THE UNIVERSITY of ADELAIDE

PETROLOGY AND GEOCHEMISTRY OF SANGEANG API AND RECENT VOLCANISM IN THE SUMBAWA-FLORES SECTOR OF THE SUNDA ARC: THE RESPONSE OF ALONG-ARC GEOCHEMISTRY TO SUBDUCTION PROCESSES.

BENJAMIN COOKE

Earth Sciences

School of Physical Sciences

University of Adelaide

This thesis is submitted in fulfilment of the requirements for the degree of Doctor of Philosophy

NOVEMBER, 2017

TABLE OF CONTENTS

Chapter 1: Introduction and thesis outline

Chapter 2: Petrological study of a mafic and ultramafic xenolith suite and host shoshonitic island arc lavas from Sangeang Api volcano in the eastern Sunda Arc

Chapter 4: Iron Isotope fractionation and disequilibrium in an arc magmatic system: Insights from the co-genetic lava and cumulate xenolith suites of Sangeang Api, Indonesia

Chapter 5: Petrological overview of the Quaternary-Tertiary volcanic centres of E. Sumbawa and W. Flores

Chapter 6: The influence of tectonic processes on the geochemistry of island arc systems: A case study of the Sunda Arc, Indonesia

Chapter 7: Conclusions and future work

ABSTRACT

This thesis documents data from an active volcano (Sangeang Api) and previously unstudied, extinct volcanoes (Wai Sano and Doro Kota and Doro Kuta) from adjacent sectors of the eastern Sunda Arc, Indonesia.

Sangeang Api erupts co-magmatic suites of lavas and cumulate xenoliths. Lavas are *ne*-normative, silica-undersaturated, volatile-rich, shoshonitic basalts to basaltic-trachyandesites. They have trace-element compositions typical of arc magmas; enrichment in LREE, alkali-earth elements and Sr, depletion in Nb, Ta, Zr and Ti and high U/Th. They are also enriched in fluid-mobile elements (Cl, Ba, Cs, etc.). The cumulate xenoliths are separated into two distinct groups; the *cpx+mgt* and *cpx+ol* pyroxenites and the *cpx+mgt+plag±amph* gabbros. These groups are compositionally distinct, with their chemistry reflecting their cumulate mineralogy and are shown to drive magma evolution in the system by fractional crystallisation. Oxidation state, water contents and pressures of crystallisation are the primary controls on the primary cumulate mineral assemblages of the xenoliths. Sangeang Api magmas degassed as they ascended through the crust, with degassing driving oxidation at depth and reduction more shallowly. Many of the cumulate xenoliths are variably contaminated by melts indicating percolation and incomplete compaction or post crystallisation intrusion.

Fe-isotope studies of the Sangeang Api products shows that the lavas record $\delta^{57}Fe$ compositions (average = 0.099‰ ±0.051) typical of arc settings. Cumulate xenoliths record heavy Fe-isotope compositions compared to the lavas (mean $\delta^{57}Fe_{gabbro}$ = 0.166‰ ±0.051; mean $\delta^{57}Fe_{pyroxenite}$ = 0.109‰ ±0.066). Using published fractionation factors, it is shown that whilst magnetite mineral separates records equilibrium compositions (mean $\delta^{57}Fe$ = 0.142‰ ±0.072), Fe-Mg silicate mineral separates display significant disequilibrium in their compositions (mean $\delta^{57}Fe_{oliv}$ = -0.313‰ ±0.284, mean $\delta^{57}Fe_{amph}$ = 0.125‰ ±0.081 and $\delta^{57}Fe_{cpx}$ = 0.109‰ ±0.090). Iron isotope disequilibria highlights the pervasiveness of post-crystallisation contaminative processes.

Lavas from the Quaternary (~2Ma) D. Kota and D. Kuta, E. Sumbawa, are geochemically and petrologically similar to those from nearby Sangeang Api. However, they are less potassic (high-K calc-alkaline) with smaller enrichments in Ba and Sr, higher Rb/Sr and lower U/Th, highlighting a role for residual amphibole in the mantle source.

Wai Sano at the far western end of Flores, is unique in the Sunda Arc, erupting adakites with characteristically low MgO, high Al_2O_3, high SiO_2, low Y and high Sr/Y. However, the Sr-Nd isotope systematics of these lavas suggests that they cannot have been produced by slab melts as is often suggested for adakites. Trace element characteristics and thermodynamic modelling suggest that a possible source of these magmas is through partial melting (10-13%) of basaltic underplates.

Ultrapotassic magmatism in the Sunda Arc is confined to the rear-arc and characterised

by trace-element and isotopic evidence of mantle metasomatism and the influence of slab tear windows. Slab window development has changed the loci and composition of volcanism on Sumbawa. Thus, highlighting the effects of local tectonic setting on arc volcanoes.

DECLARATION

I, Benjamin Cooke, certify that this work contains no material which has been accepted for the award of any other degree or diploma in my name, in any university or other tertiary institution and, to the best of my knowledge and belief, contains no material previously published or written by another person, except where due reference has been made in the text. In addition, I certify that no part of this work will, in the future, be used in a submission in my name, for any other degree or diploma in any university or other tertiary institution without the prior approval of the University of Adelaide and where applicable, any partner institution responsible for the joint-award of this degree.

I acknowledge that copyright of published works contained within this thesis resides with the copyright holder(s) of those works.

I also give permission for the digital version of my thesis to be made available on the web, via the University's digital research repository, the Library Search and also through web search engines, unless permission has been granted by the University to restrict access for a period of time.

BENJAMIN COOKE DATE

ACKNOWLEDGEMENTS

Firstly, I would like to thank my primary supervisor, Professor John Foden for all the help he has provided me throughout my research. Without your guidance, insights and feedback this thesis wouldn't exist in its current form today, and instead I would be submitting a giant pile of drivel. I would also like to thank you for all your support through the more difficult moments of my PhD candidature.

I would also like to extend my thanks to all the staff and fellow PhD students who assisted in any way with my research. Thank you to Professor Alan Collins for providing feedback on my work where possible, for the questions at various moments that stumped me and for pushing me to get some writing done at various points of my candidature. Thank you to Dr Rosalind King for your assistance during my many final year breakdowns and helping me to keep going and submit. Thank you to David Bruce for your guidance and assistance in the isotope labs, without your help my tables would be empty of data. Thank you to the other members of my research group, Christine Warwyk and Funny Meeuws. Chris, your general wizardry and patience with the Neptune was invaluable in Fe-isotope collection. Funny, thanks for all the supportive moments and moaning sessions throughout my years at Adelaide.

To my friends and family, I would like to thank you all for your support throughout the most difficult few years of my life to date. Firstly, Katelyn, thank you for constantly being by my side, putting up with way too many moaning's, emotional breakdowns and absent mindedness to count. Without your support and love I wouldn't have been able to get through this. I would like to thank my parents for their unwavering support and endless advice throughout not just my PhD, but my entire life, without it I wouldn't be where or who I am today. And finally, to my friends both in and out of university, thanks for all the awesome times (and hangovers) over the past few years. If it wasn't for my time at Adelaide University I wouldn't have met some of the best people I've ever met, people I consider to be amongst my very closest friends.

To all the people who didn't quite make the cut here, but in some small way assisted or supported me throughout this process, thank you.

I would like to acknowledge the support of the Australian Research Council in providing the funding for my field and analytical work to be completed. Finally, I would like to thank the (now defunct) School of Earth and Environmental Sciences at Adelaide University for the award of my scholarship that allowed me to move to the other side of the world and pursue my dream of achieving a PhD.

Chapter 1

Introduction and Thesis Outline

INTRODUCTION

Subduction zone magmatism is important in the development of continental crust. Fluids released by the prograde metamorphism of hydrated oceanic lithosphere during subduction act to partially melt the sub-arc mantle, creating primitive arc magmas. Primitive magmas then ascend to the surface, stalling and differentiating in crustal magma chambers. There is considerable debate about the competing influences of source region and upper platev processes in producing the characteristic signatures of subduction zone magmas. The effects of these competing processes are reflected in the characteristic major/trace element and isotopic geochemistry of arc magmas. The major, trace and isotope compositions and oxidation states of primitive, undifferentiated arc magmas are a direct result of the mantle wedge composition and any added subducted components (fluids/sediments). However, primitive magmas ascending the crust are subject to a variety of crustal magmatic processes, including fractionation, crystallisation, contamination and degassing, that can alter the primitive characteristics of the parental magma. Cross sections of island arc crust act as the primary record of crustal magmatic processes (Bouilhol et al., 2015; Clift et al., 2005; Dungan and Davidson, 2004; Hacker et al., 2008; Jagoutz, 2014). However, rare examples of co-magmatic suites of lavas and cumulate xenoliths are found in various locations around the world (Arculus and Wills, 1980; Gruender et al., 2010; Montanari et al., 2010; Price et al., 2016; Stamper et al., 2014; Tollan et al., 2012; Zernack et al., 2012). The primary aim of this thesis is to investigate the competing source and upper plate processes occurring in arc magmas through the study of magma oxidation state, degassing profiles, fractionation, stable isotope variations and along-arc radiogenic isotope variations.

Magmas produced in volcanic arc settings typically record significantly higher oxidation states than those from other tectonic settings (Carmichael, 1991; Christie et al., 1986; Evans et al., 2012). The origin of this oxidised signature is a controversial issue; contrasting evidence suggests that the mantle wedge source of arc magmas is similarly oxidised to the erupted lavas (Evans et al., 2012; Evans and Tomkins, 2011; Parkinson and Arculus, 1999; Parkinson et al., 2003; Stamper et al., 2014), OR, that it is no more oxidised than MORB-source mantle (Lee et al., 2005; Lee et al., 2010; Mallmann and O'Neill, 2009). Exponents of a relatively non-oxidised mantle source suggest that changes in redox state must occur during the ascent and transport of arc magmas. Due to the volatile-rich nature of arc magmas, magmatic degassing driven redox has been proposed as the primary agent of oxidation during arc magma ascent (Botcharnikov et al., 2005; Humphreys et al., 2015; Kelley and Cottrell, 2009). However, several studies have shown that degassing in arc volcanoes is primarily a reducing process (Kelley and Cottrell, 2012; Moussallam et al., 2014; Shorttle et al., 2015).

The oxidation state of iron exerts a fractionation effect over the stable isotopes of iron, identifying their potential as a means of recording mantle oxidation state (Beard and Johnson, 2004; Dauphas et al., 2009; Dauphas et al., 2014). Theoretically, a more oxidised source should produce partial melts with heavier iron isotopic compositions than a more reduced source (Dauphas et al., 2009). However, recent studies of subduction zone magmas suggest that they are isotopically lighter than MORB (Foden et al., In Press; Nebel et al., 2015; Teng et al., 2013). It has been suggested that this reflects successive melt depletion of the arc magma source, driving residues, and thus also partial melts, to

heavier and heavier isotopic compositions (Foden et al., In Press). Primitive arc melts are likely to then be driven to lighter isotopic compositions by the fractional crystallisation of reduced (and therefore isotopically heavy) mineral species (Sossi et al., 2012; Teng et al., 2008).

The Sunda-Banda arc system of Indonesia is home to more than 100 active and scores of extinct volcanoes. It developed through the addition of crustal blocks to a promontory of the Eurasian continent (Sundaland) since the late Jurassic (Hall, 2011; Hall, 2012; Hall and Spakman, 2015). Today, the arc system displays a unique 180˚ curvature at its easternmost point, which has been attributed to slab rollback (Hall, 2011; Hall, 2012; Spakman and Hall, 2010). Australian continental crust is impacting the subduction system and is reflected by a region of volcanic and seismic inactivity that distinguishes the Sunda Arc from the Banda Arc (Das, 2004). The influence of material derived from the Australian continent on the isotopic compositions of Sunda Arc lavas has been noted in several studies (Elburg et al., 2005; Elburg et al., 2002; Elburg et al., 2004; Hilton and Craig, 1989; Hilton et al., 1992; Stolz et al., 1990; Turner and Foden, 2001).

This thesis investigates the products of several compositionally, temporally and spatially distinct volcanic centres from the Sumbawa-Flores sector of the Sunda Arc. The primary focus of this thesis is to improve understanding of the petrogenesis of lavas and cumulate xenoliths from the active volcano of Sangeang Api. Sangeang Api erupts a suite of *ne*-normative, shoshonitic, silica-undersaturated basalts to basaltic-trachyandesites (Foden and Varne, 1980; Turner et al., 2003). Entrained within, and interpreted to be complementary to, the lavas are two distinct groups of cumulate xenoliths (gabbros and pyroxenites) (Turner et al., 2003). Previous studies have focussed primarily on U-Th-Ra disequilibria within the suite and proven a genetic link between the lavas and the cumulate xenoliths (Turner et al., 2003). This thesis studies in more detail the magmatic processes of differentiation occurring within the Sangeang Api magmatic system. As well as this the P-T-fO_2-H_2O conditions ascending magmas experienced are investigated to model the redox and degassing profile of the crustal magmatic tract. Secondly, geochemistry and petrogenetic models of previously unstudied quaternary high-K calc-alkaline volcanoes of north east Sumbawa (Doro Kota and Doro Kuta) and recent adakitic volcanics of Flores (Wai Sano) are presented. The results of the studies from Sangeang Api, Sumbawa and Flores are compared alongside a geochemical database of Sunda Arc lavas to assess the regional and local tectonic controls on volcanic composition and location. Finally, the co-existing lavas and cumulates of Sangeang Api present the perfect natural laboratory in which to investigate the stable iron isotope response to differentiation and magmatic processes within an arc volcanic system.

GEOLOGICAL BACKGROUND

The Sunda-Banda arc is a ~4800km long archipelago of Indonesian islands related to the subduction of the Indo-Australian plate beneath the Eurasian plate. The Sunda arc stretches from the Andaman Islands to Flores, to its north is continental crust of the Eurasian plate and to its south is Indian Ocean crust (Hall, 2011; Stolz et al., 1990; Turner and Foden, 2001). Banda arc volcanism is largely related to back-arc processes to the east of Timor, with Australian continental crust from the south subducting beneath Indian oceanic crust to its north (Spakman and Hall, 2010; Stolz et al., 1990). A volcanically inactive region, known as the Sunda-Banda transition, separates the Banda arc from the

Sunda arc (Elburg et al., 2004). The age of volcanism onset varied throughout the Sunda-Banda arc, with the oldest volcanism being found in the west (Java ~45Ma), followed by a younging in age to the east (Banda back-arc <12.5Ma) (Spakman and Hall, 2010). Figure 1 shows a tectonic map of the Indonesian archipelago with the locations of active volcanoes.

Located at the eastern end of the Sunda Arc, near to the Sunda-Banda transition, is the volcanically active island of Sumbawa. Sumbawa, and Lombok to its west, is almost unique within the Sunda-Banda archipelago in that it has oceanic crust both to the north and south of the island. Active volcanism on Sumbawa itself is restricted to Tambora in the north of the island (Siebert et al., 2011). Located just off the northeast corner of Sumbawa is the active volcano of Sangeang Api (erupting 13 times in the last ~100 years) (Turner et al., 2003).

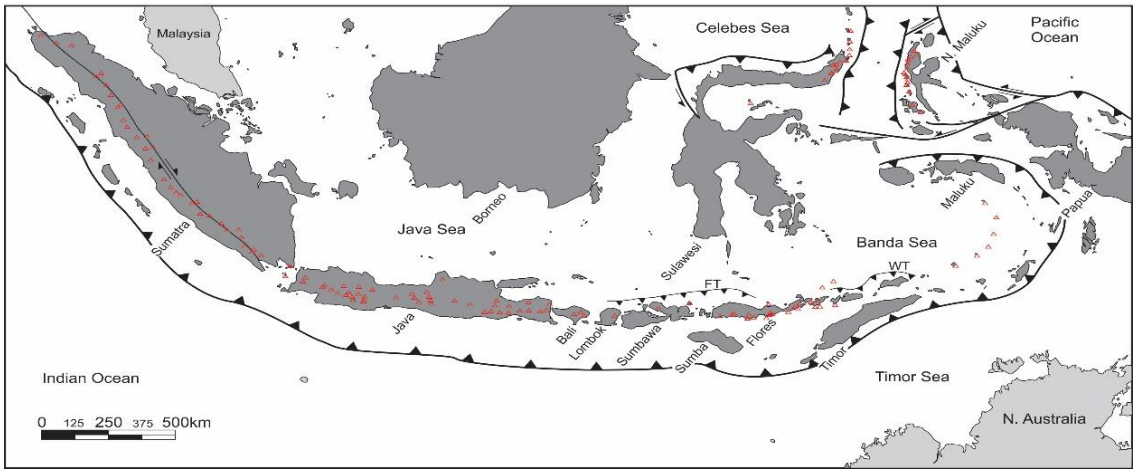

***Figure 1*:** Regional map of Indonesia and S.E. Asia showing tectonic boundaries and active volcanoes (open red triangles) (Siebert et al., 2011). FT and WT represent the Flores and Wetar thrusts respectively.

The Sunda-Banda arc formed from the convergence of the Australian, Eurasian and Pacific plates, beginning in the late Jurassic and continuing today. At its easternmost promontory, the Banda arc bends almost 180°, a feature unique to this arc. The theories surrounding the origin of this curvature hinge on the number of oceanic slabs subducting around the Banda Sea. Proponents of a two-slab theory suggest the existence of two slabs, the Australian plate subducting northwards and another plate subducting west from the Seram trough (Bowin et al., 1980; Cardwell and Isacks, 1978; Das, 2004; McCaffrey, 1989). This theory is supported by seismicity patterns, earthquake mechanisms, regional magmatism and geodetic evidence for active contraction in the Banda region (Bock et al., 2003; Das, 2004; Hinschberger et al., 2005). Whereas, supporters of the one-slab theory suggest the existence of strong curvature prior to the initiation of subduction at the Australian continental margin enclosing an oceanic embayment, followed by subduction of this oceanic crust and some continental material through the process of subduction rollback (Hall, 2011; Hall, 2012; Hall and Spakman, 2015; Spakman and Hall, 2010). Support for the slab rollback theory comes from tomographic images of the Banda slab, as seen in figures 3a-e, showing the ~300km wide slab lying flat at the base of the upper mantle (Hall, 2012; Spakman and Hall, 2010). In contrast to this, to the west of Sulawesi the slab can be observed at great depths within the mantle, suggesting different evolution of Sunda and Banda Arcs (Spakman and Hall, 2010). Slab rollback and the evolution of the Banda Arc are reflected in the ages of volcanism throughout the arc. At Java in the

west volcanism initiated 45Ma, but further east volcanism is a younger, <16Ma east of Flores and <12.5Ma in Banda back-arc basins (Hall, 2011). Slab-rollback is suggested to have begun around ~25Ma, when sections of the continental (Sula Spur) and oceanic (Banda embayment) Australian crust collided with the Sundaland Margin (a promontory of the Eurasian continent) (Hall, 2012). As Australia moved northwards, relative to Asia, subduction was transferred eastwards into the Banda embayment until it reached Australian continental crust of the Sula Spur (Hall, 2011). At this point it began to roll around the existing curved continental margin, creating the observable 180^{o} curvature observed within the arc today (Hall, 2011). The tectonic reconstructions seen in figure 2, created by Hall (2011), show this process. Rollback of a single slab had been long proposed before the two-slab theory became popular, however in more recent papers it has again been considered the most likely cause of the Banda Arc curvature and is the pre-eminent theory in the evolution of the modern Sunda-Banda Arc (Sandiford, 2010).

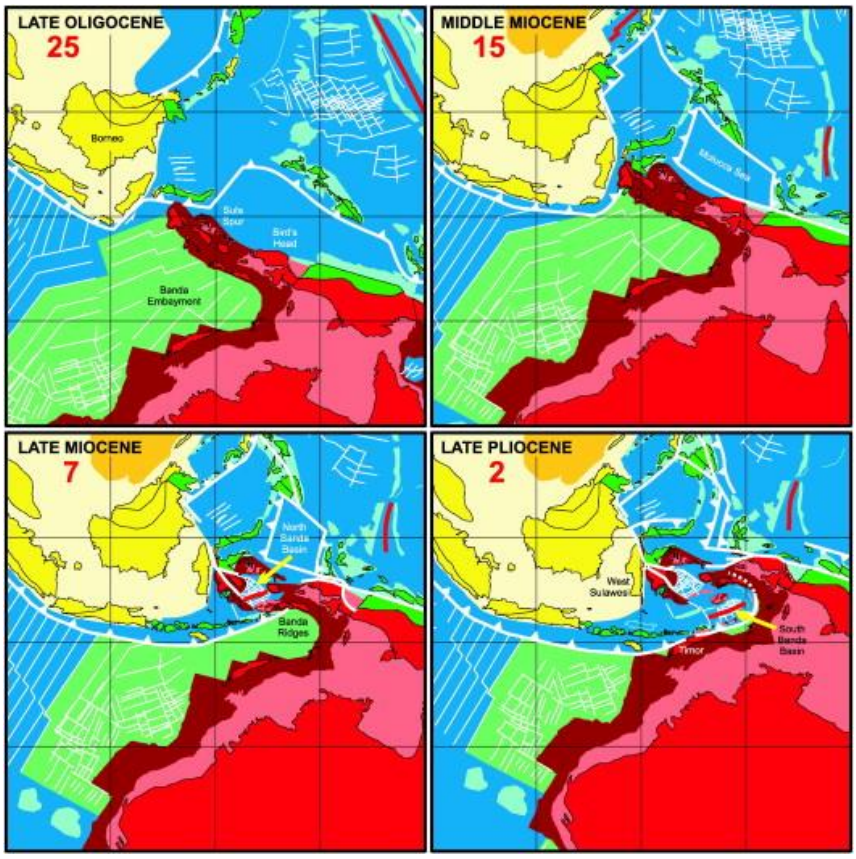

***Figure 2*:** Diagrams showing the evolution of the Sunda-Banda arc from the Late Oligocene through to the Late Pliocene. Note the interaction between the Sundaland promontory (yellow shaded area) and the Sula Spur (red shaded area), as well as the gradual subduction of the Banda Embayment (green shaded area). Taken from Hall (2011).

Spakman, 2015). It has been suggested that crustal discontinuities separating islands of the Sunda Arc exert a control over the compositions of erupted products, with Wheller et al. (1987) noting a correlation with increasing potassic and fluid-mobile element contents of erupted lavas. Various studies have noted west-east along-arc trends in the Sr, Nd, Pb

and He isotopic compositions of Sunda Arc lavas (Elburg et al., 2005; Elburg et al., 2002; Elburg et al., 2004; Hilton and Craig, 1989; Hilton et al., 1992; Turner et al., 2003; Whitford, 1975; Whitford and Jezek, 1982). The impact of subducted sedimentary material from the Australian continental crust to has been proposed as a source of these along-arc isotopic variations (Elburg et al., 2005; Hilton et al., 1992; Turner et al., 2003). Similar trends observed in the Banda Arc have likewise been used as evidence of Australian-derived material to the mantle wedge (Nebel et al., 2011; Vroon et al., 1993). Smaller isotopic variations in the Sumatra to Java section of the arc are proposed to be reflect crustal assimilation and heterogeneity of subducted sediments (Handley et al., 2014; Handley et al., 2011). Geochemical and isotopic studies of the Sunda Arc have suggested that most volcanoes are sourced from a three-component mixture of I-MORB mantle, fluids derived from the altered ocean crust and subducted sediments (Turner and Foden, 2001; Wheller et al., 1987).

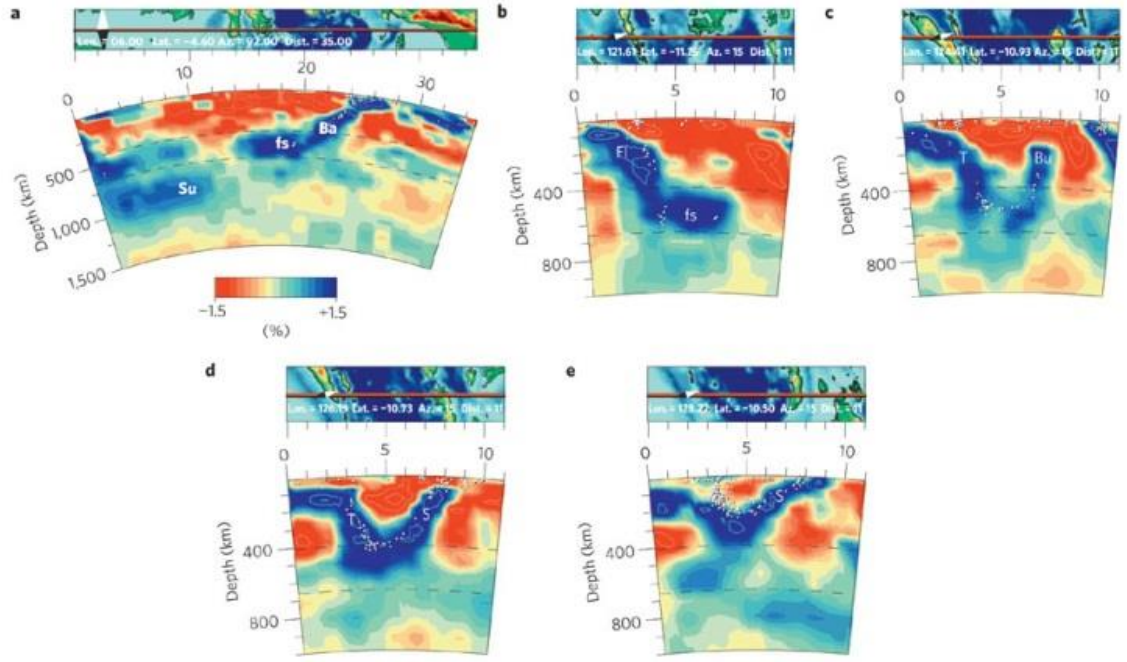

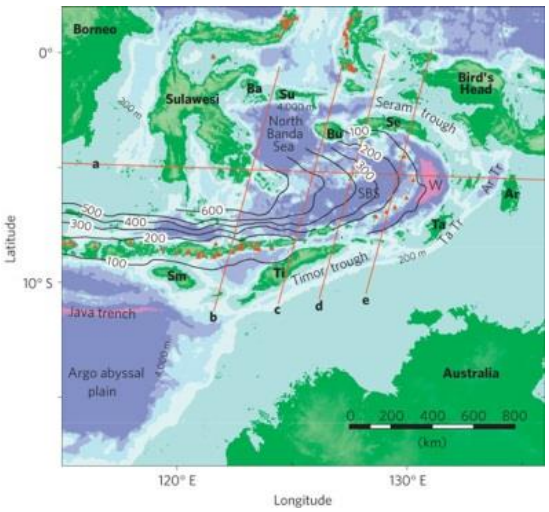

***Figure 3a-e (above)*:** Across- and along-arc tomographic sections through the Sunda-Banda arc. After Spakman and Hall (2010).

***Figure 4 (left)*:** Map of eastern Sunda-Banda arc showing Benioff Zone contours (black numbered lines) and locations of tomographic sections in figure 3a-e (red lettered lines). After Spakman and Hall (2010)

The major volcanic centres of Sumbawa appear to have migrated northwards. From the early Miocene, andesitic volcanics in the south-west of the island, through the Pleistocene, calc-alkaline volcanics in central Sumbawa; to the more recent, Pleistocene-Holocene, shoshonitic products of north-west Sumbawa and Sangeang Api (Foden and

Varne, 1980). Not only has the volcanic centre of the island migrated from south to north, but the volcanic products of the volcano appear to have become K-rich and volatile enriched (Foden and Varne, 1980). To the east of Sumbawa, active volcanism on the island of Flores appears to have shifted southwards suggesting the presence of a cross-arc structure delineating volcanic distributions between the two islands (Audley-Charles, 1975; Fiorentini and Garwin, 2010; Hamilton, 1972, 1979; Katili, 1970). Sumbawa is composed primarily of Neogene and Quaternary intrusive and extrusive volcanics (Foden and Varne, 1980; Turner et al., 2003). Associated with these volcanics are volcaniclastic units and scattered marine limestone units of similar ages (Garwin, 2000). Within the volcanics in southern Sumbawa are located a number of large intrusives of middle Miocene to Pliocene age, including the Batu Hijau copper Porphyry deposit (Fiorentini and Garwin, 2010; Garwin, 2000; Wawryk and Foden, 2017). Foden and Varne (1980) studied some of the extinct quaternary (Soromundi & Sangenges) and active volcanoes (Tambora and Sangeang Api) on or close to Sumbawa. The studied quaternary centres are characterised by ultrapotassic leucitites, whilst the active volcanoes erupt shoshonitic lavas. Several other extinct volcanic centres have been observed on Sumbawa, which have broadly been described as ~2Ma high-K calc-alkaline volcanoes (e.g. D. Kota and D. Kuta) (Garwin, 2000). Tambora has since been characterised in several studies (Foden, 1986; Gertisser et al., 2012; Self et al., 2004; Self et al., 1984; Vigouroux et al., 2012). Flores is host to many active and historically active volcanoes; including Wai Sano, Ranakah, Inierie, Inielika, Ebulobo, Iya, Kelimutu, Paluweh, Egon, Lewotobi and Lewotolo (Siebert et al., 2011). Wai Sano is the closest historically active volcano to Sumbawa and Sangeang Api and is located in the southwest corner of Flores. Very little work has been published regarding the Wai Sano products, with only two data points reported in Stolz et al. (1990), however, these two data points are highly intriguing. The reported compositions of Wai Sano lavas appear to display adakite-style geochemistry (low MgO, high Al_2O_3, high SiO_2, high Sr/Y and low Y). Adakites have been variously suggested to form from direct melting of the subducted slab (Castillo, 2012; Defant and Drummond, 1990; Defant and Kepezhinskas, 2001; Peacock et al., 1994; Yogodzinski et al., 2001), or, partial melting of mafic underplated crust (Haschke and Ben-Avraham, 2005; Ma et al., 2012; Zhang et al., 2013). Studies of these adakite-style lavas of Wai Sano are important to further describe their geochemical composition and to understand their genesis. Spatial and temporal changes in the geochemical composition of the products of active and inactive volcanic centres on Sumbawa and Flores may reflect changes within, and responses to, the tectonic environment throughout geological history and across the arc section.

Sangeang Api has been the focus of very few studies, although previous work has provided insights into its geology and geochemistry (Foden and Varne, 1980; Turner and Foden, 2001; Turner et al., 2003). Sangeang Api is a rear-arc volcano that erupts strongly alkalic-shoshonistic lavas (Turner and Foden, 2001). Similar to Tambora (Sumbawa), Sangeang Api products are potassic, trachyandesite-trachybasalt lavas that are volatile rich and silica-undersaturated (47-55% SiO_2) (Turner et al., 2003). The compositions of Sangeang Api lavas compared to those of other regional volcanoes can be seen in figure 5. These liquid products are enriched in LREE and LILEs, whilst also showing elevated concentrations of incompatible trace elements. Turner and Foden (2001) and Turner et al. (2003) suggest that Sangeang Api lavas are derived from a multi-component source region, noting high concentrations of LILEs as evidence of aqueous fluids being a principle component in the source region (as LILEs are mobile in aqueous fluids). The

proposed components include sub-arc mantle, fluids expelled from the subducted ocean crust and partial melts sourced from subducted sediment (less than 2% of which is subducted material), although both sediment and fluid input are most likely variable throughout the source region and at differing depths of subduction (Stolz et al., 1990; Turner and Foden, 2001). It is likely that these magmas were derived from exacerbated pressures, with evidence of <3% residual garnet at the source (Turner et al., 2003) $^{230}Th/^{238}U$ excesses (0.85-1.15) provide evidence for fluid addition to the mantle wedge from the subducted slab, with ^{238}U excesses, proposed to occur from addition of U to mantle wedge by fluid flux from subducting slab, suggesting that fluid addition began ~350,000 years ago (Turner and Foden, 2001; Turner et al., 2003); possibly before Australian continental crust was deep enough in the subduction zone to have any significant effect on melting (Turner and Foden, 2001). Arc magmas often show a correlation between ^{226}Ra and Ba/Th, usually used to suggest the interaction of seawater with melts. Interestingly, however, Sangeang Api shows no correlation between ^{226}Ra excesses and Ba/Th, as well as the highest ^{226}Ra excesses within the most primitive of magmas, suggesting that the excesses in ^{226}Ra reflect the mantle source and not the influence of seawater contamination (Turner et al., 2003).

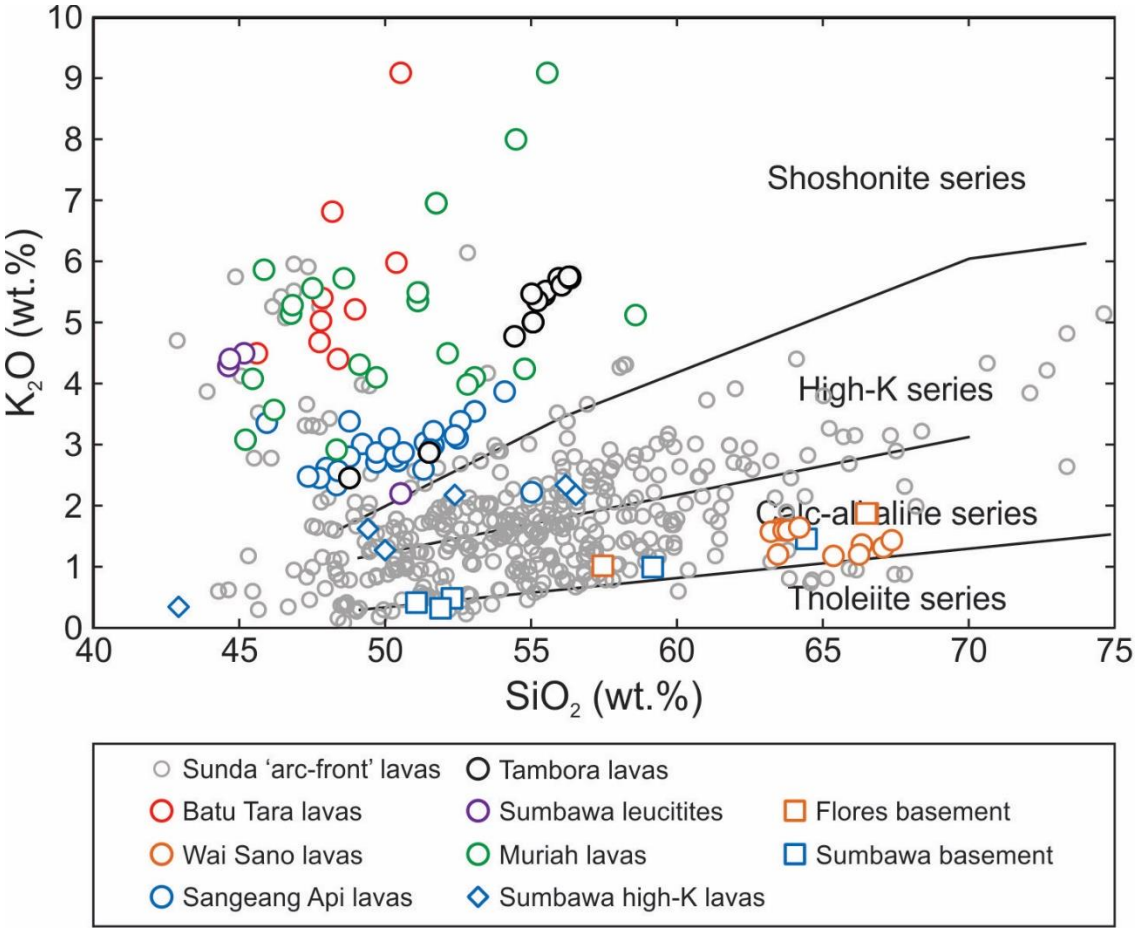

***Figure 5*:** Plot of K_2O vs. SiO_2 displaying the shoshonitic character of Sangeang Api lavas compared to other volcanoes from the Sunda Arc. Data compiled from work of this thesis and a GeoRoc database (http://georoc.mpch-mainz.gwdg.de/georoc/).

Sangeang Api lavas contain abundant entrained mafic-ultramafic cumulate xenoliths, which are suggested to be complementary to the lavas (Turner et al., 2003). Cumulates lithologies are commonly olivine-clinopyroxenite, clinopyroxenite, amphibole-gabbro and gabbro (Turner et al. 2003). Clinopyroxenites contain Ca-rich clinopyroxene, olivine,

magnetite, lesser amphibole and rare phlogopite, whereas, gabbros contain plagioclase, magnetite, clinopyroxene and amphibole (Turner et al. 2003). A key feature of Sangeang Api cumulates is the dominance of (Mg-Hastingsite) amphibole in some samples (up to 60% in some amphibole-gabbros). Complementary lavas and xenoliths provide a means of exploring the fractionation and differentiation history of Sangeang Api magmas. Turner et al. (2003) suggest that the Sangeang Api liquid line of descent is driven by fractional crystallisation of pyroxenite cumulates followed by gabbroic cumulates. Turner et al. (2003) provide a good understanding of U-Th-Ra disequilibrium processes within the Sangeang Api system and presents compelling evidence that the cumulate xenolith suite and lavas are genetically linked.

THESIS OUTLINE

Chapter 2

Chapter 2 is written for submission to the Journal of Petrology as:

Cooke, B., Foden, J. Petrological study of a mafic and ultramafic xenolith suite and host shoshonitic island arc lavas from Sangeang Api volcano in the eastern Sunda Arc.

The goal of this chapter is to build upon the work of Turner et al. (2003) and provide a detailed petrogenetic study of the Sangeang Api lavas and cumulate xenoliths. Combining petrological descriptions, mineral geochemistry and whole-rock geochemistry fractional crystallisation and petrogenetic conditions are established. Petrological textures, whole-rock and mineral geochemistry provide evidence of significant post-crystallisation disequilibrium. The composition of the mantle source from which the Sangeang Api magmas are sourced is characterised, noting the possible presence of both amphibole and phlogopite metasomatism.

Chapter 3

Chapter 3 is written for submission to Lithos as:

Cooke, B., Foden J. A window into the crustal magmatic tract of Sangeang Api, Indonesia: Insights from amphibole thermobarometry.

Amphibole is prevalent throughout the Sangeang Api suite of lavas and cumulate xenoliths. Within arc magmas amphibole is stable under a small range of pressures, temperatures and water contents (Foden and Green, 1992). It has long been recognised that the chemistry of amphibole is strongly influenced by the physical conditions they are formed under, allowing them to be used as geothermobarometers (Andersen and Smith, 1995; Blundy and Holland, 1990; Hammarstrom and Zen, 1986; Holland and Blundy, 1994; Johnson and Rutherford, 1989; Krawczynski et al., 2012; Schmidt, 1992). Noting the predominance of amphibole within the Sangeang Api suites, this chapter utilises recent advances in amphibole geothermobarometry (Ridolfi and Renzulli, 2012; Ridolfi et al., 2010) to study the P-T-fO_2-H_2O conditions under which the magmas ascended the crust. From the calculated thermobarometrical conditions an estimated degassing and redox profile for the Sangeang Api magmatic system was created.

Chapter 4

Chapter 4 is written for submission to Chemical Geology as:

Cooke, B., Foden, J., Warwyk, C. M. Iron Isotope fractionation and disequilibrium in an arc magmatic system: Insights from the co-genetic lava and cumulate xenolith suites of Sangeang Api, Indonesia.

Primitive lavas from subduction zone settings typically record lighter Fe-isotope compositions than MORB, reflecting their origin from melt-depleted and refractory peridotites stalled in the mantle wedge (Foden et al., In Press; Nebel et al., 2015). The main aim of this chapter is to understand the effect on iron-isotope fractionation by magmatic processes in an arc volcano (Sangeang Api). Iron isotope compositions of whole-rocks (both lavas and cumulate xenoliths) and cumulate mineral separates are reported. Iron isotope fractionation is tested to determine equilibrium magmatic processes, however, the Sangeang Api cumulate xenoliths record significant evidence of disequilibrium processes through post-crystallisation processes. Fe isotopic compositions of the lavas are compared to the outcomes of thermodynamic models of magma evolution. Finally, the lava compositions reported in this study lavas are compared to other arc lavas both globally and locally to determine the effects of tectonic setting and source compositional differences on Fe-isotope compositions.

Chapter 5

Chapter 5 is written for submission to the Journal of Petrology as:

Cooke, B., Foden, J. Petrological overview of the Quaternary-Tertiary volcanic centres of E. Sumbawa and W. Flores.

It has been suggested that Sumbawa and Flores are separated by an across-arc fault (Audley-Charles, 1975; Katili, 1970), leading to the observed displacement of active volcanism from the north of Sumbawa to the southern margin of Flores (Foden and Varne, 1980). Similarly, the loci of active volcanism on Sumbawa appears to have moved northwards through time (Garwin, 2000). The main goal of this chapter is to describe the petrological differences both spatially and temporally between eastern Sumbawa and western Flores. It provides the first petrological and geochemical studies of the volcanic centres of Kota & Kuta (northeast Sumbawa) and Wai Sano (southwest Flores), as well as the basement geology of northwest Flores. Detailed petrology, geochemistry, geothermobarometry and thermodynamic modelling is utilised to gain an understanding of the petrogenesis, magma ascent conditions and source region conditions and composition.

Chapter 6

Chapter 6 is written for Earth and Planetary Sciences Letters as:

Cooke, B., Foden, J. The influence of tectonic processes on the geochemistry of island arc systems: A case study of the Sunda Arc, Indonesia.

Combining petrological data from this thesis and a database of Sunda Arc lava geochemistry (http://georoc.mpch-mainz.gwdg.de/georoc/) and comparing to tectonic models of the Sunda Arc (e.g. Hall and Spakman, 2015), this chapter aims to determine the tectonic controls on the compositions and spatial distribution of volcanoes in the arc. Isotopic, major element and trace element compositions of lavas are a direct response to the composition of their source and the conditions under which that source melted. Tectonic models, earthquake foci profiles and seismic tomographic models are used to

determine tectonic controls on source compositions and partial melting conditions, and thus the geochemistry of lavas erupted at the surface. Primarily this chapter focusses on the tectonic controls on rear-arc ultrapotassic volcanism in the Sunda Arc, heterogeneous sediment input to the mantle wedge and the spatial (and temporal) distribution of volcanoes in the Sumbawa-Flores sector.

Chapter 7

Conclusions and Future Work

This chapter discusses the major findings of this thesis with regards to the main questions and issues set out in Chapter 1. Bringing together the separate studies of the Sangeang Api system to identify magmatic processes occurring within the volcano and identify possible new methods of further understanding the evolution and redox changes within the magmatic system (μ-XANES and in-situ Fe-isotopes). As well as suggesting future directions in which to further study the tectonic controls on magma composition and spatial distribution in the Sunda Arc.

REFERENCES

Andersen, J.L., Smith, D.R., 1995. The effects of temperature and fO_2 on the Al-in-hornblende barometer. American Mineralogist 80, 549-559.

Arculus, R.J., Wills, K.J.A., 1980. The petrology of plutonic blocks and inclusions from the lesser antilles island arc. Journal of Petrology 21, 743-799.

Audley-Charles, M.G., 1975. The Sumba fracture: A major discontinuity between eastern and western Indonesia. Tectonophysics 26, 213-228.

Beard, B.L., Johnson, C.M., 2004. Fe isotope variations in the modern and ancient earth and other planetary bodies, in: Johnson, C.M., Beard, B.L., Albarede, F. (Eds.), Geochemistry of Non-Traditional Stable Isotopes, pp. 319-357.

Blundy, J.D., Holland, T.J.B., 1990. Calcic amphibole equilibria and a new amphibole-plagioclase geothermometer. Contributions to Mineralogy and Petrology 104, 208-224.

Bock, Y., Prawirodirdjo, L., Genrich, J.F., Stevens, C.W., McCaffrey, R., Subarya, C., Puntodewo, S.S.O., Calais, E., 2003. Crustal motion in Indonesia from Global Positioning System measurements. Journal of Geophysical Research 108, ETG3-1-21.

Botcharnikov, R.E., Koepke, J., Holtz, F., McCammon, C., Wilke, M., 2005. The effect of water activity on the oxidation and structural state of Fe in a ferro-basaltic melt. Geochimica et Cosmochimica Acta 69, 5071-5085.

Bouilhol, P., Schmidt, M.W., Burg, J.-P., 2015. Magma Transfer and Evolution in Channels within the Arc Crust: the Pyroxenitic Feeder Pipes of Sapat (Kohistan, Pakistan). Journal of Petrology.

Bowin, C., Purdy, G.M., Johnston, C., Shor, G., Lawver, L., Hartono, H.M.S., Jezek, P., 1980. Arc-continent collision in Banda Sea region. AAPG Bulletin 64, 868-915.

Cardwell, R.K., Isacks, B.L., 1978. Geometry of subducted lithosphere beneath banda sea in eastern indonesia from seismicity and fault plane solutions. Journal of Geophysical Research 83, 2825-2838.

Carmichael, I.S.E., 1991. The redox states of basic and silicic magmas - a reflection of their source regions. Contributions to Mineralogy and Petrology 106, 129-141.

Castillo, P.R., 2012. Adakite petrogenesis. Lithos 134, 304-316.

Christie, D.M., Carmichael, I.S.E., Langmuir, C.H., 1986. Oxidation-states of midocean ridge basalt glasses. Earth and Planetary Science Letters 79, 397-411.

Clift, P.D., Draut, A.E., Kelemen, P.B., Blusztajn, J., Greene, A., 2005. Stratigraphic and geochemical evolution of an oceanic arc upper crustal section: The Jurassic Talkeetna Volcanic Formation, south-central Alaska. Geological Society of America Bulletin 117, 902-925.

Das, S., 2004. Seismicity gaps and the shape of the seismic zone in the Banda Sea region from relocated hypocenters. Journal of Geophysical Research-Solid Earth 109.

Dauphas, N., Craddock, P.R., Asimow, P.D., Bennett, V.C., Nutman, A.P., Ohnenstetter, D., 2009. Iron isotopes may reveal the redox conditions of mantle melting from Archean to Present. Earth and Planetary Science Letters 288, 255-267.

Dauphas, N., Roskosz, M., Alp, E.E., Neuville, D.R., Hu, M.Y., Sio, C.K., Tissot, F.L.H., Zhao, J., Tissandier, L., Médard, E., Cordier, C., 2014. Magma redox and structural controls on iron isotope variations in Earth's mantle and crust. Earth and Planetary Science Letters 398, 127-140.

Defant, M.J., Drummond, M.S., 1990. Derivation of some modern arc magmas by melting of young subducted lithosphere. Nature 347, 662-665.

Defant, M.J., Kepezhinskas, P., 2001. Evidence suggests slab melting in arc magmas. Eos, Transactions American Geophysical Union 82, 65-69.

Dungan, M.A., Davidson, J., 2004. Partial assimilative recycling of the mafic plutonic roots of arc volcanoes: An example from the Chilean Andes. Geology 32, 773-776.

Elburg, M.A., Foden, J.D., van Bergen, M.J., Zulkarnain, I., 2005. Australia and Indonesia in collision: geochemical sources of magmatism. Journal of Volcanology and Geothermal Research 140, 25-47.

Elburg, M.A., van Bergen, M., Hoogewerff, J., Foden, J., Vroon, P., Zulkarnain, I., Nasution, A., 2002. Geochemical trends across an arc-continent collision zone: magma sources and slab-wedge transfer processes below the Pantar Strait volcanoes, Indonesia. Geochimica et Cosmochimica Acta 66, 2771-2789.

Elburg, M.A., van Bergen, M.J., Foden, J.D., 2004. Subducted upper and lower continental crust contributes to magmatism in the collision sector of the Sunda-Banda arc, Indonesia. Geology 32, 41.

Ely, K.S., Sandiford, M., 2010. Seismic response to slab rupture and variation in lithospheric structure beneath the Savu Sea, Indonesia. Tectonophysics 483, 112-124.

Evans, K.A., Elburg, M.A., Kamenetsky, V.S., 2012. Oxidation state of subarc mantle. Geology 40, 783-786.

Evans, K.A., Tomkins, A.G., 2011. The relationship between subduction zone redox budget and arc magma fertility. Earth and Planetary Science Letters 308, 401-409.

Fiorentini, M.L., Garwin, S.L., 2010. Evidence of a mantle contribution in the genesis of magmatic rocks from the Neogene Batu Hijau district in the Sunda Arc, South Western Sumbawa, Indonesia. Contributions to Mineralogy and Petrology 159, 819-837.

Foden, J., 1986. The petrology of Tambora volcano, Indonesia: A model for the 1815 eruption. Journal of Volcanology and Geothermal Research 27, 1-41.

Foden, J., Sossi, P.A., Nebel, O., In Press. Controls on the Iron Isotopic Composition of Global Arc Magmas. Earth and Planetary Science Letters.

Foden, J., Varne, R., 1980. The petrology and tectonic setting of quaternary - recent volcanic centers of lombok and sumbawa, sunda arc. Chemical Geology 30, 201-226.

Foden, J.D., Green, D.H., 1992. Possible role of amphibole in the origin of andesite - some experimental and natural evidence. Contributions to Mineralogy and Petrology 109, 479-493.

Garwin, S.L., 2000. The setting, geometry and timing of intrusion-related hydrothermal systems in the vicinity of the Batu Hijau porphyry copper-gold deposit, Sumbawa, Indonesia. University of Western Australia, p. 320.

Gertisser, R., Self, S., Thomas, L.E., Handley, H.K., Van Calsteren, P., Wolff, J.A., 2012. Processes and Timescales of Magma Genesis and Differentiation Leading to the Great Tambora Eruption in 1815. Journal of Petrology 53, 271-297.

Gruender, K., Stewart, R.B., Foley, S., 2010. Xenoliths from the sub-volcanic lithosphere of Mt Taranaki, New Zealand. Journal of Volcanology and Geothermal Research 190, 192-202.

Hacker, B.R., Mehl, L., Kelemen, P.B., Rioux, M., Behn, M.D., Luffi, P., 2008. Reconstruction of the Talkeetna intraoceanic arc of Alaska through thermobarometry. Journal of Geophysical Research-Solid Earth 113, 16.

Hall, R., 2011. Australia- SE Asia collison: plate tectonics and crustal flow, in: Hall, R., Cottam, M.A., Wilson, M.E.J. (Eds.), The SE Asian gateway: history and tectonics of Australia-Asia collision. Geological Society of London Special Publication, pp. 75-109.

Hall, R., 2012. Late Jurassic–Cenozoic reconstructions of the Indonesian region and the Indian Ocean. Tectonophysics 570–571, 1-41.

Hall, R., Spakman, W., 2015. Mantle structure and tectonic history of SE Asia. Tectonophysics 658, 14-45.

Hamilton, W.B., 1972. Preliminary tectonic map of the Indonesian region, Open-File Report, - ed.

Hamilton, W.B., 1979. Tectonics of the Indonesian region, Professional Paper, - ed.

Hammarstrom, J.M., Zen, E., 1986. Aluminum in hornblende: an empirical igneous geobarometer. American Mineralogist 71, 1297-1313.

Handley, H.K., Blichert-Toft, J., Gertisser, R., Macpherson, C.G., Turner, S.P., Zaennudin, A., Abdurrachman, M., 2014. Insights from Pb and O isotopes into along-arc variations in subduction inputs and crustal assimilation for volcanic rocks in Java, Sunda arc, Indonesia. Geochimica et Cosmochimica Acta 139, 205-226.

Handley, H.K., Turner, S., Macpherson, C.G., Gertisser, R., Davidson, J.P., 2011. Hf–Nd isotope and trace element constraints on subduction inputs at island arcs: Limitations of Hf anomalies as sediment input indicators. Earth and Planetary Science Letters 304, 212-223.

Haschke, M., Ben-Avraham, Z., 2005. Adakites from collision-modified lithosphere. Geophysical Research Letters 32, n/a-n/a.

Hilton, D.R., Craig, H., 1989. A helium isotope transect along the Indonesian archipelago. Nature 342, 906-908.

Hilton, D.R., Hoogewerff, J.A., van Bergen, M.J., Hammerschmidt, K., 1992. Mapping magma sources in the east Sunda-Banda arcs, Indonesia: Constraints from helium isotopes. Geochimica et Cosmochimica Acta 56, 851-859.

Hinschberger, F., Malod, J.A., Rehault, J.P., Villeneuve, M., Royer, J.Y., Burhanuddin, S., 2005. Late Cenozoic geodynamic evolution of eastern Indonesia. Tectonophysics 404, 91-118.

Holland, T., Blundy, J., 1994. Non-ideal interactions in calcic amphiboles and their bearing on amphibole-plagioclase thermometry. Contributions to Mineralogy and Petrology 116, 433-447.

Humphreys, M.C.S., Brooker, R.A., Fraser, D.G., Burgisser, A., Mangan, M.T., McCammon, C., 2015. Coupled Interactions between Volatile Activity and Fe Oxidation State during Arc Crustal Processes. Journal of Petrology 56, 795-814.

Jagoutz, O., 2014. Arc crustal differentiation mechanisms. Earth and Planetary Science Letters 396, 267-277.

Johnson, M.C., Rutherford, M.J., 1989. Experimental calibration of the aluminum-in-hornblende geobarometer with application to Long Valley caldera (California) volcanic rocks. Geology 17, 837-841.

Katili, J.A., 1970. Large transcurrent faults in Southeast Asia with special reference to Indonesia. Geologische Rundschau 59, 581-600.

Kelley, K.A., Cottrell, E., 2009. Water and the Oxidation State of Subduction Zone Magmas. Science 325, 605-607.

Kelley, K.A., Cottrell, E., 2012. The influence of magmatic differentiation on the oxidation state of Fe in a basaltic arc magma. Earth and Planetary Science Letters 329–330, 109-121.

Krawczynski, M.J., Grove, T.L., Behrens, H., 2012. Amphibole stability in primitive arc magmas: effects of temperature, H2O content, and oxygen fugacity. Contributions to Mineralogy and Petrology 164, 317-339.

Kundu, B., Gahalaut, V.K., 2011. Slab detachment of subducted Indo-Australian plate beneath Sunda arc, Indonesia. Journal of Earth System Science 120, 193-204.

Lee, C.T.A., Leeman, W.P., Canil, D., Li, Z.X.A., 2005. Similar V/Sc systematics in MORB and arc basalts: Implications for the oxygen fugacities of their mantle source regions. Journal of Petrology 46, 2313-2336.

Lee, C.T.A., Luffi, P., Le Roux, V., Dasgupta, R., Albarede, F., Leeman, W.P., 2010. The redox state of arc mantle using Zn/Fe systematics. Nature 468, 681-685.

Ma, Q., Zheng, J.P., Griffin, W.L., Zhang, M., Tang, H.Y., Su, Y.P., Ping, X.Q., 2012. Triassic "adakitic" rocks in an extensional setting (North China): Melts from the cratonic lower crust. Lithos 149, 159-173.

Mallmann, G., O'Neill, H.S.C., 2009. The Crystal/Melt Partitioning of V during Mantle Melting as a Function of Oxygen Fugacity Compared with some other Elements (Al, P, Ca, Sc, Ti, Cr, Fe, Ga, Y, Zr and Nb). Journal of Petrology 50, 1765-1794.

McCaffrey, R., 1989. Seismological constraints and speculations on banda arc tectonics. Netherlands Journal of Sea Research 24, 141-152.

Montanari, D., Corti, G., Simakin, A., 2010. Magma chambers and localization of deformation during thrusting. Terra Nova 22, 390-395.

Moussallam, Y., Oppenheimer, C., Scaillet, B., Gaillard, F., Kyle, P., Peters, N., Hartley, M., Berlo, K., Donovan, A., 2014. Tracking the changing oxidation state of Erebus magmas, from mantle to surface, driven by magma ascent and degassing. Earth and Planetary Science Letters 393, 200-209.

Nebel, O., Sossi, P.A., Bénard, A., Wille, M., Vroon, P.Z., Arculus, R.J., 2015. Redox-variability and controls in subduction zones from an iron-isotope perspective. Earth and Planetary Science Letters 432, 142-151.

Nebel, O., Vroon, P.Z., van Westrenen, W., Iizuka, T., Davies, G.R., 2011. The effect of sediment recycling in subduction zones on the Hf isotope character of new arc crust, Banda arc, Indonesia. Earth and Planetary Science Letters 303, 240-250.

Parkinson, I.J., Arculus, R.J., 1999. The redox state of subduction zones: insights from arc-peridotites. Chemical Geology 160, 409-423.

Parkinson, I.J., Arculus, R.J., Eggins, S.M., 2003. Peridotite xenoliths from Grenada, Lesser Antilles Island Arc. Contributions to Mineralogy and Petrology 146, 241-262.

Peacock, S.M., Rushmer, T., Thompson, A.B., 1994. Partial melting of subducting oceanic crust. Earth and Planetary Science Letters 121, 227-244.

Price, R.C., Smith, I.E.M., Stewart, R.B., Gamble, J.A., Gruender, K., Maas, R., 2016. High-K andesite petrogenesis and crustal evolution: Evidence from mafic and ultramafic xenoliths, Egmont Volcano (Mt. Taranaki) and comparisons with Ruapehu Volcano, North Island, New Zealand. Geochimica et Cosmochimica Acta 185, 328-357.

Ridolfi, F., Renzulli, A., 2012. Calcic amphiboles in calc-alkaline and alkaline magmas: thermobarometric and chemometric empirical equations valid up to 1,130A degrees C and 2.2 GPa. Contributions to Mineralogy and Petrology 163, 877-895.

Ridolfi, F., Renzulli, A., Puerini, M., 2010. Stability and chemical equilibrium of amphibole in calc-alkaline magmas: an overview, new thermobarometric formulations and application to subduction-related volcanoes. Contributions to Mineralogy and Petrology 160, 45-66.

Sandiford, M., 2010. Geodynamics Complex subduction. Nature Geoscience 3, 518-520.

Schmidt, M.W., 1992. Amphibole composition in tonalite as a function of pressure: an experimental calibration of the Al-in-hornblende barometer. Contributions to Mineralogy and Petrology 110, 304-310.

Self, S., Gertisser, R., Thordarson, T., Rampino, M.R., Wolff, J.A., 2004. Magma volume, volatile emissions, and stratospheric aerosols from the 1815 eruption of Tambora. Geophysical Research Letters 31.

Self, S., Rampino, M.R., Newton, M.S., Wolff, J.A., 1984. Volcanological study of the great Tambora eruption of 1815. Geology 12, 659-663.

Shorttle, O., Moussallam, Y., Hartley, M.E., Maclennan, J., Edmonds, M., Murton, B.J., 2015. Fe-XANES analyses of Reykjanes Ridge basalts: Implications for oceanic crust's role in the solid Earth oxygen cycle. Earth and Planetary Science Letters 427, 272-285.

Siebert, L., Simkin, T., Kimberly, P., 2011. Volcanoes of the World : Third Edition (3). University of California Press, Berkeley, US.

Sossi, P.A., Foden, J.D., Halverson, G.P., 2012. Redox-controlled iron isotope fractionation during magmatic differentiation: an example from the Red Hill intrusion, S. Tasmania. Contributions to Mineralogy and Petrology 164, 757-772.

Spakman, W., Hall, R., 2010. Surface deformation and slab-mantle interaction during Banda arc subduction rollback. Nature Geoscience 3, 562-566.

Stamper, C.C., Blundy, J.D., Arculus, R.J., Melekhova, E., 2014. Petrology of Plutonic Xenoliths and Volcanic Rocks from Grenada, Lesser Antilles. Journal of Petrology 55, 1353-1387.

Stolz, A.J., Varne, R., Davies, G.R., Wheller, G.E., Foden, J.D., 1990. Magma source components in an arc-continent collision zone - the flores-lembata sector, sunda arc, indonesia. Contributions to Mineralogy and Petrology 105, 585-601.

Teng, F.-Z., Dauphas, N., Helz, R.T., 2008. Iron Isotope Fractionation During Magmatic Differentiation in Kilauea Iki Lava Lake. Science 320, 1620-1622.

Teng, F.-Z., Dauphas, N., Huang, S., Marty, B., 2013. Iron isotopic systematics of oceanic basalts. Geochimica et Cosmochimica Acta 107, 12-26.

Tollan, P.M.E., Bindeman, I., Blundy, J.D., 2012. Cumulate xenoliths from St. Vincent, Lesser Antilles Island Arc: a window into upper crustal differentiation of mantle-derived basalts. Contributions to Mineralogy and Petrology 163, 189-208.

Turner, S., Foden, J., 2001. U, Th and Ra disequilibria, Sr, Nd and Pb isotope and trace element variations in Sunda arc lavas: predominance of a subducted sediment component. Contributions to Mineralogy and Petrology 142, 43-57.

Turner, S., Foden, J., George, R., Evans, P., Varne, R., Elburg, M., Jenner, G., 2003. Rates and processes of potassic magma evolution beneath Sangeang Api volcano, East Sunda arc, Indonesia. Journal of Petrology 44, 491-515.

Vigouroux, N., Wallace, P.J., Williams-Jones, G., Kelley, K., Kent, A.J.R., Williams-Jones, A.E., 2012. The sources of volatile and fluid-mobile elements in the Sunda arc: A melt inclusion study from Kawah Ijen and Tambora volcanoes, Indonesia. Geochemistry Geophysics Geosystems 13, 22.

Vroon, P.Z., van Bergen, M.J., White, W.M., Varekamp, J.C., 1993. Sr-Nd-Pb isotope systematics of the Banda Arc, Indonesia: Combined subduction and assimilation of continental material. Journal of Geophysical Research: Solid Earth 98, 22349-22366.

Wawryk, C.M., Foden, J.D., 2017. Iron-isotope systematics from the Batu Hijau Cu-Au deposit, Sumbawa, Indonesia. Chemical Geology.

Wheller, G.E., Varne, R., Foden, J.D., Abbott, M.J., 1987. Geochemistry of quaternary volcanism in the Sunda-Banda arc, Indonesia, and three-component genesis of island-arc basaltic magmas. Journal of Volcanology and Geothermal Research 32, 137-160.

Whitford, D.J., 1975. Strontium isotopic studies of the volcanic rocks of the Saunda arc, Indonesia, and their petrogenetic implications. Geochimica et Cosmochimica Acta 39, 1287-1302.

Whitford, D.J., Jezek, P.A., 1982. Isotopic constraints on the role of subducted sialic material in Indonesian island-arc magmatism. Geological Society of America Bulletin 93, 504-513.

Widiyantoro, S., Pesicek, J.D., Thurber, C.H., 2011. Subducting slab structure below the eastern Sunda arc inferred from non-linear seismic tomographic imaging. Geological Society, London, Special Publications 355, 139-155.

Widiyantoro, S., van der Hilst, R., 1997. Mantle structure beneath Indonesia inferred from high-resolution tomographic imaging. Geophysical Journal International 130, 167-182.

Yogodzinski, G.M., Lees, J.M., Churikova, T.G., Dorendorf, F., Woerner, G., Volynets, O.N., 2001. Geochemical evidence for the melting of subducting oceanic lithosphere at plate edges. Nature 409, 500-504.

Zernack, A.V., Price, R.C., Smith, I.E.M., Cronin, S.J., Stewart, R.B., 2012. Temporal Evolution of a High-K Andesitic Magmatic System: Taranaki Volcano, New Zealand. Journal of Petrology 53, 325-363.

Zhang, C., Holtz, F., Koepke, J., Wolff, P.E., Ma, C., Bédard, J.H., 2013. Constraints from experimental melting of amphibolite on the depth of formation of garnet-rich restites, and implications for models of Early Archean crustal growth. Precambrian Research 231, 206-217.

Chapter 2

Petrological study of a mafic and ultramafic xenolith suite and host shoshonitic island arc lavas from Sangeang Api volcano in the eastern Sunda Arc

Statement of Authorship

Title of Paper	Petrological study of a mafic and ultramafic xenolith suite and host shoshonitic island arc lavas from Sangeang Api volcano in the eastern Sunda Arc
Publication Status	☐ Published ☐ Accepted for Publication ☐ Submitted for Publication ☑ Unpublished and Unsubmitted work written in manuscript style
Publication Details	For submission to Journal of Petrology as: Cooke, B., Foden, J. Petrological study of a mafic and ultramafic xenolith suite and host shoshonitic island arc lavas from Sangeang Api volcano in the eastern Sunda Arc.

Principal Author

Name of Principal Author (Candidate)	Benjamin Cooke		
Contribution to the Paper	Collection of samples in fieldwork, sample preparation, data collection, data processing, data interpretation, manuscript preparation and content, creation of diagrams		
Overall percentage (%)	80		
Certification:	This paper reports on original research I conducted during the period of my Higher Degree by Research candidature and is not subject to any obligations or contractual agreements with a third party that would constrain its inclusion in this thesis. I am the primary author of this paper.		
Signature		Date	13/11/2017

Co-Author Contributions

By signing the Statement of Authorship, each author certifies that:

i. the candidate's stated contribution to the publication is accurate (as detailed above);

ii. permission is granted for the candidate in include the publication in the thesis; and

iii. the sum of all co-author contributions is equal to 100% less the candidate's stated contribution.

Name of Co-Author	Professor John Foden		
Contribution to the Paper	Assistance in fieldwork, data interpretation, trace element modelling section, review		
Signature		Date	13/11/2017

ABSTRACT

Sangeang Api is a highly active volcano located in the eastern Sunda Arc of Indonesia, erupting most recently in May 2014. It erupts volatile-rich, silica-undersaturated and highly oxidised basalts to basaltic-trachyandesites. These lavas are amongst the most potassic in the Sunda Arc (2-4wt.% K_2O), and like nearby Tambora fall between the widespread calc-alkaline products of many Sunda Arc volcanoes including Rinjani and the ultrapotassic suite of Batu-Tara volcano which lies in the Flores sea, ENE of Sangeang Api. Entrained within and interpreted to be co-genetic with the lavas are a suite of cumulate xenoliths. The cumulate xenoliths can be separated mineralogically and geochemically into two distinct groups; the pyroxenites, sub-divided into *cpx-mgt* and *cpx-ol* bearing members, and the *cpx-plag-mgt-hbl* rich gabbros. The fractional crystallisation of these two distinct cumulate xenolith groups drove the differentiation profiles observed in the lavas, as evidenced by the lavas and xenoliths sharing similar mineral populations. Primitive olivine cores record Mg# of 0.8-0.85 and similarly primitive clinopyroxene cores are Cr-rich, magnesian (Mg# 0.75-0.85) and have significant Ca-Tschermak substitution, suggesting that the most primitive minerals crystallised from previously fractionated, low Al/Si ratios and high water contents. Trace element modelling suggests that the pyroxenite and gabbro cumulates crystallised somewhat in parallel from distinct magmas, with differences in pressure, aH_2O and fO_2. It also displays the effects of contamination on the cumulate xenoliths, increasing the contents of incompatible elements higher than would be expected from the fractional crystallisation of primitive cumulates. Parental magmas were likely sourced by <3% batch melting of an I-MORB source in the presence of 0.8-3.75% residual garnet, which was enriched with partial melts of ~1.5-2.5% sediment of a mixed pelagic and carbonate material. Within some of the xenoliths cumulate amphibole can be observed to breakdown in the following incongruent reaction: *Pargasite* → *Cpx* + *Oliv* + *Amph* + *Melt*. These incongruent breakdown reactions produce an alkali-rich glass which can be found in other samples were amphibole is not present. Many of the primitive clinopyroxenes display late-stage overgrowths of less magnesian clinopyroxene or amphibole and in many xenolith samples interstitial and post-cumulate amphibole and phlogopite can be readily observed. Disequilibrium textures are evidence of contamination processes altering the primitive trace element compositions of the cumulates. They are attributed to several processes; inefficient extraction of melts, melt vein intrusions, cumulate disaggregation and melt invasion and cryptic enrichment by percolative flows. Magmas experienced significant decompression degassing as they ascended to the surface, leading to melts with extremely low sulphur concentrations <500ppm. Immediately prior to eruption magmas experienced a rapid decompression and degassing event, losing approximately ~2.5wt.% H_2O and quench crystallising low-An microlites and sodic rims on plagioclase phenocrysts.

INTRODUCTION

Arc volcanism is a key part of the global subduction factory, with the emplacement of magmas in island arcs being a primary contributor to crustal growth. Primitive arc

magmas originate from partial melting of the mantle wedge peridotite and differentiate as they ascend through the crust. Most arc magmas expressed at the earth's surface differ greatly from their parental magmas, having experienced significant differentiation in the mid-lower crust. Primitive arc magmas stall and fractionate in the upper lithosphere and lower-mid crust leaving behind crystal cumulates, differentiated magmas produced then ascend towards the surface and are emplaced in upper crustal intrusives and erupted in volcanic suites. Cumulate xenoliths interpreted as co-genetic to the lavas they are entrained within are rare and are found at a limited number of active volcanoes around the world (Gruender et al., 2010; Montanari et al., 2010; Stamper et al., 2014; Tollan et al., 2012; Zernack et al., 2012). However, numerous localities worldwide display plutonic complexes that have been interpreted as exposed sections of the paleo-island arc feeder systems. Examples of these crustal sections have been described in Alaska (Clift et al., 2005; Hacker et al., 2008), Pakistan (Bouilhol et al., 2015; Bruno et al., 2009; Jagoutz, 2014) and Chile (Dungan and Davidson, 2004). These sections preserved ultramafic, mafic and felsic plutonic suites, as well as the feeder zones that transfer magmas between crustal reservoirs and the surface. Pyroxenite and olivine-pyroxene lithologies are common among the exposed magmatic systems, some of which also contain abundant amphibole.

Cumulate xenoliths provide an unparalleled insight into petrogenesis of active arc volcanic systems and thus crustal growth. Crystal cumulates preserve direct evidence of the fractionation and differentiation processes experienced by primitive parental magmas that is not observable in differentiated magmas. Xenolith suites have been used to provide evidence for primitive magma chemistry, magmatic architecture, differentiation and crustal interaction/assimilation in variety of island arcs, including the Lesser Antilles (Arculus and Wills, 1980; Stamper et al., 2014; Tollan et al., 2012), New Zealand (Gruender et al., 2010; Price et al., 2016; Zernack et al., 2012), the Aleutian Arc (Conrad and Kay, 1984; Debari et al., 1987; Yogodzinski and Kelemen, 2007) and Italy (Balassone et al., 2013; Cigolini, 2007; Giannetti, 1982).

This paper presents a study of a suite of shoshonitic silica-undersaturated, volatile-rich basalts-basaltic trachyandesites from the active volcano of Sangeang Api, located to the northeast of Sumbawa in the Sunda-Banda Arc system of Indonesia. Entrained within, and interpreted to be co-genetic with, the shoshonites are a suite of gabbro and pyroxenite cumulate xenoliths. The presence of these co-genetic xenoliths provides a unique natural laboratory in which to investigate the processes of magma evolution in arc volcanic settings.

GEOLOGICAL SETTING

Sangeang Api is an active volcano located in the Flores Strait between Flores and Sumbawa in the Sunda-Banda Arc system of Indonesia (fig. 1a&b). The island is composed of the two peaks of Sangeang Api volcano, the active cone of Doro Api (1949) and the inactive peak of Doro Mantoi (1975), which are both emplaced within the bounds of an older caldera. Sangeang Api has erupted at various times since the

earliest documented eruption in 1512, with a few larger (VEI≥3) eruptions occurring more recently in 1953, 1985-88 and 2014-2015 (Siebert et al., 2011).

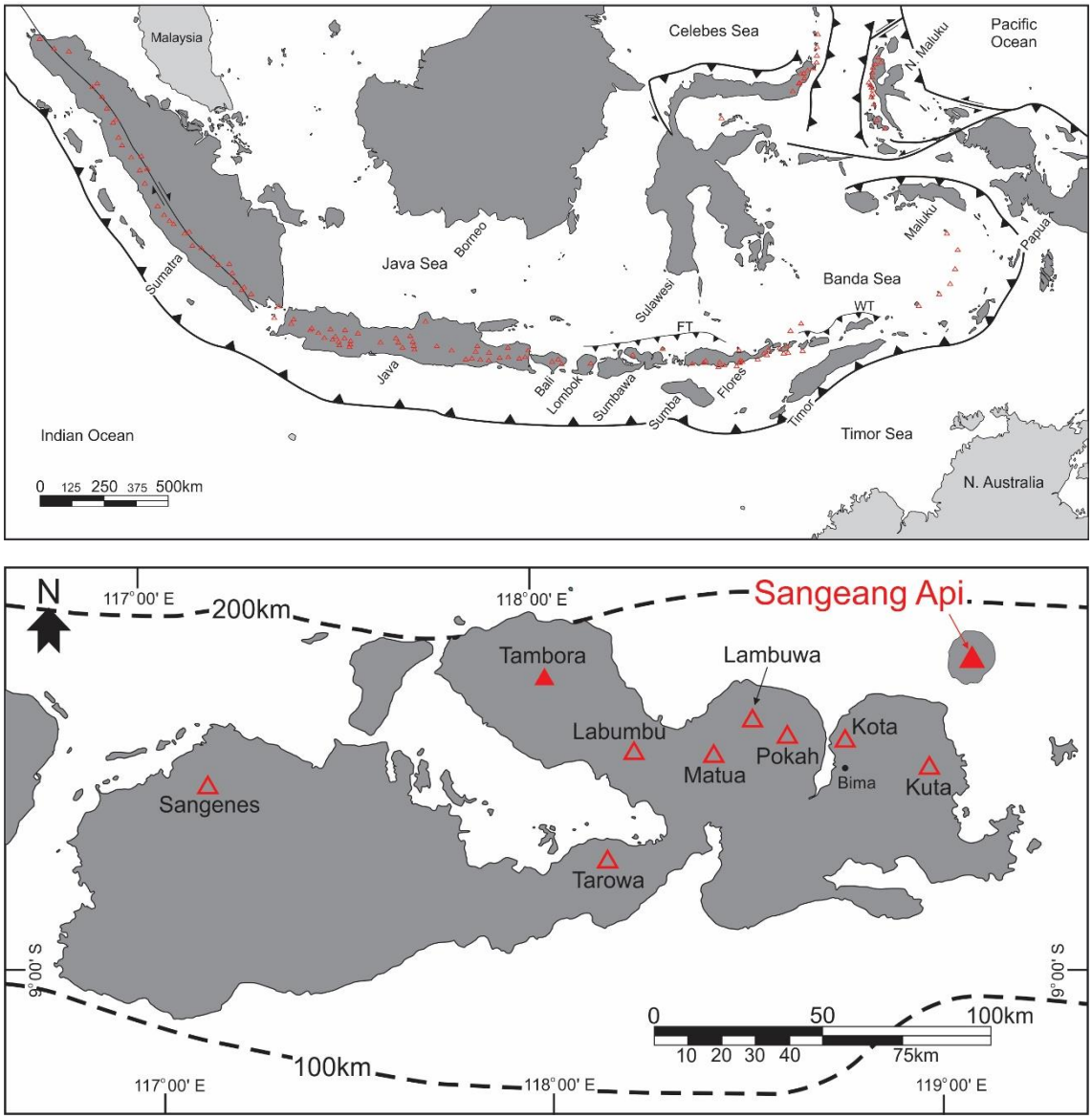

Figure 1a (top): Regional map of the Sunda-Banda Arc. Open triangles show the location of Holocene volcanoes (Siebert et al., 2011). Acronyms: FT = Flores thrust, WT = Wetar Thrust.

Figure 1b (bottom): Close-up map of Sumbawa. Closed triangles show the location of active volcanoes; including Sangeang Api (to the northeast of Sumbawa). Open triangles show the location of extinct Quaternary volcanoes. Dashed lines in the background display the depth to the Benioff zone – adapted from Spakman and Hall (2010).

The Sunda-Banda Arc is a ~4800km long tectonic feature that extends from the Andaman Islands in the Bay of Bengal in the west through to the Banda Sea in the East (fig. 1a). The Sunda Arc is dominantly east-west trending through most of its extent from Sumatra in the west to Flores in the east, with the Banda Arc continuing the system on to its eastern promontory where the arc bends 180˚ around the Banda Sea. A region of volcanic and seismic inactivity marks the transition from the Sunda Arc to the Banda Arc (Das, 2004). Subduction in this region is related to the northwards subduction of the Indo-Australian

plate beneath the Eurasian plate. Sangeang Api is found close to the transition from the subduction of Indian Oceanic crust in the western extent of the system to Australian continental crust in the eastern extent from the region of Timor.

Convergence of the Indo-Australian, Eurasian and Pacific plates from the late Jurassic through to the modern day formed the Sunda-Banda Arc system; with volcanism initiating in the west of Java (~45Ma) and younging to the east into the back-arc volcanos of the Banda Sea (<12.5Ma) (Spakman and Hall, 2010). The origin of the Banda Arc curvature was initially thought to be related to back-arc spreading (Hamilton, 1979; Hinschberger et al., 2005); or to be remnants of older Jurassic-Cretaceous age oceanic crust (Bowin et al., 1980). However, more recent studies have suggested that the Banda Sea is an embayment of oceanic crust that existed prior to the initiation of subduction in the Sulawesi region, and extended eastwards into its current position through slab rollback (Hall, 2011; Hall, 2012; Spakman and Hall, 2010). Pownall et al. (2016) proposed that a 450km long, low-angle normal fault system, termed the 'Banda Detachment', accommodated the lithospheric extension required by the eastwards slab rollback. Seismic tomographic sections clearly show this embayment of oceanic crust sitting within the mantle at depths of approximately ~600km in the west and shallowing to ~300km in the east (Spakman and Hall, 2010).

The islands of the eastern Sunda Arc (Lombok, Sumbawa, Flores, etc.) are actively faulted by northwest and northeast trending strike-slip structures. Often these structures define the breaks between islands and offset jogs on the coastlines of the islands, and are also related to the alignment of volcanic arrays on Sumbawa and Flores. Sangeang Api is found above one of these faults in the Flores Strait, a structure that also separates Sumbawa from Flores. Active volcanism in Sumbawa is to the north of the archipelago with both Tambora and Sangeang Api located ~250-300km to the rear of the trench and approximately 180km above the Benioff zone, whereas to the east of the Flores Strait fault active volcanism from Flores through to the Sunda-Banda transition zone steps to the south of the respective islands (with some notable exceptions; Batu Tara, etc.). Sumbawan volcanism dates back to the base of the Quaternary with continuous active volcanism occurring to the present day. Interestingly the site of active volcanism on Sangeang Api has moved northwards and the erupted products have become increasingly potassic with this northward shift; from the lower-quaternary, high-K calc-alkaline volcanics of Tarowa, Labumbu, Lambuwa, Kota and Kuta, to the shoshonites of the Pleistocene Sangenges and the Holocene Tambora and Sangeang Api.

ANALYTICAL METHODS

Out of 115 samples collected in the field from 2 sites on the island of Sangeang Api, 31 representative samples were selected for geochemical analysis. Samples were crushed and powdered in a tungsten-carbide mill at the University of Adelaide (UofA). Powders were ignited at 1000°C, and LOI was measured. Fused disks and pressed pellets were made in house using a lithium borate flux. These were then analysed using XRF for major and trace element concentrations by Mark Raven at CSIRO Waite Campus, Adelaide (all iron was measured as Fe_2O_3). Ferric-ferrous iron ratios were calculated using the

volumetric wet chemistry method of Wilson (1960). A further 27 samples were analysed for a full suite of trace elements using solution ICP-MS by Bureau Veritas, Adelaide. BHVO-2 and BCR-2 standards were analysed using the same method and all elements were within a 1% error.

In-situ major element concentrations of minerals and glasses were collected from selected representative samples using electron microprobe at Adelaide Microscopy, UofA (Cameca SXFive and SX51) and the Research School of Earth Sciences, Australian National University (Cameca SX100). Samples were analysed using spot sizes ranging from 5-15µm and all analysis was undertaken at 15kV and 20nA. Trace element concentrations of minerals and glass were also collected at Adelaide Microscopy, UofA using an Agilent 7500cx mass spectrometer connected to a New Wave Up-213 laser.

13 samples representative of the chemical variation within the cumulate xenolith and lava suites underwent further Sr, Nd & Sm isotopic analysis, using an IsotopX TIMS at UofA. Two standards, BCR-2 and AGV-2, were also analysed; returning $^{87}Sr/^{86}Sr$ ratios of 0.705013 and 0.703980 respectively. Lab procedural blanks are less than 1pg for Sr and 200µg for Nd, with procedural blanks from this study fitting within this range.

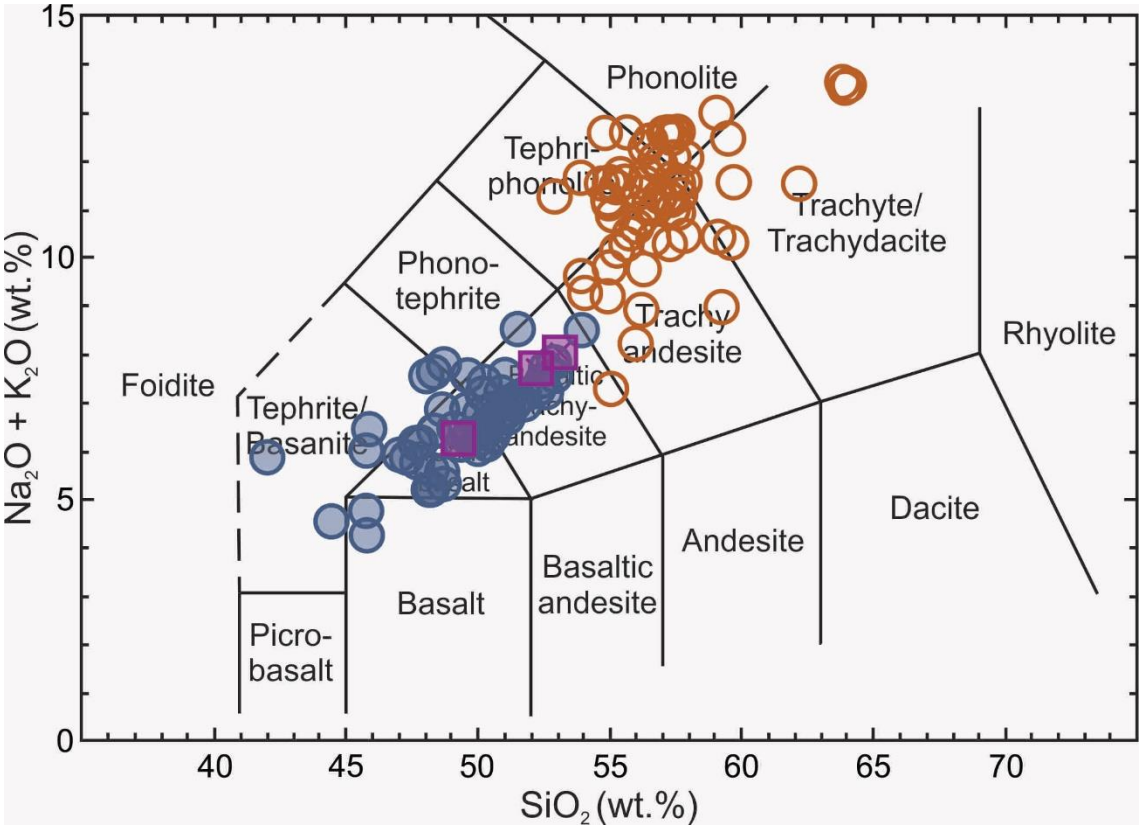

Figure 2: Total alkali versus silica plot displaying lava (filled blue circles), 2014 ash (purple squares) and groundmass glass (open orange circles) geochemistry. Note that the ash overlaps the most fractionated of the lavas and the groundmass displaying an extension of the lava fractionation trend.

LITHOLOGICAL DESCRIPTIONS

Lavas

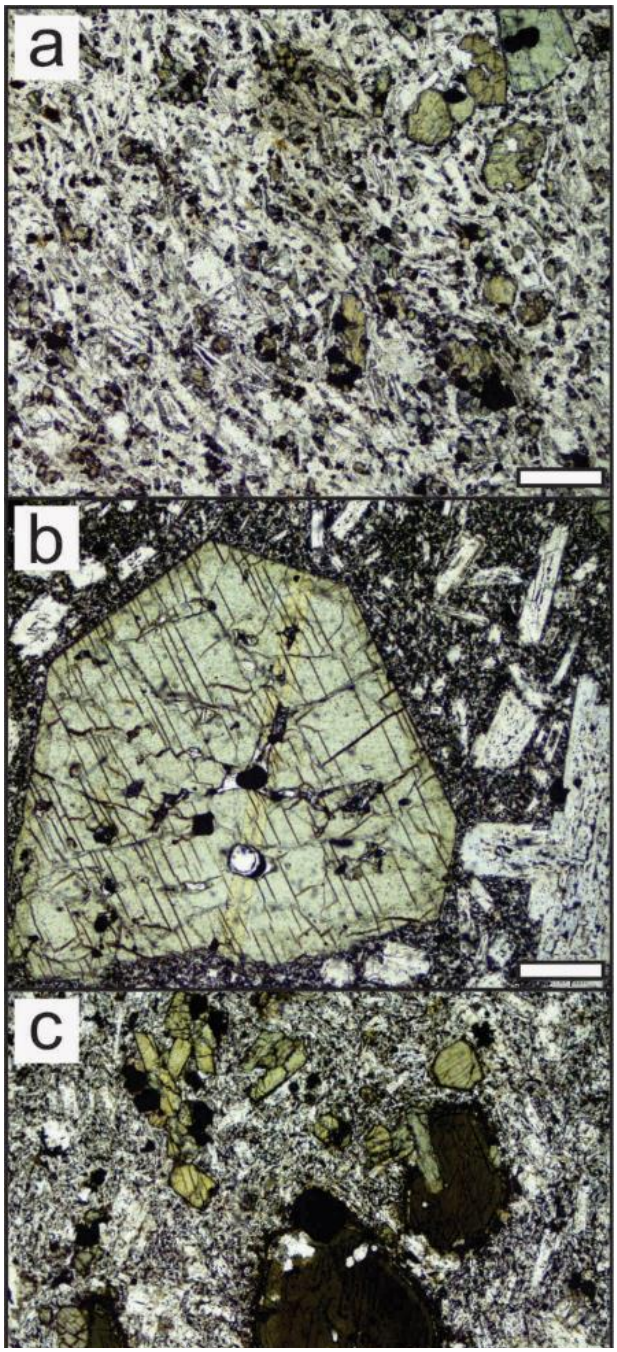

Figures 3a-c: Photomicrographs of typical lavas. Scale bars in bottom right hand corners are 500µm. a) Clinopyroxene and magnetite phenocrysts in a trachytic groundmass of *plagioclase* + *clinopyroxene* + *magnetite*. b) Clinopyroxene xenocryst and plagioclase phenocryst with sieve texture, in a groundmass of *plagioclase* + *clinopyroxene* + *magnetite*. c) Phenocrysts pf clinopyroxene and amphibole with disequilibrium rims of *magnetite* + *clinopyroxene*, in a groundmass composed of *plagioclase* + *amphibole* + *magnetite*.

Sangeang Api erupts a suite of basalts to basaltic-trachyandesites (fig. 2) that are aphanitic and porphyritic, often these are vesicular (fig. 3a-c). These host distinct populations of clinopyroxene-plagioclase-magnetite±olivine and clinopyroxene-plagioclase-magnetite-amphibole phenocrysts and microphenocrysts (see table 1 and fig. 3a-c). Alongside the phenocryst populations are diverse and variable xenocrystic and megacrystic populations of clinopyroxene-plagioclase-olivine-amphibole (fig. 3b). Often the xenocrysts are identified by their large size compared to the other phenocrysts in the sample, obviously fractured mineral edges, zoning and cores with primitive compositions – high Mg# in clinopyroxenes (Mg#>90) (fig. 12a) and amphiboles (Mg#>65) and high-An contents in plagioclase (An >88) (fig. 14). Mineral accumulates are found in a number of the samples, and are always composed of the same minerals as the phenocryst population of the lava in which they are hosted, sometimes displaying an ophitic texture.

These crystal populations are hosted in a groundmass of variable crystal populations of clinopyroxene-olivine-amphibole-magnetite-plagioclase with or without a glass. Groundmass glass compositions are highly potassic and complementary to the lavas (trachyandesites, tephra-phonolites, phonolites and trachytes) (fig. 2).

Plagioclase is ubiquitous in the lavas. When compared to the plagioclase

xenocrysts the phenocrysts are less anorthitic (An50-90), whilst microphenocrysts tend to be less anorthitic (An35-75). Plagioclase phenocrysts of all sizes often display complex zoning histories but are characterised by rims with low anorthite contents (An<70). Sieve textures with glass and magnetite inclusions are seen in some of the phenocryst, xenocryst and megacrysts of plagioclase (fig. 3b).

Xenoliths

Entrained within the lavas are a suite of cumulate xenoliths that are separated into two distinct groups; pyroxenites (group 1) and gabbros (group 2) (fig. 5a). Both groups display both adcumulate and orthocumulate textures, group 2 also display poikilitic textures. As well as the two distinct xenolith groups, a number of composite xenoliths, combining textures and mineralogies of both the gabbros and pyroxenites have been observed. Figures 4a-d show representative photomicrographs of the cumulate xenoliths.

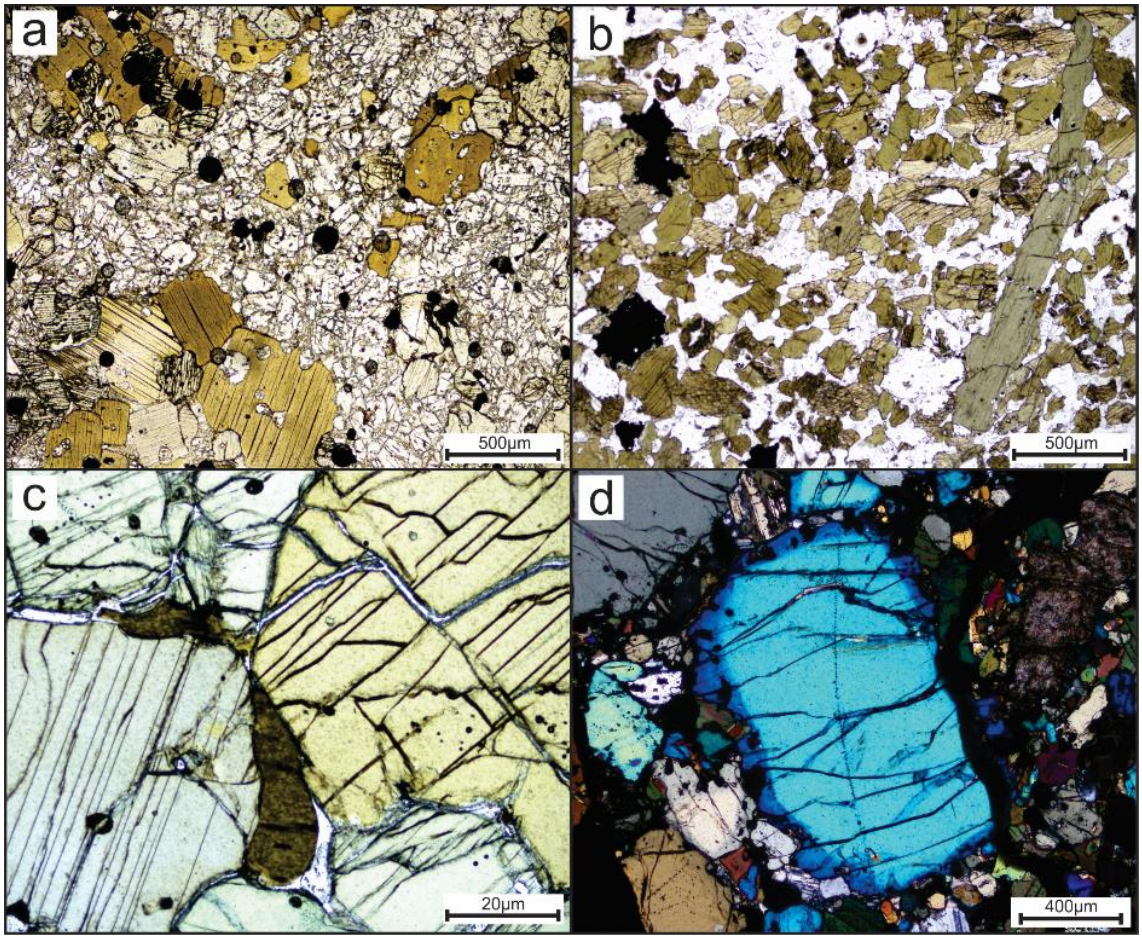

Figures 4a-d: Photomicrographs displaying representative cumulate xenolith textures. Figures 4a and 4b are group 2 gabbros, whilst 4c and 4d are group 1 pyroxenites. a) Gabbro sample (BC14/023) with early cumulate clinopyroxene and magnetite and later plagioclase and phlogopite. b) Amphibole-gabbro (BC14/048) composed of primary cumulate amphibole and later plagioclase with late magnetite. c) Clinopyroxenite sample (B1H) with primary cumulate clinopyroxene and late intracumulate amphibole. d) Clinopyroxenite xenolith region hosted in gabbro (BC14/023), composed of early cumulate clinopyroxene (with late overgrowths of clinopyroxene) and olivine, with later magnetite and plagioclase.

Group 1 Pyroxenites

The pyroxenites are dominated by the presence of highly calcic clinopyroxenes in two distinct mineral populations; clinopyroxene+magnetite and clinopyroxene+olivine (table 1). Whilst olivine and magnetite are important phases in the pyroxenites, olivine and magnetite are never found synchronously together. The olivine-clinopyroxenites are composed predominantly (60-80% modal proportion) of Ca- and Mg-rich, augitic clinopyroxene. Forsteritic olivine (~Fo80) is a primary cumulate alongside the clinopyroxene in the pyroxenites (20-40% modal proportion). Magnetite is absent from the olivine-clinopyroxenites. Rare interstitial Mg-hastingsite amphibole and phlogopite can be found in some of the samples (usually less than 5% modal proportion). The magnetite-clinopyroxenites are dominated by similarly Ca-rich, augitic clinopyroxene (fig. 12) (70-90% modal proportion) and cumulate magnetite (10-20% modal proportion). The magnetite-clinopyroxenites have lesser plagioclase, amphibole and phlogopite (up to 15% modal proportion). Apatite is present in both the magnetite- and olivine-clinopyroxenites to a minor degree (less than 1% by modal proportion).

Group 2 Gabbros

The gabbros are dominated by varying amounts of plagioclase, clinopyroxene, amphibole and magnetite (table 1). The primary cumulus minerals in the majority of these gabbros are Ca-rich clinopyroxene (fig. 12) and pargasitic and Mg-hastingsite amphibole (fig. 15) and both make 20-40% of the mineral populations. Plagioclase is found largely as a cumulus and postcumulus phase, but also as a poikolitic phase; these plagioclase are highly anorthite rich (mean anorthite content of An89 ± 7) (fig. 14), with the highest anorthite contents recorded in their cores (up to An98) and rarely have overgrowth rims of low anorthite contents (as low as An48). Clinopyroxenes in the gabbros span a broad range of compositions from augite to diopside and are Ca-rich but do not record compositions as primitive as clinopyroxenes from the pyroxenites (fig. 12). Clinopyroxene is observed only as primary cumulus or as a poikilitic mineral phase, often the cumulus clinopyroxenes display some replacement by pargasitic amphibole. Amphibole is found extensively throughout the gabbros as a primary- and post-cumulate phase. Compositionally these are pargasites and Mg-hastingsites (fig. 15); the pargasites are texturally primary cumulus phases with long elongate crystals that display simple twinning whilst the Mg-hastingsites display a broad range of textures from euhedral diamond shaped crystals, to large poikilitic crystals and in some circumstances filling in interstitial space between primary cumulates. Often the amphiboles display significant evidence of having undergone incongruent melting during ascent to the surface, producing a mixture of clinopyroxene, olivine and a highly alkaline (Na_2O+K_2O = 6-18wt.%) liquid (fig. 2).

Some of the gabbro samples display distinctive areas that are glass rich containing common hopper-quench textured plagioclase, clinopyroxene and amphibole crystallites. These samples show similar crystal populations to the gabbros, however, it seems that these samples are loose aggregates of cumulate minerals or have experienced some level of disaggregation. These groundmass glasses are highly alkaline (~7-13wt.%

Sample no.	Lithology	Mineral population	Paragenesis	Cumulate phases	Post-cumulate phases	Poikolitic phases	Xenocryst population
BC14/ 004	Lava	Plag. (80%), Cpx. (15%), Mgt. (5%)					Hbl.
BC14/ 018	Lava	Plag. (65%), Cpx. (20%), Mgt. (10%), Oliv. (5%)					Hbl. + Cpx. + Plag.
BC14/ 020	Gabbro	Plag. (60%), Cpx. (20%), Mgt. (10%), Hbl. (10%)	Mgt. > Plag. + Cpx. > Hbl.	Mgt. + Plag. + Cpx.	Hbl.		
BC14/ 025	Pyroxenite	Cpx. (60%), Plag. (20%), Biot. (15%), Mgt. (5%)	Mgt. > Cpx. > Cpx. + Plag. + Biot. > Plag.	Mgt. + Cpx. + Plag.	Cpx. + Biot. + Plag.		
BC14/ 043	Gabbro	Cpx. (35%), Plag. (40%), Biot. (10%), Hbl. (10%), Mgt. (5%)	Cpx. + Plag. + Mgt. > Biot. > Hbl.	Cpx. + Plag. + Mgt.	Biot.	Hbl.	Mgt. + Cpx. + Plag
BC14/ 048	Hornblende-Gabbro	Hbl. (60%), Plag. (35%), Mgt. (5%)	Hbl. > Mgt. > Plag.	Hbl. + Plag. + Mgt.			
BC14/ 060	Gabbro	Plag. (40%), Cpx. (30%), Mgt. (15%.), Hbl. (15%)	Plag. + Cpx. + Mgt. > Hbl.	Plag. + Cpx. + Mgt.		Hbl.	
SA12-X01	Gabbro	Plag. (60%), Cpx. (15%), Hbl. (15%), Mgt. (10%)	Hbl. + Cpx. > Plag. + Mgt.	Hbl. + Cpx.	Plag. + Mgt.		
SA12-X011	Magnetite-Pyroxenite	Cpx. (50%), Plag. (20%), Mgt. (20%), Hbl. (10%)	Mgt. > Cpx. > Plag. > Hbl.	Mgt. + Cpx.	Plag.	Hbl.	
SA12-X042B	Phlogopite-Clinopyroxenite	Cpx. (60%), Biot. (20%), Plag. (15%), Mgt. (5%)	Cpx. > Cpx. + Mgt. + Plag. > Biot.	Cpx. + Plag. + Mgt.	Biot.		

Table 1: Modal proportions and paragenetic sequences of various representative samples.

Na_2O+K_2O), volatile rich (0-296ppm S, 25-10797ppm Cl, 0-1550ppm F and 0-6902ppm Ba) (fig. 17) and more fractionated than the magmas (53-64wt.% SiO_2).

Composite xenoliths and cataclasite textures

Several cumulate xenoliths display composite textures, most commonly observed as relatively large (>5cm diameter), and often numerous, pyroxenitic regions within a gabbroic host. Mineralogically distinct xenolith regions are largely separated by distinct, relatively planar boundaries. More rarely, smaller regions of the inherited xenolithic material can be observed within the host cumulate. It is impossible that these regions formed simultaneously from the same batch of magma due to the distinct mineral assemblages and compositional variation between minerals. Instead, the contrasting xenolithic regions and sharp boundaries suggest that these xenolithic regions are created by the fragmentation and transport of previously solidified cumulate piles within later magmatic batches. Some cumulate gabbro samples also host xenocrystic cargoes of more primitive minerals (e.g. high Mg# clinopyroxene and olivine). Often the xenocrysts display overgrowths with compositions overlapping the cumulate mineralogy of the host cumulate. Xenocrystic cargoes are likely inherited from poorly aggregated, earlier cumulate piles which then stall within a crustal magma chamber and are enveloped by younger cumulates.

More rarely, cumulate xenoliths of both groups display strain fabrics and cataclasite textures characterised by thin planes of angular and finely crystalline cumulate mineralogy indicative of grain reduction processes. Indicating the presence of a deformational stress regime within the Sangeang Api magmatic tract at depths shallower than the brittle-ductile transition. This is discussed further in a later section.

BULK ROCK GEOCHEMISTRY

Whole-rock major element chemistry

Lavas

Sangeang Api erupts a suite of ne-normative, silica-undersaturated (fig. 8), volatile-enriched lavas that range in composition from basalt to basaltic-trachyandesite, with some more alkaline tephrite and phono-tephrite compositions (fig. 2). Sangeang Api lavas are amongst the most potassic in the Sunda Arc, being shoshonitic with K_2O in the range 2-4wt.% and similar to the lavas erupted by the nearby Tambora and Sangenges (fig. 6) (Foden, 1986a; Gertisser et al., 2012), they are not however as potassic as other ultrapotassic lavas from the Sunda Arc such as Batu Tara (see fig. 7) and Muriah (Edwards et al., 1991; Stolz et al., 1988). As well as sharing their potassic nature Sangeang Api lavas are similarly highly oxidised, with Fe^{3+}/Fe^{2+} ratios of 0.44-2.64. When Fe^{3+}/Fe^{2+} and SiO_2 are compared we can see a slight reduction in the iron as

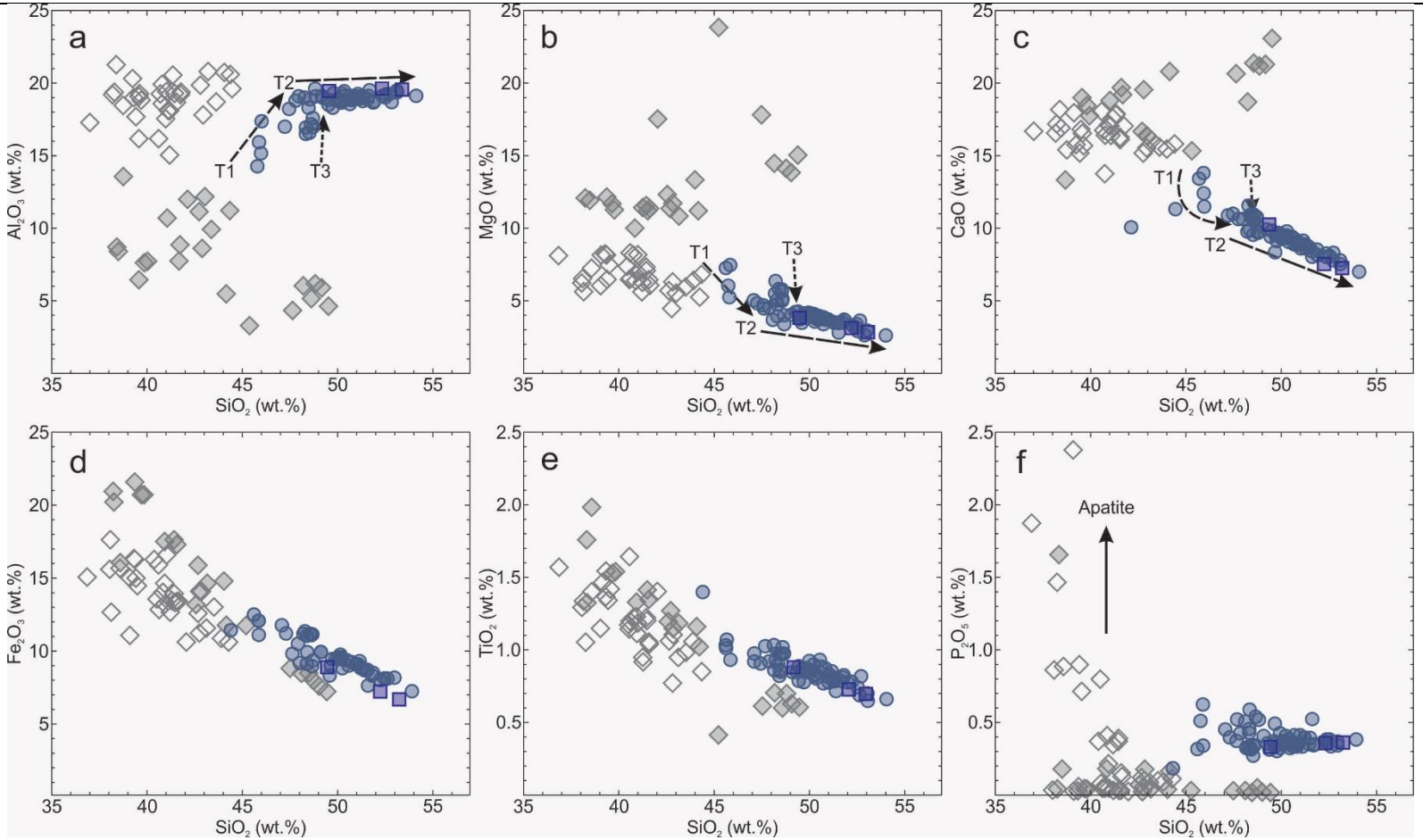

Figures 5a-f: Whole-rock major element discrimination diagrams. Coloured symbols represent data from this study; blue circles are lava data, purple squares are from 2014 ash samples, open grey diamonds are group 1 gabbroic xenoliths and closed grey diamonds are group 1 pyroxenitic xenoliths. Data collated from this study, Turner et al. (2003) and Foden and Varne (1980). The arrows T1, T2 and T3 are the lava fractionation trends 1, 2 and 3. Note the arrow in figure 5f demonstrating the effect of cumulate apatite on the P_2O_5 content of the xenoliths.

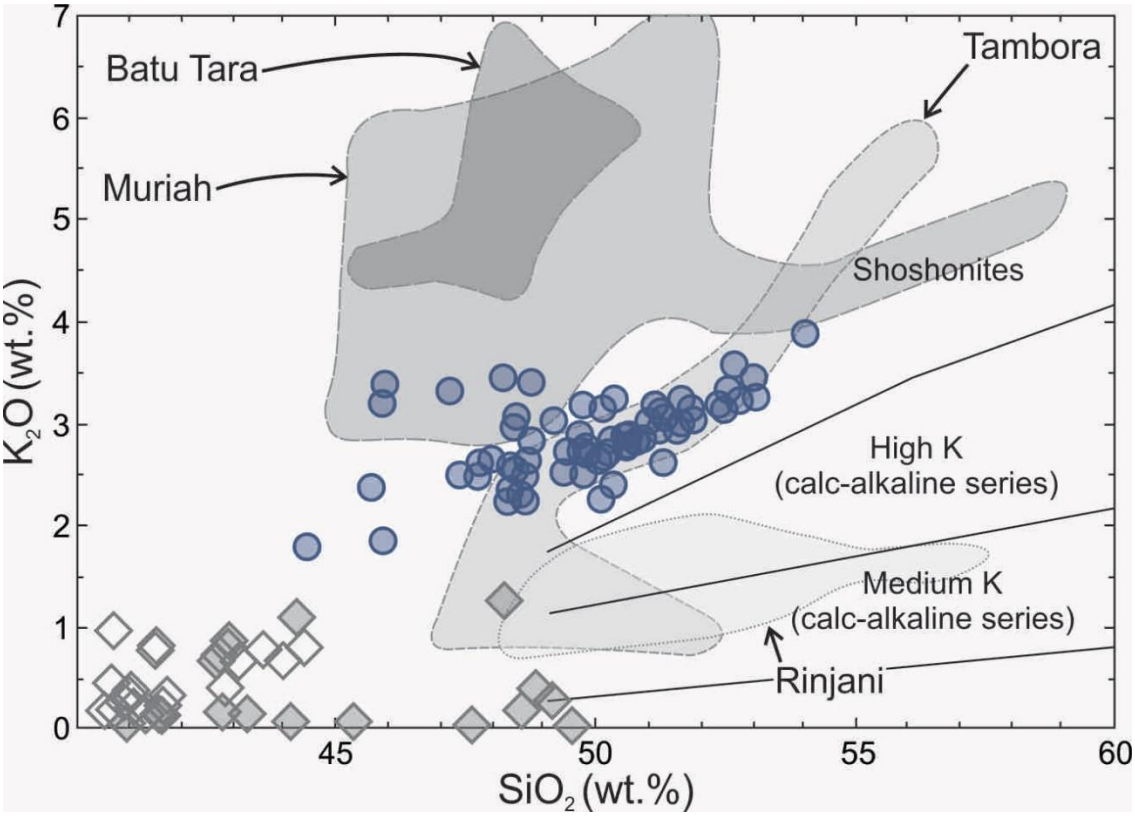

Figure 6: K_2O vs. SiO_2 diagram displaying the shoshonitic character of the Sangeang Api lavas. Symbols as in figures 5a-f. Greyed out areas in the background represent data from other calc-alkaline (Rinjani) and ultrapotassic lavas (Tambora, Batu Tara and Muriah) from the Sunda Arc.

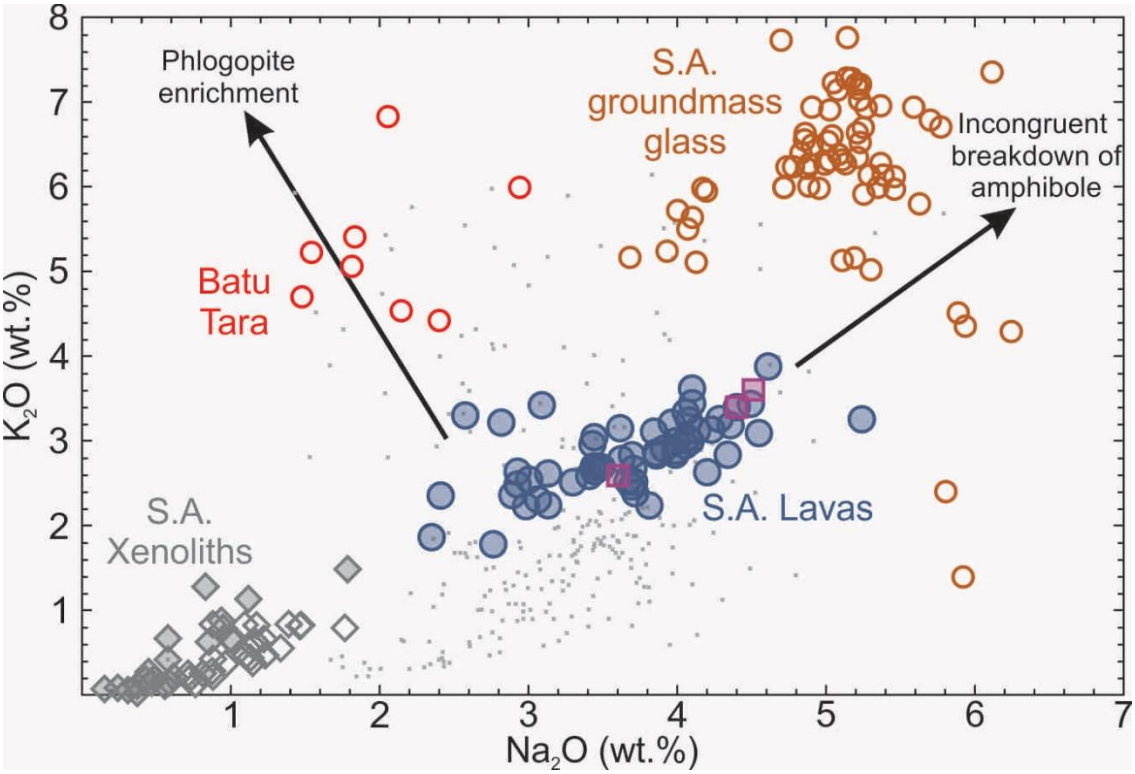

Figure 7: K_2O vs. Na_2O diagram showing Sangeang Api lavas, xenoliths and groundmass glass with Batu Tara lavas (red circles) and Sunda Arc lavas (grey crosses) for comparison. Note the arrows showing the effect of residual phlogopite and amphibole in the lithospheric source regions.

fractionation increases (increasing SiO_2). Lava Mg# range from 0.395-0.55 and, as would be expected from a differentiating suite of lavas, show a negative correlation with SiO_2.

Two distinct trends can be observed within this data (trends 1 and 2 in figure 5a-c); an initial trend (trend 1) associated with an increase in Al_2O_3 (~14-19wt.%), decreasing MgO (~7-4wt.%) and minimal increase in SiO_2 (45-48wt.%), followed by a trend (trend 2) with no increase in Al_2O_3 (~19wt.%), a shallower decrease in MgO (4-2.5wt.%) and significant increase in SiO_2 (48-54wt.%). A sub-trend (trend 3 in figures 5a-c) of the initial trend can be observed, which shows a similar increase in Al_2O_3 and decrease in MgO, but at a higher, stable SiO_2 content (~48.5wt.%). Similar trends can be observed in the Mg# composition of the lavas.

The lavas broadly have low to zero sulphur contents; however, a limited number of the samples have some sulphur content (4-740ppm S) (fig. 17). Also analysed were 3 ash samples from the most recent May 2014 eruption, these samples represent one trachybasalts and two basaltic-trachyandesites (fig. 2). All three ash samples align with trend 2 and are amongst the more evolved of the samples (figs. 5a-f). Compared to the lavas the ash samples have significantly higher sulphur contents (372-1740ppm S) (fig. 17).

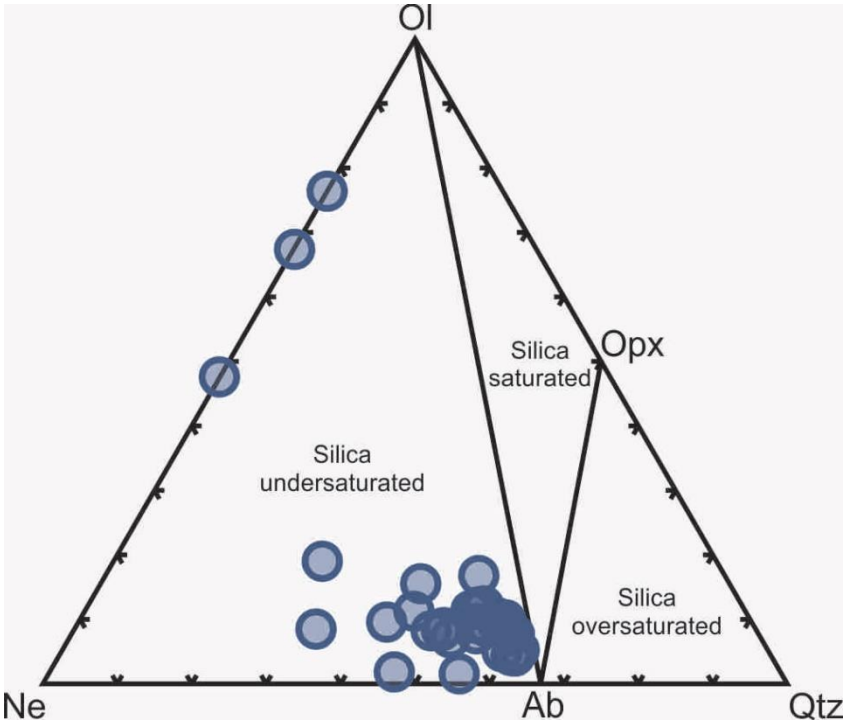

Figure 8: Nepheline-Olivine-Quartz silica saturation diagram displaying normalised values for the Sangeang Api lavas, note that all are silica undersaturated and display no clear trend in the data.

Xenoliths

As previously discussed the group 1 pyroxenite xenoliths are composed primarily of cumulate clinopyroxene and olivine or magnetite, with lesser post-cumulate plagioclase, amphibole, phlogopite and apatite. They are characterised by relatively low Al_2O_3 (3-14wt.%), high MgO (9-24wt.%) and a broad span of SiO_2 (28-50wt.%) (fig. 5a-c). This reflects the dominance of the Fe-Mg silicates and magnetite in their mineralogical make-up. Whilst most of the pyroxenites have Fe_2O_3 and TiO_2 compositions higher than the

gabbros and lavas, a small subgroup of the pyroxenite samples are characterised by low TiO_2, Fe_2O_3 and higher MgO (figs. 5d & 5e). This subgroup is composed of olivine-bearing, magnetite-free pyroxenites – often with relatively large amounts of interstitial amphibole or phlogopite. Whereas, the high TiO_2, high Fe_2O_3 and low MgO subgroup are characterised by olivine-free, magnetite-bearing mineral assemblages, sometimes with post-cumulate plagioclase and hydrous mineralogy. The magnetite-free subgroup also extends to the highest CaO concentrations of the whole-rock suite, reflecting the presence of Ca-rich clinopyroxenes, and the highest Mg# (~0.8) due to the strong influence of olivine and clinopyroxene. Whilst most of the cumulate xenoliths display near-zero P_2O_5, some samples show some extreme variation to high values (up to ~1.6wt.%) reflecting the rare appearance of apatite (fig. 5f). There is a broad decrease in Fe^{3+}/Fe^{2+} with increasing SiO_2, suggesting that the most primitive (lowest SiO_2), magnetite-bearing cumulates are more oxidised than olivine-bearing pyroxenites.

Group 2 xenoliths are gabbros composed of varying amounts of plagioclase, clinopyroxene, magnetite and hydrous minerals (amphibole and phlogopite). They are characterised by relatively high Al_2O_3 (15-22wt.%), low MgO (~4-8wt.%) and low SiO_2 (37-44wt.%) (figs. 5a-f). The influence of plagioclase on the high Al_2O_3 (>15wt.%) composition of the gabbro xenoliths is immediately clear and is also reflected in the low MgO (<~8wt.%) of this group. Gabbroic xenoliths show trends of decreasing Fe_2O_3 and TiO_2 with increasing SiO_2, reflecting a decrease in the proportion of magnetite. A few gabbro samples display elevated amounts (0.4-2.4wt.%) of P_2O_5, reflecting the presence of varying amounts of apatite. This is more common in the gabbros than the pyroxenites, suggesting a higher proportion of apatite crystallisation. The gabbros record low Mg# relative to the pyroxenites (0.41-0.56) and a similar decrease in Fe^{3+}/Fe^{2+} with increasing SiO_2, likely reflecting a decrease in magnetite content.

Whole-rock trace element characteristics

Figures 9a-f display the characteristics of selected trace-elements for the lavas and cumulate xenoliths. The trace-element compositions of the Sangeang Api suite of rocks is further described below.

Lavas

These relatively K-rich, silica-undersaturated lavas (shoshonites) have general trace element characteristics typical of subduction-related magmas. They have relative LREE- and alkali earth enrichment (fig. 10a and 10b) with strong Nb and Ta depletion and with $Nb_N > Ta_N$. Compared to primitive mantle they have very significant positive Pb anomalies. They also have positive Sr anomalies and negative Zr and Ti. It is worth noting that all the characteristics listed above describe all the Sangeang Api lavas. This implies these characteristics were inherited from primitive parental melts less fractionated than any of the Sangeang Api lavas sampled and not generated by fractionation processes involving the relationship between the lavas and their hosted xenoliths. At the same time Nb, Ta and Zr show enrichment comparable to that of Rb from the least to the most fractionated lavas indicating these are behaving incompatibly. Conversely, Sr shows

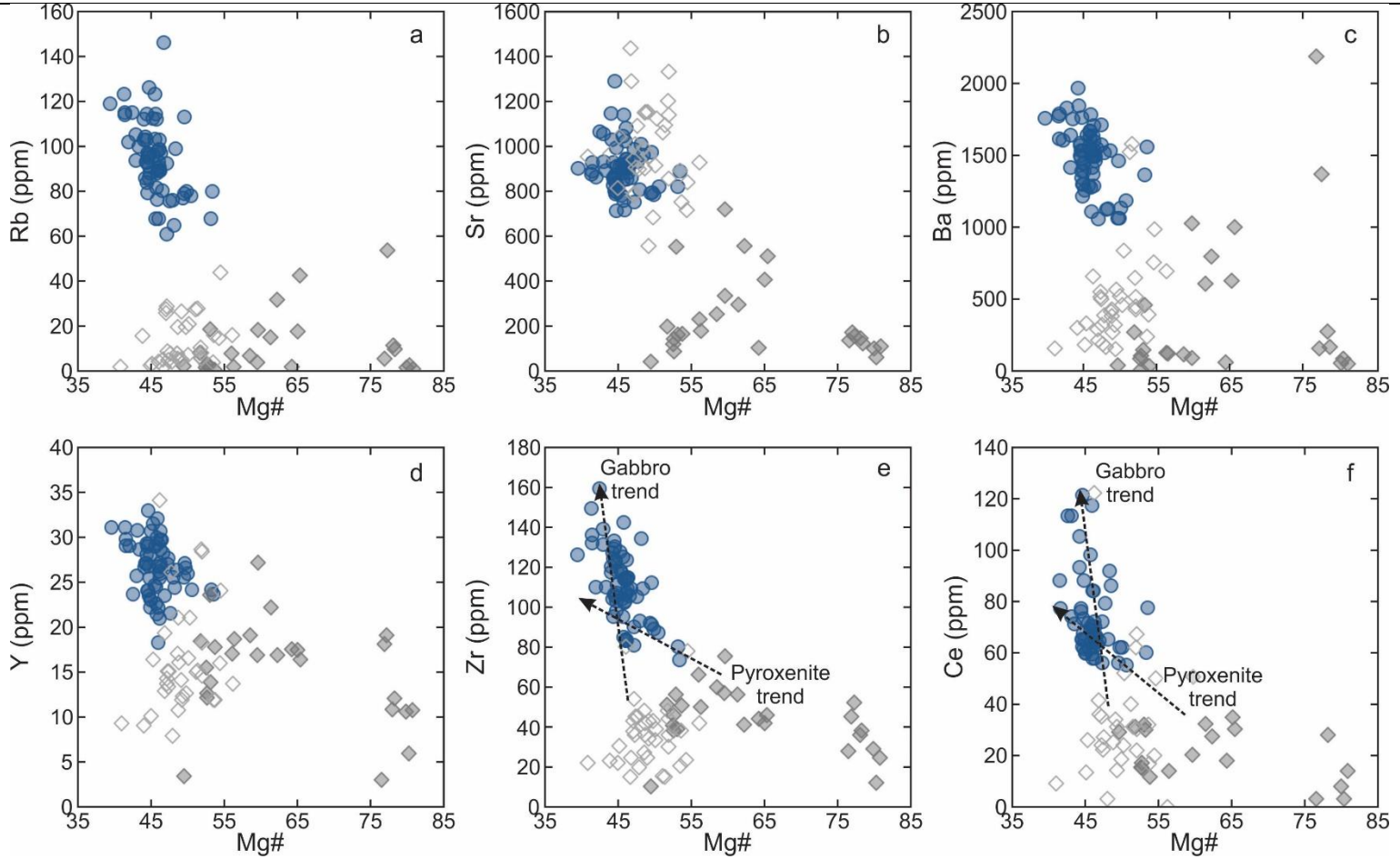

Figures 9a-f: Whole-rock trace element discrimination diagrams. Symbols as in figure 5. Data compiled from this study, Turner et al. (2003) and Foden and Varne (1980). Mg# calculated as $100[Mg/(Mg+Fe_{tot.})]$. Dashed lines in figures 9e and 9f display the effect of pyroxenite and gabbro fractionation on trace element distribution. Note the high Ba content of some xenoliths in the figure 9c, this is likely due to the addition of Ba from fractionated liquids through percolative flow processes.

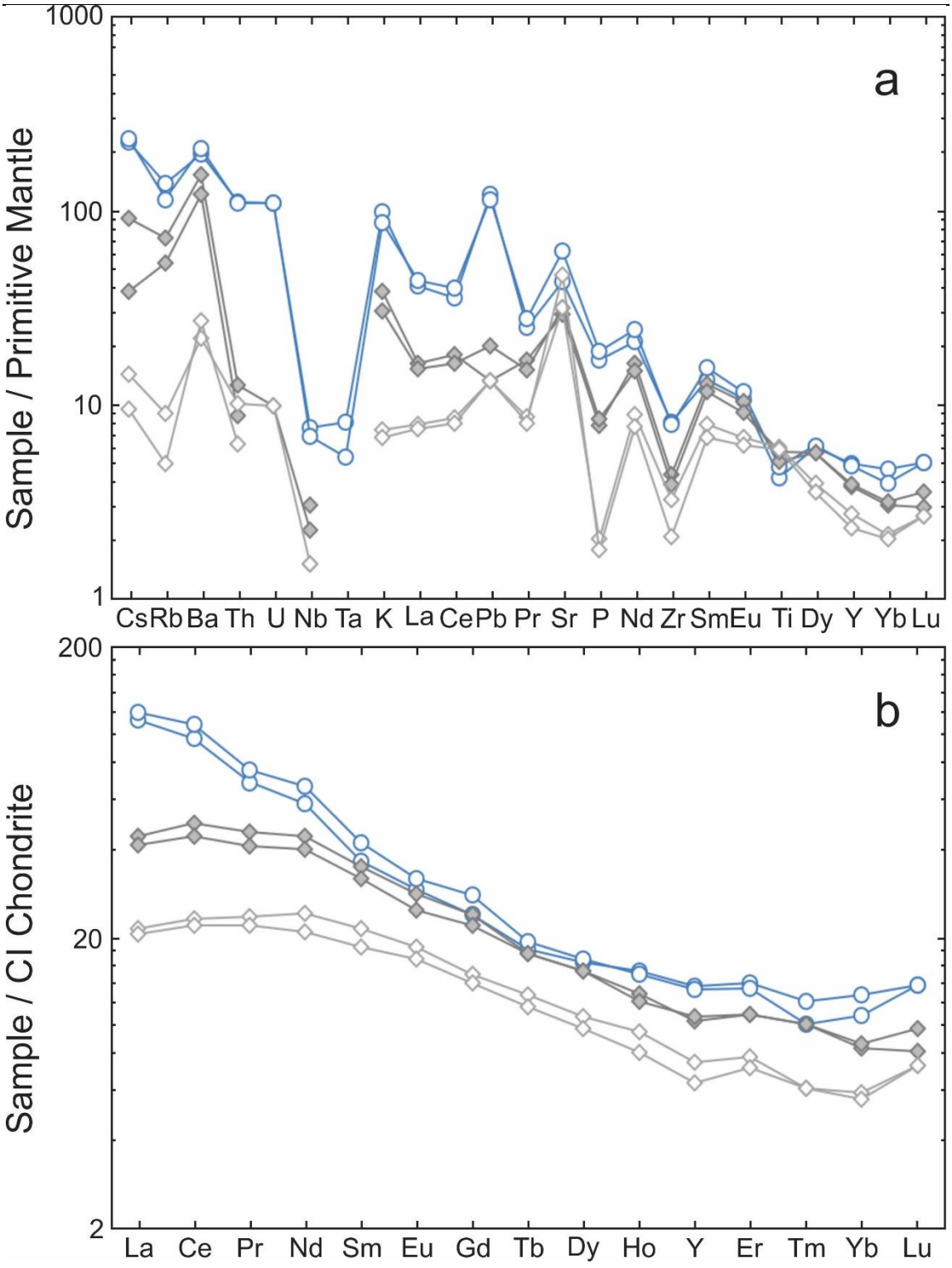

Figure 10a: Incompatible spider diagram displaying the profiles of representative lavas (open blue circles - BC14/007, BC14/076), pyroxenites (closed grey diamonds - BC14/023, BC14/041) and gabbros (open grey diamonds - BC14/071, BC14/086) relative to primitive mantle values of McDonough and Sun (1995).

Figure 10b: REE profile of representative lavas, pyroxenites and gabbros relative to CI Chondrite values of McDonough and Sun (1995). Selected samples and symbols same as figure 10a.

slight depletion, though not enough to eradicate the positive Sr anomaly. The lavas also show positive Cs and Ba anomalies. They have Th_N / U_N close to 1.

The REE patterns (fig. 10b) show relatively little change from least- to most-fractionated, implying bulk D values that approach 1. The HREE patterns have a 'spoon' shape with Er_N and Lu_N values greater than Tm_N and Yb_N. Based on the determined partition coefficients, where Kd Dy > Kd Yb & Lu, this style of REE pattern with low Dy and La/Yb ratios has been interpreted to indicate amphibole crystallization (Davidson et al., 2007). However, as demonstrated below, the relativity between clinopyroxene and amphibole REE partition coefficients are nearly the same and as a result the crystallization of either will produce the same style of REE pattern.

Xenoliths

Based on their mineralogy the xenoliths are subdivided into two groups (see earlier): 1. Pyroxenites and 2. Gabbros.

The REE patterns of these two groups are very similar (fig. 10b). In both the pyroxenites and the gabbros, by far the majority of the REE are hosted by clinopyroxene and/or amphibole. As the average modal abundance of Cpx + Amph in the gabbros is around 40% this means these have lower REE than the pyroxenites, but with similar form. The pyroxenites have MREE to HREE that are close to the values of the lavas indicating that clinopyroxene Kd values for these elements approaches 1. Given that these pyroxenes are moderately rich in Ca-Tschermak component these results are consistent with the experimentally demonstrated increase in Cpx partition coefficients for the REE as a function of increasing ^{IV}Al as Ca-Tschermaks substitution (Hill et al., 2000). The HREE patterns from Dy to Yb show a more regular decline than the lavas (fig. 10b), suggesting the Kd Dy is > Kd Yb, consistent with the complementary relative enrichment of Yb in the lavas.

As with the REEs, the gabbros tend to have lower incompatible elements than the pyroxenites, with some specific element exceptions. As discussed below, the concentration of the most incompatible elements in the xenoliths, particularly the monovalent and bivalent traces (fig. 20) seem to be strongly influenced by contamination/enrichment by melts. Accordingly, both xenolith groups show strong enrichment of Cs, Rb and Ba, particularly Cs and Ba. Both xenolith suites have large negative Nb anomalies and large positive Pb anomalies. The gabbros also have a large positive Sr anomaly reflecting plagioclase accumulation while the pyroxenites also have a significantly smaller positive Sr anomaly. Reflecting their magnetite content, gabbros are relatively enriched in Ti (and V) (figs. 20e and 20f) compared to the pyroxenites which have a slight negative Ti anomaly. Both groups show moderately strong relative depletions in P and Zr.

While gabbros are distinguished by low incompatible elements and relatively high Sr (in plagioclase) Ti and V (in magnetite), pyroxenites are relatively enriched in Sc, and slightly, but variably enriched in Cr and Ni. Although some pyroxenite samples have >200 ppm Cr (none greater than 400ppm) and most have Ni in the 10 to 70 ppm range,

these values are low by comparison with mantle pyroxenes, again reflecting the fractionated character of the xenolith suite.

$^{143}Nd/^{144}Nd$ and $^{87}Sr/^{86}Sr$ isotopic compositions

Sunda and Banda Arc lavas display an extremely broad range in Nd and Sr isotopic compositions which reflects the complex roles of different source components along the ~4800km long arc. Broadly speaking, as you move from west to east along the arc system $^{143}Nd/^{144}Nd$ ratios tend to decrease and $^{87}Sr/^{86}Sr$ ratios tend to increase. These Sunda-Banda lavas appear to sit along an array spanning between an unaltered Indian MORB and some form of sediment input (Turner and Foden 2001). Sangeang Api displays relatively low $^{143}Nd/^{144}Nd$ and high $^{87}Sr/^{86}Sr$ (fig. 11). The lavas and ash span a relatively broad range in isotopic compositions; $^{87}Sr/^{86}Sr$=0.70442-0.70535 and $^{143}Nd/^{144}Nd$=0.512609-0.512795. When compared to the other potassic magmas from the Sunda Arc (fig. 11), Sangeang Api lavas have higher $^{87}Sr/^{86}Sr$ and lower $Nd/^{144}Nd$ than Tambora, similar $^{87}Sr/^{86}Sr$ to the but higher $^{143}Nd/^{144}Nd$ than Muriah and similar $^{143}Nd/^{144}Nd$ and lower $^{87}Sr/^{86}Sr$ to Batu Tara. Both the pyroxenites and gabbros show extremely broad variations in radiogenic isotope values that overlap neatly with the Sangeang Api lavas. The pyroxenites display a spread in $^{87}Sr/^{86}Sr$ from 0.70395-0.70509 and in $^{143}Nd/^{144}Nd$ from 0.51266-0.51291. The gabbros display even broader values in $^{87}Sr/^{86}Sr$ (0.70389-0.7055) and $^{143}Nd/^{144}Nd$ (0.51257-0.5129). Figure 11 displays the Sr and Nd isotopic compositions of the Sangeang Api lavas and xenoliths compared to the products of other Sunda Arc volcanoes and arc-front sediments.

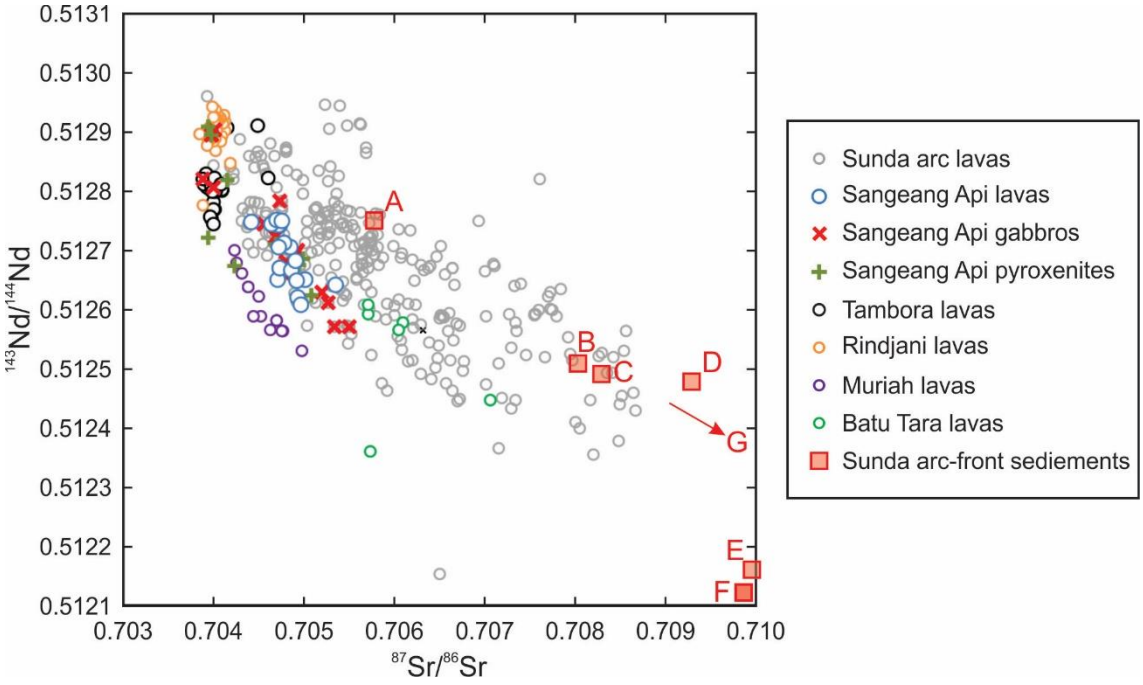

Figure 11: Sr-Nd isotope data from this and previous studies (Foden and Varne, 1980; Turner and Foden, 2001; Turner et al., 2003). See key (right of figure 10a) to identify symbols. Sunda arc-front sediment data is taken from Ben Othman et al. (1989) and Vroon et al. (1995). Tambora isotopic compositions derived from Gertisser et al. (2012), Varne and Foden (1986) and Turner and Foden (2001). Rindjani data from Foden (1983), Varne and Foden (1986) and Turner and Foden (2001). Muriah data from Edwards et al. (1991), Woodhead et al. (2001) and Nicholls and Whitford (1983). Batu Tara data from Stolz et al. (1988), Stolz et al. (1990) and van Bergen et al. (1992). Sunda arc front lavas collated from a GeoRoc database (http://georoc.mpch-mainz.gwdg.de/georoc/).

MINERAL GEOCHEMISTRY

Major element geochemistry

Whilst the mineral populations preserved in both the lavas and xenoliths are broadly similar, there are distinct compositional differences between minerals from the different lithological suites.

Clinopyroxene is a common phase in both groups of xenoliths and lavas. The compositions of clinopyroxenes within the lava and xenolith suites overlap and are span from highly calcic and magnesian diopsides to augites. However, despite the apparent similarities between the compositions there are some clear distinctions that can be drawn. Clinopyroxenes from the pyroxenites are the most calcic and magnesian of the analysed samples (fig. 13) with Mg# (molar $Mg^{2+}/Mg^{2+}+Fe^{2+}$) ranging from 0.69-0.98, whilst crystals from the lavas and gabbros display overlapping compositions (fig. 13) and are both relatively calcic and magnesian (Mg# 0.62-0.87). All clinopyroxenes display significant Ca-Tschermak ($CaAl_2SiO_6$) substitution (~0.05-0.19) (fig. 13c).

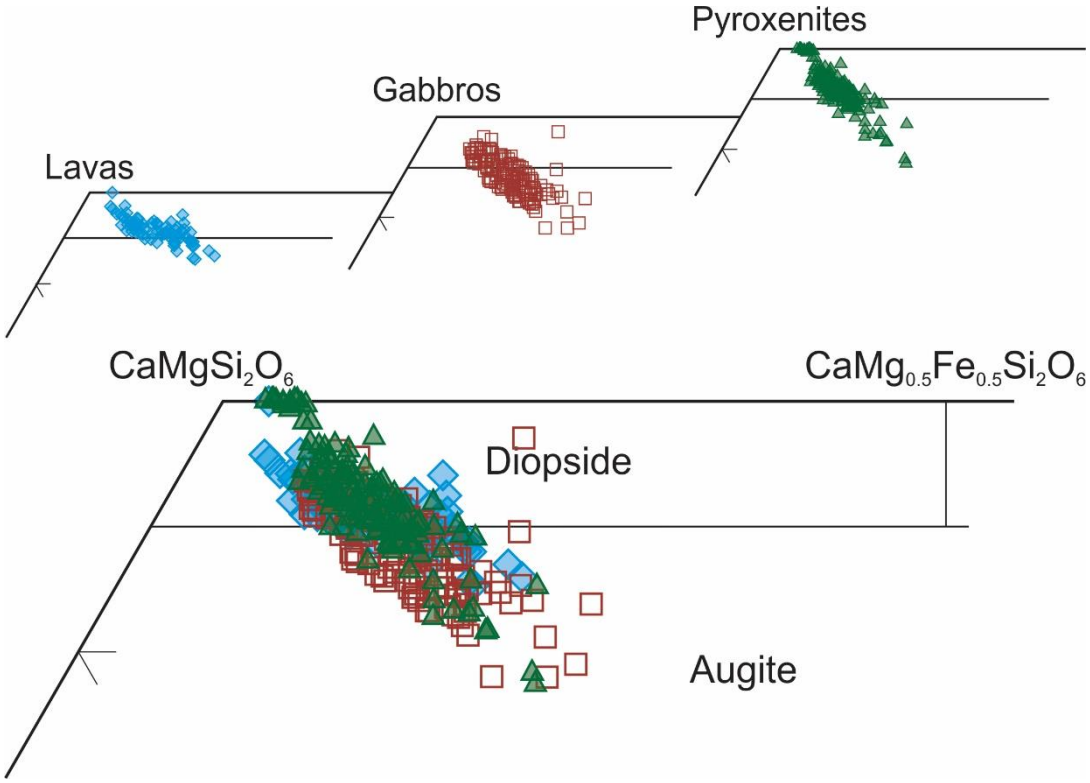

Figure 12: Clinopyroxene discrimination quadrilaterals; the top left quadrilateral shows clinopyroxenes from lavas, the centre displays those from gabbros and the far right quadrilateral shows those found in pyroxenites. Clinopyroxene chemistry stoichiometrically recalculated using the CpxBar spreadsheet of Nimis and Ulmer (1998) and Nimis (1999).

Plagioclase is common in the lavas and group 2 gabbros, as well as a rare phase in the pyroxenites. The most primitive plagioclase in the gabbros are highly calcic and anorthite rich (An90-98), and the crystals become less anorthite rich to An82 in the later formed crystals (fig. 14). Similarly, in the pyroxenites the plagioclase crystals are anorthite rich (An 83-An97) (fig. 14). These contrast strongly to plagioclase phenocrysts from the lavas that show a significant shift to lower anorthite contents (An50-90) (fig. 14). Plagioclase

phenocrysts from the lavas display complex zoning histories with much more sodic overgrowth rims. Microphenocrysts/microlites in the lavas display even more calcium-poor compositions again (An35-75) (fig. 14). These microlites share similar compositions with the later overgrowth rims, suggesting that they formed simultaneously, possibly from quenching during the final stages of degassing and decompression at eruption.

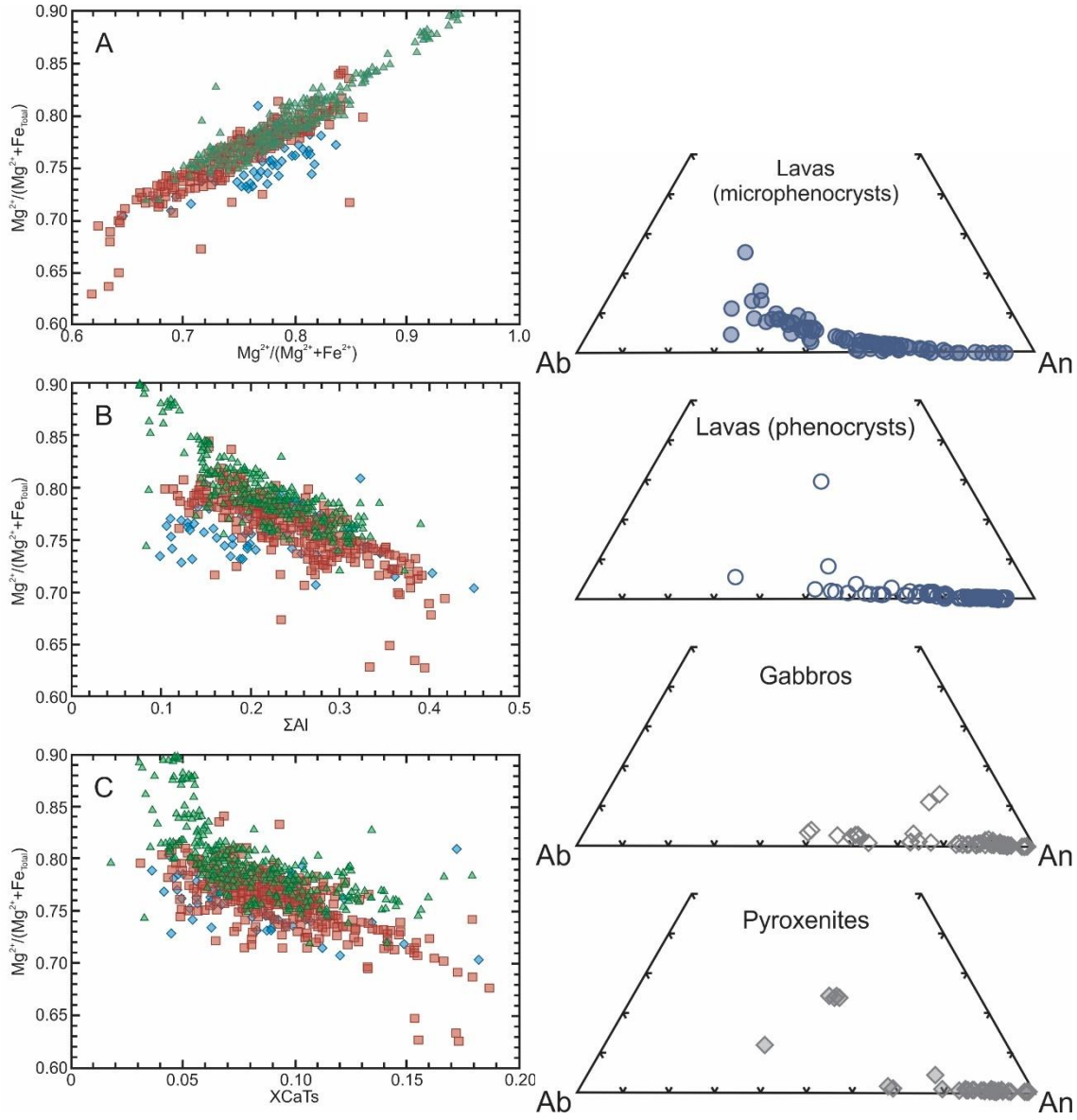

Figures 13a-c (left): Scatter plots displaying the relationship between clinopyroxene $Mg^{2+}/(Mg^{2+}+Fe_{Total})$ and $Mg^{2+}/(Mg^{2+}+Fe^{2+})$ (17a), total aluminium (17b) and Ca-Tschermak concentration (17c). Clinopyroxene chemistry stoichiometrically recalculated using the CpxBar spreadsheet of Nimis and Ulmer (1998) and Nimis (1999).

Figure 14 (right): Plagioclase ternary discrimination diagrams. Top left; microphenocrysts from lavas. Top right; phenocrysts in lavas. Bottom left; phenocrysts in gabbros. Bottom right; phenocrysts within pyroxenites.

Amphibole is found in both the lavas and the xenolith groups and they largely compositionally overlap, as can be seen in figure 15. Gabbros have both Mg-hastingsite and pargasitic amphiboles with a broad range of compositions, whereas the pargasites have significantly lower Mg# than the Mg-hastingsites (up to 0.72). The lavas have both

pargasitic and Mg-hastingsite compositions and record some of the lowest Mg#. Amphiboles in the pyroxenites are Mg-hastingsites and intermediate in composition when compared to those from the lavas and gabbros. The amphiboles display very similar REE patterns to the clinopyroxenes and probably help to exert a control over the REE profile of the gabbros and pyroxenites.

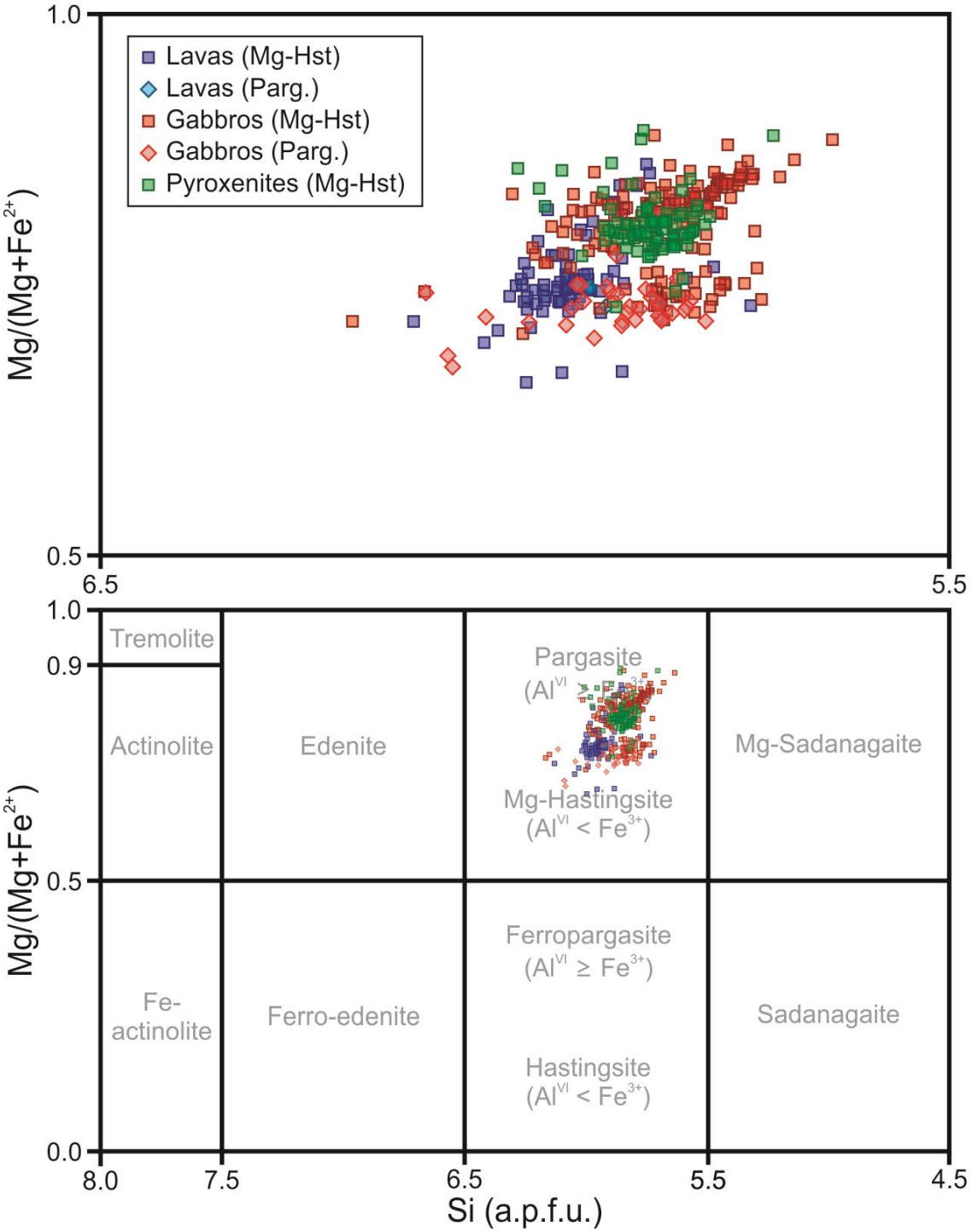

Figure 15: Amphibole discrimination diagram plotting compositions of Sangeang Api amphiboles. Amphibole chemistry recalculated stoichiometrically following the method of Locock (2014) and discrimination diagram after Leake et al. (1997).

Olivine is common amongst the pyroxenites as a primary cumulus and record Fo contents Fo80-85 and are enriched in the transition metals. Phenocrysts of olivine in the lavas have significantly lower forsterite contents of Fo60-72, whilst groundmass microphenocrysts are less forsteritic again (Fo47-68).

Magnetite is ubiquitous throughout the lava and xenolith suites. As previously mentioned magnetite and olivine are not found crystallising synchronously. Magnetites in the xenoliths are relatively MgO (3.5-4.5wt.%), Al_2O_3 (5-9wt.%) and TiO_2 (5-9.5wt.%) rich. Whilst magnetites found in the lavas are poorer in MgO (2-3.5wt%), Al_2O_3 (3-6wt.%) and TiO_2 (4-6wt.%) comparatively.

Micas within the cumulate xenolith groups are phlogopitic in composition. Phlogopite compositions do not show significant variation between the different cumulate groups, whilst even within the groups there are large variations in chemistry; crystals with the lowest Mg# often contain higher TiO2 contents and increased volatile (Ba and Cl) contents.

Trace element geochemistry

The xenoliths are composed of only five main minerals (Cpx, Amph, Mag, Ol, Plag) with phlogopite occasionally abundant and some accessory apatite. Olivine is relatively scarce and is only host to Ni and Co. Magnetite has low abundances of most trace elements except for Ti and V and plagioclase has low traces except for Sr and Eu. Both Cpx and Amph have more complex trace element compositions and it is likely that fractionation of these has a large influence on the composition of the differentiated melts. Trace element compositions of these two minerals and interstitial glass from xenoliths 88/309 and 88/310 are shown in figures 16a and 16b. The Cpx and Amph REE patterns (fig. 16b) are completely parallel, with Amph up to approximately twice the REE concentration of Cpx. Both Amph and Cpx have heavy REE concentrations that decrease continuously from Dy to Lu whereas the lavas (fig. 10b) and glass have complementary upward trending patterns between Tm and Lu. Whole rock xenolith REE patterns are like those of Cpx and Amph minerals reflecting the domination of CPX or Amphibole. The 88/310 glass is an interstitial phase invading a partly disaggregated pyroxenite. It has a more differentiated composition than any of the Sangeang Api lavas, but has similar incompatible element pattern. One obvious contrast between the Cpx and amphibole is Ba. Amphiboles have high concentrations and large positive Ba anomalies whereas in Cpx Ba is depleted. Cpx has very low Ba/Th ratios whereas by contrast amphibole has very high Ba/Th. As discussed below this may provide important implications for the understanding of the origin of the large positive $^{226}Ra/^{230}Th$ anomalies in some of the xenoliths and their minerals (Turner et al., 2003). The glass also has a significant negative Ba anomaly which could reflect the impact of amphibole fractionation.

The lavas tend to have higher U/Th ratios than the xenoliths which implies that D_U/D_{Th} for melt fractionation is < 1 if the xenoliths are driving fractionation. This is consistent with the experiments of Wood et al. (1999) that indicate that for CPX the ratio D_U/D_{Th} is <1.0 at lower pressure (less than 1.0 GPa).

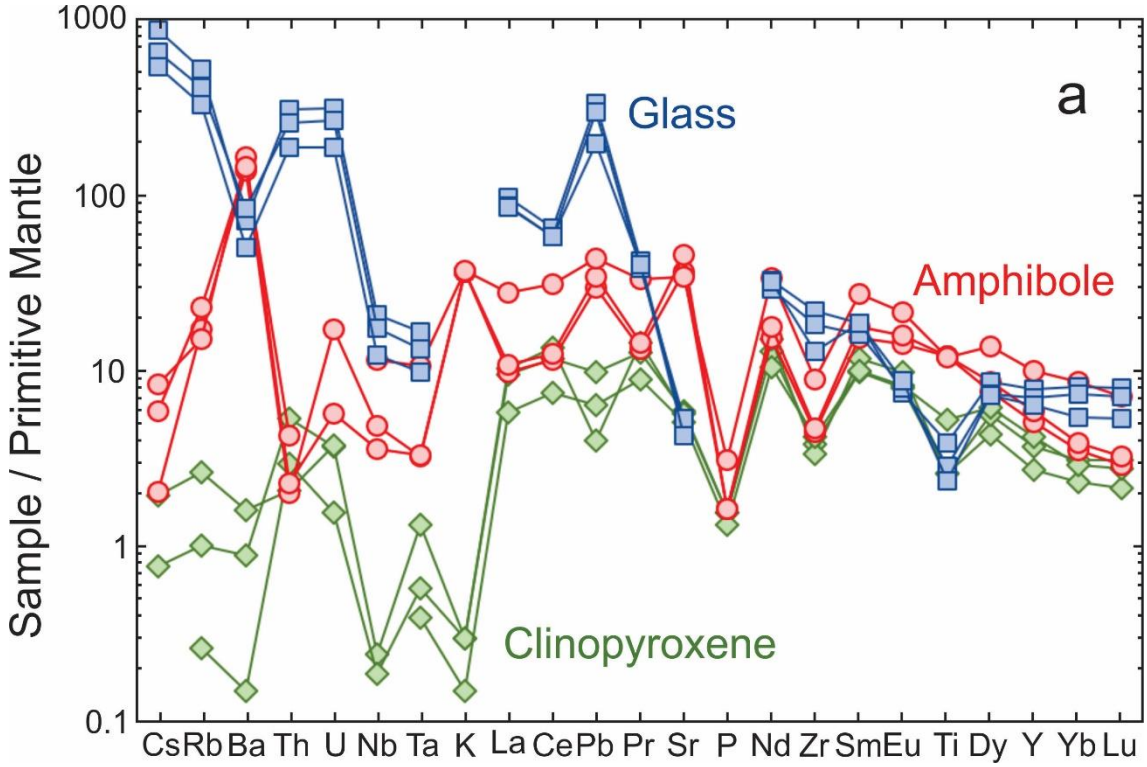

Figure 16a: Representative incompatible element profiles of clinopyroxene (green diamonds - BC14/023, BC14/048), amphibole (red circles - BC14/048, SA12-X011) and glass samples (blue squares – SA88-309, SA88-310) relative to primitive mantle values of McDonough and Sun (1995).

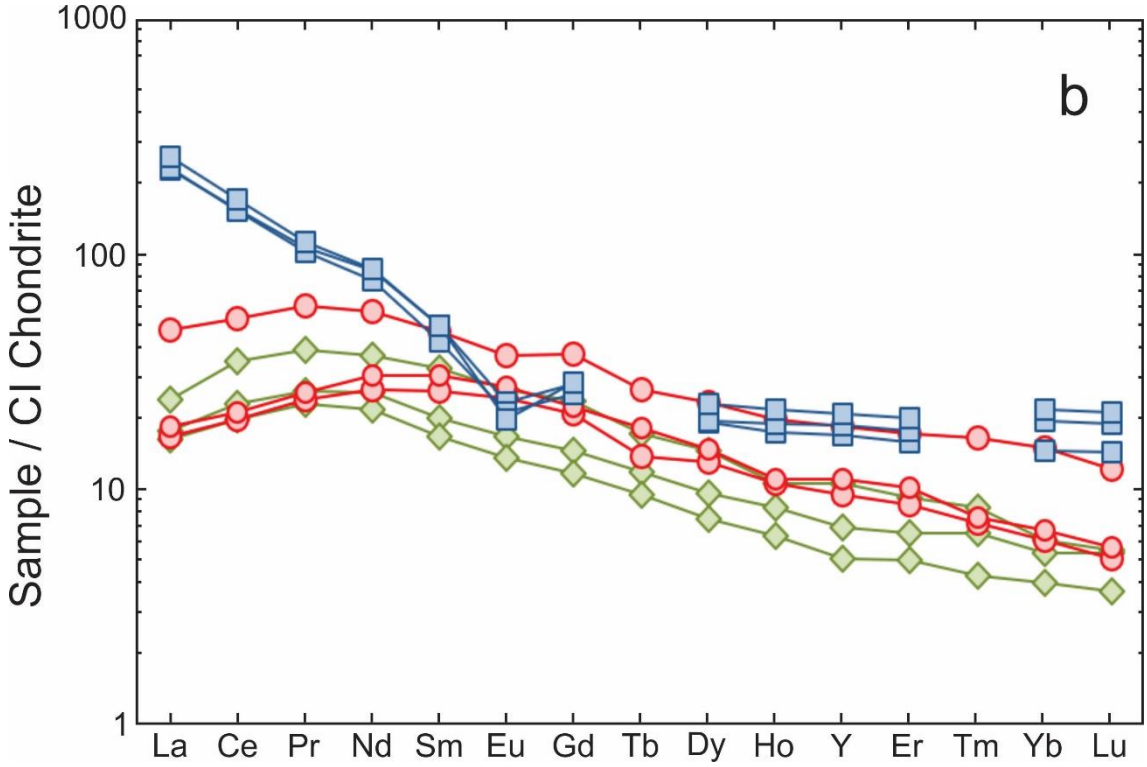

Figure 16b: Representative REE profiles of clinopyroxene, amphibole and glass relative to CI Chondrite values of McDonough and Sun (1995). Symbols and selected samples same as figure 16b.

DISCUSSION

Fractionation and differentiation in the Sangeang Api magmatic system

It appears from the whole-rock and trace element data that the Sangeang Api lavas and cumulate xenoliths are co-genetic. Major element discrimination diagrams display trends that suggest that fractional crystallisation of the xenoliths is driving the compositional variation in the lavas. This is supported by overlapping isotopic compositions and the similarity in trace element characteristics between the three suites of rocks.

Initial crystallisation in the Sangeang Api magmas is dominated by the crystallisation of both clinopyroxene and either magnetite or olivine. The most primitive cores of these minerals display Mg# in the range of 0.7-0.85 (some rare cores approach Mg# of 0.9), recording evidence of crystallisation from melts of similar Mg# to the Sangeang Api lavas. This suggests that the cumulate xenoliths were not crystallised from primitive peridotite derived melts. Rather that they crystallised from magmas that were previously fractionated or sourced from a mafic rather than ultramafic source. The presence of some rarer highly magnesian (Mg# ~0.9) cores hints at the presence of more magnesian melts that are not observed among the Sangeang Api lava suite. The most primitive clinopyroxene cores show evidence of significant Ca-Tschermak substitution and have high Wollastonite contents, suggesting that these minerals formed in equilibrium with Ca-rich and silica undersaturated melts.

$$CaAl_2SiO_6 + SiO_2 \leftrightarrow CaAl_2Si_2O_8$$

$$Ca-Tschermak + Melt \leftrightarrow Plagioclase$$

The left hand side of the equation above will be favoured at low SiO_2 activity ($aSiO_2$) and high pressures and temperatures (Arculus and Wills, 1980). Thus, at high pressures and temperatures the primitive silica undersaturated magmas of Sangeang Api are likely to crystallise clinopyroxenes with a significant Ca-Tschermak component and suppress the crystallisation of plagioclase, supporting what is observed in the pyroxenites. It is not only, however, the most primitive clinopyroxenes that display Ca-Tschermak substitution, clinopyroxenes throughout the sequence display a significant Ca-Tschermak component, suggesting that they crystallised from similarly Ca-rich and silica-undersaturated magmas. There is a negative correlation between Mg# and CaTs composition (fig. 13c), with the most primitive clinopyroxenes displaying the lowest CaTs content (~0.05). This suggests that the most primitive clinopyroxenes crystallised from melts with a low Al/Si ratio and high water content (Muntener et al., 2001). The trend observed in the clinopyroxenes to less magnesian and calcic compositions suggests that the equilibrium magmas from which they were formed were undergoing continuous fractionation and cooling under hydrous conditions (Muntener et al., 2001).

Olivine and magnetite are also primary cumulate minerals in the pyroxenites. However olivine and magnetite are never observed in the same assemblage, implying a phase change whereby olivine crystallisation is replaced by magnetite crystallisation (or vice-versa). Similar phase relationships have been observed in the Duke Island ultramafic suite

of Alaska (Irvine, 1974), with early olivine crystallisation giving way to magnetite crystallisation in later successions. This change from olivine to magnetite crystallisation is interpreted to be due to an oxidation of the magma caused by the onset of magnetite crystallisation, leading to olivine no longer being a stable phase at the solidus. A similar process is likely occurring in the Sangeang Api magmatic system, with magnetite being present in all xenoliths except for the olivine-pyroxenites. The olivine-bearing samples contain clinopyroxene with some of the highest recorded Mg#, suggesting crystallisation from the more primitive (and thus earlier) magmas. It is likely therefore that the magnetite crystallising magmas are more oxidised than those that have crystallised olivine. Olivine fractionation would act to drive the magmas to a more oxidised state, however, cumulate olivine is not seen in proportions high enough to be the sole driver of oxidation. A more likely candidate is degassing driven oxidation, with early wet and volatile-rich magmas progressively becoming oxidised by the degassing of H^+ and sulphide species (Mathez, 1984; Métrich et al., 2009).

Plagioclase is found most commonly within the gabbroic cumulates, and more rarely in small amounts in the pyroxenite cumulates. At first sight, the Sangeang Api magmas follow a uniform evolution series, with primitive melts driving plagioclase-free pyroxenite crystallisation, followed by the saturation of plagioclase and the production of the gabbroic cumulates. However, this is not observed within the trace element data, whereby, there is no sequential evolution of trace elements with Mg#. Thus, suggesting that these magmas crystallised somewhat in parallel. If the primitive melts crystallising both the gabbroic and pyroxenitic cumulates are not sequential their geochemical evolution must be driven by other processes instead. At high pressures and high aH_2O the stability field of plagioclase will decrease in size, and will only increase at shallower pressures, lower temperatures or lower aH_2O (Foden and Green, 1992; Krawczynski et al., 2012). It therefore seems likely that pyroxenite producing magmas at Sangeang Api crystallised at greater crustal depths and were saturated with respect to water, thus, suppressing plagioclase crystallisation and favouring clinopyroxene and olivine crystallisation. Therefore, the magmas producing gabbroic cumulates must have been drier and shallower, likely through magmatic decompression and degassing (Krawczynski et al., 2012). This is supported by the presence of hydrous phases (amphibole and phlogopite) being found primarily as interstitial phases in the pyroxenite cumulates and only emerge as primary cumulate phases within the gabbros. As the magmas decompress and degas the stability field of amphibole and phlogopite will expand (Foden and Green, 1992), whereas in the pyroxenite samples they likely represent the final stage of crystallisation from water-saturated, high-pressure melts. Some gabbro samples are populated only by amphibole, plagioclase and magnetite, suggesting crystallisation from relatively cold (<900˚C) magmas at moderate depths (100-650MPa) (Krawczynski et al., 2012). In some samples clinopyroxenes with primitive cores (Mg# >0.8) display amphibole replacement rims. Amphibole replacement of clinopyroxene in arc magmas and thus amphibole control over fractionation has been proposed as a common process in arc magmas (Davidson et al., 2007; Smith, 2014). Given the close similarity in trace element compositions, particularly REE profiles, between the

amphiboles and clinopyroxenes there is some suggestion that this process may be occurring in the Sangeang Api magma system.

Using the amphibole formulations of Ridolfi et al. (2010) and Ridolfi and Renzulli (2012) it is possible to calculate the chemometric and thermobarometric conditions of the magmas that crystallised the amphiboles. The results of these suggest that the amphiboles formed over a broad range of temperatures (~975-1075˚C), pressures (~350-950MPa), water-contents (~2.8-6.2wt.% H_2O) and were highly oxidised (ΔNNO ~0.1-1.2). The different lithological groups showed distinct differences in formation with the gabbros suggesting crystallisation from the deepest, wettest and hottest magmas to some of the shallowest and coolest, whilst the pyroxenites suggest crystallisation at intermediate pressures, temperatures and water content, but relatively high oxidation states. As might be suggested the amphiboles found in the lavas suggest crystallisation at the lowest pressures and temperatures, as well as water contents and redox states. It has been suggested by some that the pressures calculated by the Ridolfi formulations are not reliable (Erdmann et al., 2014), therefore it was necessary to test the calculated pressures against other barometers. Using the Nimis and Ulmer (1998) clinopyroxene barometers for samples with both clinopyroxene and amphibole shows a similar pressure range ~400-700MPa, however the highest pressure amphiboles correlate to the lowest pressure clinopyroxenes (and vice-versa). For amphiboles in the Mg# range of 74-84 it was also possible to apply the barometric solutions of Krawczynski et al. (2012); averages of their Al^{VI} and Mg# barometers return pressures hat correlate reasonably well with the pressures calculated by the Ridolfi et al. (2010) and Ridolfi and Renzulli (2012) formulations. Therefore, we believe we can be confident in the pressure ranges estimated by the amphibole formulations. These results bring up some interesting questions and are discussed further in chapter 3.

The dominant crystallisation sequences suggested by the cumulate phase relationships are as follows:

$$Pyroxenites: Cpx + Oliv \rightarrow Cpx + Mgt$$

$$Gabbros: Cpx + Plag + Mgt \rightarrow Cpx + Plag + Mgt + Hbl \pm Biot$$
$$\rightarrow Plag + Hbl + Mgt$$

In an attempt to recreate the differentiation trends and cumulate xenolith associations we applied a least squares mixing solution to 4 separate stages of the lava differentiation trend; the results of which can be seen in figure 18. These mixing solutions produce crystallisation sequences similar to those observed in the lavas and cumulates as well as producing fractional crystallites compositionally similar and overlapping to the cumulate xenolith groups observed. The initial stage of differentiation was driven by the fractional crystallisation of 83.5% clinopyroxene, 8.8% magnetite and 7.7% olivine. Whilst the stage 2 differentiation trend was driven by 85.7% clinopyroxene, 8% olivine and 6.3% plagioclase. The two initial stages of crystallisation display the importance of clinopyroxene and olivine as early forming mineral phases in driving the observed early

	CPX	OLIV	MGT	PLAG	BIOT	HBL	APAT
STAGE 1	83.5%	8.8%	7.7%				
STAGE 2	85.7%	7.9%		6.3%			
STAGE 3	33%		11.9%	47.4%	7.5%		
STAGE 4	8.1%		10.8%	38.9%		41.3%	0.8%

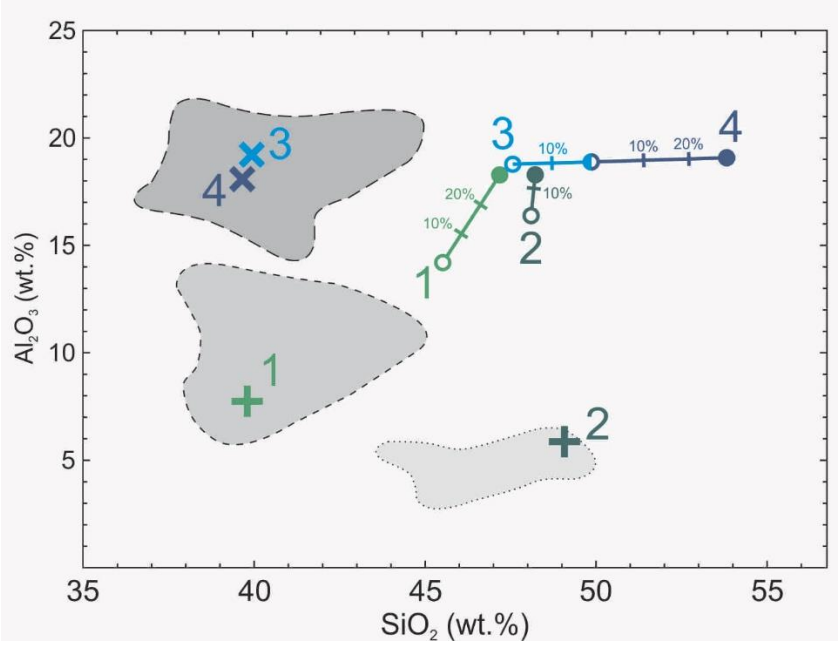

Figure 18: Diagram showing outcome of least squares mixing solutions. Each stage is numbered 1 to 4 and assigned a colour. The open symbols represent the starting melt composition and the closed circles represent the final product. Tick marks represent percentage of melt crystallised by fractional crystallisation. The cumulate products calculated by these fractional crystallisation trends are shown by crosses 1 through 4 and represent stages 1 through 4 of melt differentiation respectively. Shaded grey areas in background represent the range of Sangeang Api xenolith compositions for comparison to calculated cumulates.

differentiation trends from the primitive, parental magmas and are typical phases in the initial development of hydrous calc-alkaline magmas (Grove et al., 2003; Nandedkar et al., 2014). However, the initial stage shows that both olivine and magnetite are crystallising simultaneously, something that is not observed in the samples. Given that we observed *cpx-mgt* and *cpx-ol* cumulates, as well as late magnetite in some olivine bearing samples it is possible that the initial stage may not be crystallising both olivine and magnetite on the solidus at any given moment. Instead, there may be another parameter controlling the stability of specific phases at any given time, such as water content, oxidation state or pressure. The calculated melts display significant discrepancies in P_2O_5 and K_2O when compared to observed samples. The difference in P_2O_5 is likely due to the presence of small amounts of apatite, whereas the observed results require the addition of K_2O from elsewhere. The stage 3 differentiation trend was driven by crystallisation of 47.5% clinopyroxene, 33% clinopyroxene, 12% magnetite and 7.5% phlogopite. Stage 4 differentiation was driven by 41.3% amphibole, 38.9% plagioclase, 10.9% magnetite, 8.1% clinopyroxene and 0.8% apatite. Cumulates corresponding to these crystallisation sequences compare with average gabbro compositions. When compared to the initial fractional crystallisation trends this later differentiation is dominated by plagioclase, magnetite and hydrous minerals (phlogopite and amphibole), showing the decreasing role of clinopyroxene later in the crystallisation sequence. This is

likely due to decompression and cooling expanding the field of plagioclase, phlogopite and amphibole stability (Foden and Green, 1992).

Trace element modelling

The modelling described below has differentiated the trends produced by the basic subdivision of the xenoliths into the two groups; Group 1 the pyroxenites and Group 2 the gabbros. As illustrated by the covariation of Sc and Ce (fig. 19) the lavas show two discreet trends. One of these which shows substantial Sc depletion and limited Ce enrichment extrapolating towards the pyroxenites, while the other with significantly more enrichment of Ce for a given amount of Sc depletion extrapolates to the gabbro cumulates. These relations are also shown in figures 5e and 5f. The implication of this relationship is that the compositions of the lavas may not always result from successive pyroxenite and then, with the onset of plagioclase crystallization, of gabbroic fractionation, but the two processes may operate to some degree in parallel. This likely reflects cooling histories of different magma batches with varying water content, oxidation state and pressures.

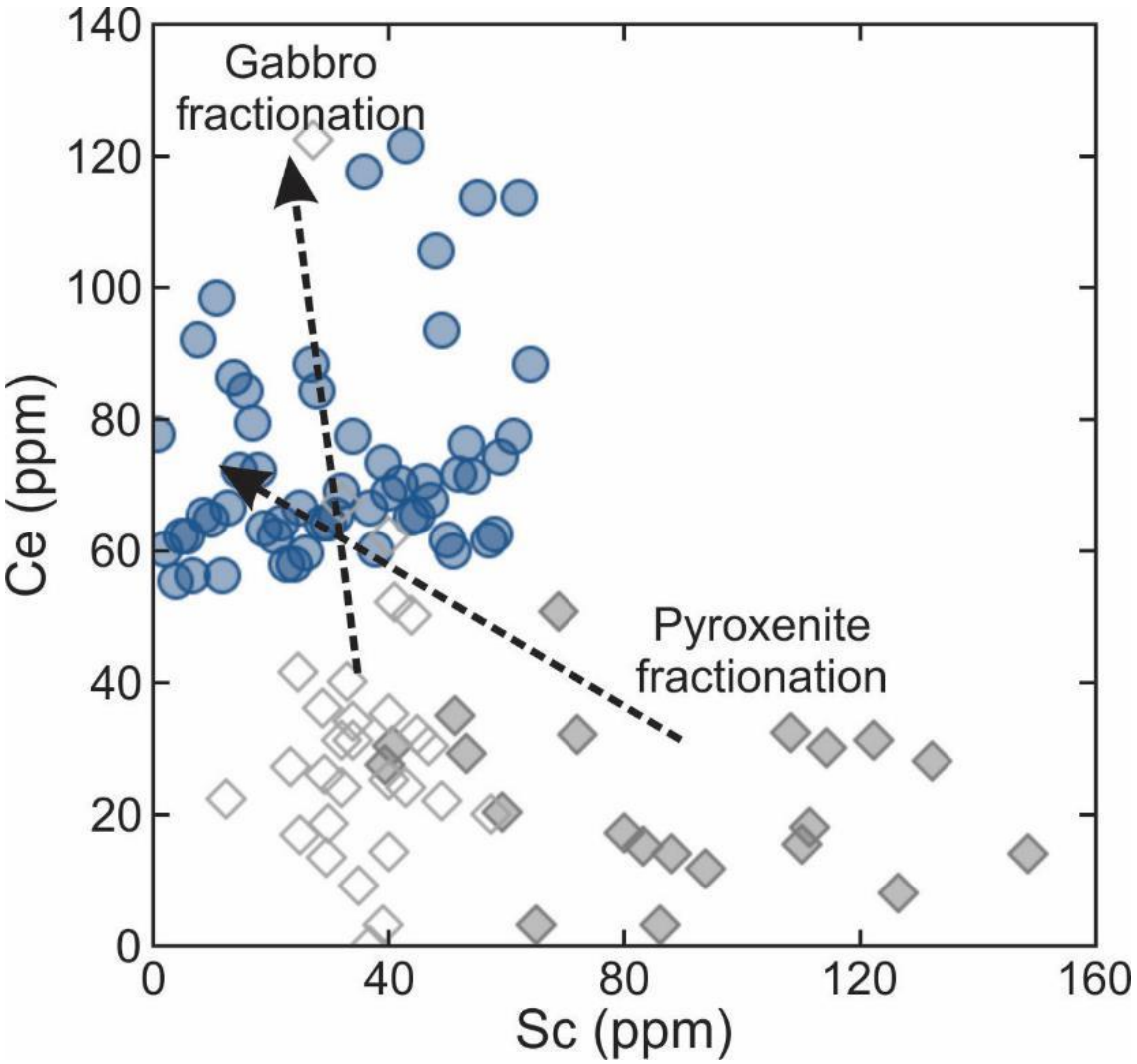

Figure 19: Sc vs. Ce diagram displaying the effects of pyroxenite vs. gabbro fractionation on the trace element composition of the Sangeang Api lavas.

The formulations of equilibrium or fractional crystallization (Shaw, 1970) describe the trace element variation of a melt based on the fraction of crystallization and the bulk distribution coefficient of a given element. These formulations allow the trace element composition of the complementary crystals and melts to be determined. It is therefore possible to assess if the Sangeang Api xenoliths have trace element compositions that are consistent with their control of the melt evolution and with appropriate partition coefficients.

Modelling of the covariation of the melt evolution of Rb and Sc (fig. 20a) is illustrative of the approach taken. The same process was applied to Sr-Rb, Zr-Sr, Y-Rb, Ti –Rb, V-Rb and Ce-Rb (figs. 20b-20g). The partition coefficients resulting from these calculations are summarized in table 2. The trace element concentration of the parental melt crystallising the pyroxenite suite (C_o) was taken as a value on the least fractionated extrapolation of the Sangeang Api lava trend. The starting composition for gabbroic series (C_o) was assumed to be slightly more fractionated. The phenocryst population of the lavas and the xenolith mineral assemblages are dominated by 5 main minerals: clinopyroxene, plagioclase, olivine, amphibole and magnetite, together with accessory apatite. If the occasional occurrence of phlogopite/phlogopite is discounted, then with respect to each of these Rb is a highly incompatible element and its enrichment during fractional crystallization of a melt becomes close to 1/F (where F is the fraction of melt remaining). The lava suite displays a range of Rb concentrations from 65ppm to 114ppm indicating a total potential % crystallization of between 40 and 50%. Figure 20a plots the covariation of Sc and Rb and the distribution coefficient that simultaneously modelled both the values and trends of the xenoliths and the lavas was determined. Because the Group 1 xenoliths are composed of varying proportions of clinopyroxene, olivine and magnetite and amongst these, Sc is only partitioned to cpx and is incompatible with respect to the other minerals the Sc distribution coefficient value determined will in fact be close to that of cpx alone and can be compared to known experimentally determined values (table 3) The result from this element pair is illustrative of that achieved for other pairs (Figs 20b-g). These calculations indicate that the compositional range of the lavas is achieved by ~45% fractional crystallization.

Each of the figures 20 show that the composition of many individual xenoliths from both the gabbros and the pyroxenites fall between the most incompatible element poor xenoliths and the lavas. The cumulate compositions that drive the melt differentiation calculated in these figures always correspond to the most incompatible element-poor xenolith bulk compositions. Each of figures 19 show that the xenoliths with greater than the minimum incompatible element concentrations lie on mixing trends between the lavas and the calculated cumulates. A single trend for each of the xenolith groups is show. This trend illustrates contamination of the cumulate mineral assemblages by melts. A large proportion of the xenoliths show contamination by <20% melt. This melt contamination may be the result of one of several processes:

- Inefficient extraction of melts that precipitated the cumulate assemblages, resulting in intercumulate growth.

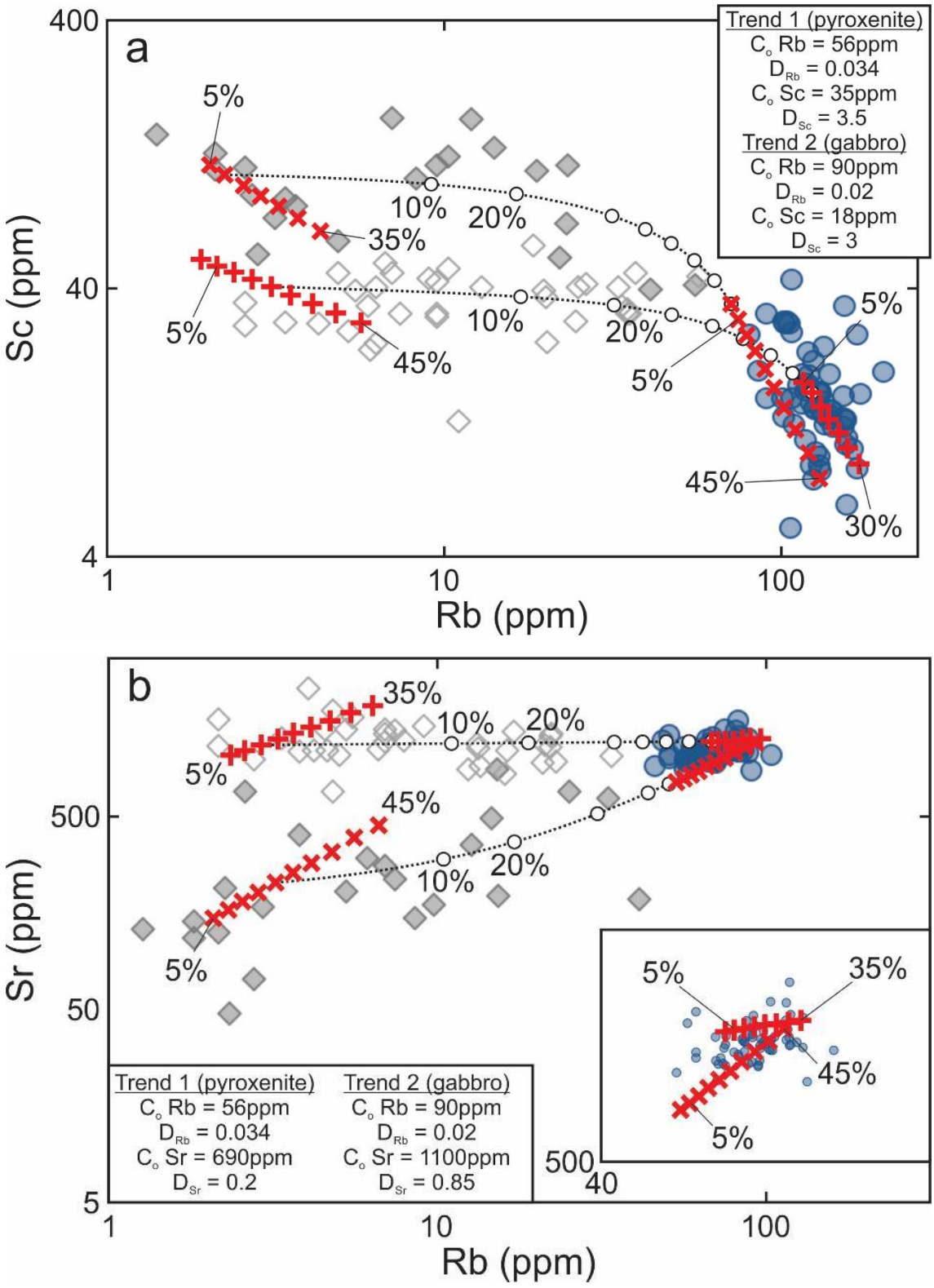
a
Trend 1 (pyroxenite)
C$_o$ Rb = 56ppm
D$_{Rb}$ = 0.034
C$_o$ Sc = 35ppm
D$_{Sc}$ = 3.5
Trend 2 (gabbro)
C$_o$ Rb = 90ppm
D$_{Rb}$ = 0.02
C$_o$ Sc = 18ppm
D$_{Sc}$ = 3
Sc (ppm)
Rb (ppm)
400
40
4
1
10
100
5%
10%
20%
35%
45%
30%
b
Sr (ppm)
Rb (ppm)
500
50
5
1
10
100
Trend 1 (pyroxenite)
C$_o$ Rb = 56ppm
D$_{Rb}$ = 0.034
C$_o$ Sr = 690ppm
D$_{Sr}$ = 0.2
Trend 2 (gabbro)
C$_o$ Rb = 90ppm
D$_{Rb}$ = 0.02
C$_o$ Sr = 1100ppm
D$_{Sr}$ = 0.85

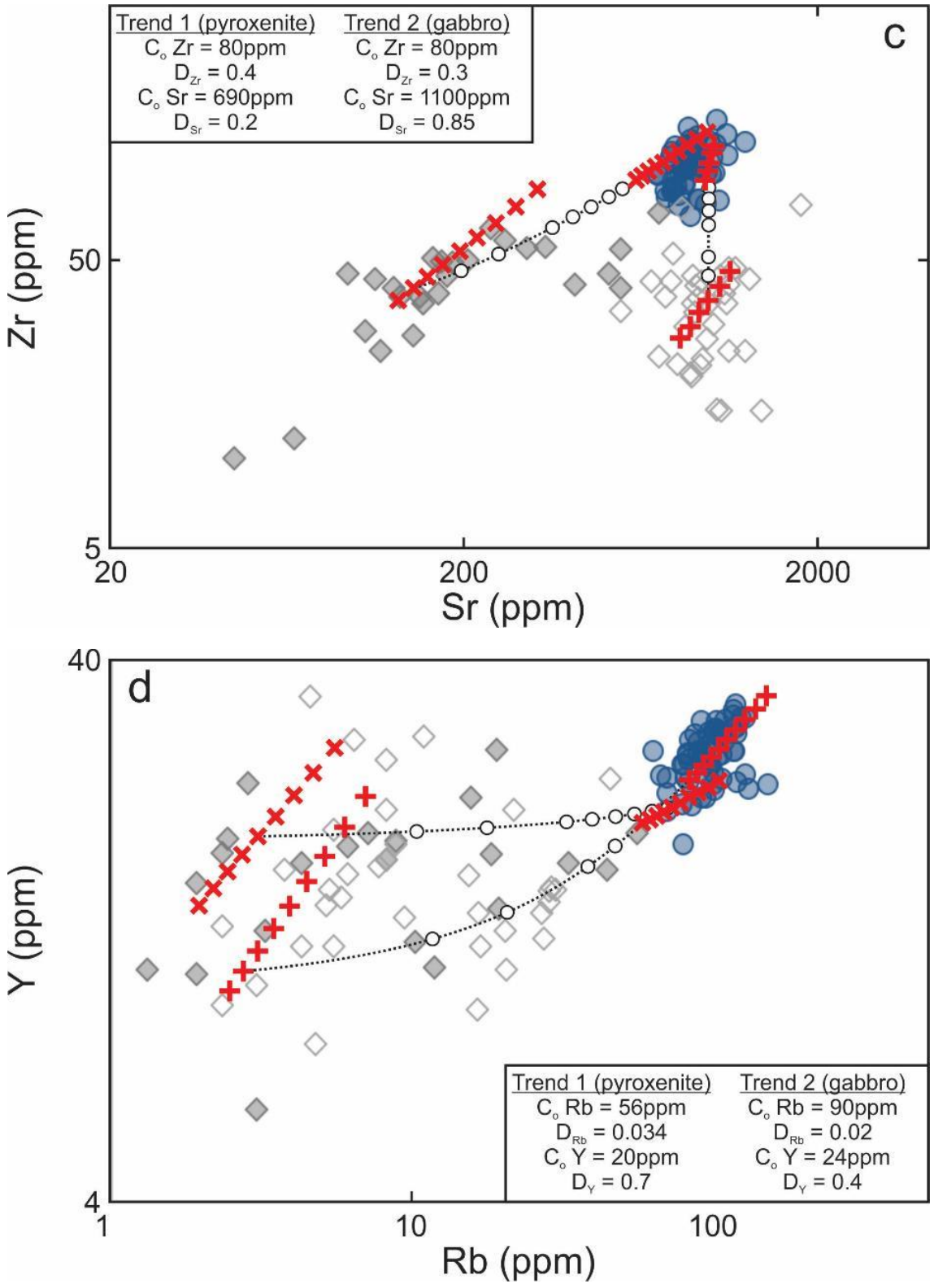
Trend 1 (pyroxenite)
C$_o$ Zr = 80ppm
D$_{Zr}$ = 0.4
C$_o$ Sr = 690ppm
D$_{Sr}$ = 0.2
Trend 2 (gabbro)
C$_o$ Zr = 80ppm
D$_{Zr}$ = 0.3
C$_o$ Sr = 1100ppm
D$_{Sr}$ = 0.85
c
Zr (ppm)
50
5
20
200
2000
Sr (ppm)
40
d
Y (ppm)
4
1
10
100
Rb (ppm)
Trend 1 (pyroxenite)
C$_o$ Rb = 56ppm
D$_{Rb}$ = 0.034
C$_o$ Y = 20ppm
D$_Y$ = 0.7
Trend 2 (gabbro)
C$_o$ Rb = 90ppm
D$_{Rb}$ = 0.02
C$_o$ Y = 24ppm
D$_Y$ = 0.4

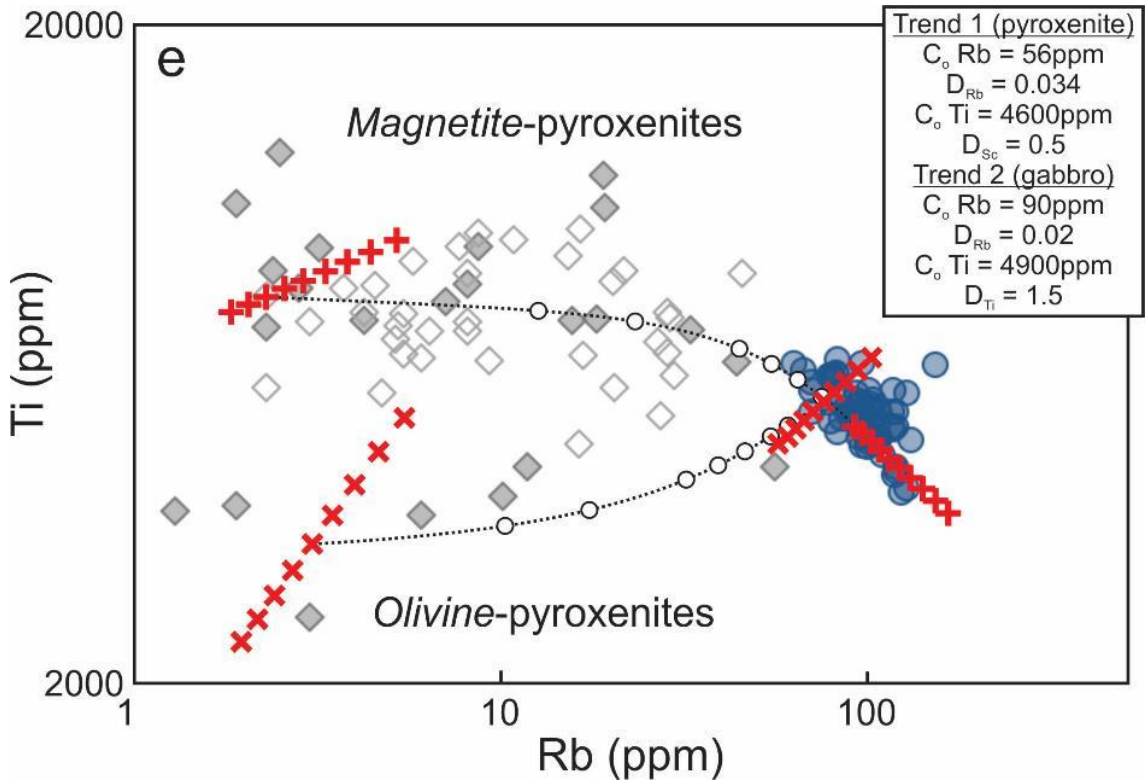
e
Magnetite-pyroxenites
Olivine-pyroxenites
Trend 1 (pyroxenite)
C$_o$ Rb = 56ppm
D$_{Rb}$ = 0.034
C$_o$ Ti = 4600ppm
D$_{Sc}$ = 0.5
Trend 2 (gabbro)
C$_o$ Rb = 90ppm
D$_{Rb}$ = 0.02
C$_o$ Ti = 4900ppm
D$_{Ti}$ = 1.5
Ti (ppm)
20000
2000
1
10
100
Rb (ppm)

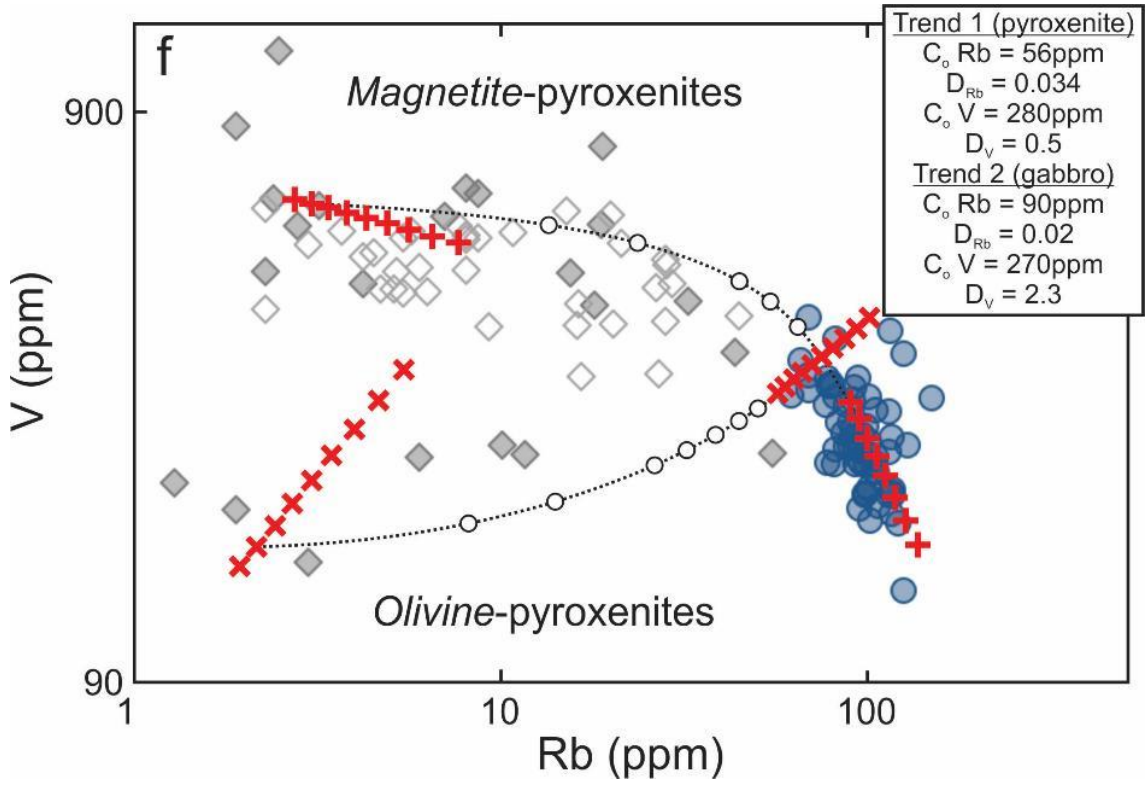
f
Magnetite-pyroxenites
Olivine-pyroxenites
Trend 1 (pyroxenite)
C$_o$ Rb = 56ppm
D$_{Rb}$ = 0.034
C$_o$ V = 280ppm
D$_V$ = 0.5
Trend 2 (gabbro)
C$_o$ Rb = 90ppm
D$_{Rb}$ = 0.02
C$_o$ V = 270ppm
D$_V$ = 2.3
V (ppm)
900
90
1
10
100
Rb (ppm)

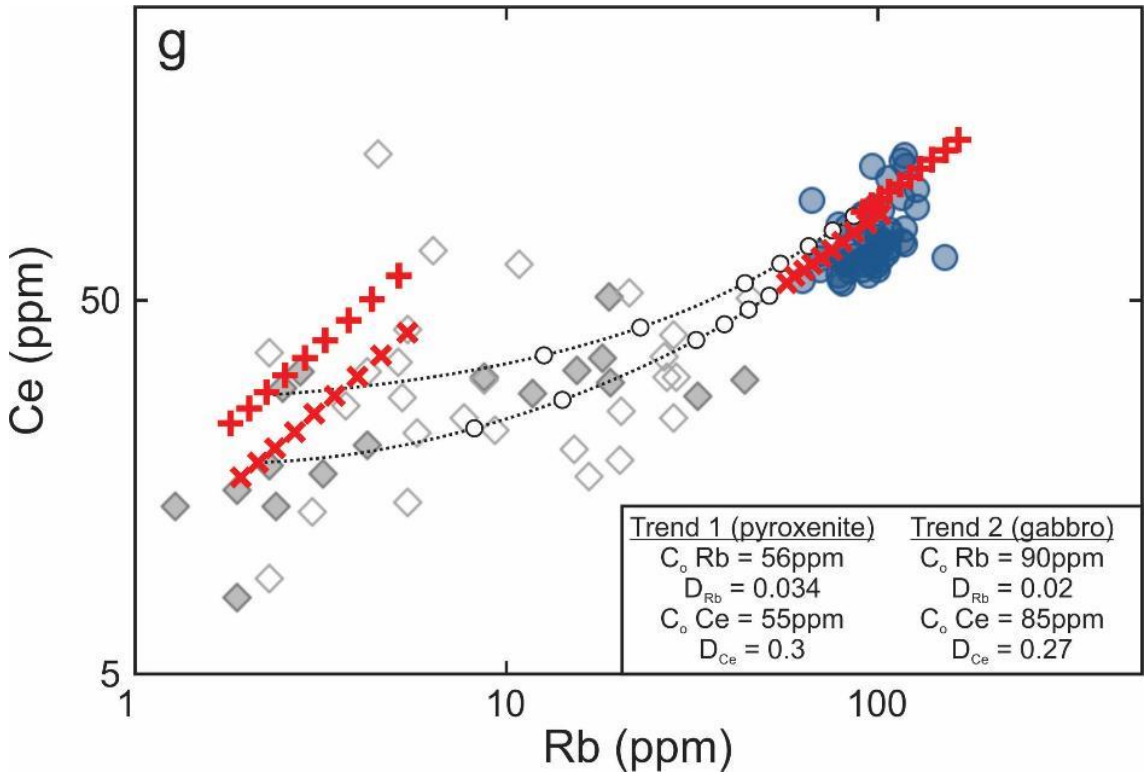

Figure 20a-g: Trace element scatter plots with fractional crystallisation models overlain. Red crosses represent melt and solid products of different degrees of fractional crystallisation of a pyroxenite. Red plus symbols represent melt and solid products of different degrees of fractional crystallisation of a gabbro. Dashed lines joining fractionated solids and liquids show the effect of contamination by melts on cumulate composition, with open circles displaying % of material added. Distribution co-efficients (D) and the initial concentration (C_o) vary between pyroxenite and gabbro fractionation and are displayed for each model and in table 2.

Element K_D	Group 1: Pyroxenite Fractionation	Group 2: Gabbro Fractionation
Rb	0.034	0.03
Sr	0.2	0.85
Sc	3.5	3
Zr	0.4	0.3
Ti	0.5	1.5
V	0.5	2.3
Y	0.7	0.4
Ce	0.3	0.27
Nd	0.4	0.25
Yb	0.6	0.4

Table 2: K_D values for elements utilised in trace element modelling.

- Intrusion of melt veins into the xenolith or to the pre-xenolith pyroxenite or gabbro intrusion during or before eruption.
- Disaggregation of loosely consolidated cumulate assemblages and their invasion by melts.

- Cryptic enrichment from percolative flow of fluids or melts resulting in grain boundary modification and reaction with the cumulate matrix, potentially resulting in amphibole or phlogopite precipitation.

Petrological evidence for these processes is observed throughout the cumulate xenolith suite and is discussed further in a later section.

If the bulk composition of the xenoliths is in fact the result of precipitation from the melts erupted as lavas, then the trace element relationship between xenolith and lava should represent a partition coefficient. These can then be used to model the impact of fractional crystallization of more primitive Sangeang Api lavas to produce more fractionated melts. This was undertaken using typical examples of xenoliths that had low incompatible elements recording minimal melt contamination. Using a more primitive lava (Ne-trachybasalt 48069) bulk distribution coefficients (D) were calculated for the pyroxenite trend using pyroxenite xenolith SA24 and the gabbroic trend utilized xenolith SA27. The bulk distribution coefficients for these two are given in table 3. The pyroxenite control is distinguished by relatively high D values >1 for Sc, Co and Ni. The gabbros bulk D values near or >1 for Ti, V, Sr and P. These reflect the presence of magnetite, plagioclase and apatite. Figures 21a and 21c show the gabbroic fractionation for the REE (fig. 21a) and for the whole incompatible suite (fig. 21c) and modelled a more differentiated Ne trachyandesite 48081. Similarly, the pyroxenite controls (figs. 21b and 21d) modelled the Ne-Trachybasalt BC14/006 (the lowest Sc sample on Sc-Ce pyroxenite trend – fig. 19). The % crystallization predicted to yield the fractionated magma was 35-45% for the gabbro fractionation and 45-55% for the pyroxenite.

The results of the trace element modelling clearly support the suggestion that the Sangeang Api xenoliths are mostly of cumulate origin and they have appropriate trace element concentrations to be the vectors that drove the fractionation lavas. The range of lava compositions are covered by up to ~50% fractionation. The conclusion based on the trace element modelling approach are also supported by:

1. The use of a least squares mixing routine and the major element composition of the lavas and xenolith minerals to estimate if the mineral assemblages of the xenoliths can drive the major element compositional variation of the lavas (see previous section) This approach also provides the relative proportions of the minerals which can then be compared to the modal determinations of the Sangeang Api xenoliths (table 1).

AND

2. The use of the thermodynamic formulation ‘MELTS’ to estimate the saturated mineral phase assemblages as they evolve during progressive cooling and crystallization. This approach allows the determination of the potential cumulate assemblages whose crystallization and segregation drives the fractionation of the lavas (see later section).

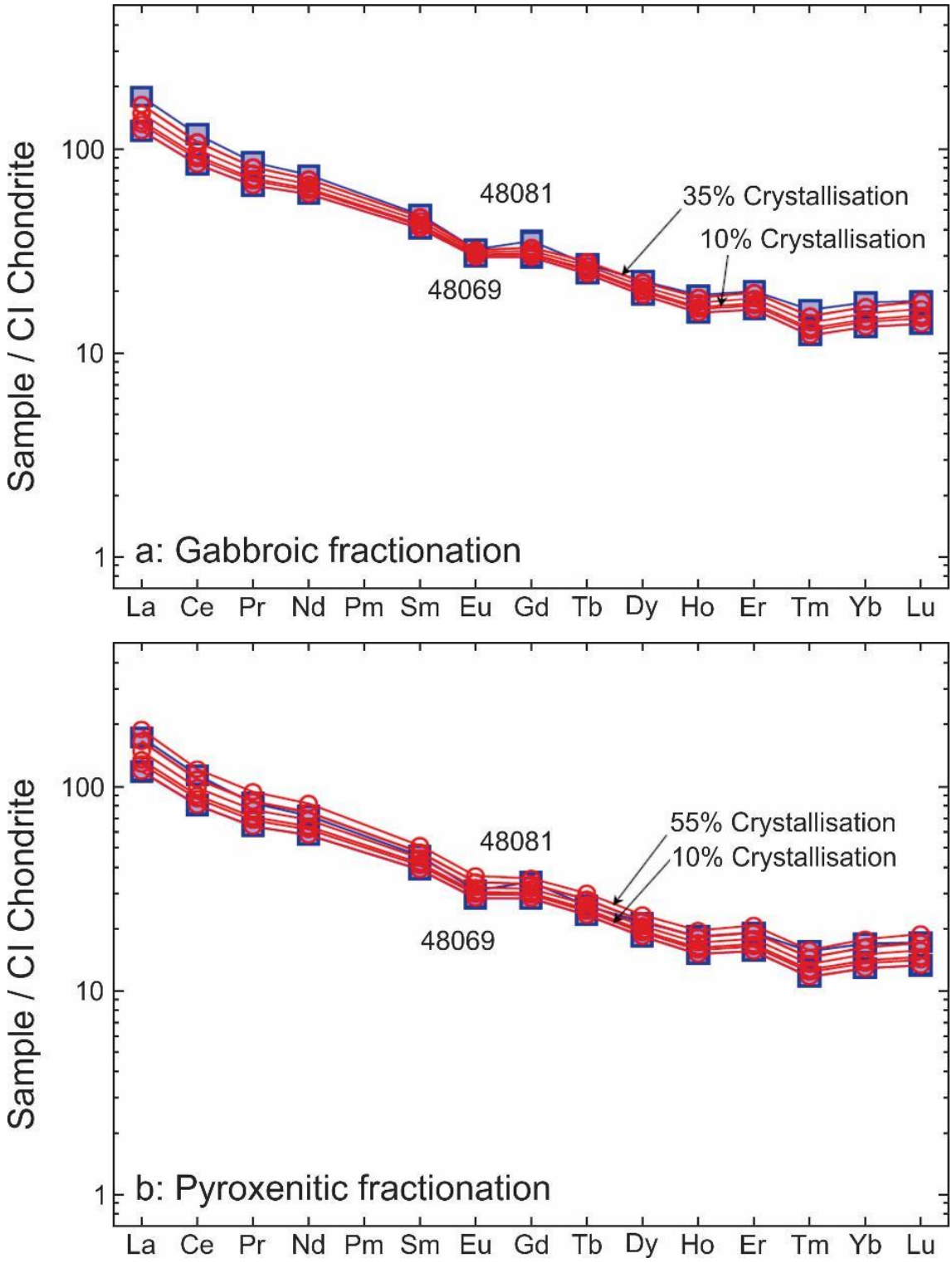
Sample / CI Chondrite
100
10
1
48081
48069
35% Crystallisation
10% Crystallisation
a: Gabbroic fractionation
La Ce Pr Nd Pm Sm Eu Gd Tb Dy Ho Er Tm Yb Lu
Sample / CI Chondrite
100
10
1
48081
48069
55% Crystallisation
10% Crystallisation
b: Pyroxenitic fractionation
La Ce Pr Nd Pm Sm Eu Gd Tb Dy Ho Er Tm Yb Lu

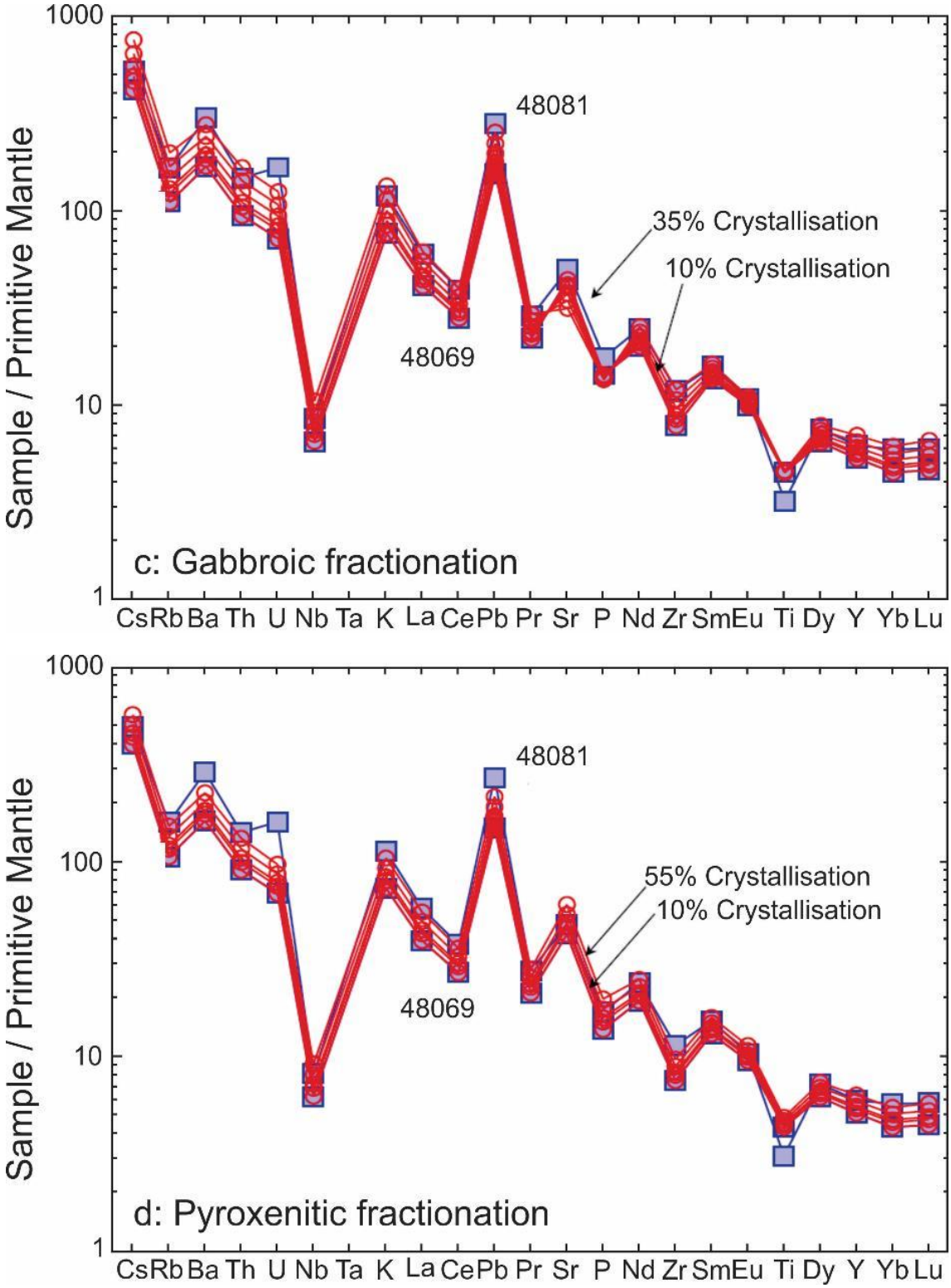

Figure 21a-d: Incompatible and REE patterns displaying the melt evolution of a primitive lava (sample 48069) using bulk distribution factors given in table 3. Figures 21a and 21c display the effects of gabbro fractionation, whilst 21b and 21d display effects of pyroxenite fractionation. A less primitive lava (sample 48081) is given for comparison.

	SA24/48069 Pyroxenite	SA27/48069 Gabbro	Group 1	Group 2	Hill et al. (2000) Cpx (4EHE)
Sc	4.400	0.960	3.5	3	2.46
V	0.751	1.352			0.51
Cs	0.182	0.009			
Rb	0.157	0.021	0.034	0.03	
Ba	0.228	0.176			0.02
Th	0.125	0.050			0.032
U	0.200	0.067			0.029
Nb	0.109	0.196			0.019
K	0.175	0.057			
La	0.214	0.321			0.089
Ce	0.326	0.419	0.3	0.27	0.148
Pb	0.136	0.182			
Pr	0.350	0.520			0.26
Sr	0.178	1.569			0.063
P	0.161	1.097			
Nd	0.407	0.611	0.4	0.25	0.38
Zr	0.414	0.282			0.283
Sm	0.550	0.700			0.49
Eu	0.582	0.818			0.75
Gd	0.625	0.750			0.7
Ti	0.732	0.969	0.5	1.5	0.512
Tb	0.591	0.682			
Dy	0.596	0.660			
Ho	0.558	0.605			0.77
Y	0.500	0.542	0.7	0.4	0.64
Tm	0.500	0.500			1.1
Er	0.519	0.558			0.76
Yb	0.455	0.477	0.6	0.4	0.8
Lu	0.412	0.412			0.61
Hf	0.500	0.500			0.58
Co	1.400	1.500			0.95
Cu	0.172	1.520			
Ga	0.439	1.122			
Ni	3.158	0.632			
Zn	0.365	0.800			

Table 3: Bulk distribution coefficients (D) calculated between pyroxenite (SA24)/gabbro (SA27) and primitive lava (48069). K_D values utilised in trace element modelling (Group 1 and Group 2) and partition co-efficients between a clinopyroxene phenocryst (4EHE) and silicate melt from Hill et al. (2000) are shown for comparison.

One key conclusion from the trace element modeling is that many of the xenoliths are contaminated or enriched probably by melts or fluids. It is possible that this process accounts for anomalies in the U-series disequilibria and for modification of the stable isotopic composition of Fe (as discussed in chapter 4). Turner et al. (2003) determined

the U-series isotopes and showed that the Sangeang Api lavas and xenoliths have significant ^{226}Ra excess, with $^{226}Ra/^{230}Th$ values up to 8. Geochemical similarities between Ra and Ba lead to the use of the Ba/Th ratio and there is a good positive correlation between Ba/Th and $^{226}Ra/^{230}Th$ (Turner and Foden, 2001; Turner et al., 2003). As illustrated in figure 16a amphibole has very high Ba and a high Ba/Th ratio, much higher than that of the melt (glass). Clinopyroxene, by contrast, has very low Ba and a very low Ba/Th ratio. Given the very high Ba content of amphibole (which in some cases may represent a cryptic enrichment of the cumulate crystal pile) and the very high $^{226}Ra/^{230}Th$ in xenolithic amphibole (Sample SA21 amphibole $^{226}Ra/^{230}Th$ = 6.617; Turner et al., 2003) it seems amphibole becomes a repository for Ba and by inference for 226Ra.

Meanwhile, the extremely low Ba/Th ratio of clinopyroxene will lead at extremely low melt fractions, perhaps during percolative grain-boundary flow through cumulate crystal piles, to significant Ra/Th fractionation. Noting that ^{226}Ra has a half-life of about 1600 years compared to that of its parent isotope (^{230}Th half-life = 75kyr), Ra anomalies will be preserved in very young xenoliths but will be extinct where enrichment is older than 8000 yrs. The concept that cryptic amphibole growth provides evidence for percolative exchange as small % melt pass through cumulate crystal piles is also important when the Fe stable isotope variations are considered (see later). The Fe stable isotope data presented in chapter 4 on minerals from the xenoliths, particularly clinopyroxene and olivine, return values inappropriate for equilibrium with the lavas and apparently shifted by diffusion from original primary values.

Melt percolation and mineral overgrowths

As discussed in the previous trace element modelling section, the cumulate xenoliths display significant geochemical evidence of post-crystallisation contamination. The possible processes leading to this contamination (inefficient extraction of melts, melt vein intrusions, cumulate disaggregation and melt invasion and cryptic enrichment by percolative flows) should leave behind observable petrological features, the evidence of which is discussed below.

Amongst many of the cumulate xenoliths the primitive anhydrous cumulate minerals display late overgrowths of less primitive material or hydrous minerals such as amphibole, suggesting that there may be percolation of previously fractionated material through cumulate piles within the Sangeang Api magma chambers. An example of these mineral overgrowths can be observed in the element map seen in figure 22 and the Mg# transect from the same crystal, there is a significant and marked compositional difference between the core (Mg# ~88) and the rim (Mg# ~80). Similarly, figure 4d displays a late clinopyroxene overgrowth rim surrounding a xenocrystic clinopyroxene phase. Some of the xenocrystic samples in the lavas display the same overgrowth textures as are observed in the cumulate xenoliths. This represents evidence of cumulate disaggregation of crystal-cumulate piles and their invasion and transport by younger melts.

Figure 22: Element map and transect showing compositional variation between core and overgrowth rim of a clinopyroxene xenocryst.

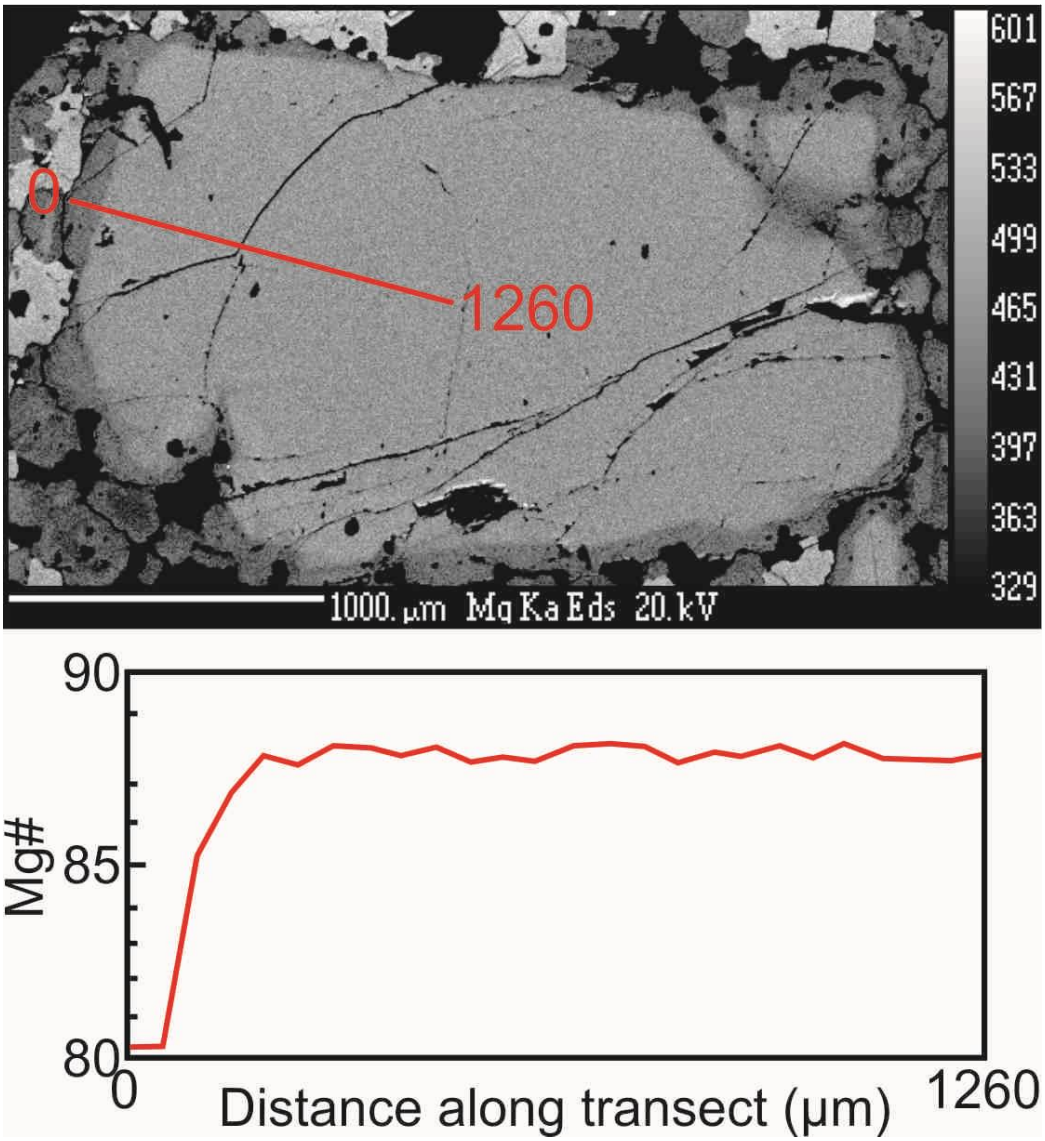

Post-cumulate amphibole and phlogopite are common in the gabbros and in some of the pyroxenites, as seen in figures 23a-c. These post-cumulate hydrous minerals display evidence of the cryptic enrichment of cumulate piles by percolative fluid flow. Post-cumulate phlogopite often displays kink-banding, suggesting that they crystallised under a stress regime (faulting?). The Mg# of these post-cumulate phases are markedly different o the primary cumulate mineralogy surrounding them, suggesting crystallisation from more fractionated melts.

Rare interstitial glass is observed within some of the cumulate samples (figs. 24a and 24c). These interstitial glasses have compositions distinct and more fractionated than would crystallise the primitive cumulates that they are surrounded by. Thus, suggesting that they crystallised from magma with a different composition to the parental melts. The source of these interstitial fluids is of keen interest, do they represent the products of fractionation or incongruent melting? This interstitial glass is hosted in the quenched areas is highly alkalic even in the absence of amphibole (rich in K_2O) suggesting that it is sourced from the incongruent breakdown of pargasite. However, the compositions of clinopyroxene overgrowths do not reflect the compositions of quenched clinopyroxene laths formed from these melts. This suggests that these clinopyroxenes cannot be sourced from the same fluids formed in these reactions. Equally the compositions of some interstitial amphiboles do not support crystallisation from such alkalic fluid (low K_2O/Na_2O ratios). Therefore, there must be two or more percolating melts that have acted to create post-cumulate overprints in the Sangeang Api magma chambers; one a product of the incongruent breakdown of amphibole and the other(s) variably fractionated partial melts. Low K_2O melt veins could have been introduced at depth within the system or during transport and eruption. The relatively low S and high Cl contents (fig. 17) suggest that these magmas were relatively degassed and thus likely represent pre- or syn-eruptive melts. Occasionally these intrusive veins of

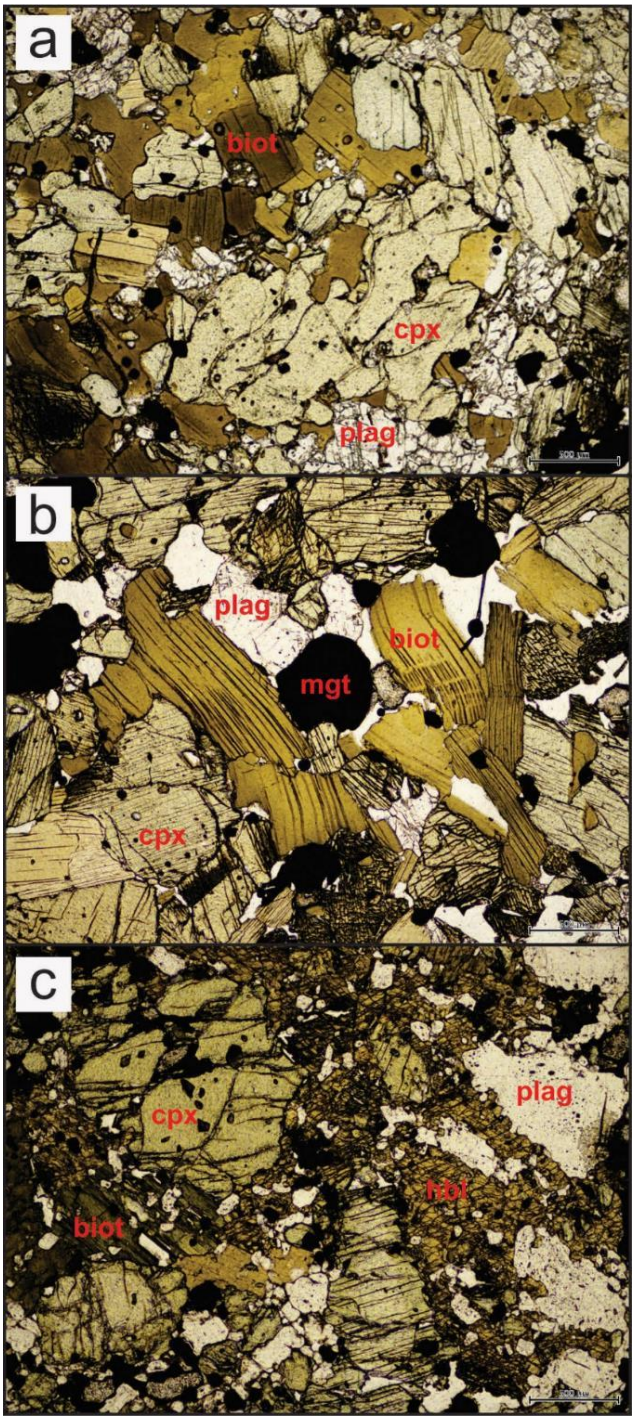

Figures 23a-c: Photomicrographs displaying textures consistent with percolative flow. 19a shows cumulate clinopyroxene with abundant post-cumulate phlogopite and smaller An-poor plagioclase. 19b shows cumulate clinopyroxene, magnetite and rare plagioclase with post-cumulate phlogopite. Note that post-cumulate phlogopite displays prominent kink-banding suggesting formation under an exacerbated stress regime such as cause by faulting. 19c shows cumulate clinopyroxene and plagioclase with prominent poikilitic hornblende and post-cumulate phlogopite.

material are composed of hydrous mineralogy (phlogopite and amphibole) rather than quenched melt (fig 24b). These likely reflect crystallisation from fractionated melts and not pargasite-breakdown melts.

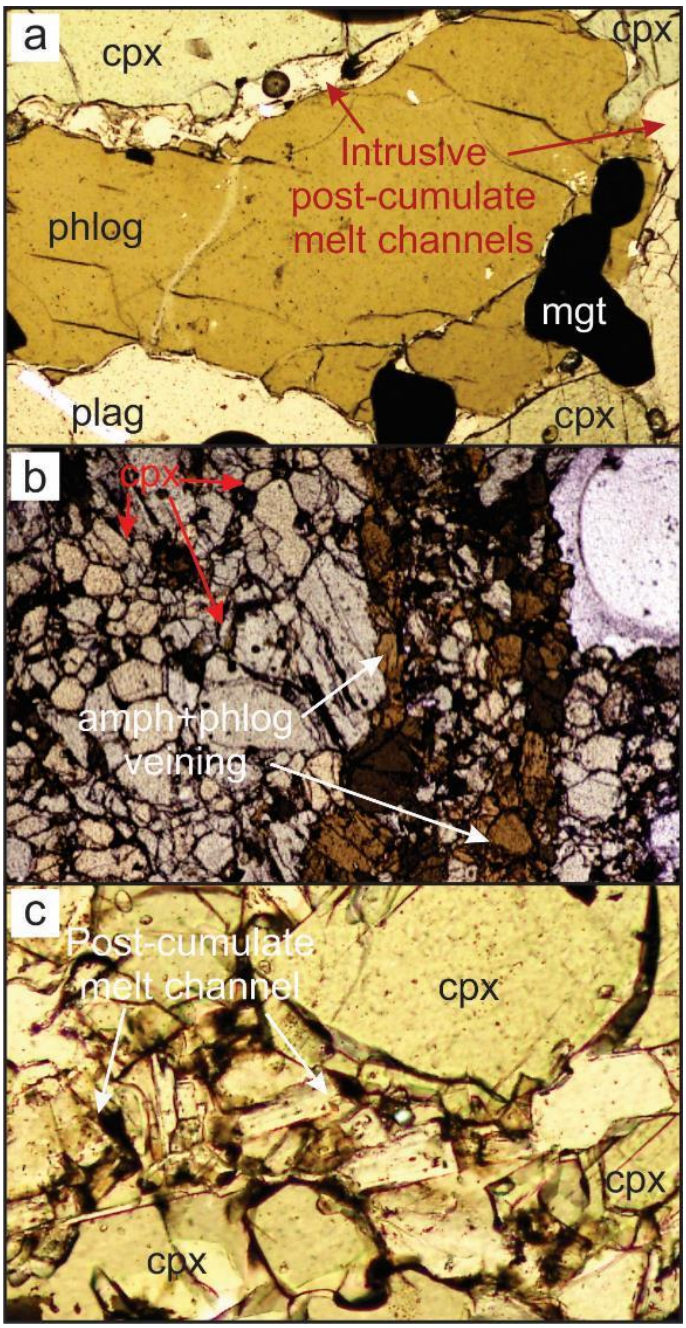

Figure 24a-c: Photomicrographs displaying evidence for the intrusion of melt channels into cumulate lithologies. Ca displays intrusive melt channels composed of low K_2O (mean K_2O = 4.98wt.%) with low An (~An60) plagioclase microlites between cumulate phlogopite, clinopyroxene and plagioclase. Cb shows amphibole and phlogopite veins intruding through a pyroxenite xenolith (note the well-developed cpx triple-junctions). Cc is a close-up of a plagioclase microlith rich (~An56) K_2O-rich (~6.5wt%) intrusive melt channel separating cumulate clinopyroxene.

Figure 4c displays an intercumulate amphibole surrounded by primary cumulate clinopyroxene within a pyroxenite sample that has not experienced disaggregation (well -eveloped triple-junctions). This intercumulate amphibole likely reflects crystallisation from a trapped melt pocket and evidences poor extraction of the melts which crystallised the surrounding cumulate mineralogy.

This begs the question of where these variably fractionated melts are sourced from and how they percolated through the cumulate pile. They may have originated from previously fractionated magmas that have ascended from deeper magma chambers. Another, possible process that could have created these observed overgrowths and late intercumulus minerals is self-convective mixing (Couch et al., 2001); whereby an open magma chamber that is being continuously or periodically heated from the base by the addition of hot, primitive magmas and cooled from the top will set up a convection cell on the scale of the magma chamber and self-mix fractionated partial melts through cumulate crystal piles. However, this seems like an unlikely process as the gabbros and pyroxenites likely

crystallised from chemically distinct magmas at different pressures and water contents, and therefore cannot have experienced magma mixing. Witham (2011) suggests that magma chambers that are injected with primitive, undegassed, volatile-rich magmas will ascend through previously degassed magmas and cumulate piles due to significant density differences. Since it is likely that the erupted Sangeang Api magmas have experienced significant decompression degassing (discussed in later section) it would suggest that degassed magmas were located in distinct crustal reservoirs and were unable to sink down and mix with previously crystallised cumulates. Throughflow of hot, undegassed melts within magma chambers may help with the disaggregation of loose cumulate piles and the entrainment of xenocrysts and more aggregated xenoliths within ascending magmas. Evidence of post-cumulate crystallisation under a stress regime suggests the presence of crustal faulting, possibly aiding in the disaggregation and entrainment of cumulate piles. Evidence of faulting within the Sangeang Api magmatic tract is discussed further in a later section.

MELTS modelling

Using the Rhyolite-MELTs program of Ghiorso & Gualda (2015) and Gualda et al. (2012) we have modelled the phase stability and melt evolution two samples (L06 and L14) under a variety of conditions between 980-1280°C and 0-8kbar. The two samples collected represent primitive end-members of the two primary major element chemistry trends (T1 and T2) observed in figure 5a-c. In an attempt to model the magma evolution and phase relationships of the Sangeang Api system we applied a variety of controls to the models to assess their effect on melt evolution; buffered vs. non-buffered fO_2, equilibrium vs. fractional crystallization and water content of the magma (1.5, 3 and 4.5wt.% H_2O). The outcomes of our modelling can be seen in figures 25 to 27. Below we discuss the outcomes and limitations of this modelling.

Firstly, it is important to acknowledge that it is very difficult, if not impossible, to crystallize all of the phases that are observed in the Sangeang Api magmas. Most important amongst these is amphibole, which makes up to 60% of the modal proportions of some xenolith samples. It has proved impossible to crystallize amphibole under any number of conditions and settings, likely this is reflecting the difficulty of crystallizing hydrous minerals (especially amphibole) within the MELTs program. Similarly, there are other phases which are found in some of the samples that have proved difficult to crystallize in these samples as well as others – particularly phlogopite. Other phases are suggested to be stable in amounts that do not reflect most of the observed xenolith or lava assemblages. Particularly garnet (figs. 25c & 25f), which is not observed in any of the samples, however, under fractional crystallization mode the program attempts to crystallize garnet below above 5kbar in both sample runs. Another, smaller problem is that the models suggest that a larger modal proportion of apatite is stable than is observed in the samples. This is most likely due to the models attempting to minimize the activity of phosphorous.

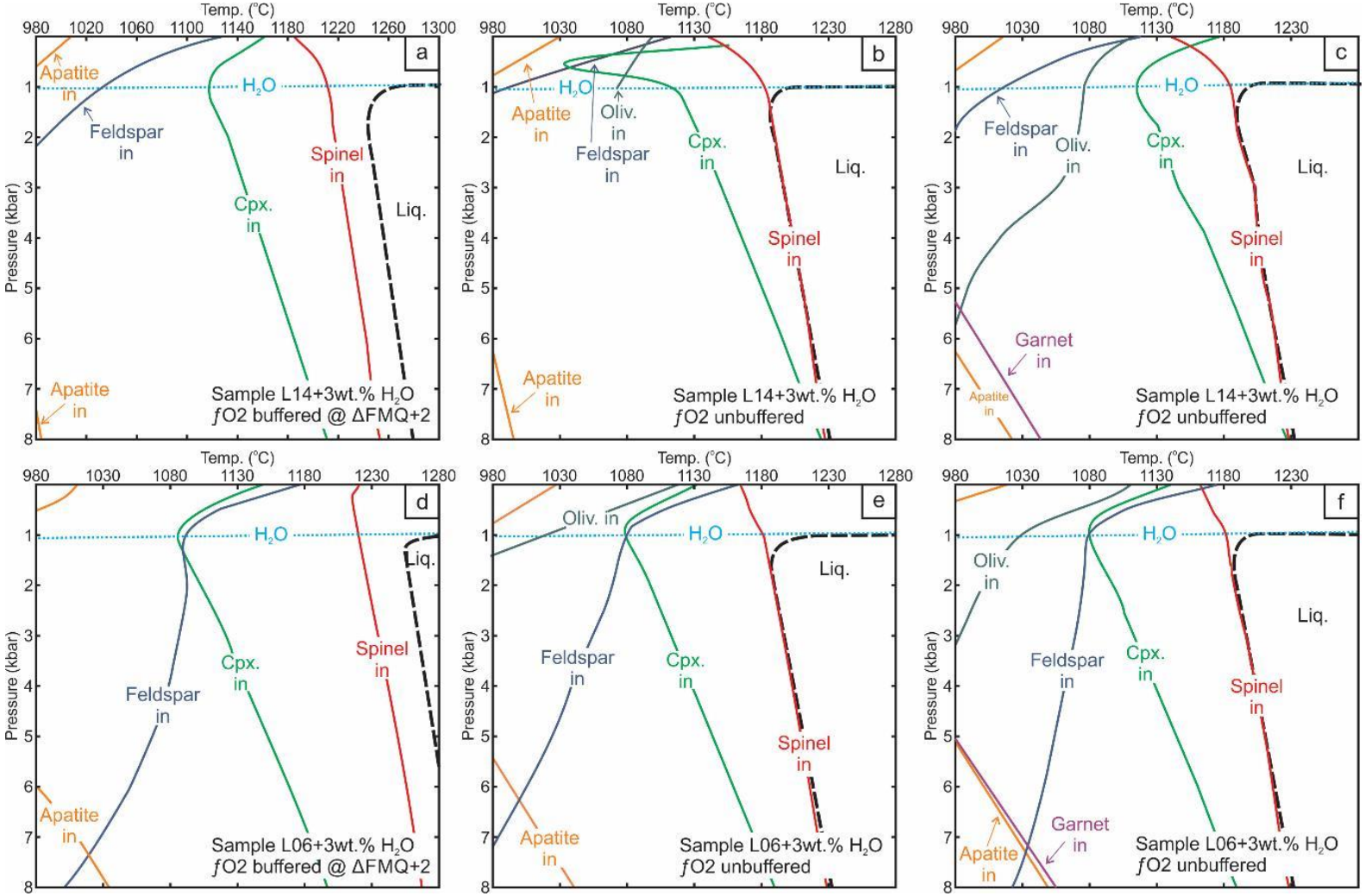

Figure 25a-f: Phase diagrams calculated using Rhyolite-MELTS (Ghiorso and Gualda, 2015; Gualda et al., 2012). Sample composition used and conditions applied to each calculation are displayed in the bottom right hand corner of each phase diagram. Sample compositions were used with an additional 3wt.% H_2O and were normalised to 100%, an initial $ƒO_2$ of ΔFMQ + 2 was used in each circumstance. Diagrams 25a, 4b, 4d & 4e were calculated in equilibrium mode. Diagrams 25c & 4f were calculated under fractionating solids mode.

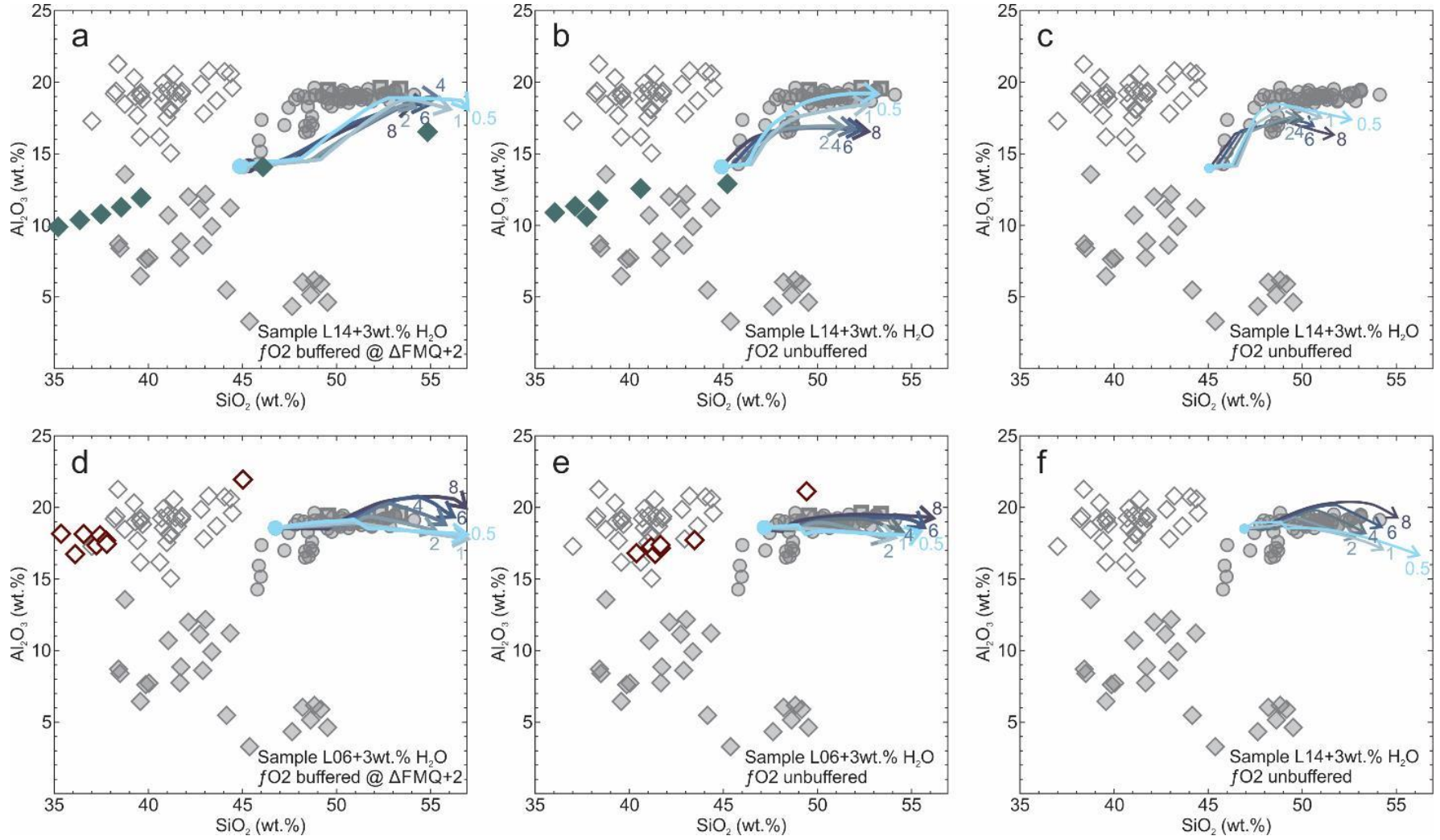
a
Sample L14+3wt.% H2O
ƒO2 buffered @ ΔFMQ+2
b
Sample L14+3wt.% H2O
ƒO2 unbuffered
c
Sample L14+3wt.% H2O
ƒO2 unbuffered
d
Sample L06+3wt.% H2O
ƒO2 buffered @ ΔFMQ+2
e
Sample L06+3wt.% H2O
ƒO2 unbuffered
f
Sample L14+3wt.% H2O
ƒO2 unbuffered
Al2O3 (wt.%)
SiO2 (wt.%)

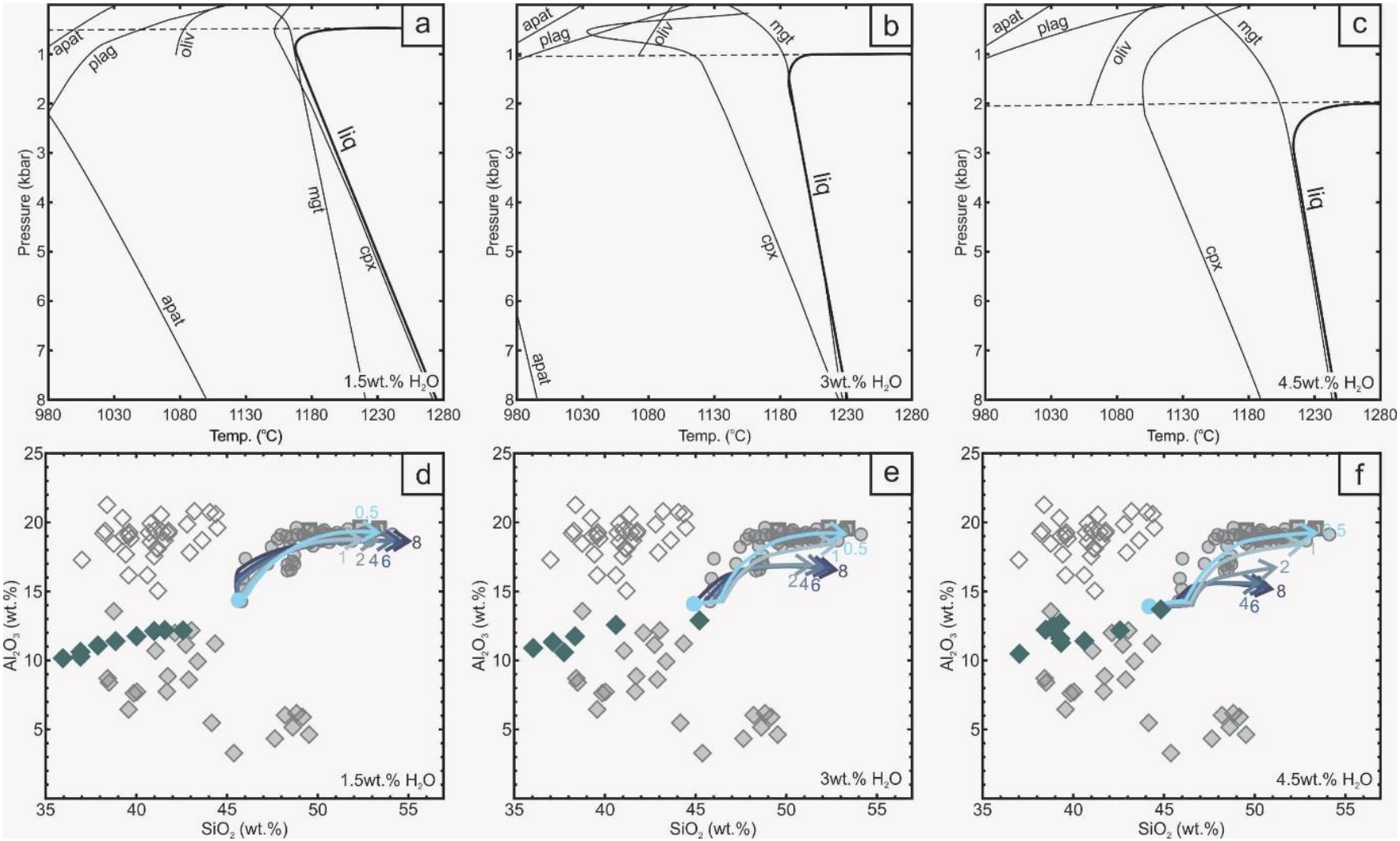
a
b
c
apat
plag
oliv
mgt
cpx
liq
bli
Pressure (kbar)
Temp. (°C)
1.5wt.% H2O
3wt.% H2O
4.5wt.% H2O
d
e
f
Al2O3 (wt.%)
SiO2 (wt.%)
0.5
1
2
4
6
8

Figure 26a-f (page 65): Liquid composition evolution calculated using Rhyolite-MELTS (Ghiorso and Gualda, 2015; Gualda et al., 2012). Sample composition used and conditions applied to each calculation are displayed in the bottom right hand corner of each diagram, all models undertaken at an initial fO_2 of ΔFMQ + 2. Sample compositions were used with an additional 3wt.% H_2O and were normalised to 100%. Diagrams 26a, 4b, 4d & 4e were calculated in equilibrium mode. Diagrams 26c & 4f were calculated with solids fractionated. Blue lines represent isobaric melt evolution trends from an initial composition (circle) towards a final melt composition at 980˚C (point of arrow head) at pressure intervals from 0.5kbar to 8kbar. Darker lines represent higher pressure melts, with coloured number symbols representing the pressure interval at which each melt trend was calculated. Coloured diamonds in diagrams 26a, 4b, 4d & 4e represent final equilibrium cumulate mineralogy at ~980˚C for each of the pressure intervals.

Figure 27a-f (***page 66)***: Diagrams displaying the effect of varying amounts of water on the phase relations and liquid evolution trends. Diagrams 27a-c display phase diagrams calculated using Rhyolite-MELTS (Ghiorso and Gualda, 2015; Gualda et al., 2012). Diagrams 27d-f display liquid composition evolution calculated using Rhyolite-MELTS (Ghiorso and Gualda, 2015; Gualda et al., 2012). All models are fO_2 water added and normalised to 100%. Blue lines represent isobaric melt evolution trends from an initial composition (circle) towards a final melt composition at 980˚C (point of arrow head) at pressure intervals from 0.5kbar to 8kbar. Darker lines represent higher pressure melts, with coloured number symbols representing the pressure interval at which each melt trend was calculated. Coloured diamonds in diagrams 27d, 27e and 27f represent final equilibrated cumulate mineralogy at ~980˚C for each of the pressure intervals. Note the changes in cumulate composition and melt trend with increasing water, due primarily to the suppression of plagioclase crystallisation and the change in initial crystallising phase (clinopyroxene to magnetite) at higher water contents.

It seems likely that the magma system is unbuffered with respect to fO_2. Whilst the phase relationships appear relatively realistic when the magmas is buffered at ΔNNO, it seems to favor earlier spinel crystallization than might be expected and increases the stability of plagioclase (figs. 25a & 25d). When fO_2 is unbuffered (figs. 25b & 25c) the liquid field increases and spinel crystallization is suppressed to lower temperatures for a given pressure. It appears that not buffering the melt also increase the likelihood of other phases crystallizing (i.e.olivine) due to an increased availability of reduced iron. The unbuffered melts themselves are driven to much more reduced oxidation states and better reflect the observed magma evolutions trends.

The effect of fractionating solid phases from the melt as they form is more significant and markedly changes the stability of most phases (see figures 25d & 25f). When compared to equilibrium mode, fractional crystallization introduces additional phases (garnet) and significantly expands the stability field of other phases (olivine, apatite and feldspar). Interestingly, it seems that when unbuffered in equilibrium mode sample L14 will not crystallize plagioclase until the melt loses water to the vapour phase, however, in fractional crystallization mode the melts will crystallize plagioclase prior to the separation of water into the vapour phase. A significant difference can be observed in how the melt evolution of both samples responds to the crystallization mode (see figure 26), with sample L14 being better modelled by fractional crystallization and sample L06 the opposite, with equilibrium mode more effective. This appears at odds with the trace element modelling, which suggests that both trends are driven by fractional crystallization with most samples experiencing contamination by varyingly fractionated liquids. Whilst equilibrium crystallization seems to fit the L06 trend best (fig. 26e), fractional

crystallization also produces realistic evolution trends at higher pressures (>4kbar) and high-mid temperatures (1280-1050°C). Similarly, the most realistic magma evolution trends for L14 are produced at higher pressures and high-mid temperatures (fig. 26c). This would suggest that the melts may have evolved at pressures above 4kbar and temperatures above 1050°C through a fractional crystallization process.

Perhaps the largest factor affecting the melt evolution and phase stabilities of these melts is water content. Increasing the water content of the melt from 1.5-4.5wt.% shows marked changes in the phase boundaries (see figure 27). Perhaps the most interesting of which is the separation of water from the melt into a co-existing vapour phase, the depth of which increases with water content (from 0.5kbar at 1.5wt.% to 2kbar at 4.5wt.%). Other significant differences are in the initial crystallising phase at the liquidus; at lower water contents clinopyroxene precedes magnetite (fig. 27a) and the higher the water content the higher the stability threshold of magnetite (and vice-versa for clinopyroxene) (fig. 27b). Increasing water content will also decrease the stability of some phases (e.g. plagioclase) and increase that of others (e.g. olivine), reflecting what we might expect from the paragenetic sequence with plagioclase crystallization suppressed until later in the sequence. The effect of these changes in phase stability are reflected in the evolution trends of the melts (figs. 27d-f), with early clinopyroxene crystallization at low water contents diving an initial increase in Al_2O_3 and at higher temperatures the higher stability of magnetite early in the sequence is reflected in a later increase in Al_2O_3.

Whilst the MELTs modelling is not perfect in replicating the paragenetic sequences that are observed in the xenolith and lava assemblages, it is useful in establishing some of the conditions under which the magmas evolved. Suggesting that the magmas were unbuffered with respect to fO_2 and crystallised at mid-lower crustal pressures from melts containing >3wt.% H_2O. It is likely that the magmas experienced a dissociation of water from the melt into the vapour phase at shallow crustal pressures (<2kbar). Initial melt composition exerts a primary control on the liquid line of descent and the phases which appear. A combination of water content and pressure play a strong role in controlling the mineral paragenesis; with higher pressures and temperatures favouring ferromagnesian phases (clinopyroxene and magnetite) and higher water contents suppressing plagioclase crystallisation at high pressures and temperatures.

Decompression processes

The groundmass glass analysed in this study display a broad compositional variation, especially with reference to volatiles which display a lot of variation suggesting that they have undergone varying amounts of degassing. The lavas display a similar distribution in sulphur contents to the groundmass analyses, suggesting that both of these have undergone similar levels of degassing. When compared to groundmass samples from the 1815 eruption of Tambora (Gertisser et al., 2012) (fig. 28), Sangeang Api groundmass records lower sulphur contents suggesting that they have undergone approximately 60% more degassing with respect to sulphur. The ash samples from the most recent eruption are significantly more S-rich than the lavas or groundmass from both Sangeang Api and Tambora and are in the range of concentrations recorded by the undegassed Tambora melt

inclusions, likely recording the rapid, shallow degassing of melts during the eruption event (Wallace, 2005). Sulphur degassing is thus an important process in the Sangeang Api magmas and may be driving reduction in the lavas. Considering that the Sangeang Api magmas are highly oxidised, sulphur degassing in the form of sulphate degassing will drive the melts to become reduced (Burgisser and Scaillet, 2007; Moussallam et al., 2014).

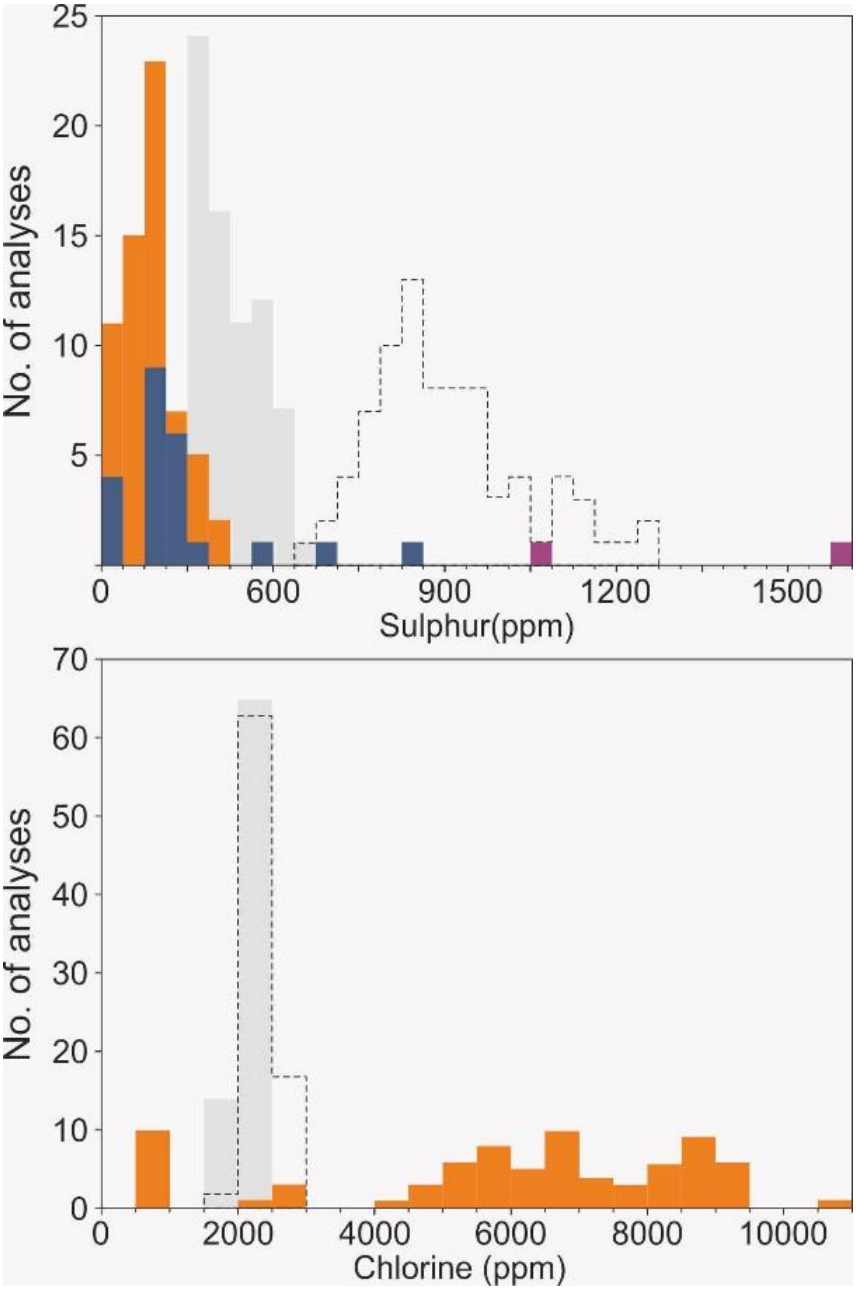

Figure 28: Histograms of groundmass glass and lava sulphur and chlorine concentrations. Sangeang Api groundmass glass are shown by orange bars, lavas by blue and ash from 2014 eruption in purple. Included for comparison are groundmass glass and melt inclusion data from Gertisser et al. (2012): grey bars are groundmass glass and dotted outline are melt inclusions.

Unlike the sulphur contents the average chlorine content (5919ppm) is significantly higher in the Sangeang Api groundmass glass compared to the Tambora samples (1511ppm) (fig. 28), suggesting that the magmas at Sangeang Api have been much less effective in degassing chlorine. This suggests that these glasses crystallised at shallow crustal depths (<5km) and were likely saturated to with an aqueous fluid+brine solution (Carroll, 2005). Given that these glasses likely solidified at shallow depths, these evolved

alkalic and Cl-rich melts may be sourced from the incongruent breakdown of amphibole during decompression. At high water contents (i.e. saturation), relatively high temperatures and shallow-intermediate depths, amphiboles incongruently breakdown in the following reaction (Foden and Green, 1992):

$$Pargasite \rightarrow 45.5\%\ Cpx + 21\%\ Olivine + 15.5\%\ Amphibole + 20.5\%\ Cl - H_2O\ melt$$

This reaction is supported by the observed modal proportions of the minerals in the xenoliths that have experienced and preserved the incongruent breakdown of amphibole. Incongruent melting of amphibole is supported by groundmass glass incompatible trace element patterns reflecting those of amphiboles – similar Rb, Ba, Nb, La, Ce, Se and Nd. It is also supported by the high Na_2O and K_2O concentrations of the glasses suggesting sourcing from an extremely amphibole-rich source (fig. 7). Magmas likely experienced a very late stage degassing and decompression event immediately prior to eruption. The decompression of water-saturated magmas and progressive water loss (~2.5wt.%) in the upper part of the crustal magmatic tract will drive magmas to crystallise An-poor plagioclase (Crabtree and Lange, 2011). Sangeang Api lavas commonly contain low-An microlites and low-An rims on plagioclase phenocrysts, suggesting that they have experienced rapid decompression and degassing in the upper magmatic tract. Based on the discrepancies between anorthite contents of plagioclase phenocryst cores and rims/microlites and the calculations of Martel et al. (1998) Sangeang Api magmas probably experienced a degassing event on the order of about 2.5wt% H_2O immediately prior to eruption. Based on the calculated water-contents of the magmas from amphibole compositions, degassing on the scale of 2.5wt.% water in the upper-crust and final exhumation of lavas would drive the final lavas to be completely (or almost nearly) anhydrous.

Faulting in magma tract

As previously mentioned, a number of the cumulate samples display cataclasic and strain fabrics suggesting that the cumulate mineral piles have been displaced along faults in the crustal magmatic tract. These textures are predominantly concentrated zones of well equilibrated, partially mylonitised, granulitic morphologies, as well as some rarer and sheared/cataclasic textures. Late-forming pargasite phases often show kink-banding (fig. 23b), suggesting crystallisation under an imposed stress regime. These textures are evidence of the disruption of cumulate piles and earlier intrusives under the external stress regime of a fault system. A faulting system would provide pathways under which new batches of magma could travel through the system. It has long been suggested that a W-E trending rear-arc thrust termed the Flores-thrust passes from the Java Sea into the Banda Sea to the north of the islands of Lombok, Sumbawa and Flores (fig. 1a) (Beckers and Lay, 1995; Koulali et al., 2016; Silver et al., 1986). Relative slip vectors indicate that strain along the Sumbawa section of the Flores Thrust is accommodated by a northwards slip of the hanging wall (Koulali et al., 2016). It has been shown that magma chambers at depth can localise deformation during thrusting events (Montanari et al., 2010). The

Sangeang Api magma chamber system may be acting to localise deformation from the Flores Thrust at depth in the crust.

Figure 29: Simple mixing models between an I-MORB source (gold star) and various sediments of the Sunda arc-front representing subducted sediments, with isotopic distributions of selected arc lavas given for comparison. Mixing models have been calculated for sediments B-G using I-MORB isotopic compositions of Rehkamper and Hofmann (1997), an I-MORB source composition from Workman and Hart (2005) and sediment isotope and trace element compositions of Ben Othman et al. (1989) and Vroon et al. (1995). I-MORB source composition of $^{143}Nd/^{144}Nd$: 0.51307, $^{87}Sr/^{86}Sr$: 0.70275, Nd: 0.67ppm and Sr 9.6ppm. Composition of sediments A (RC14-067), B (V33-79), C (V33-77), D (V33-75), E (V28-341) & G (V28-343) are taken from Ben Othman et al. (1989), whilst sediment G is an average of DSDP 262 compositions from Vroon et al. (1995). Sediments A, B, C, D and E are considered unlikely to represent mixing trends between the mantle source and subducted sediments (dotted red lines). Sediments F, a carbonate turbidite, and G, a pelagic clay, represent the most likely trends of mixing between the I-MORB source and subducted sediments (solid black lines with ticks denoting percent of sediment mixed to I-MORB source). The green dashed line displays a likely mixing trend on which the Sangeang Api lavas sit, between an I-MORB source with the addition 1% sediment F and 20% sediment G. Inset diagram (top right) shows a close-up of this mixing model with Sangeang

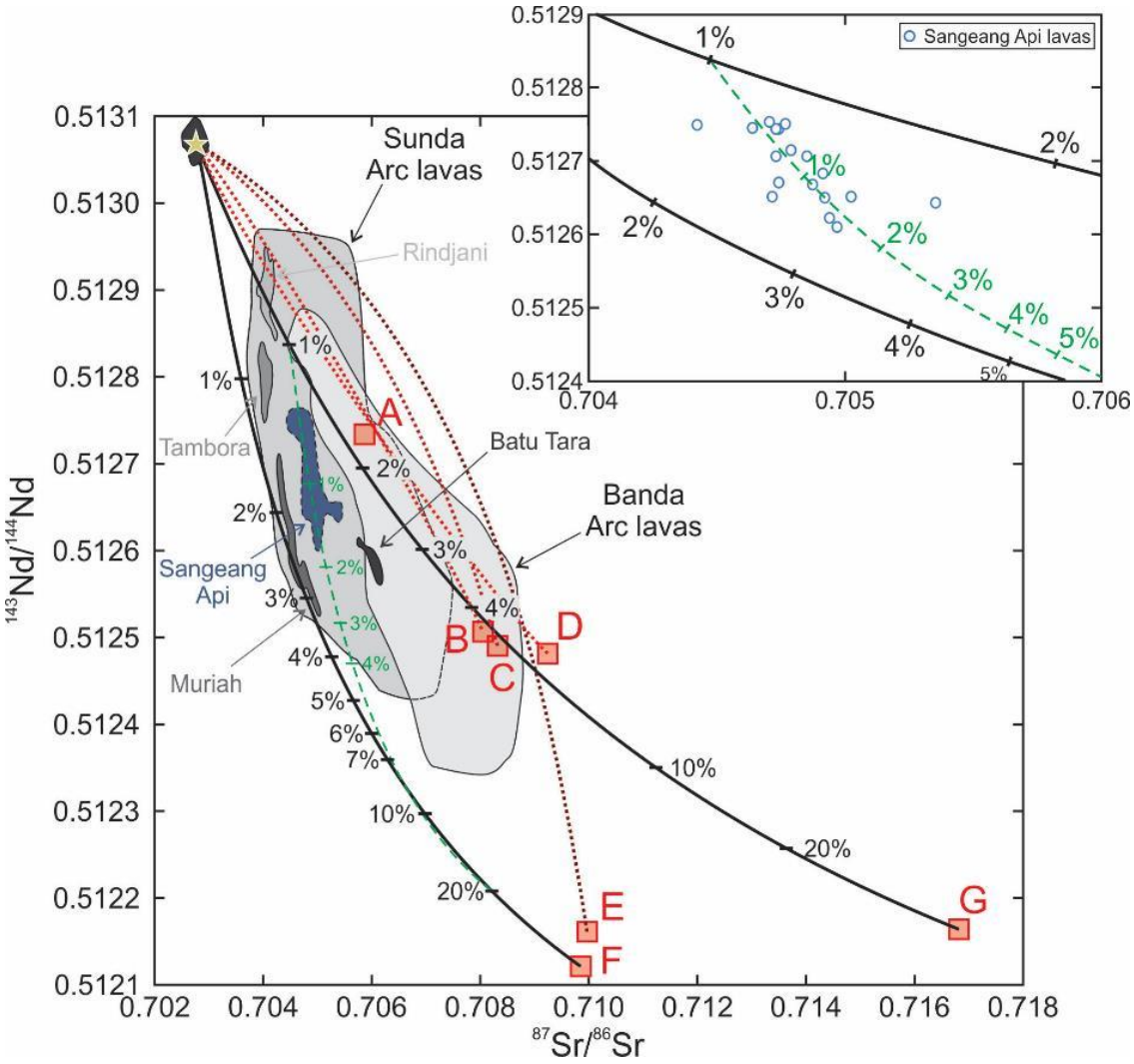

Source sediment input

As previously mentioned the Sunda-Banda Arc displays an extremely broad range in Sr and Nd isotope ratios spanning from compositions that are like I-MORB (high Nd ratios and low Sr ratios) towards lower Nd isotope and higher Sr isotope ratios. The range of

isotopic values has been proposed to be due to the influence of sediment input to the mantle source region (Stolz et al., 1990; Turner and Foden, 2001). It has been noted by many that there is a broad increase in Sr isotopes, Nd and Pb isotopes from the western Sunda Arc towards the east and the Banda Arc (Stolz et al., 1990; Turner and Foden, 2001; Wheller et al., 1987). Figure 29 displays simple mixing trends (Langmuir et al., 1978) between sediments of the Sunda arc-front, which are suggested to be representative of subducted sediment within the arc. These sediments span a range of sedimentary materials; biogenic/carbonate (sediments E & F), pelagic clay (sediment G), volcanogenic (sediment A) and terrigenous/biogenic turbidite (sediments B, C & D) material (Ben Othman et al., 1989; Vroon et al., 1995). Concave-down trends in figure 29 (sediments B, C and E) have Sr/Nd ratios higher than I-MORB source, whereas the concave-up trends (D, F and G) have Sr/Nd ratios lower than the I-MORB source. Higher Sr compositions within these sediments are related to carbonate material, whereas lower Sr compositions are related to a predominance of pelagic clay/mud sediments (Ben Othman et al., 1989; Vroon et al., 1995). The Sunda Arc lava trend appears to be bound by a concave-up trend between variously enriched sediments, suggesting that pelagic mud/clay material is the predominant subducted material throughout the arc. The majority of Sunda Arc lavas appear to be bound by the trends between an I-MORB source and sediments F & G, suggesting that the most influential subducted sediments in the source region of the Sunda Arc are carbonates and pelagic clays. The mixing trend to lower Nd compositions is trending towards an enriched mantle (EM1) style source as described by Zindler and Hart (1986), which has been supposed as a source of ocean island basalts, perhaps suggesting a role for OIB source mantle at Sangeang Api. An enriched OIB mantle source has been proposed to play a role in the genesis of the similarly ultrapotassic Batu Tara, supporting the role of an enriched mantle source in the Sunda Arc (van Bergen et al., 1992). Previous work has proposed a three-component source for the Sunda Arc magmas; mantle wedge peridotite, subducted sediment and fluids derived from altered ocean crust (AOC) (Edwards et al., 1991; Gertisser et al., 2012; Turner and Foden, 2001). Turner et al. (2003) used Sr, Nd and Pb isotopic evidence combined with trace element ratios to propose that melting of an I-MORB source region enriched by 2.5% partial melt of a Sunda sediment produced the observed trends in the Sangeang Api isotopic data. However, the Sunda sediment value utilised in their model assumes homogeneity in the subducted sediment component along the length of the arc (Plank and Langmuir, 1998), which is unlikely given the diversity of sediments found along the arc. Simple mixing models suggest that the Sangeang Api lavas are sourced from an I-MORB source mantle that has experienced mixing with a variably enriched mantle source with Sr/Nd ratios similar to a pelagic clay (see fig. 29). Thus, hinting at small-scale heterogeneity in the subducted sediment material. Both Th and the REE are fluid immobile, Turner et al. (2003) and Turner and Foden (2001) used Th/Ce ratios and $^{143}Nd/^{144}Nd$ compositions to suggest that sediment was introduced to the mantle source as a partial melt. Utilising the new sediment mixing models from this study, figure 30a compares sediment mixing models from this study to those of Turner et al. (2003). Both new mixing models support the suggestion of a mixture of sediment sources, with the mixing curves directly crossing the Sangeang Api samples.

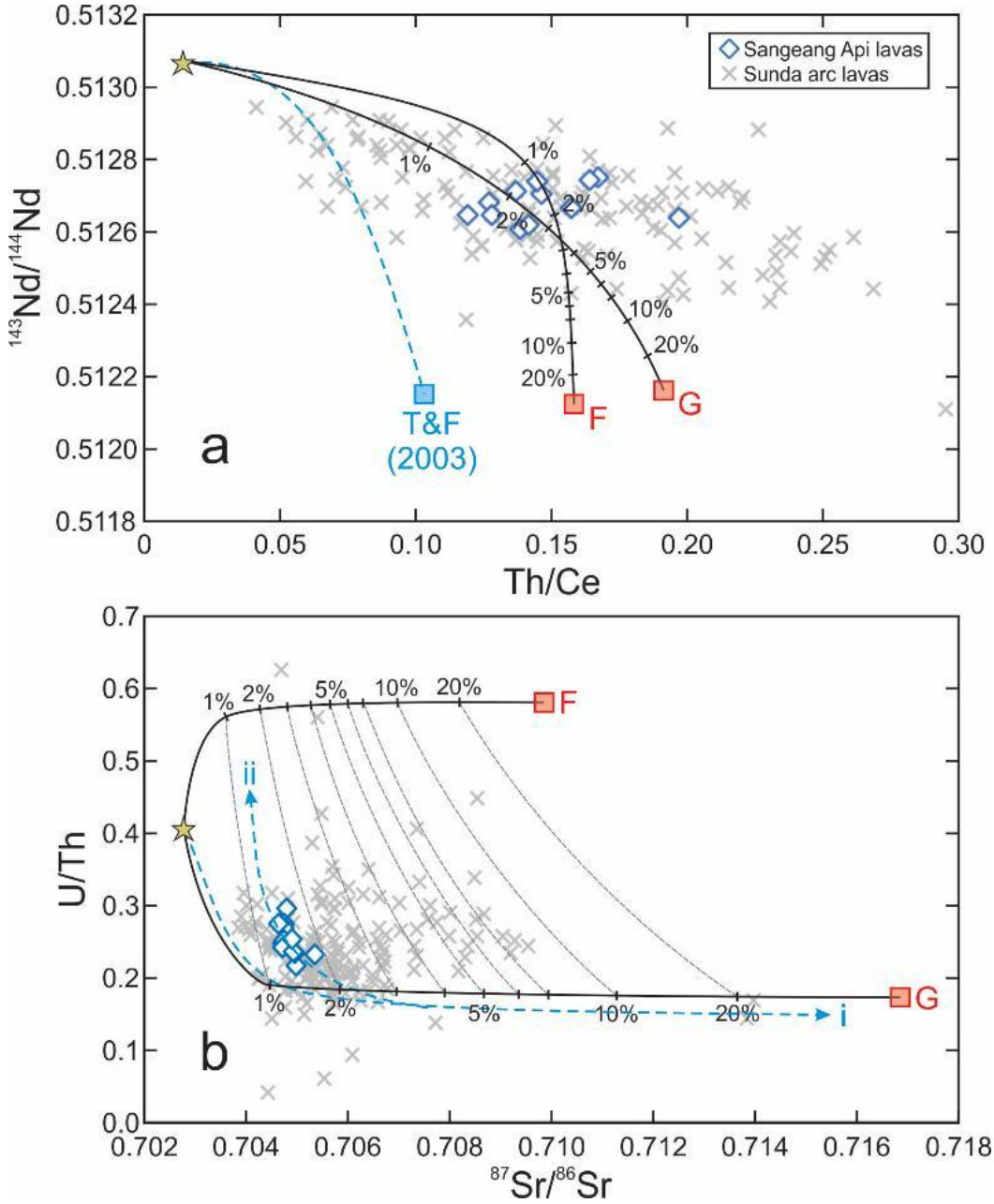

Figure 30a: Th/Ce vs. $^{143}Nd/^{144}Nd$ discrimination diagram with simple mixing models between I-MORB source (gold star) and selected Sunda front sediments. Mixing model of Turner et al. (2003) shown for comparison. Sunda arc-front sediments G & F as in figure 29. Lava symbols given in key at top right. Data sources of Sunda arc lavas and Sangeang Api lavas as in figure 10. I-MORB source composition of 0.67ppm Nd, 0.0079ppm and 0.55ppm Ce (Workman and Hart, 2005). Sediment F (DSDP 262) composition of 26.8ppm Nd, 5.264ppm Th and 33.1ppm Ce (Vroon et al., 1995). Sediment G (V28-343) composition of 23.05ppm Nd, 10.83ppm Th and 56.93ppm Ce (Ben Othman et al., 1989).

Figure 30b: $^{87}Sr/^{86}Sr$ vs. U/Th discrimination diagram with simple mixing models between an I-MORB source and selected Sunda front sediments. Sunda arc-front sediments G & F as in figure 29. Mixing models i and ii are taken from Turner and Foden (2001) and display mixing between an I-MORB source and a Java sediment (line i), and mixing between a Java sediment and fluid derived from an altered ocean crust (line ii). Lava symbols given in key at top right. Data sources of Sunda arc lavas and Sangeang Api lavas as in figure 10. I-MORB source composition of 9.6ppm Sr, 0.0079ppm Th and 0.0032ppm U (Workman and Hart, 2005). Sediment F (DSDP 262) composition of 126ppm Sr, 6.4625ppm Th and 3.75ppm U (Vroon et al., 1995). Sediment G (V28-343) composition of 132ppm U, 10.83ppm Th and 1.91ppm U (Ben Othman et al., 1989). Grey dashed lines spanning between sediment F and G represent mixing lines between 1%-20% mixes of sediment.

Turner and Foden (2001) used models of $^{87}Sr/^{86}Sr$ vs. U/Th to ascertain the role of fluids input to the source region, with their model suggesting a role for fluids derived from altered oceanic crust in the observed trace and isotopic element compositions of Sunda arc-front volcanoes. Figure 30b displays models comparing the new mixing trends with those of Turner and Foden (2001). The newer models suggest that a mixture of ~1-2% of both sediment F and G with an I-MORB source would create a similar array to the altered ocean fluid model (line ii in figure 30b) of Turner and Foden (2001). It therefore seems that the anomalous $^{143}Nd/^{144}Nd$-$^{87}Sr/^{86}Sr$ array of the Sangeang Api lavas could be created by the mixing of two heterogeneous and variably enriched sediment sources. The models presented here broadly agree with those of Turner et al. (2003), however, they identify more heterogeneity in the sediments added to the I-MORB source region, ~1-2.5% addition of variably enriched and compositionally distinct sediments. The models suggest that the sediment signature was not added by partial melts.

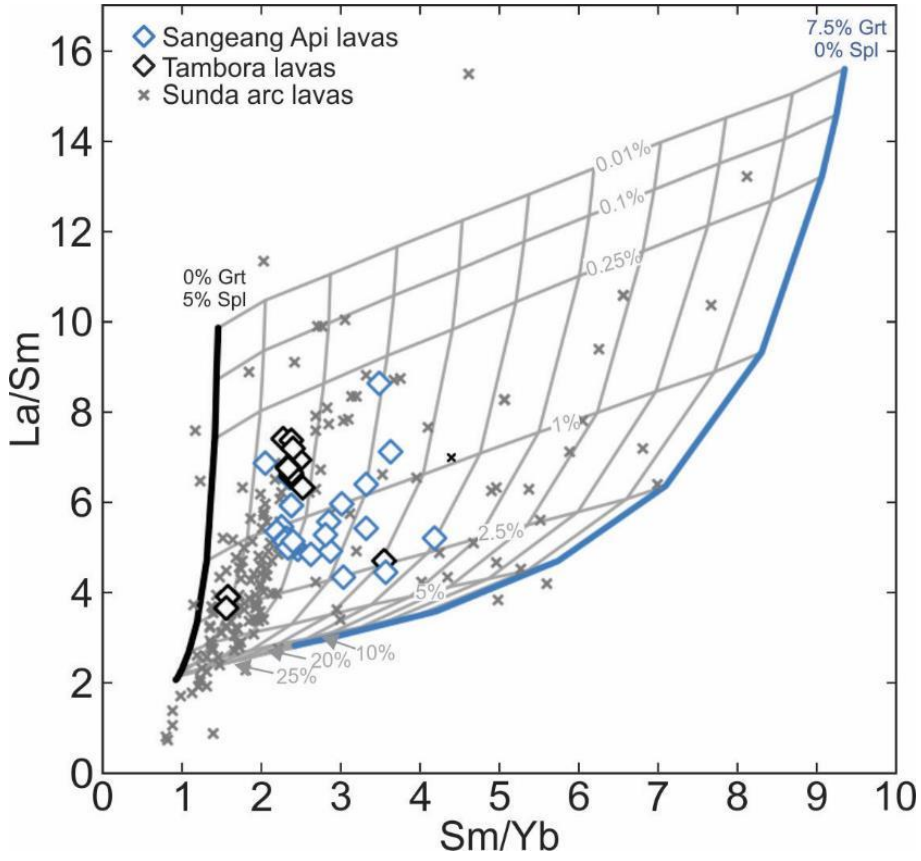

Figure 31: Sm/Yb vs. La/Sm discrimination diagram with partial melting grid overlain. Displayed are the 0.01% to 25% partial melting models of a spinel-lherzholite (black line, left) and a "metasomatized" garnet-harzburgite (blue line, right). Grey lines between the two end-member models represent partial melting models of intermediate compositions (left to right 10-90% garnet harzburgite). Compositions of lavas from Sangeang Api (blue diamonds), Tambora (black diamonds) and Sunda Arc lavas are displayed for comparison. Spinel-lherzholite composed of 56% olivine, 32% orthopyroxene, 7% clinopyroxene, and 5% spinel (melt distributions 12%, 15%, 70% and 3% respectively). Metasomatised garnet-harzburgite composed of 50% Olivine, 26% orthopyroxene, 10.5% amphibole, 7.5% garnet, 3% clinopyroxene and 3% phlogopite (melt distributions 10%, 15%, 3%, 6%, 65% and 1% respectively). Partition co-efficients taken from McKenzie and O'Nions (1991).

To test the exact conditions of melting, an equilibrium batch melting grid of Sm/Yb vs. La/Sm was created between a spinel-lherzholite source and a metasomatized garnet-harzburgite source (see figure 31). These mantle compositions were chosen as their equilibrium batch melts present outer bounds on the compositional distribution of Sunda Arc lavas. Degree of melting estimates range from 0.3-3% partial melting with 0.8-3.75% residual garnet and small degrees of metasomatism. These results are consistent with the suggestions of Turner et al. (2003), who proposed that Sangeang Api lavas were produced from 3% batch melt in the presence of up to 3% residual garnet.

It has been suggested that the magmas of the nearby Tambora were produced by 2% partial melting of a garnet free I-MORB source, contaminated by ~3% fluids from altered crust and <1% sediment material (Gertisser et al., 2012; Vigouroux et al., 2012). The sediment mixing models (fig. 29) and mantle melting models from this study (fig. 31) broadly agree with these suggestions, suggesting low degrees of batch melting (<1%) of an I-MORB source with <1.5% mixed sediments in the presence of <1.5% residual garnet. Despite only being separated by ~120km and sharing similarities in their major and trace element compositions (both shoshonitic in character, similar incompatible element and broadly similar REE profiles), there are notable differences in fluid mobile elements (lower Cl and Ba) and source characteristics (lower degrees of melting, sediment input and garnet residue) (Foden, 1986b; Gertisser et al., 2012). Tambora and Sangeang Api display significant source heterogeneity, highlighting the broad variation in the mantle along the Sunda-Banda Arc.

There is evidence that the source region for the Sangeang Api magmas is enriched in varying quantities of phlogopite and amphibole (fig. 7). Lavas with increasing concentrations of both Na_2O and K_2O correlate to source regions that may have experienced the incongruent breakdown of amphibole forming the product of these enrichment, whilst those that trend towards higher K_2O and lower Na_2O, such as those of the Batu Tara suite (Stolz et al., 1988), suggest source regions enriched in phlogopite. Sangeang Api lavas display trends towards an amphibole rich source, and the xenolith groundmass glasses show clear evidence of sourcing from an amphibole rich source. A few samples display a trend away from this towards a more Batu Tara like phlogopite enriched source. A source enriched in both phlogopite and amphibole might produce melts displaying evidence both of amphibole and phlogopite breakdown. The stability fields of amphibole and phlogopite in the mantle overlap, however phlogopite is stable to higher pressures than amphibole and will breakdown at higher temperatures (earlier) than amphibole (Frost, 2006; Wunder and Melzer, 2003). Initial partial melts favouring the breakdown of phlogopite would produce magma compositions with higher Na_2O compositions, whereas higher degrees of melting would initiate amphibole breakdown and thus drive partial melts to higher K_2O and Na_2O compositions. Alternatively, melts originating from metasomatized mantle at greater depths (in the phlogopite stability field) will display a phlogopite signature (elevated Na_2O), whereas melts originating at relatively shallower depths (in the amphibole stability field) will have an amphibole signature (high K_2O and Na_2O). Turner et al. (2003) suggest that there is little evidence for the role of amphibole or phlogopite breakdown in the source region of Sangeang Api

(low Ba/Sr and Rb/Sr), and hence no evidence of mantle metasomatism. However, it is possible that a source enriched in both phlogopite and amphibole would produce magmas with indiscernible Ba/Sr and Rb/Sr systematics. Batch melting models suggest that there is a role for the melting of a source enriched to some degree in both amphibole and phlogopite at Sangeang Api. This is at odds with the findings of Turner et al. (2003), suggesting that the Sangeang Api magmas originate from partial melts of a source region enriched in both phlogopite and amphibole. Further investigation and modelling is required to derive the composition and components of the Sangeang Api source region.

SUMMARY

Sangeang Api erupts a suite of lavas and entrained cumulate xenoliths that record the complete differentiation history of a potassic island arc magma. Below the findings of this study are summarised:

- The most primitive magmas observed within the erupted Sangeang Api lava suite are silica-undersaturated, oxidised (Fe^{3+}/Fe^{2+} >1) and water-saturated, with low Al/Si ratios and had likely experienced previous fractionation.
- Lavas produced by Sangeang Api are basaltic – basaltic-trachyandesite in composition. They are characterised by high potassium (2.5-4%), silica-undersaturation and volatile-rich. Melt evolution trends within the lavas were driven by 0-45% fractional crystallisation, leaving either a gabbroic or pyroxenitic cumulate.
- Parental magmas from the Sangeang Api system are likely sourced from 0.3-3% partial melting of a metasomatized mantle source enriched by 1-2% addition of compositionally distinct sediments. Partial melting occurred at depths great enough to stabilise up to 3.75% garnet.
    - Significant heterogeneity is noted between the source regions of Sangeang Api and the neighbouring (~120km) Tambora.
    - It is likely that Sangeang Api's source region is enriched in both phlogopite and amphibole.
- Parallel fractional crystallisation of magmas with differing aH_2O and fO_2 at different pressures drove the production of two distinct cumulate suites: *Cpx+Ol/Mgt* pyroxenites and *Cpx+Plag+Mgt+Amph±Phlog* gabbros.
    - Pyroxenite cumulates formed at high pressures and are composed of primary cumulate Cpx with either Mgt or Ol. With less oxidised and wetter melts crystallising olivine, whereas more oxidised and degassed melts crystallising magnetite.
    - Gabbro cumulates crystallised from drier melts at shallower pressures than the pyroxenite cumulates.
- Primitive cumulate xenoliths were overprinted and contaminated by interactions with younger melts.
    - Cumulates that have experienced contamination are characterised by higher concentrations of incompatible elements. Likely leading to ^{226}Ra excesses and Fe-isotopic disequilibrium.

- Intruding melts were either previously fractionated magmas or highly alkalic products of the incongruent breakdown of amphibole during decompression.
- Contamination of cumulate piles is observed as;
    - Veining of melts/hydrous mineralogy intruding primitive cumulate mineralogy.
    - Disaggregation of cumulate piles and subsequent overgrowth of less magnesian rims by more fractionated melts.
    - Inefficient extraction of crystallising melts and crystallisation of intercumulate hydrous minerals (amphibole/phlogopite)
    - Cryptic contamination by percolative melts, leading to the crystallisation of hydrous minerals such as amphibole and phlogopite.
- Percolative flow through weakly aggregated cumulate piles likely aid in the disaggregation and entrainment of xenocrysts and xenoliths in ascending lavas. This process is exacerbated by crustal faulting.
- Magmas like decompressed on a water-saturated degassing curve with parental magmas having high water contents >5wt.% H_2O. Magmas finally experienced a rapid decompression and degassing event on the scale of ~2.5wt.% loss of H_2O immediately prior to eruption.

REFERENCES

Arculus, R.J., Wills, K.J.A., 1980. The petrology of plutonic blocks and inclusions from the lesser antilles island arc. Journal of Petrology 21, 743-799.

Balassone, G., Scordari, F., Lacalamita, M., Schingaro, E., Mormone, A., Piochi, M., Petti, C., Mondillo, N., 2013. Trioctahedral micas in xenolithic ejecta from recent volcanism of the Somma-Vesuvius (Italy): Crystal chemistry and genetic inferences. Lithos 160–161, 84-97.

Beckers, J., Lay, T., 1995. Very broadband seismic analysis of the 1992 Flores, Indonesia, earthquake (Mw = 7.9). Journal of Geophysical Research: Solid Earth (1978–2012) 100, 18179-18193.

Ben Othman, D., White, W.M., Patchett, J., 1989. The geochemistry of marine sediments, island arc magma genesis, and crust-mantle recycling. Earth and Planetary Science Letters 94, 1-21.

Bouilhol, P., Schmidt, M.W., Burg, J.-P., 2015. Magma Transfer and Evolution in Channels within the Arc Crust: the Pyroxenitic Feeder Pipes of Sapat (Kohistan, Pakistan). Journal of Petrology.

Bowin, C., Purdy, G.M., Johnston, C., Shor, G., Lawver, L., Hartono, H.M.S., Jezek, P., 1980. Arc-continent collision in Banda Sea region. AAPG Bulletin 64, 868-915.

Bruno, D., Delphine, B., Carlos, J.G., Jean-Louis, B., Olivier, B., Sahid, S.H., Hamid, D., 2009. Geochemical Architecture of the Lower- to Middle-crustal Section of a Paleo-

island Arc (Kohistan Complex, Jijal-Kamila Area, Northern Pakistan): Implications for the Evolution of an Oceanic Subduction Zone. Journal of Petrology 50, 531-531.

Burgisser, A., Scaillet, B., 2007. Redox evolution of a degassing magma rising to the surface. Nature 445, 194-197.

Carroll, M.R., 2005. Chlorine solubility in evolved alkaline magmas.

Cigolini, C., 2007. Petrography and thermobarometry of high-pressure ultramafic ejecta from Mount Vesuvius, Italy: inferences on the deep feeding system. Periodico Di Mineralogia 76, 5-24.

Clift, P.D., Draut, A.E., Kelemen, P.B., Blusztajn, J., Greene, A., 2005. Stratigraphic and geochemical evolution of an oceanic arc upper crustal section: The Jurassic Talkeetna Volcanic Formation, south-central Alaska. Geological Society of America Bulletin 117, 902-925.

Conrad, W.K., Kay, R.W., 1984. Ultramafic and mafic inclusions from adak-island - crystallization history, and implications for the nature of primary magmas and crustal evolution in the aleutian arc. Journal of Petrology 25, 88-125.

Couch, S., Sparks, R.S.J., Carroll, M.R., 2001. Mineral disequilibrium in lavas explained by convective self-mixing in open magma chambers. Nature 411, 1037-1039.

Crabtree, S.M., Lange, R.A., 2011. Complex Phenocryst Textures and Zoning Patterns in Andesites and Dacites: Evidence of Degassing-Induced Rapid Crystallization? Journal of Petrology 52, 3-38.

Das, S., 2004. Seismicity gaps and the shape of the seismic zone in the Banda Sea region from relocated hypocenters. Journal of Geophysical Research-Solid Earth 109.

Davidson, J., Turner, S., Handley, H., Macpherson, C., Dosseto, A., 2007. Amphibole "sponge" in arc crust? Geology 35, 787-790.

Debari, S., Kay, S.M., Kay, R.W., 1987. Ultramafic xenoliths from adagdak volcano, adak, aleutian-islands, alaska - deformed igneous cumulates from the moho of an island-arc. Journal of Geology 95, 329-341.

Dungan, M.A., Davidson, J., 2004. Partial assimilative recycling of the mafic plutonic roots of arc volcanoes: An example from the Chilean Andes. Geology 32, 773-776.

Edwards, C., Menzies, M., Thirlwall, M., 1991. Evidence from Muriah, Indonesia, for the Interplay of Supra-Subduction Zone and Intraplate Processes in the Genesis of Potassic Alkaline Magmas. Journal of Petrology 32, 555-592.

Erdmann, S., Martel, C., Pichavant, M., Kushnir, A., 2014. Amphibole as an archivist of magmatic crystallization conditions: problems, potential, and implications for inferring magma storage prior to the paroxysmal 2010 eruption of Mount Merapi, Indonesia. Contributions to Mineralogy and Petrology 167, 1-23.

Foden, J., 1983. The Petrology of The Calcalkaline Lavas of Rindjani Volcano, East Sunda Arc: a Model for Island Arc Petrogenesis.

Foden, J., 1986a. THE PETROLOGY OF TAMBORA VOLCANO, INDONESIA - A MODEL FOR THE 1815 ERUPTION. Journal of Volcanology and Geothermal Research 27, 1-41.

Foden, J., 1986b. The petrology of Tambora volcano, Indonesia: A model for the 1815 eruption. Journal of Volcanology and Geothermal Research 27, 1-41.

Foden, J., Varne, R., 1980. The petrology and tectonic setting of quaternary - recent volcanic centers of lombok and sumbawa, sunda arc. Chemical Geology 30, 201-226.

Foden, J.D., Green, D.H., 1992. Possible role of amphibole in the origin of andesite - some experimental and natural evidence. Contributions to Mineralogy and Petrology 109, 479-493.

Frost, D.J., 2006. The Stability of Hydrous Mantle Phases. Reviews in Mineralogy and Geochemistry 62, 243-271.

Gertisser, R., Self, S., Thomas, L.E., Handley, H.K., Van Calsteren, P., Wolff, J.A., 2012. Processes and Timescales of Magma Genesis and Differentiation Leading to the Great Tambora Eruption in 1815. Journal of Petrology 53, 271-297.

Ghiorso, M.S., Gualda, G.A.R., 2015. An H2O–CO2 mixed fluid saturation model compatible with rhyolite-MELTS. Contributions to Mineralogy and Petrology 169, 53.

Giannetti, B., 1982. Cumulate inclusions from K-rich magmas, Roccamonfina volcano, Italy. Earth and Planetary Science Letters 57, 313-335.

Grove, T.L., Elkins-Tanton, L.T., Parman, S.W., Chatterjee, N., Muntener, O., Gaetani, G.A., 2003. Fractional crystallization and mantle-melting controls on calc-alkaline differentiation trends. Contributions to Mineralogy and Petrology 145, 515-533.

Gruender, K., Stewart, R.B., Foley, S., 2010. Xenoliths from the sub-volcanic lithosphere of Mt Taranaki, New Zealand. Journal of Volcanology and Geothermal Research 190, 192-202.

Gualda, G.A.R., Ghiorso, M.S., Lemons, R.V., Carley, T.L., 2012. Rhyolite-MELTS: a Modified Calibration of MELTS Optimized for Silica-rich, Fluid-bearing Magmatic Systems. Journal of Petrology 53, 875-890.

Hacker, B.R., Mehl, L., Kelemen, P.B., Rioux, M., Behn, M.D., Luffi, P., 2008. Reconstruction of the Talkeetna intraoceanic arc of Alaska through thermobarometry. Journal of Geophysical Research-Solid Earth 113, 16.

Hall, R., 2011. Australia- SE Asia collison: plate tectonics and crustal flow, in: Hall, R., Cottam, M.A., Wilson, M.E.J. (Eds.), The SE Asian gateway: history and tectonics of Australia-Asia collision. Geological Society of London Special Publication, pp. 75-109.

Hall, R., 2012. Late Jurassic–Cenozoic reconstructions of the Indonesian region and the Indian Ocean. Tectonophysics 570–571, 1-41.

Hamilton, W.B., 1979. Tectonics of the Indonesian region, Professional Paper, - ed.

Hill, E., Wood, B.J., Blundy, J.D., 2000. The effect of Ca-Tschermaks component on trace element partitioning between clinopyroxene and silicate melt. Lithos 53, 203-215.

Hinschberger, F., Malod, J.A., Rehault, J.P., Villeneuve, M., Royer, J.Y., Burhanuddin, S., 2005. Late Cenozoic geodynamic evolution of eastern Indonesia. Tectonophysics 404, 91-118.

Irvine, T.N., 1974. Petrology of the Duke Island ultramafic complex, southeastern Alaska / T. N. Irvine. Geological Society of America, Boulder, Colo.

Jagoutz, O., 2014. Arc crustal differentiation mechanisms. Earth and Planetary Science Letters 396, 267-277.

Koulali, A., Susilo, S., McClusky, S., Meilano, I., Cummins, P., Tregoning, P., Lister, G., Efendi, J., Syafi'i, M.A., 2016. Crustal strain partitioning and the associated earthquake hazard in the eastern Sunda-Banda Arc. Geophysical Research Letters 43, 1943-1949.

Krawczynski, M.J., Grove, T.L., Behrens, H., 2012. Amphibole stability in primitive arc magmas: effects of temperature, H2O content, and oxygen fugacity. Contributions to Mineralogy and Petrology 164, 317-339.

Langmuir, C.H., Vocke, R.D., Hanson, G.N., Hart, S.R., 1978. A general mixing equation with applications to Icelandic basalts. Earth and Planetary Science Letters 37, 380-392.

Leake, B.E., Woolley, A.R., Arps, C.E.S., Birch, W.D., Gilbert, M.C., Grice, J.D., Hawthorne, F.C., Kato, A., Kisch, H.J., Krivovichev, V.G., Linthout, K., Laird, J., Mandarino, J.A., Maresch, W.V., Nickel, E.H., Rock, N.M.S., Schumacher, J.C., Smith, D.C., Stephenson, N.C.N., Ungaretti, L., Whittaker, E.J.W., Guo, Y.Z., 1997. Nomenclature of amphiboles: Report of the subcommittee on amphiboles of the International Mineralogical Association, Commission on New Minerals and Mineral Names. Canadian Mineralogist 35, 219-246.

Locock, A.J., 2014. An Excel spreadsheet to classify chemical analyses of amphiboles following the IMA 2012 recommendations. Computers & Geosciences 62, 1-11.

Martel, C., Pichavant, M., Bourdier, J.L., Traineau, H., Holtz, F., Scaillet, B., 1998. Magma storage conditions and control of eruption regime in silicic volcanoes: experimental evidence from Mt. Pelée. Earth and Planetary Science Letters 156, 89-99.

Mathez, E.A., 1984. Influence of degassing on oxidation-states of basaltic magmas. Nature 310, 371-375.

McDonough, W.F., Sun, S.s., 1995. The composition of the Earth. Chemical Geology 120, 223-253.

McKenzie, D.A.N., O'Nions, R.K., 1991. Partial Melt Distributions from Inversion of Rare Earth Element Concentrations. Journal of Petrology 32, 1021-1091.

Métrich, N., Berry, A.J., O'Neill, H.S.C., Susini, J., 2009. The oxidation state of sulfur in synthetic and natural glasses determined by X-ray absorption spectroscopy. Geochimica et Cosmochimica Acta 73, 2382-2399.

Montanari, D., Corti, G., Simakin, A., 2010. Magma chambers and localization of deformation during thrusting. Terra Nova 22, 390-395.

Moussallam, Y., Oppenheimer, C., Scaillet, B., Gaillard, F., Kyle, P., Peters, N., Hartley, M., Berlo, K., Donovan, A., 2014. Tracking the changing oxidation state of Erebus magmas, from mantle to surface, driven by magma ascent and degassing. Earth and Planetary Science Letters 393, 200-209.

Muntener, O., Kelemen, P.B., Grove, T.L., 2001. The role of H2O during crystallization of primitive arc magmas under uppermost mantle conditions and genesis of igneous pyroxenites: an experimental study. Contributions to Mineralogy and Petrology 141, 643-658.

Nandedkar, R.H., Ulmer, P., Muentener, O., 2014. Fractional crystallization of primitive, hydrous arc magmas: an experimental study at 0.7 GPa. Contributions to Mineralogy and Petrology 167.

Nicholls, I.A., Whitford, D.J., 1983. Potassium-rich volcanic rocks of the Muriah complex, Java, Indonesia: Products of multiple magma sources? Journal of Volcanology and Geothermal Research 18, 337-359.

Nimis, P., 1999. Clinopyroxene geobarometry of magmatic rocks. Part 2. Structural geobarometers for basic to acid, tholeiitic and mildly alkaline magmatic systems. Contributions to Mineralogy and Petrology 135, 62-74.

Nimis, P., Ulmer, P., 1998. Clinopyroxene geobarometry of magmatic rocks Part 1: An expanded structural geobarometer for anhydrous and hydrous, basic and ultrabasic systems. Contributions to Mineralogy and Petrology 133, 122-135.

Plank, T., Langmuir, C.H., 1998. The chemical composition of subducting sediment and its consequences for the crust and mantle. Chemical Geology 145, 325-394.

Pownall, J.M., Hall, R., Lister, G.S., 2016. Rolling open Earth's deepest forearc basin. Geology 44, 947-950.

Price, R.C., Smith, I.E.M., Stewart, R.B., Gamble, J.A., Gruender, K., Maas, R., 2016. High-K andesite petrogenesis and crustal evolution: Evidence from mafic and ultramafic xenoliths, Egmont Volcano (Mt. Taranaki) and comparisons with Ruapehu Volcano, North Island, New Zealand. Geochimica et Cosmochimica Acta 185, 328-357.

Rehkamper, M., Hofmann, A.W., 1997. Recycled ocean crust and sediment in Indian Ocean MORB. Earth and Planetary Science Letters 147, 93-106.

Ridolfi, F., Renzulli, A., 2012. Calcic amphiboles in calc-alkaline and alkaline magmas: thermobarometric and chemometric empirical equations valid up to 1,130A degrees C and 2.2 GPa. Contributions to Mineralogy and Petrology 163, 877-895.

Ridolfi, F., Renzulli, A., Puerini, M., 2010. Stability and chemical equilibrium of amphibole in calc-alkaline magmas: an overview, new thermobarometric formulations and application to subduction-related volcanoes. Contributions to Mineralogy and Petrology 160, 45-66.

Siebert, L., Simkin, T., Kimberly, P., 2011. Volcanoes of the World : Third Edition (3). University of California Press, Berkeley, US.

Silver, E.A., Breen, N.A., Prasetyo, H., Hussong, D.M., 1986. Multibeam study of the Flores Backarc Thrust Belt, Indonesia. Journal of Geophysical Research: Solid Earth 91, 3489-3500.

Smith, D.J., 2014. Clinopyroxene precursors to amphibole sponge in arc crust. Nat Commun 5.

Spakman, W., Hall, R., 2010. Surface deformation and slab-mantle interaction during Banda arc subduction rollback. Nature Geoscience 3, 562-566.

Stamper, C.C., Blundy, J.D., Arculus, R.J., Melekhova, E., 2014. Petrology of Plutonic Xenoliths and Volcanic Rocks from Grenada, Lesser Antilles. Journal of Petrology 55, 1353-1387.

Stolz, A.J., Varne, R., Davies, G.R., Wheller, G.E., Foden, J.D., 1990. Magma source components in an arc-continent collision zone - the flores-lembata sector, sunda arc, indonesia. Contributions to Mineralogy and Petrology 105, 585-601.

Stolz, A.J., Varne, R., Wheller, G.E., Foden, J.D., Abbott, M.J., 1988. The geochemistry and petrogenesis of K-rich alkaline volcanics from the Batu Tara volcano, eastern Sunda arc. Contributions to Mineralogy and Petrology 98, 374-389.

Tollan, P.M.E., Bindeman, I., Blundy, J.D., 2012. Cumulate xenoliths from St. Vincent, Lesser Antilles Island Arc: a window into upper crustal differentiation of mantle-derived basalts. Contributions to Mineralogy and Petrology 163, 189-208.

Turner, S., Foden, J., 2001. U, Th and Ra disequilibria, Sr, Nd and Pb isotope and trace element variations in Sunda arc lavas: predominance of a subducted sediment component. Contributions to Mineralogy and Petrology 142, 43-57.

Turner, S., Foden, J., George, R., Evans, P., Varne, R., Elburg, M., Jenner, G., 2003. Rates and processes of potassic magma evolution beneath Sangeang Api volcano, East Sunda arc, Indonesia. Journal of Petrology 44, 491-515.

van Bergen, M.J., Vroon, P.Z., Varekamp, J.C., Poorter, R.P.E., 1992. The origin of the potassic rock suite from Batu Tara volcano (East Sunda Arc, Indonesia). LITHOS 28, 261-282.

Varne, R., Foden, J.D., 1986. Geochemical and isotopic systematics of eastern Sunda Arc volcanics: Implications for mantle sources and mantle mixing processes, in: Wezel, F.-C. (Ed.), The Origin of Arcs. Elsevier, Amsterdam, pp. 159-189.

Vigouroux, N., Wallace, P.J., Williams-Jones, G., Kelley, K., Kent, A.J.R., Williams-Jones, A.E., 2012. The sources of volatile and fluid-mobile elements in the Sunda arc: A melt inclusion study from Kawah Ijen and Tambora volcanoes, Indonesia. Geochemistry Geophysics Geosystems 13, 22.

Vroon, P.Z., van Bergen, M.J., Klaver, G.J., White, W.M., 1995. Strontium, neodymium, and lead isotopic and trace-element signatures of the East indonesian sediments: provenance and implications for banda arc magma genesis. Geochimica et Cosmochimica Acta 59, 2573-2598.

Wallace, P.J., 2005. Volatiles in subduction zone magmas: concentrations and fluxes based on melt inclusion and volcanic gas data. Journal of Volcanology and Geothermal Research 140, 217-240.

Wheller, G.E., Varne, R., Foden, J.D., Abbott, M.J., 1987. Geochemistry of quaternary volcanism in the Sunda-Banda arc, Indonesia, and three-component genesis of island-arc basaltic magmas. Journal of Volcanology and Geothermal Research 32, 137-160.

Wilson, A.D., 1960. The micro-determination of ferrous iron in silicate minerals by a volumetric and a colorimetric method. Analyst 85, 823-827.

Witham, F., 2011. Conduit convection, magma mixing, and melt inclusion trends at persistently degassing volcanoes: Reply to comment by Metrich etal. (2011). Earth and Planetary Science Letters 306, 309-311.

Wood, B.J., Blundy, J.D., Robinson, J.A.C., 1999. The role of clinopyroxene in generating U-series disequilibrium during mantle melting. Geochimica et Cosmochimica Acta 63, 1613-1620.

Woodhead, J.D., Hergt, J.M., Davidson, J.P., Eggins, S.M., 2001. Hafnium isotope evidence for 'conservative' element mobility during subduction zone processes. Earth and Planetary Science Letters 192, 331-346.

Workman, R.K., Hart, S.R., 2005. Major and trace element composition of the depleted MORB mantle (DMM). Earth and Planetary Science Letters 231, 53-72.

Wunder, B., Melzer, S., 2003. Experimental evidence on phlogopitic mantle metasomatism induced by phengite dehydration. European Journal of Mineralogy 15, 641-647.

Yogodzinski, G.M., Kelemen, P.B., 2007. Trace elements in clinopyroxenes from Aleutian xenoliths: Implications for primitive subduction magmatism in an island arc. Earth and Planetary Science Letters 256, 617-632.

Zernack, A.V., Price, R.C., Smith, I.E.M., Cronin, S.J., Stewart, R.B., 2012. Temporal Evolution of a High-K Andesitic Magmatic System: Taranaki Volcano, New Zealand. Journal of Petrology 53, 325-363.

Zindler, A., Hart, S., 1986. Chemical Geodynamics. Annual Review of Earth and Planetary Sciences 14, 493-571.

Chapter 3

A window into the crustal magmatic tract of Sangeang Api, Indonesia: Insights from amphibole thermobarometry

Statement of Authorship

Title of Paper	A window into the crustal magmatic tract of Sangeang Api, Indonesia: Insights from amphibole thermobarometry
Publication Status	☐ Published ☐ Accepted for Publication ☐ Submitted for Publication ☑ Unpublished and Unsubmitted work written in manuscript style
Publication Details	For submission to Journal of Petrology as: Cooke, B., Foden, J. Petrological study of a mafic and ultramafic xenolith suite and host shoshonitic island arc lavas from Sangeang Api volcano in the eastern Sunda Arc.

Principal Author

Name of Principal Author (Candidate)	Benjamin Cooke		
Contribution to the Paper	Collection of samples in fieldwork, sample preparation, data collection, data processing, data interpretation, manuscript preparation and content, creation of diagrams		
Overall percentage (%)	80		
Certification:	This paper reports on original research I conducted during the period of my Higher Degree by Research candidature and is not subject to any obligations or contractual agreements with a third party that would constrain its inclusion in this thesis. I am the primary author of this paper.		
Signature		Date	13/11/2017

Co-Author Contributions

By signing the Statement of Authorship, each author certifies that:

i. the candidate's stated contribution to the publication is accurate (as detailed above);

ii. permission is granted for the candidate in include the publication in the thesis; and

iii. the sum of all co-author contributions is equal to 100% less the candidate's stated contribution.

Name of Co-Author	Professor John Foden		
Contribution to the Paper	Assistance in fieldwork, data interpretation, review		
Signature		Date	13/11/2017

ABSTRACT

Sangeang Api is an active volcano in the eastern Sunda Arc of Indonesia, which erupts an alkali suite of *Ne*-basalts to *Ne*-basaltic-trachyandesites that entrain abundant cumulate xenoliths. The cumulate xenoliths form two distinct groups, gabbros and pyroxenites, and are interpreted to be co-magmatic with the lavas. Amphibole is a common phase in both groups of cumulate xenoliths and also a common phase in the lavas. The lavas contain amphibole both as microphenocrysts and phenocrysts and often as partially reacted megacrysts (up to 2mm). In the cumulate xenoliths the amphiboles are found in four textural sites; 1. Primary cumulate, 2. Intra-cumulate, 3. Poikilitic, 4. Mineral overgrowths on clinopyroxene crystals. Across all lithologies, amphiboles are predominantly Mg-hastingsite in composition, with a smaller number in the gabbros and lavas having pargasitic compositions. The composition of amphiboles respond directly to the physiochemical conditions of the melts from which they are crystallising. Recent calibrations of amphibole-melt equilibria (Ridolfi et al., 2010; 2012) have allowed the estimation of the physiochemical conditions of the magmas from which amphiboles crystallised. Applying these formulations to the Sangeang Api amphiboles provides a record of almost continual crystallisation through the lower- to mid-crust from 974-338MPa and over a relatively narrow range of temperatures (1072-976˚C). These results suggest that the magmas ascended on a water-saturated degassing curve, with water contents ranging from 6.51-3.15wt.% H_2O. Modelling of the volatile saturation contents suggest that the melts underwent initial CO_2 degassing at depths in the system from an initial content of 3900ppm. Similarly, sulfur was initially degassed as a reduced (S^{2-}) phase at lower crustal pressures and changed to oxidised (S^{4+}) sulfur degassing at pressures less than 600MPa. This change in degassing mode is reflected in the redox state of the melts. Initial decompression form Moho depths was accompanied by oxidation from ΔNNO+0.2 to ΔNNO+1.15, whereas further decompression from pressures less than 600MPa was accompanied by reduction to ΔNNO+0.05. Through this study it was possible to gain an understanding of the architecture of the magma tract, with the lower crust having two distinct magma reservoirs before moving into a mid-crustal series of overlapping magma chambers and magmatic tracts.

INTRODUCTION

The association of cumulate xenoliths and lavas in arc volcanic settings can provide key insights into our understanding of crustal magma evolution and processes (e.g. Gruender et al., 2010; Montanari et al., 2010; Stamper et al., 2014; Tollan et al., 2012; Zernack et al., 2012). Magmas from arc volcanic settings are more oxidised with than those from other tectonic settings (Carmichael, 1991; Christie et al., 1986; Evans et al., 2012). Understanding the cause behind the relative oxidation of arc magmas is a controversial issue. Opposing theories suggest that oxidation is an artefact of the source region or is caused by processes occurring as the magmas ascend (Carmichael, 1991; Evans et al., 2012; Evans and Tomkins, 2011; Lee et al., 2005; Lee et al., 2010; Mallmann and O'Neill, 2009; Parkinson and Arculus, 1999). An important process in ascending magmas is degassing, which has been proposed to be a key driver in the anomalously high oxidation

state of arc melts (Kelley and Cottrell, 2012; Mathez, 1984). Therefore, understanding the path a magma has taken to the surface and is correlating redox state along that path is important in testing this theory.

A common method for estimating the physiochemical conditions of an ascending magma is to use mineral geothermobarometers and oxybarometers, a large variety of which are available to researchers. Andersen et al. (1993) formulated the QUILF programme, which uses the equilibria between Fe-Mg-Mn-Ti Oxides and selected silicate minerals (pyroxenes, olivine and quartz) to allow for the estimation of pressure, temperature and oxygen fugacity. Thermodynamic models of the solid solution substitution between Fe-Ti oxide pairs (magnetite-ilmenite, etc.) have been formulated that allow for the estimation of temperature and oxygen fugacity (Ghiorso and Evans, 2008; Ghiorso and Sack, 1991; Lattard et al., 2005). Mineral-melt equilibria is a commonly used tool for the determination of pre-eruptive magmatic conditions (temperature, pressure and H_2O content); these include the clinopyroxene-liquid thermobarometer of Putirka et al. (2003) and the plagioclase-liquid hygrometer/thermometer of Lange et al. (2009). Similarly, the response of clinopyroxene crystal chemistry to melts of varying physiochemical conditions has been established, allowing for the use of single clinopyroxene crystals as geobarometers (Nimis, 1995, 1999; Nimis and Ulmer, 1998).

Amphiboles are a common phase in many different arc magmas and crystallise under a narrow range of pressure, temperature and water content (Foden and Green, 1992). Given the narrow stability range of amphiboles in arc magmas they have long been targeted as potential geothermometers and geobarometers. A number of early geobarometric solutions established that the Al_{VI} content of amphiboles could be used to calibrate for pressures of crystallisation (Hammarstrom and Zen, 1986; Johnson and Rutherford, 1989; Schmidt, 1992). These solutions were later expanded to account for temperature and fO_2 (Andersen and Smith, 1995; Krawczynski et al., 2012). Holland and Blundy (1994), and earlier Blundy and Holland (1990), determined that equilibria between co-existing amphibole-plagioclase assemblages can be used to calculate magmatic temperatures.

Recent advances in amphibole thermobarometry, notably Ridolfi et al. (2012, 2010), can help to unravel the physiochemical paths through which magmas ascend to the surface. Studies have found that the composition of amphiboles responds to the physical properties (pressure, temperature, water content, oxidation state and silica content) of melts that they are in equilibrium with (Ridolfi and Renzulli, 2012; Ridolfi et al., 2010). By analysing the major element composition of amphiboles and stoichiometrically calculating their chemical composition, amphiboles can be used as geothermobarometers to ascertain the physiochemical parameters of melts that they were in equilibrium with when they formed. Ridolfi and Renzulli (2012), expanding on the work of Ridolfi et al. (2010), determined algorithms for the response of cation exchange in artificially created amphiboles to specific physiochemical conditions of their equilibrium melt. These amphibole geothermobarometric formulations are outlined below;

Eq.	Variable	Equation
[1a]	Pressure	lnP (MPa) = 38.723 - 2.6957*Si - 2.3565*Ti - 1.3006*Al - 2.7780*Fe - 2.4838*Mg - 0.6614*Ca - 0.2705*Na + 0.1117*K
[1b]	Pressure	P (MPa) = 24023 - 1,925.3*Si - 1,720.6*Ti - 1,478.5*Al - 1843.2*Fe - 1746.9*Mg - 158.28*Ca - 40.444*Na + 253.52*K
[2]	Temp.	T (˚C) = 17098 - 1322.3*Si - 1035.1*Ti - 1208.2*Al - 1230.4*Fe - 1152.9*Mg - 130.40*Ca + 200.54*Na + 29.408*K + 24.410*lnP
[3]	Oxygen fugacity	ΔNNO (log units) = 214.39 - 17.042*Si - 26.080*Ti - 16.389*Al - 18.397*Fe - 15.152*Mg + 0.2162*Ca + 6.1987*Na + 14.389*K
[4]	Melt H_2O	lnH2O melt (wt%) = -65.907 + 5.0981*Si + 3.1308*Ti + 4.9211*Al + 4.9744*Fe + 4.6536*Mg + 1.0018*Ca - 0.7890*Na - 0.539*K + 0.4642*lnP
[5]	Melt SiO_2	SiO2 (wt%) = -142.31 + 22.008*Si - 15.306*Ti + 2.1880*Al + 16.455*Fe + 12.868*Mg + 0.4085*Ca + 6.7100*Na + 20.980*K - 9.6423*10^{8}P^{-4}

These geothermobarometric formulations have been applied to the products of a number of arc volcanoes around the world, including the lava suites of Merapi, Indonesia (Costa et al., 2013; Erdmann et al., 2014) and Okataina, New Zealand (Shane and Smith, 2013). These formulations have also been applied to amphibole from plutonic rocks, e.g. Grenada, Lesser Antilles (Stamper et al., 2014) and Egmont Volcano, New Zealand (Price et al., 2016).

Utilising the amphibole thermobarometers of Ridolfi et al. (2012, 2010) this study aims to provide insights into magma evolution at the active volcano of Sangeang Api located at the eastern end of Indonesia's Sunda Arc (fig. 1). Sangeang Api erupts shoshonitic basalts to basaltic-trachyandesites that entrain a suite of cumulate gabbros and clinopyroxenites, which are interpreted to be coeval to the lavas and representative of the magma chamber processes. Amphiboles can be found in all exhumed suites, being common in both the lavas and especially the gabbros. The extensive presence of amphibole throughout both Sangeang Api's lavas and their associated cumulate xenoliths provides unparalled insights into the crustal magmatic tract of an active volcano.

GEOLOGICAL SETTING

Sangeang Api is an active volcano located off the northeast coast of the island of Sumbawa in the Flores Strait near to the easternmost extent of the Sunda Arc. Figure 1 displays the location of Sangeang Api with respect to the Sunda Arc, Sumbawa and the active/inactive volcanic centres of neighbouring Sumbawa. It has a well catalogued history of eruptions that appear to be moderately cyclical, erupting most recently in May of 2014. Subduction in this region is related to the northwards movement of the Indo-Australian plate beneath the Eurasian continent. The predominantly east-west trending Sunda Arc extends from the Andaman Islands through to the island of Flores, before continuing as the Banda Arc through a 180˚ curvature around the Banda Sea. Together, the Sunda-Banda Arc system extends for ~4800km from the Bengal Sea through to the Banda Sea. The Sunda-Banda Arc system developed between the early-Cretaceous and late-Miocene, through the addition of distinct crustal blocks to a promontory of the Eurasian continent known as Sundaland (Hall, 2011; Hall, 2012; Hall and Spakman, 2015). Sangeang Api is approximately ~120km north of the trench and 180km above the

Benioff zone. Sumbawa is close to the change in subduction from Indian oceanic material

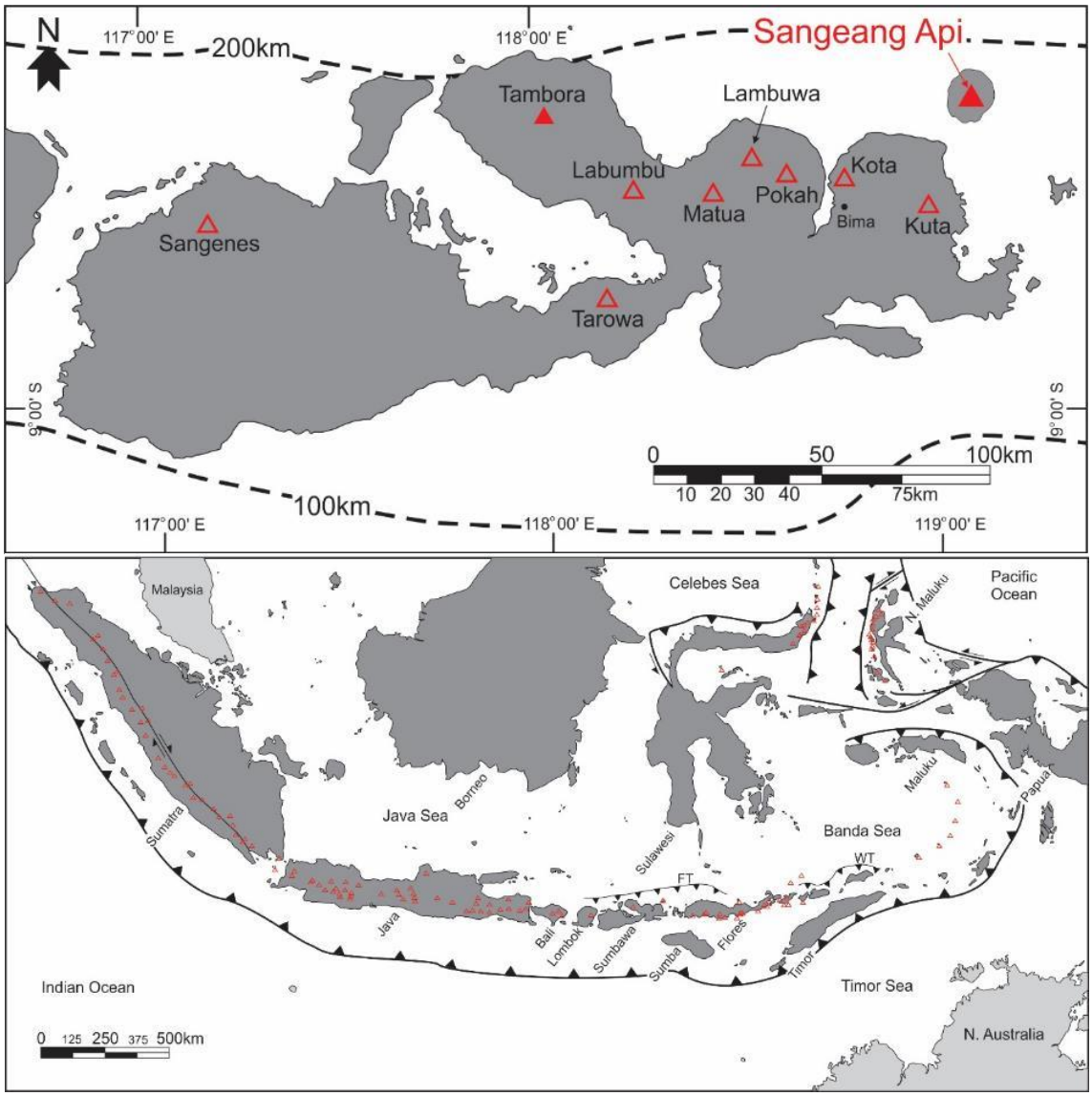

Figure 1: Map of Sunda Arc displaying the locations of active volcanoes (Siebert et al., 2011) and major tectonic boundaries, including the Flores and Wetar thrusts (FT and WT respectively). Below is a close-up image of the island of Sumbawa, displaying the location of Sangeang Api, as well as local active (closed red triangles) and inactive (open red traingles) volcanic centres. Dashed lines are contours of distance to Benioff Zone (Spakman and Hall, 2010).

to Australian continental material. Sangeang Api is emplaced upon oceanic crust with an estimated Moho depth of between ~14 and ~18km (Curray et al., 1977; Hall, 2011). Sumbawa has been volcanically active for ~8Ma, thus it is likely that the crust beneath Sumbawa has been magmatically thickened and the Moho is greater than ~14km beneath the island (Hall, 2011; Turner et al., 2003). The active volcanic cone of Doro Api is emplaced within a larger caldera structure alongside the inactive cone of Doro Mantoi. To the north of Sangeang Api is the Flores thrust, a west-east trending rear-arc thrust structure extending from the Java Sea to the north of Lombok through to the Banda Sea to the north of Flores (Beckers and Lay, 1995; Koulali et al., 2016; Silver et al., 1986). Statistical analyses of quaternary volcanic localities from Java through to western Flores have led to the identification of four approximately NW-SE trending lineaments in

volcano distribution (Pacey et al., 2013); western (west Java), central western (central Java), central eastern (eastern Java to central Sumbawa) and eastern (central Sumbawa through central Flores). However, there is a significant latitudinal gap between the most recent active volcanic centres at the north of Sumbawa (Tambora and Sangeang Api) and Lombok (Rinjani) to those at the southern edge of Flores (Wai Sano, etc.), suggesting that there may be a cross-arc sinistral wrench fault separating Sumbawa and Flores. It is likely that this crustal fault structure is controlling the location of active volcanism.

PETROLOGY OF SANGEANG API PRODUCTS

Sangeang Api erupts a suite of silica-undersaturated, shoshonitic, basalts to basaltic trachyandesites. The lavas display aphanitic and porphyritic textures, which are often vesiculated. These contain *cpx-plag-mgt±oliv* and *cpx-plag-mgt-amph* phenocryst and microphenocryst populations. In addition to these phenocryst and microphenocryst populations, the lavas also entrain a diverse population of xenocrysts and megacrysts that are interpreted to be inherited from disaggregated cumulate piles. Amphibole is a common phase both in the magmatic crystal populations and the inherited crystal populations. Often the larger phenocrysts, xenocrysts and megacrysts have incongruent breakdown rims composed of clinopyroxene, plagioclase and abundant magnetite.

Entrained within the lavas are numerous cumulate xenoliths that can be separated into two broad groups of gabbros and pyroxenites. A range of cumulate textures are observed within these two groups of xenoliths; from adcumulate, through orthocumulate and poikilitic textures. Amphibole is observed within both cumulate populations; however, it is much more common in the gabbros than the pyroxenites, up to 60% of the modal proportions in some samples. The gabbros are composed of variable amounts of plagioclase, clinopyroxene, magnetite and amphibole. Amphibole is both a cumulate, post-cumulate and poikilitic phase in the gabbro group of cumulates. Whereas, the pyroxenite cumulate group are dominated by two distinct mineral populations – *clinopyroxene-magnetite* and *clinopyroxene-olivine*. Amphibole is found much less commonly in the pyroxenites and is predominantly observed as a post-cumulate phase and less rarely as a poikilitic phase. The phenocryst populations (often disaggregated) of the lavas and the cumulate assemblages of the xenoliths are similar, suggesting a shared heritage between the lavas and cumulates. This is supported by major and trace element compositional trends, with fractional crystallisation of the cumulate phases broadly driving evolutionary trends in the lava composition, suggesting that the lavas and cumulate xenoliths are cognate. However, the lavas are not always co-magmatic with the cumulate xenoliths entrained within them. Commonly, the lava phenocryst populations and cumulate assemblages are distinctly different and in some lava samples multiple distinct cumulate assemblages are observed, rarely intermingled with one another. Within several cumulate xenoliths are post-crystallisation, cataclasite textures, evidence of a shear zone in the crustal magmatic tract. Thus, the lavas and the entrained cumulate xenoliths can be described as cognate, but not necessarily co-magmatic in every instance.

The presence of amphibole throughout each lithology and in a wide variety of textural relationships provides an unparalled opportunity to investigate the physiochemical

evolution of both the lavas and cumulate xenoliths by making use of the geothermobarometrical formulations of Ridolfi et al. (2010, 2012).

METHODS

Thin sections of 27 amphibole bearing samples were analysed using EPMA and LA-ICPMS to produce major and trace element data.

Major element compositions of amphiboles were analysed by EPMA at Adelaide Microscopy, University of Adelaide (Cameca SXFive and Cameca SX51) and the Research School of Earth Sciences, Australian National University (Cameca SX100). Polished thin sections were analysed with a 10μm spot size at 20nA and 15kV for a select group of elements. Individual spots were analysed for a total of 60 seconds with a background of 20 seconds using NIST-610 as a standard and measuring BHVO-2 and BCR-2 to test for reliability. Individual crystals were measured in along axis transects to identify any zoning within the mineral.

LA-ICPMS was used to investigate amphibole trace element compositions. Samples were analysed at Adelaide Microscopy (University of Adelaide) using a New Wave UP-213 laser ablation system attached to an Agilent 7500cx mass spectrometer. Samples were ablated for 120 seconds with a 30 second background using a 30μm spot size.

AMPHIBOLE PETROLOGY

Amphibole is present in differing proportions amongst the entire suite of rocks erupted by Sangeang Api, including both the lava and cumulate xenolith suites. Amphibole is relatively common within the lavas; it is observed as phenocrysts (fig. 2a and 2b) and to a lesser extent microphenocrysts making up the groundmass of the lava samples. Largely the phenocrysts and microphenocrysts of the lavas are euhedral and prismatic, with equant boundaries (fig. 2a), but in some samples the phenocrysts display subhedral-euhedral acicular prismatic shapes (fig. 2b). Common amongst both the phenocrysts and microphenocrysts are the presence of a surrounding overgrowth rim of Fe-oxides (fig. 2a and 2b) between 0.1-1.5μm thick. Many samples contain better developed reaction rims surrounding remnant cores of, and in some cases entirely consuming, amphibole phenocrysts. These coronas are composed predominantly of Fe-oxides and clinopyroxene with lesser plagioclase and alkalic glass.

Several samples contain larger megacrysts and xenocrysts that usually span in length from 0.5-10mm but can range up to 30mm. Megacrysts are characterised by subhedral-euhedral prismatic shapes, often displaying incongruent breakdown textures that are rich in magnetite and clinopyroxene as well as plagioclase and alkalic glass. Xenocrysts can be distinguished by their clearly fractured crystal forms, often these appear to have been similar in shapes to the megacrysts and show remnants of a euhedral-prismatic structure (fig. 2d).

Within the cumulate xenoliths amphibole displays a broad range of crystal forms and phase relationships. These are outlined in the following sections:

Gabbros

1. **Primary cumulates:** Amphibole can be observed as primary cumulates in many of the gabbroic samples (fig. 2c); such primary cumulates display both strongly prismatic as well as elongate and needle like crystal forms. Often these minerals can be up to 60mm in length along the long-axis with cross-sections up to 15mm across. Primary cumulate amphibole is observed pre-dating or crystallising alongside plagioclase, however, the cumulate amphibole crystallised after clinopyroxene and magnetite in most samples – whilst there are examples of amphibole pre- or syn-dating these minerals. Commonly these cumulate amphiboles display well established incongruent breakdown textures, which much like in the lavas are dominated by magnetite with lesser clinopyroxene, alkali glass and more rarely plagioclase and olivine. More rarely there is evidence that these amphiboles have undergone complete decompression melting, leaving behind only the breakdown products.
2. **Post-cumulate:** Post-cumulate amphibole is common within the gabbros in two different textural situations;
    a. Intra-cumulate: In a rare number of samples amphibole is observed in the interstitial spaces between the primary cumulate mineralogy. Inherently, these intra-cumulate amphiboles post-date the primary cumulate mineralogy, which in the case of the gabbros are predominantly clinopyroxene and plagioclase. Depending on the sample, the intra-cumulate amphibole was formed at the same time as, after or even before magnetite.
    b. Poikilitic: The most important post-cumulate amphibole phase found within the gabbros is that with a poikilitic texture (fig. 2e). Poikilitic amphibole is found in many of the gabbro samples and is generally large relative to the other cumulate mineralogy. The crystal populations entrained within these amphiboles range in size from 0.05-5mm. Generally, the chadacryst and oikocryst populations of the poikilitic amphiboles is the same as the cumulate populations of the sample in which they are found (fig. 2e).

Pyroxenites

Amphibole is observed in three distinct textural sites within the pyroxenite samples, these are outline below;

1. **Mineral overgrowths:** Within a few rare samples amphibole is observed overgrowing clinopyroxene cumulates. Often these are very thin overgrowths – less than 1mm in thickness. The mineral overgrowths are indented by late growing minerals of magnetite and more rarely plagioclase.
2. **Intra-cumulate:** Amphibole is often observed infilling space between the other cumulate mineralogy and post-dating all other mineralogy (fig. 2f). Textural evidence, such as that observed in figure 2f, suggests that this intra-cumulate

Figure 2a-f: Photomicrographs displaying the common textural relationships of amphibole in the Sangeang Api lavas (2a & 2b), gabbros (2c, 2d & 2e) and pyroxenites (2f). (a) Trachyte with amphibole euhedral, prismatic phenocrysts with thin opacitic rims, alongside clinopyroxene phenocrysts in a hyalopilitic groundmass. (b) Vesiculated hypocrystalline lava with abundant phenocrysts of opacitised amphibole (basal sections), clinopyroxene and plagioclase with well-developed sieve textures in a magnetite rich groundmass. (c) Hbl-gabbro composed of elongate and basal sections of primary cumulate amphibole surrounded by plagioclase. (d) Gabbro composed of primary clinopyroxene and magnetite with later plagioclase with a xenocryst of twinned, prismatic amphibole. (e) Poikilitic amphibole encasing subhedral plagioclase and magnetite crystals. (f) Pyroxenite formed of large clinopyroxene and olivine, with late intersertal amphibole.

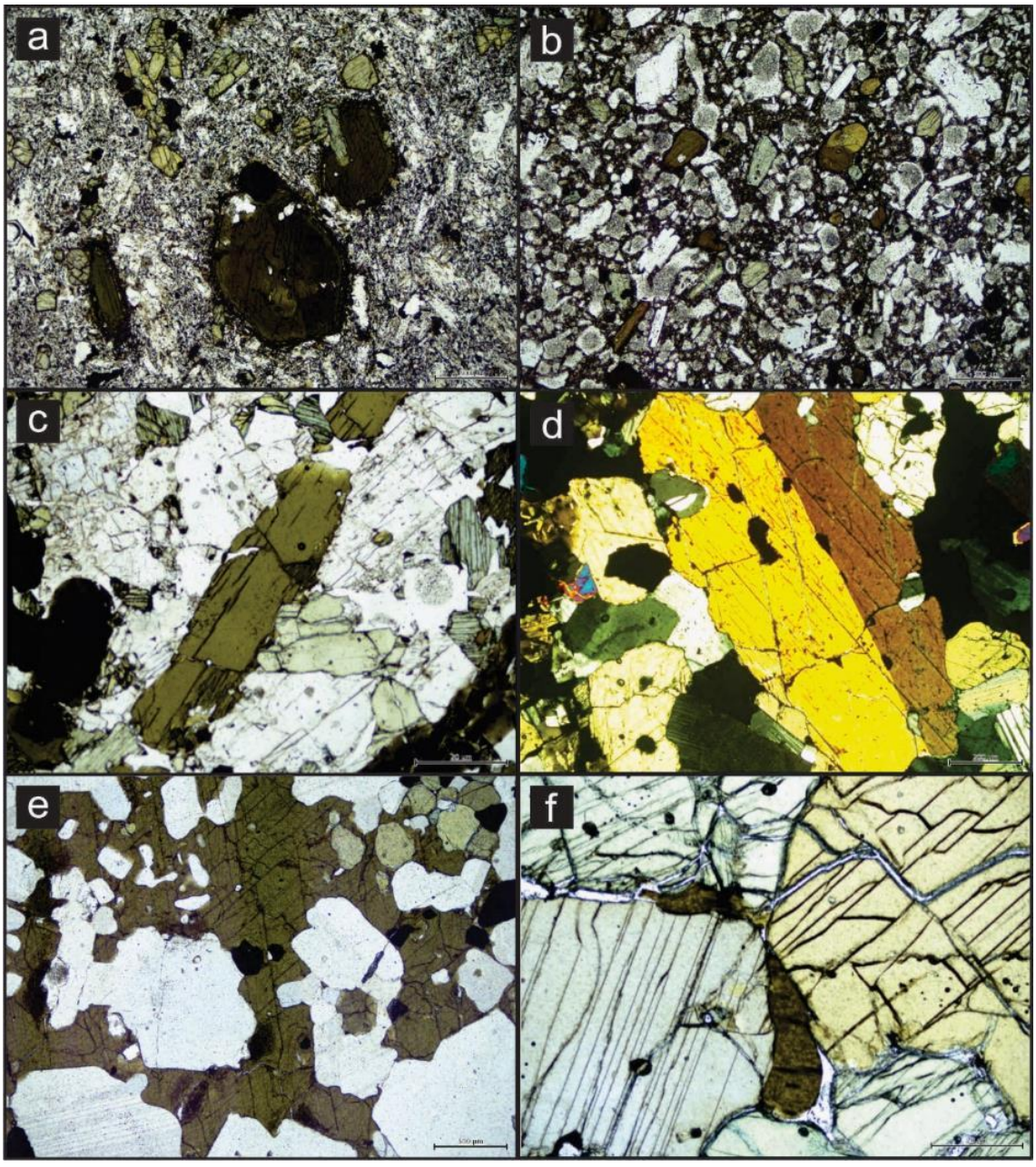

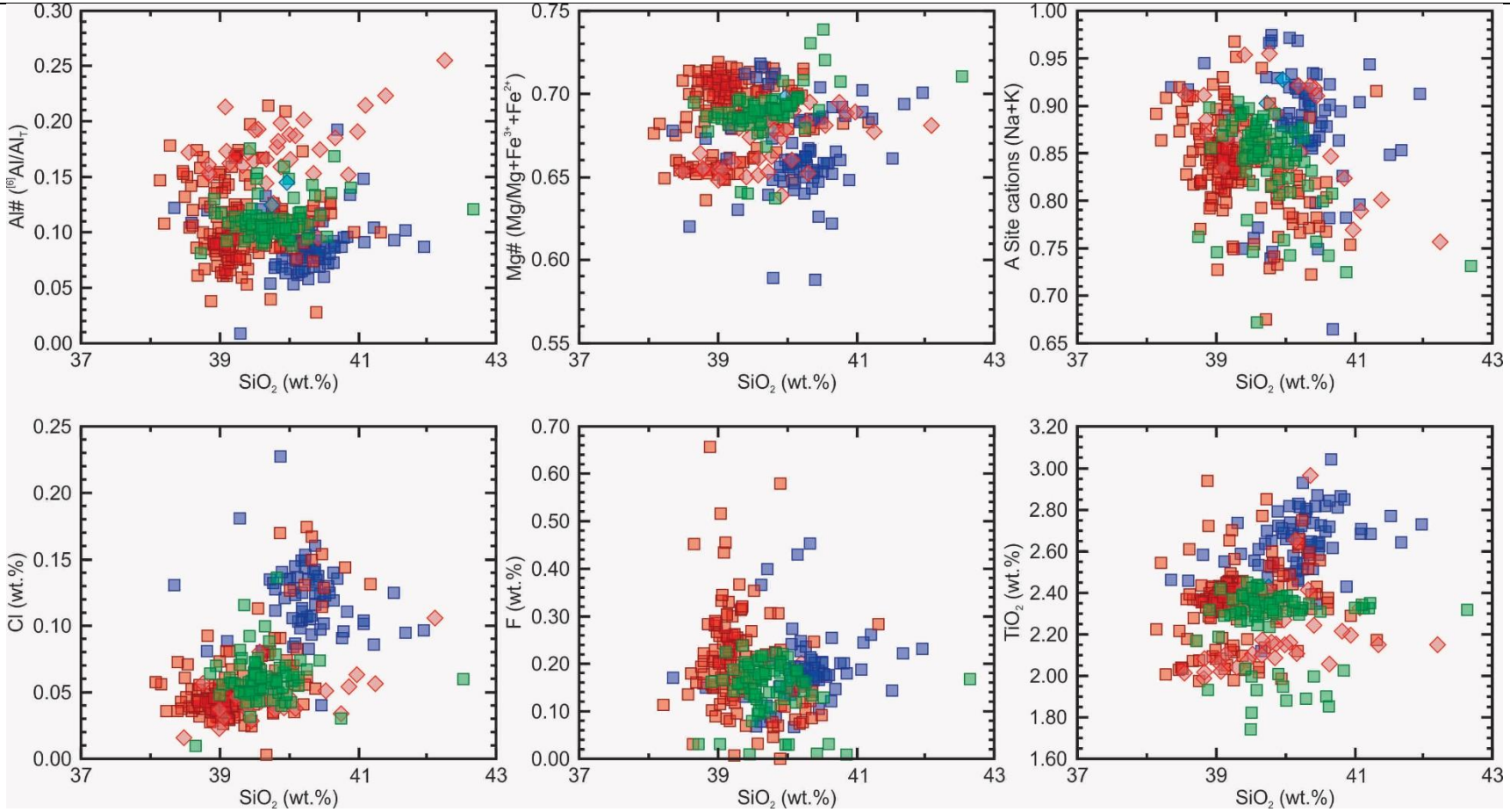

Figure 3a-f: Discrimination diagrams of amphibole chemistry. Symbols: Blue squares = Mg-hastingsite analyses from lavas, blue diamond's = pargasite analyses from lavas, red squares = Mg-hastingsite analyses from gabbros, red diamond's = pargasite analyses from gabbros and green squares = Mg-hastingsite analyses from pyroxenites. Al#, Mg# and A site cations stoichimetrically calculated using the 13-cation method of Leake et al. (1997).

Table 1: Average amphibole major element from representative amphibole-bearing samples of Sangeang Api. Mineral species abbreviations are as follows; Mg-Hst = Magnesio-Hastingsite, Parg = Pargasite. Al# calculated as Al_{VI}/Al_{Total}.

Sample No.	**B10**		**B1B**		**B24**		**B24**		**B27**		**B7**		**B7**		**B8**	
Lithology	Gabbro		Gabbro		Gabbro		Gabbro		Gabbro		Gabbro		Gabbro		Gabbro	
No. Analyses	10		6		4		11		7		15		6		27	
Element (wt.%)	Average	1s.d.	Average	1s.d.	Average	1s.d.	Average	1s.d.	Average	1s.d.	Average	1s.d.	Average	1s.d.	Average	1s.d.
SiO_2	40.38	0.37	39.59	0.76	40.18	1.09	40.64	0.78	39.33	0.58	39.73	0.53	39.89	0.43	39.17	0.46
TiO_2	2.35	0.04	2.55	0.04	2.19	0.09	2.17	0.08	2.44	0.08	2.48	0.14	2.35	0.07	2.08	0.06
Al_2O_3	13.64	0.21	13.51	0.53	15.06	0.50	15.12	0.56	14.13	0.20	13.55	0.47	13.85	0.49	14.75	0.25
Cr_2O_3	0.00	0.01	0.00	0.01	0.00	0.01	0.01	0.01	0.01	0.01	0.02	0.02			0.00	0.01
FeO	11.55	0.16	11.08	0.17	11.10	0.21	11.07	0.24	10.68	0.42	11.15	0.61	10.95	0.24	12.02	0.20
MnO	0.17	0.01	0.18	0.03	0.18	0.01	0.18	0.01	0.16	0.04	0.19	0.07	0.14	0.04	0.18	0.01
MgO	13.94	0.22	13.81	0.27	13.32	0.22	13.36	0.23	14.05	0.35	13.57	0.53	13.33	0.24	12.82	0.16
CaO	12.17	0.11	11.74	0.25	12.40	0.14	12.42	0.15	12.11	0.18	12.00	0.36	12.47	0.04	12.43	0.08
Na_2O	1.99	0.04	2.17	0.07	1.99	0.07	1.98	0.07	2.39	0.31	2.16	0.10	2.11	0.11	1.92	0.04
K_2O	1.71	0.03	1.54	0.07	1.75	0.07	1.74	0.08	1.48	0.21	1.53	0.09	1.60	0.05	1.76	0.04
F			0.10	0.03					0.11	0.07	0.09	0.05				
Cl	0.14	0.02	0.06	0.02	0.05	0.02	0.05	0.02	0.07	0.03	0.34	0.37	0.80	0.00	0.04	0.01
Total	98.04	0.86	96.34	0.60	98.23	1.19	98.73	0.79	96.95	0.73	96.72	0.59	97.41	0.33	97.16	0.64
Al#	0.11	0.01	0.11	0.01	0.19	0.03	0.20	0.03	0.12	0.01	0.13	0.03	0.16	0.02	0.16	0.02
Mineral species	Mg-Hst		Mg-Hst		Mg-Hst		Parg		Mg-Hst		Mg-Hst		Parg		Mg-Hst	

Table 1: Average amphibole major element from representative amphibole-bearing samples of Sangeang Api. Mineral species abbreviations are as follows; Mg-Hst = Magnesio-Hastingsite, Parg = Pargasite. Al# calculated as Al_{VI}/Al_{Total}.

Sample No.	**B8**		**BC14/039**		**BC14/048**		**SA12-X01**		**SA12-X011**		**SA21**		**SA22**		**BC14/004**	
Lithology	Gabbro		Gabbro		Gabbro		Gabbro		Gabbro		Gabbro		Gabbro		Lava	
No. Analyses	14		2		60		27		8		3		2		59	
Element (wt.%)	Average	1s.d.	Average	1s.d.	Average	1s.d.	Average	1s.d.	Average	1s.d.	Average	1s.d.	Average	1s.d.	Average	1s.d.
SiO_2	39.31	0.46	40.06	0.46	39.12	0.23	39.17	0.21	39.97	0.21	39.25	0.64	40.30	0.17	40.34	0.49
TiO_2	2.08	0.06	2.62	0.32	2.38	0.04	2.39	0.12	2.37	0.09	2.60	0.10	2.81	0.22	2.68	0.12
Al_2O_3	14.83	0.25	12.26	0.88	14.08	0.40	13.20	0.25	13.12	0.20	13.82	0.61	11.98	0.09	12.85	0.54
Cr_2O_3	0.00	0.01	0.02	0.03	0.01	0.01	0.01	0.01	0.01	0.01	0.03	0.06				
FeO	11.96	0.23	11.62	0.56	10.73	0.26	10.96	0.39	10.73	0.11	11.00	0.22	12.05	0.27	12.36	0.78
MnO	0.18	0.01	0.23	0.05	0.15	0.03	0.16	0.03	0.16	0.02	0.22	0.02	0.24	0.01	0.31	0.07
MgO	12.70	0.14	14.37	0.24	14.34	0.20	14.31	0.21	14.48	0.20	13.48	0.18	12.92	0.02	13.44	0.46
CaO	12.41	0.08	11.33	0.04	12.19	0.12	12.03	0.07	11.93	0.13	11.80	0.16	12.30	0.06	11.78	0.29
Na_2O	1.92	0.05	2.37	0.05	2.20	0.06	2.35	0.13	2.24	0.03	2.19	0.09	2.23	0.02	2.66	0.14
K_2O	1.77	0.04	1.16	0.01	1.45	0.05	1.34	0.05	1.46	0.08	1.62	0.07	1.44	0.01	1.44	0.19
F			0.28	0.04	0.23	0.08	0.29	0.22	0.16	0.09	0.18	0.06	0.20	0.00	0.21	0.11
Cl	0.04	0.02	0.05	0.01	0.05	0.01	0.04	0.01	0.06	0.02	0.19	0.19	0.80	0.00	0.12	0.03
Total	97.19	0.73	96.36	0.35	96.92	0.43	96.24	0.31	96.70	0.24	96.40	0.24	97.56	0.15	98.20	0.85
Al#	0.17	0.02	0.03	0.01	0.09	0.01	0.07	0.01	0.09	0.01	0.12	0.00	0.10	0.01	0.08	0.02
Mineral species	Parg		Parg		Mg-Hst		Mg-Hst		Mg-Hst		Mg-Hst		Parg		Mg-Hst	

Table 1: Average amphibole major element from representative amphibole-bearing samples of Sangeang Api. Mineral species abbreviations are as follows; Mg-Hst = Magnesio-Hastingsite, Parg = Pargasite. Al# calculated as Al_{VI}/Al_{Total}.

Sample No.	**SA18**		**SA19**		**SA26**		**SA26**		**SA8**		**B16**		**B21**		**BC14/020**	
Lithology	Lava		Lava		Lava		Lava		Lava		Pyroxenite		Pyroxenite		Pyroxenite	
No. Analyses	4		4		6		2		3		3		9		63	
Element (wt.%)	Average	1s.d.	Average	1s.d.	Average	1s.d.	Average	1s.d.	Average	1s.d.	Average	1s.d.	Average	1s.d.	Average	1s.d.
SiO_2	39.59	0.16	39.61	1.20	39.91	0.91	39.87	0.16	39.94	0.46	39.64	0.26	39.68	0.59	39.77	0.50
TiO_2	2.54	0.05	2.63	0.16	2.46	0.31	2.40	0.05	2.61	0.03	2.01	0.02	1.97	0.17	2.34	0.04
Al_2O_3	13.61	0.09	13.50	0.80	12.85	0.67	13.79	0.16	13.19	0.07	14.69	0.06	13.88	0.30	13.90	0.27
Cr_2O_3	0.02	0.01	0.02	0.02					0.01	0.00	-0.01	0.01	0.02	0.01		
FeO	10.31	0.24	11.34	0.11	12.50	1.06	11.03	0.51	10.37	0.26	12.75	0.13	10.96	0.26	11.31	0.19
MnO	0.17	0.02	0.27	0.02	0.18	0.07			0.17	0.02	0.14	0.01	0.15	0.04	0.17	0.02
MgO	14.34	0.05	13.57	0.41	12.86	0.64	13.75	0.18	14.18	0.12	12.70	0.18	13.96	0.28	14.07	0.27
CaO	11.79	0.15	11.84	0.16	12.07	0.49	12.73	0.28	11.71	0.08	12.03	0.12	11.77	0.34	12.13	0.10
Na_2O	2.07	0.04	2.39	0.07	2.17	0.16	2.18	0.28	2.33	0.10	1.88	0.01	2.19	0.05	2.28	0.08
K_2O	1.52	0.06	1.64	0.07	1.39	0.05	1.41	0.06	1.50	0.03	2.02	0.03	1.41	0.08	1.60	0.06
F	0.09	0.03	0.17	0.02					0.19	0.15			0.04	0.03	0.17	0.03
Cl	0.06	0.02	0.12	0.03	0.80	0.00	0.80	0.00	0.05	0.02	0.12	0.02	0.22	0.33	0.06	0.01
Total	96.08	0.29	97.09	1.07	97.13	0.72	97.56	0.15	96.25	0.28	97.98	0.18	96.25	0.52	97.79	0.88
Al#	0.10	0.01	0.11	0.01	0.11	0.02	0.13	0.01	0.11	0.00	0.16	0.01	0.13	0.01	0.10	0.01
Mineral species	Mg-Hst		Mg-Hst		Mg-Hst		Parg		Mg-Hst		Mg-Hst		Mg-Hst		Mg-Hst	

amphibole crystallised from magmatic remnants trapped in, or percolating through, the cumulate pile. Largely these intra-cumulate minerals represent a very small portion of the samples in which they are found (<1% modal proportion) and in some samples display 'tear-drop' shapes (fig. 2f) between well-formed cumulate phases.

3. **Poikilitic:** Large poikilitic amphibole (3-15mm across) is found in several pyroxenite samples. The mineral phases that are entrained within the poikilitic amphibole share the same mineralogy as the cumulate mineralogy surrounding them, often orders of magnitude in size smaller than the surrounding mineralogy.

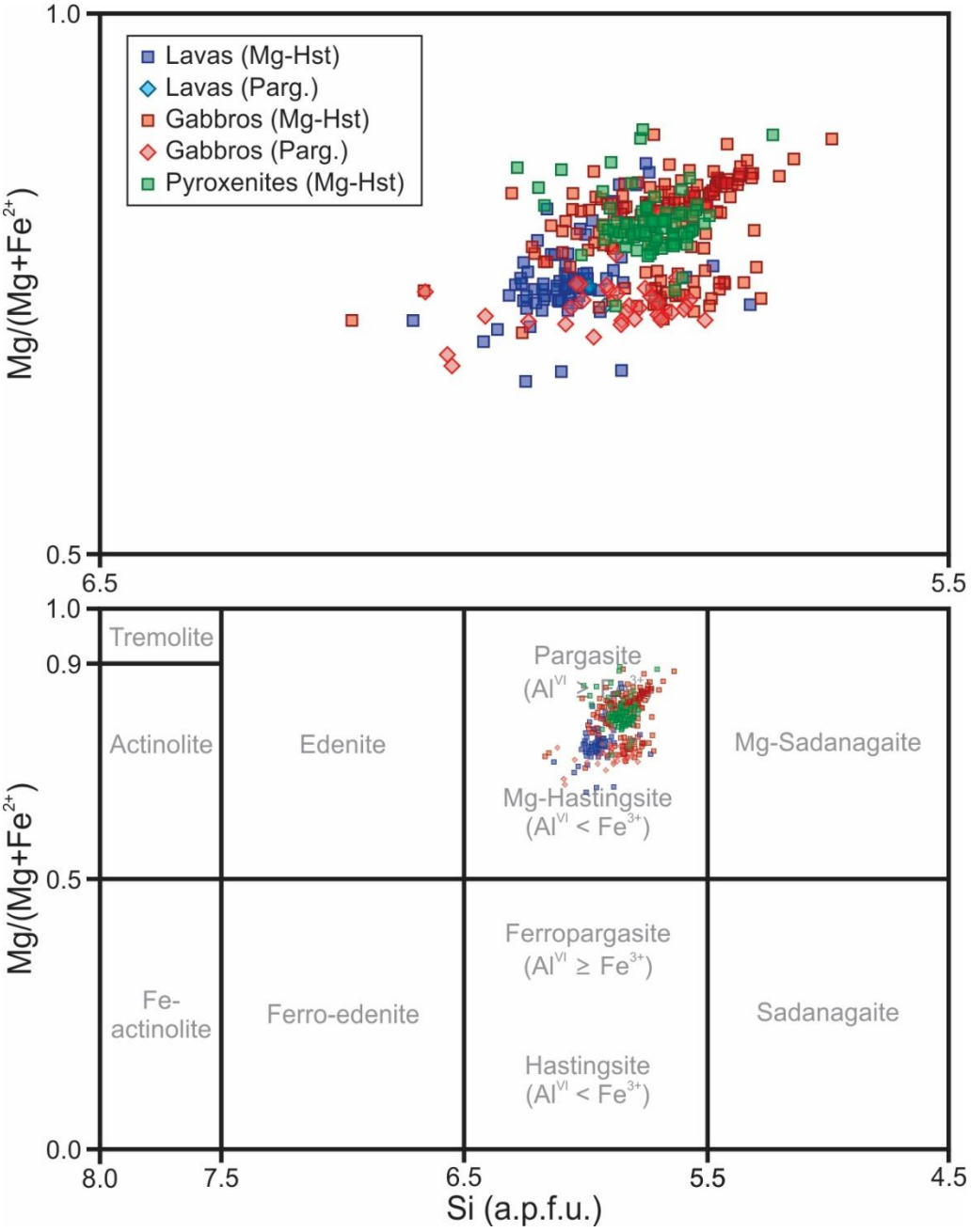

Figure 4: Amphibole classification diagram, altered from Leake et al. (1997). Symbols are the same as those in figure 3. Cations stoichimetrically calculated using the 13-cation method of Leake et al. (1997).

AMPHIBOLE CHEMISTRY

This study presents a total of 366 spots analyses; 81 lava analyses, 206 gabbro analyses and 79 pyroxenite analyses. Reflecting the diverse textural and phase relationships displayed by the amphibole population, amphibole compositions overlap between the cumulate xenolith and lava suites. Amphiboles from the gabbros, pyroxenites and lavas are predominantly Mg-Hastingsite whilst there are a smaller number of pargasites found within the gabbros and to a lesser extent the lavas. Figures 3 and 4 displays compositional variations between amphiboles from the lithological suites of Sangeang Api.

Gabbro analyses

Amphiboles within the gabbro samples display a broad chemical diversity, overlaying the compositions of the amphiboles from either the pyroxenites or lavas. Both the Mg-Hastingsites and Pargasites span a range in SiO_2 content from 38-42wt.%, whilst their other chemistry contrasts. With the Pargasites having lower Mg# (Parg=0.64-0.69, Mg-Hst=0.67-0.72), higher Al# - Al in sixfold co-ordination / Total Al (parg=0.14-0.25, Mg-Hst=0.02-0.17) and significantly lower TiO_2 (Parg=1.95-2.3wt.%, Mg-Hst=2.2-3wt.%) (fig. 3). Despite this there is little to no difference in other elements, such as Cl or F (fig. 3).

Pyroxenite analyses

The compositions of the amphiboles analysed within the pyroxenite samples are intermediate to those found within the gabbros or lavas (see figs. 3 and 4). As mentioned previously all analysed samples are Mg-Hastingsite in composition (fig. 4). The Mg-Hastingsites span a range in SiO_2 from 38.5-41wt.%, with intermediate Al# (0.08-0.12) and Mg# (0.67-0.71) (fig. 3). Despite a small number of outliers, most analysed spots from the pyroxenites are distributed in a tight pack with little compositional distinction to be made (fig. 3 and 4).

Lavas

Amphiboles analysed within the lava samples are largely Mg-Hastingsite in composition with only 2 analyses being pargasitic in composition (fig. 4). Both the pargasites and Mg-hastingsites are compositionally similar, the lavas appear to display two separate groupings within the Mg# data (0.58-0.66, 0.68-0.72) and have the lowest Al# of all lithological groups (0.05-0.10) (fig. 3). They also have the highest Cl and TiO_2 contents of any analysed samples (Cl=0.08-0.27wt.% and TiO_2=2.5-3wt.%) (fig. 3).

Across all analysed samples a positive trend can be observed between SiO_2 and Cl content (fig.3), from the gabbro analyses through to the intermediate pyroxenite samples and finally the lava analyses. A similar trend between increasing SiO_2 and increasing Cl can be observed amongst the whole-rock analyses, suggesting that this in part a product of fractionation within the system. Interestingly a similar trend is not observed in fluorine content as might be expected.

THERMOBAROMETRY RESULTS

The formulations of Ridolfi and Renzulli (2012) were applied to the amphiboles analysed in this study, the outcomes of which can be seen in figures 5a-c. This returned estimates of pressure, temperature, water content and magma redox state. Calculated pressure estimates span a near continuous range from ~974MPa to ~338MPa; within the separate lithologies and mineral end-members there are significant differences in the pressure range. These pressures are consistent with crystallisation over the range 34-12km depth. Mg-Hastingsites from the lavas span a range from 890-400MPa, whilst those analyses with a pargasitic composition record pressures of 595-600MPa. Gabbros analyses with a Mg-hastingsite composition span the entire range in pressures, however the bulk of these analyses are found in three clusters; the deepest and smallest of these spans from 850-810MPa, followed by a shallower cluster between 790-715MPa and finally a larger continuous range from 700-450MPa. Compared to this the pargasitic amphiboles from the gabbros display a smaller range in pressures from 930-390MPa, with most analyses recording pressures between 930-695MPa. Analyses from the pyroxenites display a much tighter, compact and intermediate range of recorded pressures than the gabbros – from 780-520MPa.

Temperature estimates are similarly distributed in a continuous range from 1072-976˚C (fig. 5b) and are spread between the different lithologies and mineral end-members. Pargasites from the lavas record temperature estimates from 1041-1039˚C, whilst the Mg-hastingsites span an estimated pressure range from 1057-976˚C with the majority between 1022˚C and 998˚C. Except for two outliers at ~980˚C the majority of Mg-hastingsite analyses from the gabbros samples span from 1007-1072˚C with no obvious grouping as seen in the pressure estimates. The gabbro pargasite samples span from 1062-995˚C, with most grouped between 1062-1035˚C. As observed in the pressure estimates the analyses from the pyroxenites are similarly tightly packed and intermediate in estimated temperatures between 1051 and 1011˚C.

Estimated water contents show a continuous decrease from 6.51 to 3.15wt.% H_2O to lower pressures (fig. 5a) and temperatures (fig. 5b), suggesting that these melts were continuously degassing with respect to water as they ascended to the surface. Mg-hastingsites from the lavas span this entire range in estimated melt water content, however, the majority are clustered towards the lowest end of water content (4.74-3.14wt.% H_2O). The pargasites from the lavas are intermediate in water content ~5.1wt.% H_2O. The estimated water contents of the gabbros that crystallised the Mg-hastingsite span from 6.04-3.56wt.% H_2O, whilst the pargasites span from 6.29-4.11wt.%H_2O, with the majority between 6.29 and 5.61wt.% H_2O. Analyses from the pyroxenite samples range from 5.77-4.18wt.% H_2O, with the majority between 4.71 and 4.18wt.% H_2O.

Unlike water content, which displays a range spanning from high water content at high pressures and temperatures to low water contents at low pressures and temperatures, the melts show an anticlockwise trend of oxidation at higher pressures and temperatures from the lowest depth to around 20km before trending to more reduced melts to the shallowest depths, as demonstrated in figure 5c. The Mg-hastingsite lavas are amongst the most

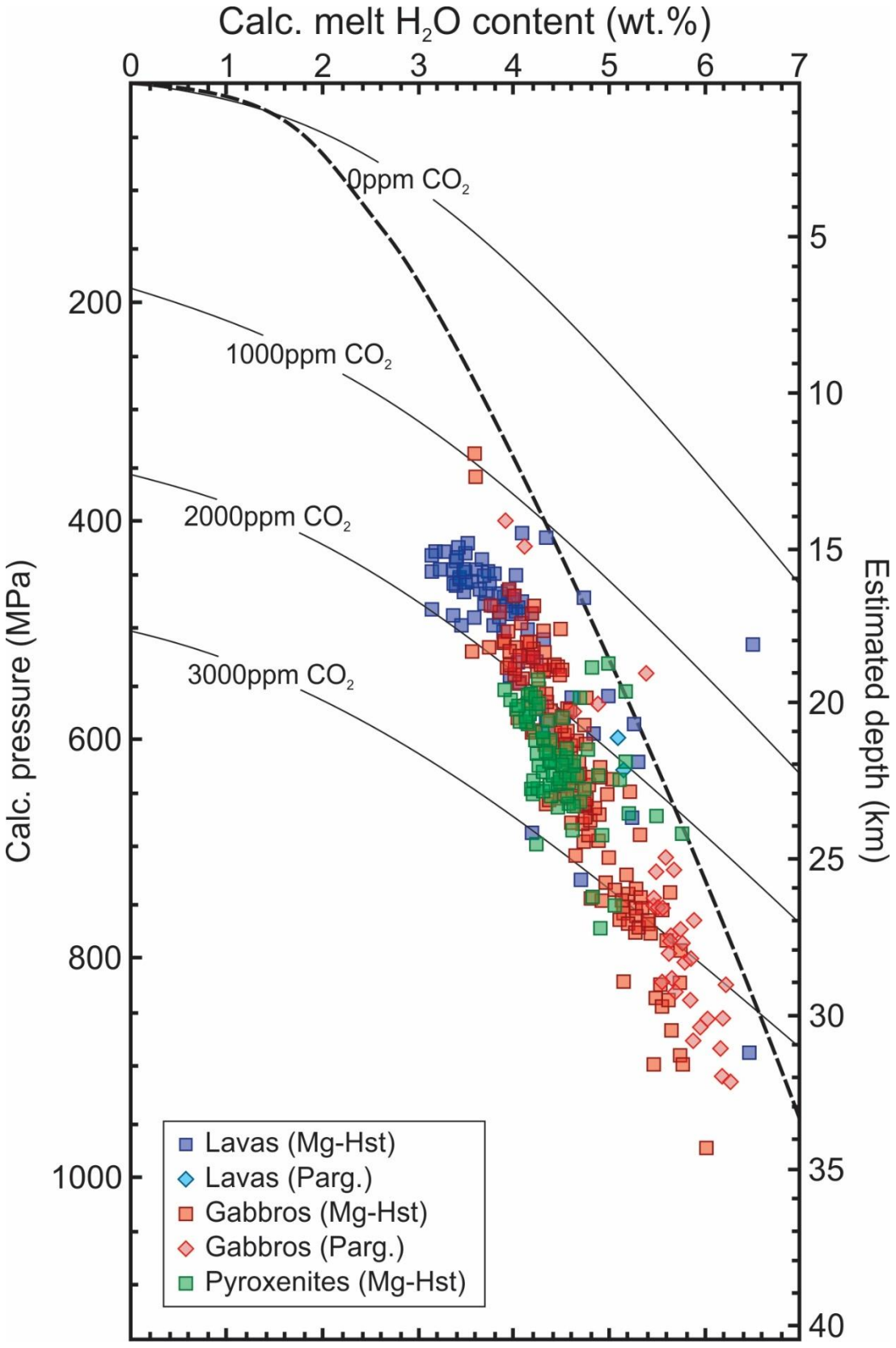

Figure 5a: Results of amphibole geothermobarometry and hygrometry calculated using the calibrations of Ridolfi and Renzulli (2012). Symbols are the same as in figure 3. Solid lines in background show vapour saturation curves at 1000°C and varying amounts of CO_2. Dashed line represents possible vapour saturated degassing curve with an initial CO_2 content of 3800ppm and continual degassing of both CO_2 and H_2O.

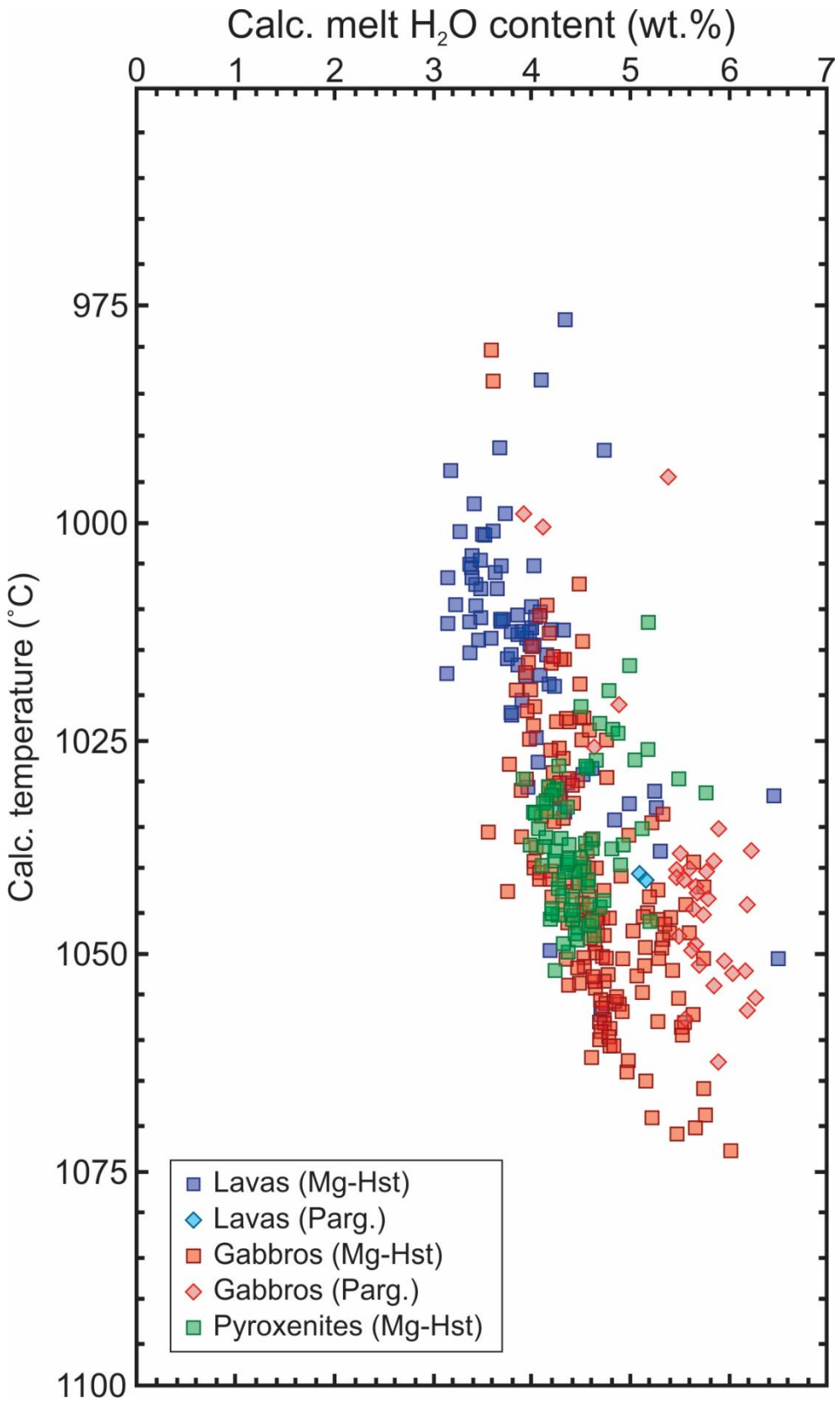

Figure 5b: Results of amphibole geothermobarometry, calculated using the calibrations of Ridolfi and Renzulli (2012). Symbols are the same as in figure 3.

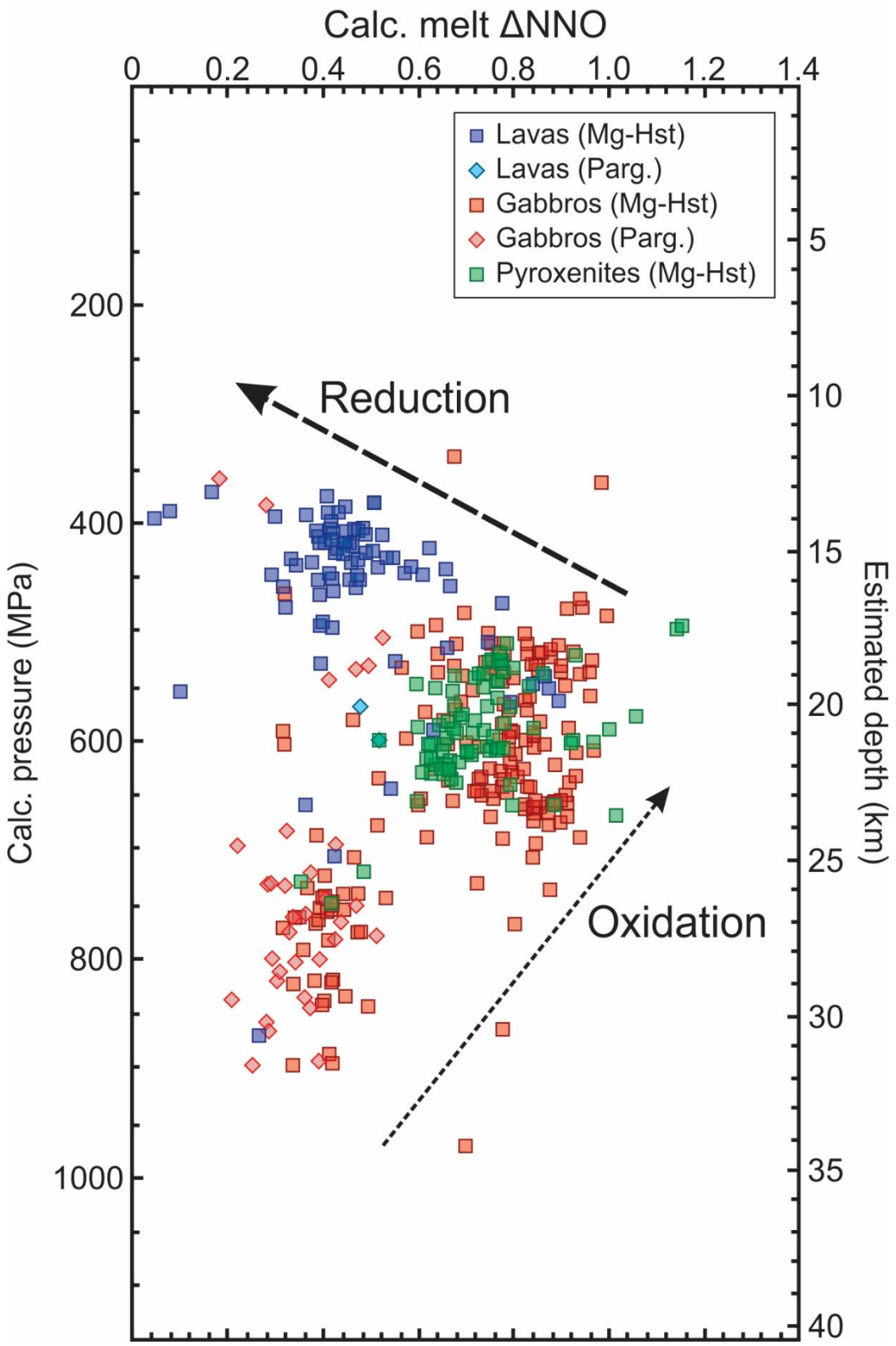

Figure 5c: Results of amphibole geothermobarometry and oxybarometry calculated using the calibrations of Ridolfi and Renzulli (2012). Symbols are the same as in figure 3. Dashed arrows show oxidation trend at pressures greater than ~600MPa and reduction trend at pressures lower than ~600MPa.

Table 2: Estimated temperature, pressure, oxidation state and water content of representative amphibole-bearing samples, calculated using the Ridolfi and Renzulli (2012) equations. Standard errors given for each condition.

Sample No.	**B10**		**B1B**		**B24**		**B24**		**B27**		**B7**		**B7**		**B8**	
Lithology No. Analyses	Gabbro 10		Gabbro 6		Gabbro 4		Gabbro 11		Gabbro 7		Gabbro 15		Gabbro 6		Gabbro 27	
Mineral species	Mg-Hst		Mg-Hst		Mg-Hst		Parg		Mg-Hst		Mg-Hst		Parg		Mg-Hst	
Element (wt.%)	Average	1s.d.	Average	1s.d.	Average	1s.d.	Average	1s.d.	Average	1s.d.	Average	1s.d.	Average	1s.d.	Average	1s.d.
T (°C) (error = 22°C)	1023.89	5.05	1027.87	17.89	1060.34	9.23	1041.25	16.88	1049.97	8.05	1025.35	11.03	1035.41	10.33	1050.68	7.20
P (MPa)	566.34	19.27	584.02	90.36	826.62	61.19	803.80	100.85	665.40	35.44	573.91	65.86	643.39	80.99	782.62	45.46
Uncertainty (Max error)	62.30	2.12	64.24	9.94	90.93	6.73	88.42	11.09	73.19	3.90	63.13	7.24	70.77	8.91	86.09	5.00
Oceanic depth (km)	19.98	0.68	20.61	3.19	29.17	2.16	28.36	3.56	23.48	1.25	20.25	2.32	22.70	2.86	27.61	1.60
Continental depth (km)	21.39	0.73	22.06	3.41	31.22	2.31	30.36	3.81	25.13	1.34	21.68	2.49	24.30	3.06	29.56	1.72
ΔNNO	0.72	0.07	0.68	0.11	0.43	0.01	0.41	0.08	0.65	0.04	0.62	0.19	0.40	0.10	0.40	0.04
logfO2 (error = 0.4)	-9.05	0.12	-9.03	0.20	-8.75	0.14	-9.04	0.23	-8.72	0.16	-9.13	0.25	-9.19	0.12	-8.92	0.11
H2Omelt (wt.%)	4.35	0.17	4.44	0.34	5.27	0.27	5.93	0.26	4.73	0.28	4.55	0.42	5.08	0.62	5.43	0.21
Uncertainty	0.65	0.03	0.67	0.05	0.79	0.04	0.89	0.04	0.71	0.04	0.68	0.06	0.76	0.09	0.81	0.03

Table 2: Estimated temperature, pressure, oxidation state and water content of representative amphibole-bearing samples, calculated using the Ridolfi and Renzulli (2012) equations. Standard errors given for each condition.

Sample No.	**B8**		**BC14/039**		**BC14/048**		**SA12-X01**		**SA12-X011**		**SA21**		**SA22**		**BC14/004**	
Lithology	Gabbro		Gabbro		Gabbro		Gabbro		Gabbro		Gabbro		Gabbro		Lava	
No. Analyses	14		2		60		27		8		3		2		59	
Mineral species	Parg		Parg		Mg-Hst		Mg-Hst		Mg-Hst		Mg-Hst		Parg		Mg-Hst	
Element (wt.%)	Average	1s.d.	Average	1s.d.	Average	1s.d.	Average	1s.d.	Average	1s.d.	Average	1s.d.	Average	1s.d.	Average	1s.d.
T (°C) (error = 22°C)	1047.83	7.11	1000.30	23.07	1051.59	7.70	1036.82	6.43	1024.26	6.06	1037.33	18.46	1000.02	1.16	1012.27	9.50
P (MPa)	807.41	46.58	420.08	81.98	654.32	61.92	540.78	30.63	515.44	25.39	640.11	93.15	412.33	15.95	479.88	66.59
Uncertainty (Max error)	88.81	5.12	46.21	9.02	71.98	6.81	59.49	3.37	56.70	2.79	70.41	10.25	45.36	1.75	52.79	7.33
Oceanic depth (km)	28.49	1.64	14.82	2.89	23.09	2.18	19.08	1.08	18.19	0.90	22.59	3.29	14.55	0.56	16.93	2.35
Continental depth (km)	30.49	1.76	15.87	3.10	24.71	2.34	20.42	1.16	19.47	0.96	24.18	3.52	15.57	0.60	18.12	2.52
ΔNNO	0.32	0.05	0.97	0.03	0.83	0.06	0.85	0.08	0.91	0.06	0.52	0.05	0.24	0.07	0.44	0.11
logfO2 (error = 0.4)	-9.04	0.12	-9.20	0.35	-8.53	0.15	-8.75	0.14	-8.87	0.11	-9.04	0.25	-9.94	0.09	-9.54	0.20
H2Omelt (wt.%)	5.72	0.23	3.91	0.43	4.71	0.28	4.20	0.27	4.07	0.17	4.57	0.23	4.02	0.13	3.84	0.62
Uncertainty	0.86	0.04	0.59	0.06	0.71	0.04	0.63	0.04	0.61	0.03	0.68	0.03	0.60	0.02	0.58	0.09

Table 2: Estimated temperature, pressure, oxidation state and water content of representative amphibole-bearing samples, calculated using the Ridolfi and Renzulli (2012) equations. Standard errors given for each condition.

Sample No.	**SA18**		**SA19**		**SA26**		**SA26**		**SA8**		**B16**		**B21**		**BC14/020**	
Lithology	Lava		Lava		Lava		Lava		Lava		Pyroxenite		Pyroxenite		Pyroxenite	
No. Analyses	4		4		6		2		3		3		9		63	
Mineral species	Mg-Hst		Mg-Hst		Mg-Hst		Parg		Mg-Hst		Mg-Hst		Mg-Hst		Mg-Hst	
Element (wt.%)	Average	1s.d.	Average	1s.d.	Average	1s.d.	Average	1s.d.	Average	1s.d.	Average	1s.d.	Average	1s.d.	Average	1s.d.
T (°C) (error = 22°C)	1032.68	1.98	1031.67	25.40	1009.47	28.16	1041.26	0.41	1023.80	9.80	1034.94	6.59	1028.91	10.26	1038.88	6.29
P (MPa)	586.80	10.86	590.31	137.42	511.65	90.18	614.80	21.11	534.02	21.43	755.23	14.86	632.12	50.07	612.43	33.36
Uncertainty (Max error)	64.55	1.19	64.93	15.12	56.28	9.92	67.63	2.32	58.74	2.36	83.07	1.63	69.53	5.51	67.37	3.67
Oceanic depth (km)	20.70	0.38	20.83	4.85	18.05	3.18	21.69	0.74	18.84	0.76	26.65	0.52	22.30	1.77	21.61	1.18
Continental depth (km)	22.16	0.41	22.29	5.19	19.32	3.41	23.22	0.80	20.17	0.81	28.52	0.56	23.87	1.89	23.13	1.26
ΔNNO	0.86	0.04	0.50	0.12	0.37	0.21	0.50	0.03	0.73	0.06	0.43	0.07	0.86	0.12	0.72	0.07
logfO2 (error = 0.4)	-8.78	0.03	-9.16	0.30	-9.64	0.55	-9.01	0.04	-9.05	0.12	-9.13	0.15	-8.82	0.12	-8.83	0.10
H2Omelt (wt.%)	4.47	0.26	4.05	0.55	4.80	0.50	5.14	0.05	4.13	0.19	4.94	0.12	5.16	0.33	4.36	0.19
Uncertainty	0.67	0.04	0.61	0.08	0.72	0.07	0.77	0.01	0.62	0.03	0.74	0.02	0.77	0.05	0.65	0.03

reduced analyses ~ΔNNO+0.90-0.05, with the pargasites in the oxidation trend around ~ΔNNO+0.52-0.48. The Mg-hastingsites are largely in the initial trend of oxidation spanning from ~ΔNNO+0.35-1.00, with a small number becoming more reduced at shallower depths. The pargasites are also largely part of the initial oxidation trend at the greater depths from ~ΔNNO+0.19-0.53. The pyroxenites appear to cluster around the most oxidised part of the trend between ΔNNO+0.40 and ΔNNO+1.15.

DISCUSSION

Validity of pressure estimates

Erdmann et al. (2014) questioned the validity of pressures estimated by the Ridolfi thermobarometers. Two groups of amphiboles were experimentally crystallised at specific pressures (200 and 400Mpa) and their final compositions measured by electron microprobe. When the Ridolfi formulations were applied to these compositions they returned a much broader and continuous range of pressures than would have been expected (160-560Mpa). Therefore, to validate the pressures estimated in this study other independent barometers are compared.

Krawczynski et al. (2012) formulated the following two independent barometers for amphiboles based on their stoichiometry normalised to 23 oxygens;

$$[6]\ P_{H_2O}(MPa) = \left(\frac{Mg\#}{52.7} - 0.014 * \Delta NNO\right)^{15.12}$$

$$[7]\ P(MPa) = 1675 * Al^{VI} - 48$$

Equation 6 is only applicable to amphiboles with Mg# between 74 and 84; therefore, analysed minerals were filtered to fit within this range. Both equations have reasonably large errors (±93 and ±111Mpa respectively) and thus averaging both barometers together provides a more accurate representation of the data (±94MPa error). When compared to the pressures calculated by the Ridolfi formulations (fig. 6a and 6b), the average of these two dependant equations provide pressure estimates that appear to largely fit with a narrower and lower pressure range; ~300-550MPa.

Nimis (1999) formulated a single clinopyroxene barometer that can be applied to hydrous, alkaline magmatic systems. Using these formulations, estimated magma temperatures range between ~300 and 775MPa (fig. 6c). Most analysed samples range from 400-650MPa. This fits well with the pressures estimated by the Sangeang Api samples.

Lange et al. (2009) provide formulations for calculating the water content of a given melt of a known temperature and pressure from the relationship between magmatic glass and plagioclase in equilibrium with it. These formulations were applied to Sangeang Api glass and plagioclase analyses (using both phenocrysts and microphenocrysts) using the pressures and temperatures calculated from the amphibole formulations to provide independent estimates of the melt water content (fig. 7a and 7b). Calculated melt water contents range from 2-7.3wt.% H_2O, a range broadly consistent with water contents estimated by the amphiboles (3.15-6.51wt.% H_2O). When the calculated water contents

are compared for each method we can see very little difference between most of the samples. Using plagioclase microphenocryst analyses to calculate water content provides estimates that are much more accurate than using phenocryst analyses. Calculated water contents using the plag-glass method are not strongly dependent on the pressure input, e.g. a 1000MPa pressure difference provides only a 1wt.% H_2O difference. However, the calculations are much more dependent on the temperature input, therefore it is possible

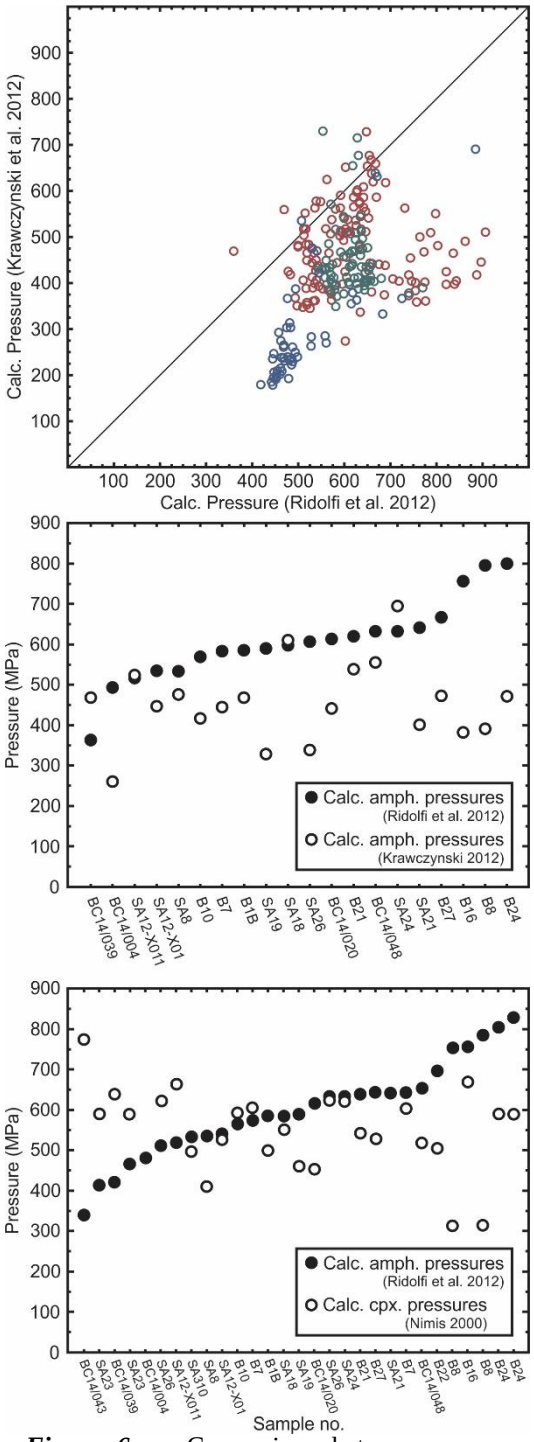

Figure 6a-c: Comparison between pressures estimated by Ridolfi and Renzulli (2012), Krawczynski et al. (2012) and Nimis (1999) thermobarometry methods. (a) Comparison between Ridolfi and Renzulli (2012) and Krawczynski et al. (2012) results for each individual analysis. Solid line represents a 1:1 ratio. (b) Comparison between Ridolfi and Renzulli (2012) and Krawczynski et al. (2012) results of averaged calculated pressures. (c) Comparison between Ridolfi and Renzulli

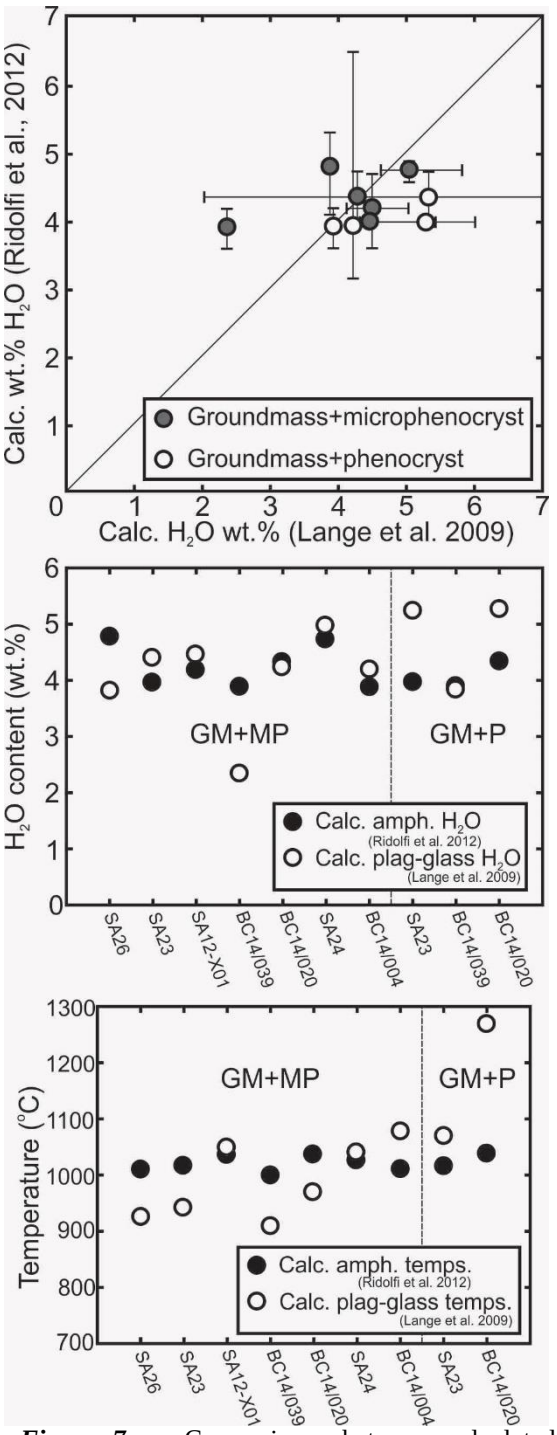

Figure 7a-c: Comparisons between calculated melt H_2O contents and temperatures for Ridolfi and Renzulli (2012) and Lange et al. (2009) methods. (a) Averaged results of Ridolfi and Renzulli (2012) and Lange et al. (2009) hygrometry methods, error bars represent maximum and minimum calculated H_2O contents. (b) Averaged results of Ridolfi and Renzulli (2012) and Lange et al. (2009) hygrometry methods, calculated at temperatures estimated by Ridolfi and Renzulli (2012) method. (c) Averaged

to use the plag-glass method as an independent test for accuracy of the amphibole temperature estimates. To calculate the same water content as the amphibole estimations requires little change in the temperature (fig. 7c). These results suggest that the plagioclase phenocrysts largely formed at lower temperatures than the amphiboles at a given water content and pressure, and the plagioclase phenocrysts at higher temperatures.

Based on these comparisons it is likely that the calculated Ridolfi and Renzulli (2012) pressures can be considered trustworthy and we therefore regard them as accurate for the purposes of this study.

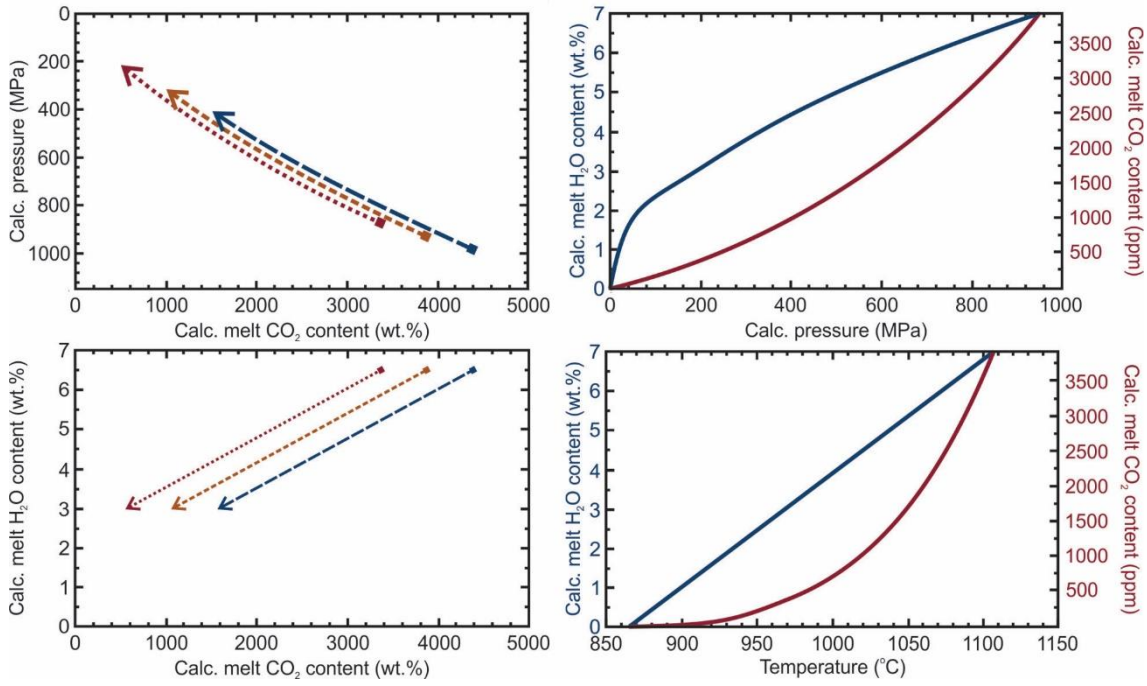

Figure 8a-d: Results of modelling calculated using VolatileCalc tool of Newman and Lowenstern (2002). (a) Dashed lines show the effect of varying CO_2 and H_2O contents (as displayed in 8b) on vapour saturation pressures, for a given temperature (1000°C) and SiO_2 content (49wt.%). (c) Estimated values of CO_2 and H_2O at vapour saturation (dashed line in figure 5a) over the pressure range 1000-0MPa. (d) Estimated values of CO_2 and H_2O at vapour saturation (dashed line in figure 5a) over the temperature range 1110°C-865°C.

Decompression degassing path

As Sangeang Api magmas ascended to the surface they progressively lost water, possibly due to decompression degassing. Using the VolatileCalc program of Newman and Lowenstern (2002) a vapour saturation curve was produced using only the temperatures and water contents calculated from amphibole thermobarometry as parameters and not taking into account CO_2 content. This achieved a vapour saturation curve that suggests pressures of vapour saturation too shallow to match the observed trend in data. Following this, varying amounts of CO_2 (1000ppm, 2000ppm and 3000ppm) were added to the same calculations to observe the effect of CO_2 content on vapour saturation. Increasing the amount of CO_2 in the melt increases the pressure of vapour saturation. Further calculations were undertaken to observe the effects of simultaneously degassing the melt of water and CO_2; vapour saturation curves created (see fig. 8) show curves more like the spread of data, and again increasing the initial CO_2 increases the depth of vapour saturation. The presence of H_2O in magmas decreases the solubility of CO_2 (Blank and

Brooker, 1994), therefore CO_2 will degas preferentially to H_2O and CO_2 will show an increased rate of degassing when compared to water at higher depths, whilst at shallow depths it is likely that both water and CO_2 will degas rapidly from the melt and drive explosive eruptions. A curve reflecting these relationships that matches the parameters calculated by amphibole thermobarometry can be estimated (see figure 5a); over the temperature range 1100-865˚C water will degas consistently from 7wt.% to 0 wt.%, whilst CO_2 will initially decrease rapidly from 3900ppm to 1500ppm and then decrease more slowly to 0ppm CO_2.

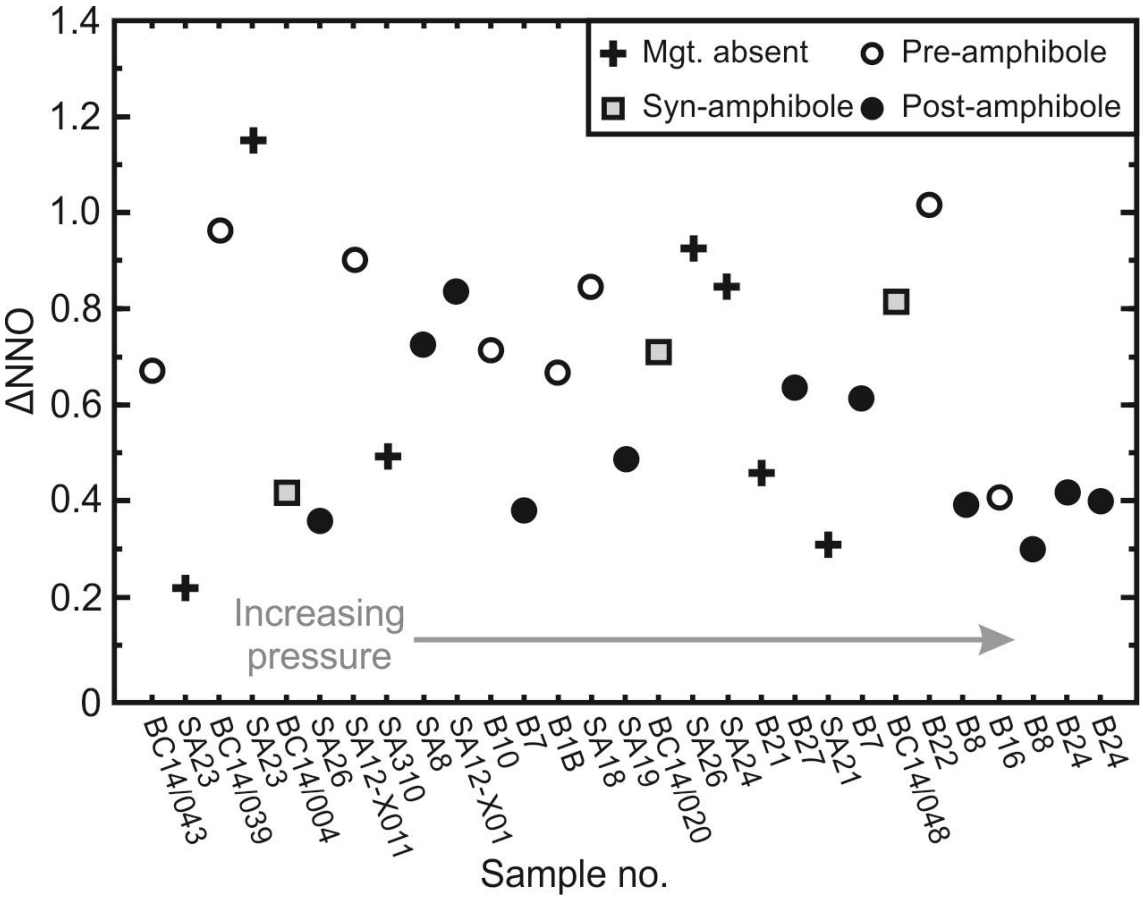

Figure 9: Averaged calculated ΔNNO values for samples arranged from left to right by increasing average pressure content. Symbols represent whether magnetite is texturally absent, prior to (pre-), synchronous to (syn-) and post-dating (post-) amphibole.

Redox processes

The deepest and thus most primitive melts begin life relatively oxidised (~ΔNNO+0.25-0.7) before becoming increasingly oxidised (to ~ΔNNO+0.6-1.2) as they ascend from the deep to mid crust. This oxidation event is seen most clearly in the gabbro pargasites and pyroxenite Mg-Hastingsites. Several processes could have created this apparent oxidation in the deep crust; fractional crystallisation of reduced species, degassing or other differentiation processes. 50% fractional crystallisation of olivine can for example cause the Fe^{3+}/Fe_T of a melt to double (Lee et al., 2010); however, the fractional crystallisation of other mineral species, such as magnetite, can act to reduce a melt. Due to the mixed redox state of iron in magnetite ($Fe^{2+}Fe^{3+}{}_2O_4$), saturation and fractional crystallisation will reduce a melt (Kelley and Cottrell, 2012). If this was the case it would be expected

to see the most reduced samples associated with early forming, pre-amphibole crystallisation magnetite. In fact, what is observed is the opposite, samples with early magnetite tend to be more oxidised than samples with late, post-amphibole magnetite (fig. 9). Similarly, olivine fractionation is unlikely to be exerting a control on redox within the system as there is no obvious correlation between the presence of olivine and high ΔNNO. Another process must thus be controlling redox in this system, with the likely cause being degassing (Humphreys et al., 2015). Considering that the magmas display a consistent decrease in water with decompression this points to water as the primary agent of oxidation. Basaltic magmas can be oxidised by the following H_2O degassing equation (Mathez, 1984):

$$[8]\ H_2O_{(melt)} \rightarrow H^+_{(melt)} + OH^-_{(melt)}$$

Burgisser and Scaillet (2007) suggest that magmas degassing water only will oxidise by up to as much 2 orders of magnitude as they ascend, but that the rate of oxidation will decrease (up to 0.5 magnitudes of order) as the percentage of excess gas in the magma increases. The Sangeang Api magma displays an initial oxidation trend on the order of a magnitude with a loss of water content (i.e. gas exsolution) of approximately 3wt.%, suggesting that the magma should have become significantly more oxidised (around 2 orders of magnitude above the NNO) if water was the only degassing agent. This also does not explain the reduction observed shallower in the system. Therefore, we must consider other that there must be other redox agents affecting the melt at the same time. Sulfur has been proposed as a method of either oxidising or reducing the melt depending on the method of degassing and the sulfur species being released, these reactions are as follows (Métrich et al., 2009):

$$[9]\ S^{2-}_{(melt)} + {Fe_2}^{3+}O_{3\,(melt)} \rightarrow SO_{2\,(gas)} + 2Fe^{2+}O_{(melt)} + O^{2-}_{(melt)}$$

$$[10]\ SO^{2-}_{4\,(melt)} + 2Fe^{2+}O_{(melt)} \rightarrow SO_{2\,(gas)} + Fe^{3+}_2O_{3\,(melt)} + O^{2-}_{(melt)}$$

Magmas primarily contain sulphur in two different oxidation states - sulphate (S^{6+}) and sulphide (S^{2-}) (Jugo, 2009; Wallace and Edmonds, 2011). Because of the 8 electron difference between the two sulphur species sulphur has a powerful oxidative or reductive potential as compared to the single electron oxidative potential of H_2O. For low initial gas contents and low sulphur contents (<200ppm S) magmas in the H-O-S system will initially oxidise as they ascend, before reducing as they ascend through the shallow crust (Burgisser and Scaillet, 2007). The initial trend of oxidation is likely controlled by a combined H_2O and sulphide (S^{2-}) degassing, whilst the later reductive trend is most likely controlled by sulphate (S^{6+}) degassing, similar to that proposed by Moussallam et al. (2014) for Erebus volcano, Antarctica. Sulfur acts much like CO_2 in its degassing profile and will degas preferentially when compared to water at higher pressures (Wallace and Edmonds, 2011), therefore CO_2 and S might be expected to act similarly in the Sangeang Api system. As the Sangeang Api magma decompresses the melt will become saturated with, and enriched in, sulfur. However, glass and magmas from the Sangeang Api system display low concentrations of sulfur, which will likely saturate the melt with sulphide deep in the magmatic system and which are too low to saturate the melt with sulphide at shallow depths (Mavrogenes and O'Neill, 1999). Using experimental data from Jugo (2009) the sulfur content at sulphide saturation for a

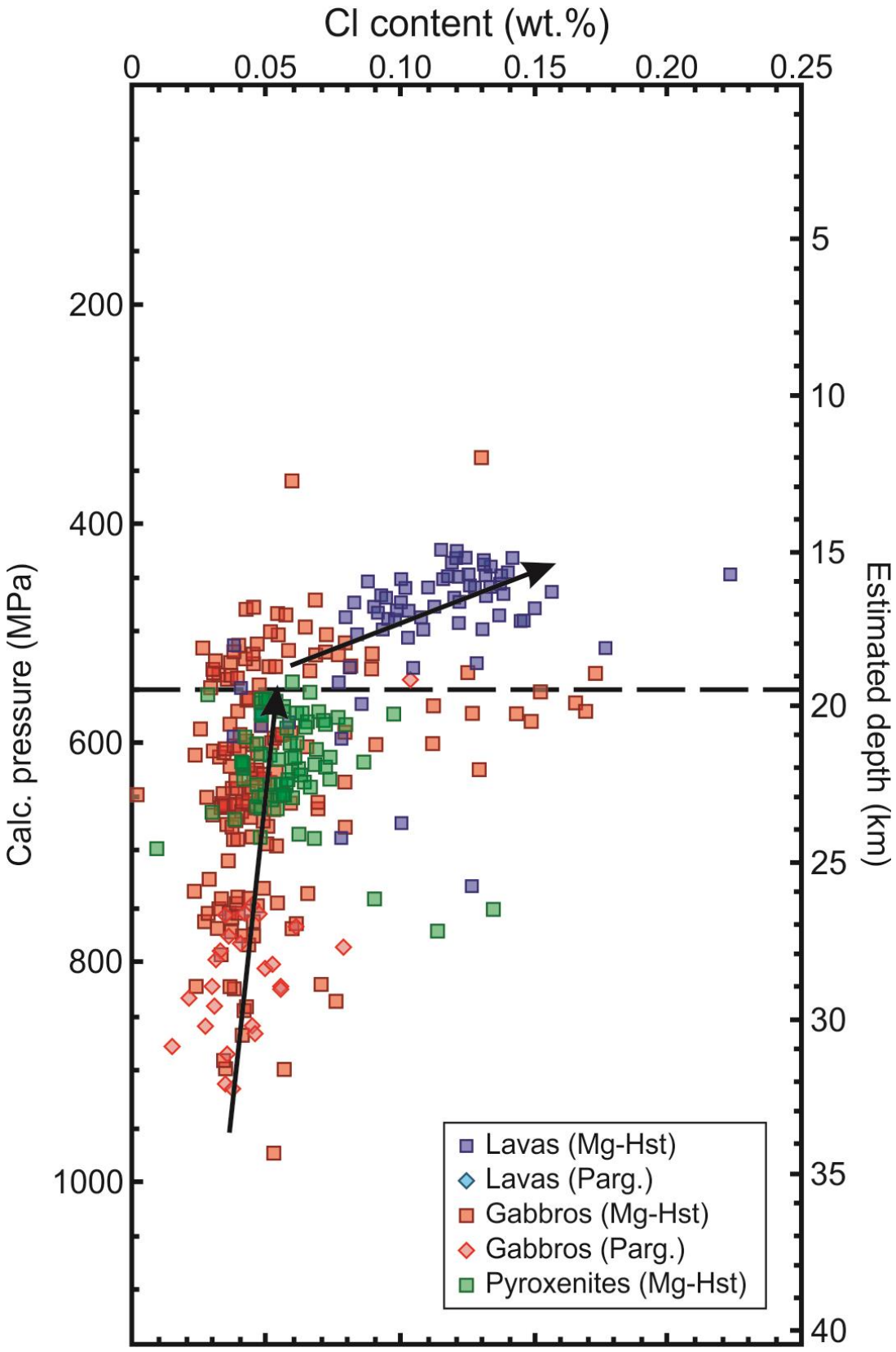

Figure 10a: Comparison between pressures calculated by Ridolfi and Renzulli (2012) and Cl content of amphibole analyses. (a) Dashed line represents change in vapour regime with solid arrows showing trends in Cl content with depth. Symbols as in figure 3.

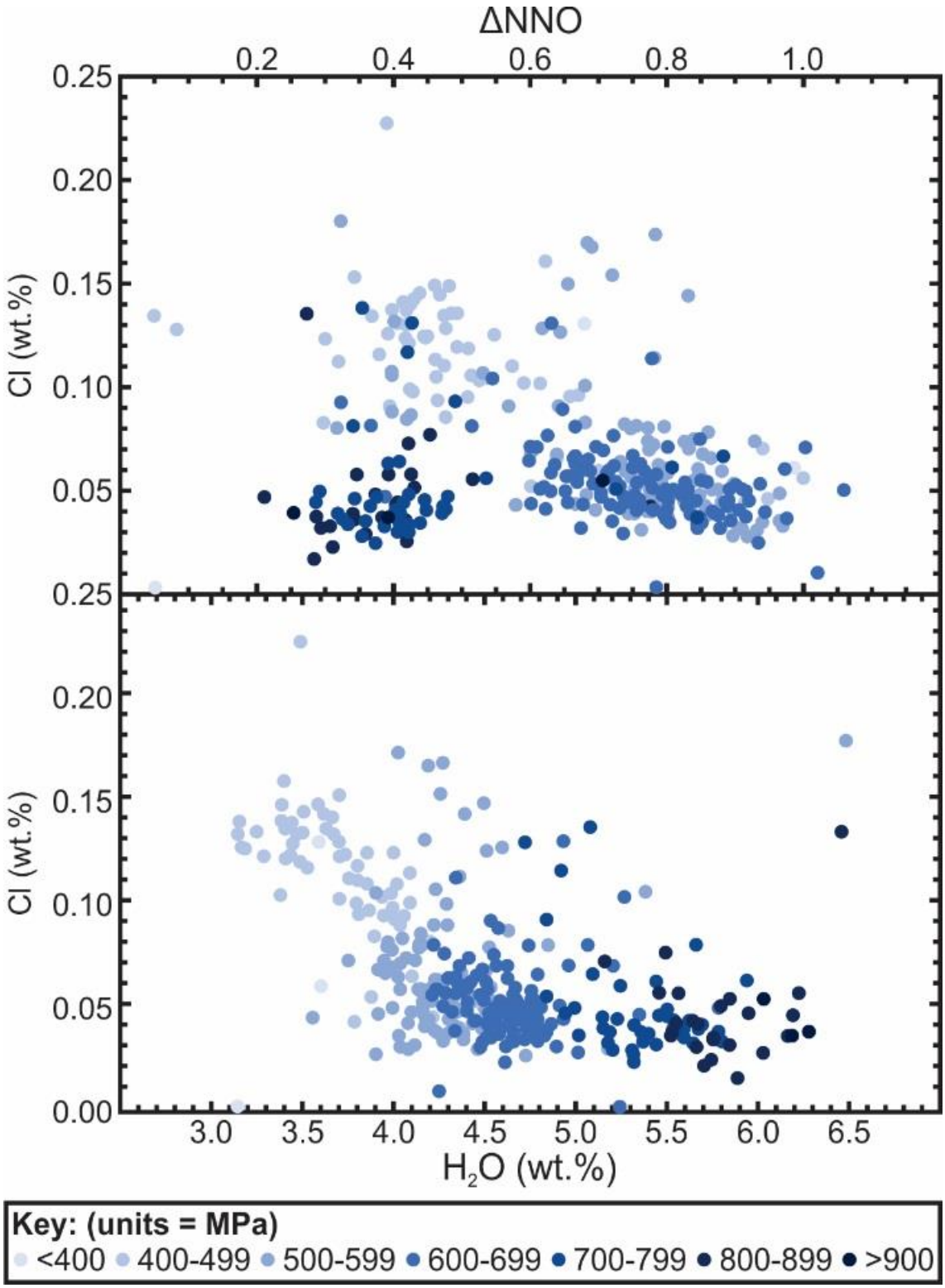

Figure 10b-c: Comparison between ΔNNO and H_2O contents calculated by Ridolfi and Renzulli (2012) and Cl content of amphibole analyses. (b) Symbol colours represent pressure levels – from darkest blue representing highest pressure to lightest blue representing lowest pressure. (c) Symbol colours represent pressure levels– from darkest blue representing highest pressure to lightest blue representing lowest pressure.

given redox state can be calculated; if the maximum oxidation state recorded by the Sangeang Api magmas records the change from a sulphide dominated vapour phase to a sulphate dominated vapour phase, an estimate of the maximum S content of the melt is ~3000ppm.

Chlorine will stay in the magma at depth in the magma system until it becomes saturated at shallower depths and will degas rapidly (Lowenstern, 2000; Wallace, 2005). Therefore, magmas and melts should become enriched in chlorine as they ascend and fractionate through the deep- to mid-crust. As previously mentioned, the Sangeang Api amphiboles display an increase in Cl content with increasing SiO_2 content. Cl content of amphiboles in this study do not show a very slight overall increase in concentration between 1000 and 600MPa (0.025-0.05wt.%), however, after this point the amphiboles become enriched in Cl at a much greater rate (0.05-0.15wt.% over ~150MPa), as shown in figure 10a. Similarly, this more rapid increase of Cl content at pressures below ~600MPa can be observed in calculated water contents of the magmas with relatively stable Cl contents at higher water contents (>4wt.%) giving way to a rapid increase in Cl content as the magmas progressively lose water) (figure 10b). This rapid increase in Cl content after ~600MPa is not associated with a similarly rapid decrease in melt water content, suggesting that it is not water degassing that is driving this increase in Cl content of the amphiboles and thus must be reflecting another change within the magma system. The high Cl amphiboles are predominantly associated with the more reduced, shallow magmas (light blue datapoints in fig. 10b), whilst the lower Cl amphiboles are associated with the high-pressure melts or oxidised mid-lower crust melts (darker blue datapoints in figure 10b). The high-Cl content of the shallower amphiboles, associated with the lower oxidation state relative to the mid-lower crustal samples supports our earlier suggestion that the vapour profile of the magma changes significantly at this level of the crust. Changes in the Cl/OH ratio of a melt due to degassing will increase the Cl content of amphiboles crystallising in equilibrium with these melts (Humphreys et al., 2009; Sato, 2004). Therefore, a major degassing event in the magmas at or above 600MPa would drive up the Cl/OH ratio of the magma, therefore increasing the Cl content of the amphiboles formed in equilibrium with these shallower melts.

Magma tract architecture

What appears at first glance to be a continuous trend in crystallisation from high to low pressure, upon further consideration there appears to be two more separate groups of data points at higher pressures (730-820MPa and 850-900Mpa). This grouping in the data can be seen more clearly in histograms of the data and is not observed in any of the other calculated parameters. It can be observed more clearly in 2D space, as in the density distribution plot (fig. 11), were the darker reds show a higher density of data points. Two separate and distinct high-density groupings can be seen at higher pressures. These two groups may be artefacts of magmas stalling and crystallising at depth in the crust. These artefacts hint that at the deepest points in the Sangeang Api system there may be stratigraphically distinct magma chambers. However, shallower as melts move into the mid-crust the continuous trend and density of data points suggests that magmas are continuously rising and crystallising, possibly as magma chambers become more interconnected and less stratigraphically distinct.

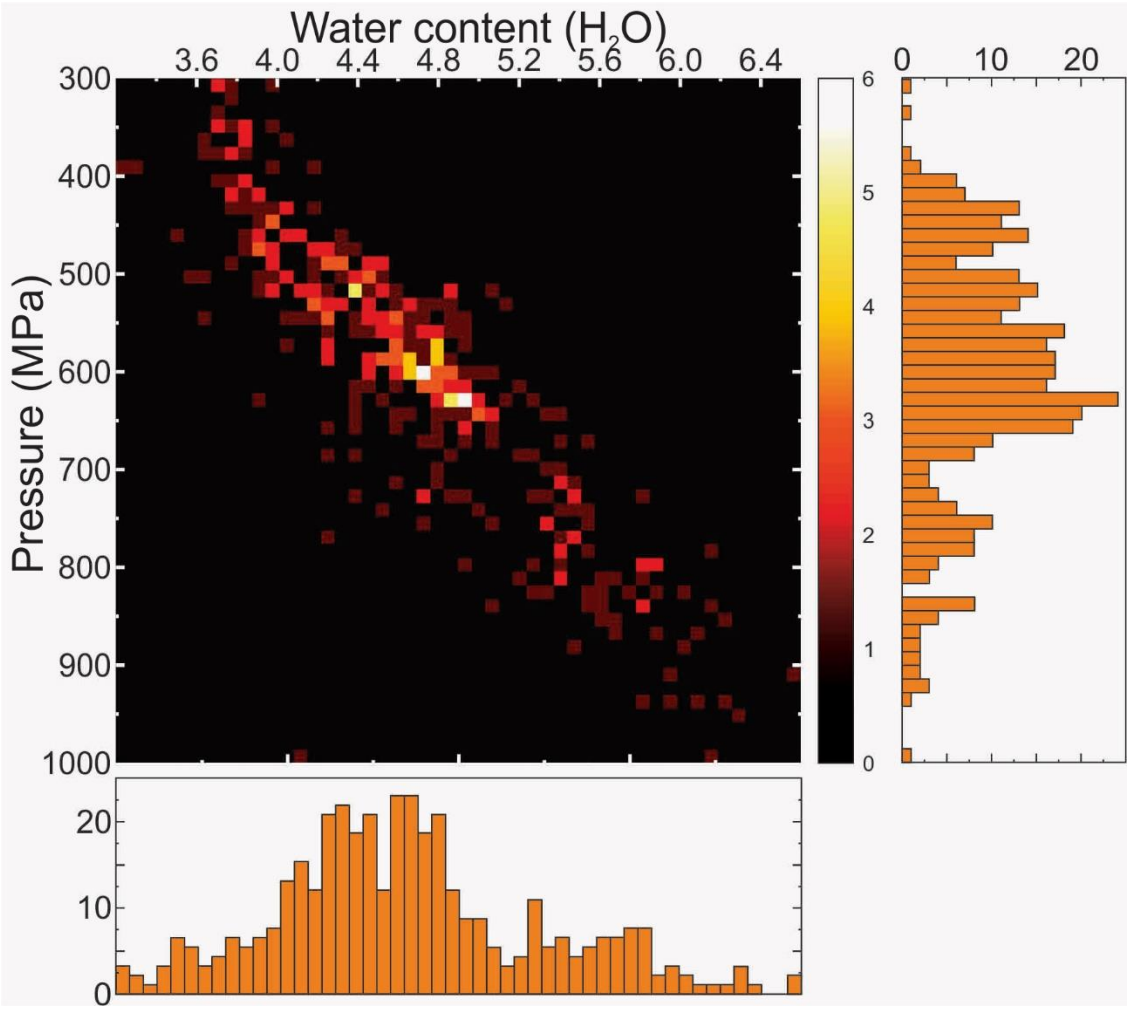

Figure 11: 2D density matrix of pressure vs. H_2O data calculated using Ridolfi and Renzulli (2012) methods. Created in MATLAB using script displayed on page 126. Brightest colours represent a high density of data points, with lower densities displayed as respectively darker colours – key observable at right of diagram. Histograms at right and below display bins used for pressure and water respectively.

Comparison with other volcanoes

The redox path of the Sangeang Api magmas can be compared directly with the redox paths of other volcanoes from a variety of tectonic settings around the world. Arc volcanoes are likely to record vertical redox profiles as they ascend the crust and degas (Humphreys et al., 2015), the crustal magmatic tract of Sangeang Api is consistent with this. Studies of the Taupo Volcanic Zone (TVZ), New Zealand, have made use of both Fe-Ti oxide oxythermobarometry and amphibole geothermobarometry to establish the redox path experienced by rhyolite magmas of different ages (Shane and Smith, 2013; Smith et al., 2005). Fe-Ti oxide results record fO_2 in the range of ΔNNO-1.3 to ΔNNO+1.4 (Smith et al., 2005), whilst amphiboles record significantly higher oxidation states from ΔNNO-0.3 to ΔNNO+2.4 (Shane and Smith, 2013). Despite this both techniques used display a trend of reduction from higher to lower temperatures – reflecting the reduction of the Sangeang Api magmas at lower temperatures and pressures. Amphiboles from Merapi volcano (Java, Indonesia) record magma temperatures and oxidation states similar to those from Sangeang Api – 905-1040˚C and

ΔNNO+0.2 to ΔNNO+1.1 (Erdmann et al., 2014). However, there is no significant and observable trend in the redox data, despite this the most oxidised magmas occur at the lowest temperatures.

A number of different volcanoes in arc settings display evidence of oxidation during ascent to the surface. Ruprecht et al. (2012) applied a combination of Fe-Ti oxythermobarometry and amphibole geothermobarometry to the products of Volcán Quizapu (Chile), returning oxidation states of ΔNNO+0.2 to ΔNNO+1.3 that display a consistent trend of oxidation from high to low temperatures. Similarly, andesites from Shiveluch volcano (Kamchatka, Russia) display a consistent oxidation from ΔNNO+1.5 to ΔNNO+2.1 with lower temperatures as calculated using co-existing oxide pairs (Humphreys et al., 2006).

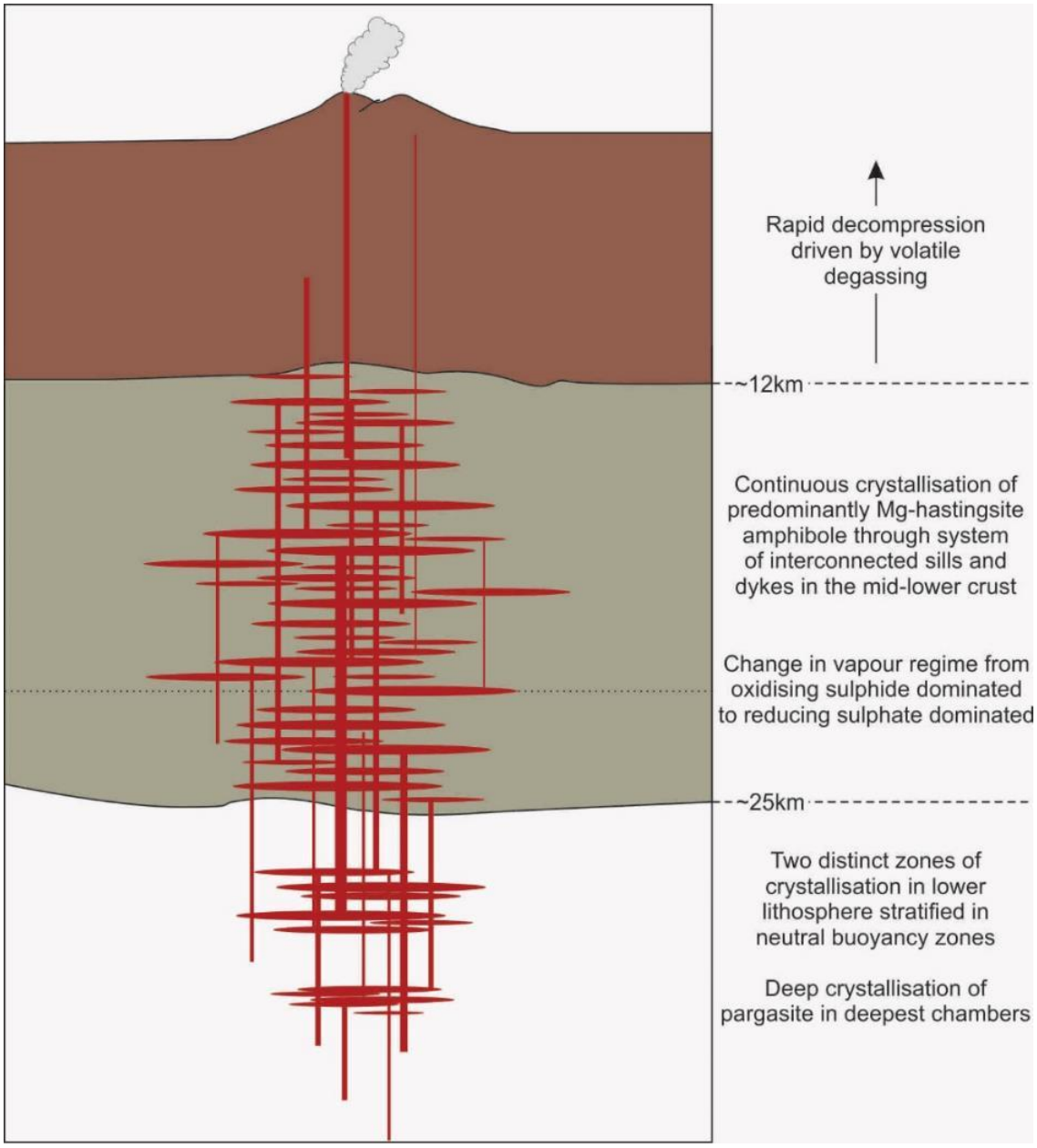

Figure 12: Conceptual model of Sangeang Api magma transfer system.

CONCLUSION

Figure 12 shows a schematic model for the crustal magmatic tract of Sangeang Api, outlining degassing and redox processes, changes to amphibole composition and structure of the magmatic system. Sangeang Api amphiboles record a crystallisation history from the Moho through to the middle crust (~35-15km). The melts from which these magmas crystallised are hot (~975-1075˚C), wet (~3.2-6.8wt.% H_2O) and relatively oxidised (~ΔNNO+0.19-1.15). Magmas likely progressively degassed as they ascended to the surface, preferentially degassing CO_2 at depth from an initial concentration of ~3900ppm as well as a preferential decrease in sulphur through sulphide degassing. At shallower depths the magmas preferentially degassed water with respect to CO_2 and volatile profile changed so that sulphate degassing took over. Chlorine initially increased slightly at greater depths and then more rapidly shallower in the system. Pressures estimates in this study suggest that the magmatic system is stratified into a distinct set of magma chambers in the lower crust, before moving up into the mid- to shallow-crust in a series of interconnected magma chambers and tracts.

REFERENCES

Andersen, D.J., Lindsley, D.H., Davidson, P.M., 1993. QUILF: A pascal program to assess equilibria among Fe-Mg-Mn-Ti oxides, pyroxenes, olivine, and quartz. Computers & Geosciences 19, 1333-1350.

Andersen, J.L., Smith, D.R., 1995. The effects of temperature and fO_2 on the Al-in-hornblende barometer. American Mineralogist 80, 549-559.

Beckers, J., Lay, T., 1995. Very broadband seismic analysis of the 1992 Flores, Indonesia, earthquake (Mw = 7.9). Journal of Geophysical Research: Solid Earth (1978–2012) 100, 18179-18193.

Blank, J.G., Brooker, R.A., 1994. Experimental studies of carbon dioxide in silicate melts; solubility, speciation, and stable carbon isotope behaviour. Reviews in Mineralogy and Geochemistry 30, 157-186.

Blundy, J.D., Holland, T.J.B., 1990. Calcic amphibole equilibria and a new amphibole-plagioclase geothermometer. Contributions to Mineralogy and Petrology 104, 208-224.

Burgisser, A., Scaillet, B., 2007. Redox evolution of a degassing magma rising to the surface. Nature 445, 194-197.

Carmichael, I.S.E., 1991. The redox states of basic and silicic magmas - a reflection of their source regions. Contributions to Mineralogy and Petrology 106, 129-141.

Christie, D.M., Carmichael, I.S.E., Langmuir, C.H., 1986. Oxidation-states of midocean ridge basalt glasses. Earth and Planetary Science Letters 79, 397-411.

Costa, F., Andreastuti, S., Bouvet de Maisonneuve, C., Pallister, J.S., 2013. Petrological insights into the storage conditions, and magmatic processes that yielded the centennial 2010 Merapi explosive eruption. Journal of Volcanology and Geothermal Research 261, 209-235.

Curray, J.R., Shor, G.G., Raitt, R.W., Henry, M., 1977. Seismic refraction and reflection studies of crustal structure of the Eastern Sunda and Western Banda Arcs. Journal of Geophysical Research 82, 2479-2489.

Erdmann, S., Martel, C., Pichavant, M., Kushnir, A., 2014. Amphibole as an archivist of magmatic crystallization conditions: problems, potential, and implications for inferring magma storage prior to the paroxysmal 2010 eruption of Mount Merapi, Indonesia. Contributions to Mineralogy and Petrology 167, 1-23.

Evans, K.A., Elburg, M.A., Kamenetsky, V.S., 2012. Oxidation state of subarc mantle. Geology 40, 783-786.

Evans, K.A., Tomkins, A.G., 2011. The relationship between subduction zone redox budget and arc magma fertility. Earth and Planetary Science Letters 308, 401-409.

Foden, J.D., Green, D.H., 1992. Possible role of amphibole in the origin of andesite - some experimental and natural evidence. Contributions to Mineralogy and Petrology 109, 479-493.

Ghiorso, M.S., Evans, B.W., 2008. Thermodynamics of Rhombohedral Oxide Solid Solutions and a Revision of the FE-TI Two-Oxide Geothermometer and Oxygen-Barometer. American Journal of Science 308, 957-1039.

Ghiorso, M.S., Sack, O., 1991. Fe-Ti oxide geothermometry: thermodynamic formulation and the estimation of intensive variables in silicic magmas. Contributions to Mineralogy and Petrology 108, 485-510.

Hall, R., 2011. Australia- SE Asia collison: plate tectonics and crustal flow, in: Hall, R., Cottam, M.A., Wilson, M.E.J. (Eds.), The SE Asian gateway: history and tectonics of Australia-Asia collision. Geological Society of London Special Publication, pp. 75-109.

Hall, R., 2012. Late Jurassic–Cenozoic reconstructions of the Indonesian region and the Indian Ocean. Tectonophysics 570–571, 1-41.

Hall, R., Spakman, W., 2015. Mantle structure and tectonic history of SE Asia. Tectonophysics 658, 14-45.

Hammarstrom, J.M., Zen, E., 1986. Aluminum in hornblende: an empirical igneous geobarometer. American Mineralogist 71, 1297-1313.

Holland, T., Blundy, J., 1994. Non-ideal interactions in calcic amphiboles and their bearing on amphibole-plagioclase thermometry. Contributions to Mineralogy and Petrology 116, 433-447.

Humphreys, M.C.S., Blundy, J.D., Sparks, R.S.J., 2006. Magma Evolution and Open-System Processes at Shiveluch Volcano: Insights from Phenocryst Zoning. Journal of Petrology 47, 2303-2334.

Humphreys, M.C.S., Brooker, R.A., Fraser, D.G., Burgisser, A., Mangan, M.T., McCammon, C., 2015. Coupled Interactions between Volatile Activity and Fe Oxidation State during Arc Crustal Processes. Journal of Petrology 56, 795-814.

Humphreys, M.C.S., Edmonds, M., Christopher, T., Hards, V., 2009. Chlorine variations in the magma of Soufrière Hills Volcano, Montserrat: Insights from Cl in hornblende and melt inclusions. Geochimica et Cosmochimica Acta 73, 5693-5708.

Gruender, K., Stewart, R.B., Foley, S., 2010. Xenoliths from the sub-volcanic lithosphere of Mt Taranaki, New Zealand. Journal of Volcanology and Geothermal Research 190, 192-202.

Johnson, M.C., Rutherford, M.J., 1989. Experimental calibration of the aluminum-in-hornblende geobarometer with application to Long Valley caldera (California) volcanic rocks. Geology 17, 837-841.

Jugo, P.J., 2009. Sulfur content at sulfide saturation in oxidized magmas. Geology 37, 415-418.

Kelley, K.A., Cottrell, E., 2012. The influence of magmatic differentiation on the oxidation state of Fe in a basaltic arc magma. Earth and Planetary Science Letters 329–330, 109-121.

Koulali, A., Susilo, S., McClusky, S., Meilano, I., Cummins, P., Tregoning, P., Lister, G., Efendi, J., Syafi'i, M.A., 2016. Crustal strain partitioning and the associated earthquake hazard in the eastern Sunda-Banda Arc. Geophysical Research Letters 43, 1943-1949.

Krawczynski, M.J., Grove, T.L., Behrens, H., 2012. Amphibole stability in primitive arc magmas: effects of temperature, H2O content, and oxygen fugacity. Contributions to Mineralogy and Petrology 164, 317-339.

Lange, R.A., Frey, H.M., Hector, J., 2009. A thermodynamic model for the plagioclase-liquid hygrometer/thermometer. American Mineralogist 94, 494-506.

Lattard, D., Sauerzapf, U., Käsemann, M., 2005. New calibration data for the Fe–Ti oxide thermo-oxybarometers from experiments in the Fe–Ti–O system at 1 bar, 1,000–1,300°C and a large range of oxygen fugacities. Contributions to Mineralogy and Petrology 149, 735-754.

Leake, B.E., Woolley, A.R., Arps, C.E.S., Birch, W.D., Gilbert, M.C., Grice, J.D., Hawthorne, F.C., Kato, A., Kisch, H.J., Krivovichev, V.G., Linthout, K., Laird, J., Mandarino, J.A., Maresch, W.V., Nickel, E.H., Rock, N.M.S., Schumacher, J.C., Smith, D.C., Stephenson, N.C.N., Ungaretti, L., Whittaker, E.J.W., Guo, Y.Z., 1997. Nomenclature of amphiboles: Report of the subcommittee on amphiboles of the International Mineralogical Association, Commission on New Minerals and Mineral Names. Canadian Mineralogist 35, 219-246.

Lee, C.T.A., Leeman, W.P., Canil, D., Li, Z.X.A., 2005. Similar V/Sc systematics in MORB and arc basalts: Implications for the oxygen fugacities of their mantle source regions. Journal of Petrology 46, 2313-2336.

Lee, C.T.A., Luffi, P., Le Roux, V., Dasgupta, R., Albarede, F., Leeman, W.P., 2010. The redox state of arc mantle using Zn/Fe systematics. Nature 468, 681-685.

Mallmann, G., O'Neill, H.S.C., 2009. The Crystal/Melt Partitioning of V during Mantle Melting as a Function of Oxygen Fugacity Compared with some other Elements (Al, P, Ca, Sc, Ti, Cr, Fe, Ga, Y, Zr and Nb). Journal of Petrology 50, 1765-1794.

Lowenstern, J.B., 2000. A review of the contrasting behavior of two magmatic volatiles: chlorine and carbon dioxide. Journal of Geochemical Exploration 69–70, 287-290.

Mathez, E.A., 1984. Influence of degassing on oxidation-states of basaltic magmas. Nature 310, 371-375.

Mavrogenes, J.A., O'Neill, H.S.C., 1999. The relative effects of pressure, temperature and oxygen fugacity on the solubility of sulfide in mafic magmas. Geochimica et Cosmochimica Acta 63, 1173-1180.

Métrich, N., Berry, A.J., O'Neill, H.S.C., Susini, J., 2009. The oxidation state of sulfur in synthetic and natural glasses determined by X-ray absorption spectroscopy. Geochimica et Cosmochimica Acta 73, 2382-2399.

Montanari, D., Corti, G., Simakin, A., 2010. Magma chambers and localization of deformation during thrusting. Terra Nova 22, 390-395.

Moussallam, Y., Oppenheimer, C., Scaillet, B., Gaillard, F., Kyle, P., Peters, N., Hartley, M., Berlo, K., Donovan, A., 2014. Tracking the changing oxidation state of Erebus magmas, from mantle to surface, driven by magma ascent and degassing. Earth and Planetary Science Letters 393, 200-209.

Newman, S., Lowenstern, J.B., 2002. VolatileCalc: a silicate melt–H2O–CO2 solution model written in Visual Basic for excel. Computers & Geosciences 28, 597-604.

Nimis, P., 1995. A clinopyroxene geobarometer for basaltic systems based on crystal-structure modeling. Contributions to Mineralogy and Petrology 121, 115-125.

Nimis, P., 1999. Clinopyroxene geobarometry of magmatic rocks. Part 2. Structural geobarometers for basic to acid, tholeiitic and mildly alkaline magmatic systems. Contributions to Mineralogy and Petrology 135, 62-74.

Nimis, P., Ulmer, P., 1998. Clinopyroxene geobarometry of magmatic rocks Part 1: An expanded structural geobarometer for anhydrous and hydrous, basic and ultrabasic systems. Contributions to Mineralogy and Petrology 133, 122-135.

Pacey, A., Macpherson, C.G., McCaffrey, K.J.W., 2013. Linear volcanic segments in the central Sunda Arc, Indonesia, identified using Hough Transform analysis: Implications for arc lithosphere control upon volcano distribution. Earth and Planetary Science Letters 369–370, 24-33.

Parkinson, I.J., Arculus, R.J., 1999. The redox state of subduction zones: insights from arc-peridotites. Chemical Geology 160, 409-423.

Price, R.C., Smith, I.E.M., Stewart, R.B., Gamble, J.A., Gruender, K., Maas, R., 2016. High-K andesite petrogenesis and crustal evolution: Evidence from mafic and ultramafic xenoliths, Egmont Volcano (Mt. Taranaki) and comparisons with Ruapehu Volcano, North Island, New Zealand. Geochimica et Cosmochimica Acta 185, 328-357.

Putirka, K.D., Mikaelian, H., Ryerson, F., Shaw, H., 2003. New clinopyroxene-liquid thermobarometers for mafic, evolved, and volatile-bearing lava compositions, with applications to lavas from Tibet and the Snake River Plain, Idaho. American Mineralogist 88, 1542-1554.

Ridolfi, F., Renzulli, A., 2012. Calcic amphiboles in calc-alkaline and alkaline magmas: thermobarometric and chemometric empirical equations valid up to 1,130A degrees C and 2.2 GPa. Contributions to Mineralogy and Petrology 163, 877-895.

Ridolfi, F., Renzulli, A., Puerini, M., 2010. Stability and chemical equilibrium of amphibole in calc-alkaline magmas: an overview, new thermobarometric formulations and application to subduction-related volcanoes. Contributions to Mineralogy and Petrology 160, 45-66.

Ruprecht, P., Bergantz, G.W., Cooper, K.M., Hildreth, W., 2012. The Crustal Magma Storage System of Volcan Quizapu, Chile, and the Effects of Magma Mixing on Magma Diversity. Journal of Petrology 53, 801-840.

Sato, H., 2004. Experimental Petrology of the 1991-1995 Unzen Dacite, Japan. Part II: Cl/OH Partitioning between Hornblende and Melt and its Implications for the Origin of Oscillatory Zoning of Hornblende Phenocrysts. Journal of Petrology 46, 339-354.

Schmidt, M.W., 1992. Amphibole composition in tonalite as a function of pressure: an experimental calibration of the Al-in-hornblende barometer. Contributions to Mineralogy and Petrology 110, 304-310.

Shane, P., Smith, V.C., 2013. Using amphibole crystals to reconstruct magma storage temperatures and pressures for the post-caldera collapse volcanism at Okataina volcano. Lithos 156–159, 159-170.

Siebert, L., Simkin, T., Kimberly, P., 2011. Volcanoes of the World : Third Edition (3). University of California Press, Berkeley, US.

Silver, E.A., Breen, N.A., Prasetyo, H., Hussong, D.M., 1986. Multibeam study of the Flores Backarc Thrust Belt, Indonesia. Journal of Geophysical Research: Solid Earth 91, 3489-3500.

Smith, V.C., Shane, P., Nairn, I.A., 2005. Trends in rhyolite geochemistry, mineralogy, and magma storage during the last 50 kyr at Okataina and Taupo volcanic centres, Taupo Volcanic Zone, New Zealand. Journal of Volcanology and Geothermal Research 148, 372-406.

Spakman, W., Hall, R., 2010. Surface deformation and slab-mantle interaction during Banda arc subduction rollback. Nature Geoscience 3, 562-566.

Stamper, C.C., Blundy, J.D., Arculus, R.J., Melekhova, E., 2014. Petrology of Plutonic Xenoliths and Volcanic Rocks from Grenada, Lesser Antilles. Journal of Petrology 55, 1353-1387.

Tollan, P.M.E., Bindeman, I., Blundy, J.D., 2012. Cumulate xenoliths from St. Vincent, Lesser Antilles Island Arc: a window into upper crustal differentiation of mantle-derived basalts. Contributions to Mineralogy and Petrology 163, 189-208.

Turner, S., Foden, J., George, R., Evans, P., Varne, R., Elburg, M., Jenner, G., 2003. Rates and processes of potassic magma evolution beneath Sangeang Api volcano, East Sunda arc, Indonesia. Journal of Petrology 44, 491-515.

Wallace, P.J., 2005. Volatiles in subduction zone magmas: concentrations and fluxes based on melt inclusion and volcanic gas data. Journal of Volcanology and Geothermal Research 140, 217-240.

Wallace, P.J., Edmonds, M., 2011. The Sulfur Budget in Magmas: Evidence from Melt Inclusions, Submarine Glasses, and Volcanic Gas Emissions. Reviews in Mineralogy and Geochemistry 73, 215-246.

Zernack, A.V., Price, R.C., Smith, I.E.M., Cronin, S.J., Stewart, R.B., 2012. Temporal Evolution of a High-K Andesitic Magmatic System: Taranaki Volcano, New Zealand. Journal of Petrology 53, 325-363.

MATLAB SCRIPT

```
data1 = x;
data2 = y;
values = hist3([data1(:) data2(:)],[50 50]);
imagesc(values)
colorbar
axis equal
axis xy
```

Chapter 4

Iron Isotope fractionation and disequilibrium in an arc magmatic system: Insights from the co-genetic lava and cumulate xenolith suites of Sangeang Api, Indonesia

Statement of Authorship

Title of Paper	Iron Isotope fractionation and disequilibrium in an arc magmatic system: Insights from the co-genetic lava and cumulate xenolith suites of Sangeang Api, Indonesia
Publication Status	☐ Published ☐ Accepted for Publication ☐ Submitted for Publication ☑ Unpublished and Unsubmitted work written in manuscript style
Publication Details	For submission to Chemical Geology as: Cooke, B., Foden, J., Warwyk, C. M. Iron Isotope fractionation and disequilibrium in an arc magmatic system: Insights from the co-genetic lava and cumulate xenolith suites of Sangeang Api, Indonesia

Principal Author

Name of Principal Author (Candidate)	Benjamin Cooke		
Contribution to the Paper	Collection of samples in fieldwork, sample preparation, sample, dissolution, data collection, data processing, data interpretation, manuscript preparation and content, creation of diagrams		
Overall percentage (%)	80		
Certification:	This paper reports on original research I conducted during the period of my Higher Degree by Research candidature and is not subject to any obligations or contractual agreements with a third party that would constrain its inclusion in this thesis. I am the primary author of this paper.		
Signature		Date	13/11/2017

Co-Author Contributions

By signing the Statement of Authorship, each author certifies that:

i. the candidate's stated contribution to the publication is accurate (as detailed above);

ii. permission is granted for the candidate in include the publication in the thesis; and

iii. the sum of all co-author contributions is equal to 100% less the candidate's stated contribution.

Name of Co-Author	Professor John Foden		
Contribution to the Paper	Assistance in fieldwork, guidance in sample preparation, data interpretation, review		
Signature		Date	13/11/2017

Name of Co-Author	Christine Warwyk		
Contribution to the Paper	Guidance in sample preparation, guidance dissolution, assistance in collection of Fe-isotope data		
Signature		Date	13/11/2017

ABSTRACT

Lavas erupted by arc volcanoes are generally more oxidised relative to lavas from other volcanic settings, i.e. mid-ocean ridge basalts(MORB). The source of this apparent oxidation is a contentious issue, either oxidised lavas reflect an oxidised mantle wedge source or oxidation is inherited through intra-crustal processes occurring during magma ascent. Iron isotopes have been identified as a means of testing the oxidation state of sub-arc mantle. All other factors being equal, partial melting of high Fe^{3+}/Total Fe (i.e. oxidised) sources will theoretically yield melts with heavier isotopic compositions than partial melting of lower Fe^{3+}/Total Fe sources (i.e. more reduced). Recent work by Nebel et al. (2015) and Foden et al. (In Press) has suggested that contrary to expectations, the mantle wedge source of arc magmas is isotopically light with respect to iron when compared to MORB. However, the processes controlling iron isotope fractionation in differentiating arc magmatic systems is poorly understood. Here, we present iron isotope data from a suite of lavas and cogenetic cumulate xenoliths and their minerals to understand iron isotope fractionation in the upper plate crustal section of ascending arc magma. The dataset comprises Fe-isotope compositions of lavas, cumulate xenoliths (gabbros and pyroxenites) and mineral separates (clinopyroxene, olivine, magnetite, amphibole and phlogopite) from Sangeang Api. Sangeang Api is an active arc volcano located ~330km to the rear of the eastern Sunda Arc of Indonesia, approximately 12km to the northeast of the island of Sumbawa. The lavas record δ^{57}Fe compositions (mean $\delta^{57}Fe = 0.099‰ \pm 0.051$) typical of the eastern Sunda Arc. Using well constrained Fe-isotope fractionation factors we tested recorded mineral separate compositions for equilibrium with primitive lavas of the suite. Magnetite separates record δ^{57}Fe compositions (mean $\delta^{57}Fe = 0.142‰ \pm 0.072$) in equilibrium with the whole-range of lava compositions, suggesting that they record their original magmatic compositions. However, the Fe-Mg silicates do not display this, recording significantly different compositions than would be expected if they were in equilibrium with the lavas. Both amphibole and clinopyroxene are heavier than anticipated (mean $\delta^{57}Fe = 0.125‰ \pm 0.081$ and $\delta^{57}Fe = 0.109‰ \pm 0.090$ respectively). Whereas, olivine separates are lighter (mean $\delta^{57}Fe = -0.313‰ \pm 0.284$) than would be expected from $\Delta^{57}Fe_{mgt\text{-}olivine}$ fractionation factors. This is reflected in the cumulate whole-rock compositions, mass balance calculations of equilibrium minerals suggest that both the gabbros and pyroxenites should be isotopically lighter than the lavas. In reality, gabbro and pyroxenite whole-rocks are heavier (mean $\delta^{57}Fe_{gabbro} = 0.166‰ \pm 0.051$ and mean $\delta^{57}Fe_{pyroxenite} = 0.109‰ \pm 0.066$) than the lavas. Iron isotope disequilibria appears pervasive throughout the cumulate xenolith suite, leading to the question of its origin. Cumulate xenoliths from Sangeang Api commonly display petrological, trace element and isotopic evidence for interactions with and contamination by variably fractionated melts percolating through the cumulate piles. Iron isotopic evidence from this study suggests that these processes are pervasive throughout the entire cumulate suite, displacing the original magmatic compositions of Fe-Mg silicate cumulate mineralogy to the observed compositions. Whereas, the Sangeang Api lavas appear to record the original Fe-isotopic signature of the mantle from which they are sourced.

INTRODUCTION

It has long been noted that island arc lavas are more oxidised than those from other tectonic settings (mid-ocean ridges and ocean island basalts) (Carmichael, 1991; Christie et al., 1986; Evans et al., 2012), the origin of which is hotly debated in the literature. Oxidation in arc magmas is predominantly measured by the $Fe^{3+}/\Sigma Fe$ ratio of the magma, as iron is the most abundant multi-valent element in arc magmas.

Arc magmas are thought to be sourced from melt depleted and metasomatised mantle wedge that has been fluxed by fluids released during progressive metamorphism of the descending slab and sediment on the surface (Grove et al., 2006; Grove et al., 2012; Kerrick and Connolly, 2001a, b; Schmidt and Poli, 1998). Mass balance calculations suggest that the overall effect of these interactions is to oxidise the mantle wedge (Evans et al., 2012; Evans and Tomkins, 2011). Thus, it can be surmised that since island arc lavas are sourced from these mantle wedge regions it is here where they inherited their oxidised character. Limited studies of sub-arc mantle xenoliths and primitive arc lavas support this notion of an oxidised mantle wedge. With thermobarometry suggesting that the sub-arc mantle have fO_2 values of 1 to 4 log units above the synthetic fayalite-magnetite-quartz buffer (ΔFMQ) (Carmichael, 1991; Evans et al., 2012; Parkinson and Arculus, 1999).

Trace element ratios, however, are in disagreement with these observations and models of an oxidised mantle (Lee et al., 2005; Lee et al., 2010; Mallmann and O'Neill, 2009). Fe and V are more incompatible at higher oxidation states, thus partition more into partial melts in oxidised sources (Lee et al., 2010; Mallmann and O'Neill, 2009). Comparing these elements with those with only one valency (Zn and Sc) and therefore a fixed partition coefficient, suggest that the source regions of arc lavas and MORB are similarly oxidised. This requires that oxidation in arc magmas must be achieved by some process outside of the source region; with speculation that redox processes in the crust can be driven by degassing, fractionation of reduced species or other crustal processes occurring during magma ascent (Burgisser and Scaillet, 2007; Kelley and Cottrell, 2012; Moussallam et al., 2014).

Stable isotopes of iron (^{54}Fe, ^{56}Fe, ^{57}Fe and ^{58}Fe) have been identified as a means of investigating the oxidation state of the mantle wedge, due to the fractionation effect exerted over iron isotopes by variations in oxidation (Beard and Johnson, 2004; Dauphas and Rouxel, 2006). Theory suggests that Fe^{3+} will have an isotopically heavier composition than Fe^{2+}. However, any oxidation effect could potentially be masked by differing degrees of partial melts, with larger melt fractions of the same source producing isotopically lighter melts (Dauphas et al., 2009). Therefore, magmas sourced from an oxidised region will be isotopically heavier than those from a more relatively reduced region. This is not what is observed however, with primitive island arc magmas around the world being characterised by light isotopes when compared to MORB ($\sim\delta^{57}Fe$+0.1-0.2), even when corrected for fractional crystallisation. Nebel et al. (2015) proposed a three-stage process to explain the light isotopic composition of arc magmas. Initial melt depletion of a peridotite lithology will drive the residues to lower $Fe^{3+}/\Sigma Fe$ (~ΔFMQ-2)

and light isotopic compositions. Fluxing by slab derived fluids that are Fe-poor, sulphate-rich and highly oxidised produces melts that are similarly oxidised but retain the isotopically light characteristics of the protolith. These isotopically light melts may then become heavier with respect to iron through the fractional crystallisation of Fe^{2+} bearing phases. However, it has been shown that isotopically light, hypersaline-/sulfate-rich fluids are released during the progressive metamorphism and devolatilisation of serpentinised peridotite (Debret et al., 2016). Therefore, our understanding of the processes required to produce oxidised and yet isotopically light island arc lavas is still unclear. In this study, we will provide further constraints on the effects of crustal magmatic processes on iron isotope fractionation in island arc systems. The intraoceanic island arc volcano of Sangeang Api (Indonesia) erupts a suite of lavas, entrained in which and coeval with are a suite of cumulate xenoliths. As such it presents the perfect natural laboratory to study the processes of stable iron isotope fractionation in crustal magmatic systems.

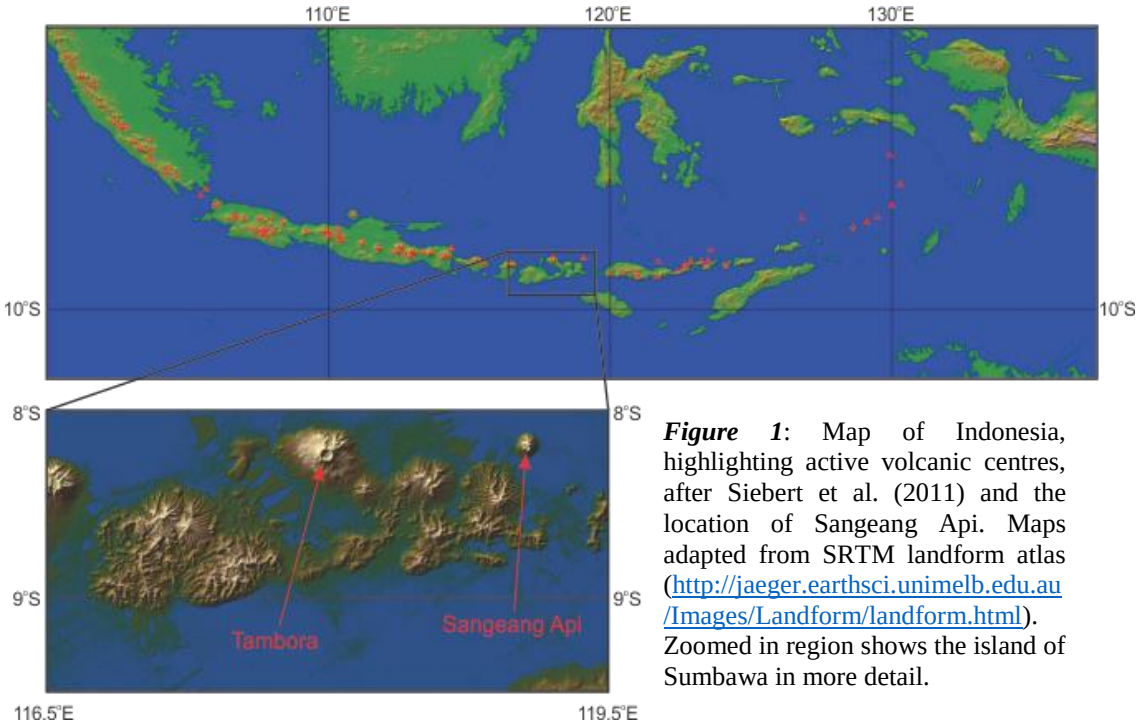

Figure 1: Map of Indonesia, highlighting active volcanic centres, after Siebert et al. (2011) and the location of Sangeang Api. Maps adapted from SRTM landform atlas (http://jaeger.earthsci.unimelb.edu.au/Images/Landform/landform.html). Zoomed in region shows the island of Sumbawa in more detail.

GEOLOGICAL BACKGROUND

Located ~330km to the rear of the trench and ~180km above the down-going slab (Syracuse and Abers, 2006), Sangeang Api is an active arc volcano located near to the island of Sumbawa in the eastern Sunda Arc of Indonesia (fig. 1). It records a history of eruptions from 1512 and culminating most recently in the eruption of May 2014 (Siebert et al., 2011). It erupts a suite of shoshonitic, volatile-rich and silica-undersaturated lavas ranging in composition from basalts to basaltic-trachyandesites (Foden and Varne, 1980; Turner et al., 2003). Entrained within these lava suites are a suite of xenoliths that can be split into two separate sub-groups based on their mineralogy and geochemistry; group 1

Figure 2a-c: Harker diagrams displaying geochemistry of whole-rock analyses from Sangeang Api, data collated from Foden and Varne (1980), Turner et al. (2003) and this thesis. Arrows in figure 2a geochemical trends driven by fractional crystallisation of cumulate mineralogy: Trend 1 = 83.5% clinopyroxene, 8.8% olivine and 7.7% magnetite. Trend 2 = 85.7% clinopyroxene, 7.9% olivine and 6.3% plagioclase. Trend 3 = 33-8.1% clinopyroxene, 11.9-10.8% magnetite, 47.4-38.9% plagioclase, 7.5-0% biotite, 0-41.3% amphibole and 0-0.8% apatite. Key for symbols can be seen in figure 2b. Fe_2O_3 in figure 2b is representative of total Fe.

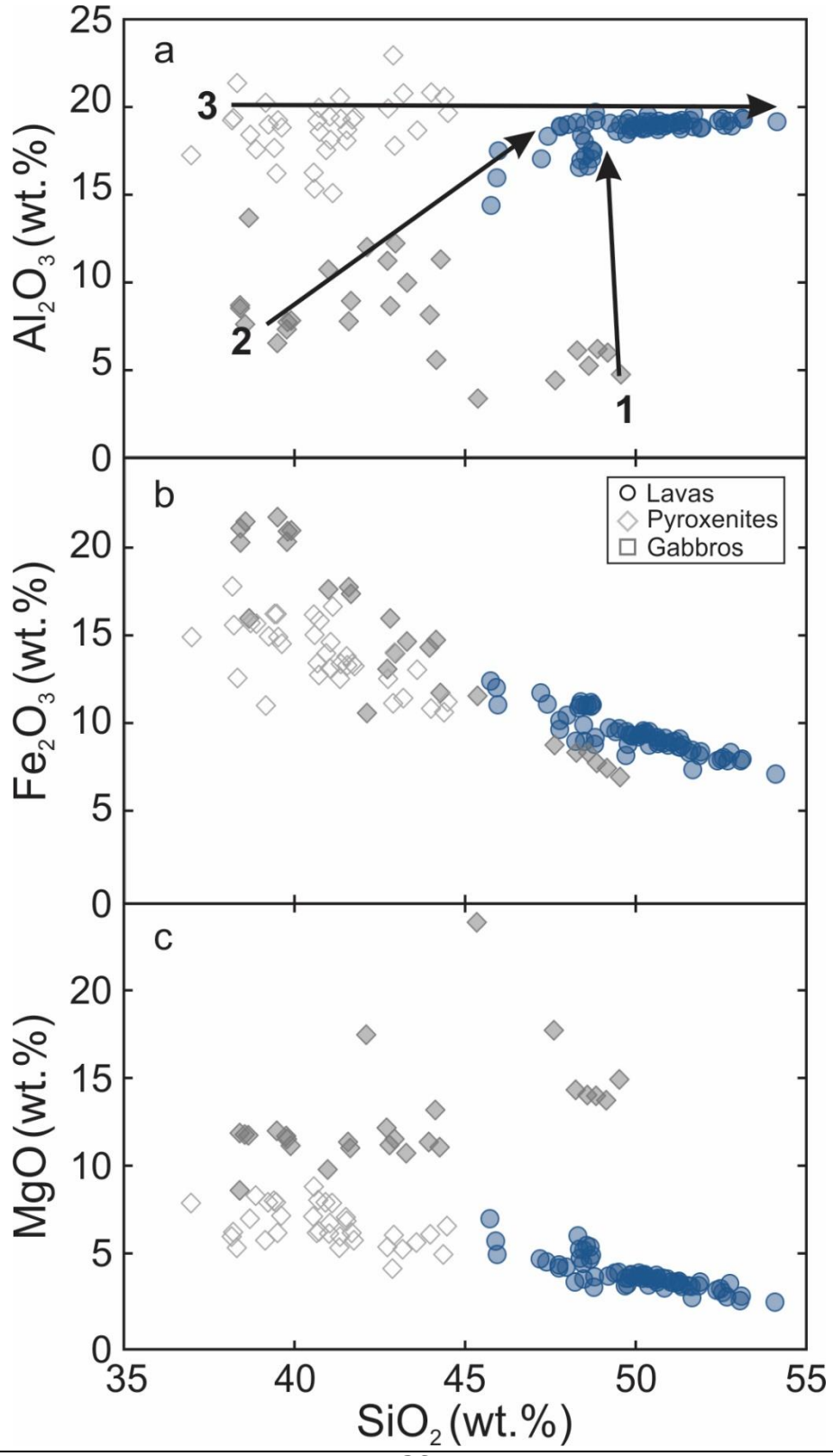

clinopyroxenites (*cpx+ol/mgt*, Al_2O_3 <12wt.% and MgO >10wt.%) and group 2 gabbros (*plag+cpx±amph±mgt*, Al_2O_3 >15wt.% and MgO <9wt.%). Figures 2a-2c display compositional variation in the lavas, gabbros and pyroxenites. Similarities between the phenocryst populations of the lavas (*cpx+plag+mgt+oliv* and *cpx+plag+mgt+amph*) and the crystal populations of the xenoliths suggests that the xenoliths bear a cumulate origin and are likely co-genetic to the lavas in which they are entrained. Not only are the phenocryst and cumulate mineral populations similar, but there is petrological evidence for the inheritance of xenocrysts in the lavas from the cumulate xenoliths; overlapping compositions and Mg# in clinopyroxene, similar anorthite contents in plagioclase and overlapping amphibole compositions. Geochemical differentiation trends within the lavas can likewise be related to the fractional crystallisation of the cumulate xenolith suites (see figure 2a). Falling $Fe^{3+}/\Sigma Fe$ with increasing Zr (indices of magma differentiation) suggests that the magmas became increasingly reduced as differentiation occurred. Estimates of magma fO_2 in equilibrium with amphiboles, calculated using the Ridolfi and Renzulli (2012) amphibole oxythermobarometer, suggest that magmas ascending through a crustal magmatic tract followed an oxidation-reduction path from ~ΔNNO+0.5 (at ~900MPa) to ~ΔNNO+1.5 (600MPa) at and finally back to ~ΔNNO+1 (at 400MPa). This has been interpreted as a change in the degassing regime of the magma from sulphide dominated at pressures above ~600MPa, to sulphate dominated at pressures below this. A number of the cumulate xenoliths display textures of cumulate-cumulate and cumulate-melt interactions, suggesting that the magma chambers were influenced by pervasive magmatic mixing and melt percolation. The chemistry of trapped percolative melts (highly alkaline: Na_2O+K_2O >10wt.%, Cl-rich: >4000ppm) hints at a pargasite breakdown origin and is supported by well-developed amphibole breakdown textures in amphibole-gabbro xenoliths.

Given the completeness of the magmatic and cumulate assemblages erupted by the Sangeang Api system, and our understanding of the magmatic processes leading to the observed chemistry and petrology, Sangeang Api volcano presents an ideal system in which to investigate and elucidate the effect on iron isotope fractionation of crustal magmatic processes. Percolative flow of pargasite-derived melts may, however, have introduced some form of disequilibrium into the system that may have complicated the iron isotope characteristics of the magmas and cumulate xenoliths.

METHODS

Sample selection and preparation

Representative samples of the lava suite and both groups of xenoliths were chosen to cover the full range of geochemical and petrological characteristics displayed. Lava samples were selected based primarily on their major element (SiO_2, Al_2O_3 & MgO), trace element (Zr, Sr & Y) and radiogenic isotope ($^{143}Nd/^{144}Nd$ & $^{87}Sr/^{86}Sr$) compositions to ensure a good coverage of the observed differentiation trends. Cumulate xenoliths were selected to ensure good coverage of observed major and trace element geochemistry, as well as mineral populations (especially ferromagnesian mineralogy). All samples were screened for evidence of alteration to ensure no possible iron isotope fractionation from post-eruptive processes.

Whole rock samples were prepared at the University of Adelaide. Samples were first crushed in a jaw crusher and a portion of the crushed cumulate xenolith samples set aside

for later mineral separation. Crushed samples were then powder using a tungsten-carbide mill. Separates of ferromagnesian minerals (clinopyroxene, olivine, amphibole and biotite) from the reserved crushed samples were then manually hand-picked using an optical microscope. Magnetite was separated from powdered whole-rock samples using a neodymium magnet to avoid potential contamination by iron. Representative minerals from separated mineral populations were then mounted in epoxy resin and polished for electron microprobe analysis.

Sample dissolution

Powdered whole rock samples and mineral separates were dissolved in a mixture of concentrated HNO_3-HCl-HF for a minimum of 12 hours at 140˚C. Following this samples were dried off, with the addition of HNO_3 to drive off HF and stop insoluble fluorides from forming. Samples were then dissolved in 6 M HCl, before again being dried and then finally dissolved again in 0.5ml 6 M HCl. Following a method similar to that of Poitrasson and Freydier (2005), iron was purified from the samples using an AG1-X4 200-400 mesh anion exchange resin previously cleaned and equilibrated with 6 M HCl. Iron was eluted using 4ml of 2M HCl to ensure no Zn elution, before being dried down and taken up in 5ml 0.05 M HCl for mass spectrometry. To test the reproducibility of our data we ran several repeat samples. All repeats were within error except for one olivine separate (BC14/089), hinting at possible iron isotope disequilibrium between cumulate mineralogy.

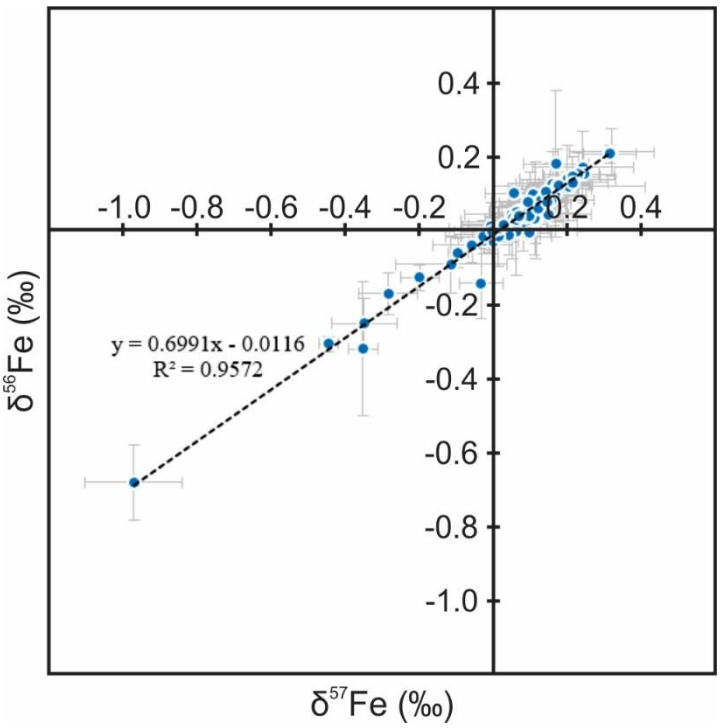

Figure 3: $\delta^{57}Fe$-$\delta^{56}Fe$ plot displaying mass fractionation of all analyses (whole-rock and mineral separates) in this study. Analyses define a slop of y = 0.6991x – 0.0116, close to the equilibrium mass dependence of 0.6780 calculated by Young et al. (2002) and have an r^2 value of 0.9572. Error bars represent 2s.d. of an average of at least 2 analyses.

Mass spectrometry

Iron isotope ratios were measured in medium resolution mode, using a H-geometry skimmer cone on a Thermo-Finnigan Neptune MC-ICPMS at CSIRO, Waite Campus. Samples were diluted to a ~4ppm iron solution in 2% HNO_3 to give a signal between 0.95-1.1V on ^{57}Fe. Samples were spiked with ~8ppm Ni to produce a signal of ~1V on ^{61}Ni.

Prior to each measurement of sample solution a baseline measurement was undertaken. Solution take-up time was set to 120 seconds. Each measurement was undertaken in static mode and consisted of 35 cycles set to 8 second

integration times. To assess the reproducibility of our data, a minimum of 3 analyses were undertaken for each sample.

Mass bias was corrected for following the Ni-spiking method of Poitrasson and Freydier (2005). All data are presented using the delta notation in parts per mil (‰) relative to the IRMM-014 standard, as represented below:

$$\delta^{57}Fe\ (‰) = \left[\left({}^{57}Fe/{}^{54}Fe_{sample}\right)/\left({}^{57}Fe/{}^{54}Fe_{IRMM-014}\right) - 1\right] \times 10^3$$

Estimates of error are represented as 2 times the standard deviation (2SD) of replicate analyses of the same sample. Three geostandards (BCR-2, BHVO-2 and AGV-2) were analysed to measure the long-term reproducibility of our procedure (table 1). BCR-2 analyses returned an average δ^{57}Fe of 0.148‰ ± 0.124. BHVO-2 analyses returned an average δ^{57}Fe of 0.155‰ ± 0.061. AGV-2 analyses returned an average δ^{57}Fe of 0.157‰ ± 0.123. Each of our geostandard averages is within analytical error of the published δ^{57}Fe (BCR-2 0.126‰, BHVO-2 0.174‰ and AGV-2 0.146‰) (Craddock and Dauphas, 2011). A procedural blank was prepared with each batch of samples (18 in total) returning an average iron concentration of 4.6ppb. Analysed data sit on a mass dependent fractionation line with a slope of y = 0.6991x – 0.0116 as observed in figure 3, close to the theoretical equilibrium mass dependent fractionation of 0.6780 of Young et al. (2002).

Standard	No. analyses	Measured values				Literature values		
		δ^{57}Fe (‰)	2s.d.	δ^{56}Fe (‰)	2s.d.	δ^{57}Fe (‰)	δ^{56}Fe (‰)	Reference
AGV-2	15	0.157	0.123	0.114	0.079	0.146	0.105	Craddock & Dauphas 2011
BCR-2	12	0.148	0.062	0.112	0.105	0.126	0.091	Craddock & Dauphas 2011
BHVO-2	17	0.154	0.061	0.116	0.074	0.174	0.114	Craddock & Dauphas 2011

Table 1: Comparison of measured geostandards from this study to published geostandard values.

Electron microprobe analysis

Major element compositions of mineral separates were determined by electron microprobe analysis using a Cameca SXFive at Adelaide Microscopy, University of Adelaide. Samples were analysed using a 15µm spot size at 15kV and 20nA, with a 20s background measurement and 40s peak measurment. Several in-house standards (Plagioclase, Astimex Almandine Garnet, Rutile, Astimex albite, Rhodonite, Chromite, Tugtupite, Astimex Apatite, Sanidine, Barite, Willemite & Astimex Anhydrite) were used for calibration. To account for zoning and polishing effects, a minimum of 10 spots was analysed for each individual crystal separate in transects aligned with the long-axis of the mineral. The data was then filtered to remove data points outside 1 standard deviation of the mean for each individual analysed crystal. Filtering was necessary to account for any effects of polishing or fracture within the crystal structure which may have caused outlying results.

Table 2: Major element and iron isotopic compositions of whole-rock samples analysed in this study. Iron isotopic compositions are the average of a minimum of two analyses, with errors given as 2 standard deviations from the mean.

Sample No.	**L01**	**L05**	**L14**	**SA7**	**BC14/ 008**	**L14 (rpt.)**	**BC14/ 017**	**SA12-XO2**	**BC14/ 066**	**BC14/ 071**	**BC14 /048**	**BC14/ 064**	**SA12-X06**
Lithology	Basaltic trachy andesite	Basaltic trachy andesite	Basalt	Trachy basalt	Phono tephrite	Basalt	Basanite	Gabbro	Gabbro	Gabbro	Hbl-Gabbro	Hbl-Gabbro	Gabbro
(wt.%)													
SiO_2	50.67	52.78	45.72	48.68	48.78	45.72	45.95	38.28	43.98	41.08	40.69	40.53	42.72
TiO_2	0.89	0.82	1.03	0.98	0.81	1.03	1.00	1.06	1.05	1.22	1.64	1.17	1.06
Al_2O_3	18.92	18.84	14.30	16.98	19.63	14.30	17.42	21.31	20.75	15.00	19.88	16.16	19.84
FeO	3.73	4.05	5.72		3.14	5.72	4.12	4.33	6.86	8.90	4.40	8.27	5.24
Fe_2O_3	4.91	3.92	6.09	11.21	5.75	6.09	6.97	7.77	4.01	7.68	8.35	7.88	6.72
MnO	0.20	0.20	0.20	0.23	0.22	0.20	0.21	0.12	0.13	0.18	0.14	0.19	0.14
MgO	3.89	3.59	7.23	5.65	3.39	7.23	5.21	5.59	6.36	8.12	8.25	7.36	5.65
CaO	9.21	8.30	13.38	10.76	9.69	13.38	11.49	18.10	15.40	17.54	13.75	17.99	15.16
Na_2O	3.63	3.98	2.41	2.94	4.41	2.41	3.08	0.87	1.64	0.80	1.67	0.74	1.53
K_2O	2.78	3.21	2.36	2.48	3.39	2.36	3.37	0.26	0.67	0.21	0.95	0.18	0.73
P_2O_5	0.33	0.34	0.32	0.33	0.53	0.32	0.62	1.46	0.08	0.04	0.07	0.36	0.12
SO_3	0.03	0.04	0.04			0.04	0.13	0.07			0.00		0.05
Cl					1059.50		174.50		515.00	292.00	466.00	322.50	
LOI	-0.02	0.05	-0.03	-0.20	0.16	-0.03	0.41	-0.20	-0.99	-0.80	0.16	-0.86	-0.11
Total	99.58	100.55	99.40	100.04	99.84	99.40	99.59	99.48	100.99	100.80	99.84	100.86	99.42
Na_2O+K_2O	6.405	7.191	4.768	5.420	7.804	4.768	6.456	1.129	2.311	1.009	2.626	0.924	2.256
Mg# ($Mg/[Mg+Fe_{Tot}]$)	0.538	0.524	0.604	0.666	0.514	0.604	0.562	0.560	0.567	0.539	0.643	0.526	0.550
Fe^{2+}/Fe^{3+}	1.686	2.292	2.085		1.212	2.085	1.314	1.238	3.801	2.575	1.170	2.334	1.734
$Fe^{3+}/\Sigma Fe$	0.372	0.304	0.324		0.452	0.324	0.432	0.447	0.208	0.280	0.461	0.300	0.366
$\delta^{57}Fe$ (‰)	**0.089**	**0.107**	**0.154**	**0.097**	**0.120**	**0.026**	**0.013**	**0.201**	**0.154**	**0.215**	**0.174**	**0.061**	**0.142**
2s.d.	0.040	0.040	0.046	0.055	0.014	0.115	0.133	0.205	0.115	0.094	0.082	0.048	0.081
$\delta^{56}Fe$ (‰)	**0.047**	**0.063**	**0.088**	**0.038**	**0.060**	**0.016**	**0.004**	**0.119**	**0.081**	**0.129**	**0.123**	**0.027**	**0.104**
2s.d.	0.021	0.065	0.016	0.040	0.051	0.082	0.095	0.148	0.093	0.053	0.061	0.056	0.036

Table 2: Major element and iron isotopic compositions of whole-rock samples analysed in this study. Iron isotopic compositions are the average of a minimum of two analyses, with errors given as 2 standard deviations from the mean.

Sample No.	**SA24**	**BC14/078**	**SA24 (repeat)**	**BC14/019**	**SA12-X04**	**SA12-X03**
Lithology	Olivine-Pyroxenite	Pyroxenite	Olivine-Pyroxenite	Olivine-Pyroxenite	Pyroxenite	Pyroxenite
(wt.%)						
SiO_2	48.84	39.47	48.84	42.69	38.63	38.51
TiO_2	0.71	1.44	0.71	1.19	1.97	1.79
Al_2O_3	6.11	6.43	6.11	11.12	13.61	7.53
FeO		8.44		6.23	6.72	8.10
Fe_2O_3	7.84	13.14	7.84	6.86	8.46	12.34
MnO	0.14	0.16	0.14	0.18	0.16	0.17
MgO	14.08	12.12	14.08	12.30	11.87	11.94
CaO	21.11	19.01	21.11	16.64	13.28	18.66
Na_2O	0.58	0.37	0.58	0.99	1.79	0.41
K_2O	0.40	0.02	0.40	0.67	1.49	0.10
P_2O_5	0.05	0.03	0.05	0.07	0.18	0.10
SO_3		0.00			0.05	0.02
Cl		299.50		236.50		
LOI	0.02	-0.67	0.02	1.02	0.28	-0.50
Total	99.88	100.67	99.88	98.98	99.25	100.05
Na_2O+K_2O	0.980	0.389	0.980	1.656	3.283	3.283
Mg# ($Mg/[Mg+Fe_{Tot}]$)	0.877	0.601	0.877	0.702	0.668	0.609
Fe^{2+}/Fe^{3+}		1.428		2.018	1.765	1.458
$Fe^{3+}/\Sigma Fe$		0.412		0.331	0.362	0.407
$\delta^{57}Fe$ (‰)	**0.068**	**0.028**	**-0.005**	**0.143**	**0.095**	**0.093**
2s.d.	0.052	0.096	0.082	0.032	0.057	0.098
$\delta^{56}Fe$ (‰)	**0.040**	**0.016**	**-0.003**	**0.078**	**-0.007**	**0.078**
2s.d.	0.050	0.082	0.062	0.016	0.019	0.072

Table 3: Major element and iron isotopic compositions of amphibole, clinopyroxene and olivine mineral separate samples analysed in this study. Iron isotopic compositions are the average of a minimum of two analyses, with errors given as 2 standard deviations from the mean. Abbreviations: 'Pyrox.' = Pyroxenite, 'Amph' = Amphibole, 'Cpx' = Clinopyroxene and 'Oliv' = Olivine. Repeat analyses of mineral separates from the same samples are denoted by a *. Major element compositions represent the average of a minimum of 5 spot analyses of a single phenocryst from the representative sample. Mg# calculated as $Mg/(Mg+Fe^{2+})$.

Sample	**BC14/ 044**	**BC14/ 048**	**BC14/ 066**	**BC14/ 049**	**SA12-X06**	**SA12-X04**	**BC14/ 049**	**BC14/ 044**	**SA12-X02**	**BC14/ 066**	**BC14/ 071**	**BC14/ 038**	**BC14/ 066***
Lithology	Gabbro	Gabbro	Gabbro	Gabbro	Pyrox.	Pyrox.	Gabbro	Gabbro	Gabbro	Gabbro	Gabbro	Gabbro	Gabbro
Mineral	Amph	Amph	Amph	Amph	Amph	Amph	Cpx	Cpx	Cpx	Cpx	Cpx	Cpx	Cpx
SiO_2	39.19	39.12	39.15	39.21	39.37	38.40		49.18	47.10	49.54	48.78	47.07	49.54
TiO_2	2.83	2.38	2.29	2.23	2.40	2.08		0.76	0.89	0.61	0.77	0.94	0.61
Al_2O_3	13.50	14.08	14.06	14.15	14.31	14.88		4.58	6.47	4.18	5.01	6.60	4.18
Cr_2O_3	0.00	0.01	0.01	0.00	0.01	0.00		0.01	0.00	0.00	0.00	0.01	0.00
FeO	10.94	10.73	10.49	10.46	10.70	11.09		7.31	8.32	6.93	7.23	7.75	6.93
MnO	0.21	0.15	0.12	0.12	0.13	0.13		0.29	0.20	0.18	0.20	0.16	0.18
MgO	13.52	14.34	14.30	14.10	14.38	13.51		13.86	12.59	14.82	14.00	12.91	14.82
CaO	11.97	12.19	12.21	12.22	12.18	12.25		0.06	0.02	0.02	0.03	0.04	0.02
Na_2O	2.36	2.20	2.19	2.07	2.18	1.98		22.72	23.29	22.73	22.97	23.30	22.73
K_2O	1.58	1.45	1.33	1.53	1.30	1.82		0.59	0.33	0.24	0.30	0.29	0.24
F	0.34	0.23	0.24	0.17	0.13	0.17		0.00	0.00	0.00	0.00	0.00	0.00
Cl	0.09	0.05	0.04	0.04	0.04	0.05		0.01	0.01	0.00	0.01	0.01	0.00
ZnO	0.04		0.03	0.04	0.02	0.03		0.00	0.02	0.01	0.00	0.01	0.01
BaO	0.15		0.10	0.10	0.09	0.13		0.00	0.01	0.01	0.01	0.01	0.01
V_2O_3	0.09		0.07	0.08	0.08	0.08		0.04	0.05	0.03	0.02	0.05	0.03
SO_3	0.02		0.01	0.02	0.01	0.01		0.01	0.01	0.01	0.02	0.01	0.01
TOTAL	96.68	96.92	96.53	96.49	97.28	96.53		99.43	99.30	99.33	99.36	99.14	99.33
Mg#	0.755	0.834	0.830	0.813	0.844	0.793		0.874	0.879	0.900	0.891	0.893	0.900
$\delta^{57}Fe$ (‰)	**0.172**	**0.152**	**0.070**	**0.105**	**0.097**	**-0.058**	**0.214**	**0.215**	**0.079**	**0.114**	**0.085**	**0.142**	**0.240**
2s.d.	0.038	0.113	0.021	0.014	0.098	0.107	0.028	0.006	0.037	0.110	0.039	0.028	0.137
$\delta^{56}Fe$ (‰)	**0.125**	**0.111**	**0.052**	**0.096**	**0.065**	**-0.040**	**0.147**	**0.143**	**-0.006**	**0.027**	**0.003**	**0.084**	**0.171**
2s.d.	0.013	0.071	0.004	0.021	0.045	0.047	0.026	0.004	0.051	0.102	0.018	0.005	0.098

Table 3: Major element and iron isotopic compositions of amphibole, clinopyroxene and olivine mineral separate samples analysed in this study. Iron isotopic compositions are the average of a minimum of two analyses, with errors given as 2 standard deviations from the mean. Abbreviations: 'Pyrox.' = Pyroxenite, 'Amph' = Amphibole, 'Cpx' = Clinopyroxene and 'Oliv' = Olivine. Repeat analyses of mineral separates from the same samples are denoted by a *. Major element compositions represent the average of a minimum of 5 spot analyses of a single phenocryst from the representative sample. Mg# calculated as $Mg/(Mg+Fe^{2+})$.

Sample	**BC14/ 086**	**SA12-X02**	**BC14/ 064**	**SA12-X026**	**BC14/ 014**	**SA24**	**BC14/ 078**	**BC14/ 041**	**BC14/ 069**	**SA24**	**BC14/ 019**	**SA12-X019**	**BC14/ 089**
Lithology	Gabbro	Gabbro	Gabbro	Gabbro	Pyrox.	Pyrox.	Pyrox.	Pyrox.	Pyrox.	Pyrox.	Pyrox.	Pyrox.	Pyrox.
Mineral	Cpx	Cpx	Cpx	Cpx	Cpx	Cpx	Cpx	Cpx	Cpx	Cpx	Cpx	Cpx	Cpx
SiO_2	49.48		50.79	47.06		49.23	47.80	48.91	48.11	49.23		48.87	48.49
TiO_2	0.67		0.47	0.96		0.65	0.80	0.74	0.82	0.65		0.74	0.76
Al_2O_3	4.28		3.56	6.45		4.55	5.76	4.96	5.69	4.55		5.35	5.75
Cr_2O_3	0.00		0.27	0.00		0.03	0.01	0.02	0.01	0.03		0.02	0.02
FeO	7.08		5.09	7.16		5.99	7.09	7.04	7.01	5.99		6.53	6.87
MnO	0.21		0.13	0.13		0.11	0.11	0.15	0.13	0.11		0.11	0.11
MgO	14.37		15.71	13.16		14.89	13.86	13.94	13.74	14.89		14.53	14.27
CaO	0.02		0.02	0.05		0.02	0.03	0.02	0.03	0.02		0.02	0.03
Na_2O	22.90		23.62	23.20		23.59	23.24	23.45	23.29	23.59		23.36	23.12
K_2O	0.34		0.27	0.34		0.23	0.24	0.37	0.31	0.23		0.22	0.22
F	0.02		0.00	0.07		0.00	0.00	0.00	0.00	0.00		0.00	0.00
Cl	0.01		0.00	0.01		0.01	0.01	0.01	0.01	0.01		0.01	0.01
ZnO	0.01		0.00	0.01		0.00	0.00	0.00	0.00	0.00		0.00	0.00
BaO	0.01		0.01	0.01		0.01	0.01	0.01	0.01	0.01		0.01	0.01
V_2O_3	0.03		0.02	0.04		0.04	0.04	0.03	0.03	0.04		0.03	0.04
SO_3	0.01		0.01	0.01		0.01	0.01	0.01	0.01	0.01		0.00	0.01
TOTAL	99.43		99.96	98.65		99.35	99.01	99.67	99.20	99.35		99.82	99.71
Mg#	0.896		0.929	0.921		0.927	0.918	0.887	0.913	0.927		0.901	0.894
$\delta^{57}Fe$ (‰)	**0.159**	**0.051**	**0.112**	**0.048**	**0.089**	**0.060**	**0.042**	**0.093**	**0.318**	**-0.011**	**0.212**	**0.196**	**-0.023**
2s.d.	0.101	0.138	0.096	0.011	0.019	0.166	0.082	0.171	0.113	0.093	0.040	0.048	0.002
$\delta^{56}Fe$ (‰)	**0.126**	**0.024**	**0.075**	**0.043**	**0.012**	**-0.002**	**-0.013**	**0.043**	**0.212**	**-0.011**	**0.144**	**0.139**	**-0.026**
2s.d.	0.086	0.102	0.110	0.005	0.030	0.121	0.053	0.050	0.064	0.049	0.010	0.017	0.017

Table 3: Major element and iron isotopic compositions of amphibole, clinopyroxene and olivine mineral separate samples analysed in this study. Iron isotopic compositions are the average of a minimum of two analyses, with errors given as 2 standard deviations from the mean. Abbreviations: 'Pyrox.' = Pyroxenite, 'Amph' = Amphibole, 'Cpx' = Clinopyroxene and 'Oliv' = Olivine. Repeat analyses of mineral separates from the same samples are denoted by a *. Major element compositions represent the average of a minimum of 5 spot analyses of a single phenocryst from the representative sample. Mg# calculated as $Mg/(Mg+Fe^{2+})$.

Sample	**SA12-X04**	**SA12-X03**	**SA12-X032**	**BC14/064**	**BC14/019**	**SA24**	**BC14/041**	**BC14/089**	**BC14/089***	**SA12-X019**	**SA12-X032**	**SA12-X03**
Lithology	Pyrox.	Pyrox.	Pyrox.	Gabbro	Pyrox.	Pyrox.	Pyrox.	Pyrox.	Pyrox.	Pyrox.	Pyrox.	Pyrox.
Mineral	Cpx	Cpx	Cpx	Oliv	Oliv	Oliv	Oliv	Oliv	Oliv	Oliv	Oliv	Oliv
SiO_2		47.14	50.65	38.25	38.22	38.07	38.74	38.43	38.43	38.99	38.42	38.72
TiO_2		1.05	0.45	0.01	0.01	0.01	0.01	0.01	0.01	0.01	0.02	0.02
Al_2O_3		6.74	3.65	0.02	0.03	0.03	0.02	0.05	0.05	0.04	0.06	0.06
Cr_2O_3		0.00	0.07	0.00	0.00	0.00	0.01	0.00	0.00	0.00	0.00	0.01
FeO		7.08	5.40	21.22	21.16	21.75	18.07	20.22	20.22	19.09	19.73	19.05
MnO		0.13	0.11	0.67	0.60	0.46	0.50	0.43	0.43	0.39	0.51	0.43
MgO		13.69	15.51	39.02	39.20	38.51	41.63	39.66	39.66	41.19	39.94	40.98
CaO		0.01	0.02	0.03	0.04	0.04	0.03	0.06	0.06	0.03	0.06	0.03
Na_2O		23.18	23.48	0.17	0.18	0.19	0.19	0.25	0.25	0.25	0.18	0.23
K_2O		0.28	0.27	0.02	0.02	0.01	0.03	0.02	0.02	0.02	0.02	0.01
F		0.00	0.00	0.00	0.00	0.00	0.00	0.00	0.00	0.00	0.00	0.00
Cl		0.00	0.01	0.00	0.00	0.01	0.01	0.01	0.01	0.00	0.01	0.00
ZnO		0.01	0.00	0.03	0.02	0.03	0.01	0.01	0.01	0.02	0.02	0.01
BaO		0.01	0.01	0.00	0.00	0.00	0.00	0.00	0.00	0.01	0.00	0.00
V_2O_3		0.03	0.02	0.00	0.01	0.01	0.01	0.01	0.01	0.00	0.01	0.00
SO_3		0.01	0.01	0.01	0.00	0.00	0.01	0.01	0.01	0.01	0.01	0.02
TOTAL		99.37	99.67	99.45	99.50	99.11	99.24	99.17	99.17	100.05	98.97	99.58
Mg#		0.882	0.915	0.767	0.770	0.760	0.807	0.778	0.778	0.794	0.783	0.794
$\delta^{57}Fe$ (‰)	**-0.034**	**0.061**	**0.055**	**-0.349**	**-0.968**	**-0.114**	**-0.443**	**-0.198**	**-0.353**	**-0.008**	**-0.284**	**-0.095**
2s.d.	0.058	0.074	0.076	0.087	0.131	0.149	0.026	0.051	0.039	0.075	0.079	0.029
$\delta^{56}Fe$ (‰)	**-0.143**	**0.049**	**0.100**	**-0.251**	**-0.680**	**-0.092**	**-0.306**	**-0.127**	**-0.319**	**0.012**	**-0.171**	**-0.060**
2s.d.	0.094	0.052	0.007	0.066	0.102	0.077	0.021	0.035	0.180	0.064	0.058	0.039

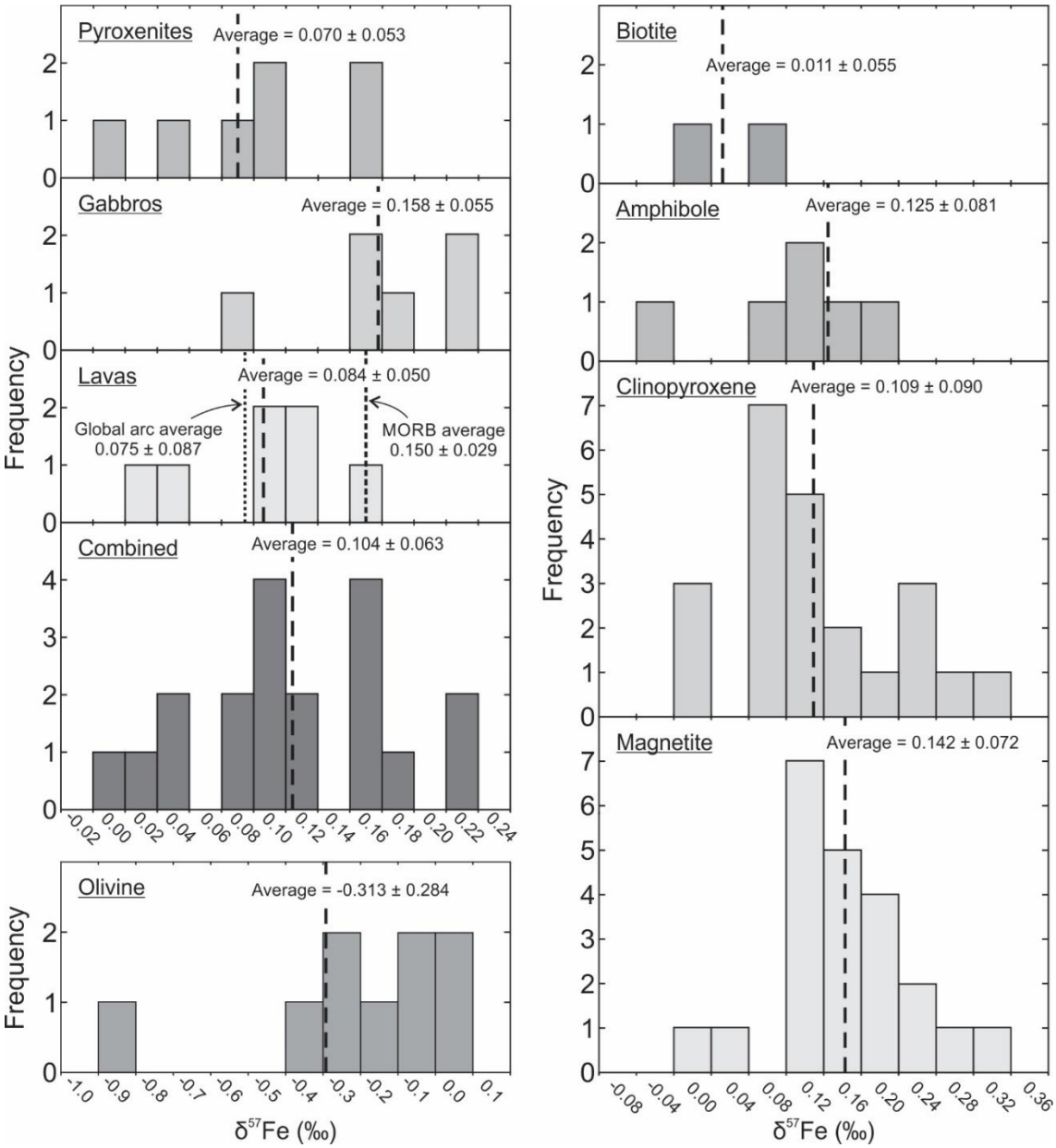

Figure 4: Histograms displaying δ^{57}Fe compositions of Sangeang Api whole-rock and mineral separates. Average Fe-isotope compositions given by dashed lines. Displayed errors are 1 standard deviation from the mean. Lava histogram shows average of global arc lavas from Foden et al. (In Press) and MORB basalts from Teng et al. (2013) for comparison.

RESULTS

Histograms displaying the range of δ^{57}Fe compositions and mean δ^{57}Fe values recorded by whole-rock and mineral separate samples from Sangeang Api can be observed in figure 4. Tables 3, 4 and 5 display the measured Fe isotope compositions of whole-rock and mineral separate analyses.

Whole-rock

Lavas

Analysed samples (n=11) range from basalts to basaltic-trachyandesites, with SiO_2 ranging from 45.7-52.8wt.% and Mg# (calculated as a molar ratio of $Mg/[Mg+Fe_{Tot}]$ for

all whole-rock analyses) spanning 0.43-0.55 (figure 2). $Fe^{3+}/\Sigma Fe$ ratios range from 0.38-0.53. Sangeang Api lavas have $\delta^{56}Fe$ compositions ranging from 0.004-0.088‰ and $\delta^{57}Fe$ from 0.013-0.120‰ (figure 4). Lavas analysed in this study record a mean $\delta^{57}Fe$ composition of 0.099‰ ± 0.051. Lava samples display a correlation between decreasing Mg# and increasing $\delta^{57}Fe$ values.

Gabbros

Gabbro samples analysed (n=10) range from 38.3-44wt.% SiO_2 (figure 2a), with Mg# spanning 0.31-0.39 and $Fe^{3+}/\Sigma Fe$ ratios range from 0.37-0.66. Gabbro samples span the largest isotopic compositions, recording $\delta^{56}Fe$ compositions spanning 0.027-0.129‰ and $\delta^{57}Fe$ compositions from 0.061-0.215‰ (figure 4). The mean $\delta^{57}Fe$ composition of gabbro xenoliths is 0.166‰ ± 0.051 (figure 4), 0.67‰ heavier than the lava analyses.

Pyroxenites

Analysed pyroxenite samples (n=10) span SiO_2 compositions from 38.6-48.8wt.%, with $Fe^{3+}/\Sigma Fe$ spanning 0.42-0.5 and Mg# 0.43-0.78. Pyroxenite samples record $\delta^{56}Fe$ compositions ranging from -0.007 to 0.078‰ and $\delta^{57}Fe$ from -0.05 to 0.143‰. This is the broadest range of compositions of any whole-rock group, recording the lightest whole-rock composition. Likely reflecting the greater presence of lighter cumulate minerals (such as olivine) in some pyroxenite samples. The pyroxenite samples record a mean $\delta^{57}Fe$ value of 0.109‰ ±0.066 (figure 4).

Mineral separates

Clinopyroxene

Clinopyroxene separates record mean $\delta^{57}Fe$ compositions of 0.109‰ ± 0.081, the full distribution of clinopyroxene samples can be seen in figure 4. Clinopyroxene separates from gabbros (n=11) have Mg# (calculated as a molar ratio of $Mg^{2+}/[Mg^{2+}/Fe^{2+}]$) from 0.87 to 0.93 and $Fe^{3+}/\Sigma Fe$ from 0.51 to 0.72. $\delta^{56}Fe$ compositions span from -0.006 to 0.171‰ and $\delta^{57}Fe$ from 0.051 to 0.240‰. Separates from pyroxenites (n=12) are similarly magnesian (Mg# 0.88-0.93) and have $Fe^{3+}/\Sigma Fe$ in a similar range (0.53-0.69). Clinopyroxenes from pyroxenites span to much lighter and heavier isotopic compositions, with $\delta^{56}Fe$ from -0.143 to 0.212‰ and $\delta^{57}Fe$ from -0.034 to 0.318‰.

Olivine

Olivine separates from this study range in Mg# (calculated as $Mg^{2+}/[Mg^{2+}+Fe^{2+}]$) from 0.76 to 0.81. A single olivine separate from a gabbro sample has $\delta^{56}Fe$ of -0.251‰ (±0.07) and $\delta^{57}Fe$ of -0.349‰ (±0.09). Separates from pyroxenite samples (n=8) have $\delta^{56}Fe$ spanning from -0.680 to 0.012‰ and $\delta^{57}Fe$ from -0.968 to -0.008‰. Olivine separates, as a whole, record a mean $\delta^{57}Fe$ composition of -0.313‰ ± 0.284 (figure 4).

Magnetite

Magnetite separates from gabbros (n=12) have $\delta^{56}Fe$ compositions spanning from -0.030 to 0.207‰ and $\delta^{57}Fe$ from 0.000 to 0.313‰. Separates from pyroxenite samples (n=10)

have δ^{56}Fe compositions from 0.060 to 0.179‰ and δ^{57}Fe from 0.094 to 0.212‰. Magnetite separates, as a whole, record a mean δ^{57}Fe composition of 0.142‰ ± 0.072.

Amphibole

Separates of amphibole from gabbros have Mg# (calculated as $Mg^{2+}/[Mg^{2+}/Fe^{2+}]$) ranging from 0.76 to 0.83 and Si contents ranging from 5.78 to 5.88 (a.p.f.u.). δ^{56}Fe compositions range from 0.052-0.125‰ and δ^{57}Fe span between 0.070 to 0.172‰. Pyroxenite separates (n=2) have Mg# spanning 0.79 to 0.84 and Si contents from 5.74-5.78. δ^{56}Fe compositions range from -0.040 to 0.065‰ and δ^{57}Fe span between -0.058 to 0.097‰. There appears to be a positive correlation between δ^{57}Fe and Si content amongst the amphibole separates. Figure 4 shows the δ^{57}Fe composition of amphiboles from all whole-rock groups, recording an average δ^{57}Fe composition of 0.125‰ ± 0.081.

Sample	Lithology	Mineral	δ^{57}Fe (‰)	2s.d.	δ^{56}Fe (‰)	2s.d.
BC14/086	Gabbro	Magnetite	0.000	0.066	-0.030	0.032
BC14/086	Gabbro	Magnetite	0.012	0.143	-0.017	0.079
BC14/066	Gabbro	Magnetite	0.245	0.039	0.152	0.003
BC14/071	Gabbro	Magnetite	0.228	0.097	0.152	0.058
SA12-X02	Gabbro	Magnetite	0.199	0.127	0.138	0.091
BC14/038	Gabbro	Magnetite	0.130	0.065	0.085	0.053
BC14/038	Gabbro	Biotite	0.050	0.074	0.034	0.037
BC14/049	Gabbro	Magnetite	0.087	0.093	0.037	0.044
BC14/086	Gabbro	Magnetite	0.313	0.069	0.207	0.025
BC14/044	Gabbro	Magnetite	0.098	0.083	0.068	0.091
BC14/064	Gabbro	Magnetite	0.098	0.083	0.068	0.091
BC14/048	Gabbro	Magnetite	0.146	0.054	0.043	0.003
SA12-X026	Gabbro	Magnetite	0.111	0.012	0.033	0.099
SA24	Pyroxenite	Magnetite	0.212	0.076	0.145	0.053
SA24	Pyroxenite	Biotite	-0.027	0.061	-0.017	0.045
BC14/019	Pyroxenite	Magnetite	0.159	0.007	0.099	0.025
BC14/078	Pyroxenite	Magnetite	0.165	0.082	0.096	0.082
SA12-X06	Pyroxenite	Magnetite	0.167	0.088	0.179	0.198
BC14/041	Pyroxenite	Magnetite	0.115	0.049	0.062	0.020
SA12-X019	Pyroxenite	Magnetite	0.172	0.096	0.121	0.099
BC14/069	Pyroxenite	Magnetite	0.107	0.072	0.065	0.013
SA12-X04	Pyroxenite	Magnetite	0.131	0.019	0.084	0.027
SA12-X04*	Pyroxenite	Magnetite	0.126	0.006	0.082	0.046
SA12-X03	Pyroxenite	Magnetite	0.094	0.072	0.060	0.066

Table 4: Iron isotopic composition of magnetite and biotite mineral separate analyses. Iron isotopic compositions are the average of a minimum of two analyses, with errors given as 2 standard deviations from the mean.

Biotite

Two biotite separates (one each from gabbros and pyroxenites) have δ^{56}Fe ranging from -0.017 to 0.034‰ and δ^{57}Fe spanning from -0.027 to 0.050‰, with biotite from the

pyroxenite having a lighter composition than that from the gabbro. Biotite separates record a mean $\delta^{57}Fe$ composition of 0.011‰ ± 0.055.

DISCUSSION

Inter-mineral fractionation

The lava and cumulate xenolith suites erupted by Sangeang Api are suggested to be co-genetic in their origin. The phenocryst populations of the lavas reflect the modal cumulate mineral proportions from the cumulate xenoliths, and likely inherited a portion of their phenocryst assemblages from the disaggregation of cumulate piles (Turner et al., 2003). Likewise, the melt evolution trends of the lavas can be modelled by fractional crystallisation of the cumulate xenolith mineral assemblages. Therefore, the products of Sangeang Api would appear to provide the ideal situation to investigate Fe-isotope fractionation in an arc magmatic system. Sossi et al. (2012) undertook one such study, analysing a differentiating suite of mafic to felsic tholeiitic magma and phenocrysts (magnetite and pyroxene). Calculating mineral-mineral and mineral-melt fractionation factors that controlled observed trends in the $\delta^{57}Fe$ evolution of the magma suite. Utilising the fractionation factors between spinel and olivine/clinopyroxene of Roskosz et al. (2015) the inter-mineral $\delta^{57}Fe$ compositions from the Sangeang Api rocks are compared to expected equilibrium fractionation factors (figure 5). Despite a few select magnetite-clinopyroxene pairs sitting on calculated equilibrium fractionation factors, it is obvious that both clinopyroxene and olivine define disequilibria arrays.

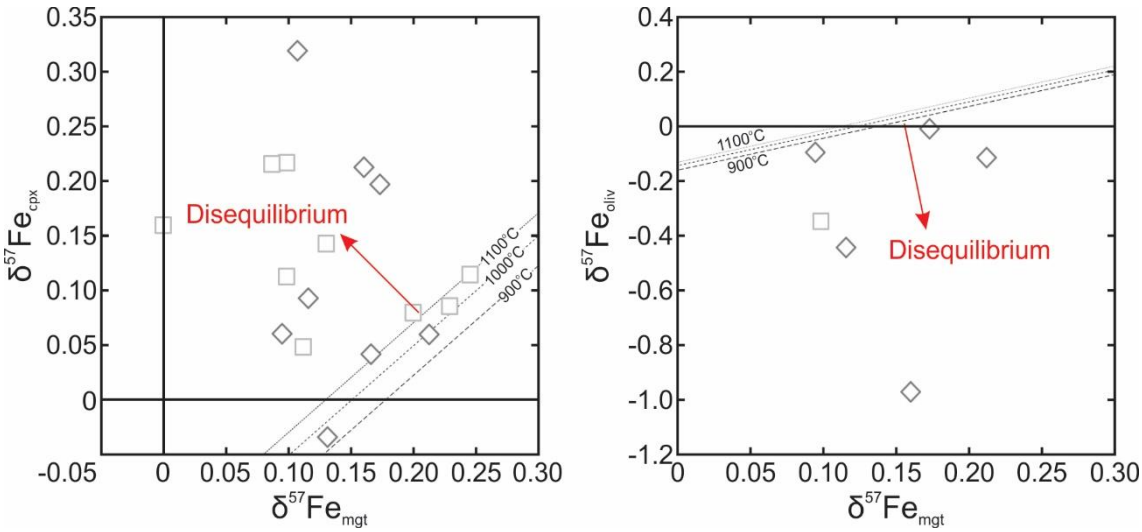

Figure 5a & b: $\delta^{57}Fe_{mgt}$ vs. $\delta^{57}Fe_{cpx}/\delta^{57}Fe_{oliv}$ diagram were fractionation factor ($\Delta^{57}Fe_{mgt\text{-}mineral}$) can be calculated by subtracting one value from another. Dashed lines represent expected $\delta^{57}Fe$ fractionation factors from 900˚C-1100˚C calculated from Roskosz et al. (2015).

Utilising mineral-melt fractionation factors of Sossi et al. (2012) the expected cumulate clinopyroxene and magnetite compositions for a given temperature and initial melt composition can be calculated. Given a magnetite-melt fractionation factor of $\delta^{57}Fe_{mtn\text{-}melt} = +0.20‰ \cdot 10^6/T^2$ (Sossi et al., 2012), an initial melt composition of $\delta^{57}Fe_{melt} = 0.02‰$ (isotopic composition of most primitive Sangeang Api lava) and a temperature of 1000˚C, the estimated equilibrium magnetite would have a composition of $\delta^{57}Fe_{mtn} = 0.143‰$. This composition is extremely close to the average analysed magnetite composition

($\delta^{57}Fe_{mtn}$ = 0.142‰ ± 0.072) of the Sangeang Api cumulates, and even at heavier melt compositions ($\delta^{57}Fe_{melt}$ = 0.15‰) the calculated equilibrium magnetite composition ($\delta^{57}Fe_{mtn}$ = 0.273‰) is within the maximum range of analysed magnetite compositions (see figure 4). The agreement between the calculated magnetite compositions and the measured magnetite compositions suggest that the analysed cumulate magnetite crystals and lavas are in equilibrium with one another. Using a pyroxene-melt fractionation factor of $\delta^{57}Fe_{px\text{-}melt} = -0.25‰ \cdot 10^6/T^2$ (Sossi et al., 2012) and the same melt composition ($\delta^{57}Fe_{melt}$ = 0.02‰) and temperature (1000˚C), the expected equilibrium pyroxene would have a composition of $\delta^{57}Fe_{px}$ = -0.134‰. This composition is much lighter than the average of the analysed cumulate clinopyroxenes ($\delta^{57}Fe_{px}$ = 0.109‰ ± 0.09) and lighter even than the lightest observed clinopyroxene ($\delta^{57}Fe_{px}$ = -0.034‰ ± 0.06). Only at higher melt compositions ($\delta^{57}Fe_{melt}$ = 0.15‰) does the equilibrium clinopyroxene ($\delta^{57}Fe_{px}$ = -0.04‰) replicate values similar to the lightest measured cumulate clinopyroxene ($\delta^{57}Fe_{px}$ = -0.034‰ ± 0.06). Thus, suggesting that the clinopyroxenes have undergone significant post-crystallisation iron isotope fractionation, resulting in the analysed cumulate clinopyroxene recording heavier than anticipated iron isotope values.

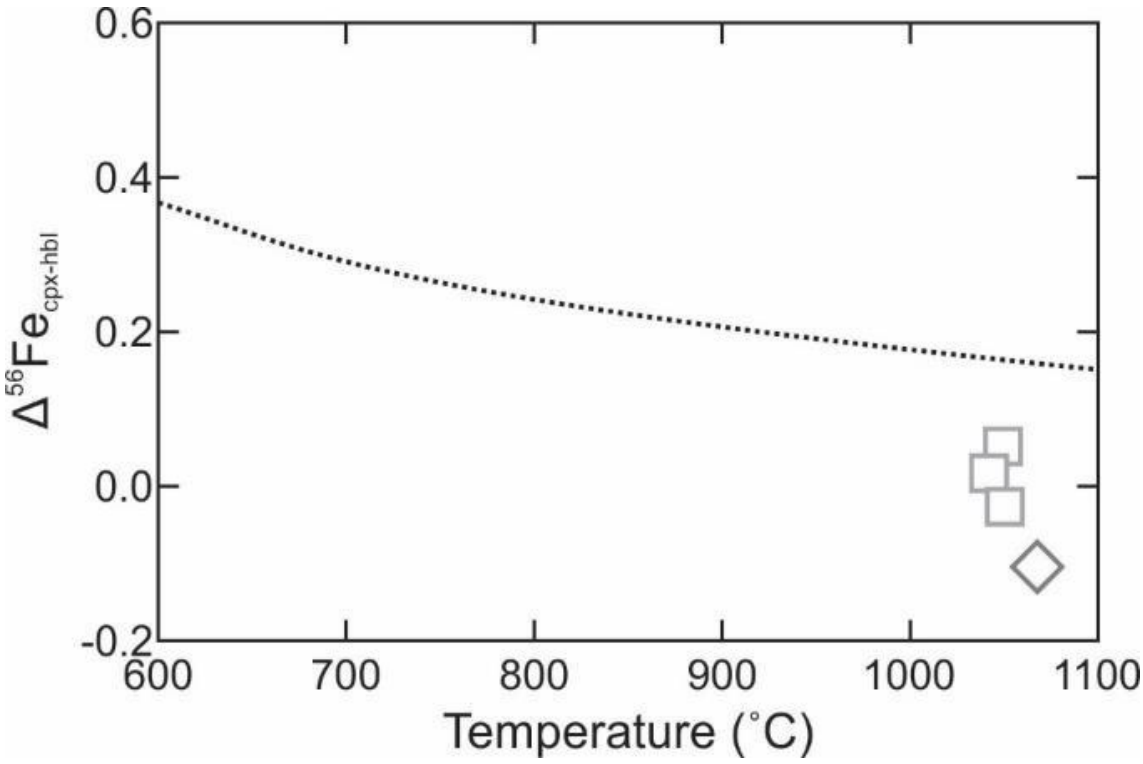

Figure 6: Temperature dependent fractionation factor and observed fractionation factor for clinopyroxene-amphibole pairs ($\Delta^{56}Fe_{(cpx\text{-}hbl)}$). Data points are observed cpx-hbl pairs from this study with temperatures estimated using the amphibole thermobarometer of Ridolfi and Renzulli (2012). Symbols as in figure 2b. Dotted line represents extrapolation of fractionation factor from Schoenberg et al. (2009) between clinopyroxene and amphibole with $Fe^{3+}/\Sigma Fe$ of 0.90 and 0.36 respectively.

Amphibole is a late crystallising phase in the cumulate xenoliths, only crystallising as a primary cumulate phase late in the melt evolution trend. Assuming a fractionation factor for amphibole the same as that of clinopyroxene (Foden et al., In Press), and crystallisation from differentiated, and therefore heavier, lavas ($\delta^{57}Fe_{melt}$ = 0.15) similarly

light equilibrium amphibole compositions ($\delta^{57}Fe_{hbl}$ = -0.04‰) would be anticipated. This is not observed in the isotopic values (average $\delta^{57}Fe_{hbl}$ = 0.125‰ ± 0.081). This suggests that the analysed amphiboles crystallised either from much more Fe^{3+} rich and therefore heavier melts or have experienced similar post-crystallisation fractionation. Schoenberg et al. (2009) investigated clinopyroxene-amphibole fractionation in a differentiating alkaline igneous rock sweet. Using Mössbauer spectroscopy they calculated the temperature dependent fractionation of $\Delta^{56}Fe_{cpx\text{-}hbl}$ for amphiboles with $Fe^{3+}/\Sigma Fe_{(amphibole)}$ = 0.36 and $Fe^{3+}/\Sigma Fe_{(clinopyroxene)}$ = 0.90. Extrapolating from their fractionation factor at 1000˚C a $\Delta^{56}Fe_{cpx\text{-}hbl}$ ~0.18‰ might be expected. Comparing measured fractionation factors from this study they span to lower temperatures than would be expected, suggesting that amphibole and clinopyroxene may not be in equilibrium (fig. 6). However, the measured $Fe^{3+}/\Sigma Fe_{(amphibole)}$ and $Fe^{3+}/\Sigma Fe_{(clinopyroxene)}$ from this study are significantly different (0.29-0.56 and 0.51-0.72 respectively) to those used in the Schoenberg et al. (2009) fractionation factors. At higher $Fe^{3+}/\Sigma Fe_{(amphibole)}$ and lower $Fe^{3+}/\Sigma Fe_{(clinopyroxene)}$ the clinopyroxene-amphibole fractionation factor is expected to be lower at a given temperature. This would suggest that the amphibole and clinopyroxene from this study are more likely to be in equilibrium with one another. Given that the clinopyroxene separates have experienced significant disequilibrium fractionation it is therefore likely that the amphibole separates have experienced similar disequilibrium fractionation.

Olivine separates record the lightest compositions of any mineral separate in this study, as low as $\delta^{57}Fe$ = -0.968‰. Shahar et al. (2008) calculated an equilibrium fractionation factor for magnetite and fayalite of $\Delta^{57}Fe_{mtn\text{-}fay} = +0.30\ (\pm 0.024) \cdot 10^6/T^2$. Utilising this equilibrium fractionation factor and a magnetite composition of $\delta^{57}Fe_{mtn}$ = 0.143‰ at 1000˚C produces an estimate of $\delta^{57}Fe_{fay}$ = -0.157‰. The average $\delta^{57}Fe_{olivine}$ of the observed olivine separates is -0.313‰ ± 0.284, lighter than the most primitive anticipated olivine composition. Similarly, light olivine compositions have been recorded by analysis of olivine fragments found in Hawaiian basalts (Sio et al., 2013; Teng et al., 2011). Equilibrium isotope fractionation has been posited as a cause of these light Fe isotope compositions, due to the preferential partitioning of isotopically light iron into Fe^{2+}-rich olivine (Teng et al., 2008). However, combined Mg and Fe isotope studies display co-variations with the Fe/Mg compositions of the olivine crystals (Teng et al., 2011). Equilibrium isotope fractionation is not able to create the observed Mg isotopic fractionation, and therefore cannot be the source of the isotopically light Fe compositions (Teng et al., 2011). Chemical diffusion has been proposed as a possible cause for Fe and Mg isotope fractionation in olivine. During diffusion olivine will gain Fe and lose Mg to the melt. During chemical diffusion light isotopes diffuse quicker than heavier isotopes (Dauphas et al., 2017), and thus will become isotopically lighter in the element they acquire from a melt (in this case Fe) and heavier in the element they lose (Mg) (Teng et al., 2011). It therefore seems likely that olivine separates from this study have experienced significant chemical diffusional fractionation. The extremely light $\delta^{57}Fe_{olivine}$ of some of the samples from this study (as light as -0.968‰) suggests significant post-crystallisation

diffusion has occurred in some of the cumulate piles, hinting at sustained percolation of melts through olivine-bearing cumulate piles.

Given the heavy $\delta^{57}Fe$ of amphibole and clinopyroxene separates and light $\delta^{57}Fe$ of olivine separates there is significant evidence from the Fe-isotope of cumulate mineralogy for pervasive post-crystallisation disequilibrium processes. The most likely cause of post-crystallisation Fe-isotope disequilibria is the percolation of fluids through the Sangeang Api cumulate piles. Many cumulate samples display petrological evidence of this, with many samples containing late crystallising hydrous phases (amphibole and biotite) interstitial to the primary cumulate mineralogy (e.g. clinopyroxene and olivine) and some samples containing intruded veinlets of quenched melts (see chapter 2). Overgrowths are observed on clearly cumulate mineralogy (primarily clinopyroxene) within several cumulate xenolith samples (see chapter 2), in the case of clinopyroxene these well-developed overgrowths typically have lower Mg# ($Mg^{2+}/[Mg^{2+}+Fe^{2+}]$). The distribution of cumulate xenolith trace element compositions also suggests that there is contamination between variably fractionated melts and cumulate piles. Turner et al. (2003) noted significant ^{226}Ra excesses in the Sangeang Api lavas and cumulate xenoliths, these were interpreted to represent rapid melt extraction from the mantle wedge and short differentiation times. However, these ^{226}Ra excesses could also be explained by melts being sourced from the incongruent breakdown of potassic phases (Turner et al., 2003). Interstitial glass present in some cumulate xenolith samples were analysed and have compositions that would be anticipated by the incongruent breakdown of pargasite. Suggesting that these ^{226}Ra excesses may reflect percolation and mixing of variably fractionated melts and melts arising from the breakdown of pargasite. Amphibole analyses from Sangeang Api commonly have high Ba contents (>800ppm), likely reflecting amphibole crystallisation from or interaction with melts rich in fluid-mobile elements. These disequilibrium processes are reflected in the unexpectedly heavy $\delta^{57}Fe$ compositions of the cumulate xenolith whole-rocks, which would be expected to be isotopically lighter than the lavas due to the fractional crystallisation of relatively Fe^{2+}-rich cumulate mineralogy (especially olivine and clinopyroxene) (Schuessler et al., 2009; Teng et al., 2008). It is therefore likely that the Sangeang Api magmatic system experienced Fe-isotopic disequilibrium fractionation processes, with only the lavas and magnetite separates recording magmatic compositions. It appears that the original magmatic compositions of cumulate mineralogy and cumulate whole-rocks has been overprinted by pervasive and long-lived melt percolation through cumulate piles in the crustal magma chamber system. The interstitial glasses were not analysed in this study and may provide avenues for future research into the cause of disequilibrium in the Sangeang Api system.

Modelled effects of fractional crystallisation

To model the expected $\delta^{57}Fe$ compositions of the cumulate assemblage and whole-rocks an estimate of the proportions of Fe oxide and Fe-Mg silicate minerals removed from the and increasing SiO_2, was divided into three stages and least squares mixing was utilised to calculate the proportions of Fe-oxide and Fe-Mg silicate minerals crystallising at each

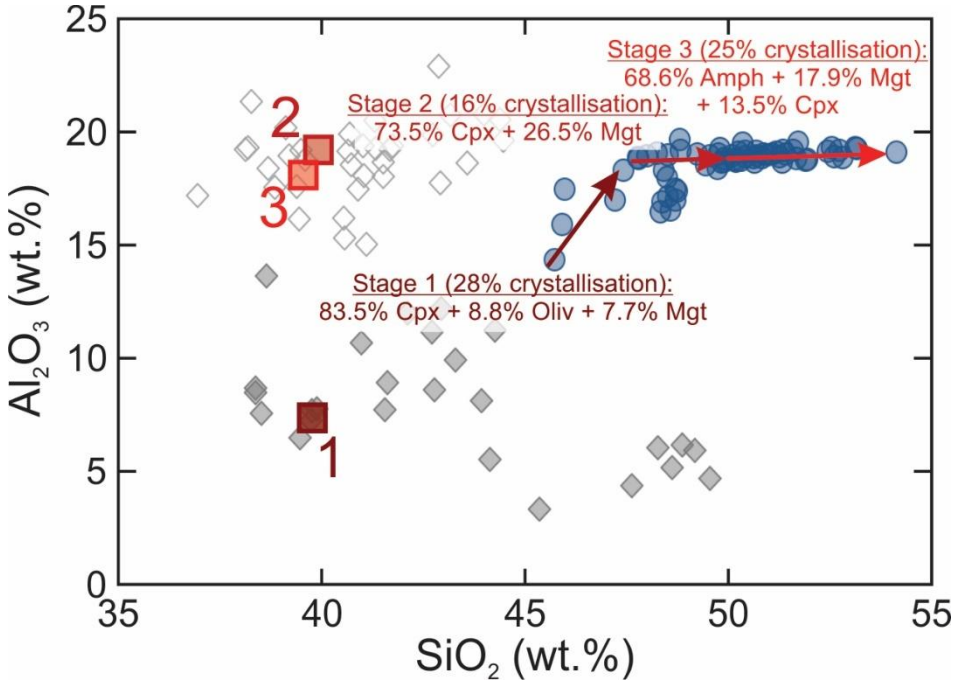

Figure 7: Diagram displaying outcome of least-squares mixing solutions. Stages 1 through 3 have been assigned a colour and represent different amounts of fractional crystallisation from an initial composition (start of arrow) to a final composition (arrowhead). Percentage of fractional crystallisation is given next to each stage and below are shown relative proportions of Fe-oxide and Fe-Mg silicates for which there are known Fe-isotope fractionation factors. Harker plot in the background shows lava, gabbro and pyroxenite samples for comparison (see diagram 2b for key to symbols).

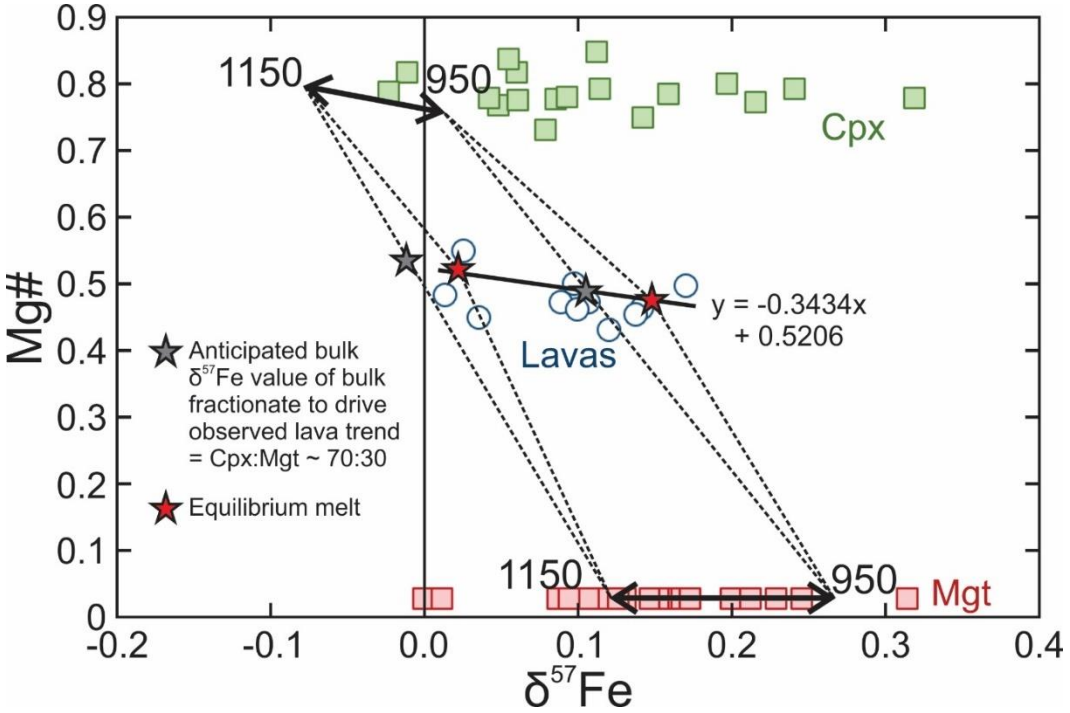

Figure 8: δ^{57}Fe vs. Mg# plot, displaying equilibrium mineral and cumulate compositions for a given initial melt composition for stage 2 of least squares mixing solution (figure 7). Initial melt δ^{57}Fe composition assumed to be 0.02‰. Arrows represent calculated equilibrium mineral (cpx – top, mgt – bottom) δ^{57}Fe values from 950˚C to 1150˚C. Dotted lines represent tie lines between lava and equilibrium bulk fractionate. Solid line represents lava trend (following the equation given) from least fractionated to most fractionated. Measured mineral separate and whole-rock compositions are given for comparison. Note the distinct difference between measured clinopyroxene compositions and calculated equilibrium clinopyroxene values.

stage (see figure 7 for more detail). Using an initial melt composition of 0.02, the calculated mineral proportions (Cpx:Mgt = 70:30) and known fractionation factors for magnetite-melt ($\delta^{57}Fe_{mtn\text{-}melt} = +0.20‰ \cdot 10^6/T^2$) and clinopyroxene-melt ($\delta^{57}Fe_{cpx\text{-}melt} = -0.25‰ \cdot 10^6/T^2$)(Sossi et al., 2012), the equilibrium cumulate composition for stage 2 can be calculated by simple mass balance. Figure 8 displays the outcome of this modelling. As previously mentioned, it is clear to see that the measured $\delta^{57}Fe$ values of clinopyroxene and amphibole are significantly heavier than are anticipated from all but evolving magma by fractional crystallisation must be calculated. To do this the lava trend seen in figure 2a, of initial rapid increase in Al_2O_3 followed by no change in melt $Al_2O_3$the most fractionated lavas. Similarly measured olivine separates spread to drastically lighter $\delta^{57}Fe$ compositions than would be expected from those in equilibrium with even the most primitive lavas. This is likewise reflected in expected equilibrium cumulate compositions,

Figure 9a-d: Outcomes of thermodynamic modelling of evolution of sample L14 by equilibrium crystallisation, with and initial fO_2 of ΔQFM+2, 1.5kbar, water content of 3.5wt.% and $\delta^{57}Fe$ of 0.15‰; calculated using Rhyolite-MELTs software (Ghiorso and Gualda, 2015; Gualda et al., 2012). 9a: SiO_2 vs. MgO harker diagram displaying modelled liquid line of descent. 9b: SiO_2 vs. $\delta^{57}Fe$ diagram displaying modelled liquid line of descent. 9c: Diagram displaying the percentage of melt remaining vs. temperature, with crystallised mineral sequences displayed. 9c: diagram displaying $\delta^{57}Fe$ fractionation with temperature, with crystallised mineral sequences displayed.

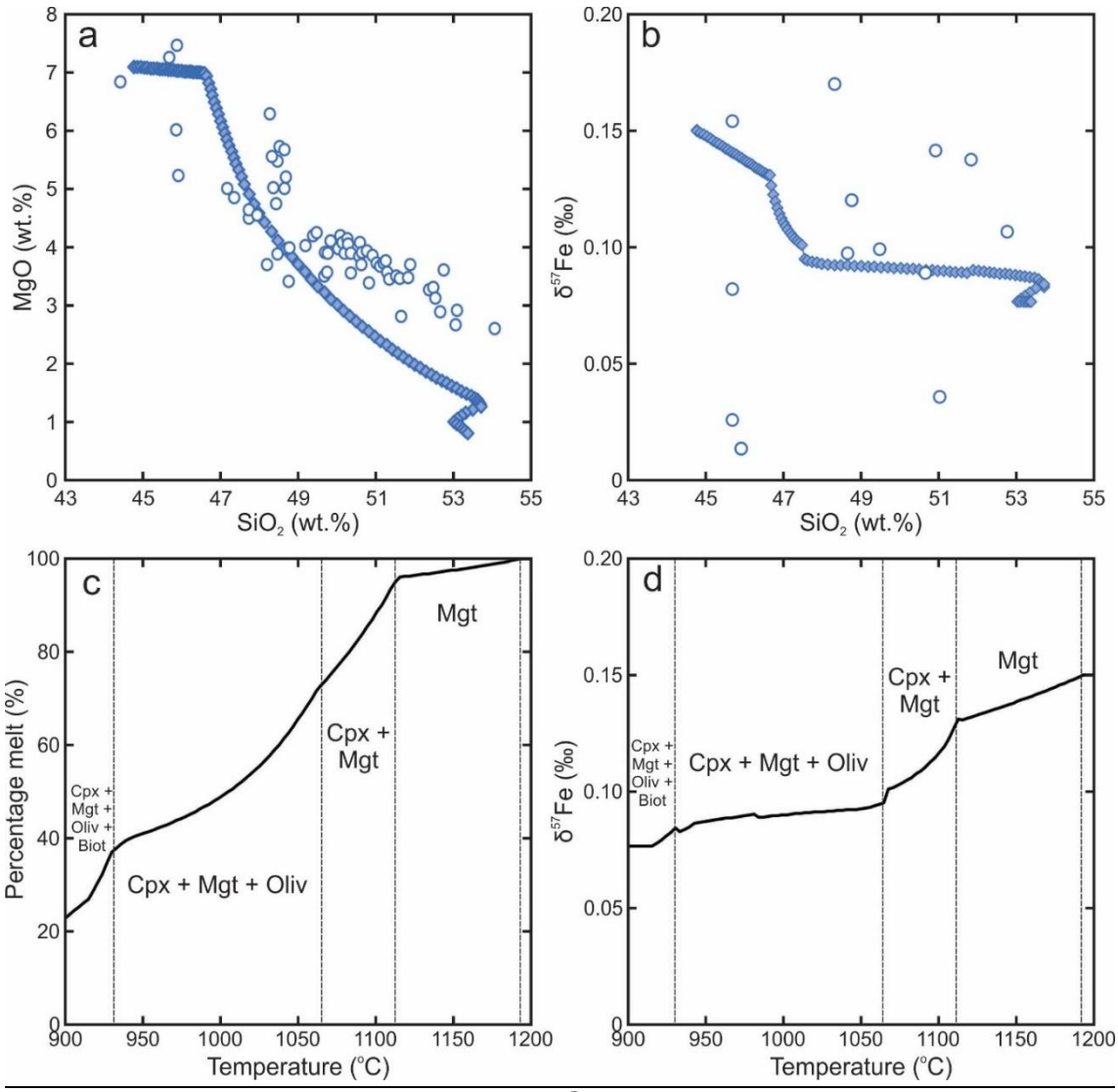

that are significantly lighter than is recorded in the measured cumulate samples, indeed we would anticipate the cumulates to be isotopically lighter than the lavas. However, both the gabbros and pyroxenites have heavier mean values (δ^{57}Fe = 0.166‰ and 0.109‰ respectively) than the lavas (δ^{57}Fe = 0.099‰). The mean δ^{57}Fe composition of both the pyroxenites and pyroxenes is the same (0.109‰), underscoring the importance of pyroxene in creating the recorded pyroxenite isotopic compositions. This further underlines the effects of iron isotopic disequilibrium in the Sangeang Api system and reflects the pervasive nature of melt percolation interacting with cumulate

piles. Following the methods of Foden et al. (In Press) lava compositions from this study were corrected for the fractional crystallisation of olivine, yielding primitive unfractionated compositions of δ^{57}Fe -0.058 to 0.103.

Rhyolite-MELTS Modelling

Thermodynamic modelling utilising Rhyolite-MELTS software (Ghiorso and Gualda, 2015; Gualda et al., 2012) has been used in previous chapters (Chapter 2) to establish P-T phase diagrams and model melt evolution under varying conditions; fO_2 buffered, fO_2 unbuffered, equilibrium crystallisation, fractional crystallisation, varying water contents, etc.. The most accurate of these models (determining an anticipated mineral-crystallisation sequence and melt evolution) used a primitive lava composition (sample L14), was fO_2 unbuffered and undertaken in equilibrium crystallisation mode. It is possible using the outcomes of Rhyolite-MELTS modelling and published fractionation factors (Polyakov et al., 2007; Polyakov and Mineev, 2000; Sossi et al., 2012) to model the Fe-isotopic fractionation of an evolving melt (Foden et al., 2015; Sossi et al., 2016; Wawryk and Foden, 2017).

It has previously been suggested that olivine-pyroxenite cumulates at Sangeang Api originated from relatively wet and less oxidised melts than magnetite-pyroxenites (see chapter 2). Based on previous Rhyolite-MELTS models, the expected Sangeang Api magma isotopic compositions were modelled in equilibrium mode using a primitive lava (L14), with water content ~3.5wt.%, at an fO_2 of ΔQFM+2 and at a pressure of 1.5kbar. Figure 9a-d displays the outcomes of this modelling. This modelling suggests the following crystallisation sequence (figure 9c):

$$Mgt \rightarrow Cpx+Mgt \rightarrow Cpx+Mgt+Oliv \rightarrow Cpx+Mgt+Oliv+Biot$$

This crystallisation sequence matches well the initial crystallising sequence estimated by least squares mixing models (figure 7), suggesting that this model is viable for the Sangeang Api system. It is worth noting that the liquid line of descent is most successful in modelling the evolution of the pyroxenite driven melt trend, and that the gabbro trend is likely crystallised by drier and more oxidised melts. Similarly, this model calculates iron isotope compositions within the measured error range of the Sangeang Api lavas. Thus, suggesting that the lavas record original isotopic values and have not been contaminated, but further supports the suggestion that cumulate minerals and whole-rocks have been contaminated by post-crystallisation processes. Rhyolite-MELTs modelling suggests that magmas crystallising magnetite and clinopyroxene are likely to be driven to

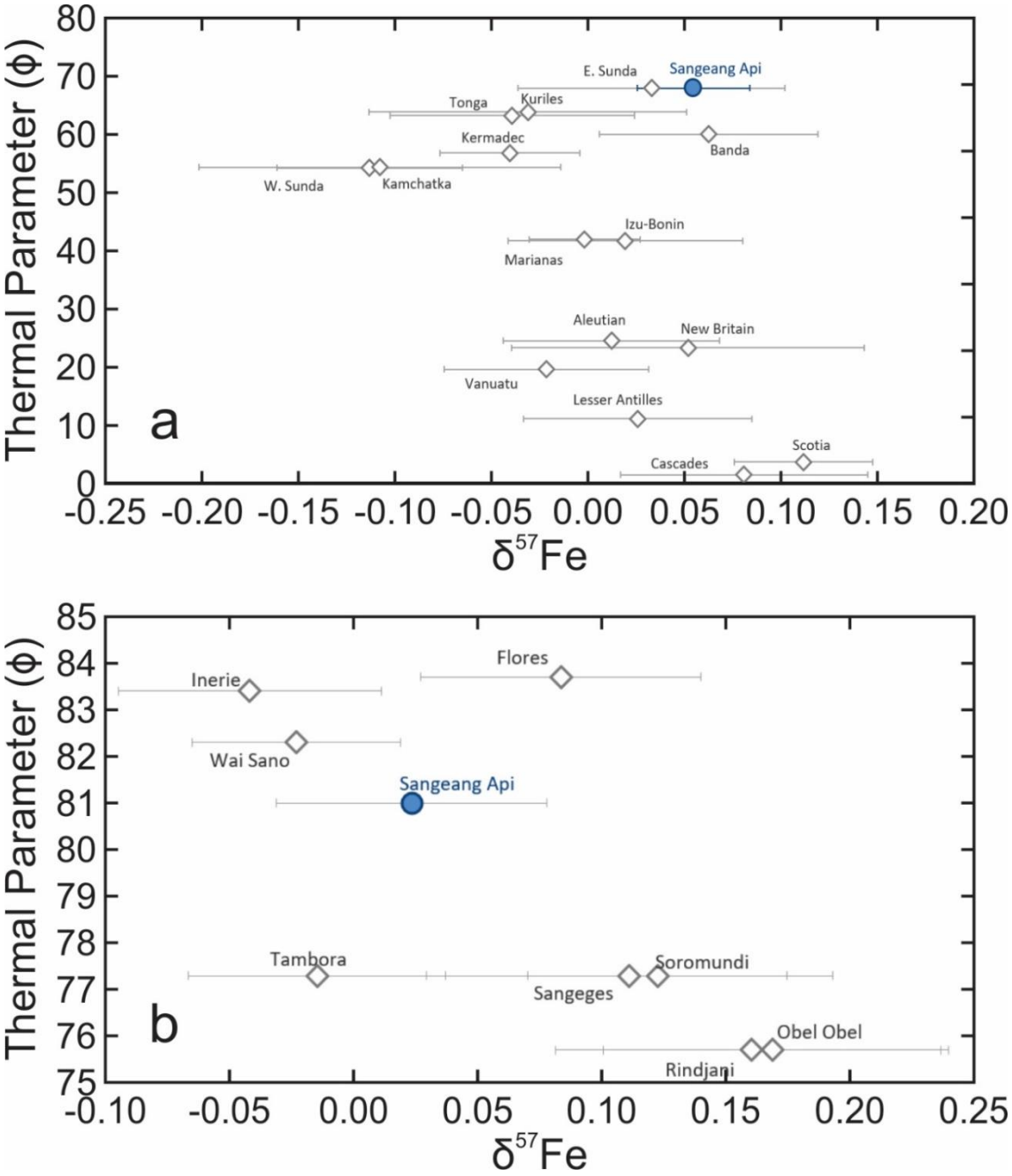

Figure 10a&b: δ^{57}Fe vs. Thermal Parameter (ϕ) diagram displaying average unfractionated Sangeang Api compositions compared to global arc averages (a) and East Sunda arc volcano averages (b). Iron isotopic compositions corrected for fractional crystallisation taken from Foden et al. (In Press). Thermal parameter (ϕ) (calculated as $[age\ of\ subducting\ slab \times slab\ descent\ rate]/100$) is taken from Syracuse and Abers (2006). Sangeang Api ϕ displayed for its section of arc (E. Sunda arc) in figure 10a and for individual volcano in figure 10b. Error bars represent 1 standard deviation from mean δ^{57}Fe value.

lighter compositions, producing isotopically heavy complementary cumulates, whilst the crystallisation of olivine will likely act to drive the melt to heavier compositions, and the complementary cumulates to light compositions. It may be supposed, therefore, that the heavier lavas might have fractionated olivine, whilst the lighter lavas will have fractionated significant amounts of magnetite and clinopyroxene. This modelling suggests that magnetite and olivine should simultaneously crystallise. However, there is

no textural evidence for olivine and magnetite occurring together, this is an issue that has previously been raised in chapter 2 and requires further investigation.

Comparison to other arc volanoes

Modelling suggests that the source regions of arc magmas should be more oxidised than the mantle source of MORB due to the flux of oxidising material into the mantle wedge (Evans et al., 2012; Evans and Tomkins, 2011). Theoretically, partial melts of more oxidised sources should be isotopically heavier than those produced by less oxidised sources (Dauphas et al., 2009). Given this, primitive mantle-wedge sourced arc magmas should be isotopically heavier than MORB magmas. However, studies of primitive arc lavas (Foden et al., In Press; Nebel et al., 2015) have revealed that on average they are lighter than MORB lavas (Teng et al., 2013) (see figure 4 for comparison). When corrected for fractional crystallisation, lavas from this study are no exception, recording mean unfractionated lava δ^{57}Fe compositions (δ^{57}Fe = 0.023‰ ± 0.051) lighter than mean MORB (δ^{57}Fe = 0.150‰ ± 0.029) (Teng et al., 2013). Both Foden et al. (In Press) and Nebel et al. (2015) suggest that repeated melt extraction of the mantle wedge by fractional melting drives residues to become increasingly light, therefore driving their fractional melts to become lighter over time. Foden et al. (In Press) noted a broadly negative correlation between the thermal parameter (ϕ) of an arc (calculated as *[age of subducting slab×slab descent rate]/100*; after Syracuse & Abers, 2006) and the average δ^{57}Fe

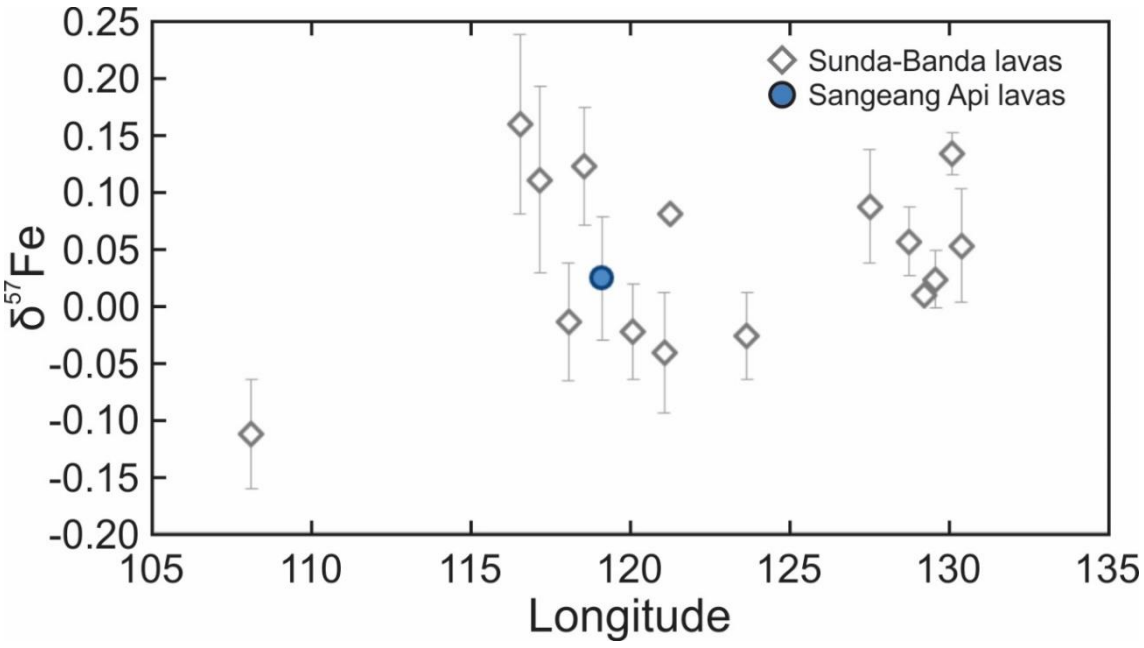

Figure 11: Longitude vs. δ^{57}Fe diagram displaying lava compositions of the Sunda-Banda arc from west to east. Key for symbols in the top right. Iron isotopic compositions corrected for fractional crystallisation taken from Foden et al. (In Press) and Nebel et al. (2015). Error bars represent standard deviation from mean unfractionated δ^{57}Fe value.

composition of unfractionated lavas erupted from that arc section. Proposing that sub-arc mantle regions stall and experience repetitive melt depletion events, conditions which are favoured by slabs with high ϕ values Foden et al. (In Press). A notable exception to this are the eastern Sunda and Banda arcs, which have high ϕ and relatively heavy δ^{57}Fe

compositions (figure 10a). Sangeang Api is typical of the eastern Sunda Arc lavas, being intermediate to other eastern Sunda Arc lavas (see figure 10b).

Several authors have noted distinct trends in radiogenic isotopes ($^{3}He/^{4}He$, $^{87}Sr/^{86}Sr$, $^{143}Nd/^{144}Nd$ and Pb isotopes) from west to east (Elburg et al., 2004; Hilton and Craig, 1989; Hilton et al., 1992; Stolz et al., 1990; Turner and Foden, 2001; Varne and Foden, 1986; Wheller et al., 1987). To determine whether similar trends can be observed in Fe stable isotopes figure 11 displays average unfractionated $\delta^{57}Fe$ compositions of volcanic centres from the Indonesian archipelago from west to east. As anticipated Galunggung on Java (western Sunda Arc - ~108˚E) displays the lightest $\delta^{57}Fe$ values. Between the western Sunda Arc and the Lombok-Flores section (eastern Sunda Arc - 115-124˚E) of the arc there is a jump to heavier $\delta^{57}Fe$ values which is followed by a trend in decreasing $\delta^{57}Fe$ from west to east, with Sangeang Api intermediate to this. The Banda arc samples (127-131˚E) display a shift to heavier isotopes from the Flores section, but do not display any distinctive trend within the group. The cause of this shift from high $\delta^{57}Fe$ compositions at the western end of the Lombok-Flores section and to the low $\delta^{57}Fe$ at the eastern end of the section is unclear. One explanation for the high $\delta^{57}Fe$ at the western end is that repeated melt depletions of the mantle wedge are unable to occur as the sub-arc peridotite is being 'refreshed' by new mantle material, indeed there is evidence for the presence of gaps in the subducting slab underlying the Lombok-Sumbawa region (Hall and Spakman, 2015; Kundu and Gahalaut, 2011). There is evidence from Pb-isotopes that these slab gaps may be introducing OIB-source type peridotite into the source regions of the Lombok-Sumbawa volcanoes. The introduction of fresh mantle material would revert the effects of progressive melt extraction, driving the mantle source to heavier $\delta^{57}Fe$ composition. Isotopically heavier mantle wedge compositions would be reflected in the $\delta^{57}Fe$ compositions of the melts extracted from this region. Alternatively, Sossi et al. (2016) noted that lavas of the New Britain Arc show a shift from light to heavy isotopes with distance from arc and increased alkalinity. Attributing this to smaller degrees of partial melting in the rear-arc. It seems unlikely that a similar process is causing this observed shift in the eastern Sunda Arc, as Tambora and Sangeang Api are further away from the trench and are the most alkalic of the studied volcanoes but are isotopically intermediate in composition. Furthermore, Tambora is suggested to be sourced by smaller degrees of partial melting than Sangeang Api (see chapter 2 and chapter 6) and yet records lighter isotopic compositions.

CONCLUSIONS

The basaltic to basaltic-trachandesitic lavas of Sangeang Api record mean $\delta^{57}Fe$ compositions of 0.099‰ ± 0.051. These values are typical $\delta^{57}Fe$ compositions for lavas of the eastern Sunda Arc, being intermediate to the products of other volcanic centres in the Lombok-Flores section of the Sunda Arc. As noted by Foden et al. (In Press), $\delta^{57}Fe$ of the eastern Sunda Arc are heavier than would be expected given the estimated thermal parameter (ϕ = 67.7). Furthermore, $\delta^{57}Fe$ values of volcanic centres tend to get heavier from Flores towards Lombok, possibly reflecting the influence of slab gaps allowing for

the introduction of 'fresh' mantle material to the mantle wedge source. Thus, driving the mantle wedge to heavier Fe-isotope conditions.

Cumulate xenoliths (gabbros and pyroxenites) and most mineral separates derived from these samples deviate drastically from what would be expected by well-constrained fractionation factors, recording pervasive disequilibrium processes. Utilising $\Delta^{57}Fe_{Mgt\text{-}Melt}$ fractionation factors and primitive melt $\delta^{57}Fe$ compositions, it can be shown that measured magnetite compositions reflect the expected magmatic compositions. However, Fe-Mg silicate (clinopyroxene, amphibole and olivine) minerals record values much different from what the expected magmatic compositions should be. Amphibole and clinopyroxene compositions show a dramatic shift to heavier than expected $\delta^{57}Fe$ compositions, whilst olivine compositions are much lighter than anticipated. These shifts are reflected in the cumulate whole-rock compositions, which are much heavier than expected mass-balanced cumulates. Many of the cumulate xenoliths display strong evidence of interactions with percolative fluids. This is displayed petrologically by intra-cumulate glass, hydrous mineralogy and mineral overgrowths. The effects of cumulate-melt interactions can be similarly observed in whole-rock trace-element compositions and ^{226}Ra excesses throughout the whole-rock suite. It is likely that cumulate piles interacted with variably fractionated and isotopically heavy melts, altering the Fe-isotopic signature of cumulate mineralogy and overprinting original magmatic Fe-isotope compositions.

Rhyolite-MELTs modelling suggests that the lava compositions measured are those of the original magmatic trend and have not experienced disequilibrium contamination like the cumulate xenoliths and mineral separates. It also supports the least-squares mixing solutions and suggests that the fractionating cumulate mineralogy exerted a primary control over lava evolution.

Whilst it appears that primitive arc lavas, such as Sangeang Api, record the iron isotopic compositions of their source mantle, their cumulate products may not reflect the equilibrium magmatic compositions that would be expected. Arc magmatic tracts are, by their very nature, open systems and therefore disequilibrium iron isotope processes are likely to be commonplace amongst magma chamber lithologies in arc settings.

REFERENCES

Beard, B.L., Johnson, C.M., 2004. Fe isotope variations in the modern and ancient earth and other planetary bodies, in: Johnson, C.M., Beard, B.L., Albarede, F. (Eds.), Geochemistry of Non-Traditional Stable Isotopes, pp. 319-357.

Burgisser, A., Scaillet, B., 2007. Redox evolution of a degassing magma rising to the surface. Nature 445, 194-197.

Carmichael, I.S.E., 1991. The redox states of basic and silicic magmas - a reflection of their source regions. Contributions to Mineralogy and Petrology 106, 129-141.

Christie, D.M., Carmichael, I.S.E., Langmuir, C.H., 1986. Oxidation-states of midocean ridge basalt glasses. Earth and Planetary Science Letters 79, 397-411.

Craddock, P.R., Dauphas, N., 2011. Iron Isotopic Compositions of Geological Reference Materials and Chondrites. Geostandards and Geoanalytical Research 35, 101-123.

Dauphas, N., Craddock, P.R., Asimow, P.D., Bennett, V.C., Nutman, A.P., Ohnenstetter, D., 2009. Iron isotopes may reveal the redox conditions of mantle melting from Archean to Present. Earth and Planetary Science Letters 288, 255-267.

Dauphas, N., John, S.G., Rouxel, O., 2017. Iron Isotope Systematics. Reviews in Mineralogy and Geochemistry 82, 415-510.

Dauphas, N., Rouxel, O., 2006. Mass spectrometry and natural variations of iron isotopes. Mass Spectrom Rev 25, 515-550.

Debret, B., Millet, M.A., Pons, M.L., Bouilhol, P., Inglis, E., Williams, H., 2016. Isotopic evidence for iron mobility during subduction. Geology 44, 215-218.

Elburg, M.A., van Bergen, M.J., Foden, J.D., 2004. Subducted upper and lower continental crust contributes to magmatism in the collision sector of the Sunda-Banda arc, Indonesia. Geology 32, 41.

Evans, K.A., Elburg, M.A., Kamenetsky, V.S., 2012. Oxidation state of subarc mantle. Geology 40, 783-786.

Evans, K.A., Tomkins, A.G., 2011. The relationship between subduction zone redox budget and arc magma fertility. Earth and Planetary Science Letters 308, 401-409.

Foden, J., Sossi, P.A., Nebel, O., In Press. Controls on the Iron Isotopic Composition of Global Arc Magmas. Earth and Planetary Science Letters.

Foden, J., Sossi, P.A., Wawryk, C.M., 2015. Fe isotopes and the contrasting petrogenesis of A-, I- and S-type granite. Lithos 212–215, 32-44.

Foden, J., Varne, R., 1980. The petrology and tectonic setting of quaternary - recent volcanic centers of lombok and sumbawa, sunda arc. Chemical Geology 30, 201-226.

Ghiorso, M.S., Gualda, G.A.R., 2015. An H2O–CO2 mixed fluid saturation model compatible with rhyolite-MELTS. Contributions to Mineralogy and Petrology 169, 53.

Grove, T.L., Chatterjee, N., Parman, S.W., Medard, E., 2006. The influence of H2O on mantle wedge melting. Earth and Planetary Science Letters 249, 74-89.

Grove, T.L., Till, C.B., Krawczynski, M.J., 2012. The role of H 2O in subduction zone magmatism, Annual Review of Earth and Planetary Sciences, pp. 413-439.

Gualda, G.A.R., Ghiorso, M.S., Lemons, R.V., Carley, T.L., 2012. Rhyolite-MELTS: a Modified Calibration of MELTS Optimized for Silica-rich, Fluid-bearing Magmatic Systems. Journal of Petrology 53, 875-890.

Hall, R., Spakman, W., 2015. Mantle structure and tectonic history of SE Asia. Tectonophysics 658, 14-45.

Hilton, D.R., Craig, H., 1989. A helium isotope transect along the Indonesian archipelago. Nature 342, 906-908.

Hilton, D.R., Hoogewerff, J.A., van Bergen, M.J., Hammerschmidt, K., 1992. Mapping magma sources in the east Sunda-Banda arcs, Indonesia: Constraints from helium isotopes. Geochimica et Cosmochimica Acta 56, 851-859.

Kelley, K.A., Cottrell, E., 2012. The influence of magmatic differentiation on the oxidation state of Fe in a basaltic arc magma. Earth and Planetary Science Letters 329–330, 109-121.

Kerrick, D.M., Connolly, J.A.D., 2001a. Metamorphic devolatilization of subducted marine sediments and the transport of volatiles into the Earth's mantle. Nature 411, 293-296.

Kerrick, D.M., Connolly, J.A.D., 2001b. Metamorphic devolatilization of subducted oceanic metabasalts: implications for seismicity, arc magmatism and volatile recycling. Earth and Planetary Science Letters 189, 19-29.

Kundu, B., Gahalaut, V.K., 2011. Slab detachment of subducted Indo-Australian plate beneath Sunda arc, Indonesia. Journal of Earth System Science 120, 193-204.

Lee, C.T.A., Leeman, W.P., Canil, D., Li, Z.X.A., 2005. Similar V/Sc systematics in MORB and arc basalts: Implications for the oxygen fugacities of their mantle source regions. Journal of Petrology 46, 2313-2336.

Lee, C.T.A., Luffi, P., Le Roux, V., Dasgupta, R., Albarede, F., Leeman, W.P., 2010. The redox state of arc mantle using Zn/Fe systematics. Nature 468, 681-685.

Mallmann, G., O'Neill, H.S.C., 2009. The Crystal/Melt Partitioning of V during Mantle Melting as a Function of Oxygen Fugacity Compared with some other Elements (Al, P, Ca, Sc, Ti, Cr, Fe, Ga, Y, Zr and Nb). Journal of Petrology 50, 1765-1794.

Moussallam, Y., Oppenheimer, C., Scaillet, B., Gaillard, F., Kyle, P., Peters, N., Hartley, M., Berlo, K., Donovan, A., 2014. Tracking the changing oxidation state of Erebus magmas, from mantle to surface, driven by magma ascent and degassing. Earth and Planetary Science Letters 393, 200-209.

Nebel, O., Sossi, P.A., Bénard, A., Wille, M., Vroon, P.Z., Arculus, R.J., 2015. Redox-variability and controls in subduction zones from an iron-isotope perspective. Earth and Planetary Science Letters 432, 142-151.

Parkinson, I.J., Arculus, R.J., 1999. The redox state of subduction zones: insights from arc-peridotites. Chemical Geology 160, 409-423.

Poitrasson, F., Freydier, R., 2005. Heavy iron isotope composition of granites determined by high resolution MC-ICP-MS. Chemical Geology 222, 132-147.

Polyakov, V.B., Clayton, R.N., Horita, J., Mineev, S.D., 2007. Equilibrium iron isotope fractionation factors of minerals: Reevaluation from the data of nuclear inelastic resonant X-ray scattering and Mössbauer spectroscopy. Geochimica et Cosmochimica Acta 71, 3833-3846.

Polyakov, V.B., Mineev, S.D., 2000. The use of Mössbauer spectroscopy in stable isotope geochemistry. Geochimica et Cosmochimica Acta 64, 849-865.

Ridolfi, F., Renzulli, A., 2012. Calcic amphiboles in calc-alkaline and alkaline magmas: thermobarometric and chemometric empirical equations valid up to 1,130A degrees C and 2.2 GPa. Contributions to Mineralogy and Petrology 163, 877-895.

Roskosz, M., Sio, C.K.I., Dauphas, N., Bi, W., Tissot, F.L.H., Hu, M.Y., Zhao, J., Alp, E.E., 2015. Spinel–olivine–pyroxene equilibrium iron isotopic fractionation and applications to natural peridotites. Geochimica et Cosmochimica Acta 169, 184-199.

Schmidt, M.W., Poli, S., 1998. Experimentally based water budgets for dehydrating slabs and consequences for arc magma generation. Earth and Planetary Science Letters 163, 361-379.

Schoenberg, R., Marks, M.A.W., Schuessler, J.A., von Blanckenburg, F., Markl, G., 2009. Fe isotope systematics of coexisting amphibole and pyroxene in the alkaline igneous rock suite of the Ilímaussaq Complex, South Greenland. Chemical Geology 258, 65-77.

Schuessler, J.A., Schoenberg, R., Sigmarsson, O., 2009. Iron and lithium isotope systematics of the Hekla volcano, Iceland — Evidence for Fe isotope fractionation during magma differentiation. Chemical Geology 258, 78-91.

Shahar, A., Young, E.D., Manning, C.E., 2008. Equilibrium high-temperature Fe isotope fractionation between fayalite and magnetite: An experimental calibration. Earth and Planetary Science Letters 268, 330-338.

Siebert, L., Simkin, T., Kimberly, P., 2011. Volcanoes of the World : Third Edition (3). University of California Press, Berkeley, US.

Sio, C.K.I., Dauphas, N., Teng, F.-Z., Chaussidon, M., Helz, R.T., Roskosz, M., 2013. Discerning crystal growth from diffusion profiles in zoned olivine by in situ Mg–Fe isotopic analyses. Geochimica et Cosmochimica Acta 123, 302-321.

Sossi, P.A., Foden, J.D., Halverson, G.P., 2012. Redox-controlled iron isotope fractionation during magmatic differentiation: an example from the Red Hill intrusion, S. Tasmania. Contributions to Mineralogy and Petrology 164, 757-772.

Sossi, P.A., Nebel, O., Foden, J., 2016. Iron isotope systematics in planetary reservoirs. Earth and Planetary Science Letters 452, 295-308.

Stolz, A.J., Varne, R., Davies, G.R., Wheller, G.E., Foden, J.D., 1990. Magma source components in an arc-continent collision zone - the flores-lembata sector, sunda arc, indonesia. Contributions to Mineralogy and Petrology 105, 585-601.

Syracuse, E.M., Abers, G.A., 2006. Global compilation of variations in slab depth beneath arc volcanoes and implications. Geochemistry Geophysics Geosystems 7, 18.

Teng, F.-Z., Dauphas, N., Helz, R., Gao, S., Huang, S., 2011. Diffusion-driven magnesium and iron isotope fractionation in Hawaiian olivine. Earth and Planetary Science Letters 308, 317-324.

Teng, F.-Z., Dauphas, N., Helz, R.T., 2008. Iron Isotope Fractionation During Magmatic Differentiation in Kilauea Iki Lava Lake. Science 320, 1620-1622.

Teng, F.-Z., Dauphas, N., Huang, S., Marty, B., 2013. Iron isotopic systematics of oceanic basalts. Geochimica et Cosmochimica Acta 107, 12-26.

Turner, S., Foden, J., 2001. U, Th and Ra disequilibria, Sr, Nd and Pb isotope and trace element variations in Sunda arc lavas: predominance of a subducted sediment component. Contributions to Mineralogy and Petrology 142, 43-57.

Turner, S., Foden, J., George, R., Evans, P., Varne, R., Elburg, M., Jenner, G., 2003. Rates and processes of potassic magma evolution beneath Sangeang Api volcano, East Sunda arc, Indonesia. Journal of Petrology 44, 491-515.

Varne, R., Foden, J.D., 1986. Geochemical and isotopic systematics of eastern Sunda Arc volcanics: Implications for mantle sources and mantle mixing processes, in: Wezel, F.-C. (Ed.), The Origin of Arcs. Elsevier, Amsterdam, pp. 159-189.

Wawryk, C.M., Foden, J.D., 2017. Iron-isotope systematics from the Batu Hijau Cu-Au deposit, Sumbawa, Indonesia. Chemical Geology.

Wheller, G.E., Varne, R., Foden, J.D., Abbott, M.J., 1987. Geochemistry of quaternary volcanism in the Sunda-Banda arc, Indonesia, and three-component genesis of island-arc basaltic magmas. Journal of Volcanology and Geothermal Research 32, 137-160.

Young, E.D., Galy, A., Nagahara, H., 2002. Kinetic and equilibrium mass-dependent isotope fractionation laws in nature and their geochemical and cosmochemical significance. Geochimica et Cosmochimica Acta 66, 1095-1104.

Chapter 5

Petrological overview of the Quaternary-Tertiary volcanic centres of E. Sumbawa and W. Flores

Statement of Authorship

Title of Paper	Petrological overview of the Quaternary-Tertiary volcanic centres of E. Sumbawa and W. Flores
Publication Status	☐ Published ☐ Accepted for Publication ☐ Submitted for Publication ☑ Unpublished and Unsubmitted work written in manuscript style
Publication Details	For submission to Journal of Petrology as: Cooke, B., Foden, J. Petrological overview of the Quaternary-Tertiary volcanic centres of E. Sumbawa and W. Flores

Principal Author

Name of Principal Author (Candidate)	Benjamin Cooke		
Contribution to the Paper	Collection of E. Sumbawa and NW Flores samples in fieldwork, sample preparation, data collection, data processing, data interpretation, manuscript preparation and content, creation of diagrams		
Overall percentage (%)	80		
Certification:	This paper reports on original research I conducted during the period of my Higher Degree by Research candidature and is not subject to any obligations or contractual agreements with a third party that would constrain its inclusion in this thesis. I am the primary author of this paper.		
Signature		Date	13/11/2017

Co-Author Contributions

By signing the Statement of Authorship, each author certifies that:

i. the candidate's stated contribution to the publication is accurate (as detailed above);

ii. permission is granted for the candidate in include the publication in the thesis; and

iii. the sum of all co-author contributions is equal to 100% less the candidate's stated contribution.

Name of Co-Author	Professor John Foden		
Contribution to the Paper	Collection of Wai Sano samples, assistance in fieldwork, data interpretation, review		
Signature		Date	13/11/2017

ABSTRACT

The eastern Sunda Arc of Indonesia is home to a range of active and extinct volcanic centres. This study focusses on the previously unstudied volcanic centres of Kota and Kuta on northeast Sumbawa, Wai Sano on southwest Flores and the andesite-dacite basement of northwest Flores. The samples collected from each locality vary greatly in petrology and geochemistry, such that each locality needs to be discussed separately. The quaternary (<2Ma) Kota and Kuta erupted high-K basalts to trachyandesites with entrained amphibole-gabbro xenoliths entrained in and associated with them. The lavas are predominantly porphyritic and host phenocryst populations of *plagioclase* + *augite* + *magnetite* ± *amphibole* in microlite-rich groundmass of similar mineralogical composition (plus minor olivine and orthopyroxene). Intruding these lavas are amphibole-rich gabbros with textures suggesting a cumulate origin. Both rhyolite-MELTS modelling, amphibole thermobarometry and clinopyroxene thermobarometry suggest the lavas and gabbros arose from a magma suite in a series of distinct magma chambers at mid-lower crustal levels (200-700MPa), with relatively low water contents (<3wt.% H_2O_{Melt}). Isotopic compositions of the lavas ($^{87}Sr/^{86}Sr$ 0.7047-0.7053; $^{143}Nd/^{144}Nd$ ~0.5128) suggest crystallisation from an I-MORB source mixed with 1-2wt.% terrigenous/biogenic sediment. REE profiles and trace element ratios suggest that this source region contained <1.7% residual garnet and likely contained residual amphibole. Wai Sano is a large, eroded quaternary to recent (~10ka) caldera in southwest Flores built on an andesitic basement. It erupted porphyritic dacites with *plagioclase* + *augite* + *hypersthene* + *amphibole* + *magnetite* in a glassy/cryptocrystalline groundmass. Thermobarometry suggests that these magmas are water rich (4.5-7.8wt.% H_2O_{Melt}), highly oxidised (ΔNNO+1.36-2.44) and crystallised at two distinct crustal levels; a shallow magma chamber (90-190MPa, 795-870°C) and a mid-crustal magma tract (300-650MPa, 950-1000°C). Wai Sano is distinct in the Sunda and Banda arcs by the adakitic characteristics of its erupted lavas; low MgO (1.1-2.5wt.%), high SiO_2 (63-67.4wt.%), high Al_2O_3 (16.9-18.3wt.%), low Y (7-12ppm) and high Sr/Y (30-50). However, the isotopic compositions of the lavas ($^{87}Sr/^{86}Sr$ 0.7062-0.7064; $^{143}Nd/^{144}Nd$ 0.5125-0.5127) are at odds with what would be anticipated if they were formed from a slab melt, as might be anticipated by the major and trace element geochemistry. Similarly, the estimated age of the subducting slab is much too old (~145Ma) to melt. It is therefore suggested that the Wai Sano magmas formed by 10-13% partial melting of basaltic underplating around ~1GPa, leaving behind a garnet-phlogopite-gabbro restite with <30% modal garnet. The calc-alkaline andesitic and dacitic basement lavas of northwest Flores are similar in their major element geochemistry to the Wai Sano dacites, however, they diverge in their trace elements. These lavas are porphyritic with phenocryst assemblages of *plagioclase* + *clinopyroxene* + *magnetite* ± *amphibole* hosted in a glassy groundmass with microcrystalline *plagioclase* + *magnetite*. Amphibole thermobarometry suggests crystallisation at similar pressures, temperatures, water contents and oxidation states to the shallow magma chamber of Wai Sano. Of the analysed samples the NW Flores samples have the most I-MORB like isotope ratios ($^{87}Sr/^{86}Sr$ ~0.7047; $^{143}Nd/^{144}Nd$ ~0.51293) and possibly suggest a three-component source mix of I-MORB mantle,

altered ocean fluid and sediment. Despite relatively low Y contents (15-20ppm) the trace element geochemistry of the NW Flores samples suggests that these magmas are not adakite related (low Sr/Y 12-15), but rather sourced from high degree partial melts of a source region with little residual garnet and pargasite.

INTRODUCTION

The Sunda Arc of Indonesia spans from the Andaman Islands in the west to the Banda Sea in the east. This study focusses on a section of the eastern Sunda Arc spanning Sumbawa across the Flores Strait and into westernmost Flores. Sangeang Api and Tambora are the only volcanoes in the study area to have erupted in recorded history (Siebert, Simkin & Kimberly 2011); Sangeang Api most recently in 2014. Tambora is well known for the VEI-7 eruption in 1815, which produced 107-113km^3 of tephra and cooled global temperatures by ~1-1.5˚C (Foden, John 1986; Gertisser et al. 2012; Self et al. 2004; Stothers 1984). Lavas erupted by Sangeang Api and Tambora share common characteristics; they are highly potassic, producing shoshonitic, ne-normative trachybasalts to trachyandesites and are at similar heights above the Benioff zone (~190km) (Foden, John 1986; Foden, J. & Varne 1980; Gertisser et al. 2012; Turner et al. 2003). The island of Sumbawa contains a number of extinct quaternary volcanic centres, including Gunung Sangenges, Soromundi, Doro Kota and Doro Kuta, that are broadly found to the south of both Tambora and Sangeang Api. G. Sangenges and Soromundi erupted highly-undersaturated, ne- and lc-normative leucitites, andesites, dacites and trachybasalts (Foden, J. & Varne 1980). Lavas of G. Sangenges and Soromundi, like those of Tambora and Sangeang Api, are highly-potassic (High-K calc-alkaline to shoshonitic) (Foden, J. & Varne 1980). D. Kota and Kuta are currently unstudied, but they are thought to be approximately ~2Ma in age and high-K calc-alkaline in composition (Garwin 2000). In the southwest corner of Sumbawa, early Miocene basement exposures record calc-alkaline trachybasalt, andesite and dacite compositions (Foden, J. & Varne 1980; Garwin 2000). For an overview of the regional geology spanning Sumbawa and western Flores see figure 1.

To the east of Sumbawa is the island of Flores, with basement composed predominantly of andesite-dacite and Miocene-Recent sediment cover. Located in the southwest corner of Flores is the largely eroded Quaternary (~10ka) caldera of Wai Sano (Siebert, Simkin & Kimberly 2011). Unlike Sumbawa where active volcanism is restricted to the northern coasts of the island, active volcanism on Flores is found predominantly on the southern coast of the island (except for Paluweh). Historically active volcanoes of Flores include (from west to east) Ranakah, Inierie, Inielika, Ebulobo, Iya, Kelimutu, Paluweh, Egon, Lewotobi and Lewotolo (Siebert, Simkin & Kimberly 2011).

Both Sumbawa and Flores are situated on oceanic crust, however the nature of the subducting slab changes from west to east. With oceanic crust being subducted beneath Sumbawa and western Flores, with the subducting crust becoming more continental in character to the east as the Australian crust begins to impact with the Indonesian arc (Bowin et al. 1980; Porritt et al. 2016). This is reflected in the isotopic compositions of the erupted products towards the incipient arc-continent collision region, with evidence

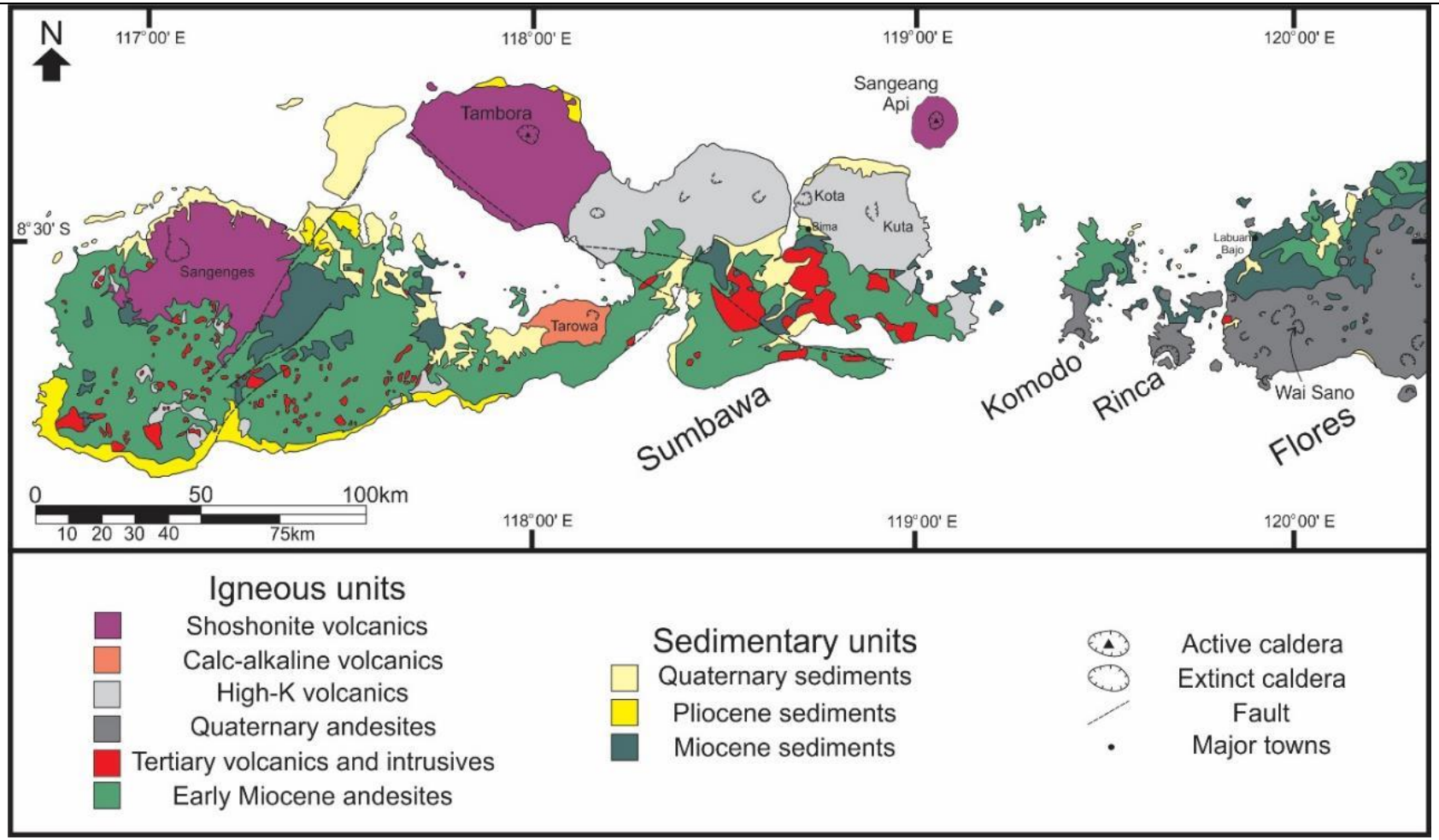

Figure 1: Simplified geological map of Sumbawa and Flores compiled from the geological maps of Sumbawa and Flores by Garwin (2000) and Indonesia Direktorat Geologi (1976) respectively.

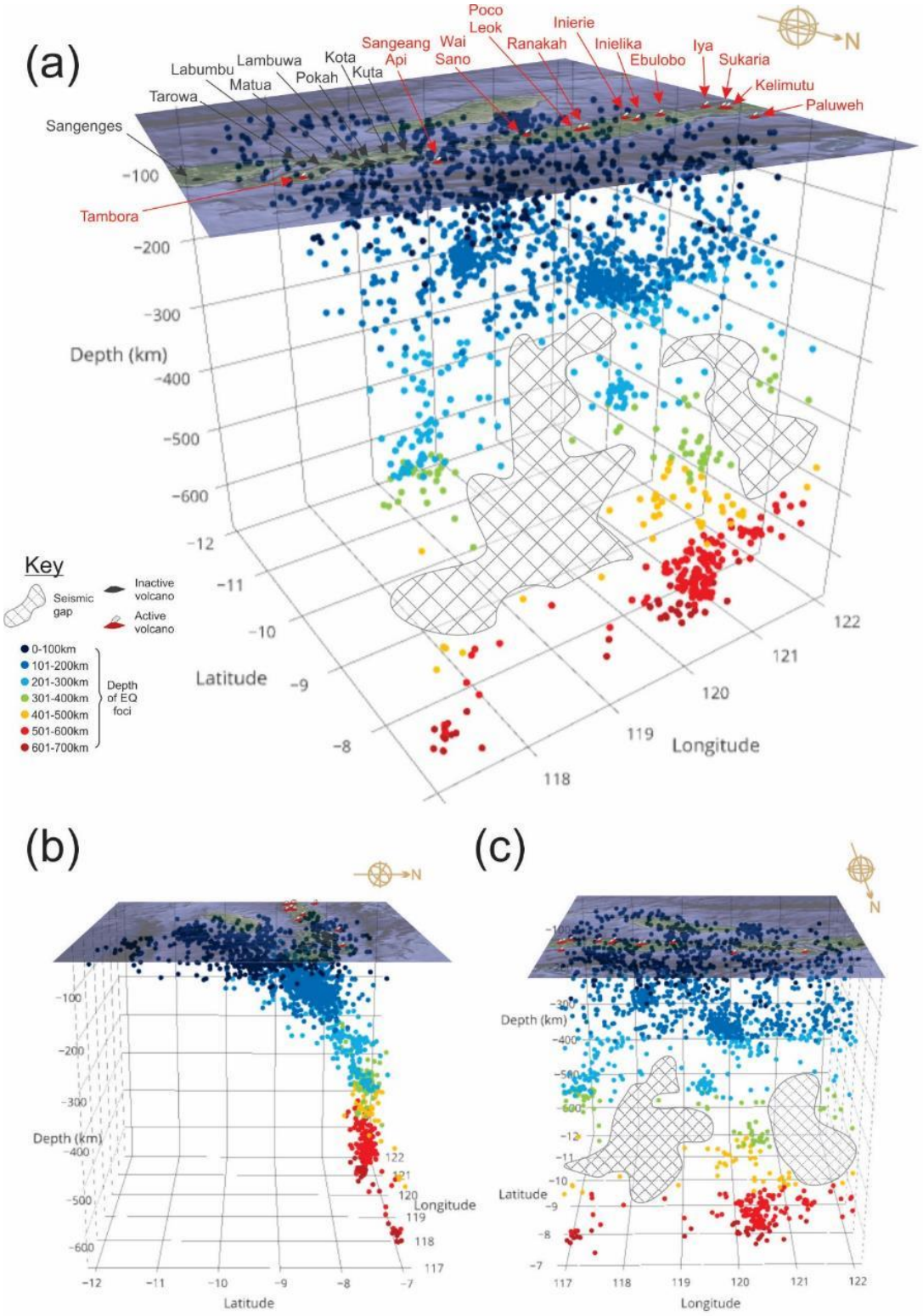

Figure 2: Earthquake foci profiles compiling all earthquakes recorded over magnitude 2.5 from International Seismological Centre (2017) with locations of quaternary volcanoes symbolised above (grey triangles). (a) Data from east Sumbawa (between 117˚40'E and 119˚20'E). (b) Data from west Flores (between 119˚40'E and 120˚10'E).

from He, Pb, Sr and Nd isotopes suggesting increased mixing and input of Australian and continental material towards the east (Elburg, M. A. et al. 2005; Elburg, Marlina A. et al. 2002; Elburg, M. A., van Bergen & Foden 2004; Hilton & Craig 1989; Hilton et al. 1992). Seismic tomography suggests that a tear in the subducting slab has developed from eastern Flores towards the Banda Sea (Ely & Sandiford 2010). Ely and Sandiford (2010) suggest that extensional regimes in the subducting slab beneath western Flores is evidence that this slab tear is extending westwards. 2D and 3D profiles of earthquake foci beneath our study region in the eastern Sunda Arc display large regions devoid of seismicity. These regions may be due to transitional regions in the subducting slab or may be evidence of existing or developing slab tear (see figure 2).

The Sunda arc formed from the gradual addition of distinct crustal blocks to a continental extension of the Eurasian plate called Sundaland. It has been proposed that these crustal blocks are expressed at the surface today by distinct islands that have been rotated and are separated by deep crustal faults (Nugroho et al. 2009; Wheller et al. 1987). The change in loci of active volcanism between Sumbawa and Flores (north to south) could be attributed to one of these deep crustal faults separating the islands, however, why this would move volcanism southwards is, as yet, unknown. Pacey, Macpherson and McCaffrey (2013) posited that the quaternary volcanoes of Northern Sumbawa (minus Tambora and Sangeang Api) and western Flores are aligned in a lineament controlled by lithospheric structure, at odds with the suggestions of others.

This study will present the first petrological and geochemical study of erupted products from northeast Sumbawa and Wai Sano, as well as the volcanogenic basement of northwest Flores.

METHODS

Samples without any sign of post-eruptive alteration and the most representative mineral populations were selected for geochemical analysis. Samples were first crushed and powdered, using a jaw crusher and tungsten-carbide ring mill respectively. Sample powders were then separated for analysis by ICP-MS, XRF and TIMS analysis.

To analyse the Rb, Sr, Sm and Nd isotopic compositions of the samples they were first dissolved in a concentrated HCl-HNO_3-HF solution. Subsequently they were dried down, with the addition of extra concentrated HNO_3 to remove HF, before dissolution in 15 M HNO_3. AG50W X8 200-400 mesh cation exchange resin was used to separate a REE fraction, Rb and Sr. Sm and Nd were then separated from the REE fraction using Eichrom Ln resin (SPS part# LNS05152). All samples were dried down again with the addition of 0.1 M H_3PO_4 and loaded on Re filaments before isotopic measurements were undertaken on an IsotopX TIMS at the University of Adelaide. Two standards, BCR-2 and AGV-2, were also analysed; returning $^{87}Sr/^{86}Sr$ ratios of 0.705013 and 0.703980 respectively. Lab procedural blanks are less than 1pg for Sr and 200µg for Nd, with procedural blanks from this study fitting within this range.

In preparation for XRF analysis and to measure LOI, sample powders were ignited at 1000˚C. Fused disks were prepared using a lithium borate flux. XRF analysis of the Wai

Sano samples was undertaken at the University of Adelaide, and the N. Sumbawa and N. Flores samples at CSIRO (Waite Campus, Adelaide). After XRF analysis fused beads of the N. Flores samples were stacked, mounted on a slide and polished. These beads were then analysed for trace element composition using an Agilent 7500cx mass spectrometer connected to a New Wave Up-213 laser (Adelaide Microscopy, University of Adelaide). 10 points on each fused disk were ablated for 120 seconds with a 30 second background using a 30μm spot size. Analyses were corrected using a NIST-610 glass standard and BHVO-2 and BCR-2 standards were measured to test reliability. The N. Sumbawa and Wai Sano samples were analysed for their trace element composition following an ICP-MS procedure by Bureau Veritas (Thebarton Laboratories, Adelaide).

Polished sections of samples were analysed for major element compositions of minerals by EPMA using a Cameca SXFive (Adelaide Microscopy, University of Adelaide). Analyses were undertaken with spot sizes of 5-15μm at 15kV and 20nA for a total of 60 seconds per spot with a 20 second background. For calibration, several in-house standards (Plagioclase, Astimex Almandine Garnet, Rutile, Astimex albite, Rhodonite, Chromite, Tugtupite, Astimex Apatite, Sanidine, Barite, Willemite & Astimex Anhydrite) were used.

EASTERN SUMBAWA PETROGRAPHY

Northeast Sumbawa High-K Calc-alkaline Lavas

Samples from the northeast corner of Sumbawa display a broad range in textures and mineral populations. Most samples are porphyritic lavas with varying degrees of phenocryst mineralogy and content, however, gabbroic textures with larger mineralogy are observed in some rare samples. Figures 3a-3f display representative textures within the N. Sumbawa samples. Table 1 outlines the common textures observed in the Eastern Sumbawan samples.

Lavas

The lavas from NE Sumbawa display both porphyritic textures as well as rare trachyte textures. The porphyritic samples contain lava phenocryst populations dominated by plagioclase, with clinopyroxene, amphibole and magnetite also common and more rarely small amounts of orthopyroxene and olivine. These are hosted in either glassy groundmass with microlites of plagioclase, clinopyroxene and magnetite (figure 3a), or, microcrystalline groundmass of similar mineral content to the microlite populations (figure 3b). In some samples, the glassy groundmass has undergone slight breakdown (figure 3c). A number of these porphyritic samples contain <10% vesicles greater than 0.7mm across. One sample displays a coarser doleritic texture with aligned amphibole and plagioclase, and lesser clinopyroxene and olivine (figure 3d). Entrained in this trachytic sample is an amphibole-gabbro xenolith (figure 3e), interestingly amphibole is more concentrated in the lava immediately adjacent to the xenolith.

Plagioclase makes up to 70% of the phenocryst populations of the NE Sumbawa lavas. Plagioclase phenocrysts display a large range in size (from 0.1-4.5mm) and in some

Locality	Lithology	Phenocryst/cumulate assemblage(s)	Texture(s)	Groundmass assemblage
Kota/Kuta	Basalts - Trachyandesite	*plagioclase+clinopyroxene+amphibole+magnetite (±orthopyroxene±olivine)*	*Porphyritic*	*plagioclase+clinopyroxene+ magnetite+glass*
		amphibole+plagioclase+clinopyroxene+olivine	*Trachytic*	*N/A*
	Gabbros	*(1) clinopyroxene+plagioclase → amphibole → magnetite* *(2) amphibole → magnetite+plagioclase → olivine*	*(1) Adcumulute* *(2) Orthocumulate*	*N/A*
Wai Sano	Dacites	*plagioclase+orthopyroxene+amphibole+magnetite (±clinopyroxene)*	*Porphyritic* *Trachytic (rare)*	*plagioclase+magnetite+ clinopyroxene+biotite+olivine +glass*
N. Flores	Dacites	*plagioclase+amphibole+magnetite*	*Porphyritic (Phaneritic zones)*	*plagioclase+chlorite*
	Andesite	*plagioclase+clinopyroxene+magnetite*	*Porphyritic*	*plagioclase*

Table 1: Outline of lithologies, textures and mineral/groundmass assemblages displayed by samples from localities in this study.

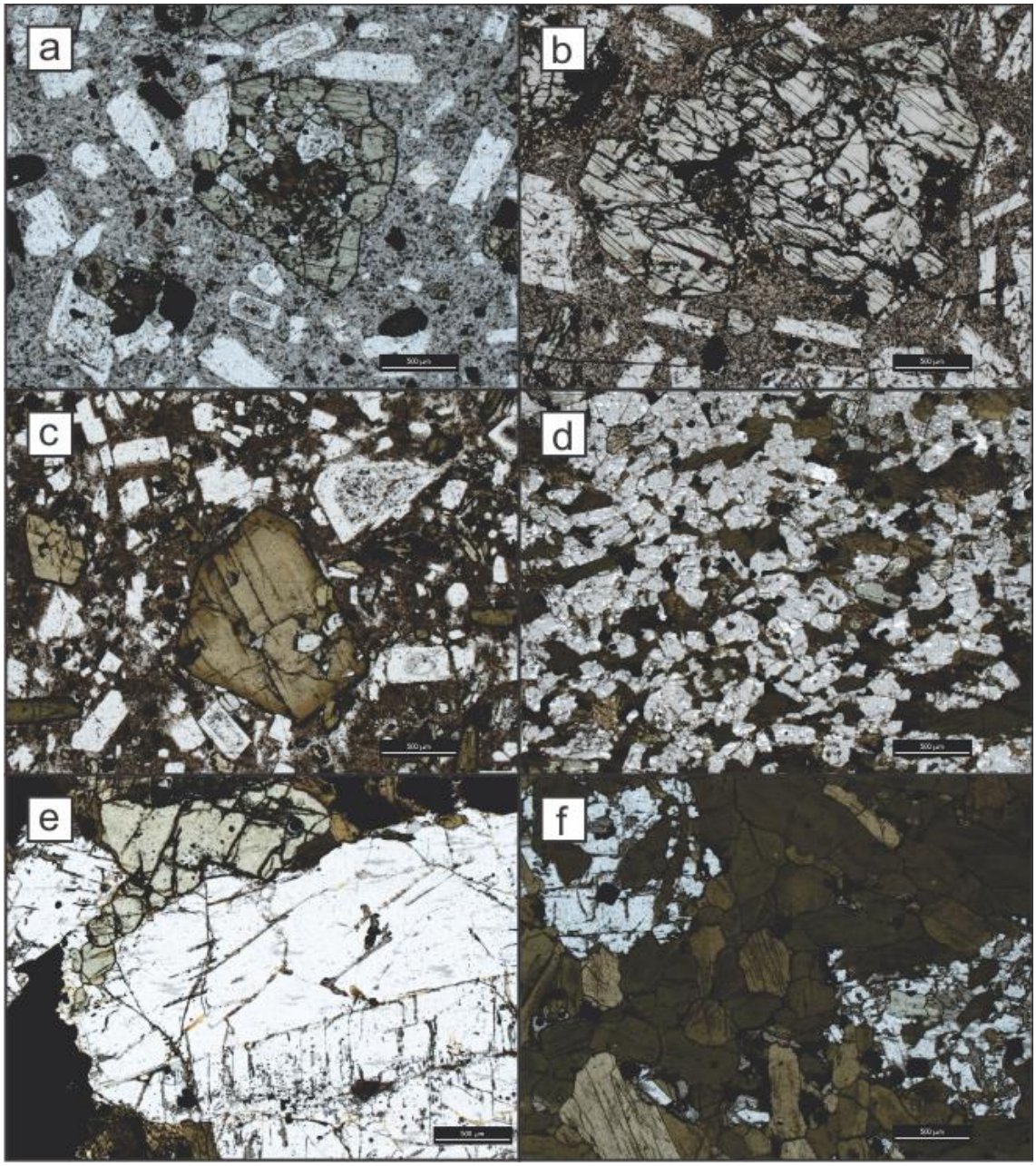

Figure 3a-f: Representative photomicrographs of lavas and gabbro xenoliths from northeast Sumbawa. (a) Lava (sample BC14/107) displaying accumulate of clinopyroxene, plagioclase and magnetite encasing an interstitial amphibole. (b) Large clinopyroxene phenocryst in microcrystalline groundmass (BC14/111). (c) Amphibole, plagioclase and clinopyroxene phenocrysts hosted in a glass rich groundmass (BC14/114). (d) Doleritic lava of sample BC14/130, composed of plagioclase, amphibole, clinopyroxene and magnetite. (e) Gabbro xenolith hosted in BC14/130; displaying large cumulate plagioclase with later olivine, magnetite and amphibole. (f) Gabbro sample (BC14/129) showing cumulate textures of amphibole and clinopyroxene, with later plagioclase and magnetite.

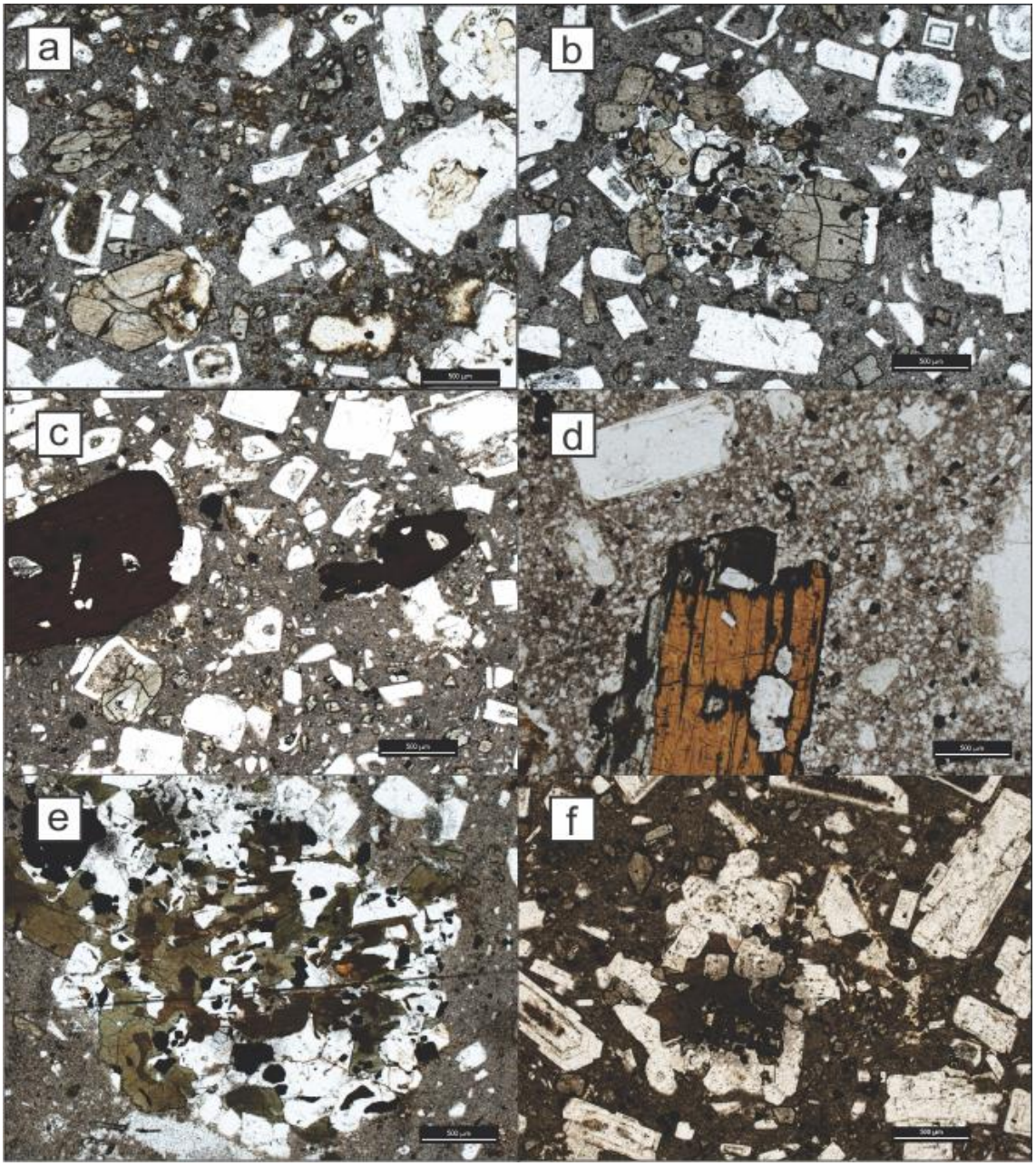

Figure 4a-f: Photomicrographs of dacites from Wai Sano. (a) Hypersthene, plagioclase and amphibole phenocrysts in a microcrystalline groundmass (SN1). (b) Porphyritic lava (SN2) with phenocrysts of hypersthene, plagioclase and magnetite. (c) Amphibole xenocryst with plagioclase inclusions in a porphyritic lava (SN4). (d) Phenocrysts of plagioclase and amphibole that has experienced partial breakdown in a crystalline groundmass (SN7). (e) Phlogopite, plagioclase and magnetite in a microcrystalline groundmass (SN10). (f) Amphibole and plagioclase phenocrysts in a glassy groundmass (SN3).

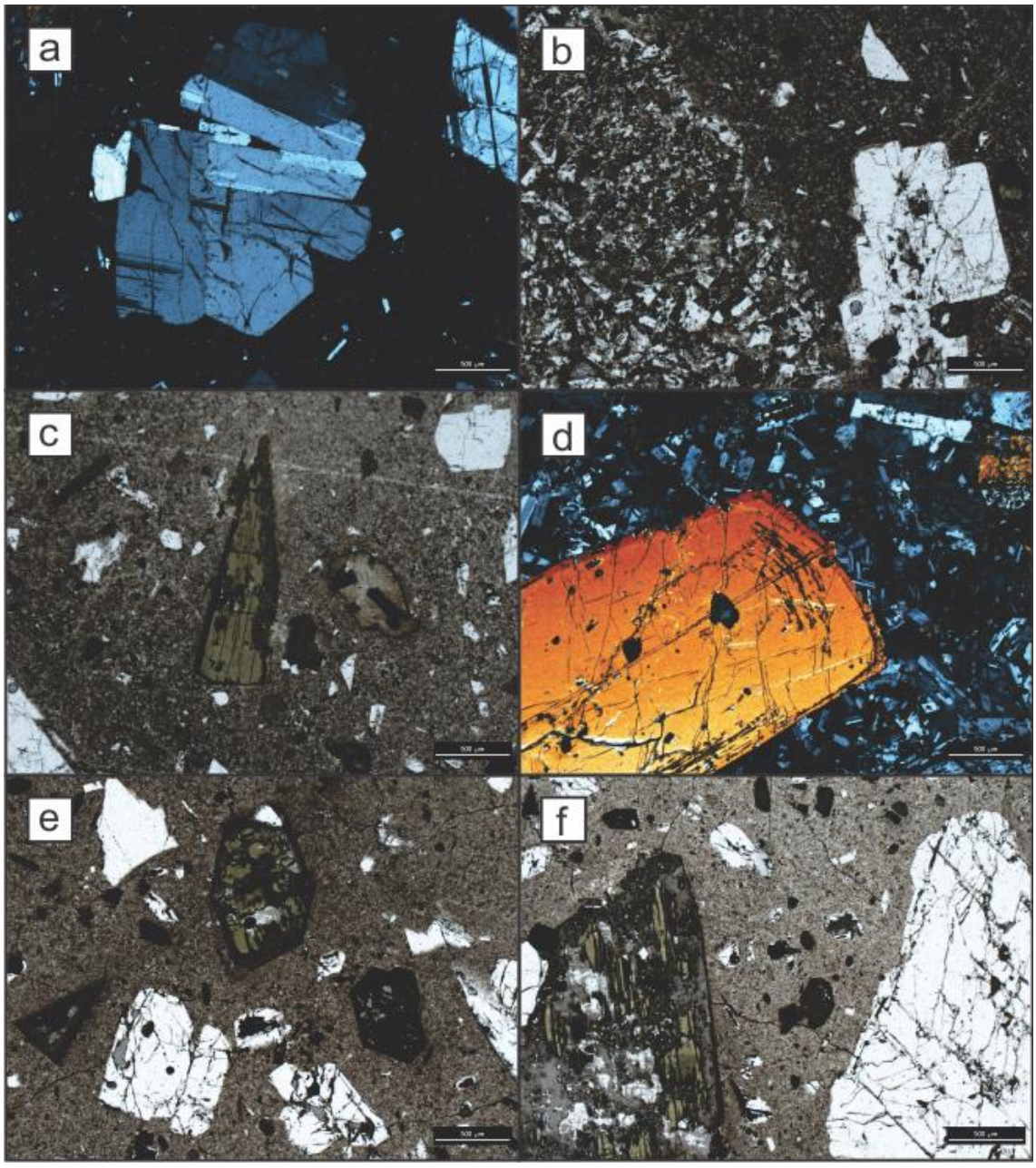

Figure 5a-f: Photomicrographs of dacite and andesite basement from northwest Flores. (a) Large plagioclase phenocrysts in microcrystalline groundmass (BC14/001). (b) Boundary between a porphyritic and crystalline lava region (BC14/001). (c) Amphibole xenocryst in porphyritic lava (BC14/001). (d) Large clinopyroxene phenocryst in crystalline groundmass (BC14/002). (e) Amphibole, plagioclase and magnetite phenocrysts in porphyritic lava (BC14/003). (f) Large plagioclase and amphibole (displaying well-developed breakdown rim) phenocryst in porphyritic lava (BC14/003).

samples megacrysts of up to 90mm can be observed. These large phenocrysts and megacrysts commonly display strong oscillatory zoning and some well-developed sieve textures that are bound by fresh rims. Plagioclase is also common as microlites and microphenocrysts in the glassy groundmass.

Clinopyroxene is observed as a common phenocryst phase in the NE Sumbawa lavas. Clinopyroxene phenocrysts make up between 4-20% of the phenocryst populations, with the crystals having well-formed, euhedral crystals between 0.4-3mm on the long-axis. Clinopyroxene microphenocrysts are common amongst the groundmass microlite populations.

Amphibole is found in several of the Sumbawa samples, making between 4 and 30% of the phenocryst/crystal populations. Amphibole in the trachyte sample is elongate and subhedral in shape, ranging between 0.3-0.8mm in length. Phenocrysts in the porphyritic samples are mostly euhedral-subhedral, ranging between 0.4 and 2.5mm in size. Commonly they display 0.5-0.2mm opacitic rims of Fe-oxides and occasionally have more well-developed breakdown textures with or without remnant amphibole cores. One sample (BC14-117) displays small amphibole phenocrysts (0.2-0.4mm across) that are rimmed by 0.1-0.2mm of clinopyroxene, possibly suggesting that the crystallising magma experienced a rapid devolatilisation during a slow cooling regime.

Magnetite is common throughout the lavas and is often observed as subhedral cubic phenocrysts ranging in size from 0.05mm to 0.6mm, with some rarer large megacrysts up to 2mm being observed in some samples. Titanium contents of the magnetites ranges from 4-6wt%. Magnetite is often observed as inclusions in clinopyroxene and plagioclase phenocrysts.

More rarely olivine and orthopyroxene is found in the lavas. Olivine is mostly observed as microphenocrysts smaller than 0.15mm in the groundmass of most samples, but in the trachyte sample it is observed as a larger (3-6mm) phase that is post-dating amphibole and plagioclase in the groundmass. Orthopyroxene is observed rarely as small phenocrysts (<0.5mm), but is primarily observed as a rare phase in the groundmass microlite population of some samples.

Gabbros

Two samples display cumulate textures (figures 3e and 3f), a xenolithic amphibole-gabbro region entrained within the trachytic lava and another amphibole-gabbro. The xenolithic sample contains large (>3mm) euhedral clinopyroxene and plagioclase that pre-date smaller (1.5-2.5mm) anhedral amphibole with later interstitial magnetite (figure 3e). The gabbro sample is predominantly made of large, elongate, euhdral amphibole (~70%) with magnetite and plagioclase interstitial to this and rare (<1%) olivine (figure 3f). In both samples, the amphibole is well preserved and doesn't display any breakdown or reaction rims suggesting rapid decompression of the samples.

Mineral Geochemistry

Plagioclase

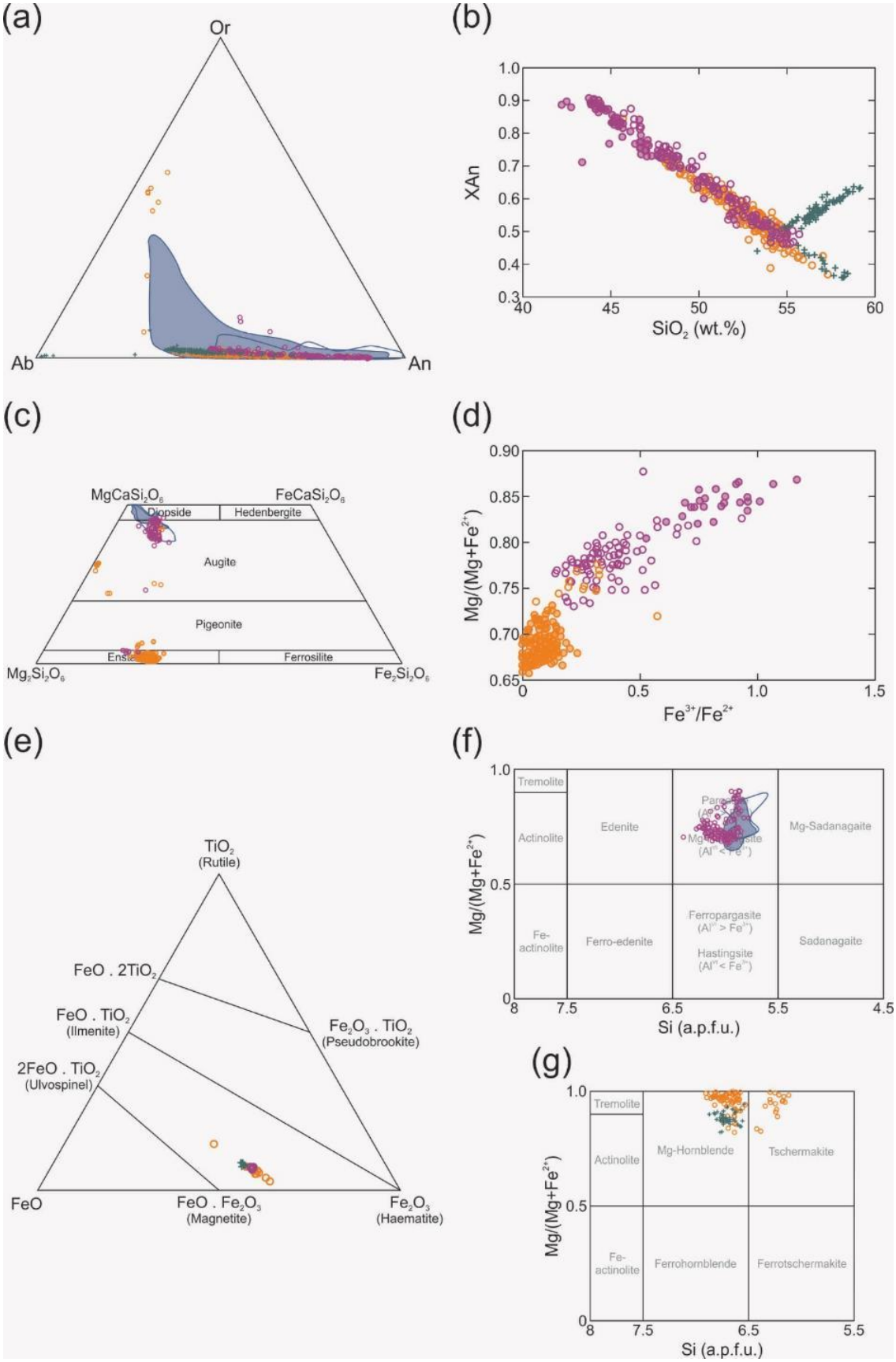
(a)
Or
Ab
An
(b)
XAn
SiO2 (wt.%)
(c)
MgCaSi2O6
FeCaSi2O6
Diopside
Hedenbergite
Augite
Pigeonite
Ferrosilite
Mg2Si2O6
Fe2Si2O6
(d)
Mg/(Mg+Fe2+)
Fe3+/Fe2+
(e)
TiO2 (Rutile)
FeO . 2TiO2
FeO . TiO2 (Ilmenite)
Fe2O3 . TiO2 (Pseudobrookite)
2FeO . TiO2 (Ulvospinel)
FeO
FeO . Fe2O3 (Magnetite)
Fe2O3 (Haematite)
(f)
Tremolite
Actinolite
Edenite
Mg-Sadanagaite
Fe-actinolite
Ferro-edenite
Ferropargasite
Hastingsite
Sadanagaite
Si (a.p.f.u.)
(g)
Tremolite
Actinolite
Mg-Hornblende
Tschermakite
Fe-actinolite
Ferrohornblende
Ferrotschermakite
Si (a.p.f.u.)

Figure 6a-f (previous page): Classification and composition diagrams displaying mineral geochemistry. (a) Plagioclase classification diagram displaying phenocryst compositions from N. Sumbawa (purple circles), Wai Sano (orange circles) and NW. Flores (green crosses). Sangeang Api lava (closed blue region) and gabbro (open blue region) compositional variations are shown for comparison. (b) SiO_2 vs. anorthite content of plagioclase phenocrysts. (c) Ca-Mg-Fe pyroxene quadrilateral classification diagrams (after Morimoto 1998), open circles represent clinopyroxene analyses and closed circles are orthopyroxene analyses. (d) Diagram displaying the ferric/ferrous iron and Mg# (Mg/[Mg+Fe^{2+}]) ratios of pyroxene analyses. (e) Oxide classification diagram, after Deer, Howie and Zussman (2013). (f) Calcic amphibole ($Na+K_A \geq 0.5$) classification diagram after Leake et al. (1997). (g) Calcic amphibole ($Na+K_A < 0.5$) classification diagram after Leake et al. (1997).

Plagioclase phenocrysts from NE Sumbawa lavas are more An-rich (~An46-An87) than those from Wai Sano, but not as An-rich as plagioclase analyses from the nearby Sangeang Api (figure 6a). Analyses of plagioclase from the gabbros range from An51-An90, and significantly overlap in composition the phenocrysts from the lavas (see figure 6b), possibly suggesting some inheritance of crystals from the cumulate to the lava.

Pyroxenes

Most pyroxene analyses from the NE Sumbawan samples are augitic clinopyroxene in composition, with Mg# (calculated as 100Mg/[Mg^{2+}+Fe^{2+}]) ranging from 72-88 in the lavas and 82-87 in the gabbros (figure 6c). Compositionally they form distinct groups, with the lavas having lower Fe^{3+}/Fe^{2+} contents (0.09-0.93) and the gabbros much higher (0.52-1.17). Compositionally they follow a well-defined path from high Mg# and high Fe^{3+}/Fe^{2+} crystals of the gabbros to low Mg# and low high Fe^{3+}/Fe^{2+} lava phenocrysts (figure 6d) – hinting at a shared differentiation history. Analyses of the rare orthopyroxene phenocrysts fall into the hypersthene field with Mg# ranging from 70-74 (figure 6c). They are significantly more Fe^{3+}-rich than the clinopyroxenes (Fe^{3+}/Fe^{2+} 7.6-18.8).

Amphibole

The compositions of the Sumbawa amphiboles are less magnesian (Mg#69-90) than those from Wai Sano/NW Flores and all analysed samples are Mg-Hastingsite (figure 6f). Interestingly these amphiboles display a correlation between increasing Mg# (Mg#69-90) and decreasing Si content (Si a.p.f.u. 5.5-6.9). Amphiboles found in the gabbros have lower Mg# (Mg#67-77) than those from the lavas (Mg#69-90) and display no increase in Mg# with decreasing Si content as the lava samples do.

Magnetite

Magnetite displays Fe^{3+}/Fe^{2+} ratios of 1.32 to 1.34. They have TiO_2 contents ranging from 6.55 to 6.72wt.% and low ZnO (0.06-0.17wt.%), Cr_2O_3 (0-0.04wt.%) and MnO (0.73-0.80wt.%). Their compositions can be observed in figure 6e.

Olivine

Olivines in the lavas have forsterite contents ranging from Fo69-70, falling close to the boundary between the Chrysolite and Hyalosiderite compositional fields. They are manganese (0.9-1.0wt.%) and titanium poor (0.18-0.23wt.%).

WAI SANO PETROGRAPHY

Wai Sano Adakitic Lavas

Wai Sano lavas are commonly porphyritic and dominated by phenocrysts of plagioclase, clinopyroxene, orthopyroxene, amphibole and magnetite entrained in a glassy or cryptocrystalline groundmass. Table 1 outlines the common textures observed in the Wai Sano samples. A few samples display magma mingling textures of two distinct magmatic textures mixing with one another. Examples of the Wei Sano lavas can be observed in figures 4a-4f. Plagioclase phenocrysts range in size from 0.1-5mm and in many samples, there are two distinct groups of plagioclase phenocrysts with different textures and crystal size distributions; a group of large (1-5mm), well-formed, euhedral phenocrysts-megacrysts that are strongly zoned and contain abundant melt inclusions in their outermost rim. Alongside these are smaller phenocrysts (up to 1.5mm) with well-developed sieve textures in the core and rimmed by a zone free of inclusions or sieve texture (see figures 4b and 4e). In other samples, there is only one group of phenocrysts that are identified by strongly euhedral crystals with strongly formed zoning often with one zone through the zoning displaying a strong sieve texture (see figure 4f).

Amphibole is a common phase throughout the Wai Sano samples, making between 2 and 10% of the phenocryst population in most samples. It is primarily observed as euhedral and subhedral crystals with a broad range of sizes spanning microphenocrysts (0.05-0.2mm) to megacrysts (>4mm). In most samples phenocrysts and microphenocrysts display well-developed Fe-oxide rims, with some larger megacrysts having undergone incongruent breakdown to Fe-oxides, clinopyroxene and lesser plagioclase (figure 4d). A rare number of samples display amphibole being enveloped by other mineralogy; with a megacryst in one sample being enveloped by a later orthopyroxene megacryst, whilst another displays what may be a xenocrystic accumulation of plagioclase, clinopyroxene and magnetite surrounding an amphibole crystal with an interstitial texture (see figures 4e and 4f).

Pyroxene phases are found in most Wai Sano lavas, with augite and enstatite co-existing in most samples. The pyroxenes make up between 4 and 34% of the phenocryst populations, with enstatite being more common (3-18%) than augite. Pyroxene phenocrysts are predominantly idiomorphic, elongate and euhedral in shape between 0.2-3mm in size, with some being significantly larger than this. Larger pyroxene phenocrysts often contain small amounts of melt and crystal inclusions (plagioclase and magnetite).

Magnetite is common throughout all of the Wai Sano lavas making between 3-8% of the phenocryst population. Magnetite crystals range in size between 0.1-1mm in size and are usually euhedral or subhedrally cubic in shape. Titanium contents of the magnetite crystals range from 2wt.% to 10wt.%. Magnetite is a common inclusion within larger pyroxene and plagioclase crystals.

Biotite and apatite are extremely rare in the Wai Sano lavas, with both being found rarely in the groundmass microphenocryst assemblage.

Sample	**SN1**		**SN4**		**SN7**		**SN10**		**BC14/001**		**BC14/003**		**BC14/114**		**BC14/129**		**BC14/130**	
Location	Wai Sano		Wai Sano		Wai Sano		Wai Sano		Wai Sano		Wai Sano		Kolo		Wai Sano		Wai Sano	
Lithology	Dacite		Dacite		Dacite		Dacite		Dacite		Dacite		Basalt		Gabbro		Dolerite	
Mineral	Amph		Amph		Amph		Amph		Amph		Amph		Amph		Amph		Amph	
	wt.%	1s.d.	wt.%	1s.d.	wt.%	1s.d.	wt.%	1s.d.	wt.%	1s.d.	wt.%	1s.d.	wt.%	1s.d.	wt.%	1s.d.	wt.%	1s.d.
SiO_2	46.18	0.46	44.48	1.23	42.89	1.42	47.37	0.48	45.42	0.71	46.41	0.33	40.71	0.90	40.38	0.59	39.89	0.44
TiO_2	1.09	0.11	1.47	0.22	1.20	0.20	1.14	0.05	1.25	0.11	1.38	0.12	2.13	0.26	2.28	0.07	2.62	0.08
Al_2O_3	7.81	0.32	10.34	1.39	11.12	1.37	6.87	0.37	7.64	0.65	7.54	0.18	13.79	0.69	12.13	0.75	12.93	0.80
Cr_2O_3	0.01	0.02	0.05	0.09	0.03	0.01	0.01	0.01	0.01	0.01	0.00	0.00	0.05	0.06	0.01	0.01	0.02	0.02
FeO	13.10	0.35	12.31	1.41	12.51	0.74	11.52	0.27	15.00	0.61	14.65	0.31	10.29	1.17	13.76	0.23	12.86	0.69
MnO	0.40	0.03	0.21	0.07	0.23	0.18	0.36	0.03	0.58	0.09	0.52	0.04	0.14	0.08	0.26	0.03	0.28	0.04
MgO	14.90	0.22	14.54	0.96	14.40	0.15	16.09	0.11	13.81	0.47	13.88	0.14	14.57	0.75	12.36	0.30	12.54	0.28
CaO	10.04	0.10	10.85	0.19	10.67	0.37	10.54	0.06	10.32	0.24	10.37	0.14	11.72	0.33	11.45	0.12	11.72	0.12
Na_2O	1.32	0.07	1.68	0.27	1.91	0.30	1.22	0.13	1.42	0.13	1.38	0.08	2.37	0.11	2.25	0.08	2.50	0.16
K_2O	0.21	0.02	0.26	0.04	0.22	0.04	0.14	0.01	0.44	0.04	0.42	0.03	1.01	0.15	1.09	0.06	0.84	0.11
F	0.09	0.04	0.06	0.02	0.03	0.03	0.04	0.05	0.18	0.09	0.10	0.02	0.11	0.03	0.23	0.09	0.15	0.03
Cl	0.06	0.01	0.04	0.03	0.03	0.03	0.04	0.01	0.22	0.02	0.20	0.02	0.03	0.03	0.06	0.01	0.05	0.02
Total	95.21	0.22	96.31	0.37	95.25	0.26	95.34	0.27	96.27	0.67	96.86	0.37	96.93	0.91	96.26	0.23	96.39	0.40

Table 2: Average amphibole major element compositions from representative phenocrysts of samples. Average values are calculated for single phenocrysts and 1 standard deviation of the phenocryst analyses is given. Mg# is calculated as $Mg/(Mg+Fe^{2+})$.

Sample	**SN1**		**SN4**		**SN7**		**SN10**		**BC14/001**		**BC14/003**		**BC14/114**		**BC14/129**		**BC14/130**	
Location	Wai Sano		Wai Sano		Wai Sano		Wai Sano		Wai Sano		Wai Sano		Kolo		Wai Sano		Wai Sano	
Lithology	Dacite		Dacite		Dacite		Dacite		Dacite		Dacite		Basalt		Gabbro		Dolerite	
Mineral	Amph		Amph		Amph		Amph		Amph		Amph		Amph		Amph		Amph	
	wt.%	1s.d.	wt.%	1s.d.	wt.%	1s.d.	wt.%	1s.d.	wt.%	1s.d.	wt.%	1s.d.	wt.%	1s.d.	wt.%	1s.d.	wt.%	1s.d.
AlIV	1.31	0.06	1.57	0.17	1.74	0.19	1.17	0.06	1.30	0.09	1.27	0.03	2.06	0.11	1.94	0.08	2.03	0.07
Ti	0.00	0.01	0.00	0.00	0.00	0.00	0.01	0.02	0.06	0.04	0.01	0.01	0.00	0.00	0.00	0.00	0.00	0.00
Tsite	*8.00*	*0.00*	*8.00*	*0.00*	*8.00*	*0.00*	*8.00*	*0.00*	*8.00*	*0.00*	*8.00*	*0.00*	*8.00*	*0.00*	*8.00*	*0.00*	*8.00*	*0.00*
AlVI	0.03	0.01	0.19	0.07	0.18	0.05	0.00	0.00	0.01	0.04	0.02	0.03	0.32	0.05	0.21	0.06	0.26	0.08
Ti	0.12	0.01	0.16	0.02	0.13	0.02	0.11	0.02	0.08	0.03	0.14	0.02	0.23	0.03	0.26	0.01	0.30	0.01
Cr	0.00	0.00	0.01	0.01	0.00	0.00	0.00	0.00	0.00	0.00	0.00	0.00	0.01	0.01	0.00	0.00	0.00	0.00
Fe3+	1.52	0.06	1.18	0.09	1.37	0.19	1.32	0.04	1.43	0.11	1.28	0.13	0.74	0.10	0.66	0.05	0.53	0.06
Mg	3.22	0.04	3.13	0.18	3.13	0.03	3.45	0.02	3.01	0.10	3.00	0.02	3.17	0.16	2.77	0.06	2.80	0.06
Fe2+	0.07	0.05	0.31	0.22	0.15	0.12	0.06	0.03	0.41	0.11	0.50	0.10	0.52	0.19	1.07	0.07	1.08	0.07
Mn	0.05	0.00	0.03	0.01	0.03	0.02	0.04	0.01	0.07	0.01	0.06	0.00	0.02	0.01	0.03	0.00	0.04	0.01
Csite	*5.00*	*0.00*	*5.00*	*0.00*	*5.00*	*0.00*	*5.00*	*0.00*	*5.00*	*0.00*	*5.00*	*0.00*	*5.00*	*0.00*	*5.00*	*0.00*	*5.00*	*0.00*
Fe2+	0.00	0.00	0.00	0.00	0.00	0.00	0.00	0.00	0.00	0.00	0.00	0.00	0.00	0.00	0.00	0.00	0.00	0.00
Ca	1.56	0.02	1.68	0.03	1.67	0.07	1.63	0.01	1.61	0.04	1.61	0.02	1.83	0.06	1.84	0.02	1.88	0.02
Na	0.37	0.02	0.32	0.03	0.32	0.05	0.34	0.03	0.37	0.03	0.38	0.02	0.17	0.06	0.16	0.02	0.12	0.02
Bsite	*1.93*	*0.03*	*2.00*	*0.00*	*1.99*	*0.03*	*1.96*	*0.03*	*1.99*	*0.02*	*1.99*	*0.02*	*2.00*	*0.00*	*2.00*	*0.00*	*2.00*	*0.00*
Na	0.00	0.00	0.15	0.10	0.22	0.12	0.01	0.01	0.03	0.04	0.01	0.02	0.51	0.05	0.50	0.04	0.61	0.05
K	0.04	0.00	0.05	0.01	0.04	0.01	0.03	0.00	0.08	0.01	0.08	0.01	0.19	0.03	0.21	0.01	0.16	0.02
Asite	*0.04*	*0.00*	*0.20*	*0.10*	*0.26*	*0.12*	*0.03*	*0.01*	*0.11*	*0.04*	*0.09*	*0.01*	*0.69*	*0.07*	*0.71*	*0.03*	*0.77*	*0.03*
Mg#	0.98	0.02	0.91	0.06	0.95	0.03	0.98	0.01	0.88	0.03	0.86	0.02	0.86	0.05	0.72	0.01	0.72	0.02

Table 3: Average amphibole major element compositions and formulae based on 13 cations (calculated from Leake et al., 1997) from representative phenocrysts of samples. Average values are calculated for single phenocrysts and 1 standard deviation of the phenocryst analyses is given. Mg# is calculated as $Mg/(Mg+Fe^{2+})$.

Sample	**SN1**		**SN4**		**SN4**		**SN7**		**SN10**		**BC14/106**		**BC14/106**		**BC14/111**		**BC14/114**		**BC14/130**	
Location	Wai Sano		Wai Sano		Wai Sano		Wai Sano		Wai Sano		Kolo		Wai Sano		Wai Sano		Wai Sano		Wai Sano	
Lithology	Dacite		Dacite		Dacite		Dacite		Dacite		Basalt		Basalt		Andesite		Basalt		Dolerite	
Mineral	Opx		Cpx		Opx		Opx		Opx		Opx		Cpx		Cpx		Cpx		Cpx	
	wt.%	1sd	wt.%	1sd	wt.%	1sd	wt.%	1sd	wt.%	1sd	wt.%	1sd	wt.%	1sd	wt.%	1sd	wt.%	1sd	wt.%	1sd
SiO_2	51.55	0.7	51.30	0.3	52.17	0.3	52.06	0.3	51.99	0.2	52.66	0.6	51.25	0.8	51.42	0.6	50.79	1.1	50.69	0.5
TiO_2	0.09	0.0	0.37	0.0	0.10	0.0	0.14	0.0	0.14	0.0	0.21	0.0	0.42	0.1	0.47	0.0	0.53	0.1	0.46	0.1
ZnO	0.04	0.0					0.05	0.0	0.05	0.0									0.03	0.0
Al_2O_3	1.15	0.7	2.02	0.3	1.29	0.7	0.88	0.2	0.87	0.2	1.38	0.4	2.18	0.8	2.25	0.3	2.97	1.1	2.56	0.6
Cr_2O_3	0.00	0.0			0.00	0.0	0.01	0.0	0.01	0.0	0.00	0.0							0.01	0.0
FeO	20.27	1.0	8.71	0.3	20.81	0.5	19.44	0.4	19.92	0.4	17.47	0.1	9.00	0.4	9.63	0.7	8.13	0.4	7.65	0.5
MnO	0.87	0.1	0.36	0.0	0.87	0.1	1.06	0.1	1.14	0.1	1.03	0.0	0.60	0.1	0.51	0.0	0.46	0.1	0.34	0.0
MgO	22.97	0.7	14.72	0.1	22.94	0.5	23.89	0.2	23.59	0.3	24.67	0.2	15.26	0.6	15.13	0.5	14.03	0.6	13.96	0.2
CaO	0.63	0.2	20.71	0.2	0.54	0.2	0.75	0.1	0.80	0.2	1.67	0.2	19.94	0.5	19.47	0.4	21.93	0.2	22.98	0.2
BaO	0.01	0.0					0.01	0.0	0.01	0.0									0.01	0.0
Na_2O	0.07	0.0	0.30	0.0	0.05	0.0	0.03	0.0	0.02	0.0	0.05	0.0	0.33	0.0	0.39	0.0	0.39	0.1	0.45	0.1
K_2O	0.01	0.0	0.00	0.0	0.01	0.0	0.01	0.0	0.00	0.0	0.01	0.0	0.00	0.0	0.01	0.0	0.00	0.0	0.01	0.0
P_2O_5	0.01	0.0					0.01	0.0	0.01	0.0									0.00	0.0
SO_3	0.03	0.1			0.01	0.0	0.00	0.0	0.00	0.0	0.00	0.0							0.01	0.0
Cl	0.02	0.0			0.02	0.0	0.00	0.0	0.01	0.0	0.00	0.0							0.01	0.0
F	0.04	0.0			0.01	0.0	0.01	0.0	0.01	0.0	0.00	0.0							0.01	0.0
Total	97.75	0.2	98.49	0.0	98.80	0.5	98.34	0.3	98.55	0.4	99.15	0.9	98.99	0.5	99.27	0.7	99.23	0.4	99.17	0.3

Table 4: Average pyroxene major element compositions from phenocrysts hosted in representative samples. Clinopyroxene analyses are denoted as 'Cpx' and orthopyroxene analyses as 'Opx'. Average values are calculated for single phenocrysts and 1 standard deviation of the phenocryst analyses is given. Blank cells in table were not analysed for the given sample.

Sample	**SN1**		**SN7**		**SN10**		**BC14/001**		**BC14/106**		**BC14/114**		**BC14/129**		**BC14/130**	
Location	Wai Sano		Wai Sano		Wai Sano		Labuan Bajo		Sumbawa (N)		Lahar (W. Kota)		Kolo		Kolo	
Lithology	Dacite		Dacite		Dacite		Dacite		Basalt		Basalt		Gabbro		Dolerite	
Mineral	Plag		Plag		Plag		Plag		Plag		Plag		Plag		Plag	
	wt.%	1s.d.	wt.%	1s.d.	wt.%	1s.d.	wt.%	1s.d.	wt.%	1s.d.	wt.%	1s.d.	wt.%	1s.d.	wt.%	1s.d.
SiO_2	52.85	0.66	53.85	1.67	48.64	0.61	57.53	0.69	53.56	0.80	51.05	0.86	46.48	0.50	44.33	0.97
TiO_2	0.01	0.01	0.01	0.01	0.01	0.01	0.01	0.01	0.04	0.02	0.02	0.02	0.01	0.01	0.01	0.01
ZnO	0.01	0.01	0.04	0.03	0.02	0.02	25.43	0.48					31.57	0.26	0.01	0.02
Al_2O_3	27.39	0.55	26.70	1.04	29.75	0.32	0.01	0.01	28.82	0.57	30.75	0.63	0.00	0.00	33.36	0.37
Cr_2O_3	0.02	0.02	0.00	0.01	0.00	0.00	0.21	0.03					0.37	0.04	0.01	0.01
FeO	0.30	0.06	0.16	0.03	0.40	0.07	0.01	0.01	0.36	0.06	0.42	0.09	0.01	0.01	0.37	0.12
MnO	0.01	0.02	0.02	0.02	0.02	0.02	0.01	0.02					0.00	0.00	0.01	0.02
MgO	0.02	0.01	0.04	0.08	0.02	0.01	0.02	0.02	0.04	0.01	0.04	0.01	0.02	0.01	0.03	0.03
CaO	11.09	0.64	10.00	1.22	14.07	0.43	8.03	0.47	10.69	0.47	12.91	0.63	15.14	0.27	17.47	0.44
BaO	0.01	0.01	0.02	0.02	0.01	0.01	0.02	0.02					0.04	0.01	0.02	0.01
Na_2O	5.27	0.36	6.10	1.01	3.38	0.23	6.85	0.23	0.31	0.03	0.12	0.02	2.56	0.19	1.34	0.19
K_2O	0.14	0.02	0.18	0.03	0.06	0.02	0.45	0.07	5.23	0.31	4.05	0.35	0.11	0.01	0.05	0.02
P_2O_5	0.01	0.01	0.00	0.00	0.01	0.01	0.03	0.05					0.01	0.01	0.00	0.00
SO_3	0.01	0.01	0.03	0.07	0.01	0.01	0.00	0.00					0.00	0.00	0.01	0.02
Cl	0.01	0.00	0.05	0.13	0.00	0.00	0.00	0.00					0.00	0.00	0.01	0.01
F	0.00	0.00	0.00	0.00	0.00	0.00	0.00	0.00					0.00	0.00	0.00	0.00
Total	97.14	0.43	97.20	0.51	96.39	0.36	98.60	0.32	99.07	0.55	99.37	0.77	96.33	0.23	97.03	0.92
Xan	0.53	0.03	0.47	0.07	0.69	0.02	0.38	0.02	0.52	0.03	0.63	0.03	0.76	0.02	0.88	0.02

Figure 5: Average plagioclase major element compositions from phenocrysts hosted in representative samples. Average values are calculated for single phenocrysts and 1 standard deviation of the phenocryst analyses is given. Blank cells in table were not analysed for the given sample. Average anorthite content of the plagioclase analyses is given as XAn.

The groundmass of the Wai Sano samples is either glassy (e.g. figure 4c) or cryptocrystalline (e.g. figure 4d) in all samples. Often the groundmass hosts abundant small microphenocryst laths (<0.2mm) of plagioclase, clinopyroxene, magnetite and olivine in varying proportions. A small number of the samples display evidence of channelized flow with trachytic texture crosscutting lavas with no alignment in groundmass mineralogy.

Mineral Geochemistry

Pyroxenes

Orthopyroxene is a more prominent phase in the Wai Sano samples than clinopyroxene. The orthopyroxene analyses have hypersthene compositions, with low Fe^{3+}/Fe^{2+} (0.01-0.32) and Mg# (65-75) compared to the Wai Sano and the NE Flores clinopyroxenes (see figure 6c). Clinopyroxenes from the Wai Sano lavas are augitic in composition, with Fe^{3+}/Fe^{2+} between 0.06-0.57 and Mg# between 68 and 80. Compositionally they overlap slightly with the least mafic lava analyses from NE Flores (as seen in figure 6d).

Plagioclase

Plagioclase compositions span anorthite compositions from An41 to An73, over a range of SiO_2 spanning 48-56wt.% (see figures 6a and 6b). Some rare outliers span to An contents as high as An84 and as low as An37. Plagioclase analyses from the Wai Sano lavas show decreasing An content with SiO_2, similar to the NE Sumbawa samples (figure 6b).

Amphiboles

Compositionally the amphiboles span a range from magnesiohornblende to tschermakite with high Mg# (~Mg#85-99) (figure 6g). Amphiboles from Wai Sano have significantly lower Na+K in the A-site than the other samples in this study. They have Mg# spanning from 82.6 to 99.9, significantly more magnesian than those from the NE Sumbawa samples.

Magnetites

Magnetites from Wai Sano display a large amount of compositional variation compared to the analyses from NE Sumbawa and N Flores. They have Fe^{3+}/Fe^{2+} ratios between 0.84 and 1.63 and TiO_2 spanning 2.8-14wt.%. The majority of samples are more Fe_2O_3 rich than magnetites from NE Sumbawa or N Flores, as observed in figure 6e.

Phlogopite

Rare phlogopite in the Wai Sano lavas have Mg/Fe^{2+} ratios between 2.15 and 2.88 and Na/K ratios between 0.19 and 0.24. Average Cl contents (0.10wt.%) are slightly higher than those from the nearby Sangeang Api (0.07wt.%), whilst average F contents are significantly lower (0.22 compared to 0.42wt.%).

Groundmass glass

Groundmass glass was analysed in one sample (SN10). These glasses are SiO_2 rich (73-83wt.%) with Al_2O_3 between 9.6-15.1wt.%. Average MgO and FeO_{tot} are low (0.63wt.% and 1.24wt.% respectively), whereas total alkali contents are relatively high (6wt.% Na_2O+K_2O). These groundmass glass are also volatile poor (0-85ppm S, 0-16ppm Cl and 0ppm F), suggesting that they crystallised from strongly degassed magmas.

Apatite

Apatite samples from the Wai Sano samples contain significant volatiles (729-827ppm Cl, 6-184ppm S and 0-42ppm Ba).

NORTHWEST FLORES PETROGRAPHY

Northwest Flores Lavas

Three samples were collected from lava flows at the northwest corner of Flores near to the town of Labuan Bajo. Photomicrographic examples of representative volcanogenic basement from northern Sumbawa are displayed in figure 5a to 5f and table 1 outlines the common textures observed in these samples. All three samples display porphyritic textures with a lot of variation in groundmass texture; finely crystalline groundmass composed primarily of plagioclase, clinopyroxene and magnetite with some interstitial glass (figure 5b and 5d), glassy groundmass with microcrystalline plagioclase (figure 5f) and cryptocrystalline groundmass (figure 5b). One sample (BC14-001) displays magma mingling textures between phaneritic and porphyritic lavas (see figure 5b). Phenocryst populations differ between samples; however, plagioclase is a dominant phase in all the samples with lesser amphibole or clinopyroxene depending on the sample. Plagioclase is observed as phenocrysts varying in size from 0.1-3mm, often displaying strong oscillatory zoning profiles with some crystals having well-developed sieve textures. Clinopyroxene is observed as euhedral phenocrysts ranging in size from 0.5-4mm with minor magnetite inclusions (figure 5d). Amphibole and clinopyroxene are not observed as co-existing phenocryst phases. Amphibole phenocrysts display breakdown rims to Fe-oxides, clinopyroxene, plagioclase and glass with remnant cores of amphibole, these dehydrated amphiboles preserve euhedral diamond and elongate crystal forms (figure 5c and 5f).

Mineral Geochemistry

Plagioclase

Plagioclase phenocrysts range in composition from An36-73 and display increasing K contents with decreasing An contents (figure 6a). Two divergent groups are displayed in XAn content versus SiO_2, with one group increasing in XAn with increasing SiO_2 content and another of decreasing XAn with increasing SiO_2 (figure 6b). Interestingly both groups appear to diverge from an 'initial composition' of XAn ~0.5 and ~55wt.% SiO_2, as can be observed in figure 6b.

Amphibole

Amphiboles from northwest Flores are Mg-Hornblende in composition with lower Mg# than amphiboles observed at Wai Sano (~Mg#82-94) (figure 6g).

Magnetite

Magnetite range in Fe^{3+}/Fe^{2+} from 1.17-1.23, compositionally poorer in Fe_2O_3 (49.2-51.2wt.%) and richer in TiO_2 (7.3-8.6wt.%) than the NE Sumbawa samples. They also contain lower ZnO (0-0.13wt.%) and Cr_2O_3 (0-0.03wt.%), and higher MnO (1.5-2.6wt.%). Their compositions can be observed in figure 6g.

GEOCHEMISTRY

Distinct compositional differences are observed in the Sumbawan volcanics and basement. The most distinctive difference across the island is a broad increase in potassic content of magmas with distance north from the trench and age. See figures 7 and 8 for compositions of products from the study area, and figures 9a-j for selected major and trace element compositions of analyses from this study.

The modern day eruptive centres of Tambora and Sangeang Api at the north of Sumbawa erupt suites of ultrapotassic, shoshonites spanning ultramafic to intermediate compositions. Tambora erupts lavas spanning 47-57wt.% SiO_2 from basalts, through basaltic-andesite, trachybasalt and basaltic-trachyandesite with the majority falling into trachyandesite and tephri-phonolite. The majority of the Tambora products are shoshonitic (~1.7-5.9wt.% K_2O), with a few outliers having calc-alkaline compositions (~0.8-0.9wt.% K_2O). Sangeang Api erupts magmas with SiO_2 content spanning ~42-54wt.% SiO_2 and compositions from basalt through tephrite-basanite, trachybasalt, basaltic-trachyandesite, phono-tephrite to trachyandesite. Similar to the Tambora eruptives, Sangeang Api lavas are predominantly shoshonitic (~1.8-5.3wt.% K_2O), with some rare high-K calc-alkaline outliers (~1.5-2.3wt.% K_2O). When compared to Tambora lavas, for a given SiO_2 content the Sangeang Api magmas are generally more potassic. The compositions of Tambora, Sangeang Api and the quaternary volcanoes of our study area can be observed in figures 7 and 8. Figures 9a to 9j display selected major and minor element variation with SiO_2 of volcanics in this study and the compositional variations of lavas from Sangeang Api for comparison.

Northeast Sumbawa High-K Calc-alkaline Lavas

To the south of Sangeang Api are the High-K, calc-alkaline, tertiary (~2Ma) magmatic centres of Kota and Kuta, samples from this area range in SiO_2 content from 49-57wt.% SiO_2 from basalts, through basalts, to basaltic-trachyandesites and trachyandesites. These older and more southerly lavas cover a range of SiO_2 concentrations similar to those of Sangeang Api and Tambora, however, they are distinctly less potassic (~0.3-2.3wt.%K_2O) at a given SiO_2 content. They display slightly convex chondrite normalised rare earth element plots (as seen in figure 10b) with average La_N/Yb_N of 7.29, relatively steep LREE profile (average La_N/Sm_N – 2.76) and an average Eu anomaly of 0.85 (Eu/Eu* calculated as Eu/[(Sm+Gd)*0.5]). Characteristic of these lavas are low Rb/Sr

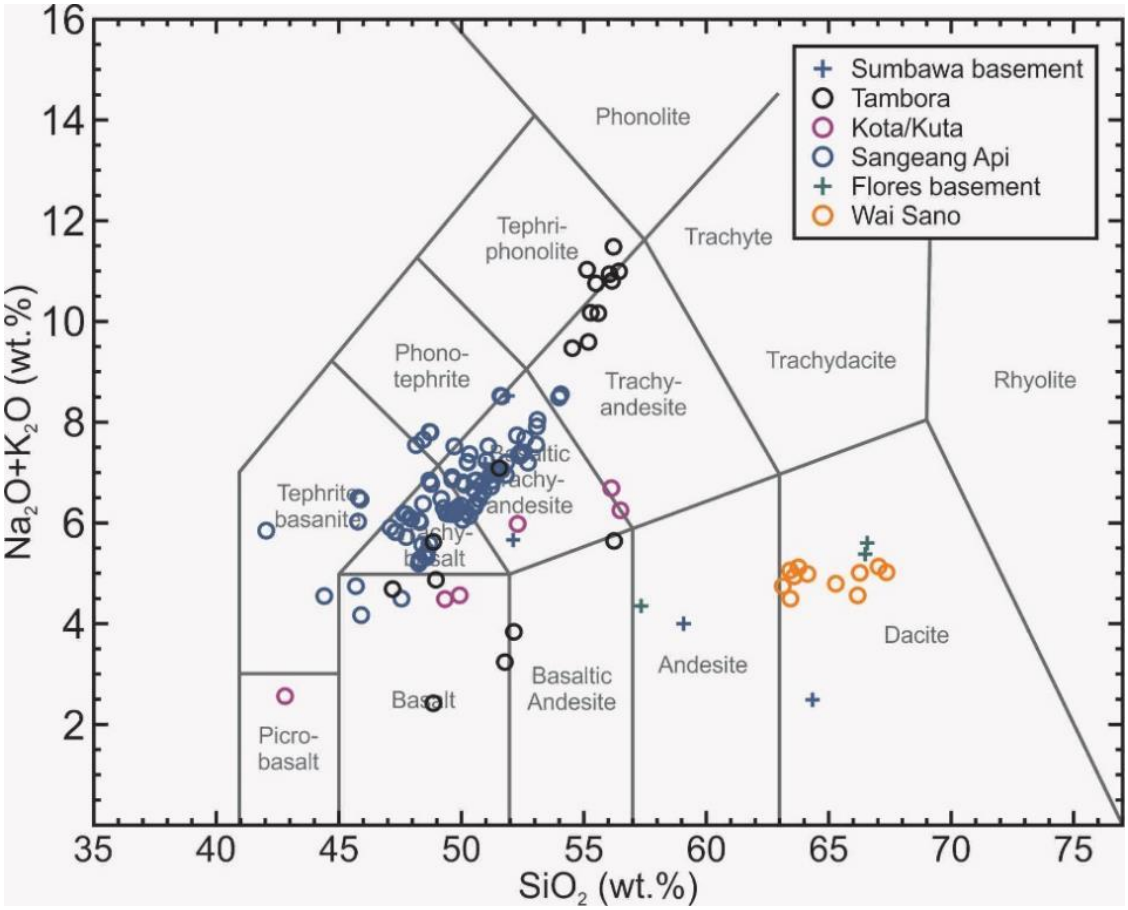

Figure 7: TAS diagram displaying whole rock analyses from this study, as well as Foden, J. and Varne (1980), Foden, John (1986), Gertisser et al. (2012), Turner et al. (2003) and Wheller et al. (1987).

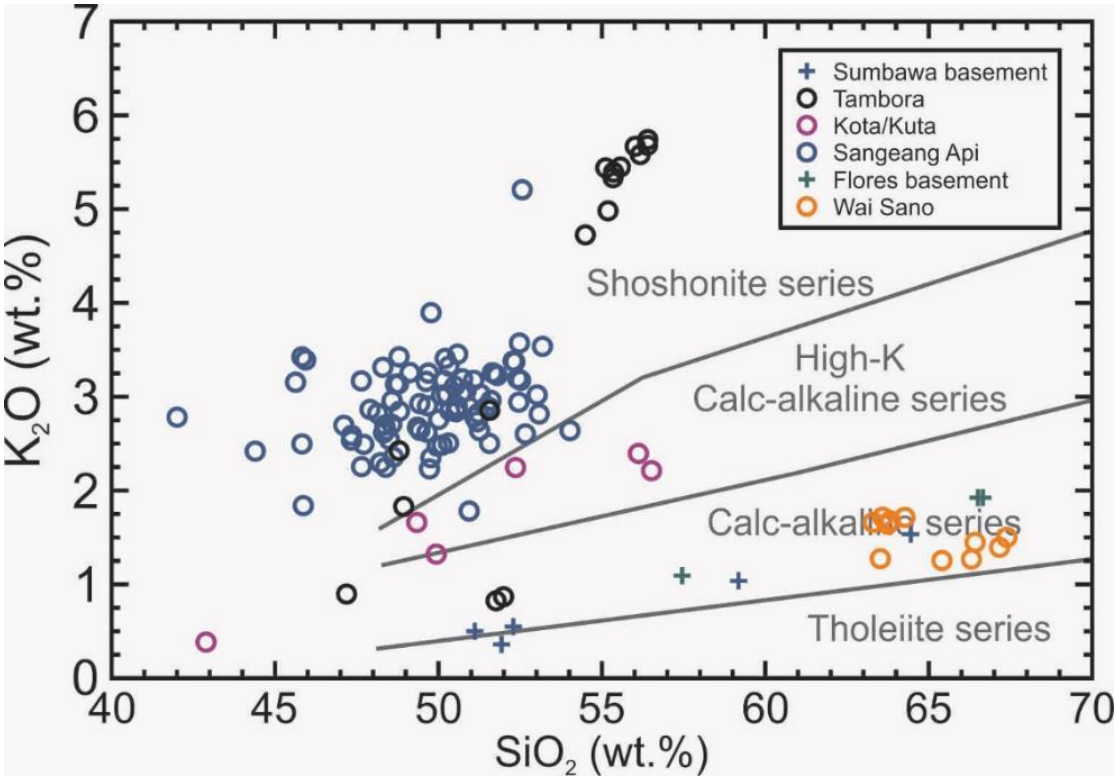

Figure 8: SiO_2 vs K_2O diagram showing the varying affinities of whole rock analyses from this study, as well as Foden, J. and Varne (1980), Foden, John (1986), Gertisser et al. (2012), Turner et al. (2003) and Wheller et al. (1987).

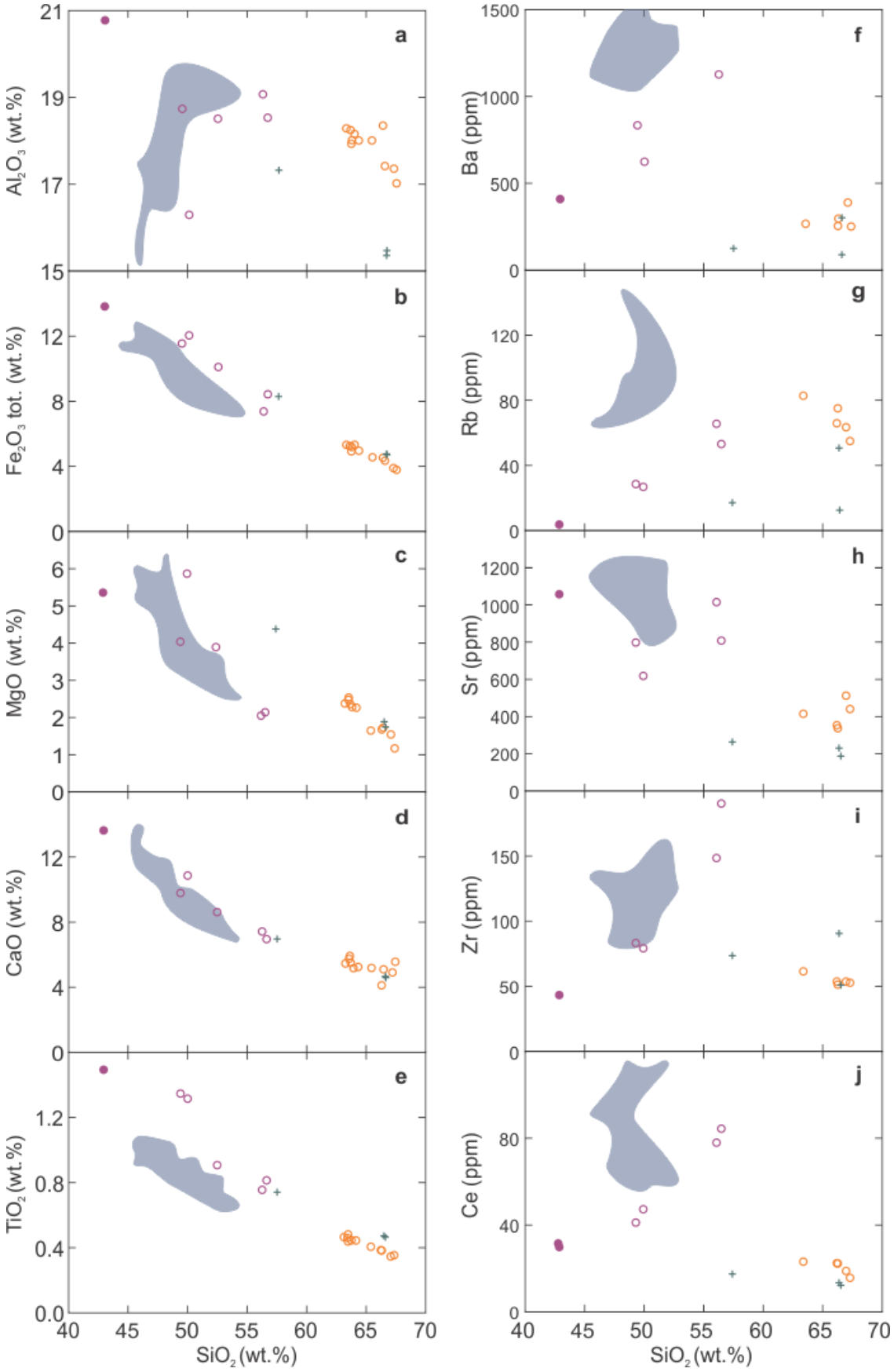

Figure 9a-j: Harker diagrams displaying major (a-e) and trace element (f-j) geochemistry of N. Sumbawa (lavas = open purple circles, gabbro = closed purple circle), Wai Sano (open orange circles) and N. Flores basement (green crosses). With blue region representing variation in nearby Sangeang Api lavas.

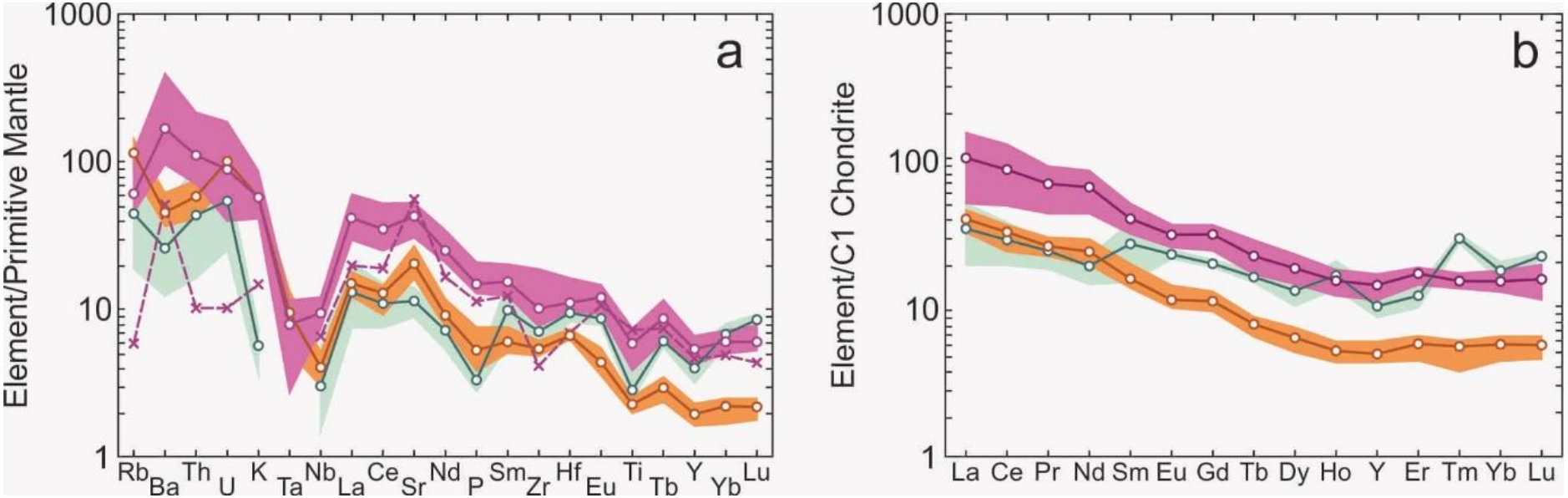

Figure 10a & 10b: Normalised incompatible and rare earth element spider diagrams. Incompatible elements normalised relative to primitive values of McDonough and Sun (1995). Rare earth elements normalised relative to CI Chondrite values of McDonough and Sun (1995). Shaded areas in the background represent the full range of analysed values (purple = N. Sumbawa, orange = Wai Sano & green = N. Flores), solid lines with white circles represent lava analyses purple = N. Sumbawa, orange = Wai Sano & green = N. Flores) and dashed purple line with crosses represents gabbro sample BC14/126 from N. Sumbawa.

Sample	**SN2**	**SN5**	**SN7**	**SN9**	**SN11**	**BC14/ 001**	**BC14/ 002**	**BC14/ 003**	**BC14/ 102**	**BC14/ 110**	**BC14/ 117**	**BC14/ 125**	**BC14/ 126**
Location	Wai Sano	Wai Sano	Wai Sano	Wai Sano	Wai Sano	Labuan Bajo	Labuan Bajo	Labuan Bajo	Sumbawa (N)	W. Kota	Kolo	Kolo	Kolo
Lithology	Dacite	Dacite	Dacite	Dacite	Dacite	Dacite	Andesite	Dacite	Trachy-andesite	Trachy-andesite	Basalt	Basalt	Gabbro
SiO_2	63.52	67.07	66.24	66.34	67.35	66.52	57.45	66.48	56.20	56.53	49.98	49.39	42.93
TiO_2	0.43	0.34	0.38	0.38	0.35	0.46	0.74	0.47	0.75	0.81	1.31	1.34	1.49
Al_2O_3	17.88	17.32	18.31	17.37	16.97	15.41	17.26	15.31	19.03	18.47	16.24	18.71	20.73
Fe_2O_3	4.86	3.79	4.38	4.26	3.70	4.66	8.19	4.61	7.28	8.37	11.90	11.45	13.70
MnO	0.11	0.08	0.09	0.09	0.08	0.12	0.16	0.13	0.22	0.16	0.19	0.20	0.21
MgO	2.46	1.51	1.65	1.68	1.15	1.73	4.37	1.85	2.04	2.13	5.84	4.04	5.34
CaO	5.83	4.85	4.06	5.04	5.54	4.58	6.90	4.57	7.38	6.92	10.79	9.73	13.55
Na_2O	3.39	3.76	3.33	3.62	3.57	3.68	3.27	3.44	4.31	4.01	3.27	2.85	2.18
K_2O	1.65	1.35	1.23	1.39	1.45	1.89	1.04	1.89	2.35	2.19	1.30	1.64	0.38
P_2O_5	0.10	0.11	0.10	0.10	0.09	0.12	0.15	0.12	0.40	0.29	0.25	0.28	0.21
SO_3	b.d.l.	b.d.l.	b.d.l.	b.d.l.	b.d.l.	b.d.l.	b.d.l.	b.d.l.	0.09	b.d.l.	b.d.l.	b.d.l.	0.01
Cl						128.00	55.50	109.00	190.00	155.50	136.50	91.50	449.00
LOI						0.81	0.47	1.12	-0.07	0.10	-1.08	0.35	-0.76
Total	100.23	100.18	99.77	100.27	100.25	99.19	99.53	98.88	100.07	99.90	101.08	99.65	100.76
Mg#	0.50	0.44	0.43	0.44	0.38	0.27	0.35	0.29	0.22	0.20	0.33	0.26	0.28
Na_2O+K_2O	5.04	5.11	4.56	5.01	5.02	5.57	4.31	5.33	6.66	6.20	4.57	4.49	2.56

Table 6: Whole-rock major element analyses from this study. All analyses measured by XRF. Samples with compositions below the detection limit labelled as b.d.l.. Blank cells in table were not analysed for this sample.

Sample	**SN2**	**SN5**	**SN7**	**SN9**	**SN11**	**BC14/ 001**	**BC14/ 002**	**BC14/ 003**	**BC14/ 102**	**BC14/ 110**	**BC14/ 117**	**BC14/ 125**	**BC14/ 126**
Location	Wai Sano	Wai Sano	Wai Sano	Wai Sano	Wai Sano	Labuan Bajo	Labuan Bajo	Labuan Bajo	Sumb. (N)	W. Kota	Kolo	Kolo	Kolo
Lithology	Dacite	Dacite	Dacite	Dacite	Dacite	Dacite	Andesite	Dacite	T-A	T-A	Basalt	Basalt	Gabbro
Method	ICPMS	ICPMS	ICPMS	ICPMS	ICPMS	LA-ICPMS	LA-ICPMS	LA-ICPMS	ICPMS	ICPMS	ICPMS	ICPMS	ICPMS
As	13	16	10	13	16	b.d.l.	b.d.l.	b.d.l.	6	4	4	2	b.d.l.
Ba	262	382	246	288	246	81	119	296	2490	1120	618	832	360
Be	3	2	2	3	2	b.d.l.	b.d.l.	b.d.l.	2.5	2	1	b.d.l.	b.d.l.
Bi	0.3	0.3	0.2	0.3	0.2	b.d.l.	b.d.l.	b.d.l.	b.d.l.	b.d.l.	b.d.l.	b.d.l.	b.d.l.
Co	78	100	72	36	60	20.89	27.27	22.40	48	34	66	58	58
Cr	b.d.l.	b.d.l.	b.d.l.	b.d.l.	b.d.l.	37.32	42.58	b.d.l.	b.d.l.	b.d.l.	70	b.d.l.	b.d.l.
Cs	11.1	9.2	8.8	9.4	8	b.d.l.	b.d.l.	1.38	1.4	1.3	0.5	0.8	1
Cu	26	16	20	14	22	22.51	32.53	11.87	108	42	106	118	44
Ga	19.2	20	19.6	21.2	21.4	11.47	16.51	12.75	22	21	21.4	20.8	23.4
Hf	2	2	1.8	1.8	1.8	2.37	b.d.l.	2.87	4	4.4	2.8	2.8	1.8
In	b.d.l.	b.d.l.	b.d.l.	b.d.l.	b.d.l.	b.d.l.	b.d.l.	0.78	b.d.l.	b.d.l.	b.d.l.	b.d.l.	b.d.l.
Li	30	50	40	30	30				10	10	b.d.l.	10	b.d.l.
Mo	1	1.5	1.5	b.d.l.	1	b.d.l.	b.d.l.	b.d.l.	b.d.l.	1.5	1	b.d.l.	b.d.l.
Nb	3	2.5	2.5	2.5	2	1.00	1.59	3.15	7.5	7.5	5	4.5	4
Ni	8	4	8	10	10	9.63	19.81	b.d.l.	b.d.l.	8	26	12	6
Pb	18	19	17	14	15	3.33	2.19	8.58	14	13	7	9	4
Rb	82.2	63	65.2	74.4	54.2	11.73	16.78	50.12	64.8	52.8	26	28.4	3.2
Sb	0.8	1	0.7	0.8	0.9	b.d.l.	b.d.l.	b.d.l.	0.3	0.3	0.3	0.2	<0.1
Sc	11	9	12	12	11	19.91	30.45	11.02	9	13	39	28	30
Sn	2.1	1	1.9	2.7	1.6	b.d.l.	b.d.l.	b.d.l.	1.2	0.8	1.1	1	1
Sr	405	508	343	333	439	180	263	226	1010	803	613	788	1050
Ta	0.5	0.5	0.4	0.2	0.2	b.d.l.	b.d.l.	b.d.l.	0.4	0.4	0.1	0.2	b.d.l.

Table 7a: Whole-rock trace element analyses from this study. Methods of analysis given in table. Samples with compositions below the detection limit labelled as b.d.l.. Blank cells in table were not analysed for this sample. Abbreviation - T-A: Trachy-andesite

Sample	**SN2**	**SN5**	**SN7**	**SN9**	**SN11**	**BC14/ 001**	**BC14/ 002**	**BC14/ 003**	**BC14/ 102**	**BC14/ 110**	**BC14/ 117**	**BC14/ 125**	**BC14/ 126**
Location	Wai Sano	Wai Sano	Wai Sano	Wai Sano	Wai Sano	Labuan Bajo	Labuan Bajo	Labuan Bajo	Sumbawa (N)	W. Kota	Kolo	Kolo	Kolo
Lithology	Dacite	Dacite	Dacite	Dacite	Dacite	Dacite	Andesite	Dacite	T-A	T-A	Basalt	Basalt	Gabbro
Method	ICPMS	ICPMS	ICPMS	ICPMS	ICPMS	LA-ICPMS	LA-ICPMS	LA-ICPMS	ICPMS	ICPMS	ICPMS	ICPMS	ICPMS
Th	4.3	5.6	4.5	4.6	3.3	1.29	1.65	6.89	16.3	14.2	6.2	5.9	0.8
Tl	0.5	0.4	0.4	0.3	0.4	b.d.l.	b.d.l.	b.d.l.	0.2	b.d.l.	b.d.l.	b.d.l.	b.d.l.
U	2.2	2.1	2.1	2.3	1.5	b.d.l.	0.65	1.85	3.7	3.1	1.3	0.8	0.2
V	75	55	85	80	85	133	194	63	115	165	320	345	385
W	406	370	330	114	264	42.9	60.00	116.82	155	84	128	142	130
Y	9.3	8.5	8	7.5	7.1	13.89	21.16	14.12	24.2	25.6	28	18.1	20.1
Zn	62	66	62	68	70	39.04	47.14	37.52	98	78	78	90	102
Zr	61	53	53	51	52	50.16	72.62	89.70	148	189	79	82	43
La	10.3	9.3	9.8	11.2	8.1	4.98	7.38	12.47	36.4	37.9	25	18.8	12.7
Ce	22.5	18.1	22	22.1	15.3	12.58	18.46	23.59	77.3	83.8	46.7	41	31
Pr	2.65	2.35	2.6	2.8	2.2	1.805	2.44	2.65	8.6	8.8	6.2	5.45	4.3
Nd	11.9	9.95	12.4	13.7	9.6	6.93	10.37	9.59	40.9	38.7	31.2	27	20.9
Sm	2.3	2.1	2.6	2.95	2.1	2.27	5.77	b.d.l.	7.85	6.35	7.05	5.3	4.95
Eu	0.6	0.7	0.6	0.8	0.65	1.25	1.38	b.d.l.	2.15	1.75	2.05	1.5	1.6
Gd	2.4	2.2	2.2	2.6	2	b.d.l.	4.41	3.56	7.4	6.2	7.6	5.2	6
Tb	0.32	0.28	0.3	0.32	0.24	0.575	0.64	b.d.l.	1	0.8	1.06	0.64	0.72
Dy	1.7	1.55	1.5	1.85	1.3	2.54	3.66	3.42	5.25	4.65	5.85	3.75	4.1
Ho	0.34	0.3	0.32	0.32	0.26	0.76	0.86	1.14	0.92	0.92	1.06	0.74	0.88
Er	1.05	1	0.95	1	0.75	1.675	2.15	b.d.l.	3.1	3.1	3	2.4	2.6
Tm	0.15	0.15	0.15	0.15	0.1	b.d.l.	0.74	b.d.l.	0.4	0.45	0.4	0.35	0.35
Yb	1	1	1.05	0.95	0.75	2.49	3.26	b.d.l.	2.95	3	2.6	2.25	2.15
Lu	0.14	0.16	0.16	0.14	0.12	0.535		0.58	0.44	0.5	0.42	0.36	0.3

Table 7b: Whole-rock trace element analyses from this study. Methods of analysis given in table. Samples with compositions below the detection limit labelled as b.d.l.. Blank cells in table were not analysed for this sample. Abbreviation - T-A: Trachy-andesite

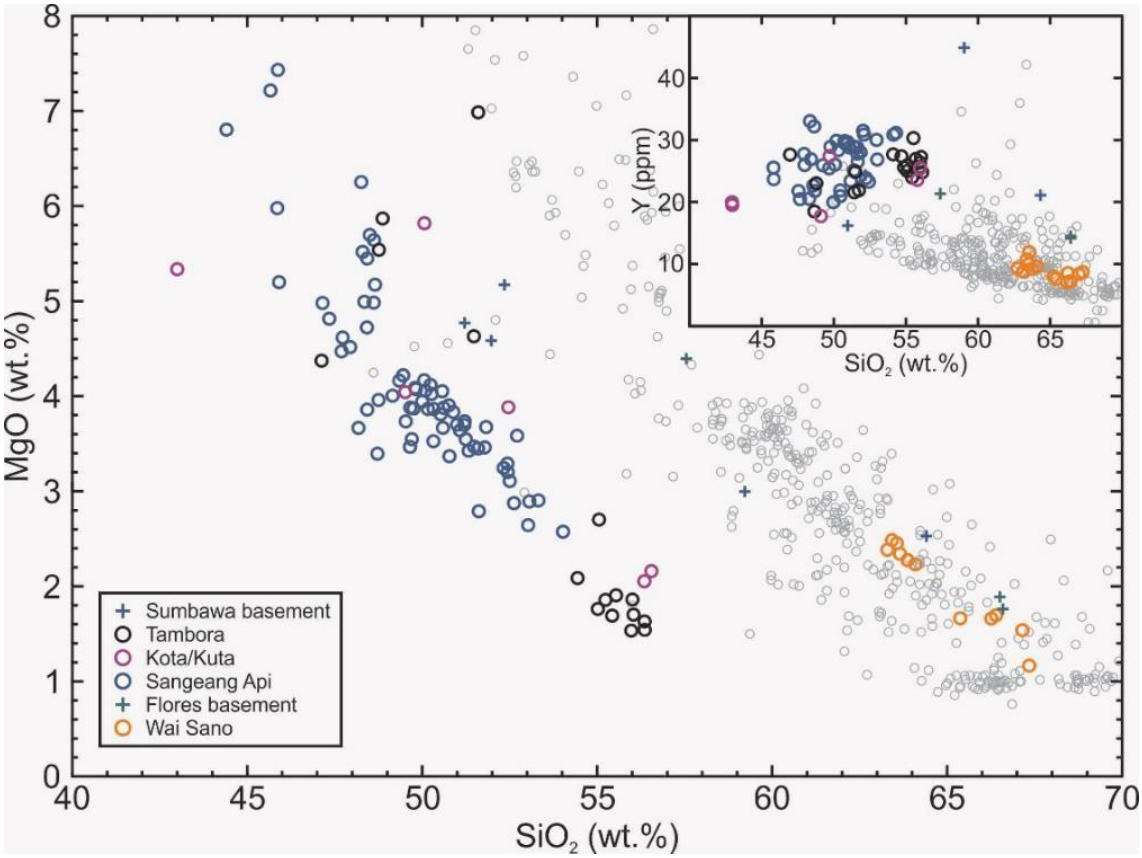

Figure 11: SiO_2 vs MgO diagram with SiO_2 vs Y diagram inset, showing adakitic character of Wai Sano lavas. Coloured symbols as in figure 4, open grey circles represent data taken from a global adakite database sourced from GEOROC database (http://georoc.mpch-mainz.gwdg.de/georoc/).

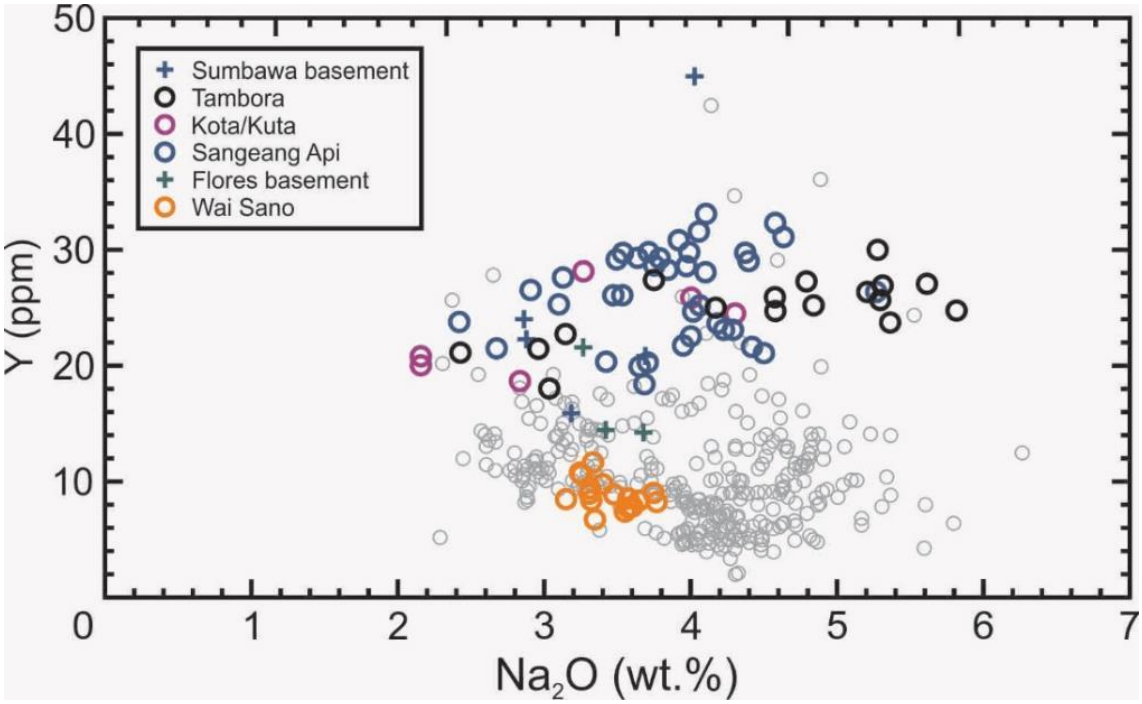

Figure 12: Na_2O vs. Y diagram showing adakitic character of Wai Sano lavas. Coloured symbols as in figure 4, open grey circles represent data taken from a global adakite database sourced from GEOROC database (http://georoc.mpch-mainz.gwdg.de/georoc/).

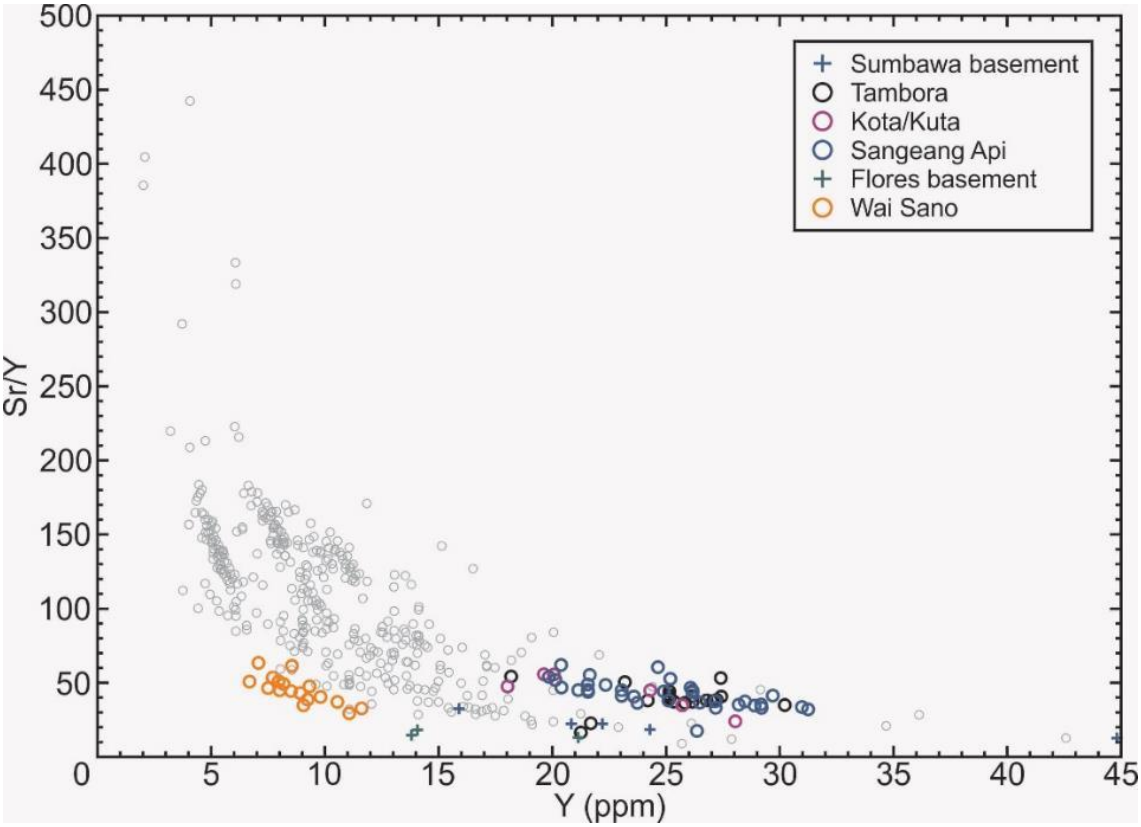

Figure 13: Y vs. Sr/Y diagram showing adakitic character of Wai Sano lavas. Coloured symbols as in figure 4, open grey circles represent data taken from a global adakite database sourced from GEOROC database (http://georoc.mpch-mainz.gwdg.de/georoc/).

ratios (0.036-0.066), high Ba (832-2490ppm) and high Nb/Rb (0.12-0.19). Also collected with the Kota/Kuta lava samples was a gabbro xenolith (BC14/126). This gabbro xenolith is characterised by low SiO_2 (43wt.%), low K_2O (0.4wt.%) and high CaO (13.6wt.%). The chondrite normalised REE profile of the gabbro xenolith is very similar to those of the lavas, but with a shallower profile (La_N/Yb_N – 4.0), especially in the LREE (La_N/Sm_N – 1.6). This sample contains lower Ba (360ppm), Rb/Sr (0.003) and higher Nb/Rb (1.25) than the lavas.

Sumbawa Basement

The tertiary basement of southwest Sumbawa (<20Ma) is composed primarily of calc-alkaline and tholeiitic basaltic-trachyandesite, with andesites and dacites. The distinctly older magmas of the Sumbawa basement display an even more distinct depreciation in their K_2O content (~0.3-0.9wt.%K_2O) for a given SiO_2 content as compared to the younger and more potassic lavas of Kota, Kuta, Sangeang Api and Tambora.

Wai Sano

Lavas from Wai Sano, located in the southwest corner of Flores, display compositions with the characteristics of adakite type lavas. Figures 11 through 13 display these adakitic characteristics. They are dacites with 63-67wt.% SiO_2, 1.1-2.5wt.% MgO and 17-18.3wt.% Al_2O_3. Alongside this, are trace element compositions with low Y (7.1-

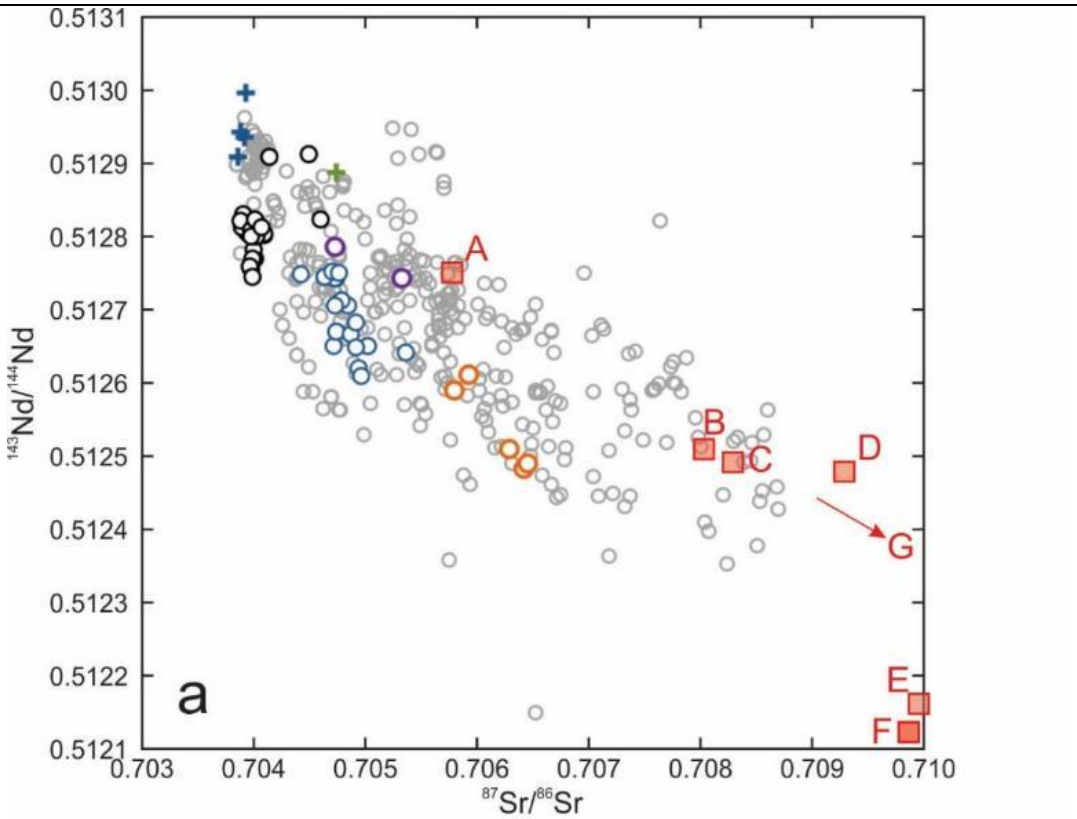
a
$^{143}Nd/^{144}Nd$
$^{87}Sr/^{86}Sr$
A
B
C
D
E
F
G

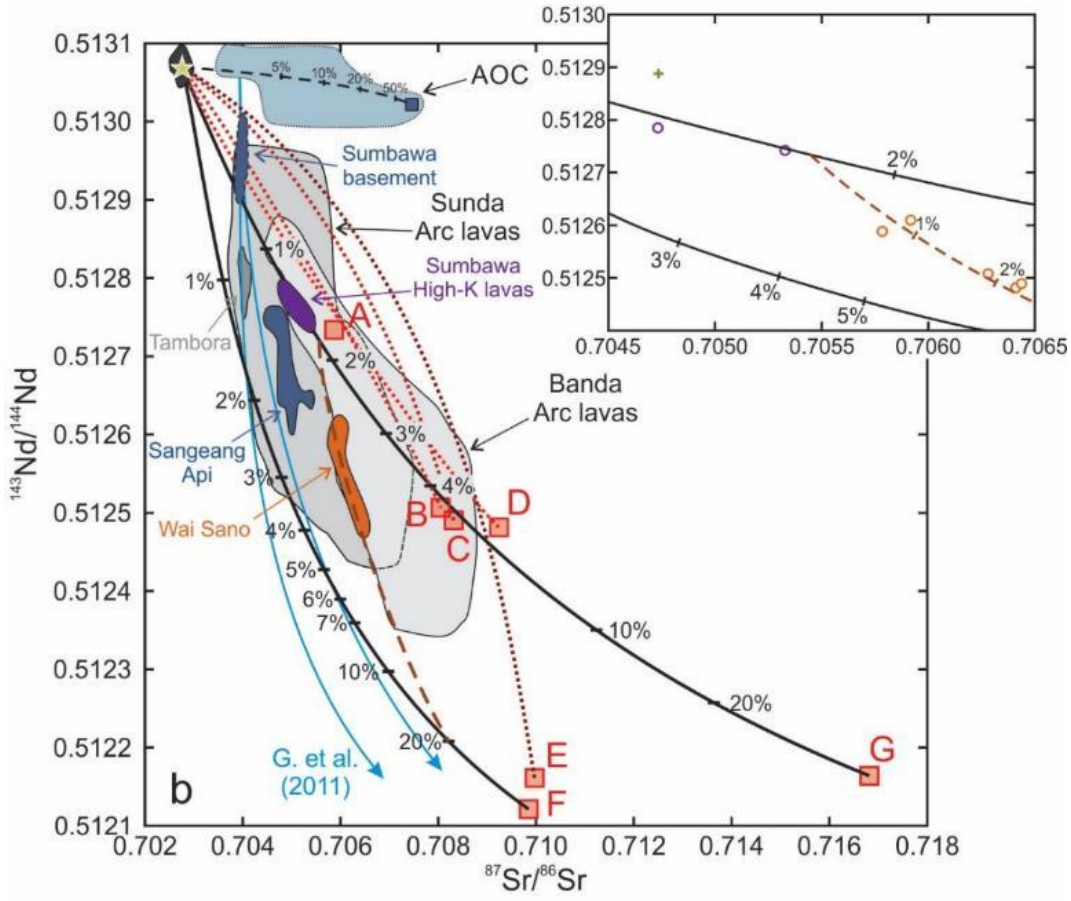
b
AOC
Sumbawa basement
Sunda Arc lavas
Sumbawa High-K lavas
Tambora
Sangeang Api
Wai Sano
Banda Arc lavas
G. et al. (2011)
$^{143}Nd/^{144}Nd$
$^{87}Sr/^{86}Sr$

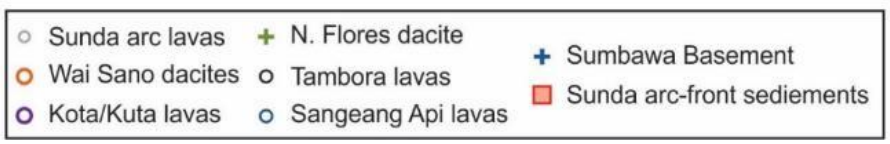
Sunda arc lavas
Wai Sano dacites
Kota/Kuta lavas
N. Flores dacite
Tambora lavas
Sangeang Api lavas
Sumbawa Basement
Sunda arc-front sediements

Figure 14a (previous page): $^{87}Sr/^{86}Sr$ vs. $^{143}Nd/^{144}Nd$ discrimination diagram displaying isotope data from this study and previous studies (Foden, J. & Varne 1980; Gertisser et al. 2012; Turner & Foden 2001; Turner et al. 2003). Symbol key displayed beneath 14b. Sunda arc-front lavas taken from a GeoRoc database (http://georoc.mpch-mainz.gwdg.de/georoc/). Red squares represent Sunda front sediment data values; sediments A (RC14-067), B (V33-79), C (V33-77), D (V33-75), E (V28-341) & G (V28-343) from Ben Othman, White and Patchett (1989) and sediment F (average of DSDP 262) from Vroon et al. (1995). Note the enriched character (low $^{143}Nd/^{144}Nd$ and high $^{87}Sr/^{86}Sr$) of the Wai Sano magmas.

Figure 14b (previous page): Simple mixing models between an I-MORB source, altered ocean crust (AOC) and the Sunda front sediment. Close-up of mixing models inset with compositions of Wai Sano, Kota/Kuta and N-Flores lavas. I-MORB isotopes compositions from Rehkamper and Hofmann (1997) and trace element concentrations from Workman and Hart (2005). Sunda front sediment names are as in figure Na, with isotope and trace element compositions taken from Ben Othman, White and Patchett (1989) and Vroon et al. (1995). Altered ocean crust composition taken from Staudigel et al. (1995). Red dashed lines between I-MORB source and sediments B, C, D and E are considered unlikely mixing trends for the Sunda arc front lavas. Dashed black mixing line represents in main figure displays a mixing line between an I-MORB source and AOC. Solid black lines between I-MORB and sediments F and G bound the majority of Sunda and Banda arc front lavas and as such are considered the most representative sediment mixtures for the Sunda Arc. Numbered ticks represent percentage of material added to I-MORB source. Dashed brown line (main figure and inset) is a representative mixing model for the Wai Sano source region. Blue mixing lines with arrowheads are three-component mixing models argued to be representative of Tambora source region by Gertisser et al. (2012). I-MORB source composition of $^{143}Nd/^{144}Nd$: 0.51307, $^{87}Sr/^{86}Sr$: 0.70275, Nd: 0.67ppm and Sr 9.6ppm.

9.3ppm), low Ba (246-382ppm), low Th/U (1.95-2.7) and low V (55-85) (figure 10a). Compared to the N. Sumbawa lavas, the Wai Sano adakites have much lower Nb/Rb (0.033-0.04) and significantly higher Rb/Sr ratios (0.12-0.22). Chondrite normalised REE profiles are similar to those of the N. Sumbawa samples (see figure 10b), but slightly shallower (average La_N/Yb_N – 6.96) with steeper HREE profiles (average Sm_N/Yb_N 2.76 compared to 2.68) and similar Eu anomalies (average Eu/Eu* - 0.86).

Northwest Flores

Lava samples collected from the northwest corner of Flores, near to the town of Labuan Bajo, are similar in some of their characteristics to the Wai Sano lavas, but show some distinct differences. Compositionally they range from andesites to dacites with 57.5-66.5wt.% SiO_2, 15.3-17.3wt.% Al_2O_3 and 1.7-4.4wt.% MgO. Chondrite normalised REE profiles of the N. Flores lavas are much less steep than those of the Wai Sano and N. Sumbawa samples (La_N/Yb_N 1.35-1.54) (figure 10b). They also display significant differences between the andesitic and dacitic samples, with the dacites having steeper LREE profile (La_N/Sm_N 1.4 compared to 0.8), shallower HREE (Sm_N/Yb_N 0.99 compared to 1.93) and drastically different Eu anomalies (Eu/Eu* of 2.9 compared to 0.8). Similarly, in the trace element compositions the dacites and andesites display compositional differences, with the dacites more depleted in Y (~14ppm compared to 21ppm), Sr (179-226ppm compared to 263ppm) and Sc (11-19ppm compared to 30ppm), whilst all three samples are relatively depleted in Ba (81-295ppm).

ISOTOPIC COMPOSITIONS

The samples from Sumbawa and Flores are isotopically distinct from one another and display significant difference between different volcanic centres. Figure 14a displays isotope variation of the Wai Sano, N. Flores, N. Sumbawa and Sumbawa basement

samples, alongside the range of Sunda Arc lavas, as well as Tambora and Sangeang Api lavas for comparison. Samples from Wai Sano have the highest $^{87}Sr/^{86}Sr$ ratios (0.7062811-0.7064375) and lowest $^{143}Nd/^{144}Nd$ (0.5125392-0.5126607). Basement from both S.W. Sumbawa and Flores (Labuan Bajo) have the highest$^{143}Nd/^{144}Nd$ (between 0.512907 and 0.512994) but contrast in their $^{87}Sr/^{86}Sr$ compositions (0.703874-0.703940 for SW. Sumbawa and 0.7047392 at NW. Flores). Samples from the Pliocene volcanoes of N. Sumbawa are intermediate to those from N. Flores and Wai Sano, with $^{87}Sr/^{86}Sr$ ranging from 0.7047371-0.7053299 and $^{143}Nd/^{144}Nd$ from 0.5127836-0.5128305. The lavas analysed in this study contrast with those of the active volcanoes of the same arc segment (Tambora and Sangeang Api). Due to their proximity it may be expected that the lavas of northern Sumbawa to be most similar to those of the active volcanic centres; indeed they display $^{87}Sr/^{86}Sr$ values in the range recorded by Sangeang Api, however, their $^{143}Nd/^{144}Nd$ values are in the range of those recorded by Tambora.

DISCUSSION

Thermobarometry

Thermobarometry based on mineral-mineral, mineral-glass and single mineral geochemistry is a commonly used tool to determine the physical conditions of a melt in equilibrium with the phenocrysts crystallised from it. Here amphibole (Ridolfi & Renzulli 2012), plagioclase-glass (Lange, Frey & Hector 2009) and clinopyroxene (Nimis 1999) thermobarometry are applied to the analysed mineral compositions of phenocrysts analysed in this study.

Amphibole thermobarometry of Ridolfi and Renzulli (2012) provides estimated pressure, temperature, water content and oxidation state of the magmas in equilibrium with these amphiboles. Figures 15a to 15c display thermobarometrical estimates calculated using the amphibole thermobarometer. The calculated conditions from each sample site are distinct thermobaormetrically. The samples from D. Kota and D. Kuta in northeast Sumbawa record amphibole crystallisation at mid-lower crustal depths (220-700MPa, 7.75-25km), high temperatures (915-1040˚C), moderate water contents (3.8-1.2wt.% H_2O) and relatively low oxidation states (ΔNNO+0.01-1.21). These values are similar to those recorded by the nearby Sangeang Api volcano, which are broadly speaking hotter, deeper, and more oxidised with similar water contents. Compared to this most lavas from Flores are estimated to be significantly shallower (90-190MPa, 3.2-6.8km) and cooler (795-870˚C), with similar water contents (4.5-7.8wt.% H_2O) and are significantly more oxidised (ΔNNO+1.36-2.44). The northwest Flores lavas are to the higher end of temperature, pressure and water contents but to the lower end of oxidation states. The Wai Sano lavas contain two distinct amphibole populations (Mg-Hornblende and Tschermakite) the majority of these are Mg-Hornblende in composition and crystallised from the low P and T samples, whereas the Tschermakite samples record crystallisation at higher pressures (275-380MPa, 9.8-13.4km) and temperatures (910-940˚C), with higher water contents (6.3-7.8wt% H_2O) and lower oxidation states (ΔNNO+1.08-1.60). This suggests two distinct regions of amphibole crystallisation in the crust one at mid-

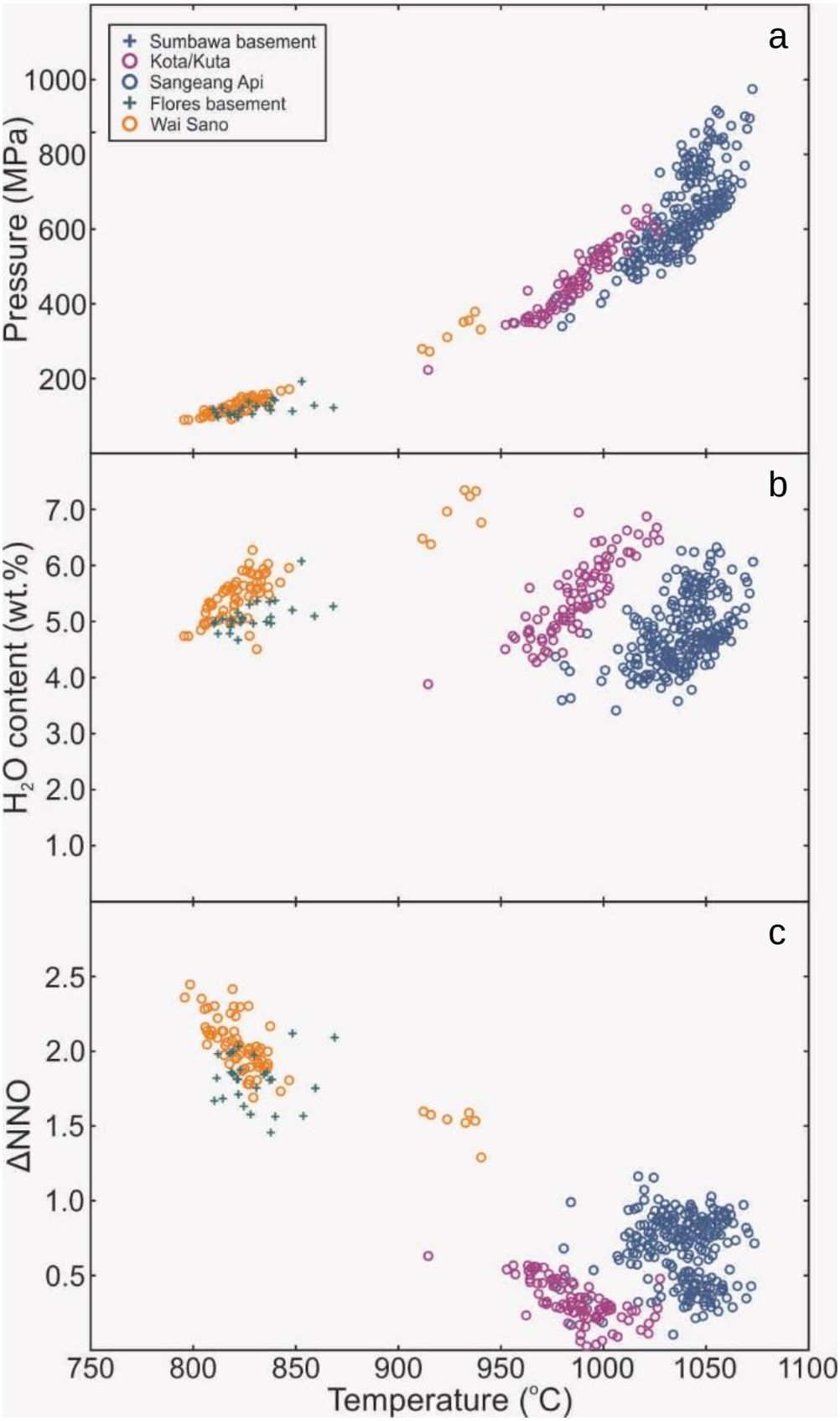

Figure 15a-c: Amphibole thermobarometry estimates determined using Ridolfi & Renzulli (2012) calibrations. Symbols as in figure 4. Oa: Pressure (MPa) vs temperature (°C) estimates. Ob: H_2O_{Melt} (wt.%) vs temperature (°C) estimates. Oc: fO_2 relative to NiNiO buffer (ΔNNO) vs temperature (°C) estimates.

lower crustal depths and one shallower in the crust. Likely these two regions of crystallisation reflect layers of negative buoyancy in the magmatic system of Wai Sano.

Applying the CpxBar program of Nimis & Ulmer (1998) and Nimis (1999) estimates of crystallisation pressure were calculated for the Wai Sano and N. Sumbawan samples at 1000 ˚C. Wai Sano estimates range from 320-650MPa (average of 440MPa), or crustal depths of approximately 11-23km, whilst the N. Sumbawa estimates range from 350-1190MPa (average of 630MPa), equivalent to depths of 12-40km. Clinopyroxene pressure estimates from both Wai Sano and N. Sumbawa overlap with the highest pressure amphibole estimates and extend to even higher pressures, suggesting that in both systems the onset of clinopyroxene crystallisation proceeds that of amphibole. The pressure estimates also suggest that the Wai Sano system is shallower than that of the N. Sumbawan volcanoes, echoing the evidence from amphibole thermobarometry. It seems likely therefore that the magmas from which clinopyroxene crystallised in both systems was more primitive than that which crystallised amphibole.

Northern Sumbawa petrogenesis

The quaternary lavas of northern Sumbawa share many geochemical, mineralogical and petrological features with Sangeang Api, located only ~20km to the north. The major element geochemistry is broadly similar, following similar fractionation trends and broadly similar lithological classifications (basalts-trachyandesites). However, there are a few differences; the SiO_2 content extends to slightly higher contents (42.9-56.5wt.% SiO_2), the northern Sumbawan samples are more sodic (2.2-4.3wt.% Na_2O) and most obviously have lower K_2O contents (0.4-2.4wt.% K_2O), falling into the high-K calc-alkaline trend (figure 8). Trace element compositions of the N. Sumbawa samples are very similar to those of the Sangeang Api samples. The LREE to MREE (La-Dy) profiles are very similar between the N. Sumbawa and Sangeang Api samples, whilst the HREE (Dy-Lu) profile is slightly steeper in the N. Sumbawa lavas and the Eu anomaly is slightly more negative (Eu/Eu*0.85). Incompatible trace element patterns are broadly similar with some differences; more depleted in Rb, Ba and Sr, with stronger depletion in U compared to Th, and enrichment in some of the more incompatible elements (Sm, Hf, Ti, Tb, Yb and Lu) figure Ma). The major and trace element geochemistry of the N. Sumbawa lavas suggests that they formed from a similar process and from a similar source to the Sangeang Api magmas, but with some differences. The more pronounced negative Eu anomaly suggests that the lavas fractionated from a more plagioclase rich cumulate mineralogy. REE profiles suggest that the magmas formed from a combination of smaller melt fractions of a source region with less residual garnet, likely suggesting lower pressures of partial melting in the mantle.

To further constrain the residual mineralogy of the source region, trace element ratios can be interpreted – such as those affected by garnet presence (LREE vs. HREE, etc.). Sm/Yb vs. La/Sm ratios suggest that the source region of the contained approximately 0.6-3.5% modal garnet and formed from low to moderate degree (0.9-10%) equilibrium batch melts. There appears to be an increasing influence of garnet in the source with increasing amounts of partial melting, possibly suggesting progressive melt depletion of the

peridotite source at higher pressures could be stabilising garnet. Ba/Rb vs. Rb/Sr ratios suggest that the source contained some amount of residual amphibole (low Rb/Sr <0.08 and high Ba/Rb >22) due to Rb being more compatible in amphibole than Ba or Sr, whereas the Sangeang Api magmas do not appear to have melted from a source containing residual amphibole. This is supported by Nb/Rb vs. Nb ratios which suggest the influence of amphibole with increased Nb/Rb ratios for a given Nb (Nb more incompatible in amphibole than Rb).

The analysed lavas and gabbro follow distinct geochemical evolution trends of increasing SiO_2, K_2O and Na_2O with decreasing Fe_2O_3, CaO, TiO_2 and Al_2O_3 from the amphibole-gabbro (BC14/126) to the trachyandesitic lavas (e.g. BC14/110) suggesting that they are linked genetically (see figures 9a to 9e). The higher Al_{tot} and lower Mg# of amphibole phenocrysts in the gabbroic samples suggests crystallisation at higher pressures than those crystallised in the lavas (Schmidt 1992). Comparison between clinopyroxene from gabbro and lava samples show that the magmas from which the gabbro had higher average Mg# (~0.85 compared to ~0.80, calculated as $Mg^{2+}/[Mg^{2+}+Fe^{2+}]$) and Fe^{3+}/Fe^{3+} (~0.84 compared to ~0.36). This suggests that the melts from which the gabbroic clinopyroxenes, and hence the gabbros themselves, were formed were more mafic and oxidised than those from which the lava phenocrysts formed. Whilst the Sangeang Api clinopyroxenes overlap considerably in composition, this is not the case for the N. Sumbawa samples, with little to no overlap in the compositions of clinopyroxenes between the xenoliths and lavas. Despite the lack of overlap, the compositions fall on the same evolutionary trend suggesting that they formed from the same parent melt. Phenocrysts of plagioclase within the lavas often show very low anorthite contents suggesting that the magmas from which they formed had undergone significant degassing prior to the onset of plagioclase crystallisation. Recent studies have, however, suggested that plagioclase antecrysts inherited from deep crustal mineral mushes that crystallised from high water content parent magmas may have low An contents (Yanagida et al., 2018; Zellmer et al., 2016). It seems unlikely that this is the case in N. Sumbawa as we observe phenocrysts with anorthite rich cores (~An80) and An-poor overgrowths (~An60), in fitting with a rapid degassing event prior to eruption. Such anorthitic core compositions are similar to analyses from the gabbroic samples with average compositions of ~An79.5. This suggests that the phenocrysts with high anorthite cores represent crystals that could have been inherited from the cumulate suite, however, this seems unlikely as there is no overlap between the compositions of lava and gabbro hosted plagioclase suites overall. The high anorthite contents of the gabbroic feldspars hints at the melts in equilibrium with the crystallising plagioclase having high water contents (>5wt.%) (Feig, Koepke & Snow, 2006).

Rhyolite-MELTS was used to determine phase relationships and magma evolution paths of a primitive N. Sumbawa sample (BC14/110) over a range of pressures (600MPa, 400MPa, 200MPa and 100MPa) and water contents (4.5, 3 and 1.5wt.% H_2O), and the results can be observed in figures 16a-16i. All calculations were undertaken in equilibrium mode, with an initial fO_2 at the Ni-Ni-O buffer and were subsequently unbuffered with respect to fO_2. Varying the water content of the modelled melts has the

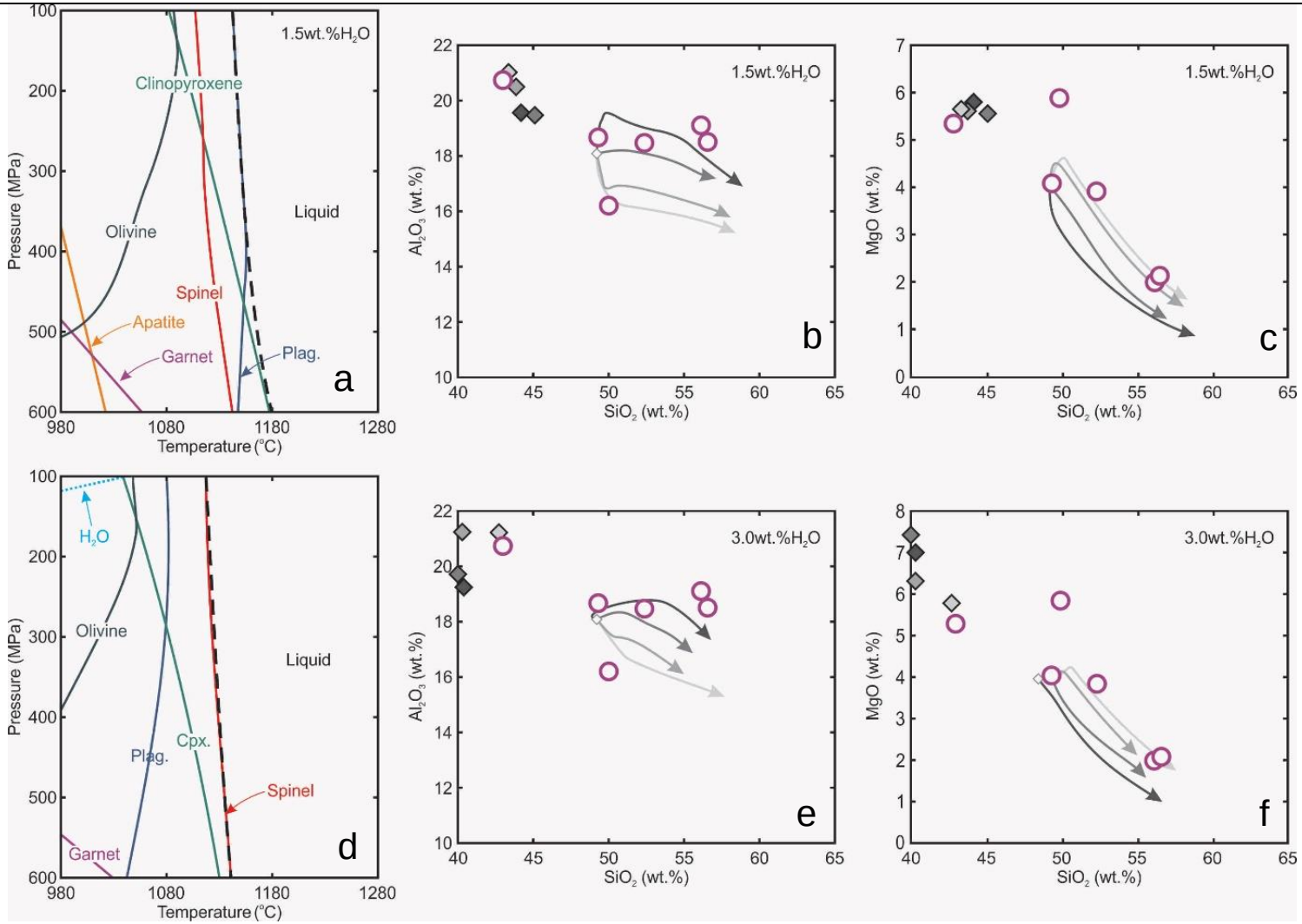
1.5wt.%H2O
Clinopyroxene
Olivine
Liquid
Spinel
Apatite
Garnet
Plag.
a
Pressure (MPa)
Temperature (°C)
b
c
SiO2 (wt.%)
Al2O3 (wt.%)
MgO (wt.%)
3.0wt.%H2O
H2O
Cpx.
d
e
f

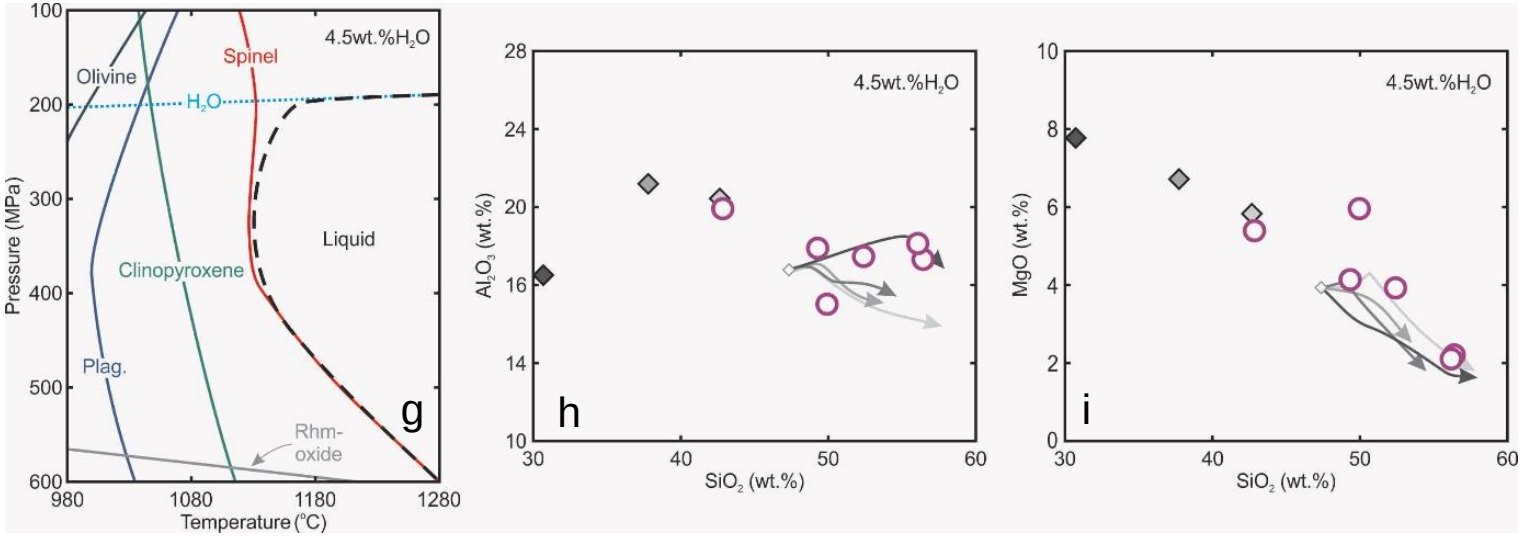

Figure 16a-i (previous page and above): Rhyolite-MELTS modelling for north Sumbawa samples. 16a, 16d & 16g: Phase diagrams between 100-600MPa and 980-1280°C, calculated with 1.5, 3 and 4.5wt.% H_2O respectively. Pb, 16e & 16h: Al_2O_3 vs SiO_2 diagrams displaying N. Sumbawa samples (purple circles), starting model compositions (white diamond), melt evolution paths (grey arrows) and cumulate assemblage compositions (grey diamonds). 16c, 16f & 16i: MgO vs SiO_2 diagrams displaying N. Sumbawa samples, starting model compositions melt evolution paths and cumulate assemblage compositions (symbols for each as in 16b, 16e & 16h).

largest effect on the magma evolution, phase stability and cumulate composition. Decreasing the water content increases the stability field of garnet, apatite, olivine, clinopyroxene and plagioclase whilst simultaneously decreasing the stability of field of magnetite (spinel), hematite (rhm-oxide) and a fluid phase. The threshold for plagioclase becoming stable prior to clinopyroxene increases to greater temperatures at lower water contents. It is difficult to replicate entirely the mineralogical suites of the lavas and gabbros, the most important mineral missing from the modelled suites is amphibole. Melt evolution paths fit well for most of the water contents at all pressures, however, it is difficult to model the Mg content of the lavas without crystallisation at pressures below 200MPa. Cumulate compositions of the final equilibrium assemblage fit the composition of the analysed gabbro only at low pressures (~100MPa) and low water contents (1.5wt.%) (see figures 16a-c), suggesting that the gabbro sample analysed crystallised at mid-lower crustal pressures and low water contents. Thus, the magma from which the gabbroic sample accumulated must have undergone a relatively large amount of degassing at a relatively deep level. Most lava samples appear to fit well with the different pressure trends suggesting that lava chemistry and petrology may reflect melt extraction from distinct magma chambers, located at various pressures throughout the crust. The low water contents of the trends that appear to fit with some of the lava analyses suggests that some of the magmas had undergone a large amount of degassing and devolatilisation. Lava-hosted plagioclase analyses with low An-contents support the suggestion that some of the magmas had low water contents prior to eruption. Despite these models not being able to stabilise amphibole, they agree with amphibole thermobarometry estimates of pressure, temperature and water contents that all suggest mid-lower crustal crystallisation of amphibole-rich lithologies (cumulate gabbros) from magmas with low water content (<3wt.% H_2O).

Wai Sano Adakite characteristics and genesis

Wai Sano magmas bear the major and trace element geochemical signatures of adakites, magmas that are most often interpreted to have formed by slab melting processes (Casillo 2012; Defant & Drummond 1990; Defant & Kepezhinskas 2001; Peacock, Rushmer & Thompson 1994; Yogodzinski et al. 2001). However, a key feature of typical adakitic magmas are primitive isotopic signatures ($^{87}Sr/^{86}Sr$ <0.7045) reflecting their origin from a mid-ocean ridge basalt type slabs. In this characteristic, the Wai Sano magmas diverge from typical adakites as the isotopic values ($^{87}Sr/^{86}Sr$ >0.7062, figure 14) suggest that the region from which they are sourced experienced significant sediment input. Given the high temperatures required to produce a slab melt (>800˚C), it has been suggested that the subducting slab from which the melts originate must be young (<25Ma), and therefore hot, oceanic crust (Defant & Drummond 1990). However, more recent work by Plank et al. (2009), utilising H_2O/Ce ratios of primitive basalts from various different arc settings, suggests that temperatures at the slab surface of old, cold and slowly subducting slabs can be high enough to cause slab melting. Despite this, with the estimated age of the subducted crust being ~145Ma (Syracuse & Abers 2006) and the more radiogenic isotopic compositions require that the Wai Sano magmas could not have formed in a typical slab-melt scenario, therefore other theories for the origin of these magmas must be considered.

The first scenario we must consider is contamination of slab melts by a crustal reservoir with more radiogenic isotope ratios. The crust in this region is predominantly composed of quaternary andesites (fig. 1), contamination of the Wai Sano magmas to the extent required to influence the isotopic values would require the assimilation of so much material as to dramatically alter the chemical composition of the melts. The second possibility is that these are partial melts derived from arc basalts that have underplated the crust. Modern magmas from this region have a significant sediment-derived isotopic composition (Elburg, M. A., van Bergen & Foden 2004; Turner & Foden 2001), similar to that of the Wai Sano magmas. Therefore, basaltic-basanitic melts originated from the partial melting of a garnet-lherzolite mixed with ~2.5-3% sediment of a mixed sediment type including some carbonate component before stalling and crystallising at the base of the lithosphere and not ascending to the surface. Stevenson et al. (2005) found direct evidence for the partial melting of underplated crust in the Pembroke Granulite of New Zealand. Modelling supports the origin of adakitic partial melts from a source region with the bulk composition of an observed dioritic orthogneiss leaving behind a peritectic garnet phase; similar to what would be anticipated by partial melting of underplated mafic roots. There are other modern and fossil adakites around the globe which cannot have originated from the melting of a subducted slab, either because there is no subducted slab in the area to cause melting (e.g. Jaraquay volcanics, Baja California & Arid Hills Papua New Guinea) (Haschke & Ben-Avraham 2005; Peacock, Rushmer & Thompson 1994) or have formed in intraplate settings (e.g. Lingqiu Basin, North China Craton) (Ma et al. 2012; Wang, Liu & Liu 2006). Studies of these slab melt free adakites have supported theories of partial melts of mafic underplating in equilibrium with amphibole and garnet to produce adakite-type magmas (Zhang et al. 2013). Partial melting of a mafic-underplated crust in equilibrium with garnet therefore seems the most likely origin of the Wai Sano adakitic signal. This scenario brings into question the processes required to melt a basalt underplated crust. Typical mantle wedge P-T conditions at the base of the crust would be unable to raise the temperatures to a significant point of melting underplated crust, this presents two options from which partial melting of these stalled mafic bodies would be able to partially melt: fluxing of the upper mantle and lower crust by fluids released from the slab or a metasomatised mantle – a process which would lower the melting point of the mafic underplating and likely alter the isotopic characteristics of any melts to more radiogenic compositions. It seems unlikely that fluids released from the slab or mantle wedge would be able to reach the base of the lithosphere without creating partial melts of the mantle wedge itself. Indeed, there is evidence that adakite signatures are more strongly developed in less hydrous volcanic systems associated with shallow subduction (Zellmer et al., 2012). Or alternatively the thermal structure of the mantle wedge needs to be altered to raise the temperature at the base of the crust. Slab tears can induce the upwelling of deeper, hotter asthenosphere, altering the thermal structure and possibly approaching the melting point of the mafic underplating – a similar process as that suggested to have created the adakitic magmas of Baja California (Negrete-Aranda, Contreras & Spelz 2013).

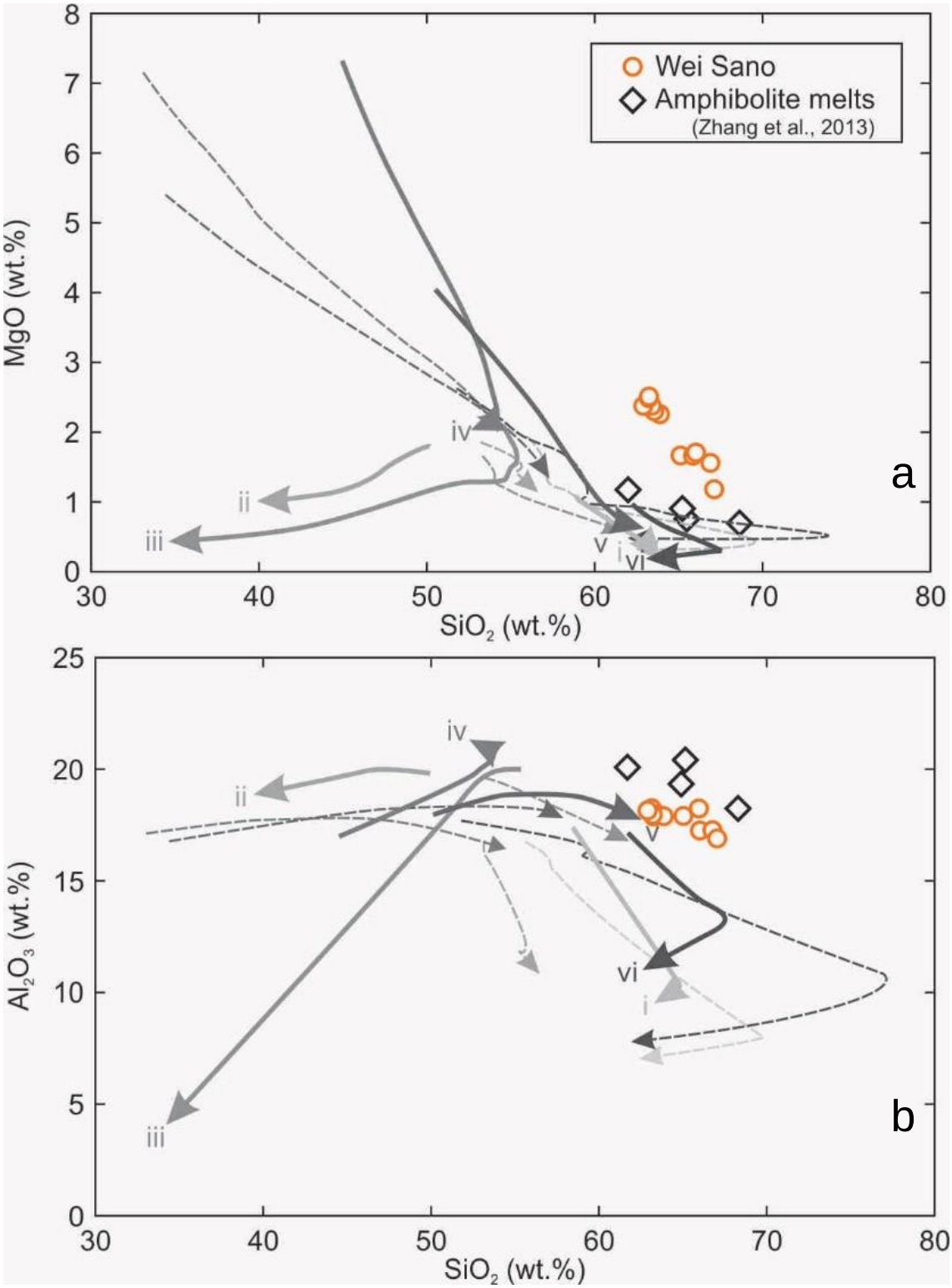

Figure 17a & b: p-MELTS and rhyolite-MELTS modelling of ~5-30% partial melting at 1GPa (solid lines) and 0.5GPa (dashed lines), with Wai Sano analyses from this study (open orange circles), amphibolite melts of Zhang et al. (2013)(open black diamonds) and modelled partial melting evolution trends (i-vi); i: basalt 1 (Le Maitre, 1976), ii: basanite (Le Maitre, 1976), iii: typical Sunda basalt (Turner et al., 2001), iv: garnet hornblendite (Garrido, 2006), v: amphibolite (Zhang et al., 2013) & vi: basalt 2 (Le Maitre, 1976) 17a: MgO vs SiO_2 diagram. 17b: Al_2O_3 vs SiO_2 diagram.

As previously discussed, it has been proposed that the melting of mafic underplated crust in the presence of residual garnet and possibly amphibole could produce a melt with an adakite-type composition. To model the compositional evolution of magmas and restites produced by the partial melting of different lithologies at lower lithospheric pressures (0.5-1GPa) it is possible to use the pMELTS and rhyolite-MELTS software of Ghiorso et al. (2002), Gualda et al. (2012) and Ghiorso and Gualda (2015). To model the P-T conditions and starting composition required to create magma similar to the Wai Sano adakitic lavas, five different starting compositions were subjected to partial melting at 0.5, 0.75 and 1GPa, the results of which can be seen in figures 17a and 17b. pMELTS was used for models at 1GPa and rhyolite-MELTS was used for those at 0.5 and 0.75GPa. The initial materials used are a basanite (Le Maitre, 1976), basalt (Le Maitre, 1976), typical Sunda Arc basalt (Turner et al., 2001), gabbro (Le Maitre, 1976), garnet-hornblendite (Garrido 2006) and amphibolite (Zhang et al., 2013). At each pressure interval ~2-30% partial melts were produced and compared to each other and the Wai Sano magmas. Moderate degree partial melts (10-13%) of basalt and gabbro are most similar to Wai Sano over all three pressure windows, however, they are most similar at 1GPa, producing melts with typical adakite-like characterisitics (SiO_2 >56wt.%, MgO <3wt.%, and Al_2O_3 >15wt.%). Basanites, amphibolites, garnet hornblendites and the Sunda basalt produce melts with MgO and Al_2O_3 in the range expected but do not approach the elevated SiO_2 contents, with all falling below 56wt.%. Based on the compositions of the partial melts produced by both the gabbro and basalt it appears that these are the most likely sources of underplate melting at ~1GPa. To further constrain the source the composition of the restite and the temperatures of melting can be considered. Trace element geochemistry (high Sr, low Y and low Yb) suggests that adakites sources must have residual garnet, therefore any restite produced by the partial melting must have stabilised garnet. Both basalt and gabbro restites produced by this modelling contained up to 30% restitic garnet, consistent with experimental melting of amphibolites under similar conditions (Zhang et al. 2013). The remaining restite mineralogy produced by both models are dominated by sodic plagioclase, clinopyroxene and phlogopite with minor olivine and orthopyroxene. The estimated temperatures of melting for the basalts and gabbros are 720-830°C and 780-880°C respectively. These modelled melting tempertures suggest that these solidified and underplated basaltic/gabbroic sources must be in a region cooler than this before melting can initiate to produce an adakite-type melt. In a typical island arc system for the depth above the slab of ~94km that we would anticipate at Wai Sano (Syracuse & Abers, 2006) (Syracuse & Abers 2006) the expected temperature at 1GPa or ~35km would be approximately ~750-800°C (Kelemen et al. 2013). These estimated temperatures suggest that a mantle diapir of the basaltic composition would not have solidified to be able to remelt at these temperatures, whereas a gabbroic diapir would be more likely to have crystallised under these P-T conditions. To raise the mantle geotherm to a sufficient point to melt stalled lenses or underplated gabbroic material we must consider a novel tectonic setting for the Wai Sano magmas. There is significant evidence of a slab tear underneath western Flores, suggested by Ely and Sandiford (2010) and supported by earthquake foci profiles of the eastern Sunda Arc. It therefore appears possible that the Wai Sano magmas could be produced by 10-13%

partial melting of an underplated region with a 'gabbroic' composition, leaving behind a phlogopite-gabbro restite containing ~20-30% garnet.

Previous studies have suggested that to produce adakitic melts the source needs to be in equilibrium with both amphibole and garnet, however, our modelling suggests that phlogopite is stable at the expense of amphibole. This is likely due to the elevated pressures (~1GPa) that is inferred by the modelling; phlogopite is stable to higher pressures in the mantle than amphibole. Trace element geochemistry supports the viability of these models, with trace element ratios supporting the presence of phlogopite (high Rb/Sr, low Ba/Rb) and garnet (high Sm/Yb) in the source. However, the extremely high amount of garnet inferred from the restite seems unrealistic, despite other authors noting the importance of garnet as a control on melt composition (Zellmer et al., 2012). The evidence presented here supports notions that adakite-type magmas can be formed without any direct influence of slab melting. Adakite magmas can form in island arc systems above old, cold slabs that should, and will not, produce slab melting in a tectonic and geodynamic setting whereby crust underplated by basalts or stalled basaltic diapirs are raised above the threshold for melting and undergo moderate degrees of partial melting leaving behind phlogopite- and garnet-bearing restites.

NW. Flores andesite & dacite petrogenesis

Lavas from the northwest corner of Flores range in composition from andesites to dacites. They appear to be intermediate in their chemistry between the Wai Sano adakites and the potassic volcanics of Sumbawa; relatively low MgO (2-4wt.%), moderate Al_2O_3 (15-17.5wt.%) and low K_2O compared to the Sumbawan volcanics (>2wt.%). The major element geochemistry of these samples might suggest that they formed from the same processes as the Wai Sano adakites to the south. Indeed, they do appear to have some adakitic characteristics such as low Y (15-20ppm) (figure 12) and relatively low $^{87}Sr/^{86}Sr$ (0.7047) and high $^{143}Nd/^{144}Nd$ (0.51293) (figure 14) suggesting origin from a relatively MORB-like source. However, this is not born out by the remaining trace element geochemistry with low Sr/Y (<20) (figure 13) and low Sm/Yb (0.91-1.8) ratios suggesting origin from a source with little to no residual garnet, something incompatible with adakite genesis. Chondrite normalised REE profiles of the andesites and dacites display large variations in the REE profile (figure 10b), with the andesites being more enriched in the HREE than the LREE, and similarly display large variations in Eu anomalies (Eu/Eu* 0.8 to 2.9), suggesting that the dacites accumulated plagioclase whilst fractionation of significant amounts of plagioclase produced the andesites. The magmas have low Ba contents (81-295ppm) and moderate Rb/Sr (0.06-0.22) ratios, suggesting the source region was amphibole poor with a minor amount of pargasite. Plagioclase is a common phase in the NW. Flores magmas with compositions of larger phenocrysts ranging from An40-61 and smaller microlites being very sodic (<Ab96), suggesting that the magmas were relatively water poor at the onset of plagioclase crystallisation and had degassed almost completely at the time of groundmass crystallisation. This is supported by the presence of well-developed decompression breakdown rims on amphibole phenocrysts within the magma. Amphibole thermobarometry suggests shallow crystallisation

(<200MPa) of relatively water-rich magmas (>4.5wt.% H_2O). Likely suggesting that the magmas experienced rapid degassing post-amphibole crystallisation.

Comparison of source regions between volcanic centres

The volcanic centres display significant differences in their isotopic compositions, with perhaps the most striking of these being the high $^{87}Sr/^{86}Sr$ and low $^{143}Nd/^{144}Nd$ of the Wai Sano products. Each volcanic centre can be looked at separately; however, when looked at together they appear to fall on a simple mixing line between an I-MORB source and broadly the regional ocean-floor sediments (figure 14). It has been noted by a number of authors that amongst the active and recent volcanoes of the Sunda-Banda Arc there is a general increase from west to east in $^{87}Sr/^{86}Sr$ and vice-versa in Nd isotopes (Elburg, Marlina A. et al. 2002; Elburg, M. A., van Bergen & Foden 2004; Handley et al. 2014; Turner & Foden 2001). This has been attributed to a general increase in sediment input and a greater influence of Australian continental material towards the east. The samples from northeast Sumbawa sit on this trend, whereas the samples from Flores sit on opposite sides of these trends. Sr- and Nd-isotopes of the Wai Sano samples suggest that these melts may have experienced significant sediment input at the source of melting. Another possible source of these uplifted Sr-isotope values could be interaction with a crustal carbonate reservoir, similar to that of Merapi volcano in central Java (Deegan et al. 2010). This, however, is an unlikely causation of these increased Sr-isotope values as there is no petrological evidence of mingling with a carbonate source and is not reflected in the geochemistry of the samples (relatively low calcium content). Compared to this the nearby, but significantly older, samples from the basement of northwest Flores show depressed Sr isotope values; likely reflecting the lack of sediment and continental material from the impact of the Australian continent.

Simple mixing curves provide evidence for several different sediments that have influenced the source region of this segment and that sediments may have change both spatially and temporally. The northeast Sumbawa samples fall on a mixing line between an I-MORB source and a modern day Sunda front sediment of terrigenous/biogenic composition (figure 14b), likely analogous to sediment input at the source region. Theses samples also sit very close to the broader regional mixing trend between an I-MORB source and modern day Sunda front pelagic clay. Likely these samples were mixed with approximately 1-2% terrigenous/biogenic material. The Wai Sano samples are significantly different to this and reflect a trend away from the regional pelagic mixing trend towards a mixing curve with a Sunda front carbonate sediment (figure 14b), suggesting that these samples have been experienced a mixing event with a combination of both pelagic and biogenic material. Our mixing model suggests that these samples have experienced mixing with around 1.7% pelagic material and 0.8-2.1% biogenic material. Given that these samples likely represent partial melts of stalled basaltic melts, their isotopic composition likely reflect the mantle wedge composition from which their basaltic 'parent' was sourced.

Basement samples from both Sumbawa and Flores define Sr-Nd arrays that span to isotopic compositions above the regional isotopic trend between the I-MORB source and

sediment G (see figure 14b). Gertisser et al. (2012) proposed that the lavas of Tambora are sourced from an I-MORB mantle mixed with ~3% fluids from altered ocean crust (AOC) and <1% sedimentary material of a sediment like sediment F from this study. Figure 14b shows that the SW. Sumbawan basement defines an array lying directly on the mixing line defined by their study, suggesting that fluids derived from AOC played a role in the source region of the Sumbawa Basement, but with less sediment input (<0.5%). It is impossible to conclude from one sample which mixing model suits the NW Flores basement best, however, given its isotopic similarity to the SW Sumbawa samples there is a suggestion of a similar three-component source region with a greater influence of AOC fluids (<5%).

CONCLUSIONS & FURTHER QUESTIONS

Despite their close geographical spacing, the volcanic centres and basement lavas display significant differences in their geochemistry and petrology. From the high-K calc-alkaline basalts-trachandesites of Kota & Kuta in northeast Sumbawa, to the calc-alkaline andesites and dacites of northwest Flores and the adakitic dacites of Wai Sano. Complex tectonic and geodynamic processes need to have occurred throughout this small region to create such distinctive products. From earthquake foci and the work of Ely and Sandiford (2010) it is clear that there is a developing slab tear underneath west Flores and possibly east Sumbawa. It has also been suggested that there are deep crustal faults between the islands of Sumbawa and Flores. This geodynamic and tectonic setting presents an interesting laboratory to investigate the processes of slab rollback, slab tear and crustal faulting on the temporo-spatial petrology and geochemistry of volcanism.

Whilst at first glance the magmas of Sangeang Api and Kota/Kuta seem similar, the petrological processes that have driven magma evolution at the distinct volcanic centres and the tectonic settings under which they formed appear very different. The tectonic evolution of eastern Sumbawa in the ~2Ma since the eruption of the Kota/Kuta volcanics has had a dramatic effect on the geochemistry and petrology of the erupted products. How the geochemistry of the centres and the tectonic evolution of the area relate requires further investigation.

Geothermohygrobarometry provides evidence that all systems studied were hydrous (4-7.5wt.% H_2O) and in each system clinopyroxene is likely to have crystallised at greater depths than amphibole, but with distinct differences in P-T-fO_2 crystallisation conditions. The Wai Sano and Northwest Flores samples share many similaraties, both crystallising at shallow depths (less than 400MPa), low temperatures (less than 950˚C) and being highly oxidised (up to ΔNNO+2.5). However, the Wai Sano samples are slightly more oxidised than the Northwest Flores lavas and contain some amphibole antecrysts that record deeper, hotter and wetter conditions. Northest Sumbawa lavas record conditions more similar to those of the nearby Sangeang Api, however, they tend to be slightly shallower, cooler and less oxidised whilst being slightly wetter.

This study presents evidence for the production of adakite-style magmas in active volcanic arcs were slab melting is unlikely, if not impossible. It is common in island arcs

throughout the globe for the crust to be underplated by stalled basaltic melts. In the majority of circumstances these mafic underplates will crystallise and remain untouched geologic processes. However, in rare circumstances were the geotherm of the lower crust can be raised, either by slab tearing combined with corner flow, or other processes, these mafic underplates will melt. It has previously been proposed that partial melting of basalt or amphibolite at pressures ~1GPa will produce adakitic style melts, leaving behind garnet-rich restites. Previously, these processes have been observed in intraplate regions or continental arcs, here we present evidence for the partial melting of mafic underplates in an oceanic arc setting.

REFERENCES

Ben Othman, D, White, WM & Patchett, J 1989, 'The geochemistry of marine sediments, island arc magma genesis, and crust-mantle recycling', *Earth and Planetary Science Letters*, vol. 94, no. 1, 1989/08/01, pp. 1-21.

Bowin, C, Purdy, GM, Johnston, C, Shor, G, Lawver, L, Hartono, HMS & Jezek, P 1980, 'Arc-continent collision in Banda Sea region', *AAPG Bulletin*, vol. 64, no. 6, pp. 868-915.

Castillo, PR 2012, 'Adakite petrogenesis', *Lithos*, vol. 134, Mar, pp. 304-316.

Centre, IS 2017, 'On-line Event Bibliography', Internatl. Seis. Cent., Thatcham, United Kingdom, <http://www.isc.ac.uk/event_bibliography>.

Deegan, FM, Troll, VR, Freda, C, Misiti, V, Chadwick, JP, McLeod, CL & Davidson, JP 2010, 'Magma–Carbonate Interaction Processes and Associated CO2 Release at Merapi Volcano, Indonesia: Insights from Experimental Petrology', *Journal of Petrology*, vol. 51, no. 5, pp. 1027-1051.

Deer, WA, Howie, RA & Zussman, J 2013, *An introduction to the rock-forming minerals*, Third edition. edn, eds RAa Howie & Ja Zussman, The Mineralogical Society.

Defant, MJ & Drummond, MS 1990, 'Derivation of some modern arc magmas by melting of young subducted lithosphere', *Nature*, vol. 347, no. 6294, 10/18/print, pp. 662-665.

Defant, MJ & Kepezhinskas, P 2001, 'Evidence suggests slab melting in arc magmas', *Eos, Transactions American Geophysical Union*, vol. 82, no. 6, pp. 65-69.

Elburg, MA, Foden, JD, van Bergen, MJ & Zulkarnain, I 2005, 'Australia and Indonesia in collision: geochemical sources of magmatism', *Journal of Volcanology and Geothermal Research*, vol. 140, no. 1–3, 1/30/, pp. 25-47.

Elburg, MA, van Bergen, M, Hoogewerff, J, Foden, J, Vroon, P, Zulkarnain, I & Nasution, A 2002, 'Geochemical trends across an arc-continent collision zone: magma sources and slab-wedge transfer processes below the Pantar Strait volcanoes, Indonesia', *Geochimica et Cosmochimica Acta*, vol. 66, no. 15, 8/1/, pp. 2771-2789.

Elburg, MA, van Bergen, MJ & Foden, JD 2004, 'Subducted upper and lower continental crust contributes to magmatism in the collision sector of the Sunda-Banda arc, Indonesia', *Geology*, vol. 32, no. 1, p. 41.

Ely, KS & Sandiford, M 2010, 'Seismic response to slab rupture and variation in lithospheric structure beneath the Savu Sea, Indonesia', *Tectonophysics*, vol. 483, no. 1-2, Mar, pp. 112-124.

Foden, J 1986, 'The petrology of Tambora volcano, Indonesia: A model for the 1815 eruption', *Journal of Volcanology and Geothermal Research*, vol. 27, no. 1, 1986/01/01, pp. 1-41.

Foden, J & Varne, R 1980, 'The petrology and tectonic setting of quaternary - recent volcanic centers of lombok and sumbawa, sunda arc', *Chemical Geology*, vol. 30, no. 3, 1980, pp. 201-226.

Garrido, CJ 2006, 'Petrogenesis of Mafic Garnet Granulite in the Lower Crust of the Kohistan Paleo-arc Complex (Northern Pakistan): Implications for Intra-crustal Differentiation of Island Arcs and Generation of Continental Crust', *Journal of Petrology*, vol. 47, no. 10, pp. 1873-1914.

Garwin, SL 2000, 'The setting, geometry and timing of intrusion-related hydrothermal systems in the vicinity of the Batu Hijau porphyry copper-gold deposit, Sumbawa, Indonesia', Ph.D. thesis, University of Western Australia.

Geologi, ID 1976, *Geology, Flores (west): sub-region no. 3, Nusa Tenggara Timur*, Nusa Tenggara Timur, Indonesia Direktorat Geologi, Indonesia.

Gertisser, R, Self, S, Thomas, LE, Handley, HK, Van Calsteren, P & Wolff, JA 2012, 'Processes and Timescales of Magma Genesis and Differentiation Leading to the Great Tambora Eruption in 1815', *Journal of Petrology*, vol. 53, no. 2, Feb, pp. 271-297.

Ghiorso, MS & Gualda, GAR 2015, 'An H2O–CO2 mixed fluid saturation model compatible with rhyolite-MELTS', *Contributions to Mineralogy and Petrology*, vol. 169, no. 6, p. 53.

Ghiorso, MS, Hirschmann, MM, Reiners, PW & Kress, VC 2002, 'The pMELTS: A revision of MELTS for improved calculation of phase relations and major element partitioning related to partial melting of the mantle to 3 GPa', *Geochemistry, Geophysics, Geosystems*, vol. 3, no. 5, pp. 1-35.

Gualda, GAR, Ghiorso, MS, Lemons, RV & Carley, TL 2012, 'Rhyolite-MELTS: a Modified Calibration of MELTS Optimized for Silica-rich, Fluid-bearing Magmatic Systems', *Journal of Petrology*, vol. 53, no. 5, pp. 875-890.

Handley, HK, Blichert-Toft, J, Gertisser, R, Macpherson, CG, Turner, SP, Zaennudin, A & Abdurrachman, M 2014, 'Insights from Pb and O isotopes into along-arc variations in subduction inputs and crustal assimilation for volcanic rocks in Java, Sunda arc, Indonesia', *Geochimica et Cosmochimica Acta*, vol. 139, pp. 205-226.

Haschke, M & Ben-Avraham, Z 2005, 'Adakites from collision-modified lithosphere', *Geophysical Research Letters*, vol. 32, no. 15, pp. n/a-n/a.

Hilton, DR & Craig, H 1989, 'A helium isotope transect along the Indonesian archipelago', *Nature*, vol. 342, no. 6252, 12/28/print, pp. 906-908.

Hilton, DR, Hoogewerff, JA, van Bergen, MJ & Hammerschmidt, K 1992, 'Mapping magma sources in the east Sunda-Banda arcs, Indonesia: Constraints from helium isotopes', *Geochimica et Cosmochimica Acta*, vol. 56, no. 2, 1992/02/01/, pp. 851-859.

Kelemen, PB, Rilling, JL, Parmentier, EM, Mehl, L & Hacker, BR 2013, 'Thermal Structure due to Solid-State Flow in the Mantle Wedge Beneath Arcs', in *Inside the Subduction Factory*, American Geophysical Union, pp. 293-311.

Lange, RA, Frey, HM & Hector, J 2009, 'A thermodynamic model for the plagioclase-liquid hygrometer/thermometer', *American Mineralogist*, vol. 94, no. 4, Apr, pp. 494-506.

Leake, BE, Woolley, AR, Arps, CES, Birch, WD, Gilbert, MC, Grice, JD, Hawthorne, FC, Kato, A, Kisch, HJ, Krivovichev, VG, Linthout, K, Laird, J, Mandarino, JA, Maresch, WV, Nickel, EH, Rock, NMS, Schumacher, JC, Smith, DC, Stephenson, NCN, Ungaretti, L, Whittaker, EJW & Guo, YZ 1997, 'Nomenclature of amphiboles: Report of the subcommittee on amphiboles of the International Mineralogical Association, Commission on New Minerals and Mineral Names', *Canadian Mineralogist*, vol. 35, Feb, pp. 219-246.

Ma, Q, Zheng, JP, Griffin, WL, Zhang, M, Tang, HY, Su, YP & Ping, XQ 2012, 'Triassic "adakitic" rocks in an extensional setting (North China): Melts from the cratonic lower crust', *Lithos*, vol. 149, Sep, pp. 159-173.

McDonough, WF & Sun, Ss 1995, 'The composition of the Earth', *Chemical Geology*, vol. 120, no. 3–4, 3/1/, pp. 223-253.

Morimoto, N 1988, 'Nomenclature of Pyroxenes', *Mineralogy and Petrology*, vol. 39, no. 1, September 01, pp. 55-76.

Negrete-Aranda, R, Contreras, J & Spelz, RM 2013, 'Viscous dissipation, slab melting, and post-subduction volcanism in south-central Baja California, Mexico', *Geosphere*, vol. 9, no. 6, pp. 1714-1728.

Nimis, P 1999, 'Clinopyroxene geobarometry of magmatic rocks. Part 2. Structural geobarometers for basic to acid, tholeiitic and mildly alkaline magmatic systems', *Contributions to Mineralogy and Petrology*, vol. 135, no. 1, 1999/04/01, pp. 62-74.

Nugroho, H, Harris, R, Lestariya, AW & Maruf, B 2009, 'Plate boundary reorganization in the active Banda Arc–continent collision: Insights from new GPS measurements', *Tectonophysics*, vol. 479, no. 1, 2009/12/10/, pp. 52-65.

Pacey, A, Macpherson, CG & McCaffrey, KJW 2013, 'Linear volcanic segments in the central Sunda Arc, Indonesia, identified using Hough Transform analysis: Implications for arc lithosphere control upon volcano distribution', *Earth and Planetary Science Letters*, vol. 369–370, no. 0, 5//, pp. 24-33.

Peacock, SM, Rushmer, T & Thompson, AB 1994, 'Partial melting of subducting oceanic crust', *Earth and Planetary Science Letters*, vol. 121, no. 1, 1994/01/01/, pp. 227-244.

Plank, T., Cooper, L.B., Manning, C.E., 2009. Emerging geothermometers for estimating slab surface temperatures. Nature Geoscience 2, 611-615.

Porritt, RW, Miller, MS, O'Driscoll, LJ, Harris, CW, Roosmawati, N & Teofilo da Costa, L 2016, 'Continent–arc collision in the Banda Arc imaged by ambient noise tomography', *Earth and Planetary Science Letters*, vol. 449, 9/1/, pp. 246-258.

Rehkamper, M & Hofmann, AW 1997, 'Recycled ocean crust and sediment in Indian Ocean MORB', *Earth and Planetary Science Letters*, vol. 147, no. 1–4, 3//, pp. 93-106.

Ridolfi, F & Renzulli, A 2012, 'Calcic amphiboles in calc-alkaline and alkaline magmas: thermobarometric and chemometric empirical equations valid up to 1,130A degrees C and 2.2 GPa', *Contributions to Mineralogy and Petrology*, vol. 163, no. 5, May, pp. 877-895.

Self, S, Gertisser, R, Thordarson, T, Rampino, MR & Wolff, JA 2004, 'Magma volume, volatile emissions, and stratospheric aerosols from the 1815 eruption of Tambora', *Geophysical Research Letters*, vol. 31, no. 20.

Siebert, L, Simkin, T & Kimberly, P 2011, *Volcanoes of the World: Third Edition (3)*, University of California Press, Berkeley, US.

Staudigel, H, Davies, GR, Hart, SR, Marchant, KM & Smith, BM 1995, 'Large scale isotopic Sr, Nd and O isotopic anatomy of altered oceanic crust: DSDP/ODP sites417/418', *Earth and Planetary Science Letters*, vol. 130, no. 1, pp. 169-185.

Stevenson, JA, Daczko, NR, Clarke, GL, Pearson, N & Klepeis, KA 2005, 'Direct observation of adakite melts generated in the lower continental crust, Fiordland, New Zealand', *Terra Nova*, vol. 17, no. 1, pp. 73-79.

Stothers, RB 1984, 'The Great Tambora Eruption in 1815 and its Aftermath', *Science*, vol. 224, no. 4654, pp. 1191-1198.

Syracuse, EM & Abers, GA 2006, 'Global compilation of variations in slab depth beneath arc volcanoes and implications', *Geochemistry Geophysics Geosystems*, vol. 7, May, p. 18.

Turner, S & Foden, J 2001, 'U, Th and Ra disequilibria, Sr, Nd and Pb isotope and trace element variations in Sunda arc lavas: predominance of a subducted sediment component', *Contributions to Mineralogy and Petrology*, vol. 142, no. 1, Oct, pp. 43-57.

Turner, S, Foden, J, George, R, Evans, P, Varne, R, Elburg, M & Jenner, G 2003, 'Rates and processes of potassic magma evolution beneath Sangeang Api volcano, East Sunda arc, Indonesia', *Journal of Petrology*, vol. 44, no. 3, Mar, pp. 491-515.

Vroon, PZ, van Bergen, MJ, Klaver, GJ & White, WM 1995, 'Strontium, neodymium, and lead isotopic and trace-element signatures of the East indonesian sediments:

provenance and implications for banda arc magma genesis', *Geochimica et Cosmochimica Acta*, vol. 59, no. 12, pp. 2573-2598.

Wang, X-C, Liu, Y-S & Liu, X-M 2006, 'Mesozoic adakites in the Lingqiu Basin of the central North China Craton: Partial melting of underplated basaltic lower crust', *Geochemical Journal*, vol. 40, no. 5, pp. 447-461.

Wheller, GE, Varne, R, Foden, JD & Abbott, MJ 1987, 'Geochemistry of quaternary volcanism in the Sunda-Banda arc, Indonesia, and three-component genesis of island-arc basaltic magmas', *Journal of Volcanology and Geothermal Research*, vol. 32, no. 1, 1987/06/01, pp. 137-160.

Workman, RK & Hart, SR 2005, 'Major and trace element composition of the depleted MORB mantle (DMM)', *Earth and Planetary Science Letters*, vol. 231, no. 1–2, 2/28/, pp. 53-72.

Yanagida, Y., Nakamura, M., Yasuda, A., Kuritani, T., Nakagawa, M., Yoshida, T., 2018. Differentiation of a Hydrous Arc Magma Recorded in Melt Inclusions in Deep Crustal Cumulate Xenoliths from Ichinomegata Maar, NE Japan. Geochemistry, Geophysics, Geosystems 19, 838-864.

Yogodzinski, GM, Lees, JM, Churikova, TG, Dorendorf, F, Woerner, G & Volynets, ON 2001, 'Geochemical evidence for the melting of subducting oceanic lithosphere at plate edges', *Nature*, vol. 409, no. 6819, 01/25/print, pp. 500-504.

Zellmer, G., Iizuka, Y., Miyoshi, M., Tamura, Y., Tatsumi, Y., 2012. Lower crustal H2O controls on the formation of adakitic melts.

Zellmer, G.F., Pistone, M., Iizuka, Y., Andrews, B.J., Gómez-Tuena, A., Straub, S.M., Cottrell, E., 2016. Petrogenesis of antecryst-bearing arc basalts from the Trans-Mexican Volcanic Belt: Insights into along-arc variations in magma-mush ponding depths, H2O contents, and surface heat flux. American Mineralogist 101, 2405-2422.

Zhang, C, Holtz, F, Koepke, J, Wolff, PE, Ma, C & Bédard, JH 2013, 'Constraints from experimental melting of amphibolite on the depth of formation of garnet-rich restites, and implications for models of Early Archean crustal growth', *Precambrian Research*, vol. 231, pp. 206-217.

Chapter 6

The influence of tectonic processes on the geochemistry of island arc systems: A case study of the Sunda Arc, Indonesia

Statement of Authorship

Title of Paper	The influence of tectonic processes on the geochemistry of island arc systems: A case study of the Sunda Arc, Indonesia
Publication Status	☐ Published ☐ Accepted for Publication ☐ Submitted for Publication ☑ Unpublished and Unsubmitted work written in manuscript style
Publication Details	For submission to Earth and Planetary Science Letters as: Cooke, B., Foden, J. The influence of tectonic processes on the geochemistry of island arc systems: A case study of the Sunda Arc, Indonesia

Principal Author

Name of Principal Author (Candidate)	Benjamin Cooke		
Contribution to the Paper	Database creation, data processing, data interpretation, manuscript preparation and content, creation of diagrams		
Overall percentage (%)	80		
Certification:	This paper reports on original research I conducted during the period of my Higher Degree by Research candidature and is not subject to any obligations or contractual agreements with a third party that would constrain its inclusion in this thesis paper.		
Signature		Date	13/11/2017

Co-Author Contributions

By signing the Statement of Authorship, each author certifies that:

i. the candidate's stated contribution to the publication is accurate (as detailed above);

ii. permission is granted for the candidate in include the publication in the thesis; and

iii. the sum of all co-author contributions is equal to 100% less the candidate's stated contribution.

Name of Co-Author	Professor John Foden		
Contribution to the Paper	Data interpretation and review		
Signature		Date	13/11/2017

ABSTRACT

Host to >100 active volcanoes, the Sunda-Banda island-arc system of Indonesia stretches ~5000km from the Indian Ocean in the west to the Banda Sea in the east. Lavas erupted along its length are typical of island arc systems, spanning calc-alkaline to ultrapotassic compositions. Co-variations in along-arc isotopic compositions highlight the increasing influence of continental derived material towards the Banda Sea and collision of the Australian continent with the arc system. With Sr and Pb isotopes increasing from 0.7050-0.7098 and 38.5-29.5 respectively and Nd isotopes decreasing from 0.5128-0.5124. The Java sector of the arc displays smaller co-variance in Sr and Nd isotopes, but no significant change in Pb isotopes, suggesting small amounts of source heterogeneity and interaction between ascending melts and the continental crust upon which the active volcanoes are built. Across-arc the Sunda lavas display compositional variations, most notably increasing K_2O with increasing depth-to-slab (H). Increasing H is also associated with increasing Nd isotopes, decreasing Sr isotopes and increasing La/Yb (normalised to chondrite values). These variations suggest larger amounts of garnet in the source region and thus an increasing depth of partial melting. There also appears to be an increase in the influence of residual phlogopite with depth to slab (high Rb/Sr and low Ba/Rb). It therefore appears that these arc-rear ultrapotassic magmas are associated with deep melting of metasomatized (primarily phlogopite enriched) mantle wedge. Earthquake foci profiles and seismic tomographic sections suggest that a number of these ultrapotassic volcanic centres are located above slab tear windows. Pb isotopic compositions of the ultrapotassic volcanoes hosted above the slab windows (Muriah, Sangeang Api & Tambora) suggest the influence of asthenosphere with an Indian Ocean Island Basalt (I-OIB) signature. This suggests that the influx of asthenosphere through these slab windows has not only raised the mantle geotherm allowing for the partial melting of metasomatic veins (above the garnet stability threshold) but mixed in asthenosphere with an I-OIB signature. The island of Sumbawa provides an example for the developing influence of slab tears on the expression of lavas at the surface. With >2Ma high-K volcanics giving way to ultrapotassic leucitites and modern shoshonitic lavas. Initial high-K lavas are representative of 'normal' Sunda arc-front magmatism, prior to the development of a slab window. Miocene leucitites occur from the initial small degree partial melting of phlogopite-enriched metasomatic veining as upwelling hot asthenosphere raises the mantle geotherm. Modern shoshonitic volcanism is a product of increasing degrees of metasomatic vein partial melting and may have moved away from the trench as the slab window moved northwards with respect to the trench. Earthquake profiles likewise suggest that these slab windows are bound by discontinuities in the subducting slab, channelling fluid-mobile elements from the slab and overriding sediments to the shallow lithosphere. This is paired with lithospheric faulting, which further channels these metasomatic melts and disaggregates cumulate xenolith piles, enhancing their entrainment in ascending magmas. Lavas of the Sunda arc evidence the strong influence that tectonic processes exert on magma production in the sub-arc mantle and the geochemistry of erupted products.

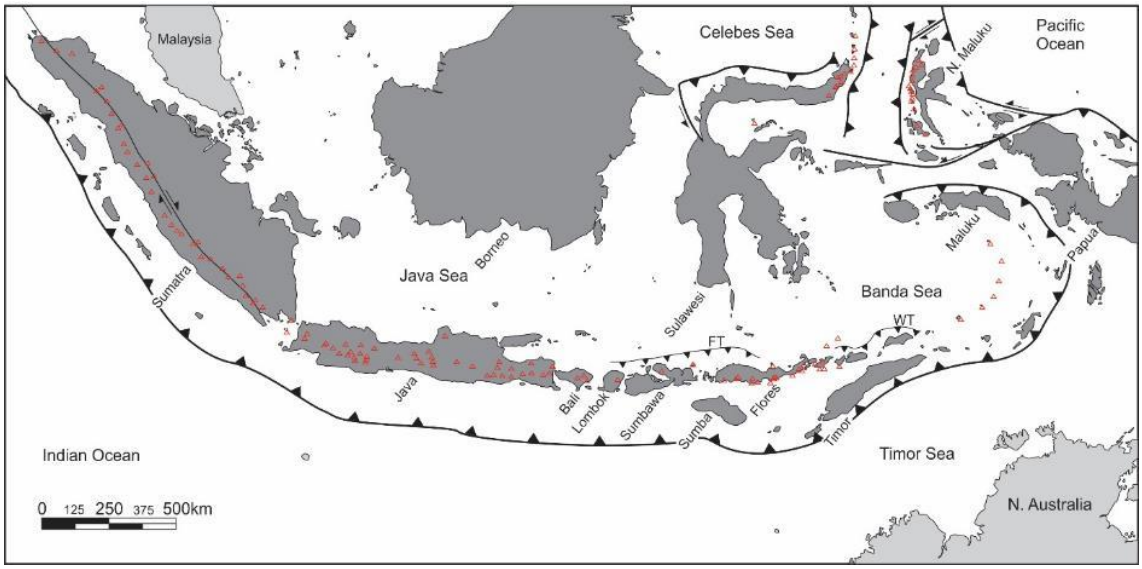

Figure 1: Tectonic map of the Sunda Arc displaying the locations of Holocene volcanic centres (Siebert et al., 2011). FT and WT are the Flores Thrust and Wetar Thrust respectively.

INTRODUCTION

The Sunda Arc of Indonesia is a near ~5000km long archipelago stretching from the Andaman Islands in the west to the lesser Sunda Islands in the east and is home to more than 100 volcanoes (figure 1), including some of the most violent volcanoes in recorded history; including the 1883 eruption of Krakatau, the 1815 eruption of Tambora and the eruption of the Lake Toba super-volcano approximately 74,000 years ago (Siebert et al., 2011). At its eastern flank, the Sunda Arc is separated from the Banda Arc by a ~300km region of seismic and volcanic activity. The Banda Arc curves 180˚ around the eastern edge of the Banda Sea from Wetar in the southwest to Seram in the north.

Today, the Sunda-Banda Arc is composed of continental and oceanic crust of the Eurasian plate that has evolved by the edition of blocks of crustal material rifted during the break-up of the Indian and Australian continents from the early Cretaceous to the modern day (Hall, 2011; Hall, 2012). The western Sunda Arc is built on a promontory of the Eurasian continental crust known as Sundaland, a region of thin weak lithosphere composed of Jurassic and older Tethyan and Gondwanan material (Hall, 2011). This Sundaland core extends through Southeast Asia to the eastern edge of the island of Sumatra. During the late Jurassic and early Cretaceous the Sundaland promontory experienced subduction both from the south (northwards subduction of Meso-Tethyan Ocean) and the north (southwards subduction of the Pacific Ocean), before the collision of Australian crustal fragments around 90Ma largely terminated subduction in the region (Hall, 2011). Around 45Ma subduction on the Sundaland margins initiated once again as the Australian continent rifted from Antarctica and began to move northwards. A spur of Australian continental crust (Sula Spur) collided with the eastern extent of the Sundaland promontory around 25Ma (Hall, 2011). Around 15Ma, as the Sula Spur pushed northwards, subduction rollback initiated into the embayment of oceanic crust separating the Sula Spur from the Australian Continental crust (Hall, 2011; Hall, 2012). This continues to the modern day with the 180˚ curvature of the Banda Sea. Initially this was

thought to have developed by two slabs subducting with opposite polarity (Bowin et al., 1980; Cardwell and Isacks, 1978; Das, 2004; McCaffrey, 1989), however more recent studies have attributed this curvature to subduction rollback (Hall, 2012; Spakman and Hall, 2010), indeed seismic tomography shows this concave oceanic embayment sitting in the mantle beneath the Banda Sea (Hall and Spakman, 2015; Spakman and Hall, 2010).

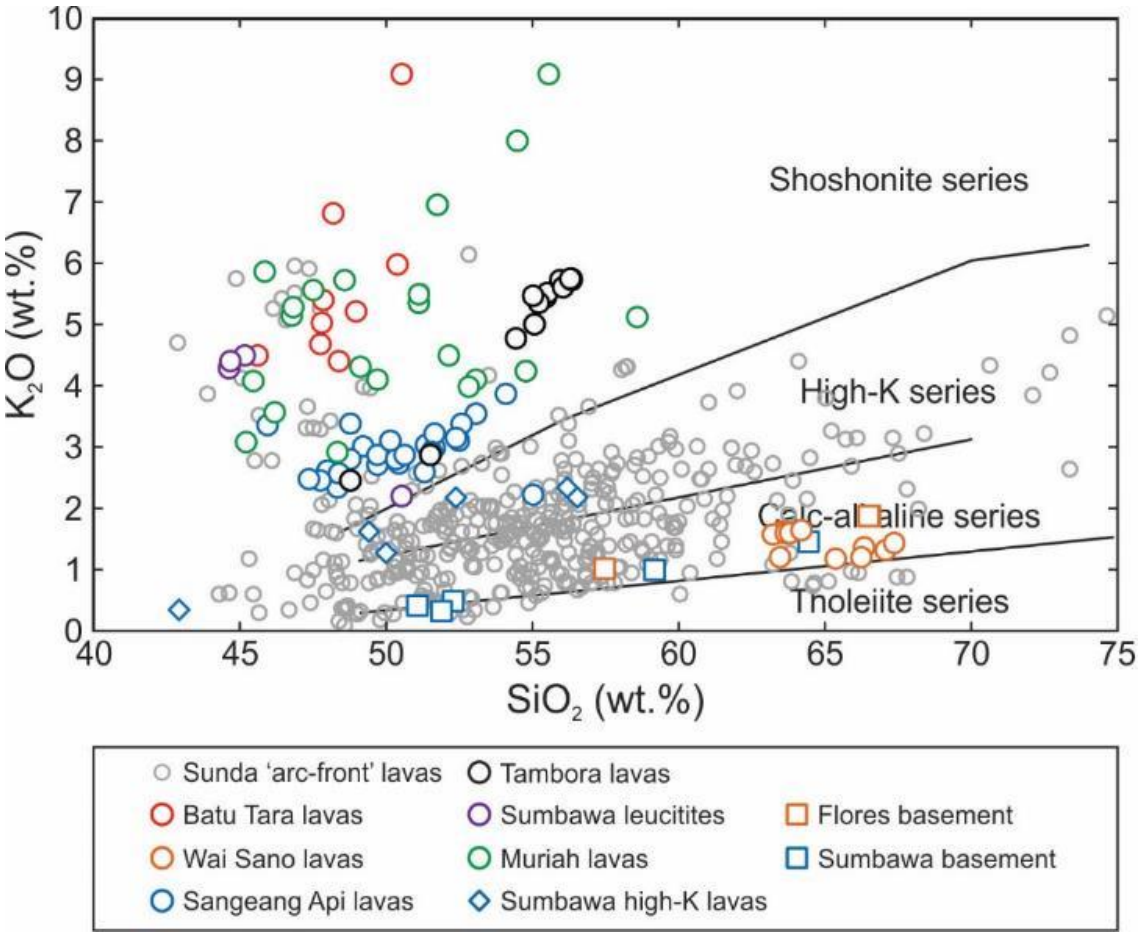

Figure 2: K_2O vs. SiO_2 diagram displaying compositions of Sunda Arc lavas, lavas of selected volcanic centres and volcanogenic/intrusive basement geology. Data compiled from a GeoRoc database (http://georoc.mpch-mainz.gwdg.de/georoc/), previous work of this thesis, Gertisser et al. (2012) and unpublished data provided by Professor John Foden. Symbols are given in table below diagram.

Volcanism in the Sunda Arc is predominantly hosted on the southern edges of the islands of the archipelago. Largely, the lavas of these volcanoes belong to the typical island arc calc-alkaline to high-K calc-alkaline series (Wheller et al., 1987). A small number of active volcanoes in the arc stand out from this near-trench pattern, volcanoes such as Muriah, Tambora, Sangeang Api and Batu Tara are located at greater distances from the trench (up to 390km) and the slab surface (up to 294km). Figure 2 shows compositional differences of Sunda Arc lavas and basement geology, note that most lavas fall into the calc-alkaline or high-K series with some notable distinctions (e.g. Muriah, Tambora, Sanegang Api, Batu Tara and the Sumbawan leucitites). These volcanoes are also distinctive in their chemical and isotopic compositions, with high K_2O contents, elevated $^{87}Sr/^{86}Sr$ and low $^{143}Nd/^{144}Nd$ values. Pacey et al. (2013) proposed that quaternary volcanoes in the central Sunda Arc (from Java through to Flores) are distributed in four

linear segments; further suggesting that the quaternary centres in the eastern section (Central Sumbawa through to Central Flores) are aligned in a NNW-SSE linear segment controlled by weaknesses in the arc lithosphere. Their calculations do not, however, take into account the active, ultrapotassic volcanic centres of Sangeang Api and Tambora, whose distributions they suggest are not controlled by the same processes as the other volcanic centres of the central Sunda Arc. Wheller et al. (1987) determined four sectors in the Sunda-Banda Arc based on the numerical parameter K_{Si} (average of $100.K_2O/[SiO_2\text{-}40]$) from major element analyses of samples from specific volcanoes.

Various studies have displayed distinct trends in the products of volcanoes across the entirety of the Sunda Arc, as well as smaller sections of the arc (Foden and Varne, 1980; Gasparon and Varne, 1998; Handley et al., 2014; Handley et al., 2011; Pacey et al., 2013; Stolz et al., 1990; Turner and Foden, 2001; Wheller et al., 1987; Whitford, 1975; Whitford and Jezek, 1982; Whitford et al., 1979). From west to east a broad increase in $^{87}Sr/^{86}Sr$ values and Pb isotopes ($^{206}Pb/^{204}Pb$, $^{207}Pb/^{204}Pb$ and $^{208}Pb/^{204}Pb$), and similarly a decrease in $^{143}Nd/^{144}Nd$ isotopes has been noted (Turner and Foden, 2001), with particularly steep trends in the isotopic data towards the Sunda-Banda transition (Elburg et al., 2004). These trends have been suggested to be due to increasing influence of sediment and slab-derived fluids in the source regions of the arc magmas (Elburg et al., 2005; Elburg et al., 2004; Turner and Foden, 2001). This increase in sediment and fluid has been attributed to the influence of continental detritus entering the subduction zone via the incipient impact of the Australian continental crust. The influence of the Australian continent in the mantle wedge has been supported by He isotopes, which suggest the addition of a component from the degassing of continental crust. Small-scale variations in these trends and those of other isotopes ($\delta^{18}O$ and $^{176}Hf/^{177}Hf$) have been noted in the Java region, with increasing $^{87}Sr/^{86}Sr$ and $^{208}Pb/^{204}Pb$ from west to central Java and decreasing from central to east Java (Handley et al., 2014; Handley et al., 2011). Java is built on continental crust, unlike the arc to the east towards the Sunda-Banda transition. The trends across Java have been proposed to be due to a combination of crustal assimilation (ophiolitic/carbonate material) processes and heterogeneity in the sediment composition inputted to the source region (Handley et al., 2014; Handley et al., 2011). To the east of the Sunda Arc, beyond the Sunda-Banda transition, opposing trends in isotopic data can be observed with $^{176}Hf/^{177}Hf$ and $^{143}Nd/^{144}Nd$ increasing, alongside $^{87}Sr/^{86}Sr$ and Pb isotope values from the southwest into the northeast Banda Sea (Nebel et al., 2011; Vroon et al., 1993). This has similarly been suggested to reflect the influence of the incipient collision of the Australian continental crust in the Sunda-Banda transition zone and the loss of this influence to the northeast of the Banda Sea (Nebel et al., 2011; Vroon et al., 1993).

This work attempts to forge an understanding of the links between the along- and across-arc variations in geochemistry and the evolving tectonic climate of the Sunda Arc. Particularly in the development of 'rear-arc' ultrapotassic volcanism.

METHODS OF DATA SELECTION

To further investigate along and across arc variations in the geochemistry of the Sunda Arc volcanoes a database of lavas from the Andaman Islands in the west to the Banda Sea

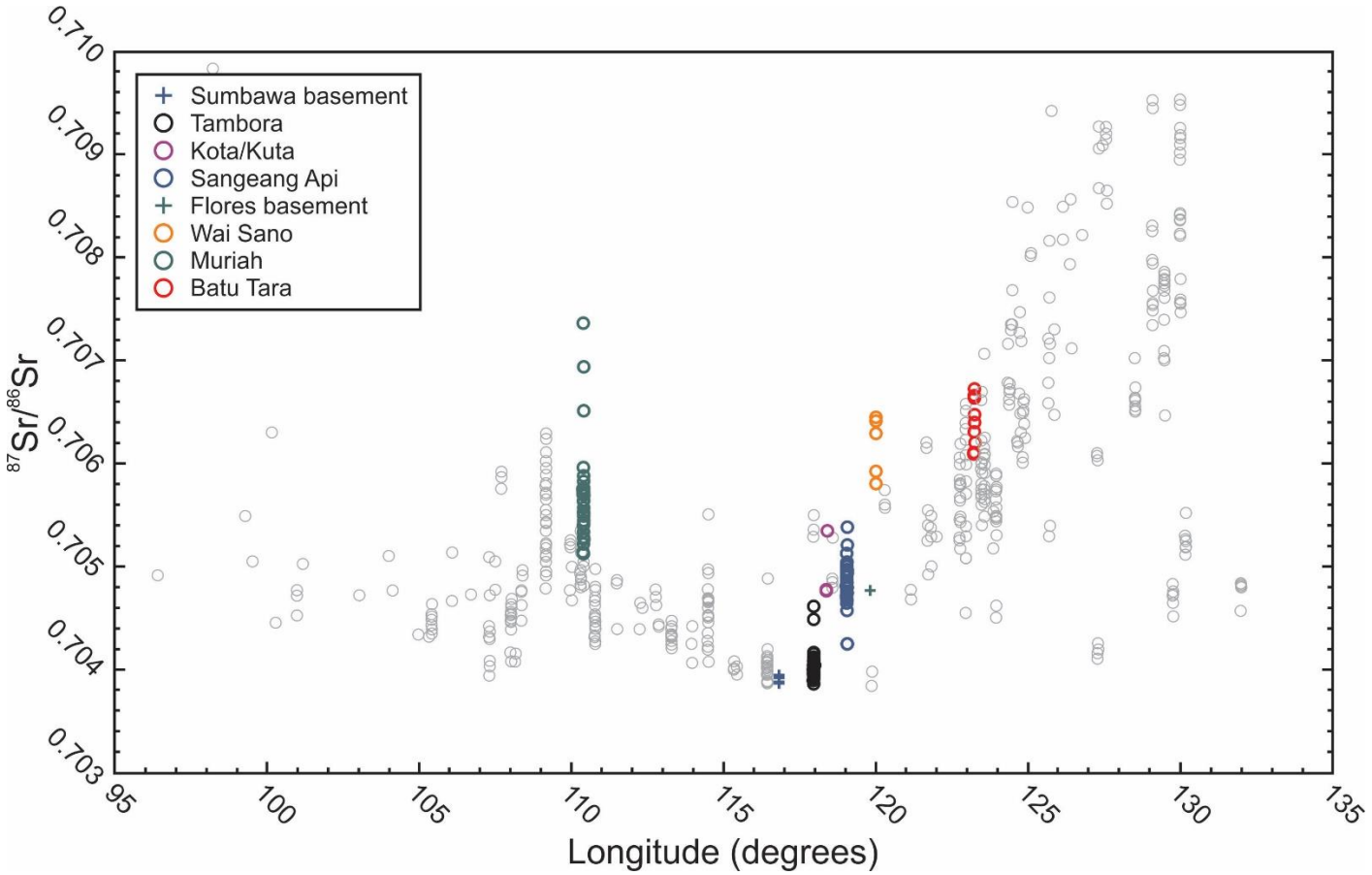

Figure 3: Along-arc variation in $^{87}Sr/^{86}Sr$ from 95˚E to 130˚E. Symbols represent Sunda arc-front lavas (open grey circles), Muriah lavas (open green circles), Sumbawa basement (blue crosses), Tambora lavas (open black circles), Sangeang Api lavas (open blue circles), Flores basement (orange crosses), Wai Sano lavas (open orange circles) and Batu Tara lavas (open red circles). Data compiled from GeoRoc database (http://georoc.mpch-mainz.gwdg.de/georoc/), Gertisser et al. (2012) and unpublished data from this thesis.

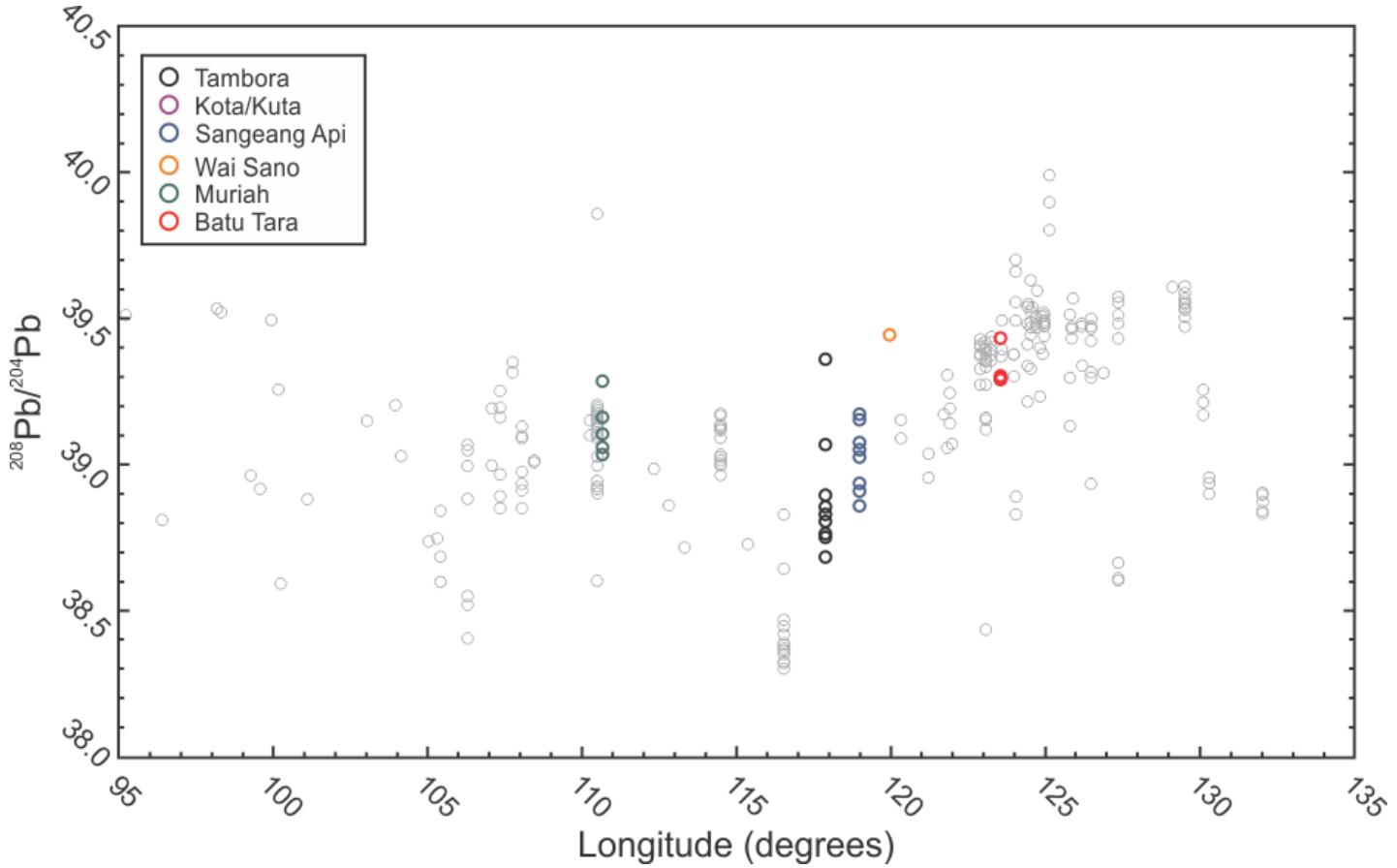

Figure 4: Along-arc variation in $^{208}Pb/^{204}Pb$ from 95˚E to 130˚E. Symbols as in figure 3. Data compiled from GeoRoc database (http://georoc.mpch-mainz.gwdg.de/georoc/) and Gertisser et al. (2012).

in the east was collated. Geochemical and isotopic data was collated from GeoRoc (http://georoc.mpch-mainz.gwdg.de/georoc/), previous work from this thesis and from other sources (e.g. Gertisser et al. 2012). Slab parameters of modern volcanoes were taken from Syracuse and Abers (2006) and matched to the geochemical data.

RESULTS

Lavas erupted by the volcanos of the Sunda Arc display distinct trends in their radiogenic isotope compositions (Sr, Nd and Pb) with longitude. From west to east there is a broad increase in $^{87}Sr/^{86}Sr$, a decrease in $^{143}Nd/^{144}Nd$ and Pb isotopic compositions. Figures 3 and 4 display Sr and Pb isotope variations with longitude. First, the along-arc Sr and Nd isotope variations are considered. $^{87}Sr/^{86}Sr$ and $^{143}Nd/^{144}Nd$ variation within the Sunda lavas appear to have responded in the opposite fashion to each other (i.e. where Sr values are high, Nd values are low – and vice versa), therefore for the purposes of this study and to simplify the discussion Sr isotopic variation will be focussed upon. The isotopic composition of Sunda lavas broadly increase from west to east (96-133°E) (figure 3). The pattern is, however, more complex than this simple west to east increase, with an increase in the Sr isotopic compositions from 96 to 110°E latitude (Andaman Islands to Central Java), followed by a steep drop to lower values again and then an increase again to the east and the Banda arc (118-133°E). Lead isotopes similarly show along-arc variation from west to east (figure 4). With a flat and slightly shallow decline in $^{208}Pb/^{204}Pb$ (39.5-38.3) from the Andaman Islands (97°E) to Rindjani (Lombok, ~116.5°E), before a steep increase (38.6-40.0) from Tambora (Sumbawa, ~118°E) to the Lesser Sunda Islands in the east (132°E).

Ultrapotassic magmas of the Sunda-Banda Arc (e.g. Muriah, Tambora, Sangeang Api & Batu Tara) display unique chemical characteristics that distinguish them from the other arc-front volcanoes. There is a general trend of increasing H (depth to slab) with increasing K_2O, likewise this is reflected in high $^{143}Nd/^{144}Nd$, low $^{87}Sr/^{86}Sr$ and high La_N/Yb_N.

DISCUSSION

Radiogenic isotope trends

The lavas of the Sunda Banda Arc show a broad increase in values from east to west, which has been suggested to be an indication of the influence of Australian derived continental material, due to the impact of Australia with the Sunda Arc beginning around 120°E (Elburg et al., 2005; Elburg et al., 2002; Elburg et al., 2004; Hilton et al., 1992; Stolz et al., 1990; Turner and Foden, 2001). This does not, however, explain the variation in the compositions from the Andaman Islands to Central Java, where there can be no influence of continental material entering into the mantle due to the lack of a crustal impactor. Handley et al. (2014) suggested that these inflated values were created as a result of crustal contamination processes by carbonate and basaltic/ophiolitic sources. The majority of Sunda lavas appear to have experienced varying levels of mixing between an I-MORB source and pelagic, continentally derived subducted sediment (mixing curve to sediment G in fig. 5a). There are a variety of samples that do not stick to the observed

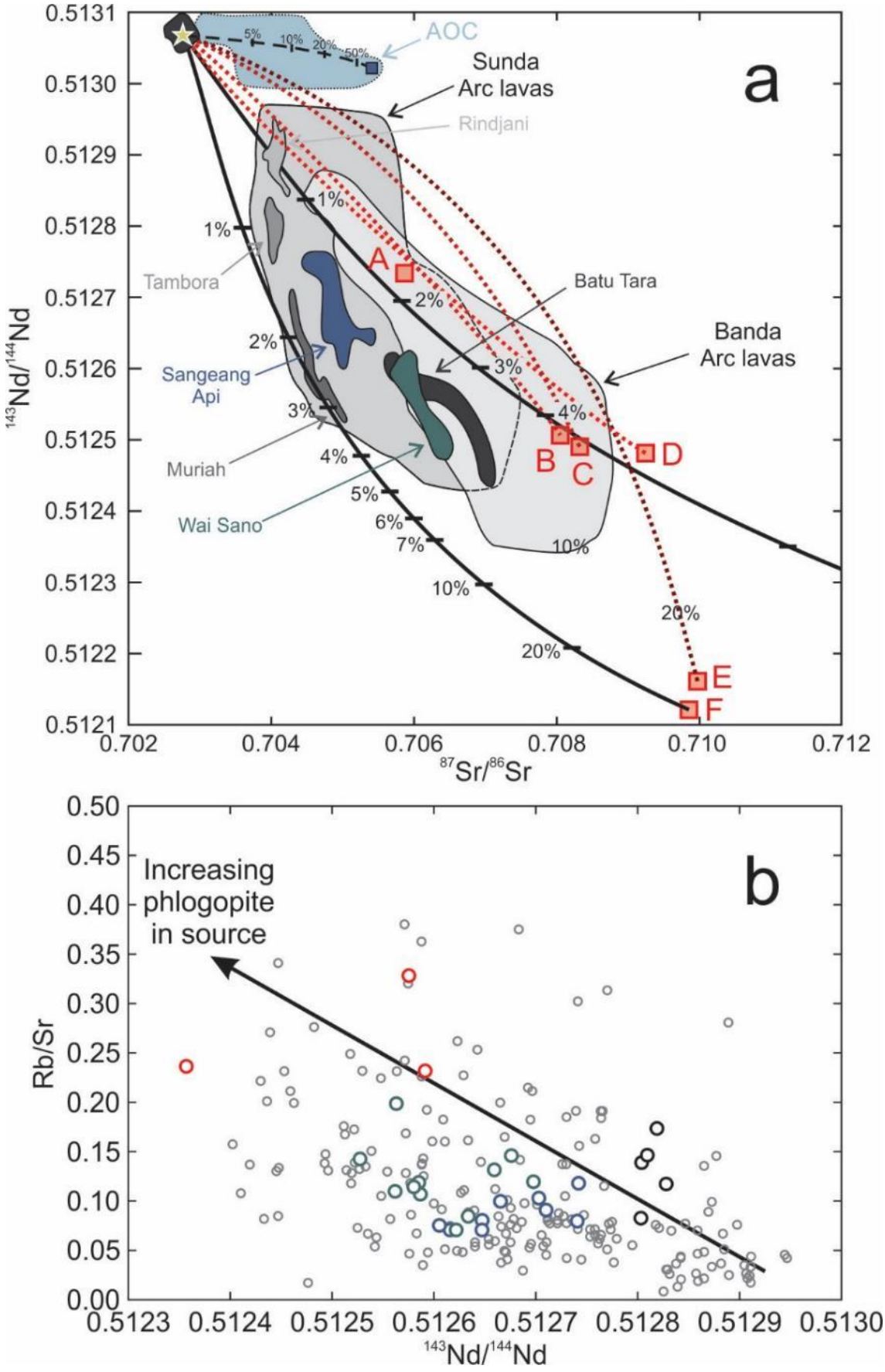
a
AOC
Sunda
Arc lavas
Rindjani
Tambora
Batu Tara
Banda
Arc lavas
Sangeang
Api
Muriah
Wai Sano
A
B
C
D
E
F
1%
2%
3%
4%
5%
6%
7%
10%
20%
50%
$^{143}Nd/^{144}Nd$
$^{87}Sr/^{86}Sr$
0.5131
0.5130
0.5129
0.5128
0.5127
0.5126
0.5125
0.5124
0.5123
0.5122
0.5121
0.702
0.704
0.706
0.708
0.710
0.712
b
Increasing
phlogopite
in source
Rb/Sr
$^{143}Nd/^{144}Nd$
0.50
0.45
0.40
0.35
0.30
0.25
0.20
0.15
0.10
0.05
0.00
0.5123
0.5124
0.5125
0.5126
0.5127
0.5128
0.5129
0.5130

Figure 5a (previous page): $^{143}Nd/^{144}Nd$ vs. $^{87}Sr/^{86}Sr$ displaying isotopic variation of I-MORB field (dark grey field) Sunda front lavas (mid grey field), Banda lavas (light grey field), Indian Ocean altered ocean crust (light blue field) Muriah lavas, Tambora lavas, Sangeang Api lavas, Wai Sano lavas and Batu Tara lavas. I-MORB and lava data compiled from GeoRoc database (http://georoc.mpch-mainz.gwdg.de/georoc/), Gertisser et al. (2012) and unpublished data from this thesis. I-MORB isotopic values from Rehkamper and Hofmann (1997) and I-MORB source composition from Workman and Hart (2005). Altered ocean crust (AOC) values taken from Staudigel et al. (1995). Red squares represent composition of Sunda front sediments, with sediments A (RC14-067), B (V33-79), C (V33-77), D (V33-75), E (V28-341) & G (V28-343) are taken from Ben Othman et al. (1989), whilst sediment G is an average of DSDP 262 compositions from Vroon et al. (1995). Sediments A, B, C, D and E are considered unlikely to represent mixing trends between the mantle source and subducted sediments (dotted red lines). Sediments F, a carbonate turbidite, and G, a pelagic clay, represent the most likely trends of mixing between the I-MORB source and subducted sediments as they present bounds on the Sunda arc-front lavas (solid black lines with ticks denoting percent of sediment mixed to I-MORB source). Black dashed line represents mixing line between an I-MORB mantle source and AOC fluid. I-MORB source composition of $^{143}Nd/^{144}Nd$: 0.51307, $^{87}Sr/^{86}Sr$: 0.70275, Nd: 0.67ppm and Sr 9.6ppm. Note that curvature of sediment mixing trends is controlled by Sr/Nd ratio of sediment value compared to I-MORB composition, with Sr/Nd ratios higher than I-MORB composition resulting in a concave down trend and Sr/Nd ratio slower than I-MORB composition producing a concave up trend.

Figure 5b (previous page): Rb/Sr vs. $^{143}Nd/^{144}Nd$ values of Sunda arc lavas noting the influence of residual phlogopite on trace element and isotopic composition. Symbols as in figure 3. Data compiled from GeoRoc database (http://georoc.mpch-mainz.gwdg.de/georoc/), Gertisser et al. (2012) and

regional variation trend, primarily the ultrapotassic magmas of Sangeang Api and Batu Tara, as well as the possibly crustally contaminated lavas of west-central Java and the adakitic Wei Sano lavas. They appear to show lower $^{143}Nd/^{144}Nd$ for a given $^{87}Sr/^{86}Sr$, suggesting influence of another source. Given that the west-central Java samples have displayed evidence of mixing with crustal carbonates (Handley et al., 2014), similar processes must be considered for the ultrapotassic volcanoes. This, however, is an unlikely process in most of these volcanoes as the best evidence suggests that the ultrapotassic volcanoes are built on arc-thickened and magmatically underplated oceanic crust with little carbonate present. Thus, suggesting another be required to create the isotopic signatures of these magmas. A simple mixing trend between an I-MORB source and a carbonate sediment sample from the Sunda Arc follows a similar trend of lower Nd at a given Sr value, suggesting this may be a source (mixing curve to sediment F in fig. 5a). Indeed, it appears that the ultrapotassic magmas trend away from the 'regional mixing curve' and towards the biogenic mixing curve, perhaps suggesting that they inherited their unique characteristics from sources with mixed sediment inputs. Lavas erupted by Muriah on Java share these distinct isotopic characteristics, however, they do not seem to follow the trend towards a pelagic, continentally derived, sediment and instead sit directly on the mixing curve towards a more enriched biogenic carbonate sediment (mixing curve to sediment F in fig. Ea). Some Sunda arc-front lavas define arrays above the two regional mixing trends towards compositions with higher $^{143}Nd/^{144}Nd$ for a given $^{87}Sr/^{86}Sr$ (figure 5a). A number of studies have suggested that Sunda Arc lavas are sourced from an I-MORB mantle source influenced by the addition of both altered ocean crust (AOC) fluids and sediment material (Gertisser et al., 2012; Stolz et al., 1990; Turner and Foden, 2001; Turner et al., 2003). Figure 5a shows a simple mixing trend between AOC derived fluids and an I-MORB mantle source, it can clearly be seen from this diagram that the Sunda Arc lavas define arrays between this I-MORB mantle/AOC fluid mixing trend and

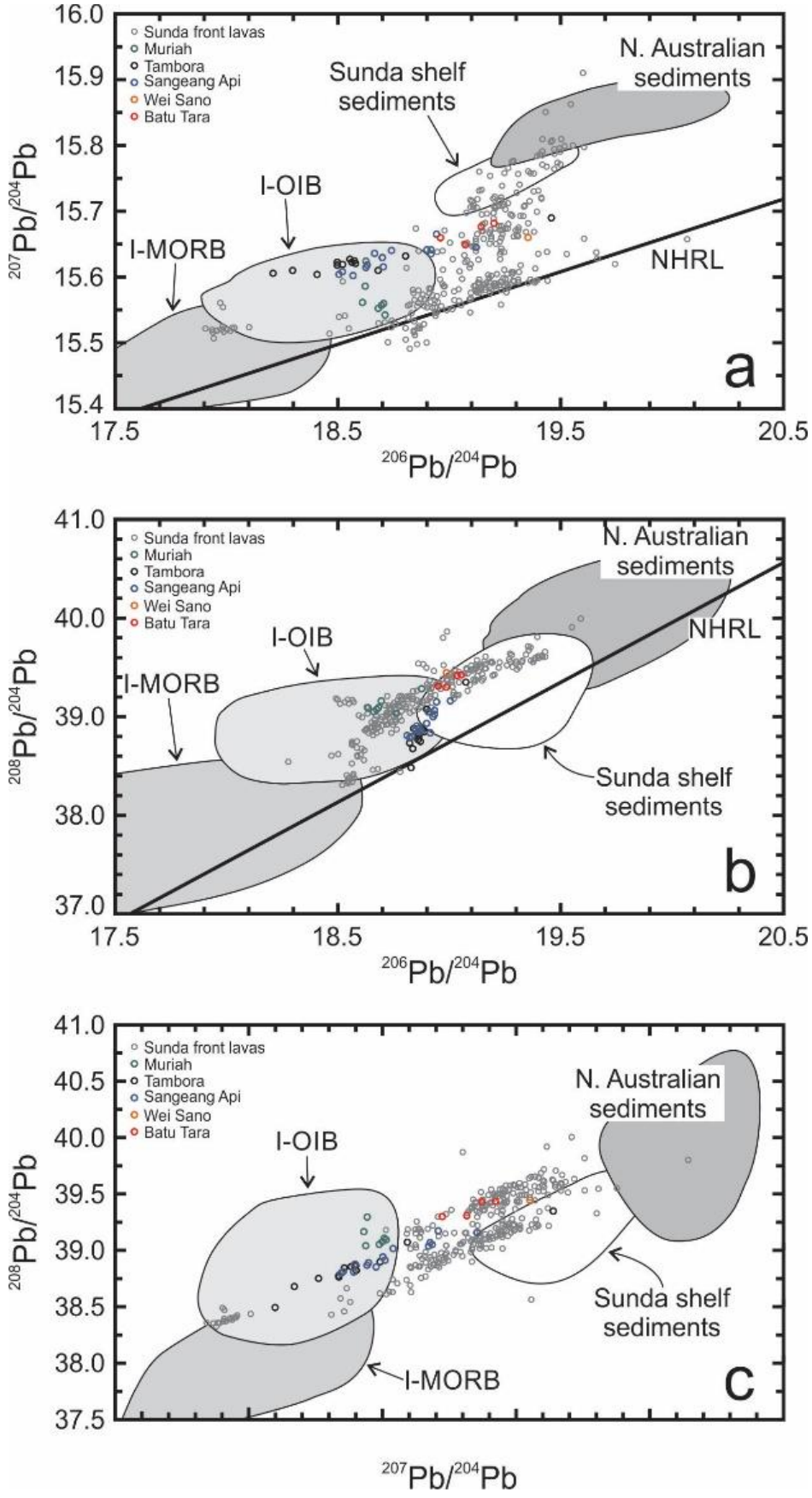

Figure 6a-c: Pb isotope compositions of Sunda Arc lavas. I-OIB, I-MORB and sediment fields adapted from Elburg et al. (2002). Symbols as in figure 3. Data compiled from GeoRoc database (http://georoc.mpch-mainz.gwdg.de/georoc/) and Gertisser et al. (2012).

sediments of the Sunda front. It therefore appears clear that fluid release from AOC and mixing of variably enriched subducted sediments are strong controls on the composition of Sunda Arc mantle wedge sources.

Similar east-to-west trends and variations in the Pb-isotope data roughly follow a mixing trend between an I-OIB/I-MORB source region towards the Sunda Shelf sediments and Australian continental sediments. The adakites of Wei Sano stand apart from these regional trends with inflated $^{208}Pb/^{204}Pb$ that correspond closely to sediments of the Sunda Front (figures 6a-6c), hinting at a strong sediment influence in the source. Ultrapotassic magmas from Muriah, Sangeang Api and Tambora display evidence for input from an I-OIB source (figures 6a-6c). However, this is not observed in the Batu Tara magmas – hinting at some source region differences between the two volcanic centres.

Magmas of the Aeolian Arc display similar isotopic variations to the Sunda Arc lavas, suggesting that they formed from sources mixed with variable amounts of both terrigenous and biogenic sediment material (Peccerillo, 2001; Schiavi et al., 2012). Similarly, there is evidence for mixing with an OIB-like source component in the Aeolian Arc (Conticelli et al., 2009b). Lavas of the Izu-Bonin arc display along-arc isotopic variations that are likely controlled by addition of varying amounts of slab-derived fluid, volcaniclastic and pelagic material (Ishizuka et al., 2007). Thus, it seems along-arc isotopic variation in the Sunda Arc arises from heterogeneities in the source region related to mixing with distinct mantle, sediment and possibly fluid sources. Isotopic variation in the western section of the arc (Andaman Islands to Java) are controlled both by compositional heterogeneity in sediments mixed into the source region and crustal contamination processes, reflecting their location on thicker continental crust (Handley et al., 2014). To the east of Java isotopic variation is dependent on two main factors;

- compositional heterogeneity in fluids and sediment inputs to the source region.
- increasing influence of Australian continental derived material towards the incipient impact of the Australian continental crust.

Rear-arc ultrapotassic volcanism

The ultrapotassic volcanics of the Sunda Arc stand out distinctively from the majority of the active volcanics in the region not only in their chemistry and isotopic compositions (figs. 2 and 5a), but also their geography (fig. 1). They are located much further from the trench than the 'normal' arc front volcanics and are significantly higher above the slab, with depths to the slab (H) 150km and greater – see figure 7a (Syracuse and Abers, 2006). It seems likely then that it is this set of tectonic parameters exerting a control upon the geochemistry. This is supported by increasing potassium contents of lavas with increasing H (figure 7a). Similarly, the greater distance between the slab surface and the volcanos, the lower the $^{143}Nd/^{144}Nd$ ratios (figure 7b) and the steeper the REE profiles (La_N/Yb_N) (figure 7c). These co-variations with increasing H suggest that slab depth is exerting a significant control over the composition of the partially melting mantle. To determine if the depth of partial melting is a control on the composition of magmas in the system, it can be useful to establish the amount of garnet in the source region (garnet stability in the

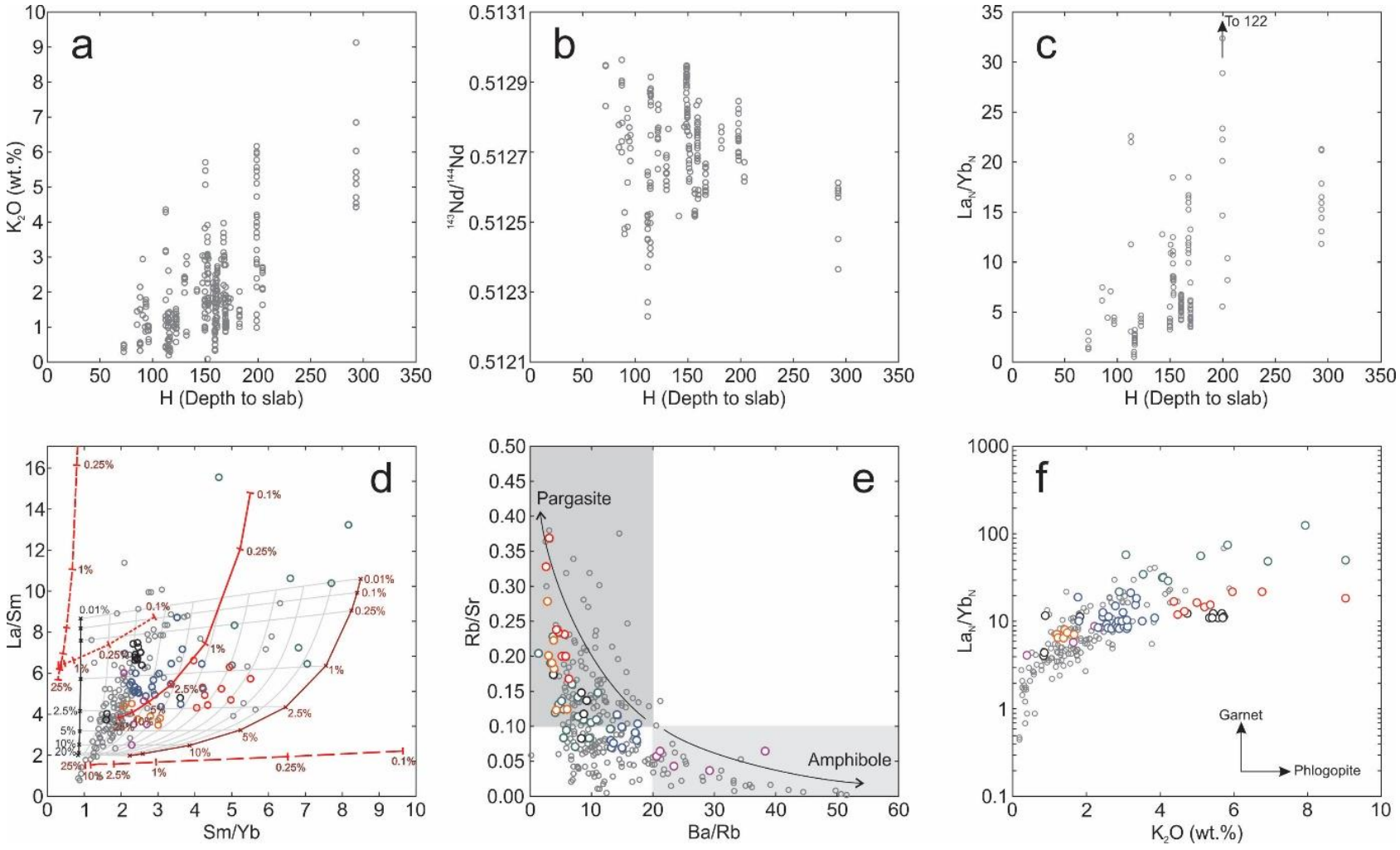
a
K2O (wt.%)
H (Depth to slab)
b
143Nd/144Nd
H (Depth to slab)
c
To 122
LaN/YbN
H (Depth to slab)
d
La/Sm
Sm/Yb
0.25%
0.1%
1%
0.01%
2.5%
5%
10%
20%
25%
e
Pargasite
Amphibole
Rb/Sr
Ba/Rb
f
LaN/YbN
Garnet
Phlogopite
K2O (wt.%)

Figure 7a-f (previous page): Diagrams displaying isotopic and geochemical variations with depth to slab (7a-c) and trace element covariations noting the influence of residual mineral phases (7d-f). Symbols as in figure 3. Data compiled from GeoRoc database (http://georoc.mpch-mainz.gwdg.de/georoc/), Gertisser et al. (2012) and unpublished data from this thesis. Figure 7c displays a partial melting grid between spinel and garnet bearing lherzolites, details of model constraints can be found in appendix 4. Red lines in figure 7c represent batch partial melting models of data from Finero phlogopite-peridotite (central solid line, Zanetti et al. 1999), Papua New Guinea orthopyroxenite (left medium dashed line, McInnes et al. 2001), Japan amphibole-peridotite (centre-left small dashed line, Khedr & Arai 2009) and Kamchatka orthopyroxene-amphibole-peridotite (bottom long dashed line, Ishimaru et al. 2006), dashes represent degrees of partial melting (with amounts stated next to them) and details of model constraints can be found in appendix 4. Figure 7e distinguishes between the influence of residual phlogopite and residual amphibole in erupted lavas, after Furman & Graham (1999). Figure 7f displays the effect of residual garnet and phlogopite on lava REE (La/Yb normalised to chondrite values of McDonough & Sun 1995) and major element geochemistry (K_2O).

mantle is confined to depths greater than ~35-40km) (O'Hara et al., 1971). As garnet strongly partitions the HREE relative to the LREE, the rare earth contents of lavas sourced from garnet-bearing mantle peridotite regions display steeper MREE/HREE ratios than those sourced from garnet poor peridotite. For a given La_N/Sm_N value, lavas sourced from a more garnet-rich peridotite will have a higher Sm_N/Yb_N (see figure 7d). This relationship is displayed by the ultrapotassic lavas of the Sunda Arc, especially those of Batu Tara and Muriah, hinting at a more garnet-rich peridotite source and thus elevated pressures of partial melting. Likewise, phlogopite is stable in mantle compositions to greater pressures and temperatures than amphibole (Konzett and Ulmer, 1999; Sudo and Tatsumi, 1990; Wunder and Melzer, 2003). Melting of a phlogopite enriched source will increase the Rb/Sr ratio of a lava, whereas amphibole enriched peridotite will increase the Ba/Rb ratio of a lava (LaTourrette et al., 1995), whilst a primitive mantle source will show neither an increase in Ba/Rb or Rb/Sr, allowing for the distinction of sources enriched by either phase. Ultrapotassic lavas of the Sunda arc display inflated Rb/Sr values (>0.1) and low Ba/Rb values (<20) (figure 7e), suggesting a source enriched in phlogopite and lacking amphibole, again hinting at partial melting occurring at elevated pressures. This is most prominent in the lavas of Muriah and Batu Tara (Rb/Sr 0.08-0.38), but less so in Sangeang Api and Tambora (0.08-0.18), suggesting that the sources of Muriah and Batu Tara contain more residual phlogopite. Whereas, the source of Sangeang Api and Tambora may contain less residual phlogopite and perhaps a little residual amphibole. It therefore seems likely that the ultrapotassic magmas of the Sunda Arc are sourced from partial melts of phlogopite (± amphibole) and garnet bearing peridotite at pressures greater than 12kbar. It has been proposed that Sr and Nd isotopic decoupling can happen in mantle metasomatised by amphibole and phlogopite, with metasomatised peridotite xenoliths trending to lower $^{143}Nd/^{144}Nd$ values with increased amounts of metasomatism (Ionov et al., 2002). As previously mentioned, the Sunda arc ultrapotassic lavas record low $^{143}Nd/^{144}Nd$ values for a given $^{87}Sr/^{86}Sr$, supporting their sourcing from a metasomatised mantle (figure 5a). Similarly, the Rb/Sr ratios of the magmas increase with decreasing $^{143}Nd/^{144}Nd$ (figure 5b), again supporting partial melting of a phlogopite enriched source. The ultrapotassic magmas of the Roman Province and Aeolian Arc display similar chemical and isotopic compositions to the Sunda ultrapotassics (Avanzinelli et al., 2008; Balcone-Boissard et al., 2016; Conticelli et al., 2015; Conticelli et al., 2009a; Peccerillo, 1998). The Aeolian magmas display large isotopic variations both geographically and

temporally (Conticelli et al., 2009a; Peccerillo, 1998; Peccerillo, 2001), this has been attributed variously to crustal contamination processes (Conticelli, 1998; Perini and Conticelli, 2002) and small-scale heterogeneity of sediments mixed into the source region (Peccerillo, 1998; Peccerillo, 2001; Schiavi et al., 2012). Schiavi et al. (2012) presented evidence from primitive olivine hosted melt inclusions (from Stromboli) displaying variable trace element and isotopic compositions suggesting the presence of distinct metasomatized mantle regions.

Muriah produces magmas with similar geochemical compositions to the other Sunda ultrapotassic lavas, but with Sr-Nd isotopic compositions that suggest mixing with purely biogenic carbonate material. Whether this happened in the source or by the assimilation of crustal carbonate is difficult to discern entirely from the geochemical and isotopic compositions of the lavas. Other nearby volcanoes in eastern Java show no influence of biogenic sediment input in the source region (Handley et al., 2014). Edwards et al. (1991) proposed that the Muriah ultrapotassic were sourced from a metasomatised I-MORB source which was enriched by pelagic sediment and included some assimilation from the upper crust. Whilst the surface geology surrounding Muriah (volcanic and alluvial deposits) does not support there being carbonate in the source, there are significant carbonate deposits in the Rembang Zone in which it is located (Smyth et al., 2005), outcropping immediately to the east (Smyth et al., 2008). If these carbonate deposits extend into the crust hosting the magmatic system, assimilation into the magmatic system could produce the isotopic and geochemical characteristics of the ultrapotassic lavas. The Muriah ultrapotassic signature possibly arises from complex interactions between metasomatised mantle melts and assimilation of a carbonate hosting crust and requires further investigation.

Sr and Nd isotopes from Tambora are less radiogenic than those of the other ultrapotassic magmas (figure 5a), they sit close to I-MORB values and overlap slightly the I-OIB field (Gertisser et al., 2012). Previous studies have suggested that the Tambora lavas are sourced from an I-MORB source enriched with 3% altered ocean crust fluids and <1% sediment melt (Gertisser et al., 2012). Pb isotopes indicate the influence of an I-OIB component in the source region. Trace element ratios suggest the influence of residual phlogopite, with little influence of garnet suggesting moderate pressures of partial melting in the mantle. The relatively low Sr and high Nd isotopes compared to the other ultrapotassic magmas suggest melting from a source only moderately metasomatized.

This all brings into question the process of developing phlogopite enriched mantle and the conditions necessary to create a partial melt of such a source. Phengite dehydration reactions in the subducting slab can metasomatise mantle peridotite, stabilising phlogopite at pressures greater than amphibole phase stability (Wunder and Melzer, 2003). Ratios of fluid mobile (Ba,U, etc.) and fluid immobile (Th, Nb, etc.) have been interpreted in an attempt to constrain the source of hydrous mineralogy in the mantle, whether it be by fluid metasomatism or the emplacement of sediment melts (Elliott, 2013; Plank and Langmuir, 1998). The lavas of Sangeang Api (and Tambora to a lesser extent) are depleted in the fluid immobile elements (Th <12ppm and Nb <10ppm), whereas the lavas of Batu Tara have much higher fluid immobile element concentrations (Nb >10ppm

and Th >11ppm). Suggesting a lack of sediment melts and a strong influence of fluid enrichment in the Sumbawan ultrapotassics and the predominance of a sediment melt derived signature in the Batu Tara and Muriah samples. Indeed, Sangeang Api records some of the largest Ba/Th ratios in the entire arc, likely reflecting significant fluid input to the source. Turner et al. (2003) support the suggestion of a fluid component to the source of the Sangeang Api magmas, however, they do not support the suggestion that small amounts of residual phlogopite (± amphibole) are to be found in the source of Sangeang Api. Turner and Foden (2001) suggested that the sediment characteristics of the Sunda arc lavas were formed from the addition of sediment partial melts, with some lavas showing evidence for a fluid component, again supporting the evidence for complex heterogeneity between individual volcanoes of the arc. At odds with the findings of Turner and Foden (2001), however, are suggestions of large fluid inputs from the slab can be associated with rear arc volcanics (Sangeang Api).

Metasomatised peridotite has been reported in mantle xenoliths (e.g. Kamchatka and Papua New Guinea) and exhumed ultramafic terranes (e.g. Italy and Japan) in various locations around the world (Arai et al., 2003; Coltorti et al., 2007; Ernst, 1981; Ishimaru et al., 2006; Kepezhinskas et al., 1996; Khedr and Arai, 2009; Lu et al., 1997; Marocchi et al., 2007; McInnes et al., 2001; Zanetti et al., 1999). Experimental studies have shown that partial melting of a phlogopite-peridotite at 3GPa, within the garnet stability field, will produce foiditic to trachybasaltic melts over a range of melting (0.8-25.6 wt.%) (Condamine et al., 2016). Batch partial melting models, following the method of O'Nions and McKenzie (1988), have been calculated for various metasomatised mantle peridotites (see figure 7d): Finero phlogopite-peridotite (Zanetti et al., 1999), Papua New Guinea orthopyroxenite (McInnes et al., 2001), Japan amphibole-peridotite (Khedr and Arai, 2009) and Kamchatka orthopyroxene-amphibole-peridotite (Ishimaru et al., 2006). The compositions of batch partial melts produced from these samples display distinct differences, suggesting that metasomatic style plays a key role in the composition of the magmatic products of partial melting. From the models produced in this study, the most similar source region to produce the trace element dynamics of the Sunda ultrapotassics (relatively increased Sm/Yb ratios for a given La/Sm) is the Finero peridotite massif (Italy). Thus, supporting earlier conclusions that residual phlogopite metasomatism has played a key role in the production of ultrapotassic lavas in the Sunda Arc.

Influence of slab tears

Slab tears and developing slab ruptures have been noted in various regions of the Sunda slab (Ely and Sandiford, 2010; Hall and Spakman, 2015; Kundu and Gahalaut, 2011; Widiyantoro et al., 2011; Widiyantoro and van der Hilst, 1997). The largest notable slab tears are suggested to be beneath Sumatra, Java and Lombok-Sumbawa (Hall and Spakman, 2015; Kundu and Gahalaut, 2011). Tomographic models suggest that there are two distinctive styles of slab tear in the arc; a tear in the slab beneath Sumatra and gaps in the slab beneath central Java and Sumbawa (Fiorentini and Garwin, 2010; Hall and Spakman, 2015). Hall and Spakman (2015) suggest that the gaps in the slab formed from the impact of more buoyant oceanic plateaus and temporary blocking of the subduction zone, a process supported for the Sumbawan slab window (Fiorentini and Garwin, 2010).

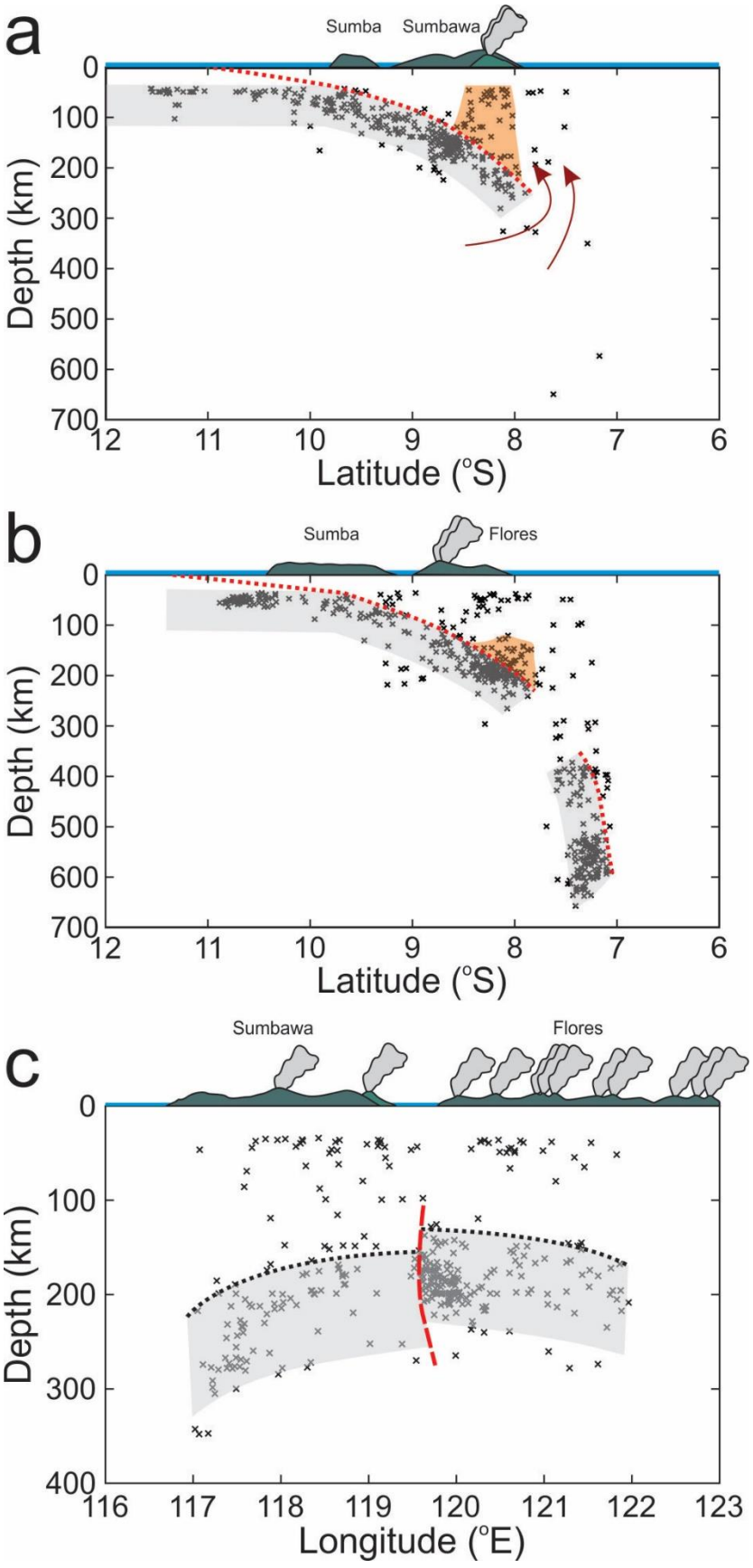

Figure 8a-c: Across-arc and along-arc earthquake profiles. Earthquake data from USGS earthquake catalogue (Engdahl and Villaseñor, 2002). Locations of islands and volcanoes (grey clouds) are observed above cross-sections. Coloured regions in figures 8a and 8b represent subducting slab (grey area), approximate slab surface (red dashed lines), region of partial melting and melt transfer (orange region) and asthenospheric flow (dark red arrows). Across-arc profiles are located between 118˚E-119˚E (8a), and 119˚40'E-120˚40'E (8b). Figure 8c displays an along-arc earthquake profile between 7˚30'S and 8 ˚30'S, with slab (grey region), approximate slab surface (dashed black line) and estimated discontinuity surface (red dashed line).

It is notable that these slab gaps are found immediately underneath some of the ultrapotassic volcanoes (Muriah, Tambora and Sangeang Api). It has been suggested that these slab tears have influenced the production of ultrapotassic volcanoes through the partial melting of mantle peridotite without the influence of slab derived fluids (Hall and Spakman, 2015). This cannot, however, explain the anomalously low $^{143}Nd/^{144}Nd$ ratios of the ultrapotassic volcanics. Kundu and Gahalaut (2011) proposed that the quaternary volcanics of the eastern Sunda Arc displayed geochemical evidence (high Sr/Y, Cr and Ni) for slab edge melting due to the influx of hot asthenosphere at the borders of slab tears. Despite the high Sr/Y ratios of the ultrapotassic magmas their Y contents are too high (23-47ppm) to originate from a slab melting source (<12ppm). It is likely, however, that these slab tears play a key role in the origin of ultrapotassic magmatism.

Sumbawa may provide the best environment to observe the effects of a slab tear in the Sunda Arc (figure 8a). Sumbawa is host to ~2Ma high-K calc-alkaline volcanics (e.g. Kota and Kuta), quaternary leucitites (e.g. Soromundi and Sangenges) and modern day shoshonites (e.g. Tambora and Sangeang Api). The compositional variation from arc front-like magmatism, through leucititic and ultrapotassic volcano hints strongly at an evolving arc source. Conticelli et al. (2009) noted a similar progression in the lavas of Roccamonfina from the Roman Magmatic Province (RMP), with a progression from ultrapotassic leucite-bearing lavas between 630-400ka, to shoshonitic leucite-free lavas between 385-230ka and high-K calc-alkaline magmatism from 155-50ka. Progressive partial melting of metasomatized mantle channels has been proposed to account for these temporal changes, with progressive melting depleting the metasomatic character (Conticelli et al., 2009b). Like Sumbawa, the RMP is suggested to be underlain by a slab tear (Faccenna et al., 2001). It has been proposed that this slab tear has allowed for an influx of hot asthenosphere, raising the geotherm in the mantle wedge and melting the metasomatic channels in the mantle wedge (Conticelli et al., 2009b). This influx of hot asthenosphere is evidenced in the Roccamonfina lavas by OIB-like Pb isotopic values (Conticelli et al., 2009b). The ultrapotassics of Sumbawa display Pb isotope values overlapping the I-OIB field, suggesting that a similar influx of hot asthenospheric material from the sub-Sumbawa slab gap. Foley (1992) suggests that potassic magmas develop from the melting of veined and metasomatized mantle. Metasomatic veins have a lower melting point than surrounding mantle peridotite, thus with the initial influx of hot asthenospheric material partial melting will be concentrated in the metasomatic veining, producing melt extremely rich in K and incompatible elements. As more hot asthenosphere is introduced via the slab gap, temperatures of the mantle wedge continue to rise, leading to the initiation of partial melting of the host peridotite (Foley, 1992). These higher degree partial melts should be poorer in K (but still K-rich), more magnesian and retain similar incompatible element characteristics to the vein melts. Interestingly these relationships are not entirely carried out in the Sumbawa region; with the leucitites being more enriched in Rb, Sc and Ni, and depleted in Sr and Ba when compared to the shoshonites of Tambora and Sangeang Api (Foden and Varne, 1980). Rb/Sr ratios (0.066-0.381) in the leucitite magmas suggest partial melting in the presence of varying amounts of phlogopite (figure 7e), whilst Nb/Rb ratios suggest melting from a source in the

presence of little to no residual amphibole. These leucitites therefore are likely the products of initial small degree partial melts of phlogopite-bearing metasomatic veins (low Rb/Sr and high $^{143}Nd/^{144}Nd$). The high-K calc-alkaline quaternary centres on Sumbawa (e.g. Kota/Kuta) are similar in composition to other arc-front calc-alkaline magmas and lack evidence of partial melting in the presence of phlogopite. Similarly, they fall on an isotopic mixing path with pelagic sediment and show no evidence for mixing with biogenic sediments. The high-K calc-alkaline volcanoes are therefore likely to represent partial melts of "normal" Sunda mantle wedge without the influence of a slab window, thus providing geographical and temporal bounds on the age of the slab tear. This slab window must have reached the mantle wedge after eruption of the Kota and Kuta volcanic centres, but prior to Sangenges and Soromundi. It also appears that the slab window may have moved northwards and raised the geotherm of the local mantle wedge, allowing for the northwards movement of active volcanism and transition from leucitite to shoshonite magmas. Fiorentini and Garwin (2010) suggest that a slab window has developed through the subduction of the relatively buoyant Roo Rise (a seamount chain on the Indo-Australian plate). Their theory suggests that the impact of this buoyant crust has caused instability in the slab and the development of an arc-transverse fault zone on the western boundary of Sumbawa, allowing for the upwelling of hot asthenospheric melts.

Slab tears appear to be absent beneath the island of Batu Tara, suggesting that another process must be controlling the creation of ultrapotassic magmatism beneath the island. Batu Tara is found significantly further to the rear of the arc than any of the other ultrapotassic volcanoes, and at a greater depth to the Benioff zone ~300km. Despite the lack of a tear in the slab the island is located close to the Banda Sea, which displays a characteristic concave slab (Hall and Spakman, 2015). This unique slab-rollback form likely drives asthenospheric flow parallel to the slab borders and away from the subducted Banda slab (Di Leo et al., 2012). Batu Tara displays evidence for the input of significant Sunda Shelf sediment, as well as partial melting from a region of phlogopite-enriched metasomatized mantle. Strong slab-parallel asthenospheric flow could both raise mantle wedge temperatures to facilitate the melting of metasomatic veining, but also provide a flux of sediment material.

Earthquake foci display another possible slab window below western Flores (figure 8b), albeit smaller than the Sumbawan window. There is however, no ultrapotassic volcanism on the island of Flores, instead the predominant style of volcanism is calc-alkaline, except for Wai Sano which displays adakite-type characteristics (low Y, low MgO and high Al_2O_3). Wai Sano is distinct from atypical adakites by its high Sr isotopes ($^{87}Sr/^{86}Sr$ >0.7062) that suggest it does not form from the melting of oceanic slab material, as is typically thought of as the origin of adakite-style melts. Instead it appears to have been formed by partial melting of mafic underplating at pressures ~1GPa. To melt these previously stalled mafic underplates requires the local mantle geotherm to raise. Initial influx of hot asthenosphere through a slab window, would raise temperatures in the mantle wedge. One Pb isotope analysis has been undertaken for the Wai Sano samples, and suggests mixing with shelf sediments and lack of an I-OIB signature as in the

ultrapotassic magmas. Upwelling of asthenosphere must have not had sufficient time to mix into the source region of these volcanics yet, but enough time to impose a raised geotherm upon the mantle wedge.

Distribution of active volcanism between Sumbawa and Flores

The distinctive change in the loci of active volcanism from the northern edge of Sumbawa to the southern edge of Flores has been noted by a number of authors (Audley-Charles, 1975; Fiorentini and Garwin, 2010; Foden and Varne, 1980; Garwin, 2000). Several authors have proposed the presence of a dextral strike-slip fault separating the islands of Sumbawa and Flores (Audley-Charles, 1975; Hamilton, 1972, 1979; Katili, 1970), whilst Fiorentini and Garwin (2010) suggested the presence of tears in the subducting slab. Wheller et al. (1987) noted an association of this crustal discontinuity with increases in potassium and fluid-mobile elements of erupted products. This is indeed displayed in the closest modern lavas from Sangeang Api, which are rich in K and fluid-mobile elements (e.g. Ba and Sr). Interestingly, entrained in the Sangeang Api lavas are a suite of cumulate xenoliths, which in some circumstances display granular textures, suggesting the presence of a crustal faulting system. This may evidence the interaction of the proposed strike-slip fault system with the plumbing system of Sangeang Api and may assist in the disaggregation and entrainment of xenolithic fragments. Tears in the subducting slab are more difficult to distinguish, present tomographic images do not support the presence of a slab tear, however, along-arc 'images' of the slab display a clear discontinuity with a pronounced cluster of earthquakes around 119.8˚E (figure 8c). This discontinuity can also be observed in the dips of the slab, with the slab beneath Sumbawa (117-119˚E) dipping at approximately 44.7˚ until the slab window begins at ~200-300km depth (figure 8a). Whereas, underneath Flores (119.5-121˚E) the slab dips at approximately 26˚ before a small region of aseismicity (~50km) followed by a dramatic steepening of the slab to ~80.5˚ (figure 8b). The earthquake foci evidence supports the suggestion of Fiorentini and Garwin (2010) that the slab window beneath Sumbawa is framed by a slab tear. Nugroho et al. (2009) suggest that the islands of Sumbawa and Flores are separated by two distinct crustal domains, with the initiation of subduction polarity occurring beneath Flores. This discontinuity is also reflected in a change from down-dip extensional region in the shallow slab to a down-dip compressional regime beneath western Flores (Ely and Sandiford, 2010). This slab discontinuity may be channelling fluids into the mantle above, increasing the amount of metasomatism in the mantle. This is evidenced by differences between Tambora and Sangeang Api, which both are found above the same slab window and thus should experience similar mantle conditions and melting processes. Tambora displays lower Ba/La ratios (16.5-35 compared to 27-53) and average Sr contents (915ppm compared to 990ppm) supporting a smaller input of fluid-mobile elements. The evidence thus suggests that these crustal and slab discontinuities are delineating slab windows and channelling fluid flow into the sub-arc mantle. The quaternary volcanics of Kota and Kuta found immediately to the south of Sangeang Api should display similar fluid enrichment if the slab discontinuity was present during their formation, however, their Ba/La ratios (6-17) and Sr contents (average 884ppm) suggest they are poor in fluid-mobile elements, thus putting bounds on the age of the slab rupture and discontinuity and

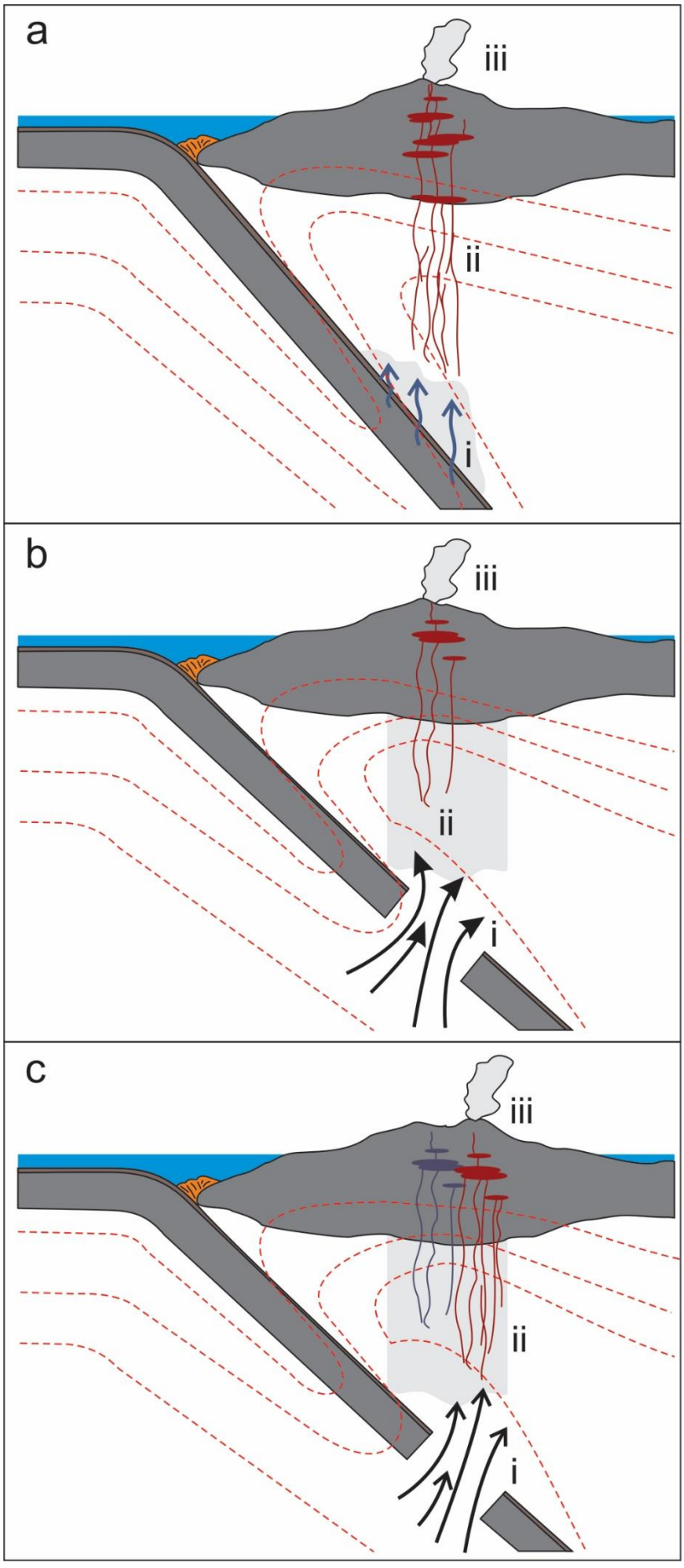

Figure 9a-c: Evolutionary models of arc system from normal arc-front volcano (9a) through leucitite centers (9b) to shoshonite volcanoes (9c). **9a**: i. fluid released from progressive metamorphism of sediments and subducted slab, triggering partial melting and partially metasomatizing the overriding mantle wedge. ii. Hydrous partial melts ascend the mantle wedge, producing phlogopite enriched metasomatic veins. iii. Calc-alkaline to high-K lavas ascend the crust and in thicker continental regions assimilate crustal material. **9b**: i. slab window opens and asthenosphere with an I-OIB signature begins to influx the mantle wedge. ii. Geotherm of the mantle wedge begins to raise, triggering small degrees of partial melting of metasomatized mantle veining rich in hydrous mineralogy (phlogopite/amphibole). iii. Extremely potassic, leucite-normative melts ascend to the surface. **9c**: i. Slab window moves further from the trench and asthenosphere continues to influx the mantle wedge. ii. Asthenosphere with an I-OIB signature begins to mix with metasomatized regions of the mantle wedge, larger fractions of partial melts are produced, and wall-rocks begin to partially melt. iii. Shoshonitic magmas with mixed I-OIB and metasomatism isotopic signature ascend the crust.

suggesting that it formed at a similar time to the slab window. It therefore appears that the slab window and discontinuity formed simultaneously and that the process of their formation was likely related. Previous work has suggested that this slab window is related to the impact of the buoyant Roo Rise producing asthenospheric weaknesses (Fiorentini and Garwin, 2010). A slab window linked to the collision of the Australian continent is present to the east of Flores and is likely propagating slowly westwards (Ely and Sandiford, 2010), however, this is a region free of volcanism.

CONCLUSIONS

Complex tectonic and geodynamic processes occurring in the Sunda Arc of Indonesia have had a large impact on the magmatic products expressed at the surface. The majority of active volcanism in the arc are located proximal to the trench, with distance from the trench controlled largely by the dip of the subducting slab. These arc-front volcanoes largely belong the calc-alkaline to high-K calc-alkaline series. A series of anomalous shoshonitic to leucitic volcanoes (Muriah, Batu Tara, Sangeang Api, Tambora, Sangenges and Soromundi) are found dispersed throughout the arc. These shoshonitic lavas are discovered to the rear of the arc at depths above the Benioff zone are >150km. These ultrapotassic volcanoes are distinguishable by La/Yb (normalised) ratios >10, Rb/Sr >0.08 and Ba/Rb <20. Consistent with other studies (Elburg et al., 2005; Elburg et al., 2004; Hilton and Craig, 1989; Hilton et al., 1992; Turner and Foden, 2001; Wheller et al., 1987) this study presents evidence of along-arc isotopic variations suggesting an increasing influence of continental derived material in the source region towards the Banda Sea and collision zone of the Australian continent. Small variations can be noted in the Java section of the arc and likely reflect the influence of crustal contamination and compositional heterogeneity of sediment on the subducting slab. Ultrapotassic magmatism is associated both with phlogopite-enriched metasomatic regions of the mantle and windows in the subducting slab. It is possible that the opening of tears in the subducting slab are allowing asthenosphere with an I-OIB signature to influx the mantle wedge, raising the mantle geotherm and creating partial melts of metasomatic veins in the rear-arc. The slab window beneath Sumbawa is likely bounded by discontinuities in the subducting slab increasing the flux of fluid-mobile elements to the mantle wedge. The association of this slab discontinuity with a crustal-scale faulting system has channelled melts enriched in fluid-mobile elements into the lithosphere and aided in the disaggregation and entrainment of crustal xenoliths. Figures 9a-c display the proposed model of arc system evolution during the development of mantle metasomatism and slab windows.

REFERENCES

Arai, S., Ishimaru, S., Okrugin, V.M., 2003. Metasomatized harzburgite xenoliths from Avacha volcano as fragments of mantle wedge of the Kamchatka arc: Implication for the metasomatic agent. Island Arc 12, 233-246.

Audley-Charles, M.G., 1975. The Sumba fracture: A major discontinuity between eastern and western Indonesia. Tectonophysics 26, 213-228.

Avanzinelli, R., Elliott, T., Tommasini, S., Conticelli, S., 2008. Constraints on the genesis of potassium-rich Italian volcanic rocks from U/Th disequilibrium. Journal of Petrology 49, 195-223.

Balcone-Boissard, H., Boudon, G., Cioni, R., Webster, J.D., Zdanowicz, G., Orsi, G., Civetta, L., 2016. Chlorine as a geobarometer for alkaline magmas: Evidence from a systematic study of the eruptions of Mount Somma-Vesuvius. 6, 21726.

Ben Othman, D., White, W.M., Patchett, J., 1989. The geochemistry of marine sediments, island arc magma genesis, and crust-mantle recycling. Earth and Planetary Science Letters 94, 1-21.

Bowin, C., Purdy, G.M., Johnston, C., Shor, G., Lawver, L., Hartono, H.M.S., Jezek, P., 1980. Arc-continent collision in Banda Sea region. AAPG Bulletin 64, 868-915.

Cardwell, R.K., Isacks, B.L., 1978. Geometry of subducted lithosphere beneath banda sea in eastern indonesia from seismicity and fault plane solutions. Journal of Geophysical Research 83, 2825-2838.

Coltorti, M., Bonadiman, C., Faccini, B., Grégoire, M., O'Reilly, S.Y., Powell, W., 2007. Amphiboles from suprasubduction and intraplate lithospheric mantle. Lithos 99, 68-84.

Condamine, P., Médard, E., Devidal, J.-L., 2016. Experimental melting of phlogopite-peridotite in the garnet stability field. Contributions to Mineralogy and Petrology 171.

Conticelli, S., 1998. The effect of crustal contamination on ultrapotassic magmas with lamproitic affinity: mineralogical, geochemical and isotope data from the Torre Alfina lavas and xenoliths, Central Italy. Chemical Geology 149, 51-81.

Conticelli, S., Avanzinelli, R., Ammannati, E., Casalini, M., 2015. The role of carbon from recycled sediments in the origin of ultrapotassic igneous rocks in the Central Mediterranean. Lithos 232, 174-196.

Conticelli, S., Guarnieri, L., Farinelli, A., Mattei, M., Avanzinelli, R., Bianchini, G., Boari, E., Tommasini, S., Tiepolo, M., Prelević, D., Venturelli, G., 2009a. Trace elements and Sr–Nd–Pb isotopes of K-rich, shoshonitic, and calc-alkaline magmatism of the Western Mediterranean Region: Genesis of ultrapotassic to calc-alkaline magmatic associations in a post-collisional geodynamic setting. Lithos 107, 68-92.

Conticelli, S., Marchionni, S., Rosa, D., Giordano, G., Boari, E., Avanzinelli, R., 2009b. Shoshonite and sub-alkaline magmas from an ultrapotassic volcano: Sr–Nd–Pb isotope data on the Roccamonfina volcanic rocks, Roman Magmatic Province, Southern Italy. Contributions to Mineralogy and Petrology 157, 41-63.

Das, S., 2004. Seismicity gaps and the shape of the seismic zone in the Banda Sea region from relocated hypocenters. Journal of Geophysical Research-Solid Earth 109.

Di Leo, J.F., Wookey, J., Hammond, J.O.S., Kendall, J.M., Kaneshima, S., Inoue, H., Yamashina, T., Harjadi, P., 2012. Mantle flow in regions of complex tectonics: Insights from Indonesia. Geochemistry, Geophysics, Geosystems 13, n/a-n/a.

Edwards, C., Menzies, M., Thirlwall, M., 1991. Evidence from Muriah, Indonesia, for the Interplay of Supra-Subduction Zone and Intraplate Processes in the Genesis of Potassic Alkaline Magmas. Journal of Petrology 32, 555-592.

Elburg, M.A., Foden, J.D., van Bergen, M.J., Zulkarnain, I., 2005. Australia and Indonesia in collision: geochemical sources of magmatism. Journal of Volcanology and Geothermal Research 140, 25-47.

Elburg, M.A., van Bergen, M., Hoogewerff, J., Foden, J., Vroon, P., Zulkarnain, I., Nasution, A., 2002. Geochemical trends across an arc-continent collision zone: magma sources and slab-wedge transfer processes below the Pantar Strait volcanoes, Indonesia. Geochimica et Cosmochimica Acta 66, 2771-2789.

Elburg, M.A., van Bergen, M.J., Foden, J.D., 2004. Subducted upper and lower continental crust contributes to magmatism in the collision sector of the Sunda-Banda arc, Indonesia. Geology 32, 41.

Elliott, T., 2013. Tracers of the Slab, Inside the Subduction Factory. American Geophysical Union, pp. 23-45.

Ely, K.S., Sandiford, M., 2010. Seismic response to slab rupture and variation in lithospheric structure beneath the Savu Sea, Indonesia. Tectonophysics 483, 112-124.

Engdahl, E.R., Villaseñor, A., 2002. Global Seismicity: 1900–1999, in: W.H.K. Lee, H.K., P.C. Jennings, and C. Kisslinger (Ed.), International Handbook of Earthquake and Engineering Seismology, Part A. Academic Press, pp. 665–690.

Ernst, W.G., 1981. Petrogenesis of eclogites and peridotites from the Western and Ligurian Alps. American Mineralogist 66, 443.

Faccenna, C., Becker, T.W., Lucente, F.P., Jolivet, L., Rossetti, F., 2001. History of subduction and back arc extension in the Central Mediterranean. Geophysical Journal International 145, 809-820.

Fiorentini, M.L., Garwin, S.L., 2010. Evidence of a mantle contribution in the genesis of magmatic rocks from the Neogene Batu Hijau district in the Sunda Arc, South Western Sumbawa, Indonesia. Contributions to Mineralogy and Petrology 159, 819-837.

Foden, J., Varne, R., 1980. The petrology and tectonic setting of quaternary - recent volcanic centers of lombok and sumbawa, sunda arc. Chemical Geology 30, 201-226.

Foley, S., 1992. Vein-plus-wall-rock melting mechanisms in the lithosphere and the origin of potassic alkaline magmas. Lithos 28, 435-453.

Furman, T., Graham, D., 1999. Erosion of lithospheric mantle beneath the East African Rift system: geochemical evidence from the Kivu volcanic province. Lithos 48, 237-262.

Garwin, S.L., 2000. The setting, geometry and timing of intrusion-related hydrothermal systems in the vicinity of the Batu Hijau porphyry copper-gold deposit, Sumbawa, Indonesia. University of Western Australia, p. 320.

Gasparon, M., Varne, R., 1998. Crustal assimilation versus subducted sediment input in west Sunda arc volcanics: An evaluation. Mineralogy and Petrology 64, 89-117.

Gertisser, R., Self, S., Thomas, L.E., Handley, H.K., Van Calsteren, P., Wolff, J.A., 2012. Processes and Timescales of Magma Genesis and Differentiation Leading to the Great Tambora Eruption in 1815. Journal of Petrology 53, 271-297.

Hall, R., 2011. Australia- SE Asia collison: plate tectonics and crustal flow, in: Hall, R., Cottam, M.A., Wilson, M.E.J. (Eds.), The SE Asian gateway: history and tectonics of Australia-Asia collision. Geological Society of London Special Publication, pp. 75-109.

Hall, R., 2012. Late Jurassic–Cenozoic reconstructions of the Indonesian region and the Indian Ocean. Tectonophysics 570–571, 1-41.

Hall, R., Spakman, W., 2015. Mantle structure and tectonic history of SE Asia. Tectonophysics 658, 14-45.

Hamilton, W.B., 1972. Preliminary tectonic map of the Indonesian region, Open-File Report, - ed.

Hamilton, W.B., 1979. Tectonics of the Indonesian region, Professional Paper, - ed.

Handley, H.K., Blichert-Toft, J., Gertisser, R., Macpherson, C.G., Turner, S.P., Zaennudin, A., Abdurrachman, M., 2014. Insights from Pb and O isotopes into along-arc variations in subduction inputs and crustal assimilation for volcanic rocks in Java, Sunda arc, Indonesia. Geochimica et Cosmochimica Acta 139, 205-226.

Handley, H.K., Turner, S., Macpherson, C.G., Gertisser, R., Davidson, J.P., 2011. Hf–Nd isotope and trace element constraints on subduction inputs at island arcs: Limitations of Hf anomalies as sediment input indicators. Earth and Planetary Science Letters 304, 212-223.

Hilton, D.R., Craig, H., 1989. A helium isotope transect along the Indonesian archipelago. Nature 342, 906-908.

Hilton, D.R., Hoogewerff, J.A., van Bergen, M.J., Hammerschmidt, K., 1992. Mapping magma sources in the east Sunda-Banda arcs, Indonesia: Constraints from helium isotopes. Geochimica et Cosmochimica Acta 56, 851-859.

Ionov, D.A., Mukasa, S.B., Bodinier, J.-L., 2002. Sr–Nd–Pb Isotopic Compositions of Peridotite Xenoliths from Spitsbergen: Numerical Modelling Indicates Sr–Nd Decoupling in the Mantle by Melt Percolation Metasomatism. Journal of Petrology 43, 2261-2278.

Ishimaru, S., Arai, S., Ishida, Y., Shirasaka, M., Okrugin, V.M., 2006. Melting and Multi-stage Metasomatism in the Mantle Wedge beneath a Frontal Arc Inferred from Highly Depleted Peridotite Xenoliths from the Avacha Volcano, Southern Kamchatka. Journal of Petrology 48, 395-433.

Ishizuka, O., Taylor, R.N., Yuasa, M., Milton, J.A., Nesbitt, R.W., Uto, K., Sakamoto, I., 2007. Processes controlling along-arc isotopic variation of the southern Izu-Bonin arc. Geochemistry, Geophysics, Geosystems 8, n/a-n/a.

Katili, J.A., 1970. Large transcurrent faults in Southeast Asia with special reference to Indonesia. Geologische Rundschau 59, 581-600.

Kepezhinskas, P., Defant, M.J., Drummond, M.S., 1996. Progressive enrichment of island arc mantle by melt-peridotite interaction inferred from Kamchatka xenoliths. Geochimica et Cosmochimica Acta 60, 1217-1229.

Khedr, M.Z., Arai, S., 2009. Geochemistry of metasomatized peridotites above subducting slab: a case study of hydrous metaperidotites from Happo-O'ne complex, central Japan. Journal of Mineralogical and Petrological Sciences 104, 313-318.

Konzett, J., Ulmer, P., 1999. The Stability of Hydrous Potassic Phases in Lherzolitic Mantle—an Experimental Study to 9.5 GPa in Simplified and Natural Bulk Compositions. Journal of Petrology 40, 629-652.

Kundu, B., Gahalaut, V.K., 2011. Slab detachment of subducted Indo-Australian plate beneath Sunda arc, Indonesia. Journal of Earth System Science 120, 193-204.

LaTourrette, T., Hervig, R.L., Holloway, J.R., 1995. Trace element partitioning between amphibole, phlogopite, and basanite melt. Earth and Planetary Science Letters 135, 13-30.

Lu, M., Hofmann, A.W., Mazzucchelli, M., Rivalenti, G., 1997. The mafic-ultramafic complex near Finero (Ivrea-Verbano Zone), II. Geochronology and isotope geochemistry. Chemical Geology 140, 223-235.

Marocchi, M., Hermann, J., Morten, L., 2007. Evidence for multi-stage metasomatism of chlorite-amphibole peridotites (Ulten Zone, Italy): Constraints from trace element compositions of hydrous phases. Lithos 99, 85-104.

McCaffrey, R., 1989. Seismological constraints and speculations on banda arc tectonics. Netherlands Journal of Sea Research 24, 141-152.

McDonough, W.F., Sun, S.s., 1995. The composition of the Earth. Chemical Geology 120, 223-253.

McInnes, B.I.A., Gregoire, M., Binns, R.A., Herzig, P.M., Hannington, M.D., 2001. Hydrous metasomatism of oceanic sub-arc mantle, Lihir, Papua New Guinea: petrology and geochemistry of fluid-metasomatised mantle wedge xenoliths. Earth and Planetary Science Letters 188, 169-183.

Nebel, O., Vroon, P.Z., van Westrenen, W., Iizuka, T., Davies, G.R., 2011. The effect of sediment recycling in subduction zones on the Hf isotope character of new arc crust, Banda arc, Indonesia. Earth and Planetary Science Letters 303, 240-250.

Nugroho, H., Harris, R., Lestariya, A.W., Maruf, B., 2009. Plate boundary reorganization in the active Banda Arc–continent collision: Insights from new GPS measurements. Tectonophysics 479, 52-65.

O'Hara, M.J., Richardson, S.W., Wilson, G., 1971. Garnet-peridotite stability and occurrence in crust and mantle. Contributions to Mineralogy and Petrology 32, 48-68.

O'Nions, R.K., McKenzie, D.P., 1988. Melting and continent generation. Earth and Planetary Science Letters 90, 449-456.

Pacey, A., Macpherson, C.G., McCaffrey, K.J.W., 2013. Linear volcanic segments in the central Sunda Arc, Indonesia, identified using Hough Transform analysis: Implications for arc lithosphere control upon volcano distribution. Earth and Planetary Science Letters 369–370, 24-33.

Peccerillo, A., 1998. Relationships between ultrapotassic and carbonate-rich volcanic rocks in central Italy: petrogenetic and geodynamic implications. Lithos 43, 267-279.

Peccerillo, A., 2001. Geochemical similarities between the Vesuvius, Phlegraean Fields and Stromboli Volcanoes: petrogenetic, geodynamic and volcanological implications. Mineralogy and Petrology 73, 93-105.

Perini, G., Conticelli, S., 2002. Crystallization conditions of leucite-bearing magmas and their implications on the magmatological evolution of ultrapotassic magmas: the Vico Volcano, Central Italy. Mineralogy and Petrology 74, 253-276.

Plank, T., Langmuir, C.H., 1998. The chemical composition of subducting sediment and its consequences for the crust and mantle. Chemical Geology 145, 325-394.

Rehkamper, M., Hofmann, A.W., 1997. Recycled ocean crust and sediment in Indian Ocean MORB. Earth and Planetary Science Letters 147, 93-106.

Schiavi, F., Kobayashi, K., Nakamura, E., Tiepolo, M., Vannucci, R., 2012. Trace element and Pb–B–Li isotope systematics of olivine-hosted melt inclusions: insights into source metasomatism beneath Stromboli (southern Italy). Contributions to Mineralogy and Petrology 163, 1011-1031.

Siebert, L., Simkin, T., Kimberly, P., 2011. Volcanoes of the World : Third Edition (3). University of California Press, Berkeley, US.

Smyth, H., Hall, R., Hamilton, J., Kinny, P., 2005. East Java: Cenozoic basins, volcanoes and ancient basement. Indonesian Petroleum Association, Proceedings 30th Annual Convention, 251-266.

Smyth, H.R., Hall, R., Nichols, G.J., 2008. Significant Volcanic Contribution to Some Quartz-Rich Sandstones, East Java, Indonesia. Journal of Sedimentary Research 78, 335-356.

Spakman, W., Hall, R., 2010. Surface deformation and slab-mantle interaction during Banda arc subduction rollback. Nature Geoscience 3, 562-566.

Staudigel, H., Davies, G.R., Hart, S.R., Marchant, K.M., Smith, B.M., 1995. Large scale isotopic Sr, Nd and O isotopic anatomy of altered oceanic crust: DSDP/ODP sites417/418. Earth and Planetary Science Letters 130, 169-185.

Stolz, A.J., Varne, R., Davies, G.R., Wheller, G.E., Foden, J.D., 1990. Magma source components in an arc-continent collision zone - the flores-lembata sector, sunda arc, indonesia. Contributions to Mineralogy and Petrology 105, 585-601.

Sudo, A., Tatsumi, Y., 1990. Phlogopite and K-amphibole in the upper mantle: Implication for magma genesis in subduction zones. Geophysical Research Letters 17, 29-32.

Syracuse, E.M., Abers, G.A., 2006. Global compilation of variations in slab depth beneath arc volcanoes and implications. Geochemistry Geophysics Geosystems 7, 18.

Turner, S., Foden, J., 2001. U, Th and Ra disequilibria, Sr, Nd and Pb isotope and trace element variations in Sunda arc lavas: predominance of a subducted sediment component. Contributions to Mineralogy and Petrology 142, 43-57.

Turner, S., Foden, J., George, R., Evans, P., Varne, R., Elburg, M., Jenner, G., 2003. Rates and processes of potassic magma evolution beneath Sangeang Api volcano, East Sunda arc, Indonesia. Journal of Petrology 44, 491-515.

Vroon, P.Z., van Bergen, M.J., Klaver, G.J., White, W.M., 1995. Strontium, neodymium, and lead isotopic and trace-element signatures of the East indonesian sediments: provenance and implications for banda arc magma genesis. Geochimica et Cosmochimica Acta 59, 2573-2598.

Vroon, P.Z., van Bergen, M.J., White, W.M., Varekamp, J.C., 1993. Sr-Nd-Pb isotope systematics of the Banda Arc, Indonesia: Combined subduction and assimilation of continental material. Journal of Geophysical Research: Solid Earth 98, 22349-22366.

Wheller, G.E., Varne, R., Foden, J.D., Abbott, M.J., 1987. Geochemistry of quaternary volcanism in the Sunda-Banda arc, Indonesia, and three-component genesis of island-arc basaltic magmas. Journal of Volcanology and Geothermal Research 32, 137-160.

Whitford, D.J., 1975. Strontium isotopic studies of the volcanic rocks of the Saunda arc, Indonesia, and their petrogenetic implications. Geochimica et Cosmochimica Acta 39, 1287-1302.

Whitford, D.J., Jezek, P.A., 1982. Isotopic constraints on the role of subducted sialic material in Indonesian island-arc magmatism. Geological Society of America Bulletin 93, 504-513.

Whitford, D.J., Nicholls, I.A., Taylor, S.R., 1979. Spatial variations in the geochemistry of quaternary lavas across the Sunda arc in Java and Bali. Contributions to Mineralogy and Petrology 70, 341-356.

Widiyantoro, S., Pesicek, J.D., Thurber, C.H., 2011. Subducting slab structure below the eastern Sunda arc inferred from non-linear seismic tomographic imaging. Geological Society, London, Special Publications 355, 139-155.

Widiyantoro, S., van der Hilst, R., 1997. Mantle structure beneath Indonesia inferred from high-resolution tomographic imaging. Geophysical Journal International 130, 167-182.

Workman, R.K., Hart, S.R., 2005. Major and trace element composition of the depleted MORB mantle (DMM). Earth and Planetary Science Letters 231, 53-72.

Wunder, B., Melzer, S., 2003. Experimental evidence on phlogopitic mantle metasomatism induced by phengite dehydration. European Journal of Mineralogy 15, 641-647.

Zanetti, A., Mazzucchelli, M., Rivalenti, G., Vannucci, R., 1999. The Finero phlogopite-peridotite massif: an example of subduction-related metasomatism. Contributions to Mineralogy and Petrology 134, 107-122.

Chapter 7

Conclusions and future work

This thesis investigated petrological and geochemical processes occurring in several young or active volcanoes in the Sumbawa-Flores sector of the eastern Sunda Arc of Indonesia. The primary goal of this thesis was to investigate the competing influence of source region and upper plate processes on the compositions of erupted arc magmas. Through the investigation of fractionation, redox profiles, cumulate contamination and iron stable isotope fractionation the upper plate controls on magma geochemistry were studied. Similarly, source region controls on magma compositions were investigated using trace element geochemistry, Fe-stable isotope variations and radiogenic isotope compositions. These findings are outlined in this conclusions chapter.

Firstly, Chapters 2, 3 and 4 investigated the petrogenesis of Sangeang Api volcano; focussing on the relationship between the ultrapotassic lavas and the two groups of entrained cumulate xenoliths, composition of the source mantle, partial melting conditions at the source, magma ascent processes in the crustal magmatic tract and iron isotope fractionation within the arc magmatic suite. Following this, Chapter 5 outlined the petrology and geochemistry of some previously unstudied volcanic centres from Sumbawa (D. Kota and D. Kuta) and Flores (Wai Sano), as well as the basement geology of northwest Flores. This chapter outlined significant differences in the petrology and geochemistry of the volcanoes. Noting that whilst the quaternary volcanoes of NE Sumbawa are relatively similar in their petrogenesis to the modern Sangeang Api, Wai Sano in SW Flores is highly distinctive, both with its adakitic characteristics and its novel genesis from partial melting of underplated crust. Chapter 6 provided evidence for regional and local controls on the geochemistry of erupted Sunda Arc lavas. Focussing on along- and across-arc variations in lava major-element, trace-element and isotopic compositions and identifying the influence of heterogeneities in subducted sediments, windows and tears in the subducting slab and crustal faulting processes. This chapter brings together the findings of this thesis and based on these provides future directions for research.

CONCLUSIONS

Sumbawa and its close neighbour Sangeang Api are host to arc magmatic intrusions and volcanoes stretching from the Neogene Batu Hijau porphyry Cu-Au deposit (Fiorentini and Garwin, 2010; Garwin, 2000; Wawryk and Foden, 2017), through quaternary high-K calc-alkaline volcanics, such as D. Kuta and D. Kota, quaternary leucitites of Sangenges and Soromundi (Foden and Varne, 1980) and the active modern volcanoes of Tambora and Sangeang Api. The development and northwards movement of a slab tear gap beneath the Lombok-Sumbawa region (Kundu and Gahalaut, 2011) likely precipitated the observed spatial and temporal distribution of volcanoes on Sumbawa. It has been suggested that the buoyant Roo Rise collided with the Sunda Arc, blocking the subduction zone and leading to the development of slab tears (Fiorentini and Garwin, 2010; Garwin, 2000). This thesis proposed that the influx of hot mantle through a slab window has raised the mantle geotherm, progressively melting metasomatic veining in the mantle wedge. Similar processes have been suggested to be occurring in the Roman Magmatic Province, where the magmas share many similarities with those of the

Sumbawa sector (Conticelli et al., 2009; Rosenbaum et al., 2008). Thus, highlighting source region controls in the eastern Sunda Arc.

A primary goal of this thesis was to further understand the source, differentiation, ascent and redox processes occurring throughout the Sangeang Api magmatic system to further understand how arc magmas are affected by upper plate processes. This thesis presents evidence that the Sangeang Api magmas were sourced by <3% partial melts of an MORB-source enriched by the addition of 1.5-2.5% mixed sediments and possibly metasomatized by the addition of phlogopite and amphibole at pressures large enough to stabilise 0.8-3.75% garnet. This both supports and disagrees with previous work by (Turner et al., 2003), who suggested similar amounts of partial melting and sediment input, but only of a single sediment, and who argued for no role of mantle metasomatism. Trace element modelling, MELTs modelling and least squares mixing models suggest that lava evolution was driven predominantly by the fractional crystallisation of the cumulate xenoliths. However, despite previous suggestions that pyroxenite crystallisation was succeeded by gabbro crystallisation (Turner et al., 2003), this thesis suggests that the two groups of cumulates crystallised in parallel with pressure, water content, oxidation state and melt composition controlling phase stability. Evidence from Pb isotopes suggests the influence of I-OIB style mantle in the Sangeang Api source, further supporting suggestions for the presence of a slab window beneath Sumbawa. Given that the quaternary lavas of Kota and Kuta (NE Sumbawa) appear to follow a differentiation path similar to the gabbro trend of Sangeang Api and the entrainment of a single gabbro xenolith, it might be assumed that the most primitive magmas from their system were drier and formed at shallower depths. This is supported by amphibole thermobarometry, which suggests that the NE Sumbawa lavas formed at shallow depths and low water contents relative to the Sangeang Api magma system.

Turner et al. (2003) proposed that Sangeang Api magmas were contaminated by a maximum assimilation of <15% Indian Ocean crust. However, the findings of this thesis demonstrate that contamination within the Sangeang Api magmatic system is caused by post-crystallisation interaction of variably fractionated fluids with accumulated crystal piles. Contamination of cumulate piles is reflected in exacerbated incompatible element contents of cumulate xenoliths and Fe-isotope disequilibrium within the cumulate xenolith whole-rocks and Fe-Mg silicate mineral separates. Petrological textures of post-crystallisation contamination are shown by the introduction of liquids into the cumulate piles through the inefficient extraction of fractionated melts, the disaggregation of poorly welded cumulate piles and subsequent entrainment in later fluids, post-crystallisation overgrowths on disaggregated cumulate minerals, intrusion of melt veins into cumulate piles and cryptic enrichment through the late crystallisation of post-cumulate amphibole. These contamination effects are likely reflected in ^{226}Ra excesses noted throughout the Sangeang Api magmatic system by Turner et al. (2003). ^{226}Ra excesses are suggested to be formed by rapid melt extraction and transport through the crust (Turner et al., 2001), preferential melting of phlogopite/amphibole in the mantle source (Feineman and DePaolo, 2003) or from the incongruent breakdown of amphibolite facies lower crust (Dufek and Cooper, 2005). An analysis of cumulate amphibole from a Sangeang Api

cumulate xenolith records very high $^{226}Ra/^{230}Th$ (~8.7), as does an interstitial glass (~2.3) (Turner et al., 2003). Therefore, it might be surmised that cumulate xenolith samples that have experienced post-crystallisation contamination would record relatively high $^{226}Ra/^{230}Th$, and vice-versa those which are relatively primitive would have low $^{226}Ra/^{230}Th$. Cumulate xenolith studies analysed in the study of Turner et al. (2003) show this relationship, with samples poor in incompatible elements (primitive) having low $^{226}Ra/^{230}Th$ more enriched in incompatibles (contaminated) have higher $^{226}Ra/^{230}Th$. Thus, putting the conclusions presented by Turner et al. (2003) of rapid melt extraction from the mantle source into doubt, and highlighting the effects of melt contamination in the Sangeang Api magmatic system. Similarly, evidence of metasomatism by hydrous phases (amphibole and phlogopite) in the source mantle of the Sangeang Api system may provide another source of $^{226}Ra/^{230}Th$ excesses.

A key problem this thesis aimed to answer is the source of arc magma oxidation, specifically the role of degassing during magma decompression and its effect on magma oxidation state. Sangeang Api amphiboles studied in this thesis (see Chapter 3) provide evidence of the Sangeang Api magmas following an anticlockwise path of oxidation followed by reduction associated with decompression. This was linked to decreasing water content, models of magma volatile content and lava and glass volatile contents to suggest sulphur as the primary redox agent in the Sangeang Api system. Similarly, the Sangeang Api lavas display decreasing $Fe^{3+}/\Sigma Fe$ with increasing indices of differentiation (SiO_2, Zr, etc.). This evidence suggests that there are competing redox processes at play at different levels of the Sangeang Api crust. Previous studies of volatiles in arc systems have suggested that magmas either oxidise or reduce as they ascend to the surface (Botcharnikov et al., 2005; Crabtree and Lange, 2011; Humphreys et al., 2015; Kelley and Cottrell, 2009; Moussallam et al., 2014), but that redox paths do not change during decompression. This thesis supports that magmatic degassing can alter redox state, but, proposes that redox state is controlled by the dominant degassing regime at any given point within a magmatic system. Initial sulphur content of a primitive magma likely determines the redox path followed by a magma, similarly melt contamination by sulphide- or sulphate-rich fluids/materials at a certain crustal horizon will drive changes in magma redox path. The redox state of intrusive magmas is an important factor in determining the metal species concentrated in economic ore deposits (Hart et al., 2004; Richards, 2015; Tomkins et al., 2012), and thus understanding how magma redox evolves during ascent of the crust and how it relates to magma volatile content is important in our understanding of the formation of economic ore deposits. Ultimately, this thesis supports a mantle source for the initial oxidation of primitive arc magmas, suggesting that crustal degassing processes act to alter this initial oxidised nature.

Fracture and entrainment of cumulate xenoliths, along with the disaggregation, and infiltration of fluids through, cumulate piles was likely facilitated by crustal faulting. Faulting above the brittle-ductile transition is evidenced by grain size reduction textures (cataclasite and mylonite textures). Faulting may act to channelize the flow of fluids and melts throughout the cumulate piles. This, therefore, suggests that the Sangeang Api cumulates must have formed above the brittle-ductile transition. Amphibole

thermobarometry suggests the magmas ascended rapidly from the mid-crust to the surface. Rapid decompression of magmas from the mid-crust may have been aided by faulting in the upper crust.

Wai Sano is unique amongst the Sunda Arc in erupting lavas with an adakitic character (SiO_2 >63wt%, Al_2O_3 >17wt.%, MgO <2.5wt.%, Y <9ppm, Yb <1ppm and Sr/Y >31). Typically, adakites have low $^{87}Sr/^{86}Sr$ compositions, reflecting their origin as partial melts of the subducting oceanic slab (Castillo, 2012; Defant and Drummond, 1990; Defant and Kepezhinskas, 2001; Peacock et al., 1994; Yogodzinski et al., 2001). However, the Wai Sano magmas have high Sr isotope compositions ($^{87}Sr/^{86}Sr$ >0.706) suggesting that they cannot be sourced from melting of basaltic oceanic crust. These differences in isotopic characteristics have been interpreted to reflect partial melting of basaltic underplating with isotopic characteristics typically of the eastern Sunda Arc. pMELTS modelling supports this conclusion, suggesting that, as anticipated, melting of a basaltic/gabbroic can produce melt compositions like those of the Wai Sano lavas. Trace element data suggests that the Wai Sano lavas were produced in equilibrium with garnet and phlogopite, hinting at elevated pressures of melting. This suggests that the geodynamic setting from which they are sourced must have an elevated geotherm, possibly through edge flow related to slab tearing. Basement lavas of NW Flores display characteristics intermediate to the Sumbawan volcanics and Wai Sano, possibly showing evidence for the intermediate magmas between basaltic underplate partial melts and typical eastern Sunda Arc compositions.

Geodynamic controls on the geochemical compositions of Sangeang Api lavas have been highlighted by this thesis. The rear-arc ultrapotassic volcanoes of the Sunda Arc (e.g. Batu Tara, Sangeang Api and Muriah) share several characteristics that are controlled by similarities in their local tectonic setting; high K, depletion in HREE and enriched isotopic compositions. These typically reflect their source characteristics; deep partial melting (stabilising garnet) of metasomatized mantle (typically phlogopite enriched), possibly above slab tears and/or slab windows. Likewise, along-arc variations in isotopic compositions reflect local and regional heterogeneities in the subducting slab, with increasing influence of Australian continental material to the east and possible crustal assimilation and subducted sediment heterogeneity in Java. These findings are in agreement with previous studies of the Sunda Arc and further highlight the increasing influence on mantle wedge compositions of Australian continental collision with the arc closer to the Sunda-Banda transition (Elburg et al., 2005; Elburg et al., 2002; Elburg et al., 2004; Handley et al., 2014; Handley et al., 2011; Hilton and Craig, 1989; Hilton et al., 1992; Stolz et al., 1990; Turner and Foden, 2001; Wheller et al., 1987). Local geodynamic settings are a primary control on the composition of erupted products and their spatial distribution. Developing tectonic settings are reflected in the spatial distribution and chemistry of progressively younger volcanoes (e.g. Sumbawa).

FUTURE WORK

$^{226}Ra/^{230}Th$ excesses in the Sangeang Api system have previously been posited to be evidence of rapid melt extraction from the mantle. However, the multitudinous evidence

for cumulate xenolith contamination by the percolation of melts and crystallisation of hydrated mineral species puts these suggestions into doubt, possibly accounting for the observed $^{226}Ra/^{230}Th$ excesses. Similarly, the evidence for a metasomatized source mantle presented in this study could provide a further source of $^{226}Ra/^{230}Th$ excesses. To provide better constraints on the origin of ^{226}Ra excesses within the Sangeang Api system detailed U-series isotope studies of the cumulate and post-cumulate mineralogy, along with that of interstitial glass and intrusive melt veins could be undertaken. This would provide evidence of the effects of contamination on the U-series isotopic character of the cumulate xenoliths and the lavas. ^{226}Ra excesses can originate from amphibolite metamorphism and breakdown in the lower crust (Dufek and Cooper, 2005). Berlo et al. (2006) argue that these processes are primarily going to be important in adakite settings. Given the adakitic nature of Wai Sano, as well as the suggestion that phlogopite is an important phase in the basaltic underplate source, it might be surmised that Wai Sano would record large ^{226}Ra excesses, thus presenting an interesting direction for future research.

Cumulate mineral separates from Sangeang Api record significant Fe-isotope disequilibria, however, the sample selection and analytical methods utilised in this study only record evidence of the bulk Fe-isotope composition of an entire crystal grain and lack textural evidence of their exact cumulate origin (e.g. primary cumulate or post-cumulate). Recent developments in SIMS (Marin-Carbonne et al., 2011) and femtosecond LA-MC-ICPMS techniques (Horn and von Blanckenburg, 2007; Horn et al., 2006) have allowed for the in-situ analysis of Fe-isotopes, providing Fe-isotope data accurate to ~0.3‰ (Dauphas et al., 2017) from targeted textural sites within a sample. Fe-isotope disequilibrium profiles within olivine phenocrysts were measured by Sio et al. (2013) using SIMS, femtosecond LA-ICP-MS and microdrilling techniques. All three methods provided results in agreement with one another, suggesting that either of these techniques can be used (Sio et al., 2013). The microdrilling process is as follows; place a drop of water on the sample, drill the targeted textural site and remove the produced slurry using a pipette which (Dauphas et al., 2017; Sio et al., 2013). The slurry can then be dried down and undergo a typical acid digestion process and anion exchange column purification. Due to the possible iron isotope fractionation effects experienced during LA-ICP-MS and SIMS analysis, as well its relative simplicity, the microdrilling technique presents the best possible candidate for in-situ Fe-isotope analysis of selected textural sites in the Sangeang Api cumulate suite.

This thesis presents evidence of redox changes in the Sangeang Api magmatic system through the application of amphibole geooxythermobarometry (Ridolfi and Renzulli, 2012; Ridolfi et al., 2010) and the determination of lava oxidation state by wet chemistry (Wilson, 1960). Direct evidence of Fe and S oxidation state in interstitial glass and melt inclusions, as well as volatile content (e.g. H_2O, S, etc.), can be obtained from μ-XANES spectral analysis (Berry et al., 2013; Botcharnikov et al., 2005; Dyar et al., 2012; Kelley and Cottrell, 2012; Métrich et al., 2009; Moussallam et al., 2014; Shorttle et al., 2015). The proposed redox path of the Sangeang Api magmas could be assessed by the direct analysis of progressively degassed melt inclusions representing different stages of magma fractionation (from primitive to fractionated). Alternatively, recent advances in the

determination of the water content of nominally anhydrous minerals (NAMs, e.g. clinopyroxene and olivine) in trace amounts allows for the calculation of water contents of magmas from which the NAMs crystallised (Lloyd et al., 2016; Turner et al., 2017). Lloyd et al. (2016) provide evidence that zoned clinopyroxene phenocrysts record decreasing trace amounts of water towards their rim, evidencing magmatic degassing during ascent. The oxidation state of iron in clinopyroxene phenocrysts reflects that of the magma that they have crystallised from, thus by combining direct measurements of Fe oxidation state in the phenocryst, melt inclusion data and water content it should be possible to assess degassing processes associated with redox changes.

Further study of the Wai Sano products and nearby volcanic centres would aid in developing models of the production of the adakitic character of the Wai Sano lavas. Further targets for geochemical and petrological studies include the basement of SW Flores, the other active volcanoes of western Flores (Ranakah, Poco Leok, etc.) and the nearby islands that separate Flores and Sumbawa (Komodo, Rinca and Banta). Similarly, more in-depth studies (geochemisty and geochronology) of the extinct volcanic centres and basement geology of Sumbawa would help to further understanding of how volcanism has developed across Sumbawa in response to changes in the geodynamic and tectonic setting.

REFERENCES

Berlo, K., Turner, S., Blundy, J., Hawkesworth, C., 2006. $^{226}Ra/^{230}Th$ excess generated in the lower crust: Implications for magma transport and storage time scales: Comment and Reply. COMMENT 34, e101-e102.

Berry, A.J., Yaxley, G.M., Hanger, B.J., Woodland, A.B., de Jonge, M.D., Howard, D.L., Paterson, D., Kamenetsky, V.S., 2013. Quantitative mapping of the oxidative effects of mantle metasomatism. Geology 41, 683-686.

Botcharnikov, R.E., Koepke, J., Holtz, F., McCammon, C., Wilke, M., 2005. The effect of water activity on the oxidation and structural state of Fe in a ferro-basaltic melt. Geochimica et Cosmochimica Acta 69, 5071-5085.

Castillo, P.R., 2012. Adakite petrogenesis. Lithos 134, 304-316.

Conticelli, S., Marchionni, S., Rosa, D., Giordano, G., Boari, E., Avanzinelli, R., 2009. Shoshonite and sub-alkaline magmas from an ultrapotassic volcano: Sr–Nd–Pb isotope data on the Roccamonfina volcanic rocks, Roman Magmatic Province, Southern Italy. Contributions to Mineralogy and Petrology 157, 41-63.

Crabtree, S., Lange, R., 2011. An evaluation of the effect of degassing on the oxidation state of hydrous andesite and dacite magmas: A comparison of pre- and post-eruptive Fe 2+ concentrations.

Dauphas, N., John, S.G., Rouxel, O., 2017. Iron Isotope Systematics. Reviews in Mineralogy and Geochemistry 82, 415-510.

Defant, M.J., Drummond, M.S., 1990. Derivation of some modern arc magmas by melting of young subducted lithosphere. Nature 347, 662-665.

Defant, M.J., Kepezhinskas, P., 2001. Evidence suggests slab melting in arc magmas. Eos, Transactions American Geophysical Union 82, 65-69.

Dufek, J., Cooper, K.M., 2005. $^{226}Ra/^{230}Th$ excess generated in the lower crust: Implications for magma transport and storage time scales. Geology 33, 833-836.

Dyar, M.D., Breves, E.A., Emerson, E., Bell, S.W., Nelms, M., Ozanne, M.V., Peel, S.E., Carmosino, M.L., Tucker, J.M., Gunter, M.E., Delaney, J.S., Lanzirotti, A., Woodland, A.B., 2012. Accurate determination of ferric iron in garnets by bulk Mössbauer spectroscopy and synchrotron micro-XANES. American Mineralogist 97, 1726-1740.

Elburg, M.A., Foden, J.D., van Bergen, M.J., Zulkarnain, I., 2005. Australia and Indonesia in collision: geochemical sources of magmatism. Journal of Volcanology and Geothermal Research 140, 25-47.

Elburg, M.A., van Bergen, M., Hoogewerff, J., Foden, J., Vroon, P., Zulkarnain, I., Nasution, A., 2002. Geochemical trends across an arc-continent collision zone: magma sources and slab-wedge transfer processes below the Pantar Strait volcanoes, Indonesia. Geochimica et Cosmochimica Acta 66, 2771-2789.

Elburg, M.A., van Bergen, M.J., Foden, J.D., 2004. Subducted upper and lower continental crust contributes to magmatism in the collision sector of the Sunda-Banda arc, Indonesia. Geology 32, 41.

Feineman, M.D., DePaolo, D.J., 2003. Steady-state $^{226}Ra/^{230}Th$ disequilibrium in mantle minerals: Implications for melt transport rates in island arcs. Earth and Planetary Science Letters 215, 339-355.

Fiorentini, M.L., Garwin, S.L., 2010. Evidence of a mantle contribution in the genesis of magmatic rocks from the Neogene Batu Hijau district in the Sunda Arc, South Western Sumbawa, Indonesia. Contributions to Mineralogy and Petrology 159, 819-837.

Foden, J., Varne, R., 1980. The petrology and tectonic setting of quaternary - recent volcanic centers of lombok and sumbawa, sunda arc. Chemical Geology 30, 201-226.

Garwin, S.L., 2000. The setting, geometry and timing of intrusion-related hydrothermal systems in the vicinity of the Batu Hijau porphyry copper-gold deposit, Sumbawa, Indonesia. University of Western Australia, p. 320.

Handley, H.K., Blichert-Toft, J., Gertisser, R., Macpherson, C.G., Turner, S.P., Zaennudin, A., Abdurrachman, M., 2014. Insights from Pb and O isotopes into along-arc variations in subduction inputs and crustal assimilation for volcanic rocks in Java, Sunda arc, Indonesia. Geochimica et Cosmochimica Acta 139, 205-226.

Handley, H.K., Turner, S., Macpherson, C.G., Gertisser, R., Davidson, J.P., 2011. Hf–Nd isotope and trace element constraints on subduction inputs at island arcs: Limitations of

Hf anomalies as sediment input indicators. Earth and Planetary Science Letters 304, 212-223.

Hart, C., L. Mair, J., Goldfarb, R., Groves, D., 2004. Source and redox controls on metallogenic variations in intrusion-related ore systems, Tombstone-Tungsten Belt, Yukon Territory, Canada.

Hilton, D.R., Craig, H., 1989. A helium isotope transect along the Indonesian archipelago. Nature 342, 906-908.

Hilton, D.R., Hoogewerff, J.A., van Bergen, M.J., Hammerschmidt, K., 1992. Mapping magma sources in the east Sunda-Banda arcs, Indonesia: Constraints from helium isotopes. Geochimica et Cosmochimica Acta 56, 851-859.

Horn, I., von Blanckenburg, F., 2007. Investigation on elemental and isotopic fractionation during 196 nm femtosecond laser ablation multiple collector inductively coupled plasma mass spectrometry. Spectrochimica Acta Part B: Atomic Spectroscopy 62, 410-422.

Horn, I., von Blanckenburg, F., Schoenberg, R., Steinhoefel, G., Markl, G., 2006. In situ iron isotope ratio determination using UV-femtosecond laser ablation with application to hydrothermal ore formation processes. Geochimica et Cosmochimica Acta 70, 3677-3688.

Humphreys, M.C.S., Brooker, R.A., Fraser, D.G., Burgisser, A., Mangan, M.T., McCammon, C., 2015. Coupled Interactions between Volatile Activity and Fe Oxidation State during Arc Crustal Processes. Journal of Petrology 56, 795-814.

Kelley, K.A., Cottrell, E., 2009. Water and the Oxidation State of Subduction Zone Magmas. Science 325, 605-607.

Kelley, K.A., Cottrell, E., 2012. The influence of magmatic differentiation on the oxidation state of Fe in a basaltic arc magma. Earth and Planetary Science Letters 329–330, 109-121.

Kundu, B., Gahalaut, V.K., 2011. Slab detachment of subducted Indo-Australian plate beneath Sunda arc, Indonesia. Journal of Earth System Science 120, 193-204.

Lloyd, A.S., Ferriss, E., Ruprecht, P., Hauri, E.H., Jicha, B.R., Plank, T., 2016. An Assessment of Clinopyroxene as a Recorder of Magmatic Water and Magma Ascent Rate. Journal of Petrology 57, 1865-1886.

Marin-Carbonne, J., Rollion-Bard, C., Luais, B., 2011. In-situ measurements of iron isotopes by SIMS: MC-ICP-MS intercalibration and application to a magnetite crystal from the Gunflint chert. Chemical Geology 285, 50-61.

Métrich, N., Berry, A.J., O'Neill, H.S.C., Susini, J., 2009. The oxidation state of sulfur in synthetic and natural glasses determined by X-ray absorption spectroscopy. Geochimica et Cosmochimica Acta 73, 2382-2399.

Moussallam, Y., Oppenheimer, C., Scaillet, B., Gaillard, F., Kyle, P., Peters, N., Hartley, M., Berlo, K., Donovan, A., 2014. Tracking the changing oxidation state of Erebus magmas, from mantle to surface, driven by magma ascent and degassing. Earth and Planetary Science Letters 393, 200-209.

Peacock, S.M., Rushmer, T., Thompson, A.B., 1994. Partial melting of subducting oceanic crust. Earth and Planetary Science Letters 121, 227-244.

Richards, J.P., 2015. The oxidation state, and sulfur and Cu contents of arc magmas: implications for metallogeny. Lithos 233, 27-45.

Ridolfi, F., Renzulli, A., 2012. Calcic amphiboles in calc-alkaline and alkaline magmas: thermobarometric and chemometric empirical equations valid up to 1,130A degrees C and 2.2 GPa. Contributions to Mineralogy and Petrology 163, 877-895.

Ridolfi, F., Renzulli, A., Puerini, M., 2010. Stability and chemical equilibrium of amphibole in calc-alkaline magmas: an overview, new thermobarometric formulations and application to subduction-related volcanoes. Contributions to Mineralogy and Petrology 160, 45-66.

Rosenbaum, G., Gasparon, M., Lucente, F.P., Peccerillo, A., Miller, M.S., 2008. Kinematics of slab tear faults during subduction segmentation and implications for Italian magmatism. Tectonics 27, n/a-n/a.

Shorttle, O., Moussallam, Y., Hartley, M.E., Maclennan, J., Edmonds, M., Murton, B.J., 2015. Fe-XANES analyses of Reykjanes Ridge basalts: Implications for oceanic crust's role in the solid Earth oxygen cycle. Earth and Planetary Science Letters 427, 272-285.

Sio, C.K.I., Dauphas, N., Teng, F.-Z., Chaussidon, M., Helz, R.T., Roskosz, M., 2013. Discerning crystal growth from diffusion profiles in zoned olivine by in situ Mg–Fe isotopic analyses. Geochimica et Cosmochimica Acta 123, 302-321.

Stolz, A.J., Varne, R., Davies, G.R., Wheller, G.E., Foden, J.D., 1990. Magma source components in an arc-continent collision zone - the flores-lembata sector, sunda arc, indonesia. Contributions to Mineralogy and Petrology 105, 585-601.

Tomkins, A.G., Rebryna, K.C., Weinberg, R.F., Schaefer, B.F., 2012. Magmatic Sulfide Formation by Reduction of Oxidized Arc Basalt. Journal of Petrology 53, 1537-1567.

Turner, M., Turner, S., Mironov, N., Portnyagin, M., Hoernle, K., 2017. Can magmatic water contents be estimated from clinopyroxene phenocrysts in some lavas? A case study with implications for the origin of the Azores Islands. Chemical Geology 466, 436-445.

Turner, S., Evans, P., Hawkesworth, C., 2001. Ultrafast Source-to-Surface Movement of Melt at Island Arcs from ^{226}Ra-^{230}Th Systematics. Science 292, 1363-1366.

Turner, S., Foden, J., 2001. U, Th and Ra disequilibria, Sr, Nd and Pb isotope and trace element variations in Sunda arc lavas: predominance of a subducted sediment component. Contributions to Mineralogy and Petrology 142, 43-57.

Turner, S., Foden, J., George, R., Evans, P., Varne, R., Elburg, M., Jenner, G., 2003. Rates and processes of potassic magma evolution beneath Sangeang Api volcano, East Sunda arc, Indonesia. Journal of Petrology 44, 491-515.

Wawryk, C.M., Foden, J.D., 2017. Iron-isotope systematics from the Batu Hijau Cu-Au deposit, Sumbawa, Indonesia. Chemical Geology.

Wheller, G.E., Varne, R., Foden, J.D., Abbott, M.J., 1987. Geochemistry of quaternary volcanism in the Sunda-Banda arc, Indonesia, and three-component genesis of island-arc basaltic magmas. Journal of Volcanology and Geothermal Research 32, 137-160.

Wilson, A.D., 1960. The micro-determination of ferrous iron in silicate minerals by a volumetric and a colorimetric method. Analyst 85, 823-827.

Yogodzinski, G.M., Lees, J.M., Churikova, T.G., Dorendorf, F., Woerner, G., Volynets, O.N., 2001. Geochemical evidence for the melting of subducting oceanic lithosphere at plate edges. Nature 409, 500-504.

Appendix 1

Appendix 1 is the accompaniment to chapters 2, 3 and 4

Includes whole-rock and mineral geochemical data from Sangeang Api samples

Sample no.	BC14/ 004	BC14/ 005	BC14/ 006	BC14/ 007	BC14/ 008	BC14/ 010	BC14/ 011	BC14/ 012
Lith.	**Lava**	**Lava**	**Lava**	**Lava**	**Lava**	**Lava**	**Lava**	**Lava**
SiO_2	51.68	49.71	51.32	50.32	48.78	52.51	51.56	50.65
TiO_2	0.71	0.78	0.80	0.84	0.81	0.76	0.79	0.79
Al_2O_3	19.53	18.37	19.15	19.47	19.63	19.26	19.15	19.12
Fe_2O_3	7.47	8.25	8.72	9.46	8.89	8.06	8.42	8.94
MnO	0.20	0.20	0.22	0.22	0.22	0.20	0.20	0.21
MgO	2.80	3.48	3.55	4.03	3.39	3.29	3.48	3.67
CaO	7.95	8.37	8.65	9.44	9.69	8.18	8.59	8.85
Na_2O	5.26	4.00	4.21	4.36	4.41	4.26	4.06	3.93
K_2O	3.23	2.88	2.61	2.83	3.39	3.13	2.94	2.89
P_2O_5	0.52	0.34	0.38	0.35	0.53	0.35	0.35	0.36
SO_3	0.00	b.d.l.	b.d.l.	b.d.l.	b.d.l.	b.d.l.	b.d.l.	b.d.l.
Cl	1048	284.5	409	810.5	1059.5	378	147.5	654
LOI	0.55	3.61	0.34	-1.39	0.16	-0.05	0.45	0.52
Total	99.45	96.39	99.66	101.39	99.84	100.05	99.55	99.48
Mg#	0.43	0.45	0.45	0.46	0.43	0.45	0.45	0.45
Be	4	2	2.5	2	3.5	2.5	2.5	2
Sc	6.2	8.7	5.1	12.3	9.8	9.4	8.3	8.7
V	192	192.8	217.5	257.7	218.4	192	192.8	217.5
Cr	3.9		2.6	4	4.8	40.7	40.7	40.7
Co	61	43	50	38	38	40	58	48
Ni	15	15	15	15	15	15	15	15
Cu	122	134	93	175	122	134	134	136
Zn	100	98	108	98	100	94	98	100
Ga	22	20.4	20.4	19.2	19.6	19.8	20.8	20.2
As	10	4	2	2	3	4	6	4
Rb	115	96	79.4	81.6	93.6	96	96.8	91.2
Sr	1200	880	984	856	1190	888	912	896
Y	23.6	24.6	26.7	21.4	25.6	23.4	22.9	22.1
Zr	159	118	122	85	131	123	111	98
Nb	12	6	6	5	11	6	5.5	5
Mo	3	2	1.5	1.5	3	1.5	2	1.5
Sn	0.9	1.5	1.2	0.9	1.1	1	1.4	0.9
Sb	0.8	0.4	0.4	0.3	0.5	0.5	0.4	0.4
Cs	8.8	5.5	5	4.7	7.3	5.5	5.2	5.5
Ba	1820	1280	1210	1270	1410	1290	1250	1380

Table 1a: Whole-rock major and trace element geochemistry. All major elements analysed by XRF, trace elements analysed by solution-ICP-MS and XRF (samples analysed by XRF denoted with a *). Abbreviations: Pyrox. = pyroxenite, Hbl = Hornblende, Ol = olivine

Sample no.	BC14/ 004	BC14/ 005	BC14/ 006	BC14/ 007	BC14/ 008	BC14/ 010	BC14/ 011	BC14/ 012
Lith.	**Lava**	**Lava**	**Lava**	**Lava**	**Lava**	**Lava**	**Lava**	**Lava**
La	62.2	29.6	31.3	26.5	57.4	28.9	27.8	30.2
Ce	113	61.4	67.5	59.3	113	61.4	59.6	64.9
Pr	11.4	6.5	7.3	6.35	11.5	6.3	6.45	6.95
Nd	39.7	26.7	28.4	26.5	43.6	26.3	24.9	27.8
Sm	7.2	5.65	6.2	5.45	8.05	5.6	5.55	6.1
Eu	2.05	1.7	1.8	1.65	2.4	1.6	1.6	1.75
Gd	6	5	6	4.8	6.8	4.8	5	5.2
Tb	0.82	0.74	0.82	0.66	0.92	0.7	0.72	0.7
Dy	4.5	4.5	4.85	4.05	5.1	4.25	4.4	4.2
Ho	0.9	0.92	1	0.84	1.02	0.9	0.94	0.84
Er	2.35	2.55	2.85	2.25	2.6	2.5	2.55	2.25
Tm	0.3	0.35	0.35	0.3	0.3	0.3	0.3	0.3
Yb	2.05	2.4	2.55	2.05	2.2	2.4	2.35	2.1
Lu	0.3	0.38	0.42	0.34	0.38	0.38	0.38	0.34
Hf	3.2	2.8	3	2.2	3	2.8	2.8	2.4
Ta	0.5	0.4	0.3	0.3	0.5	0.3	0.3	0.3
W	214	84	105	57	87	87	167	110
Pb	30	18	19	18	34	19	18	17
Th	24.8	10.2	10.6	8.7	22.3	10.3	10.1	10
U	6.1	2.6	2.6	2.2	5.2	2.5	2.5	2.3
Th/Ce	0.219	0.166	0.157	0.147	0.197	0.168	0.169	0.154
U/Th	0.246	0.255	0.245	0.253	0.233	0.243	0.248	0.230
Zr/Nb	13.250	19.667	20.333	17.000	11.909	20.500	20.182	19.600
La/Sm	8.639	5.239	5.048	4.862	7.130	5.161	5.009	4.951
Sm/Yb	3.512	2.354	2.431	2.659	3.659	2.333	2.362	2.905
Ba/Th	73.4	125.5	114.2	146.0	63.2	125.2	123.8	138.0
Sm/Nd	0.181	0.212	0.218	0.206	0.185	0.213	0.223	0.219
$^{87}Sr/^{86}Sr$				0.70473	0.705352	0.704703		
$^{143}Nd/^{144}Nd$				0.512706	0.512643	0.512752		
εNd				1.319	0.089	2.215		

Table 1b: Whole-rock trace element and isotope geochemistry. Trace elements analysed by solution-ICP-MS and XRF (samples analysed by XRF denoted with a *). Abbreviations: Pyrox. = pyroxenite, Hbl = Hornblende, Ol = olivine

Sample no.	BC14/ 013	BC14/ 014	BC14/ 015	BC14/ 016	BC14/ 017	BC14/ 018	BC14/ 019*	BC14/ 022
Lith.	**Lava**	**Lava**	**Lava**	**Lava**	**Lava**	**Pyrox.**	**Pyrox.**	**Hbl Pyrox.**
SiO2	48.80	50.16	47.76	52.40	45.95	45.92	42.69	43.28
TiO2	0.83	0.84	0.89	0.77	1.00	1.06	1.19	1.18
Al2O3	19.17	18.69	18.85	19.14	17.42	15.19	11.12	9.89
Fe2O3	9.26	9.47	9.74	7.99	11.09	11.90	13.09	14.62
MnO	0.20	0.20	0.20	0.20	0.21	0.19	0.18	0.21
MgO	3.97	4.06	4.48	3.25	5.21	7.45	12.30	10.87
CaO	9.74	9.35	10.59	7.97	11.49	13.74	16.64	19.68
Na2O	3.98	3.63	3.70	4.16	3.08	2.37	0.99	0.59
K2O	2.83	3.13	2.47	3.17	3.37	1.84	0.67	0.14
P2O5	0.52	0.34	0.52	0.36	0.62	0.33	0.07	0.04
SO3	b.d.l.	0.19	0.01	b.d.l.	0.13	0.00	b.d.l.	0.02
Cl	304.5	108	748.5	160	174.5	338	236.5	316
LOI	0.66	-0.07	0.73	0.57	0.41	-0.03	1.02	-0.54
Total	99.34	100.07	99.27	99.43	99.59	100.03	98.98	100.54
Mg#	0.46	0.46	0.48	0.45	0.48	0.55	0.65	0.60
Be	3	2	2.5	2.5	3.5	1.5		
Sc	10.8	13.2	15.5	7.7	19.6	39.1	51	59.1
V	257.7	218.4	277.2	181.9	330.2	354	410	451.6
Cr	40.7	40.7	40.7	40.7	40.7	40.7	291	15
Co	48	39	42	58	43	58	62	73
Ni	20	20	30	15	25	40	46	50
Cu	136	117	154	141	182	78	27	143
Zn	98	92	98	100	96	90	55	78
Ga	20.2	18.2	20.6	20.4	18.2	19.4	15	16.2
As	7		9	4	3	2		
Rb	88	76.4	75.8	92.8	64.8	80.8	20	4.2
Sr	1040	808	1050	904	1140	779	460	378
Y	22.1	18.2	21.5	24	24.3	20.2	17	16.8
Zr	114	102	105	129	134	79	42	57
Nb	8.5	5	7.5	6	7	5		
Mo	2.5	1	1.5	1	2	1		
Sn	1	0.7	1	1.2	1.1	1.1		1.4
Sb	0.5	0.2	0.5	0.4	0.3	0.2		
Cs	6	4	5.6	5	6.1	3.5		0.4
Ba	1490	1100	1510	1380	1120	896	617	86

Table 1c: Whole-rock major and trace element geochemistry. All major elements analysed by XRF, trace elements analysed by solution-ICP-MS and XRF (samples analysed by XRF denoted with a *). Abbreviations: Pyrox. = pyroxenite, Hbl = Hornblende, Ol = olivine

Sample no.	BC14/ 013	BC14/ 014	BC14/ 015	BC14/ 016	BC14/ 017	BC14/ 018	BC14/ 019*	BC14/ 022
Lith.	**Lava**	**Lava**	**Lava**	**Lava**	**Lava**	**Pyrox.**	**Pyrox.**	**Hbl Pyrox.**
La	42	27	37.3	30.1	41.8	24.2		6.6
Ce	84	57.6	79.1	62.4	91.6	55.7	38	20.4
Pr	8.65	6.45	8.4	6.6	9.8	6.55		3.4
Nd	31.7	25.4	32.7	26.2	39.8	26.2	28	17.7
Sm	6.55	5.1	6.25	5.85	8	6		5.3
Eu	1.9	1.5	1.85	1.65	2.4	1.8		1.5
Gd	5.6	4.4	5.6	5.2	6.6	5.2		5.2
Tb	0.76	0.64	0.76	0.74	0.94	0.76		0.74
Dy	4.3	3.65	4.55	4.65	5.3	4.25		4
Ho	0.84	0.72	0.84	0.94	0.94	0.78		0.72
Er	2.4	1.95	2.3	2.6	2.4	2.1		1.9
Tm	0.3	0.25	0.25	0.35	0.25	0.25		0.25
Yb	1.95	1.8	2.05	2.4	1.9	1.65		1.35
Lu	0.34	0.28	0.36	0.42	0.28	0.28		0.2
Hf	2.6	2.4	2.6	3	3	2.2		2.6
Ta	0.4	0.3	0.4	0.4	0.3	0.2		
W	113	76.5	71	175	63	105		117
Pb	28	11	25	20	12	5		2
Th	17	9.9	15.3	10.7	11	7.1	11	0.6
U	4.2	2.3	3.7	2.6	2.6	1.8		0.2
Th/Ce	0.202	0.172	0.193	0.171	0.120	0.127	0.291	0.029
U/Th	0.247	0.232	0.242	0.243	0.236	0.254		0.333
Nb/Rb	13.412	20.400	14.000	21.500	19.143	15.800		
La/Sm	6.412	5.294	5.968	5.145	5.225	4.033		1.245
Sm/Yb	3.359	2.833	3.049	2.438	4.211	3.636		3.926
Ba/Th	87.6	111.1	98.7	129.0	101.8	126.2	56.6	143.3
Sm/Nd	0.207	0.201	0.191	0.223	0.201	0.229		0.299
$^{87}Sr/^{86}Sr$					0.704921	0.70491		0.704946
$^{143}Nd/^{144}Nd$					0.51265	0.512682		0.512675
εNd					0.225	0.863		0.719

Table 1d: Whole-rock trace element and isotope geochemistry. Trace elements analysed by solution-ICP-MS and XRF (samples analysed by XRF denoted with a *). Abbreviations: Pyrox. = pyroxenite, Hbl = Hornblende, Ol = olivine

Sample no.	BC14/ 023	BC14/ 033	BC14/ 038	BC14/ 041	BC14/ 048*	BC14/ 064	BC14/ 066	BC14/ 069
Lith.	**Pyrox.**	**Gabbro**	**Gabbro**	**Ol-Pyrox.**	**Hbl-Gabbro**	**Hbl-Gabbro**	**Gabbro**	**Pyrox.**
SiO2	44.25	41.72	39.44	42.93	40.69	40.53	43.98	39.76
TiO2	1.02	1.03	1.36	1.15	1.64	1.17	1.05	1.53
Al2O3	11.20	19.35	16.13	12.14	19.88	16.16	20.75	7.64
Fe2O3	11.75	13.28	16.19	13.98	12.75	16.15	10.87	20.78
MnO	0.21	0.18	0.16	0.21	0.14	0.19	0.13	0.20
MgO	11.21	6.04	8.12	11.67	8.25	7.36	6.36	11.68
CaO	17.76	16.98	16.77	16.37	13.75	17.99	15.40	18.39
Na2O	1.12	1.01	0.65	0.93	1.67	0.74	1.64	0.60
K2O	1.10	0.34	0.57	0.88	0.95	0.18	0.67	0.20
P2O5	0.16	0.14	0.05	0.17	0.07	0.36	0.08	0.04
SO3	0.02	b.d.l.	0.01	0.00	0.00	b.d.l.	b.d.l.	b.d.l.
Cl	363	281.5	197	351.5	466	322.5	515	302.5
LOI	0.17	-0.09	0.51	-0.47	0.16	-0.86	-0.99	-0.84
Total	99.83	100.09	99.49	100.47	99.84	100.86	100.99	100.84
Mg#	0.65	0.47	0.50	0.62	0.56	0.47	0.54	0.53
Be	1							
Sc	40.6	12.7	29.9	39.4	33.2	23.5	25.1	79.8
V	342.3	379	596.6	420.4	429.7	473.5	310.7	618.1
Cr	342.8	2.9	4.1	177.7		67.9	4.3	56.7
Co	61	61	81	72	67.2	73	57	74
Ni	70	25	30	90		35	35	75
Cu	38	62	771	175	102.1	30	32	34
Zn	74	82	84	90	54.1	96	68	84
Ga	14	20.2	19.2	17.4	18.1	21.6	18.8	16.4
As								
Rb	42.8	9.2	19.8	32	16	5.2	16.4	3.2
Sr	578	1140	773	628	1044.2	1020	848	162
Y	16.3	13.3	12.6	16.8	13.6	15	11.8	12.6
Zr	46	36	43	41	41.6	45	38	38
Nb	1.5	1	1	2		1	1.5	1
Mo							1	
Sn	1	0.9	1.2	1		1.2	1	1.4
Sb								
Cs	1.9	0.5	0.5	0.8	12.2	0.3	1	
Ba	994	314	516	792	680.4	181	385	104

Table 1e: Whole-rock major and trace element geochemistry. All major elements analysed by XRF, trace elements analysed by solution-ICP-MS and XRF (samples analysed by XRF denoted with a *). Abbreviations: Pyrox. = pyroxenite, Hbl = Hornblende, Ol = olivine

Sample no.	BC14/ 023	BC14/ 033	BC14/ 038	BC14/ 041	BC14/ 048*	BC14/ 064	BC14/ 066	BC14/ 069
Lith.	**Pyrox.**	**Gabbro**	**Gabbro**	**Ol-Pyrox.**	**Hbl-Gabbro**	**Hbl-Gabbro**	**Gabbro**	**Pyrox.**
La	10.6	8.8	6.3	9.9	23	9.3	7.4	5
Ce	30.3	22.3	18.5	27.4	35.4	27.2	16.8	17.1
Pr	4.3	3.05	2.85	3.85		3.95	2.15	2.75
Nd	20.5	14.7	14.3	18.5	17.9	19.5	10.2	14.1
Sm	5.2	3.85	4.3	4.75	16.5	5	2.75	4.05
Eu	1.6	1.3	1.35	1.4		1.45	0.9	1.15
Gd	4.8	3.6	4.2	4.4		4.6	2.8	4
Tb	0.64	0.52	0.56	0.64		0.64	0.42	0.54
Dy	3.8	3	3	3.8		3.55	2.55	3
Ho	0.7	0.58	0.58	0.66		0.62	0.5	0.52
Er	1.75	1.4	1.4	1.75		1.55	1.35	1.35
Tm	0.25	0.2	0.15	0.25		0.2	0.2	0.15
Yb	1.35	1.15	1	1.4		1.15	1.1	0.95
Lu	0.2	0.18	0.18	0.24		0.2	0.22	0.16
Hf	1.8	1.4	2	1.6		1.8	1.4	1.8
Ta								
W	90	125	140	80		111	99	71.5
Pb	2	3	5	3		2	5	
Th	1	1	0.7	0.7	11.7	0.9	2.3	0.5
U	0.2	0.3	0.3			0.2	0.6	
Th/Ce	0.033	0.045	0.038	0.026	0.331	0.033	0.137	0.029
U/Th	0.200	0.300	0.429			0.222	0.261	
Nb/Rb	30.667	36.000	43.000	20.500		45.000	25.333	38.000
La/Sm	2.038	2.286	1.465	2.084	1.394	1.860	2.691	1.235
Sm/Yb	3.852	3.348	4.300	3.393		4.348	2.500	4.263
Ba/Th	994.0	314.0	737.1	1131.4	58.2	201.1	167.4	208.0
Sm/Nd	0.254	0.262	0.301	0.257	0.922	0.256	0.270	0.287
$^{87}Sr/^{86}Sr$		0.704906		0.70499				
$^{143}Nd/^{144}Nd$		0.512695		0.512687				
εNd		1.109		0.950				

Table 1f: Whole-rock trace element and isotope geochemistry. Trace elements analysed by solution-ICP-MS and XRF (samples analysed by XRF denoted with a *). Abbreviations: Pyrox. = pyroxenite, Hbl = Hornblende, Ol = olivine

Sample no.	BC14/ 071	BC14/ 076	BC14/ 078	BC14/ 080	BC14/ 086	LAB ('14)*	SAB ('14)*	RINCA*
Lith.	**Gabbro**	**Lava**	**Pyrox.**	**Lava**	**Gabbro**	**Ash**	**Ash**	**Ash**
SiO2	41.08	47.39	39.47	48.39	40.71	53.20	52.31	49.43
TiO2	1.22	0.96	1.44	1.02	1.18	0.69	0.72	0.87
Al2O3	15.00	18.27	6.43	18.29	18.51	19.50	19.61	19.28
Fe2O3	16.58	11.16	21.59	11.25	15.79	6.82	7.35	9.10
MnO	0.18	0.22	0.16	0.20	0.18	0.19	0.19	0.20
MgO	8.12	4.82	12.12	5.00	6.53	2.90	3.18	3.71
CaO	17.54	10.94	19.01	9.84	16.33	7.24	7.62	10.27
Na2O	0.80	3.31	0.37	3.43	0.93	4.48	4.39	3.68
K2O	0.21	2.49	0.02	2.58	0.20	3.52	3.33	2.60
P2O5	0.04	0.39	0.03	0.43	0.04	0.36	0.35	0.33
SO3	b.d.l.	0.01	0.00	b.d.l.	b.d.l.	0.26	0.09	0.43
Cl	292	902	299.5	792.5	167.5	446	372	1129
LOI	-0.80	-0.04	-0.67	-0.50	-0.42			-0.03
Total	100.80	100.04	100.67	100.50	100.42	99.21	99.18	100.03
Mg#	0.49	0.46	0.53	0.47	0.45	0.30	0.30	0.29
Be		1.5		2				
Sc	40	15.5	83	19.4	29.7			
V	542.7	310.9	575.5	283.6	527.7	147.3	153.4	173.6
Cr	19.6	3.6	31.7	18	3.8	11.5		
Co	71	50	97	66	76	15.2	14.1	19.6
Ni	45	20	100	40	30			
Cu	18	203	14	146	105	151.4	168.1	135.7
Zn	88	100	76	108	94	310.6	84.9	75.6
Ga	18.8	18.6	17	20.6	20.4	18.5	18.6	19.1
As		2						
Rb	5.4	68	0.4	146	3	123	120.8	95.7
Sr	627	1220	99	968	920	868.3	937.6	983.3
Y	11.8	20.9	12.1	23.4	10	23.8	25.3	23.1
Zr	34	83	46	109	22	139.9	136.8	111.8
Nb	1	4.5		6.5	1			
Mo		1.5		1	1			
Sn	1.1	1	1.5	1.2	0.9			
Sb		0.3		0.2				
Cs	0.3	4.9		4.2	0.2	18.3	11.5	18.6
Ba	145	1360	7	1050	177	1594.4	1657.8	1523.3

Table 1g: Whole-rock major and trace element geochemistry. All major elements analysed by XRF, trace elements analysed by solution-ICP-MS and XRF (samples analysed by XRF denoted with a *). Abbreviations: Pyrox. = pyroxenite, Hbl = Hornblende, Ol = olivine

Sample no.	BC14/ 071	BC14/ 076	BC14/ 078	BC14/ 080	BC14/ 086	LAB ('14)*	SAB ('14)*	RINCA*
Lith.	**Gabbro**	**Lava**	**Pyrox.**	**Lava**	**Gabbro**	**Ash**	**Ash**	**Ash**
La	5.1	28.2	4	27.4	4.9	42.4	33.8	46.4
Ce	14.3	66.3	15	64.5	13.5	71.3	56.3	74.5
Pr	2.2	7	2.75	7.4	2.05			
Nd	11.1	30.3	15	29.3	9.6	30	29.8	20.7
Sm	3.2	6.3	4.5	6.3	2.75			
Eu	1.05	1.8	1.3	1.95	0.95			
Gd	3	5.6	4.6	6.2	2.8			
Tb	0.46	0.7	0.6	0.8	0.42			
Dy	2.65	4.15	3.3	4.45	2.4			
Ho	0.52	0.82	0.58	0.94	0.44			
Er	1.25	2.15	1.35	2.4	1.15			
Tm	0.15	0.25	0.15	0.3	0.15			
Yb	0.95	1.75	0.9	2.05	0.9			
Lu	0.18	0.34	0.12	0.34	0.18			
Hf	1.4	2.4	2.4	2.8	1			
Ta		0.2		0.3				
W	116	84	118	131	147			
Pb	2	17		12	2	22.6	16	13.3
Th	0.8	8.6	0.2	7	0.5	22.6	22.5	21
U	0.2	2.2		1.5		12.1	11.2	12.5
Th/Ce	0.056	0.130	0.013	0.109	0.037	0.317	0.400	0.282
U/Th	0.250	0.256		0.214		0.535	0.498	0.595
Nb/Rb	34.000	18.444		16.769	22.000			
La/Sm	1.594	4.476	0.889	4.349	1.782			
Sm/Yb	3.368	3.600	5.000	3.073	3.056			
Ba/Th	181.3	158.1	35.0	150.0	354.0	70.5	73.7	72.5
Sm/Nd	0.288	0.208	0.300	0.215	0.286			
$^{87}Sr/^{86}Sr$			0.705087				0.704763	
$^{143}Nd/^{144}Nd$			0.512625				0.51275	
εNd			-0.256				2.182	

Table 1h: Whole-rock trace element and isotope geochemistry. Trace elements analysed by solution-ICP-MS and XRF (samples analysed by XRF denoted with a *). Abbreviations: Pyrox. = pyroxenite, Hbl = Hornblende, Ol = olivine

Analysis name	B10_Cpx1-1	B10_Cpx1-1	B10_Cpx1-1	B10_Cpx1-1	B10_Cpx1-1	B10_Cpx1-1	B10_Cpx1-1	B10_Cpx1-1	B10_Cpx2-1	B10_Cpx2-3	B10_Cpx2-4	B10_Cpx2-5	B10_Cpx2-6	B10_Cpx2-7	B10_Cpx3-1	B10_Cpx3-1	B10_Cpx3-1
SiO_2	48.82	49.19	48.93	48.73	49.08	48.35	49.56	50.45	48.99	47.12	50.74	49.33	50.75	49.47	50.83	48.90	50.52
TiO_2	0.70	0.70	0.81	0.84	0.81	0.84	0.73	0.68	0.69	1.23	0.80	0.74	0.78	0.84	0.56	0.88	0.56
Al_2O_3	4.96	4.90	5.77	5.86	5.87	6.45	5.07	4.56	5.02	7.58	5.15	5.11	5.21	5.20	3.96	6.04	4.47
Cr_2O_3	0.00	0.01	0.00	0.00	0.01	0.01	0.00	0.02	0.01	0.01	0.00	0.00	0.00	0.01	0.01	-0.01	-0.01
FeO	6.96	7.17	7.32	7.41	7.36	7.63	7.15	7.01	6.91	8.30	7.11	7.23	7.02	7.35	6.61	7.44	6.63
NiO	0.00	0.02	0.01	0.04	0.00	0.00	-0.01	0.00	0.01	0.01	0.01	0.00	0.02	0.01	-0.03	-0.03	-0.03
MnO	0.21	0.22	0.19	0.20	0.20	0.19	0.21	0.21	0.20	0.18	0.21	0.22	0.22	0.21	0.21	0.19	0.22
MgO	14.35	14.53	14.09	13.97	13.85	13.68	14.42	14.54	14.32	12.82	14.48	14.23	14.37	13.97	15.22	13.68	15.21
CaO	23.09	22.88	22.98	23.17	23.20	23.37	23.34	23.28	23.30	22.82	23.13	23.00	22.94	22.89	22.75	22.87	22.67
BaO																	
Na_2O	0.28	0.25	0.31	0.29	0.28	0.29	0.31	0.30	0.27	0.32	0.28	0.34	0.31	0.33	0.26	0.33	0.25
K_2O	0.02	0.00	0.01	0.00	0.00	0.01	0.01	0.03	0.00	0.00	0.02	0.01	0.00	0.01	0.00	0.01	0.02
P_2O_5	0.49	0.48	0.52	0.48	0.54	0.43	0.53	0.51	0.54	0.50	0.42	0.58	0.48	0.47	0.45	0.55	0.39
SO_3																	
Cl	0.02	0.01	0.02	0.02	0.00	-0.01	-0.01	0.00	0.00	0.01	0.00	0.01	-0.01	0.02	0.00	-0.01	0.01
F																	
Total	99.90	100.3	100.9	101.0	101.2	101.2	101.3	101.6	100.2	100.8	102.3	100.8	102.1	100.7	100.8	100.8	100.9

Table 2: Major element compositions of clinopyroxene analyses from gabbro samples. All analyses carried out by electron microprobe.

Analysis name	B10_ Cpx3 -1	B10_ Cpx3 -1	B10_ Cpx4 -1	B1B_ Cpx1 -1	B1B_ Cpx1 -2	B1B_ Cpx2 -1	B1B_ Cpx3 -1	B1B_ Cpx3 -2	B1B_ Cpx3 -3	B1B_ Cpx5 -1	B1B_ Cpx6 -2	B1B_ Cpx6 -3	B21_ Cpx1 -1	B21_ Cpx1 -4	B21_ Cpx1 -5	B21_ Cpx2 -2
SiO_2	50.52	50.69	48.50	49.83	49.51	50.12	47.55	49.89	49.42	48.03	49.40	48.81	50.68	50.42	49.05	49.30
TiO_2	0.56	0.55	0.54	0.76	0.76	0.57	1.00	0.58	0.60	0.96	0.63	0.70	0.48	0.55	0.44	0.67
Al_2O_3	4.47	3.97	3.53	4.72	4.94	3.64	6.00	4.06	3.92	5.71	4.24	4.61	3.89	4.06	4.29	4.19
Cr_2O_3	-0.01	0.02	0.01	0.00	0.00	0.00	0.01	0.00	0.00	0.00	0.00	0.00	0.04	0.04	0.06	0.06
FeO	6.63	6.77	6.65	7.12	7.28	6.94	7.66	7.04	7.12	7.39	7.08	7.11	6.08	5.35	6.09	6.08
NiO	-0.03	0.00	0.02	0.00	0.01	0.03	0.00	0.00	0.00	0.00	0.00	0.02	0.04	0.03	0.00	0.01
MnO	0.22	0.20	0.24	0.19	0.26	0.28	0.19	0.24	0.20	0.23	0.23	0.24	0.16	0.06	0.12	0.13
MgO	15.21	15.18	14.74	13.87	13.98	14.46	13.22	14.34	14.31	13.10	13.93	13.93	14.81	15.23	14.72	14.56
CaO	22.67	23.03	22.50	22.54	22.45	22.26	22.44	22.12	22.24	22.45	22.60	22.57	22.88	22.25	22.99	22.87
BaO				0.01	0.03	0.00	0.01	0.00	0.00	0.00	0.07	0.00	0.00	0.02	0.02	0.03
Na_2O	0.25	0.26	0.31	0.36	0.36	0.31	0.33	0.41	0.35	0.38	0.34	0.35	0.27	0.22	0.33	0.31
K_2O	0.02	0.00	0.02	0.01	0.00	0.00	0.00	0.00	0.03	0.00	0.01	0.00	0.01	0.01	0.01	0.01
P_2O_5	0.39	0.58	0.45	0.02	0.02	0.02	0.00	0.01	0.02	0.05	0.00	0.00	0.06	0.02	0.02	0.01
SO_3																
Cl	0.01	-0.01	0.01	0.00	0.01	0.01	0.00	0.00	0.01	0.00	0.00	0.00	0.01	0.00	0.00	0.00
F				0.00	0.00	0.00	0.00	0.00	0.00	0.00	0.00	0.00	0.00	0.00	0.00	0.00
Total	101.0	101.3	97.5	99.4	99.6	98.6	98.4	98.7	98.2	98.3	98.5	98.4	99.4	98.3	98.1	98.2

Table 2: Major element compositions of clinopyroxene analyses. All analyses carried out by electron microprobe.

Analysis name	B21_ Cpx3 -1	B21_ Cpx3 -2	B21_ Cpx3 -3	B21_ Cpx4 -1	B21_ Cpx4 -2	B21_ Cpx4 -3	B21_ Cpx4 -4	B21_ Cpx4 -5	B21_ Cpx4 -6	B21_ Cpx4 -7	B21_ Cpx4 -9	B21_ Cpx5 -2	B21_ Cpx5 -3	B21_ Cpx5 -5	B24_ Cpx2 -1	B24_ Cpx2 -1
SiO_2	49.58	49.25	49.30	49.37	49.19	48.74	49.55	48.54	49.31	49.48	49.18	49.05	49.62	49.43	49.08	49.08
TiO_2	0.59	0.65	0.56	0.53	0.65	0.65	0.64	0.73	0.64	0.64	0.69	0.66	0.61	0.66	0.69	0.69
Al_2O_3	3.91	5.02	4.97	4.34	5.14	4.95	4.14	5.49	4.17	4.28	5.15	5.49	4.90	5.17	5.20	5.20
Cr_2O_3	0.05	0.02	0.05	0.04	0.01	0.10	0.06	0.04	0.05	0.00	0.04	0.01	0.05	0.02	0.01	0.01
FeO	6.73	7.09	6.81	6.42	7.21	6.97	6.07	7.20	6.12	6.25	7.09	7.04	6.53	6.94	7.23	7.23
NiO	0.00	0.03	0.00	0.03	0.00	0.00	0.00	0.01	0.00	0.03	0.00	0.04	0.00	0.00	0.01	0.01
MnO	0.15	0.18	0.19	0.11	0.13	0.21	0.14	0.20	0.14	0.12	0.22	0.21	0.17	0.19	0.24	0.24
MgO	14.48	13.76	14.06	14.44	13.74	14.09	14.62	13.54	14.67	14.60	14.16	13.51	14.17	13.68	13.78	13.78
CaO	22.60	22.92	22.62	22.74	22.62	22.53	22.92	22.27	22.81	22.66	22.69	22.93	22.97	22.38	23.49	23.49
BaO	0.01	0.03	0.01	0.00	0.01	0.01	0.02	0.04	0.00	0.00	0.01	0.01	0.04	0.05		
Na_2O	0.34	0.34	0.31	0.29	0.31	0.30	0.25	0.32	0.23	0.26	0.34	0.32	0.30	0.36	0.29	0.29
K_2O	0.00	0.00	0.00	0.00	0.01	0.01	0.03	0.00	0.00	0.01	0.00	0.00	0.00	0.00	0.00	0.00
P_2O_5	0.02	0.01	0.03	0.00	0.00	0.01	0.00	0.01	0.01	0.00	0.00	0.00	0.00	0.00	0.44	0.44
SO_3																
Cl	0.01	0.01	0.00	0.01	0.00	0.01	0.02	0.02	0.01	0.01	0.02	0.01	0.00	0.00	0.00	0.00
F	0.00	0.00	0.00	0.00	0.00	0.00	0.00	0.00	0.00	0.00	0.00	0.00	0.00	0.00		
Total	98.5	99.3	98.9	98.3	99.0	98.6	98.5	98.4	98.2	98.3	99.6	99.3	99.4	98.9	100.5	100.5

Table 2: Major element compositions of clinopyroxene analyses from gabbro samples. All analyses carried out by electron microprobe.

Analysis name	B24_Cpx2-1	B24_Cpx2-1	B24_Cpx2-1	B24_Cpx2-1	B24_Cpx2-1	B24_Cpx2-1	B24_Cpx2-1	B24_Cpx2-1	B24_Cpx2-1	B24_Cpx2-1	B24_Cpx2-1	B24_Cpx2-1	B24_Cpx3-1	B24_Cpx3-1	B24_Cpx3-1	B24_Cpx3-1
SiO_2	46.45	46.45	49.09	49.09	45.07	48.14	46.13	49.46	49.46	46.66	50.11	50.11	47.50	47.58	47.72	47.19
TiO_2	1.16	1.16	0.68	0.68	1.45	0.92	1.26	0.66	0.66	1.25	0.70	0.70	1.11	1.10	1.13	1.22
Al_2O_3	8.04	8.04	5.17	5.17	9.53	6.52	8.70	5.18	5.18	8.74	5.21	5.21	7.14	7.57	8.11	8.33
Cr_2O_3	0.00	0.00	0.00	0.00	-0.01	0.00	-0.01	-0.01	-0.01	0.00	0.02	0.02	-0.01	0.00	0.01	-0.01
FeO	8.50	8.50	7.48	7.48	8.92	7.71	8.60	7.41	7.41	8.83	7.29	7.29	8.03	7.76	8.19	8.40
NiO	-0.02	-0.02	0.00	0.00	0.00	0.01	0.02	0.03	0.03	-0.01	0.00	0.00	0.01	-0.01	-0.01	0.00
MnO	0.20	0.20	0.20	0.20	0.21	0.23	0.21	0.22	0.22	0.24	0.21	0.21	0.23	0.20	0.21	0.20
MgO	12.03	12.03	13.64	13.64	11.26	13.20	11.77	13.78	13.78	11.74	13.59	13.59	12.48	12.46	12.12	12.15
CaO	23.36	23.36	23.59	23.59	23.50	23.42	23.61	23.75	23.75	23.36	23.71	23.71	23.47	23.45	23.53	23.62
BaO																
Na_2O	0.39	0.39	0.30	0.30	0.35	0.45	0.34	0.30	0.30	0.33	0.35	0.35	0.48	0.35	0.40	0.37
K_2O	0.00	0.00	0.00	0.00	0.00	0.01	0.00	0.00	0.00	0.00	0.00	0.00	0.00	-0.01	0.00	0.00
P_2O_5	0.42	0.42	0.46	0.46	0.44	0.47	0.46	0.41	0.41	0.49	0.45	0.45	0.42	0.46	0.43	0.42
SO_3																
Cl	-0.01	-0.01	0.00	0.00	0.00	0.01	-0.01	0.01	0.01	0.00	0.01	0.01	0.00	0.00	-0.01	0.00
F																
Total	100.6	100.6	100.6	100.6	100.7	101.1	101.1	101.2	101.2	101.6	101.7	101.7	100.9	100.9	101.8	101.9

Table 2: Major element compositions of clinopyroxene analyses from gabbro samples. All analyses carried out by electron microprobe.

Analysis name	B24_Cpx3-1	B7	B7	B7_Cpx1-1	B7_Cpx1-4	B7_Cpx2-1	B7_Cpx4-1	B7_Cpx4-2	B7_Cpx4-3	B7_Cpx6-2	B8_Cpx2-1	B8_Cpx2-2	B8_Cpx2-3	B8_Cpx2-4	B8_Cpx3-1	B8_Cpx3-1
SiO_2	49.38	42.67	42.15	48.18	48.61	47.78	48.11	47.64	49.20	49.57	47.46	45.64	45.68	47.30	46.95	45.95
TiO_2	0.89	2.62	3.69	0.91	0.99	0.95	1.01	1.10	0.84	0.77	0.94	1.26	1.20	0.90	0.68	0.94
Al_2O_3	6.53	12.32	12.58	5.88	5.69	5.53	5.88	6.03	5.01	3.62	6.61	8.35	8.33	6.48	5.05	6.35
Cr_2O_3	0.01			0.00	0.03	0.01	0.00	0.02	0.00	0.00	-0.02	0.02	0.01	0.00	-0.01	0.01
FeO	7.36	8.09	9.06	7.14	7.37	7.35	6.90	7.43	6.83	7.06	8.33	9.04	8.94	8.07	7.91	8.34
NiO	0.00			0.01	0.00	0.03	0.01	0.00	0.04	0.04	-0.01	0.01	-0.02	0.01	0.00	0.00
MnO	0.20			0.25	0.22	0.17	0.18	0.20	0.16	0.29	0.23	0.20	0.22	0.21	0.21	0.24
MgO	13.31	10.21	9.30	13.44	13.37	13.48	13.63	13.53	14.41	14.43	12.46	11.62	11.58	12.57	13.06	12.34
CaO	23.52	22.86	23.19	22.55	23.12	22.28	22.37	22.59	22.71	21.83	23.61	23.83	23.81	23.56	23.29	23.37
BaO				0.04	0.03	0.00	0.07	0.00	0.00	0.01						
Na_2O	0.35	0.54	0.47	0.31	0.31	0.31	0.30	0.31	0.31	0.38	0.33	0.33	0.34	0.34	0.33	0.34
K_2O	-0.01			0.01	0.02	0.00	0.00	0.00	0.01	0.01	-0.01	0.00	0.00	0.00	0.01	0.01
P_2O_5	0.46			0.01	0.03	0.00	0.00	0.06	0.00	0.02	0.38	0.41	0.40	0.45	0.32	0.40
SO_3																
Cl	0.01			0.01	0.01	0.00	0.00	0.01	0.00	0.00	0.00	0.01	0.00	0.00	0.02	-0.01
F				0.00	0.00	0.00	0.00	0.00	0.00	0.00						
Total	102.0	99.4	100.4	98.7	99.8	97.9	98.5	98.9	99.5	98.0	100.3	100.7	100.5	99.9	97.8	98.3

Table 2: Major element compositions of clinopyroxene analyses from gabbro samples. All analyses carried out by electron microprobe.

Analysis name	B8_C px3-1	B8_C px3-1	B8_C px3-1	B8_C px3-1	B8_C px3-1	B8_C px3-1	B8_C px3-1	b9_1	b9_10	b9_11	b9_12	b9_15	b9_18	b9_19	b9_2	b9_20
SiO_2	46.38	46.49	47.84	48.02	46.92	47.97	47.89	50.58	49.54	49.27	49.62	49.50	49.44	48.98	50.84	50.18
TiO_2	0.92	0.84	0.68	0.66	0.79	0.67	0.66	0.44	0.58	0.56	0.57	0.51	0.72	0.65	0.45	0.56
Al_2O_3	6.01	6.08	4.81	4.78	6.00	5.00	5.19	3.45	4.38	4.13	4.44	4.22	4.78	4.69	3.43	4.55
Cr_2O_3	-0.02	0.00	-0.01	0.02	0.00	0.00	0.00									
FeO	8.52	8.18	7.84	7.82	8.13	7.80	7.74	5.56	6.08	5.98	6.08	5.75	6.20	6.35	5.22	6.19
NiO	0.02	-0.01	-0.01	0.01	0.03	0.03	0.02									
MnO	0.23	0.20	0.24	0.20	0.24	0.20	0.24	0.08	0.08	0.09	0.12	0.14	0.10	0.13	0.12	0.15
MgO	12.27	12.65	13.26	13.39	12.70	13.26	13.21	15.37	15.00	14.79	14.91	14.78	14.63	14.83	15.49	14.69
CaO	23.26	23.49	23.52	23.60	23.55	23.58	23.65	23.11	23.42	23.75	23.53	23.52	23.24	23.37	23.40	22.86
BaO								0.00	0.00	0.04	0.00	0.00	0.07	0.00	0.09	0.00
Na_2O	0.37	0.33	0.26	0.28	0.35	0.32	0.29	0.22	0.20	0.23	0.22	0.20	0.20	0.20	0.15	0.21
K_2O	0.01	0.01	0.00	0.00	0.00	0.01	0.00	0.01	0.02	0.00	0.00	0.00	0.00	0.00	0.00	0.00
P_2O_5	0.39	0.38	0.39	0.37	0.42	0.36	0.39	0.02	0.06	0.05	0.00	0.00	0.00	0.00	0.03	0.01
SO_3								0.01	0.00	0.00	0.00	0.00	0.00	0.00	0.00	0.00
Cl	0.01	0.00	-0.01	0.01	0.01	0.01	0.00	0.00	0.01	0.02	0.00	0.00	0.00	0.00	0.00	0.01
F								0.28	0.00	0.04	0.00	0.00	0.00	0.00	0.00	0.00
Total	98.4	98.7	98.8	99.2	99.2	99.2	99.3	99.1	99.4	99.0	99.5	98.6	99.4	99.2	99.3	99.4

Table 2: Major element compositions of clinopyroxene analyses. All analyses carried out by electron microprobe.

Analysis name	b9_45	b9_5	b9_6	BC14/038_Cpx1	BC14/038_Cpx1	BC14/038_Cpx1	BC14/038_Cpx2	BC14/038_Cpx2	BC14/038_Cpx2	BC14/038_Cpx2	BC14/038_Cpx2	BC14/038_Cpx3	BC14/038_Cpx3	BC14/038_Cpx3	BC14/038_Cpx4	BC14/038_Cpx4
SiO_2	49.56	50.99	51.00	45.98	46.71	46.79	46.72	45.41	47.46	46.41	46.32	45.96	45.62	47.30	46.99	46.44
TiO_2	0.62	0.44	0.39	1.22	1.01	1.07	0.99	1.19	0.97	1.07	1.12	1.08	1.18	1.12	1.17	1.06
Al_2O_3	4.45	3.34	3.04	0.00	0.01	0.09	0.03	0.00	0.03	0.08	0.08	0.00	0.07	0.00	0.00	0.02
Cr_2O_3				7.00	6.30	6.44	6.04	7.88	5.97	6.79	6.89	7.07	7.56	7.13	5.93	6.75
FeO	6.03	5.73	5.12	0.00	0.01	0.02	0.00	0.00	0.00	0.01	0.00	0.00	0.02	0.00	0.02	0.02
NiO				7.58	7.43	7.54	7.33	7.67	6.65	7.89	7.90	7.76	7.64	8.04	7.41	7.45
MnO	0.13	0.08	0.12	0.17	0.19	0.22	0.15	0.14	0.18	0.18	0.12	0.23	0.18	0.14	0.16	0.18
MgO	14.74	15.33	15.95	12.72	13.12	13.19	13.11	12.25	13.89	12.75	12.95	12.54	12.47	13.57	13.17	12.73
CaO	23.43	23.20	23.27	23.25	23.37	23.05	23.22	23.35	23.34	23.31	23.33	23.27	23.24	23.12	23.24	23.44
BaO	0.00	0.00	0.06	0.00	0.01	0.01	0.01	0.01	0.02	0.04	0.00	0.00	0.02	0.01	0.00	0.00
Na_2O	0.20	0.15	0.17	0.35	0.28	0.34	0.41	0.36	0.35	0.40	0.36	0.31	0.29	0.32	0.26	0.32
K_2O	0.00	0.01	0.02	0.00	0.00	0.00	0.01	0.00	0.00	0.01	0.00	0.01	0.00	0.00	0.00	0.00
P_2O_5	0.00	0.09	0.03	0.00	0.00	0.00	0.00	0.00	0.00	0.01	0.03	0.00	0.00	0.01	0.00	0.00
SO_3	0.01	0.00	0.01	0.00	0.00	0.00	0.00	0.01	0.01	0.00	0.00	0.02	0.00	0.00	0.00	0.00
Cl	0.02	0.02	0.01	0.00	0.01	0.01	0.01	0.00	0.02	0.00	0.01	0.00	0.00	0.00	0.01	0.00
F	0.00	0.00	0.12	0.00	0.00	0.00	0.00	0.00	0.00	0.03	0.00	0.00	0.00	0.00	0.00	0.00
Total	99.2	99.4	99.3	98.3	98.5	98.8	98.0	98.3	98.9	99.0	99.1	98.2	98.3	100.8	98.4	98.4

Table 2: Major element compositions of clinopyroxene analyses from gabbro samples. All analyses carried out by electron microprobe.

Analysis name	BC14/038_Cpx4	BC14/038_Cpx4	BC14/038_Cpx4	BC14/038_Cpx4	BC14/038_Cpx4	BC14/038_Cpx5	BC14/038_Cpx5	BC14/038_Cpx5	BC14/038_Cpx5	BC14/038_Cpx5	BC14/038_Cpx6	BC14/038_Cpx6	BC14/038_Cpx6	BC14/038_Cpx6	BC14/038_Cpx6	BC14/038_Cpx7
SiO_2	46.81	47.89	46.22	47.01	47.69	45.24	47.31	47.36	47.18	48.49	44.97	46.07	44.81	45.75	45.27	47.02
TiO_2	0.95	0.91	1.16	0.93	0.82	1.17	0.90	0.99	0.89	0.75	1.23	0.90	1.23	1.11	1.19	0.98
Al_2O_3	0.00	0.00	0.00	0.04	0.00	0.10	0.00	0.04	0.00	0.04	0.10	0.00	0.01	0.00	0.11	0.03
Cr_2O_3	6.27	5.44	7.03	6.24	6.29	7.96	5.37	5.51	5.97	5.30	8.05	6.74	8.20	7.63	8.70	6.13
FeO	0.01	0.01	0.04	0.00	0.00	0.01	0.00	0.02	0.01	0.01	0.02	0.04	0.00	0.00	0.00	0.00
NiO	7.66	7.17	7.72	7.72	7.31	7.86	7.61	7.76	7.84	7.56	8.24	8.14	8.43	7.82	8.03	7.36
MnO	0.18	0.18	0.15	0.17	0.19	0.21	0.19	0.17	0.14	0.27	0.14	0.17	0.16	0.17	0.19	0.17
MgO	13.11	13.56	12.79	13.09	13.58	12.21	13.53	13.33	13.18	13.69	11.97	12.78	12.11	12.55	12.20	12.92
CaO	23.39	23.27	23.50	23.41	23.21	23.10	23.16	23.25	23.23	23.09	23.23	23.34	23.31	23.51	22.93	23.31
BaO	0.02	0.03	0.01	0.01	0.00	0.01	0.01	0.01	0.01	0.01	0.00	0.00	0.03	0.01	0.00	0.03
Na_2O	0.33	0.37	0.32	0.31	0.43	0.26	0.36	0.32	0.32	0.42	0.40	0.32	0.24	0.26	0.39	0.35
K_2O	0.01	0.01	0.01	0.00	0.00	0.01	0.00	0.01	0.01	0.00	0.00	0.00	0.01	0.02	0.04	0.00
P_2O_5	0.01	0.01	0.00	0.01	0.00	0.01	0.02	0.01	0.00	0.00	0.00	0.00	0.00	0.01	0.02	0.00
SO_3	0.00	0.02	0.00	0.00	0.03	0.00	0.01	0.00	0.00	0.00	0.00	0.01	0.01	0.00	0.01	0.00
Cl	0.00	0.00	0.01	0.00	0.00	0.00	0.00	0.01	0.00	0.00	0.00	0.00	0.00	0.00	0.02	0.00
F	0.10	0.00	0.03	0.09	0.00	0.00	0.00	0.00	0.00	0.00	0.00	0.00	0.00	0.00	0.00	0.00
Total	98.8	98.9	99.0	99.0	99.6	98.2	98.5	98.8	98.8	99.6	98.4	98.5	98.6	98.8	99.1	98.3

Table 2: Major element compositions of clinopyroxene analyses from gabbro samples. All analyses carried out by electron microprobe.

Analysis name	BC14/038_Cpx7	BC14/038_Cpx7	BC14/038_Cpx7	BC14/038_Cpx7	BC14/038_Cpx7	BC14/038_Cpx7	BC14/038_Cpx7	BC14/038_Cpx7	BC14/038_Cpx7	BC14/048_Cpx1	BC14/048_Cpx1	BC14/048_Cpx1	BC14/048_Cpx1	BC14/048_Cpx1	BC14/048_Cpx1	BC14/048_Cpx1
SiO_2	47.04	46.25	47.07	47.25	47.39	46.85	47.12	47.18	46.82	48.54	45.05	44.60	45.49	45.12	44.59	49.44
TiO_2	0.94	1.10	0.98	0.97	0.97	0.97	0.88	1.14	1.09	0.65	1.47	1.58	1.35	1.48	1.58	0.64
Al_2O_3	0.02	0.03	0.00	0.00	0.00	0.03	0.13	0.04	0.01	5.32	8.32	8.72	7.77	8.50	8.83	4.66
Cr_2O_3	5.89	7.11	6.25	6.15	6.05	6.11	5.97	6.02	7.21	0.01	0.02	0.00	0.01	0.03	0.01	0.00
FeO	0.00	0.00	0.00	0.00	0.03	0.01	0.00	0.01	0.02	7.00	8.19	8.72	8.13	8.62	8.65	7.12
NiO	7.55	7.77	7.57	7.62	7.51	8.12	8.45	7.33	7.88	0.00	0.00	0.00	0.00	0.00	0.00	0.03
MnO	0.20	0.23	0.21	0.21	0.20	0.16	0.17	0.13	0.16	0.22	0.15	0.13	0.15	0.18	0.17	0.21
MgO	13.18	12.60	13.26	13.21	12.95	13.14	12.86	13.26	12.93	13.62	12.34	12.09	12.80	12.14	12.18	14.11
CaO	23.29	23.13	22.99	22.93	23.23	23.05	23.17	23.70	23.01	22.30	22.78	22.59	22.96	22.65	22.76	22.64
BaO	0.02	0.03	0.02	0.00	0.02	0.01	0.00	0.00	0.00	0.03	0.00	0.00	0.00	0.00	0.01	0.00
Na_2O	0.44	0.35	0.30	0.31	0.40	0.46	0.36	0.33	0.36	0.35	0.31	0.33	0.31	0.31	0.29	0.28
K_2O	0.00	0.00	0.01	0.01	0.00	0.01	0.00	0.00	0.01	0.01	0.01	0.00	0.01	0.00	0.01	0.01
P_2O_5	0.01	0.01	0.01	0.01	0.01	0.00	0.00	0.00	0.00	0.02	0.00	0.00	0.00	0.02	0.00	0.09
SO_3	0.00	0.00	0.00	0.00	0.00	0.02	0.01	0.00	0.02	0.00	0.00	0.00	0.00	0.01	0.00	0.00
Cl	0.00	0.01	0.00	0.01	0.00	0.00	0.00	0.00	0.00	0.01	0.01	0.00	0.00	0.00	0.01	0.02
F	0.00	0.00	0.00	0.00	0.00	0.00	0.00	0.02	0.00	0.00	0.02	0.00	0.00	0.00	0.00	0.00
Total	98.6	98.6	98.7	98.7	98.8	99.0	99.1	99.2	99.5	98.1	98.7	98.7	99.0	99.1	99.1	99.3

Table 2: Major element compositions of clinopyroxene analyses from gabbro samples. All analyses carried out by electron microprobe.

Analysis name	BC14/048_Cpx1	BC14/048_Cpx1	BC14/048_Cpx1	BC14/048_Cpx1	BC14/048_Cpx1	BC14/048_Cpx1	BC14/048_Cpx1	BC14/048_Cpx1	BC14/048_Cpx1	BC14/048_Cpx1	BC14/048_Cpx1	BC14/048_Cpx1	BC14/048_Cpx1	BC14/048_Cpx2	BC14/048_Cpx2	BC14/048_Cpx2
SiO_2	47.24	47.56	47.01	45.62	46.93	46.40	46.22	46.81	49.96	49.90	50.01	50.08	50.07	46.12	46.35	48.41
TiO_2	1.07	1.00	1.13	1.38	1.16	1.26	1.29	1.22	0.66	0.62	0.64	0.66	0.64	1.14	1.13	0.83
Al_2O_3	6.47	6.35	6.67	7.97	6.74	7.19	7.56	7.21	4.46	4.41	4.34	4.25	4.48	7.08	7.32	5.00
Cr_2O_3	0.00	0.00	0.00	0.00	0.00	0.00	0.01	0.00	0.00	0.01	0.00	0.01	0.01	0.00	0.02	0.01
FeO	8.15	8.09	8.25	8.02	8.32	8.46	8.48	8.24	7.22	7.15	7.10	7.13	7.20	8.08	8.01	7.77
NiO	0.01	0.00	0.02	0.01	0.00	0.00	0.03	0.00	0.00	0.03	0.00	0.00	0.00	0.02	0.01	0.00
MnO	0.18	0.20	0.22	0.18	0.17	0.22	0.21	0.21	0.24	0.22	0.20	0.21	0.20	0.17	0.18	0.24
MgO	12.86	12.99	12.95	12.89	12.78	12.70	12.59	12.90	14.21	14.39	14.38	14.48	14.21	12.86	12.80	13.41
CaO	22.93	22.76	22.78	23.00	22.94	22.86	22.91	22.84	22.73	22.82	23.01	22.85	22.82	22.47	22.24	22.61
BaO	0.00	0.00	0.02	0.00	0.01	0.03	0.01	0.01	0.04	0.02	0.00	0.00	0.01	0.00	0.00	0.00
Na_2O	0.33	0.33	0.31	0.24	0.34	0.34	0.34	0.33	0.35	0.32	0.29	0.31	0.31	0.33	0.35	0.42
K_2O	0.00	0.00	0.00	0.00	0.00	0.00	0.00	0.01	0.00	0.02	0.00	0.00	0.00	0.03	0.02	0.01
P_2O_5	0.00	0.05	0.00	0.11	0.00	0.00	0.00	0.00	0.00	0.00	0.00	0.00	0.04	0.01	0.04	0.00
SO_3	0.00	0.00	0.00	0.00	0.00	0.00	0.00	0.00	0.00	0.00	0.01	0.00	0.00	0.00	0.00	0.01
Cl	0.00	0.01	0.01	0.00	0.01	0.00	0.02	0.01	0.00	0.00	0.00	0.01	0.00	0.00	0.00	0.01
F	0.00	0.00	0.00	0.00	0.00	0.00	0.00	0.00	0.00	0.00	0.00	0.00	0.02	0.00	0.02	0.00
Total	99.3	99.3	99.4	99.4	99.4	99.5	99.7	99.8	99.9	99.9	100.0	100.0	100.0	98.3	98.5	98.7

Table 2: Major element compositions of clinopyroxene analyses from gabbro samples. All analyses carried out by electron microprobe.

Analysis name	BC14/048_Cpx2	BC14/048_Cpx2	BC14/048_Cpx2	BC14/048_Cpx2	BC14/048_Cpx2	BC14/048_Cpx2	BC14/048_Cpx2	SA12-XO11_Cpx1	SA12-XO11_Cpx1	SA12-XO11_Cpx1	SA12-XO11_Cpx1	SA12-XO11_Cpx1	SA12-XO11_Cpx1	SA12-XO11_Cpx1	SA12-XO11_Cpx1	SA12-XO11_Cpx1
SiO_2	47.70	47.41	47.49	48.53	48.83	49.24	47.03	48.22	48.44	47.84	49.23	48.38	49.83	49.69	48.55	48.16
TiO_2	0.97	1.00	0.95	0.83	0.77	0.75	1.11	0.87	0.86	0.86	0.78	0.78	0.62	0.66	0.86	0.85
Al_2O_3	5.81	6.04	6.09	5.12	4.77	4.67	6.82	5.90	5.51	6.14	4.68	5.94	4.13	4.35	5.77	6.05
Cr_2O_3	0.00	0.00	0.00	0.01	0.04	0.00	0.00	0.01	0.00	0.00	0.00	0.01	0.02	0.04	0.00	0.02
FeO	7.67	7.72	7.83	7.96	7.67	7.62	8.07	7.05	6.77	7.08	6.93	6.94	6.93	6.91	7.23	7.22
NiO	0.02	0.00	0.02	0.01	0.05	0.00	0.00	0.00	0.00	0.01	0.00	0.04	0.00	0.01	0.00	0.03
MnO	0.19	0.16	0.22	0.29	0.25	0.21	0.24	0.13	0.18	0.11	0.18	0.20	0.20	0.21	0.17	0.15
MgO	13.43	13.39	13.30	13.25	13.52	13.88	13.15	13.80	14.27	13.85	14.42	14.07	14.53	14.49	13.87	13.87
CaO	22.72	22.81	22.78	22.59	22.82	22.69	22.72	22.82	22.82	23.04	22.67	22.77	22.77	22.75	22.79	22.85
BaO	0.01	0.03	0.00	0.01	0.00	0.00	0.00	0.03	0.02	0.00	0.01	0.00	0.05	0.02	0.00	0.00
Na_2O	0.33	0.34	0.31	0.43	0.39	0.40	0.37	0.25	0.28	0.26	0.44	0.26	0.42	0.36	0.30	0.24
K_2O	0.00	0.01	0.01	0.00	0.00	0.01	0.00	0.01	0.00	0.02	0.00	0.01	0.00	0.01	0.00	0.01
P_2O_5	0.04	0.10	0.00	0.00	0.06	0.00	0.00	0.00	0.00	0.00	0.00	0.02	0.00	0.00	0.00	0.09
SO_3	0.00	0.00	0.00	0.00	0.00	0.00	0.00	0.00	0.00	0.00	0.03	0.00	0.00	0.00	0.00	0.02
Cl	0.00	0.00	0.01	0.01	0.00	0.00	0.00	0.02	0.00	0.00	0.01	0.00	0.01	0.00	0.01	0.01
F	0.00	0.01	0.00	0.00	0.08	0.00	0.03	0.00	0.00	0.00	0.00	0.00	0.00	0.00	0.00	0.00
Total	98.9	99.0	99.0	99.0	99.3	99.5	99.5	99.1	99.2	99.2	99.4	99.4	99.5	99.5	99.6	99.6

Table 2: Major element compositions of clinopyroxene analyses from gabbro samples. All analyses carried out by electron microprobe.

Analysis name	SA12-XO11_Cpx1	SA12-XO11_Cpx1	SA12-XO11_Cpx1	SA12-XO11_Cpx1	SA12-XO11_Cpx2	SA12-XO11_Cpx2	SA12-XO11_Cpx2	SA12-XO11_Cpx2	SA12-XO11_Cpx2	SA12-XO11_Cpx2	SA12-XO11_Cpx2	SA12-XO11_Cpx2	SA12-XO11_Cpx2	SA12-XO11_Cpx2	SA12-XO11_Cpx2	SA12-XO11_Cpx2
SiO_2	48.09	49.72	49.80	49.83	47.12	48.05	47.34	47.41	49.70	49.63	48.50	47.16	49.81	48.29	48.68	47.92
TiO_2	0.92	0.64	0.67	0.67	0.95	0.88	0.93	0.97	0.70	0.71	0.77	0.96	0.68	0.85	0.69	0.88
Al_2O_3	6.12	4.30	4.48	4.81	6.39	5.70	6.60	6.63	3.98	4.31	5.46	6.67	3.96	5.84	5.36	6.14
Cr_2O_3	0.00	0.00	0.00	0.00	0.00	0.01	0.00	0.02	0.00	0.00	0.00	0.01	0.00	0.01	0.02	0.00
FeO	7.02	6.92	6.96	6.83	7.17	6.79	7.16	7.08	7.47	6.44	6.78	7.39	7.43	6.95	6.80	7.01
NiO	0.05	0.02	0.00	0.00	0.00	0.00	0.00	0.00	0.00	0.00	0.00	0.00	0.00	0.02	0.00	0.00
MnO	0.16	0.21	0.25	0.20	0.11	0.15	0.15	0.17	0.21	0.14	0.15	0.13	0.14	0.13	0.13	0.18
MgO	13.95	14.71	14.48	14.64	13.41	14.04	13.41	13.47	13.90	14.38	14.29	13.37	13.91	13.97	14.15	13.81
CaO	23.00	22.70	22.73	22.50	23.03	22.90	23.16	23.02	22.68	23.21	23.04	23.33	22.88	23.14	23.33	23.26
BaO	0.00	0.00	0.04	0.00	0.02	0.00	0.03	0.02	0.02	0.01	0.01	0.01	0.04	0.04	0.00	0.02
Na_2O	0.26	0.39	0.39	0.42	0.27	0.27	0.20	0.26	0.49	0.28	0.27	0.25	0.45	0.21	0.23	0.27
K_2O	0.00	0.00	0.00	0.00	0.00	0.01	0.00	0.00	0.00	0.01	0.01	0.00	0.00	0.01	0.00	0.00
P_2O_5	0.00	0.00	0.00	0.00	0.00	0.04	0.00	0.00	0.02	0.02	0.00	0.00	0.00	0.00	0.04	0.00
SO_3	0.00	0.00	0.00	0.00	0.00	0.00	0.00	0.00	0.00	0.00	0.00	0.00	0.00	0.00	0.02	0.00
Cl	0.00	0.00	0.00	0.01	0.00	0.00	0.00	0.01	0.00	0.00	0.00	0.00	0.00	0.00	0.00	0.00
F	0.00	0.00	0.06	0.00	0.00	0.00	0.04	0.00	0.00	0.05	0.00	0.00	0.00	0.01	0.02	0.00
Total	99.6	99.6	99.9	99.9	98.5	98.8	99.0	99.0	99.2	99.2	99.3	99.3	99.3	99.5	99.5	99.5

Table 2: Major element compositions of clinopyroxene analyses from gabbro samples. All analyses carried out by electron microprobe.

Analysis name	SA12-XO11_Cpx2	SA12-XO11_Cpx2	SA12-XO11_Cpx2	SA12-XO11_Cpx2	SA12-XO11_Cpx2	SA12-XO11_Cpx3	SA12-XO11_Cpx3	SA12-XO11_Cpx3	SA12-XO11_Cpx3	SA12-XO11_Cpx3	SA12-XO11_Cpx3	SA12-XO11_Cpx3	SA12-XO11_Cpx3	SA12-XO11_Cpx3	SA12-XO11_Cpx4	SA12-XO11_Cpx4
SiO_2	47.71	47.14	49.00	49.19	48.24	46.45	47.05	47.34	47.16	47.96	46.96	47.05	47.00	47.30	45.81	45.53
TiO_2	0.95	0.96	0.67	0.77	0.83	1.09	1.03	0.99	1.00	0.95	1.04	1.00	1.04	1.00	0.83	1.12
Al_2O_3	6.49	7.34	5.26	5.10	6.45	7.30	6.84	6.72	6.88	6.13	7.17	7.12	7.03	7.07	6.67	7.94
Cr_2O_3	0.00	0.00	0.00	0.02	0.00	0.00	0.03	0.00	0.00	0.00	0.01	0.03	0.02	0.00	0.00	0.02
FeO	7.19	7.53	7.14	6.58	7.63	7.55	7.28	7.46	7.42	7.24	7.47	7.53	7.39	7.43	7.09	7.79
NiO	0.01	0.00	0.00	0.00	0.03	0.00	0.04	0.00	0.00	0.00	0.00	0.03	0.02	0.00	0.01	0.00
MnO	0.16	0.17	0.16	0.12	0.17	0.16	0.17	0.18	0.13	0.16	0.13	0.10	0.13	0.13	0.14	0.13
MgO	13.60	13.24	13.69	14.07	13.20	13.02	13.29	13.16	13.36	13.50	13.17	13.15	13.44	13.38	13.02	12.60
CaO	23.05	22.83	23.26	23.63	23.19	23.05	23.06	22.93	22.90	23.02	23.10	23.17	23.12	23.20	22.94	23.09
BaO	0.00	0.04	0.00	0.00	0.01	0.03	0.00	0.02	0.06	0.04	0.01	0.01	0.00	0.01	0.01	0.00
Na_2O	0.25	0.33	0.41	0.27	0.34	0.25	0.26	0.28	0.24	0.29	0.25	0.25	0.24	0.25	0.25	0.23
K_2O	0.01	0.00	0.00	0.00	0.00	0.00	0.01	0.00	0.00	0.00	0.01	0.01	0.00	0.00	0.02	0.01
P_2O_5	0.00	0.04	0.11	0.04	0.09	0.00	0.00	0.00	0.01	0.00	0.10	0.00	0.03	0.04	0.00	0.03
SO_3	0.01	0.03	0.00	0.00	0.00	0.00	0.00	0.02	0.00	0.00	0.00	0.00	0.00	0.00	0.03	0.01
Cl	0.00	0.00	0.00	0.00	0.01	0.01	0.01	0.01	0.01	0.00	0.01	0.00	0.01	0.01	0.01	0.00
F	0.08	0.00	0.00	0.06	0.07	0.00	0.00	0.00	0.10	0.00	0.00	0.00	0.00	0.07	0.00	0.00
Total	99.5	99.7	99.7	99.9	100.3	98.9	99.1	99.1	99.3	99.3	99.4	99.4	99.5	99.9	96.8	98.5

Table 2: Major element compositions of clinopyroxene analyses from gabbro samples. All analyses carried out by electron microprobe.

Analysis name	SA12-XO11_Cpx4	SA12-XO11_Cpx4	SA12-XO11_Cpx4	SA12-XO11_Cpx4	SA12-XO11_Cpx4	SA12-XO11_Cpx4	SA12-XO11_Cpx4	SA12-XO11_Cpx4	SA12-XO11_Cpx4	SA12-XO11_Cpx4	SA12-XO11_Cpx4	SA12-XO11_Cpx4	SA12-XO11_Cpx4	SA12-XO11_Cpx5	SA12-XO11_Cpx5	SA12-XO11_Cpx5
SiO_2	48.91	47.31	47.66	45.50	47.62	48.59	46.99	47.58	44.87	46.18	46.93	48.39	46.75	47.75	47.78	47.98
TiO_2	0.58	0.95	0.87	1.19	0.79	0.68	0.94	0.87	1.37	1.11	0.99	0.84	0.62	0.65	0.92	0.88
Al_2O_3	3.74	6.13	5.84	7.95	5.82	5.01	6.51	6.15	8.62	7.47	7.12	5.62	9.84	4.60	5.69	5.41
Cr_2O_3	0.04	0.04	0.00	0.00	0.00	0.00	0.00	0.02	0.00	0.00	0.00	0.03	0.02	0.01	0.04	0.00
FeO	7.38	7.06	6.77	8.01	7.06	6.83	7.15	7.18	8.18	7.68	7.49	6.81	6.47	7.07	6.98	7.23
NiO	0.00	0.00	0.01	0.00	0.03	0.00	0.09	0.00	0.02	0.00	0.00	0.03	0.00	0.00	0.03	0.00
MnO	0.25	0.15	0.17	0.12	0.13	0.19	0.15	0.17	0.14	0.19	0.19	0.17	0.18	0.19	0.12	0.18
MgO	14.55	13.77	13.99	12.54	13.89	14.51	13.56	13.72	12.28	12.85	13.24	14.21	13.78	13.31	14.10	13.49
CaO	22.65	23.05	23.09	23.32	23.33	22.76	23.36	23.10	23.25	23.22	23.02	23.10	21.46	22.61	22.97	23.31
BaO	0.00	0.00	0.01	0.02	0.01	0.00	0.02	0.00	0.04	0.00	0.03	0.00	0.02	0.01	0.01	0.01
Na_2O	0.35	0.26	0.25	0.19	0.24	0.34	0.24	0.23	0.26	0.26	0.25	0.28	0.37	0.43	0.29	0.44
K_2O	0.04	0.00	0.00	0.01	0.00	0.01	0.00	0.02	0.00	0.01	0.01	0.00	0.02	0.03	0.01	0.03
P_2O_5	0.07	0.02	0.07	0.06	0.00	0.00	0.00	0.00	0.00	0.00	0.00	0.01	0.00	0.00	0.00	0.00
SO_3	0.00	0.00	0.00	0.00	0.00	0.00	0.00	0.00	0.00	0.01	0.01	0.00	0.02	0.01	0.00	0.01
Cl	0.00	0.01	0.01	0.00	0.01	0.01	0.00	0.01	0.01	0.00	0.01	0.00	0.02	0.03	0.00	0.00
F	0.02	0.00	0.04	0.00	0.00	0.00	0.00	0.00	0.00	0.15	0.00	0.00	0.00	0.05	0.00	0.00
Total	98.6	98.8	98.8	98.9	98.9	98.9	99.0	99.0	99.0	99.1	99.3	99.5	99.6	96.7	98.9	99.0

Table 2: Major element compositions of clinopyroxene analyses from gabbro samples. All analyses carried out by electron microprobe.

Analysis name	SA12-XO11_Cpx5	SA12-XO11_Cpx5	SA12-XO11_Cpx5	SA12-XO11_Cpx5	SA12-XO11_Cpx5	SA12-XO11_Cpx5	SA12-XO11_Cpx5	SA12-XO11_Cpx5	SA12-XO11_Cpx5	SA12-XO11_Cpx6	SA12-XO11_Cpx6	SA12-XO11_Cpx6	SA12-XO11_Cpx6	SA12-XO11_Cpx6	SA12-XO11_Cpx6	SA12-XO11_Cpx6
SiO_2	49.48	47.90	47.29	48.77	48.01	49.50	48.72	50.03	49.68	46.49	48.52	47.57	48.60	48.86	48.23	45.95
TiO_2	0.59	0.85	1.00	0.71	0.86	0.57	0.73	0.50	0.78	0.89	0.69	0.90	0.74	0.65	0.85	1.17
Al_2O_3	4.03	5.87	6.49	5.16	5.66	3.97	5.32	4.13	6.20	6.47	5.14	6.25	5.21	4.95	5.98	7.86
Cr_2O_3	0.00	0.05	0.04	0.03	0.03	0.00	0.02	0.01	0.02	0.01	0.01	0.00	0.01	0.05	0.01	0.00
FeO	6.99	7.07	7.23	6.85	7.37	7.26	7.20	6.54	6.83	7.06	6.94	7.17	6.87	6.77	7.09	7.99
NiO	0.04	0.00	0.01	0.00	0.00	0.08	0.00	0.05	0.00	0.03	0.00	0.00	0.00	0.04	0.02	0.03
MnO	0.21	0.15	0.16	0.16	0.11	0.21	0.15	0.19	0.14	0.16	0.15	0.18	0.13	0.13	0.18	0.17
MgO	14.42	13.79	13.71	14.30	13.75	14.32	14.18	14.99	14.79	13.31	14.13	13.80	14.20	14.39	13.80	12.71
CaO	22.76	22.95	22.92	22.84	23.16	22.95	22.85	22.74	22.33	22.82	23.15	23.01	23.17	23.12	22.83	23.08
BaO	0.00	0.01	0.01	0.00	0.00	0.00	0.00	0.00	0.02	0.00	0.04	0.01	0.00	0.02	0.03	0.00
Na_2O	0.45	0.30	0.30	0.33	0.35	0.43	0.30	0.31	0.35	0.27	0.22	0.28	0.27	0.24	0.27	0.21
K_2O	0.00	0.01	0.01	0.01	0.00	0.01	0.00	0.02	0.01	0.02	0.00	0.01	0.01	0.01	0.01	0.00
P_2O_5	0.00	0.06	0.00	0.05	0.00	0.14	0.00	0.08	0.00	0.04	0.00	0.00	0.00	0.01	0.01	0.00
SO_3	0.00	0.00	0.01	0.00	0.01	0.02	0.00	0.01	0.00	0.05	0.00	0.00	0.00	0.00	0.00	0.00
Cl	0.00	0.00	0.01	0.01	0.01	0.00	0.00	0.00	0.01	0.02	0.01	0.00	0.00	0.00	0.00	0.00
F	0.00	0.03	0.03	0.00	0.04	0.00	0.00	0.00	0.00	0.00	0.00	0.03	0.00	0.00	0.00	0.19
Total	99.0	99.1	99.2	99.2	99.4	99.4	99.5	99.6	101.1	97.6	99.0	99.2	99.2	99.2	99.3	99.4

Table 2: Major element compositions of clinopyroxene analyses from gabbro samples. All analyses carried out by electron microprobe.

Analysis name	SA12-XO11_Cpx6	SA12-XO11_Cpx6	SA12-XO11_Cpx6	SA12-XO11_Cpx6	SA12-XO11_Cpx6	SA12-XO11_Cpx6	SA12-XO11_Cpx6	SA12-XO11_Cpx6	SA23	SA23	SA23	SA26	SA26	SA26	SA26	SA26
SiO_2	49.03	49.00	48.68	48.99	48.98	47.42	48.59	49.02	49.50	47.72	48.56	47.32	46.90	47.54	48.39	48.59
TiO_2	0.70	0.70	0.73	0.70	0.72	0.99	0.80	0.69	0.55	1.14	0.77	0.94	0.94	0.83	0.73	0.76
Al_2O_3	5.03	4.88	5.21	5.20	5.10	6.83	5.78	4.90	4.57	6.41	6.11	5.90	6.42	6.14	6.02	5.73
Cr_2O_3	0.00	0.03	0.05	0.02	0.01	0.00	0.00	0.00				0.17				
FeO	6.81	6.87	6.97	6.79	7.03	7.33	6.92	7.01	6.72	8.36	7.51	7.75	8.33	8.21	7.37	7.19
NiO	0.00	0.00	0.04	0.00	0.00	0.00	0.01	0.00								
MnO	0.08	0.16	0.12	0.19	0.14	0.13	0.17	0.14	0.18	0.12						
MgO	14.39	14.33	14.44	14.30	14.42	13.63	14.26	14.46	13.42	12.68	12.84	12.33	12.16	12.21	13.19	13.36
CaO	23.12	23.25	23.09	23.16	23.05	23.05	22.90	23.27	23.13	21.86	23.46	23.74	23.53	23.79	23.20	23.28
BaO	0.00	0.05	0.03	0.00	0.00	0.01	0.00	0.03								
Na_2O	0.21	0.20	0.24	0.27	0.23	0.27	0.25	0.23	0.54	0.47	0.48	0.40	0.24	0.29	0.29	0.29
K_2O	0.00	0.00	0.00	0.00	0.00	0.00	0.01	0.00								
P_2O_5	0.08	0.07	0.00	0.03	0.00	0.04	0.05	0.00								
SO_3	0.00	0.01	0.00	0.01	0.00	0.01	0.01	0.00								
Cl	0.00	0.00	0.02	0.00	0.01	0.01	0.00	0.00								
F	0.00	0.00	0.00	0.03	0.00	0.00	0.06	0.07								
Total	99.4	99.5	99.6	99.7	99.7	99.7	99.8	99.8	98.6	98.8	99.7	98.4	98.5	99.0	99.2	99.2

Table 2: Major element compositions of clinopyroxene analyses from gabbro samples. All analyses carried out by electron microprobe.

Analysis name	SA26	SA26	SA26	SA26	SA26	SA26	SA26	SA26	SA26	SA88-301_Cpx1-1	SA88-301_Cpx1-2	SA88-301_Cpx4-1	SA88-301_Cpx4-2	SA88-301_Cpx4-4	SA88-301_Cpx5-2
SiO_2	48.54	47.65	44.95	47.53	44.65	47.57	47.75	49.01	50.38	47.75	48.76	47.42	48.61	48.47	46.75
TiO_2	0.76	0.89	1.74	1.00	1.71	1.06	0.88	0.86	0.79	1.09	1.07	0.90	0.77	0.80	1.81
Al_2O_3	5.80	6.22	9.10	6.40	8.88	6.17	6.16	5.46	4.77	6.22	5.71	5.79	4.81	5.01	7.36
Cr_2O_3										0.00	0.02	0.00	0.01	0.02	0.00
FeO	7.38	8.16	9.63	8.23	11.03	8.60	8.26	7.70	6.73	9.15	8.52	8.27	7.56	7.79	5.83
NiO										0.01	0.09	0.02	0.00	0.00	0.04
MnO		0.21	0.16	0.18	0.19		0.26	0.14	0.13	0.39	0.35	0.32	0.32	0.28	0.18
MgO	13.23	12.40	11.33	12.18	10.39	12.12	12.46	12.77	14.34	12.38	13.72	12.93	13.76	13.69	13.76
CaO	23.37	23.62	22.32	23.81	22.50	23.95	23.79	23.90	23.23	22.20	22.06	22.28	22.23	21.99	21.91
BaO										0.05	0.05	0.00	0.00	0.00	0.03
Na_2O	0.31	0.28	0.34	0.36	0.41	0.33	0.37	0.28	0.63	0.47	0.37	0.36	0.33	0.35	0.65
K_2O										0.00	0.01	0.01	0.01	0.01	0.01
P_2O_5										0.00	0.02	0.02	0.02	0.01	0.02
SO_3															
Cl									0.09	0.01	0.00	0.01	0.00	0.00	0.00
F										0.00	0.00	0.00	0.00	0.00	0.00
Total	99.4	99.4	99.6	99.7	99.8	99.8	99.9	100.1	101.1	99.7	100.7	98.3	98.4	98.4	98.3

Table 2: Major element compositions of clinopyroxene analyses from gabbro samples. All analyses carried out by electron microprobe.

Analysis name	B16_ Cpx	B16_ Cpx	B16_ Cpx	B16_ Cpx	B16_ Cpx	B16_ Cpx	B16_ Cpx	B16_ Cpx1-1	B16_ Cpx1-1	B16_ Cpx1-1	B16_ Cpx2-1	B16_ Cpx2-1	B16_ Cpx2-1	B16_ Cpx2-1	B16_ Cpx2-1	B16_ Cpx2-1
SiO_2	46.37	47.32	46.95	47.33	48.22	48.02	48.08	48.49	47.84	48.66	46.79	46.60	46.67	47.78	47.44	48.16
TiO_2	1.10	0.97	1.18	0.98	0.90	1.07	0.95	0.69	0.74	0.73	0.86	0.96	0.91	0.72	0.88	0.80
Al_2O_3	7.36	6.90	7.40	7.06	6.73	7.07	6.91	4.65	5.13	4.74	6.58	6.83	6.71	5.35	6.18	5.71
Cr_2O_3	0.00	-0.01	0.02	-0.01	0.02	0.00	0.00	0.00	0.00	0.00	0.01	-0.01	0.01	0.01	0.00	-0.01
FeO	7.28	7.10	7.50	7.25	7.01	7.61	7.16	5.94	6.51	6.16	6.83	7.23	7.14	6.56	7.56	6.85
NiO	0.03	0.01	-0.02	0.00	0.02	0.00	-0.02	0.02	0.01	0.01	0.02	-0.01	0.04	0.01	0.00	-0.01
MnO	0.13	0.12	0.13	0.12	0.12	0.12	0.12	0.13	0.13	0.12	0.11	0.13	0.12	0.11	0.13	0.13
MgO	12.84	13.05	12.72	13.17	13.11	12.48	13.27	14.05	13.69	13.87	12.91	12.93	13.32	14.34	12.79	13.47
CaO	23.17	23.23	23.34	23.37	23.36	23.15	23.43	23.42	23.70	23.56	23.16	23.39	23.27	23.51	23.50	23.33
BaO																
Na_2O	0.26	0.28	0.26	0.26	0.29	0.29	0.28	0.27	0.28	0.28	0.36	0.33	0.32	0.24	0.30	0.33
K_2O	0.01	0.00	0.01	0.00	0.00	0.00	0.00	0.01	0.00	0.01	0.24	0.00	0.00	0.00	0.00	0.02
P_2O_5	0.46	0.50	0.49	0.49	0.47	0.51	0.47	0.44	0.47	0.44	0.48	0.47	0.47	0.47	0.49	0.45
SO_3																
Cl	0.01	0.01	0.00	0.01	0.02	0.00	0.01	0.01	0.01	0.00	0.02	0.01	0.01	0.01	0.00	0.02
F																
Total	99.0	99.5	100.0	100.1	100.3	100.3	100.7	98.1	98.5	98.6	98.4	98.9	99.0	99.1	99.3	99.3

Table 3: Major element compositions of clinopyroxene analyses from pyroxenite samples. All analyses carried out by electron microprobe.

Analysis name	B16_ Cpx2-1	B16_ Cpx2-1	B16_ Cpx3-1	B16_ Cpx3-1	B16_ Cpx3-1	B16_ Cpx3-1	B16_ Cpx3-1	B16_ Cpx3-1	B16_ Cpx3-1	B16_ Cpx3-1	B1A_ Cpx1	B1A_ Cpx1	B1A_ Cpx1	B1A_ Cpx1	B1A_ Cpx1	B1A_ Cpx1
SiO_2	48.28	47.43	48.41	46.87	47.00	47.51	47.58	47.52	48.61	47.77	50.04	49.98	49.45	49.42	49.59	50.24
TiO_2	0.75	0.96	0.95	1.07	1.02	0.98	1.02	1.08	0.86	1.09	0.64	0.67	0.81	0.80	0.76	0.66
Al_2O_3	5.69	6.74	7.34	7.19	7.09	6.97	6.91	7.18	6.48	7.36	4.63	4.93	5.46	5.64	5.49	4.84
Cr_2O_3	0.01	0.00	0.00	0.00	-0.01	0.00	0.02	0.03	0.01	-0.02	0.00	0.05	0.00	0.00	0.00	0.00
FeO	6.59	7.82	6.51	7.27	7.49	7.31	7.26	7.21	7.08	7.30	6.93	6.88	7.31	7.44	7.21	6.86
NiO	0.01	0.01	-0.01	0.01	0.02	0.01	-0.01	0.02	0.00	0.02	0.00	0.00	0.00	0.00	0.00	0.02
MnO	0.12	0.15	0.11	0.12	0.12	0.11	0.12	0.13	0.13	0.11	0.21	0.20	0.23	0.21	0.23	0.22
MgO	13.91	12.45	13.18	12.93	12.74	12.81	13.05	12.88	13.36	13.15	14.34	14.31	14.10	13.95	14.05	14.74
CaO	23.26	23.30	22.08	23.38	23.41	23.26	23.30	23.31	23.48	23.54	22.96	22.90	22.89	22.83	23.01	22.79
BaO											0.00	0.01	0.01	0.05	0.00	0.00
Na_2O	0.29	0.37	0.36	0.28	0.32	0.26	0.29	0.27	0.30	0.28	0.30	0.33	0.28	0.30	0.28	0.32
K_2O	0.02	0.00	0.03	0.01	0.01	0.00	0.01	0.00	0.00	0.01	0.02	0.02	0.01	0.00	0.01	0.01
P_2O_5	0.50	0.47	0.49	0.49	0.49	0.50	0.48	0.48	0.49	0.49	0.00	0.01	0.05	0.00	0.03	0.00
SO_3											0.02	0.00	0.00	0.00	0.00	0.01
Cl	0.01	-0.01	0.05	0.00	-0.01	0.00	0.00	0.01	0.00	0.00	0.01	0.01	0.00	0.00	0.01	0.01
F											0.00	0.00	0.00	0.00	0.00	0.00
Total	99.4	99.7	99.5	99.6	99.7	99.7	100.0	100.1	100.8	101.1	100.1	100.3	100.6	100.6	100.7	100.7

Table 3: Major element compositions of clinopyroxene analyses from pyroxenite samples. All analyses carried out by electron microprobe.

Analysis name	B1A_ Cpx1	B1A_ Cpx1	B1A_ Cpx2	B1A_ Cpx2	B1A_ Cpx2	B1A_ Cpx2	B1A_ Cpx2	B1A_ Cpx2	B1A_ Cpx2	B1A_ Cpx2	B1A_ Cpx3	B1A_ Cpx3	B1A_ Cpx3	B1A_ Cpx3	B1A_ Cpx3	B1A_ Cpx3
SiO_2	51.38	50.49	49.90	48.91	48.35	48.56	49.92	50.32	50.35	48.51	47.79	49.74	47.76	49.71	48.81	49.92
TiO_2	0.55	0.69	0.66	0.93	1.00	0.97	0.70	0.67	0.69	1.10	0.96	0.79	1.04	0.77	0.90	0.78
Al_2O_3	3.79	4.84	5.15	6.24	6.97	6.80	5.49	5.04	5.00	7.59	7.00	5.64	7.53	5.78	6.70	5.74
Cr_2O_3	0.01	0.00	0.00	0.01	0.00	0.02	0.00	0.02	0.01	0.00	0.02	0.00	0.02	0.00	0.00	0.01
FeO	6.82	7.10	6.45	6.90	7.01	7.11	6.71	6.86	6.91	7.19	7.05	6.73	7.43	6.87	6.99	6.61
NiO	0.00	0.00	0.00	0.00	0.02	0.00	0.01	0.02	0.00	0.00	0.00	0.01	0.00	0.00	0.00	0.02
MnO	0.23	0.23	0.15	0.17	0.09	0.12	0.14	0.19	0.23	0.12	0.12	0.12	0.17	0.19	0.13	0.15
MgO	15.07	14.36	14.49	13.99	13.76	13.83	14.64	14.49	14.65	13.87	13.47	14.53	13.57	14.26	14.17	14.55
CaO	22.72	23.12	23.21	23.07	23.40	23.28	23.12	23.10	23.02	23.27	23.04	23.16	23.17	23.06	23.36	23.24
BaO	0.00	0.01	0.00	0.03	0.00	0.00	0.03	0.05	0.00	0.00	0.04	0.01	0.02	0.02	0.03	0.03
Na_2O	0.32	0.29	0.27	0.32	0.30	0.24	0.27	0.31	0.29	0.23	0.28	0.24	0.28	0.35	0.24	0.26
K_2O	0.00	0.00	0.02	0.01	0.00	0.00	0.01	0.01	0.00	0.02	0.02	0.00	0.00	0.02	0.01	0.00
P_2O_5	0.08	0.00	0.00	0.00	0.00	0.00	0.00	0.00	0.09	0.00	0.00	0.03	0.06	0.02	0.00	0.04
SO_3	0.01	0.00	0.00	0.02	0.00	0.00	0.00	0.01	0.00	0.00	0.00	0.00	0.00	0.00	0.00	0.00
Cl	0.01	0.00	0.01	0.00	0.00	0.00	0.00	0.01	0.00	0.00	0.00	0.00	0.00	0.00	0.01	0.02
F	0.00	0.00	0.00	0.00	0.00	0.10	0.00	0.00	0.00	0.00	0.04	0.03	0.00	0.01	0.00	0.00
Total	101.0	101.1	100.3	100.6	100.9	101.0	101.0	101.1	101.2	101.9	99.8	101.0	101.0	101.1	101.4	101.4

Table 3: Major element compositions of clinopyroxene analyses from pyroxenite samples. All analyses carried out by electron microprobe.

Analysis name	B1A_ Cpx4	B1A_ Cpx4	B1A_ Cpx4	B1A_ Cpx4	B1A_ Cpx4	B1A_ Cpx4	B1A_ Cpx4	B1A_ Cpx4	B1A_ Cpx4	B1A_ Cpx4	B1A_ Cpx5	B1A_ Cpx5	B1A_ Cpx5	B22_ Cpx1-2	B22_ Cpx1-4	B22_ Cpx1-6
SiO_2	49.25	47.47	48.89	49.06	48.08	49.37	50.31	48.53	49.81	49.21	49.48	50.54	49.95	48.16	48.46	46.42
TiO_2	0.66	1.05	0.89	0.93	1.02	0.81	0.70	0.99	0.73	0.94	0.81	0.64	0.70	0.79	0.67	0.87
Al_2O_3	4.71	7.45	6.26	6.34	7.41	6.13	5.06	6.79	5.78	6.51	5.34	4.35	5.19	5.42	4.64	6.25
Cr_2O_3	0.01	0.00	0.01	0.00	0.00	0.01	0.04	0.01	0.02	0.00	0.00	0.03	0.02	0.08	0.00	0.00
FeO	6.57	7.09	6.76	6.78	7.18	6.90	6.82	6.87	6.81	6.75	7.17	6.96	6.94	7.14	6.94	7.82
NiO	0.00	0.00	0.00	0.03	0.02	0.01	0.00	0.00	0.00	0.00	0.03	0.02	0.04	0.03	0.01	0.00
MnO	0.15	0.11	0.18	0.10	0.15	0.14	0.15	0.14	0.14	0.12	0.24	0.24	0.20	0.22	0.21	0.14
MgO	13.94	13.31	13.92	14.10	13.49	13.97	14.35	13.98	14.30	14.20	13.98	14.35	14.17	13.91	14.17	12.72
CaO	22.54	23.03	22.83	23.16	23.14	23.14	23.06	23.27	23.22	23.16	22.67	22.69	22.83	22.93	22.95	22.29
BaO	0.01	0.00	0.01	0.00	0.01	0.00	0.03	0.02	0.02	0.04	0.00	0.00	0.02	0.00	0.05	0.04
Na_2O	0.30	0.27	0.32	0.26	0.26	0.32	0.31	0.26	0.28	0.22	0.38	0.38	0.33	0.32	0.30	0.28
K_2O	0.03	0.02	0.02	0.00	0.00	0.00	0.01	0.00	0.00	0.00	0.00	0.01	0.00	0.01	0.01	0.01
P_2O_5	0.01	0.00	0.00	0.02	0.00	0.00	0.03	0.00	0.00	0.00	0.04	0.00	0.00	0.02	0.00	0.02
SO_3	0.03	0.01	0.00	0.00	0.00	0.00	0.02	0.00	0.00	0.00	0.00	0.00	0.00			
Cl	0.01	0.01	0.00	0.00	0.00	0.00	0.00	0.00	0.00	0.00	0.00	0.01	0.00	0.00	0.00	0.01
F	0.01	0.07	0.00	0.00	0.04	0.00	0.00	0.06	0.00	0.00	0.00	0.00	0.00	0.00	0.00	0.00
Total	98.2	99.9	100.1	100.8	100.8	100.8	100.9	100.9	101.1	101.2	100.1	100.2	100.4	99.0	98.4	96.9

Table 3: Major element compositions of clinopyroxene analyses from pyroxenite samples. All analyses carried out by electron microprobe.

Analysis name	B22_ Cpx2-1	B22_ Cpx2-4	B22_ Cpx3-4	B22_ Cpx4-1	B22_ Cpx4-4	B22_ CpxT 1-1	B22_ CpxT 1-10	B22_ CpxT 1-2	B22_ CpxT 1-3	B22_ CpxT 1-4	B22_ CpxT 1-5	B22_ CpxT 1-6	B22_ CpxT 1-7	B22_ CpxT 1-8	B23_ 4	B23_ 7
SiO_2	47.02	45.20	46.50	50.13	48.10	47.88	47.72	47.73	47.68	48.99	48.84	52.98	49.41	48.00	49.63	49.37
TiO_2	0.96	1.03	0.75	0.50	0.82	0.93	0.94	0.90	0.87	0.73	0.72	0.22	0.53	0.77	0.45	0.46
Al_2O_3	6.64	6.71	5.25	3.75	5.59	6.30	6.15	6.51	6.44	4.77	5.18	2.38	4.16	4.97	4.04	4.03
Cr_2O_3	0.00	0.00	0.01	0.36	0.12	0.02	0.06	0.02	0.04	0.01	0.11	0.29	0.30	0.00		
FeO	7.27	7.58	7.13	5.44	6.96	7.77	7.54	7.67	7.26	6.83	6.59	4.73	6.15	7.15	5.49	5.92
NiO	0.05	0.00	0.07	0.01	0.00	0.00	0.05	0.00	0.02	0.00	0.03	0.05	0.01	0.04		
MnO	0.21	0.13	0.21	0.11	0.20	0.16	0.23	0.16	0.16	0.23	0.17	0.12	0.12	0.19	0.12	0.11
MgO	13.41	12.84	13.40	14.73	13.67	13.33	13.37	13.22	13.43	14.41	14.41	16.22	14.47	13.94	14.62	14.68
CaO	22.86	22.25	22.66	22.71	23.04	23.03	22.55	22.55	22.48	22.36	22.58	23.10	22.42	22.54	23.50	23.56
BaO	0.02	0.01	0.02	0.00	0.00	0.01	0.00	0.02	0.04	0.09	0.03	0.00	0.00	0.00	0.00	0.00
Na_2O	0.29	0.26	0.29	0.32	0.33	0.26	0.30	0.25	0.30	0.35	0.35	0.26	0.29	0.28	0.22	0.26
K_2O	0.00	0.01	0.00	0.02	0.03	0.01	0.00	0.01	0.01	0.01	0.01	0.00	0.00	0.02	0.00	0.01
P_2O_5	0.03	0.00	0.02	0.01	0.00	0.01	0.02	0.02	0.01	0.00	0.03	0.00	0.00	0.00	0.00	0.02
SO_3															0.00	0.02
Cl	0.01	0.00	0.01	0.04	0.02	0.01	0.00	0.01	0.02	0.00	0.00	0.00	0.00	0.00	0.02	0.00
F	0.00	0.00	0.00	0.00	0.00	0.00	0.00	0.00	0.00	0.00	0.00	0.00	0.00	0.00	0.14	0.00
Total	98.8	96.0	96.3	98.1	98.9	99.7	98.9	99.1	98.8	98.8	99.0	100.3	97.9	97.9	98.2	98.4

Table 3: Major element compositions of clinopyroxene analyses from pyroxenite samples. All analyses carried out by electron microprobe.

Analysis name	B23_8	B23_9	B23_Cpx4	B23_Cpx4	B23_Cpx4	B235_6	B2H_Cpx1-1	B2H_Cpx1-10	B2H_Cpx1-2	B2H_Cpx1-4	B2H_Cpx1-5	B2H_Cpx1-6	B2H_Cpx1-7	B2H_Cpx1-8	B2H_Cpx1-9	B2H_Cpx2-1
SiO_2	49.40	49.62	49.20	49.20	48.46	49.12	48.46	49.37	48.95	47.77	48.51	47.43	50.19	48.50	48.72	48.02
TiO_2	0.58	0.53	0.51	0.50	0.74	0.58	0.89	0.80	0.72	1.01	0.99	0.98	0.80	0.77	0.70	0.87
Al_2O_3	4.38	4.41	3.91	4.02	5.11	4.67	5.54	5.24	4.90	5.82	6.09	5.76	4.98	5.02	4.87	5.08
Cr_2O_3			0.07	0.10	0.07		0.00	0.00	0.01	0.01	-0.01	0.00	0.01	-0.02	0.01	0.00
FeO	5.88	5.86	5.95	5.91	6.40	6.11	7.06	7.12	7.05	7.41	7.58	7.47	6.96	7.30	7.06	7.24
NiO			0.00	0.00	0.04		0.01	-0.02	-0.03	0.01	0.00	-0.01	0.03	0.01	-0.01	-0.02
MnO	0.12	0.16	0.09	0.12	0.12	0.03	0.23	0.22	0.21	0.23	0.21	0.24	0.21	0.20	0.22	0.22
MgO	14.58	14.57	14.81	14.90	14.12	14.55	13.56	14.16	13.76	13.49	13.28	13.37	13.74	14.03	14.08	13.71
CaO	23.37	23.40	23.13	23.10	22.95	23.60	23.12	23.54	23.13	23.40	23.60	23.07	23.48	23.24	23.12	22.76
BaO	0.00	0.00	0.02	0.04	0.01	0.00										
Na_2O	0.24	0.25	0.25	0.25	0.23	0.26	0.41	0.43	0.41	0.41	0.39	0.39	0.41	0.38	0.40	0.49
K_2O	0.00	0.00	0.00	0.01	0.01	0.00	0.01	0.01	0.02	0.00	0.01	0.01	0.01	0.00	0.00	0.01
P_2O_5	0.04	0.00	0.09	0.01	0.05	0.00	0.45	0.44	0.43	0.41	0.49	0.40	0.44	0.42	0.45	0.39
SO_3	0.00	0.00	0.01	0.01	0.00	0.02										
Cl	0.01	0.00	0.01	0.00	0.01	0.00	0.01	-0.01	0.01	0.00	0.01	0.02	0.00	0.00	0.00	0.01
F	0.30	0.20	0.06	0.01	0.00	0.00										
Total	99.0	99.0	98.1	98.2	98.3	98.9	99.7	101.3	99.6	100.0	101.2	99.1	101.3	99.9	99.6	98.8

Table 3: Major element compositions of clinopyroxene analyses from pyroxenite samples. All analyses carried out by electron microprobe.

Analysis name	B2H_ Cpx2-2	B2H_ Cpx2-3	B2H_ Cpx2-4	B2H_ Cpx2-5	B2H_ Cpx2-6	B2H_ Cpx2-7	B2H_ Cpx2-8	B2H_ Cpx2-9	B2H_ Cpx3-1	B2H_ Cpx3-2	B2H_ Cpx3-3	B2H_ Cpx3-7	B2H_ Cpx3-8	B2H_ Cpx3-9	B2H_ Cpx4-1	B2H_ Cpx4-2
SiO_2	48.92	49.50	48.76	48.35	47.65	47.60	47.72	48.01	48.27	47.51	48.21	48.55	48.45	49.27	47.06	47.07
TiO_2	0.83	0.73	0.75	0.74	0.88	0.73	0.85	0.89	0.90	0.80	0.73	0.80	0.94	0.56	0.98	0.96
Al_2O_3	5.51	4.90	4.87	4.54	5.60	4.92	5.18	5.57	5.72	5.22	4.82	5.12	5.87	3.70	5.88	5.66
Cr_2O_3	0.00	0.00	0.01	0.01	-0.01	0.00	-0.02	-0.01	0.01	-0.01	-0.01	0.00	-0.01	0.01	-0.01	-0.01
FeO	7.28	7.06	7.06	6.82	7.34	7.27	6.90	7.16	7.44	7.27	7.65	7.33	7.62	6.93	7.38	7.29
NiO	0.03	0.00	0.03	0.01	-0.01	0.00	0.00	0.00	0.01	0.00	0.00	-0.01	-0.02	0.00	0.04	0.01
MnO	0.22	0.21	0.22	0.28	0.23	0.22	0.23	0.24	0.24	0.22	0.24	0.22	0.23	0.24	0.22	0.23
MgO	14.09	13.98	14.21	14.14	13.53	13.65	13.76	13.53	13.74	13.94	13.77	13.59	13.50	14.75	13.26	13.46
CaO	23.18	23.47	23.18	22.63	22.99	23.03	23.13	22.95	23.22	23.04	22.96	23.25	23.50	22.87	23.15	23.11
BaO																
Na_2O	0.37	0.40	0.40	0.37	0.38	0.39	0.45	0.36	0.40	0.40	0.42	0.43	0.40	0.46	0.45	0.41
K_2O	0.00	0.01	0.00	0.00	-0.01	0.01	0.01	0.01	0.01	0.01	0.00	-0.01	0.01	0.00	0.00	0.00
P_2O_5	0.46	0.47	0.38	0.41	0.42	0.45	0.41	0.41	0.45	0.41	0.47	0.43	0.46	0.43	0.46	0.40
SO_3																
Cl	0.01	0.00	0.00	0.02	0.00	0.02	0.01	0.00	0.02	0.00	0.01	0.01	0.00	0.01	0.01	0.00
F																
Total	100.9	100.7	99.9	98.3	99.0	98.3	98.6	99.1	100.4	98.8	99.3	99.7	101.0	99.2	98.9	98.6

Table 3: Major element compositions of clinopyroxene analyses from pyroxenite samples. All analyses carried out by electron microprobe.

Analysis name	B2H_ Cpx4-4	B2H_ Cpx4-5	B2H_ Cpx4-6	B2H_ Cpx4-7	B2H_ Cpx4-8	B2H_ Cpx5-1	B2H_ Cpx5-2	B2H_ Cpx5-4	B2H_ Cpx5-5	B2H_ Cpx5-7	B2H_ Cpx6-1	B2H_ Cpx6-2	B2H_ Cpx6-3	B2H_ Cpx6-4	B2H_ Cpx6-5	B2H_ Cpx6-7
SiO_2	48.20	48.86	47.98	47.57	47.41	48.82	48.67	48.74	49.15	46.81	48.87	47.68	47.50	46.66	48.27	46.60
TiO_2	0.73	0.75	0.83	1.06	1.04	0.79	0.75	0.77	0.75	0.99	0.78	1.02	1.02	0.74	0.79	1.00
Al_2O_3	4.99	4.90	5.07	5.84	6.10	4.89	5.19	4.79	4.46	6.16	4.67	5.72	5.66	4.90	5.00	5.90
Cr_2O_3	0.00	0.00	-0.03	0.00	0.00	0.00	0.00	0.00	0.02	0.00	-0.02	0.01	0.01	-0.01	-0.01	0.00
FeO	7.02	7.10	6.99	7.44	7.60	6.98	6.99	7.13	6.94	7.30	7.46	7.73	7.93	7.50	7.40	7.78
NiO	-0.02	0.00	0.02	0.00	0.01	0.02	0.01	-0.02	0.02	0.02	-0.01	0.00	0.02	-0.02	0.02	0.01
MnO	0.22	0.23	0.23	0.22	0.23	0.23	0.23	0.24	0.23	0.24	0.27	0.22	0.27	0.25	0.24	0.23
MgO	13.86	13.82	13.25	12.94	13.24	14.02	14.02	13.90	14.01	13.34	13.78	12.77	13.19	13.26	13.61	12.93
CaO	23.26	23.19	22.89	23.01	23.00	23.16	23.24	23.10	23.10	22.93	22.85	22.82	22.96	22.71	22.96	22.95
BaO																
Na_2O	0.40	0.40	0.45	0.41	0.41	0.41	0.40	0.39	0.39	0.43	0.46	0.47	0.46	0.42	0.38	0.42
K_2O	0.01	0.00	0.01	0.02	0.01	0.01	0.01	0.01	0.01	-0.01	0.00	0.01	0.00	0.01	-0.01	0.00
P_2O_5	0.45	0.46	0.40	0.46	0.40	0.42	0.39	0.44	0.45	0.41	0.42	0.44	0.40	0.37	0.45	0.42
SO_3																
Cl	0.02	-0.01	0.04	0.02	0.01	0.02	0.00	0.01	0.01	0.02	0.01	0.01	-0.01	0.00	0.00	0.00
F																
Total	99.2	99.7	98.2	99.0	99.5	99.8	99.9	99.5	99.5	98.6	99.6	98.9	99.4	96.8	99.1	98.3

Table 3: Major element compositions of clinopyroxene analyses from pyroxenite samples. All analyses carried out by electron microprobe.

Analysis name	B2H_ Cpx7-1	B2H_ Cpx7-2	B2H_ Cpx7-3	B2H_ Cpx7-4	B2H_ Cpx7-5	B2H_ Cpx7-6	B2H_ Cpx7-7	BC14 /023_ Cpx	BC14 /023_ Cpx	BC14 /023_ Cpx	BC14 /023_ Cpx	BC14 /023_ Cpx	BC14 /023_ Cpx	BC14 /023_ Cpx	BC14 /023_ Cpx	BC14 /023_ Cpx
SiO_2	47.81	47.49	47.87	48.01	48.97	47.09	46.83	46.53	49.10	50.55	51.68	50.56	47.63	51.84	50.62	50.98
TiO_2	0.81	0.92	0.79	0.86	0.92	0.98	0.90	1.16	0.58	0.47	0.32	0.47	1.35	0.32	0.46	0.48
Al_2O_3	5.02	5.26	5.23	5.26	5.23	5.87	5.44	7.47	4.40	3.35	2.62	3.52	6.49	2.58	3.47	3.32
Cr_2O_3	0.01	0.00	0.00	0.01	0.00	0.01	-0.01	0.04	0.02	0.00	0.42	0.06	0.00	0.43	0.01	0.02
FeO	7.22	7.46	7.29	7.23	7.43	7.73	7.68	7.40	7.03	5.32	4.04	5.23	7.55	4.05	5.27	5.25
NiO	0.03	-0.01	-0.01	-0.01	-0.02	0.00	-0.01	0.00	0.01	0.03	0.03	0.00	0.00	0.00	0.03	0.00
MnO	0.24	0.25	0.23	0.25	0.26	0.20	0.24	0.20	0.27	0.08	0.11	0.09	0.24	0.07	0.13	0.09
MgO	14.04	13.42	13.79	13.70	13.63	12.94	13.12	12.59	14.24	15.61	16.55	15.53	13.11	16.61	15.67	15.72
CaO	22.84	22.64	22.82	22.86	22.82	23.20	23.21	22.05	22.32	23.03	22.77	23.11	21.98	22.72	23.00	22.82
BaO								0.02	0.00	0.05	0.03	0.02	0.00	0.04	0.01	0.00
Na_2O	0.42	0.48	0.38	0.40	0.51	0.38	0.40	0.47	0.40	0.23	0.19	0.22	0.49	0.20	0.23	0.23
K_2O	0.00	0.00	0.00	0.01	0.00	0.01	0.00	0.01	0.01	0.00	0.02	0.01	0.00	0.00	0.00	0.01
P_2O_5	0.36	0.40	0.40	0.44	0.43	0.41	0.43	0.10	0.06	0.07	0.03	0.00	0.00	0.00	0.00	0.00
SO_3								0.00	0.00	0.00	0.00	0.00	0.00	0.01	0.00	0.00
Cl	0.01	0.00	0.00	0.00	0.00	0.00	0.02	0.01	0.00	0.00	0.01	0.00	0.02	0.00	0.00	0.01
F								0.00	0.00	0.00	0.00	0.00	0.00	0.00	0.00	0.00
Total	98.8	98.3	98.8	99.0	100.2	98.8	98.3	98.1	98.4	98.8	98.8	98.8	98.8	98.9	98.9	98.9

Table 3: Major element compositions of clinopyroxene analyses from pyroxenite samples. All analyses carried out by electron microprobe.

Analysis name	BC14/023_Cpx	BC14/023_Cpx	BC14/023_Cpx	BC14/023_Cpx	BC14/023_Cpx	BC14/023_Cpx	BC14/023_Cpx	BC14/023_Cpx	BC14/023_Cpx	BC14/023_Cpx	BC14/023_Cpx	BC14/023_Cpx	BC14/023_Cpx	BC14/023_Cpx	BC14/023_Cpx	BC14/023_Cpx
SiO_2	47.40	49.96	47.52	49.13	47.52	50.84	50.50	50.77	50.63	47.57	48.26	49.00	50.86	50.82	51.17	48.79
TiO_2	1.36	0.57	1.09	0.96	1.33	0.46	0.51	0.48	0.50	1.07	0.59	0.85	0.43	0.48	0.48	0.79
Al_2O_3	6.69	3.88	7.05	5.05	6.65	3.30	3.65	3.45	3.47	6.65	7.84	5.36	3.28	3.40	3.24	5.28
Cr_2O_3	0.02	0.05	0.01	0.00	0.00	0.04	0.01	0.03	0.04	0.02	0.00	0.01	0.04	0.05	0.05	0.00
FeO	7.39	7.09	7.36	7.08	7.42	5.25	6.86	5.33	5.35	7.42	6.78	6.91	5.21	5.23	5.10	7.03
NiO	0.04	0.02	0.00	0.03	0.01	0.07	0.00	0.00	0.04	0.00	0.00	0.02	0.00	0.00	0.02	0.02
MnO	0.20	0.26	0.21	0.23	0.25	0.08	0.28	0.10	0.10	0.16	0.28	0.24	0.13	0.10	0.10	0.20
MgO	13.14	14.42	12.98	13.99	13.20	15.81	14.71	15.63	15.68	13.36	13.72	14.01	15.76	15.79	15.78	14.21
CaO	22.11	22.24	22.32	22.05	22.03	22.98	21.97	23.02	22.95	22.30	21.04	22.16	23.12	23.02	22.96	22.42
BaO	0.02	0.00	0.04	0.01	0.00	0.00	0.00	0.00	0.02	0.02	0.04	0.01	0.05	0.05	0.00	0.00
Na_2O	0.49	0.53	0.43	0.43	0.48	0.20	0.49	0.23	0.20	0.48	0.47	0.47	0.23	0.22	0.25	0.37
K_2O	0.01	0.00	0.00	0.01	0.01	0.00	0.01	0.01	0.00	0.00	0.03	0.00	0.00	0.00	0.01	0.01
P_2O_5	0.00	0.00	0.00	0.05	0.03	0.00	0.07	0.02	0.00	0.03	0.00	0.04	0.01	0.00	0.00	0.03
SO_3	0.00	0.00	0.00	0.00	0.00	0.00	0.01	0.00	0.03	0.00	0.03	0.00	0.00	0.00	0.00	0.00
Cl	0.02	0.00	0.00	0.01	0.01	0.00	0.00	0.00	0.01	0.00	0.01	0.01	0.00	0.00	0.00	0.01
F	0.05	0.00	0.00	0.00	0.09	0.00	0.00	0.00	0.06	0.00	0.00	0.00	0.00	0.00	0.00	0.00
Total	99.0	99.0	99.0	99.0	99.0	99.0	99.1	99.1	99.1	99.1	99.1	99.1	99.1	99.2	99.2	99.2

Table 3: Major element compositions of clinopyroxene analyses from pyroxenite samples. All analyses carried out by electron microprobe.

Analysis name	BC14/023_Cpx	BC14/023_Cpx	BC14/023_Cpx	BC14/023_Cpx	BC14/023_Cpx	BC14/023_Cpx	BC14/023_Cpx	BC14/023_Cpx	BC14/023_Cpx	BC14/023_Cpx	BC14/023_Cpx	BC14/023_Cpx	BC14/023_Cpx	BC14/023_Cpx	BC14/023_Cpx	BC14/023_Cpx
SiO_2	51.00	51.92	47.68	51.89	49.86	50.61	50.97	50.91	50.82	51.21	51.93	50.21	52.06	53.12	52.48	50.31
TiO_2	0.46	0.29	1.33	0.33	0.70	0.60	0.48	0.49	0.47	0.45	0.31	0.61	0.33	0.20	0.33	0.73
Al_2O_3	3.34	2.56	6.54	2.57	4.65	3.84	3.36	3.48	3.64	3.34	2.56	4.08	2.58	1.77	2.34	4.39
Cr_2O_3	0.01	0.45	0.01	0.36	0.00	0.01	0.00	0.05	0.01	0.04	0.48	0.00	0.45	0.32	0.20	0.00
FeO	5.86	3.98	7.70	4.15	6.80	6.48	6.58	5.28	6.78	5.35	4.16	6.73	4.16	3.56	4.39	6.83
NiO	0.02	0.05	0.03	0.03	0.00	0.03	0.00	0.01	0.00	0.02	0.00	0.00	0.03	0.00	0.00	0.00
MnO	0.20	0.08	0.22	0.06	0.23	0.26	0.31	0.09	0.25	0.13	0.09	0.27	0.10	0.14	0.12	0.26
MgO	15.22	16.73	13.18	16.82	14.29	14.71	15.09	15.86	14.75	15.76	16.84	14.89	16.73	17.19	16.58	14.42
CaO	22.66	22.87	22.05	22.78	22.13	22.20	22.03	22.96	22.14	22.86	22.88	22.21	22.82	22.93	22.82	22.12
BaO	0.03	0.05	0.01	0.01	0.02	0.00	0.05	0.00	0.03	0.00	0.00	0.00	0.00	0.00	0.02	0.00
Na_2O	0.39	0.19	0.48	0.21	0.48	0.45	0.46	0.23	0.48	0.26	0.17	0.45	0.20	0.16	0.25	0.48
K_2O	0.00	0.00	0.00	0.01	0.01	0.00	0.00	0.00	0.01	0.01	0.00	0.01	0.00	0.00	0.00	0.02
P_2O_5	0.00	0.03	0.00	0.01	0.00	0.02	0.00	0.00	0.03	0.00	0.01	0.00	0.00	0.13	0.00	0.00
SO_3	0.00	0.01	0.01	0.00	0.00	0.00	0.00	0.01	0.00	0.00	0.00	0.00	0.01	0.01	0.01	0.00
Cl	0.01	0.01	0.00	0.02	0.01	0.01	0.01	0.01	0.00	0.01	0.00	0.01	0.00	0.00	0.01	0.00
F	0.00	0.00	0.00	0.00	0.07	0.04	0.00	0.00	0.00	0.00	0.00	0.00	0.01	0.00	0.00	0.00
Total	99.2	99.2	99.2	99.2	99.2	99.3	99.3	99.4	99.4	99.4	99.4	99.5	99.5	99.5	99.6	99.6

Table 3: Major element compositions of clinopyroxene analyses from pyroxenite samples. All analyses carried out by electron microprobe.

Analysis name	BC14/023_Cpx	BC14/023_Cpx	BC14/023_Cpx	BC14/023_Cpx	BC14/023_Cpx	BC14/023_Cpx	BC14/023_Cpx	BC14/023_Cpx	BC14/023_Cpx	BC14/023_Cpx	BC14/023_Cpx	BC14/023_Cpx	BC14/023_Cpx	BC14/023_Cpx	BC14/023_Cpx	BC14/023_Cpx
SiO_2	52.75	52.30	52.03	51.35	52.78	50.00	53.28	51.99	53.33	52.06	52.09	52.18	52.22	52.11	53.35	50.79
TiO_2	0.21	0.29	0.30	0.44	0.24	0.68	0.23	0.33	0.21	0.31	0.33	0.32	0.32	0.33	0.23	0.62
Al_2O_3	1.90	2.31	2.57	3.31	1.89	7.44	1.78	2.77	1.78	2.59	2.59	2.53	2.61	2.53	1.77	3.88
Cr_2O_3	0.28	0.25	0.46	0.02	0.31	0.09	0.33	0.45	0.39	0.50	0.46	0.44	0.44	0.52	0.39	0.02
FeO	3.71	4.16	4.23	6.46	3.86	5.81	3.62	4.39	3.52	4.18	4.18	4.22	4.19	4.13	3.51	6.76
NiO	0.06	0.00	0.02	0.00	0.04	0.03	0.00	0.03	0.04	0.02	0.01	0.03	0.03	0.00	0.05	0.06
MnO	0.11	0.10	0.08	0.27	0.08	0.22	0.10	0.11	0.10	0.08	0.12	0.07	0.11	0.13	0.09	0.28
MgO	17.33	16.95	16.83	15.23	17.19	12.95	17.29	16.59	17.34	16.74	16.79	16.72	16.77	16.70	17.30	14.78
CaO	22.99	22.93	22.82	21.99	22.99	20.48	22.81	22.77	22.75	22.79	22.84	22.91	22.80	22.92	22.85	22.11
BaO	0.02	0.02	0.01	0.00	0.00	0.03	0.00	0.00	0.01	0.03	0.01	0.03	0.00	0.00	0.00	0.03
Na_2O	0.19	0.21	0.21	0.47	0.24	1.34	0.16	0.22	0.20	0.21	0.19	0.21	0.18	0.25	0.17	0.45
K_2O	0.01	0.00	0.02	0.00	0.01	0.47	0.00	0.00	0.00	0.02	0.01	0.00	0.00	0.00	0.00	0.01
P_2O_5	0.00	0.07	0.00	0.07	0.00	0.00	0.06	0.02	0.00	0.06	0.09	0.05	0.01	0.08	0.01	0.00
SO_3	0.02	0.00	0.01	0.00	0.00	0.00	0.00	0.00	0.00	0.01	0.02	0.00	0.02	0.01	0.01	0.02
Cl	0.00	0.00	0.00	0.01	0.01	0.10	0.00	0.00	0.00	0.00	0.00	0.01	0.01	0.00	0.00	0.00
F	0.00	0.00	0.00	0.00	0.00	0.00	0.00	0.00	0.00	0.10	0.00	0.00	0.00	0.00	0.00	0.00
Total	99.6	99.6	99.6	99.6	99.6	99.6	99.7	99.7	99.7	99.7	99.7	99.7	99.7	99.7	99.7	99.8

Table 3: Major element compositions of clinopyroxene analyses from pyroxenite samples. All analyses carried out by electron microprobe.

Analysis name	BC14/023_Cpx	BC14/023_Cpx	BC14/023_Cpx	BC14/023_Cpx	BC14/023_Cpx	BC14/023_Cpx	BC14/023_Cpx	BC14/023_Cpx	BC14/023_Cpx	BC14/039_Cpx1	BC14/039_Cpx1	BC14/039_Cpx1	BC14/039_Cpx1	BC14/039_Cpx1	BC14/039_Cpx1	BC14/039_Cpx1
SiO_2	52.41	52.24	50.93	53.46	52.67	51.62	53.34	53.63	53.48	49.54	47.50	48.18	48.34	47.43	49.40	47.64
TiO_2	0.31	0.30	0.50	0.22	0.25	0.39	0.23	0.25	0.21	0.60	0.94	0.84	0.84	0.98	0.60	0.95
Al_2O_3	2.50	2.56	3.69	1.77	2.00	2.90	1.79	1.75	1.77	0.00	0.02	0.06	0.00	0.00	0.02	0.00
Cr_2O_3	0.45	0.47	0.02	0.36	0.28	0.54	0.40	0.32	0.36	3.84	5.27	4.94	4.95	5.48	3.83	5.41
FeO	4.06	4.19	6.86	3.56	4.75	5.68	3.56	3.59	3.63	0.01	0.02	0.01	0.00	0.00	0.00	0.00
NiO	0.02	0.00	0.00	0.01	0.00	0.06	0.05	0.03	0.04	5.57	6.90	6.70	6.48	7.32	6.40	7.11
MnO	0.09	0.11	0.26	0.08	0.18	0.16	0.12	0.09	0.03	0.15	0.14	0.14	0.14	0.17	0.13	0.14
MgO	16.79	16.74	14.80	17.27	16.66	15.70	17.25	17.37	17.33	15.03	14.15	14.33	14.51	14.07	15.02	14.16
CaO	22.94	22.91	22.34	22.94	22.75	22.37	22.99	22.88	22.98	22.97	23.03	22.92	22.95	22.88	22.90	23.07
BaO	0.01	0.01	0.00	0.02	0.00	0.00	0.00	0.01	0.00	0.00	0.00	0.01	0.04	0.00	0.01	0.03
Na_2O	0.20	0.22	0.44	0.16	0.32	0.42	0.16	0.14	0.20	0.28	0.32	0.26	0.28	0.28	0.26	0.25
K_2O	0.00	0.00	0.00	0.00	0.01	0.00	0.00	0.00	0.02	0.00	0.01	0.00	0.00	0.00	0.00	0.01
P_2O_5	0.02	0.08	0.01	0.00	0.01	0.04	0.07	0.00	0.02	0.00	0.02	0.00	0.00	0.00	0.02	0.00
SO_3	0.00	0.00	0.00	0.00	0.01	0.01	0.02	0.01	0.00	0.00	0.01	0.00	0.00	0.00	0.02	0.00
Cl	0.00	0.00	0.00	0.00	0.00	0.01	0.00	0.01	0.02	0.01	0.00	0.01	0.02	0.00	0.01	0.00
F	0.01	0.00	0.00	0.00	0.03	0.05	0.00	0.00	0.05	0.00	0.01	0.00	0.00	0.00	0.02	0.00
Total	99.8	99.8	99.8	99.9	99.9	99.9	100.0	100.1	100.1	98.0	98.3	98.4	98.5	98.6	98.6	98.8

Table 3: Major element compositions of clinopyroxene analyses from pyroxenite samples. All analyses carried out by electron microprobe.

Analysis name	BC14/039_Cpx1	BC14/039_Cpx1	BC14/039_Cpx1	BC14/039_Cpx1	BC14/039_Cpx1	BC14/039_Cpx1	BC14/039_Cpx2	BC14/039_Cpx2	BC14/039_Cpx2	BC14/039_Cpx2	BC14/039_Cpx2	BC14/039_Cpx2	BC14/039_Cpx2	BC14/039_Cpx2	BC14/039_Cpx2	BC14/039_Cpx2
SiO_2	49.58	49.94	49.88	50.03	50.20	50.47	49.20	49.14	48.55	48.34	48.73	48.84	49.92	49.25	49.74	48.56
TiO_2	0.59	0.57	0.57	0.58	0.55	0.53	0.64	0.73	0.71	0.79	0.76	0.71	0.60	0.65	0.69	0.84
Al_2O_3	0.04	0.06	0.04	0.00	0.09	0.09	0.00	0.00	0.03	0.00	0.00	0.00	0.06	0.02	0.00	0.00
Cr_2O_3	3.78	3.64	3.51	3.62	3.46	3.37	4.38	4.39	4.73	4.91	4.84	4.63	3.72	4.27	4.06	4.97
FeO	0.00	0.00	0.01	0.01	0.02	0.00	0.01	0.00	0.01	0.01	0.00	0.00	0.00	0.00	0.00	0.00
NiO	6.25	6.22	6.35	6.24	6.20	6.23	6.53	6.64	6.67	7.09	6.70	6.62	6.71	6.64	6.35	7.01
MnO	0.11	0.15	0.16	0.13	0.19	0.15	0.17	0.23	0.18	0.22	0.18	0.16	0.20	0.19	0.19	0.20
MgO	15.12	15.12	15.33	15.18	15.33	15.41	14.81	14.48	14.55	14.20	14.36	14.54	14.98	14.94	14.91	14.25
CaO	23.01	23.00	23.00	23.16	22.99	22.98	22.43	22.64	22.88	22.86	23.00	23.02	22.55	22.70	22.75	22.82
BaO	0.00	0.00	0.01	0.00	0.02	0.02	0.00	0.00	0.03	0.01	0.01	0.00	0.00	0.01	0.00	0.03
Na_2O	0.26	0.27	0.23	0.23	0.28	0.25	0.27	0.38	0.31	0.37	0.24	0.41	0.22	0.30	0.31	0.34
K_2O	0.00	0.00	0.02	0.01	0.00	0.01	0.01	0.01	0.01	0.00	0.00	0.00	0.01	0.00	0.00	0.00
P_2O_5	0.01	0.00	0.01	0.00	0.03	0.00	0.04	0.00	0.00	0.00	0.02	0.00	0.00	0.00	0.00	0.00
SO_3	0.02	0.00	0.01	0.01	0.00	0.00	0.03	0.00	0.01	0.00	0.01	0.00	0.00	0.00	0.00	0.00
Cl	0.00	0.01	0.00	0.00	0.01	0.00	0.00	0.01	0.01	0.00	0.01	0.01	0.00	0.01	0.00	0.00
F	0.00	0.00	0.00	0.00	0.00	0.00	0.00	0.00	0.00	0.00	0.00	0.01	0.00	0.00	0.01	0.03
Total	98.8	99.0	99.1	99.2	99.4	99.5	98.5	98.6	98.7	98.8	98.9	98.9	99.0	99.0	99.0	99.0

Table 3: Major element compositions of clinopyroxene analyses from pyroxenite samples. All analyses carried out by electron microprobe.

Analysis name	BC14/039_Cpx2	BC14/039_Cpx2	BC14/039_Cpx2	BC14/039_Cpx2	BC14/039_Cpx2	BC14/039_Cpx2	BC14/039_Cpx2	BC14/039_Cpx2	BC14/039_Cpx2	BC14/039_Cpx3	BC14/039_Cpx3	BC14/039_Cpx3	BC14/039_Cpx3	BC14/039_Cpx3	BC14/039_Cpx3	BC14/039_Cpx3
SiO_2	48.83	48.63	49.55	48.68	48.80	49.56	49.03	49.61	50.45	47.18	47.95	46.58	47.31	48.07	48.00	46.91
TiO_2	0.76	0.78	0.65	0.84	0.72	0.71	0.78	0.66	0.57	1.01	0.88	1.11	1.04	0.77	0.81	1.10
Al_2O_3	0.00	0.00	0.04	0.00	0.00	0.04	0.00	0.09	0.09	0.00	0.01	0.00	0.04	0.00	0.00	0.00
Cr_2O_3	4.86	4.97	3.96	4.98	4.82	4.32	4.67	4.22	3.62	5.80	5.17	6.35	6.16	5.25	5.44	6.24
FeO	0.01	0.04	0.00	0.01	0.02	0.00	0.00	0.00	0.01	0.02	0.01	0.00	0.00	0.00	0.00	0.01
NiO	6.83	6.86	6.70	7.26	7.01	6.65	7.04	6.71	6.79	7.44	7.18	7.83	7.33	6.81	6.81	7.96
MnO	0.14	0.16	0.16	0.19	0.19	0.20	0.20	0.17	0.23	0.20	0.23	0.16	0.20	0.15	0.13	0.22
MgO	14.35	14.42	15.17	14.17	14.38	14.93	14.68	14.91	15.38	13.75	14.01	13.46	13.72	14.22	14.04	13.47
CaO	22.97	22.90	22.61	22.77	22.99	22.59	22.66	22.73	22.57	22.38	22.42	22.42	22.38	22.80	22.97	22.43
BaO	0.01	0.00	0.00	0.03	0.00	0.03	0.00	0.05	0.01	0.00	0.00	0.00	0.02	0.04	0.00	0.01
Na_2O	0.32	0.35	0.31	0.25	0.30	0.28	0.31	0.25	0.27	0.37	0.31	0.31	0.24	0.35	0.36	0.28
K_2O	0.01	0.01	0.01	0.00	0.00	0.00	0.00	0.01	0.00	0.01	0.00	0.00	0.01	0.00	0.00	0.01
P_2O_5	0.00	0.00	0.02	0.00	0.01	0.00	0.00	0.00	0.00	0.00	0.00	0.02	0.00	0.01	0.00	0.01
SO_3	0.00	0.00	0.00	0.00	0.00	0.01	0.00	0.00	0.00	0.01	0.01	0.01	0.01	0.00	0.00	0.00
Cl	0.00	0.00	0.00	0.00	0.01	0.01	0.00	0.02	0.00	0.01	0.00	0.00	0.00	0.00	0.00	0.01
F	0.00	0.05	0.00	0.00	0.00	0.00	0.00	0.00	0.00	0.00	0.00	0.00	0.00	0.07	0.00	0.00
Total	99.1	99.1	99.2	99.2	99.2	99.3	99.4	99.4	100.0	98.2	98.2	98.2	98.5	98.5	98.6	98.6

Table 3: Major element compositions of clinopyroxene analyses from pyroxenite samples. All analyses carried out by electron microprobe.

Analysis name	BC14/039_Cpx3	BC14/039_Cpx6	BC14/039_Cpx6	BC14/039_Cpx6	BC14/039_Cpx6	BC14/039_Cpx6	BC14/039_Cpx6	BC14/039_Cpx6	BC14/039_Cpx6	BC14/039_Cpx6	BC14/039_Cpx6	BC14/043_Cpx1	BC14/043_Cpx1	BC14/043_Cpx1	BC14/043_Cpx1	BC14/043_Cpx1
SiO_2	49.06	45.23	47.51	47.64	47.54	47.55	46.70	48.18	46.53	46.67	47.27	46.85	48.72	48.78	47.10	47.37
TiO_2	0.76	1.02	0.93	0.87	0.95	0.92	0.90	0.90	1.12	1.11	0.99	0.98	0.69	0.65	0.98	0.94
Al_2O_3	0.00	0.05	0.00	0.00	0.06	0.00	0.09	0.03	0.00	0.04	0.03	6.63	4.73	4.77	6.57	6.35
Cr_2O_3	4.74	8.72	5.65	5.32	5.64	5.55	6.78	5.32	6.63	6.57	5.96	0.00	0.01	0.03	0.00	0.00
FeO	0.00	0.00	0.04	0.04	0.02	0.04	0.01	0.01	0.01	0.00	0.00	7.45	6.88	6.84	7.39	7.34
NiO	6.84	7.08	6.93	7.31	7.00	7.32	7.32	7.08	7.96	8.02	7.85	0.00	0.00	0.02	0.00	0.07
MnO	0.17	0.19	0.19	0.18	0.21	0.18	0.18	0.16	0.18	0.20	0.20	0.17	0.17	0.15	0.12	0.19
MgO	14.62	12.74	13.79	13.98	13.90	13.94	13.51	14.12	13.42	13.24	13.61	13.21	14.25	14.28	13.33	13.51
CaO	22.84	22.09	22.68	22.69	22.74	22.48	22.63	22.53	22.60	22.64	22.76	23.06	23.09	23.15	23.19	23.01
BaO	0.01	0.00	0.01	0.00	0.00	0.02	0.02	0.04	0.02	0.01	0.05	0.02	0.04	0.01	0.00	0.00
Na_2O	0.27	0.32	0.29	0.29	0.30	0.38	0.28	0.37	0.34	0.30	0.35	0.25	0.24	0.23	0.30	0.30
K_2O	0.02	0.03	0.00	0.00	0.00	0.00	0.01	0.06	0.00	0.01	0.01	0.01	0.01	0.01	0.00	0.00
P_2O_5	0.00	0.01	0.00	0.00	0.00	0.01	0.00	0.00	0.01	0.01	0.00	0.09	0.00	0.05	0.07	0.02
SO_3	0.00	0.03	0.01	0.00	0.00	0.01	0.00	0.00	0.00	0.02	0.00	0.00	0.00	0.01	0.00	0.00
Cl	0.00	0.00	0.00	0.00	0.00	0.00	0.00	0.01	0.01	0.01	0.00	0.00	0.01	0.00	0.00	0.00
F	0.00	0.00	0.04	0.00	0.00	0.01	0.00	0.00	0.00	0.00	0.00	0.12	0.03	0.00	0.00	0.00
Total	99.3	97.5	98.0	98.3	98.4	98.4	98.4	98.8	98.8	98.8	99.1	98.8	98.9	99.0	99.0	99.1

Table 3: Major element compositions of clinopyroxene analyses from pyroxenite samples. All analyses carried out by electron microprobe.

Analysis name	BC14/043_Cpx1	BC14/043_Cpx1	BC14/043_Cpx1	BC14/043_Cpx1	BC14/043_Cpx1	BC14/043_Cpx1	BC14/043_Cpx1	BC14/043_Cpx1	BC14/043_Cpx1	BC14/043_Cpx1	BC14/043_Cpx1	BC14/043_Cpx1	BC14/043_Cpx1	BC14/043_Cpx1	BC14/043_Cpx2	BC14/043_Cpx2
SiO_2	46.69	46.72	49.29	46.74	46.86	48.60	48.83	49.15	49.17	49.39	49.67	49.70	49.82	49.58	48.66	48.63
TiO_2	1.04	1.07	0.63	1.07	1.04	0.85	0.66	0.68	0.65	0.64	0.64	0.66	0.61	0.64	0.85	0.81
Al_2O_3	6.98	7.03	4.56	7.00	6.93	5.11	4.86	4.85	4.71	4.73	4.49	4.60	4.55	4.63	4.88	4.88
Cr_2O_3	0.07	0.00	0.01	0.01	0.00	0.00	0.02	0.00	0.00	0.01	0.00	0.00	0.05	0.03	0.04	0.05
FeO	7.85	7.76	6.75	7.76	7.76	7.73	6.83	6.86	6.80	6.88	6.71	6.86	6.86	6.83	7.59	7.63
NiO	0.00	0.00	0.02	0.04	0.04	0.00	0.06	0.01	0.01	0.00	0.08	0.00	0.02	0.01	0.00	0.03
MnO	0.14	0.13	0.14	0.13	0.14	0.27	0.16	0.13	0.15	0.15	0.15	0.12	0.15	0.12	0.26	0.24
MgO	12.98	13.12	14.41	13.01	13.12	13.61	14.48	14.53	14.55	14.53	14.69	14.50	14.68	14.60	13.61	13.50
CaO	22.97	23.00	23.12	23.16	23.10	22.50	23.28	23.19	23.27	23.16	23.12	23.12	23.08	23.21	22.55	22.70
BaO	0.06	0.03	0.02	0.00	0.00	0.02	0.00	0.01	0.00	0.00	0.03	0.00	0.02	0.01	0.06	0.00
Na_2O	0.28	0.24	0.22	0.27	0.26	0.53	0.25	0.24	0.23	0.23	0.22	0.24	0.21	0.28	0.48	0.47
K_2O	0.00	0.00	0.00	0.01	0.00	0.01	0.01	0.00	0.01	0.00	0.01	0.00	0.00	0.00	0.01	0.01
P_2O_5	0.04	0.00	0.00	0.05	0.00	0.06	0.00	0.00	0.08	0.00	0.00	0.05	0.02	0.14	0.01	0.07
SO_3	0.00	0.00	0.00	0.00	0.00	0.00	0.00	0.02	0.00	0.02	0.00	0.00	0.00	0.00	0.00	0.00
Cl	0.00	0.00	0.00	0.01	0.00	0.00	0.00	0.01	0.01	0.00	0.00	0.00	0.00	0.01	0.01	0.00
F	0.00	0.02	0.07	0.00	0.00	0.00	0.08	0.00	0.04	0.00	0.00	0.00	0.00	0.00	0.00	0.00
Total	99.1	99.1	99.2	99.3	99.3	99.3	99.5	99.7	99.7	99.7	99.8	99.8	100.1	100.1	99.0	99.0

Table 3: Major element compositions of clinopyroxene analyses from pyroxenite samples. All analyses carried out by electron microprobe.

Analysis name	BC14/043_Cpx2	SA12/X01_Cpx1	SA12/X01_Cpx1	SA12/X01_Cpx1	SA12/X01_Cpx2	SA12/X01_Cpx2	SA12/X01_Cpx2	SA12/X01_Cpx2	SA12/X01_Cpx2	SA12/X01_Cpx2	SA12/X01_Cpx2	SA12/X01_Cpx2	SA12/X01_Cpx2	SA12/X01_Cpx2	SA12/X01_Cpx3	SA12/X01_Cpx3
SiO_2	49.17	47.76	46.57	48.36	49.37	46.67	49.39	48.75	47.43	49.51	49.16	49.31	50.50	51.57	45.79	45.95
TiO_2	0.72	0.76	1.09	0.77	0.55	0.98	0.55	0.73	0.91	0.57	0.62	0.62	0.77	0.41	1.25	1.22
Al_2O_3	4.53	0.00	0.00	0.09	0.00	0.00	0.00	0.01	0.11	0.00	0.00	0.00	0.07	0.06	0.08	0.03
Cr_2O_3	0.05	5.13	6.57	4.89	3.78	6.25	3.85	4.43	5.67	3.77	4.10	4.16	2.67	1.81	7.02	7.06
FeO	7.31	0.01	0.00	0.01	0.02	0.00	0.01	0.01	0.02	0.00	0.00	0.00	0.00	0.00	0.01	0.00
NiO	0.02	7.54	7.91	7.28	6.02	7.51	6.26	6.69	7.37	6.30	6.66	6.50	7.08	7.69	7.85	7.75
MnO	0.18	0.24	0.16	0.18	0.14	0.20	0.18	0.19	0.18	0.20	0.17	0.20	0.33	0.61	0.19	0.16
MgO	14.21	13.42	13.27	14.12	15.07	13.54	14.99	14.40	13.77	15.01	14.72	14.72	14.96	16.27	13.02	12.89
CaO	22.51	22.83	22.67	22.62	22.78	22.69	22.84	22.88	22.74	22.90	22.90	22.93	21.92	20.12	22.55	22.65
BaO	0.00	0.01	0.04	0.00	0.01	0.00	0.00	0.01	0.05	0.02	0.00	0.07	0.00	0.00	0.01	0.00
Na_2O	0.52	0.40	0.32	0.34	0.25	0.30	0.29	0.28	0.29	0.26	0.28	0.23	0.56	0.58	0.25	0.36
K_2O	0.00	0.01	0.00	0.00	0.01	0.00	0.00	0.00	0.00	0.01	0.01	0.00	0.01	0.01	0.01	0.02
P_2O_5	0.00	0.00	0.00	0.00	0.00	0.00	0.00	0.00	0.00	0.00	0.00	0.00	0.00	0.00	0.00	0.00
SO_3	0.00	0.01	0.00	0.00	0.01	0.00	0.01	0.00	0.00	0.00	0.01	0.00	0.00	0.00	0.00	0.00
Cl	0.01	0.00	0.01	0.00	0.00	0.01	0.00	0.00	0.00	0.01	0.00	0.00	0.00	0.00	0.00	0.00
F	0.13	0.00	0.04	0.00	0.00	0.00	0.00	0.00	0.03	0.00	0.04	0.00	0.01	0.01	0.01	0.00
Total	99.4	98.1	98.6	98.7	98.0	98.2	98.4	98.4	98.5	98.6	98.7	98.7	98.9	99.1	98.0	98.1

Table 3: Major element compositions of clinopyroxene analyses from pyroxenite samples. All analyses carried out by electron microprobe.

Analysis name	SA12/ X01_ Cpx3	SA12/ X01_ Cpx3	SA12/ X01_ Cpx3	SA12/ X01_ Cpx3	SA12/ X01_ Cpx3	SA12/ X01_ Cpx3	SA12/ X01_ Cpx3	SA12/ X01_ Cpx3	SA12/ X01_ Cpx3	SA12/ X01_ Cpx3	SA12/ X01_ Cpx3	SA12/ X01_ Cpx3
SiO_2	46.23	48.13	46.76	48.86	48.03	47.19	46.49	50.85	47.84	49.32	46.89	46.92
TiO_2	1.13	0.78	1.08	0.66	0.85	1.00	1.09	0.53	0.82	0.65	0.99	0.98
Al_2O_3	0.00	0.04	0.05	0.05	0.02	0.01	0.06	0.01	0.03	0.03	0.06	0.01
Cr_2O_3	6.85	4.92	6.56	4.32	5.05	6.09	6.56	2.38	5.24	4.04	6.32	6.27
FeO	0.01	0.00	0.03	0.00	0.03	0.00	0.01	0.00	0.02	0.01	0.02	0.00
NiO	7.92	6.95	7.42	6.60	7.12	7.29	7.74	7.03	7.47	6.52	7.55	7.69
MnO	0.16	0.21	0.21	0.18	0.14	0.22	0.17	0.41	0.17	0.16	0.15	0.17
MgO	13.06	14.13	13.35	14.50	13.94	13.59	13.25	15.48	13.92	14.68	13.50	13.60
CaO	22.64	22.87	22.64	22.97	22.88	22.79	22.83	21.29	22.77	22.94	22.75	22.77
BaO	0.00	0.00	0.00	0.03	0.02	0.00	0.02	0.01	0.00	0.00	0.03	0.00
Na_2O	0.28	0.34	0.31	0.29	0.37	0.30	0.30	0.55	0.23	0.24	0.33	0.31
K_2O	0.00	0.00	0.00	0.00	0.00	0.01	0.00	0.00	0.01	0.01	0.00	0.01
P_2O_5	0.00	0.00	0.00	0.00	0.00	0.00	0.00	0.00	0.01	0.00	0.01	0.00
SO_3	0.03	0.00	0.00	0.00	0.01	0.00	0.00	0.00	0.02	0.01	0.00	0.00
Cl	0.00	0.00	0.01	0.00	0.00	0.00	0.01	0.00	0.00	0.00	0.00	0.00
F	0.00	0.00	0.00	0.00	0.00	0.00	0.00	0.00	0.00	0.00	0.00	0.00
Total	98.3	98.4	98.4	98.5	98.5	98.5	98.5	98.6	98.6	98.6	98.6	98.7

Table 3: Major element compositions of clinopyroxene analyses from pyroxenite samples. All analyses carried out by electron microprobe.

Analysis name	SA12/X01_Cpx3	SA12/X01_Cpx4	SA12/X01_Cpx4	SA12/X01_Cpx4	SA19_Cpx9	SA19_Cpx10	SA19_Cpx11	SA19_Cpx12	SA19_Cpx13	SA19_Cpx14	SA19_Cpx15	SA19_Cpx16
SiO_2	46.08	50.14	46.67	50.46	48.09	49.61	48.97	49.76	49.04	49.41	49.93	48.73
TiO_2	1.24	0.56	1.18	0.59	0.92	0.65	0.88	0.70	0.75	0.75	0.59	0.86
Al_2O_3	0.06	0.04	0.10	0.00	5.58	4.02	5.03	4.17	4.38	4.45	3.73	4.79
Cr_2O_3	7.30	2.22	5.18	2.32	0.00	0.00	0.00	0.00	0.00	0.05	0.01	0.03
FeO	0.00	0.00	0.02	0.01	7.58	7.35	7.44	7.45	7.24	7.35	7.18	7.53
NiO	7.90	7.02	9.27	6.80	0.00	0.01	0.00	0.03	0.01	0.02	0.04	0.00
MnO	0.17	0.51	0.40	0.44	0.21	0.30	0.25	0.32	0.33	0.29	0.29	0.31
MgO	13.14	14.93	13.09	15.27	13.36	13.88	13.44	13.72	14.08	13.79	14.23	13.77
CaO	22.68	21.60	21.39	21.83	22.96	22.52	22.54	22.05	22.49	22.54	22.50	22.78
BaO	0.00	0.00	0.00	0.04	0.00	0.05	0.00	0.00	0.00	0.03	0.03	0.04
Na_2O	0.29	0.58	0.48	0.60	0.40	0.60	0.43	0.50	0.40	0.53	0.47	0.46
K_2O	0.01	0.02	0.01	0.01	0.01	0.03	0.00	0.00	0.01	0.02	0.01	0.02
P_2O_5	0.00	0.00	0.00	0.01	0.02	0.01	0.03	0.04	0.02	0.02	0.00	0.00
SO_3	0.00	0.00	0.00	0.00								
Cl	0.00	0.01	0.00	0.01	0.01	0.08	0.03	0.05	0.05	0.01	0.00	0.01
F	0.03	0.00	0.00	0.00	0.00	0.00	0.00	0.00	0.00	0.00	0.00	0.00
Total	98.9	97.6	97.8	98.4	99.1	99.1	99.1	98.8	98.8	99.2	99.0	99.3

Table 3: Major element compositions of clinopyroxene analyses from pyroxenite samples. All analyses carried out by electron microprobe.

Analysis name	SA25	SA25	SA25	SA25	SA25	SA310_1	SA310_10	SA310_11	SA310_12	SA310_2	SA310_25	SA310_26
SiO_2	49.61	48.90	48.27	48.94	47.16	48.94	48.81	48.74	48.73	48.39	49.09	48.95
TiO_2	0.62	0.66	0.49	0.70	1.03	0.64	0.69	0.74	0.65	0.83	0.64	0.68
Al_2O_3	5.29	4.85	5.49	5.38	6.87	4.60	4.80	5.15	5.17	4.93	4.85	4.89
Cr_2O_3												
FeO	4.84	7.05	7.65	7.40	8.39	6.73	6.55	6.80	6.73	6.96	7.01	6.89
NiO												
MnO					0.17	0.16	0.11	0.11	0.13	0.12	0.10	0.12
MgO	13.01	12.91	12.76	12.59	12.08	14.66	14.41	14.34	14.05	14.25	14.23	14.09
CaO	24.86	24.08	23.88	24.32	24.20	23.02	23.37	23.04	23.04	23.11	23.30	23.32
BaO						0.00	0.00	0.00	0.00	0.00	0.00	0.00
Na_2O		0.15	0.32	0.17	0.36	0.27	0.25	0.26	0.21	0.27	0.23	0.20
K_2O						0.00	0.01	0.01	0.01	0.01	0.00	0.00
P_2O_5						0.01	0.00	0.03	0.00	0.00	0.03	0.00
SO_3						0.00	0.02	0.00	0.00	0.01	0.00	0.00
Cl						0.00	0.00	0.02	0.04	0.01	0.01	0.00
F						0.18	0.10	0.20	0.02	0.18	0.02	0.00
Total	98.2	98.6	98.9	99.5	100.3	99.2	99.2	99.5	98.8	99.1	99.5	99.2

Table 3: Major element compositions of clinopyroxene analyses from pyroxenite samples. All analyses carried out by electron microprobe.

Analysis name	SA310_29	SA310_30	SA310_37	SA310_38	SA310_39	SA310_41	SA310_42	SA310_7
SiO_2	49.46	49.32	49.13	50.79	49.50	48.94	48.97	48.97
TiO_2	0.67	0.68	0.75	0.51	0.66	0.71	0.74	0.68
Al_2O_3	5.00	4.98	5.07	3.58	4.52	4.91	5.06	4.86
Cr_2O_3								
FeO	6.88	7.18	6.61	6.12	6.64	6.80	6.73	6.65
NiO								
MnO	0.12	0.14	0.11	0.14	0.14	0.10	0.11	0.16
MgO	14.54	14.43	14.38	15.17	14.61	14.26	14.33	14.30
CaO	23.28	23.26	23.46	23.08	22.72	23.10	23.04	23.22
BaO	0.00	0.00	0.00	0.00	0.00	0.00	0.03	0.05
Na_2O	0.28	0.23	0.22	0.21	0.25	0.26	0.23	0.25
K_2O	0.00	0.00	0.00	0.00	0.01	0.01	0.02	0.00
P_2O_5	0.00	0.00	0.01	0.00	0.03	0.00	0.00	0.00
SO_3	0.00	0.01	0.00	0.01	0.00	0.00	0.00	0.00
Cl	0.01	0.01	0.03	0.03	0.00	0.01	0.00	0.01
F	0.06	0.02	0.20	0.04	0.00	0.14	0.00	0.00
Total	100.3	100.3	100.0	99.7	99.1	99.3	99.3	99.2

Table 3: Major element compositions of clinopyroxene analyses from pyroxenite samples. All analyses carried out by electron microprobe.

Analysis name	B25_ Cpx1-3	B25_ Cpx2-1	B25_ Cpx2-6	B25_ Cpx3-2	B25_ Cpx3-3	B25_ Cpx3-7	B25_ Cpx4-3	B25_ Cpx4-6	B25_ Cpx4-7	B25_ Cpx5-6	B25_ Cpx5-7	B25_ Cpx5-8	B25_ Cpx5-9	B25_ Cpx6-2	B25_ Cpx6-3	B25_ Cpx6-5
SiO_2	45.72	48.30	47.88	47.78	47.21	47.20	46.78	47.38	48.46	47.66	47.63	47.20	46.20	48.61	45.80	45.33
TiO_2	1.22	0.93	0.78	0.81	1.00	1.02	0.88	1.11	0.69	0.87	0.82	0.80	1.13	0.73	1.25	1.51
Al_2O_3	7.49	4.55	4.51	4.81	6.22	6.24	5.44	6.45	3.82	5.77	5.48	5.21	7.23	4.29	7.39	8.12
Cr_2O_3	0.01	0.01	0.00	-0.02	0.00	-0.01	-0.01	0.01	0.00	0.01	0.01	0.00	-0.01	0.02	0.00	-0.02
FeO	7.87	8.12	7.60	7.60	8.62	7.17	7.97	7.89	7.32	7.03	7.08	7.11	7.31	7.34	7.95	8.58
NiO	-0.01	0.01	-0.02	0.01	0.01	0.00	-0.03	0.00	0.01	0.02	0.02	0.01	-0.01	0.01	0.01	0.01
MnO	0.17	0.33	0.24	0.27	0.22	0.18	0.28	0.24	0.27	0.17	0.17	0.16	0.15	0.28	0.23	0.25
MgO	12.80	14.10	14.29	14.62	13.43	13.57	13.78	13.16	14.79	13.72	13.92	13.98	13.12	14.61	12.98	12.42
CaO	23.16	21.96	22.48	22.48	22.26	23.09	21.89	22.60	22.39	23.19	23.36	23.06	23.56	22.56	22.66	22.52
BaO																
Na_2O	0.28	0.37	0.26	0.28	0.21	0.31	0.33	0.36	0.29	0.24	0.20	0.26	0.23	0.27	0.39	0.37
K_2O	0.02	0.06	0.01	0.02	0.03	0.03	0.08	0.04	0.02	0.04	0.02	0.05	0.03	0.04	0.07	0.04
P_2O_5	0.48	0.48	0.48	0.43	0.54	0.38	0.53	0.48	0.49	0.50	0.50	0.39	0.48	0.44	0.41	0.45
SO_3																
Cl	0.01	0.02	0.02	0.04	0.06	0.01	0.05	0.03	0.01	0.02	0.01	0.01	0.02	0.02	0.01	0.02
F																
Total	99.2	99.2	98.5	99.1	99.8	99.2	98.0	99.7	98.6	99.3	99.2	98.2	99.5	99.2	99.2	99.6

Table 4: Major element compositions of clinopyroxene analyses from lava samples. All analyses carried out by electron microprobe.

Analysis name	B25_ Cpx6-6	B25_ Cpx7-1	B25_ Cpx7-1	B25_ Cpx7-1	B25_ Cpx7-1	B25_ Cpx7-1	B25_ Cpx7-1	B25_ Cpx7-1	B25_ Cpx7-1	B25_ Cpx7-1	B25_ Cpx7-1	B25_ Cpx7-1	B25_ Cpx7-1	B27_ Cpx10	B27_ Cpx11	B27_ Cpx12
SiO_2	49.07	45.74	47.50	46.71	46.61	47.55	48.22	47.32	47.30	47.15	48.49	47.55	48.80	49.56	48.38	49.59
TiO_2	0.77	1.05	0.85	0.83	1.04	0.85	0.66	0.93	0.96	1.02	0.92	0.93	0.81	0.64	0.91	0.73
Al_2O_3	3.42	6.92	5.18	5.82	6.51	5.18	4.70	5.66	5.75	5.92	5.66	6.49	5.88	4.18	5.73	4.76
Cr_2O_3	0.01	-0.01	0.00	0.02	-0.01	0.01	-0.01	0.01	0.00	0.00	0.00	-0.01	0.01	0.00	0.04	0.05
FeO	6.51	7.26	6.81	7.47	7.16	6.96	6.88	6.86	6.79	6.92	6.83	7.50	7.09	7.77	7.29	7.24
NiO	-0.01	0.01	0.01	0.01	-0.02	-0.03	0.02	0.02	-0.02	0.00	0.00	-0.01	-0.02	0.00	0.00	0.00
MnO	0.39	0.15	0.20	0.21	0.17	0.19	0.23	0.16	0.18	0.15	0.20	0.20	0.19	0.37	0.18	0.24
MgO	14.83	12.92	14.09	13.44	13.19	14.31	14.08	14.08	14.05	14.15	13.99	13.26	14.36	13.64	13.33	13.93
CaO	22.14	23.23	23.04	23.34	23.42	23.01	23.42	23.25	23.28	23.44	23.26	23.59	23.15	22.73	23.21	22.96
BaO														0.09	0.07	0.03
Na_2O	0.55	0.30	0.31	0.34	0.29	0.31	0.33	0.31	0.30	0.29	0.31	0.29	0.43	0.55	0.29	0.41
K_2O	0.02	0.04	0.02	0.02	0.01	0.01	0.03	0.01	0.03	0.00	0.02	0.02	0.15	0.02	0.00	0.01
P_2O_5	0.51	0.49	0.47	0.44	0.43	0.55	0.46	0.41	0.45	0.43	0.43	0.49	0.41	0.00	0.00	0.00
SO_3																
Cl	0.01	0.03	0.03	0.01	0.01	0.02	0.02	0.01	0.01	0.01	0.01	0.01	0.04	0.00	0.00	0.00
F														0.00	0.00	0.00
Total	98.2	98.1	98.5	98.7	98.8	99.0	99.0	99.0	99.1	99.5	100.1	100.3	101.3	99.5	99.4	100.0

Table 4: Major element compositions of clinopyroxene analyses from lava samples. All analyses carried out by electron microprobe.

Analysis name	B27_ Cpx13	B27_ Cpx14	B27_ Cpx15	B27_ Cpx17	B27_ Cpx18	B27_ Cpx19	B27_ Cpx20	B27_ Cpx21	B27_ Cpx22	B27_ Cpx3	B27_ Cpx4	B27_ Cpx5	B27_ Cpx6	B27_ Cpx7	B27_ Cpx8	B27_ Cpx9
SiO_2	46.86	44.81	49.07	47.21	48.41	46.93	48.84	48.67	49.86	45.55	44.25	49.79	50.06	50.03	47.31	47.27
TiO_2	1.03	1.70	0.85	1.39	0.91	0.99	0.92	1.06	0.78	1.26	1.72	0.72	0.65	0.57	0.97	1.07
Al_2O_3	6.80	9.03	5.90	6.53	6.03	6.73	5.08	5.74	3.99	7.66	7.83	3.88	3.92	3.24	6.45	6.60
Cr_2O_3	0.00	0.01	0.00	0.00	0.00	0.00	0.00	0.00	0.02	0.00	0.00	0.01	0.00	0.00	0.04	0.00
FeO	7.29	9.21	7.72	8.37	7.02	8.16	8.13	8.46	7.28	8.58	8.93	7.38	7.03	6.54	6.99	7.10
NiO	0.01	0.03	0.09	0.00	0.06	0.00	0.04	0.00	0.04	0.05	0.02	0.03	0.01	0.01	0.02	0.04
MnO	0.15	0.25	0.17	0.43	0.16	0.19	0.29	0.46	0.43	0.26	0.25	0.31	0.34	0.38	0.23	0.22
MgO	13.55	11.35	13.78	12.97	13.84	13.06	12.93	13.25	14.37	12.01	11.78	14.51	14.41	14.75	13.41	13.60
CaO	23.05	22.67	23.50	21.50	23.11	22.50	22.80	21.56	22.23	22.01	21.85	22.50	22.31	22.08	22.92	23.37
BaO	0.03	0.06	0.00	0.08	0.00	0.04	0.02	0.02	0.03	0.07	0.02	0.00	0.00	0.01	0.00	0.03
Na_2O	0.26	0.33	0.36	0.49	0.30	0.38	0.61	0.55	0.46	0.48	0.42	0.32	0.46	0.41	0.26	0.29
K_2O	0.00	0.00	0.00	0.03	0.00	0.00	0.01	0.03	0.02	0.01	0.00	0.01	0.00	0.02	0.01	0.00
P_2O_5	0.02	0.04	0.06	0.07	0.02	0.00	0.00	0.07	0.05	0.07	0.00	0.06	0.00	0.02	0.00	0.00
SO_3																
Cl	0.00	0.00	0.00	0.00	0.01	0.00	0.00	0.01	0.00	0.00	0.00	0.02	0.00	0.00	0.00	0.01
F	0.00	0.00	0.00	0.00	0.00	0.00	0.00	0.00	0.00	0.00	0.00	0.00	0.00	0.00	0.00	0.00
Total	99.1	99.5	101.5	99.1	99.9	99.0	99.7	99.9	99.6	98.0	97.1	99.5	99.2	98.1	98.6	99.6

Table 4: Major element compositions of clinopyroxene analyses from lava samples. All analyses carried out by electron microprobe.

Analysis name	B29_ Cpx2	B29_ Cpx6	B29_ Cpx6	B29_ Cpx6	B29_ Cpx6	B29_ Cpx8	B29_ Cpx8	B35_ Cpx2	B35_ Cpx2	B35_ Cpx2	B35_ Cpx7	B35_ Cpx7	B37_ Cpx	B37_ Cpx	B37_ Cpx	B37_ Cpx
SiO_2	48.29	49.11	49.53	49.15	49.51	48.86	50.26	49.26	50.64	50.50	47.80	49.39	48.01	48.50	49.25	48.99
TiO_2	0.81	0.69	0.78	0.86	0.80	0.79	0.69	0.64	0.51	0.70	1.10	0.76	0.95	0.82	0.72	0.79
Al_2O_3	5.07	4.81	5.50	5.92	5.43	5.55	4.82	4.09	3.25	4.47	6.76	5.14	6.07	5.60	5.12	5.48
Cr_2O_3	0.00	0.00	0.01	0.00	0.00	0.05	0.02	0.00	0.00	0.02	0.01	0.02	0.02	0.00	0.01	0.00
FeO	6.92	7.10	7.01	7.26	6.99	7.32	6.92	7.07	7.14	6.89	8.24	7.13	7.29	7.14	6.90	7.13
NiO	0.04	0.00	0.00	0.00	0.00	0.00	0.02	0.00	0.01	0.00	0.03	0.00	0.05	0.00	0.00	0.02
MnO	0.17	0.20	0.16	0.18	0.14	0.17	0.21	0.24	0.31	0.26	0.21	0.22	0.16	0.23	0.18	0.17
MgO	13.84	14.17	14.16	13.83	14.26	13.95	14.44	14.28	14.26	14.32	13.08	14.31	13.06	13.70	13.89	13.82
CaO	22.59	23.06	22.87	22.78	23.03	23.03	22.84	22.10	22.34	22.38	22.26	22.58	22.88	22.80	22.70	22.81
BaO	0.03	0.04	0.00	0.00	0.05	0.05	0.03	0.04	0.02	0.00	0.03	0.00	0.03	0.03	0.00	0.02
Na_2O	0.30	0.29	0.32	0.36	0.36	0.31	0.32	0.36	0.48	0.39	0.33	0.28	0.31	0.31	0.35	0.31
K_2O	0.00	0.01	0.01	0.00	0.01	0.00	0.01	0.00	0.00	0.00	0.01	0.01	0.01	0.01	0.03	0.00
P_2O_5	0.01	0.00	0.00	0.04	0.00	0.00	0.06	0.00	0.00	0.04	0.02	0.05	0.00	0.00	0.03	0.01
SO_3	0.00	0.00	0.00	0.00	0.01	0.00	0.00	0.01	0.00	0.00	0.00	0.01	0.00	0.01	0.01	0.00
Cl	0.01	0.00	0.00	0.02	0.01	0.00	0.00	0.00	0.00	0.00	0.01	0.00	0.01	0.02	0.03	0.01
F	0.00	0.00	0.00	0.03	0.00	0.07	0.00	0.00	0.00	0.06	0.00	0.00	0.02	0.00	0.01	0.03
Total	98.1	99.5	100.4	100.4	100.6	100.1	100.6	98.1	99.0	100.0	99.9	99.9	98.9	99.2	99.2	99.6

Table 4: Major element compositions of clinopyroxene analyses from lava samples. All analyses carried out by electron microprobe.

Analysis name	B37_ Cpx1	B37_ Cpx1	B37_ Cpx1	B37_ Cpx1	B37_ Cpx1	B37_ Cpx1	B37_ Cpx2	B37_ Cpx2	B37_ Cpx2	B37_ Cpx3	B37_ Cpx3	B37_ Cpx3	B37_ Cpx3	B37_ Cpx3	B37_ Cpx4	B37_ Cpx4
SiO_2	49.71	50.41	51.29	50.17	50.51	49.93	49.53	48.75	49.87	49.73	49.57	48.62	49.93	44.12	48.99	49.34
TiO_2	0.89	0.81	0.62	0.81	0.79	0.79	0.61	0.86	0.68	0.59	0.70	0.83	0.58	1.29	0.84	0.88
Al_2O_3	5.03	4.50	3.58	4.54	4.18	5.42	3.87	4.28	2.78	3.59	3.68	4.51	2.95	5.05	4.47	4.31
Cr_2O_3	0.00	0.00	0.00	0.00	0.02	0.03	0.02	0.00	0.00	0.01	0.00	0.00	0.03	0.00	0.02	0.00
FeO	8.05	8.20	7.58	8.67	8.43	6.67	8.89	8.76	8.94	7.94	8.18	8.24	8.03	16.61	8.50	8.90
NiO	0.01	0.00	0.00	0.04	0.00	0.01	0.00	0.03	0.01	0.01	0.00	0.02	0.03	0.01	0.00	0.00
MnO	0.27	0.30	0.27	0.37	0.36	0.21	0.43	0.36	0.33	0.27	0.28	0.27	0.34	0.38	0.31	0.36
MgO	13.99	14.16	15.05	13.96	14.27	14.43	14.45	13.32	13.47	14.17	13.85	13.53	14.38	12.18	13.82	13.55
CaO	21.83	21.68	21.90	21.64	21.59	23.01	19.57	21.32	21.99	21.32	21.27	21.60	21.36	19.29	21.13	21.32
BaO	0.05	0.02	0.03	0.00	0.00	0.00	0.03	0.01	0.01	0.01	0.01	0.01	0.00	0.01	0.03	0.00
Na_2O	0.41	0.44	0.28	0.40	0.42	0.28	0.39	0.40	0.46	0.39	0.48	0.40	0.41	0.41	0.40	0.44
K_2O	0.02	0.00	0.00	0.01	0.00	0.01	0.13	0.02	0.02	0.00	0.01	0.01	0.00	0.02	0.01	0.01
P_2O_5	0.00	0.02	0.04	0.05	0.08	0.02	0.06	0.00	0.79	0.00	0.03	0.04	0.10	0.03	0.02	0.03
SO_3	0.01	0.00	0.00	0.00	0.00	0.00	0.01	0.00	0.00	0.00	0.00	0.00	0.01	0.00	0.00	0.00
Cl	0.03	0.00	0.01	0.01	0.00	0.00	0.05	0.01	0.02	0.01	0.00	0.01	0.00	0.00	0.01	0.00
F	0.05	0.09	0.00	0.00	0.07	0.00	0.00	0.00	0.07	0.09	0.04	0.05	0.00	0.14	0.00	0.14
Total	100.3	100.6	100.7	100.7	100.7	100.8	98.0	98.1	99.4	98.1	98.1	98.1	98.1	99.6	98.5	99.3

Table 4: Major element compositions of clinopyroxene analyses from lava samples. All analyses carried out by electron microprobe.

Analysis name	B37_ Cpx4	SA17 _Cpx 1	SA17 _Cpx 2	SA17 _Cpx 2	SA17 _Cpx 2	SA17 _Cpx 3	SA17 _Cpx 3	SA17 _Cpx 3	SA17 _Cpx 3	SA17 _Cpx 3	SA17 _Cpx 4	SA17 _Cpx 4	SA17 _Cpx 4	SA17 _Cpx 4	SA17 _Cpx 4	SA17 _Cpx 4
SiO_2	50.92	49.86	50.50	51.11	50.89	49.60	49.92	50.44	50.28	50.33	50.33	50.48	50.83	50.58	50.15	50.78
TiO_2	0.59	0.54	0.65	0.53	0.61	0.62	0.59	0.51	0.54	0.53	0.50	0.48	0.44	0.52	0.59	0.56
Al_2O_3	3.16	3.08	3.96	3.46	3.77	3.77	3.54	3.15	3.51	3.39	3.29	3.11	3.00	3.35	3.84	3.42
Cr_2O_3	0.00	0.04	0.00	0.02	0.00	0.02	0.01	0.00	0.00	0.01	0.00	0.00	0.00	0.00	0.00	0.00
FeO	7.99	7.07	6.97	6.67	6.81	6.96	7.09	6.79	6.90	6.93	6.74	6.89	7.36	6.78	7.46	7.03
NiO	0.05	0.00	0.00	0.03	0.00	0.00	0.01	0.00	0.00	0.02	0.00	0.03	0.00	0.03	0.00	0.00
MnO	0.37	0.35	0.34	0.32	0.34	0.33	0.35	0.34	0.34	0.32	0.30	0.33	0.39	0.36	0.31	0.33
MgO	14.64	14.48	14.44	14.94	14.66	14.31	14.37	14.64	14.32	14.40	14.60	14.59	14.31	14.64	14.07	14.63
CaO	21.33	22.20	22.46	22.40	22.42	22.15	22.11	22.15	22.12	22.23	22.13	22.37	22.18	22.46	22.34	22.23
BaO	0.01	0.00	0.02	0.01	0.02	0.00	0.02	0.05	0.00	0.00	0.01	0.00	0.00	0.00	0.03	0.00
Na_2O	0.41	0.42	0.37	0.40	0.37	0.42	0.40	0.37	0.36	0.38	0.45	0.41	0.47	0.39	0.43	0.42
K_2O	0.00	0.01	0.01	0.00	0.01	0.00	0.01	0.00	0.01	0.00	0.00	0.00	0.00	0.01	0.01	0.01
P_2O_5	0.05	0.04	0.06	0.00	0.04	0.00	0.00	0.00	0.01	0.00	0.00	0.02	0.00	0.00	0.01	0.00
SO_3	0.01	0.00	0.00	0.00	0.00	0.00	0.00	0.00	0.01	0.00	0.02	0.00	0.00	0.00	0.00	0.00
Cl	0.00	0.00	0.01	0.00	0.01	0.00	0.00	0.00	0.00	0.01	0.00	0.01	0.00	0.00	0.01	0.00
F	0.00	0.00	0.03	0.00	0.00	0.08	0.00	0.00	0.09	0.00	0.00	0.03	0.00	0.00	0.03	0.00
Total	99.5	98.1	99.8	99.9	99.9	98.3	98.4	98.5	98.5	98.5	98.4	98.7	99.0	99.1	99.3	99.4

Table 4: Major element compositions of clinopyroxene analyses from lava samples. All analyses carried out by electron microprobe.

Analysis name	SA17_Cpx4	SA17_Cpx4	SA17_Cpx4	SA17_Cpx5	SA17_Cpx5	SA17_Cpx5	SA17_Cpx5	SA17_Hbl1	SA17_Hbl1	SA17_Hbl1	SA17_Hbl1	SA18_Cpx10	SA18_Cpx2	SA18_Cpx3	SA18_Cpx4	SA18_Cpx5
SiO_2	50.72	50.28	50.83	50.36	50.36	50.82	50.14	50.76	50.78	50.02	50.87	50.97	48.56	47.17	46.51	46.91
TiO_2	0.58	0.65	0.50	0.57	0.58	0.50	0.63	0.55	0.54	0.70	0.53	0.56	0.81	1.08	1.18	1.19
Al_2O_3	3.45	3.98	3.22	3.58	3.63	3.24	3.93	3.46	3.36	4.13	3.39	2.87	4.96	6.56	6.77	6.97
Cr_2O_3	0.01	0.01	0.04	0.04	0.00	0.00	0.01	0.00	0.00	0.01	0.01	0.00	0.00	0.00	0.01	0.00
FeO	6.73	7.11	7.39	7.19	6.96	6.98	7.18	7.02	7.02	7.26	7.04	6.54	6.72	7.14	7.01	7.07
NiO	0.00	0.05	0.00	0.00	0.03	0.00	0.00	0.00	0.01	0.00	0.00	0.00	0.01	0.00	0.00	0.11
MnO	0.31	0.32	0.37	0.33	0.36	0.32	0.32	0.34	0.37	0.36	0.33	0.26	0.19	0.13	0.13	0.12
MgO	14.76	14.41	14.17	14.39	14.57	14.71	14.41	14.47	14.41	14.15	14.66	15.23	14.20	13.39	13.46	13.12
CaO	22.38	22.27	22.40	22.31	22.30	22.45	22.37	22.44	22.35	22.43	22.37	22.17	22.62	23.06	22.70	22.87
BaO	0.04	0.01	0.01	0.02	0.00	0.00	0.00	0.00	0.04	0.00	0.00	0.00	0.00	0.02	0.07	0.00
Na_2O	0.41	0.43	0.49	0.36	0.41	0.38	0.39	0.39	0.47	0.41	0.39	0.55	0.28	0.31	0.24	0.31
K_2O	0.00	0.00	0.00	0.00	0.00	0.00	0.01	0.00	0.00	0.00	0.00	0.13	0.01	0.02	0.00	0.01
P_2O_5	0.11	0.00	0.12	0.00	0.06	0.00	0.00	0.00	0.08	0.04	0.00	0.00	0.06	0.03	0.03	0.00
SO_3	0.00	0.00	0.00	0.01	0.00	0.00	0.00	0.00	0.00	0.00	0.00					
Cl	0.01	0.00	0.01	0.00	0.00	0.00	0.01	0.00	0.00	0.00	0.00	0.12	0.01	0.02	0.02	0.03
F	0.02	0.00	0.00	0.04	0.01	0.00	0.07	0.00	0.00	0.06	0.00	0.00	0.00	0.00	0.00	0.00
Total	99.5	99.5	99.5	99.2	99.3	99.4	99.5	99.4	99.4	99.6	99.6	99.4	98.4	98.9	98.1	98.7

Table 4: Major element compositions of clinopyroxene analyses from lava samples. All analyses carried out by electron microprobe.

Analysis name	SA18_Cpx6	SA18_Cpx7	SA18_Cpx8	SA18_Cpx9	SA18_Hbl11	SA18_hbl12	SA18_Hbl12	SA18_hbl12	SA18_Hbl14	SA18_Hbl15	SA18_Hbl16	SA18_Hbl18	SA18_Hbl2	SA18_Hbl3	SA18_Hbl5	SA18_Hbl7
SiO_2	49.24	47.78	47.30	49.07	49.40	47.30	48.60	47.92	47.64	48.73	50.15	48.30	47.33	48.42	46.77	47.94
TiO_2	0.74	0.84	0.99	0.81	0.92	0.98	0.93	0.95	1.14	0.81	0.64	0.80	1.13	0.85	0.89	0.98
Al_2O_3	4.87	4.69	5.92	4.53	4.44	6.40	5.12	6.04	6.24	4.77	3.28	5.20	6.92	5.23	5.85	5.65
Cr_2O_3	0.01	0.00	0.00	0.03	0.03	0.01	0.00	0.00	0.01	0.00	0.00	0.04	0.00	0.00	0.02	0.01
FeO	6.80	6.77	7.37	7.05	7.08	6.92	6.68	6.41	7.61	6.63	6.41	6.41	7.29	7.10	6.50	6.97
NiO	0.00	0.00	0.00	0.00	0.04	0.02	0.00	0.00	0.00	0.00	0.00	0.05	0.00	0.00	0.00	0.03
MnO	0.20	0.27	0.26	0.24	0.28	0.14	0.17	0.13	0.22	0.26	0.24	0.13	0.23	0.26	0.13	0.23
MgO	14.32	14.24	13.66	14.55	14.16	13.85	14.15	14.16	13.45	14.39	15.10	14.47	13.39	13.90	14.04	13.92
CaO	22.87	22.65	22.49	22.46	21.70	22.85	22.64	23.44	22.71	22.49	22.41	23.13	23.22	22.76	22.13	22.73
BaO	0.00	0.04	0.01	0.04	0.00	0.05	0.02	0.05	0.00	0.01	0.04	0.00	0.07	0.06	0.04	0.02
Na_2O	0.31	0.34	0.29	0.42	0.38	0.20	0.43	0.30	0.36	0.31	0.30	0.27	0.28	0.33	0.23	0.29
K_2O	0.01	0.01	0.00	0.03	0.00	0.03	0.09	0.00	0.02	0.00	0.00	0.01	0.01	0.01	0.02	0.01
P_2O_5	0.05	0.01	0.00	0.02	0.02	0.02	0.00	0.00	0.00	0.04	0.01	0.00	0.01	0.03	0.00	0.01
SO_3																
Cl	0.03	0.01	0.00	0.00	0.00	0.01	0.04	0.00	0.00	0.00	0.00	0.01	0.00	0.00	0.03	0.01
F	0.00	0.00	0.00	0.00	0.00	0.00	0.00	0.00	0.00	0.00	0.00	0.00	0.00	0.00	0.00	0.00
Total	99.5	97.7	98.3	99.3	98.5	98.8	98.9	99.4	99.4	98.4	98.6	98.8	99.9	99.0	96.7	98.8

Table 4: Major element compositions of clinopyroxene analyses from lava samples. All analyses carried out by electron microprobe.

Analysis name	SA18_Hbl8	SA8_Cpx1-3	SA8_Cpx1-4	SA8_Cpx2-3
SiO_2	49.44	48.29	49.76	50.71
TiO_2	0.83	0.86	0.59	0.50
Al_2O_3	4.41	5.18	3.38	3.70
Cr_2O_3	0.01	0.00	0.01	0.00
FeO	6.71	7.53	7.70	6.83
NiO	0.00	0.00	0.05	0.00
MnO	0.21	0.24	0.42	0.23
MgO	14.58	13.53	13.45	14.72
CaO	22.73	22.30	22.54	22.33
BaO	0.00	0.01	0.00	0.03
Na_2O	0.38	0.41	0.57	0.27
K_2O	0.00	0.01	0.00	0.00
P_2O_5	0.01	0.06	0.00	0.00
SO_3				
Cl	0.01	0.03	0.00	0.02
F	0.00	0.00	0.00	0.00
Total	99.3	98.5	98.5	99.3

Table 4: Major element compositions of clinopyroxene analyses from lava samples. All analyses carried out by electron microprobe.

Appendix 1

	B10_Hbl1-1	B10_Hbl1-2	B10_Hbl1-3	B10_Hbl1-4	B10_Hbl1-5	B10_Hbl2-1	B10_Hbl2-1	B10_Hbl2-1	B10_Hbl2-1	B10_Hbl2-1	B1B_Hbl18	B1B_Hbl19	B1B_Hbl21
Lithology	Gabbro	Gabbro	Gabbro	Gabbro	Gabbro	Gabbro	Gabbro	Gabbro	Gabbro	Gabbro	Gabbro	Gabbro	Gabbro
SiO_2	40.61	39.66	40.95	40.12	40.61	40.37	40.60	39.97	40.44	40.45	40.07	39.81	39.84
TiO_2	2.32	2.36	2.29	2.33	2.35	2.32	2.37	2.34	2.43	2.39	2.49	2.60	2.54
Al_2O_3	13.73	13.78	13.95	13.20	13.69	13.42	13.62	13.57	13.66	13.74	13.03	13.69	12.98
Cr_2O_3	0.00	-0.01	-0.01	0.01	0.01	0.02	0.01	0.00	0.02	-0.01	0.00	0.00	0.01
FeO	11.53	11.39	11.91	11.39	11.40	11.64	11.61	11.63	11.46	11.55	11.18	11.06	11.21
MnO	0.17	0.17	0.16	0.18	0.17	0.16	0.16	0.18	0.18	0.15	0.15	0.24	0.15
MgO	14.11	14.01	14.31	13.54	13.81	14.06	14.04	13.75	14.01	13.78	14.20	13.70	13.81
CaO	12.18	12.08	12.18	11.97	12.39	12.16	12.26	12.12	12.23	12.15	11.76	11.97	11.29
Na_2O	1.94	2.00	2.05	1.94	1.97	2.00	2.02	1.99	2.05	1.94	2.22	2.09	2.26
K_2O	1.73	1.68	1.68	1.64	1.69	1.73	1.71	1.72	1.73	1.74	1.52	1.67	1.49
F											0.1418	0.0663	0.0697
Cl	0.1135	0.1128	0.1437	0.126	0.1276	0.1732	0.1536	0.1692	0.1667	0.1491	0.0733	0.0431	0.0804
Total	98.4	97.2	99.6	96.4	98.2	98.1	98.6	97.4	98.4	98.0	96.8	96.9	95.7
Species	Mg-Hst	Mg-Hst	Mg-Hst	Mg-Hst	Mg-Hst	Mg-Hst	Mg-Hst	Mg-Hst	Mg-Hst	Mg-Hst	Mg-Hst	Mg-Hst	Mg-Hst
T (°C)	1023	1034	1023	1014	1024	1021	1023	1026	1027	1023	1017	1031	1010
error (σest)	22	22	22	22	22	22	22	22	22	22	22	22	22
P (MPa)	567	600	573	537	574	537	555	572	565	582	502	599	511
error (Max error)	62	66	63	59	63	59	61	63	62	64	55	66	56
ΔNNO	0.79	0.78	0.84	0.65	0.62	0.79	0.72	0.69	0.69	0.66	0.83	0.58	0.76
error (σest)	0.4	0.4	0.4	0.4	0.4	0.4	0.4	0.4	0.4	0.4	0.4	0.4	0.4
H_2Omelt (wt.%)	4.37	4.33	4.40	4.52	4.61	4.03	4.26	4.28	4.20	4.50	3.95	4.44	4.16
error*	0.65	0.65	0.66	0.68	0.69	0.60	0.64	0.64	0.63	0.68	0.59	0.67	0.62

Table 5: Major element compositions of amphibole electron microprobe analyses. Element compositions reported as wt.%. P-T-H_2O-fO_2 estimates calculated using formulations of Ridolfi et al. (2012).

Appendix 1

	B1B_Hbl24	B1B_Hbl25	B24_Hbl3-1	B24_Hbl3-1	B24_Hbl3-1	B24_Hbl3-1	B27	B27	B27	B27	B27	B27	B27
Lithology	Gabbro	Gabbro	Gabbro	Gabbro	Gabbro	Gabbro	Gabbro	Gabbro	Gabbro	Gabbro	Gabbro	Gabbro	Gabbro
SiO_2	38.22	40.33	38.15	38.47	39.27	39.71	38.95	38.63	39.79	39.17	39.02	39.39	40.35
TiO_2	2.54	2.59	2.22	2.22	2.38	2.13	2.43	2.39	2.53	2.45	2.35	2.37	2.56
Al_2O_3	14.41	13.34	15.11	14.78	14.54	15.20	14.21	13.90	14.07	14.05	14.54	14.02	14.12
Cr_2O_3	0.01	0.00	0.00	0.01	0.00	0.00	0.00	0.00	0.01	0.04	0.00	0.00	0.00
FeO	11.20	10.75	11.16	11.24	11.08	11.28	11.10	11.12	10.20	10.50	10.29	11.14	10.41
MnO	0.18	0.16	0.18	0.17	0.17	0.18	0.19	0.21	0.12	0.15	0.12	0.18	0.18
MgO	13.47	14.03	13.07	13.13	13.30	13.35	13.77	13.64	14.45	14.13	14.27	13.66	14.42
CaO	11.92	11.86	12.29	12.41	12.19	12.41	12.24	12.02	11.92	12.27	12.39	12.00	11.96
Na_2O	2.23	2.13	1.98	2.01	2.12	2.03	2.10	2.29	2.87	2.26	2.22	2.16	2.80
K_2O	1.57	1.52	1.76	1.78	1.79	1.82	1.59	1.61	1.11	1.61	1.51	1.66	1.24
F	0.1137	0.1216					0.09	0.03	0.08	0.08	0.26	0.07	0.14
Cl	0.0553	0.0401	0.0572	0.0718	0.0476	0.0768	0.04	0.07	0.08	0.06	0.05	0.07	0.13
Total	95.9	96.9	96.0	96.3	96.9	98.2	96.7	95.9	97.2	96.8	97.0	96.7	98.3
Species	Mg-Hst	Mg-Hst	Mg-Hst	Mg-Hst	Mg-Hst	Mg-Hst	Mg-Hst	Mg-Hst	Mg-Hst	Mg-Hst	Mg-Hst	Mg-Hst	Mg-Hst
T (°C)	1061	1019	1071	1065	1051	1055	1052	1051	1047	1054	1064	1040	1041
error (σest)	22	22	22	22	22	22	22	22	22	22	22	22	22
P (MPa)	746	541	898	822	749	838	690	660	638	657	732	655	627
error (Max error)	82	59	99	90	82	92	76	73	70	72	81	72	69
ΔNNO	0.54	0.70	0.43	0.43	0.42	0.45	0.63	0.61	0.67	0.68	0.73	0.61	0.64
error (σest)	0.4	0.4	0.4	0.4	0.4	0.4	0.4	0.4	0.4	0.4	0.4	0.4	0.4
H_2Omelt (wt.%)	4.83	4.50	5.48	5.17	4.93	5.50	4.79	4.35	5.05	4.39	4.98	4.61	4.92
error*	0.72	0.67	0.82	0.78	0.74	0.82	0.72	0.65	0.76	0.66	0.75	0.69	0.74

Table 5: Major element compositions of amphibole electron microprobe analyses. Element compositions reported as wt.%. P-T-H_2O-fO_2 estimates calculated using formulations of Ridolfi et al. (2012).

Appendix 1

	B7	B7	B7_Hbl 10	B7_Hbl 11	B7_Hbl 12	B7_Hbl 1-2	B7_Hbl 13	B7_Hbl 1-3	B7_Hbl 1-5	B7_Hbl 2	B7_Hbl 4	B7_Hbl 5	B7_Hbl 6
Lithology	Gabbro	Gabbro	Gabbro	Gabbro	Gabbro	Gabbro	Gabbro	Gabbro	Gabbro	Gabbro	Gabbro	Gabbro	Gabbro
SiO_2	38.85	39.28	39.89	39.56	39.24	39.19	39.79	38.91	38.94	40.49	39.98	40.22	40.18
TiO_2	2.37	2.43	2.54	2.37	2.48	2.65	2.38	2.72	2.38	2.56	2.48	2.66	2.62
Al_2O_3	13.69	13.37	13.43	13.86	13.96	13.43	14.10	13.56	14.06	12.99	13.07	13.27	12.86
Cr_2O_3			0.00	0.02	0.01	0.02	0.00	0.04	0.00	0.00	0.03	0.02	0.00
FeO	11.34	11.31	10.34	10.59	10.64	12.33	10.71	12.82	12.03	11.49	11.32	10.80	10.91
MnO			0.13	0.11	0.12	0.26	0.08	0.32	0.29	0.15	0.17	0.22	0.22
MgO	13.35	13.45	14.26	14.47	13.89	12.73	14.10	12.59	12.75	13.65	13.70	14.09	13.81
CaO	12.16	12.37	11.89	11.84	11.67	11.66	11.90	11.51	11.72	11.76	11.79	11.81	11.63
Na_2O	2.15	2.22	2.00	2.12	2.10	2.21	2.04	2.16	2.12	2.22	2.22	2.27	2.29
K_2O	1.47	1.69	1.43	1.48	1.47	1.60	1.44	1.62	1.53	1.45	1.54	1.61	1.51
F			0.0004	0.0322	0.0078	0.1238	0.0472	0.1036	0.1512	0.092	0.1094	0.1204	0.1526
Cl	0.8	0.8	0.0432	0.0238	0.0284	0.0798	0.0021	0.0918	0.0459	0.0519	0.0901	0.0821	0.0653
Total	96.2	96.9	96.0	96.5	95.6	96.3	96.6	96.4	96.0	96.9	96.5	97.2	96.2
Species	Mg-Hst	Mg-Hst	Mg-Hst	Mg-Hst	Mg-Hst	Mg-Hst	Mg-Hst	Mg-Hst	Mg-Hst	Mg-Hst	Mg-Hst	Mg-Hst	Mg-Hst
T (°C)	1041	1038	1025	1037	1036	1023	1035	1025	1034	1007	1016	1022	1011
error (σest)	22	22	22	22	22	22	22	22	22	22	22	22	22
P (MPa)	637	582	563	612	651	590	649	604	687	500	521	532	495
error (Max error)	70	64	62	67	72	65	71	66	76	55	57	59	54
ΔNNO	0.52	0.47	0.83	0.94	0.74	0.32	0.79	0.33	0.39	0.60	0.65	0.68	0.64
error (σest)	0.4	0.4	0.4	0.4	0.4	0.4	0.4	0.4	0.4	0.4	0.4	0.4	0.4
H_2Omelt (wt.%)	4.92	4.06	4.77	4.60	5.00	4.53	5.22	4.53	5.33	4.49	4.23	3.97	4.10
error*	0.74	0.61	0.71	0.69	0.75	0.68	0.78	0.68	0.80	0.67	0.63	0.60	0.62

Table 5: Major element compositions of amphibole electron microprobe analyses. Element compositions reported as wt.%. P-T-H_2O-fO_2 estimates calculated using formulations of Ridolfi et al. (2012).

Appendix 1

	B7_Hbl 7	B7_Hbl 8	B8_Hbl 1-5	B8_Hbl 1-4	B8_Hbl 1-3	B8_Hbl 1-2	B8_Hbl 1-1	B8_Hbl 1-0	B8_Hbl 1-1	B8_Hbl 1-3	B8_Hbl 1-4	B8_Hbl 1-7	B8_Hbl 2-1
Lithology	Gabbro	Gabbro	Gabbro	Gabbro	Gabbro	Gabbro	Gabbro	Gabbro	Gabbro	Gabbro	Gabbro	Gabbro	Gabbro
SiO_2	40.25	40.21	38.51	38.48	38.53	38.60	39.01	39.00	39.45	39.26	39.44	39.26	39.08
TiO_2	2.75	2.64	2.04	2.03	2.03	2.18	2.08	2.13	2.18	2.12	2.03	2.14	2.18
Al_2O_3	12.84	13.05	14.59	15.16	14.78	14.46	14.40	14.54	14.47	14.62	14.67	14.81	14.51
Cr_2O_3	0.00	0.08	0.01	-0.02	0.02	0.01	-0.01	0.02	-0.01	0.00	0.01	0.00	0.01
FeO	10.78	11.00	12.04	11.83	11.99	12.05	11.73	11.89	11.86	12.18	11.93	12.03	12.26
MnO	0.22	0.23	0.16	0.17	0.18	0.18	0.16	0.19	0.18	0.19	0.16	0.19	0.20
MgO	14.11	14.14	13.01	12.89	12.75	12.74	12.95	12.81	12.89	13.00	12.95	13.18	12.81
CaO	11.70	11.70	12.46	12.52	12.50	12.52	12.48	12.48	12.41	12.49	12.52	12.42	12.36
Na_2O	2.30	2.31	1.97	1.85	1.86	1.86	1.97	1.91	1.87	1.93	1.94	1.96	1.80
K_2O	1.37	1.37	1.68	1.75	1.77	1.82	1.70	1.79	1.81	1.81	1.78	1.70	1.86
F	0.1051	0.077											
Cl	0.0585	0.0552	0.0419	0.0351	0.0369	0.0455	0.0341	0.0276	0.024	0.033	0.0621	0.046	0.0398
Total	96.5	96.9	96.5	96.7	96.5	96.5	96.5	96.8	97.1	97.6	97.5	97.7	97.1
Species	Mg-Hst	Mg-Hst	Mg-Hst	Mg-Hst	Mg-Hst	Mg-Hst	Mg-Hst	Mg-Hst	Mg-Hst	Mg-Hst	Mg-Hst	Mg-Hst	Mg-Hst
T (°C)	1013	1016	1058	1066	1058	1055	1049	1050	1043	1049	1047	1052	1046
error (σest)	22	22	22	22	22	22	22	22	22	22	22	22	22
P (MPa)	484	502	778	890	823	764	744	765	737	753	767	777	746
error (Max error)	53	55	86	98	90	84	82	84	81	83	84	85	82
ΔNNO	0.71	0.75	0.48	0.42	0.39	0.35	0.41	0.36	0.38	0.42	0.40	0.48	0.41
error (σest)	0.4	0.4	0.4	0.4	0.4	0.4	0.4	0.4	0.4	0.4	0.4	0.4	0.4
H_2Omelt (wt.%)	4.21	4.32	5.30	5.76	5.53	5.13	5.35	5.30	5.30	5.16	5.42	5.44	5.14
error*	0.63	0.65	0.79	0.86	0.83	0.77	0.80	0.79	0.79	0.77	0.81	0.82	0.77

Table 5: Major element compositions of amphibole electron microprobe analyses. Element compositions reported as wt.%. P-T-H_2O-fO_2 estimates calculated using formulations of Ridolfi et al. (2012).

Appendix 1

	B8_Hbl 2-2	B8_Hbl 2-6	B8_Hbl 3	B8_Hbl 3	B8_Hbl 3	B8_Hbl 3	B8_Hbl 3	B8_Hbl 3	B8_Hbl 4	B8_Hbl 4	B8_Hbl 4	B8_Hbl 4	B8_Hbl 4
Lithology	Gabbro	Gabbro	Gabbro	Gabbro	Gabbro	Gabbro	Gabbro	Gabbro	Gabbro	Gabbro	Gabbro	Gabbro	Gabbro
SiO_2	39.14	40.18	38.71	38.76	38.95	39.08	39.25	39.17	39.38	38.77	38.29	39.22	39.62
TiO_2	2.03	2.12	2.17	1.97	2.09	2.08	1.98	2.05	2.10	2.07	2.01	2.13	2.04
Al_2O_3	14.96	15.11	14.49	14.97	14.50	14.33	14.63	14.64	14.58	15.02	15.19	14.58	14.68
Cr_2O_3	0.00	-0.03	-0.01	0.02	0.00	-0.02	0.00	0.02	0.00	0.00	-0.01	-0.01	0.01
FeO	12.04	12.53	12.03	12.18	12.13	12.08	12.16	12.22	12.32	12.09	12.26	12.00	11.91
MnO	0.18	0.18	0.20	0.16	0.19	0.19	0.18	0.19	0.19	0.19	0.17	0.19	0.18
MgO	12.87	12.92	12.86	12.80	12.79	12.86	12.78	12.68	12.95	12.86	12.70	12.93	13.06
CaO	12.31	12.50	12.33	12.42	12.32	12.44	12.40	12.48	12.35	12.36	12.57	12.34	12.50
Na_2O	1.91	1.88	1.92	1.93	1.91	1.91	1.95	1.94	1.88	1.94	1.97	1.90	1.88
K_2O	1.72	1.80	1.77	1.74	1.73	1.76	1.78	1.83	1.81	1.76	1.72	1.79	1.73
F													
Cl	0.0251	0.0345	0.0379	0.0433	0.0376	0.0297	0.0322	0.0382	0.0443	0.0426	0.0354	0.0294	0.0401
Total	97.2	99.2	96.5	97.0	96.7	96.7	97.1	97.3	97.6	97.1	96.9	97.1	97.6
Species	Mg-Hst	Mg-Hst	Mg-Hst	Mg-Hst	Mg-Hst	Mg-Hst	Mg-Hst	Mg-Hst	Mg-Hst	Mg-Hst	Mg-Hst	Mg-Hst	Mg-Hst
T (°C)	1051	1042	1051	1057	1047	1045	1046	1048	1044	1058	1069	1046	1044
error (σest)	22	22	22	22	22	22	22	22	22	22	22	22	22
P (MPa)	823	794	759	840	755	725	769	773	742	844	899	756	756
error (Max error)	91	87	84	92	83	80	85	85	82	93	99	83	83
ΔNNO	0.42	0.36	0.41	0.41	0.40	0.41	0.39	0.32	0.45	0.41	0.35	0.43	0.45
error (σest)	0.4	0.4	0.4	0.4	0.4	0.4	0.4	0.4	0.4	0.4	0.4	0.4	0.4
H_2Omelt (wt.%)	5.76	5.75	5.17	5.65	5.38	5.19	5.43	5.34	5.21	5.56	5.77	5.28	5.58
error*	0.86	0.86	0.78	0.85	0.81	0.78	0.81	0.80	0.78	0.83	0.87	0.79	0.84

Table 5: Major element compositions of amphibole electron microprobe analyses. Element compositions reported as wt.%. P-T-H_2O-fO_2 estimates calculated using formulations of Ridolfi et al. (2012).

	B8_Hbl 4	B8_Hbl 4	B8_Hbl 4	BC14/03 9_Hbl1	BC14/03 9_Hbl1	BC14/04 3_Hbl1	BC14/04 8_Hbl1	BC14/04 8_Hbl1	BC14/04 8_Hbl1	BC14/04 8_Hbl1	BC14/04 8_Hbl1	BC14/04 8_Hbl1	BC14/04 8_Hbl1
Lithology	Gabbro	Gabbro	Gabbro	Gabbro	Gabbro	Gabbro	Gabbro	Gabbro	Gabbro	Gabbro	Gabbro	Gabbro	Gabbro
SiO_2	38.66	39.96	39.63	40.38	39.73	41.32	39.14	38.67	38.79	39.07	39.29	38.93	38.96
TiO_2	2.07	1.98	2.02	2.39	2.85	2.17	2.33	2.37	2.36	2.31	2.29	2.28	2.33
Al_2O_3	14.83	14.64	14.84	11.64	12.88	11.29	13.98	14.17	14.08	14.14	14.47	14.21	14.13
Cr_2O_3	0.02	0.00	-0.01	0.04	0.00	0.00	0.00	0.00	0.03	0.03	0.00	0.00	0.00
FeO	11.97	11.79	11.84	12.02	11.23	11.45	10.41	10.41	10.45	10.56	10.45	10.46	10.51
MnO	0.15	0.18	0.16	0.26	0.19	0.20	0.17	0.17	0.15	0.11	0.13	0.15	0.18
MgO	12.77	13.15	13.04	14.20	14.54	13.83	14.66	14.56	14.55	14.63	14.83	14.62	14.60
CaO	12.53	12.45	12.49	11.30	11.35	12.36	12.31	12.29	12.34	12.41	12.31	12.34	12.36
Na_2O	1.96	1.93	1.97	2.41	2.33	2.27	2.17	2.17	2.21	2.20	2.31	2.22	2.24
K_2O	1.74	1.70	1.75	1.17	1.15	1.39	1.36	1.45	1.38	1.40	1.39	1.39	1.38
F				0.246	0.307	0.284	0.257	0.451	0.221	0.159	0.183	0.215	0.230
Cl	0.039	0.040	0.044	0.061	0.046	0.131	0.052	0.051	0.044	0.040	0.039	0.049	0.035
Total	96.7	97.8	97.8	96.1	96.6	96.7	96.8	96.8	96.6	97.1	97.7	96.9	97.0
Species	Mg-Hst	Mg-Hst	Mg-Hst	Mg-Hst	Mg-Hst	Mg-Hst	Mg-Hst	Mg-Hst	Mg-Hst	Mg-Hst	Mg-Hst	Mg-Hst	Mg-Hst
T (°C)	1059	1039	1047	984	1017	980	1053	1062	1060	1058	1061	1060	1059
error (σest)	22	22	22	22	22	22	22	22	22	22	22	22	22
P (MPa)	825	741	785	362	478	339	634	677	660	656	690	672	658
error (Max error)	91	82	86	40	53	37	70	74	73	72	76	74	72
ΔNNO	0.34	0.48	0.42	0.99	0.95	0.68	0.94	0.91	0.89	0.91	0.95	0.92	0.90
error (σest)	0.4	0.4	0.4	0.4	0.4	0.4	0.4	0.4	0.4	0.4	0.4	0.4	0.4
H_2Omelt (wt.%)	5.54	5.65	5.61	3.61	4.22	3.59	4.75	4.62	4.71	4.71	4.82	4.78	4.71
error*	0.83	0.85	0.84	0.54	0.63	0.54	0.71	0.69	0.71	0.71	0.72	0.72	0.71

Table 5: Major element compositions of amphibole electron microprobe analyses. Element compositions reported as wt.%. P-T-H_2O-fO_2 estimates calculated using formulations of Ridolfi et al. (2012).

	BC14/048_Hbl1	BC14/048_Hbl1	BC14/048_Hbl1	BC14/048_Hbl1	BC14/048_Hbl1	BC14/048_Hbl1	BC14/048_Hbl1	BC14/048_Hbl1	BC14/048_Hbl1	BC14/048_Hbl1	BC14/048_Hbl1	BC14/048_Hbl1	BC14/048_Hbl1
Lithology	Gabbro	Gabbro	Gabbro	Gabbro	Gabbro	Gabbro	Gabbro	Gabbro	Gabbro	Gabbro	Gabbro	Gabbro	Gabbro
SiO_2	39.11	38.95	38.91	39.11	38.92	38.99	38.85	39.03	39.06	38.56	39.04	39.11	39.16
TiO_2	2.34	2.38	2.28	2.31	2.39	2.34	2.33	2.36	2.33	2.37	2.39	2.35	2.35
Al_2O_3	14.02	14.10	14.09	14.08	14.22	14.07	14.43	14.16	14.27	14.74	14.13	14.14	14.20
Cr_2O_3	0.00	0.01	0.02	0.01	0.00	0.00	0.00	0.00	0.02	0.00	0.00	0.00	0.00
FeO	10.42	10.55	10.41	10.44	10.60	10.44	10.55	10.47	10.46	10.51	10.51	10.45	10.41
MnO	0.12	0.12	0.13	0.13	0.14	0.07	0.13	0.13	0.12	0.10	0.15	0.15	0.15
MgO	14.68	14.48	14.61	14.62	14.46	14.54	14.46	14.46	14.55	14.32	14.41	14.51	14.52
CaO	12.37	12.31	12.36	12.31	12.31	12.31	12.29	12.29	12.27	12.27	12.34	12.28	12.33
Na_2O	2.20	2.14	2.20	2.21	2.19	2.18	2.24	2.09	2.23	2.16	2.14	2.28	2.25
K_2O	1.36	1.43	1.38	1.39	1.40	1.39	1.38	1.43	1.44	1.41	1.42	1.39	1.36
F	0.085	0.186	0.157	0.260	0.205	0.204	0.283	0.201	0.126	0.137	0.171	0.453	0.220
Cl	0.045	0.039	0.036	0.050	0.037	0.044	0.036	0.031	0.038	0.061	0.042	0.034	0.045
Total	96.7	96.7	96.6	96.9	96.9	96.6	97.0	96.7	96.9	96.6	96.8	97.1	97.0
Species	Mg-Hst	Mg-Hst	Mg-Hst	Mg-Hst	Mg-Hst	Mg-Hst	Mg-Hst	Mg-Hst	Mg-Hst	Mg-Hst	Mg-Hst	Mg-Hst	Mg-Hst
T (°C)	1056	1056	1058	1055	1059	1056	1062	1055	1058	1069	1056	1056	1057
error (σest)	22	22	22	22	22	22	22	22	22	22	22	22	22
P (MPa)	640	658	659	651	675	656	709	667	678	770	665	661	668
error (Max error)	70	72	72	72	74	72	78	73	75	85	73	73	74
ΔNNO	0.93	0.87	0.92	0.91	0.85	0.89	0.85	0.88	0.88	0.81	0.83	0.85	0.85
error (σest)	0.4	0.4	0.4	0.4	0.4	0.4	0.4	0.4	0.4	0.4	0.4	0.4	0.4
H_2Omelt (wt.%)	4.72	4.72	4.74	4.72	4.81	4.77	5.00	4.87	4.75	5.23	4.85	4.78	4.91
error*	0.71	0.71	0.71	0.71	0.72	0.72	0.75	0.73	0.71	0.78	0.73	0.72	0.74

Table 5: Major element compositions of amphibole electron microprobe analyses. Element compositions reported as wt.%. P-T-H_2O-fO_2 estimates calculated using formulations of Ridolfi et al. (2012).

	BC14/048_Hbl2	BC14/048_Hbl2	BC14/048_Hbl2	BC14/048_Hbl2	BC14/048_Hbl2	BC14/048_Hbl2	BC14/048_Hbl2	BC14/048_Hbl2	BC14/048_Hbl2	BC14/048_Hbl2	BC14/048_Hbl3	BC14/048_Hbl3	BC14/048_Hbl3
Lithology	Gabbro	Gabbro	Gabbro	Gabbro	Gabbro	Gabbro	Gabbro	Gabbro	Gabbro	Gabbro	Gabbro	Gabbro	Gabbro
SiO_2	38.96	39.16	38.92	39.09	39.11	39.33	39.23	39.29	39.21	39.28	39.22	39.32	39.48
TiO_2	2.35	2.37	2.42	2.37	2.37	2.34	2.37	2.36	2.37	2.36	2.42	2.42	2.42
Al_2O_3	13.85	13.64	13.91	13.89	13.70	13.72	13.86	13.66	13.75	13.57	13.69	13.81	14.06
Cr_2O_3	0.00	0.00	0.00	0.00	0.00	0.02	0.01	0.03	0.05	0.04	0.03	0.00	0.00
FeO	10.98	11.10	11.24	11.24	10.99	10.93	10.92	10.99	10.88	11.07	11.07	10.96	11.27
MnO	0.17	0.15	0.12	0.17	0.18	0.20	0.18	0.15	0.15	0.19	0.17	0.19	0.16
MgO	14.33	14.15	14.07	14.10	14.17	14.27	14.23	14.15	14.18	14.09	14.32	14.42	14.30
CaO	12.14	12.11	12.15	12.17	12.15	12.13	12.14	12.09	12.12	12.20	12.09	12.07	12.12
Na_2O	2.12	2.22	2.29	2.19	2.20	2.22	2.22	2.21	2.21	2.13	2.22	2.21	2.28
K_2O	1.42	1.39	1.43	1.44	1.44	1.46	1.41	1.44	1.43	1.46	1.42	1.49	1.44
F	0.284	0.243	0.149	0.167	0.305	0.312	0.224	0.306	0.300	0.255	0.224	0.315	0.270
Cl	0.042	0.041	0.047	0.054	0.035	0.053	0.044	0.053	0.047	0.049	0.055	0.039	0.050
Total	96.7	96.6	96.8	96.9	96.6	97.0	96.9	96.7	96.7	96.7	96.9	97.3	97.9
Species	Mg-Hst	Mg-Hst	Mg-Hst	Mg-Hst	Mg-Hst	Mg-Hst	Mg-Hst	Mg-Hst	Mg-Hst	Mg-Hst	Mg-Hst	Mg-Hst	Mg-Hst
T (°C)	1048	1042	1050	1047	1044	1042	1046	1041	1044	1040	1043	1044	1046
error (σest)	22	22	22	22	22	22	22	22	22	22	22	22	22
P (MPa)	622	594	634	628	606	600	621	596	610	586	594	604	630
error (Max error)	68	65	70	69	67	66	68	66	67	64	65	66	69
ΔNNO	0.89	0.81	0.74	0.78	0.80	0.83	0.81	0.80	0.80	0.78	0.85	0.87	0.80
error (σest)	0.4	0.4	0.4	0.4	0.4	0.4	0.4	0.4	0.4	0.4	0.4	0.4	0.4
H_2Omelt (wt.%)	4.63	4.58	4.55	4.66	4.52	4.48	4.68	4.53	4.60	4.51	4.44	4.32	4.62
error*	0.70	0.69	0.68	0.70	0.68	0.67	0.70	0.68	0.69	0.68	0.67	0.65	0.69

Table 5: Major element compositions of amphibole electron microprobe analyses. Element compositions reported as wt.%. P-T-H_2O-fO_2 estimates calculated using formulations of Ridolfi et al. (2012).

Lithology	BC14/048_Hbl3 Gabbro	BC14/048_Hbl3 Gabbro	BC14/048_Hbl3 Gabbro	BC14/048_Hbl3 Gabbro	BC14/048_Hbl3 Gabbro	BC14/048_Hbl3 Gabbro	BC14/048_Hbl4 Gabbro	BC14/048_Hbl4 Gabbro	BC14/048_Hbl4 Gabbro	BC14/048_Hbl4 Gabbro	BC14/048_Hbl4 Gabbro	BC14/048_Hbl4 Gabbro	BC14/048_Hbl4 Gabbro
SiO_2	39.13	39.34	39.13	39.89	39.39	38.97	38.79	39.09	39.02	39.30	39.07	39.14	39.21
TiO_2	2.42	2.37	2.38	2.38	2.46	2.36	2.36	2.35	2.40	2.36	2.38	2.36	2.38
Al_2O_3	13.84	13.94	13.97	14.91	13.91	13.84	14.34	14.14	14.07	13.83	14.13	14.03	14.03
Cr_2O_3	0.02	0.01	0.01	0.04	0.00	0.00	0.00	0.01	0.00	0.01	0.04	0.02	0.00
FeO	10.94	10.93	10.93	10.40	10.87	10.88	10.85	11.00	10.60	10.94	10.51	10.70	10.63
MnO	0.12	0.13	0.14	0.14	0.14	0.19	0.14	0.18	0.14	0.14	0.16	0.18	0.12
MgO	14.18	14.30	14.09	14.68	14.15	13.98	14.32	14.25	14.38	14.28	14.44	14.39	14.40
CaO	12.04	12.07	12.12	11.88	12.08	12.15	12.04	12.12	12.24	12.24	12.24	12.32	12.25
Na_2O	2.21	2.24	2.11	2.32	2.18	2.16	2.23	2.17	2.08	2.21	2.12	2.15	2.17
K_2O	1.45	1.49	1.47	1.49	1.50	1.49	1.46	1.46	1.50	1.48	1.49	1.47	1.51
F	0.237	0.195	0.142	0.577	0.250	0.267	0.178	0.275	0.114	0.175	0.343	0.229	0.158
Cl	0.037	0.047	0.040	0.066	0.047	0.052	0.055	0.046	0.034	0.034	0.054	0.038	0.050
Total	96.6	97.1	96.5	98.8	97.0	96.3	96.8	97.1	96.6	97.0	97.0	97.0	96.9
Species	Mg-Hst	Mg-Hst	Mg-Hst	Mg-Hst	Mg-Hst	Mg-Hst	Mg-Hst	Mg-Hst	Mg-Hst	Mg-Hst	Mg-Hst	Mg-Hst	Mg-Hst
T (°C)	1045	1045	1046	1052	1044	1047	1058	1051	1053	1046	1054	1053	1051
error (σest)	22	22	22	22	22	22	22	22	22	22	22	22	22
P (MPa)	622	627	643	738	626	636	695	660	655	613	662	643	644
error (Max error)	68	69	71	81	69	70	76	73	72	67	73	71	71
ΔNNO	0.80	0.83	0.78	0.89	0.76	0.73	0.85	0.83	0.86	0.81	0.86	0.84	0.84
error (σest)	0.4	0.4	0.4	0.4	0.4	0.4	0.4	0.4	0.4	0.4	0.4	0.4	0.4
H_2Omelt (wt.%)	4.57	4.51	4.79	5.08	4.60	4.67	4.74	4.75	4.65	4.47	4.67	4.64	4.55
error*	0.69	0.68	0.72	0.76	0.69	0.70	0.71	0.71	0.70	0.67	0.70	0.70	0.68

Table 5: Major element compositions of amphibole electron microprobe analyses. Element compositions reported as wt.%. P-T-H_2O-fO_2 estimates calculated using formulations of Ridolfi et al. (2012).

	BC14/048_Hbl4	BC14/048_Hbl4	BC14/048_Hbl5	BC14/048_Hbl5	BC14/048_Hbl5	BC14/048_Hbl5	BC14/048_Hbl5	BC14/048_Hbl5	BC14/048_Hbl5	BC14/048_Hbl5	BC14/048_Hbl5	BC14/048_Hbl5	BC14/048_Hbl5
Lithology	Gabbro	Gabbro	Gabbro	Gabbro	Gabbro	Gabbro	Gabbro	Gabbro	Gabbro	Gabbro	Gabbro	Gabbro	Gabbro
SiO_2	38.77	38.79	39.17	39.65	39.27	39.33	39.06	39.44	39.02	39.11	39.34	39.21	39.20
TiO_2	2.36	2.35	2.42	2.40	2.40	2.41	2.44	2.42	2.42	2.39	2.45	2.49	2.46
Al_2O_3	14.25	15.34	13.65	13.79	13.96	13.73	14.06	14.00	16.03	13.59	14.03	14.00	14.17
Cr_2O_3	0.00	0.02	0.01	0.00	0.03	0.00	0.05	0.01	0.00	0.02	0.00	0.00	0.04
FeO	10.84	10.49	11.16	10.97	10.77	11.01	10.62	10.63	10.88	10.87	10.52	10.59	10.45
MnO	0.12	0.16	0.17	0.17	0.16	0.13	0.15	0.13	0.13	0.16	0.15	0.09	0.14
MgO	14.10	14.22	14.22	14.46	14.27	14.06	14.26	14.32	14.09	13.90	14.25	14.16	14.22
CaO	12.20	12.11	12.09	12.15	12.18	12.12	12.19	12.14	11.82	12.11	12.17	12.15	12.11
Na_2O	2.07	2.09	2.28	2.26	2.12	2.23	2.25	2.23	2.23	2.16	2.18	2.21	2.17
K_2O	1.50	1.48	1.49	1.53	1.51	1.46	1.51	1.50	1.48	1.45	1.49	1.50	1.51
F	0.195	0.206	0.170	0.192	0.171	0.249	0.331	0.156	0.259	0.204	0.320	0.261	0.221
Cl	0.051	0.042	0.060	0.057	0.050	0.041	0.042	0.040	0.054	0.046	0.044	0.035	0.040
Total	96.4	97.3	96.9	97.6	96.9	96.8	97.0	97.0	98.4	96.0	96.9	96.7	96.7
Species	Mg-Hst	Mg-Hst	Mg-Hst	Mg-Hst	Mg-Hst	Mg-Hst	Mg-Hst	Mg-Hst	Mg-Hst	Mg-Hst	Mg-Hst	Mg-Hst	Mg-Hst
T (°C)	1056	1070	1044	1042	1047	1041	1054	1047	1073	1040	1048	1049	1051
error (σest)	22	22	22	22	22	22	22	22	22	22	22	22	22
P (MPa)	692	867	592	593	633	606	654	635	974	603	647	647	671
error (Max error)	76	95	65	65	70	67	72	70	107	66	71	71	74
ΔNNO	0.79	0.78	0.80	0.85	0.81	0.73	0.77	0.79	0.71	0.71	0.76	0.72	0.76
error (σest)	0.4	0.4	0.4	0.4	0.4	0.4	0.4	0.4	0.4	0.4	0.4	0.4	0.4
H_2Omelt (wt.%)	4.89	5.68	4.21	4.21	4.60	4.56	4.50	4.58	6.04	4.67	4.71	4.64	4.77
error*	0.73	0.85	0.63	0.63	0.69	0.68	0.67	0.69	0.91	0.70	0.71	0.70	0.72

Table 5: Major element compositions of amphibole electron microprobe analyses. Element compositions reported as wt.%. P-T-H_2O-fO_2 estimates calculated using formulations of Ridolfi et al. (2012).

	BC14/048_Hbl5	SA12/X01_Hbl1	SA12/X01_Hbl1	SA12/X01_Hbl1	SA12/X01_Hbl1	SA12/X01_Hbl1	SA12/X01_Hbl1	SA12/X01_Hbl1	SA12/X01_Hbl1	SA12/X01_Hbl1	SA12/X01_Hbl2	SA12/X01_Hbl2	SA12/X01_Hbl2
Lithology	Gabbro	Gabbro	Gabbro	Gabbro	Gabbro	Gabbro	Gabbro	Gabbro	Gabbro	Gabbro	Gabbro	Gabbro	Gabbro
SiO_2	39.35	39.42	38.95	39.24	39.09	39.31	39.13	39.22	39.14	39.32	38.88	38.68	38.78
TiO_2	2.45	2.32	2.32	2.41	2.36	2.27	2.39	2.39	2.33	2.33	2.94	2.28	2.43
Al_2O_3	14.02	13.21	13.20	13.19	13.00	13.01	13.21	13.46	13.04	13.10	12.97	13.75	13.73
Cr_2O_3	0.01	0.02	0.02	0.00	0.00	0.00	0.02	0.01	0.00	0.02	0.00	0.00	0.03
FeO	10.56	11.55	11.10	11.46	10.23	11.16	10.82	11.04	11.19	11.15	11.59	11.04	11.25
MnO	0.15	0.15	0.15	0.12	0.21	0.13	0.20	0.19	0.23	0.17	0.19	0.12	0.11
MgO	14.18	14.21	14.15	13.92	14.70	14.12	14.31	14.16	14.07	14.00	14.03	14.49	14.26
CaO	12.21	12.07	12.02	11.91	12.14	11.95	11.98	12.01	12.04	12.01	11.99	12.18	12.08
Na_2O	2.19	2.35	2.56	2.29	2.49	2.26	2.56	2.33	2.55	2.34	2.28	2.15	2.27
K_2O	1.49	1.31	1.31	1.38	1.35	1.33	1.33	1.31	1.25	1.29	1.33	1.36	1.30
F	0.238	0.166	0.290	0.262	1.180	0.157	0.329	0.133	0.239	0.183	0.654	0.160	0.159
Cl	0.054	0.054	0.048	0.038	0.073	0.042	0.036	0.040	0.038	0.030	0.047	0.035	0.031
Total	96.9	96.8	96.1	96.2	96.8	95.7	96.3	96.3	96.1	96.0	96.9	96.3	96.4
Species	Mg-Hst	Mg-Hst	Mg-Hst	Mg-Hst	Mg-Hst	Mg-Hst	Mg-Hst	Mg-Hst	Mg-Hst	Mg-Hst	Mg-Hst	Mg-Hst	Mg-Hst
T (°C)	1048	1032	1041	1030	1043	1027	1040	1038	1035	1030	1037	1052	1048
error (σest)	22	22	22	22	22	22	22	22	22	22	22	22	22
P (MPa)	648	531	547	540	518	521	544	573	528	533	511	611	608
error (Max error)	71	58	60	59	57	57	60	63	58	59	56	67	67
ΔNNO	0.73	0.85	0.78	0.76	0.93	0.86	0.81	0.79	0.75	0.77	0.69	0.98	0.85
error (σest)	0.4	0.4	0.4	0.4	0.4	0.4	0.4	0.4	0.4	0.4	0.4	0.4	0.4
H_2Omelt (wt.%)	4.75	4.29	4.11	4.30	3.75	4.34	4.04	4.57	4.24	4.47	3.92	4.50	4.60
error*	0.71	0.64	0.62	0.65	0.56	0.65	0.61	0.69	0.64	0.67	0.59	0.68	0.69

Table 5: Major element compositions of amphibole electron microprobe analyses. Element compositions reported as wt.%. P-T-H_2O-fO_2 estimates calculated using formulations of Ridolfi et al. (2012).

	SA12/X 01_Hbl2	SA12/X 01_Hbl2	SA12/X 01_Hbl2	SA12/X 01_Hbl3	SA12/X 01_Hbl3	SA12/X 01_Hbl3	SA12/X 01_Hbl4	SA12/X 01_Hbl4	SA12/X 01_Hbl4	SA12/X 01_Hbl4	SA12/X 01_Hbl4	SA12/X 01_Hbl5	SA12/X 01_Hbl5
Lithology	Gabbro	Gabbro	Gabbro	Gabbro	Gabbro	Gabbro	Gabbro	Gabbro	Gabbro	Gabbro	Gabbro	Gabbro	Gabbro
SiO_2	39.15	39.11	39.51	39.04	39.30	39.35	39.40	39.36	39.18	38.94	39.55	39.06	39.10
TiO_2	2.44	2.41	2.40	2.40	2.39	2.39	2.32	2.35	2.39	2.31	2.38	2.39	2.42
Al_2O_3	13.41	13.56	13.00	13.17	13.02	13.38	12.72	13.10	13.29	13.52	13.01	13.12	13.14
Cr_2O_3	0.00	0.00	0.01	0.00	0.03	0.00	0.01	0.00	0.05	0.01	0.00	0.00	0.03
FeO	10.67	10.70	10.81	10.74	10.79	10.48	11.08	10.40	10.44	10.60	10.43	11.41	11.07
MnO	0.14	0.16	0.16	0.17	0.18	0.14	0.18	0.15	0.18	0.14	0.18	0.16	0.17
MgO	14.61	14.47	14.17	14.46	14.30	14.48	14.45	14.63	14.56	14.37	14.53	14.15	14.29
CaO	12.15	12.21	12.03	12.00	11.97	12.00	12.02	12.00	12.07	12.08	11.99	11.98	11.91
Na_2O	2.13	2.31	2.38	2.36	2.60	2.52	2.44	2.29	2.33	2.16	2.37	2.27	2.23
K_2O	1.36	1.35	1.34	1.35	1.46	1.33	1.31	1.34	1.39	1.29	1.41	1.35	1.26
F	0.204	0.209	0.353	0.513	0.367	0.142	0.215	0.171	0.196	0.281	0.215	0.180	0.434
Cl	0.048	0.037	0.039	0.031	0.046	0.044	0.044	0.032	0.030	0.026	0.027	0.047	0.052
Total	96.3	96.5	96.2	96.2	96.5	96.3	96.2	95.8	96.1	95.7	96.1	96.1	96.1
Species	Mg-Hst	Mg-Hst	Mg-Hst	Mg-Hst	Mg-Hst	Mg-Hst	Mg-Hst	Mg-Hst	Mg-Hst	Mg-Hst	Mg-Hst	Mg-Hst	Mg-Hst
T (°C)	1042	1047	1029	1039	1036	1041	1028	1034	1041	1043	1031	1034	1033
error (σest)	22	22	22	22	22	22	22	22	22	22	22	22	22
P (MPa)	560	584	518	538	521	561	479	527	550	589	514	530	532
error (Max error)	62	64	57	59	57	62	53	58	61	65	57	58	59
ΔNNO	0.97	0.86	0.77	0.91	0.79	0.84	0.92	0.98	0.92	0.92	0.90	0.85	0.90
error (σest)	0.4	0.4	0.4	0.4	0.4	0.4	0.4	0.4	0.4	0.4	0.4	0.4	0.4
H_2Omelt (wt.%)	4.35	4.39	4.22	4.04	3.56	4.20	3.79	4.13	4.08	4.74	3.91	4.16	4.43
error*	0.65	0.66	0.63	0.61	0.53	0.63	0.57	0.62	0.61	0.71	0.59	0.62	0.66

Table 5: Major element compositions of amphibole electron microprobe analyses. Element compositions reported as wt.%. P-T-H_2O-fO_2 estimates calculated using formulations of Ridolfi et al. (2012).

Appendix 1

	SA12/X 01_Hbl5	SA12/X 01_Hbl5	SA12-XO11	SA12-XO11	SA12-XO11	SA12-XO11	SA12-XO11	SA12-XO11	SA12-XO11	SA12-XO11	SA21 Core 1	SA21 Core 2	SA21 Rim 2
Lithology	Gabbro	Gabbro	Gabbro	Gabbro	Gabbro	Gabbro	Gabbro	Gabbro	Gabbro	Gabbro	Gabbro	Gabbro	Gabbro
SiO_2	39.33	39.07	40.34	40.11	39.88	39.80	39.89	39.88	39.69	40.17	39.90	38.62	39.23
TiO_2	2.36	2.35	2.52	2.44	2.26	2.41	2.43	2.28	2.31	2.31	2.50	2.61	2.70
Al_2O_3	13.02	13.03	12.98	12.74	13.33	13.12	13.12	13.33	13.23	13.14	13.12	14.20	14.15
Cr_2O_3	0.00	0.01	0.00	0.00	0.03	0.02	0.03	0.00	0.00	0.00	0.00	0.10	0.00
FeO	11.53	11.18	10.54	10.82	10.66	10.85	10.71	10.66	10.83	10.75	11.09	11.16	10.75
MnO	0.16	0.17	0.14	0.16	0.14	0.16	0.20	0.14	0.17	0.18	0.21	0.24	0.21
MgO	14.20	14.17	14.85	14.49	14.62	14.33	14.38	14.60	14.31	14.24	13.52	13.29	13.64
CaO	12.05	12.01	11.83	11.82	12.06	11.88	11.87	12.16	12.01	11.85	11.62	11.85	11.93
Na_2O	2.40	2.16	2.28	2.22	2.24	2.25	2.19	2.21	2.26	2.25	2.30	2.12	2.16
K_2O	1.28	1.38	1.42	1.38	1.37	1.49	1.50	1.43	1.54	1.58	1.55	1.69	1.63
F	0.147	0.244	0.086	0.084	0.306	0.224	0.111	0.205	0.220	0.073	0.230	0.180	0.120
Cl	0.041	0.043	0.055	0.069	0.034	0.078	0.059	0.034	0.067	0.069	0.090	0.410	0.080
Total	96.5	95.8	97.0	96.3	96.9	96.6	96.5	96.9	96.6	96.6	96.1	96.5	96.6
Species	Mg-Hst	Mg-Hst	Mg-Hst	Mg-Hst	Mg-Hst	Mg-Hst	Mg-Hst	Mg-Hst	Mg-Hst	Mg-Hst	Mg-Hst	Mg-Hst	Mg-Hst
T (°C)	1031	1032	1020	1015	1030	1025	1024	1032	1030	1020	1016	1050	1046
error (σest)	22	22	22	22	22	22	22	22	22	22	22	22	22
P (MPa)	512	524	484	470	538	520	517	539	536	520	534	708	678
error (Max error)	56	58	53	52	59	57	57	59	59	57	59	78	75
ΔNNO	0.84	0.89	1.00	0.94	0.97	0.87	0.89	0.95	0.86	0.84	0.57	0.47	0.52
error (σest)	0.4	0.4	0.4	0.4	0.4	0.4	0.4	0.4	0.4	0.4	0.4	0.4	0.4
H_2Omelt (wt.%)	4.17	4.19	3.88	4.01	4.39	4.00	4.04	4.27	3.96	3.99	4.30	4.67	4.72
error*	0.63	0.63	0.58	0.60	0.66	0.60	0.61	0.64	0.59	0.60	0.65	0.70	0.71

Table 5: Major element compositions of amphibole electron microprobe analyses. Element compositions reported as wt.%. P-T-H_2O-fO_2 estimates calculated using formulations of Ridolfi et al. (2012).

	SA23	B24_Hb l2-1	B24_Hb l2-3	B24_Hb l4-1	B24_Hb l4-1	B24_Hb l4-1	B24_Hb l4-1	B24_Hb l4-1	B24_Hb l4-1	B24_Hb l4-1	B24_Hb l4-1	B7
Lithology	Gabbro	Gabbro	Gabbro	Gabbro	Gabbro	Gabbro	Gabbro	Gabbro	Gabbro	Gabbro	Gabbro	Gabbro
SiO_2	39.66	42.25	41.40	40.99	39.91	40.10	39.55	40.67	41.12	40.20	40.03	40.86	39.78
TiO_2	2.77	2.15	2.15	2.20	2.15	2.16	2.10	2.05	2.33	2.11	2.27	2.21	2.41
Al_2O_3	12.42	13.60	15.48	15.31	15.60	15.37	15.14	15.19	15.06	14.86	15.61	15.09	13.35
Cr_2O_3		0.01	0.01	0.01	-0.01	0.00	0.00	0.00	-0.01	0.01	0.04	0.00	
FeO	11.70	11.32	11.31	11.01	11.17	11.13	11.18	11.17	10.88	10.76	11.23	10.58	11.19
MnO	0.15	0.20	0.17	0.18	0.18	0.19	0.18	0.19	0.18	0.17	0.17	0.16	
MgO	13.16	13.58	13.32	13.67	13.23	13.20	13.00	13.41	13.51	13.47	12.99	13.55	13.62
CaO	12.23	12.03	12.57	12.29	12.49	12.43	12.43	12.54	12.37	12.56	12.49	12.44	12.50
Na_2O	2.30	2.16	1.96	1.98	1.90	1.96	1.91	2.01	1.99	1.95	1.97	1.96	2.18
K_2O	1.46	1.53	1.78	1.77	1.76	1.79	1.73	1.80	1.72	1.71	1.75	1.80	1.68
F													
Cl	0.800	0.106	0.057	0.054	0.036	0.047	0.028	0.051	0.063	0.038	0.039	0.034	0.800
Total	96.7	98.9	100.2	99.4	98.4	98.4	97.3	99.1	99.2	97.8	98.6	98.7	97.5
Species	Mg-Hst	Parg	Parg	Parg	Parg	Parg	Parg	Parg	Parg	Parg	Parg	Parg	Parg
T (°C)	1017	995	1038	1039	1057	1051	1052	1044	1036	1046	1055	1041	1034
error (σest)	22	22	22	22	22	22	22	22	22	22	22	22	22
P (MPa)	464	541	824	800	910	863	855	804	766	775	914	789	565
error (Max error)	51	59	91	88	100	95	94	88	84	85	101	87	62
ΔNNO	0.33	0.53	0.35	0.52	0.40	0.38	0.36	0.43	0.41	0.47	0.26	0.44	0.50
error (σest)	0.4	0.4	0.4	0.4	0.4	0.4	0.4	0.4	0.4	0.4	0.4	0.4	0.4
H_2Omelt (wt.%)	3.98	5.40	6.24	5.86	6.19	5.97	6.05	5.80	5.91	5.76	6.29	5.78	4.15
error*	0.60	0.81	0.94	0.88	0.93	0.89	0.91	0.87	0.89	0.86	0.94	0.87	0.62

Table 5: Major element compositions of amphibole electron microprobe analyses. Element compositions reported as wt.%. P-T-H_2O-fO_2 estimates calculated using formulations of Ridolfi et al. (2012).

	B7	B7	B7	B7	B7	B8_Cpx 1-1	B8_Hbl 1-2	B8_Hbl 1-6	B8_Hbl 2-3	B8_Hbl 2-4	B8_Hbl 2-7	B8_Hbl 3	B8_Hbl 3
Lithology	Gabbro	Gabbro	Gabbro	Gabbro	Gabbro	Gabbro	Gabbro	Gabbro	Gabbro	Gabbro	Gabbro	Gabbro	Gabbro
SiO_2	39.50	40.36	40.45	39.85	39.42	38.85	39.34	39.16	39.88	39.82	40.02	38.86	39.08
TiO_2	2.32	2.41	2.24	2.31	2.42	1.99	2.04	2.10	2.09	2.16	2.15	2.08	2.06
Al_2O_3	14.34	13.51	13.35	14.27	14.27	14.83	14.44	14.85	14.83	14.65	15.36	14.90	14.91
Cr_2O_3						0.00	-0.01	-0.02	0.01	0.01	0.01	0.00	0.01
FeO	11.07	11.16	10.57	10.81	10.92	11.65	11.78	11.91	11.77	12.05	12.58	11.89	11.91
MnO				0.11	0.16	0.17	0.17	0.18	0.19	0.20	0.19	0.19	0.18
MgO	13.25	13.47	13.52	13.14	13.00	12.91	12.78	12.62	12.92	12.74	12.52	12.61	12.66
CaO	12.41	12.47	12.44	12.50	12.48	12.49	12.36	12.36	12.43	12.47	12.41	12.39	12.37
Na_2O	1.96	2.17	2.12	2.01	2.23	2.00	1.89	1.88	1.88	1.88	1.92	1.90	1.92
K_2O	1.54	1.64	1.59	1.62	1.55	1.73	1.77	1.81	1.80	1.84	1.76	1.73	1.79
F													
Cl	0.800	0.800	0.800	0.800	0.800	0.057	0.046	0.031	0.042	0.049	0.046	0.032	0.023
Total	97.2	98.0	97.1	97.4	97.3	96.7	96.6	96.9	97.8	97.9	99.0	96.6	96.9
Species	Parg	Parg	Parg	Parg	Parg	Parg	Parg	Parg	Parg	Parg	Parg	Parg	Parg
T (°C)	1043	1026	1021	1040	1048	1058	1041	1049	1042	1040	1044	1054	1051
error (σest)	22	22	22	22	22	22	22	22	22	22	22	22	22
P (MPa)	721	576	568	709	722	822	746	820	781	754	857	839	832
error (Max error)	79	63	62	78	79	90	82	90	86	83	94	92	91
ΔNNO	0.43	0.42	0.47	0.33	0.23	0.39	0.38	0.30	0.37	0.29	0.21	0.31	0.31
error (σest)	0.4	0.4	0.4	0.4	0.4	0.4	0.4	0.4	0.4	0.4	0.4	0.4	0.4
H_2Omelt (wt.%)	5.69	4.64	4.89	5.61	5.51	5.57	5.48	5.68	5.67	5.48	6.21	5.85	5.72
error*	0.85	0.70	0.73	0.84	0.83	0.84	0.82	0.85	0.85	0.82	0.93	0.88	0.86

Table 5: Major element compositions of amphibole electron microprobe analyses. Element compositions reported as wt.%. P-T-H_2O-fO_2 estimates calculated using formulations of Ridolfi et al. (2012).

Appendix 1

	B8_Hbl 3	B8_Hbl 4	B8_Hbl 4	B8_Hbl 4	B8_Hbl 4	B8_Hbl 4	SA23	SA23	BC14-004	BC14-004	BC14-004	BC14-004	BC14-004
Lithology	Gabbro	Gabbro	Gabbro	Gabbro	Gabbro	Gabbro	Gabbro	Gabbro	Lava	Lava	Lava	Lava	Lava
SiO_2	38.57	39.10	39.51	38.86	39.68	39.68	40.42	40.18	40.20	39.91	39.96	40.23	40.31
TiO_2	2.01	2.02	2.07	2.02	2.17	2.10	2.96	2.65	2.81	2.79	2.69	2.72	2.80
Al_2O_3	15.02	15.20	14.59	14.63	14.61	14.81	11.91	12.04	13.02	12.84	12.94	12.95	12.66
Cr_2O_3	-0.02	0.01	0.00	0.00	-0.01	0.00							
FeO	11.90	12.12	12.17	11.86	12.10	11.79	12.24	11.86	12.76	12.51	12.28	12.32	12.09
MnO	0.17	0.17	0.20	0.17	0.16	0.16	0.24	0.23	0.24	0.27	0.25	0.27	0.21
MgO	12.59	12.52	12.68	12.63	12.66	12.90	12.90	12.93	13.50	13.37	13.38	13.45	13.61
CaO	12.62	12.31	12.44	12.38	12.30	12.37	12.34	12.25	11.70	11.69	11.50	11.70	11.73
Na_2O	1.88	1.90	1.88	1.91	1.93	2.03	2.24	2.21	2.51	2.64	2.58	2.55	2.67
K_2O	1.74	1.72	1.78	1.75	1.80	1.74	1.43	1.45	1.65	1.67	1.63	1.60	1.53
F								0.200	0.192	0.204	0.192	0.161	0.178
Cl	0.016	0.037	0.036	0.033	0.044	0.081	0.800	0.800	0.149	0.140	0.134	0.148	0.105
Total	96.5	97.1	97.3	96.2	97.5	97.7	97.5	96.8	98.7	98.0	97.5	98.1	97.9
Species	Parg	Parg	Parg	Parg	Parg	Parg	Parg	Parg	Mg-Hst	Mg-Hst	Mg-Hst	Mg-Hst	Mg-Hst
T (°C)	1063	1052	1042	1050	1039	1045	999	1001	1015	1018	1014	1014	1012
error (σest)	22	22	22	22	22	22	22	22	22	22	22	22	22
P (MPa)	876	884	756	797	755	785	401	424	488	483	497	489	459
error (Max error)	96	97	83	88	83	86	44	47	54	53	55	54	50
ΔNNO	0.29	0.29	0.33	0.34	0.29	0.34	0.19	0.29	0.48	0.42	0.48	0.46	0.46
error (σest)	0.4	0.4	0.4	0.4	0.4	0.4	0.4	0.4	0.4	0.4	0.4	0.4	0.4
H_2Omelt (wt.%)	5.90	6.18	5.58	5.62	5.52	5.65	3.93	4.12	3.39	3.16	3.48	3.60	3.38
error*	0.88	0.93	0.84	0.84	0.83	0.85	0.59	0.62	0.51	0.47	0.52	0.54	0.51

Table 5: Major element compositions of amphibole electron microprobe analyses. Element compositions reported as wt.%. P-T-H_2O-fO_2 estimates calculated using formulations of Ridolfi et al. (2012).

Appendix 1

	BC14-004	BC14-004	BC14-004	BC14-004	BC14-004	BC14-004	BC14-004	BC14-004	BC14-004	BC14-004	BC14-004	BC14-004	BC14-004
Lithology	Lava	Lava	Lava	Lava	Lava	Lava	Lava	Lava	Lava	Lava	Lava	Lava	Lava
SiO_2	40.08	39.31	40.07	39.73	40.50	40.29	40.25	40.15	40.03	39.96	40.11	40.36	40.39
TiO_2	2.82	2.74	2.74	2.70	2.62	2.76	2.54	2.50	2.66	2.71	2.70	2.62	2.74
Al_2O_3	13.30	13.29	12.56	12.28	12.36	12.59	12.52	12.57	12.70	12.49	12.42	12.56	12.75
Cr_2O_3													
FeO	11.90	14.06	12.60	13.07	12.76	12.59	13.16	12.53	12.51	12.80	12.88	13.07	12.75
MnO	0.23	0.34	0.37	0.33	0.33	0.32	0.38	0.31	0.34	0.34	0.32	0.36	0.35
MgO	13.57	13.45	13.50	13.00	13.48	13.55	13.13	13.57	13.43	13.17	13.20	13.20	13.32
CaO	11.87	13.61	11.64	11.64	11.73	11.70	11.65	11.79	11.61	11.74	11.76	11.79	11.78
Na_2O	2.60	2.53	2.74	2.63	2.64	2.67	2.49	2.79	2.64	2.48	2.52	2.56	2.48
K_2O	1.47	0.29	1.53	1.56	1.41	1.54	1.53	1.33	1.51	1.54	1.54	1.59	1.55
F	0.241	0.185	0.272	0.399	0.204	0.187	0.178	0.430	0.148	0.134	0.194	0.145	0.198
Cl	0.084	0.180	0.128	0.134	0.118	0.134	0.143	0.103	0.135	0.120	0.136	0.140	0.142
Total	98.2	100.0	98.1	97.5	98.2	98.3	98.0	98.1	97.7	97.5	97.8	98.4	98.4
Species	Mg-Hst	Mg-Hst	Mg-Hst	Mg-Hst	Mg-Hst	Mg-Hst	Mg-Hst	Mg-Hst	Mg-Hst	Mg-Hst	Mg-Hst	Mg-Hst	Mg-Hst
T (°C)	1025	1051	1012	1007	1002	1010	1001	1011	1011	1008	1006	1005	1008
error (σest)	22	22	22	22	22	22	22	22	22	22	22	22	22
P (MPa)	531	513	447	433	423	446	445	450	465	448	438	446	463
error (Max error)	58	56	49	48	47	49	49	50	51	49	48	49	51
ΔNNO	0.42	0.33	0.48	0.37	0.51	0.49	0.47	0.53	0.50	0.43	0.42	0.42	0.43
error (σest)	0.4	0.4	0.4	0.4	0.4	0.4	0.4	0.4	0.4	0.4	0.4	0.4	0.4
H_2Omelt (wt.%)	4.05	6.51	3.16	3.15	3.54	3.24	3.62	3.70	3.50	3.49	3.41	3.39	3.67
error*	0.61	0.98	0.47	0.47	0.53	0.49	0.54	0.56	0.52	0.52	0.51	0.51	0.55

Table 5: Major element compositions of amphibole electron microprobe analyses. Element compositions reported as wt.%. P-T-H_2O-fO_2 estimates calculated using formulations of Ridolfi et al. (2012).

	BC14-004	BC14-004	BC14-004	BC14-004	BC14-004	BC14-004	BC14-004	BC14-004	BC14-004	BC14-004	BC14-004	BC14-004	BC14-004
Lithology	Lava	Lava	Lava	Lava	Lava	Lava	Lava	Lava	Lava	Lava	Lava	Lava	Lava
SiO_2	40.64	40.47	40.19	40.43	40.58	40.25	39.90	40.52	40.27	40.10	40.39	40.59	40.33
TiO_2	2.72	2.63	2.46	2.81	2.82	2.93	2.72	2.72	2.51	2.67	2.74	2.69	2.60
Al_2O_3	12.72	12.40	12.74	12.68	12.73	12.86	12.39	12.83	12.86	12.27	13.00	12.33	12.79
Cr_2O_3													
FeO	12.77	12.88	12.41	12.60	12.52	12.68	12.48	12.50	12.30	12.39	12.62	12.37	12.13
MnO	0.37	0.35	0.27	0.39	0.34	0.37	0.35	0.30	0.31	0.34	0.35	0.34	0.27
MgO	13.44	13.25	13.50	13.30	13.49	13.21	13.08	13.49	13.55	13.19	13.26	13.36	13.55
CaO	11.77	11.64	11.78	11.66	11.81	11.72	11.53	11.91	11.80	11.70	11.69	11.60	11.80
Na_2O	2.69	2.70	2.59	2.58	2.62	2.52	2.58	2.53	2.66	2.44	2.55	2.60	2.75
K_2O	1.55	1.55	1.37	1.52	1.56	1.55	1.52	1.52	1.38	1.54	1.54	1.53	1.33
F	0.121	0.167	0.175	0.173	0.172	0.157	0.151	0.178	0.235	0.172	0.165	0.174	0.212
Cl	0.140	0.123	0.125	0.137	0.129	0.153	0.227	0.123	0.106	0.145	0.125	0.124	0.092
Total	98.9	98.2	97.6	98.3	98.8	98.4	96.9	98.6	98.0	97.0	98.4	97.7	97.9
Species	Mg-Hst	Mg-Hst	Mg-Hst	Mg-Hst	Mg-Hst	Mg-Hst	Mg-Hst	Mg-Hst	Mg-Hst	Mg-Hst	Mg-Hst	Mg-Hst	Mg-Hst
T (°C)	1007	1001	1010	1006	1010	1012	1005	1012	1013	1002	1011	998	1012
error (σest)	22	22	22	22	22	22	22	22	22	22	22	22	22
P (MPa)	454	430	470	457	455	476	446	467	479	431	490	425	474
error (Max error)	50	47	52	50	50	52	49	51	53	47	54	47	52
ΔNNO	0.43	0.42	0.55	0.40	0.42	0.35	0.39	0.45	0.52	0.44	0.39	0.45	0.47
error (σest)	0.4	0.4	0.4	0.4	0.4	0.4	0.4	0.4	0.4	0.4	0.4	0.4	0.4
H_2Omelt (wt.%)	3.44	3.28	4.01	3.63	3.45	3.70	3.50	3.71	3.99	3.51	3.86	3.44	4.01
error*	0.52	0.49	0.60	0.54	0.52	0.56	0.52	0.56	0.60	0.53	0.58	0.52	0.60

Table 5: Major element compositions of amphibole electron microprobe analyses. Element compositions reported as wt.%. P-T-H_2O-fO_2 estimates calculated using formulations of Ridolfi et al. (2012).

Appendix 1

	BC14-004	BC14-004	BC14-004	BC14-004	BC14-004	BC14-004	BC14-004	BC14-004	BC14-004	BC14-004	BC14-004	BC14-004	BC14-004
Lithology	Lava	Lava	Lava	Lava	Lava	Lava	Lava	Lava	Lava	Lava	Lava	Lava	Lava
SiO_2	40.37	40.10	41.52	40.19	40.17	40.10	39.12	40.39	40.34	40.06	40.69	39.78	39.80
TiO_2	2.65	2.71	2.77	2.46	2.54	2.58	2.55	2.59	2.58	2.49	2.61	2.40	2.52
Al_2O_3	12.83	12.31	12.83	12.87	12.88	12.99	13.26	12.59	13.31	13.00	15.74	13.01	12.20
Cr_2O_3													
FeO	12.68	12.84	12.48	12.31	12.43	12.31	12.00	12.45	12.01	12.28	11.59	11.49	14.94
MnO	0.35	0.37	0.38	0.28	0.34	0.27	0.31	0.31	0.28	0.25	0.36	0.43	0.49
MgO	13.24	12.94	13.64	13.43	13.35	13.31	13.11	13.22	13.46	13.39	12.93	13.28	12.00
CaO	11.87	11.77	11.77	11.80	11.83	11.79	11.74	11.83	11.61	11.90	10.99	11.53	11.60
Na_2O	2.62	2.59	2.64	2.72	2.71	2.62	2.56	2.52	2.93	2.84	2.49	2.91	2.79
K_2O	1.39	1.55	1.53	1.38	1.39	1.41	1.31	1.55	1.35	1.41	1.51	1.37	1.60
F	0.207	0.147	0.145	0.180	0.169	0.069	0.221	0.191	0.453	0.136	0.147	0.866	0.209
Cl	0.115	0.122	0.124	0.110	0.098	0.086	0.088	0.130	0.107	0.105	0.135	0.132	0.127
Total	98.3	97.5	99.8	97.7	97.9	97.5	96.3	97.8	98.4	97.9	99.2	97.2	98.3
Species	Mg-Hst	Mg-Hst	Mg-Hst	Mg-Hst	Mg-Hst	Mg-Hst	Mg-Hst	Mg-Hst	Mg-Hst	Mg-Hst	Mg-Hst	Mg-Hst	Mg-Hst
T (°C)	1011	1004	999	1014	1014	1016	1029	1005	1019	1021	1032	1019	994
error (σest)	22	22	22	22	22	22	22	22	22	22	22	22	22
P (MPa)	475	435	448	485	487	500	564	457	530	503	887	527	430
error (Max error)	52	48	49	53	54	55	62	50	58	55	98	58	47
ΔNNO	0.38	0.30	0.45	0.48	0.43	0.43	0.40	0.41	0.40	0.40	0.27	0.40	0.08
error (σest)	0.4	0.4	0.4	0.4	0.4	0.4	0.4	0.4	0.4	0.4	0.4	0.4	0.4
H_2Omelt (wt.%)	4.09	3.41	3.73	4.03	4.00	4.15	4.63	3.71	4.24	3.91	6.47	4.17	3.19
error*	0.61	0.51	0.56	0.60	0.60	0.62	0.69	0.56	0.64	0.59	0.97	0.63	0.48

Table 5: Major element compositions of amphibole electron microprobe analyses. Element compositions reported as wt.%. P-T-H_2O-fO_2 estimates calculated using formulations of Ridolfi et al. (2012).

	BC14-004	BC14-004	BC14-004	BC14-004	BC14-004	BC14-004	BC14-004	BC14-004	BC14-004	BC14-004	BC14-004	BC14-004	BC14-004
Lithology	Lava	Lava	Lava	Lava	Lava	Lava	Lava	Lava	Lava	Lava	Lava	Lava	Lava
SiO_2	40.76	40.40	41.96	40.19	40.50	39.80	41.09	41.68	40.64	40.80	40.29	41.08	40.47
TiO_2	2.81	2.51	2.73	2.83	2.64	2.65	2.70	2.64	2.84	2.87	2.80	2.68	2.87
Al_2O_3	12.67	12.42	13.57	12.75	12.98	12.95	13.06	13.22	12.59	12.80	12.85	14.63	12.73
Cr_2O_3													
FeO	12.37	14.92	11.31	11.41	11.47	12.75	11.47	11.37	11.11	11.15	12.15	10.74	11.29
MnO	0.28	0.49	0.22	0.22	0.25	0.26	0.19	0.23	0.23	0.23	0.31	0.28	0.23
MgO	13.46	11.95	14.91	13.90	14.05	13.15	14.27	14.47	13.98	14.05	13.24	14.19	13.81
CaO	11.86	11.67	12.06	11.86	11.95	11.82	11.86	11.94	11.87	11.84	11.75	11.50	11.90
Na_2O	2.63	2.70	3.07	2.61	2.58	2.85	2.87	2.75	2.78	2.75	2.77	2.83	2.77
K_2O	1.34	1.58	1.35	1.32	1.34	1.41	1.37	1.37	1.30	1.31	1.31	1.32	1.34
F	0.202	0.173	0.231	0.228	0.201	0.218	0.246	0.222	0.255	0.202	0.189	0.186	0.185
Cl	0.090	0.134	0.096	0.103	0.101	0.111	0.101	0.095	0.118	0.095	0.082	0.103	0.097
Total	98.5	99.0	101.5	97.4	98.1	98.0	99.2	100.0	97.7	98.1	97.7	99.5	97.7
Species	Mg-Hst	Mg-Hst	Mg-Hst	Mg-Hst	Mg-Hst	Mg-Hst	Mg-Hst	Mg-Hst	Mg-Hst	Mg-Hst	Mg-Hst	Mg-Hst	Mg-Hst
T (°C)	1005	992	1022	1018	1018	1022	1016	1011	1013	1014	1013	1031	1017
error (σest)	22	22	22	22	22	22	22	22	22	22	22	22	22
P (MPa)	452	436	497	470	486	496	478	480	450	465	485	672	467
error (Max error)	50	48	55	52	53	55	53	53	49	51	53	74	51
ΔNNO	0.40	0.05	0.67	0.54	0.62	0.32	0.59	0.66	0.49	0.51	0.30	0.55	0.43
error (σest)	0.4	0.4	0.4	0.4	0.4	0.4	0.4	0.4	0.4	0.4	0.4	0.4	0.4
H_2Omelt (wt.%)	4.04	3.67	3.81	3.94	4.10	3.80	3.79	4.06	3.81	3.95	4.20	5.25	3.87
error*	0.61	0.55	0.57	0.59	0.61	0.57	0.57	0.61	0.57	0.59	0.63	0.79	0.58

Table 5: Major element compositions of amphibole electron microprobe analyses. Element compositions reported as wt.%. P-T-H_2O-fO_2 estimates calculated using formulations of Ridolfi et al. (2012).

Appendix 1

	BC14-004	BC14-004	SA18	SA18	SA18	SA18	SA19	SA19	SA19	SA19	SA26	SA26	SA26
Lithology	Lava	Lava	Lava	Lava	Lava	Lava	Lava	Lava	Lava	Lava	Lava	Lava	Lava
SiO_2	41.23	40.19	39.77	39.39	39.56	39.62	40.85	40.38	38.36	38.83	40.65	40.45	39.67
TiO_2	2.68	2.68	2.47	2.59	2.55	2.53	2.85	2.63	2.46	2.58	3.04	2.35	2.12
Al_2O_3	12.98	12.55	13.73	13.56	13.51	13.62	13.03	12.62	14.25	14.10	12.16	12.66	13.79
Cr_2O_3			0.01	0.02	0.00	0.03	0.00	0.03	0.04	0.00			
FeO	11.51	11.35	10.49	10.31	10.45	9.97	11.38	11.35	11.18	11.43	13.51	13.39	11.12
MnO	0.19	0.24	0.14	0.18	0.17	0.19	0.29	0.26	0.28	0.26	0.17	0.12	
MgO	14.04	13.74	14.39	14.35	14.34	14.28	14.02	13.81	13.22	13.22	12.48	12.56	13.80
CaO	11.91	11.91	11.65	11.69	11.81	11.99	11.90	11.62	11.99	11.84	11.54	11.78	12.44
Na_2O	2.97	2.81	2.12	2.08	2.05	2.04	2.38	2.40	2.29	2.47	2.33	2.25	2.28
K_2O	1.34	1.32	1.57	1.52	1.55	1.43	1.55	1.65	1.64	1.73	1.42	1.40	1.30
F	0.261	0.247	0.090	0.130	0.070	0.080	0.180	0.190	0.170	0.150			
Cl	0.085	0.112	0.040	0.050	0.050	0.080	0.110	0.160	0.130	0.080	0.800	0.800	0.800
Total	99.2	97.1	96.5	95.9	96.1	95.9	98.5	97.1	96.0	96.7	98.1	97.8	97.3
Species	Mg-Hst	Mg-Hst	Mg-Hst	Mg-Hst	Mg-Hst	Mg-Hst	Mg-Hst	Mg-Hst	Mg-Hst	Mg-Hst	Mg-Hst	Mg-Hst	Mg-Hst
T (°C)	1013	1016	1030	1034	1032	1035	1029	1013	1007	1057	1050	984	992
error (σest)	22	22	22	22	22	22	22	22	22	22	22	22	22
P (MPa)	472	458	594	584	573	596	580	484	461	730	686	413	471
error (Max error)	52	50	65	64	63	66	64	53	51	80	75	45	52
ΔNNO	0.48	0.46	0.90	0.88	0.87	0.80	0.85	0.58	0.63	0.43	0.37	0.17	0.34
error (σest)	0.4	0.4	0.4	0.4	0.4	0.4	0.4	0.4	0.4	0.4	0.4	0.4	0.4
H_2Omelt (wt.%)	3.90	3.76	4.37	4.35	4.30	4.86	4.54	3.86	3.40	4.71	4.21	4.09	4.75
error*	0.59	0.56	0.66	0.65	0.65	0.73	0.68	0.58	0.51	0.71	0.63	0.61	0.71

Table 5: Major element compositions of amphibole electron microprobe analyses. Element compositions reported as wt.%. P-T-H_2O-fO_2 estimates calculated using formulations of Ridolfi et al. (2012).

Appendix 1

	SA26	SA26	SA26	SA8_Hbl1-1	SA8_Hbl7	SA8_Hbl8	SA26	SA26	B16_Int Hbl1-1	B16_Int Hbl1-2	B16_Int Hbl1-4	B21	B21
Lithology	Lava	Lava	Lava	lava	lava	lava	Lava	Lava	Pyrox.	Pyrox.	Pyrox.	Pyrox.	Pyrox.
SiO_2	40.89	39.19	38.59	40.47	39.62	39.72	39.75	39.98	39.93	39.44	39.54	39.47	39.62
TiO_2	2.43	2.33	2.46	2.58	2.61	2.64	2.43	2.36	2.00	2.03	2.00	2.27	1.93
Al_2O_3	12.07	13.18	13.25	13.11	13.20	13.26	13.67	13.90	14.65	14.76	14.66	13.31	13.78
Cr_2O_3				0.00	0.01	0.01			-0.02	0.00	0.00	0.02	0.02
FeO	12.44	11.31	13.21	10.60	10.09	10.40	11.39	10.67	12.67	12.69	12.90	11.27	11.11
MnO		0.14	0.28	0.15	0.17	0.19			0.14	0.15	0.12	0.19	0.17
MgO	12.83	13.42	12.09	14.20	14.30	14.05	13.62	13.88	12.51	12.72	12.87	13.73	14.16
CaO	11.57	12.54	12.53	11.62	11.77	11.74	12.92	12.53	11.90	12.07	12.13	11.80	11.20
Na_2O	2.23	1.93	2.02	2.22	2.41	2.37	1.98	2.37	1.89	1.89	1.87	2.11	2.15
K_2O	1.44	1.40	1.40	1.47	1.49	1.52	1.45	1.36	2.04	2.03	1.99	1.44	1.48
F				0.105	0.366	0.113						0.010	0.100
Cl	0.800	0.800	0.800	0.040	0.080	0.043	0.800	0.800	0.137	0.116	0.093	0.050	0.050
Total	96.7	96.2	96.6	96.6	96.1	96.1	98.0	97.9	97.9	97.9	98.2	95.7	95.8
Species	Mg-Hst	Mg-Hst	Mg-Hst	Mg-Hst	Mg-Hst	Mg-Hst	Parg	Parg	Mg-Hst	Mg-Hst	Mg-Hst	Mg-Hst	Mg-Hst
T (°C)	1038	977	1033	1033	1013	1031	1028	1041	1042	1027	1040	1038	1023
error (σest)	22	22	22	22	22	22	22	22	22	22	22	22	22
P (MPa)	621	416	561	587	510	543	549	600	630	752	772	743	560
error (Max error)	68	46	62	65	56	60	60	66	69	83	85	82	62
ΔNNO	0.64	0.42	0.56	0.11	0.78	0.75	0.67	0.49	0.52	0.36	0.42	0.49	0.76
error (σest)	0.4	0.4	0.4	0.4	0.4	0.4	0.4	0.4	0.4	0.4	0.4	0.4	0.4
H_2Omelt (wt.%)	5.31	4.35	5.00	5.28	4.34	3.97	4.09	5.10	5.18	5.07	4.91	4.83	4.70
error*	0.80	0.65	0.75	0.79	0.65	0.60	0.61	0.77	0.78	0.76	0.74	0.72	0.70

Table 5: Major element compositions of amphibole electron microprobe analyses. Element compositions reported as wt.%. P-T-H_2O-fO_2 estimates calculated using formulations of Ridolfi et al. (2012).

Appendix 1

	B21	B21	B21	B21	B21	B21	B21	B22	BC14-020	BC14-020	BC14-020	BC14-020	BC14-020
Lithology	Pyrox.	Pyrox.	Pyrox.	Pyrox.	Pyrox.	Pyrox.	Pyrox.	Pyrox.	Pyrox.	Pyrox.	Pyrox.	Pyrox.	Pyrox.
SiO_2	39.04	39.56	40.06	40.88	38.92	40.00	39.53	38.74	39.37	39.60	40.25	39.55	39.87
TiO_2	2.19	1.82	1.88	2.02	1.93	1.95	1.74	2.17	2.31	2.31	2.31	2.34	2.32
Al_2O_3	14.19	13.87	13.92	13.56	13.92	14.21	14.19	14.38	13.39	13.61	13.59	14.10	13.98
Cr_2O_3	0.00		0.00	0.03		0.02	0.02	0.00					
FeO	11.20	11.11	10.57	10.57	11.07	10.90	10.86	11.26	11.00	11.19	11.03	11.36	11.11
MnO	0.21	0.16	0.16	0.13	0.11	0.16	0.09	0.18	0.17	0.16	0.18	0.16	0.14
MgO	13.76	13.80	14.40	14.39	13.64	13.90	13.89	14.38	14.12	14.21	14.30	14.15	14.32
CaO	11.47	12.20	11.69	11.74	12.31	11.84	11.70	11.80	12.13	12.23	12.13	12.13	12.15
Na_2O	2.18	2.18	2.26	2.25	2.21	2.16	2.21	2.01	2.27	2.29	2.34	2.20	2.32
K_2O	1.53	1.47	1.35	1.31	1.41	1.43	1.30	1.73	1.57	1.56	1.57	1.68	1.60
F	0.030		0.030	0.010		0.030	0.080	0.030	0.238	0.208	0.143	0.188	0.222
Cl	0.070	0.800	0.070	0.030	0.800	0.040	0.050	0.010	0.050	0.073	0.055	0.059	0.057
Total	95.9	97.0	96.4	96.9	96.3	96.6	95.7	96.7	96.6	97.4	97.9	97.9	98.1
Species	Mg-Hst	Mg-Hst	Mg-Hst	Mg-Hst	Mg-Hst	Mg-Hst	Mg-Hst	Mg-Hst	Mg-Hst	Mg-Hst	Mg-Hst	Mg-Hst	Mg-Hst
T (°C)	1019	1037	1035	1026	1012	1046	1030	1031	1052	1037	1040	1031	1045
error (σest)	22	22	22	22	22	22	22	22	22	22	22	22	22
P (MPa)	609	686	637	619	556	667	668	687	695	563	578	562	639
error (Max error)	67	75	70	68	61	73	74	76	76	62	64	62	70
ΔNNO	1.06	0.81	0.78	1.01	0.94	0.69	0.80	0.89	1.03	0.78	0.78	0.77	0.77
error (σest)	0.4	0.4	0.4	0.4	0.4	0.4	0.4	0.4	0.4	0.4	0.4	0.4	0.4
H_2Omelt (wt.%)	4.79	4.95	5.12	5.18	5.19	5.21	5.51	5.77	4.23	4.00	4.12	4.17	4.23
error*	0.72	0.74	0.77	0.78	0.78	0.78	0.83	0.87	0.64	0.60	0.62	0.63	0.63

Table 5: Major element compositions of amphibole electron microprobe analyses. Element compositions reported as wt.%. P-T-H_2O-fO_2 estimates calculated using formulations of Ridolfi et al. (2012).

Lithology	BC14-020 Pyrox.	BC14-020 Pyrox.	BC14-020 Pyrox.	BC14-020 Pyrox.	BC14-020 Pyrox.	BC14-020 Pyrox.	BC14-020 Pyrox.	BC14-020 Pyrox.	BC14-020 Pyrox.	BC14-020 Pyrox.	BC14-020 Pyrox.	BC14-020 Pyrox.	BC14-020 Pyrox.
SiO_2	40.07	39.61	39.09	39.79	39.41	39.63	39.72	39.47	39.55	39.61	40.03	39.68	39.65
TiO_2	2.35	2.43	2.42	2.34	2.39	2.44	2.32	2.45	2.42	2.24	2.31	2.34	2.28
Al_2O_3	13.90	13.87	13.96	14.06	14.05	14.19	14.11	14.12	14.15	13.55	13.55	13.77	13.88
Cr_2O_3													
FeO	11.24	11.11	11.25	11.14	11.03	11.62	11.34	11.37	11.25	11.52	11.28	11.36	11.47
MnO	0.16	0.20	0.16	0.17	0.15	0.19	0.19	0.16	0.18	0.17	0.14	0.19	0.20
MgO	14.24	14.10	14.00	14.31	14.25	14.15	14.14	13.96	13.87	14.07	14.22	13.98	13.96
CaO	12.01	12.09	12.24	12.22	12.17	12.17	12.17	12.19	12.16	11.98	12.14	12.19	12.08
Na_2O	2.21	2.24	2.19	2.36	2.23	2.36	2.23	2.28	2.22	2.36	2.29	2.31	2.24
K_2O	1.62	1.59	1.58	1.54	1.55	1.52	1.56	1.55	1.57	1.57	1.54	1.60	1.65
F	0.164	0.177	0.166	0.109	0.204	0.215	0.185	0.184	0.133	0.206	0.149	0.216	0.174
Cl	0.048	0.062	0.048	0.062	0.056	0.068	0.053	0.049	0.049	0.072	0.053	0.064	0.076
Total	98.0	97.5	97.1	98.1	97.5	98.5	98.0	97.8	97.6	97.4	97.7	97.7	97.7
Species	Mg-Hst	Mg-Hst	Mg-Hst	Mg-Hst	Mg-Hst	Mg-Hst	Mg-Hst	Mg-Hst	Mg-Hst	Mg-Hst	Mg-Hst	Mg-Hst	Mg-Hst
T (°C)	1041	1034	1040	1050	1045	1047	1047	1042	1047	1044	1034	1031	1039
error (σest)	22	22	22	22	22	22	22	22	22	22	22	22	22
P (MPa)	615	600	613	638	625	637	640	638	648	657	570	560	599
error (Max error)	68	66	67	70	69	70	70	70	71	72	63	62	66
ΔNNO	0.79	0.80	0.73	0.71	0.76	0.78	0.71	0.76	0.65	0.63	0.79	0.78	0.68
error (σest)	0.4	0.4	0.4	0.4	0.4	0.4	0.4	0.4	0.4	0.4	0.4	0.4	0.4
H_2Omelt (wt.%)	4.28	4.31	4.35	4.40	4.41	4.46	4.47	4.58	4.58	4.72	4.05	4.22	4.24
error*	0.64	0.65	0.65	0.66	0.66	0.67	0.67	0.69	0.69	0.71	0.61	0.63	0.64

Table 5: Major element compositions of amphibole electron microprobe analyses. Element compositions reported as wt.%. P-T-H_2O-fO_2 estimates calculated using formulations of Ridolfi et al. (2012).

Lithology	BC14-020 Pyrox.	BC14-020 Pyrox.	BC14-020 Pyrox.	BC14-020 Pyrox.	BC14-020 Pyrox.	BC14-020 Pyrox.	BC14-020 Pyrox.	BC14-020 Pyrox.	BC14-020 Pyrox.	BC14-020 Pyrox.	BC14-020 Pyrox.	BC14-020 Pyrox.	BC14-020 Pyrox.
SiO_2	40.25	39.58	39.76	39.58	39.67	39.72	40.56	39.61	39.64	40.04	39.42	39.38	40.04
TiO_2	2.30	2.32	2.35	2.37	2.33	2.30	2.31	2.33	2.30	2.39	2.33	2.30	2.31
Al_2O_3	13.49	13.96	13.55	13.98	13.81	13.87	14.30	14.09	13.93	14.00	13.91	13.70	14.06
Cr_2O_3													
FeO	11.15	11.50	11.73	11.41	11.37	11.44	11.64	11.38	11.25	11.45	11.40	11.24	11.38
MnO	0.20	0.17	0.19	0.18	0.18	0.17	0.18	0.17	0.17	0.16	0.19	0.16	0.19
MgO	14.40	13.96	13.82	13.95	14.13	13.99	14.53	14.18	14.08	14.08	13.69	13.82	14.11
CaO	12.14	12.16	11.94	12.21	12.12	12.21	12.17	12.27	12.11	12.33	12.14	12.11	12.15
Na_2O	2.51	2.30	2.31	2.27	2.31	2.29	2.28	2.24	2.27	2.27	2.15	2.14	2.30
K_2O	1.40	1.63	1.54	1.63	1.52	1.58	1.61	1.58	1.57	1.57	1.64	1.56	1.54
F	0.163	0.126	0.141	0.148	0.164	0.177	0.129	0.171	0.117	0.178	0.170	0.162	0.186
Cl	0.062	0.064	0.100	0.065	0.061	0.053	0.074	0.066	0.043	0.063	0.076	0.071	0.043
Total	98.1	97.8	97.4	97.8	97.7	97.8	99.8	98.1	97.5	98.5	97.1	96.6	98.3
Species	Mg-Hst	Mg-Hst	Mg-Hst	Mg-Hst	Mg-Hst	Mg-Hst	Mg-Hst	Mg-Hst	Mg-Hst	Mg-Hst	Mg-Hst	Mg-Hst	Mg-Hst
T (°C)	1038	1031	1042	1028	1043	1039	1040	1037	1046	1040	1040	1040	1037
error (σest)	22	22	22	22	22	22	22	22	22	22	22	22	22
P (MPa)	613	545	623	573	629	600	611	620	635	620	614	633	606
error (Max error)	67	60	69	63	69	66	67	68	70	68	68	70	67
ΔNNO	0.73	0.79	0.69	0.68	0.67	0.75	0.70	0.85	0.75	0.75	0.67	0.63	0.70
error (σest)	0.4	0.4	0.4	0.4	0.4	0.4	0.4	0.4	0.4	0.4	0.4	0.4	0.4
H_2Omelt (wt.%)	4.27	4.27	4.29	4.30	4.33	4.38	4.39	4.40	4.44	4.45	4.50	4.54	4.56
error*	0.64	0.64	0.64	0.64	0.65	0.66	0.66	0.66	0.67	0.67	0.67	0.68	0.68

Table 5: Major element compositions of amphibole electron microprobe analyses. Element compositions reported as wt.%. P-T-H_2O-fO_2 estimates calculated using formulations of Ridolfi et al. (2012).

Lithology	BC14-020 Pyrox.	BC14-020 Pyrox.	BC14-020 Pyrox.	BC14-020 Pyrox.	BC14-020 Pyrox.	BC14-020 Pyrox.	BC14-020 Pyrox.	BC14-020 Pyrox.	BC14-020 Pyrox.	BC14-020 Pyrox.	BC14-020 Pyrox.	BC14-020 Pyrox.	BC14-020 Pyrox.
SiO_2	40.14	39.13	39.52	39.99	40.03	40.28	39.38	39.90	40.15	39.92	39.86	39.94	39.59
TiO_2	2.36	2.29	2.33	2.38	2.32	2.33	2.26	2.30	2.32	2.38	2.37	2.35	2.29
Al_2O_3	14.03	14.06	14.04	13.49	13.72	13.85	13.50	13.65	13.65	13.60	13.67	13.49	14.16
Cr_2O_3													
FeO	11.29	11.31	11.28	11.31	11.30	11.18	10.89	11.25	11.18	11.26	11.14	10.99	11.58
MnO	0.15	0.15	0.14	0.18	0.14	0.18	0.19	0.20	0.22	0.16	0.17	0.19	0.13
MgO	14.05	13.81	13.84	14.20	14.41	14.48	13.99	14.16	14.20	14.23	14.03	14.19	13.96
CaO	12.17	12.17	12.22	11.99	12.02	12.20	12.12	12.11	12.13	12.09	12.20	12.16	12.19
Na_2O	2.28	2.26	2.26	2.32	2.26	2.25	2.22	2.25	2.35	2.18	2.29	2.24	2.26
K_2O	1.56	1.55	1.53	1.62	1.62	1.66	1.62	1.62	1.60	1.60	1.63	1.58	1.72
F	0.186	0.224	0.132	0.127	0.212	0.162	0.149	0.181	0.118	0.203	0.184	0.155	0.096
Cl	0.043	0.056	0.058	0.068	0.065	0.074	0.081	0.079	0.058	0.058	0.059	0.053	0.059
Total	98.3	97.0	97.3	97.7	98.1	98.6	96.4	97.7	98.0	97.7	97.6	97.3	98.0
Species	Mg-Hst	Mg-Hst	Mg-Hst	Mg-Hst	Mg-Hst	Mg-Hst	Mg-Hst	Mg-Hst	Mg-Hst	Mg-Hst	Mg-Hst	Mg-Hst	Mg-Hst
T (°C)	1038	1037	1048	1044	1030	1033	1035	1037	1034	1032	1032	1036	1032
error (σest)	22	22	22	22	22	22	22	22	22	22	22	22	22
P (MPa)	623	620	659	645	553	572	583	583	577	572	567	586	560
error (Max error)	69	68	73	71	61	63	64	64	63	63	62	64	62
ΔNNO	0.72	0.68	0.66	0.63	0.78	0.87	0.84	0.74	0.78	0.74	0.81	0.68	0.76
error (σest)	0.4	0.4	0.4	0.4	0.4	0.4	0.4	0.4	0.4	0.4	0.4	0.4	0.4
H_2Omelt (wt.%)	4.62	4.63	4.64	4.74	3.92	4.03	4.07	4.14	4.14	4.14	4.15	4.16	4.17
error*	0.69	0.69	0.70	0.71	0.59	0.60	0.61	0.62	0.62	0.62	0.62	0.62	0.63

Table 5: Major element compositions of amphibole electron microprobe analyses. Element compositions reported as wt.%. P-T-H_2O-fO_2 estimates calculated using formulations of Ridolfi et al. (2012).

Lithology	BC14-020 Pyrox.	BC14-020 Pyrox.	BC14-020 Pyrox.	BC14-020 Pyrox.	BC14-020 Pyrox.	BC14-020 Pyrox.	BC14-020 Pyrox.	BC14-020 Pyrox.	BC14-020 Pyrox.	BC14-020 Pyrox.	BC14-020 Pyrox.	BC14-020 Pyrox.	BC14-020 Pyrox.
SiO_2	40.17	39.39	39.87	39.25	39.93	39.53	40.16	40.38	39.46	38.93	42.68	39.95	39.32
TiO_2	2.35	2.39	2.31	2.37	2.34	2.38	2.34	2.35	2.33	2.32	2.31	2.32	2.30
Al_2O_3	13.63	14.02	13.77	14.03	14.18	14.23	14.19	13.66	14.10	14.12	15.01	13.65	14.00
Cr_2O_3													
FeO	11.06	11.30	11.12	11.21	11.38	11.29	11.12	11.53	11.23	11.43	11.18	11.39	11.29
MnO	0.20	0.19	0.17	0.15	0.19	0.16	0.18	0.19	0.17	0.21	0.15	0.17	0.17
MgO	14.14	13.82	14.20	13.93	14.06	14.00	14.19	13.72	13.75	13.50	15.43	14.10	13.85
CaO	12.19	12.19	12.13	12.29	12.00	12.29	12.02	11.90	12.20	12.04	11.99	12.10	12.16
Na_2O	2.19	2.23	2.26	2.15	2.29	2.17	2.39	2.32	2.16	2.10	2.59	2.36	2.27
K_2O	1.64	1.71	1.58	1.68	1.68	1.67	1.60	1.59	1.67	1.69	1.58	1.58	1.71
F	0.184	0.194	0.140	0.143	0.196	0.147	0.173	0.133	0.199	0.163	0.169	0.221	0.159
Cl	0.064	0.051	0.044	0.057	0.058	0.031	0.059	0.068	0.049	0.064	0.060	0.050	0.056
Total	97.8	97.5	97.6	97.3	98.3	97.9	98.4	97.8	97.3	96.6	103.2	97.9	97.3
Species	Mg-Hst	Mg-Hst	Mg-Hst	Mg-Hst	Mg-Hst	Mg-Hst	Mg-Hst	Mg-Hst	Mg-Hst	Mg-Hst	Mg-Hst	Mg-Hst	Mg-Hst
T (°C)	1045	1031	1045	1037	1049	1039	1048	1039	1021	1044	1046	1028	1034
error (σest)	22	22	22	22	22	22	22	22	22	22	22	22	22
P (MPa)	648	573	646	593	648	642	663	638	580	658	682	632	575
error (Max error)	71	63	71	65	71	71	73	70	64	72	75	70	63
ΔNNO	0.69	0.73	0.62	0.77	0.67	0.72	0.68	0.72	0.60	0.62	0.60	0.98	0.73
error (σest)	0.4	0.4	0.4	0.4	0.4	0.4	0.4	0.4	0.4	0.4	0.4	0.4	0.4
H_2Omelt (wt.%)	4.22	4.24	4.26	4.31	4.33	4.36	4.47	4.51	4.52	4.60	4.61	4.66	4.16
error*	0.63	0.64	0.64	0.65	0.65	0.65	0.67	0.68	0.68	0.69	0.69	0.70	0.62

Table 5: Major element compositions of amphibole electron microprobe analyses. Element compositions reported as wt.%. P-T-H_2O-fO_2 estimates calculated using formulations of Ridolfi et al. (2012).

	BC14-020	BC14-020	BC14-020	BC14-020	BC14-020	BC14-020	SA24	SA24	SA310_35	SA310_36
Lithology	Pyrox.	Pyrox.	Pyrox.	Pyrox.	Pyrox.	Pyrox.	Pyrox.	Pyrox.	Pyrox.	Pyrox.
SiO_2	39.68	39.23	39.68	39.47	39.80	39.67	40.34	40.68	40.45	40.63
TiO_2	2.33	2.29	2.42	2.37	2.24	2.35	1.89	1.85	2.00	1.90
Al_2O_3	13.63	13.99	14.07	13.82	13.91	14.16	14.04	14.03	13.33	13.25
Cr_2O_3										
FeO	11.72	11.35	11.39	11.30	12.03	11.38	10.56	9.98	9.84	9.41
MnO	0.19	0.18	0.13	0.20	0.21	0.16			0.04	0.13
MgO	13.74	13.70	14.06	13.80	13.58	13.93	14.40	14.45	15.04	14.98
CaO	12.10	12.08	12.22	12.22	11.71	12.01	11.83	11.86	12.25	11.97
Na_2O	2.28	2.19	2.38	2.30	2.36	2.34	2.30	2.25	2.02	2.10
K_2O	1.56	1.69	1.55	1.55	1.57	1.58	1.63	1.60	1.33	1.29
F	0.098	0.188	0.179	0.138	0.201	0.168			0.013	0.030
Cl	0.067	0.061	0.043	0.042	0.088	0.054	0.800	0.800	0.800	0.800
Total	97.4	97.0	98.1	97.2	97.7	97.8	97.8	97.5	97.1	96.5
Species	Mg-Hst	Mg-Hst	Mg-Hst	Mg-Hst	Mg-Hst	Mg-Hst	Mg-Hst	Mg-Hst	Mg-Hst	Mg-Hst
T (°C)	1046	1033	1043	1045	1042	1028	1041	1029	1024	1024
error (σest)	22	22	22	22	22	22	22	22	22	22
P (MPa)	645	584	650	633	618	616	651	630	632	534
error (Max error)	71	64	72	70	68	68	72	69	69	59
ΔNNO	0.66	0.64	0.64	0.66	0.61	0.65	0.67	0.93	0.93	1.15
error (σest)	0.4	0.4	0.4	0.4	0.4	0.4	0.4	0.4	0.4	0.4
H_2Omelt (wt.%)	4.20	4.38	4.40	4.43	4.50	4.57	4.57	4.58	4.89	4.84
error*	0.63	0.66	0.66	0.66	0.68	0.68	0.69	0.69	0.73	0.73

Table 5: Major element compositions of amphibole electron microprobe analyses. Element compositions reported as wt.%. P-T-H_2O-fO_2 estimates calculated using formulations of Ridolfi et al. (2012).

	BC14038-Plag4	BC14038-Plag4	BC14038-Plag4	BC14038-Plag5	BC14038-Plag5	BC14038-Plag5	BC14038-Plag5	BC14038-Plag6	BC14038-Plag6	BC14038-Plag6	BC14038-Plag6	BC14039-Plag4
SiO_2	43.19	43.07	43.29	42.83	42.97	43.14	43.60	43.51	43.43	43.71	43.85	48.45
TiO_2	0.00	0.01	0.03	0.01	0.01	0.01	0.01	0.01	0.02	0.01	0.02	0.03
Al_2O_3	33.06	33.11	33.24	33.04	33.24	33.32	33.25	32.95	33.36	33.45	33.32	29.79
Cr_2O_3												
FeO	0.59	0.56	0.54	0.52	0.47	0.51	0.51	0.54	0.52	0.49	0.51	0.80
MgO	0.06	0.06	0.05	0.06	0.04	0.05	0.04	0.03	0.04	0.01	0.03	0.11
CaO	18.58	18.79	18.73	18.71	18.60	18.60	18.61	18.35	18.50	18.35	18.55	14.47
BaO												
Na_2O	0.63	0.68	0.64	0.77	0.78	0.72	0.85	0.84	0.87	0.80	0.87	2.96
K_2O	0.06	0.06	0.05	0.05	0.07	0.06	0.06	0.05	0.05	0.05	0.05	0.22
P_2O_5												
Cl												
Total	96.2	96.3	96.6	96.0	96.2	96.4	96.9	96.3	96.8	96.9	97.2	96.8

Table 6: Major element compositions of plagioclase electron microprobe analyses. Element compositions reported as wt.%.

	BC14039-Plag4	SA23-Plag6	BC14004-Plag6	BC14004-Plag6	BC14004-Plag6	BC14004-Plag6	BC14015-Plag11	BC14015-Plag11	BC14015-Plag11	BC14015-Plag11	BC14015-Plag12	BC14015-Plag12
SiO_2	51.96	50.22	57.73	51.67	49.92	52.74	44.15	45.14	43.66	45.23	42.91	42.92
TiO_2	0.04	0.03	0.06	0.04	0.04	0.03	0.03	0.01	0.01	0.01	0.00	0.00
Al_2O_3	27.79	27.82	23.86	27.91	29.23	28.40	31.98	31.75	32.88	32.08	33.22	33.68
Cr_2O_3												
FeO	0.69	0.48	0.41	0.58	0.61	0.60	0.52	0.52	0.57	0.64	0.58	0.50
MgO	0.08	0.06	0.04	0.04	0.05	0.07	0.05	0.03	0.05	0.05	0.05	0.02
CaO	11.80	12.00	6.46	11.80	13.47	11.53	17.36	17.02	18.10	16.91	18.51	18.87
BaO												
Na_2O	4.40	4.07	6.84	4.43	3.64	4.85	1.38	1.70	1.02	1.77	0.84	0.68
K_2O	0.45	0.43	0.91	0.27	0.21	0.34	0.09	0.08	0.06	0.08	0.04	0.05
P_2O_5												
Cl												
Total	97.2	95.1	96.3	96.7	97.2	98.6	95.6	96.3	96.3	96.8	96.2	96.7

Table 6: Major element compositions of plagioclase electron microprobe analyses. Element compositions reported as wt.%.

	BC14015-Plag12	BC14015-Plag12	BC14015-Plag13	BC14015-Plag13	BC14015-Plag13	BC14015-Plag2	BC14015-Plag2	BC14015-Plag2	BC14015-Plag2	BC14015-Plag4	BC14015-Plag4	BC14015-Plag4
SiO_2	43.48	43.50	44.45	43.13	43.77	48.04	46.19	49.57	47.91	43.45	43.44	44.04
TiO_2	0.02	0.01	0.02	0.01	0.03	0.03	0.03	0.03	0.03	0.00	0.01	0.01
Al_2O_3	33.30	33.61	32.08	33.29	33.01	29.54	30.96	28.99	30.05	32.24	32.45	32.43
Cr_2O_3												
FeO	0.56	0.51	0.59	0.56	0.40	0.69	0.66	0.66	0.57	0.55	0.65	0.51
MgO	0.04	0.06	0.03	0.03	0.04	0.04	0.06	0.05	0.05	0.04	0.03	0.05
CaO	18.58	18.43	17.64	18.92	18.56	14.57	16.41	13.52	15.11	18.18	18.31	18.37
BaO												
Na_2O	0.83	0.79	1.41	0.68	1.02	3.05	2.16	3.62	2.89	1.07	1.04	0.94
K_2O	0.04	0.06	0.07	0.03	0.06	0.14	0.09	0.18	0.14	0.04	0.05	0.04
P_2O_5												
Cl												
Total	96.9	97.0	96.3	96.6	96.9	96.1	96.6	96.6	96.7	95.6	96.0	96.4

Table 6: Major element compositions of plagioclase electron microprobe analyses. Element compositions reported as wt.%.

	BC14015-Plag4	BC14015-Plag5	BC14015-Plag5	BC14015-Plag5	BC14015-Plag5	BC14015-Plag6	BC14015-Plag6	BC14015-Plag6	BC14015-Plag6	BC14015-Plag8	BC14015-Plag8	BC14015-Plag8
SiO_2	44.02	44.49	43.82	43.73	44.02	42.62	46.76	45.99	43.50	44.01	44.85	47.31
TiO_2	0.00	0.02	0.02	0.00	0.01	0.01	0.02	0.03	0.02	0.02	0.02	0.04
Al_2O_3	32.78	31.94	32.84	32.76	33.26	33.36	30.72	31.51	33.57	32.76	32.24	30.51
Cr_2O_3												
FeO	0.57	0.58	0.49	0.52	0.63	0.52	0.61	0.62	0.62	0.59	0.58	0.63
MgO	0.02	0.02	0.01	0.04	0.03	0.06	0.05	0.06	0.04	0.02	0.02	0.02
CaO	18.33	17.51	18.29	18.38	18.16	18.60	15.77	16.34	18.65	17.88	17.13	15.44
BaO												
Na_2O	0.88	1.45	0.96	1.00	1.06	0.74	2.32	2.00	0.81	1.17	1.60	2.52
K_2O	0.04	0.07	0.05	0.04	0.05	0.05	0.10	0.10	0.05	0.07	0.09	0.18
P_2O_5												
Cl												
Total	96.6	96.1	96.5	96.5	97.2	96.0	96.3	96.6	97.3	96.5	96.5	96.6

Table 6: Major element compositions of plagioclase electron microprobe analyses. Element compositions reported as wt.%.

	BC14015-Plag8	SA88301-Plag4	SA88301-Plag4	SA88301-Plag4	SA88301-Plag4	BC14020-Plag1	BC14020-Plag1	BC14020-Plag1	BC14020-Plag1	BC14020-Plag2	BC14020-Plag2	BC14020-Plag2
SiO_2	45.18	44.29	44.36	44.58	43.83	43.90	43.89	44.24	44.53	43.90	44.13	44.52
TiO_2	0.01	0.01	0.02	0.01	0.00	0.01	0.01	0.01	0.02	0.02	0.01	0.01
Al_2O_3	32.40	32.63	32.64	32.62	33.20	32.08	32.77	32.49	32.17	32.65	32.81	33.83
Cr_2O_3												
FeO	0.65	0.66	0.56	0.54	0.60	0.62	0.59	0.58	0.58	0.60	0.51	0.63
MgO	0.04	0.03	0.04	0.05	0.03	0.05	0.04	0.04	0.06	0.05	0.03	0.06
CaO	17.12	17.60	17.92	17.70	18.26	18.05	17.82	17.81	17.51	17.90	18.09	18.39
BaO												
Na_2O	1.72	1.22	1.11	1.24	0.92	1.20	1.20	1.24	1.54	1.10	1.02	1.02
K_2O	0.08	0.10	0.08	0.06	0.06	0.07	0.06	0.08	0.15	0.07	0.06	0.08
P_2O_5												
Cl												
Total	97.2	96.5	96.7	96.8	96.9	96.0	96.4	96.5	96.6	96.3	96.7	98.5

Table 6: Major element compositions of plagioclase electron microprobe analyses. Element compositions reported as wt.%.

	BC14020-Plag6	BC14020-Plag8	BC14020-Plag8	BC14020-Plag8	BC14023-Plag1	BC14023-Plag1	BC14023-Plag1	BC14023-Plag1	BC14023-Plag2	BC14023-Plag2	BC14023-Plag2	BC14023-Plag2
SiO_2	56.11	43.16	45.85	44.09	46.13	45.18	45.49	45.59	47.25	47.62	48.44	48.37
TiO_2	0.08	0.01	0.03	0.01	0.01	0.02	0.02	0.00	0.85	0.84	0.86	0.83
Al_2O_3	23.39	33.29	31.53	33.27	30.68	31.37	31.92	31.89	23.87	23.63	23.69	23.67
Cr_2O_3												
FeO	0.54	0.47	0.53	0.41	0.49	0.53	0.55	0.54	0.25	0.28	0.29	0.25
MgO	0.05	0.01	0.07	0.02	0.06	0.13	0.05	0.02	0.01	0.01	0.01	0.00
CaO	6.99	18.76	16.63	18.58	15.37	16.85	16.95	17.05	13.48	13.74	13.84	14.21
BaO												
Na_2O	5.93	0.62	1.83	0.81	2.20	1.65	1.62	1.61	5.29	5.87	5.50	5.39
K_2O	2.08	0.03	0.14	0.04	0.82	0.16	0.16	0.14	6.43	6.66	6.44	6.46
P_2O_5												
Cl												
Total	95.2	96.4	96.6	97.3	95.8	95.9	96.8	96.9	97.4	98.6	99.1	99.2

Table 6: Major element compositions of plagioclase electron microprobe analyses. Element compositions reported as wt.%.

	SA12X01 1-Plag2	SA12X01 1-Plag2	SA12X01 1-Plag2	SA12X01 1-Plag3	SA12X01 1-Plag3	SA12X01 1-Plag3	SA12X01 1-Plag4	SA12X01 1-Plag4	SA12X01 1-Plag4	SA12X01 1-Plag4	BC14015 -Plag14	BC14015 -Plag14
SiO_2	45.77	46.80	46.61	47.23	46.80	47.74	43.78	43.20	43.40	43.54	45.05	46.35
TiO_2	1.30	1.02	1.12	1.00	1.07	0.98	0.02	0.01	0.01	0.00	0.01	0.02
Al_2O_3	7.77	6.79	7.16	6.39	6.79	6.19	33.23	33.65	33.70	33.65	31.45	31.01
Cr_2O_3												
FeO	7.79	7.40	7.50	7.05	7.28	6.89	0.54	0.50	0.50	0.48	0.74	0.76
MgO	12.36	12.88	12.78	13.19	13.20	13.46	0.03	0.05	0.05	0.04	0.06	0.02
CaO	23.15	23.24	23.31	23.28	23.16	23.22	18.16	18.73	18.70	18.78	16.78	16.08
BaO												
Na_2O	0.25	0.31	0.29	0.31	0.30	0.32	0.95	0.70	0.70	0.76	1.89	2.18
K_2O	0.00	0.01	0.00	0.01	0.01	0.00	0.05	0.04	0.03	0.04	0.06	0.10
P_2O_5												
Cl												
Total	98.4	98.4	98.8	98.4	98.6	98.8	96.8	96.9	97.1	97.3	96.0	96.5

Table 6: Major element compositions of plagioclase electron microprobe analyses. Element compositions reported as wt.%.

	BC14015-Plag3	BC14015-Plag3	BC14015-Plag3	BC14015-Plag3	BC14015-Plag7	BC14015-Plag7	BC14015-Plag9	BC14020-Plag3	BC14020-Plag3	BC14020-Plag4	BC14020-Plag4	BC14020-Plag5
SiO_2	56.93	49.38	51.08	44.38	47.04	45.25	50.95	43.32	43.80	43.98	45.28	53.70
TiO_2	0.09	0.05	0.06	0.00	0.01	0.01	0.05	0.01	0.01	0.01	0.02	0.05
Al_2O_3	23.51	28.35	27.51	32.38	30.54	32.31	28.23	33.08	33.14	32.42	32.40	25.17
Cr_2O_3												
FeO	0.64	0.74	0.85	0.60	0.61	0.76	0.91	0.48	0.47	0.52	0.48	0.61
MgO	0.07	0.04	0.04	0.03	0.05	0.05	0.03	0.04	0.03	0.04	0.03	0.05
CaO	6.20	13.11	12.01	17.88	15.44	16.98	12.32	18.55	18.46	18.19	17.43	9.23
BaO												
Na_2O	7.06	3.65	4.25	1.33	2.56	1.85	4.22	0.77	0.88	1.06	1.45	5.30
K_2O	0.88	0.20	0.25	0.04	0.10	0.07	0.21	0.04	0.06	0.05	0.09	1.02
P_2O_5												
Cl												
Total	95.4	95.5	96.0	96.6	96.3	97.3	96.9	96.3	96.9	96.3	97.2	95.1

Table 6: Major element compositions of plagioclase electron microprobe analyses. Element compositions reported as wt.%.

	BC14020-Plag9	BC14020-Plag9	BC14039-Plag1	BC14039-Plag2	BC14039-Plag3	BC14039-Plag3	SA12X01-Plag1	SA12X01-Plag1	SA12X01-Plag1	SA12X01-Plag1	SA12X01-Plag2	SA12X01-Plag2
SiO_2	54.19	54.33	55.24	56.76	55.83	57.54	49.89	55.72	50.37	54.25	51.39	50.64
TiO_2	0.12	0.06	0.15	0.10	0.09	0.13	0.03	0.05	0.05	0.05	0.05	0.05
Al_2O_3	24.94	25.63	23.60	23.79	23.91	22.90	28.08	24.61	28.03	25.85	26.40	27.61
Cr_2O_3												
FeO	0.91	0.69	1.18	0.96	0.98	1.01	0.80	0.47	0.79	0.69	0.89	0.94
MgO	0.15	0.08	0.26	0.13	0.13	0.13	0.07	0.04	0.05	0.05	0.07	0.10
CaO	8.97	9.57	7.98	7.60	8.16	6.89	12.68	8.08	12.47	9.64	11.15	12.22
BaO												
Na_2O	5.29	5.11	5.77	6.12	5.75	6.30	3.62	5.71	3.91	5.05	4.53	3.95
K_2O	1.43	1.12	1.52	1.45	1.25	1.57	0.50	1.54	0.55	1.03	0.77	0.55
P_2O_5												
Cl												
Total	96.0	96.6	95.7	96.9	96.1	96.5	95.7	96.2	96.2	96.6	95.2	96.0

Table 6: Major element compositions of plagioclase electron microprobe analyses. Element compositions reported as wt.%.

	SA12X01-Plag2	SA12X01-Plag2	SA12X01-Plag3	SA12X01-Plag3	SA12X01-Plag5	SA12X01-Plag5	SA12X01-Plag5	SA12X01-Plag6	SA12X01-Plag6	SA12X01-Plag6	SA12X01-Plag6	SA12X01-Plag7
SiO_2	50.79	50.23	53.71	52.21	50.20	51.83	51.49	49.03	49.32	49.78	50.47	49.39
TiO_2	0.05	0.04	0.06	0.05	0.04	0.04	0.05	0.04	0.03	0.04	0.03	0.05
Al_2O_3	27.50	28.09	25.58	26.51	27.89	26.91	27.23	28.86	28.82	28.67	28.14	28.67
Cr_2O_3												
FeO	1.00	0.97	0.60	0.87	0.72	0.73	0.74	0.72	0.77	0.73	0.72	0.85
MgO	0.08	0.08	0.06	0.05	0.08	0.07	0.06	0.05	0.06	0.07	0.05	0.07
CaO	12.10	12.59	9.60	10.82	12.71	11.24	11.54	13.46	13.49	13.03	12.52	13.37
BaO												
Na_2O	4.06	3.73	4.97	4.58	3.76	4.45	4.30	3.44	3.27	3.49	3.86	3.34
K_2O	0.60	0.54	1.13	0.80	0.55	0.70	0.68	0.45	0.43	0.50	0.58	0.44
P_2O_5												
Cl												
Total	96.2	96.3	95.7	95.9	95.9	96.0	96.1	96.0	96.2	96.3	96.4	96.2

Table 6: Major element compositions of plagioclase electron microprobe analyses. Element compositions reported as wt.%.

	SA12X01-Plag7	SA12X01-Plag8	SA12X01-Plag8	SA24-Plag1	SA24-Plag2	SA24-Plag3	SA24-Plag4	SA24-Plag5	SA24-Plag5	SA24-Plag6	SA24-Plag6	SA24-Plag7
SiO_2	55.08	55.52	49.63	55.92	49.81	58.50	53.41	49.14	53.41	49.32	50.87	48.91
TiO_2	0.07	0.05	0.02	0.05	0.03	0.06	0.04	0.04	0.02	0.01	0.01	0.02
Al_2O_3	25.12	25.26	29.18	24.01	28.08	22.45	25.65	28.79	25.90	28.47	27.69	28.84
Cr_2O_3												
FeO	0.57	0.54	0.83	0.43	0.45	0.34	0.43	0.48	0.48	0.57	0.46	0.51
MgO	0.04	0.03	0.09	0.07	0.04	0.06	0.05	0.05	0.04	0.05	0.08	0.10
CaO	8.75	8.41	13.34	7.54	12.49	5.77	9.68	13.36	9.86	12.96	11.91	13.35
BaO												
Na_2O	5.43	5.56	3.33	5.78	3.91	6.90	5.16	3.29	5.22	3.45	4.08	3.16
K_2O	1.36	1.38	0.43	1.47	0.29	2.03	0.71	0.25	0.55	0.28	0.45	0.30
P_2O_5												
Cl												
Total	96.4	96.7	96.8	95.3	95.1	96.1	95.1	95.4	95.5	95.1	95.5	95.2

Table 6: Major element compositions of plagioclase electron microprobe analyses. Element compositions reported as wt.%.

	SA24-Plag7	SA24-Plag8	SA24-Plag8	SA24-Plag8	SA24-Plag8	SA24-Plag9	SA24-Plag9	SA26-Plag1	SA26-Plag1	SA26-Plag1	SA26-Plag1	SA26-Plag2
SiO_2	54.64	53.70	53.86	48.61	48.57	46.86	49.71	58.14	56.31	57.15	56.51	54.37
TiO_2	0.05	0.05	0.04	0.02	0.04	0.02	0.02	0.28	0.34	0.10	0.08	0.07
Al_2O_3	24.95	25.42	25.23	28.79	29.29	30.19	28.07	20.80	21.07	23.30	24.44	24.73
Cr_2O_3												
FeO	0.53	0.51	0.46	0.53	0.45	0.54	0.51	1.60	2.62	0.78	0.86	1.14
MgO	0.07	0.07	0.06	0.06	0.05	0.05	0.05	0.25	0.71	0.08	0.08	0.10
CaO	8.81	9.10	9.39	13.41	13.81	14.69	12.75	4.71	6.31	6.68	7.76	8.50
BaO												
Na_2O	5.57	5.18	5.26	3.45	3.23	2.49	3.63	5.52	5.67	5.88	5.95	5.04
K_2O	0.90	1.11	0.85	0.34	0.23	0.19	0.31	4.31	2.68	2.31	1.52	1.61
P_2O_5												
Cl												
Total	95.5	95.1	95.1	95.2	95.7	95.0	95.1	95.6	95.7	96.3	97.2	95.6

Table 6: Major element compositions of plagioclase electron microprobe analyses. Element compositions reported as wt.%.

	SA26-Plag2	SA26-Plag2	SA26-Plag2	SA88301-Plag1	SA88301-Plag1	SA88301-Plag1	SA88301-Plag2	SA88301-Plag3	SA88301-Plag3	SA88301-Plag3	SA88301-Plag5	SA88301-Plag5
SiO_2	57.31	55.93	54.90	49.39	53.85	47.45	49.92	54.43	52.28	55.02	48.96	46.75
TiO_2	0.10	0.12	0.14	0.04	0.08	0.03	0.05	0.08	0.06	0.08	0.02	0.01
Al_2O_3	23.26	24.11	24.46	29.34	26.13	30.60	29.08	24.51	27.58	25.78	29.54	30.87
Cr_2O_3												
FeO	0.74	1.09	1.34	0.73	0.80	0.87	0.84	0.74	0.68	0.81	0.70	0.69
MgO	0.05	0.14	0.21	0.10	0.05	0.09	0.07	0.06	0.07	0.08	0.09	0.10
CaO	6.45	7.66	8.65	13.74	9.97	15.35	13.61	8.41	11.54	9.33	14.16	16.11
BaO												
Na_2O	6.22	5.69	5.43	3.14	5.02	2.51	3.61	5.50	4.50	5.07	3.05	2.22
K_2O	2.32	1.74	1.38	0.40	1.03	0.26	0.34	1.30	0.63	1.53	0.35	0.17
P_2O_5												
Cl												
Total	96.5	96.5	96.5	96.9	96.9	97.2	97.5	95.0	97.3	97.7	96.9	96.9

Table 6: Major element compositions of plagioclase electron microprobe analyses. Element compositions reported as wt.%.

	SA88301 -Plag5	SA88301 -Plag6	SA88301 -Plag6	SA88301 -Plag6	B10_Plag1 -1	B10_Plag1 -2	B10_Plag1 -3	B10_Plag1 -4	B10_Plag1 -5	B10_Plag2 -1	B10_Plag2 -1	B10_Plag2 -1
SiO_2	48.30	48.26	47.70	50.33	45.83	45.61	45.93	46.65	46.34	45.53	45.07	45.79
TiO_2	0.02	0.03	0.02	0.05	0.02	0.02	0.00	0.02	-0.01	0.04	0.01	-0.01
Al_2O_3	30.03	29.15	29.79	28.86	35.81	35.37	35.91	36.73	36.72	34.54	35.58	35.65
Cr_2O_3					0.01	0.02	-0.01	-0.01	0.02	0.01	0.02	0.01
FeO	0.82	0.70	0.71	0.75	0.61	0.59	0.56	0.63	0.58	0.72	0.52	0.51
MgO	0.11	0.13	0.10	0.09	0.03	0.03	0.03	0.01	-0.01	0.10	-0.01	0.04
CaO	14.96	14.20	14.80	13.42	18.20	18.28	18.39	18.90	18.79	17.79	18.35	18.19
BaO												
Na_2O	2.68	2.92	2.72	3.53	0.98	1.02	1.04	0.74	0.79	1.10	0.96	1.00
K_2O	0.24	0.31	0.27	0.41	0.07	0.08	0.08	0.05	0.07	0.31	0.06	0.09
P_2O_5					0.38	0.33	0.47	0.44	0.44	0.53	0.39	0.37
Cl					0.01	0.01	0.00	0.00	-0.01	0.01	0.00	0.00
Total	97.2	95.7	96.1	97.4	102.0	101.4	102.4	104.2	103.8	100.7	101.0	101.7

Table 6: Major element compositions of plagioclase electron microprobe analyses. Element compositions reported as wt.%.

	B10_Plag 2-1	B10_Plag 2-1	B10_Plag 3-1	B10_Plag 3-1	B10_Plag 3-1	B10_Plag 3-1	B10_Plag 3-1	B10_Plag 3-1	B10_Plag 3-1	B10_Plag 3-1	B10_Plag 3-1	B10_Plag 3-1
SiO_2	45.01	45.40	45.91	45.70	45.61	45.59	45.30	45.24	44.34	45.60	45.79	45.65
TiO_2	-0.01	0.01	0.02	0.00	0.01	0.01	0.01	0.01	0.01	0.00	0.02	0.01
Al_2O_3	35.48	35.56	35.11	35.63	33.78	35.93	35.07	35.59	35.56	35.99	35.15	36.02
Cr_2O_3	0.00	0.00	-0.02	-0.01	0.00	0.01	0.02	0.00	0.00	0.00	-0.01	-0.01
FeO	0.55	0.58	0.52	0.54	0.58	0.53	0.58	0.55	0.56	0.51	0.56	0.61
MgO	-0.01	0.03	0.03	-0.01	0.04	0.02	-0.01	0.02	0.04	0.02	0.00	0.02
CaO	18.74	18.32	18.05	18.09	17.57	18.54	18.33	18.44	18.22	18.57	18.17	18.18
BaO												
Na_2O	0.89	0.93	1.01	1.03	1.01	0.80	0.90	0.86	0.90	0.80	1.02	0.97
K_2O	0.05	0.07	0.09	0.07	0.24	0.05	0.06	0.06	0.05	0.05	0.07	0.06
P_2O_5	0.36	0.48	0.27	0.32	0.30	0.38	0.42	0.34	0.44	0.32	0.38	0.43
Cl	0.01	0.00	0.01	-0.01	0.08	0.00	0.00	0.01	0.01	0.00	0.00	0.00
Total	101.1	101.4	101.0	101.4	99.2	101.9	100.7	101.1	100.1	101.9	101.2	102.0

Table 6: Major element compositions of plagioclase electron microprobe analyses. Element compositions reported as wt.%.

	B10_Plag 4-1	B10_Plag 4-1	B10_Plag 4-1	B10_Plag 4-1	B10_Plag 4-1	B10_Plag 5-1	B10_Plag 5-1	B10_Plag 5-1	B10_Plag 5-1	B10_Plag 5-1	B10_Plag 5-1	B25_Plag 1-1
SiO_2	44.25	44.83	45.53	45.03	45.21	46.02	45.86	45.45	45.21	40.51	44.09	45.84
TiO_2	0.01	0.02	0.01	0.01	0.03	0.01	0.01	0.01	0.00	0.07	0.01	0.03
Al_2O_3	35.00	35.20	35.19	34.78	34.67	35.72	35.82	35.50	35.23	29.55	35.59	34.59
Cr_2O_3	0.01	0.01	0.00	0.00	-0.01	0.00	0.01	-0.01	0.01	0.00	-0.01	0.01
FeO	0.52	0.59	0.59	0.59	0.54	0.60	0.54	0.52	0.51	0.77	0.51	0.67
MgO	0.01	0.03	0.02	-0.01	0.05	0.00	0.00	0.02	0.01	0.17	0.02	0.05
CaO	18.58	18.50	18.32	18.22	18.00	18.59	18.71	18.50	18.28	15.79	18.85	17.78
BaO												
Na_2O	0.81	0.91	0.97	1.05	1.14	0.89	0.86	0.88	1.00	1.06	0.80	1.17
K_2O	0.06	0.06	0.06	0.07	0.08	0.06	0.07	0.06	0.08	0.24	0.05	0.12
P_2O_5	0.41	0.44	0.29	0.36	0.33	0.44	0.39	0.51	0.39	0.37	0.31	0.31
Cl	0.00	-0.01	0.01	0.00	0.02	0.01	0.02	0.01	0.01	0.06	0.00	-0.01
Total	99.7	100.6	101.0	100.1	100.1	102.3	102.3	101.5	100.7	88.6	100.2	100.6

Table 6: Major element compositions of plagioclase electron microprobe analyses. Element compositions reported as wt.%.

	B25_Plag 1-2	B25_Plag 1-3	B25_Plag 1-4	B25_Plag 1-5	B25_Plag 1-6	B25_Plag 1-7	B25_Plag 1-8	B25_Plag 1-9	B25_Plag 2-1	B25_Plag 2-2	B25_Plag 2-3	B25_Plag 2-4
SiO_2	44.43	45.05	44.86	45.25	44.61	44.49	44.53	45.65	48.65	47.77	48.60	47.61
TiO_2	0.01	0.00	0.03	0.03	0.01	0.01	0.02	0.04	0.05	0.01	0.02	0.03
Al_2O_3	33.61	34.12	33.93	34.69	33.81	34.26	34.32	33.61	29.40	31.59	31.94	31.56
Cr_2O_3	0.00	-0.01	-0.01	-0.01	0.00	0.00	0.02	0.02	0.01	0.00	0.00	0.01
FeO	0.69	0.70	0.65	0.55	0.57	0.58	0.52	0.68	0.79	0.80	0.78	0.84
MgO	0.08	0.05	0.07	0.07	0.05	0.05	0.05	0.06	0.10	0.07	0.09	0.11
CaO	17.51	17.71	17.91	18.07	17.75	18.16	18.13	17.30	13.40	15.16	15.31	15.38
BaO												
Na_2O	1.25	1.18	1.18	1.05	1.14	1.07	1.01	1.45	3.30	2.45	2.41	2.48
K_2O	0.10	0.11	0.13	0.10	0.10	0.10	0.10	0.15	0.57	0.33	0.36	0.36
P_2O_5	0.36	0.30	0.41	0.38	0.31	0.39	0.28	0.29	0.28	0.32	0.33	0.28
Cl	0.01	0.00	0.01	0.01	0.01	0.01	0.00	0.01	0.02	0.01	0.01	0.01
Total	98.1	99.2	99.2	100.2	98.4	99.1	99.0	99.3	96.5	98.5	99.9	98.7

Table 6: Major element compositions of plagioclase electron microprobe analyses. Element compositions reported as wt.%.

	B25_Plag 3-1	B25_Plag 3-2	B25_Plag 3-3	B25_Plag 3-4	B25_Plag 3-5	B25_Plag 3-6	B25_Plag 3-7	B25_Plag 4-1	B25_Plag 4-2	B25_Plag 4-3	B25_Plag 4-4	B25_Plag 4-5
SiO_2	47.00	45.55	47.69	48.88	47.78	49.13	44.24	53.97	47.59	46.85	48.61	48.40
TiO_2	0.04	0.06	0.04	0.05	0.04	0.03	0.03	0.10	0.04	0.04	0.04	0.04
Al_2O_3	31.64	32.22	31.42	31.32	31.70	31.19	32.40	27.92	30.86	31.28	31.83	32.27
Cr_2O_3	0.00	0.00	-0.01	0.00	0.00	0.01	0.00	0.02	0.00	-0.01	0.01	-0.01
FeO	0.68	0.67	0.76	0.77	0.80	0.72	0.68	0.90	0.80	0.77	0.79	0.79
MgO	0.09	0.05	0.11	0.05	0.12	0.09	0.02	0.09	0.07	0.11	0.08	0.09
CaO	15.22	16.23	15.19	14.55	15.49	14.58	17.00	10.10	14.74	15.21	14.72	15.41
BaO												
Na_2O	2.44	1.98	2.54	2.71	2.28	2.71	1.57	4.50	2.65	2.40	2.69	2.41
K_2O	0.37	0.20	0.31	0.36	0.40	0.41	0.16	1.44	0.32	0.33	0.36	0.32
P_2O_5	0.30	0.36	0.30	0.38	0.31	0.39	0.32	0.25	0.35	0.34	0.37	0.28
Cl	0.01	0.00	0.01	0.01	0.04	0.02	0.01	0.02	0.01	0.00	0.01	0.02
Total	97.8	97.3	98.4	99.1	99.0	99.3	96.5	99.3	97.5	97.3	99.5	100.0

Table 6: Major element compositions of plagioclase electron microprobe analyses. Element compositions reported as wt.%.

	B25_Plag4-6	B25_Plag4-7	B25_Plag5	B25_Plag5	B25_Plag5	B25_Plag5	B25_Plag5	B25_Plag5	B25_Plag5	B25_Plag5	B25_Plag5	B25_Plag5
SiO_2	48.30	46.49	47.20	43.77	44.62	44.46	45.68	43.74	1.46	44.12	44.25	44.47
TiO_2	0.03	0.02	0.02	0.03	0.02	0.02	0.04	0.02	0.04	0.01	0.02	0.03
Al_2O_3	30.69	32.22	32.57	34.31	33.92	33.59	33.78	32.70	0.57	34.13	34.24	33.85
Cr_2O_3	0.00	0.02	0.00	0.00	0.00	0.02	0.02	-0.02	0.01	0.00	0.01	-0.01
FeO	0.67	0.66	0.66	0.71	0.71	0.60	0.66	0.65	0.36	0.70	0.68	0.71
MgO	0.07	0.04	0.04	0.07	0.07	0.07	0.08	0.10	0.22	0.07	0.07	0.03
CaO	14.39	15.83	15.79	17.95	17.90	17.68	17.53	17.26	0.87	17.70	17.82	17.90
BaO												
Na_2O	2.93	2.16	2.19	1.11	1.20	1.19	1.34	1.33	0.40	1.17	1.21	1.18
K_2O	0.40	0.24	0.27	0.13	0.14	0.15	0.14	0.20	0.56	0.10	0.14	0.13
P_2O_5	0.31	0.33	0.33	0.38	0.34	0.39	0.36	0.39	-0.05	0.37	0.39	0.38
Cl	0.01	0.00	0.02	0.01	0.00	0.01	0.01	0.02	0.24	0.00	0.01	0.00
Total	97.8	98.0	99.1	98.5	98.9	98.2	99.6	96.4	4.7	98.4	98.8	98.7

Table 6: Major element compositions of plagioclase electron microprobe analyses. Element compositions reported as wt.%.

	B25_Plag 6-1	B25_Plag 6-2	B25_Plag 6-3	B25_Plag 6-4	B25_Plag 6-5	B25_Plag 6-6	B25_Plag 6-7	B24_Plag 1-1	B24_Plag 1-1	B24_Plag 1-1	B24_Plag 1-1	B24_Plag 1-1
SiO_2	46.64	46.51	43.69	45.17	46.52	47.94	59.36	43.60	44.49	44.48	44.38	44.29
TiO_2	0.03	0.03	0.02	0.04	0.03	0.04	0.09	0.01	0.02	0.00	0.02	0.01
Al_2O_3	31.89	31.71	30.39	31.13	31.87	33.10	24.41	35.72	35.62	35.37	35.74	35.76
Cr_2O_3	0.00	-0.01	0.01	0.00	0.01	0.00	0.00	-0.01	0.00	-0.01	0.02	-0.01
FeO	0.69	0.61	0.70	0.74	0.65	0.71	0.70	0.51	0.49	0.56	0.45	0.53
MgO	0.05	0.04	0.07	0.07	0.06	0.06	0.14	0.03	0.01	-0.02	0.00	0.03
CaO	15.22	15.34	15.54	15.60	15.80	16.20	0.35	17.96	18.03	18.02	18.01	18.22
BaO												
Na_2O	2.42	2.35	2.06	2.04	2.18	2.21	1.19	0.95	1.01	0.98	0.95	0.99
K_2O	0.26	0.22	0.29	0.25	0.23	0.30	15.13	0.04	0.05	0.05	0.05	0.05
P_2O_5	0.35	0.21	0.36	0.24	0.35	0.32	0.05	0.39	0.41	0.42	0.42	0.41
Cl	0.01	0.02	0.04	0.03	0.01	0.01	0.13	0.02	0.01	0.00	0.00	0.00
Total	97.6	97.1	93.2	95.4	97.7	100.9	101.6	99.2	100.2	99.9	100.0	100.3

Table 6: Major element compositions of plagioclase electron microprobe analyses. Element compositions reported as wt.%.

	B24_Plag 2-1	B24_Plag 2-1	B24_Plag 2-1	B24_Plag 2-1	B24_Plag 2-1	B24_Plag 3-1	B24_Plag 3-1	B24_Plag 3-1	B24_Plag 3-1	B24_Plag 3-1	B24_Plag 3-1	B24_Plag 4-1
SiO_2	42.90	43.55	43.50	44.54	44.35	44.74	44.60	44.87	45.22	44.78	43.53	45.70
TiO_2	0.02	0.03	0.02	0.03	0.00	0.01	0.03	0.03	0.02	0.02	0.02	0.00
Al_2O_3	35.62	35.78	35.49	34.73	35.17	35.34	34.92	34.44	34.31	34.54	35.04	36.03
Cr_2O_3	0.01	-0.01	0.00	0.00	-0.01	0.01	0.01	0.02	0.00	-0.02	0.01	-0.02
FeO	0.54	0.43	0.45	0.48	0.56	0.49	0.54	0.60	0.64	0.65	0.49	0.54
MgO	0.01	0.01	0.01	-0.03	0.03	0.01	0.02	0.02	0.03	0.00	0.01	0.01
CaO	18.26	18.69	18.36	18.29	18.23	18.00	18.05	17.64	17.31	17.74	18.32	18.17
BaO												
Na_2O	0.89	0.77	0.94	1.03	1.11	1.19	1.12	1.42	1.53	1.26	0.98	1.06
K_2O	0.05	0.04	0.04	0.05	0.07	0.06	0.05	0.08	0.09	0.07	0.05	0.05
P_2O_5	0.36	0.41	0.32	0.37	0.39	0.33	0.31	0.34	0.30	0.31	0.35	0.37
Cl	0.00	0.00	0.00	0.00	0.01	0.00	0.01	0.01	0.01	0.00	0.01	-0.01
Total	98.7	99.7	99.1	99.6	99.9	100.2	99.7	99.5	99.5	99.4	98.8	101.9

Table 6: Major element compositions of plagioclase electron microprobe analyses. Element compositions reported as wt.%.

	B24_Plag4-1	B24_Plag4-1	B24_Plag4-1	B24_Plag4-1	B24_Plag4-1	B8_Plag1-1	B8_Plag1-1	B8_Plag1-1	B8_Plag1-1	B8_Plag1-1	B8_Plag2	B8_Plag2
SiO_2	45.70	44.32	45.37	45.67	47.05	43.24	44.20	43.54	43.54	43.20	43.80	42.68
TiO_2	0.00	0.02	0.01	0.01	0.02	0.01	0.00	0.00	0.02	0.02	0.02	0.01
Al_2O_3	36.03	36.54	36.27	35.63	37.39	35.84	35.40	35.41	35.11	35.63	35.78	34.38
Cr_2O_3	-0.02	0.01	0.00	0.00	0.01	0.02	0.00	0.00	-0.01	0.01	-0.02	0.01
FeO	0.54	0.46	0.47	0.47	0.53	0.52	0.56	0.51	0.56	0.74	0.50	0.57
MgO	0.01	0.01	0.01	0.03	0.02	0.00	0.04	-0.01	0.01	0.03	0.03	0.01
CaO	18.17	18.82	18.56	18.03	18.40	18.95	18.46	18.72	18.37	18.82	18.94	18.23
BaO												
Na_2O	1.06	0.83	0.94	1.19	1.11	0.72	0.92	0.89	0.98	0.73	0.77	0.84
K_2O	0.05	0.03	0.05	0.06	0.06	0.05	0.07	0.05	0.06	0.04	0.04	0.06
P_2O_5	0.37	0.37	0.36	0.37	0.38	0.34	0.36	0.36	0.38	0.34	0.31	0.31
Cl	-0.01	-0.01	0.01	0.01	-0.01	0.00	0.00	0.01	0.00	0.00	0.00	0.00
Total	101.9	101.4	102.1	101.5	105.0	99.7	100.0	99.5	99.0	99.6	100.2	97.1

Table 6: Major element compositions of plagioclase electron microprobe analyses. Element compositions reported as wt.%.

	B8_Plag2	B8_Plag2	B8_Plag2	B8_Plag2	B8_Plag2	B8_Plag2	B8_Plag2	B8_Plag2	B8_Plag3-1	B8_Plag3-2	B8_Plag3-3	B8_Plag3-4
SiO_2	44.38	44.92	44.76	44.69	44.59	44.37	43.93	44.36	45.33	44.44	44.99	44.93
TiO_2	0.02	0.00	-0.01	0.00	0.01	0.02	0.00	0.00	0.02	0.02	0.02	0.00
Al_2O_3	35.22	34.75	35.46	35.37	35.05	35.43	35.82	36.01	35.23	36.18	35.96	36.48
Cr_2O_3	0.00	0.01	-0.01	0.03	0.02	-0.01	0.00	0.00	0.02	-0.01	0.00	-0.01
FeO	0.56	0.54	0.51	0.58	0.55	0.57	0.50	0.52	0.62	0.54	0.60	0.57
MgO	0.02	0.02	0.04	0.03	0.01	0.04	0.02	0.04	0.02	0.00	0.01	0.02
CaO	18.42	18.18	18.41	18.45	18.56	18.48	18.89	18.93	18.53	18.89	18.89	18.90
BaO												
Na_2O	1.01	1.02	0.99	1.00	0.96	0.92	0.74	0.72	0.92	0.75	0.78	0.77
K_2O	0.05	0.06	0.06	0.06	0.06	0.05	0.04	0.03	0.17	0.04	0.04	0.04
P_2O_5	0.34	0.33	0.38	0.37	0.31	0.31	0.32	0.36	0.36	0.34	0.39	0.33
Cl	-0.01	0.00	0.01	0.01	-0.01	0.00	0.00	-0.01	0.01	0.01	0.01	-0.01
Total	100.0	99.8	100.6	100.6	100.1	100.2	100.3	101.0	101.3	101.2	101.7	102.0

Table 6: Major element compositions of plagioclase electron microprobe analyses. Element compositions reported as wt.%.

	B8_Plag3-5	B8_Plag3-6	B8_Plag3-7	B8_Plag	B8_Plag	B8_Plag	B8_Plag	B8_Plag	B8_Plag	B8_Plag	B8_Plag	B8_Plag
SiO_2	43.63	44.43	45.76	43.91	44.52	43.55	44.47	43.19	44.45	42.96	43.43	44.50
TiO_2	0.03	0.01	0.01	0.02	0.00	0.00	0.02	-0.01	0.01	0.03	0.07	0.01
Al_2O_3	35.29	35.31	36.84	35.62	35.68	34.30	35.33	34.57	35.08	34.09	34.54	35.37
Cr_2O_3	0.01	-0.01	-0.01	0.00	-0.01	-0.02	0.00	0.01	0.00	0.01	0.00	-0.01
FeO	0.51	0.55	0.57	0.55	0.52	0.58	0.56	0.63	0.52	0.65	0.62	0.63
MgO	0.02	0.04	0.02	0.03	0.01	0.03	0.02	0.15	-0.01	0.05	0.13	0.03
CaO	18.62	18.47	18.97	18.86	18.69	18.36	18.46	18.70	18.54	18.10	18.69	18.71
BaO												
Na_2O	0.81	0.88	0.77	0.71	0.84	0.95	1.02	1.17	0.97	0.86	0.91	0.87
K_2O	0.04	0.06	0.04	0.04	0.06	0.06	0.06	0.13	0.06	0.18	0.08	0.06
P_2O_5	0.32	0.33	0.38	0.33	0.33	0.32	0.33	0.34	0.31	0.30	0.32	0.35
Cl	0.01	0.00	0.00	0.01	0.00	0.01	0.01	0.05	0.00	0.01	0.07	0.00
Total	99.3	100.1	103.4	100.1	100.6	98.2	100.3	99.0	100.0	97.3	98.9	100.5

Table 6: Major element compositions of plagioclase electron microprobe analyses. Element compositions reported as wt.%.

	B8_Plag	B8_Plag	B8_Plag	B8_Plag	B8_Plag	B8_Plag	B8_Plag5-1	B8_Plag5-1	B8_Plag5-1	B8_Plag5-1	B8_Plag5-1	B8_Plag5-1
SiO_2	44.74	44.52	44.12	43.99	44.03	44.59	43.48	43.41	42.54	44.32	44.39	44.07
TiO_2	-0.01	0.01	0.02	0.01	0.01	0.00	0.02	0.00	0.02	0.01	-0.01	0.02
Al_2O_3	35.41	35.59	35.29	35.40	35.16	36.34	35.82	35.12	33.30	35.52	35.35	35.18
Cr_2O_3	-0.02	0.01	0.01	-0.02	0.00	-0.02	0.00	0.00	0.02	-0.01	0.01	0.00
FeO	0.66	0.63	0.54	0.52	0.53	0.56	0.57	0.52	0.53	0.59	0.59	0.64
MgO	0.00	0.02	0.01	0.00	0.05	0.01	0.02	0.03	0.05	0.00	0.01	0.00
CaO	18.70	18.61	18.67	18.70	18.63	19.02	18.94	18.98	17.78	18.58	18.65	18.54
BaO												
Na_2O	0.88	0.89	0.89	0.83	0.86	0.73	0.75	0.65	0.79	0.90	0.86	0.91
K_2O	0.05	0.05	0.06	0.05	0.06	0.04	0.05	0.04	0.09	0.05	0.04	0.05
P_2O_5	0.35	0.33	0.31	0.33	0.35	0.36	0.34	0.33	0.27	0.36	0.34	0.35
Cl	0.01	0.00	0.00	0.00	0.02	0.01	0.01	0.01	0.11	0.00	0.01	0.00
Total	100.8	100.7	99.9	99.8	99.7	101.7	100.0	99.1	95.5	100.4	100.3	99.8

Table 6: Major element compositions of plagioclase electron microprobe analyses. Element compositions reported as wt.%.

	B8_Plag5-1	B8_Plag5-1	B8_Plag5-1	B8_Plag5-1	B2H_Plag1	B2H_Plag1	B2H_Plag1	B2H_Plag1	B2H_Plag1	B2H_Plag1	B2H_Plag2	B2H_Plag2
SiO_2	44.14	43.97	46.63	43.88	45.01	44.77	45.05	44.99	44.77	44.45	45.09	44.74
TiO_2	0.02	0.03	0.17	0.02	0.03	0.01	0.03	0.00	0.01	0.02	0.02	0.02
Al_2O_3	35.43	35.66	29.73	35.29	35.27	34.97	34.99	34.98	35.57	35.53	35.34	35.18
Cr_2O_3	0.01	0.02	0.00	-0.01	-0.01	0.00	0.01	0.00	0.00	0.00	-0.01	-0.01
FeO	0.56	0.57	2.33	0.61	0.55	0.44	0.48	0.47	0.51	0.72	0.55	0.48
MgO	0.03	0.03	0.53	0.02	0.01	0.01	0.03	0.01	0.03	-0.01	-0.03	0.02
CaO	18.82	18.67	14.07	18.56	18.20	18.29	17.93	17.97	18.39	18.44	18.27	18.35
BaO												
Na_2O	0.86	0.85	1.98	0.92	1.12	1.08	1.09	1.11	1.09	0.96	1.08	1.12
K_2O	0.04	0.06	1.86	0.06	0.09	0.08	0.07	0.08	0.08	0.06	0.07	0.07
P_2O_5	0.31	0.33	0.27	0.36	0.35	0.37	0.37	0.38	0.39	0.37	0.33	0.36
Cl	0.01	0.01	0.20	0.00	0.01	0.01	0.01	0.00	0.01	0.00	0.00	0.01
Total	100.2	100.2	97.9	99.7	100.6	100.0	100.1	100.0	100.9	100.6	100.8	100.4

Table 6: Major element compositions of plagioclase electron microprobe analyses. Element compositions reported as wt.%.

	B2H_Plag2	B2H_Plag2	B2H_Plag2	B2H_Plag3-2	B2H_Plag3-2	B2H_Plag3-2	B2H_Plag3-2	B2H_Plag3-2	B2H_Plag3-2	B2H_Plag3-2	B2H_Plag3-2	B2H_Plag4
SiO_2	44.63	45.17	44.79	44.21	44.35	44.31	44.89	44.63	44.40	44.43	44.68	48.57
TiO_2	0.02	0.02	0.02	0.01	0.02	0.02	0.01	0.02	-0.01	0.02	0.02	0.03
Al_2O_3	35.33	35.24	35.27	34.66	34.77	34.10	34.93	34.85	35.46	35.16	35.85	32.10
Cr_2O_3	0.00	0.00	-0.01	-0.01	0.00	0.02	-0.01	0.02	-0.01	0.02	-0.01	-0.01
FeO	0.54	0.58	0.54	0.51	0.60	0.57	0.59	0.51	0.54	0.58	0.64	0.55
MgO	0.02	0.01	0.00	0.02	0.03	0.03	0.00	0.03	0.03	0.05	0.02	0.00
CaO	18.36	18.38	18.16	17.78	18.06	17.98	18.06	17.94	18.36	18.22	18.62	14.63
BaO												
Na_2O	1.06	0.99	1.09	1.19	1.10	1.08	1.21	1.15	1.10	1.04	0.99	2.78
K_2O	0.06	0.07	0.07	0.09	0.08	0.10	0.09	0.08	0.07	0.06	0.06	0.22
P_2O_5	0.34	0.36	0.37	0.35	0.36	0.32	0.40	0.37	0.36	0.34	0.34	0.31
Cl	0.01	0.00	0.01	0.01	0.01	0.02	0.00	0.02	0.04	0.00	0.01	0.01
Total	100.4	100.8	100.4	98.8	99.4	98.5	100.2	99.6	100.4	99.9	101.2	99.2

Table 6: Major element compositions of plagioclase electron microprobe analyses. Element compositions reported as wt.%.

	B2H_Plag 4	B2H_Plag 4	B2H_Plag 4	B2H_Plag 4	B2H_Plag 4	B2H_Plag 4	B2H_Plag 4	B2H_Plag 4	B27_Plag 1	B27_Plag 2	B27_Plag 3	B27_Plag 4
SiO_2	44.48	44.55	44.43	43.99	44.71	44.69	44.71	45.26	49.06	44.86	45.69	43.22
TiO_2	0.01	0.01	0.02	-0.01	0.00	0.01	0.00	0.01	0.01	0.00	0.00	0.00
Al_2O_3	34.53	34.36	34.49	34.79	34.90	34.47	34.32	33.99	31.39	34.47	34.22	34.16
Cr_2O_3	0.00	0.01	0.03	0.00	0.02	-0.02	-0.01	0.01	0.00	0.00	0.01	0.00
FeO	0.52	0.43	0.42	0.38	0.47	0.43	0.52	0.54	0.63	0.54	0.62	0.68
MgO	0.01	0.05	0.03	0.04	0.02	0.03	0.03	0.02	0.02	0.00	0.00	0.02
CaO	17.62	17.61	17.50	17.87	17.86	17.70	17.90	17.04	14.31	18.28	17.81	18.53
BaO									0.06	0.00	0.01	0.02
Na_2O	1.16	1.28	1.27	1.17	1.17	1.21	1.25	1.77	3.02	0.89	1.11	0.80
K_2O	0.07	0.09	0.07	0.10	0.08	0.09	0.08	0.08	0.18	0.02	0.07	0.04
P_2O_5	0.36	0.34	0.34	0.37	0.33	0.35	0.33	0.32	0.02	0.00	0.03	0.00
Cl	0.00	0.01	0.01	0.02	0.01	0.00	0.01	0.00	0.00	0.00	0.00	0.00
Total	98.8	98.8	98.6	98.7	99.6	99.0	99.2	99.1	98.7	99.1	99.6	97.5

Table 6: Major element compositions of plagioclase electron microprobe analyses. Element compositions reported as wt.%.

	B27_Plag5	B27_Plag6	B27_Plag7	B27_PlagInc2	SA18_Plag1	SA18_Plag2	SA18_Plag3	SA18_Plag4	SA18_Plag5	SA18_Plag6	SA18_Plag7	SA18_Plag8
SiO_2	43.86	49.31	44.70	48.69	44.56	43.36	43.85	43.50	9.31	42.95	44.50	44.55
TiO_2	0.01	0.08	0.01	0.13	0.01	0.02	0.01	0.00	0.01	0.07	0.02	0.03
Al_2O_3	35.21	30.79	34.54	31.47	34.41	34.49	34.18	34.42	10.10	34.52	34.22	34.33
Cr_2O_3	0.04	0.02	0.00	0.00	0.00	0.02	0.02	0.00	0.00	0.01	0.00	0.00
FeO	0.64	0.67	0.61	0.91	0.55	0.55	0.53	0.67	0.23	0.54	0.59	0.57
MgO	0.00	0.00	0.05	0.09	0.03	0.05	0.05	0.01	0.00	0.02	0.05	0.05
CaO	18.77	13.17	18.07	14.46	17.91	18.10	17.98	18.04	6.01	18.25	17.88	17.95
BaO	0.02	0.03	0.04	0.07	0.00	0.03	0.00	0.02	0.02	0.01	0.01	0.06
Na_2O	0.75	4.22	0.88	2.85	1.08	0.95	0.98	0.74	0.66	0.72	1.12	1.08
K_2O	0.01	0.19	0.06	0.54	0.07	0.06	0.06	0.06	0.04	0.05	0.06	0.06
P_2O_5	0.02	0.00	0.01	0.06	0.02	0.05	0.00	0.01	0.00	0.00	0.00	0.03
Cl	0.00	0.24	0.01	0.09	0.02	0.05	0.00	0.01	0.04	0.00	0.03	0.01
Total	99.4	98.8	99.0	99.4	98.7	97.7	97.7	97.5	26.5	97.2	98.5	98.7

Table 6: Major element compositions of plagioclase electron microprobe analyses. Element compositions reported as wt.%.

	SA19_plag1	SA19_Plag2	SA19_Plag3	SA19_Plag4	SA19_Plag5	SA19_Plag6	SA19_Plag7	SA19_Plag01	SA19_Plag10	SA19_Plag11	SA19_Plag2	SA19_Plag3
SiO_2	44.29	43.63	45.04	45.68	44.57	45.59	46.82	44.48	45.38	44.76	45.40	43.82
TiO_2	0.00	0.03	0.02	0.06	0.01	0.01	0.00	0.03	0.04	0.01	0.03	0.00
Al_2O_3	34.48	32.81	33.82	34.12	33.46	34.36	33.66	34.26	34.55	34.08	33.99	34.36
Cr_2O_3	0.00	0.01	0.01	0.02	0.00	0.00	0.00	0.00	0.00	0.00	0.02	0.00
FeO	0.45	0.49	0.46	0.63	0.55	0.45	0.55	0.50	0.53	0.46	0.72	0.57
MgO	0.02	0.02	0.02	0.02	0.04	0.00	0.01	0.06	0.02	0.06	0.00	0.02
CaO	17.68	17.02	16.93	17.51	16.96	17.75	16.52	17.68	17.82	17.57	17.05	17.45
BaO	0.05	0.04	0.04	0.06	0.01	0.02	0.05	0.04	0.05	0.08	0.00	0.01
Na_2O	1.02	1.15	1.40	1.52	1.54	1.20	1.72	1.26	1.23	1.15	1.45	1.20
K_2O	0.04	0.09	0.08	0.06	0.07	0.08	0.09	0.06	0.07	0.07	0.10	0.07
P_2O_5	0.00	0.03	0.00	0.00	0.00	0.03	0.00	0.00	0.02	0.00	0.06	0.02
Cl	0.02	0.01	0.00	0.05	0.05	0.00	0.03	0.06	0.05	0.02	0.02	0.01
Total	98.1	95.3	97.8	99.7	97.3	99.5	99.5	98.5	99.8	98.3	98.9	97.6

Table 6: Major element compositions of plagioclase electron microprobe analyses. Element compositions reported as wt.%.

	SA19_Plag4	SA19_Plag5	SA19_Plag6	SA19_Plag7	SA19_Plag8	B22_Plag1-2	B21_Plag1-1	B21_Plag1-2	SA88-301_Plag1-1	SA88-301_Plag1-2	SA88-301_Plag1-3	SA88-301_Plag1-4
SiO_2	45.17	45.93	45.66	43.88	43.92	43.48	45.59	44.65	47.07	54.69	55.23	52.08
TiO_2	0.05	0.00	0.04	0.00	0.00	0.04	0.03	0.00	0.05	0.15	0.05	0.04
Al_2O_3	33.69	33.66	33.59	34.35	34.95	34.99	33.86	34.38	33.29	26.67	27.52	29.06
Cr_2O_3	0.00	0.00	0.00	0.00	0.01	0.02	0.02	0.02	0.06	0.00	0.00	0.01
FeO	0.47	0.57	0.54	0.52	0.46	0.55	0.50	0.51	0.45	0.93	0.39	0.76
MgO	0.03	0.02	0.02	0.02	0.02	0.02	0.03	0.02	0.00	0.41	0.03	0.05
CaO	16.57	16.81	17.05	17.47	18.10	18.23	17.18	17.69	16.54	9.91	9.62	11.94
BaO	0.07	0.12	0.02	0.02	0.06	0.03	0.00	0.00	0.08	0.16	0.12	0.12
Na_2O	1.68	1.49	1.44	1.13	0.85	0.84	1.29	1.04	1.98	5.28	5.28	4.16
K_2O	0.10	0.09	0.11	0.05	0.04	0.04	0.08	0.06	0.09	0.71	0.61	0.51
P_2O_5	0.04	0.01	0.03	0.00	0.03	0.02	0.03	0.04	0.03	0.07	0.02	0.04
Cl	0.03	0.00	0.03	0.02	0.00	0.00	0.01	0.01	0.00	0.01	0.00	0.00
Total	97.9	98.7	98.5	97.5	98.4	98.3	98.6	98.4	99.6	99.0	98.9	98.8

Table 6: Major element compositions of plagioclase electron microprobe analyses. Element compositions reported as wt.%.

	SA88-301_Plag2-1	SA88-301_Plag2-2	SA88-301_Plag2-3	SA88-301_Plag3-1	SA88-301_Plag3-2	SA88-301_Plag3-3	SA88-301_Plag4-1	SA88-301_Plag4-2	SA88-301_Plag4-3	SA88-301_Plag5-1	SA88-301_Plag5-2	SA88-301_Plag5-3
SiO_2	47.14	45.99	45.67	46.13	45.31	45.21	47.76	52.51	51.61	44.06	44.07	44.98
TiO_2	0.42	0.02	0.04	0.00	0.00	0.00	0.02	0.01	0.01	0.06	0.00	0.01
Al_2O_3	28.76	33.58	33.70	33.50	34.48	33.69	32.21	29.25	29.58	34.36	34.42	34.29
Cr_2O_3	0.02	0.00	0.02	0.00	0.01	0.02	0.03	0.01	0.00	0.00	0.00	0.02
FeO	3.40	0.65	0.76	0.64	0.65	0.70	0.53	0.51	0.46	0.66	0.63	0.56
MgO	1.16	0.02	0.06	0.03	0.00	0.04	0.03	0.04	0.02	0.03	0.04	0.05
CaO	13.65	16.70	16.88	16.54	17.75	17.12	14.70	11.12	11.71	17.73	17.48	17.50
BaO	0.17	0.00	0.01	0.02	0.04	0.05	0.09	0.13	0.12	0.00	0.04	0.04
Na_2O	1.56	1.45	1.46	1.63	1.14	1.49	2.43	4.71	4.18	0.96	1.05	1.22
K_2O	2.10	0.14	0.09	0.08	0.09	0.09	0.19	0.50	0.52	0.06	0.07	0.09
P_2O_5	0.23	0.03	0.00	0.04	0.04	0.04	0.01	0.03	0.00	0.00	0.02	0.00
Cl	0.05	0.02	0.02	0.00	0.00	0.02	0.01	0.00	0.01	0.01	0.01	0.00
Total	98.8	98.6	98.7	98.7	99.5	98.5	98.1	98.8	98.3	97.9	97.9	98.8

Table 6: Major element compositions of plagioclase electron microprobe analyses. Element compositions reported as wt.%.

	SA88-301_Plag 5-4	SA88-301_Plag 6-1	SA88-301_Plag 6-2	SA88-301_Plag 6-3	SA88-301_Plag 6-4	SA88-301_Plag 6-5	B21_Plag 1-1	B21_Plag 1-2	B1B_Plag 1-1	B1B_Plag 1-2	B1B_Plag 1-3	B1B_Plag 1-4
SiO_2	45.47	44.17	46.47	45.83	44.91	46.06	45.59	44.65	49.83	49.51	48.59	50.12
TiO_2	0.00	0.03	0.05	0.00	0.00	0.02	0.03	0.00	0.76	0.76	0.81	0.57
Al_2O_3	34.23	34.02	33.51	33.74	33.87	33.70	33.86	34.38	4.72	4.94	4.62	3.64
Cr_2O_3	0.00	0.02	0.02	0.00	0.00	0.00	0.02	0.02	0.00	0.00	0.05	0.00
FeO	0.60	0.52	0.65	0.60	0.63	0.66	0.50	0.51	7.12	7.28	7.33	6.94
MgO	0.04	0.01	0.02	0.02	0.02	0.04	0.03	0.02	13.87	13.98	13.72	14.46
CaO	17.49	17.52	16.68	16.82	16.73	16.61	17.18	17.69	22.54	22.45	21.79	22.26
BaO	0.05	0.05	0.05	0.03	0.00	0.01	0.00	0.00	0.01	0.03	0.02	0.00
Na_2O	1.22	1.13	1.67	1.50	1.43	1.41	1.29	1.04	0.36	0.36	0.46	0.31
K_2O	0.08	0.06	0.10	0.08	0.08	0.07	0.08	0.06	0.01	0.00	0.00	0.00
P_2O_5	0.00	0.03	0.02	0.02	0.03	0.01	0.03	0.04	0.02	0.02	0.00	0.02
Cl	0.01	0.00	0.02	0.07	0.00	0.00	0.01	0.01	0.00	0.00	0.00	0.00
Total	99.3	97.6	99.3	98.8	97.7	98.7	98.6	98.4	99.4	99.6	97.6	98.6

Table 6: Major element compositions of plagioclase electron microprobe analyses. Element compositions reported as wt.%.

	B1B_Plag 1-1	B1B_Plag 1-2	B1B_Plag 1-3	B1B_Plag 1-4	B1B_Plag 1-5	B1B_Plag 1-6	B1B_Plag 1-7	B1B_Plag 1-8	B1B_Plag 1-9	B1B_Plag 1-10	B1B_Plag 1-11	B1B_Plag 1-12
SiO_2	47.55	49.89	49.42	48.03	49.13	49.40	48.81	48.18	48.61	47.78	48.11	47.64
TiO_2	1.00	0.58	0.60	0.96	0.68	0.63	0.70	0.91	0.99	0.95	1.01	1.10
Al_2O_3	6.00	4.06	3.92	5.71	3.99	4.24	4.61	5.88	5.69	5.53	5.88	6.03
Cr_2O_3	0.01	0.00	0.00	0.00	0.00	0.00	0.00	0.00	0.03	0.01	0.00	0.02
FeO	7.66	7.04	7.12	7.39	6.68	7.08	7.11	7.14	7.37	7.35	6.90	7.43
MgO	13.22	14.34	14.31	13.10	14.13	13.93	13.93	13.44	13.37	13.48	13.63	13.53
CaO	22.44	22.12	22.24	22.45	22.04	22.60	22.57	22.55	23.12	22.28	22.37	22.59
BaO	0.01	0.00	0.00	0.00	0.03	0.07	0.00	0.04	0.03	0.00	0.07	0.00
Na_2O	0.33	0.41	0.35	0.38	0.37	0.34	0.35	0.31	0.31	0.31	0.30	0.31
K_2O	0.00	0.00	0.03	0.00	0.00	0.01	0.00	0.01	0.02	0.00	0.00	0.00
P_2O_5	0.00	0.01	0.02	0.05	0.01	0.00	0.00	0.01	0.03	0.00	0.00	0.06
Cl	0.00	0.00	0.00	0.00	0.00	0.00	0.00	0.00	0.00	0.00	0.00	0.00
Total	98.4	98.7	98.2	98.3	97.4	98.5	98.4	98.7	99.8	97.9	98.5	98.9

Table 6: Major element compositions of plagioclase electron microprobe analyses. Element compositions reported as wt.%.

	SA5_Plag 3	SA5_Plag 3	SA5_Plag 3	SA5_Plag 3	SA5_Plag 4	SA5_Plag 4	B29_Plag 1	SA17_Plag 1	SA17_Plag 1	SA17_Plag 1	SA17_Plag 1	SA17_Plag 1
SiO_2	49.94	49.15	48.34	52.20	52.55	49.91	45.27	44.41	44.70	45.85	46.24	44.82
TiO_2	0.02	0.08	0.01	0.02	0.02	0.02	0.01	0.02	0.02	0.02	0.00	0.01
Al_2O_3	28.82	27.55	29.93	27.25	26.45	28.01	34.19	34.20	33.70	33.30	33.05	33.78
Cr_2O_3	0.02	0.03	0.00	0.01	0.01	0.00	0.03	0.00	0.01	0.04	0.00	0.00
FeO	0.62	1.14	0.71	0.65	0.54	0.54	0.69	0.45	0.56	0.60	0.59	0.52
MgO	0.04	0.15	0.03	0.04	0.04	0.02	0.04	0.06	0.03	0.05	0.02	0.03
CaO	12.99	11.90	13.97	10.94	10.20	12.32	17.86	18.23	17.82	17.05	16.70	17.70
BaO	0.07	0.08	0.04	0.14	0.10	0.08	0.04	0.02	0.00	0.01	0.02	0.01
Na_2O	3.71	4.17	3.05	4.81	5.22	4.00	1.06	0.91	1.06	1.55	1.67	1.17
K_2O	0.27	0.71	0.22	0.43	0.48	0.31	0.09	0.07	0.05	0.10	0.09	0.07
P_2O_5	0.09	0.06	0.03	0.04	0.01	0.03	0.00	0.00	0.01	0.00	0.00	0.07
Cl	0.00	0.12	0.00	0.01	0.01	0.02	0.01	0.01	0.00	0.00	0.00	0.01
Total	96.6	95.3	96.4	96.6	95.7	95.3	99.3	98.4	98.0	98.6	98.4	98.2

Table 6: Major element compositions of plagioclase electron microprobe analyses. Element compositions reported as wt.%.

	SA17_Plag 1	SA17_Plag 1	SA17_Plag 1	B37_Plag 1	B37_Plag 1	B37_Plag 1	B37_Plag 1	B37_Plag 1	B37_Plag 1	B1A_Plag 1	B1A_Plag 1	B1A_Plag 1
SiO_2	44.73	45.47	44.22	44.27	44.15	44.79	44.94	44.58	43.86	45.57	45.43	45.22
TiO_2	0.02	0.02	0.01	0.01	0.00	0.02	0.01	0.00	0.01	0.02	0.02	0.03
Al_2O_3	33.90	33.11	33.79	34.42	34.10	34.76	35.22	34.48	33.82	35.33	35.38	35.58
Cr_2O_3	0.01	0.00	0.00	0.01	0.00	0.01	0.01	0.03	0.00	0.00	0.01	0.03
FeO	0.55	0.51	0.50	0.47	0.61	0.56	0.51	0.56	0.52	0.61	0.63	0.62
MgO	0.03	0.02	0.03	0.00	0.09	0.00	0.02	0.00	0.00	0.04	0.00	0.01
CaO	17.72	17.30	17.98	18.16	18.09	18.28	18.18	18.04	18.01	18.06	18.20	18.24
BaO	0.00	0.02	0.03	0.00	0.03	0.03	0.05	0.00	0.05	0.03	0.05	0.00
Na_2O	1.15	1.41	0.93	0.85	0.85	0.84	0.95	0.87	0.84	1.04	0.93	0.85
K_2O	0.06	0.10	0.06	0.05	0.07	0.05	0.05	0.04	0.05	0.05	0.04	0.04
P_2O_5	0.00	0.04	0.00	0.00	0.00	0.05	0.05	0.01	0.06	0.05	0.00	0.00
Cl	0.01	0.02	0.01	0.02	0.05	0.00	0.00	0.00	0.01	0.00	0.01	0.00
Total	98.2	98.0	97.6	98.3	98.1	99.5	100.0	98.6	97.3	100.8	100.7	100.6

Table 6: Major element compositions of plagioclase electron microprobe analyses. Element compositions reported as wt.%.

	B1A_Plag 1	B1A_Plag 1	B1A_Plag 2	B1A_Plag 2	B1A_Plag 2	B1A_Plag 2	B1A_Plag 2	B1A_Plag 2	B1A_Plag 3	B1A_Plag 3	B1A_Plag 3	B1A_Plag 3
SiO_2	45.52	45.42	50.97	42.21	45.17	45.50	45.77	45.26	45.33	44.74	45.06	50.51
TiO_2	0.01	0.02	0.05	0.01	0.02	0.01	0.01	0.01	0.02	0.01	0.01	0.03
Al_2O_3	35.44	35.18	31.49	32.94	34.69	35.76	35.09	35.47	35.82	35.43	35.95	31.51
Cr_2O_3	0.00	0.00	0.01	0.02	0.00	0.03	0.01	0.02	0.01	0.00	0.01	0.02
FeO	0.64	0.71	0.64	0.54	0.61	0.53	0.63	0.59	0.40	0.48	0.40	0.61
MgO	0.00	0.02	0.05	0.04	0.00	0.00	0.01	0.02	0.01	0.01	0.00	0.02
CaO	18.12	18.09	13.86	17.30	17.77	18.24	17.78	18.17	18.36	18.24	18.49	13.78
BaO	0.01	0.01	0.09	0.01	0.00	0.04	0.01	0.05	0.01	0.04	0.00	0.02
Na_2O	1.04	0.97	3.63	0.95	1.10	0.97	1.26	0.92	0.88	0.83	0.87	3.43
K_2O	0.06	0.04	0.26	0.08	0.06	0.02	0.07	0.04	0.04	0.04	0.04	0.17
P_2O_5	0.01	0.00	0.01	0.00	0.00	0.04	0.02	0.09	0.01	0.00	0.00	0.01
Cl	0.01	0.00	0.01	0.02	0.02	0.00	0.00	0.00	0.01	0.01	0.00	0.00
Total	100.9	100.5	101.1	94.2	99.5	101.2	100.7	100.7	100.9	99.9	100.8	100.1

Table 6: Major element compositions of plagioclase electron microprobe analyses. Element compositions reported as wt.%.

	B1A_Plag3	B1A_Plag3	B1A_Plag3	B1A_Plag3	B2H_PlagInc1-1	B2H_PlagInc1-2	B2H_PlagInc2-1	B2H_PlagInc2-2	B2H_PlagInc2-3	B2H_PlagInc2-4	B21	B21
SiO_2	45.38	46.54	45.81	48.21	45.62	44.78	46.12	44.79	45.39	44.35	44.78	44.64
TiO_2	0.00	0.02	0.02	0.01	0.01	0.02	0.03	0.03	0.03	0.06		
Al_2O_3	35.40	35.07	35.69	33.89	34.68	33.71	33.70	34.43	34.64	34.03	35.75	35.25
Cr_2O_3	0.05	0.00	0.00	0.00	-0.01	0.00	-0.01	0.02	0.01	0.00		
FeO	0.43	0.52	0.44	0.57	0.69	0.68	0.80	0.78	1.17	1.25	0.57	0.57
MgO	0.00	0.01	0.00	0.00	0.02	0.04	0.01	0.03	0.02	0.01		0.11
CaO	18.05	17.49	18.12	16.08	17.57	17.31	16.70	17.82	17.69	17.52	18.13	17.99
BaO	0.00	0.02	0.00	0.02								
Na_2O	0.97	1.51	1.07	2.27	1.42	1.35	1.88	1.26	1.19	1.23	1.38	1.21
K_2O	0.02	0.06	0.05	0.11	0.14	0.13	0.17	0.10	0.10	0.11	0.10	0.10
P_2O_5	0.00	0.10	0.03	0.01	0.34	0.36	0.30	0.36	0.38	0.31		
Cl	0.00	0.01	0.00	0.00	0.02	0.00	0.02	0.01	0.01	0.00		
Total	100.3	101.4	101.3	101.2	100.5	98.4	99.7	99.6	100.6	98.9	100.7	99.9

Table 6: Major element compositions of plagioclase electron microprobe analyses. Element compositions reported as wt.%.

	B7	B7	B7	SA23	SA24	SA24	SA26	SA26	SA26	SA26	SA26	SA26
SiO_2	53.75	55.30	53.51	46.23	56.43	49.71	43.79	43.53	43.69	44.00	55.99	57.70
TiO_2					1.21						0.20	0.13
Al_2O_3	29.93	29.03	29.76	34.43	20.64	31.94	33.45	34.36	33.98	33.10	26.24	24.99
Cr_2O_3							0.11					
FeO	0.64	0.57	0.59	0.55	4.94	0.52	0.68	0.51	0.61	0.57	0.72	0.72
MgO	0.22	0.23	0.27		0.74		0.10		0.19	0.15	0.16	0.17
CaO	12.55	11.51	12.57	17.08	2.15	13.23	18.62	19.22	19.26	18.42	9.37	7.96
BaO												
Na_2O	4.06	4.60	4.13	1.55	4.58	3.57	1.09	0.82	0.95	1.01	4.94	5.48
K_2O	0.68	0.88	0.62	0.13	6.15	0.32	0.07		0.09	0.09	1.23	1.76
P_2O_5												
Cl					0.82							
Total	101.8	102.1	101.5	100.0	97.7	99.3	97.8	98.4	98.8	97.3	98.9	98.9

Table 6: Major element compositions of plagioclase electron microprobe analyses. Element compositions reported as wt.%.

	SA12/ X01_Plag 1	SA12/ X01_Plag 1	SA12/ X01_Plag 1	SA12/ X01_Plag 1	SA12/ X01_Plag 1	SA12/ X01_Plag 1	SA12/ X01_Plag 1	SA12/ X01_Plag 1	SA12/ X01_Plag 1	SA12/ X01_Plag 1	SA12/ X01_Plag 1	SA12/ X01_Plag 2
SiO_2	44.59	43.78	44.42	44.19	44.07	43.95	43.26	43.97	43.72	44.16	43.24	45.21
TiO_2	0.00	0.01	0.01	0.00	0.01	0.02	0.02	0.01	0.00	0.02	0.01	0.01
Al_2O_3	32.30	32.72	33.04	33.15	33.33	33.18	32.86	33.46	32.87	32.98	32.98	32.92
Cr_2O_3	0.00	0.00	0.00	0.00	0.00	0.00	0.00	0.00	0.00	0.00	0.00	0.01
FeO	0.58	0.57	0.59	0.59	0.57	0.61	0.53	0.53	0.59	0.53	0.58	0.57
MgO	0.05	0.05	0.07	0.05	0.05	0.04	0.09	0.06	0.05	0.06	0.04	0.04
CaO	16.91	17.44	17.46	17.79	17.90	17.81	17.90	17.81	17.58	17.73	17.62	17.19
BaO	0.05	0.01	0.02	0.01	0.00	0.03	0.02	0.03	0.01	0.02	0.03	0.00
Na_2O	1.62	1.31	1.23	1.21	1.22	1.15	1.03	1.12	1.14	1.20	1.14	1.53
K_2O	0.12	0.10	0.06	0.06	0.05	0.07	0.06	0.06	0.06	0.07	0.07	0.12
P_2O_5	0.01	0.01	0.00	0.00	0.01	0.00	0.00	0.00	0.00	0.00	0.00	0.01
Cl	0.00	0.03	0.00	0.01	0.00	0.00	0.01	0.00	0.01	0.00	0.00	0.01
Total	96.2	96.1	96.9	97.1	97.3	96.9	95.8	97.1	96.1	96.8	95.7	97.6

Table 6: Major element compositions of plagioclase electron microprobe analyses. Element compositions reported as wt.%.

	SA12/ X01_Plag 2	SA12/ X01_Plag 2	SA12/ X01_Plag 3	SA12/ X01_Plag 3	SA12/ X01_Plag 3	SA12/ X01_Plag 3	SA12/ X01_Plag 3	SA12/ X01_Plag 3	SA12/ X01_Plag 3	SA12/ X01_Plag 4	SA12/ X01_Plag 4	SA12/ X01_Plag 4
SiO_2	44.83	44.75	55.67	53.33	59.56	59.44	62.45	54.58	53.31	51.75	49.70	54.95
TiO_2	0.01	0.02	0.07	0.02	0.84	0.79	0.79	0.06	0.02	0.04	0.04	0.58
Al_2O_3	32.58	32.68	25.37	26.64	18.81	18.73	19.72	25.61	26.78	27.46	29.25	18.83
Cr_2O_3	0.00	0.00	0.00	0.01	0.00	0.00	0.00	0.01	0.01	0.00	0.01	0.00
FeO	0.59	0.65	0.52	0.67	3.78	3.99	3.60	0.74	0.70	0.75	0.77	4.73
MgO	0.06	0.05	0.07	0.07	1.15	1.17	1.27	0.08	0.08	0.08	0.07	1.13
CaO	17.15	17.12	8.49	10.36	2.17	2.20	2.22	8.93	10.37	11.43	13.09	3.56
BaO	0.04	0.01	0.27	0.15	0.15	0.17	0.15	0.31	0.15	0.11	0.05	0.07
Na_2O	1.50	1.38	5.88	5.24	6.35	6.22	7.06	5.41	5.12	4.74	3.95	6.45
K_2O	0.11	0.13	1.36	0.92	7.25	7.31	7.01	1.46	0.88	0.69	0.43	5.84
P_2O_5	0.02	0.02	0.00	0.02	0.27	0.24	0.29	0.02	0.00	0.01	0.02	0.50
Cl	0.00	0.01	0.01	0.00	0.63	0.65	0.63	0.01	0.00	0.01	0.01	0.54
Total	96.9	96.8	97.8	97.5	101.0	101.0	105.3	97.2	97.5	97.1	97.5	97.3

Table 6: Major element compositions of plagioclase electron microprobe analyses. Element compositions reported as wt.%.

	SA12/ X01_Plag 5	SA12/ X01_Plag 5	SA12/ X01_Plag 5	BC14/ 038_Plag 1	BC14/ 038_Plag 1	BC14/ 038_Plag 1	BC14/ 038_Plag 1	BC14/ 038_Plag 1	BC14/ 038_Plag 1	BC14/ 038_Plag 1	BC14/ 038_Plag 1	BC14/ 038_Plag 1
SiO_2	49.71	49.74	51.83	43.71	43.14	43.22	43.25	43.10	43.32	43.24	43.22	43.20
TiO_2	0.04	0.03	0.03	0.00	0.02	0.02	0.01	0.02	0.02	0.00	0.00	0.01
Al_2O_3	29.01	28.77	27.57	33.57	33.89	33.81	34.06	33.87	33.93	34.05	34.10	34.05
Cr_2O_3	0.04	0.00	0.00	0.02	0.00	0.02	0.00	0.00	0.05	0.00	0.03	0.00
FeO	0.83	0.77	1.04	0.54	0.48	0.43	0.43	0.47	0.52	0.42	0.32	0.39
MgO	0.08	0.07	0.06	0.08	0.04	0.05	0.01	0.03	0.04	0.02	0.03	0.03
CaO	12.85	12.88	11.28	18.26	18.55	18.65	18.57	18.73	18.63	18.67	18.50	18.65
BaO	0.08	0.04	0.12	0.02	0.00	0.03	0.02	0.02	0.00	0.00	0.02	0.00
Na_2O	4.01	3.88	4.77	1.08	0.83	0.71	0.77	0.71	0.63	0.77	0.77	0.63
K_2O	0.49	0.49	0.73	0.07	0.05	0.06	0.05	0.06	0.04	0.05	0.04	0.04
P_2O_5	0.04	0.01	0.04	0.00	0.00	0.00	0.00	0.00	0.02	0.00	0.01	0.00
Cl	0.00	0.01	0.01	0.00	0.00	0.00	0.00	0.00	0.00	0.00	0.00	0.00
Total	97.2	96.7	97.5	97.4	97.0	97.0	97.2	97.0	97.2	97.2	97.1	97.0

Table 6: Major element compositions of plagioclase electron microprobe analyses. Element compositions reported as wt.%.

	BC14/038 _Plag1	BC14/038 _Plag1	BC14/038 _Plag1	BC14/038 _Plag1	BC14/038 _Plag1	BC14/038 _Plag1	BC14/038 _Plag1	BC14/038 _Plag1	BC14/038 _Plag2	BC14/038 _Plag2	BC14/038 _Plag2	BC14/038 _Plag2
SiO_2	42.83	42.83	43.04	42.98	43.08	43.24	43.74	43.58	43.50	43.51	43.59	42.32
TiO_2	0.01	0.00	0.02	0.00	0.00	0.00	0.01	0.01	0.00	0.01	0.00	0.03
Al_2O_3	34.28	34.10	34.02	33.92	34.12	33.71	33.69	33.33	33.85	33.76	33.38	35.84
Cr_2O_3	0.01	0.03	0.02	0.00	0.02	0.00	0.01	0.02	0.00	0.00	0.03	0.00
FeO	0.38	0.41	0.40	0.46	0.45	0.46	0.58	0.62	0.48	0.52	0.47	0.58
MgO	0.03	0.04	0.04	0.05	0.04	0.06	0.05	0.07	0.04	0.06	0.04	0.13
CaO	18.57	18.65	18.65	18.49	18.54	18.71	18.06	18.06	18.50	18.47	18.05	16.86
BaO	0.02	0.05	0.01	0.01	0.00	0.02	0.02	0.01	0.03	0.03	0.02	0.02
Na_2O	0.67	0.68	0.83	0.75	0.73	0.83	0.87	1.01	0.74	0.77	1.02	0.96
K_2O	0.04	0.05	0.04	0.04	0.05	0.05	0.07	0.07	0.05	0.06	0.07	0.09
P_2O_5	0.02	0.00	0.00	0.02	0.00	0.01	0.00	0.00	0.00	0.01	0.00	0.01
Cl	0.00	0.01	0.01	0.00	0.01	0.00	0.00	0.00	0.00	0.00	0.00	0.00
Total	96.9	96.9	97.1	96.8	97.1	97.1	97.1	96.8	97.2	97.2	96.7	96.9

Table 6: Major element compositions of plagioclase electron microprobe analyses. Element compositions reported as wt.%.

	BC14/ 038_Plag 2	BC14/ 038_Plag 2	BC14/ 038_Plag 2	BC14/ 038_Plag 2	BC14/ 038_Plag 2	BC14/ 038_Plag 2	BC14/ 039_FLd 1	BC14/ 039_FLd 1	BC14/ 039_FLd 1	BC14/ 039_FLd 1	BC14/ 039_FLd 2	BC14/ 039_FLd 2
SiO_2	43.57	43.39	43.17	43.68	43.11	43.61	48.06	48.42	48.49	49.98	49.33	48.09
TiO_2	0.00	0.02	0.01	0.02	0.01	0.02	0.04	0.02	0.04	0.05	0.05	0.05
Al_2O_3	33.54	33.73	33.60	33.87	33.52	34.01	30.06	30.14	29.86	29.10	29.39	30.30
Cr_2O_3	0.00	0.00	0.02	0.00	0.00	0.01	0.00	0.00	0.00	0.02	0.00	0.00
FeO	0.63	0.43	0.54	0.51	0.55	0.58	0.79	0.80	0.84	0.76	0.84	0.70
MgO	0.06	0.03	0.04	0.04	0.06	0.05	0.12	0.10	0.11	0.11	0.08	0.09
CaO	18.27	18.31	18.35	18.45	18.32	18.53	14.71	14.56	14.22	13.08	13.62	14.82
BaO	0.03	0.02	0.02	0.02	0.03	0.01	0.04	0.07	0.04	0.08	0.08	0.01
Na_2O	0.88	0.88	0.83	0.81	0.76	0.77	2.80	3.00	3.35	3.84	3.60	2.90
K_2O	0.06	0.06	0.06	0.06	0.05	0.05	0.24	0.25	0.27	0.31	0.29	0.24
P_2O_5	0.03	0.00	0.00	0.01	0.00	0.01	0.03	0.00	0.02	0.00	0.01	0.00
Cl	0.00	0.00	0.00	0.00	0.01	0.00	0.00	0.00	0.00	0.01	0.00	0.00
Total	97.1	96.9	96.7	97.5	96.5	97.7	96.9	97.4	97.2	97.4	97.3	97.2

Table 6: Major element compositions of plagioclase electron microprobe analyses. Element compositions reported as wt.%.

	BC14/ 039_Plag 1	BC14/ 039_Plag 1	BC14 /039_Plag 1	BC14 /039_Plag 1	BC14/ 039_Plag 1	BC14/ 039_Plag 1	BC14/ 039_Plag 1	BC14/ 039_Plag 1	BC14/ 039_Plag 2	BC14/ 039_Plag 2	BC14/ 039_Plag 2	BC14/ 039_Plag 2
SiO_2	45.40	43.96	44.25	43.57	45.04	43.86	43.03	52.38	43.30	44.14	44.26	44.47
TiO_2	0.03	0.00	0.03	0.01	0.03	0.00	0.00	0.06	0.01	0.00	0.01	0.00
Al_2O_3	32.17	33.33	33.32	33.75	32.44	33.46	33.42	29.51	33.63	33.26	33.56	33.21
Cr_2O_3	0.00	0.01	0.00	0.00	0.00	0.00	0.00	0.00	0.00	0.00	0.00	0.00
FeO	0.66	0.49	0.55	0.55	0.66	0.61	0.60	0.46	0.66	0.76	0.60	0.64
MgO	0.14	0.05	0.06	0.03	0.07	0.04	0.06	0.17	0.04	0.05	0.06	0.07
CaO	16.93	18.09	17.85	18.32	16.98	18.06	18.34	6.08	18.46	18.03	17.93	17.58
BaO	0.02	0.03	0.03	0.04	0.05	0.00	0.03	0.34	0.02	0.04	0.00	0.03
Na_2O	1.68	0.94	1.14	0.80	1.60	1.04	0.76	6.19	0.82	1.01	1.04	1.27
K_2O	0.12	0.06	0.06	0.04	0.09	0.07	0.06	1.10	0.05	0.04	0.05	0.08
P_2O_5	0.03	0.02	0.05	0.04	0.02	0.00	0.00	0.17	0.00	0.00	0.00	0.00
Cl	0.01	0.00	0.00	0.01	0.00	0.01	0.00	0.06	0.00	0.01	0.00	0.00
Total	97.2	97.0	97.4	97.2	97.0	97.2	96.4	96.8	97.0	97.4	97.5	97.4

Table 6: Major element compositions of plagioclase electron microprobe analyses. Element compositions reported as wt.%.

	BC14/ 039_Plag 2	BC14/ 039_Plag 2	BC14 /039_Plag 2	BC14/ 039_Plag 2	BC14/ 039_Plag 2	BC14 /039_Plag 3	BC14/ 039_Plag 3	BC14/ 039_Plag 3	BC14/ 039_Plag 3	BC14/ 039_Plag 3	BC14 /039_Plag 3	BC14/ 039_Plag 3
SiO_2	44.60	45.22	44.64	44.24	44.11	43.75	44.00	44.36	43.98	44.32	45.07	45.04
TiO_2	0.02	0.02	0.03	0.02	0.02	0.00	0.02	0.01	0.02	0.00	0.02	0.00
Al_2O_3	32.95	32.88	33.13	33.17	33.28	33.96	33.52	33.13	33.14	33.10	32.52	32.73
Cr_2O_3	0.00	0.00	0.00	0.01	0.00	0.03	0.00	0.01	0.00	0.02	0.00	0.00
FeO	0.59	0.56	0.62	0.54	0.52	0.62	0.61	0.54	0.57	0.66	0.64	0.63
MgO	0.08	0.07	0.06	0.06	0.07	0.05	0.07	0.06	0.07	0.06	0.06	0.07
CaO	17.55	17.30	17.68	17.77	18.00	18.45	18.17	17.82	17.90	17.67	17.28	17.20
BaO	0.00	0.03	0.04	0.00	0.04	0.01	0.01	0.01	0.02	0.03	0.05	0.01
Na_2O	1.48	1.50	1.24	1.16	0.96	0.94	1.02	1.06	1.26	1.30	1.49	1.55
K_2O	0.08	0.08	0.07	0.07	0.05	0.05	0.06	0.07	0.06	0.07	0.08	0.08
P_2O_5	0.01	0.00	0.00	0.00	0.01	0.00	0.00	0.00	0.01	0.00	0.00	0.01
Cl	0.01	0.00	0.01	0.00	0.00	0.00	0.00	0.00	0.00	0.00	0.00	0.00
Total	97.4	97.7	97.6	97.0	97.1	97.9	97.7	97.1	97.1	97.2	97.3	97.3

Table 6: Major element compositions of plagioclase electron microprobe analyses. Element compositions reported as wt.%.

	BC14/ 039_Plag 3	BC14/ 039_Plag 3	BC14/ 039_Plag 3	BC14/ 039_Plag 3	BC14/ 039_Plag 3	BC14/ 039_Plag 3	BC14/ 039_Plag 3	BC14/ 039_Plag 3	BC14/ 039_Plag 4	BC14/ 039_Plag 4	BC14/ 039_Plag 5	BC14/ 039_Plag 5
SiO_2	45.16	45.48	44.36	44.77	44.24	44.69	45.26	43.60	58.05	48.97	60.75	58.72
TiO_2	0.01	0.04	0.00	0.02	0.01	0.02	0.03	0.00	0.68	0.04	0.23	0.28
Al_2O_3	32.54	32.32	33.05	32.80	33.49	32.96	33.92	33.82	16.33	29.95	20.79	20.94
Cr_2O_3	0.01	0.00	0.00	0.00	0.00	0.00	0.00	0.00	0.03	0.03	0.01	0.00
FeO	0.60	0.58	0.63	0.60	0.62	0.66	0.55	0.61	6.30	0.82	1.60	2.45
MgO	0.08	0.11	0.07	0.08	0.07	0.06	0.08	0.06	1.71	0.11	0.26	0.63
CaO	17.21	16.96	17.81	17.45	18.00	17.61	17.51	18.35	2.86	13.93	4.04	5.65
BaO	0.02	0.04	0.05	0.00	0.04	0.00	0.01	0.01	0.14	0.04	0.39	0.26
Na_2O	1.53	1.64	1.21	1.33	0.94	1.27	1.37	0.87	5.48	3.25	6.54	6.70
K_2O	0.08	0.10	0.06	0.08	0.06	0.08	0.08	0.04	6.13	0.25	4.57	2.37
P_2O_5	0.01	0.02	0.00	0.01	0.04	0.00	0.00	0.00	0.92	0.00	0.18	0.35
Cl	0.00	0.00	0.00	0.00	0.00	0.00	0.00	0.00	0.76	0.01	0.03	0.10
Total	97.3	97.3	97.2	97.2	97.5	97.4	98.9	97.4	99.6	97.5	99.5	98.6

Table 6: Major element compositions of plagioclase electron microprobe analyses. Element compositions reported as wt.%.

	BC14/ 039_PlagIn c1	BC14/ 039_PlagIn c1	BC14/ 039_PlagIn c1	BC14/ 039_PlagIn c1	BC14/ 039_PlagIn c1	BC14/ 015_Pla g1	BC14/ 015_Pla g1	BC14/ 015_Pla g1	BC14/ 015_Pla g1	BC14/ 015_Pla g2	BC14/ 015_Pla g2	BC14/ 015_Pla g2
SiO_2	43.90	44.71	42.87	44.03	44.81	44.44	42.32	42.84	44.37	45.72	46.16	45.18
TiO_2	0.01	0.03	0.02	0.01	0.02	0.03	0.01	0.00	0.03	0.03	0.02	0.01
Al_2O_3	33.74	32.65	33.26	31.75	32.68	31.33	31.82	32.46	31.11	30.36	30.08	31.09
Cr_2O_3	0.00	0.00	0.00	0.00	0.00	0.01	0.01	0.00	0.00	0.00	0.01	0.01
FeO	0.57	0.61	0.66	0.56	0.73	0.73	0.61	0.64	0.66	0.55	0.53	0.55
MgO	0.06	0.07	0.09	0.07	0.12	0.05	0.05	0.03	0.04	0.05	0.07	0.08
CaO	18.27	17.35	16.86	16.87	17.13	16.15	17.20	17.28	15.64	15.20	14.78	15.83
BaO	0.00	0.01	0.04	0.08	0.02	0.03	0.02	0.05	0.04	0.04	0.04	0.05
Na_2O	0.95	1.50	1.25	1.60	1.64	1.88	1.24	1.25	2.16	2.49	2.62	2.11
K_2O	0.04	0.08	0.11	0.10	0.11	0.09	0.07	0.04	0.10	0.15	0.19	0.13
P_2O_5	0.02	0.00	0.00	0.00	0.00	0.00	0.02	0.02	0.01	0.01	0.00	0.00
Cl	0.00	0.00	0.03	0.02	0.01	0.02	0.01	0.01	0.02	0.00	0.00	0.00
Total	97.6	97.1	95.2	95.1	97.4	94.8	93.4	94.7	94.2	94.6	94.5	95.1

Table 6: Major element compositions of plagioclase electron microprobe analyses. Element compositions reported as wt.%.

	BC14/ 015_Plag 2	BC14/ 015_Plag 2	BC14/ 015_Plag 2	BC14/ 015_Plag 2	BC14/ 015_Plag 2	BC14/ 015_Plag 2	BC14/ 015_Plag 3	BC14/ 015_Plag 3	BC14/ 015_Plag 3	BC14/ 015_Plag 3	BC14/ 015_Plag 4	BC14/ 015_Plag 4
SiO_2	43.29	42.58	42.38	43.63	42.55	42.24	48.53	44.42	43.14	44.91	48.24	44.26
TiO_2	0.03	0.01	0.01	0.01	0.01	0.01	0.06	0.02	0.01	0.02	0.04	0.02
Al_2O_3	31.99	32.48	32.71	32.84	32.49	32.79	28.05	31.37	32.05	31.00	28.64	31.23
Cr_2O_3	0.00	0.00	0.00	0.01	0.02	0.01	0.00	0.00	0.00	0.01	0.00	0.00
FeO	0.53	0.56	0.52	0.65	0.51	0.57	0.68	0.54	0.60	0.62	0.73	0.62
MgO	0.05	0.03	0.02	0.03	0.03	0.01	0.07	0.04	0.03	0.06	0.03	0.05
CaO	17.18	17.60	17.98	16.96	17.68	18.04	12.06	16.17	17.02	15.73	13.05	16.26
BaO	0.05	0.01	0.02	0.04	0.02	0.03	0.14	0.02	0.03	0.04	0.07	0.03
Na_2O	1.33	0.98	0.90	1.43	1.00	0.77	4.07	1.86	1.32	2.06	3.64	1.87
K_2O	0.07	0.04	0.04	0.05	0.04	0.02	0.23	0.10	0.05	0.10	0.15	0.09
P_2O_5	0.00	0.00	0.00	0.00	0.00	0.00	0.01	0.02	0.01	0.00	0.01	0.00
Cl	0.00	0.00	0.00	0.01	0.00	0.00	0.01	0.01	0.00	0.00	0.00	0.00
Total	94.6	94.3	94.6	95.7	94.4	94.5	94.0	94.6	94.3	94.6	94.6	94.4

Table 6: Major element compositions of plagioclase electron microprobe analyses. Element compositions reported as wt.%.

	BC14/ 015_Plag 4	BC14/ 015_Plag 4	BC14/ 015_Plag 4	BC14/ 015_Plag 5	BC14/ 015_Plag 5	BC14/ 015_Plag 5	BC14/ 015_Plag 5	BC14/ 015_Plag 6	BC14/ 015_Plag 6	BC14/ 015_Plag 6	BC14/ 015_Plag 6	BC14/ 015_Plag 7
SiO_2	44.60	43.57	45.33	42.58	44.67	44.49	43.46	48.00	46.79	43.31	47.49	45.90
TiO_2	0.03	0.02	0.01	0.01	0.01	0.01	0.03	0.04	0.03	0.02	0.03	0.03
Al_2O_3	30.87	32.15	30.25	33.80	31.26	31.15	32.04	29.08	29.72	32.10	29.12	30.08
Cr_2O_3	0.00	0.00	0.00	0.00	0.00	0.01	0.01	0.00	0.00	0.02	0.02	0.00
FeO	0.63	0.52	0.63	0.73	0.60	0.60	0.63	0.72	0.59	0.55	0.64	0.66
MgO	0.04	0.03	0.03	0.09	0.05	0.05	0.04	0.04	0.06	0.03	0.04	0.04
CaO	15.90	16.93	15.01	16.06	16.24	16.18	17.10	13.28	14.32	17.06	13.56	14.76
BaO	0.04	0.04	0.05	0.02	0.06	0.03	0.04	0.08	0.07	0.01	0.09	0.08
Na_2O	1.95	1.59	2.62	1.48	1.81	1.92	1.35	3.60	2.92	1.34	3.39	2.74
K_2O	0.07	0.04	0.13	0.13	0.10	0.10	0.07	0.18	0.16	0.04	0.16	0.13
P_2O_5	0.01	0.00	0.01	0.01	0.02	0.01	0.00	0.01	0.01	0.02	0.03	0.00
Cl	0.00	0.00	0.00	0.04	0.00	0.00	0.00	0.00	0.01	0.00	0.00	0.00
Total	94.2	94.9	94.1	95.0	94.8	94.6	94.8	95.1	94.7	94.5	94.6	94.5

Table 6: Major element compositions of plagioclase electron microprobe analyses. Element compositions reported as wt.%.

	BC14/ 015_Plag7	BC14/ 015_Plag7	BC14 /015_Plag7	BC14/ 015_Plag7	BC14/ 015_Plag7	BC14/ 015_Plag7	BC14/ 015_Plag7	BC14/ 015_Plag7	BC14/ 015_Plag7	BC14/ 015_PlagInc1	BC14/ 015_PlagInc1
SiO_2	42.36	42.10	40.21	38.61	42.91	42.21	42.21	42.40	45.32	22.06	43.20
TiO_2	0.02	0.01	0.00	0.01	0.02	0.00	0.01	0.02	0.02	0.48	0.02
Al_2O_3	32.46	32.71	31.58	35.98	32.37	32.82	32.78	32.74	30.72	11.25	31.97
Cr_2O_3	0.01	0.00	0.01	0.00	0.00	0.02	0.00	0.00	0.00	0.02	0.01
FeO	0.52	0.62	0.55	0.59	0.59	0.59	0.50	0.61	0.70	0.66	0.63
MgO	0.03	0.02	0.08	0.18	0.05	0.04	0.04	0.01	0.04	0.23	0.03
CaO	17.83	18.11	16.51	16.31	17.34	18.16	18.00	17.93	15.31	8.74	17.13
BaO	0.02	0.02	0.05	0.02	0.03	0.03	0.03	0.03	0.06	0.01	0.04
Na_2O	0.86	0.70	0.90	0.74	1.21	0.72	0.85	0.90	2.46	1.54	1.39
K_2O	0.03	0.03	0.13	0.06	0.06	0.04	0.04	0.03	0.12	0.43	0.08
P_2O_5	0.00	0.00	0.02	0.02	0.00	0.00	0.01	0.01	0.01	0.19	0.02
Cl	0.00	0.00	0.09	0.03	0.00	0.01	0.00	0.01	0.00	1.53	0.01
Total	94.1	94.3	90.2	92.6	94.6	94.7	94.5	94.7	94.8	47.6	94.5

Table 6: Major element compositions of plagioclase electron microprobe analyses. Element compositions reported as wt.%.

	B10_Ox1-1	B10_Ox2-1	B10_Ox2-2	B25_Ox1-1	B25_Ox1-2	B24_Ox1-1	B24_Ox1-2	B8_Ox1-1	B8_Ox1-2	B2H_Ox1-1	B2H_Ox1-2	B2H_Ox1-3	B2H_Ox1-4
SiO_2	0.03	0.11	0.11	0.08	0.09	0.03	0.04	0.06	0.06	0.08	0.03	0.10	0.02
TiO_2	5.50	5.35	5.28	5.12	5.16	4.80	4.87	5.00	5.00	5.67	5.61	5.66	5.68
ZnO													
Al_2O_3	5.75	5.55	5.35	8.23	7.72	5.54	5.35	5.92	5.86	6.65	6.65	6.53	6.39
Cr_2O_3	0.03	0.03	0.04	0.01	0.01	0.01	0.02	-0.01	0.02	0.02	0.01	0.01	0.03
FeO	77.51	76.82	76.94	72.70	72.24	76.79	77.03	77.00	76.75	74.91	74.12	75.25	74.84
NiO	0.02	0.03	0.04	0.00	-0.02	-0.01	0.00	0.01	0.01	0.05	0.05	0.01	0.02
MnO	0.43	0.44	0.43	0.47	0.53	0.58	0.56	0.52	0.54	0.54	0.55	0.51	0.58
MgO	3.51	3.43	3.37	4.68	4.47	3.37	3.48	3.13	3.10	4.57	4.40	4.45	4.59
CaO	0.02	0.01	0.05	0.05	0.03	0.02	0.03	0.02	0.01	0.03	0.02	0.01	0.03
BaO													
Na_2O	0.03	0.01	0.01	0.08	0.03	0.02	0.01	0.00	0.02	0.00	0.07	-0.01	0.07
K_2O	0.02	0.01	0.00	0.03	0.02	0.00	0.00	0.01	0.00	0.01	0.01	0.01	-0.01
P_2O_5	0.04	-0.07	0.04	-0.03	-0.02	0.01	0.00	0.03	0.03	0.00	-0.01	-0.01	0.00
Cl	0.00	0.01	0.01	0.01	-0.01	0.01	-0.01	-0.01	-0.01	0.00	0.00	0.01	0.00
F													
V_2O_5													
TOTAL	92.9	91.8	91.7	91.5	90.3	91.2	91.4	91.7	91.4	92.5	91.5	92.5	92.2

Table 7: Major element compositions of magnetite electron microprobe analyses. Element compositions reported as wt.%.

	B2H_ Ox2-1	B2H_ Ox2-2	B2H_ Ox2-3	B2H_ Ox2-4	B2H_ OxInc1 -1	B2H_ OxInc1 -2	B16_O x1-1	B16_O x1-2	B16_O x1-3	B16_O x1-4	B16_O x1-5	B27_O x1	B27_O x2
SiO_2	0.09	0.09	1.48	0.05	0.10	0.06	0.03	0.05	0.05	0.06	0.08	0.11	0.08
TiO_2	5.11	4.69	5.88	5.83	7.45	7.67	4.03	4.11	4.09	4.15	4.11	5.26	6.25
ZnO													
Al_2O_3	6.36	6.28	6.39	6.36	3.63	3.31	5.83	5.88	5.93	5.79	5.70	5.80	6.35
Cr_2O_3	0.01	-0.01	0.02	0.03	0.03	0.04	0.03	0.03	0.01	0.03	0.02	0.07	0.01
FeO	76.09	76.46	73.72	75.20	75.81	75.24	78.24	77.99	78.44	78.01	78.22	74.98	75.02
NiO	0.04	0.04	0.03	0.04	0.05	0.03	0.02	0.03	0.03	0.03	0.01	0.05	0.05
MnO	0.48	0.59	0.44	0.58	0.56	0.60	0.36	0.37	0.38	0.36	0.37	0.59	0.90
MgO	4.17	3.95	4.39	4.39	3.91	3.47	3.48	3.19	3.10	3.31	3.11	3.33	3.30
CaO	0.02	0.02	0.21	0.05	0.02	0.03	0.03	0.01	0.03	0.01	0.01	0.01	0.01
BaO												0.06	0.09
Na_2O	0.03	0.11	0.29	0.02	0.01	0.09	0.03	0.00	0.01	0.03	0.03	0.00	0.00
K_2O	0.00	0.00	0.14	0.00	-0.01	0.00	0.00	0.00	0.00	0.02	0.00	0.00	0.00
P_2O_5	0.00	-0.01	0.01	0.00	0.00	-0.02	0.00	0.00	0.02	0.01	0.01	0.03	0.04
Cl	0.01	0.01	0.01	0.01	0.00	0.02	0.00	-0.01	0.01	0.00	0.00	0.01	0.00
F												0.14	0.15
V_2O_5													
TOTAL	92.4	92.3	93.0	92.5	91.6	90.6	92.1	91.7	92.1	91.8	91.7	90.4	92.2

Table 7: Major element compositions of magnetite electron microprobe analyses. Element compositions reported as wt.%.

	B27_Ox3	B27_Ox4	B27_Ox5	SA18_Ox1	SA18_Ox2	SA18_Ox3	SA18_Ox4	SA18_Ox5	SA19_Ox1	SA19_Ox2	SA19_Ox3	SA19_Ox4	SA19_Ox5
SiO_2	0.11	0.08	0.11	0.13	0.04	0.06	0.05	0.11	0.08	0.10	0.08	0.08	0.14
TiO_2	5.92	5.94	6.39	5.66	5.73	5.80	5.90	5.76	5.26	5.95	7.07	5.61	6.92
ZnO													
Al_2O_3	7.80	5.54	5.78	6.84	7.02	6.91	7.01	6.92	3.74	4.08	4.75	4.24	4.63
Cr_2O_3	0.00	0.00	0.02	0.00	0.05	0.02	0.04	0.03	0.00	0.00	0.00	0.00	0.01
FeO	72.90	76.99	76.19	73.89	73.35	74.50	74.26	74.28	78.62	75.58	72.07	74.89	70.57
NiO	0.04	0.04	0.07	0.12	0.04	0.03	0.00	0.01	0.00	0.00	0.00	0.00	0.00
MnO	0.58	0.74	0.87	0.42	0.44	0.51	0.60	0.44	0.66	0.30	0.06	0.20	0.20
MgO	3.59	3.14	2.72	4.45	4.47	4.63	4.54	4.52	2.57	1.75	2.15	1.76	2.16
CaO	0.04	0.01	0.03	0.02	0.02	0.00	0.00	0.01	0.03	0.00	0.19	0.05	0.13
BaO	0.11	0.07	0.16	0.11	0.17	0.09	0.13	0.06	0.13	0.16	0.09	0.08	0.11
Na_2O	0.00	0.00	0.00	0.00	0.00	0.00	0.00	0.00	0.00	0.01	0.00	0.00	0.19
K_2O	0.01	0.02	0.01	0.00	0.00	0.00	0.02	0.03	0.02	0.03	0.07	0.04	0.12
P_2O_5	0.02	0.01	0.00	0.00	0.01	0.00	0.00	0.00	0.00	0.04	0.11	0.02	0.02
Cl	0.00	0.01	0.03	0.00	0.02	0.00	0.00	0.01	0.01	0.50	0.50	0.47	0.49
F	0.19	0.14	0.18	0.09	0.13	0.15	0.16	0.16	0.18	0.12	0.13	0.14	0.17
V_2O_5													
TOTAL	91.3	92.7	92.6	91.7	91.5	92.7	92.7	92.3	91.3	88.6	87.3	87.6	85.9

Table 7: Major element compositions of magnetite electron microprobe analyses. Element compositions reported as wt.%.

	B22_Ox1-1	B22_Ox1-2	B22_Ox1-3	B22_Ox2-1	B22_Ox2-2	B22_Ox3-1	B22_Ox3-2	B22_Ox3-3	B22_Ox4-1	B22_Ox4-2	B22_Ox4-3	SA88-301_Ox1-1	SA88-301_Ox2-2
SiO_2	0.11	0.12	0.03	0.07	0.27	0.07	0.06	0.06	0.23	0.10	0.06	0.07	0.11
TiO_2	5.14	5.23	5.26	5.20	5.10	5.19	5.21	5.08	4.79	5.25	5.22	7.36	9.11
ZnO													
Al_2O_3	6.09	6.11	6.18	6.13	6.04	6.07	6.21	6.27	5.24	6.16	6.07	12.08	9.08
Cr_2O_3	0.13	0.10	0.09	0.12	0.12	0.28	0.35	0.32	0.14	0.20	0.14	0.02	0.00
FeO	76.39	76.21	76.34	75.45	74.23	76.26	74.42	75.00	72.74	76.03	75.18	64.78	65.62
NiO	0.04	0.03	0.01	0.08	0.07	0.05	0.02	0.01	0.00	0.02	0.04	0.10	0.05
MnO	0.51	0.38	0.36	0.42	0.49	0.47	0.43	0.45	0.44	0.51	0.42	0.70	0.71
MgO	3.69	3.47	3.64	3.68	3.52	3.59	3.58	3.65	2.86	3.57	3.55	7.32	7.22
CaO	0.00	0.00	0.01	0.01	0.01	0.01	0.00	0.00	0.01	0.02	0.03	0.18	0.28
BaO	0.07	0.16	0.06	0.12	0.09	0.12	0.10	0.03	0.17	0.01	0.15	0.11	0.14
Na_2O	0.01	0.00	0.00	0.00	0.00	0.00	0.00	0.00	0.00	0.00	0.00	0.00	0.01
K_2O	0.01	0.00	0.00	0.00	0.02	0.00	0.00	0.01	0.03	0.00	0.00	0.01	0.03
P_2O_5	0.00	0.01	0.00	0.00	0.03	0.00	0.02	0.04	0.00	0.00	0.02	0.06	0.03
Cl	0.00	0.00	0.00	0.00	0.00	0.00	0.01	0.01	0.01	0.00	0.02	0.00	0.02
F	0.15	0.16	0.13	0.15	0.10	0.17	0.18	0.14	0.12	0.13	0.13	0.06	0.06
V_2O_5													
TOTAL	92.4	92.0	92.1	91.4	90.1	92.3	90.6	91.1	86.8	92.0	91.0	92.8	92.5

Table 7: Major element compositions of magnetite electron microprobe analyses. Element compositions reported as wt.%.

	SA88-301_Ox3-1	B21_Ox1-1	B21_Ox1-2	B21_Ox1-3	B21_Ox2-1	B21_Ox2-2	B21_Ox2-3	B1B_Ox1-1	B1B_Ox2-1	B1B_Ox2-2	B1B_Ox3-1	B1B_Ox3-2	B1B_Ox3-3
SiO_2	0.15	0.10	0.08	0.28	0.09	0.03	0.08	0.09	0.08	33.56	0.13	0.06	0.09
TiO_2	9.18	4.43	4.43	4.02	3.51	3.55	3.54	7.06	5.79	0.35	5.67	5.80	5.64
ZnO													
Al_2O_3	4.28	5.59	5.67	6.05	6.57	6.55	6.39	6.40	5.99	1.02	6.13	5.91	5.88
Cr_2O_3	0.00	0.00	0.00	0.07	0.45	0.41	0.36	0.03	0.00	0.04	0.02	0.03	0.01
FeO	72.25	76.48	76.64	73.37	75.71	77.27	75.49	75.27	76.46	27.18	75.84	76.22	75.32
NiO	0.06	0.04	0.03	0.09	0.12	0.09	0.01	0.03	0.00	0.08	0.03	0.01	0.00
MnO	0.92	0.41	0.42	0.43	0.37	0.39	0.37	0.54	0.55	0.80	0.47	0.46	0.52
MgO	2.78	3.02	3.05	3.21	3.37	3.44	3.14	3.23	2.97	27.83	3.37	3.09	3.50
CaO	0.03	0.00	0.00	0.01	0.00	0.02	0.04	0.04	0.02	2.29	0.04	0.03	0.00
BaO	0.27	0.02	0.18	0.07	0.01	0.12	0.05	0.07	0.08	0.00	0.12	0.12	0.11
Na_2O	0.00	0.00	0.00	0.00	0.00	0.00	0.06	0.00	0.00	0.02	0.00	0.00	0.00
K_2O	0.05	0.01	0.00	0.02	0.00	0.02	0.04	0.00	0.01	0.01	0.01	0.01	0.02
P_2O_5	0.00	0.00	0.00	0.00	0.00	0.00	0.00	0.02	0.04	0.21	0.01	0.03	0.01
Cl	0.02	0.00	0.03	0.00	0.00	0.00	0.08	0.00	0.00	0.01	0.01	0.01	0.01
F	0.13	0.16	0.16	0.13	0.13	0.17	0.19	0.13	0.19	0.00	0.13	0.11	0.16
V_2O_5													
TOTAL	90.1	90.3	90.7	87.8	90.3	92.1	89.8	92.9	92.2	93.4	92.0	91.9	91.3

Table 7: Major element compositions of magnetite electron microprobe analyses. Element compositions reported as wt.%.

	B1B_Ox4-1	B1B_Ox4-2	B1B_Ox5	B7_Ox1-1	B7_Ox1-2	SA8_Ox1-1	SA8_Ox1-2	SA8_Ox1-3	SA8_Ox2-1	SA8_Ox2-2	SA8_Ox2-3	B35_Ox1	B35_Ox1
SiO_2	0.06	0.13	0.10	0.06	0.05	0.07	0.04	0.12	0.10	0.11	0.07	0.09	0.05
TiO_2	5.79	5.89	9.09	5.45	5.55	5.21	5.65	5.31	5.63	5.77	5.47	5.17	1.06
ZnO													
Al_2O_3	5.97	6.27	7.15	5.58	5.38	5.08	5.56	4.58	5.32	5.15	5.01	5.58	5.13
Cr_2O_3	0.04	0.04	0.03	0.04	0.04	0.00	0.01	0.06	0.03	0.02	0.00	0.00	0.04
FeO	75.39	74.11	69.30	75.52	75.99	76.39	75.84	74.69	76.93	77.34	75.85	76.44	79.10
NiO	0.03	0.07	0.00	0.00	0.04	0.06	0.00	0.00	0.01	0.00	0.01	0.00	0.05
MnO	0.51	0.57	0.42	0.55	0.51	0.60	0.70	0.67	0.64	0.60	0.64	0.79	0.86
MgO	3.58	3.20	4.36	3.51	3.59	3.06	3.15	3.49	3.07	2.57	3.82	2.82	2.91
CaO	0.03	0.02	0.04	0.01	0.00	0.02	0.01	0.04	0.00	0.00	0.01	0.00	0.01
BaO	0.14	0.22	0.18	0.10	0.12	0.16	0.14	0.13	0.14	0.12	0.10	0.00	0.00
Na_2O	0.00	0.00	0.00	0.00	0.00	0.00	0.00	0.00	0.00	0.00	0.00	0.00	0.00
K_2O	0.00	0.00	0.00	0.00	0.01	0.02	0.01	0.04	0.00	0.00	0.02	0.00	0.00
P_2O_5	0.01	0.03	0.01	0.00	0.00	0.00	0.02	0.02	0.05	0.00	0.02	0.00	0.02
Cl	0.00	0.01	0.02	0.02	0.00	0.01	0.01	0.01	0.00	0.00	0.01	0.00	0.00
F	0.12	0.17	0.14	0.16	0.12	0.13	0.14	0.11	0.13	0.16	0.16	0.68	0.66
V_2O_5													
TOTAL	91.7	90.7	90.8	91.0	91.4	90.8	91.3	89.3	92.0	91.9	91.2	91.6	89.9

Table 7: Major element compositions of magnetite electron microprobe analyses. Element compositions reported as wt.%.

	B35_O x1	B23_O x1	B23_O x1	B29_O x1	B29_O x1	B29_O x2	B29_O x2	B29_O x2	B29_O x2	B37_O x1	B37_O x1	B37_O x1	B37_O x1
SiO_2	0.11	0.12	0.16	0.17	0.07	0.21	0.11	0.14	0.07	0.22	0.09	0.09	0.06
TiO_2	11.23	4.69	4.68	4.76	5.84	4.07	6.50	5.31	4.48	8.59	9.49	9.51	9.47
ZnO													
Al_2O_3	3.61	7.47	7.48	7.11	8.71	7.75	8.76	8.96	8.89	3.72	4.60	4.56	4.50
Cr_2O_3	0.03	0.94	0.94	0.18	0.15	0.16	0.22	0.21	0.18	0.06	0.03	0.05	0.01
FeO	70.92	73.13	72.48	71.91	70.79	68.67	72.32	74.02	68.21	68.49	75.55	75.35	75.13
NiO	0.01	0.10	0.07	0.07	0.09	0.05	0.04	0.03	0.04	0.00	0.00	0.00	0.06
MnO	0.76	0.32	0.31	0.40	0.38	0.51	0.43	0.51	0.39	0.61	0.79	0.73	0.69
MgO	2.15	5.06	4.98	3.62	4.40	4.03	3.88	3.82	4.52	1.31	1.70	1.75	1.61
CaO	0.02	0.03	0.02	0.06	0.06	0.13	0.02	0.01	0.02	0.19	0.01	0.01	0.02
BaO	0.07	0.00	0.02	0.01	0.00	0.04	0.00	0.05	0.00	0.00	0.01	0.02	0.02
Na_2O	0.04	0.00	0.00	0.05	0.17	0.07	0.00	0.00	0.00	0.07	0.01	0.00	0.03
K_2O	0.00	0.01	0.00	0.01	0.02	0.00	0.00	0.01	0.00	0.03	0.00	0.00	0.01
P_2O_5	0.02	0.00	0.00	0.02	0.03	0.00	0.03	0.00	0.05	0.00	0.00	0.00	0.06
Cl	0.00	0.00	0.00	0.03	0.04	0.01	0.00	0.01	0.00	0.06	0.01	0.00	0.04
F	0.66	0.64	0.59	0.59	0.64	0.50	0.63	0.60	0.63	0.73	0.70	0.64	0.66
V_2O_5													
TOTAL	89.6	92.5	91.7	89.0	91.4	86.2	92.9	93.7	87.5	84.1	93.0	92.7	92.4

Table 7: Major element compositions of magnetite electron microprobe analyses. Element compositions reported as wt.%.

	B1A_Ox1	B1A_Ox1	B1A_Ox1	B1A_Ox1	B1A_Ox1	B1A_Ox2	B1A_Ox2	SA12/X01_Mgt1	SA12/X01_Mgt1	BC14/038_Mgt1	BC14/038_Mgt1	BC14/038_Mgt1	BC14/015_Mgt1
SiO_2	0.07	0.09	0.15	0.09	0.36	0.59	0.09	0.15	0.10	0.56	0.08	0.07	0.20
TiO_2	4.72	4.77	4.75	4.76	4.80	4.46	5.01	8.77	8.82	5.04	5.17	5.14	5.77
ZnO								0.06	0.05	0.06	0.09	0.04	0.08
Al_2O_3	7.90	7.59	7.69	7.39	7.89	6.51	7.06	3.99	3.92	9.38	8.39	8.09	7.14
Cr_2O_3	0.01	0.00	0.01	0.02	0.05	0.01	0.02	0.02	0.02	0.02	0.03	0.02	0.05
FeO	73.74	73.92	73.18	73.42	72.04	65.66	74.64	73.53	73.99	71.42	74.07	72.53	70.42
NiO	0.07	0.06	0.09	0.05	0.03	0.06	0.00						
MnO	0.41	0.41	0.39	0.48	0.34	0.44	0.47	0.72	0.72	0.42	0.53	0.41	0.68
MgO	3.78	4.02	3.82	4.04	4.21	2.82	3.80	3.94	4.00	4.85	5.01	4.87	3.21
CaO	0.01	0.02	0.05	0.02	0.03	0.16	0.01	0.03	0.03	0.06	0.06	0.02	0.02
BaO	0.00	0.00	0.00	0.00	0.00	0.02	0.01	0.04	0.00	0.00	0.01	0.00	0.00
Na_2O	0.00	0.00	0.02	0.00	0.03	0.10	0.00	0.00	0.00	0.01	0.00	0.00	0.05
K_2O	0.00	0.01	0.00	0.00	0.02	0.04	0.00	0.02	0.02	0.02	0.00	0.00	0.01
P_2O_5	0.02	0.07	0.03	0.02	0.00	0.00	0.00	0.02	0.00	0.01	0.00	0.02	0.00
Cl	0.00	0.00	0.00	0.00	0.00	0.03	0.00	0.00	0.00	0.02	0.01	0.00	0.00
F	0.67	0.52	0.61	0.65	0.62	0.55	0.56	0.27	0.24	0.30	0.26	0.32	0.26
V_2O_5													
TOTAL	91.4	91.5	90.8	90.9	90.4	81.5	91.7	91.4	91.8	92.0	93.6	91.4	87.8

Table 7: Major element compositions of magnetite electron microprobe analyses. Element compositions reported as wt.%.

	BC14/015_Mgt1	BC14/015_Mgt1	BC14/015_Mgt1	BC14/015_Mgt1	BC14/015_Mgt1	BC14/015_Mgt1	BC14/015_Mgt1	SA12X026_Mgt1	SA12X026_Mgt1	SA12X026_Mgt1	SA12X026_Mgt1	SA12X026_Mgt1	SA12X026_Mgt2
SiO_2	0.10	0.24	1.31	0.12	0.27	0.14	0.11	0.07	0.09	0.10	0.08	0.13	0.15
TiO_2	4.87	4.76	4.36	4.85	8.39	9.23	9.76	5.03	5.19	5.16	5.16	5.20	5.02
ZnO	0.05	0.12	0.05	0.08	0.12	0.13	0.17	0.03	0.03	0.08	0.04	0.02	0.03
Al_2O_3	7.56	7.88	21.02	7.96	3.89	2.71	2.40	7.38	7.63	7.56	7.61	7.60	7.47
Cr_2O_3	0.06	0.07	0.05	0.08	0.05	0.02	0.02	0.04	0.04	0.05	0.05	0.02	0.03
FeO	71.06	69.60	61.39	69.99	71.90	73.14	72.08	81.64	82.41	81.52	80.92	81.14	80.72
NiO													
MnO	0.48	0.41	0.43	0.45	0.94	0.98	1.08	0.39	0.39	0.41	0.40	0.38	0.40
MgO	4.45	4.50	4.83	4.74	1.71	1.50	1.48	4.60	4.43	4.50	4.64	4.59	4.45
CaO	0.01	0.04	0.24	0.03	0.07	0.04	0.12	0.00	0.00	0.01	0.00	0.00	0.00
BaO	0.00	0.00	0.01	0.01	0.00	0.00	0.00	0.07	0.13	0.06	0.08	0.07	0.08
Na_2O	0.02	0.05	0.19	0.02	0.01	0.00	0.01	0.06	0.00	0.02	0.05	0.00	0.01
K_2O	0.00	0.01	0.04	0.00	0.03	0.02	0.01	0.00	0.00	0.00	0.00	0.00	0.00
P_2O_5	0.00	0.01	0.01	0.00	0.01	0.00	0.00						
Cl	0.00	0.01	0.04	0.00	0.00	0.00	0.00	0.01	0.00	0.00	0.00	0.01	0.01
F	0.25	0.28	0.13	0.31	0.26	0.30	0.27	0.00	0.08	0.00	0.04	0.00	0.02
V_2O_5								0.45	0.49	0.44	0.48	0.46	0.46
TOTAL	88.8	87.8	94.1	88.5	87.5	88.1	87.4	99.8	100.9	100.0	99.6	99.6	98.9

Table 7: Major element compositions of magnetite electron microprobe analyses. Element compositions reported as wt.%.

	BC14/019_Olivine1	BC14/019_Olivine1	BC14/019_Olivine1	BC14/019_Olivine1	BC14/019_Olivine1	BC14/019_Olivine2	BC14/019_Olivine2	BC14/019_Olivine2	BC14/019_Olivine2	BC14/019_Olivine2	BC14/019_Olivine3	BC14/019_Olivine3	BC14/019_Olivine3
SiO_2	37.86	37.87	38.94	38.26	38.60	38.34	38.86	38.42	37.91	38.25	38.02	38.05	38.23
TiO_2	0.03	0.01	0.02	0.01	0.01	0.00	0.00	0.00	0.00	0.00	0.01	0.00	0.00
ZnO	0.00	0.04	0.05	0.05	0.07	0.03	0.06	0.04	0.05	0.02	0.01	0.02	0.00
Al_2O_3	0.04	0.02	0.05	0.12	0.03	0.04	0.02	0.04	0.01	0.02	0.02	0.03	0.05
Cr_2O_3	0.00	0.00	0.00	0.01	0.00	0.00	0.00	0.02	0.02	0.00	0.02	0.01	0.01
FeO	21.58	20.85	20.96	20.77	20.68	21.89	21.88	20.57	21.03	20.21	20.73	21.22	20.96
MnO	0.57	0.67	0.56	0.60	0.55	0.61	0.58	0.63	0.61	0.60	0.58	0.63	0.61
MgO	38.56	38.88	39.83	39.91	40.26	39.45	40.01	39.19	39.22	39.54	39.07	38.91	38.82
CaO	0.19	0.16	0.18	0.18	0.18	0.16	0.17	0.18	0.17	0.19	0.21	0.19	0.21
BaO	0.00	0.00	0.00	0.00	0.00	0.00	0.00	0.02	0.02	0.00	0.00	0.00	0.00
Na_2O	0.00	0.00	0.00	0.00	0.00	0.05	0.07	0.03	0.00	0.00	0.04	0.00	0.05
K_2O	0.00	0.00	0.01	0.00	0.00	0.01	0.00	0.00	0.00	0.00	0.00	0.00	0.01
SO_3	0.00	0.00	0.00	0.00	0.01	0.01	0.00	0.01	0.00	0.01	0.00	0.00	0.01
Cl	0.00	0.00	0.00	0.00	0.00	0.01	0.00	0.00	0.01	0.00	0.00	0.01	0.01
F	0.04	0.05	0.00	0.00	0.05	0.05	0.00	0.00	0.05	0.00	0.07	0.00	0.00
TOTAL	98.9	98.5	100.6	99.9	100.4	100.6	101.7	99.2	99.1	98.9	98.8	99.1	98.9

Table 8: Major element compositions of olivine electron microprobe analyses. Element compositions reported as wt.%.

	BC14/019_Olivine3	BC14/019_Olivine3	BC14/019_Olivine3	BC14/019_Olivine3	BC14/019_Olivine3	BC14/019_Olivine3	BC14/019_Olivine3	BC14/041_Olivine1	BC14/041_Olivine1	BC14/041_Olivine1	BC14/041_Olivine1	BC14/041_Olivine1	BC14/041_Olivine1
SiO_2	38.31	38.32	37.76	38.23	38.30	37.86	38.05	38.88	39.00	38.80	38.79	39.10	39.04
TiO_2	0.02	0.07	0.00	0.00	0.00	0.05	0.03	0.00	0.00	0.02	0.02	0.02	0.03
ZnO	0.07	0.01	0.00	0.03	0.03	0.07	0.05	0.00	0.08	0.00	0.04	0.03	0.01
Al_2O_3	0.03	0.05	0.04	0.01	0.03	0.02	0.02	0.00	0.00	0.00	0.01	0.01	0.02
Cr_2O_3	0.00	0.00	0.00	0.00	0.00	0.00	0.00	0.00	0.00	0.00	0.00	0.00	0.00
FeO	21.79	21.78	21.28	21.46	20.99	21.33	21.24	17.69	17.42	17.09	17.01	17.34	17.72
MnO	0.62	0.61	0.60	0.63	0.63	0.59	0.59	0.46	0.44	0.46	0.45	0.42	0.44
MgO	39.24	38.87	39.07	38.79	38.74	38.74	38.84	42.82	42.67	42.58	42.41	42.12	42.20
CaO	0.17	0.17	0.19	0.18	0.17	0.19	0.22	0.18	0.21	0.20	0.21	0.20	0.20
BaO	0.00	0.00	0.00	0.02	0.01	0.00	0.00	0.00	0.00	0.00	0.00	0.00	0.00
Na_2O	0.00	0.00	0.06	0.01	0.01	0.01	0.00	0.07	0.05	0.02	0.00	0.03	0.00
K_2O	0.00	0.00	0.00	0.00	0.00	0.00	0.00	0.00	0.00	0.01	0.00	0.00	0.00
SO_3	0.00	0.00	0.02	0.01	0.03	0.00	0.00	0.00	0.00	0.02	0.03	0.00	0.00
Cl	0.00	0.01	0.02	0.00	0.00	0.00	0.00	0.03	0.00	0.01	0.00	0.01	0.00
F	0.02	0.03	0.03	0.00	0.00	0.00	0.02	0.00	0.00	0.00	0.01	0.07	0.00
TOTAL	100.3	99.9	99.1	99.4	98.9	98.9	99.1	100.1	99.9	99.2	99.0	99.3	99.7

Table 8: Major element compositions of olivine electron microprobe analyses. Element compositions reported as wt.%.

	BC14/041_Olivine1	BC14/041_Olivine1	BC14/041_Olivine1	BC14/041_Olivine2	BC14/041_Olivine2	BC14/041_Olivine2	BC14/041_Olivine2	BC14/041_Olivine3	BC14/041_Olivine3	BC14/041_Olivine3	BC14/041_Olivine3	BC14/041_Olivine3	BC14/041_Olivine3
SiO_2	38.76	38.60	38.67	38.34	38.90	38.08	38.43	38.45	38.72	38.59	39.06	38.89	38.76
TiO_2	0.01	0.02	0.00	0.00	0.01	0.01	0.05	0.00	0.00	0.00	0.00	0.02	0.02
ZnO	0.02	0.03	0.01	0.09	0.03	0.08	0.04	0.04	0.00	0.05	0.04	0.01	0.01
Al_2O_3	0.00	0.03	0.05	0.03	0.01	0.01	0.02	0.03	0.03	0.03	0.02	0.02	0.02
Cr_2O_3	0.01	0.01	0.00	0.00	0.03	0.00	0.01	0.03	0.02	0.01	0.01	0.00	0.00
FeO	18.14	17.51	18.52	17.74	18.25	19.04	19.95	19.92	19.01	19.17	18.42	17.09	17.29
MnO	0.47	0.52	0.51	0.48	0.48	0.55	0.60	0.66	0.61	0.57	0.50	0.50	0.45
MgO	42.15	41.43	41.28	41.36	41.25	40.48	40.26	39.67	40.49	40.87	41.73	42.16	42.29
CaO	0.20	0.19	0.20	0.20	0.20	0.19	0.16	0.18	0.19	0.19	0.19	0.20	0.17
BaO	0.00	0.00	0.01	0.00	0.00	0.00	0.00	0.00	0.00	0.00	0.00	0.00	0.00
Na_2O	0.02	0.04	0.01	0.04	0.08	0.00	0.00	0.01	0.00	0.00	0.00	0.15	0.00
K_2O	0.00	0.00	0.00	0.00	0.00	0.00	0.00	0.00	0.00	0.00	0.00	0.00	0.01
SO_3	0.00	0.01	0.00	0.03	0.00	0.00	0.03	0.03	0.00	0.00	0.00	0.01	0.00
Cl	0.00	0.00	0.01	0.01	0.00	0.01	0.03	0.01	0.01	0.00	0.00	0.01	0.00
F	0.00	0.00	0.03	0.00	0.00	0.00	0.00	0.00	0.01	0.00	0.00	0.01	0.02
TOTAL	99.8	98.4	99.3	98.3	99.2	98.4	99.6	99.0	99.1	99.5	100.0	99.1	99.0

Table 8: Major element compositions of olivine electron microprobe analyses. Element compositions reported as wt.%.

	BC14/041_Olivine3	SA24_Olivine 1	SA24_Olivine 1	SA24_Olivine 1	SA24_Olivine 1	SA24_Olivine 1	SA24_Olivine 1	SA24_Olivine 1	SA24_Olivine 1	SA24_Olivine 1	SA24_Olivine 1	SA24_Olivine 2	SA24_Olivine 2
SiO_2	38.92	37.71	38.01	37.88	38.27	38.05	38.18	37.85	37.99	38.36	37.84	38.10	38.83
TiO_2	0.00	0.00	0.00	0.00	0.00	0.00	0.01	0.06	0.01	0.00	0.00	0.01	0.00
ZnO	0.02	0.03	0.05	0.10	0.00	0.03	0.00	0.00	0.05	0.02	0.01	0.11	0.00
Al_2O_3	0.01	0.01	0.01	0.02	0.03	0.01	0.03	0.04	0.06	0.02	0.00	0.02	0.03
Cr_2O_3	0.00	0.00	0.02	0.00	0.02	0.00	0.00	0.00	0.01	0.01	0.00	0.00	0.01
FeO	17.02	24.54	23.41	22.18	21.95	21.82	21.55	20.85	21.36	20.67	20.95	22.46	22.24
MnO	0.40	0.59	0.55	0.39	0.45	0.45	0.44	0.39	0.41	0.45	0.49	0.56	0.49
MgO	42.33	37.28	37.77	38.48	38.61	38.70	38.84	39.06	39.07	38.65	37.97	37.54	38.80
CaO	0.20	0.17	0.18	0.20	0.20	0.20	0.20	0.19	0.19	0.19	0.20	0.14	0.19
BaO	0.00	0.00	0.00	0.00	0.00	0.00	0.00	0.00	0.00	0.00	0.01	0.00	0.00
Na_2O	0.00	0.00	0.01	0.00	0.02	0.03	0.00	0.10	0.03	0.00	0.00	0.00	0.04
K_2O	0.00	0.00	0.00	0.00	0.00	0.00	0.00	0.00	0.00	0.01	0.00	0.01	0.00
SO_3	0.03	0.00	0.01	0.00	0.01	0.00	0.00	0.00	0.01	0.00	0.00	0.00	0.00
Cl	0.00	0.00	0.00	0.01	0.02	0.02	0.03	0.00	0.02	0.02	0.00	0.01	0.00
F	0.00	0.03	0.04	0.00	0.01	0.00	0.00	0.00	0.05	0.05	0.00	0.00	0.08
TOTAL	98.9	100.4	100.0	99.3	99.6	99.3	99.3	98.6	99.2	98.4	97.5	99.0	100.7

Table 8: Major element compositions of olivine electron microprobe analyses. Element compositions reported as wt.%.

	SA24_ Olivine 2	SA24_ Olivine 2	SA24_ Olivine 2	SA24_ Olivine 3	SA24_ Olivine 3	SA24_ Olivine 3	SA24_ Olivine 3	SA24_ Olivine 3	SA24_ Olivine 4	SA24_ Olivine 4	SA24_ Olivine 4	SA24_ Olivine 4	SA24_ Olivine 4
SiO_2	37.89	38.34	37.86	36.98	38.60	38.02	38.30	38.06	38.25	38.23	38.10	37.89	38.05
TiO_2	0.00	0.01	0.01	0.00	0.01	0.02	0.01	0.02	0.02	0.00	0.00	0.01	0.03
ZnO	0.07	0.02	0.04	0.04	0.07	0.04	0.06	0.08	0.05	0.00	0.07	0.02	0.03
Al_2O_3	0.02	0.01	0.03	0.03	0.00	0.04	0.04	0.04	0.04	0.03	0.01	0.04	0.04
Cr_2O_3	0.00	0.00	0.00	0.00	0.00	0.00	0.00	0.00	0.00	0.00	0.00	0.00	0.03
FeO	21.59	21.15	22.93	22.75	20.78	22.19	21.27	21.14	21.25	21.61	20.81	21.50	20.85
MnO	0.41	0.43	0.55	0.52	0.45	0.55	0.44	0.41	0.46	0.38	0.40	0.47	0.43
MgO	38.94	38.99	37.40	36.94	38.77	38.39	38.91	38.67	39.29	39.22	38.82	38.72	38.88
CaO	0.20	0.18	0.18	0.18	0.20	0.18	0.20	0.18	0.21	0.20	0.20	0.16	0.17
BaO	0.02	0.02	0.00	0.00	0.00	0.00	0.03	0.00	0.00	0.00	0.00	0.00	0.00
Na_2O	0.00	0.00	0.00	0.00	0.00	0.00	0.01	0.03	0.00	0.02	0.00	0.00	0.00
K_2O	0.00	0.00	0.00	0.00	0.00	0.00	0.00	0.00	0.00	0.00	0.00	0.00	0.00
SO_3	0.00	0.02	0.00	0.00	0.00	0.00	0.01	0.01	0.02	0.01	0.00	0.01	0.01
Cl	0.00	0.01	0.00	0.00	0.01	0.01	0.00	0.00	0.00	0.00	0.02	0.00	0.02
F	0.00	0.08	0.00	0.06	0.00	0.07	0.03	0.05	0.01	0.02	0.03	0.08	0.02
TOTAL	99.1	99.2	99.0	97.5	98.9	99.5	99.3	98.7	99.6	99.7	98.5	98.9	98.6

Table 8: Major element compositions of olivine electron microprobe analyses. Element compositions reported as wt.%.

	BC14/064_Olivine1	BC14/064_Olivine1	BC14/064_Olivine1	BC14/064_Olivine1	BC14/064_Olivine1	BC14/064_Olivine2	BC14/064_Olivine2	BC14/064_Olivine2	BC14/064_Olivine2	BC14/064_Olivine2	BC14/064_Olivine3	BC14/064_Olivine3	BC14/064_Olivine3
SiO_2	37.85	38.45	38.37	38.06	38.05	38.10	38.14	38.22	37.98	38.31	38.28	38.24	38.42
TiO_2	0.00	0.00	0.06	0.03	0.00	0.00	0.02	0.00	0.00	0.02	0.00	0.03	0.00
ZnO	0.01	0.01	0.01	0.02	0.02	0.04	0.01	0.02	0.05	0.04	0.03	0.05	0.05
Al_2O_3	0.02	0.03	0.01	0.02	0.03	0.02	0.04	0.00	0.02	0.05	0.02	0.01	0.03
Cr_2O_3	0.00	0.00	0.00	0.00	0.00	0.00	0.00	0.00	0.01	0.00	0.00	0.00	0.00
FeO	21.35	21.68	21.34	21.66	21.55	21.01	20.88	21.75	21.10	21.22	21.46	22.24	21.45
MnO	0.65	0.66	0.68	0.70	0.66	0.62	0.66	0.58	0.61	0.67	0.69	0.68	0.67
MgO	39.24	39.14	39.20	39.16	39.14	38.61	39.02	39.07	39.21	38.95	38.88	39.00	39.23
CaO	0.15	0.17	0.14	0.17	0.15	0.15	0.19	0.18	0.19	0.17	0.14	0.17	0.16
BaO	0.00	0.00	0.01	0.00	0.02	0.00	0.00	0.00	0.00	0.00	0.00	0.02	0.01
Na_2O	0.02	0.01	0.00	0.03	0.01	0.01	0.02	0.05	0.01	0.02	0.00	0.01	0.01
K_2O	0.00	0.00	0.00	0.00	0.00	0.00	0.01	0.00	0.00	0.00	0.00	0.00	0.00
SO_3	0.00	0.00	0.00	0.00	0.00	0.01	0.00	0.03	0.01	0.01	0.03	0.00	0.01
Cl	0.00	0.02	0.00	0.01	0.02	0.00	0.00	0.00	0.00	0.00	0.00	0.00	0.04
F	0.10	0.06	0.01	0.11	0.00	0.01	0.00	0.01	0.02	0.08	0.07	0.00	0.00
TOTAL	99.3	100.2	99.8	99.9	99.7	98.6	99.0	99.9	99.2	99.5	99.6	100.5	100.1

Table 8: Major element compositions of olivine electron microprobe analyses. Element compositions reported as wt.%.

	BC14/064_Olivine3	BC14/064_Olivine3	BC14/064_Olivine3	BC14/064_Olivine3	BC14/064_Olivine3	BC14/064_Olivine3	BC14/064_Olivine3	BC14/064_Olivine4	BC14/064_Olivine4	BC14/064_Olivine4	BC14/064_Olivine4	BC14/064_Olivine4	SA12X019_Olivine1
SiO_2	38.36	38.53	38.45	38.60	38.37	38.39	38.30	38.21	38.45	37.82	38.15	38.13	38.92
TiO_2	0.03	0.02	0.00	0.00	0.00	0.00	0.00	0.00	0.00	0.01	0.04	0.00	0.01
ZnO	0.03	0.06	0.04	0.03	0.03	0.03	0.01	0.02	0.06	0.06	0.03	0.04	0.07
Al_2O_3	0.00	0.03	0.02	0.01	0.03	0.01	0.04	0.01	0.03	0.04	0.04	0.01	0.05
Cr_2O_3	0.00	0.01	0.02	0.00	0.00	0.00	0.00	0.01	0.01	0.00	0.02	0.00	0.00
FeO	21.54	20.82	20.50	20.86	20.12	20.56	20.86	21.85	21.61	20.88	20.81	21.31	19.32
MnO	0.66	0.63	0.70	0.68	0.69	0.67	0.71	0.69	0.71	0.74	0.67	0.66	0.34
MgO	39.12	39.01	39.00	39.02	39.03	38.96	39.22	38.98	38.67	38.88	39.01	38.76	41.10
CaO	0.18	0.18	0.19	0.20	0.20	0.16	0.17	0.15	0.16	0.19	0.16	0.15	0.24
BaO	0.00	0.01	0.00	0.00	0.02	0.00	0.00	0.00	0.00	0.00	0.00	0.00	0.00
Na_2O	0.00	0.01	0.00	0.01	0.04	0.00	0.03	0.01	0.03	0.06	0.00	0.05	0.03
K_2O	0.00	0.00	0.00	0.01	0.00	0.00	0.00	0.00	0.00	0.00	0.00	0.00	0.00
SO_3	0.00	0.00	0.01	0.03	0.01	0.00	0.00	0.00	0.02	0.03	0.01	0.00	0.00
Cl	0.00	0.00	0.00	0.01	0.00	0.00	0.00	0.00	0.00	0.00	0.00	0.00	0.00
F	0.00	0.00	0.00	0.02	0.00	0.05	0.00	0.00	0.06	0.02	0.05	0.09	0.01
TOTAL	99.9	99.3	98.9	99.5	98.5	98.8	99.3	99.9	99.8	98.7	99.0	99.2	100.1

Table 8: Major element compositions of olivine electron microprobe analyses. Element compositions reported as wt.%.

	SA12X019_Olivine1	SA12X019_Olivine1	SA12X019_Olivine1	SA12X019_Olivine1	SA12X019_Olivine1	SA12X019_Olivine2	SA12X019_Olivine2	SA12X019_Olivine2	SA12X019_Olivine2	SA12X019_Olivine2	SA12X019_Olivine2	SA12X019_Olivine2	SA12X019_Olivine2
SiO_2	39.80	39.58	38.86	39.11	39.22	38.88	39.00	38.95	38.87	38.96	38.69	38.80	38.80
TiO_2	0.00	0.00	0.00	0.01	0.03	0.00	0.00	0.00	0.04	0.01	0.00	0.02	0.00
ZnO	0.00	0.03	0.03	0.01	0.04	0.04	0.01	0.06	0.04	0.02	0.05	0.01	0.06
Al_2O_3	0.02	0.02	0.04	0.04	0.05	0.04	0.05	0.03	0.04	0.02	0.07	0.04	0.05
Cr_2O_3	0.00	0.01	0.00	0.00	0.00	0.01	0.00	0.01	0.00	0.00	0.00	0.00	0.00
FeO	18.42	19.24	19.13	19.26	19.18	18.97	19.72	18.97	19.37	18.73	19.19	18.66	18.58
MnO	0.44	0.43	0.38	0.36	0.37	0.42	0.39	0.37	0.36	0.38	0.37	0.45	0.42
MgO	42.24	41.95	41.00	41.29	40.93	40.98	41.13	41.14	41.20	41.31	41.00	41.07	40.77
CaO	0.24	0.25	0.24	0.23	0.24	0.24	0.23	0.27	0.24	0.26	0.27	0.24	0.24
BaO	0.00	0.01	0.00	0.03	0.00	0.01	0.00	0.02	0.01	0.02	0.00	0.00	0.00
Na_2O	0.01	0.02	0.00	0.00	0.00	0.00	0.02	0.03	0.00	0.02	0.04	0.01	0.09
K_2O	0.00	0.00	0.00	0.00	0.00	0.00	0.00	0.00	0.00	0.00	0.00	0.00	0.00
SO_3	0.01	0.02	0.00	0.00	0.02	0.00	0.00	0.02	0.02	0.00	0.03	0.00	0.01
Cl	0.03	0.00	0.00	0.00	0.00	0.00	0.00	0.00	0.00	0.00	0.01	0.00	0.00
F	0.06	0.00	0.01	0.00	0.00	0.05	0.00	0.08	0.04	0.00	0.00	0.02	0.05
TOTAL	101.2	101.6	99.7	100.3	100.1	99.6	100.5	99.9	100.2	99.7	99.7	99.3	99.0

Table 8: Major element compositions of olivine electron microprobe analyses. Element compositions reported as wt.%.

	SA12X019_Olivine2	SA12X019_Olivine2	SA12X019_Olivine3	SA12X019_Olivine3	SA12X019_Olivine3	SA12X019_Olivine3	SA12X019_Olivine3	SA12X03_Olivine1	SA12X03_Olivine1	SA12X03_Olivine1	SA12X03_Olivine2	SA12X03_Olivine2	SA12X03_Olivine2
SiO_2	38.96	39.32	38.72	38.69	38.56	38.64	39.47	38.44	39.43	38.34	38.90	38.38	38.72
TiO_2	0.02	0.00	0.00	0.00	0.03	0.03	0.00	0.00	0.00	0.00	0.01	0.01	0.00
ZnO	0.03	0.02	0.06	0.05	0.02	0.03	0.04	0.06	0.03	0.03	0.00	0.04	0.01
Al_2O_3	0.04	0.03	0.04	0.04	0.04	0.05	0.06	0.03	0.03	0.03	0.03	0.05	0.04
Cr_2O_3	0.00	0.00	0.00	0.00	0.00	0.01	0.00	0.00	0.02	0.01	0.00	0.00	0.02
FeO	19.04	18.70	19.04	19.67	18.98	19.43	19.28	19.50	18.95	18.75	19.10	19.28	19.07
MnO	0.38	0.45	0.42	0.39	0.40	0.37	0.40	0.45	0.43	0.43	0.42	0.42	0.42
MgO	41.30	40.87	40.87	41.20	40.96	40.68	42.06	40.78	41.74	41.04	41.46	40.19	41.03
CaO	0.24	0.25	0.26	0.26	0.25	0.26	0.25	0.24	0.21	0.23	0.23	0.25	0.24
BaO	0.00	0.00	0.00	0.00	0.01	0.00	0.00	0.00	0.00	0.00	0.02	0.00	0.00
Na_2O	0.00	0.03	0.00	0.00	0.00	0.00	0.07	0.01	0.00	0.00	0.00	0.02	0.03
K_2O	0.00	0.00	0.00	0.00	0.00	0.00	0.00	0.00	0.00	0.00	0.00	0.00	0.00
SO_3	0.01	0.03	0.02	0.02	0.00	0.00	0.03	0.00	0.04	0.03	0.01	0.01	0.01
Cl	0.00	0.01	0.01	0.00	0.00	0.00	0.00	0.01	0.00	0.00	0.00	0.00	0.00
F	0.03	0.00	0.05	0.01	0.00	0.00	0.01	0.00	0.01	0.00	0.02	0.00	0.00
TOTAL	100.0	99.7	99.5	100.3	99.2	99.5	101.7	99.5	100.9	98.9	100.2	98.7	99.6

Table 8: Major element compositions of olivine electron microprobe analyses. Element compositions reported as wt.%.

	SA12X03_Olivine2	SA12X03_Olivine3	SA12X03_Olivine3	SA12X032_Olivine1	SA12X032_Olivine1	SA12X032_Olivine1	SA12X032_Olivine1	SA12X032_Olivine1	SA12X032_Olivine1	SA12X032_Olivine1	SA12X032_Olivine1	SA12X032_Olivine1	SA12X032_Olivine2
SiO_2	38.55	38.26	39.44	38.44	38.30	38.43	38.32	38.14	38.62	38.86	38.75	38.62	38.37
TiO_2	0.00	0.13	0.02	0.00	0.01	0.00	0.00	0.01	0.09	0.04	0.00	0.00	0.00
ZnO	0.05	0.08	0.01	0.00	0.06	0.04	0.03	0.07	0.03	0.04	0.04	0.07	0.10
Al_2O_3	0.03	0.19	0.11	0.01	0.01	0.04	0.05	0.03	0.02	0.03	0.04	0.04	0.09
Cr_2O_3	0.00	0.00	0.00	0.01	0.00	0.00	0.00	0.02	0.03	0.00	0.00	0.00	0.00
FeO	19.24	19.12	18.40	19.85	19.40	19.57	19.64	20.17	19.56	19.55	20.18	20.76	20.30
MnO	0.46	0.44	0.44	0.50	0.50	0.52	0.50	0.52	0.48	0.53	0.52	0.57	0.51
MgO	40.84	40.29	41.48	39.99	39.90	39.86	39.78	39.94	40.18	40.03	40.18	40.25	39.08
CaO	0.23	0.21	0.23	0.15	0.17	0.18	0.19	0.16	0.18	0.17	0.17	0.17	0.22
BaO	0.00	0.00	0.00	0.00	0.00	0.01	0.00	0.00	0.01	0.00	0.00	0.00	0.00
Na_2O	0.03	0.02	0.00	0.03	0.07	0.02	0.00	0.02	0.00	0.00	0.03	0.00	0.01
K_2O	0.00	0.00	0.00	0.00	0.00	0.00	0.01	0.00	0.00	0.00	0.00	0.00	0.00
SO_3	0.04	0.02	0.03	0.02	0.04	0.00	0.00	0.00	0.00	0.00	0.01	0.00	0.01
Cl	0.01	0.00	0.02	0.00	0.00	0.00	0.00	0.00	0.01	0.03	0.00	0.00	0.00
F	0.00	0.00	0.05	0.05	0.01	0.03	0.00	0.03	0.03	0.06	0.05	0.00	0.00
TOTAL	99.5	98.8	100.2	99.0	98.5	98.7	98.5	99.1	99.2	99.3	99.9	100.5	98.7

Table 8: Major element compositions of olivine electron microprobe analyses. Element compositions reported as wt.%.

	SA12X032_Olivine2	SA12X032_Olivine2	SA12X032_Olivine3	SA12X032_Olivine3	SA12X032_Olivine3	SA12X032_Olivine3	BC14/089_Olivine1	BC14/089_Olivine1	BC14/089_Olivine1	BC14/089_Olivine1	BC14/089_Olivine2	BC14/089_Olivine3	BC14/089_Olivine3
SiO_2	39.01	37.60	38.13	38.93	37.96	38.26	38.54	38.80	38.66	38.31	38.75	38.30	38.91
TiO_2	0.02	0.01	0.00	0.00	0.01	0.06	0.00	0.03	0.02	0.02	0.05	0.00	0.01
ZnO	0.11	0.00	0.09	0.05	0.13	0.06	0.09	0.03	0.06	0.07	0.09	0.01	0.04
Al_2O_3	0.06	0.06	0.10	0.15	0.21	0.02	0.03	0.05	0.04	0.05	0.06	0.05	0.05
Cr_2O_3	0.01	0.01	0.00	0.00	0.01	0.00	0.00	0.00	0.00	0.00	0.00	0.00	0.01
FeO	18.85	20.31	19.51	19.15	19.84	19.06	20.63	19.66	20.60	20.73	19.39	20.00	20.24
MnO	0.54	0.50	0.50	0.49	0.52	0.50	0.45	0.42	0.48	0.40	0.39	0.49	0.39
MgO	40.64	39.33	39.69	40.71	39.14	40.29	39.51	40.21	39.75	39.96	40.73	39.02	40.22
CaO	0.18	0.17	0.18	0.18	0.19	0.17	0.24	0.25	0.26	0.25	0.28	0.25	0.25
BaO	0.00	0.00	0.00	0.00	0.00	0.00	0.00	0.01	0.00	0.00	0.00	0.00	0.02
Na_2O	0.03	0.01	0.04	0.06	0.00	0.00	0.01	0.00	0.02	0.02	0.05	0.00	0.02
K_2O	0.00	0.00	0.00	0.00	0.00	0.01	0.00	0.00	0.00	0.00	0.00	0.00	0.01
SO_3	0.00	0.00	0.00	0.02	0.00	0.01	0.02	0.00	0.03	0.01	0.00	0.00	0.01
Cl	0.01	0.01	0.00	0.03	0.04	0.00	0.01	0.05	0.02	0.01	0.00	0.00	0.00
F	0.04	0.00	0.00	0.02	0.02	0.04	0.00	0.03	0.00	0.00	0.00	0.03	0.00
TOTAL	99.5	98.1	98.2	99.8	98.1	98.4	99.5	99.6	99.9	99.8	99.8	98.1	100.2

Table 8: Major element compositions of olivine electron microprobe analyses. Element compositions reported as wt.%.

	BC14/089_Olivine3	BC14/089_Olivine4	BC14/089_Olivine4	BC14/089_Olivine5	BC14/089_Olivine5	BC14-043_OLIVINE1	BC14-043_OLIVINE1	BC14-043_OLIVINE1	BC14-043_OLIVINE1	BC14-043_OLIVINE1	BC14-043_OLIVINE1	BC14-043_OLIVINE1	BC14-043_OLIVINE1
SiO_2	38.56	38.16	37.98	38.25	37.96	38.39	38.19	38.05	38.32	38.09	38.17	38.54	38.41
TiO_2	0.01	0.00	0.00	0.00	0.02	0.01	0.00	0.00	0.00	0.01	0.00	0.01	0.01
ZnO	0.09	0.08	0.07	0.10	0.02								
Al_2O_3	0.06	0.04	0.08	0.03	0.06	0.01	0.01	0.03	0.00	0.01	0.01	0.02	0.02
Cr_2O_3	0.00	0.00	0.00	0.02	0.00								
FeO	19.80	20.23	20.38	20.41	20.52	22.32	22.20	22.03	22.49	22.50	22.42	22.66	22.16
MnO	0.42	0.42	0.42	0.42	0.42	0.73	0.75	0.72	0.71	0.75	0.77	0.71	0.72
MgO	39.68	39.06	39.20	39.31	39.22	39.90	39.72	39.64	40.02	39.93	39.63	40.52	40.11
CaO	0.24	0.24	0.24	0.22	0.26	0.19	0.16	0.26	0.17	0.17	0.18	0.20	0.21
BaO	0.00	0.00	0.01	0.00	0.00								
Na_2O	0.02	0.00	0.05	0.02	0.00								
K_2O	0.00	0.00	0.00	0.00	0.00								
SO_3	0.00	0.04	0.00	0.00	0.03								
Cl	0.00	0.04	0.01	0.00	0.01								
F	0.04	0.00	0.03	0.00	0.03	0.04	0.00	0.00	0.01	0.01	0.00	0.03	0.00
TOTAL	98.9	98.3	98.5	98.8	98.5	101.6	101.0	100.7	101.7	101.5	101.2	102.7	101.6

Table 8: Major element compositions of olivine electron microprobe analyses. Element compositions reported as wt.%.

	BC14-043_OLIVINE1	BC14-043_OLIVINE1	BC14-043_OLIVINE1	BC14-043_OLIVINE1	BC14-043_OLIVINE1	BC14-043_OLIVINE1	BC14-043_OLIVINE1	BC14-043_OLIVINE1	BC14-043_OLIVINE1	BC14-043_OLIVINE1	BC14-043_OLIVINE1	BC14-043_OLIVINE1	BC14-043_OLIVINE1
SiO_2	38.21	38.24	36.50	38.41	38.33	38.43	38.55	38.34	38.56	38.69	37.65	38.25	38.22
TiO_2	0.00	0.00	0.00	0.00	0.01	0.01	0.00	0.00	0.00	0.00	0.01	0.01	0.00
ZnO													
Al_2O_3	0.04	0.01	0.07	0.02	0.02	0.03	0.03	0.02	0.01	0.01	0.07	0.02	0.02
Cr_2O_3													
FeO	22.37	22.49	22.14	22.18	22.18	22.13	22.02	22.01	22.38	22.26	22.11	22.00	22.12
MnO	0.70	0.71	0.68	0.74	0.65	0.73	0.71	0.74	0.72	0.72	0.66	0.74	0.72
MgO	40.18	39.94	37.56	40.16	40.12	40.05	40.31	40.08	40.49	40.46	39.51	39.93	40.00
CaO	0.21	0.21	0.22	0.20	0.20	0.20	0.20	0.22	0.19	0.19	0.21	0.21	0.20
BaO													
Na_2O													
K_2O													
SO_3													
Cl													
F	0.00	0.00	0.03	0.03	0.00	0.00	0.02	0.03	0.01	0.07	0.00	0.02	0.03
TOTAL	101.7	101.6	97.2	101.7	101.5	101.6	101.8	101.4	102.4	102.4	100.2	101.2	101.3

Table 8: Major element compositions of olivine electron microprobe analyses. Element compositions reported as wt.%.

	BC14-043_OLIVINE1	BC14-043_OLIVINE1	BC14-043_OLIVINE1	BC14-043_OLIVINE1	BC14-043_OLIVINE1	BC14-043_OLIVINE1	BC14-043_OLIVINE1	BC14-043_OLIVINE1	BC14-043_OLIVINE1	BC14-043_OLIVINE1	BC14-043_OLIVINE1	BC14-043_OLIVINE1	BC14-043_OLIVINE1
SiO_2	38.49	38.30	38.42	38.60	38.41	38.71	38.70	38.16	38.45	37.88	38.42	38.41	38.18
TiO_2	0.01	0.02	0.02	0.02	0.01	0.01	0.00	0.00	0.01	0.01	0.01	0.00	0.00
ZnO													
Al_2O_3	0.00	0.02	0.00	0.02	0.01	0.01	0.04	0.02	0.04	0.04	0.02	0.02	0.00
Cr_2O_3													
FeO	22.39	21.94	22.18	22.18	22.12	22.18	21.88	22.07	22.20	22.12	22.75	22.67	22.55
MnO	0.70	0.71	0.74	0.75	0.76	0.71	0.69	0.69	0.75	0.73	0.76	0.73	0.76
MgO	40.57	40.20	40.14	39.88	40.16	40.55	40.67	39.48	40.04	39.13	40.16	40.02	39.96
CaO	0.20	0.20	0.20	0.19	0.19	0.20	0.19	0.19	0.18	0.18	0.17	0.19	0.18
BaO													
Na_2O													
K_2O													
SO_3													
Cl													
F	0.00	0.03	0.03	0.00	0.06	0.00	0.01	0.00	0.00	0.01	0.01	0.02	0.02
TOTAL	102.3	101.4	101.7	101.6	101.7	102.4	102.2	100.6	101.7	100.1	102.3	102.1	101.7

Table 8: Major element compositions of olivine electron microprobe analyses. Element compositions reported as wt.%.

	BC14-043_OLIVINE1	BC14-043_OLIVINE1	BC14-043_OLIVINE1	BC14-043_OLIVINE1	BC14-043_OLIVINE1	BC14-043_OLIVINE1	BC14-043_OLIVINE1	BC14-043_OLIVINE1	BC14-043_OLIVINE1	BC14-043_OLIVINE1	BC14-043_OLIVINE1	BC14/039_Ol1	BC14/039_Ol1
SiO_2	38.55	38.15	38.54	38.60	38.36	38.34	38.39	38.32	38.12	38.17	38.53	42.28	38.19
TiO_2	0.00	0.00	0.01	0.00	0.01	0.00	0.00	0.00	0.01	0.00	0.00	0.15	0.00
ZnO												0.10	0.01
Al_2O_3	0.02	0.06	0.02	0.02	0.02	0.01	0.02	0.03	0.01	0.02	0.01	22.27	0.00
Cr_2O_3												0.00	0.00
FeO	22.66	22.47	22.53	22.36	22.79	22.51	22.92	22.90	22.61	22.91	22.68	5.24	20.65
MnO	0.71	0.70	0.73	0.76	0.75	0.75	0.72	0.80	0.77	0.78	0.78	0.15	0.57
MgO	39.73	39.50	39.90	39.92	39.48	39.59	39.85	39.63	39.31	39.22	39.65	8.53	41.11
CaO	0.19	0.21	0.23	0.19	0.18	0.17	0.16	0.17	0.18	0.16	0.17	6.69	0.18
BaO												0.12	0.03
Na_2O												2.57	0.00
K_2O												1.60	0.00
SO_3												0.06	0.00
Cl												0.15	0.00
F	0.02	0.07	0.00	0.01	0.01	0.00	0.01	0.00	0.01	0.00	0.00	0.00	0.00
TOTAL	101.9	101.1	102.0	101.9	101.6	101.4	102.1	101.8	101.0	101.3	101.8	90.1	100.7

Table 8: Major element compositions of olivine electron microprobe analyses. Element compositions reported as wt.%.

	BC14/039_Ol1	BC14/039_Ol1	BC14/039_Ol1	BC14/039_Ol1	BC14/039_Ol1	BC14/039_Ol1	BC14/039_Ol1	BC14/039_Ol1	BC14/039_Ol1	BC14/039_Ol1	BC14/039_Ol1	BC14/039_Ol1	BC14/039_Ol1
SiO_2	38.15	38.24	38.14	38.33	38.49	38.01	38.73	38.09	38.25	38.20	37.75	38.13	38.06
TiO_2	0.00	0.00	0.01	0.01	0.01	0.00	0.00	0.02	0.01	0.00	0.01	0.00	0.02
ZnO	0.04	0.00	0.00	0.10	0.04	0.00	0.02	0.03	0.07	0.02	0.00	0.02	0.03
Al_2O_3	0.01	0.02	0.02	0.03	0.02	0.02	1.12	0.03	0.04	0.03	0.00	0.01	0.02
Cr_2O_3	0.00	0.03	0.00	0.02	0.00	0.00	0.00	0.00	0.00	0.00	0.00	0.00	0.03
FeO	20.51	20.37	20.41	20.31	19.98	20.05	20.22	20.93	20.17	20.22	20.10	20.22	20.41
MnO	0.57	0.57	0.57	0.61	0.59	0.52	0.54	0.52	0.58	0.59	0.59	0.60	0.60
MgO	41.02	40.67	40.74	40.85	40.85	40.46	41.91	40.93	41.07	40.72	40.66	40.60	40.50
CaO	0.18	0.19	0.21	0.18	0.19	0.18	0.20	0.20	0.17	0.17	0.18	0.19	0.19
BaO	0.00	0.02	0.00	0.02	0.02	0.01	0.00	0.03	0.00	0.00	0.00	0.00	0.02
Na_2O	0.00	0.02	0.02	0.01	0.00	0.00	0.03	0.00	0.02	0.02	0.05	0.00	0.02
K_2O	0.00	0.01	0.01	0.01	0.00	0.00	0.00	0.00	0.00	0.00	0.00	0.00	0.00
SO_3	0.00	0.00	0.00	0.00	0.00	0.00	0.01	0.00	0.00	0.00	0.02	0.00	0.00
Cl	0.00	0.00	0.00	0.00	0.00	0.01	0.00	0.00	0.00	0.01	0.00	0.01	0.01
F	0.00	0.02	0.02	0.00	0.00	0.00	0.00	0.00	0.00	0.01	0.03	0.04	0.00
TOTAL	100.5	100.2	100.1	100.5	100.2	99.3	102.8	100.8	100.4	100.0	99.4	99.8	99.9

Table 8: Major element compositions of olivine electron microprobe analyses. Element compositions reported as wt.%.

	BC14/039_Ol1	BC14/039_Ol1	BC14/039_Ol1	BC14/039_Ol1	BC14/039_Ol1	BC14/039_Ol2	BC14/039_Ol2	BC14/039_Ol2	BC14/039_Ol2	BC14/039_Ol2	BC14/039_Ol2	BC14/039_Ol2	BC14/039_Ol2
SiO_2	37.81	38.12	35.49	10.60	35.62	37.79	38.24	39.61	8.59	12.30	38.39	37.85	38.29
TiO_2	0.00	0.00	0.00	0.00	0.03	0.02	0.01	0.00	0.01	0.01	0.00	0.00	0.00
ZnO	0.17	0.12	0.00	0.00	0.03	0.03	0.00	0.00	0.02	0.05	0.04	0.00	0.07
Al_2O_3	0.02	0.01	4.07	1.51	9.81	0.03	0.00	0.08	0.30	0.77	0.01	0.04	0.01
Cr_2O_3	0.04	0.00	0.00	0.00	0.00	0.01	0.00	0.00	0.01	0.00	0.00	0.01	0.00
FeO	20.92	20.30	18.53	4.39	16.95	20.65	20.74	20.97	3.34	2.96	20.94	21.23	20.63
MnO	0.65	0.54	0.55	0.15	0.54	0.61	0.61	0.72	0.20	0.12	0.63	0.61	0.66
MgO	40.55	40.85	36.29	8.56	37.46	40.34	41.03	42.37	6.97	9.77	40.90	40.66	41.13
CaO	0.18	0.19	0.31	0.15	0.31	0.19	0.18	0.20	0.12	0.13	0.19	0.17	0.17
BaO	0.00	0.00	0.00	0.05	0.00	0.00	0.06	0.00	0.00	0.00	0.00	0.00	0.00
Na_2O	0.02	0.03	0.09	0.07	0.08	0.01	0.00	0.00	0.02	0.04	0.01	0.09	0.00
K_2O	0.00	0.00	0.05	0.02	0.03	0.00	0.00	0.01	0.01	0.02	0.01	0.01	0.00
SO_3	0.00	0.00	0.06	0.06	0.00	0.00	0.00	0.00	0.01	0.06	0.00	0.00	0.00
Cl	0.01	0.00	0.02	1.19	0.00	0.00	0.01	0.01	1.21	1.41	0.00	0.00	0.01
F	0.07	0.00	0.00	0.00	0.00	0.00	0.00	0.01	0.01	0.00	0.03	0.05	0.02
TOTAL	100.4	100.2	95.5	26.7	100.9	99.7	100.9	104.0	21.0	27.8	101.1	100.7	101.0

Table 8: Major element compositions of olivine electron microprobe analyses. Element compositions reported as wt.%.

	BC14/039_Ol2	BC14/039_Ol2	BC14/039_Ol2	B25_Ol1-1	SA88-301_Ol1-1	B23_Cpx6	B35_Olivine1	B37_Ol1	B37_Ol1	B37_Ol1	B37_Ol1	B37_Ol2	B37_Ol2
SiO_2	38.02	38.02	39.23	35.14	35.54	36.23	35.32	35.45	35.41	35.35	35.60	34.99	36.61
TiO_2	0.00	0.00	0.02	0.03	0.01	0.01	0.01	0.02	0.02	0.01	0.01	0.03	0.02
ZnO	0.07	0.05	0.00										
Al_2O_3	1.39	0.03	0.88	0.02	0.03	0.03	0.05	0.02	0.02	0.01	0.00	0.01	2.62
Cr_2O_3	0.00	0.00	0.00	-0.01	0.00	0.00	0.01	0.01	0.02	0.02	0.04	0.01	0.05
FeO	19.85	20.51	19.28	27.76	30.64	18.29	28.35	37.60	37.20	37.80	36.64	37.21	36.04
MnO	0.59	0.67	0.57	1.26	1.56	0.34	1.20	1.53	1.65	1.62	1.68	1.56	1.61
MgO	39.83	40.81	41.22	31.89	30.49	40.22	32.43	24.92	25.18	24.40	25.74	24.89	20.78
CaO	0.22	0.18	0.25	0.48	0.42	0.23	0.31	0.38	0.36	0.35	0.36	0.38	1.11
BaO	0.00	0.00	0.00		0.00	0.05	0.02	0.00	0.00	0.03	0.00	0.00	0.00
Na_2O	0.04	0.01	0.26	0.03	0.00	0.00	0.03	0.04	0.02	0.02	0.03	0.01	0.62
K_2O	0.03	0.00	0.10	0.06	0.04	0.01	0.04	0.00	0.01	0.00	0.00	0.00	0.09
SO_3	0.02	0.00	0.02			0.00	0.00	0.01	0.00	0.00	0.01	0.00	0.01
Cl	0.01	0.01	0.14	0.01	0.01	0.00	0.00	0.03	0.01	0.01	0.00	0.02	0.02
F	0.06	0.00	0.00		0.00	0.05	0.11	0.19	0.27	0.36	0.21	0.16	0.16
TOTAL	100.1	100.3	101.9	96.9	98.9	95.5	98.2	100.2	100.3	100.0	100.4	99.3	99.8

Table 8: Major element compositions of olivine electron microprobe analyses. Element compositions reported as wt.%.

	B37_Ol2	B37_Ol2	B37_Ol2	B37_Ol3	b9_7	b9_8	b9_9	b9_16magm	b9_16	b9_17	b9_26	b9_27	b9_28
SiO_2	34.81	34.66	34.71	32.48	39.03	39.42	39.40	38.29	38.44	38.45	38.63	39.06	39.48
TiO_2	0.00	0.03	0.01	0.18	0.00	0.00	0.02	0.01	0.02	0.04	0.00	0.02	0.04
ZnO													
Al_2O_3	0.01	0.03	0.04	0.30	0.03	0.04	0.02	0.03	0.04	0.03	0.00	0.02	0.02
Cr_2O_3	0.00	0.00	0.02	0.00									
FeO	38.58	37.77	38.27	33.74	18.23	17.99	18.13	18.68	18.70	18.84	19.23	19.00	19.47
MnO	1.64	1.64	1.69	1.27	0.28	0.38	0.39	0.41	0.49	0.39	0.36	0.37	0.30
MgO	23.78	23.83	23.31	23.89	43.00	42.72	43.32	42.01	42.42	41.76	41.96	42.31	42.83
CaO	0.34	0.53	0.44	0.40	0.19	0.23	0.21	0.24	0.17	0.20	0.21	0.22	0.18
BaO	0.00	0.01	0.02	0.00	0.00	0.00	0.07	0.00	0.06	0.00	0.00	0.00	0.00
Na_2O	0.00	0.00	0.05	0.06	0.02	0.00	0.01	0.01	0.01	0.04	0.00	0.00	0.00
K_2O	0.00	0.01	0.03	0.04	0.00	0.03	0.00	0.00	0.00	0.02	0.00	0.00	0.00
SO_3	0.02	0.01	0.03	0.01	0.01	0.00	0.02	0.00	0.00	0.00	0.00	0.01	0.00
Cl	0.01	0.01	0.03	0.03	0.01	0.02	0.01	0.00	0.00	0.04	0.00	0.01	0.03
F	0.15	0.26	0.18	0.25	0.00	0.00	0.00	0.00	0.00	0.00	0.00	0.00	0.02
TOTAL	99.4	99.1	99.0	92.6	100.8	100.9	101.6	99.7	100.4	99.9	100.6	101.0	102.4

Table 8: Major element compositions of olivine electron microprobe analyses. Element compositions reported as wt.%.

	SA310_19	SA310_20	SA310_21	SA310_22	SA310_23	SA310_24	SA310_34	B23_1	B23_2	B23_3
SiO_2	38.56	38.67	38.69	38.49	38.80	38.73	38.83	38.58	38.53	38.64
TiO_2	0.00	0.03	0.00	0.03	0.00	0.00	0.03	0.03	0.00	0.00
ZnO										
Al_2O_3	0.02	0.00	0.00	0.03	0.04	0.02	0.02	0.03	0.02	0.03
Cr_2O_3										
FeO	20.21	19.58	19.81	19.76	19.76	19.40	19.77	18.29	18.30	18.40
MnO	0.47	0.41	0.37	0.46	0.47	0.41	0.40	0.36	0.30	0.39
MgO	41.59	41.54	41.72	41.56	41.50	41.92	41.62	42.33	42.31	41.87
CaO	0.20	0.22	0.20	0.20	0.23	0.23	0.16	0.23	0.25	0.24
BaO	0.00	0.02	0.00	0.00	0.00	0.04	0.02	0.00	0.00	0.02
Na_2O	0.00	0.00	0.00	0.00	0.00	0.00	0.03	0.02	0.00	0.00
K_2O	0.01	0.00	0.01	0.00	0.00	0.01	0.00	0.01	0.00	0.01
SO_3	0.00	0.00	0.02	0.00	0.00	0.00	0.01	0.00	0.00	0.00
Cl	0.01	0.01	0.01	0.00	0.00	0.00	0.01	0.00	0.00	0.02
F	0.00	0.14	0.05	0.00	0.11	0.24	0.00	0.14	0.00	0.00
TOTAL	101.1	100.7	100.9	100.6	100.9	101.1	100.9	100.0	99.7	99.7

Table 8: Major element compositions of olivine electron microprobe analyses. Element compositions reported as wt.%.

	B24_Apat1-1	B27_Apt1	SA19_Apt01	SA19_Apt2	B22_Apt1-1	B22_Apt1-2	B22_Apt1-3	B21_Apt1-1	B21_Apt1-2
SiO_2	0.81	0.37	0.37	0.46	0.48	0.40	0.78	0.41	0.34
TiO_2	0.01	0.01	0.00	0.01	0.00	0.01	0.00	0.00	0.00
Al_2O_3	0.01	0.01	0.01	0.01	0.00	0.08	0.02	0.00	0.00
Cr_2O_3	-0.02	0.00	0.03	0.00	0.00	0.03	0.00	0.01	0.00
FeO	0.25	0.03	0.28	0.23	0.35	0.29	0.40	0.26	0.24
NiO	-0.01	0.00	0.00	0.00	0.00	0.00	0.04	0.00	0.04
MnO	0.07	0.03	0.08	0.08	0.10	0.04	0.02	0.02	0.12
MgO	0.15	0.16	0.15	0.14	0.21	0.17	0.17	0.15	0.18
CaO	54.56	53.73	52.79	52.44	53.03	52.77	47.26	51.59	52.51
BaO		0.02	0.00	0.01	0.00	0.01	0.01	0.00	0.07
Na_2O	0.12	0.00	0.00	0.00	0.00	0.00	0.00	0.00	0.00
K_2O	0.01	0.00	0.05	0.03	0.00	0.00	0.02	0.00	0.02
P_2O_5	38.26	42.08	42.08	41.31	37.46	43.17	42.28	42.06	41.69
Cl	0.68	0.52	0.60	0.56	0.37	0.41	0.37	0.49	0.53
F		1.77	1.99	2.09	1.39	1.40	1.78	1.24	1.27
TOTAL	94.9	98.7	98.4	97.4	93.4	98.8	93.1	96.2	97.0

Table 9: Major element compositions of apatite electron microprobe analyses. Element compositions reported as wt.%.

SAMPLE	B10_Biot1-1	B10_Biot1-2	B10_Biot1-3	B10_Biot1-4	B10_Biot1-5	B10_Biot1-6	B10_Biot1-7	B10_Biot1-8	B10_Biot1-9	B10_Biot2-1	B10_Biot2-2	B10_Biot2-3	B10_Biot2-4
SiO_2	37.61	37.02	36.55	37.56	37.46	38.02	37.08	36.94	37.30	38.42	36.87	37.86	36.99
TiO_2	2.86	2.87	2.85	2.83	2.91	2.77	3.20	3.24	3.13	3.19	3.17	3.16	3.20
Al_2O_3	17.02	16.87	17.04	16.97	16.96	17.10	16.91	17.13	17.13	16.98	16.57	16.80	16.55
Cr_2O_3	0.00	0.01	-0.01	0.02	0.00	0.02	0.00	0.02	0.00	0.00	0.00	-0.02	0.00
FeO	11.64	11.36	11.61	11.55	11.43	11.33	11.31	11.36	11.49	11.08	11.10	11.18	11.34
NiO	0.02	-0.02	0.00	0.03	0.00	0.03	0.00	-0.01	0.01	0.03	0.03	0.01	0.01
MnO	0.10	0.08	0.08	0.09	0.10	0.10	0.12	0.10	0.10	0.09	0.09	0.09	0.09
MgO	17.49	17.31	17.29	17.64	17.51	17.66	18.10	18.11	18.15	17.58	17.50	17.83	17.37
CaO	0.04	0.03	0.05	0.02	0.10	0.10	0.06	0.02	0.02	0.08	0.13	0.06	0.18
BaO													
Na_2O	0.75	0.76	0.76	0.73	0.76	0.78	0.78	0.72	0.70	0.83	0.83	0.82	0.83
K_2O	8.42	8.15	8.26	8.35	8.10	8.15	9.61	9.61	9.68	9.43	9.34	9.41	9.42
P_2O_5	0.02	-0.01	0.07	-0.08	0.01	-0.03	-0.03	-0.01	-0.03	0.00	0.11	0.09	-0.01
SO_3													
Cl	0.06	0.07	0.06	0.07	0.06	0.08	0.08	0.08	0.09	0.15	0.15	0.11	0.09
F													
TOTAL	96.0	94.5	94.6	95.9	95.4	96.1	97.2	97.3	97.8	97.9	95.9	97.4	96.1

Table 10: Major element compositions of phlogopite electron microprobe analyses. Element compositions reported as wt.%.

SAMPLE	B25_Hbl1-1	B25_Hbl1-2	B25_Hbl1-3	B25_Hbl1-4	B25_Hbl1-5	B25_Hbl1-6	B25_Hbl1-7	B25_Hbl1-8	B24_Biot1-1	B24_Biot1-1	B24_Biot1-1	B16_Biot1-1	B16_Biot1-1
SiO_2	34.67	35.24	35.36	34.72	35.80	34.49	35.59	35.58	37.90	37.04	37.13	35.18	35.37
TiO_2	3.98	3.96	4.03	3.92	4.01	4.03	4.08	3.98	3.28	3.37	3.31	2.44	2.33
Al_2O_3	16.44	16.30	16.17	15.97	16.33	15.72	16.42	16.05	16.64	16.36	16.77	17.17	16.73
Cr_2O_3	0.00	0.01	-0.01	0.01	0.01	0.00	0.00	0.00	0.01	0.01	0.00	0.00	0.00
FeO	10.84	10.82	11.94	10.76	10.89	10.97	11.00	10.94	11.42	11.83	11.81	10.77	11.06
NiO	-0.03	-0.05	-0.01	-0.01	0.02	0.00	-0.01	-0.02	0.01	0.00	0.01	0.00	0.01
MnO	0.14	0.11	0.13	0.13	0.13	0.12	0.15	0.13	0.13	0.13	0.14	0.09	0.07
MgO	17.90	17.63	17.67	17.74	17.63	17.14	17.95	17.58	17.57	17.15	17.07	17.52	17.45
CaO	0.04	0.01	0.27	0.03	0.09	0.09	0.03	0.04	0.06	0.02	0.05	0.01	0.02
BaO													
Na_2O	0.93	0.92	0.99	0.94	0.88	0.88	0.95	0.82	0.90	0.83	0.85	0.65	0.65
K_2O	9.35	9.37	9.05	9.19	9.42	9.35	9.50	9.40	8.74	8.78	8.87	9.14	9.20
P_2O_5	0.02	0.01	0.03	-0.04	-0.05	0.02	0.03	0.07	0.02	-0.01	-0.04	0.00	0.02
SO_3													
Cl	0.07	0.06	0.06	0.07	0.05	0.11	0.07	0.07	0.06	0.04	0.05	0.05	0.05
F													
TOTAL	94.4	94.4	95.7	93.5	95.2	92.9	95.8	94.7	96.7	95.5	96.1	93.0	93.0

Table 10: Major element compositions of phlogopite electron microprobe analyses. Element compositions reported as wt.%.

SAMPLE	B16_Biot1-1	B16_Biot1-1	B16_Biot1-1	B16_Biot1-1	B16_Biot1-1	B16_Biot1-1	B16_Biot1-1	B16_Biot1-1	B16_Biot1-1	B16_Biot1-1	B16_Biot1-1	B16_Biot1-1	B16_Biot1-1
SiO_2	34.40	35.55	35.98	36.00	36.23	36.30	36.44	36.17	35.60	35.80	36.61	35.90	35.41
TiO_2	2.37	2.38	2.42	2.29	2.34	2.23	2.24	2.34	2.31	2.36	2.32	2.46	2.42
Al_2O_3	16.55	17.27	17.25	17.58	17.12	17.14	17.63	17.36	17.36	17.07	17.57	17.34	17.18
Cr_2O_3	0.00	0.00	-0.01	0.00	0.00	-0.01	0.00	-0.01	0.00	-0.01	0.01	0.00	0.02
FeO	10.89	10.91	11.05	11.07	11.11	11.11	10.91	11.12	10.99	11.28	10.97	11.12	11.39
NiO	0.03	0.01	0.01	0.04	0.00	0.01	0.00	0.02	0.01	-0.02	0.02	0.01	0.02
MnO	0.08	0.06	0.08	0.08	0.08	0.07	0.07	0.08	0.09	0.09	0.10	0.07	0.08
MgO	17.06	17.85	17.73	18.00	18.03	17.64	17.71	17.89	17.76	17.71	18.01	17.47	17.42
CaO	0.02	0.04	0.02	0.02	0.02	0.01	0.02	0.08	0.03	0.03	0.02	0.02	0.03
BaO													
Na_2O	0.64	0.63	0.60	0.59	0.60	0.60	0.61	0.71	0.60	0.62	0.63	0.62	0.64
K_2O	9.23	9.22	9.25	9.13	9.35	9.25	9.35	9.29	9.27	9.31	9.30	9.26	9.29
P_2O_5	-0.03	-0.02	-0.01	-0.01	0.03	0.00	0.00	-0.01	0.00	-0.02	0.02	0.02	0.00
SO_3													
Cl	0.05	0.06	0.05	0.05	0.06	0.05	0.06	0.06	0.05	0.05	0.07	0.04	0.07
F													
TOTAL	91.3	94.0	94.4	94.8	95.0	94.4	95.0	95.1	94.1	94.3	95.6	94.3	94.0

Table 10: Major element compositions of phlogopite electron microprobe analyses. Element compositions reported as wt.%.

SAMPLE	B16_Biot2-1	B16_Biot2-1	B16_Biot2-1	B16_Biot2-1	B16_Biot2-1	B16_Biot2-1	B16_Biot2-1	B16_Biot2-1	B16_Biot3-1	B16_Biot3-1	B16_Biot3-1	B16_Biot3-1	B16_Biot3-1
SiO_2	35.18	35.49	35.92	35.84	36.32	36.41	36.60	37.02	38.29	37.51	36.94	37.83	37.58
TiO_2	2.72	2.70	2.68	2.66	2.74	2.71	2.73	2.67	2.59	2.48	2.40	2.34	2.32
Al_2O_3	16.67	16.90	16.91	16.89	17.24	17.20	17.27	17.48	17.94	17.66	17.49	17.44	17.49
Cr_2O_3	0.00	-0.01	0.01	0.02	-0.01	0.00	0.00	0.01	0.00	0.00	0.00	0.02	0.00
FeO	12.46	12.37	12.55	12.68	12.74	12.59	12.62	12.53	12.19	12.35	12.17	12.03	12.18
NiO	-0.01	0.05	0.03	0.00	0.02	0.01	0.04	0.02	0.03	0.04	0.03	0.02	0.01
MnO	0.09	0.10	0.10	0.09	0.09	0.11	0.09	0.08	0.08	0.09	0.09	0.08	0.09
MgO	16.14	16.42	16.42	16.39	16.29	16.63	16.39	16.49	17.27	17.36	17.22	17.05	16.94
CaO	0.04	0.02	0.04	0.03	0.04	0.03	0.04	0.01	0.07	0.05	0.05	0.02	0.02
BaO													
Na_2O	0.67	0.50	0.64	0.67	0.70	0.66	0.66	0.67	0.76	0.70	0.70	0.68	0.65
K_2O	9.15	8.65	9.13	9.31	9.39	9.45	9.49	9.56	9.52	9.54	9.68	9.78	9.62
P_2O_5	0.01	-0.01	-0.01	0.01	0.01	0.01	0.00	-0.02	0.02	0.01	0.00	0.00	-0.02
SO_3													
Cl	0.06	0.06	0.06	0.07	0.06	0.07	0.09	0.07	0.07	0.07	0.06	0.08	0.06
F													
TOTAL	93.2	93.3	94.5	94.6	95.6	95.9	96.0	96.6	98.8	97.8	96.8	97.4	97.0

Table 10: Major element compositions of phlogopite electron microprobe analyses. Element compositions reported as wt.%.

SAMPLE	B16_Biot3-1	B16_Biot3-1	B16_Biot3-1	B16_Biot3-1	B16_Biot3-1	B16_IntBiot1-1	B16_IntBiot1-1	B16_IntBiot1-1	B16_IntBiot1-1	B16_IntBiot2-1	B16_IntBiot2-2	B16_IntBiot2-3	SA19_Biot1
SiO_2	37.89	37.26	37.16	37.23	36.98	35.51	35.76	34.93	35.92	36.12	36.47	35.52	35.26
TiO_2	2.44	2.49	2.53	2.60	2.60	2.49	2.46	2.47	2.52	2.54	2.51	2.54	3.73
Al_2O_3	17.78	17.62	17.27	17.40	17.11	17.13	17.53	17.31	17.60	17.04	17.40	17.18	15.41
Cr_2O_3	0.00	-0.01	-0.01	-0.02	-0.01	0.01	0.01	0.00	-0.01	-0.01	0.00	0.01	0.03
FeO	12.27	12.38	11.79	12.21	12.07	11.69	11.59	11.49	11.91	12.26	12.50	12.34	11.81
NiO	0.01	0.00	0.00	0.05	0.01	0.04	0.02	0.02	0.00	0.02	0.01	0.01	0.00
MnO	0.07	0.08	0.08	0.08	0.11	0.10	0.08	0.09	0.09	0.08	0.07	0.09	0.18
MgO	17.34	17.16	16.69	16.78	16.85	16.80	17.03	16.66	17.36	16.46	16.93	16.73	17.31
CaO	0.06	0.05	0.01	0.01	0.03	0.04	0.07	0.05	0.03	0.13	0.13	0.11	0.05
BaO													1.09
Na_2O	0.72	0.73	0.64	0.67	0.66	0.70	0.81	0.73	0.68	0.79	0.73	0.77	0.81
K_2O	9.78	9.76	9.58	9.73	9.66	9.65	9.58	9.45	9.83	9.45	9.41	9.56	8.62
P_2O_5	0.00	0.01	0.03	0.02	0.00	0.01	0.00	0.05	0.00	0.01	0.01	0.03	0.02
SO_3													
Cl	0.07	0.07	0.10	0.07	0.05	0.08	0.16	0.10	0.08	0.26	0.10	0.17	0.14
F													0.34
TOTAL	98.4	97.6	95.9	96.9	96.1	94.3	95.1	93.3	96.0	95.2	96.3	95.1	94.8

Table 10: Major element compositions of phlogopite electron microprobe analyses. Element compositions reported as wt.%.

SAMPLE	B37_Biot1	B37_Biot1	B37_Biot1	B37_Biot1	B37_Biot1	SA17_Biotite 1	SA17_Biotite 1	SA17_Biotite 1	SA17_Biotite 1	SA17_Biotite 1	SA17_Biotite 1	SA17_Biotite 2	SA17_Biotite 2
SiO_2	39.17	38.91	38.81	39.20	39.56	35.98	36.01	36.12	36.03	36.17	36.00	36.35	36.22
TiO_2	3.63	3.46	3.59	3.44	3.55	3.03	3.04	3.13	3.03	3.07	3.14	3.46	3.51
Al_2O_3	13.38	13.28	13.18	13.43	13.37	15.54	15.67	15.79	15.47	15.85	15.78	15.87	15.83
Cr_2O_3	0.01	0.00	0.00	0.01	0.00	0.03	0.02	0.00	0.00	0.00	0.00	0.00	0.00
FeO	10.54	10.15	11.78	10.93	10.30	10.47	10.58	10.56	10.55	10.69	10.64	10.62	10.84
NiO	0.00	0.00	0.03	0.00	0.03	0.02	0.03	0.03	0.00	0.01	0.00	0.00	0.01
MnO	0.15	0.17	0.15	0.15	0.16	0.14	0.12	0.16	0.08	0.10	0.12	0.10	0.16
MgO	19.00	19.04	18.14	19.00	19.50	17.69	17.79	17.73	17.71	17.78	17.74	17.69	17.60
CaO	0.02	0.02	0.02	0.03	0.02	0.00	0.02	0.00	0.00	0.00	0.01	0.02	0.03
BaO	0.06	0.09	0.04	0.06	0.04	1.17	1.18	1.15	1.14	1.20	1.13	1.19	1.19
Na_2O	0.45	0.47	0.50	0.46	0.49	0.90	0.84	0.84	0.88	0.90	0.88	0.85	0.91
K_2O	9.83	9.69	9.77	9.72	9.85	8.67	8.67	8.67	8.65	8.69	8.62	8.49	8.45
P_2O_5	0.00	0.03	0.01	0.02	0.00	0.00	0.02	0.05	0.01	0.00	0.09	0.00	0.01
SO_3	0.00	0.00	0.00	0.01	0.00	0.00	0.02	0.00	0.00	0.00	0.01	0.02	0.00
Cl	0.10	0.11	0.08	0.11	0.09	0.04	0.04	0.03	0.04	0.03	0.03	0.03	0.05
F	5.74	5.82	5.81	5.99	6.06	0.52	0.58	0.47	0.49	0.49	0.57	0.36	0.45
TOTAL	102.1	101.2	101.9	102.6	103.0	94.2	94.6	94.7	94.1	95.0	94.8	95.1	95.2

Table 10: Major element compositions of phlogopite electron microprobe analyses. Element compositions reported as wt.%.

SAMPLE	SA17_ Biotite 2	SA17_ Biotite 2	SA17_ Biotite 3	SA17_ Biotite 3	SA17_ Biotite 3	SA17_ Biotite 3	SA17_ Biotite 3	SA12/X 01_Biot 1	SA12/X 01_Biot 1	SA12/X 01_Biot 1	SA12/X 01_Biot 1	BC14/0 38_Biot 1	BC14/0 38_Bio t1
SiO_2	36.57	36.22	34.32	34.64	34.66	34.79	34.46	36.24	35.49	36.31	35.80	35.35	35.11
TiO_2	3.56	3.60	3.89	3.91	3.77	3.70	3.88	5.14	5.39	5.31	5.38	2.96	2.94
Al_2O_3	15.85	16.13	14.85	15.05	14.84	14.96	14.84	15.76	15.28	15.26	14.76	16.34	16.26
Cr_2O_3	0.00	0.03	0.03	0.00	0.01	0.03	0.00	0.01	0.00	0.00	0.00	0.00	0.00
FeO	10.95	10.97	11.22	11.28	11.22	11.02	10.99	8.20	7.97	7.84	7.91	9.61	9.60
NiO	0.00	0.00	0.01	0.01	0.00	0.03	0.00						
MnO	0.12	0.11	0.12	0.18	0.12	0.11	0.13	0.08	0.07	0.09	0.05	0.10	0.05
MgO	17.84	17.52	16.58	16.96	16.85	16.93	16.69	19.20	18.58	18.85	18.71	18.80	18.70
CaO	0.04	0.02	0.02	0.00	0.03	0.03	0.05	0.07	0.05	0.05	0.03	0.06	0.02
BaO	1.18	1.38	1.46	1.40	1.29	1.24	1.28	0.32	0.43	0.48	0.48	0.91	0.91
Na_2O	0.90	0.85	0.90	0.96	0.87	1.02	0.94	0.69	0.71	0.86	0.70	0.82	0.95
K_2O	8.57	8.55	8.52	8.55	8.54	8.65	8.57	9.22	9.22	9.25	9.14	8.97	8.86
P_2O_5	0.00	0.00	0.01	0.05	0.00	0.00	0.00	0.03	0.01	0.00	0.03	0.01	0.01
SO_3	0.00	0.00	0.00	0.00	0.00	0.00	0.00	0.00	0.00	0.00	0.01	0.01	0.02
Cl	0.03	0.04	0.03	0.03	0.02	0.04	0.04	0.09	0.10	0.12	0.12	0.02	0.02
F	0.45	0.43	0.41	0.33	0.44	0.44	0.47	1.11	0.84	0.89	1.15	0.31	0.32
TOTAL	96.1	95.9	92.4	93.4	92.7	93.0	92.3	95.8	93.8	94.9	93.8	94.1	93.6

Table 10: Major element compositions of phlogopite electron microprobe analyses. Element compositions reported as wt.%.

SAMPLE	BC14/038_Biot1	BC14/038_Biot1	BC14/038_Biot1	BC14/038_Biot1	BC14/038_Biot1	BC14/038_Biot1	BC14/038_Biot1	BC14/038_Biot1	BC14/038_Biot1	BC14/038_Biot1	BC14/038_Biot1	BC14/038_Biot1	BC14/038_Biot1
SiO_2	35.32	35.34	34.58	34.66	34.71	35.13	35.16	34.80	35.18	34.66	34.80	35.36	35.30
TiO_2	2.91	2.82	2.84	2.86	2.76	2.73	2.74	2.83	2.80	2.86	2.98	2.94	2.96
Al_2O_3	16.22	16.22	16.26	16.71	16.57	16.80	16.91	16.90	16.69	16.40	17.10	16.90	16.68
Cr_2O_3	0.02	0.00	0.01	0.00	0.00	0.03	0.00	0.00	0.01	0.00	0.02	0.00	0.02
FeO	9.61	10.13	9.79	10.24	9.80	9.89	10.32	10.12	10.47	9.83	9.70	10.00	9.44
NiO													
MnO	0.10	0.10	0.06	0.07	0.11	0.09	0.11	0.08	0.11	0.10	0.10	0.12	0.13
MgO	18.70	18.77	18.08	18.21	18.19	18.37	18.52	18.48	18.58	18.23	18.02	18.43	18.73
CaO	0.06	0.04	0.08	0.08	0.08	0.09	0.06	0.04	0.04	0.06	0.10	0.06	0.09
BaO	0.90	0.83	0.85	0.88	0.88	0.83	0.88	0.92	0.91	0.91	0.91	0.94	0.93
Na_2O	0.80	0.82	0.84	0.71	0.70	0.83	0.77	0.86	0.79	0.81	0.84	0.68	0.77
K_2O	8.90	9.06	8.66	8.56	8.50	8.75	8.68	8.76	8.95	8.72	8.51	8.55	8.51
P_2O_5	0.00	0.02	0.01	0.00	0.06	0.02	0.00	0.02	0.00	0.02	0.06	0.01	0.04
SO_3	0.02	0.03	0.05	0.06	0.06	0.05	0.03	0.06	0.04	0.06	0.09	0.05	0.04
Cl	0.03	0.03	0.06	0.04	0.06	0.03	0.04	0.04	0.03	0.04	0.04	0.03	0.03
F	0.39	0.43	0.33	0.34	0.28	0.29	0.33	0.41	0.44	0.32	0.32	0.26	0.36
TOTAL	93.8	94.5	92.4	93.4	92.7	94.0	94.4	94.2	94.8	92.9	93.5	94.3	94.0

Table 10: Major element compositions of phlogopite electron microprobe analyses. Element compositions reported as wt.%.

SAMPLE	BC14/038_Biot2	BC14/038_Biot2	BC14/038_Biot2	BC14/038_Biot2	BC14/038_Biot2	BC14/038_Biot2	BC14/038_Biot2	BC14/038_Biot2	BC14/038_Biot2	BC14/038_Biot2	BC14/038_Biot3	BC14/038_Biot3	BC14/038_Biot3
SiO_2	35.55	35.65	35.48	35.53	35.30	35.64	35.51	35.40	35.72	35.88	35.62	35.16	35.88
TiO_2	2.99	3.02	3.04	3.04	3.06	2.94	2.96	3.04	2.90	2.95	2.98	2.90	2.86
Al_2O_3	16.55	16.43	16.42	16.40	16.49	16.63	16.70	16.44	16.45	16.64	16.63	16.28	16.34
Cr_2O_3	0.03	0.00	0.00	0.00	0.00	0.00	0.00	0.02	0.02	0.04	0.00	0.00	0.01
FeO	9.65	9.48	9.87	9.87	10.13	10.43	10.07	9.75	9.69	9.68	9.71	9.90	10.00
NiO													
MnO	0.10	0.05	0.06	0.12	0.07	0.11	0.09	0.13	0.09	0.10	0.07	0.12	0.09
MgO	19.09	18.85	18.92	19.03	18.80	19.06	18.78	18.79	19.07	19.29	18.79	18.12	18.98
CaO	0.07	0.07	0.05	0.04	0.08	0.06	0.06	0.03	0.04	0.07	0.05	0.04	0.03
BaO	1.01	1.03	0.94	0.90	0.91	0.90	0.91	0.89	0.88	0.98	0.92	1.05	0.80
Na_2O	0.79	0.87	0.80	0.78	0.79	0.74	0.84	0.71	0.73	0.74	0.92	0.86	0.77
K_2O	8.62	8.76	8.77	8.68	8.82	8.78	8.92	8.98	8.76	8.80	8.64	8.68	8.93
P_2O_5	0.01	0.01	0.02	0.01	0.00	0.00	0.00	0.01	0.02	0.01	0.05	0.00	0.01
SO_3	0.05	0.01	0.01	0.02	0.02	0.03	0.03	0.03	0.04	0.04	0.04	0.00	0.03
Cl	0.02	0.03	0.02	0.03	0.01	0.03	0.03	0.02	0.03	0.04	0.02	0.04	0.03
F	0.45	0.40	0.30	0.34	0.35	0.35	0.44	0.40	0.37	0.35	0.30	0.40	0.54
TOTAL	94.9	94.6	94.6	94.7	94.7	95.6	95.2	94.5	94.7	95.5	94.6	93.4	95.2

Table 10: Major element compositions of phlogopite electron microprobe analyses. Element compositions reported as wt.%.

SAMPLE	BC14/038_Biot3	BC14/038_Biot3	BC14/038_Biot3	BC14/038_Biot3	BC14/038_Biot3	BC14/038_Biot3	BC14/038_Biot3	BC14/038_Biot3	BC14/038_Biot3	BC14/038_BiotInc1
SiO_2	35.28	35.38	35.23	35.45	35.87	36.30	36.30	47.24	46.55	35.79
TiO_2	2.89	2.89	2.95	2.90	2.92	2.94	2.92	0.97	1.08	2.93
Al_2O_3	16.45	16.55	16.41	16.63	16.47	16.61	16.99	5.94	6.84	16.23
Cr_2O_3	0.01	0.00	0.03	0.00	0.01	0.00	0.01	0.02	0.00	0.04
FeO	9.96	10.34	10.23	10.15	9.68	9.93	9.72	7.23	7.83	9.03
NiO										
MnO	0.10	0.07	0.11	0.11	0.09	0.08	0.10	0.19	0.14	0.10
MgO	18.60	18.73	18.39	18.76	18.79	19.21	19.48	13.48	12.74	18.77
CaO	0.04	0.03	0.04	0.03	0.03	0.04	0.12	23.05	23.16	0.13
BaO	0.82	0.91	0.88	0.84	0.91	1.01	1.11	0.02	0.02	0.88
Na_2O	0.87	0.83	0.80	0.74	0.80	0.91	0.72	0.29	0.40	0.79
K_2O	8.88	8.87	9.04	8.86	8.82	8.89	8.84	0.00	0.01	8.87
P_2O_5	0.00	0.00	0.00	0.03	0.04	0.00	0.02	0.04	0.00	0.03
SO_3	0.01	0.01	0.02	0.04	0.03	0.01	0.01	0.00	0.02	0.03
Cl	0.01	0.03	0.03	0.04	0.04	0.02	0.03	0.00	0.00	0.03
F	0.37	0.31	0.36	0.40	0.41	0.38	0.36	0.00	0.00	0.42
TOTAL	94.2	94.8	94.4	94.8	94.7	96.2	96.6	98.5	98.8	94.0

Table 10: Major element compositions of phlogopite electron microprobe analyses. Element compositions reported as wt.%.

SAMPLE	BC140 15-GM1	BC140 15-GM2	BC140 15-GM3	BC140 15-GM4	BC140 15-GM5	BC140 20-GM1	BC140 20-GM2	BC140 20-GM3	BC140 20-GM4	BC140 20-GM5	BC140 20-GM6	BC140 20-GM7	BC140 20-GM8
SiO_2	57.42	64.03	59.20	55.99	62.29	57.43	57.95	56.81	56.82	57.93	57.36	59.50	57.26
TiO_2	0.04	0.08	0.10	0.06	0.05	0.83	0.79	0.73	0.82	0.86	0.89	0.58	0.84
Al_2O_3	22.94	18.77	20.94	22.92	20.45	17.10	17.28	16.79	17.03	17.30	16.45	17.36	17.20
FeO	0.48	0.37	0.42	0.74	0.44	5.83	5.60	5.62	5.25	4.75	5.95	3.34	5.67
MgO	0.04	0.01	0.02	0.06	0.03	1.04	1.05	1.08	1.03	0.97	1.07	0.64	1.10
CaO	0.51	0.92	2.58	3.86	2.24	1.92	2.46	2.31	2.21	2.36	2.75	1.92	2.21
BaO	0.03	0.42	3.17	0.77	0.13	0.04	0.07	0.04	0.08	0.04	0.07	0.44	0.01
Na_2O	7.53	6.11	5.89	6.24	7.44	5.23	5.03	4.91	4.78	4.92	4.95	4.69	4.86
K_2O	7.81	7.41	4.54	4.33	4.03	7.07	6.93	6.99	6.27	6.54	6.01	7.77	6.61
P_2O_5	0.03	0.00	0.05	0.03	0.00	0.50	0.48	0.57	0.46	0.58	0.52	0.28	0.41
SO_3	0.00	0.00	0.00	0.01	0.04	0.03	0.00	0.01	0.03	0.04	0.03	0.01	0.04
Cl	0.02	0.01	0.00	0.04	0.01	0.53	0.53	0.60	0.58	0.61	0.67	0.44	0.66
F	0.00	0.00	0.00	0.00	0.00	0.10	0.09	0.07	0.04	0.05	0.01	0.00	0.07
TOTAL	96.9	98.1	96.9	95.0	97.2	97.5	98.1	96.4	95.2	96.8	96.6	96.9	96.8

Table 11: Major element compositions of groundmass glass electron microprobe analyses. Element compositions reported as wt.%.

SAMPLE	BC14004-GM7	SA26-GM1	SA26-GM1	SA26-GM1	SA26-GM1	SA26-GM2	SA26-GM2	SA26-GM2	SA26-GM2	SA23-GM2	SA23-GM2	SA23-GM3	SA23-GM4
SiO_2	59.26	54.88	55.35	55.17	56.43	55.56	54.77	53.98	55.74	59.61	56.01	56.73	59.74
TiO_2	0.06	0.72	0.83	0.76	0.72	0.60	0.73	0.68	0.57	0.08	0.13	0.43	0.42
Al_2O_3	22.73	16.72	16.91	16.72	17.16	16.90	17.00	16.54	16.72	21.07	22.25	17.59	16.95
FeO	0.33	7.48	7.83	7.26	6.20	7.16	7.89	7.99	6.56	0.41	1.34	4.69	3.48
MgO	0.05	1.05	1.68	1.90	1.67	1.48	1.38	1.70	1.28	0.03	0.21	0.84	0.62
CaO	4.53	1.80	2.32	2.06	2.02	2.84	2.79	2.15	1.95	3.92	6.39	2.77	1.49
BaO	0.25	0.03	0.13	0.13	0.12	0.09	0.14	0.06	0.03	0.77	0.31	0.12	0.14
Na_2O	7.01	5.57	4.19	5.35	5.36	5.44	5.63	5.46	5.70	5.93	5.80	5.30	5.38
K_2O	1.95	6.96	5.96	6.12	6.32	6.01	5.83	6.15	6.83	4.36	2.40	5.04	6.17
P_2O_5	0.10	0.71	0.71	0.62	0.57	0.82	0.62	0.73	0.75	0.04	0.31	0.29	0.29
SO_3	0.06	0.07	0.03	0.00	0.02	0.01	0.04	0.06	0.03	0.00	0.00	0.02	0.00
Cl	0.03	0.94	0.66	0.54	0.49	0.69	0.72	0.76	0.84	0.00	0.16	0.74	0.54
F	0.00	0.16	0.09	0.05	0.06	0.05	0.06	0.04	0.06	0.00	0.00	0.01	0.00
TOTAL	96.4	96.8	96.5	96.6	97.0	97.5	97.4	96.1	96.8	96.2	95.3	94.4	95.1

Table 11: Major element compositions of groundmass glass electron microprobe analyses. Element compositions reported as wt.%.

SAMPLE	SA23-GM5	SA23-GM6	SA23-GM7	SA23-GM8	SA23-GM9	SA23-GM9	SA23-GM10	SA12X01-GM1	SA12X01-GM2	SA12X01-GM3	SA12X01-GM5	SA12X01-GM6	SA12X01-GM6
SiO_2	57.93	57.77	55.12	57.37	54.98	53.03	55.56	57.44	57.11	57.24	57.51	57.16	57.24
TiO_2	0.25	0.35	0.07	0.18	0.43	0.37	0.55	0.66	0.71	0.66	0.79	0.79	0.81
Al_2O_3	17.42	16.71	23.48	17.97	16.39	15.94	17.03	18.19	17.98	17.95	17.97	18.00	17.77
FeO	3.20	3.17	0.67	1.90	6.35	7.74	5.88	4.01	4.04	3.97	3.99	3.88	4.04
MgO	1.99	0.92	0.06	0.77	1.38	1.57	1.09	1.05	1.13	1.13	1.13	1.19	1.12
CaO	2.87	2.32	7.38	3.57	1.68	2.06	1.84	2.18	2.15	2.23	2.18	2.29	2.12
BaO	0.28	0.17	0.45	0.33	0.00	0.00	0.00	0.23	0.19	0.19	0.20	0.19	0.19
Na_2O	5.19	5.29	5.90	5.12	4.91	5.26	5.05	5.14	5.08	5.22	5.18	5.24	5.21
K_2O	5.20	6.18	1.40	5.16	6.21	5.96	6.64	7.31	7.18	7.24	7.34	7.28	7.26
P_2O_5	0.16	0.39	0.02	0.27	0.49	0.31	0.34	0.31	0.28	0.28	0.30	0.33	0.25
SO_3	0.01	0.02	0.00	0.03	0.05	0.06	0.01	0.00	0.03	0.01	0.01	0.04	0.03
Cl	0.23	0.58	0.01	0.24	0.56	0.69	0.60	0.68	0.69	0.65	0.66	0.66	0.64
F	0.00	0.00	0.00	0.00	0.00	0.00	0.00	0.02	0.00	0.07	0.02	0.00	0.04
TOTAL	94.7	93.7	94.6	92.9	93.3	92.8	94.5	97.1	96.4	96.7	97.1	96.9	96.6

Table 11: Major element compositions of groundmass glass electron microprobe analyses. Element compositions reported as wt.%.

SAMPLE	SA12X01-GM7	SA12X01-GM8	BC14039-GM1	BC14039-GM1	BC14039-GM1	BC14039-GM1	BC14039-GM1	BC14039-GM2	BC14039-GM2	SA24-GM1	SA24-GM1	SA24-GM1	SA24-GM2
SiO_2	56.42	56.62	55.12	54.14	55.77	54.91	54.04	56.40	56.20	57.68	56.39	55.61	56.29
TiO_2	0.74	0.71	0.85	0.83	0.69	0.87	0.80	0.70	0.84	0.87	0.85	1.07	0.46
Al_2O_3	18.12	18.51	16.29	16.50	17.09	16.46	16.72	17.05	15.97	19.85	19.62	19.33	17.39
FeO	3.89	3.82	6.72	7.67	6.07	7.34	7.27	6.11	6.67	4.09	4.18	4.23	5.80
MgO	1.09	1.17	2.57	2.81	2.13	2.81	2.68	1.88	2.53	0.70	0.83	0.66	1.22
CaO	2.19	2.07	3.69	4.07	3.53	3.84	3.86	3.09	3.43	1.10	1.40	1.31	1.90
BaO	0.20	0.18	0.17	0.24	0.17	0.17	0.21	0.18	0.17	0.02	0.03	0.04	0.00
Na_2O	5.05	5.37	4.10	4.14	4.19	3.93	4.07	4.01	3.69	4.89	5.27	5.04	4.91
K_2O	7.26	7.00	5.69	5.14	5.99	5.26	5.52	5.74	5.19	6.04	6.94	6.51	6.35
P_2O_5	0.22	0.25	0.67	0.63	0.67	0.77	0.62	0.79	0.99	0.28	0.18	0.26	0.31
SO_3	0.03	0.02	0.03	0.06	0.05	0.03	0.04	0.03	0.04	0.01	0.00	0.01	0.00
Cl	0.62	0.74	0.55	0.59	0.49	0.53	0.55	0.58	0.56	0.64	0.70	0.78	0.87
F	0.00	0.06	0.03	0.05	0.02	0.03	0.03	0.00	0.07	0.00	0.00	0.01	0.00
TOTAL	95.7	96.3	96.3	96.7	96.7	96.8	96.3	96.4	96.2	96.0	96.2	94.7	95.3

Table 11: Major element compositions of groundmass glass electron microprobe analyses. Element compositions reported as wt.%.

SAMPLE	SA24-GM2	SA24-GM2	SA24-GM2	SA24-GM3	SA24-GM3	SA24-GM3	SA24-GM4	SA24-GM4	SA24-GM5	SA24-GM5	SA24-GM6	SA24-GM6	SA24-GM7
SiO_2	56.14	56.23	55.01	57.11	57.77	57.24	57.25	56.94	56.79	56.62	56.30	56.92	56.90
TiO_2	0.43	0.45	0.44	0.54	0.55	0.52	0.61	0.51	0.57	0.59	0.53	0.55	0.53
Al_2O_3	17.31	17.62	17.29	17.57	17.73	17.70	17.96	18.07	17.52	17.57	17.64	17.73	17.64
FeO	5.70	5.84	7.20	5.49	5.44	5.09	4.72	4.84	5.39	5.31	5.47	5.38	5.27
MgO	1.22	1.20	1.32	1.23	1.26	1.07	1.23	1.20	1.39	1.45	1.11	1.21	1.35
CaO	1.89	1.87	2.14	1.39	1.39	1.57	1.35	1.39	1.55	1.45	1.63	1.70	1.51
BaO	0.04	0.02	0.04	0.01	0.00	0.00	0.00	0.00	0.00	0.01	0.02	0.00	0.00
Na_2O	4.99	4.70	4.88	5.21	4.89	5.22	4.82	5.20	4.95	5.14	4.89	5.01	4.86
K_2O	6.31	6.04	6.30	6.67	6.30	6.58	6.43	6.42	6.53	6.35	6.26	6.35	6.66
P_2O_5	0.22	0.23	0.27	0.28	0.28	0.23	0.24	0.27	0.27	0.22	0.24	0.35	0.31
SO_3	0.02	0.02	0.00	0.03	0.03	0.04	0.04	0.00	0.03	0.02	0.01	0.03	0.03
Cl	0.86	0.91	0.85	0.88	0.84	1.08	0.75	0.82	0.86	0.91	0.84	0.89	0.83
F	0.00	0.00	0.00	0.01	0.00	0.02	0.00	0.03	0.00	0.00	0.00	0.00	0.00
TOTAL	94.9	94.9	95.6	96.2	96.3	96.1	95.2	95.5	95.6	95.4	94.7	95.9	95.7

Table 11: Major element compositions of groundmass glass electron microprobe analyses. Element compositions reported as wt.%.

SAMPLE	SA24-GM7	SA24-GM8	SA24-GM8	SA24-GM8	SA24-GM8	SA24-GM9	SA88301-GM1	SA88301-GM2	SA88301-GM4	SA88301-GM5	BC14/039_GM1	BC14/039_GM1	BC14/039_GM1
SiO_2	57.44	55.17	56.45	56.57	55.94	56.82	57.59	64.00	59.12	63.84	58.90	58.43	56.72
TiO_2	0.56	0.49	0.50	0.53	0.47	0.51	0.86	0.14	0.53	0.24	0.46	0.49	0.69
Al_2O_3	17.81	17.07	17.53	17.06	17.79	17.72	17.70	18.48	18.86	18.20	17.63	17.77	16.89
FeO	5.23	7.19	5.28	5.79	5.21	5.36	6.27	0.50	2.91	0.63	5.33	5.47	6.29
MgO	1.27	1.71	1.23	1.30	1.24	1.28	0.17	0.00	0.18	0.02	1.49	1.78	2.03
CaO	1.41	1.23	1.48	1.45	1.61	1.52	1.25	1.07	1.51	1.06	2.75	2.85	3.08
BaO	0.00	0.00	0.00	0.00	0.02	0.00	0.02	0.00	0.02	0.00	0.20	0.18	0.19
Na_2O	5.25	4.69	5.11	4.74	5.02	5.09	5.76	5.14	5.14	5.01	6.20	5.57	5.22
K_2O	6.74	6.13	6.35	6.27	6.62	6.39	6.73	8.34	7.80	8.57	6.51	6.27	5.76
P_2O_5	0.23	0.29	0.29	0.29	0.33	0.31	0.00	0.02	0.21	0.03	0.80	0.76	0.87
SO_3	0.04	0.01	0.01	0.00	0.01	0.03	0.03	0.01	0.03	0.00	0.07	0.08	0.07
Cl	0.91	0.89	0.93	0.86	0.88	0.91	0.22	0.02	0.48	0.03	0.62	0.59	0.60
F	0.00	0.00	0.00	0.00	0.00	0.00	0.00	0.00	0.07	0.00	0.00	0.00	0.00
TOTAL	96.7	94.7	94.9	94.7	94.9	95.7	96.5	97.7	96.7	97.6	101.2	100.5	98.6

Table 11: Major element compositions of groundmass glass electron microprobe analyses. Element compositions reported as wt.%.

SAMPLE	BC14/039_GM1	BC14-018_GM1	BC14-018_GM1	BC14-018_GM1	BC14-018_GM2	BC14-018_GM2	BC14-018_GM2
SiO_2	57.64	57.53	57.82	57.50	58.05	58.27	58.62
TiO_2	0.71	0.04	0.03	0.03	0.05	0.03	0.05
Al_2O_3	15.63	24.29	24.37	24.20	24.76	24.64	24.91
FeO	6.87	0.29	0.31	0.29	0.33	0.32	0.33
MgO	2.31	0.05	0.00	0.01	0.00	0.00	0.00
CaO	3.12	0.13	0.00	0.01	0.00	0.00	0.02
BaO	0.14	0.00	0.02	0.00	0.00	0.00	0.00
Na_2O	5.21	0.33	0.28	0.34	0.36	0.29	0.35
K_2O	6.05	16.03	15.47	14.88	15.21	15.11	14.14
P_2O_5	0.99	0.05	0.02	0.00	0.01	0.01	0.01
SO_3	0.12	0.01	0.00	0.01	0.00	0.00	0.00
Cl	0.67	0.01	0.01	0.00	0.01	0.00	0.00
F	0.03	0.00	0.00	0.00	0.00	0.00	0.00
TOTAL	99.7	98.8	98.3	97.3	98.8	98.7	98.4

Table 11: Major element compositions of groundmass glass electron microprobe analyses. Element compositions reported as wt.%.

Element	BC14/023_1	BC14/023_2	BC14023_3	BC14023_4	BC14023_5	BC14023_6	BC14023_7
Mineral	Plag	Plag	Plag	Plag	Plag	Plag	Plag
Sc	9.65	9.84	9.57	9.23	9.87	8.8	9.95
Ti	64.39	64.29	62.07	204.08	61.39	55.29	77.36
V	0.67	0.66	0.31	12.29	0.65	0.38	0.34
Cr	<2.64	<2.98	2.66	<3.02	<3.72	<3.10	<3.53
Mn	38.62	41.66	41.36	64.29	43	40.47	41.13
Co	<0.111	0.429	0.305	1.99	0.39	0.302	0.268
Ni	<0.42	<0.27	0.86	2.91	0.84	0.49	0.93
Cu	<0.21	0.67	3.95	89.69	1.72	<0.28	4.91
Zn	<1.15	4.09	3.27	7.19	2.21	1.58	<1.66
As	5.11	19.56	1.05	2.16	4.82	2.7	<1.02
Rb	0.271	0.7	0.181	0.075	0.251	0.163	0.111
Sr	2272.39	2504.8	2448.02	2408.51	3160.5	2669.89	2406.25
Y	0.223	0.317	0.174	0.225	0.277	0.315	0.219
Zr	1.31	8.84	0.315	0.7	0.55	0.253	0.133
Nb	<0.038	<0.017	<0.018	<0.046	<0.043	<0.0208	<0.042
Cd	<0.21	<0.15	<0.24	0.14	<0.232	0.26	<0.34
Sb	<0.076	<0.084	<0.075	<0.092	<0.083	<0.085	<0.069
Cs	<0.0148	<0.0146	<0.0096	<0.0138	<0.020	<0.0161	<0.0132
Ba	222.6	212.03	222.7	238.65	236.15	237.14	280.19
La	2.62	5.4	2.56	3.05	9.95	5.14	2.96
Ce	3.91	7.87	3.77	4.35	13.38	7.46	4.95
Pr	0.386	0.76	0.335	0.435	1.15	0.711	0.419
Nd	1.3	2.19	1.29	1.61	3.15	2.61	1.6
Sm	0.218	0.406	0.169	0.165	0.48	0.42	<0.115
Eu	0.433	0.47	0.36	0.271	0.78	0.543	0.397
Gd	0.188	0.314	0.14	<0.083	0.42	0.141	0.131
Tb	0.022	0.0181	0.0215	0.0139	0.0107	0.011	<0.015
Dy	<0.062	0.061	0.052	0.063	<0.051	<0.070	0.067
Ho	0.0201	0.0123	0.0117	0.0151	0.0151	0.0151	0.049
Er	<0.0314	<0.031	<0.037	0.035	<0.032	<0.044	<0.044
Tm	<0.0097	<0.0124	<0.0058	<0.0096	<0.0123	0.0139	<0.0177
Yb	<0.072	<0.036	0.057	<0.062	<0.072	<0.044	<0.036
Lu	<0.0083	0.0137	<0.0086	<0.0123	<0.0182	<0.0101	<0.0186
Hf	0.054	0.114	0.048	<0.036	0.038	<0.037	0.03
Ta	<0.0131	<0.0129	<0.0150	<0.0079	<0.0165	<0.0138	<0.0131
Pb	3.36	3.58	3.45	4.16	3.99	3.86	4.38
Th	0.0106	0.021	<0.0097	0.018	0.013	<0.0081	<0.0134
U	0.022	0.0224	0.0136	0.0062	<0.0117	0.0149	<0.00

Table 12: In-situ mineral trace element analyses. All values reported in ppm. Analysed by LA-ICMPS.

Element	BC14023_8	BC14023_9	BC14023_10	BC14023_11	BC14023_12	BC14023_13	BC14023_14
Mineral	Cpx	Cpx	Cpx	Cpx	Cpx	Cpx	Cpx
Sc	88.4	104.37	108.45	107.58	81.46	81.13	85.31
Ti	2738.69	1749.28	1764.57	1944.4	1298.08	1310.79	1352.57
V	181.3	100.36	102.88	99.53	105.62	106.93	109.77
Cr	129.22	295.08	184.27	173.32	2578.93	2685.61	2657.07
Mn	1784.39	820.73	743.31	721.52	756.19	771.01	760.2
Co	32.38	31.07	30.44	29.38	28.5	29.89	29.68
Ni	45.79	66.01	62.48	65.29	79.25	78.71	82.66
Cu	1.09	0.53	0.47	0.51	0.99	0.67	1.01
Zn	45.24	26.32	20.41	22.95	19.02	19.82	15.97
As	41.25	6.89	17.48	4.91	<0.81	1.62	3.55
Rb	1.48	0.174	0.575	0.172	0.058	<0.050	0.1
Sr	104.73	121.34	115.25	119.36	79.14	85.11	84.35
Y	27.02	6.72	6.52	6.1	3.93	3.73	3.95
Zr	98.67	18.66	21.89	19.1	5.81	5.4	5.19
Nb	0.496	0.03	0.038	0.071	<0.028	<0.024	0.04
Cd	0.33	<0.23	<0.20	<0.17	0.4	0.29	<0.180
Sb	<0.173	<0.042	<0.057	<0.057	<0.062	0.11	<0.087
Cs	0.017	<0.0099	0.0181	0.0125	<0.0123	<0.0113	<0.0158
Ba	12.1	2.68	6.29	1.88	0.164	0.53	0.98
La	14.43	3.32	3.14	3.46	0.99	0.95	0.881
Ce	45.69	10.89	9.99	10.55	3.5	3.52	3.38
Pr	7.46	1.84	1.73	1.7	0.601	0.69	0.589
Nd	33.39	8.99	10.24	10.51	3.77	3.47	3.13
Sm	8.26	2.71	2.38	2.3	0.78	1.1	1.14
Eu	2.2	0.88	0.93	0.8	0.341	0.321	0.352
Gd	7.6	2.17	2.37	2.32	1.18	1.17	1.25
Tb	1.23	0.336	0.347	0.305	0.142	0.158	0.162
Dy	6.38	1.52	1.7	2	0.89	0.83	1.04
Ho	1.3	0.324	0.257	0.305	0.16	0.19	0.163
Er	3.06	0.79	0.542	0.67	0.464	0.399	0.353
Tm	0.354	0.091	0.101	0.069	0.05	0.054	0.044
Yb	2.78	0.35	0.475	0.429	0.3	0.304	0.378
Lu	0.373	0.078	0.06	0.055	0.041	0.045	0.057
Hf	4.05	1.05	1.12	1.12	0.627	0.38	0.506
Ta	0.086	<0.0088	<0.0076	0.0108	<0.0106	<0.0091	<0.0111
Pb	1.45	0.286	0.509	0.391	0.094	0.113	0.114
Th	1.34	0.122	0.106	0.098	0.043	0.023	0.0261
U	0.178	0.065	0.041	0.013	<0.0086	0.0046	<0.0111

Table 12: In-situ mineral trace element analyses. All values reported in ppm. Analysed by LA-ICMPS.

Element	BC14023_15	BC14023_16	BC14023_17	BC14023_18	BC14023_19	BC14023_20	BC14023_2
Mineral	Cpx	Cpx	Cpx	Cpx	Cpx	Cpx	Biot
Sc	79.93	78.06	66.78	64.67	65.85	60.69	5.99
Ti	1276.67	1245.22	2866.25	2030.74	933.45	896.77	5223.61
V	107.55	103.29	219.17	184.81	85.02	86.08	111.13
Cr	2723.63	2448.49	79.56	48.9	2227.27	2230.2	13.13
Mn	728.91	705.8	2110.11	2132.28	692.98	665.54	294.05
Co	29.74	28.51	35.8	36.09	27.84	26.18	28.39
Ni	83.35	73.25	40.32	37.54	92.78	90.47	29.83
Cu	0.92	6.39	0.83	0.87	0.38	0.37	0.21
Zn	15.12	18.61	50.13	49.56	18.39	25.38	33.29
As	0.88	122.74	<0.95	5.12	5.32	<1.12	41.7
Rb	0.04	2.3	<0.039	0.095	0.217	<0.053	258.86
Sr	85.57	83.78	170.69	127.97	75.79	74.39	39.36
Y	4.01	3.83	28.93	28.19	2.85	2.69	0.15
Zr	5.38	16.34	64.17	68.55	3.66	2.3	6.88
Nb	<0.043	0.145	0.191	0.053	<0.041	<0.035	5.44
Cd	<0.24	0.79	<0.27	0.35	<0.20	<0.33	<7.67
Sb	<0.083	0.211	<0.071	<0.055	<0.058	<0.091	<5.64
Cs	<0.0106	<0.114	<0.0151	<0.0122	<0.0071	<0.0192	653.26
Ba	0.138	19.19	0.163	1.7	1.86	0.18	2971.93
La	0.95	1.03	13.36	11.66	0.751	0.592	0.089
Ce	3.21	3.61	45.01	39.23	2.39	2.39	0.041
Pr	0.627	0.69	7.06	6.52	0.479	0.436	<0.051
Nd	3.22	3.9	35.06	33.59	2.74	2.4	<0.076
Sm	1.14	0.74	9.26	8.19	0.65	0.67	<0.26
Eu	0.338	0.48	2.94	2.49	0.26	0.224	4.9
Gd	1.17	1.1	9.29	7.44	0.72	0.68	<0.21
Tb	0.177	0.238	1.33	1.2	0.119	0.122	<0.26
Dy	0.79	0.75	6.99	6.37	0.76	0.67	0.18
Ho	0.2	0.201	1.3	1.27	0.151	0.137	<0.17
Er	0.344	<0.31	3.15	2.78	0.356	0.334	<0.00
Tm	0.057	<0.097	0.402	0.444	0.035	0.061	1.08
Yb	0.247	<0.63	2.45	2.64	0.182	0.146	<0.52
Lu	0.035	0.088	0.346	0.408	0.036	0.031	<0.81
Hf	0.209	0.57	2.95	3.13	0.248	0.114	1.97
Ta	<0.0210	0.035	0.0184	0.0237	<0.0122	<0.0110	9.78
Pb	0.163	1.34	0.413	0.61	0.19	<0.078	15.02
Th	0.0162	0.1	0.38	0.295	0.0151	<0.0159	<0.24
U	<0.0105	0.054	0.062	0.022	0.0097	<0.0055	2.79

Table 12: In-situ mineral trace element analyses. All values reported in ppm. Analysed by LA-ICMPS.

Element	BC14023_3	BC14023_4	BC14023_5	BC14023_6	BC14023_7	BC14023_8	BC14023_9
Mineral	Biot	Biot	Olivine	Olivine	Olivine	Olivine	Cpx
Sc	4.25	2.3	11.31	10.03	14.61	12.16	59.56
Ti	3882.56	1811.39	28.53	29.56	23.19	31.69	3056.79
V	83.73	39.71	1.77	1.73	1.66	1.56	129.66
Cr	8.06	3.65	<0.79	0.71	1.03	<0.94	28.82
Mn	223.81	104.53	4847.18	4256.56	5754.74	4920.83	738.49
Co	20.83	9.98	192.63	168	228.83	189.92	20.68
Ni	21.05	9.73	163.73	147.22	210	166.62	23.58
Cu	0.24	0.07	1.35	1.13	2.11	1.51	0.48
Zn	23.67	11.55	178.49	158.21	222.53	171.53	13.92
As	46.69	48.18	9.78	14.33	45.62	20.01	<4.66
Rb	198.42	98.27	0.31	0.089	0.22	<0.120	0.077
Sr	27.83	14.44	0.14	0.039	0.072	0.057	59.16
Y	0.038	0.061	0.34	0.301	0.5	0.54	17.77
Zr	4.65	2.77	0.28	0.19	0.33	0.27	19.13
Nb	3.49	1.89	<0.041	<0.043	<0.087	<0.054	0.12
Cd	<3.25	<1.52	<6.35	<6.85	<7.35	<7.92	<4.48
Sb	<1.80	1.64	<5.12	<5.47	<5.73	<6.51	<4.66
Cs	490.23	240.11	<3.09	<3.25	<4.00	<4.54	<3.25
Ba	1734.44	771.23	0.66	0.36	0.49	0.3	0.14
La	0.035	0.026	<0.017	0.022	<0.016	0.021	5.55
Ce	0.02	0.053	0.0184	<0.0142	<0.020	0.02	11.09
Pr	<0.022	<0.0144	<0.027	0.072	<0.069	<0.068	12.12
Nd	<0.020	<0.013	<0.069	<0.063	<0.045	<0.079	14.69
Sm	<0.14	<0.082	<0.136	<0.33	<0.30	<0.27	15.29
Eu	2.11	1.2	<0.20	<0.13	<0.13	<0.19	15.4
Gd	<0.11	0.085	<0.24	<0.21	<0.18	<0.27	16.75
Tb	<0.134	0.09	<0.17	0.44	<0.30	<0.50	18.67
Dy	0.028	<0.051	<0.13	<0.17	<0.122	<0.21	15.86
Ho	<0.091	<0.09	<0.45	0.46	<0.21	<0.36	16.72
Er	<0.16	<0.061	<0.32	<0.25	<0.51	<0.26	14.84
Tm	<0.50	<0.17	1.6	<0.69	<0.99	1.17	17.12
Yb	0.31	<0.15	0.91	1.62	<0.70	3.28	13.75
Lu	0.69	0.26	4.38	3.84	3.07	4.2	17.39
Hf	1.25	0.72	0.17	0.21	<0.31	0.32	7.98
Ta	6.41	3.35	<0.27	<0.21	<0.25	<0.26	0.21
Pb	10.15	5.11	<0.61	0.69	1.3	1.02	2.17
Th	<0.13	0.24	<0.26	<0.31	<0.33	<0.25	2.32
U	1.36	1.01	0.36	<0.48	<0.48	0.6	1.4

Table 12: In-situ mineral trace element analyses. All values reported in ppm. Analysed by LA-ICMPS.

Element	BC14023_10	BC14023_11	BC14023_12	BC14023_13	BC14-038_1	BC14-038_2	BC14-038_3
Mineral	Cpx	Cpx	Cpx	Cpx	Plag	Plag	Plag
Sc	78.6	74.9	74.5	76.7	4.0	3.9	3.2
Ti	2010.5	2897.6	2077.1	2515.1	113.1	70.2	62.4
V	75.2	125.7	84.0	88.9	3.2	0.5	0.6
Cr	31.1	65.8	44.2	40.8	<0.75	1.1	<1.17
Mn	510.5	499.1	449.3	461.0	52.2	31.5	29.8
Co	20.8	19.4	19.8	20.2	0.6	0.2	0.2
Ni	24.2	24.2	24.5	24.5	0.2	<0.24	<0.31
Cu	0.3	0.9	0.2	0.3	13.2	0.5	1.2
Zn	10.6	10.2	8.3	9.5	3.9	2.0	1.5
As	25.9	23.6	11.4	<5.52	<0.00	<0.00	<0.00
Rb	0.4	0.5	0.1	<0.090	1.4	0.0	<0.062
Sr	73.9	79.4	68.6	70.5	2215.5	2318.6	2348.0
Y	10.8	15.6	10.4	11.8	0.4	0.1	0.2
Zr	19.2	24.9	16.7	19.9	1.2	<0.061	<0.075
Nb	0.1	0.3	<0.050	<0.062	0.1	<0.028	<0.034
Cd	<7.36	<5.09	<6.01	<4.86	<0.84	<0.93	<1.54
Sb	<4.13	<4.86	<4.20	<5.05	0.1	0.2	<0.139
Cs	<2.67	<2.77	<2.39	<3.05	0.1	<0.03	<0.04
Ba	0.8	0.7	0.4	0.2	213.5	162.9	166.0
La	7.5	8.9	6.0	7.0	4.2	4.7	4.4
Ce	12.4	15.9	11.4	13.2	5.4	6.7	5.7
Pr	11.0	14.8	11.1	13.0	0.5	0.6	0.5
Nd	12.5	17.2	12.9	15.2	1.6	1.6	1.9
Sm	14.4	16.4	11.0	13.3	0.3	<0.14	0.2
Eu	9.7	14.3	10.8	10.4	0.4	0.4	0.5
Gd	11.2	15.5	10.4	12.7	<0.1	0.2	0.2
Tb	13.1	16.4	12.6	13.7	<0.01	0.0	<0.028
Dy	9.1	12.5	7.8	10.2	<0.07	0.1	<0.109
Ho	10.2	14.2	10.2	10.7	<0.02	<0.02	<0.026
Er	9.8	11.4	8.6	8.5	<0.05	<0.06	<0.076
Tm	9.0	12.6	7.8	8.5	<0.02	<0.02	<0.028
Yb	7.5	10.1	6.4	10.0	<0.07	<0.09	<0.117
Lu	9.1	11.6	8.7	8.5	<0.02	<0.02	<0.032
Hf	6.3	10.0	6.4	7.9	<0.05	<0.07	<0.107
Ta	0.3	<0.34	<0.22	<0.26	<0.02	<0.03	<0.029
Pb	3.5	7.0	2.0	2.0	1.6	2.4	2.2
Th	4.6	7.0	1.9	2.8	0.1	<0.031	<0.041
U	3.2	4.7	3.7	1.2	0.0	<0.025	<0.034

Table 12: In-situ mineral trace element analyses. All values reported in ppm. Analysed by LA-ICMPS.

Element	BC14-038_4	BC14-038_5	BC14-038_6	BC14-038_7	BC14-038_8	BC14-038_9	BC14-038_10
Mineral	Plag	Plag	Cpx	Cpx	Cpx	Cpx	Cpx
Sc	3.29	2.93	74.17	77.41	76.43	82.21	80.56
Ti	57.86	65.75	6893.51	6156.24	6292.17	5432.48	5903.83
V	0.741	0.702	372.15	352.58	331.91	309.55	324.95
Cr	<1.42	<1.87	<0.34	<0.40	<0.39	<0.40	<0.38
Mn	30.15	30.54	1273.93	1354.33	1222.53	1366.85	1395.98
Co	0.29	0.188	35.95	36.39	36.21	40.05	36.39
Ni	<0.36	<0.51	8.11	7.61	6.62	7.42	7.72
Cu	0.81	0.72	1.62	2.02	1.344	1.56	46.99
Zn	1.97	2.43	41.05	35.29	25.2	27.91	26.94
As	<0.00	<0.00	<0.00	<0.00	<0.00	<0.00	<0.00
Rb	<0.074	0.199	<0.018	0.148	0.027	<0.020	0.68
Sr	2133.66	2230.46	115.03	117.16	119.44	112.07	116.89
Y	0.13	0.182	24.37	23.28	22.63	22.99	22.32
Zr	<0.093	<0.122	81.05	76.87	74.27	81.43	72.69
Nb	<0.041	<0.058	0.19	0.172	0.167	0.111	0.167
Cd	<1.89	<2.27	<0.41	<0.52	<0.44	<0.44	<0.47
Sb	<0.168	<0.23	<0.046	0.058	<0.045	<0.051	<0.051
Cs	<0.040	<0.055	0.0108	<0.0106	<0.0111	<0.0108	0.056
Ba	157.24	157.32	<0.074	1.72	<0.069	<0.074	8.78
La	3.96	3.52	8.95	8.45	7.74	8.75	7.8
Ce	5.5	5.04	33.63	31.94	29.31	31.83	28.44
Pr	0.48	0.557	5.5	5.22	4.86	5.38	4.63
Nd	1.52	1.72	26.98	25.12	24.69	26.17	23.22
Sm	<0.21	<0.26	7.5	7.08	7.46	7.42	6.78
Eu	0.356	0.444	2.39	2.29	2.29	2.14	2.08
Gd	<0.22	<0.28	7.81	7.1	7.01	6.91	6.48
Tb	<0.033	<0.043	1.002	0.952	0.948	0.91	0.889
Dy	<0.135	<0.169	5.48	5.23	5.15	5.39	5.18
Ho	<0.037	<0.052	0.9	0.806	0.78	0.84	0.86
Er	<0.112	<0.148	2.38	2.11	2.12	2.24	1.9
Tm	<0.036	<0.048	0.301	0.273	0.259	0.245	0.289
Yb	0.132	<0.22	1.56	1.59	1.5	1.49	1.68
Lu	<0.035	<0.044	0.197	0.225	0.213	0.214	0.222
Hf	<0.114	<0.154	2.74	2.78	2.73	3.07	2.52
Ta	<0.044	<0.050	0.0308	0.0192	0.0241	0.0183	0.012
Pb	2.01	2.92	0.18	0.322	0.172	0.222	0.529
Th	<0.049	<0.072	0.593	0.507	0.452	0.458	0.336
U	<0.037	<0.052	0.117	0.107	0.144	0.119	0.0383

Table 12: In-situ mineral trace element analyses. All values reported in ppm. Analysed by LA-ICMPS.

Element	BC14-038_11	BC14-038_12	BC14-038_13	BC14-038_14	BC14-038_15	BC14-038_16	BC14-038_17
Mineral	Cpx	Cpx	Cpx	Cpx	Cpx	Cpx	Cpx
Sc	77.15	94.67	74.89	108.23	77.42	81.85	78.99
Ti	6154.54	7277.47	6544.4	5259.28	5511.54	5873.87	5701.57
V	333.24	373.74	371.15	304.92	317.24	318.64	323.67
Cr	<0.41	<0.40	<0.33	0.42	<0.41	<0.44	0.5
Mn	1318.16	1250.57	1262.76	1248.54	1209.35	1286.77	1263.49
Co	37.61	36.03	35.2	34.76	37.01	35.89	37.18
Ni	7.82	7.25	7.95	7.87	7.59	7.37	7.32
Cu	1.71	2.94	1.69	1.44	1.49	1.68	24.37
Zn	26.92	26.87	27.56	24.72	23.59	24.69	25.65
As	<0.00	<0.00	<0.00	<0.00	<0.00	<0.00	<0.00
Rb	<0.020	1.054	1.138	0.028	<0.0195	<0.021	<0.018
Sr	115.38	120.84	128.9	102.92	122.73	112.5	122.94
Y	23.12	25.96	22.8	21.42	21.31	22.86	22.34
Zr	76.56	98.43	77.18	76.92	68.38	82.15	71.53
Nb	0.153	0.28	0.282	0.151	0.128	0.163	0.183
Cd	0.67	<0.46	0.93	<0.41	<0.49	0.76	1.13
Sb	<0.053	<0.048	0.095	<0.055	0.067	<0.065	<0.048
Cs	<0.0106	0.149	0.164	<0.0076	<0.0103	<0.0112	<0.0092
Ba	<0.078	11.01	15.45	0.139	<0.073	<0.081	0.326
La	7.99	9.7	9.26	7.12	7.55	8.4	8
Ce	30.03	34.87	35.98	28.04	28.86	29.88	30.54
Pr	4.9	5.91	5.41	4.53	4.87	5.02	5.12
Nd	25.45	28.53	25.76	22.35	24.5	25.24	25.77
Sm	7.36	8.23	7.27	6.96	7.35	7.59	7.7
Eu	2.25	2.48	2.28	2.1	2.25	2.25	2.27
Gd	7.33	8.05	6.75	6.51	6.85	7.35	7.28
Tb	0.96	1.12	0.94	0.92	0.96	0.93	0.97
Dy	5.46	6.08	5.41	5.04	5	5.54	5.44
Ho	0.91	0.98	0.84	0.8	0.88	0.84	0.87
Er	2.23	2.53	2.22	2.01	2.1	2.21	2.09
Tm	0.293	0.322	0.289	0.254	0.257	0.319	0.307
Yb	1.54	1.76	1.29	1.47	1.7	1.67	1.55
Lu	0.209	0.245	0.189	0.208	0.209	0.217	0.22
Hf	2.59	3.66	2.43	3.22	2.68	3.02	2.68
Ta	0.0219	0.0447	0.021	0.0173	0.0259	0.043	0.0256
Pb	0.188	0.426	0.852	0.225	0.185	0.17	0.407
Th	0.409	0.778	0.77	0.389	0.301	0.42	0.37
U	0.09	0.149	0.218	0.077	0.082	0.074	0.127

Table 12: In-situ mineral trace element analyses. All values reported in ppm. Analysed by LA-ICMPS.

Element	BC14-038_18	BC14-038_19	BC14-038_20	BC14-039_1	BC14-039_2	BC14-039_3	BC14-039_4
Mineral	Biot	Biot	Biot	Cpx	Cpx	Cpx	Cpx
Sc	6	6.2	5.59	59.62	60.4	58.07	57.63
Ti	9509.55	8820.7	7661.38	2560.92	2345.72	2149.98	2252.2
V	263.36	243.93	222.97	213.24	195.95	192.9	202.1
Cr	0.24	0.17	0.21	4.14	3.35	<2.93	<3.17
Mn	354.9	354.16	337.22	1121.62	1108.9	1150.44	1164.5
Co	52.37	49.67	45.47	40.95	36.24	37.65	38.17
Ni	19.91	18.68	17.17	44.08	44.26	42.24	34.58
Cu	1027.73	2743.45	1103.61	2	1.88	1.93	1
Zn	42.2	64.93	39.94	30.77	30.76	34.87	32.28
As	<0.00	<0.00	<0.00	<1.65	<2.00	<2.05	<2.02
Rb	222.01	207.42	191.07	<0.135	<0.133	0.171	<0.162
Sr	98.88	85.29	79.54	80.89	75.69	73.87	75.02
Y	0.524	0.068	0.0472	11.52	11.11	11.03	11.6
Zr	4.63	4.93	5.02	21.98	19.58	18.31	19.99
Nb	1.79	1.66	1.297	<0.090	<0.090	<0.096	<0.114
Cd	<0.17	<0.19	<0.14	<2.49	<2.36	<2.32	<2.34
Sb	0.106	0.15	0.059	<0.28	<0.30	<0.31	<0.38
Cs	4.84	4.16	3.66	<0.091	<0.076	<0.088	<0.095
Ba	4207.2	3904.1	3424.16	<0.72	<0.72	0.78	<0.76
La	0.0106	0.014	0.0129	2.06	1.98	1.8	1.56
Ce	0.0253	0.021	0.0193	7.05	6.66	6.14	6.73
Pr	<0.0031	0.0051	0.0054	1.4	1.072	1.227	1.27
Nd	<0.017	0.02	<0.016	7.86	6.95	6.87	6.76
Sm	<0.021	<0.024	0.02	2.78	2.07	2.88	2.18
Eu	0.179	0.164	0.154	0.63	0.79	0.82	0.57
Gd	<0.027	<0.024	0.028	1.78	2.75	3.12	2.6
Tb	<0.0038	0.0035	<0.0033	0.5	0.355	0.439	0.501
Dy	0.017	<0.016	0.034	2.49	1.92	2.94	1.68
Ho	<0.0036	<0.0036	<0.0031	0.461	0.51	0.452	0.425
Er	<0.0125	<0.0101	<0.0104	0.87	1.23	1.2	1.32
Tm	<0.0044	<0.0045	<0.0040	0.156	<0.091	0.177	0.238
Yb	<0.015	<0.017	0.035	0.94	1.2	1.28	0.78
Lu	<0.0042	<0.0045	0.0088	<0.100	0.1	0.183	0.139
Hf	0.161	0.179	0.141	1.28	1.08	0.63	1.31
Ta	0.282	0.279	0.221	<0.112	<0.114	<0.105	<0.144
Pb	1.1	1.39	1.14	<0.36	<0.34	<0.37	<0.39
Th	0.018	0.0053	0.0092	<0.163	<0.182	<0.169	<0.211
U	0.115	0.495	0.195	<0.162	<0.150	<0.177	<0.202

Table 12: In-situ mineral trace element analyses. All values reported in ppm. Analysed by LA-ICMPS.

Element	BC14-039_5	BC14-039_6	BC14-039_7	BC14-039_8	BC14-039_9	BC14-039_10	BC14-039_11
Mineral	Cpx	Cpx	Cpx	Cpx	Cpx	Cpx	Plag
Sc	66.96	70.37	62.35	67.07	67.02	66.83	15.86
Ti	3196.26	3749.45	3359.12	3370.59	3371.58	3451.63	121.78
V	250.24	287.27	252.15	275	271.34	277.73	0.85
Cr	<3.18	<3.16	<3.42	<3.40	<3.04	<3.39	<5.19
Mn	1150.57	1428.94	1437.4	1374.09	1376.52	1382.14	41.33
Co	36.91	39.13	37.49	36.45	36.94	37.58	1.21
Ni	38.01	22.11	18.96	17.72	16.81	16.56	2.36
Cu	1.66	2.29	1.52	2.12	1.6	2.03	2.25
Zn	33.73	37.31	35.21	35.69	34.8	42.27	<4.75
As	<2.15	<1.83	<2.09	<2.43	<2.07	<2.27	<3.28
Rb	<0.141	<0.162	<0.151	<0.155	<0.131	<0.165	0.29
Sr	81.91	87.86	88.39	89.41	88.98	86.6	2317.18
Y	16.97	25.09	21.09	22.56	22.33	22.45	<0.149
Zr	33.64	56.8	46.15	51.67	52.57	52.5	<0.27
Nb	<0.111	0.136	<0.103	<0.126	<0.101	<0.110	<0.171
Cd	<2.38	<2.07	<2.55	<2.82	<2.42	<2.86	<4.38
Sb	<0.33	<0.31	<0.36	<0.39	<0.33	<0.38	<0.50
Cs	<0.103	<0.098	<0.102	<0.110	<0.086	<0.098	<0.159
Ba	0.64	<0.80	0.82	<0.75	<0.79	<0.91	313.78
La	2.72	4.06	3.53	3.38	3.61	3.6	2.78
Ce	9.71	14.69	12.37	12.95	12.89	12.78	3.89
Pr	1.7	2.77	2.32	2.39	2.4	2.25	0.303
Nd	10.25	16.44	13.79	14.53	15.29	14.2	1.09
Sm	4.01	5.1	3.61	4.81	5.23	4.81	<1.07
Eu	1.33	1.68	1.42	1.21	1.46	1.78	0.53
Gd	3.72	6.34	5.43	5.15	5.82	5.4	<0.85
Tb	0.566	0.833	0.689	0.725	0.884	0.92	<0.164
Dy	3.76	5.04	4.35	5.14	5.12	4.82	<0.77
Ho	0.734	1.202	0.918	0.973	0.965	0.929	<0.169
Er	1.73	2.54	2.22	2.41	2.38	2.75	<0.50
Tm	0.299	0.354	0.241	0.311	0.331	0.329	<0.173
Yb	1.38	2.18	1.87	1.37	1.8	1.64	<0.77
Lu	<0.128	0.275	0.3	0.322	0.346	0.338	<0.188
Hf	1.27	2.85	2.16	2.6	2.72	2.89	<0.71
Ta	<0.130	<0.132	<0.126	<0.132	<0.128	<0.136	<0.203
Pb	0.42	<0.41	<0.36	<0.44	<0.38	<0.42	2.13
Th	<0.182	0.198	<0.200	<0.224	<0.171	0.195	<0.30
U	<0.162	<0.200	<0.194	<0.223	<0.183	<0.208	<0.28

Table 12: In-situ mineral trace element analyses. All values reported in ppm. Analysed by LA-ICMPS.

Element	BC14-039_12	BC14-039_13	BC14-039_14	BC14-039_15	BC14-039_16	BC14-039_17	BC14-039_18
Mineral	Plag	Plag	Plag	Plag	Plag	Plag	Plag
Sc	13.69	13.42	14.52	14	14.41	13.87	14.45
Ti	71.82	77.66	78.4	143.05	79.44	69.47	92.46
V	0.98	1.05	0.89	0.92	1.15	<0.52	0.92
Cr	<5.17	<4.66	<4.83	<4.37	<4.60	<4.87	<4.07
Mn	37.12	34.9	35.66	44.1	36.62	33.79	37.1
Co	0.97	0.98	0.9	1.02	1.24	1.05	1.11
Ni	1.74	<1.53	<1.52	<1.39	2.23	<1.42	<1.47
Cu	<1.31	<1.19	1.65	2.2	<1.17	<1.18	<1.18
Zn	4.77	5.65	4.56	<3.90	5.96	<4.16	4.28
As	12.33	4.88	<3.38	42.17	26.25	7.91	15.67
Rb	0.88	0.474	<0.225	1.47	0.84	0.248	0.47
Sr	1890.63	1916.74	1929.39	1958.01	1909.77	1917.75	2030.56
Y	0.162	<0.126	<0.139	0.174	0.321	<0.128	0.171
Zr	1.18	0.81	0.29	5.84	3.35	0.85	0.98
Nb	<0.157	<0.172	<0.146	<0.152	<0.132	<0.164	<0.159
Cd	<4.24	<3.15	<3.58	<2.91	<3.36	<3.63	<3.06
Sb	<0.53	<0.55	<0.54	<0.52	<0.43	<0.49	<0.38
Cs	<0.168	<0.123	<0.150	<0.143	<0.121	<0.134	<0.139
Ba	163.87	173	175.13	188.38	176.6	165.85	198.94
La	2.17	2.09	2.18	2.38	2.19	2.47	2.33
Ce	2.76	3.09	2.8	3.24	3.14	2.85	3.44
Pr	0.329	0.326	0.343	0.354	0.327	0.34	0.343
Nd	1.13	1.7	1.26	1.03	<0.73	0.9	1.34
Sm	<0.82	<0.80	<0.82	<0.92	<0.78	<0.94	<0.93
Eu	0.4	<0.25	0.4	0.52	0.44	<0.24	<0.27
Gd	<0.83	<0.84	<0.85	<0.77	0.73	<0.73	0.98
Tb	<0.158	<0.144	<0.142	<0.127	0.134	<0.119	<0.124
Dy	<0.65	<0.60	<0.57	<0.57	<0.62	<0.57	<0.56
Ho	<0.183	<0.130	<0.146	<0.132	<0.155	<0.155	<0.161
Er	<0.47	<0.45	<0.46	<0.42	<0.49	<0.42	<0.43
Tm	<0.138	<0.140	<0.161	<0.125	<0.162	<0.130	<0.146
Yb	<0.83	<0.72	<0.60	<0.62	<0.64	<0.65	<0.68
Lu	<0.155	<0.169	<0.158	<0.133	<0.157	<0.185	<0.164
Hf	<0.72	<0.60	<0.63	<0.46	<0.62	<0.58	<0.57
Ta	<0.220	<0.167	<0.173	<0.176	<0.174	<0.195	<0.152
Pb	1.82	1.59	1.2	2.26	1.72	1.58	1.66
Th	<0.27	<0.250	<0.26	<0.253	<0.24	<0.25	<0.25
U	<0.29	<0.25	<0.23	<0.26	<0.25	<0.230	<0.29

Table 12: In-situ mineral trace element analyses. All values reported in ppm. Analysed by LA-ICMPS.

Element	BC14-039_19	BC14-039_20	BC14-039_21	BC14-039_22	BC14-039_23	BC14-039_24	BC14-039_26
Mineral	Plag	Plag	Olivine	Olivine	Olivine	Olivine	Olivine
Sc	13.86	14.27	8.98	15.55	17.68	17.15	82.88
Ti	85.7	85.66	21.01	31.58	34.04	39.84	186.71
V	1	0.87	1.58	2.59	3.8	3.2	10.94
Cr	<4.56	5.41	<2.12	<3.47	<3.96	<3.80	<46.61
Mn	35.18	37.03	3167.16	5537.71	6338.21	5882.27	29508.98
Co	1.07	1.24	161.87	280	321.68	305.93	1508.75
Ni	1.7	<1.61	267.67	461.1	530.95	506.28	2314.54
Cu	1.25	2.44	2.96	5.26	9.36	50.79	39.42
Zn	<4.13	4.53	175.35	298.53	368.46	348.51	1728.85
As	<3.25	<3.02	8.62	<2.35	<2.68	2.92	<28.30
Rb	<0.22	<0.206	0.243	0.186	0.67	<0.162	<2.19
Sr	2018.28	2054.17	0.499	0.137	8.19	0.304	<1.46
Y	0.228	0.274	0.114	0.18	0.213	0.309	<1.15
Zr	0.25	0.24	1.25	0.231	0.38	0.31	<2.18
Nb	<0.159	<0.135	<0.069	<0.106	<0.128	<0.096	<1.31
Cd	<3.37	<2.92	<1.56	<2.67	<3.17	2.46	<35.77
Sb	<0.55	<0.44	<0.181	<0.35	<0.39	<0.41	<4.20
Cs	<0.142	<0.133	<0.064	<0.104	0.099	<0.101	<1.19
Ba	197.06	198.27	2.62	2.29	16.82	2.1	<10.49
La	2.77	2.54	<0.060	<0.099	0.154	<0.103	<1.11
Ce	3.46	3.45	<0.051	0.211	0.168	<0.100	<0.99
Pr	0.304	0.402	<0.044	<0.066	<0.093	<0.075	<1.01
Nd	<0.72	<0.83	<0.30	<0.45	<0.60	<0.51	<5.41
Sm	<0.86	1.06	<0.35	<0.60	<0.72	<0.66	<8.60
Eu	<0.24	<0.29	<0.098	<0.172	<0.210	<0.188	1.85
Gd	<0.87	<0.88	<0.32	<0.62	<0.58	<0.54	<7.48
Tb	<0.126	<0.119	<0.052	<0.081	<0.103	<0.102	1.45
Dy	0.57	<0.62	<0.23	<0.37	<0.52	<0.45	<5.12
Ho	0.159	<0.136	<0.061	<0.115	<0.126	<0.108	<1.36
Er	<0.39	<0.43	<0.156	<0.28	<0.32	<0.33	<4.22
Tm	<0.137	<0.151	<0.052	<0.105	<0.116	<0.114	<1.27
Yb	<0.79	<0.77	<0.29	<0.53	<0.46	<0.53	<6.61
Lu	<0.132	<0.174	<0.069	<0.114	<0.125	<0.125	<1.34
Hf	<0.53	<0.64	<0.234	<0.46	<0.37	<0.48	<4.91
Ta	<0.181	<0.190	<0.070	<0.113	<0.140	<0.098	<1.67
Pb	1.35	1.34	<0.23	<0.39	<0.50	<0.44	<4.85
Th	<0.27	<0.26	<0.093	<0.165	<0.192	<0.200	2.2
U	<0.25	<0.27	<0.110	<0.193	<0.197	0.24	<2.42

Table 12: In-situ mineral trace element analyses. All values reported in ppm. Analysed by LA-ICMPS.

Element	BC14-039_27	BC14-039_28	BC14-039_29	BC14-048_1	BC14-048_2	BC14-048_3	BC14-048_4
Mineral	Olivine	Olivine	Olivine	Amph	Amph	Amph	Amph
Sc	10.33	16.97	11.67	57.17	50.41	64.01	59.16
Ti	20.4	34.23	16.63	10421.64	9984.78	11045.3	10179.12
V	2.03	3.31	2.57	548.85	470.4	549.18	540.58
Cr	<2.68	<4.40	<3.20	<15.12	<11.15	<19.10	18.13
Mn	4238.88	6442.12	4558.21	998.52	887.94	1019.92	965.6
Co	200.45	324.5	227.51	64.15	47.71	65.25	64.99
Ni	319.01	522.88	365.33	28.71	21.77	19.02	23.01
Cu	3.35	4.93	3.57	30.34	8.01	26.98	17.7
Zn	225.84	363.99	261.52	91.63	57.09	80.49	105.89
As	<1.76	<2.89	<2.11	1.46	<3.33	<7.95	<5.58
Rb	<0.123	<0.190	<0.129	7.7	6.67	6.51	8.03
Sr	0.106	<0.126	0.105	799.73	714.28	814.9	797.13
Y	0.117	0.182	0.188	20.32	17.32	19.7	20.33
Zr	0.204	<0.199	0.178	35.31	33.95	36.44	38.4
Nb	<0.076	<0.157	<0.095	3.52	2.1	1.92	2.16
Cd	<1.80	<2.89	<2.08	0.68	<0.00	0.66	<0.00
Sb	<0.26	<0.32	<0.29	0.069	<0.00	<0.130	<0.115
Cs	<0.067	<0.134	<0.077	0.214	<0.028	<0.034	0.029
Ba	<0.60	<0.87	<0.61	943.53	824.45	944.87	936.16
La	<0.068	<0.118	<0.068	4.94	4.84	5.7	5.55
Ce	<0.075	0.131	<0.063	15.97	14.55	17.96	17.7
Pr	<0.058	<0.101	<0.065	2.67	2.66	2.76	3.16
Nd	<0.32	<0.62	<0.39	14.81	15	19.09	19.55
Sm	<0.49	<0.67	<0.51	6.26	4.75	5.51	5.79
Eu	<0.108	<0.202	<0.142	1.98	1.74	1.95	1.83
Gd	<0.46	<0.65	<0.47	5.29	5.1	5.98	6.03
Tb	<0.061	<0.087	<0.077	0.71	0.86	0.75	0.74
Dy	<0.32	<0.47	<0.35	5.03	4.83	4.18	3.97
Ho	<0.063	<0.134	<0.095	0.87	0.84	0.92	0.87
Er	<0.200	<0.34	<0.25	2.06	2.05	2.05	2.17
Tm	<0.073	<0.141	<0.086	0.262	0.146	0.31	0.265
Yb	0.47	<0.67	0.4	1.26	1.09	1.59	1.32
Lu	<0.086	<0.137	<0.104	0.205	0.281	0.226	0.296
Hf	<0.27	<0.44	<0.38	1.79	1.48	2.11	1.81
Ta	<0.104	<0.131	0.112	0.112	0.119	0.13	0.061
Pb	<0.28	<0.49	<0.38	2.37	1.54	2.01	1.45
Th	<0.129	<0.27	<0.143	0.059	0.176	0.191	0.24
U	<0.156	<0.20	<0.158	0.178	0.309	0.51	0.288

Table 12: In-situ mineral trace element analyses. All values reported in ppm. Analysed by LA-ICMPS.

Element	BC14-048_5	BC14-048_6	BC14-048_7	BC14-048_8	BC14-048_9	BC14-048_10	BC14-048_11
Mineral	Amph	Amph	Amph	Amph	Amph	Amph	Cpx
Sc	56.75	48.05	47.63	42.27	47.19	40.16	89.14
Ti	11409.56	10236.3	11076.03	10667.77	11247.86	10706.28	5023.7
V	546.02	469.73	540.9	533.91	527.24	548.98	346.83
Cr	<16.15	<13.72	<18.61	<18.49	<20.23	<24.27	<21.30
Mn	988.39	845.61	966.03	1148.82	1170.78	1171.26	1156.36
Co	58.62	52.53	64.55	65.77	62.36	62.93	34.03
Ni	19.21	28.64	33.87	16.01	10.89	11.46	65.04
Cu	<6.35	<5.35	<6.53	77.83	44.8	53.32	<7.37
Zn	77.28	79.09	93.51	117.48	114.34	88.99	56.09
As	6.61	<3.41	<5.37	74.26	71.36	62.43	74.15
Rb	8.85	7.06	9.08	9.05	12.93	8.56	1.82
Sr	795.89	735.56	768.12	686.58	738.42	720.7	106.66
Y	21.73	17.29	19.61	20.56	22.1	21.71	24.52
Zr	38.69	39.27	43.29	45.06	46.8	46.15	59.42
Nb	2.08	2.01	2.02	2.46	3.49	3.53	<0.165
Cd	<1.19	<1.55	1.31	<1.29	<1.39	<0.00	0.67
Sb	<0.00	<0.155	<0.242	0.148	<0.138	<0.196	0.133
Cs	0.035	<0.0282	<0.031	<0.047	<0.035	0.042	<0.051
Ba	946.45	843.54	873.71	834.09	954.86	904.09	14.11
La	5.53	4.86	4.73	6.06	6.34	6.29	5.18
Ce	17.66	16.16	17.39	19.54	19.09	18.7	16.41
Pr	2.44	2.62	2.86	3.29	3.38	3.36	3.03
Nd	16.65	16.2	16.18	18.42	19.52	19.04	17.05
Sm	5.56	5.39	5.55	6.06	5.73	6.53	5.8
Eu	2.43	1.93	2.19	2.22	2.03	2.16	1.56
Gd	5.26	5.83	5.53	5.93	7.33	6.17	6.93
Tb	0.79	0.78	0.88	0.97	0.8	0.647	0.88
Dy	4.49	3.23	3.87	5.44	4.97	4.62	5.52
Ho	0.89	0.588	0.8	0.77	0.9	1.06	0.97
Er	2.46	1.8	2.05	2.02	2.41	2.04	2.53
Tm	0.156	0.212	0.243	0.261	0.247	0.269	0.247
Yb	1.08	1.29	1.87	1.34	1.71	1.55	1.42
Lu	0.155	0.169	0.211	0.19	0.21	0.183	0.272
Hf	2.44	2.06	1.64	2.09	2.39	1.94	3.06
Ta	0.029	0.077	0.103	0.086	0.086	0.185	0.022
Pb	1.21	1.4	1.24	2.3	2.25	1.72	0.69
Th	0.135	0.148	0.097	0.164	0.183	0.128	0.266
U	0.102	0.088	0.065	0.319	0.405	0.299	0.072

Table 12: In-situ mineral trace element analyses. All values reported in ppm. Analysed by LA-ICMPS.

Element	BC14-048_12	BC14-048_13	BC14-048_14	BC14-048_15	BC14-048_16	BC14-048_17	BC14-048_18
Mineral	Cpx	Cpx	Cpx	Cpx	Cpx	Plag	Plag
Sc	59.86	45.46	52.72	45.93	50.3	17.15	18.75
Ti	2955.33	3009.71	5503.26	4636.55	2727.29	135.7	101.96
V	233.1	243.57	314.88	295.62	219.68	<4.51	5.3
Cr	<20.94	<25.89	<22.83	<18.78	<25.17	<24.62	<40.25
Mn	1242.4	1610.56	1505.49	1316.06	1503.53	48.05	45.87
Co	32.09	36.8	39.06	35.43	37.2	<2.03	<2.24
Ni	10.32	6.07	8.14	9.03	8.3	<8.36	5.5
Cu	<5.98	<6.78	<7.18	<6.87	<6.40	<10.83	<11.56
Zn	56.87	44.29	68.06	37.02	33.55	<23.99	<18.67
As	69.01	23.34	73.81	62.44	10.55	201.43	98.77
Rb	1.3	<0.35	1.88	2.03	0.29	3.68	2.81
Sr	87.18	105.91	111.33	104.36	98.02	2539.79	2448.16
Y	14.24	14.84	22.38	20.14	14.09	<0.26	0.58
Zr	36.9	34.56	69.05	60.73	27.2	12.72	10.07
Nb	<0.085	<0.100	0.256	<0.176	0.098	<0.24	0.22
Cd	<1.26	<2.08	0.68	<1.83	0.72	0.9	<2.20
Sb	0.091	<0.289	<0.225	<0.126	<0.125	<0.20	<0.214
Cs	<0.055	0.04	0.051	0.047	0.054	<0.050	<0.094
Ba	11.32	6.09	14.39	14.35	2.21	292.81	245.2
La	2.68	3.25	5.17	4.68	2.88	2.37	2.25
Ce	9.59	10.93	17.77	15.42	10.47	3.73	3.36
Pr	1.71	1.96	3.27	2.9	1.88	0.298	0.228
Nd	9.3	12	17.61	16.98	11.61	1.26	0.94
Sm	3.11	3.06	4.57	4.58	3.46	<0.33	0.36
Eu	1.02	1.17	1.66	1.7	0.98	0.47	0.36
Gd	3.72	4.6	5.51	5.65	3.69	<0.208	<0.23
Tb	0.539	0.606	0.81	0.84	0.482	0.043	<0.035
Dy	3.1	3.7	4.82	4.88	3.24	<0.00	0.073
Ho	0.651	0.67	0.94	0.86	0.505	<0.033	<0.00
Er	1.69	1.38	2.03	1.85	1.24	<0.00	<0.00
Tm	0.172	0.168	0.31	0.266	0.164	<0.043	<0.047
Yb	0.99	1.35	1.53	1.5	0.98	<0.144	<0.156
Lu	0.137	0.141	0.212	0.159	0.095	<0.00	<0.034
Hf	1.86	1.57	2.78	2.95	1.58	0.48	0.54
Ta	<0.029	0.0065	<0.021	<0.021	<0.029	0.028	<0.035
Pb	0.64	0.42	0.66	0.74	0.341	2.7	2.54
Th	0.11	0.113	0.179	0.116	0.118	0.031	0.019
U	<0.022	0.077	0.071	0.05	<0.031	0.096	0.057

Table 12: In-situ mineral trace element analyses. All values reported in ppm. Analysed by LA-ICMPS.

Element	BC14-048_19	BC14-048_20	BC14-048_21	BC14-048_22	BC14-048_23	BC14-048_24	BC14-048_25
Mineral	Plag	Plag	Plag	Plag	Plag	Plag	Plag
Sc	13.09	14	18.86	89.75	77.52	74.28	83.8
Ti	108.4	<43.61	46.71	20511.88	19316.6	16823.02	17642.63
V	<4.70	<5.30	<6.07	942.4	919.93	739	733.99
Cr	28.19	<22.98	<31.09	<97.98	<79.14	<65.06	<83.83
Mn	40.57	34.62	39.65	2153.39	1988.59	1431.98	1416.93
Co	<1.77	2.05	<2.33	126.05	100.51	90.82	82.08
Ni	<11.02	<6.40	<0.00	28.95	31.53	23.95	44.33
Cu	9.54	<9.85	<12.06	97.9	<26.87	46.86	<24.02
Zn	<19.59	30.89	27.19	133.43	89.31	92.92	81.55
As	117.13	83.49	131.67	<17.27	10.9	24.17	<7.79
Rb	4.07	1.66	2.69	12.95	14.14	8.77	8.36
Sr	2259.46	2068.2	2331.25	1303.31	1219.33	1064.53	1047.06
Y	0.27	<0.116	0.21	42.12	38.18	26.78	27.38
Zr	13.71	8.21	10.56	78.82	71.18	53.85	55.83
Nb	0.065	<0.124	0.057	4.83	4.51	3.4	3.1
Cd	<0.00	<2.54	0.82	<1.38	<2.43	<0.00	0.41
Sb	<0.193	<0.174	0.079	<0.20	<0.32	<0.244	<0.178
Cs	<0.049	0.021	<0.077	<0.046	<0.066	<0.057	<0.041
Ba	240.91	186.37	253.29	1631.96	1514.05	1234	1173.82
La	1.87	1.65	2.21	11.78	10.73	7.07	7.32
Ce	2.86	2.8	3.02	36.2	32.06	23.52	22.62
Pr	0.375	0.312	0.305	6.14	5.77	4.09	4.4
Nd	1.44	1	1.05	34.32	28.57	24.71	22.21
Sm	<0.32	<0.20	0.28	10.19	11.66	7.67	8.03
Eu	0.087	0.18	0.47	3.78	3.53	2.83	2.71
Gd	0.2	0.17	0.084	11.71	9.15	8.15	8.54
Tb	0.044	<0.00	0.013	1.74	1.54	1.24	1.13
Dy	0.27	<0.00	0.052	9.22	8.54	6.4	6.6
Ho	<0.032	<0.00	<0.035	1.71	1.38	0.98	1.15
Er	<0.00	<0.144	0.038	4.19	3.33	2.64	2.75
Tm	<0.00	<0.027	0.036	0.503	0.422	0.376	0.322
Yb	<0.243	0.18	<0.155	2.46	2.33	1.45	1.63
Lu	<0.00	<0.0277	<0.00	0.34	0.354	0.229	0.2
Hf	0.5	0.178	0.44	3.86	3.63	2.78	2.63
Ta	0.015	<0.028	0.013	0.208	0.19	0.131	0.166
Pb	3.18	2.14	2.47	2.77	2.65	2.28	2.14
Th	0.07	<0.043	0.085	0.276	0.313	0.261	0.136
U	0.048	0.033	0.122	0.096	0.048	0.07	0.109

Table 12: In-situ mineral trace element analyses. All values reported in ppm. Analysed by LA-ICMPS.

Element	BC14-048_26	BC14-048_27	BC14-048_28	BC14-048_29	BC14-048_30	BC14-048_31	BC14-048_32
Mineral	Plag	Amph	Amph	Amph	Amph	Cpx	Cpx
Sc	96.53	66.65	67.15	56.46	29.63	56.74	50.91
Ti	18881.66	12624.44	16458.14	13837.48	14560.48	5228.27	6843.79
V	802.03	553.89	657.2	544.69	504.71	257.56	283.89
Cr	<84.63	<66.79	<75.74	<68.80	<70.40	<86.34	<79.29
Mn	1524.76	922.4	1269.08	1183.6	1234.81	1421	1413.49
Co	87.18	55.52	67.11	62.38	66.67	32.95	37.38
Ni	45.71	28.24	18.83	11.03	12.26	12.86	8.91
Cu	<24.57	69.6	26.8	<18.11	42.59	<19.13	<17.67
Zn	78.45	76.86	70.68	61.79	80.39	17.59	50.23
As	<11.30	21.09	<12.99	<7.33	<9.67	<9.07	<7.86
Rb	11.38	7.84	10.14	7.74	7.78	0.46	0.55
Sr	1122.5	724.23	863.01	721.7	699.89	103.08	105.1
Y	30.73	17.9	26.95	23.33	22.29	15.18	19.65
Zr	51.53	37.55	51.63	46.19	41.97	31.84	55.99
Nb	3.24	1.51	3.67	2.39	3.15	0.18	<0.113
Cd	1.05	0.78	<1.50	<0.00	1.05	0.97	<0.85
Sb	<0.200	<0.161	<0.148	<0.130	<0.156	0.081	0.04
Cs	0.051	<0.043	<0.034	0.037	<0.036	0.037	<0.027
Ba	1227	827.9	994.73	856.44	878.28	3.61	1.03
La	6.92	4.82	7.16	6.23	6.7	3.2	4.48
Ce	22.9	14.41	22.14	20.35	20.97	11.76	14.68
Pr	4.02	2.46	4.16	3.52	3.61	2.19	2.58
Nd	22.78	16.06	22.43	21.11	21.21	13.5	15.41
Sm	7.29	4.37	7.56	6.37	5.64	3.45	4.57
Eu	2.84	1.84	2.23	2.18	2.31	1.08	1.51
Gd	7.87	4.9	6.41	6.64	6.76	4.15	4.71
Tb	1.09	0.74	0.99	0.96	0.92	0.64	0.78
Dy	6.89	3.8	5.96	5.19	5.18	3.35	4.1
Ho	1.29	0.77	1.04	0.99	0.83	0.81	0.81
Er	3.25	2.12	2.84	2.14	2.32	1.5	1.59
Tm	0.424	0.251	0.346	0.233	0.231	0.296	0.168
Yb	2.01	1.11	1.67	1.53	1.64	0.88	1.71
Lu	0.27	0.172	0.286	0.186	0.249	0.159	0.171
Hf	2.65	2.24	2.86	2.03	1.92	1.84	2.86
Ta	0.158	0.069	0.134	0.108	0.164	0.016	0.0154
Pb	1.99	1.62	1.79	1.71	1.43	0.42	0.303
Th	0.186	0.154	0.173	0.15	0.113	0.083	0.151
U	<0.022	0.122	0.041	0.048	0.04	0.094	0.019

Table 12: In-situ mineral trace element analyses. All values reported in ppm. Analysed by LA-ICMPS.

Element	BC14-048_33	BC14-048_34	BC14-048_35	BC14-048_36	BC14-048_37	BC14-048_38	BC14-048_39
Mineral	Cpx	Cpx	Cpx	Amph	Amph	Amph	Amph
Sc	56.2	53.46	51.7	68.14	68.48	85.71	74.86
Ti	8060.85	7090	5991.29	17972.78	22675.07	33466.34	23034.12
V	340.06	309.42	275.39	489.68	533.36	690.16	590.28
Cr	<89.87	<93.40	<116.93	<96.57	<98.06	<154.25	<127.64
Mn	1389.52	1380.48	1986	901.9	1080.29	1426.98	1092.93
Co	30.15	28.87	40.65	54.77	66.02	88.69	60.77
Ni	<6.30	<9.69	<10.85	24.13	30.97	59.96	35.19
Cu	<19.92	<20.56	35.93	64.93	172.47	81.73	45.18
Zn	34.79	52.51	34.67	31.8	53.11	51.01	44.05
As	<8.77	27.48	<8.75	<5.72	7.71	<17.49	<14.43
Rb	<0.38	0.98	<0.52	5.82	10.99	9.9	9.05
Sr	112.35	99.39	135.08	732.4	846.7	1119.74	878.85
Y	21.58	18.1	23.24	19.95	24.37	30.82	24.73
Zr	59.35	56.7	51.26	37.43	45.04	64.04	49.16
Nb	<0.127	0.039	<0.168	1.92	2.17	2.63	2.54
Cd	<0.95	<0.92	0.94	<1.91	<0.99	<2.28	0.67
Sb	<0.131	0.08	<0.173	<0.092	<0.096	<0.35	<0.122
Cs	0.011	<0.029	<0.039	0.044	0.43	<0.035	0.041
Ba	0.41	6.41	0.18	855.75	1028.11	1333.72	1074.14
La	4.85	4.48	6.16	5.15	6.54	8.96	6.92
Ce	15.25	14.62	20.42	15.56	19.94	26.83	20.32
Pr	3.55	2.52	3.21	2.88	3.2	4.47	3.76
Nd	17.66	15.47	19.2	16.68	22.42	27.16	20.8
Sm	5.34	4.82	6.65	5.08	5.92	10.29	7.04
Eu	1.75	1.33	1.57	1.82	2.22	2.97	2.59
Gd	6.04	5.05	5.74	4.5	7.77	9.73	5.87
Tb	0.85	0.85	0.82	0.79	1.04	1.4	1.03
Dy	4.59	4.97	4.9	4.15	6.08	7.14	5.41
Ho	0.73	0.75	0.85	0.71	0.97	1.27	0.83
Er	2.19	1.84	2.03	2.06	2.46	3.17	2.52
Tm	0.31	0.308	0.26	0.197	0.281	0.255	0.37
Yb	1.61	1.81	1.71	1.51	1.56	1.93	1.77
Lu	0.183	0.147	0.27	0.172	0.197	0.33	0.167
Hf	2.9	2.88	2.39	1.61	2.39	3.44	2.15
Ta	0.015	0.0118	0.023	0.095	0.1	0.193	0.091
Pb	0.191	0.61	0.49	1.74	3.76	2.28	1.91
Th	0.174	0.164	0.121	0.118	0.154	0.31	0.139
U	0.035	0.035	0.04	0.205	0.136	0.035	0.081

Table 12: In-situ mineral trace element analyses. All values reported in ppm. Analysed by LA-ICMPS.

Element	SA12-X011_1	SA12-X011_2	SA12-X011_3	SA12-X011_4	SA12-X011_5	SA12-X011_6	SA12-X011_7
Mineral	Amph	Amph	Amph	Cpx	Cpx	Cpx	Cpx
Sc	105.24	104.75	105.49	70.42	78.82	81.68	79.43
Ti	15399.87	14797.5	15288.95	3383.83	3786.73	2428.18	3700.76
V	762.06	732.69	748.23	247.62	261.7	200.84	258.78
Cr	13.33	13.06	9.43	<3.05	<3.16	<3.47	<3.05
Mn	1682.8	1656.07	1712.88	1388.8	1178.96	1111.38	1076.79
Co	99.66	96.29	98.21	39.04	34.38	36.25	36.78
Ni	73.93	72.79	76.05	21.04	25	29.84	21.98
Cu	2.75	3.19	3.01	<0.98	<1.01	<1.00	<1.02
Zn	104.33	107.22	110.8	41.06	34.8	33.98	26.49
As	<3.21	<3.25	<2.90	<2.02	2.09	4.2	2.95
Rb	13.34	12.85	14.31	0.19	<0.121	<0.130	0.135
Sr	669.72	657.49	684.54	88.63	97.29	84.57	91.27
Y	42.16	41.07	42.73	17.19	16.9	12.2	14.72
Zr	94.99	86.68	92.73	32.94	43.66	27.6	35.22
Nb	7.49	7.27	7.68	0.103	<0.098	<0.087	0.102
Cd	<3.02	<3.09	<3.21	<1.89	<1.62	<2.18	<1.49
Sb	<0.43	<0.44	<0.49	<0.28	<0.30	<0.24	<0.187
Cs	<0.131	0.121	<0.125	<0.086	<0.078	<0.081	<0.081
Ba	942.71	899.39	967.57	1.99	<0.64	1.27	<0.60
La	18.24	17.08	17.69	4.43	4.3	2.66	3.45
Ce	52.03	49.73	52.59	13.24	14.06	9.24	11.29
Pr	8.27	8.19	8.39	2.33	2.81	1.8	2.36
Nd	40.79	40.01	42.38	14.17	14.04	10.21	11.95
Sm	12.23	9.99	10.45	4.48	4.76	3.31	4.52
Eu	3.3	3.11	3.42	0.97	1.39	0.95	1.34
Gd	11.68	11.13	12.06	5.17	4.69	3.01	3.72
Tb	1.41	1.59	1.65	0.62	0.673	0.455	0.649
Dy	9.62	7.93	9.55	3.77	3.77	2.61	3.26
Ho	1.83	1.71	1.6	0.576	0.732	0.476	0.715
Er	4.42	4.19	4.37	2.14	1.75	1.34	1.55
Tm	0.68	0.6	0.504	0.123	0.307	0.209	0.155
Yb	3.4	4.23	3.57	1.38	1.39	1.06	0.76
Lu	0.379	0.58	0.46	0.222	0.146	<0.105	0.169
Hf	4.11	3.43	4.16	1.61	2.67	1.85	1.94
Ta	0.42	0.345	0.387	<0.101	<0.092	<0.098	<0.097
Pb	3.01	2.82	2.55	<0.30	0.3	<0.35	<0.37
Th	0.37	0.28	0.35	0.427	0.468	<0.164	<0.168
U	<0.22	<0.27	<0.28	<0.150	0.185	<0.151	<0.164

Table 12: In-situ mineral trace element analyses. All values reported in ppm. Analysed by LA-ICMPS.

Element	SA12-X011_8	SA12-X011_9	SA12-X011_10
Mineral	Cpx	Cpx	Cpx
Sc	75.15	70.58	77.13
Ti	3997.76	3039.91	3173.42
V	272.05	233.44	238.29
Cr	<2.90	3.32	5.22
Mn	1051.93	1101.65	1099.3
Co	35.95	37.72	37.34
Ni	25.03	23.41	26.55
Cu	1.11	<1.01	1.83
Zn	26.43	36.06	26.7
As	3.46	4.72	<2.15
Rb	<0.136	<0.154	<0.138
Sr	93.26	90.12	94.67
Y	15.99	13.34	14.07
Zr	41.93	33.69	38.38
Nb	<0.077	<0.081	<0.090
Cd	<2.30	<2.23	<1.70
Sb	<0.29	<0.23	<0.22
Cs	<0.077	<0.075	<0.079
Ba	<0.72	<0.62	<0.51
La	3.7	3.25	3.61
Ce	13.23	11.78	12.58
Pr	2.38	2.06	2.22
Nd	13.67	11.09	12.94
Sm	4.32	3.63	3.88
Eu	1.43	1.17	0.96
Gd	4.77	4.8	4.57
Tb	0.539	0.492	0.552
Dy	3.36	3.29	3.4
Ho	0.678	0.615	0.606
Er	1.72	1.57	1.44
Tm	0.189	0.178	0.182
Yb	0.79	0.93	1.04
Lu	0.102	0.218	0.098
Hf	1.55	1.98	2.14
Ta	<0.098	<0.105	<0.091
Pb	0.35	<0.30	<0.33
Th	0.153	0.209	<0.161
U	<0.156	<0.155	<0.142

Table 12: In-situ mineral trace element analyses. All values reported in ppm. Analysed by LA-ICMPS.

Analysis no.	my18e06 06	my18f06 06	my18g11 11	my18g16 16	my18d14 14	my18d15 15	my18d18 18
Element	glass	glass	glass	glass	SA88/309 glass	SA88/309 glass	SA88/309 glass
Sc	5.02	4.74	2.88	5.74	6.42	5.83	5.38
Ti	3370.00	4030.00	2810.00	4450.00	4410.00	4590.00	4160.00
V	75.43	85.82	50.65	87.11	113.00	109.00	93.31
Cr	<0.701	<0.832	<0.550	<0.778	0.96	<0.905	<0.768
Co	15.15	12.86	8.79	13.85	16.16	15.00	13.21
Ni	0.21	0.30	0.37	0.24	0.28	0.26	0.17
Cu	100.00	59.90	26.51	80.66	94.72	99.31	118.00
Zn	194.00	158.00	110.00	177.00	194.00	192.00	189.00
As	16.99	15.36	11.38	17.50	17.93	18.59	17.24
Rb	242.00	248.00	194.00	305.00	302.00	308.00	280.00
Sr	105.00	164.00	83.87	94.90	84.84	93.17	87.18
Y	29.67	27.59	27.03	33.14	32.96	33.18	32.66
Zr	188.00	214.00	134.00	239.00	220.00	224.00	213.00
Nb	11.39	11.97	7.98	13.44	13.20	13.41	13.17
Cd	0.12	0.12	<0.0967	<0.146	0.15	0.18	0.14
Sb	0.85	0.80	0.60	0.95	0.92	1.00	0.87
Cs	13.47	13.94	11.06	17.76	16.95	17.77	15.88
Ba	543.00	602.00	325.00	445.00	423.00	467.00	509.00
La	55.57	50.49	54.39	57.74	59.20	61.69	61.86
Ce	94.96	86.68	95.75	100.00	103.00	106.00	108.00
Pr	9.58	8.68	10.03	10.01	10.44	10.60	10.86
Nd	35.65	32.30	39.21	36.60	37.89	39.96	40.10
Sm	6.39	6.09	7.45	6.95	7.07	7.40	7.31
Eu	1.21	1.11	1.33	1.09	1.10	1.13	1.26
Gd	5.12	4.89	5.65	5.68	5.59	5.71	5.83
Dy	4.89	4.72	4.81	5.48	5.65	5.76	5.54
Ho	1.05	0.99	0.97	1.17	1.18	1.21	1.17
Er	2.87	2.69	2.57	3.31	3.24	3.25	3.09
Yb	3.18	2.99	2.36	3.58	3.46	3.53	3.49
Lu	0.47	0.46	0.36	0.54	0.54	0.53	0.53
Hf	3.96	4.39	2.84	5.08	4.59	4.67	4.54
Ta	0.49	0.55	0.36	0.62	0.58	0.61	0.59
Pb	43.75	40.20	29.03	44.08	47.34	49.25	46.28
Th	19.98	21.19	14.66	23.75	23.43	23.99	23.30
U	5.27	5.41	3.70	6.14	6.13	6.26	5.99

Table 13: Trace element compositions of groundmass glass from LA-ICP-MS analysis. All data reported in ppm.

Appendix 2

Appendix 2 is an accompaniment to chapter 4

Includes iron isotope measurements of geostandards, images of peak shapes from MC-ICP-MS and records of analytical blanks

Date	^{53}Cr (V)	^{54}Fe (V)	^{56}Fe (V)	56.924 (V)	^{60}Ni (V)	^{61}Ni (V)	1ppm ^{57}Fe (V)	Fe conc. (ppb)
15.08.16	0.0002	0.0019	0.0311	0.0008	0.0008	0.0001	0.22	***3.4740***
15.08.16	0.0001	0.0007	0.0031	0.0001	0.0005	0.0001	0.22	***0.3924***
16.08.16	0.0001	0.0013	0.0204	0.0005	0.0156	0.0007	0.17	***2.9063***
18.08.16	0.0001	0.0011	0.0174	0.0004	0.0264	0.0012	0.17	***2.4473***
22.08.16	0.0001	0.0016	0.0257	0.0006	0.0302	0.0014	0.21	***3.1407***
23.08.16	0.0001	0.0013	0.0208	0.0005	0.0294	0.0013	0.19	***2.6712***
23.08.16	0.0001	0.0014	0.0220	0.0006	0.0319	0.0015	0.19	***2.9377***
24.08.16	0.0001	0.0019	0.0296	0.0007	0.0224	0.0010	0.19	***3.6748***
24.08.16	0.0001	0.0025	0.0396	0.0010	0.0273	0.0013	0.19	***5.1554***
25.08.16	0.0001	0.0019	0.0314	0.0008	0.0232	0.0011	0.16	***4.8533***
29.08.16	0.0001	0.0023	0.0370	0.0009	0.0282	0.0013	0.18	***4.9379***
29.08.16	0.0002	0.0032	0.0550	0.0011	0.0333	0.0015	0.18	***6.2033***
30.08.16	0.0008	0.0036	0.0551	0.0013	0.0007	0.0001	0.19	***7.0187***
05.09.16	0.0008	0.0035	0.0542	0.0013	0.0006	0.0000	0.21	***6.2451***
05.09.16	0.0009	0.0038	0.0589	0.0014	0.0014	0.0001	0.21	***6.8065***
06.09.16	0.0007	0.0031	0.0477	0.0012	0.0007	0.0001	0.18	***6.3992***
08.09.16	0.0007	0.0032	0.0490	0.0012	0.0019	0.0001	0.15	***8.0306***

Table 1: Records of analytical and procedural blanks. Blanks calculated from measured voltage on a given cup (56.924) and known voltage produced by concentration of 1ppm Fe.

GEO STANDARD	BCR-2		BHVO-2		AGV-2	
	δ^{57}Fe	**δ^{56}Fe**	**δ^{57}Fe**	**δ^{56}Fe**	**δ^{57}Fe**	**δ^{56}Fe**
	0.164	0.119	0.134	0.077	0.231	0.168
	0.196	0.144	0.187	0.151	0.113	0.084
	0.210	0.141	0.167	0.109	0.104	0.076
	0.177	0.138	0.170	0.124	0.176	0.103
	0.142	0.069	0.154	0.118	0.167	0.123
	0.208	0.142	0.107	0.081	0.203	0.115
	0.198	0.146	0.181	0.121	0.160	0.119
	0.179	0.102	0.158	0.132	0.229	0.149
	0.158	0.110	0.128	0.114	0.204	0.130
	0.064	0.044	0.102	0.040	0.240	0.160
	0.059	0.061	0.167	0.184	0.139	0.096
	0.193	0.125	0.198	0.138	0.223	0.158
	0.080	0.052			0.182	0.144
	0.018	0.047			0.057	0.041
	0.171	0.241			0.063	0.041
					0.112	0.150
					0.072	0.088
AVERAGE	***0.148***	***0.112***	***0.154***	***0.116***	***0.166***	***0.114***
1 s.d.	***0.062***	***0.052***	***0.031***	***0.037***	***0.062***	***0.040***

Table 2: Fe-isotope measurements of geostandards.

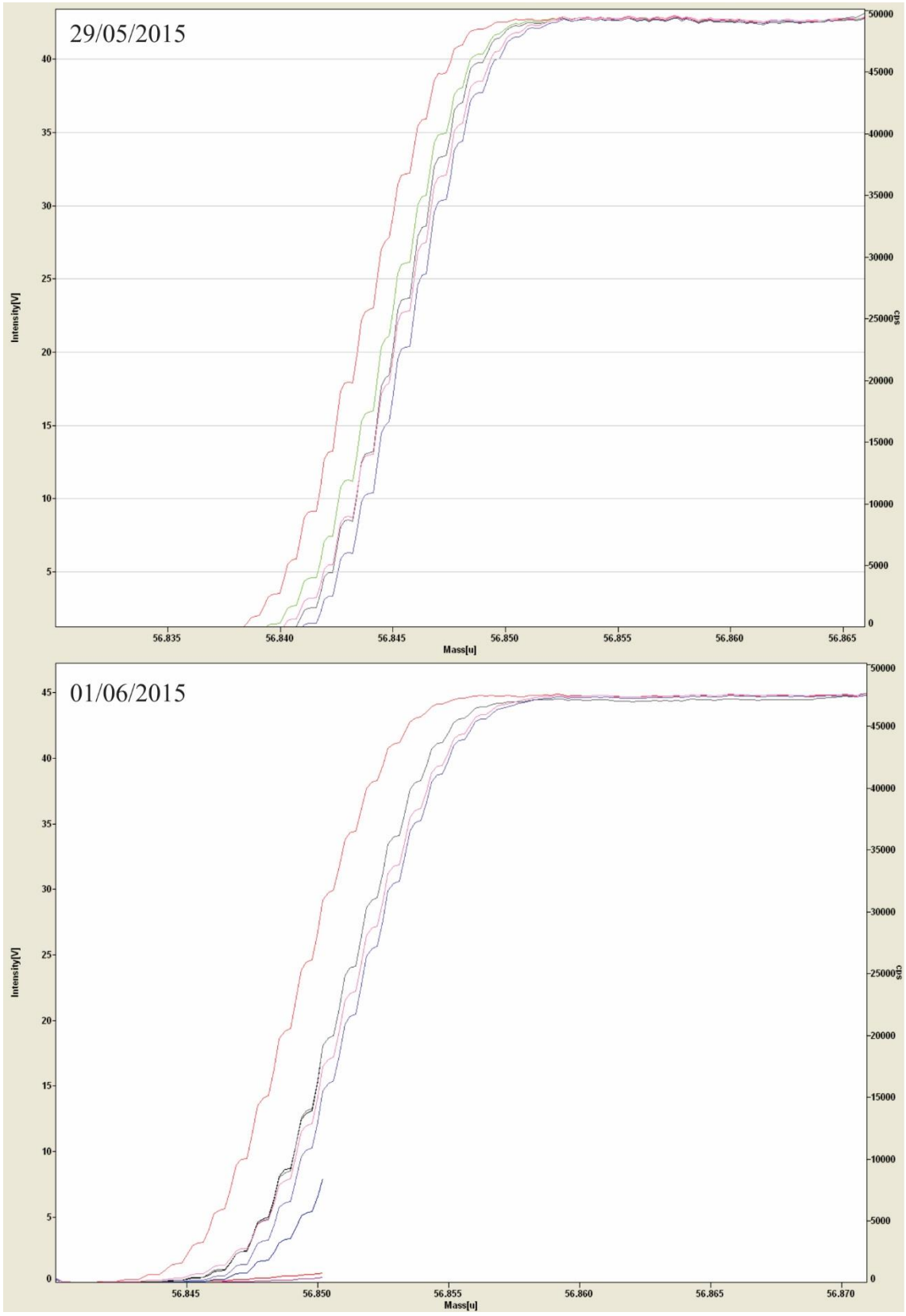

Figure 1: Representative peak scans from data collection, dates of peak scans given in top left-hand corner of each image.

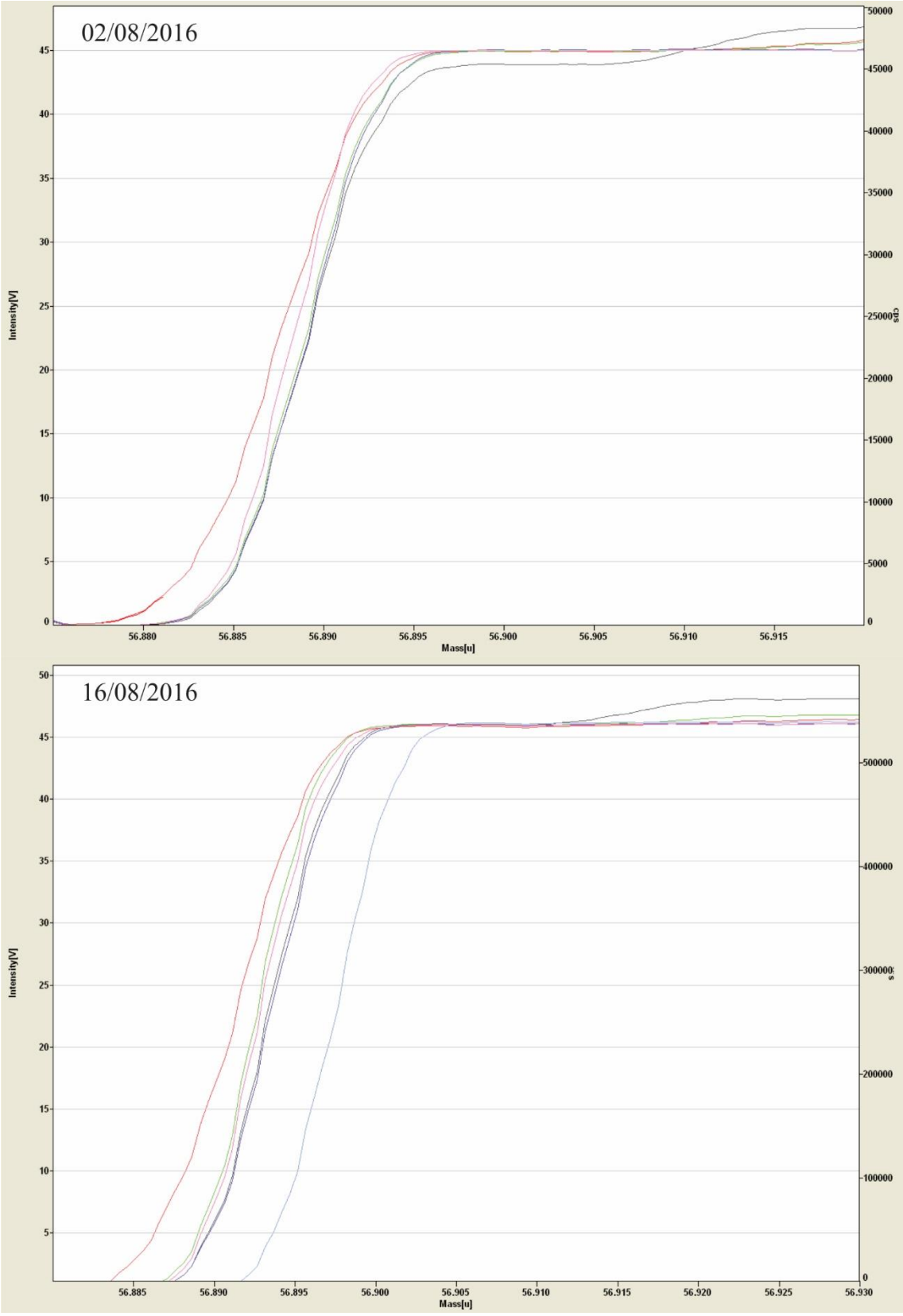

Figure 2: Representative peak scans from data collection, dates of peak scans given in top left-hand corner of each image.

Appendix 3

Appendix 3 is an accompaniment to chapter 5

Contains mineral geochemistry analyses and amphibole thermobarometry results from Wai Sano, NE Sumbawa and NW Flores

	SiO_2	TiO_2	Al_2O_3	Cr_2O_3	FeO	MnO	MgO
SN1_Hbl1	43.52	1.71	10.77	0.10	10.71	0.11	15.13
SN1_Hbl1	43.27	1.51	10.87	0.01	11.96	0.11	14.80
SN1_Hbl4	46.08	1.28	7.68	0.00	13.41	0.38	14.86
SN1_Hbl4	45.69	1.26	8.00	0.00	13.02	0.37	14.67
SN1_Hbl4	46.29	1.07	7.91	0.00	13.07	0.41	14.97
SN1_Hbl4	47.15	1.04	7.15	0.02	12.41	0.39	15.39
SN1_Hbl4	46.45	1.03	7.62	0.03	12.77	0.38	15.04
SN1_Hbl4	46.18	1.02	7.88	0.04	13.40	0.42	14.80
SN1_Hbl4	46.26	1.07	7.74	0.00	13.13	0.44	14.82
SN1_Hbl4	45.63	1.06	8.14	0.00	13.53	0.37	14.72
SN1_Hbl4	45.87	0.99	8.21	0.00	13.17	0.43	14.80
SN4_Hbl001	42.99	1.06	11.89	0.00	12.82	0.16	13.96
SN4_Hbl001	43.74	1.40	11.39	0.00	10.15	0.12	15.71
SN4_Hbl001	46.23	1.76	8.57	0.00	13.61	0.26	14.22
SN4_Hbl001	43.94	1.58	10.34	0.27	13.33	0.27	13.40
SN4_Hbl001	45.96	1.40	8.90	0.07	12.79	0.30	14.41
SN4_Hbl001	43.64	1.75	10.47	0.12	13.59	0.25	13.29
SN4_Hbl001	45.99	1.56	8.42	0.00	13.18	0.28	14.55
SN4_Hbl001	44.23	1.44	11.34	0.01	10.32	0.16	15.98
SN4_Hbl001	43.57	1.33	11.76	0.00	11.03	0.12	15.31
SN4_Hbl002	46.10	1.66	8.43	0.01	12.78	0.31	14.24
SN4_Hbl002	45.94	1.36	8.80	0.02	13.54	0.34	14.58
SN4_Hbl002	45.93	1.61	8.55	0.01	13.58	0.27	14.28
SN4_Hbl003	45.64	2.19	8.39	0.00	12.51	0.22	14.43
SN4_Hbl004	43.21	1.45	11.75	0.05	10.33	0.10	15.69
SN4_Hbl004	43.04	1.48	11.93	0.00	11.92	0.12	14.87
SN4_Hbl004	43.13	1.42	11.66	0.00	12.20	0.14	14.50
SN4_Hbl004	42.77	1.48	12.14	0.00	11.71	0.17	14.84
SN7_Hbl1	47.16	0.82	7.39	0.01	12.45	0.54	15.37
SN7_Hbl1	46.80	0.90	7.34	0.00	12.60	0.52	15.22
SN7_Hbl1	47.16	0.83	7.01	0.00	12.97	0.56	15.42
SN7_Hbl1	46.19	0.90	7.91	0.03	13.21	0.57	14.59
SN7_Hbl1	47.08	0.83	7.26	0.00	12.99	0.59	15.17
SN7_Hbl1	46.22	0.87	8.12	0.00	13.28	0.61	14.74
SN7_Hbl1	45.64	0.89	8.18	0.01	13.44	0.57	14.74
SN7_Hbl1	47.25	0.80	7.16	0.02	12.63	0.64	15.10
SN7_Hbl1	46.57	0.84	7.86	0.03	13.01	0.60	15.09
SN7_Hbl1	46.03	0.87	8.43	0.00	13.53	0.56	14.48
SN7_Hbl1	47.05	0.88	7.47	0.00	12.36	0.50	15.51
SN7_Hbl2	47.19	1.11	7.51	0.00	11.92	0.32	15.42
SN7_Hbl2	47.24	1.25	7.01	0.02	11.56	0.39	15.81
SN7_Hbl2	47.32	0.95	6.99	0.03	12.45	0.46	15.58
SN7_Hbl2	45.86	1.00	8.36	0.01	13.20	0.47	15.01
SN7_Hbl2	45.35	0.93	8.59	0.01	13.33	0.46	14.56
SN7_Hbl2	46.66	0.92	7.31	0.00	12.99	0.60	15.51

Table 1: Wai Sano amphibole analyses and thermobarometrical estimates. All analyses reported as wt.% unless otherwise stated. P-T-H_2O-fO_2 calculated using the formulations of Ridolfi et al. (2012).

	CaO	Na_2O	K_2O	F	Cl	Total	T (°C)
SN1_Hbl1	10.92	1.88	0.29	0.01	0.03	95.2	916
SN1_Hbl1	10.70	1.91	0.26	0.00	0.03	95.4	912
SN1_Hbl4	10.11	1.30	0.19	0.09	0.05	95.4	830
SN1_Hbl4	10.23	1.36	0.21	0.02	0.05	94.9	825
SN1_Hbl4	9.99	1.34	0.20	0.14	0.05	95.4	827
SN1_Hbl4	9.93	1.22	0.18	0.09	0.05	95.0	814
SN1_Hbl4	10.09	1.24	0.22	0.06	0.07	95.0	822
SN1_Hbl4	10.06	1.27	0.23	0.13	0.08	95.5	827
SN1_Hbl4	9.95	1.33	0.24	0.08	0.06	95.1	823
SN1_Hbl4	10.00	1.43	0.19	0.09	0.07	95.2	829
SN1_Hbl4	9.97	1.38	0.23	0.13	0.06	95.3	832
SN4_Hbl001	10.96	1.82	0.24	0.03	0.03	96.0	924
SN4_Hbl001	11.15	2.00	0.26	0.07	0.02	96.0	930
SN4_Hbl001	10.71	1.35	0.25	0.04	0.03	97.0	833
SN4_Hbl001	10.83	1.63	0.31	0.08	0.10	96.1	884
SN4_Hbl001	10.63	1.38	0.25	0.07	0.04	96.2	839
SN4_Hbl001	10.86	1.68	0.35	0.08	0.07	96.1	892
SN4_Hbl001	10.64	1.35	0.24	0.10	0.06	96.4	833
SN4_Hbl001	11.09	1.95	0.22	0.04	0.01	96.8	924
SN4_Hbl001	10.81	1.93	0.25	0.05	0.02	96.2	927
SN4_Hbl002	10.76	1.52	0.26	0.15	0.09	96.3	835
SN4_Hbl002	10.41	1.65	0.27	0.22	0.07	97.2	840
SN4_Hbl002	10.78	1.52	0.23	0.20	0.07	97.0	839
SN4_Hbl003	10.90	1.61	0.44	0.27	0.08	96.7	849
SN4_Hbl004	11.07	2.09	0.26	0.03	0.04	96.1	942
SN4_Hbl004	10.91	2.06	0.31	0.00	0.02	96.7	937
SN4_Hbl004	10.97	1.95	0.31	0.00	0.02	96.3	928
SN4_Hbl004	11.03	2.05	0.29	0.03	0.04	96.5	945
SN7_Hbl1	10.25	1.33	0.22	0.10	0.04	95.7	809
SN7_Hbl1	10.26	1.33	0.20	0.07	0.03	95.3	809
SN7_Hbl1	10.18	1.22	0.25	0.09	0.05	95.7	818
SN7_Hbl1	10.31	1.34	0.30	0.04	0.03	95.4	818
SN7_Hbl1	10.22	1.30	0.17	0.08	0.02	95.7	808
SN7_Hbl1	10.22	1.26	0.21	0.07	0.03	95.6	829
SN7_Hbl1	10.13	1.37	0.25	0.12	0.07	95.4	832
SN7_Hbl1	10.18	1.08	0.20	0.11	0.04	95.2	812
SN7_Hbl1	10.17	1.39	0.25	0.07	0.05	95.9	821
SN7_Hbl1	10.11	1.53	0.26	0.15	0.06	96.0	824
SN7_Hbl1	10.07	1.65	0.25	0.21	0.10	96.1	806
SN7_Hbl2	10.20	1.15	0.15	0.16	0.04	95.2	819
SN7_Hbl2	10.74	1.31	0.13	0.09	0.02	95.6	807
SN7_Hbl2	10.15	1.18	0.17	0.08	0.05	95.4	812
SN7_Hbl2	10.21	1.46	0.27	0.17	0.05	96.1	833
SN7_Hbl2	10.27	1.37	0.30	0.00	0.05	95.2	836
SN7_Hbl2	10.12	1.69	0.19	0.07	0.05	96.1	827

Table 1: Wai Sano amphibole analyses and thermobarometrical estimates. All analyses reported as wt.% unless otherwise stated. P-T-H_2O-fO_2 calculated using the formulations of Ridolfi et al. (2012).

	error (σest)	P (MPa)	Max error	ΔNNO	error (σest)	H_2Omelt (wt.%)	error *
SN1_Hbl1	22	275	30	1.58	0.4	6.37	0.95
SN1_Hbl1	22	280	31	1.60	0.4	6.47	0.97
SN1_Hbl4	22	126	14	1.98	0.4	5.37	0.40
SN1_Hbl4	22	139	15	1.88	0.4	5.63	0.40
SN1_Hbl4	22	133	15	2.01	0.4	5.46	0.40
SN1_Hbl4	22	110	12	2.14	0.4	5.08	0.40
SN1_Hbl4	22	125	14	2.04	0.4	5.37	0.40
SN1_Hbl4	22	132	15	1.98	0.4	5.44	0.40
SN1_Hbl4	22	129	14	1.97	0.4	5.34	0.40
SN1_Hbl4	22	142	16	1.97	0.4	5.58	0.40
SN1_Hbl4	22	144	16	1.98	0.4	5.61	0.40
SN4_Hbl001	22	359	90	1.40	0.4	7.78	1.17
SN4_Hbl001	22	310	34	1.73	0.4	6.64	1.00
SN4_Hbl001	22	155	17	1.48	0.4	6.07	0.40
SN4_Hbl001	22	249	62	1.17	0.4	6.99	1.05
SN4_Hbl001	22	170	19	1.62	0.4	6.38	0.40
SN4_Hbl001	22	258	28	1.08	0.4	6.84	1.03
SN4_Hbl001	22	151	17	1.67	0.4	5.88	0.40
SN4_Hbl001	22	297	33	1.82	0.4	6.61	0.99
SN4_Hbl001	22	336	37	1.71	0.4	7.05	1.06
SN4_Hbl002	22	153	17	1.45	0.4	5.97	0.40
SN4_Hbl002	22	163	18	1.69	0.4	5.75	0.40
SN4_Hbl002	22	155	17	1.51	0.4	5.89	0.40
SN4_Hbl003	22	152	17	1.33	0.4	5.01	0.40
SN4_Hbl004	22	338	37	1.72	0.4	6.63	0.99
SN4_Hbl004	22	351	39	1.51	0.4	6.83	1.02
SN4_Hbl004	22	335	37	1.44	0.4	6.98	1.05
SN4_Hbl004	22	372	41	1.48	0.4	7.04	1.06
SN7_Hbl1	22	117	13	2.14	0.4	5.28	0.40
SN7_Hbl1	22	116	13	2.11	0.4	5.30	0.40
SN7_Hbl1	22	106	12	2.26	0.4	4.97	0.40
SN7_Hbl1	22	135	15	1.91	0.4	5.62	0.40
SN7_Hbl1	22	113	12	2.11	0.4	5.33	0.40
SN7_Hbl1	22	140	15	1.97	0.4	5.84	0.40
SN7_Hbl1	22	143	16	2.00	0.4	5.59	0.40
SN7_Hbl1	22	111	12	2.09	0.4	5.42	0.40
SN7_Hbl1	22	131	14	2.07	0.4	5.41	0.40
SN7_Hbl1	22	151	17	1.87	0.4	5.90	0.40
SN7_Hbl1	22	119	13	2.16	0.4	4.97	0.40
SN7_Hbl2	22	120	13	2.08	0.4	5.57	0.40
SN7_Hbl2	22	107	12	2.14	0.4	5.14	0.40
SN7_Hbl2	22	106	12	2.22	0.4	5.01	0.40
SN7_Hbl2	22	148	16	2.02	0.4	5.50	0.40
SN7_Hbl2	22	159	18	1.91	0.4	5.86	0.40
SN7_Hbl2	22	114	13	2.30	0.4	5.05	0.40

Table 1: Wai Sano amphibole analyses and thermobarometrical estimates. All analyses reported as wt.% unless otherwise stated. P-T-H_2O-fO_2 calculated using the formulations of Ridolfi et al. (2012).

	SiO_2	TiO_2	Al_2O_3	Cr_2O_3	FeO	MnO	MgO
SN7_Hbl2	45.65	0.90	8.39	0.04	13.82	0.69	14.18
SN7_Hbl2	45.39	0.97	8.50	0.03	13.64	0.55	14.43
SN7_Hbl3	45.75	0.95	8.27	0.01	13.56	0.53	14.51
SN7_Hbl3	45.71	0.86	8.33	0.01	13.42	0.50	14.44
SN7_Hbl3	46.58	0.99	7.20	0.00	13.17	0.52	14.93
SN7_Hbl3	46.42	1.04	7.61	0.00	13.04	0.48	14.87
SN7_Hbl3	46.57	0.92	7.84	0.00	12.29	0.54	15.17
SN7_Hbl3	45.25	0.86	8.61	0.01	13.61	0.57	14.37
SN7_Hbl3	46.67	0.90	7.43	0.06	12.70	0.51	15.30
SN7_Hbl3	45.56	0.91	8.37	0.04	13.70	0.56	14.78
SN7_Hbl4	45.49	0.89	8.27	0.00	13.37	0.49	14.83
SN7_Hbl4	46.00	0.98	7.84	0.00	12.88	0.46	14.85
SN7_Hbl4	45.09	1.06	8.85	0.01	13.59	0.52	14.29
SN7_Hbl4	46.23	0.92	7.90	0.01	13.34	0.55	14.69
SN7_Hbl4	45.46	0.91	8.35	0.00	14.13	0.49	14.10
SN7_Hbl5	42.28	1.43	11.43	0.05	11.63	0.14	14.25
SN7_Hbl5	42.79	1.38	11.29	0.03	12.02	0.15	14.58
SN7_Hbl5	42.25	1.21	11.80	0.03	12.23	0.13	14.51
SN7_Hbl5	42.00	1.12	12.09	0.03	12.89	0.19	14.23
SN7_Hbl5	42.28	1.17	11.76	0.01	12.53	0.19	14.31
SN7_Hbl6	45.75	0.88	8.38	0.04	13.75	0.60	14.50
SN7_Hbl6	45.56	0.87	8.34	0.01	13.94	0.65	14.42
SN7_Hbl6	45.72	0.87	8.40	0.00	13.70	0.61	14.43
SN7_Hbl6	45.74	0.86	8.26	0.00	13.69	0.67	14.53
SN7_Hbl7	46.10	1.01	7.69	0.02	13.15	0.51	15.15
SN7_Hbl7	46.41	0.91	7.66	0.01	12.64	0.55	14.97
SN7_Hbl7	45.98	0.89	8.07	0.03	13.18	0.63	14.67
SN7_Hbl7	46.04	0.85	8.12	0.00	13.14	0.61	14.87
SN7_Hbl7	46.71	0.77	7.59	0.00	12.87	0.71	14.96
SN7_Hbl7	46.42	0.79	7.72	0.00	13.23	0.70	14.89
SN7_Hbl7	46.19	0.76	7.73	0.01	13.49	0.69	14.87
SN10_Hbl1	47.37	1.17	6.73	0.04	11.67	0.37	15.90
SN10_Hbl3	47.55	1.08	6.55	0.00	11.65	0.38	16.04
SN10_Hbl3	48.05	0.96	6.35	0.00	11.41	0.45	16.31
SN10_Hbl4	48.05	1.07	6.45	0.01	11.26	0.35	16.28
SN10_Hbl4	47.61	1.15	6.83	0.00	11.46	0.36	16.13
SN10_Hbl4	46.74	1.17	7.51	0.00	11.74	0.32	15.93
SN10_Hbl4	46.83	1.18	7.19	0.03	11.79	0.40	16.00
SN10_Hbl4	47.38	1.18	6.85	0.02	11.18	0.33	16.14
SN10_Hbl4	47.25	1.16	6.53	0.00	11.84	0.38	16.02
SN10_Hbl4	47.74	1.08	6.77	0.03	11.36	0.38	16.13
SN10_Hbl11	44.96	1.13	8.93	0.01	13.44	0.48	14.46
SN10_Hbl11	45.45	1.05	8.57	0.03	12.65	0.48	14.72
SN10_Hbl11	46.42	0.92	7.85	0.04	12.63	0.46	15.32

Table 1: Wai Sano amphibole analyses and thermobarometrical estimates. All analyses reported as wt.% unless otherwise stated. P-T-H_2O-fO_2 calculated using the formulations of Ridolfi et al. (2012).

	CaO	Na_2O	K_2O	F	Cl	Total	T (°C)
SN7_Hbl2	10.34	1.44	0.29	0.13	0.07	95.9	827
SN7_Hbl2	10.34	1.35	0.26	0.09	0.04	95.6	835
SN7_Hbl3	10.30	1.26	0.26	0.13	0.05	95.6	832
SN7_Hbl3	10.20	1.35	0.23	0.06	0.06	95.1	828
SN7_Hbl3	10.07	1.38	0.17	0.10	0.11	95.2	807
SN7_Hbl3	10.32	1.32	0.20	0.18	0.05	95.5	815
SN7_Hbl3	10.71	2.09	0.40	0.09	0.04	96.7	831
SN7_Hbl3	10.18	1.37	0.26	0.08	0.04	95.2	837
SN7_Hbl3	10.31	1.31	0.23	0.16	0.05	95.6	815
SN7_Hbl3	10.17	1.39	0.24	0.05	0.06	95.8	837
SN7_Hbl4	10.27	1.43	0.25	0.05	0.06	95.4	831
SN7_Hbl4	10.32	2.07	0.30	0.03	0.16	95.9	828
SN7_Hbl4	10.21	1.68	0.34	0.11	0.07	95.8	843
SN7_Hbl4	10.12	1.36	0.22	0.05	0.03	95.4	821
SN7_Hbl4	10.32	1.42	0.29	0.09	0.04	95.6	826
SN7_Hbl5	11.13	2.18	0.29	0.07	0.04	94.9	940
SN7_Hbl5	10.82	1.93	0.20	0.01	0.02	95.2	924
SN7_Hbl5	10.73	1.95	0.21	0.00	0.01	95.1	935
SN7_Hbl5	10.54	2.08	0.21	0.04	0.02	95.5	937
SN7_Hbl5	10.78	1.95	0.19	0.00	0.02	95.2	932
SN7_Hbl6	10.01	1.33	0.25	0.06	0.08	95.6	832
SN7_Hbl6	9.99	1.44	0.26	0.17	0.06	95.7	832
SN7_Hbl6	9.86	1.39	0.23	0.12	0.06	95.4	835
SN7_Hbl6	9.93	1.36	0.24	0.09	0.06	95.4	833
SN7_Hbl7	10.26	1.33	0.21	0.16	0.04	95.6	837
SN7_Hbl7	10.25	1.32	0.21	0.08	0.07	95.1	815
SN7_Hbl7	10.07	1.47	0.22	0.09	0.05	95.4	821
SN7_Hbl7	10.13	1.39	0.25	0.21	0.05	95.7	828
SN7_Hbl7	10.15	1.24	0.21	0.06	0.05	95.3	817
SN7_Hbl7	10.26	1.21	0.23	0.13	0.04	95.6	823
SN7_Hbl7	10.06	1.40	0.23	0.17	0.09	95.7	822
SN10_Hbl1	10.59	1.10	0.14	0.23	0.03	95.3	820
SN10_Hbl3	10.45	1.26	0.15	0.01	0.03	95.2	804
SN10_Hbl3	10.29	1.27	0.11	0.09	0.04	95.3	799
SN10_Hbl4	10.47	1.28	0.14	0.10	0.05	95.5	796
SN10_Hbl4	10.57	1.18	0.14	0.08	0.03	95.5	806
SN10_Hbl4	10.59	1.28	0.13	0.00	0.04	95.5	820
SN10_Hbl4	10.57	1.44	0.15	0.10	0.04	95.7	823
SN10_Hbl4	10.60	1.17	0.13	0.00	0.04	95.0	807
SN10_Hbl4	10.53	1.14	0.14	0.00	0.03	95.0	819
SN10_Hbl4	10.46	1.04	0.13	0.01	0.03	95.2	810
SN10_Hbl11	10.44	1.39	0.32	0.13	0.06	95.7	847
SN10_Hbl11	10.13	1.48	0.27	0.12	0.05	95.0	834
SN10_Hbl11	10.08	1.50	0.22	0.08	0.06	95.6	820

Table 1: Wai Sano amphibole analyses and thermobarometrical estimates. All analyses reported as wt.% unless otherwise stated. P-T-H_2O-fO_2 calculated using the formulations of Ridolfi et al. (2012).

	error (σest)	P (MPa)	Max error	ΔNNO	error (σest)	H2Omelt (wt.%)	error *
SN7_Hbl2	22	151	17	1.78	0.4	5.93	0.40
SN7_Hbl2	22	156	17	1.87	0.4	5.94	0.40
SN7_Hbl3	22	146	16	1.90	0.4	5.84	0.40
SN7_Hbl3	22	150	16	1.90	0.4	6.02	0.40
SN7_Hbl3	22	113	12	2.05	0.4	5.22	0.40
SN7_Hbl3	22	125	14	1.97	0.4	5.51	0.40
SN7_Hbl3	22	131	14	1.81	0.4	4.50	0.40
SN7_Hbl3	22	161	18	1.89	0.4	6.03	0.40
SN7_Hbl3	22	118	13	2.14	0.4	5.18	0.40
SN7_Hbl3	22	149	16	2.01	0.4	5.61	0.40
SN7_Hbl4	22	146	16	2.03	0.4	5.59	0.40
SN7_Hbl4	22	133	15	1.82	0.4	4.73	0.40
SN7_Hbl4	22	170	19	1.73	0.4	5.69	0.40
SN7_Hbl4	22	134	15	1.95	0.4	5.62	0.40
SN7_Hbl4	22	151	17	1.79	0.4	5.88	0.40
SN7_Hbl5	22	333	37	1.29	0.4	6.75	1.01
SN7_Hbl5	22	314	35	1.54	0.4	6.96	1.04
SN7_Hbl5	22	356	39	1.58	0.4	7.23	1.08
SN7_Hbl5	22	380	42	1.53	0.4	7.30	1.09
SN7_Hbl5	22	353	39	1.53	0.4	7.35	1.10
SN7_Hbl6	22	151	17	1.93	0.4	5.80	0.40
SN7_Hbl6	22	149	16	1.91	0.4	5.71	0.40
SN7_Hbl6	22	151	17	1.90	0.4	5.85	0.40
SN7_Hbl6	22	146	16	1.95	0.4	5.71	0.40
SN7_Hbl7	22	126	14	2.17	0.4	5.47	0.40
SN7_Hbl7	22	127	14	2.04	0.4	5.56	0.40
SN7_Hbl7	22	140	15	1.96	0.4	5.69	0.40
SN7_Hbl7	22	140	15	2.02	0.4	5.61	0.40
SN7_Hbl7	22	124	14	2.06	0.4	5.56	0.40
SN7_Hbl7	22	127	14	2.05	0.4	5.55	0.40
SN7_Hbl7	22	128	14	2.09	0.4	5.38	0.40
SN10_Hbl1	22	99	11	2.30	0.4	5.16	0.40
SN10_Hbl3	22	95	10	2.35	0.4	4.83	0.40
SN10_Hbl3	22	90	10	2.44	0.4	4.73	0.40
SN10_Hbl4	22	92	10	2.36	0.4	4.74	0.40
SN10_Hbl4	22	101	11	2.28	0.4	4.94	0.40
SN10_Hbl4	22	120	13	2.23	0.4	5.29	0.40
SN10_Hbl4	22	111	12	2.29	0.4	5.01	0.40
SN10_Hbl4	22	102	11	2.29	0.4	4.98	0.40
SN10_Hbl4	22	95	10	2.41	0.4	4.99	0.40
SN10_Hbl4	22	100	11	2.30	0.4	5.00	0.40
SN10_Hbl11	22	173	19	1.81	0.4	5.94	0.40
SN10_Hbl11	22	159	18	1.92	0.4	5.87	0.40
SN10_Hbl11	22	131	14	2.13	0.4	5.29	0.40

Table 1: Wai Sano amphibole analyses and thermobarometrical estimates. All analyses reported as wt.% unless otherwise stated. P-T-H_2O-fO_2 calculated using the formulations of Ridolfi et al. (2012).

SAMPLE	SiO_2	TiO_2	ZnO	Al_2O_3	Cr_2O_3	FeO	MnO	MgO
SN4_Cpx001	52.39	0.24		1.11		9.01	0.40	15.40
SN4_Cpx001	52.31	0.24		1.21		9.26	0.46	15.44
SN4_Cpx002	51.43	0.34		1.87		9.19	0.38	14.75
SN4_Cpx002	51.37	0.43		1.86		9.31	0.40	14.71
SN4_Cpx002	51.34	0.25		1.70		9.16	0.37	14.34
SN4_Cpx003	51.07	0.42		2.34		8.76	0.34	14.63
SN4_Cpx003	51.22	0.34		1.67		9.01	0.36	14.76
SN4_Cpx003	51.16	0.37		1.92		8.71	0.37	14.85
SN4_Cpx003	51.77	0.35		2.13		8.36	0.36	14.64
SN4_Cpx004	52.01	0.21		1.15		8.86	0.39	15.55
SN4_Opx001	52.58	0.20		1.02	0.00	18.42	0.69	24.00
SN4_Opx001	51.76	0.20		1.81	0.02	18.98	0.56	23.67
SN4_Opx001	52.70	0.13		0.58	0.02	19.40	0.68	24.21
SN4_Opx001	52.78	0.14		0.48	0.00	19.45	0.71	23.53
SN4_Opx001	52.51	0.15		0.83	0.00	18.50	0.66	23.95
SN4_Opx002	51.77	0.19		0.98	0.00	21.12	0.67	22.64
SN4_Opx002	52.21	0.13		0.77	0.00	21.12	0.94	23.00
SN4_Opx002	52.74	0.06		0.47	0.00	20.67	0.87	23.00
SN4_Opx002	52.02	0.11		0.46	0.01	20.43	0.75	22.84
SN4_Opx002	52.66	0.17		0.99	0.00	19.14	0.83	23.62
SN4_Opx003	53.22	0.10		0.50	0.00	18.56	0.66	24.75
SN4_Opx003	52.29	0.16		1.86	0.00	18.70	0.70	23.20
SN4_Opx004	52.84	0.14		0.57	0.01	18.99	0.69	24.16
SN4_Opx004	51.88	0.14		0.96	0.00	18.99	0.71	23.65
SN4_Opx005	51.18	0.16		2.05	0.00	21.61	0.68	22.61
SN4_Opx005	51.81	0.18		1.62	0.00	20.49	0.69	22.48
SN4_Opx005	52.31	0.09		0.80	0.00	21.26	0.82	23.03
SN4_Opx005	51.64	0.14		0.76	0.00	21.39	0.83	22.97
SN4_Opx006	52.12	0.09		1.20	0.00	20.74	0.96	23.14
SN4_Opx006	52.11	0.12		1.27	0.00	20.91	0.91	23.32
SN4_Opx006	51.75	0.09		3.68	0.00	19.64	0.83	21.18
SN4_Opx006	52.04	0.08		1.44	0.00	20.92	0.91	22.60
SN4_Opx006	52.08	0.09		1.21	0.00	20.94	0.88	23.03
SN4_Opx006	52.20	0.11		1.26	0.00	21.07	0.86	23.01
SN4_Opx006	52.27	0.13		1.31	0.00	19.82	0.85	22.95
SN4_Opx006	52.33	0.11		1.19	0.00	21.21	0.92	23.15
SN4_Opx006	52.04	0.11		1.29	0.00	21.17	0.88	22.99
SN4_Opx006	51.78	0.11		1.28	0.01	20.69	0.87	22.88
SN4_Opx006	51.91	0.09		1.27	0.00	21.14	0.77	22.86
SN4_Opx006	51.91	0.09		1.32	0.00	20.79	0.81	22.77
SN4_Opx006	52.26	0.21		1.21	0.00	20.62	0.86	22.95
SN4_Opx006	52.62	0.04		0.71	0.00	20.86	0.95	23.38
SN4_Opx006	52.57	0.07		0.74	0.00	20.99	0.83	23.52
SN4_Opx006	52.51	0.05		0.57	0.00	21.35	0.88	23.36
SN4_Opx006	52.31	0.11		0.89	0.00	20.88	0.82	22.92
SN4_Opx007	52.20	0.08		1.12	0.00	21.30	0.87	22.74
SN4_Opx007	52.13	0.10		1.15	0.00	20.98	0.83	22.66
SN4_Opx007	51.96	0.11		1.27	0.01	21.45	0.97	22.84
SN4_Opx007	51.74	0.10		1.87	0.00	20.91	0.91	22.50
SN4_Opx007	51.62	0.11		1.83	0.00	21.73	0.85	22.90

Table 2: Electron microprobe analyses of pyroxenes from Wai Sano. All values reported as wt.%.

SAMPLE	CaO	Na_2O	K_2O	P_2O_5	SO_3	Cl	F	TOTAL
SN4_Cpx001	20.45	0.28	0.00					99.3
SN4_Cpx001	19.80	0.29	0.01					99.0
SN4_Cpx002	20.94	0.29	0.00					99.2
SN4_Cpx002	20.52	0.33	0.00					98.9
SN4_Cpx002	20.70	0.40	0.01					98.3
SN4_Cpx003	20.57	0.28	0.01					98.4
SN4_Cpx003	20.87	0.29	0.00					98.5
SN4_Cpx003	20.87	0.29	0.00					98.5
SN4_Cpx003	20.53	0.33	0.01					98.5
SN4_Cpx004	20.34	0.22	0.00					98.7
SN4_Opx001	1.12	0.04	0.01		0.00	0.01	0.01	98.1
SN4_Opx001	1.18	0.02	0.00		0.04	0.00	0.01	98.2
SN4_Opx001	1.11	0.05	0.02		0.00	0.03	0.00	98.9
SN4_Opx001	1.35	0.06	0.01		0.00	0.01	0.02	98.5
SN4_Opx001	1.18	0.04	0.00		0.01	0.03	0.01	97.9
SN4_Opx002	0.91	0.04	0.00		0.03	0.01	0.00	98.4
SN4_Opx002	0.68	0.04	0.00		0.01	0.00	0.00	98.9
SN4_Opx002	0.98	0.01	0.00		0.03	0.01	0.00	98.8
SN4_Opx002	1.45	0.00	0.00		0.01	0.00	0.04	98.1
SN4_Opx002	0.93	0.03	0.01		0.00	0.00	0.00	98.4
SN4_Opx003	1.18	0.00	0.00		0.00	0.01	0.03	99.0
SN4_Opx003	0.89	0.02	0.04		0.00	0.03	0.00	97.9
SN4_Opx004	1.47	0.03	0.01		0.02	0.01	0.06	99.0
SN4_Opx004	1.64	0.04	0.00		0.01	0.01	0.04	98.0
SN4_Opx005	0.91	0.10	0.00		0.00	0.06	0.00	99.4
SN4_Opx005	0.96	0.06	0.00		0.00	0.01	0.06	98.3
SN4_Opx005	0.84	0.03	0.00		0.01	0.00	0.00	99.2
SN4_Opx005	0.83	0.14	0.00		0.00	0.09	0.02	98.8
SN4_Opx006	0.42	0.03	0.00		0.00	0.02	0.01	98.7
SN4_Opx006	0.46	0.06	0.00		0.02	0.00	0.03	99.2
SN4_Opx006	0.49	0.06	0.05		0.03	0.01	0.02	97.8
SN4_Opx006	0.51	0.02	0.01		0.02	0.01	0.01	98.5
SN4_Opx006	0.48	0.05	0.00		0.01	0.02	0.00	98.8
SN4_Opx006	0.44	0.02	0.00		0.00	0.00	0.02	99.0
SN4_Opx006	0.99	0.05	0.03		0.01	0.03	0.00	98.4
SN4_Opx006	0.48	0.12	0.01		0.00	0.05	0.00	99.6
SN4_Opx006	0.45	0.08	0.02		0.00	0.02	0.00	99.0
SN4_Opx006	0.46	0.03	0.00		0.00	0.00	0.00	98.1
SN4_Opx006	0.56	0.04	0.00		0.01	0.01	0.00	98.6
SN4_Opx006	0.64	0.08	0.01		0.00	0.03	0.01	98.4
SN4_Opx006	0.66	0.01	0.00		0.00	0.01	0.00	98.8
SN4_Opx006	0.44	0.02	0.00		0.00	0.01	0.00	99.0
SN4_Opx006	0.44	0.05	0.00		0.00	0.01	0.02	99.3
SN4_Opx006	0.51	0.14	0.00		0.01	0.07	0.03	99.5
SN4_Opx006	0.81	0.04	0.01		0.00	0.01	0.00	98.8
SN4_Opx007	0.69	0.03	0.01		0.00	0.01	0.02	99.1
SN4_Opx007	0.69	0.02	0.00		0.00	0.00	0.00	98.6
SN4_Opx007	0.61	0.03	0.00		0.01	0.00	0.00	99.3
SN4_Opx007	0.46	0.03	0.00		0.00	0.00	0.01	98.5
SN4_Opx007	0.45	0.03	0.00		0.02	0.00	0.00	99.5

Table 2: Electron microprobe analyses of pyroxenes from Wai Sano. All values reported as wt.%.

SAMPLE	SiO_2	TiO_2	ZnO	Al_2O_3	Cr_2O_3	FeO	MnO	MgO
SN4_Opx007	51.67	0.08		1.78	0.01	21.00	0.84	22.84
SN4_Opx007	51.59	0.05		1.56	0.00	21.06	0.83	22.74
SN4_Opx007	51.87	0.09		1.52	0.02	20.71	0.77	22.85
SN4_Opx007	52.37	0.12		1.40	0.00	20.83	0.83	22.97
SN4_Opx007	51.85	0.12		1.18	0.02	20.12	0.81	22.87
SN4_Opx007	52.00	0.16		1.03	0.00	20.07	0.82	22.88
SN4_Opx007	52.67	0.12		0.67	0.00	21.20	0.77	23.22
SN4_Opx007	51.98	0.11		0.76	0.00	20.96	0.83	22.95
SN4_Opx007	52.35	0.10		1.06	0.00	20.53	0.87	23.23
SN4_Opx008	51.92	0.11		1.23	0.00	21.51	0.94	22.38
SN4_Opx008	52.13	0.14		1.07	0.00	21.25	0.92	22.48
SN4_Opx008	52.35	0.10		1.18	0.01	21.19	0.93	22.93
SN4_Opx008	51.99	0.13		1.09	0.00	21.05	0.85	22.72
SN4_Opx008	52.27	0.10		1.10	0.00	20.92	0.86	23.13
SN4_Opx008	52.27	0.15		1.11	0.00	20.50	0.89	23.05
SN4_Opx008	51.19	0.25		1.88	0.00	20.22	0.78	22.33
SN4_Opx008	52.27	0.11		1.04	0.00	20.46	0.88	23.33
SN4_Opx008	52.13	0.12		1.03	0.00	21.03	0.87	22.96
SN4_Opx008	52.39	0.13		1.21	0.00	20.80	0.91	22.72
SN4_Opx008	52.14	0.07		1.07	0.00	20.56	0.82	23.34
SN4_Opx008	52.26	0.10		0.88	0.01	21.19	0.85	23.12
SN4_Opx008	51.48	0.07		1.27	0.03	21.33	0.90	22.93
SN4_Opx008	51.80	0.08		1.23	0.00	21.63	0.95	22.71
SN4_Opx008	52.06	0.06		1.24	0.00	21.83	0.95	22.81
SN4_Opx009	52.56	0.13		0.92	0.00	19.00	0.71	24.22
SN4_Opx009	52.94	0.18		0.93	0.00	19.79	0.83	24.24
SN4_Opx009	52.72	0.09		0.44	0.00	19.52	0.84	23.63
SN4_Opx009	51.21	0.16		0.79	0.01	19.83	0.85	22.64
SN1_Cpx1	51.90	0.13	0.05	0.81	0.03	19.40	0.73	23.64
SN1_Cpx1	51.54	0.08	0.14	0.89	0.00	20.52	0.90	23.03
SN1_Cpx1	51.71	0.10	0.00	1.04	0.00	20.62	0.91	22.81
SN1_Cpx1	51.54	0.11	0.02	0.92	0.01	21.36	0.85	22.77
SN1_Cpx1	51.63	0.10	0.08	0.83	0.00	20.80	0.84	22.81
SN1_Cpx1	51.59	0.11	0.02	0.97	0.03	21.06	0.86	22.80
SN1_Cpx1	51.82	0.10	0.05	0.94	0.00	21.37	0.86	23.05
SN1_Cpx1	51.75	0.08	0.07	0.82	0.01	20.57	0.88	22.94
SN1_Cpx1	51.82	0.10	0.06	0.85	0.01	21.11	0.85	22.89
SN1_Opx1	52.57	0.13	0.07	0.54	0.04	18.81	0.69	24.68
SN1_Opx1	51.64	0.07	0.03	0.78	0.00	21.07	0.89	23.15
SN1_Opx1	51.99	0.05	0.07	0.61	0.01	21.48	0.93	22.96
SN1_Opx1	51.85	0.05	0.07	0.59	0.00	20.45	0.95	23.24
SN1_Opx1	52.03	0.07	0.04	0.59	0.00	21.04	0.95	23.37
SN1_Opx1	51.98	0.07	0.03	0.66	0.00	21.08	0.92	23.15
SN1_Opx1	51.77	0.06	0.10	0.61	0.00	20.63	0.93	22.98
SN1_Opx1	52.00	0.05	0.00	0.60	0.00	21.35	1.01	23.29
SN1_Opx1	52.09	0.07	0.11	0.65	0.00	20.95	0.92	23.23
SN1_Opx1	52.16	0.06	0.06	0.71	0.03	20.75	0.94	23.17
SN1_Opx2	52.33	0.12	0.04	0.77	0.00	19.41	0.84	23.32
SN1_Opx2	51.64	0.17	0.11	0.56	0.00	18.87	0.76	23.74
SN1_Opx2	52.33	0.12	0.09	0.53	0.05	20.10	0.79	23.50

Table 2: Electron microprobe analyses of pyroxenes from Wai Sano. All values reported as wt.%.

SAMPLE	CaO	Na_2O	K_2O	P_2O_5	SO_3	Cl	F	TOTAL
SN4_Opx007	0.51	0.04	0.01		0.00	0.00	0.00	98.8
SN4_Opx007	0.51	0.01	0.00		0.00	0.00	0.04	98.4
SN4_Opx007	0.55	0.01	0.00		0.00	0.00	0.01	98.4
SN4_Opx007	0.61	0.03	0.00		0.00	0.00	0.00	99.2
SN4_Opx007	0.71	0.00	0.00		0.00	0.00	0.03	97.7
SN4_Opx007	0.86	0.03	0.00		0.00	0.01	0.00	97.9
SN4_Opx007	0.95	0.03	0.00		0.00	0.01	0.00	99.6
SN4_Opx007	1.29	0.04	0.00		0.02	0.01	0.00	99.0
SN4_Opx007	0.77	0.05	0.00		0.01	0.01	0.01	99.0
SN4_Opx008	0.49	0.00	0.00		0.00	0.00	0.04	98.6
SN4_Opx008	0.88	0.03	0.00		0.00	0.00	0.00	98.9
SN4_Opx008	0.69	0.00	0.00		0.01	0.00	0.02	99.4
SN4_Opx008	1.20	0.02	0.00		0.03	0.01	0.00	99.1
SN4_Opx008	0.72	0.02	0.01		0.02	0.01	0.00	99.1
SN4_Opx008	0.70	0.01	0.00		0.03	0.01	0.02	98.7
SN4_Opx008	2.29	0.12	0.01		0.00	0.00	0.00	99.1
SN4_Opx008	0.60	0.01	0.00		0.00	0.00	0.04	98.7
SN4_Opx008	0.77	0.02	0.00		0.02	0.00	0.00	99.0
SN4_Opx008	0.66	0.01	0.00		0.00	0.00	0.03	98.8
SN4_Opx008	0.70	0.04	0.00		0.00	0.00	0.00	98.7
SN4_Opx008	0.73	0.02	0.01		0.00	0.00	0.03	99.2
SN4_Opx008	0.52	0.01	0.01		0.00	0.00	0.00	98.5
SN4_Opx008	0.48	0.01	0.00		0.00	0.00	0.04	98.9
SN4_Opx008	0.45	0.01	0.01		0.00	0.00	0.01	99.4
SN4_Opx009	1.10	0.04	0.01		0.02	0.00	0.03	98.7
SN4_Opx009	1.05	0.03	0.00		0.00	0.01	0.00	100.0
SN4_Opx009	1.21	0.04	0.01		0.00	0.01	0.00	98.5
SN4_Opx009	2.67	0.02	0.01		0.01	0.04	0.09	98.3
SN1_Cpx1	1.05	0.03	0.01	0.00	0.00	0.01	0.00	97.8
SN1_Cpx1	0.85	0.01	0.02	0.08	0.00	0.00	0.06	98.1
SN1_Cpx1	0.86	0.02	0.00	0.00	0.00	0.00	0.06	98.1
SN1_Cpx1	0.84	0.02	0.00	0.01	0.01	0.00	0.00	98.5
SN1_Cpx1	0.83	0.07	0.01	0.02	0.00	0.00	0.00	98.0
SN1_Cpx1	0.80	0.04	0.00	0.00	0.00	0.00	0.00	98.3
SN1_Cpx1	0.76	0.04	0.01	0.02	0.00	0.01	0.00	99.0
SN1_Cpx1	0.75	0.14	0.00	0.00	0.01	0.04	0.00	98.1
SN1_Cpx1	0.80	0.06	0.00	0.00	0.00	0.00	0.01	98.5
SN1_Opx1	1.05	0.05	0.00	0.00	0.00	0.01	0.00	98.6
SN1_Opx1	0.47	0.00	0.00	0.00	0.00	0.00	0.00	98.1
SN1_Opx1	0.45	0.02	0.00	0.00	0.00	0.00	0.02	98.6
SN1_Opx1	0.47	0.03	0.00	0.01	0.00	0.00	0.02	97.7
SN1_Opx1	0.49	0.01	0.00	0.00	0.00	0.00	0.10	98.6
SN1_Opx1	0.49	0.03	0.01	0.02	0.00	0.00	0.05	98.5
SN1_Opx1	0.46	0.02	0.00	0.00	0.01	0.01	0.00	97.6
SN1_Opx1	0.49	0.03	0.00	0.00	0.00	0.01	0.00	98.8
SN1_Opx1	0.49	0.01	0.01	0.02	0.00	0.01	0.00	98.5
SN1_Opx1	0.50	0.05	0.01	0.00	0.01	0.01	0.07	98.5
SN1_Opx2	0.94	0.08	0.01	0.00	0.00	0.02	0.00	97.9
SN1_Opx2	1.07	0.66	0.03	0.01	0.06	0.09	0.00	97.8
SN1_Opx2	1.06	0.03	0.00	0.00	0.00	0.01	0.03	98.7

Table 2: Electron microprobe analyses of pyroxenes from Wai Sano. All values reported as wt.%.

SAMPLE	SiO_2	TiO_2	ZnO	Al_2O_3	Cr_2O_3	FeO	MnO	MgO
SN1_Opx2	52.04	0.12	0.02	0.53	0.02	20.12	0.76	23.46
SN1_Opx2	51.91	0.12	0.03	0.68	0.01	20.08	0.86	23.37
SN1_Opx2	51.74	0.12	0.06	1.00	0.00	19.96	0.77	23.21
SN1_Opx2	52.32	0.13	0.00	1.01	0.00	20.54	0.85	23.66
SN1_Opx2	51.57	0.14	0.03	1.01	0.01	20.11	0.83	23.17
SN1_Opx2	51.65	0.15	0.04	1.02	0.03	20.50	0.75	23.42
SN1_Opx2	51.89	0.16	0.05	0.95	0.00	20.78	0.84	23.04
SN1_Opx3	53.57	0.10	0.03	1.05	0.02	18.89	0.81	24.07
SN1_Opx3	52.07	0.08	0.04	0.52	0.00	20.73	0.94	23.09
SN1_Opx3	51.82	0.11	0.00	0.89	0.00	21.12	0.99	22.79
SN1_Opx3	52.34	0.08	0.11	0.32	0.00	20.49	0.94	23.17
SN1_Opx3	52.41	0.09	0.08	0.80	0.00	20.07	0.88	22.30
SN1_Opx4	52.72	0.12	0.06	0.50	0.01	18.07	0.57	24.72
SN1_Opx4	51.47	0.10	0.08	1.08	0.01	21.23	0.95	22.72
SN1_Opx4	51.38	0.06	0.04	1.09	0.01	21.20	0.91	22.74
SN1_Opx4	51.43	0.08	0.01	1.19	0.00	20.79	0.99	22.52
SN1_Opx4	51.58	0.12	0.02	1.27	0.00	20.70	0.92	22.63
SN1_Opx4	50.76	0.10	0.02	1.97	0.00	21.02	0.85	22.12
SN1_Opx4	51.00	0.10	0.09	1.07	0.00	21.19	0.95	22.44
SN1_Opx4	51.89	0.11	0.04	0.61	0.00	20.92	0.92	22.87
SN1_Opx4	51.41	0.09	0.03	1.06	0.00	21.37	0.90	22.63
SN1_Opx4	52.64	0.16	0.10	0.98	0.02	19.14	0.71	23.65
SN1_Opx5	52.13	0.18	0.00	1.03	0.01	18.43	0.62	24.23
SN1_Opx5	51.49	0.17	0.03	1.04	0.00	19.41	0.75	23.80
SN1_Opx5	51.71	0.15	0.05	1.08	0.00	19.38	0.89	23.68
SN1_Opx5	51.68	0.16	0.07	1.18	0.00	20.28	0.83	23.08
SN1_Opx5	50.72	0.11	0.04	1.58	0.02	20.20	0.81	23.11
SN1_Opx6	51.82	0.21	0.11	1.27	0.00	19.16	0.65	24.20
SN1_Opx6	52.78	0.13	0.07	0.68	0.00	18.57	0.61	25.04
SN1_Opx6	52.61	0.09	0.11	0.41	0.00	19.16	0.85	24.25
SN1_Opx6	52.36	0.11	0.07	0.77	0.04	18.87	0.61	24.22
SN1_Opx6	52.10	0.16	0.00	0.92	0.00	18.97	0.62	24.06
SN1_Opx7	52.08	0.20	0.04	1.09	0.00	18.31	0.67	24.43
SN1_Opx7	52.55	0.12	0.13	0.53	0.00	19.72	0.84	23.72
SN1_Opx7	51.44	0.18	0.05	1.02	0.01	20.20	0.81	23.05
SN1_Opx7	51.97	0.18	0.06	1.22	0.00	18.11	0.62	24.05
SN1_Opx8	52.67	0.15	0.06	1.41	0.00	19.25	0.74	22.38
SN1_Opx8	50.72	0.12	0.01	0.82	0.02	19.66	0.85	22.65
SN1_Opx8	51.90	0.16	0.06	0.91	0.02	20.06	0.80	23.30
SN1_Opx8	51.52	0.14	0.04	1.25	0.02	20.10	0.93	23.19
SN1_Opx8	51.65	0.14	0.05	0.94	0.00	19.46	0.78	22.72
SN1_Opx9	51.17	0.10	0.03	1.02	0.01	21.42	0.88	22.74
SN1_Opx9	51.43	0.15	0.10	0.93	0.01	20.68	0.85	22.66
SN1_Opx9	51.33	0.15	0.02	1.18	0.01	18.09	0.70	23.80
SN1_Opx10	52.52	0.12	0.03	0.55	0.01	18.27	0.63	24.49
SN1_Opx10	51.98	0.05	0.05	0.57	0.00	20.65	0.93	22.91
SN1_Opx10	51.75	0.06	0.01	0.61	0.01	20.32	0.90	22.94
SN1_Opx10	50.70	0.12	0.02	2.07	0.00	21.05	0.80	22.53
SN1_Opx10	50.57	0.11	0.13	1.99	0.01	21.34	0.92	22.20
SN1_Opx10	51.52	0.10	0.01	1.01	0.00	20.61	0.93	22.63

Table 2: Electron microprobe analyses of pyroxenes from Wai Sano. All values reported as wt.%.

SAMPLE	CaO	Na_2O	K_2O	P_2O_5	SO_3	Cl	F	TOTAL
SN1_Opx2	1.03	0.03	0.00	0.01	0.00	0.00	0.02	98.2
SN1_Opx2	0.97	0.02	0.00	0.00	0.01	0.00	0.00	98.1
SN1_Opx2	0.92	0.01	0.01	0.02	0.01	0.00	0.04	97.9
SN1_Opx2	0.93	0.01	0.01	0.00	0.00	0.00	0.01	99.5
SN1_Opx2	0.91	0.01	0.00	0.01	0.01	0.02	0.02	97.9
SN1_Opx2	0.95	0.02	0.01	0.02	0.01	0.00	0.00	98.6
SN1_Opx2	0.99	0.05	0.00	0.01	0.00	0.01	0.00	98.8
SN1_Opx3	0.83	0.11	0.06	0.00	0.00	0.00	0.04	99.6
SN1_Opx3	0.76	0.01	0.00	0.00	0.02	0.01	0.00	98.3
SN1_Opx3	0.65	0.02	0.00	0.00	0.00	0.00	0.01	98.4
SN1_Opx3	0.81	0.01	0.01	0.00	0.02	0.00	0.08	98.4
SN1_Opx3	0.89	0.11	0.05	0.01	0.01	0.02	0.00	97.7
SN1_Opx4	1.09	0.01	0.00	0.01	0.00	0.00	0.05	97.9
SN1_Opx4	0.58	0.01	0.00	0.02	0.01	0.00	0.00	98.2
SN1_Opx4	0.58	0.05	0.00	0.03	0.00	0.01	0.01	98.1
SN1_Opx4	0.52	0.06	0.00	0.02	0.00	0.00	0.00	97.6
SN1_Opx4	0.69	0.04	0.00	0.00	0.00	0.01	0.01	98.0
SN1_Opx4	0.67	0.02	0.00	0.02	0.00	0.01	0.05	97.6
SN1_Opx4	0.51	0.01	0.00	0.03	0.01	0.00	0.03	97.4
SN1_Opx4	0.83	0.02	0.00	0.00	0.00	0.00	0.00	98.2
SN1_Opx4	0.65	0.06	0.00	0.00	0.00	0.00	0.00	98.2
SN1_Opx4	1.10	0.05	0.01	0.00	0.00	0.01	0.00	98.6
SN1_Opx5	1.06	0.02	0.02	0.01	0.00	0.00	0.00	97.7
SN1_Opx5	1.00	0.02	0.00	0.02	0.00	0.00	0.00	97.7
SN1_Opx5	0.87	0.03	0.01	0.02	0.00	0.00	0.04	97.9
SN1_Opx5	0.82	0.03	0.01	0.01	0.01	0.00	0.00	98.2
SN1_Opx5	0.63	0.04	0.00	0.02	0.01	0.01	0.00	97.3
SN1_Opx6	1.10	0.04	0.00	0.00	0.01	0.00	0.00	98.6
SN1_Opx6	1.12	0.02	0.00	0.00	0.00	0.01	0.00	99.0
SN1_Opx6	0.79	0.02	0.00	0.01	0.00	0.00	0.01	98.3
SN1_Opx6	1.16	0.04	0.01	0.01	0.00	0.00	0.00	98.3
SN1_Opx6	0.98	0.02	0.01	0.01	0.02	0.02	0.00	97.9
SN1_Opx7	1.12	0.05	0.00	0.05	0.01	0.01	0.00	98.1
SN1_Opx7	1.02	0.02	0.00	0.00	0.01	0.00	0.01	98.7
SN1_Opx7	1.02	0.01	0.01	0.00	0.02	0.01	0.02	97.9
SN1_Opx7	1.21	0.00	0.01	0.08	0.01	0.01	0.08	97.6
SN1_Opx8	1.07	0.09	0.15	0.02	0.00	0.01	0.00	98.0
SN1_Opx8	0.91	0.03	0.00	0.00	0.00	0.07	0.00	95.8
SN1_Opx8	0.97	0.04	0.00	0.01	0.00	0.01	0.00	98.3
SN1_Opx8	0.98	0.03	0.01	0.02	0.01	0.02	0.00	98.3
SN1_Opx8	0.92	0.62	0.02	0.02	0.01	0.23	0.00	97.5
SN1_Opx9	0.66	0.03	0.00	0.00	0.00	0.00	0.01	98.1
SN1_Opx9	0.86	0.07	0.00	0.01	0.03	0.01	0.02	97.8
SN1_Opx9	1.47	0.01	0.01	0.37	0.00	0.02	0.01	97.2
SN1_Opx10	1.07	0.05	0.00	0.01	0.00	0.01	0.07	97.8
SN1_Opx10	0.51	0.03	0.01	0.01	0.03	0.01	0.02	97.7
SN1_Opx10	0.54	0.10	0.02	0.00	0.21	0.02	0.00	97.5
SN1_Opx10	0.49	0.03	0.00	0.01	0.03	0.00	0.06	97.9
SN1_Opx10	0.50	0.05	0.01	0.00	0.00	0.02	0.04	97.9
SN1_Opx10	0.57	0.05	0.01	0.00	0.00	0.01	0.11	97.5

Table 2: Electron microprobe analyses of pyroxenes from Wai Sano. All values reported as wt.%.

SAMPLE	SiO_2	TiO_2	ZnO	Al_2O_3	Cr_2O_3	FeO	MnO	MgO
SN1_Opx10	51.67	0.09	0.01	1.15	0.01	20.20	0.93	22.83
SN1_Opx10	51.38	0.12	0.05	1.65	0.00	20.83	0.94	22.55
SN1_Opx10	50.76	0.10	0.02	2.00	0.00	20.86	0.97	22.39
SN1_Opx10	51.42	0.05	0.09	0.60	0.00	20.57	0.99	22.96
SN1_Opx10	52.74	0.11	0.04	0.44	0.00	18.30	0.67	24.29
SN1_Opx11	51.60	0.14	0.01	1.03	0.00	20.31	0.83	22.68
SN1_Opx11	51.15	0.13	0.08	1.18	0.00	20.08	0.92	23.09
SN1_Opx11	51.79	0.15	0.08	1.13	0.02	20.08	0.80	23.33
SN1_Opx11	51.46	0.13	0.06	1.05	0.02	19.35	0.82	23.19
SN1_Opx11	51.70	0.13	0.07	1.11	0.00	20.24	0.74	23.18
SN1_Opx11	51.72	0.14	0.01	1.28	0.00	20.21	0.80	23.16
SN1_Opx11	51.63	0.14	0.03	1.04	0.00	19.47	0.78	23.33
SN1_Opx11	51.64	0.18	0.01	1.15	0.01	20.01	0.80	23.28
SN1_Opx11	51.75	0.12	0.00	1.62	0.00	20.33	0.80	22.48
SN1_Opx11	51.47	0.09	0.09	1.05	0.00	20.13	0.89	22.66
SN7_Opx1	52.47	0.14	0.03	0.44	0.00	19.07	1.07	23.40
SN7_Opx1	51.83	0.15	0.08	0.95	0.00	19.47	1.08	23.50
SN7_Opx1	51.43	0.16	0.12	1.51	0.01	20.21	1.05	23.47
SN7_Opx1	51.42	0.16	0.02	1.45	0.01	18.74	1.10	21.68
SN7_Opx2	52.44	0.08	0.05	0.62	0.00	18.77	0.94	24.48
SN7_Opx2	51.75	0.11	0.07	0.90	0.00	19.33	0.98	23.98
SN7_Opx2	51.89	0.11	0.07	0.89	0.00	19.29	0.94	24.01
SN7_Opx2	51.85	0.13	0.00	1.00	0.00	19.06	0.97	23.94
SN7_Opx2	51.16	0.15	0.03	1.59	0.00	19.99	1.09	23.36
SN7_Opx2	51.75	0.18	0.02	1.02	0.00	19.28	1.09	23.50
SN7_Opx2	52.45	0.09	0.00	0.39	0.00	19.21	1.13	23.95
SN7_Opx2	52.35	0.13	0.01	0.37	0.00	19.18	1.07	24.19
SN7_Opx2	52.48	0.10	0.11	0.38	0.00	19.16	1.15	24.08
SN7_Opx2	52.06	0.14	0.00	0.60	0.00	19.78	1.11	23.82
SN7_Opx3	52.29	0.10	0.12	0.57	0.01	19.79	1.10	23.88
SN7_Opx3	51.65	0.16	0.08	1.15	0.00	19.68	1.10	23.93
SN7_Opx3	51.68	0.18	0.05	0.93	0.00	19.96	1.04	23.75
SN7_Opx3	52.25	0.15	0.03	0.80	0.00	18.97	1.12	23.62
SN7_Opx3	52.16	0.15	0.00	0.82	0.00	19.05	1.08	23.82
SN7_Opx3	51.88	0.20	0.00	1.16	0.01	19.75	1.09	23.82
SN7_Opx3	51.82	0.14	0.09	1.05	0.02	19.39	0.99	24.23
SN7_Opx3	52.08	0.11	0.01	0.89	0.00	19.52	1.01	24.16
SN7_Opx3	52.75	0.10	0.04	0.56	0.01	18.88	0.96	23.77
SN7_Opx4	53.62	0.22	0.11	2.40	0.00	17.18	0.97	20.35
SN7_Opx5	50.75	0.31	0.05	2.01	0.00	20.42	0.97	22.72
SN7_Opx5	51.58	0.15	0.07	0.93	0.00	20.45	1.14	23.03
SN7_Opx5	51.62	0.13	0.00	0.85	0.01	20.17	1.20	22.94
SN7_Opx5	50.05	0.26	0.04	1.70	0.01	17.99	0.97	21.78
SN7_Opx6	52.28	0.21	0.13	0.37	0.03	19.11	0.77	23.66
SN7_Opx6	51.36	0.17	0.09	1.29	0.03	19.88	1.08	23.53
SN7_Opx6	51.87	0.12	0.07	0.91	0.00	19.50	1.07	23.97
SN7_Opx6	51.05	0.16	0.11	1.50	0.00	19.91	1.08	23.53
SN7_Opx6	51.50	0.17	0.03	1.10	0.02	19.86	1.07	23.53
SN10_Pyx1	52.07	0.13	0.04	1.11	0.00	19.61	1.05	23.57
SN10_Pyx1	51.75	0.11	0.05	1.04	0.02	19.73	1.08	23.53

Table 2: Electron microprobe analyses of pyroxenes from Wai Sano. All values reported as wt.%.

SAMPLE	CaO	Na_2O	K_2O	P_2O_5	SO_3	Cl	F	TOTAL
SN1_Opx10	0.51	0.11	0.02	0.00	0.01	0.05	0.08	97.6
SN1_Opx10	0.55	0.01	0.01	0.00	0.00	0.01	0.00	98.1
SN1_Opx10	0.48	0.02	0.00	0.00	0.00	0.00	0.05	97.6
SN1_Opx10	0.50	0.14	0.01	0.06	0.02	0.02	0.00	97.4
SN1_Opx10	1.17	0.14	0.01	0.05	0.01	0.06	0.04	98.1
SN1_Opx11	0.80	0.08	0.00	0.00	0.00	0.01	0.00	97.5
SN1_Opx11	0.72	0.04	0.00	0.00	0.00	0.01	0.00	97.4
SN1_Opx11	0.87	0.00	0.00	0.00	0.01	0.00	0.01	98.3
SN1_Opx11	0.96	0.02	0.00	0.02	0.00	0.00	0.04	97.1
SN1_Opx11	0.80	0.04	0.00	0.00	0.00	0.01	0.05	98.0
SN1_Opx11	0.88	0.06	0.01	0.02	0.00	0.00	0.03	98.3
SN1_Opx11	0.93	0.00	0.00	0.00	0.00	0.00	0.00	97.4
SN1_Opx11	0.87	0.02	0.00	0.01	0.00	0.00	0.02	98.0
SN1_Opx11	0.71	0.03	0.01	0.00	0.00	0.01	0.00	97.9
SN1_Opx11	0.75	0.01	0.00	0.02	0.00	0.00	0.00	97.2
SN7_Opx1	0.87	0.47	0.01	0.00	0.02	0.24	0.03	98.2
SN7_Opx1	0.98	0.06	0.00	0.00	0.00	0.00	0.00	98.1
SN7_Opx1	0.84	0.03	0.00	0.02	0.00	0.00	0.01	98.9
SN7_Opx1	0.82	0.07	0.01	0.00	0.00	0.01	0.00	95.5
SN7_Opx2	0.70	0.03	0.01	0.01	0.01	0.02	0.00	98.2
SN7_Opx2	0.65	0.06	0.01	0.02	0.00	0.00	0.00	97.9
SN7_Opx2	0.64	0.30	0.01	0.00	0.03	0.08	0.00	98.3
SN7_Opx2	0.66	0.05	0.00	0.00	0.00	0.00	0.09	97.7
SN7_Opx2	0.80	0.01	0.00	0.01	0.00	0.01	0.03	98.2
SN7_Opx2	0.98	0.05	0.01	0.01	0.00	0.00	0.01	97.9
SN7_Opx2	0.79	0.03	0.01	0.02	0.00	0.00	0.00	98.1
SN7_Opx2	0.83	0.05	0.00	0.00	0.01	0.01	0.04	98.2
SN7_Opx2	0.85	0.07	0.01	0.00	0.00	0.01	0.00	98.4
SN7_Opx2	0.80	0.02	0.00	0.01	0.00	0.00	0.00	98.4
SN7_Opx3	0.60	0.02	0.00	0.01	0.00	0.01	0.00	98.5
SN7_Opx3	0.84	0.01	0.01	0.00	0.00	0.00	0.06	98.6
SN7_Opx3	0.71	0.01	0.01	0.00	0.00	0.00	0.01	98.3
SN7_Opx3	1.05	0.03	0.02	0.00	0.00	0.00	0.04	98.1
SN7_Opx3	0.73	0.11	0.02	0.00	0.00	0.01	0.00	98.0
SN7_Opx3	0.82	0.03	0.01	0.00	0.01	0.00	0.00	98.8
SN7_Opx3	0.65	0.03	0.00	0.01	0.00	0.01	0.00	98.4
SN7_Opx3	0.65	0.02	0.01	0.00	0.01	0.00	0.00	98.5
SN7_Opx3	0.66	0.04	0.00	0.04	0.00	0.00	0.00	97.8
SN7_Opx4	1.38	0.09	0.43	0.00	0.00	0.02	0.00	96.8
SN7_Opx5	1.13	0.13	0.00	0.00	0.02	0.01	0.00	98.5
SN7_Opx5	0.81	0.07	0.00	0.01	0.01	0.00	0.00	98.3
SN7_Opx5	0.83	0.07	0.00	0.02	0.01	0.01	0.00	97.9
SN7_Opx5	2.92	0.33	0.03	0.00	0.01	0.02	0.00	96.1
SN7_Opx6	1.57	0.04	0.01	0.02	0.01	0.01	0.01	98.2
SN7_Opx6	0.85	0.29	0.02	0.00	0.01	0.06	0.00	98.6
SN7_Opx6	0.75	0.02	0.00	0.00	0.01	0.01	0.02	98.3
SN7_Opx6	0.76	0.06	0.00	0.01	0.00	0.00	0.02	98.2
SN7_Opx6	0.79	0.04	0.00	0.00	0.02	0.00	0.08	98.2
SN10_Pyx1	0.64	0.04	0.00	0.01	0.02	0.00	0.00	98.3
SN10_Pyx1	0.47	0.04	0.00	0.00	0.00	0.01	0.00	97.8

Table 2: Electron microprobe analyses of pyroxenes from Wai Sano. All values reported as wt.%.

SAMPLE	SiO_2	TiO_2	ZnO	Al_2O_3	Cr_2O_3	FeO	MnO	MgO
SN10_Pyx1	51.73	0.17	0.02	0.80	0.00	19.55	1.19	23.36
SN10_Pyx1	51.80	0.12	0.05	0.85	0.01	19.85	1.10	23.58
SN10_Pyx1	52.38	0.12	0.03	0.60	0.05	19.19	1.12	23.57
SN10_Pyx1	52.27	0.11	0.07	0.43	0.02	19.21	1.04	23.87
SN10_Pyx1	51.96	0.12	0.02	0.78	0.00	19.48	1.04	23.74
SN10_Pyx1	51.07	0.18	0.10	1.50	0.01	19.46	1.09	23.02
SN10_Pyx1	52.00	0.09	0.07	0.93	0.00	20.25	1.11	23.82
SN10_Pyx1	51.65	0.11	0.08	1.07	0.00	19.92	0.99	23.71
SN10_Pyx2	53.65	0.15	0.07	1.43	0.00	17.16	0.91	21.06
SN10_Pyx2	52.78	0.28	0.02	2.01	0.00	18.86	0.92	20.05
SN10_Pyx2	52.63	0.19	0.11	1.63	0.00	16.46	0.88	20.90
SN10_Pyx2	47.45	0.92	0.00	6.32	0.00	11.65	0.47	15.88
SN10_Pyx2	52.97	0.21	0.09	1.75	0.00	16.12	0.94	21.04
SN10_Pyx3	52.22	0.15	0.09	0.76	0.00	20.05	1.09	23.42
SN10_Pyx3	51.88	0.17	0.01	0.78	0.01	19.92	1.21	23.50
SN10_Pyx3	51.81	0.15	0.02	1.09	0.01	20.26	1.16	23.34
SN10_Pyx3	52.10	0.09	0.08	0.66	0.00	19.55	1.09	23.94
SN10_Pyx3	52.23	0.10	0.12	0.82	0.01	19.56	1.12	24.18
SN10_Pyx3	52.21	0.15	0.04	0.70	0.00	19.50	1.08	23.79
SN10_Pyx3	51.81	0.17	0.00	1.06	0.00	20.29	1.26	23.37
SN10_Pyx3	51.73	0.13	0.05	1.25	0.00	20.55	1.13	23.27
SN10_Pyx3	52.11	0.12	0.01	0.71	0.00	20.08	1.20	23.70
SN10_Pyx3	51.76	0.11	0.07	0.86	0.02	19.47	1.06	23.44
SN10_Pyx5	52.56	0.22	0.11	1.79	0.00	16.89	1.04	20.63
SN10_Pyx5	52.70	0.22	0.07	1.65	0.02	17.14	1.06	20.85
SN10_Pyx5	52.97	0.20	0.01	1.65	0.00	17.06	1.08	20.86
SN10_Pyx5	52.79	0.20	0.09	1.67	0.00	16.77	1.07	20.74
SN10_Pyx5	51.15	0.29	0.03	2.74	0.02	16.05	0.91	20.14
SN10_Pyx6	51.76	0.11	0.07	0.94	0.00	19.46	1.04	23.87
SN10_Pyx6	51.96	0.09	0.08	0.56	0.03	19.52	1.04	24.24
SN10_Pyx6	51.70	0.10	0.10	0.59	0.00	19.08	1.06	24.06
SN10_Pyx6	51.90	0.14	0.02	0.96	0.01	19.08	1.00	23.98
SN10_Pyx6	51.98	0.10	0.03	0.89	0.00	19.92	1.03	23.87
SN10_Pyx7	51.31	0.11	0.00	1.52	0.00	19.20	0.98	23.61
SN10_Pyx7	47.23	0.91	0.04	7.40	0.06	11.76	0.43	15.50

Table 2: Electron microprobe analyses of pyroxenes from Wai Sano. All values reported as wt.%.

SAMPLE	CaO	Na_2O	K_2O	P_2O_5	SO_3	Cl	F	TOTAL
SN10_Pyx1	0.94	0.04	0.00	0.01	0.00	0.01	0.01	97.8
SN10_Pyx1	0.75	0.02	0.01	0.00	0.01	0.00	0.00	98.1
SN10_Pyx1	0.92	0.00	0.00	0.02	0.00	0.00	0.06	98.1
SN10_Pyx1	0.95	0.01	0.01	0.00	0.00	0.01	0.02	98.0
SN10_Pyx1	0.71	0.02	0.01	0.00	0.00	0.00	0.00	97.9
SN10_Pyx1	1.14	0.05	0.01	0.05	0.00	0.01	0.00	97.7
SN10_Pyx1	0.51	0.02	0.01	0.02	0.00	0.00	0.00	98.8
SN10_Pyx1	0.53	0.12	0.01	0.01	0.00	0.02	0.00	98.2
SN10_Pyx2	1.27	0.32	0.01	0.00	0.00	0.03	0.04	96.1
SN10_Pyx2	1.36	0.51	0.30	0.01	0.08	0.02	0.08	97.2
SN10_Pyx2	1.40	0.30	0.01	0.00	0.03	0.03	0.14	94.6
SN10_Pyx2	10.12	1.15	0.12	0.00	0.00	0.02	0.00	94.1
SN10_Pyx2	1.54	0.38	0.00	0.03	0.02	0.02	0.09	95.2
SN10_Pyx3	0.84	0.00	0.01	0.00	0.00	0.00	0.00	98.6
SN10_Pyx3	0.87	0.00	0.01	0.00	0.00	0.00	0.00	98.3
SN10_Pyx3	0.78	0.01	0.00	0.01	0.00	0.01	0.00	98.6
SN10_Pyx3	0.63	0.00	0.00	0.00	0.00	0.01	0.00	98.1
SN10_Pyx3	0.65	0.03	0.00	0.00	0.00	0.00	0.03	98.9
SN10_Pyx3	1.26	0.02	0.00	0.01	0.00	0.01	0.00	98.8
SN10_Pyx3	0.78	0.03	0.00	0.00	0.00	0.00	0.04	98.8
SN10_Pyx3	0.79	0.04	0.00	0.00	0.00	0.00	0.00	99.0
SN10_Pyx3	0.76	0.03	0.00	0.02	0.02	0.02	0.00	98.8
SN10_Pyx3	0.64	0.03	0.00	0.00	0.00	0.01	0.04	97.5
SN10_Pyx5	1.45	0.28	0.04	0.00	0.01	0.01	0.05	95.1
SN10_Pyx5	1.37	0.29	0.01	0.00	0.00	0.02	0.09	95.5
SN10_Pyx5	1.33	0.26	0.00	0.02	0.00	0.02	0.09	95.5
SN10_Pyx5	1.37	0.32	0.00	0.01	0.00	0.02	0.03	95.1
SN10_Pyx5	3.02	0.49	0.09	0.01	0.01	0.02	0.13	95.1
SN10_Pyx6	0.57	0.03	0.01	0.00	0.00	0.01	0.04	97.9
SN10_Pyx6	0.63	0.00	0.00	0.00	0.00	0.00	0.00	98.1
SN10_Pyx6	0.66	0.02	0.00	0.00	0.00	0.00	0.04	97.4
SN10_Pyx6	0.61	0.02	0.00	0.00	0.03	0.00	0.00	97.8
SN10_Pyx6	0.53	0.01	0.00	0.02	0.01	0.00	0.04	98.4
SN10_Pyx7	0.73	0.14	0.01	0.00	0.09	0.01	0.00	97.7
SN10_Pyx7	10.01	1.12	0.16	0.02	0.00	0.05	0.18	94.8

Table 2: Electron microprobe analyses of pyroxenes from Wai Sano. All values reported as wt.%.

SAMPLE	SiO_2	TiO_2	ZnO	Al_2O_3	Cr_2O_3	FeO	MnO	MgO
SN4_Plag001	60.15	0.03		24.48		0.39		0.03
SN4_Plag001	53.57	0.03		29.00		0.43		0.02
SN4_Plag001	53.69	0.03		28.53		0.45		0.05
SN4_Plag001	53.32	0.01		28.85		0.39		0.03
SN4_Plag001	53.50	0.00		28.78		0.28		0.03
SN4_Plag001	54.54	0.04		28.20		0.36		0.04
SN4_Plag001	54.14	0.00		28.44		0.46		0.04
SN4_Plag001	53.81	0.02		28.23		0.45		0.04
SN4_Plag002	54.81	0.04		28.20		0.42		0.05
SN4_Plag002	53.04	0.02		29.44		0.27		0.02
SN4_Plag002	51.87	0.00		30.23		0.33		0.03
SN4_Plag002	52.79	0.00		29.46		0.18		0.00
SN4_Plag002	52.09	0.00		29.29		0.23		0.01
SN4_Plag002	54.57	0.05		28.16		0.18		0.02
SN4_Plag002	52.62	0.02		29.06		0.23		0.04
SN4_Plag002	51.67	0.00		30.01		0.26		0.02
SN4_Plag002	51.36	0.03		30.48		0.30		0.04
SN4_Plag002	50.50	0.03		31.21		0.61		0.04
SN4_Plag003	52.46	0.04		28.96		0.52		0.05
SN4_Plag003	54.05	0.01		28.44		0.33		0.03
SN4_Plag003	52.70	0.01		29.49		0.36		0.03
SN4_Plag003	52.19	0.02		29.77		0.31		0.01
SN4_Plag003	52.34	0.04		29.15		0.31		0.05
SN4_Plag003	52.39	0.00		29.57		0.32		0.02
SN4_Plag003	51.63	0.03		29.95		0.25		0.01
SN4_Plag003	51.21	0.00		30.26		0.28		0.03
SN4_Plag003	51.59	0.03		30.22		0.31		0.03
SN4_Plag003	54.24	0.01		28.55		0.32		0.03
SN4_Plag003	51.33	0.02		30.57		0.35		0.03
SN4_Plag003	53.76	0.02		28.74		0.30		0.01
SN4_Plag003	54.02	0.00		28.56		0.30		0.02
SN4_Plag003	52.32	0.05		29.74		0.23		0.02
SN4_Plag003	51.78	0.00		30.00		0.37		0.01
SN4_Plag003	53.06	0.01		29.35		0.24		0.04
SN4_Plag003	52.62	0.03		29.51		0.36		0.03
SN4_Plag003	53.01	0.02		29.45		0.32		0.05
SN4_Plag003	53.28	0.05		28.94		0.36		0.05
SN4_Plag004	53.50	0.05		28.93		0.31		0.03
SN4_Plag004	53.63	0.04		28.87		0.31		0.01
SN4_Plag004	54.20	0.00		28.71		0.17		0.03
SN4_Plag004	53.94	0.00		28.32		0.22		0.03
SN4_Plag004	54.36	0.00		28.73		0.17		0.06
SN4_Plag004	53.86	0.01		28.39		0.21		0.04
SN4_Plag004	53.33	0.00		29.23		0.23		0.01
SN4_Plag004	53.68	0.00		28.24		0.24		0.03
SN4_Plag004	53.35	0.00		28.92		0.20		0.02
SN4_Plag004	53.35	0.00		29.02		0.27		0.03
SN4_Plag004	54.81	0.04		28.10		0.30		0.03
SN4_Plag004	54.23	0.00		28.60		0.32		0.01
SN4_Plag004	52.45	0.03		29.80		0.36		0.03

Table 3: Electron microprobe analyses of pyroxenes from Wai Sano. All values reported as wt.%.

SAMPLE	CaO	BaO	Na_2O	K_2O	P_2O_5	SO_3	Cl	F	TOTAL
SN4_Plag001	8.70			4.75	0.44				98.99
SN4_Plag001	10.97			5.24	0.19				99.44
SN4_Plag001	10.94			5.10	0.20				98.98
SN4_Plag001	11.28			4.88	0.19				98.94
SN4_Plag001	11.16			5.06	0.20				99.02
SN4_Plag001	10.50			5.26	0.24				99.18
SN4_Plag001	10.64			5.29	0.21				99.22
SN4_Plag001	10.74			5.27	0.22				98.78
SN4_Plag002	10.33			5.40	0.25				99.50
SN4_Plag002	11.61			4.85	0.19				99.44
SN4_Plag002	12.49			4.33	0.15				99.44
SN4_Plag002	11.42			4.93	0.19				98.98
SN4_Plag002	11.72			4.68	0.19				98.22
SN4_Plag002	10.35			5.27	0.21				98.80
SN4_Plag002	11.34			4.90	0.17				98.37
SN4_Plag002	12.26			4.51	0.13				98.86
SN4_Plag002	12.68			4.16	0.15				99.20
SN4_Plag002	13.31			3.63	0.11				99.44
SN4_Plag003	11.59			4.78	0.15				98.55
SN4_Plag003	10.76			4.99	0.21				98.81
SN4_Plag003	11.51			4.75	0.16				99.02
SN4_Plag003	11.76			4.70	0.16				98.92
SN4_Plag003	11.60			4.60	0.14				98.23
SN4_Plag003	11.86			4.71	0.13				99.01
SN4_Plag003	12.28			4.19	0.12				98.47
SN4_Plag003	12.71			4.15	0.13				98.78
SN4_Plag003	12.66			4.11	0.16				99.10
SN4_Plag003	10.89			5.18	0.21				99.42
SN4_Plag003	12.86			4.17	0.13				99.46
SN4_Plag003	10.82			5.29	0.16				99.10
SN4_Plag003	10.77			5.35	0.18				99.22
SN4_Plag003	11.97			4.44	0.13				98.90
SN4_Plag003	12.33			4.45	0.14				99.09
SN4_Plag003	11.51			4.86	0.17				99.25
SN4_Plag003	11.78			4.76	0.14				99.22
SN4_Plag003	11.78			4.63	0.18				99.42
SN4_Plag003	11.29			4.93	0.19				99.09
SN4_Plag004	11.03			4.83	0.21				98.88
SN4_Plag004	10.97			5.10	0.17				99.08
SN4_Plag004	10.66			5.37	0.18				99.32
SN4_Plag004	10.29			5.42	0.17				98.41
SN4_Plag004	10.37			5.63	0.16				99.48
SN4_Plag004	10.38			5.53	0.17				98.60
SN4_Plag004	11.21			5.06	0.17				99.24
SN4_Plag004	10.75			5.27	0.20				98.40
SN4_Plag004	10.99			5.25	0.19				98.92
SN4_Plag004	10.87			5.18	0.18				98.89
SN4_Plag004	10.07			5.81	0.20				99.36
SN4_Plag004	10.63			5.19	0.19				99.17
SN4_Plag004	12.06			4.50	0.16				99.40

Table 3: Electron microprobe analyses of pyroxenes from Wai Sano. All values reported as wt.%.

SAMPLE	SiO_2	TiO_2	ZnO	Al_2O_3	Cr_2O_3	FeO	MnO	MgO
SN4_Plag005	52.71	0.02		28.84		0.49		0.04
SN4_Plag005	51.41	0.03		30.28		0.42		0.05
SN4_Plag005	50.60	0.02		30.75		0.45		0.05
SN4_Plag005	51.49	0.02		30.18		0.43		0.05
SN4_Plag005	53.08	0.02		29.05		0.47		0.03
SN4_Plag006	53.54	0.00		28.73		0.51		0.06
SN4_Plag006	53.78	0.02		28.10		0.33		0.05
SN4_Plag006	54.87	0.00		27.93		0.48		0.05
SN4_Plag006	52.50	0.01		29.27		0.44		0.04
SN4_Plag006	53.68	0.00		28.47		0.52		0.04
SN4_Plag006	53.95	0.01		28.01		0.48		0.04
SN4_Plag006	54.96	0.00		27.79		0.25		0.06
SN4_Plag006	53.19	0.06		28.91		0.46		0.09
SN4_Plag007	54.11	0.03		28.47		0.48		0.06
SN4_Plag007	51.20	0.00		30.61		0.40		0.03
SN4_Plag007	50.57	0.00		30.96		0.37		0.02
SN4_Plag007	54.35	0.00		28.23		0.32		0.03
SN4_Plag007	54.50	0.00		28.19		0.27		0.04
SN4_Plag007	54.37	0.01		28.17		0.41		0.04
SN4_Plag007	52.96	0.00		29.27		0.37		0.04
SN4_Plag007	51.71	0.00		30.03		0.31		0.02
SN4_Plag007	54.79	0.04		28.11		0.39		0.02
SN4_Plag007	54.24	0.02		28.27		0.45		0.01
SN4_Plag007	53.96	0.05		28.09		0.29		0.03
SN4_Plag007	51.99	0.04		29.82		0.34		0.02
SN4_Plag007	50.79	0.07		30.44		0.39		0.03
SN4_Plag007	54.13	0.01		28.39		0.36		0.03
SN4_Plag008	51.61	0.03		30.02		0.55		0.05
SN4_Plag008	53.61	0.00		28.68		0.31		0.03
SN4_Plag008	45.66	0.06		34.35		0.60		0.07
SN4_Plag008	53.66	0.02		28.48		0.32		0.05
SN4_Plag008	52.80	0.04		29.09		0.55		0.05
SN1_Plag1	51.24	0.02	0.07	28.56	0.00	0.38	0.02	0.04
SN1_Plag1	51.88	0.01	0.01	27.85	0.01	0.33	0.00	0.03
SN1_Plag1	51.01	0.02	0.00	28.29	0.03	0.43	0.03	0.02
SN1_Plag1	50.51	0.02	0.04	29.00	0.00	0.40	0.02	0.03
SN1_Plag1	50.85	0.01	0.02	28.10	0.02	0.47	0.02	0.04
SN1_Plag2	67.85	0.33	0.00	10.65	0.00	4.73	0.14	3.02
SN1_Plag2	73.55	0.40	0.01	13.21	0.01	1.62	0.07	0.36
SN1_Plag2	73.31	0.41	0.03	13.34	0.02	1.44	0.08	0.37
SN1_Plag2	73.60	0.43	0.00	13.13	0.06	1.45	0.04	0.30
SN1_Plag2	70.00	0.31	0.02	15.90	0.00	1.09	0.03	0.15
SN1_Plag3	52.43	0.03	0.03	27.60	0.00	0.49	0.02	0.05
SN1_Plag3	53.53	0.00	0.00	26.90	0.01	0.28	0.00	0.03
SN1_Plag3	51.50	0.00	0.07	28.85	0.01	0.30	0.00	0.02
SN1_Plag3	53.56	0.01	0.00	27.16	0.05	0.25	0.00	0.02
SN1_Plag4	52.89	0.00	0.06	28.18	0.00	0.55	0.00	0.01
SN1_Plag4	53.26	0.02	0.00	27.67	0.00	0.34	0.05	0.02
SN1_Plag4	52.48	0.01	0.00	27.16	0.02	0.30	0.03	0.04
SN1_Plag4	52.30	0.00	0.04	27.78	0.02	0.49	0.00	0.07

Table 3: Electron microprobe analyses of pyroxenes from Wai Sano. All values reported as wt.%.

SAMPLE	CaO	BaO	Na_2O	K_2O	P_2O_5	SO_3	Cl	F	TOTAL
SN4_Plag005	11.16			4.88	0.19				98.3
SN4_Plag005	12.62			4.21	0.15				99.2
SN4_Plag005	13.18			3.85	0.14				99.0
SN4_Plag005	12.61			4.17	0.16				99.1
SN4_Plag005	11.29			4.76	0.21				98.9
SN4_Plag006	11.10			4.96	0.20				99.1
SN4_Plag006	10.54			5.36	0.22				98.4
SN4_Plag006	10.13			5.46	0.25				99.2
SN4_Plag006	11.53			4.77	0.18				98.7
SN4_Plag006	10.81			5.16	0.20				98.9
SN4_Plag006	10.54			5.25	0.24				98.5
SN4_Plag006	10.10			5.68	0.26				99.1
SN4_Plag006	11.16			5.36	0.18				99.4
SN4_Plag007	11.02			4.77	0.18				99.1
SN4_Plag007	12.84			3.84	0.13				99.0
SN4_Plag007	13.22			3.86	0.13				99.1
SN4_Plag007	10.53			5.15	0.21				98.8
SN4_Plag007	10.50			5.47	0.21				99.2
SN4_Plag007	10.29			5.66	0.22				99.2
SN4_Plag007	11.36			4.92	0.20				99.1
SN4_Plag007	12.38			4.29	0.13				98.9
SN4_Plag007	10.28			5.40	0.23				99.2
SN4_Plag007	10.43			5.44	0.21				99.1
SN4_Plag007	10.31			5.47	0.21				98.4
SN4_Plag007	12.15			4.38	0.17				98.9
SN4_Plag007	12.69			3.99	0.13				98.5
SN4_Plag007	10.81			5.15	0.19				99.1
SN4_Plag008	11.97			4.15	0.17				98.6
SN4_Plag008	10.83			5.16	0.22				98.8
SN4_Plag008	16.95			1.70	0.03				99.4
SN4_Plag008	10.97			5.25	0.24				99.0
SN4_Plag008	11.40			4.93	0.16				99.0
SN1_Plag1	12.40	0.02	4.65	0.11	0.00	0.00	0.02	0.00	97.5
SN1_Plag1	11.72	0.00	4.65	0.15	0.01	0.01	0.01	0.00	96.7
SN1_Plag1	12.15	0.00	4.43	0.08	0.04	0.00	0.00	0.00	96.5
SN1_Plag1	12.75	0.04	4.42	0.10	0.00	0.01	0.01	0.00	97.4
SN1_Plag1	12.27	0.05	4.35	0.11	0.00	0.01	0.01	0.00	96.3
SN1_Plag2	0.54	0.08	1.61	4.02	0.07	0.02	0.16	0.03	93.2
SN1_Plag2	0.53	0.13	2.64	5.03	0.09	0.05	0.21	0.00	97.8
SN1_Plag2	0.53	0.06	2.78	4.98	0.08	0.04	0.21	0.00	97.7
SN1_Plag2	0.49	0.10	2.71	4.91	0.03	0.02	0.17	0.00	97.4
SN1_Plag2	2.37	0.08	4.29	2.96	0.04	0.02	0.07	0.00	97.3
SN1_Plag3	11.06	0.00	5.22	0.19	0.00	0.01	0.01	0.00	97.2
SN1_Plag3	10.41	0.00	5.40	0.17	0.02	0.00	0.00	0.00	96.8
SN1_Plag3	12.30	0.01	4.65	0.11	0.00	0.00	0.02	0.00	97.8
SN1_Plag3	10.71	0.00	5.11	0.16	0.00	0.00	0.00	0.00	97.0
SN1_Plag4	11.28	0.00	5.20	0.12	0.02	0.00	0.00	0.00	98.3
SN1_Plag4	11.07	0.00	5.32	0.14	0.03	0.00	0.01	0.00	97.9
SN1_Plag4	10.79	0.02	5.09	0.14	0.02	0.02	0.01	0.00	96.1
SN1_Plag4	11.23	0.00	5.62	0.13	0.00	0.09	0.17	0.00	97.9

Table 3: Electron microprobe analyses of pyroxenes from Wai Sano. All values reported as wt.%.

SAMPLE	SiO_2	TiO_2	ZnO	Al_2O_3	Cr_2O_3	FeO	MnO	MgO
SN1_Plag5	51.54	0.02	0.05	27.89	0.01	0.57	0.00	0.04
SN1_Plag5	51.84	0.00	0.00	28.30	0.01	0.45	0.02	0.05
SN1_Plag5	48.47	0.00	0.01	30.17	0.03	0.48	0.01	0.03
SN1_Plag5	53.15	0.01	0.00	26.96	0.02	0.37	0.00	0.03
SN1_Plag5	53.46	0.00	0.02	26.73	0.02	0.38	0.01	0.04
SN1_Plag5	52.57	0.01	0.00	27.40	0.01	0.35	0.00	0.01
SN1_Plag6	51.86	0.01	0.00	28.17	0.04	0.38	0.04	0.02
SN1_Plag6	53.55	0.00	0.00	26.85	0.00	0.34	0.02	0.02
SN1_Plag6	52.64	0.00	0.02	27.28	0.00	0.25	0.00	0.02
SN1_Plag6	53.31	0.01	0.00	26.95	0.02	0.26	0.00	0.03
SN1_Plag6	52.89	0.01	0.02	27.69	0.03	0.28	0.00	0.03
SN7_Plag1	54.00	0.01	0.00	26.71	0.00	0.43	0.01	0.02
SN7_Plag1	54.02	0.00	0.00	26.63	0.02	0.17	0.00	0.02
SN7_Plag1	54.81	0.01	0.00	25.90	0.00	0.20	0.02	0.01
SN7_Plag1	55.59	0.01	0.01	25.94	0.00	0.21	0.01	0.04
SN7_Plag1	54.18	0.01	0.00	25.89	0.00	0.47	0.00	0.02
SN7_Plag2	55.04	0.02	0.00	26.10	0.02	0.21	0.00	0.02
SN7_Plag2	50.17	0.01	0.00	29.00	0.00	0.20	0.05	0.01
SN7_Plag2	52.21	0.01	0.05	27.87	0.01	0.13	0.01	0.02
SN7_Plag2	55.84	0.00	0.09	25.64	0.00	0.17	0.03	0.01
SN7_Plag2	53.95	0.01	0.00	26.29	0.00	0.15	0.00	0.02
SN7_Plag2	53.34	0.03	0.03	27.08	0.01	0.12	0.00	0.00
SN7_Plag2	54.17	0.00	0.09	26.51	0.00	0.20	0.00	0.02
SN7_Plag2	53.99	0.01	0.03	25.78	0.00	0.11	0.03	0.26
SN7_Plag2	54.24	0.02	0.06	26.59	0.00	0.16	0.01	0.01
SN7_Plag2	55.55	0.01	0.03	26.11	0.00	0.17	0.04	0.01
SN7_Plag3	54.12	0.02	0.00	26.50	0.00	0.38	0.00	0.01
SN7_Plag3	54.15	0.02	0.01	26.06	0.01	0.32	0.00	0.02
SN7_Plag4	53.80	0.02	0.00	25.96	0.02	0.20	0.00	0.00
SN7_Plag4	53.67	0.01	0.07	26.23	0.02	0.22	0.02	0.02
SN7_Plag4	55.53	0.01	0.06	25.82	0.00	0.21	0.02	0.03
SN7_Plag4	54.14	0.00	0.00	25.77	0.02	0.18	0.00	0.02
SN7_Plag4	51.67	0.02	0.00	27.84	0.02	0.22	0.00	0.02
SN7_Plag4	53.08	0.02	0.00	26.84	0.00	0.18	0.02	0.00
SN7_Plag4	54.25	0.00	0.06	26.35	0.03	0.16	0.06	0.04
SN7_Plag4	53.94	0.00	0.07	26.53	0.01	0.13	0.00	0.03
SN10_Plag1	52.39	0.01	0.07	27.35	0.02	0.26	0.02	0.02
SN10_Plag1	53.09	0.00	0.00	26.79	0.01	0.19	0.00	0.02
SN10_Plag1	54.52	0.00	0.10	26.38	0.02	0.24	0.02	0.01
SN10_Plag1	53.63	0.00	0.01	26.81	0.01	0.19	0.00	0.01
SN10_Plag1	54.75	0.00	0.01	26.16	0.00	0.19	0.00	0.01
SN10_Plag1	50.35	0.02	0.05	28.95	0.00	0.20	0.00	0.00
SN10_Plag1	53.74	0.02	0.00	26.69	0.00	0.16	0.00	0.02
SN10_Plag1	52.83	0.01	0.03	27.25	0.00	0.21	0.00	0.01
SN10_Plag1	51.23	0.00	0.02	28.49	0.00	0.24	0.00	0.00
SN10_Plag2	53.83	0.00	0.00	26.89	0.00	0.25	0.01	0.02
SN10_Plag2	53.50	0.01	0.00	27.21	0.00	0.16	0.03	0.01
SN10_Plag2	55.27	0.01	0.00	26.17	0.01	0.13	0.00	0.00
SN10_Plag2	48.47	0.01	0.00	30.28	0.00	0.16	0.00	0.00
SN10_Plag2	53.51	0.01	0.07	26.91	0.00	0.25	0.03	0.02

Table 3: Electron microprobe analyses of pyroxenes from Wai Sano. All values reported as wt.%.

SAMPLE	CaO	BaO	Na_2O	K_2O	P_2O_5	SO_3	Cl	F	TOTAL
SN1_Plag5	11.87	0.02	4.81	0.12	0.03	0.00	0.00	0.04	97.0
SN1_Plag5	12.03	0.02	4.58	0.10	0.00	0.01	0.00	0.00	97.4
SN1_Plag5	14.59	0.00	2.99	0.06	0.01	0.00	0.02	0.00	96.9
SN1_Plag5	10.68	0.00	5.41	0.19	0.00	0.00	0.00	0.00	96.8
SN1_Plag5	10.54	0.00	5.38	0.14	0.02	0.00	0.01	0.00	96.8
SN1_Plag5	10.28	0.00	5.15	0.15	0.01	0.01	0.01	0.00	96.0
SN1_Plag6	12.06	0.00	4.81	0.10	0.02	0.01	0.00	0.00	97.5
SN1_Plag6	10.47	0.02	5.55	0.16	0.00	0.01	0.00	0.00	97.0
SN1_Plag6	11.01	0.00	5.16	0.15	0.00	0.00	0.00	0.00	96.5
SN1_Plag6	10.59	0.00	5.69	0.15	0.03	0.01	0.01	0.00	97.1
SN1_Plag6	11.31	0.03	5.12	0.14	0.01	0.00	0.01	0.00	97.6
SN7_Plag1	10.23	0.04	5.90	0.14	0.02	0.00	0.02	0.00	97.5
SN7_Plag1	10.08	0.03	6.03	0.20	0.00	0.00	0.00	0.00	97.2
SN7_Plag1	9.15	0.01	6.59	0.23	0.00	0.00	0.01	0.00	96.9
SN7_Plag1	8.98	0.02	6.70	0.22	0.02	0.02	0.00	0.00	97.8
SN7_Plag1	9.01	0.05	5.91	0.22	0.01	0.03	0.03	0.00	95.8
SN7_Plag2	9.35	0.01	6.47	0.20	0.00	0.01	0.00	0.00	97.5
SN7_Plag2	12.80	0.00	4.19	0.14	0.00	0.01	0.00	0.00	96.6
SN7_Plag2	11.23	0.01	5.14	0.13	0.00	0.00	0.00	0.00	96.8
SN7_Plag2	8.71	0.04	6.72	0.22	0.00	0.00	0.00	0.00	97.5
SN7_Plag2	9.90	0.05	6.12	0.17	0.01	0.00	0.02	0.00	96.7
SN7_Plag2	10.40	0.03	5.57	0.16	0.00	0.03	0.00	0.00	96.8
SN7_Plag2	9.69	0.05	6.26	0.21	0.01	0.01	0.01	0.00	97.2
SN7_Plag2	9.23	0.01	7.97	0.22	0.00	0.22	0.42	0.00	98.2
SN7_Plag2	9.67	0.03	5.97	0.19	0.00	0.01	0.00	0.00	97.0
SN7_Plag2	8.99	0.00	6.64	0.19	0.00	0.00	0.00	0.00	97.7
SN7_Plag3	9.72	0.00	6.01	0.20	0.00	0.01	0.02	0.00	97.0
SN7_Plag3	9.56	0.02	5.94	0.24	0.01	0.00	0.01	0.00	96.4
SN7_Plag4	9.39	0.01	6.07	0.22	0.00	0.01	0.01	0.00	95.7
SN7_Plag4	9.76	0.02	6.01	0.17	0.00	0.02	0.01	0.00	96.2
SN7_Plag4	8.79	0.01	6.65	0.19	0.01	0.02	0.03	0.00	97.4
SN7_Plag4	9.19	0.00	6.29	0.17	0.03	0.01	0.01	0.00	95.8
SN7_Plag4	11.53	0.00	5.11	0.13	0.04	0.00	0.00	0.00	96.6
SN7_Plag4	10.30	0.00	5.64	0.14	0.00	0.02	0.00	0.01	96.3
SN7_Plag4	9.68	0.00	6.08	0.18	0.02	0.03	0.03	0.00	96.9
SN7_Plag4	9.96	0.00	5.86	0.19	0.01	0.00	0.01	0.00	96.7
SN10_Plag1	11.22	0.04	5.11	0.12	0.00	0.00	0.02	0.00	96.7
SN10_Plag1	10.53	0.03	5.53	0.13	0.00	0.00	0.00	0.00	96.3
SN10_Plag1	9.65	0.03	6.10	0.14	0.00	0.03	0.00	0.03	97.2
SN10_Plag1	10.21	0.03	5.81	0.14	0.00	0.00	0.00	0.00	96.8
SN10_Plag1	9.60	0.01	6.16	0.16	0.00	0.00	0.00	0.00	97.0
SN10_Plag1	12.63	0.01	4.29	0.09	0.00	0.02	0.01	0.00	96.6
SN10_Plag1	10.12	0.03	5.94	0.15	0.00	0.00	0.00	0.00	96.9
SN10_Plag1	10.83	0.00	5.50	0.14	0.01	0.01	0.00	0.00	96.8
SN10_Plag1	12.08	0.03	4.58	0.12	0.00	0.00	0.00	0.00	96.8
SN10_Plag2	10.28	0.01	5.80	0.16	0.00	0.00	0.01	0.00	97.3
SN10_Plag2	10.60	0.00	5.46	0.15	0.00	0.00	0.01	0.00	97.2
SN10_Plag2	9.23	0.03	6.55	0.21	0.03	0.00	0.01	0.00	97.6
SN10_Plag2	14.38	0.02	3.37	0.07	0.01	0.01	0.00	0.00	96.8
SN10_Plag2	10.39	0.02	5.64	0.15	0.00	0.00	0.01	0.00	97.0

Table 3: Electron microprobe analyses of pyroxenes from Wai Sano. All values reported as wt.%.

SAMPLE	SiO_2	TiO_2	ZnO	Al_2O_3	Cr_2O_3	FeO	MnO	MgO
SN10_Plag3	49.65	0.01	0.01	28.57	0.02	0.45	0.00	0.07
SN10_Plag3	49.65	0.03	0.07	29.42	0.01	0.44	0.04	0.03
SN10_Plag3	50.14	0.03	0.00	28.89	0.00	0.37	0.03	0.02
SN10_Plag4	54.87	0.01	0.00	26.51	0.00	0.41	0.00	0.08
SN10_Plag4	51.09	0.01	0.00	28.26	0.00	0.39	0.00	0.03
SN10_Plag5	49.70	0.00	0.05	29.36	0.00	0.40	0.00	0.01
SN10_Plag5	48.01	0.00	0.00	29.88	0.01	0.37	0.01	0.03
SN10_Plag5	48.91	0.01	0.01	29.42	0.00	0.46	0.06	0.01
SN10_Plag5	48.27	0.01	0.00	29.65	0.00	0.27	0.02	0.02
SN10_Plag5	49.47	0.00	0.00	29.36	0.00	0.34	0.00	0.03
SN10_Plag5	48.04	0.02	0.03	30.14	0.00	0.49	0.01	0.03
SN10_Plag5	48.04	0.01	0.00	30.06	0.00	0.46	0.00	0.02
SN10_Plag5	48.27	0.01	0.03	30.19	0.00	0.47	0.03	0.02
SN10_Plag5	48.68	0.01	0.04	29.87	0.01	0.35	0.00	0.03
SN10_Plag5	49.00	0.02	0.00	29.59	0.00	0.36	0.03	0.01
SN10_Plag6	47.91	0.02	0.03	30.41	0.03	0.23	0.00	0.00
SN10_Plag6	48.86	0.00	0.00	29.72	0.00	0.22	0.00	0.01
SN10_Plag6	53.11	0.01	0.03	27.32	0.01	0.22	0.02	0.00
SN10_Plag6	50.34	0.01	0.00	29.15	0.01	0.27	0.01	0.00
SN10_Plag6	48.12	0.00	0.00	30.32	0.03	0.23	0.00	0.00
SN10_Plag7	52.59	0.00	0.03	27.48	0.00	0.33	0.00	0.03
SN10_Plag7	49.82	0.00	0.07	29.41	0.00	0.42	0.03	0.03
SN10_Plag7	77.46	0.19	0.00	10.98	0.00	0.43	0.00	0.31
SN10_Plag7	77.70	0.22	0.00	10.45	0.00	0.65	0.03	0.36
SN10_Plag8	52.04	0.03	0.01	28.07	0.00	0.37	0.02	0.02
SN10_Plag9	52.10	0.01	0.00	28.06	0.03	0.21	0.01	0.00
SN10_Plag9	56.37	0.00	0.00	25.33	0.00	0.18	0.02	0.03
SN10_Plag9	54.34	0.00	0.00	26.51	0.01	0.15	0.01	0.01
SN10_Plag9	53.67	0.00	0.00	26.92	0.00	0.18	0.02	0.00
SN10_Plag9	54.24	0.02	0.02	26.36	0.00	0.12	0.03	0.03
SN10_Plag9	50.25	0.00	0.00	29.27	0.02	0.19	0.00	0.02
SN10_Plag9	53.20	0.00	0.01	26.92	0.00	0.22	0.02	0.01
SN10_Plag9	51.92	0.01	0.00	28.09	0.04	0.28	0.02	0.01
SN10_Plag10	52.06	0.02	0.01	27.66	0.00	0.38	0.04	0.03
SN10_Plag10	54.51	0.01	0.00	26.27	0.02	0.26	0.00	0.02
SN10_Plag10	52.87	0.00	0.00	27.55	0.03	0.52	0.00	0.03
SN10_Plag10	54.92	0.02	0.02	26.10	0.00	0.32	0.00	0.02
SN10_Plag11	49.07	0.00	0.00	29.70	0.03	0.40	0.01	0.04
SN10_Plag11	53.36	0.01	0.00	27.26	0.00	0.23	0.02	0.02
SN10_Plag11	55.67	0.00	0.05	25.77	0.03	0.20	0.00	0.00
SN10_Plag11	52.76	0.03	0.05	24.08	0.00	0.17	0.06	0.03
SN10_Plag11	53.71	0.02	0.00	27.10	0.02	0.15	0.04	0.00
SN10_Plag11	55.42	0.00	0.02	25.82	0.00	0.18	0.02	0.01
SN10_Plag11	56.95	0.01	0.00	24.97	0.00	0.21	0.00	0.04
SN10_Plag11	57.24	0.00	0.00	24.58	0.00	0.18	0.03	0.02
SN10_Plag11	55.55	0.00	0.00	26.06	0.02	0.17	0.01	0.02
SN10_Plag11	49.48	0.02	0.00	29.32	0.00	0.37	0.00	0.04
SN10_PlagInc1	51.05	0.01	0.00	28.54	0.02	0.49	0.02	0.02
SN10_PlagInc1	51.13	0.00	0.00	29.03	0.01	0.38	0.01	0.02

Table 3: Electron microprobe analyses of pyroxenes from Wai Sano. All values reported as wt.%.

SAMPLE	CaO	BaO	Na_2O	K_2O	P_2O_5	SO_3	Cl	F	TOTAL
SN10_Plag3	12.71	0.00	4.10	0.09	0.01	0.00	0.01	0.00	95.7
SN10_Plag3	13.44	0.01	3.93	0.10	0.02	0.00	0.01	0.00	97.2
SN10_Plag3	12.87	0.02	4.13	0.09	0.00	0.00	0.01	0.00	96.6
SN10_Plag4	10.32	0.02	5.92	0.15	0.01	0.01	0.00	0.00	98.3
SN10_Plag4	12.29	0.00	4.55	0.10	0.00	0.01	0.00	0.00	96.7
SN10_Plag5	13.37	0.03	3.81	0.07	0.02	0.00	0.00	0.00	96.8
SN10_Plag5	14.44	0.00	3.09	0.05	0.02	0.03	0.00	0.00	95.9
SN10_Plag5	13.88	0.00	3.60	0.06	0.00	0.00	0.00	0.00	96.4
SN10_Plag5	14.07	0.01	3.34	0.08	0.00	0.02	0.00	0.00	95.8
SN10_Plag5	13.51	0.00	3.67	0.07	0.01	0.01	0.00	0.00	96.5
SN10_Plag5	14.54	0.00	3.26	0.05	0.01	0.00	0.00	0.00	96.6
SN10_Plag5	14.43	0.01	3.18	0.04	0.00	0.04	0.00	0.00	96.3
SN10_Plag5	14.56	0.01	3.26	0.04	0.00	0.01	0.00	0.00	96.9
SN10_Plag5	14.14	0.02	3.21	0.08	0.01	0.01	0.01	0.00	96.5
SN10_Plag5	13.71	0.00	3.37	0.07	0.00	0.00	0.01	0.00	96.2
SN10_Plag6	14.65	0.00	3.03	0.07	0.00	0.01	0.01	0.00	96.4
SN10_Plag6	13.64	0.00	3.59	0.07	0.00	0.04	0.00	0.02	96.2
SN10_Plag6	10.84	0.03	5.38	0.12	0.00	0.01	0.00	0.00	97.1
SN10_Plag6	12.96	0.00	4.22	0.07	0.00	0.00	0.02	0.00	97.0
SN10_Plag6	14.53	0.02	2.97	0.07	0.03	0.02	0.00	0.00	96.4
SN10_Plag7	11.03	0.02	5.22	0.11	0.00	0.01	0.00	0.00	96.9
SN10_Plag7	13.39	0.00	3.90	0.07	0.01	0.00	0.00	0.00	97.1
SN10_Plag7	0.88	0.06	2.56	3.97	0.05	0.00	0.00	0.00	96.9
SN10_Plag7	0.82	0.05	2.20	3.85	0.07	0.02	0.02	0.00	96.4
SN10_Plag8	11.86	0.02	4.73	0.10	0.00	0.00	0.00	0.00	97.3
SN10_Plag9	11.63	0.03	5.12	0.12	0.00	0.01	0.00	0.00	97.3
SN10_Plag9	8.37	0.00	6.91	0.25	0.00	0.00	0.00	0.00	97.5
SN10_Plag9	9.86	0.03	5.94	0.16	0.00	0.00	0.00	0.00	97.0
SN10_Plag9	10.44	0.02	5.82	0.14	0.01	0.00	0.01	0.00	97.2
SN10_Plag9	9.72	0.03	5.95	0.17	0.00	0.00	0.00	0.00	96.7
SN10_Plag9	13.09	0.02	4.09	0.09	0.00	0.02	0.01	0.02	97.1
SN10_Plag9	10.46	0.00	5.75	0.16	0.00	0.00	0.01	0.00	96.7
SN10_Plag9	11.63	0.01	4.93	0.11	0.00	0.00	0.01	0.00	97.1
SN10_Plag10	11.58	0.00	5.23	0.13	0.00	0.01	0.00	0.00	97.1
SN10_Plag10	9.58	0.00	6.37	0.15	0.00	0.00	0.00	0.00	97.2
SN10_Plag10	11.20	0.00	5.07	0.12	0.01	0.00	0.00	0.00	97.4
SN10_Plag10	9.51	0.01	6.18	0.16	0.00	0.02	0.00	0.00	97.3
SN10_Plag11	13.82	0.02	3.45	0.06	0.01	0.02	0.00	0.00	96.6
SN10_Plag11	10.49	0.00	5.65	0.15	0.00	0.01	0.00	0.00	97.2
SN10_Plag11	8.84	0.02	6.62	0.23	0.02	0.02	0.00	0.00	97.4
SN10_Plag11	9.24	0.02	5.60	0.22	0.00	0.00	0.01	0.00	92.3
SN10_Plag11	10.30	0.00	5.59	0.16	0.01	0.00	0.00	0.00	97.1
SN10_Plag11	9.14	0.00	6.35	0.22	0.02	0.01	0.01	0.00	97.2
SN10_Plag11	8.61	0.00	6.19	0.40	0.00	0.00	0.00	0.04	97.4
SN10_Plag11	7.70	0.03	7.15	0.33	0.00	0.02	0.00	0.00	97.3
SN10_Plag11	9.06	0.04	6.80	0.20	0.00	0.07	0.00	0.02	98.0
SN10_Plag11	13.48	0.01	3.81	0.07	0.01	0.01	0.01	0.00	96.6
SN10_PlagInc1	12.09	0.03	4.56	0.11	0.02	0.01	0.00	0.00	97.0
SN10_PlagInc1	12.55	0.00	4.24	0.10	0.02	0.00	0.00	0.00	97.5

Table 3: Electron microprobe analyses of pyroxenes from Wai Sano. All values reported as wt.%.

SAMPLE	SN7_Mgt1	SN7_Mgt1	SN10_Mgt1	SN10_Mgt1	SN10_Mgt1	SN10_Mgt2	SN10_Mgt2	SN10_Mgt3	SN10_Mgt3	SN10_Mgt3	SN10_Mgt3
SiO_2	0.07	0.13	0.06	0.03	0.11	0.08	0.59	0.07	0.03	0.05	0.01
TiO_2	4.79	4.84	2.62	3.49	6.41	13.25	5.95	5.04	5.70	5.51	35.93
ZnO	0.06	0.08	0.10	0.17	0.05	0.07	0.10	0.13	0.10	0.08	0.00
Al_2O_3	2.89	2.60	2.84	2.73	2.99	2.04	2.13	2.22	2.19	2.33	0.29
Cr_2O_3	0.05	0.05	0.03	0.05	0.04	0.05	0.05	0.08	0.04	0.04	0.00
FeO	80.78	80.72	80.82	81.71	74.70	72.37	77.45	81.18	81.70	80.41	55.38
MnO	0.47	0.45	0.32	0.51	0.59	0.83	0.44	0.41	0.44	0.52	0.43
MgO	0.95	0.86	1.09	1.03	1.40	2.03	1.21	1.30	1.29	1.37	1.91
CaO	0.02	0.01	0.08	0.04	0.11	0.02	0.04	0.01	0.00	0.02	0.00
BaO	0.00	0.00	0.00	0.00	0.02	0.00	0.04	0.00	0.02	0.00	0.00
Na2O	0.05	0.05	0.05	0.00	0.02	0.00	0.16	0.03	0.01	0.01	0.01
K2O	0.01	0.00	0.01	0.00	0.02	0.00	0.02	0.00	0.00	0.00	0.00
P2O5	0.00	0.00	0.01	0.00	0.00	0.01	0.05	0.00	0.01	0.00	0.02
SO3	0.00	0.00	0.00	0.00	0.00	0.00	0.00	0.00	0.00	0.00	0.00
Cl	0.01	0.01	0.00	0.00	0.00	0.00	0.01	0.00	0.00	0.00	0.00
F	0.37	0.37	0.30	0.26	0.42	0.32	0.23	0.31	0.38	0.25	0.15
TOTAL	90.4	90.0	88.2	89.9	86.7	90.9	88.4	90.6	91.8	90.5	94.1

Table 4: Electron microprobe analyses of magnetites from Wai Sano. All values reported as wt.%.

SAMPLE	SN1_Apat1	SN1_Apat1	SN1_Apat1	SN10_Apat1	SN10_Apat1	SN10_Apat1	SN10_Apat1
SiO_2	0.14	0.83	0.12	0.07	0.08	0.03	0.04
TiO_2	0.02	0.00	0.00	0.00	0.00	0.00	0.00
ZnO	0.01	0.00	0.00	0.03	0.00	0.11	0.00
Al_2O_3	0.02	0.58	0.00	0.03	0.00	0.01	0.00
Cr_2O_3	0.00	0.00	0.00	0.00	0.03	0.00	0.00
FeO	0.62	0.61	0.67	0.52	0.51	0.35	0.33
MnO	0.11	0.11	0.13	0.15	0.14	0.17	0.19
MgO	0.19	0.19	0.20	0.20	0.17	0.16	0.18
CaO	53.25	52.30	53.10	53.64	53.98	54.13	53.69
BaO	0.01	0.00	0.01	0.02	0.00	0.00	0.02
Na2O	0.04	0.08	0.11	0.04	0.03	0.04	0.03
K2O	0.00	0.00	0.02	0.00	0.01	0.01	0.00
P2O5	42.44	41.57	42.49	43.06	43.14	43.27	43.17
SO3	0.10	0.14	0.10	0.15	0.07	0.08	0.00
Cl	1.06	1.20	1.10	1.12	1.08	1.08	1.15
F	0.00	0.00	0.00	0.00	0.00	0.00	0.00
TOTAL	97.8	97.3	97.8	98.8	99.0	99.2	98.5

Table 5: Electron microprobe analyses of apatites from Wai Sano. All values reported as wt.%.

SAMPLE	SN10_Biot1	SN10_Biot1	SN10_Biot1	SN10_Biot1
SiO_2	37.35	37.35	36.98	36.43
TiO_2	3.50	3.25	3.27	3.23
ZnO	0.00	0.00	0.08	0.06
Al_2O_3	14.84	14.44	14.47	14.36
Cr_2O_3	0.03	0.00	0.00	0.01
FeO	10.37	11.68	13.13	13.22
MnO	0.10	0.14	0.10	0.11
MgO	16.77	16.25	16.04	15.97
CaO	0.06	0.18	0.11	0.04
BaO	0.29	0.23	0.29	0.24
Na2O	0.91	0.88	1.06	1.04
K2O	7.24	6.82	6.86	7.29
P2O5	0.00	0.01	0.00	0.02
SO3	0.02	0.03	0.05	0.05
Cl	0.09	0.11	0.10	0.10
F	0.16	0.47	0.15	0.08
TOTAL	91.6	91.6	92.6	92.2

Table 6: Electron microprobe analyses of phlogopites from Wai Sano. All values reported as wt.%.

SAMPLE	SN10_GM1	SN10_GM2	SN10_GM3	SN10_GM4	SN10_GM4	SN10_GM4
SiO2	83.1591	72.6147	74.5153	74.2848	73.15	51.3886
TiO2	0.108517	0.213778	0.201335	0.250451	0.225362	0.017534
ZnO	0	0	0	0.01456	0	0
Al2O3	9.63633	15.1111	14.6641	10.5985	14.403	28.0458
Cr2O3	0.003834	0	0.003429	0	0	0.000661
FeO	0.336005	0.437221	0.479793	4.04925	0.896079	0.358187
MnO	0.024092	0.015133	0.035379	0.27377	0.046592	0
MgO	0.023317	0.0274	0.14081	2.48519	0.482195	0
CaO	2.67055	2.68443	2.14914	0.655228	2.3338	11.8923
BaO	0.023029	0.054971	0.035827	0.07115	0.057031	0
Na2O	2.40393	3.97997	4.31896	2.72647	3.83095	4.75941
K2O	0.200581	2.94499	2.91004	3.56177	3.10316	0.106075
P2O5	0.04991	0.051687	0.008891	0.052544	0.05928	0.018856
SO3	0	0	0.07038	0	0	0
Cl	0	0.016928	0.011497	0.006221	0.023347	0.010871
F	0	0	0	0	0	0
TOTAL	98.6392	98.1485	99.5423	99.0285	98.6055	96.5958

Table 7: Electron microprobe analyses of groundmass glass from Wai Sano. All values reported as wt.%.

SAMPLE	SiO_2	TiO_2	Al_2O_3	Cr_2O_3	FeO	MnO	MgO
BC14114_hbl1	39.97	2.72	13.33	0.00	12.17	0.25	13.01
BC14114_hbl1	42.18	2.54	11.00	0.00	12.98	0.35	13.58
BC14114_hbl1	39.42	2.51	14.23	0.02	12.44	0.22	12.94
BC14114_hbl1	40.40	2.42	14.01	0.00	12.51	0.19	13.08
BC14114_hbl1	42.06	2.38	11.62	0.00	13.87	0.45	12.70
BC14114_hbl1	39.27	2.25	14.42	0.00	13.66	0.27	12.51
BC14114_hbl1	41.26	2.55	12.40	0.00	12.53	0.28	13.02
BC14114_hbl2	42.02	2.67	10.45	0.00	13.53	0.42	12.93
BC14114_hbl2	41.83	2.33	11.38	0.00	14.85	0.50	12.20
BC14114_hbl2	41.49	1.38	11.87	0.05	13.72	0.40	12.76
BC14114_hbl2	41.35	2.35	11.50	0.00	14.52	0.35	12.00
BC14114_hbl3	41.99	2.63	11.47	0.00	12.53	0.36	13.29
BC14114_hbl3	42.03	2.66	11.16	0.00	13.11	0.43	13.02
BC14114_hbl3	41.61	2.57	11.49	0.01	13.41	0.31	13.05
BC14114_hbl4	40.32	2.35	13.74	0.00	11.93	0.19	13.34
BC14114_hbl4	39.32	2.30	13.65	0.01	15.03	0.26	11.78
BC14114_hbl5	40.25	2.55	13.50	0.03	11.03	0.12	14.49
BC14114_hbl5	39.71	2.51	13.53	0.02	10.98	0.13	14.24
BC14114_hbl6	39.72	2.40	14.29	0.00	11.50	0.20	13.57
BC14114_hbl7	41.95	2.62	11.06	0.01	12.76	0.36	13.12
BC14114_hbl7	41.98	2.57	11.38	0.00	13.39	0.37	13.21
BC14114_hbl8	40.01	2.15	13.51	0.00	12.33	0.13	13.46
BC14114_hbl8	40.84	2.23	13.10	0.00	10.89	0.14	14.26
BC14114_hbl8	41.54	2.72	12.20	0.02	12.98	0.39	13.17
BC14114_hbl9	39.63	2.45	13.94	0.00	11.48	0.12	13.36
BC14114_hbl9	40.68	2.45	13.47	0.01	11.01	0.13	14.56
BC14114_hbl9	39.56	2.17	13.91	0.01	11.72	0.14	13.55
BC14114_hbl9	39.99	2.36	13.69	0.00	11.13	0.12	14.06
BC14114_hbl10	41.38	2.67	11.86	0.00	13.35	0.32	12.52
BC14114_hbl10	41.76	2.55	13.59	0.00	11.65	0.27	13.83
BC14114_hbl10	39.56	2.09	14.14	0.00	10.76	0.12	14.25
BC14114_hbl10	40.08	2.03	13.86	0.06	9.42	0.10	15.01
BC14114_hbl10	40.31	2.02	14.17	0.14	9.72	0.09	15.11
BC14114_hbl10	40.26	1.89	13.87	0.15	9.41	0.10	15.20
BC14114_hbl10	41.05	1.90	14.06	0.15	9.51	0.11	15.23
BC14114_hbl10	40.14	2.03	13.92	0.00	9.57	0.09	15.18
BC14114_hbl10	40.22	2.01	14.11	0.07	9.71	0.11	15.21
BC14114_hbl10	39.88	2.12	14.26	0.00	9.87	0.08	14.44
BC14114_hbl10	40.00	2.12	14.16	0.03	10.16	0.09	14.47
BC14114_hbl10	41.26	1.83	13.61	0.01	9.44	0.08	14.58
BC14114_hbl10	41.15	2.10	14.66	0.03	9.80	0.10	14.87
BC14114_hbl10	42.86	2.51	12.86	0.00	11.65	0.25	14.14
BC14114_hbl11	41.16	2.63	11.55	0.00	13.55	0.33	12.56
BC14114_hbl11	41.23	2.58	11.97	0.00	12.59	0.25	13.57
BC14114_hbl12	41.19	2.87	11.33	0.00	13.29	0.29	12.72
BC14114_hbl12	42.01	2.76	11.18	0.00	13.63	0.40	12.81
BC14114_hbl12	41.86	2.21	13.46	0.02	12.66	0.30	13.06
BC14114_hbl12	42.13	2.54	11.46	0.00	13.32	0.33	13.11
BC14114_hbl12	41.55	2.50	11.64	0.00	13.13	0.38	12.86

Table 8: NE Sumbawa amphibole analyses and thermobarometrical estimates. All analyses reported as wt.% unless otherwise stated. P-T-H_2O-fO_2 calculated using the formulations of Ridolfi et al. (2012).

SAMPLE	CaO	Na_2O	K_2O	F	Cl	Total	T (°C)
BC14114_hbl1	11.70	2.38	0.67	0.09	0.02	96.3	1011
BC14114_hbl1	11.37	2.41	0.63	0.15	0.07	97.3	945
BC14114_hbl1	11.75	2.47	0.83	0.12	0.03	97.0	1032
BC14114_hbl1	11.67	2.47	0.77	0.15	0.02	97.7	1014
BC14114_hbl1	11.25	2.35	0.69	0.13	0.08	97.6	945
BC14114_hbl1	11.63	2.55	0.74	0.14	0.03	97.5	1030
BC14114_hbl1	11.57	2.44	0.60	0.08	0.03	96.8	977
BC14114_hbl2	11.22	2.27	0.67	0.09	0.11	96.4	930
BC14114_hbl2	11.31	2.33	0.62	0.13	0.05	97.5	941
BC14114_hbl2	11.23	2.44	0.64	0.09	0.07	96.1	951
BC14114_hbl2	11.31	2.48	0.64	0.20	0.06	96.8	950
BC14114_hbl3	11.26	2.34	0.68	0.10	0.10	96.8	952
BC14114_hbl3	11.30	2.42	0.67	0.07	0.10	97.0	946
BC14114_hbl3	11.35	2.44	0.66	0.08	0.08	97.1	957
BC14114_hbl4	11.63	2.64	0.65	0.09	0.03	96.9	1015
BC14114_hbl4	11.52	2.45	0.74	0.11	0.03	97.2	1008
BC14114_hbl5	11.52	2.58	0.67	0.13	0.01	96.9	1020
BC14114_hbl5	11.67	2.46	0.65	0.01	0.01	95.9	1025
BC14114_hbl6	11.67	2.50	0.84	0.13	0.02	96.8	1032
BC14114_hbl7	11.22	2.44	0.64	0.13	0.09	96.4	944
BC14114_hbl7	11.18	2.45	0.59	0.13	0.08	97.3	948
BC14114_hbl8	11.69	2.45	0.66	0.10	0.03	96.5	1013
BC14114_hbl8	11.62	2.53	0.72	0.15	0.03	96.5	1004
BC14114_hbl8	11.22	2.63	0.63	0.09	0.07	97.7	970
BC14114_hbl9	11.84	2.36	0.68	0.11	0.03	96.0	1028
BC14114_hbl9	11.60	2.60	0.68	0.02	0.03	97.2	1015
BC14114_hbl9	11.57	2.47	0.77	0.11	0.02	96.0	1024
BC14114_hbl9	11.74	2.52	0.72	0.11	0.03	96.5	1024
BC14114_hbl10	11.07	2.49	0.83	0.11	0.12	96.7	958
BC14114_hbl10	11.06	2.43	0.73	0.14	0.09	98.1	988
BC14114_hbl10	11.79	2.40	0.99	0.13	0.02	96.3	1038
BC14114_hbl10	11.91	2.34	1.09	0.09	0.01	96.0	1034
BC14114_hbl10	11.78	2.36	1.13	0.10	0.02	96.9	1034
BC14114_hbl10	11.97	2.20	1.16	0.10	0.01	96.3	1032
BC14114_hbl10	11.82	2.26	1.13	0.11	0.02	97.3	1023
BC14114_hbl10	11.94	2.47	1.12	0.13	0.02	96.6	1038
BC14114_hbl10	12.02	2.24	1.13	0.04	0.01	96.9	1037
BC14114_hbl10	11.85	2.28	1.14	0.10	0.01	96.0	1038
BC14114_hbl10	11.85	2.44	0.97	0.09	0.01	96.4	1035
BC14114_hbl10	11.88	2.30	1.03	0.19	0.01	96.2	1010
BC14114_hbl10	11.88	2.45	0.98	0.10	0.01	98.1	1031
BC14114_hbl10	11.30	2.58	0.73	0.12	0.05	99.0	971
BC14114_hbl11	11.07	2.34	0.76	0.11	0.11	96.2	954
BC14114_hbl11	11.33	2.56	0.73	0.11	0.09	97.0	975
BC14114_hbl12	11.19	2.21	0.87	0.08	0.13	96.2	954
BC14114_hbl12	11.06	2.39	0.77	0.12	0.13	97.3	941
BC14114_hbl12	11.15	2.55	0.78	0.12	0.06	98.2	980
BC14114_hbl12	11.15	2.36	0.82	0.14	0.14	97.5	947
BC14114_hbl12	11.07	2.31	0.83	0.13	0.16	96.6	952

Table 8: NE Sumbawa amphibole analyses and thermobarometrical estimates. All analyses reported as wt.% unless otherwise stated. P-T-H_2O-fO_2 calculated using the formulations of Ridolfi et al. (2012).

SAMPLE	error (σest)	P (MPa)	Max error	ΔNNO	error (σest)	H2Omelt (wt.%)	error *
BC14114_hbl1	22	550	60	0.38	0.4	6.68	1.00
BC14114_hbl1	22	298	33	0.72	0.4	5.12	0.77
BC14114_hbl1	22	674	74	0.37	0.4	6.73	1.01
BC14114_hbl1	22	619	68	0.43	0.4	6.85	1.03
BC14114_hbl1	22	349	38	0.49	0.4	5.90	0.89
BC14114_hbl1	22	699	77	0.34	0.4	7.10	1.06
BC14114_hbl1	22	430	47	0.43	0.4	6.42	0.96
BC14114_hbl2	22	270	30	0.56	0.4	5.02	0.75
BC14114_hbl2	22	332	37	0.38	0.4	6.03	0.90
BC14114_hbl2	22	382	42	0.76	0.4	6.33	0.95
BC14114_hbl2	22	352	39	0.25	0.4	6.01	0.90
BC14114_hbl3	22	338	37	0.59	0.4	5.61	0.84
BC14114_hbl3	22	316	35	0.49	0.4	5.41	0.81
BC14114_hbl3	22	340	37	0.54	0.4	5.47	0.82
BC14114_hbl4	22	589	65	0.50	0.4	6.78	1.02
BC14114_hbl4	22	598	66	0.19	0.4	6.86	1.03
BC14114_hbl5	22	540	59	0.89	0.4	5.92	0.89
BC14114_hbl5	22	567	62	0.83	0.4	6.20	0.93
BC14114_hbl6	22	678	75	0.58	0.4	6.60	0.99
BC14114_hbl7	22	313	34	0.54	0.4	5.40	0.81
BC14114_hbl7	22	327	36	0.61	0.4	5.57	0.84
BC14114_hbl8	22	561	62	0.68	0.4	6.62	0.99
BC14114_hbl8	22	502	55	0.86	0.4	6.04	0.91
BC14114_hbl8	22	400	44	0.47	0.4	5.80	0.87
BC14114_hbl9	22	636	70	0.52	0.4	7.01	1.05
BC14114_hbl9	22	530	58	0.90	0.4	5.95	0.89
BC14114_hbl9	22	632	69	0.69	0.4	6.54	0.98
BC14114_hbl9	22	585	64	0.76	0.4	6.28	0.94
BC14114_hbl10	22	383	42	0.32	0.4	5.57	0.84
BC14114_hbl10	22	528	58	0.71	0.4	6.62	0.99
BC14114_hbl10	22	656	72	0.89	0.4	5.98	0.90
BC14114_hbl10	22	609	67	1.10	0.4	5.49	0.82
BC14114_hbl10	22	631	69	1.14	0.4	5.49	0.82
BC14114_hbl10	22	601	66	1.21	0.4	5.41	0.81
BC14114_hbl10	22	602	66	1.19	0.4	5.68	0.85
BC14114_hbl10	22	607	67	1.13	0.4	5.22	0.78
BC14114_hbl10	22	624	69	1.18	0.4	5.49	0.82
BC14114_hbl10	22	678	75	0.90	0.4	5.93	0.89
BC14114_hbl10	22	653	72	0.90	0.4	6.08	0.91
BC14114_hbl10	22	571	63	0.96	0.4	6.17	0.93
BC14114_hbl10	22	682	75	0.94	0.4	6.44	0.97
BC14114_hbl10	22	435	48	0.73	0.4	6.06	0.91
BC14114_hbl11	22	358	39	0.43	0.4	5.56	0.83
BC14114_hbl11	22	380	42	0.66	0.4	5.24	0.79
BC14114_hbl12	22	339	37	0.42	0.4	5.10	0.77
BC14114_hbl12	22	315	35	0.45	0.4	5.18	0.78
BC14114_hbl12	22	522	57	0.51	0.4	6.76	1.01
BC14114_hbl12	22	334	37	0.58	0.4	5.24	0.79
BC14114_hbl12	22	359	39	0.54	0.4	5.48	0.82

Table 8: NE Sumbawa amphibole analyses and thermobarometrical estimates. All analyses reported as wt.% unless otherwise stated. P-T-H_2O-fO_2 calculated using the formulations of Ridolfi et al. (2012).

SAMPLE	SiO_2	TiO_2	Al_2O_3	Cr_2O_3	FeO	MnO	MgO
BC14114_hbl12	41.64	2.75	11.32	0.00	13.33	0.34	12.75
BC14114_hbl12	42.03	2.73	11.63	0.02	12.84	0.39	12.96
BC14114_hbl12	42.31	2.80	10.90	0.01	13.27	0.32	13.09
BC14114_hbl12	41.06	2.76	11.93	0.00	13.79	0.35	12.71
BC14114_hbl12	40.67	2.73	12.67	0.00	13.16	0.31	13.03
BC14/129_Hbl1	40.55	2.47	11.40	0.00	13.49	0.29	12.67
BC14/129_Hbl1	40.86	2.19	11.42	0.05	13.58	0.28	12.78
BC14/129_Hbl1	41.15	2.18	11.33	0.00	13.56	0.28	12.64
BC14/129_Hbl1	40.74	2.16	11.54	0.00	13.86	0.24	12.48
BC14/129_Hbl1	40.09	2.25	12.08	0.02	14.01	0.29	12.30
BC14/129_Hbl1	39.52	2.25	12.44	0.02	14.20	0.27	11.95
BC14/129_Hbl1	39.30	2.31	12.75	0.03	14.15	0.25	12.02
BC14/129_Hbl1	39.67	2.37	12.49	0.02	14.23	0.28	11.99
BC14/129_Hbl1	40.59	2.29	11.56	0.00	13.52	0.26	12.84
BC14/129_Hbl2	39.89	2.47	12.22	0.02	13.52	0.31	12.46
BC14/129_Hbl2	39.44	2.28	12.89	0.00	13.98	0.29	11.87
BC14/129_Hbl2	39.58	2.16	13.03	0.00	13.88	0.24	12.12
BC14/129_Hbl2	39.40	2.16	13.11	0.02	13.95	0.30	12.06
BC14/129_Hbl2	39.41	2.16	13.26	0.00	14.08	0.25	11.98
BC14/129_Hbl2	39.48	2.06	12.98	0.01	13.78	0.28	12.11
BC14/129_Hbl2	39.32	2.23	12.90	0.00	13.98	0.27	11.94
BC14/129_Hbl2	40.35	2.30	11.90	0.00	13.57	0.34	12.51
BC14/129_Hbl2	40.04	2.44	12.63	0.05	13.52	0.27	12.39
BC14/129_Hbl3	40.31	2.25	11.56	0.00	14.05	0.29	12.45
BC14/129_Hbl3	39.97	2.40	12.07	0.00	14.14	0.26	12.16
BC14/129_Hbl3	39.54	2.27	12.48	0.00	14.17	0.23	12.08
BC14/129_Hbl3	40.02	2.21	11.77	0.02	14.01	0.27	12.43
BC14/129_Hbl1	40.38	2.32	12.32	0.00	13.19	0.23	12.73
BC14/129_Hbl1	39.67	2.24	12.96	0.00	14.05	0.28	11.94
BC14/129_Hbl1	39.59	2.11	12.53	0.00	14.18	0.29	12.07
BC14/129_Hbl2	39.75	2.18	12.58	0.00	13.99	0.29	12.03
BC14/129_Hbl2	39.20	2.15	13.31	0.00	13.97	0.30	11.91
BC14/129_Hbl2	39.67	2.12	13.19	0.02	13.48	0.23	12.16
BC14/129_Hbl2	39.58	2.16	13.08	0.00	13.72	0.28	12.02
BC14/129_Hbl2	39.72	2.18	12.87	0.00	13.90	0.25	11.94
BC14/129_Hbl2	39.98	2.24	12.41	0.00	14.03	0.27	12.02
BC14/129_Hbl2	40.61	2.30	11.36	0.01	13.48	0.28	12.83
BC14/129_Hbl2	40.02	2.31	12.39	0.01	13.94	0.33	12.08
BC14/129_Hbl2	40.47	2.25	11.72	0.01	14.02	0.28	12.24
BC14/129_Hbl3	40.02	2.24	11.84	0.00	13.50	0.30	12.72
BC14/129_Hbl5	39.95	2.16	11.93	0.01	13.81	0.26	12.48
BC14/129_Hbl4	39.05	2.34	12.61	0.03	14.49	0.26	11.93
BC14/129_Hbl4	39.12	2.23	12.75	0.00	14.11	0.28	12.01
BC14/129_Hbl4	39.92	2.30	12.05	0.00	13.63	0.28	12.57
BC14/129_Hbl6	40.10	2.30	11.71	0.00	13.75	0.28	12.52
BC14/129_Hbl6	39.25	2.15	13.87	0.00	13.66	0.27	12.04
BC14/129_Hbl6	40.81	2.28	11.49	0.00	13.75	0.23	12.65
BC14/129_Hbl6	40.88	2.33	11.57	0.01	13.70	0.30	12.57
BC14/129_Hbl6	40.93	2.26	11.51	0.00	13.56	0.24	12.80
BC14/129_Hbl6	40.88	2.18	12.23	0.01	13.20	0.28	12.45

Table 8: NE Sumbawa amphibole analyses and thermobarometrical estimates. All analyses reported as wt.% unless otherwise stated. P-T-H_2O-fO_2 calculated using the formulations of Ridolfi et al. (2012).

SAMPLE	CaO	Na_2O	K_2O	F	Cl	Total	T (°C)
BC14114_hbl12	11.16	2.35	0.79	0.13	0.15	96.7	949
BC14114_hbl12	11.16	2.41	0.85	0.08	0.14	97.2	952
BC14114_hbl12	11.04	2.49	0.82	0.11	0.12	97.3	938
BC14114_hbl12	11.23	2.42	0.90	0.09	0.10	97.3	968
BC14114_hbl12	11.46	2.42	0.61	0.09	0.06	97.2	988
BC14/129_Hbl1	11.52	2.33	1.15	0.14	0.08	96.1	969
BC14/129_Hbl1	11.64	2.28	1.06	0.29	0.04	96.5	965
BC14/129_Hbl1	11.58	2.25	1.12	0.08	0.06	96.2	958
BC14/129_Hbl1	11.59	2.27	1.09	0.20	0.06	96.2	965
BC14/129_Hbl1	11.51	2.28	1.12	0.32	0.05	96.3	979
BC14/129_Hbl1	11.49	2.38	1.13	0.15	0.07	95.9	990
BC14/129_Hbl1	11.50	2.38	1.09	0.19	0.08	96.0	999
BC14/129_Hbl1	11.61	2.42	1.11	0.14	0.06	96.4	993
BC14/129_Hbl1	11.52	2.38	1.04	0.22	0.05	96.3	971
BC14/129_Hbl2	11.45	2.43	1.09	0.17	0.08	96.1	988
BC14/129_Hbl2	11.56	2.34	1.02	0.18	0.07	95.9	998
BC14/129_Hbl2	11.61	2.43	1.00	0.14	0.03	96.2	1001
BC14/129_Hbl2	11.47	2.34	1.04	0.27	0.05	96.2	1001
BC14/129_Hbl2	11.54	2.35	1.04	0.11	0.04	96.2	1004
BC14/129_Hbl2	11.52	2.35	0.98	0.25	0.05	95.8	998
BC14/129_Hbl2	11.48	2.37	1.07	0.22	0.06	95.8	999
BC14/129_Hbl2	11.40	2.41	1.16	0.06	0.12	96.1	976
BC14/129_Hbl2	10.84	2.33	1.19	0.07	0.19	96.0	981
BC14/129_Hbl3	11.50	2.40	1.04	0.21	0.07	96.1	971
BC14/129_Hbl3	11.47	2.37	1.07	0.19	0.06	96.2	981
BC14/129_Hbl3	11.52	2.31	1.15	0.27	0.06	96.1	991
BC14/129_Hbl3	11.47	2.30	1.08	0.08	0.05	95.7	976
BC14/129_Hbl1	11.51	2.48	1.02	0.16	0.06	96.4	986
BC14/129_Hbl1	11.57	2.31	1.10	0.26	0.07	96.5	997
BC14/129_Hbl1	11.61	2.25	1.11	0.24	0.05	96.0	991
BC14/129_Hbl2	11.54	2.37	1.07	0.21	0.07	96.1	990
BC14/129_Hbl2	11.59	2.41	1.08	0.15	0.05	96.1	1009
BC14/129_Hbl2	11.62	2.34	1.04	0.23	0.04	96.1	1002
BC14/129_Hbl2	11.51	2.33	1.05	0.18	0.04	96.0	999
BC14/129_Hbl2	11.59	2.40	1.09	0.35	0.05	96.3	996
BC14/129_Hbl2	11.63	2.36	1.08	0.18	0.04	96.2	986
BC14/129_Hbl2	11.54	2.32	1.15	0.16	0.06	96.1	968
BC14/129_Hbl2	11.55	2.35	1.12	0.30	0.08	96.5	986
BC14/129_Hbl2	11.49	2.32	1.06	0.22	0.07	96.2	969
BC14/129_Hbl3	11.46	2.38	1.18	0.27	0.10	96.0	981
BC14/129_Hbl5	11.54	2.34	1.04	0.24	0.05	95.8	981
BC14/129_Hbl4	11.49	2.37	1.08	0.25	0.06	96.0	999
BC14/129_Hbl4	11.61	2.42	1.05	0.13	0.06	95.8	1003
BC14/129_Hbl4	11.59	2.34	1.10	0.23	0.07	96.1	986
BC14/129_Hbl6	11.58	2.29	1.03	0.23	0.05	95.8	976
BC14/129_Hbl6	11.32	2.38	1.02	0.26	0.06	96.3	1012
BC14/129_Hbl6	11.56	2.18	1.09	0.02	0.06	96.1	964
BC14/129_Hbl6	11.56	2.23	1.11	0.19	0.06	96.5	964
BC14/129_Hbl6	11.43	2.28	1.15	0.29	0.07	96.5	963
BC14/129_Hbl6	11.15	2.11	1.13	0.14	0.07	95.8	964

Table 8: NE Sumbawa amphibole analyses and thermobarometrical estimates. All analyses reported as wt.% unless otherwise stated. P-T-H_2O-fO_2 calculated using the formulations of Ridolfi et al. (2012).

SAMPLE	error (σest)	P (MPa)	Max error	ΔNNO	error (σest)	H2Omelt (wt.%)	error *
BC14114_hbl12	22	332	37	0.43	0.4	5.29	0.79
BC14114_hbl12	22	351	39	0.44	0.4	5.34	0.80
BC14114_hbl12	22	293	32	0.51	0.4	4.70	0.71
BC14114_hbl12	22	382	42	0.40	0.4	5.15	0.77
BC14114_hbl12	22	452	50	0.46	0.4	6.23	0.94
BC14/129_Hbl1	22	353	39	0.44	0.4	4.30	0.64
BC14/129_Hbl1	22	350	39	0.54	0.4	4.67	0.70
BC14/129_Hbl1	22	343	38	0.50	0.4	4.65	0.70
BC14/129_Hbl1	22	365	40	0.46	0.4	4.82	0.72
BC14/129_Hbl1	22	419	46	0.39	0.4	5.04	0.76
BC14/129_Hbl1	22	468	52	0.25	0.4	5.22	0.78
BC14/129_Hbl1	22	502	55	0.26	0.4	5.43	0.81
BC14/129_Hbl1	22	468	51	0.21	0.4	5.23	0.79
BC14/129_Hbl1	22	364	40	0.54	0.4	4.60	0.69
BC14/129_Hbl2	22	435	48	0.35	0.4	4.92	0.74
BC14/129_Hbl2	22	523	58	0.19	0.4	5.93	0.89
BC14/129_Hbl2	22	532	58	0.28	0.4	5.92	0.89
BC14/129_Hbl2	22	544	60	0.31	0.4	5.95	0.89
BC14/129_Hbl2	22	562	62	0.26	0.4	6.08	0.91
BC14/129_Hbl2	22	531	58	0.34	0.4	6.07	0.91
BC14/129_Hbl2	22	524	58	0.25	0.4	5.72	0.86
BC14/129_Hbl2	22	400	44	0.42	0.4	4.65	0.70
BC14/129_Hbl2	22	473	52	0.44	0.4	5.16	0.77
BC14/129_Hbl3	22	369	41	0.44	0.4	4.67	0.70
BC14/129_Hbl3	22	421	46	0.30	0.4	5.04	0.76
BC14/129_Hbl3	22	470	52	0.31	0.4	5.19	0.78
BC14/129_Hbl3	22	391	43	0.47	0.4	4.79	0.72
BC14/129_Hbl1	22	438	48	0.43	0.4	5.19	0.78
BC14/129_Hbl1	22	523	58	0.22	0.4	5.81	0.87
BC14/129_Hbl1	22	475	52	0.35	0.4	5.46	0.82
BC14/129_Hbl2	22	481	53	0.28	0.4	5.56	0.83
BC14/129_Hbl2	22	577	64	0.21	0.4	6.00	0.90
BC14/129_Hbl2	22	554	61	0.29	0.4	6.12	0.92
BC14/129_Hbl2	22	543	60	0.27	0.4	6.05	0.91
BC14/129_Hbl2	22	516	57	0.20	0.4	5.76	0.86
BC14/129_Hbl2	22	459	50	0.24	0.4	5.45	0.82
BC14/129_Hbl2	22	349	38	0.54	0.4	4.24	0.64
BC14/129_Hbl2	22	454	50	0.25	0.4	5.31	0.80
BC14/129_Hbl2	22	383	42	0.36	0.4	5.00	0.75
BC14/129_Hbl3	22	397	44	0.53	0.4	4.40	0.66
BC14/129_Hbl5	22	408	45	0.47	0.4	4.98	0.75
BC14/129_Hbl4	22	490	54	0.26	0.4	5.29	0.79
BC14/129_Hbl4	22	509	56	0.26	0.4	5.52	0.83
BC14/129_Hbl4	22	417	46	0.44	0.4	4.84	0.73
BC14/129_Hbl6	22	385	42	0.46	0.4	4.87	0.73
BC14/129_Hbl6	22	648	71	0.29	0.4	6.56	0.98
BC14/129_Hbl6	22	357	39	0.52	0.4	4.75	0.71
BC14/129_Hbl6	22	364	40	0.45	0.4	4.77	0.72
BC14/129_Hbl6	22	356	39	0.56	0.4	4.48	0.67
BC14/129_Hbl6	22	429	47	0.49	0.4	5.56	0.83

Table 8: NE Sumbawa amphibole analyses and thermobarometrical estimates. All analyses reported as wt.% unless otherwise stated. P-T-H_2O-fO_2 calculated using the formulations of Ridolfi et al. (2012).

SAMPLE	SiO_2	TiO_2	Al_2O_3	Cr_2O_3	FeO	MnO	MgO
BC14/129_Hbl6	41.14	2.21	11.27	0.02	13.61	0.30	12.61
BC14/129_Hbl6	40.97	2.26	11.37	0.04	13.76	0.26	12.64
BC14/129_Hbl6	39.95	2.34	12.31	0.00	14.02	0.22	12.23
BC14/129_Hbl6	39.98	2.37	12.41	0.00	14.05	0.23	12.04
BC14/129_Hbl6	40.23	2.36	12.38	0.00	13.94	0.26	12.07
BC14/129_Hbl6	39.84	2.29	12.72	0.00	14.01	0.28	12.08
BC14/129_Hbl6	39.93	2.25	12.89	0.00	13.92	0.29	11.94
BC14/129_Hbl7	38.72	2.31	13.77	0.01	13.82	0.25	11.78
BC14/129_Hbl7	39.11	2.11	13.31	0.00	13.52	0.22	12.11
BC14/129_Hbl7	39.13	2.16	13.61	0.04	13.76	0.30	12.12
BC14/129_Hbl7	40.91	2.38	11.44	0.01	13.48	0.31	12.90
BC14/129_Hbl5	40.21	2.32	11.67	0.00	13.67	0.24	12.59
BC14/129_Hbl5	39.91	2.17	12.35	0.00	13.83	0.29	12.26
BC14/129_Hbl5	39.51	2.17	12.84	0.00	13.96	0.26	12.10
BC14/129_Hbl5	39.19	2.24	12.95	0.00	13.94	0.30	11.98
BC14/130_Hbl1	40.50	2.57	12.02	0.00	13.17	0.25	12.65
BC14/130_Hbl1	40.18	2.62	12.27	0.01	12.87	0.30	12.55
BC14/130_Hbl1	40.38	2.46	12.34	0.03	12.12	0.28	12.96
BC14/130_Hbl1	39.66	2.56	13.54	0.02	11.14	0.21	13.47
BC14/130_Hbl1	39.86	2.55	12.74	0.00	12.62	0.26	12.65
BC14/130_Hbl2	40.01	2.67	12.24	0.03	13.72	0.35	12.02
BC14/130_Hbl2	40.25	2.64	12.53	0.02	13.88	0.29	12.24
BC14/130_Hbl2	40.23	2.71	12.41	0.03	13.26	0.34	12.51
BC14/130_Hbl2	39.54	2.71	13.06	0.03	12.52	0.22	12.54
BC14/130_Hbl2	39.75	2.58	13.59	0.00	12.08	0.27	12.51
BC14/130_Hbl2	39.40	2.57	13.65	0.03	12.38	0.25	12.76
BC14/130_Hbl2	39.76	2.61	13.78	0.04	12.35	0.24	12.59
BC14/130_Hbl2	39.36	2.66	13.60	0.00	12.20	0.27	12.71
BC14/130_Hbl2	40.68	2.45	11.50	0.00	13.36	0.27	12.95
BC14/130_Hbl5	42.49	2.42	9.57	0.00	13.35	0.28	13.03
BC14/130_Hbl5	40.61	2.65	11.34	0.00	14.24	0.30	12.15
BC14/130_Hbl6	40.38	2.54	11.51	0.00	14.03	0.33	12.34
BC14/130_Hbl6	39.16	2.40	13.08	0.00	14.65	0.36	11.66
BC14/130_Hbl6	39.19	2.27	13.28	0.05	14.24	0.33	11.61
BC14/130_Hbl6	40.19	2.56	11.67	0.00	13.86	0.33	12.28
BC14/130_Hbl8	40.33	2.66	11.78	0.00	13.50	0.31	12.57
BC14/130_Hbl8	39.35	2.40	12.78	0.00	14.39	0.35	11.65
BC14/130_Hbl8	39.77	2.36	12.97	0.00	14.21	0.42	11.46
BC14/130_Hbl9	41.11	2.61	11.66	0.02	13.54	0.40	12.68
BC14/130_Hbl9	39.99	2.64	12.09	0.00	13.64	0.36	12.16
BC14/130_Hbl9	40.43	2.71	11.27	0.01	13.69	0.32	12.46
BC14/130_Hbl10	39.41	2.59	12.72	0.00	14.21	0.31	11.59
BC14/130_Hbl10	39.56	2.56	12.48	0.00	14.69	0.32	11.65
BC14/130_Hbl10	39.42	2.70	12.29	0.01	14.63	0.31	11.64

Table 8: NE Sumbawa amphibole analyses and thermobarometrical estimates. All analyses reported as wt.% unless otherwise stated. P-T-H_2O-fO_2 calculated using the formulations of Ridolfi et al. (2012).

SAMPLE	CaO	Na_2O	K_2O	F	Cl	Total	T (°C)
BC14/129_Hbl6	11.39	2.19	1.20	0.31	0.08	96.3	953
BC14/129_Hbl6	11.42	2.12	1.12	0.28	0.06	96.3	957
BC14/129_Hbl6	11.49	2.29	1.14	0.29	0.06	96.3	985
BC14/129_Hbl6	11.44	2.33	1.03	0.12	0.05	96.1	983
BC14/129_Hbl6	11.45	2.26	1.05	0.24	0.06	96.3	979
BC14/129_Hbl6	11.59	2.32	1.03	0.26	0.06	96.5	992
BC14/129_Hbl6	11.49	2.31	1.07	0.33	0.05	96.5	991
BC14/129_Hbl7	11.56	2.47	1.03	0.21	0.06	96.0	1022
BC14/129_Hbl7	11.79	2.39	1.00	0.26	0.06	95.9	1014
BC14/129_Hbl7	11.59	2.47	1.04	0.17	0.05	96.4	1016
BC14/129_Hbl7	11.50	2.39	1.12	0.10	0.07	96.6	967
BC14/129_Hbl5	11.54	2.33	1.05	0.21	0.05	95.9	975
BC14/129_Hbl5	11.46	2.25	1.06	0.18	0.05	95.8	983
BC14/129_Hbl5	11.38	2.30	1.10	0.24	0.06	95.9	994
BC14/129_Hbl5	11.51	2.34	1.08	0.07	0.06	95.7	1002
BC14/130_Hbl1	11.68	2.49	0.99	0.18	0.07	96.6	984
BC14/130_Hbl1	11.56	2.38	1.04	0.08	0.07	95.9	988
BC14/130_Hbl1	11.84	2.26	1.10	0.20	0.07	96.0	993
BC14/130_Hbl1	11.91	2.55	0.72	0.16	0.03	96.0	1028
BC14/130_Hbl1	11.76	2.43	0.99	0.12	0.07	96.1	1003
BC14/130_Hbl2	11.63	2.19	0.94	0.15	0.08	96.0	984
BC14/130_Hbl2	11.66	2.59	0.82	0.12	0.06	97.1	992
BC14/130_Hbl2	11.58	2.45	0.86	0.14	0.04	96.6	990
BC14/130_Hbl2	11.69	2.57	0.78	0.11	0.04	95.8	1013
BC14/130_Hbl2	11.65	2.70	0.84	0.20	0.06	96.2	1018
BC14/130_Hbl2	11.97	2.45	0.77	0.16	0.03	96.4	1026
BC14/130_Hbl2	11.85	2.57	0.75	0.18	0.03	96.8	1022
BC14/130_Hbl2	11.75	2.64	0.74	0.15	0.04	96.1	1025
BC14/130_Hbl2	11.69	2.37	1.07	0.12	0.07	96.5	974
BC14/130_Hbl5	11.52	2.17	0.98	0.09	0.08	96.0	915
BC14/130_Hbl5	11.46	2.46	0.85	0.03	0.08	96.2	963
BC14/130_Hbl6	11.73	2.33	0.87	0.12	0.07	96.3	972
BC14/130_Hbl6	11.65	2.41	0.88	0.14	0.06	96.5	1005
BC14/130_Hbl6	11.64	2.41	0.93	0.16	0.07	96.2	1007
BC14/130_Hbl6	11.76	2.23	1.07	0.17	0.05	96.2	978
BC14/130_Hbl8	11.69	2.52	0.90	0.18	0.06	96.5	982
BC14/130_Hbl8	11.70	2.52	0.74	0.24	0.05	96.2	999
BC14/130_Hbl8	11.48	2.27	0.82	0.26	0.06	96.1	989
BC14/130_Hbl9	11.75	2.42	1.16	0.17	0.07	97.6	973
BC14/130_Hbl9	11.74	2.34	1.21	0.14	0.06	96.4	989
BC14/130_Hbl9	11.70	2.27	1.11	0.23	0.07	96.3	971
BC14/130_Hbl10	11.77	2.20	0.87	0.13	0.07	95.9	997
BC14/130_Hbl10	11.50	2.39	0.90	0.22	0.08	96.3	989
BC14/130_Hbl10	11.58	2.48	0.97	0.28	0.07	96.4	992

Table 8: NE Sumbawa amphibole analyses and thermobarometrical estimates. All analyses reported as wt.% unless otherwise stated. P-T-H_2O-fO_2 calculated using the formulations of Ridolfi et al. (2012).

SAMPLE	error (σest)	P (MPa)	Max error	ΔNNO	error (σest)	H2Omelt (wt.%)	error *
BC14/129_Hbl6	22	339	37	0.53	0.4	4.46	0.67
BC14/129_Hbl6	22	345	38	0.56	0.4	4.69	0.70
BC14/129_Hbl6	22	444	49	0.34	0.4	5.10	0.77
BC14/129_Hbl6	22	457	50	0.26	0.4	5.55	0.83
BC14/129_Hbl6	22	450	50	0.27	0.4	5.62	0.84
BC14/129_Hbl6	22	491	54	0.26	0.4	5.74	0.86
BC14/129_Hbl6	22	512	56	0.22	0.4	5.94	0.89
BC14/129_Hbl7	22	652	72	0.11	0.4	6.35	0.95
BC14/129_Hbl7	22	583	64	0.26	0.4	6.17	0.93
BC14/129_Hbl7	22	613	67	0.26	0.4	6.11	0.92
BC14/129_Hbl7	22	348	38	0.53	0.4	4.31	0.65
BC14/129_Hbl5	22	380	42	0.47	0.4	4.75	0.71
BC14/129_Hbl5	22	452	50	0.41	0.4	5.47	0.82
BC14/129_Hbl5	22	510	56	0.35	0.4	5.63	0.84
BC14/129_Hbl5	22	533	59	0.26	0.4	5.71	0.86
BC14/130_Hbl1	22	407	45	0.31	0.4	5.02	0.75
BC14/130_Hbl1	22	441	48	0.30	0.4	5.23	0.78
BC14/130_Hbl1	22	445	49	0.42	0.4	5.23	0.78
BC14/130_Hbl1	22	587	65	0.47	0.4	6.42	0.96
BC14/130_Hbl1	22	495	54	0.29	0.4	5.58	0.84
BC14/130_Hbl2	22	441	48	0.17	0.4	5.78	0.87
BC14/130_Hbl2	22	456	50	0.15	0.4	5.77	0.87
BC14/130_Hbl2	22	446	49	0.26	0.4	5.65	0.85
BC14/130_Hbl2	22	536	59	0.19	0.4	6.19	0.93
BC14/130_Hbl2	22	609	67	0.13	0.4	6.52	0.98
BC14/130_Hbl2	22	609	67	0.27	0.4	6.63	0.99
BC14/130_Hbl2	22	621	68	0.17	0.4	6.82	1.02
BC14/130_Hbl2	22	607	67	0.22	0.4	6.51	0.98
BC14/130_Hbl2	22	356	39	0.50	0.4	4.40	0.66
BC14/130_Hbl5	22	220	24	0.62	0.4	3.85	0.58
BC14/130_Hbl5	22	349	38	0.22	0.4	5.04	0.76
BC14/130_Hbl6	22	364	40	0.30	0.4	5.14	0.77
BC14/130_Hbl6	22	542	60	0.10	0.4	6.26	0.94
BC14/130_Hbl6	22	574	63	0.08	0.4	6.44	0.97
BC14/130_Hbl6	22	381	42	0.28	0.4	4.84	0.73
BC14/130_Hbl8	22	385	42	0.29	0.4	4.96	0.74
BC14/130_Hbl8	22	509	56	0.05	0.4	6.40	0.96
BC14/130_Hbl8	22	531	58	0.05	0.4	6.89	1.03
BC14/130_Hbl9	22	363	40	0.32	0.4	4.42	0.66
BC14/130_Hbl9	22	424	47	0.16	0.4	4.75	0.71
BC14/130_Hbl9	22	343	38	0.31	0.4	4.33	0.65
BC14/130_Hbl10	22	503	55	0.03	0.4	6.37	0.96
BC14/130_Hbl10	22	468	51	0.09	0.4	5.83	0.88
BC14/130_Hbl10	22	451	50	0.01	0.4	5.37	0.80

Table 8: NE Sumbawa amphibole analyses and thermobarometrical estimates. All analyses reported as wt.% unless otherwise stated. P-T-H_2O-fO_2 calculated using the formulations of Ridolfi et al. (2012).

SAMPLE	SiO_2	TiO_2	ZnO	Al_2O_3	Cr_2O_3	FeO	MnO	MgO
BC14106_cpx1	51.98	0.35		1.31		8.56	0.78	15.92
BC14106_cpx1	52.03	0.24		1.41		8.99	0.69	15.77
BC14106_cpx1	51.95	0.41		1.44		8.51	0.65	15.89
BC14106_cpx1	51.12	0.42		2.62		8.86	0.33	15.10
BC14106_cpx1	51.61	0.38		1.72		8.75	0.55	15.39
BC14106_cpx1	50.03	0.50		2.95		9.31	0.63	14.65
BC14106_cpx1	50.94	0.51		2.77		9.26	0.59	14.91
BC14106_cpx1	50.34	0.55		3.21		9.75	0.60	14.47
BC14106_cpx2	51.29	0.45		2.24		8.94	0.56	15.36
BC14106_cpx2	50.90	0.52		3.03		8.64	0.58	14.83
BC14106_cpx2	48.43	0.74		5.69		9.32	0.45	13.37
BC14106_cpx2	51.38	0.45		2.15		8.55	0.60	14.95
BC14106_cpx2	52.35	0.38		2.34		8.25	0.49	15.62
BC14106_cpx2	50.54	0.60		3.07		8.77	0.60	14.53
BC14106_cpx2	51.38	0.40		2.38		8.65	0.56	15.14
BC14106_cpx3	51.12	0.42		2.33		8.41	0.43	14.81
BC14106_cpx3	51.95	0.24		1.59		9.20	0.56	15.60
BC14106_cpx3	51.98	0.26		1.98		8.20	0.58	15.47
BC14106_cpx3	52.17	0.38		1.89		8.73	0.62	15.57
BC14106_cpx4	51.20	0.33		2.38		7.84	0.41	15.12
BC14106_cpx4	48.98	0.67		4.28		9.49	0.43	13.53
BC14106_cpx4	49.98	0.58		4.23		8.95	0.45	14.56
BC14106_cpx4	51.15	0.44		2.29		9.04	0.54	15.16
BC14106_cpx4	50.56	0.55		3.72		8.23	0.41	15.14
BC14106_cpx4	51.48	0.39		2.34		8.56	0.50	15.26
BC14106_cpx4	50.89	0.37		2.57		8.80	0.44	14.84
BC14106_cpx5	46.45	1.47		7.20		8.50	0.20	12.94
BC14106_cpx5	51.12	0.49		2.78		5.87	0.15	16.11
BC14106_cpx5	49.67	0.83		3.89		9.11	0.44	14.49
BC14106_cpx6	51.53	0.40		1.77		8.70	0.57	15.74
BC14106_cpx6	49.79	0.56		3.84		8.87	0.39	14.31
BC14106_cpx6	51.93	0.28		1.60		8.42	0.60	15.92
BC14106_cpx1	50.02	0.51		3.55		8.51	0.33	14.10
BC14106_cpx1	49.92	0.49		3.82		7.97	0.27	14.12
BC14106_cpx1	49.51	0.53		3.91		8.43	0.35	13.60
BC14106_cpx1	49.01	0.76		4.98		8.44	0.22	14.14
BC14106_cpx2	50.32	0.54		3.14		9.68	0.51	14.33
BC14106_cpx2	50.27	0.41		3.11		8.99	0.48	14.37
BC14106_cpx2	50.78	0.49		3.39		10.02	0.64	15.13
BC14106_cpx2	52.06	0.40		1.63		9.80	0.51	15.65
BC14106_cpx2	50.34	0.57		3.28		9.35	0.52	14.30
BC14106_cpx2	48.84	0.72		5.00		9.00	0.38	13.35
BC14111_Cpx1	51.29	0.51		2.06		9.74	0.54	15.29
BC14111_Cpx1	50.72	0.49		2.73		9.15	0.46	14.87
BC14111_Cpx1	52.48	0.41		2.10		9.89	0.50	15.43
BC14111_Cpx1	51.98	0.48		1.89		9.00	0.49	15.85
BC14111_Cpx1	51.35	0.40		2.01		9.06	0.51	15.45
BC14111_Cpx1	50.69	0.50		2.62		9.67	0.56	14.71

Table 9: Electron microprobe analyses of pyroxenes from NE Sumbawa. All values reported as wt.%.

SAMPLE	CaO	BaO	Na_2O	K_2O	P_2O_5	SO_3	Cl	F	TOTAL
BC14106_cpx1	19.83		0.30	0.00					99.0
BC14106_cpx1	20.16		0.31	0.00					99.6
BC14106_cpx1	19.73		0.27	0.00					98.8
BC14106_cpx1	20.73		0.30	0.00					99.5
BC14106_cpx1	20.18		0.34	0.00					98.9
BC14106_cpx1	19.62		0.39	0.00					98.1
BC14106_cpx1	20.16		0.36	0.00					99.5
BC14106_cpx1	19.12		0.39	0.00					98.4
BC14106_cpx2	20.03		0.35	0.00					99.2
BC14106_cpx2	19.94		0.34	0.00					98.8
BC14106_cpx2	19.68		0.38	0.03					98.1
BC14106_cpx2	20.53		0.31	0.00					98.9
BC14106_cpx2	20.24		0.31	0.01					100.0
BC14106_cpx2	20.29		0.36	0.00					98.8
BC14106_cpx2	20.27		0.34	0.00					99.1
BC14106_cpx3	20.80		0.30	0.00					98.6
BC14106_cpx3	19.39		0.32	0.01					98.9
BC14106_cpx3	20.14		0.32	0.01					98.9
BC14106_cpx3	19.79		0.41	0.00					99.6
BC14106_cpx4	20.90		0.31	0.00					98.5
BC14106_cpx4	20.37		0.35	0.01					98.1
BC14106_cpx4	20.20		0.33	0.01					99.3
BC14106_cpx4	19.96		0.35	0.01					98.9
BC14106_cpx4	20.27		0.23	0.01					99.1
BC14106_cpx4	20.25		0.31	0.00					99.1
BC14106_cpx4	20.33		0.43	0.01					98.7
BC14106_cpx5	21.34		0.40	0.00					98.5
BC14106_cpx5	21.78		0.20	0.01					98.5
BC14106_cpx5	20.16		0.37	0.00					99.0
BC14106_cpx6	19.83		0.33	0.00					98.9
BC14106_cpx6	20.44		0.35	0.00					98.6
BC14106_cpx6	20.02		0.28	0.01					99.1
BC14106_cpx1	21.69		0.43	0.00					99.2
BC14106_cpx1	21.64		0.41	0.01					98.7
BC14106_cpx1	21.83		0.43	0.01					98.6
BC14106_cpx1	21.31		0.31	0.01					99.2
BC14106_cpx2	19.52		0.40	0.02					98.5
BC14106_cpx2	20.31		0.42	0.00					98.4
BC14106_cpx2	18.64		0.43	0.02					99.6
BC14106_cpx2	19.17		0.29	0.01					99.6
BC14106_cpx2	19.97		0.41	0.01					98.8
BC14106_cpx2	21.10		0.44	0.01					98.8
BC14111_Cpx1	19.44		0.36	0.00					99.2
BC14111_Cpx1	19.60		0.39	0.01					98.4
BC14111_Cpx1	19.42		0.41	0.01					100.6
BC14111_Cpx1	19.56		0.38	0.00					99.6
BC14111_Cpx1	19.97		0.29	0.00					99.0
BC14111_Cpx1	19.70		0.44	0.00					98.9

Table 9: Electron microprobe analyses of pyroxenes from NE Sumbawa. All values reported as wt.%.

SAMPLE	SiO_2	TiO_2	ZnO	Al_2O_3	Cr_2O_3	FeO	MnO	MgO
BC14111_Cpx1	51.43	0.49		2.38		10.87	0.51	14.30
BC14114_cpx1	51.38	0.41		2.25		8.17	0.51	14.48
BC14114_cpx1	51.14	0.46		2.63		7.68	0.48	14.01
BC14114_cpx1	50.82	0.44		2.69		7.83	0.57	13.94
BC14114_cpx1	51.16	0.43		2.41		7.76	0.48	14.17
BC14114_cpx1	51.26	0.45		2.49		8.34	0.42	14.10
BC14114_cpx1	51.24	0.60		2.50		8.26	0.50	13.99
BC14114_cpx1	51.69	0.40		2.07		7.72	0.52	15.28
BC14114_cpx1	49.50	0.72		4.41		8.97	0.45	13.08
BC14114_cpx1	51.57	0.41		2.21		7.74	0.56	14.27
BC14114_cpx1	50.93	0.48		2.72		8.14	0.51	14.17
BC14114_cpx1	47.83	0.86		5.92		8.68	0.26	12.78
BC14114_cpx1	51.57	0.52		2.63		7.81	0.42	14.24
BC14114_cpx1	50.16	0.69		3.71		8.52	0.28	13.87
BC14114_cpx2	51.07	0.56		3.28		8.05	0.25	14.37
BC14114_cpx2	51.09	0.50		2.55		8.07	0.50	14.34
BC14114_cpx2	50.74	0.53		2.74		7.81	0.28	14.52
BC14114_cpx2	50.48	0.68		3.42		7.85	0.26	14.10
BC14114_cpx3	50.00	0.59		3.46		8.67	0.34	13.90
BC14114_cpx3	50.13	0.54		3.29		8.22	0.29	14.00
BC14114_cpx3	49.65	0.51		3.26		8.61	0.28	13.91
BC14114_cpx3	49.53	0.74		4.11		9.35	0.29	13.48
BC14114_cpx3	49.82	0.53		3.63		9.28	0.44	12.74
BC14106_cpx1	47.86	0.92		5.88		10.17	0.37	13.24
BC14106_cpx1	47.98	0.86		5.56		9.97	0.44	12.84
BC14106_cpx2	51.70	0.39		2.10		8.35	0.53	15.35
BC14106_cpx2	50.71	0.40		2.95		8.13	0.52	15.26
BC14106_cpx2	51.27	0.33		1.61		8.38	0.62	15.20
BC14106_cpx2	51.79	0.32		1.39		7.93	0.64	15.64
BC14106_cpx2	51.91	0.30		1.62		8.58	0.62	15.68
BC14106_cpx2	51.81	0.33		1.63		7.81	0.57	15.36
BC14106_cpx2	51.00	0.38		1.88		8.61	0.46	15.63
BC14106_cpx2	51.61	0.38		1.58		8.11	0.63	15.54
BC14106_opx1	53.02	0.17		0.98	0.00	18.32	0.84	24.22
BC14106_opx2	52.79	0.19		0.82	0.00	17.49	1.07	24.97
BC14106_opx2	52.26	0.21		1.62	0.00	17.34	1.06	24.59
BC14106_opx2	53.44	0.22		1.64	0.00	17.62	0.98	24.72
BC14106_opx2	52.15	0.22		1.44	0.00	17.44	1.03	24.38
BC14/130_Cpx1	51.30	0.27	0.01	1.68	0.00	7.37	0.37	14.23
BC14/130_Cpx1	50.57	0.49	0.07	2.83	0.00	7.78	0.41	13.89
BC14/130_Cpx1	49.86	0.67	0.04	3.58	0.03	7.91	0.40	13.44
BC14/130_Cpx1	50.27	0.58	0.00	2.75	0.00	7.04	0.29	13.87
BC14/130_Cpx1	51.18	0.51	0.00	2.09	0.00	7.44	0.34	14.13
BC14/130_Cpx1	50.88	0.49	0.04	2.41	0.00	7.69	0.41	14.13
BC14/130_Cpx1	50.82	0.42	0.03	2.42	0.00	7.81	0.35	14.01
BC14/130_Cpx1	50.58	0.47	0.00	2.58	0.00	7.95	0.43	13.84
BC14/130_Cpx1	50.83	0.39	0.03	2.17	0.00	7.59	0.45	14.02
BC14/130_Cpx1	50.45	0.45	0.02	2.51	0.00	7.64	0.36	13.97

Table 9: Electron microprobe analyses of pyroxenes from NE Sumbawa. All values reported as wt.%.

SAMPLE	CaO	BaO	Na_2O	K_2O	P_2O_5	SO_3	Cl	F	TOTAL
BC14111_Cpx1	18.59		0.43	0.05					99.0
BC14114_cpx1	22.08		0.37	0.01					99.7
BC14114_cpx1	22.15		0.45	0.00					99.0
BC14114_cpx1	21.83		0.37	0.00					98.5
BC14114_cpx1	22.06		0.42	0.01					98.9
BC14114_cpx1	22.09		0.44	0.00					99.6
BC14114_cpx1	21.96		0.38	0.01					99.4
BC14114_cpx1	21.45		0.32	0.00					99.4
BC14114_cpx1	21.59		0.44	0.00					99.2
BC14114_cpx1	21.86		0.45	0.00					99.1
BC14114_cpx1	21.90		0.40	0.00					99.3
BC14114_cpx1	21.96		0.39	0.00					98.7
BC14114_cpx1	21.92		0.41	0.00					99.5
BC14114_cpx1	22.31		0.28	0.00					99.8
BC14114_cpx2	22.06		0.30	0.00					99.9
BC14114_cpx2	21.58		0.45	0.03					99.1
BC14114_cpx2	22.43		0.28	0.00					99.3
BC14114_cpx2	22.08		0.28	0.01					99.2
BC14114_cpx3	21.35		0.33	0.00					98.6
BC14114_cpx3	21.68		0.32	0.00					98.5
BC14114_cpx3	21.77		0.25	0.00					98.2
BC14114_cpx3	21.59		0.37	0.00					99.5
BC14114_cpx3	22.32		0.40	0.00					99.2
BC14106_cpx1	20.25		0.31	0.01					99.0
BC14106_cpx1	20.78		0.38	0.01					98.8
BC14106_cpx2	20.84		0.39	0.00					99.6
BC14106_cpx2	19.37		0.28	0.00					97.7
BC14106_cpx2	19.87		0.29	0.01					97.6
BC14106_cpx2	20.53		0.31	0.01					98.6
BC14106_cpx2	19.64		0.35	0.01					98.7
BC14106_cpx2	20.65		0.37	0.00					98.6
BC14106_cpx2	19.38		0.31	0.01					97.7
BC14106_cpx2	20.02		0.29	0.00					98.2
BC14106_opx1	1.56		0.03	0.01		0.03	0.02	0.00	99.19
BC14106_opx2	1.45		0.02	0.00		0.00	0.00	0.01	98.81
BC14106_opx2	1.84		0.03	0.00		0.00	0.02	0.00	98.97
BC14106_opx2	1.66		0.10	0.02		0.00	0.00	0.00	100.41
BC14106_opx2	1.73		0.04	0.00		0.00	0.00	0.00	98.41
BC14/130_Cpx1	23.00	0.01	0.43	0.01	0.00	0.00	0.00	0.00	98.7
BC14/130_Cpx1	23.02	0.02	0.57	0.00	0.00	0.00	0.00	0.00	99.6
BC14/130_Cpx1	23.11	0.02	0.46	0.00	0.00	0.00	0.00	0.00	99.5
BC14/130_Cpx1	23.36	0.00	0.39	0.00	0.00	0.01	0.00	0.00	98.6
BC14/130_Cpx1	23.00	0.00	0.54	0.00	0.00	0.01	0.01	0.00	99.3
BC14/130_Cpx1	23.02	0.00	0.44	0.00	0.00	0.00	0.00	0.00	99.5
BC14/130_Cpx1	22.95	0.00	0.43	0.00	0.01	0.00	0.00	0.00	99.3
BC14/130_Cpx1	22.73	0.02	0.56	0.01	0.03	0.00	0.00	0.00	99.2
BC14/130_Cpx1	22.86	0.00	0.42	0.00	0.00	0.00	0.00	0.00	98.8
BC14/130_Cpx1	23.01	0.00	0.34	0.00	0.01	0.00	0.00	0.00	98.8

Table 9: Electron microprobe analyses of pyroxenes from NE Sumbawa. All values reported as wt.%.

SAMPLE	SiO_2	TiO_2	ZnO	Al_2O_3	Cr_2O_3	FeO	MnO	MgO
BC14/130_Cpx2	50.33	0.60	0.00	2.99	0.02	8.30	0.38	13.59
BC14/130_Cpx2	50.62	0.55	0.08	2.99	0.01	7.37	0.32	13.93
BC14/130_Cpx2	49.76	0.59	0.00	3.65	0.04	7.12	0.28	14.07
BC14/130_Cpx2	51.30	0.27	0.00	2.08	0.00	6.99	0.29	14.36
BC14/130_Cpx2	50.70	0.36	0.04	2.34	0.00	7.23	0.34	14.16
BC14/130_Cpx2	50.13	0.52	0.11	2.74	0.01	7.66	0.34	13.89
BC14/130_Cpx2	50.92	0.54	0.00	2.73	0.01	7.78	0.37	13.85
BC14/130_Cpx2	51.23	0.36	0.01	1.80	0.02	8.06	0.34	13.77
BC14/130_Cpx2	50.79	0.44	0.05	2.39	0.00	7.83	0.38	13.83
BC14/130_Cpx2	51.09	0.37	0.00	1.95	0.02	8.11	0.41	14.19
BC14/130_Cpx3	50.06	0.51	0.03	2.78	0.02	7.91	0.46	13.66
BC14/130_Cpx3	50.27	0.56	0.02	3.16	0.00	8.36	0.44	13.66
BC14/130_Cpx3	49.60	0.54	0.00	3.06	0.01	7.94	0.49	13.47
BC14/130_Cpx3	49.36	0.58	0.06	3.14	0.00	7.93	0.42	13.29
BC14/130_Cpx3	49.53	0.68	0.02	3.31	0.01	8.36	0.41	13.21
BC14/130_Cpx3	49.97	0.63	0.00	3.22	0.00	8.57	0.44	13.56

Table 9: Electron microprobe analyses of pyroxenes from NE Sumbawa. All values reported as wt.%.

SAMPLE	CaO	BaO	Na_2O	K_2O	P_2O_5	SO_3	Cl	F	TOTAL
BC14/130_Cpx2	22.88	0.01	0.57	0.01	0.00	0.00	0.00	0.00	99.7
BC14/130_Cpx2	23.19	0.01	0.44	0.00	0.00	0.00	0.01	0.02	99.5
BC14/130_Cpx2	23.30	0.00	0.24	0.02	0.00	0.00	0.01	0.01	99.1
BC14/130_Cpx2	23.23	0.00	0.42	0.01	0.00	0.00	0.02	0.00	99.0
BC14/130_Cpx2	23.28	0.00	0.38	0.01	0.00	0.00	0.00	0.00	98.8
BC14/130_Cpx2	22.71	0.06	0.54	0.00	0.00	0.02	0.00	0.00	98.7
BC14/130_Cpx2	22.85	0.01	0.47	0.01	0.00	0.01	0.01	0.00	99.6
BC14/130_Cpx2	22.76	0.00	0.53	0.00	0.01	0.01	0.00	0.05	98.9
BC14/130_Cpx2	22.84	0.00	0.47	0.00	0.00	0.01	0.01	0.00	99.0
BC14/130_Cpx2	22.77	0.01	0.47	0.01	0.00	0.00	0.00	0.00	99.4
BC14/130_Cpx3	22.96	0.00	0.41	0.00	0.00	0.00	0.00	0.03	98.8
BC14/130_Cpx3	22.88	0.00	0.38	0.00	0.01	0.00	0.01	0.00	99.8
BC14/130_Cpx3	22.82	0.01	0.44	0.00	0.00	0.01	0.01	0.00	98.4
BC14/130_Cpx3	22.84	0.00	0.45	0.00	0.01	0.00	0.00	0.00	98.1
BC14/130_Cpx3	22.88	0.00	0.42	0.01	0.02	0.00	0.00	0.00	98.9
BC14/130_Cpx3	22.78	0.00	0.46	0.00	0.00	0.00	0.00	0.00	99.6

Table 9: Electron microprobe analyses of pyroxenes from NE Sumbawa. All values reported as wt.%.

SAMPLE	SiO_2	TiO_2	ZnO	Al_2O_3	Cr_2O_3	FeO	MnO	MgO
BC14106_plag1	52.62	0.04		29.28		0.56		0.02
BC14106_plag1	54.92	0.02		27.84		0.36		0.03
BC14106_plag1	53.61	0.03		28.30		0.53		0.05
BC14106_plag1	54.74	0.07		27.03		1.59		0.95
BC14106_plag1	52.44	0.07		29.67		0.60		0.04
BC14106_plag1	51.67	0.12		30.12		0.69		0.05
BC14106_plag2	55.39	0.04		28.00		0.41		0.05
BC14106_plag2	53.10	0.03		28.73		0.51		0.05
BC14106_plag2	53.23	0.03		28.81		0.40		0.05
BC14106_plag3	53.32	0.05		28.63		0.39		0.03
BC14106_plag3	53.05	0.07		28.58		0.34		0.05
BC14106_plag3	53.42	0.02		28.79		0.39		0.03
BC14106_plag3	52.99	0.04		29.19		0.49		0.03
BC14106_plag3	52.59	0.03		29.01		0.30		0.06
BC14106_plag3	51.89	0.03		30.46		0.36		0.04
BC14106_plag3	53.32	0.02		28.44		0.32		0.03
BC14106_plag3	53.60	0.08		28.73		0.38		0.05
BC14106_plag3	53.67	0.03		28.72		0.38		0.05
BC14106_plag3	53.24	0.06		29.35		0.42		0.04
BC14106_plag3	52.12	0.05		29.92		0.40		0.05
BC14106_plag3	54.36	0.07		28.24		0.32		0.05
BC14106_plag3	54.13	0.03		29.14		0.43		0.03
BC14106_plag3	54.39	0.06		28.77		0.32		0.05
BC14106_plag3	54.16	0.06		28.67		0.36		0.04
BC14106_plag3	55.04	0.05		28.48		0.40		0.05
BC14106_plag3	52.96	0.02		29.15		0.26		0.04
BC14106_plag3	53.88	0.04		28.75		0.42		0.05
BC14106_plag3	53.86	0.04		28.37		0.35		0.05
BC14106_plag3	53.73	0.04		28.80		0.42		0.03
BC14106_plag3	54.51	0.02		28.38		0.29		0.02
BC14106_plag3	54.07	0.07		27.83		0.35		0.05
BC14106_plag3	54.61	0.03		28.05		0.26		0.06
BC14106_plag3	52.52	0.02		29.26		0.39		0.02
BC14106_plag4	55.19	0.01		27.60		0.46		0.04
BC14106_plag4	54.60	0.04		28.24		0.62		0.06
BC14106_plag4	54.69	0.04		28.47		0.45		0.05
BC14106_plag4	53.21	0.07		28.84		0.43		0.04
BC14106_plag4	54.09	0.00		28.09		0.41		0.06
BC14106_plag4	52.14	0.07		30.52		0.63		0.11
BC14106_plag4	53.04	0.08		28.98		0.43		0.04
BC14106_plag4	54.98	0.05		28.11		0.58		0.05
BC14106_plag4	54.86	0.05		27.76		0.39		0.06
BC14106_plag5	53.35	0.07		28.65		0.57		0.06
BC14106_plag5	50.90	0.02		30.22		0.43		0.06
BC14106_plag5	52.94	0.03		29.18		0.41		0.06
BC14106_plag5	52.20	0.04		29.23		0.37		0.04
BC14106_plag5	54.99	0.05		27.71		0.43		0.05
BC14106_plag6	50.39	0.02		30.55		0.55		0.07
BC14106_plag6	48.85	0.03		32.41		0.51		0.03

Table 10: Electron microprobe plagioclase analyses from NE Sumbawa. All values reported as wt.%.

SAMPLE	CaO	BaO	Na_2O	K_2O	P_2O_5	SO_3	Cl	F	TOTAL
BC14106_plag1	11.47		4.64	0.38					99.0
BC14106_plag1	9.85		5.52	0.46					99.0
BC14106_plag1	10.50		5.22	0.43					98.7
BC14106_plag1	9.15		5.58	0.45					99.6
BC14106_plag1	12.09		4.33	0.43					99.7
BC14106_plag1	10.74		4.84	0.49					98.7
BC14106_plag2	9.50		5.68	0.44					99.5
BC14106_plag2	10.93		4.98	0.34					98.7
BC14106_plag2	10.91		4.94	0.32					98.7
BC14106_plag3	10.80		5.26	0.33					98.8
BC14106_plag3	10.52		5.19	0.34					98.1
BC14106_plag3	10.70		5.27	0.32					98.9
BC14106_plag3	10.97		5.15	0.30					99.2
BC14106_plag3	11.20		5.02	0.27					98.5
BC14106_plag3	11.25		4.76	0.28					99.1
BC14106_plag3	10.73		5.12	0.31					98.3
BC14106_plag3	10.60		5.25	0.32					99.0
BC14106_plag3	10.64		5.27	0.33					99.1
BC14106_plag3	11.26		4.92	0.29					99.6
BC14106_plag3	11.88		4.47	0.25					99.1
BC14106_plag3	10.26		5.53	0.32					99.1
BC14106_plag3	10.76		5.31	0.30					100.1
BC14106_plag3	10.62		5.44	0.31					100.0
BC14106_plag3	10.41		5.49	0.32					99.5
BC14106_plag3	10.28		5.66	0.32					100.3
BC14106_plag3	11.03		4.96	0.30					98.7
BC14106_plag3	10.44		5.24	0.32					99.1
BC14106_plag3	10.56		5.26	0.31					98.8
BC14106_plag3	10.67		5.14	0.31					99.1
BC14106_plag3	10.05		5.66	0.36					99.3
BC14106_plag3	9.85		5.67	0.39					98.3
BC14106_plag3	9.93		5.67	0.37					99.0
BC14106_plag3	11.14		4.85	0.29					98.5
BC14106_plag4	9.41		5.81	0.39					98.9
BC14106_plag4	9.68		5.68	0.38					99.3
BC14106_plag4	10.41		5.53	0.31					100.0
BC14106_plag4	10.88		5.07	0.27					98.8
BC14106_plag4	9.68		5.90	0.36					98.6
BC14106_plag4	10.06		4.95	0.31					98.8
BC14106_plag4	11.01		4.86	0.27					98.7
BC14106_plag4	10.00		5.69	0.33					99.8
BC14106_plag4	10.03		5.48	0.34					99.0
BC14106_plag5	10.76		5.23	0.33					99.0
BC14106_plag5	12.43		4.04	0.24					98.3
BC14106_plag5	11.19		5.00	0.32					99.1
BC14106_plag5	11.42		4.71	0.30					98.3
BC14106_plag5	9.41		5.79	0.42					98.9
BC14106_plag6	13.20		3.43	0.52					98.7
BC14106_plag6	14.56		2.94	0.16					99.5

Table 10: Electron microprobe plagioclase analyses from NE Sumbawa. All values reported as wt.%.

SAMPLE	SiO_2	TiO_2	ZnO	Al_2O_3	Cr_2O_3	FeO	MnO	MgO
BC14106_plag6	49.86	0.01		31.06		0.51		0.05
BC14106_plag6	55.33	0.08		26.55		0.85		0.16
BC14106_plag6	49.49	0.05		31.68		0.46		0.04
BC14106_plag6	52.70	0.06		28.52		0.77		0.13
BC14106_plag6	55.72	0.15		25.93		1.16		0.22
BC14106_plag6	50.84	0.02		30.45		0.38		0.06
BC14114_plag1	45.74	0.00		34.70		0.56		0.00
BC14114_plag1	46.33	0.00		34.59		0.48		0.03
BC14114_plag1	46.14	0.01		35.54		0.52		0.03
BC14114_plag2	48.82	0.02		32.08		0.41		0.04
BC14114_plag2	48.16	0.03		32.88		0.29		0.03
BC14114_plag2	48.77	0.03		32.31		0.42		0.06
BC14114_plag3	49.66	0.03		31.23		0.52		0.09
BC14114_plag3	48.19	0.01		31.81		0.41		0.04
BC14114_plag3	47.69	0.04		32.39		0.47		0.05
BC14114_plag3	51.44	0.05		31.08		0.53		0.10
BC14114_plag4	52.58	0.03		29.76		0.56		0.04
BC14114_plag4	53.78	0.00		29.53		0.50		0.02
BC14114_plag4	51.75	0.02		30.00		0.41		0.05
BC14114_plag4	54.16	0.02		28.52		0.32		0.07
BC14114_plag4	52.27	0.03		29.21		0.46		0.08
BC14114_plag5	51.80	0.05		30.00		0.80		0.26
BC14114_plag5	50.63	0.00		31.14		0.51		0.04
BC14114_plag5	51.71	0.01		30.20		0.48		0.04
BC14114_plag5	49.60	0.05		31.62		0.45		0.05
BC14114_plag6	52.10	0.02		29.98		0.40		0.02
BC14114_plag6	51.87	0.05		30.07		0.39		0.03
BC14114_plag6	51.01	0.02		30.66		0.33		0.04
BC14114_plag6	50.21	0.05		31.04		0.30		0.04
BC14114_plag6	50.28	0.01		31.11		0.46		0.05
BC14114_plag6	50.99	0.00		31.49		0.35		0.05
BC14114_plag6	50.33	0.00		30.75		0.40		0.04
BC14114_plag6	50.48	0.04		30.60		0.39		0.05
BC14114_plag6	51.79	0.01		31.87		0.47		0.05
BC14114_plag6	50.04	0.01		31.06		0.40		0.03
BC14114_plag6	50.88	0.04		30.68		0.42		0.03
BC14114_plag6	51.89	0.00		30.21		0.43		0.07
BC14114_plag6	50.21	0.02		31.36		0.66		0.03
BC14114_plag6	52.66	0.02		29.61		0.50		0.03
BC14114_plag7	48.03	0.02		32.90		0.66		0.06
BC14114_plag7	48.21	0.03		32.43		0.56		0.06
BC14114_plag7	48.35	0.03		32.65		0.54		0.04
BC14114_plag7	49.60	0.04		32.29		0.37		0.08
BC14114_plag7	48.72	0.04		34.04		0.48		0.07
BC14114_plag7	48.22	0.04		32.29		0.50		0.07
BC14114_plag7	48.32	0.03		32.30		0.37		0.05
BC14114_plag7	50.19	0.00		33.96		0.49		0.06
BC14114_plag7	50.81	0.02		30.01		0.55		0.07
BC14114_plag7	50.58	0.03		30.50		0.52		0.05

Table 10: Electron microprobe plagioclase analyses from NE Sumbawa. All values reported as wt.%.

SAMPLE	CaO	BaO	Na_2O	K_2O	P_2O_5	SO_3	Cl	F	TOTAL
BC14106_plag6	13.82		3.02	0.48					98.8
BC14106_plag6	9.92		4.26	1.84					99.0
BC14106_plag6	14.09		3.35	0.16					99.3
BC14106_plag6	11.62		3.52	1.30					98.6
BC14106_plag6	9.50		4.14	2.01					98.8
BC14106_plag6	12.73		3.94	0.20					98.6
BC14114_plag1	17.17		1.53	0.03					99.7
BC14114_plag1	16.83		1.71	0.05					100.0
BC14114_plag1	17.25		1.37	0.05					100.9
BC14114_plag2	14.52		3.08	0.10					99.1
BC14114_plag2	15.22		2.63	0.08					99.3
BC14114_plag2	14.84		2.97	0.12					99.5
BC14114_plag3	13.55		3.29	0.12					98.5
BC14114_plag3	14.49		3.07	0.10					98.1
BC14114_plag3	15.34		2.58	0.07					98.6
BC14114_plag3	12.75		4.08	0.13					100.1
BC14114_plag4	11.60		4.65	0.19					99.4
BC14114_plag4	11.04		5.23	0.22					100.3
BC14114_plag4	10.90		4.87	0.18					98.2
BC14114_plag4	10.10		5.69	0.21					99.1
BC14114_plag4	11.51		4.74	0.20					98.5
BC14114_plag5	12.14		4.25	0.17					99.5
BC14114_plag5	13.40		3.82	0.13					99.7
BC14114_plag5	12.31		4.41	0.15					99.3
BC14114_plag5	13.95		3.42	0.11					99.2
BC14114_plag6	12.15		4.43	0.14					99.2
BC14114_plag6	12.20		4.43	0.13					99.2
BC14114_plag6	13.00		4.07	0.12					99.3
BC14114_plag6	13.37		3.88	0.10					99.0
BC14114_plag6	13.39		3.73	0.10					99.1
BC14114_plag6	13.26		3.77	0.11					100.0
BC14114_plag6	13.39		3.71	0.10					98.7
BC14114_plag6	13.15		3.86	0.11					98.7
BC14114_plag6	13.31		4.02	0.11					101.6
BC14114_plag6	13.29		3.77	0.11					98.7
BC14114_plag6	12.74		4.03	0.11					98.9
BC14114_plag6	12.04		4.64	0.12					99.4
BC14114_plag6	13.74		3.71	0.19					99.9
BC14114_plag6	11.71		4.70	0.15					99.4
BC14114_plag7	15.04		2.59	0.08					99.4
BC14114_plag7	14.82		2.87	0.08					99.1
BC14114_plag7	15.15		2.78	0.08					99.6
BC14114_plag7	14.28		3.14	0.08					99.9
BC14114_plag7	15.46		2.62	0.06					101.5
BC14114_plag7	14.90		2.85	0.08					98.9
BC14114_plag7	14.94		2.72	0.07					98.8
BC14114_plag7	14.67		2.98	0.07					102.4
BC14114_plag7	12.79		4.08	0.13					98.5
BC14114_plag7	12.84		3.93	0.12					98.6

Table 10: Electron microprobe plagioclase analyses from NE Sumbawa. All values reported as wt.%.

SAMPLE	SiO_2	TiO_2	ZnO	Al_2O_3	Cr_2O_3	FeO	MnO	MgO
BC14114_plag8	51.66	0.08		30.11		0.51		0.06
BC14114_plag8	46.31	0.00		33.59		0.33		0.03
BC14114_plag8	46.65	0.01		33.91		0.23		0.00
BC14114_plag8	46.69	0.03		33.83		0.38		0.02
BC14114_plag8	46.65	0.03		33.80		0.30		0.03
BC14114_plag8	48.94	0.01		31.40		0.47		0.06
BC14114_plag8	51.02	0.03		30.30		0.43		0.08
BC14/130_Plag1	49.99	0.01	0.02	29.91	0.00	0.43	0.01	0.04
BC14/130_Plag1	53.82	0.00	0.02	27.33	0.00	0.28	0.00	0.03
BC14/130_Plag1	51.97	0.02	0.00	28.10	0.00	0.29	0.00	0.01
BC14/130_Plag1	48.57	0.00	0.08	30.79	0.00	0.28	0.00	0.02
BC14/130_Plag2	45.58	0.01	0.03	32.37	0.01	0.28	0.00	0.01
BC14/130_Plag2	44.06	0.02	0.00	32.94	0.00	0.32	0.03	0.02
BC14/130_Plag2	43.79	0.01	0.06	33.45	0.01	0.46	0.04	0.01
BC14/130_Plag3	44.31	0.01	0.01	32.89	0.01	0.28	0.01	0.01
BC14/130_Plag3	44.05	0.02	0.01	33.74	0.02	0.26	0.01	0.01
BC14/130_Plag3	44.14	0.02	0.01	33.30	0.00	0.35	0.00	0.01
BC14/130_Plag3	44.51	0.02	0.00	33.16	0.02	0.35	0.01	0.00
BC14/130_Plag3	44.42	0.03	0.00	33.20	0.00	0.39	0.01	0.01
BC14/130_Plag3	44.42	0.02	0.02	33.12	0.00	0.39	0.00	0.01
BC14/130_Plag3	42.20	0.00	0.03	33.65	0.02	0.39	0.02	0.09
BC14/130_Plag3	44.01	0.01	0.00	33.07	0.02	0.29	0.04	0.01
BC14/130_Plag3	44.34	0.01	0.00	33.34	0.01	0.32	0.05	0.00
BC14/130_Plag3	44.09	0.01	0.04	33.60	0.00	0.35	0.04	0.00
BC14/130_Plag3	44.09	0.00	0.05	33.66	0.00	0.31	0.00	0.00
BC14/130_Plag3	43.89	0.00	0.04	33.75	0.00	0.31	0.04	0.02
BC14/130_Plag3	44.18	0.00	0.00	33.60	0.03	0.31	0.02	0.03
BC14/130_Plag3	45.25	0.00	0.03	32.84	0.00	0.29	0.00	0.04
BC14/130_Plag3	44.65	0.00	0.00	33.44	0.04	0.26	0.02	0.01
BC14/130_Plag4	46.65	0.02	0.00	33.53	0.00	0.78	0.06	0.10
BC14/130_Plag4	45.37	0.03	0.08	33.07	0.02	0.39	0.01	0.02
BC14/130_Plag4	44.86	0.01	0.00	33.50	0.00	0.34	0.00	0.03
BC14/130_Plag4	42.50	0.02	0.00	34.54	0.00	0.38	0.01	0.06
BC14/130_Plag4	44.09	0.00	0.01	33.51	0.00	0.31	0.00	0.00
BC14/130_Plag4	44.31	0.01	0.00	33.22	0.00	0.37	0.00	0.04
BC14/130_Plag4	44.35	0.00	0.00	33.43	0.00	0.34	0.00	0.00
BC14/130_Plag4	42.76	0.05	0.00	33.03	0.00	0.37	0.00	0.11
BC14/130_Plag4	44.00	0.01	0.00	33.44	0.04	0.39	0.02	0.04
BC14/130_Plag4	44.41	0.01	0.02	33.29	0.01	0.37	0.00	0.02
BC14/130_Plag4	43.91	0.00	0.00	33.07	0.00	0.31	0.02	0.00
BC14/130_Plag4	44.33	0.00	0.02	33.32	0.00	0.28	0.03	0.01
BC14/130_Plag4	44.16	0.01	0.00	33.14	0.03	0.34	0.01	0.01
BC14/130_Plag4	44.75	0.00	0.00	33.16	0.01	0.33	0.00	0.01
BC14/130_Plag4	44.55	0.01	0.00	33.10	0.00	0.33	0.00	0.01
BC14/130_Plag5	45.69	0.00	0.01	32.54	0.04	0.39	0.01	0.01
BC14/130_Plag5	45.70	0.01	0.02	31.84	0.00	0.35	0.00	0.03
BC14/130_Plag5	46.75	0.01	0.00	31.87	0.00	0.31	0.00	0.02
BC14/130_Plag5	48.14	0.00	0.02	30.95	0.00	0.39	0.04	0.01
BC14/130_Plag6	47.70	0.02	0.01	31.31	0.00	0.47	0.04	0.00

Table 10: Electron microprobe plagioclase analyses from NE Sumbawa. All values reported as wt.%.

SAMPLE	CaO	BaO	Na_2O	K_2O	P_2O_5	SO_3	Cl	F	TOTAL
BC14114_plag8	12.05		4.41	0.15					99.0
BC14114_plag8	16.45		1.92	0.05					98.7
BC14114_plag8	16.27		2.04	0.05					99.2
BC14114_plag8	16.12		1.97	0.04					99.1
BC14114_plag8	16.47		1.97	0.07					99.3
BC14114_plag8	14.21		3.30	0.10					98.5
BC14114_plag8	12.71		4.02	0.15					98.7
BC14/130_Plag1	13.17	0.04	4.10	0.20	0.01	0.01	0.01	0.00	98.0
BC14/130_Plag1	10.47	0.03	5.21	0.32	0.01	0.00	0.00	0.00	97.5
BC14/130_Plag1	11.58	0.07	4.93	0.26	0.01	0.01	0.00	0.00	97.2
BC14/130_Plag1	14.56	0.02	3.11	0.13	0.01	0.02	0.00	0.00	97.6
BC14/130_Plag2	16.80	0.03	1.91	0.07	0.00	0.00	0.01	0.00	97.1
BC14/130_Plag2	17.71	0.03	1.33	0.04	0.00	0.00	0.01	0.00	96.5
BC14/130_Plag2	18.11	0.06	1.05	0.05	0.00	0.00	0.01	0.00	97.1
BC14/130_Plag3	17.51	0.01	1.41	0.05	0.00	0.00	0.00	0.00	96.5
BC14/130_Plag3	18.18	0.00	1.10	0.03	0.00	0.00	0.00	0.00	97.4
BC14/130_Plag3	18.11	0.04	1.22	0.04	0.02	0.00	0.00	0.00	97.2
BC14/130_Plag3	17.81	0.00	1.40	0.03	0.01	0.00	0.00	0.00	97.3
BC14/130_Plag3	17.56	0.02	1.31	0.03	0.00	0.00	0.01	0.00	97.0
BC14/130_Plag3	17.61	0.02	1.33	0.03	0.02	0.01	0.00	0.00	97.0
BC14/130_Plag3	17.41	0.00	1.24	0.06	0.01	0.06	0.02	0.00	95.2
BC14/130_Plag3	17.83	0.03	1.24	0.04	0.00	0.00	0.00	0.00	96.6
BC14/130_Plag3	18.01	0.05	1.13	0.02	0.01	0.00	0.00	0.00	97.3
BC14/130_Plag3	18.21	0.00	1.25	0.04	0.02	0.00	0.01	0.00	97.6
BC14/130_Plag3	17.99	0.01	1.21	0.04	0.00	0.00	0.00	0.00	97.4
BC14/130_Plag3	18.11	0.04	1.20	0.04	0.00	0.00	0.00	0.00	97.4
BC14/130_Plag3	17.89	0.01	1.24	0.03	0.00	0.02	0.00	0.00	97.4
BC14/130_Plag3	17.11	0.00	1.70	0.05	0.00	0.01	0.01	0.00	97.3
BC14/130_Plag3	17.60	0.01	1.42	0.05	0.00	0.02	0.00	0.00	97.5
BC14/130_Plag4	16.20	0.05	1.67	0.07	0.01	0.00	0.00	0.00	99.1
BC14/130_Plag4	17.05	0.02	1.73	0.04	0.00	0.00	0.00	0.00	97.8
BC14/130_Plag4	17.41	0.02	1.39	0.05	0.00	0.00	0.01	0.00	97.6
BC14/130_Plag4	17.11	0.01	1.07	0.07	0.00	0.02	0.01	0.00	95.8
BC14/130_Plag4	17.89	0.03	1.11	0.03	0.00	0.00	0.00	0.00	97.0
BC14/130_Plag4	17.98	0.02	1.31	0.04	0.00	0.01	0.01	0.00	97.3
BC14/130_Plag4	17.83	0.00	1.23	0.05	0.00	0.01	0.01	0.00	97.3
BC14/130_Plag4	17.36	0.03	1.29	0.08	0.02	0.07	0.03	0.00	95.2
BC14/130_Plag4	17.64	0.02	1.22	0.04	0.00	0.00	0.00	0.00	96.9
BC14/130_Plag4	17.59	0.04	1.37	0.03	0.00	0.00	0.01	0.00	97.2
BC14/130_Plag4	17.50	0.00	1.22	0.05	0.00	0.00	0.01	0.00	96.1
BC14/130_Plag4	17.71	0.02	1.45	0.04	0.00	0.00	0.00	0.00	97.2
BC14/130_Plag4	17.67	0.00	1.20	0.05	0.00	0.00	0.00	0.00	96.6
BC14/130_Plag4	17.49	0.01	1.48	0.04	0.00	0.00	0.00	0.00	97.3
BC14/130_Plag4	17.63	0.02	1.39	0.03	0.00	0.01	0.00	0.00	97.1
BC14/130_Plag5	16.80	0.01	1.87	0.08	0.01	0.00	0.00	0.00	97.5
BC14/130_Plag5	16.56	0.00	2.05	0.07	0.03	0.00	0.00	0.00	96.7
BC14/130_Plag5	15.99	0.04	2.59	0.09	0.00	0.01	0.00	0.00	97.7
BC14/130_Plag5	14.83	0.02	3.03	0.11	0.00	0.00	0.01	0.00	97.5
BC14/130_Plag6	15.21	0.02	2.84	0.08	0.04	0.00	0.00	0.00	97.7

Table 10: Electron microprobe plagioclase analyses from NE Sumbawa. All values reported as wt.%.

SAMPLE	SiO_2	TiO_2	ZnO	Al_2O_3	Cr_2O_3	FeO	MnO	MgO
BC14/130_Plag6	45.53	0.00	0.00	31.88	0.00	0.83	0.00	0.09
BC14/130_Plag6	48.40	0.02	0.01	30.49	0.02	0.35	0.02	0.03
BC14/130_Plag6	47.06	0.00	0.08	31.57	0.03	0.44	0.02	0.01
BC14/130_Plag6	47.12	0.03	0.00	31.83	0.00	0.60	0.04	0.03
BC14/130_Plag7	46.74	0.00	0.00	31.83	0.05	0.39	0.03	0.02
BC14/130_Plag7	49.94	0.00	0.00	30.42	0.00	0.35	0.04	0.04
BC14/130_Plag7	48.56	0.00	0.04	30.48	0.01	0.40	0.00	0.04
BC14/130_Plag7	47.79	0.00	0.05	30.88	0.00	0.37	0.00	0.05
BC14/130_Plag7	45.44	0.01	0.06	32.24	0.02	0.47	0.03	0.04
BC14/130_PlagInc1	46.69	0.03	0.02	31.89	0.00	0.60	0.00	0.01
BC14/130_PlagInc1	46.16	0.03	0.00	32.28	0.00	0.59	0.00	0.02
BC14/129_Plag1	51.19	0.02	29.12	0.04	0.41	0.00	0.02	0.03
BC14/129_Plag1	48.65	0.01	30.89	0.02	0.38	0.00	0.00	0.02
BC14/129_Plag1	48.51	0.01	31.11	0.00	0.37	0.04	0.02	0.00
BC14/129_Plag1	48.92	0.01	30.60	0.00	0.35	0.01	0.00	0.00
BC14/129_Plag1	47.96	0.02	31.13	0.00	0.37	0.00	0.02	0.02
BC14/129_Plag2	43.40	0.14	35.50	0.00	0.86	0.04	0.00	0.48
BC14/129_Plag2	47.16	0.01	31.69	0.00	0.40	0.00	0.02	0.03
BC14/129_Plag2	47.86	0.02	31.46	0.01	0.34	0.00	0.02	0.02
BC14/129_Plag2	47.69	0.01	30.85	0.00	0.39	0.02	0.01	0.01
BC14/129_Plag2	48.12	0.02	30.86	0.00	0.44	0.00	0.03	0.03
BC14/129_Plag3	45.19	0.01	32.87	0.00	0.35	0.00	0.02	0.04
BC14/129_Plag3	45.39	0.00	32.69	0.00	0.37	0.00	0.00	0.00
BC14/129_Plag3	45.14	0.02	32.71	0.00	0.32	0.00	0.00	0.01
BC14/129_Plag3	45.26	0.01	32.70	0.05	0.35	0.04	0.00	0.02
BC14/129_Plag3	45.18	0.00	32.78	0.00	0.39	0.00	0.01	0.02
BC14/129_Plag4	46.42	0.00	31.54	0.00	0.40	0.00	0.00	0.02
BC14/129_Plag4	46.94	0.02	31.47	0.00	0.34	0.00	0.01	0.05
BC14/129_Plag4	46.71	0.02	31.41	0.00	0.34	0.01	0.01	0.02
BC14/129_Plag4	46.69	0.00	31.42	0.00	0.32	0.02	0.00	0.02
BC14/129_Plag4	45.66	0.01	32.03	0.00	0.43	0.00	0.00	0.01
BC14/129_Plag5	47.33	0.01	31.07	0.00	0.38	0.01	0.03	0.02
BC14/129_Plag5	50.31	0.01	28.94	0.01	0.34	0.00	0.00	0.01
BC14/129_Plag5	52.01	0.00	27.99	0.00	0.27	0.03	0.00	0.03
BC14/129_Plag5	47.06	0.00	30.85	0.00	0.33	0.02	0.01	0.04
BC14/129_Plag5	46.78	0.00	30.85	0.00	0.36	0.00	0.00	0.02
BC14/129_Plag6	45.07	0.01	33.18	0.00	0.34	0.00	0.01	0.01
BC14/129_Plag6	44.15	0.03	33.28	0.00	0.36	0.00	0.00	0.00
BC14/129_Plag6	44.33	0.00	33.22	0.01	0.38	0.02	0.02	0.02
BC14/129_Plag6	45.07	0.01	32.69	0.00	0.34	0.00	0.00	0.01
BC14/129_Plag6	47.01	0.01	31.08	0.00	0.40	0.02	0.00	0.01
BC14/129_Plag7	47.72	0.01	31.23	0.03	0.42	0.01	0.00	0.02
BC14/129_Plag7	47.84	0.01	31.30	0.00	0.43	0.00	0.00	0.02
BC14/129_Plag7	44.96	0.01	30.91	0.01	0.46	0.00	0.00	0.08

Table 10: Electron microprobe plagioclase analyses from NE Sumbawa. All values reported as wt.%.

SAMPLE	CaO	BaO	Na_2O	K_2O	P_2O_5	SO_3	Cl	F	TOTAL
BC14/130_Plag6	16.52	0.00	1.78	0.08	0.04	0.00	0.01	0.00	96.8
BC14/130_Plag6	14.46	0.03	3.35	0.13	0.01	0.01	0.01	0.00	97.3
BC14/130_Plag6	15.64	0.04	2.63	0.07	0.02	0.00	0.00	0.00	97.6
BC14/130_Plag6	15.71	0.02	2.45	0.08	0.00	0.00	0.00	0.00	97.9
BC14/130_Plag7	15.93	0.00	2.26	0.10	0.01	0.00	0.00	0.00	97.4
BC14/130_Plag7	13.48	0.01	3.89	0.18	0.00	0.02	0.01	0.06	98.4
BC14/130_Plag7	14.48	0.02	3.45	0.14	0.00	0.01	0.00	0.00	97.6
BC14/130_Plag7	14.62	0.00	3.03	0.13	0.00	0.02	0.01	0.00	97.0
BC14/130_Plag7	16.60	0.02	1.98	0.08	0.00	0.01	0.01	0.00	97.0
BC14/130_PlagInc1	15.81	0.04	2.53	0.11	0.01	0.00	0.00	0.01	97.7
BC14/130_PlagInc1	16.26	0.01	2.15	0.08	0.00	0.00	0.00	0.00	97.6
BC14/129_Plag1	12.41	0.07	4.27	0.24	0.02	0.01	0.01	0.00	97.9
BC14/129_Plag1	14.33	0.08	2.94	0.13	0.00	0.03	0.00	0.00	97.5
BC14/129_Plag1	14.53	0.06	2.90	0.13	0.00	0.00	0.01	0.00	97.7
BC14/129_Plag1	14.09	0.01	3.38	0.15	0.02	0.00	0.00	0.00	97.6
BC14/129_Plag1	14.68	0.06	3.01	0.14	0.01	0.01	0.02	0.00	97.4
BC14/129_Plag2	11.66	0.04	2.55	0.20	0.03	0.13	0.04	0.00	95.1
BC14/129_Plag2	15.34	0.07	2.61	0.09	0.03	0.03	0.00	0.00	97.5
BC14/129_Plag2	14.84	0.02	2.85	0.13	0.11	0.00	0.00	0.00	97.7
BC14/129_Plag2	14.64	0.04	2.95	0.12	0.13	0.00	0.00	0.00	96.9
BC14/129_Plag2	14.59	0.04	2.98	0.13	0.00	0.00	0.00	0.00	97.3
BC14/129_Plag3	16.12	0.04	1.85	0.09	0.00	0.01	0.00	0.04	96.6
BC14/129_Plag3	16.51	0.03	1.92	0.07	0.00	0.00	0.00	0.00	97.0
BC14/129_Plag3	16.53	0.04	1.79	0.06	0.07	0.01	0.00	0.00	96.7
BC14/129_Plag3	16.59	0.02	1.82	0.05	0.07	0.01	0.00	0.00	97.0
BC14/129_Plag3	16.59	0.07	1.78	0.05	0.00	0.02	0.00	0.00	96.9
BC14/129_Plag4	15.37	0.04	2.53	0.11	0.03	0.01	0.00	0.00	96.4
BC14/129_Plag4	14.75	0.03	2.72	0.13	0.00	0.00	0.00	0.00	96.4
BC14/129_Plag4	15.19	0.05	2.65	0.11	0.00	0.00	0.01	0.00	96.5
BC14/129_Plag4	14.99	0.03	2.65	0.12	0.00	0.00	0.00	0.00	96.3
BC14/129_Plag4	15.39	0.06	2.24	0.10	0.00	0.00	0.00	0.00	96.0
BC14/129_Plag5	14.61	0.02	2.91	0.13	0.07	0.02	0.01	0.00	96.6
BC14/129_Plag5	12.08	0.03	4.32	0.24	0.00	0.00	0.00	0.00	96.3
BC14/129_Plag5	10.90	0.09	5.06	0.33	0.01	0.01	0.00	0.00	96.7
BC14/129_Plag5	14.64	0.06	2.96	0.13	0.00	0.02	0.00	0.00	96.1
BC14/129_Plag5	14.65	0.04	2.89	0.12	0.07	0.03	0.00	0.02	95.8
BC14/129_Plag6	16.83	0.02	1.56	0.05	0.00	0.00	0.00	0.00	97.1
BC14/129_Plag6	17.21	0.03	1.39	0.05	0.01	0.00	0.00	0.00	96.5
BC14/129_Plag6	17.11	0.00	1.49	0.05	0.00	0.03	0.00	0.00	96.7
BC14/129_Plag6	16.51	0.03	1.84	0.06	0.00	0.01	0.00	0.00	96.6
BC14/129_Plag6	14.87	0.00	2.76	0.13	0.00	0.01	0.00	0.00	96.3
BC14/129_Plag7	14.76	0.02	2.91	0.12	0.00	0.00	0.01	0.00	97.3
BC14/129_Plag7	14.73	0.04	2.80	0.12	0.03	0.01	0.00	0.00	97.3
BC14/129_Plag7	14.44	0.05	2.36	0.12	0.02	0.02	0.06	0.00	93.5

Table 10: Electron microprobe plagioclase analyses from NE Sumbawa. All values reported as wt.%.

SAMPLE	BC1411 1_Oliv1	BC1411 1_Oliv1	BC1411 1_Oliv1	BC1411 1_Oliv1	BC1411 1_Oliv1	BC1411 1_Oliv1	BC1411 1_Oliv1	BC1411 1_Oliv1	BC14/13 0_Mgt1	BC14/13 0_Mgt1	BC14/13 0_Mgt1	BC14/13 0_Mgt1	BC14/13 0_Mgt1
Mineral	**Oliv**	**Oliv**	**Oliv**	**Oliv**	**Oliv**	**Oliv**	**Oliv**	**Oliv**	**Mgt**	**Mgt**	**Mgt**	**Mgt**	**Mgt**
SiO2	51.11	50.21	51.58	52.82	52.60	52.57	52.36	52.40	0.08	0.10	0.35	0.28	0.10
TiO2	0.44	0.59	0.49	0.25	0.18	0.20	0.23	0.21	6.53	6.48	6.36	6.38	6.47
ZnO									0.11	0.07	0.16	0.15	0.06
Al2O3	1.99	2.96	2.18	1.28	1.24	1.31	1.22	1.09	2.16	2.18	2.24	3.14	2.09
Cr2O3									0.00	0.04	0.04	0.00	0.05
FeO	9.36	10.25	9.27	18.96	18.13	18.61	18.85	19.03	80.75	80.78	80.45	79.81	80.79
MnO	0.54	0.49	0.49	1.01	0.99	1.00	0.90	0.95	0.78	0.71	0.72	0.74	0.76
MgO	15.21	14.27	15.15	24.16	23.94	23.82	24.02	23.81	1.59	1.50	1.43	1.65	1.54
CaO	19.41	19.63	19.60	1.38	1.37	1.39	1.43	1.46	0.01	0.01	0.03	0.02	0.01
BaO									0.00	0.00	0.04	0.00	0.00
Na2O									0.01	0.04	0.05	0.05	0.00
K2O									0.01	0.00	0.01	0.00	0.00
P2O5									0.02	0.00	0.00	0.01	0.01
SO3									0.00	0.00	0.00	0.00	0.00
Cl									0.02	0.01	0.00	0.02	0.01
F	0.00	0.00	0.00	0.00	0.03	0.06	0.01	0.02	0.29	0.34	0.28	0.25	0.28
TOTAL	98.1	98.4	98.8	99.9	98.5	98.9	99.0	99.0	92.2	92.1	92.0	92.4	92.0

Table 11: Electron microprobe magnetite and olivine analyses from NE Sumbawa. All values reported as wt.%.

SAMPLE	SiO_2	TiO_2	Al_2O_3	Cr_2O_3	FeO	MnO	MgO
BC14003_hbl1	47.05	1.38	6.99	0.00	14.88	0.59	14.28
BC14003_hbl1	46.50	1.23	7.25	0.00	14.77	0.52	14.07
BC14003_hbl1	45.08	1.57	8.45	0.00	14.92	0.53	13.43
BC14003_hbl1	45.39	1.31	8.19	0.00	14.76	0.49	13.54
BC14003_hbl2	46.38	1.55	7.57	0.00	14.43	0.54	13.67
BC14003_hbl2	45.77	1.40	7.58	0.01	15.10	0.51	13.74
BC14003_hbl2	46.35	1.36	7.64	0.00	14.73	0.48	13.95
BC14003_hbl2	46.64	1.31	7.56	0.00	14.78	0.53	14.07
BC14003_hbl2	46.77	1.59	7.84	0.00	14.07	0.50	13.79
BC14003_hbl2	46.55	1.27	7.49	0.01	14.63	0.61	13.93
BC14003_hbl2	46.64	1.30	7.20	0.00	14.85	0.50	14.01
BC14003_hbl2	46.15	1.31	7.44	0.00	14.60	0.52	13.92
BC14003_hbl3	45.83	1.37	8.19	0.00	14.97	0.62	13.43
BC14003_hbl3	46.60	1.19	7.23	0.01	14.68	0.53	14.06
BC14003_hbl3	46.46	1.30	7.35	0.02	15.10	0.51	13.76
BC14003_hbl3	46.17	1.32	7.63	0.00	14.88	0.55	13.98
BC14003_hbl3	47.44	1.03	6.60	0.00	14.60	0.67	14.20
BC14003_hbl4	47.65	1.25	6.96	0.02	13.90	0.54	14.69
BC14003_hbl4	46.40	1.27	7.47	0.00	13.99	0.55	14.23
BC14/001_Hbl	47.00	1.25	6.62	0.00	13.88	0.47	14.88
BC14/001_Hbl	45.03	1.27	8.14	0.00	16.03	0.69	13.15
BC14/001_Hbl	44.89	1.26	8.14	0.01	15.99	0.72	13.17
BC14/001_Hbl	45.19	1.24	7.82	0.01	15.63	0.69	13.26
BC14/001_Hbl	46.58	1.15	7.03	0.05	14.95	0.65	14.06
BC14/001_Hbl	46.05	1.25	7.51	0.00	15.27	0.60	13.79
BC14/001_Hbl	45.84	1.33	7.64	0.00	15.01	0.52	13.80
BC14/001_Hbl	45.04	1.06	9.38	0.00	14.22	0.56	13.63
BC14/001_Hbl	45.40	1.42	7.15	0.00	14.66	0.55	13.93
BC14/001_Hbl	45.09	1.18	7.65	0.00	14.99	0.63	13.72
BC14/001_Hbl	44.99	1.21	7.49	0.00	15.17	0.59	13.52
BC14/001_Hbl	45.44	1.11	7.18	0.00	14.89	0.55	14.24
BC14/001_Hbl	44.63	1.47	7.61	0.00	14.53	0.43	13.95
BC14/001_Hbl	44.65	1.26	7.51	0.00	14.73	0.53	14.22
BC14/001_hbl	46.19	1.29	7.89	0.00	14.81	0.56	14.37
BC14/001_hbl	46.08	1.27	7.52	0.01	14.95	0.54	14.03
BC14/001_hbl	46.20	1.29	7.47	0.00	14.79	0.48	13.93
BC14/001_hbl	46.23	1.29	7.47	0.00	14.75	0.54	13.99
BC14/001_hbl	46.59	1.26	7.15	0.02	14.70	0.60	14.24
BC14/001_hbl	46.65	1.23	7.04	0.02	14.75	0.56	14.39
BC14/001_hbl	46.97	1.15	6.78	0.00	14.43	0.56	14.49
BC14/001_hbl	45.69	1.12	7.44	0.00	14.02	0.56	14.21
BC14/001_hbl	47.35	1.16	6.66	0.01	14.29	0.55	14.61
BC14/001_hbl	47.06	1.20	6.78	0.00	14.30	0.54	14.59
BC14/001_hbl	46.47	1.26	7.02	0.03	14.60	0.50	14.15
BC14/001_hbl	46.22	1.29	7.33	0.00	14.67	0.53	14.15
BC14/001_hbl	46.76	1.30	6.84	0.02	14.30	0.48	14.58

Table 12: NW Flores amphibole analyses and thermobarometrical estimates. All analyses reported as wt.% unless otherwise stated. P-T-H_2O-fO_2 calculated using the formulations of Ridolfi et al. (2012).

SAMPLE	CaO	Na_2O	K_2O	F	Cl	Total	T (°C)
BC14003_hbl1	10.18	1.32	0.35	0.08	0.17	97.3	823
BC14003_hbl1	10.22	1.20	0.40	0.09	0.17	96.4	819
BC14003_hbl1	10.45	1.50	0.50	0.09	0.22	96.7	836
BC14003_hbl1	10.29	1.45	0.46	0.13	0.24	96.3	824
BC14003_hbl2	10.59	1.37	0.38	0.12	0.16	96.8	809
BC14003_hbl2	10.39	1.31	0.41	0.11	0.19	96.5	825
BC14003_hbl2	10.29	1.32	0.40	0.09	0.20	96.8	814
BC14003_hbl2	10.25	1.50	0.46	0.14	0.20	97.4	807
BC14003_hbl2	10.57	1.45	0.39	0.09	0.19	97.2	812
BC14003_hbl2	10.25	1.48	0.42	0.13	0.22	97.0	803
BC14003_hbl2	10.28	1.32	0.45	0.09	0.21	96.8	810
BC14003_hbl2	10.33	1.31	0.44	0.07	0.23	96.3	811
BC14003_hbl3	10.18	1.44	0.45	0.12	0.25	96.8	820
BC14003_hbl3	10.22	1.30	0.38	0.08	0.18	96.4	808
BC14003_hbl3	10.33	1.33	0.44	0.13	0.18	96.9	807
BC14003_hbl3	10.37	1.37	0.41	0.09	0.19	97.0	819
BC14003_hbl3	10.03	1.16	0.35	0.12	0.16	96.3	797
BC14003_hbl4	10.43	1.29	0.35	0.13	0.19	97.4	803
BC14003_hbl4	10.35	1.31	0.42	0.12	0.19	96.3	810
BC14/001_Hbl	10.67	1.50	0.35	0.19	0.18	97.0	822
BC14/001_Hbl	10.14	1.79	0.50	0.11	0.27	97.1	838
BC14/001_Hbl	10.15	1.53	0.50	0.14	0.25	96.8	840
BC14/001_Hbl	10.13	1.39	0.48	0.16	0.24	96.2	827
BC14/001_Hbl	10.20	1.34	0.40	0.33	0.20	97.0	818
BC14/001_Hbl	10.41	1.35	0.46	0.14	0.21	97.0	822
BC14/001_Hbl	10.55	1.38	0.48	0.19	0.24	97.0	824
BC14/001_Hbl	9.86	1.39	0.49	0.02	0.24	95.9	853
BC14/001_Hbl	10.49	1.38	0.46	0.19	0.23	95.8	838
BC14/001_Hbl	10.16	1.31	0.42	0.20	0.23	95.6	837
BC14/001_Hbl	10.22	1.32	0.41	0.20	0.22	95.4	831
BC14/001_Hbl	10.29	1.30	0.42	0.10	0.21	95.7	848
BC14/001_Hbl	10.72	1.48	0.42	0.15	0.21	95.6	859
BC14/001_Hbl	10.43	1.41	0.42	0.36	0.22	95.7	868
BC14/001_hbl	10.31	1.54	0.47	0.13	0.24	97.8	835
BC14/001_hbl	10.33	1.39	0.45	0.20	0.23	97.0	824
BC14/001_hbl	10.34	1.42	0.45	0.29	0.25	96.9	810
BC14/001_hbl	10.42	1.41	0.44	0.19	0.21	96.9	814
BC14/001_hbl	10.40	1.34	0.42	0.27	0.20	97.2	820
BC14/001_hbl	10.20	1.34	0.40	0.26	0.20	97.0	829
BC14/001_hbl	10.21	1.26	0.41	0.12	0.21	96.6	818
BC14/001_hbl	10.00	1.29	0.41	0.22	0.27	95.2	823
BC14/001_hbl	10.29	1.24	0.38	0.15	0.18	96.9	812
BC14/001_hbl	10.32	1.23	0.37	0.23	0.21	96.8	818
BC14/001_hbl	10.41	1.35	0.40	0.27	0.21	96.7	812
BC14/001_hbl	10.37	1.34	0.44	0.12	0.23	96.7	821
BC14/001_hbl	10.56	1.31	0.38	0.28	0.21	97.0	820

Table 12: NW Flores amphibole analyses and thermobarometrical estimates. All analyses reported as wt.% unless otherwise stated. P-T-H_2O-fO_2 calculated using the formulations of Ridolfi et al. (2012).

SAMPLE	error (σest)	P (MPa)	Max error	ΔNNO	error (σest)	H2Omelt (wt.%)	error *
BC14003_hbl1	22	105	12	1.85	0.4	5.02	0.4
BC14003_hbl1	22	114	13	1.77	0.4	5.03	0.4
BC14003_hbl1	22	155	17	1.36	0.4	5.31	0.4
BC14003_hbl1	22	146	16	1.50	0.4	5.38	0.4
BC14003_hbl2	22	124	14	1.42	0.4	5.36	0.4
BC14003_hbl2	22	125	14	1.66	0.4	5.27	0.4
BC14003_hbl2	22	125	14	1.62	0.4	5.13	0.4
BC14003_hbl2	22	121	13	1.66	0.4	4.86	0.4
BC14003_hbl2	22	131	14	1.39	0.4	5.51	0.4
BC14003_hbl2	22	120	13	1.62	0.4	5.03	0.4
BC14003_hbl2	22	112	12	1.71	0.4	4.86	0.4
BC14003_hbl2	22	120	13	1.65	0.4	4.99	0.4
BC14003_hbl3	22	144	16	1.45	0.4	5.49	0.4
BC14003_hbl3	22	113	12	1.74	0.4	5.02	0.4
BC14003_hbl3	22	117	13	1.61	0.4	5.02	0.4
BC14003_hbl3	22	125	14	1.69	0.4	5.17	0.4
BC14003_hbl3	22	97	11	1.82	0.4	4.79	0.4
BC14003_hbl4	22	104	11	1.84	0.4	4.87	0.4
BC14003_hbl4	22	121	13	1.72	0.4	5.02	0.4
BC14/001_Hbl	22	97	11	2.03	0.4	4.66	0.4
BC14/001_Hbl	22	144	16	1.46	0.4	5.07	0.4
BC14/001_Hbl	22	144	16	1.56	0.4	5.35	0.4
BC14/001_Hbl	22	134	15	1.58	0.4	5.29	0.4
BC14/001_Hbl	22	108	12	1.85	0.4	5.01	0.4
BC14/001_Hbl	22	122	13	1.71	0.4	5.15	0.4
BC14/001_Hbl	22	126	14	1.63	0.4	5.04	0.4
BC14/001_Hbl	22	193	21	1.57	0.4	6.07	0.4
BC14/001_Hbl	22	114	13	1.81	0.4	4.94	0.4
BC14/001_Hbl	22	129	14	1.80	0.4	5.33	0.4
BC14/001_Hbl	22	125	14	1.75	0.4	5.36	0.4
BC14/001_Hbl	22	114	13	2.12	0.4	5.17	0.4
BC14/001_Hbl	22	129	14	1.76	0.4	5.08	0.4
BC14/001_Hbl	22	125	14	2.09	0.4	5.26	0.4
BC14/001_hbl	22	130	14	1.85	0.4	5.00	0.4
BC14/001_hbl	22	122	13	1.78	0.4	5.06	0.4
BC14/001_hbl	22	121	13	1.67	0.4	4.95	0.4
BC14/001_hbl	22	121	13	1.68	0.4	5.00	0.4
BC14/001_hbl	22	111	12	1.85	0.4	4.98	0.4
BC14/001_hbl	22	107	12	1.97	0.4	4.94	0.4
BC14/001_hbl	22	101	11	1.98	0.4	4.78	0.4
BC14/001_hbl	22	122	13	1.87	0.4	4.96	0.4
BC14/001_hbl	22	98	11	1.98	0.4	4.77	0.4
BC14/001_hbl	22	101	11	1.99	0.4	4.89	0.4
BC14/001_hbl	22	108	12	1.82	0.4	4.96	0.4
BC14/001_hbl	22	116	13	1.81	0.4	4.99	0.4
BC14/001_hbl	22	103	11	1.99	0.4	4.95	0.4

Table 12: NW Flores amphibole analyses and thermobarometrical estimates. All analyses reported as wt.% unless otherwise stated. P-T-H_2O-fO_2 calculated using the formulations of Ridolfi et al. (2012).

SAMPLE	SiO_2	TiO_2	ZnO	Al_2O_3	Cr_2O_3	FeO	MnO	MgO
BC14/001_PlagR	54.64	0.02	27.20	0.00	0.27	0.01	0.01	0.04
BC14/001_PlagR	56.00	0.01	25.84	0.01	0.57	0.07	0.04	0.29
BC14/001_PlagR	56.90	0.01	26.00	0.00	0.21	0.00	0.01	0.00
BC14/001_PlagR	54.04	0.01	27.59	0.01	0.22	0.00	0.03	0.02
BC14/001_PlagR	56.00	0.00	26.52	0.02	0.19	0.00	0.03	0.01
BC14/001_PlagR	56.55	0.00	25.97	0.01	0.25	0.00	0.03	0.01
BC14/001_PlagR	58.24	0.00	25.06	0.04	0.29	0.00	0.00	0.12
BC14/001_PlagR	55.60	0.01	26.63	0.02	0.23	0.00	0.00	0.01
BC14/001_PlagR	54.03	0.01	27.73	0.03	0.24	0.01	0.02	0.02
BC14/001_PlagR	58.41	0.01	25.00	0.01	0.21	0.00	0.04	0.01
BC14/001_PlagR	57.03	0.02	26.05	0.03	0.25	0.00	0.03	0.01
BC14/001_PlagR	58.23	0.00	25.08	0.00	0.18	0.03	0.02	0.02
BC14/001_PlagR	57.73	0.02	25.48	0.00	0.20	0.00	0.00	0.00
BC14/001_PlagR	57.09	0.01	25.53	0.00	0.25	0.00	0.02	0.01
BC14/001_PlagR	56.20	0.00	26.41	0.03	0.27	0.02	0.01	0.06
BC14/001_PlagR	57.63	0.02	25.07	0.01	0.23	0.00	0.00	0.03
BC14/001_PlagR	58.09	0.02	25.17	0.00	0.20	0.01	0.00	0.00
BC14/001_PlagR	58.22	0.02	24.83	0.00	0.16	0.00	0.00	0.02
BC14/001_PlagR	56.97	0.02	25.54	0.01	0.19	0.03	0.00	0.02
BC14/001_PlagR	57.19	0.00	25.60	0.00	0.19	0.00	0.00	0.01
BC14/001_PlagR	51.68	0.00	29.22	0.04	0.43	0.00	0.01	0.03
BC14/001_PlagR	65.99	0.00	21.37	0.00	0.04	0.00	0.01	0.01
BC14/001_PlagR	67.75	0.01	20.14	0.00	0.06	0.01	0.04	0.00
BC14/001_PlagR	68.28	0.00	20.19	0.00	0.02	0.00	0.02	0.00
BC14/001_PlagR	66.88	0.00	20.17	0.00	0.10	0.02	0.02	0.08
BC14003_Plag1	56.27	0.03	27.16		0.31		0.00	
BC14003_Plag1	56.30	0.01	27.01		0.33		0.00	
BC14003_Plag1	57.64	0.03	25.97		0.39		0.00	
BC14003_Plag1	56.35	0.00	26.91		0.35		0.02	
BC14003_Plag1	55.97	0.01	27.41		0.30		0.00	
BC14003_Plag1	56.19	0.01	27.33		0.34		0.01	
BC14003_Plag1	56.01	0.02	27.56		0.30		0.04	
BC14003_Plag1	54.98	0.02	28.40		0.28		0.01	
BC14003_Plag1	54.90	0.02	28.35		0.26		0.03	
BC14003_Plag1	55.04	0.01	28.02		0.31		0.02	
BC14003_Plag1	54.85	0.04	27.98		0.25		0.04	
BC14003_Plag1	55.12	0.03	27.84		0.29		0.01	
BC14003_Plag1	54.68	0.02	27.84		0.26		0.06	
BC14003_Plag1	54.84	0.01	28.17		0.25		0.04	
BC14003_Plag1	55.50	0.01	27.57		0.28		0.02	
BC14003_Plag1	56.10	0.00	27.27		0.33		0.00	
BC14003_Plag1	57.02	0.00	26.83		0.34		0.02	
BC14003_Plag1	57.12	0.03	26.76		0.38		0.01	
BC14003_Plag1	58.70	0.01	25.79		0.43		0.02	
BC14003_Plag1	55.97	0.02	26.90		0.31		0.04	
BC14003_Plag2	56.13	0.03	27.45		0.44		0.05	
BC14003_Plag2	56.74	0.02	26.71		0.34		0.01	
BC14003_Plag2	57.02	0.01	26.91		0.35		0.05	
BC14003_Plag2	56.59	0.03	27.60		0.36		0.03	

Table 13: Electron microprobe plagioclase analyses from NW Flores. All values reported as wt.%.

SAMPLE	CaO	BaO	Na_2O	K_2O	P_2O_5	SO_3	Cl	F	TOTAL
BC14/001_PlagR	10.24	0.02	5.65	0.30	0.06	0.00	0.00	0.00	98.4
BC14/001_PlagR	8.78	0.00	6.05	0.42	0.00	0.00	0.00	0.00	98.1
BC14/001_PlagR	8.69	0.03	6.42	0.37	0.00	0.00	0.00	0.00	98.7
BC14/001_PlagR	10.48	0.02	5.41	0.27	0.09	0.00	0.01	0.00	98.2
BC14/001_PlagR	9.16	0.00	6.15	0.34	0.08	0.00	0.00	0.00	98.5
BC14/001_PlagR	8.77	0.00	6.21	0.33	0.00	0.00	0.01	0.00	98.1
BC14/001_PlagR	7.72	0.02	6.92	0.39	0.00	0.00	0.00	0.00	98.8
BC14/001_PlagR	9.51	0.01	6.03	0.33	0.01	0.00	0.00	0.00	98.4
BC14/001_PlagR	10.87	0.00	5.16	0.25	0.08	0.01	0.00	0.00	98.5
BC14/001_PlagR	7.65	0.00	6.91	0.46	0.00	0.00	0.00	0.00	98.7
BC14/001_PlagR	8.70	0.04	6.65	0.37	0.00	0.01	0.01	0.00	99.2
BC14/001_PlagR	7.66	0.04	7.10	0.47	0.14	0.01	0.01	0.00	99.0
BC14/001_PlagR	8.12	0.02	6.78	0.43	0.00	0.01	0.00	0.00	98.8
BC14/001_PlagR	8.33	0.00	6.63	0.41	0.00	0.01	0.01	0.00	98.3
BC14/001_PlagR	8.89	0.00	6.38	0.34	0.00	0.00	0.00	0.00	98.6
BC14/001_PlagR	7.70	0.00	6.98	0.63	0.00	0.00	0.00	0.00	98.3
BC14/001_PlagR	7.59	0.02	7.13	0.47	0.02	0.00	0.00	0.00	98.7
BC14/001_PlagR	7.51	0.00	7.09	0.49	0.10	0.00	0.00	0.00	98.4
BC14/001_PlagR	8.15	0.00	6.87	0.43	0.02	0.00	0.01	0.00	98.3
BC14/001_PlagR	7.98	0.03	6.90	0.42	0.00	0.00	0.00	0.00	98.3
BC14/001_PlagR	12.65	0.02	4.34	0.18	0.02	0.00	0.00	0.00	98.6
BC14/001_PlagR	0.99	0.00	11.33	0.07	0.00	0.02	0.01	0.00	99.9
BC14/001_PlagR	0.51	0.05	11.92	0.09	0.00	0.00	0.00	0.00	100.6
BC14/001_PlagR	0.31	0.00	12.06	0.05	0.03	0.00	0.00	0.00	101.0
BC14/001_PlagR	0.57	0.00	11.64	0.09	0.00	0.01	0.01	0.00	99.6
BC14003_Plag1	9.06		6.21	0.27					99.3
BC14003_Plag1	8.84		6.34	0.21					99.0
BC14003_Plag1	7.80		6.73	0.15					98.7
BC14003_Plag1	8.85		6.41	0.14					99.0
BC14003_Plag1	9.38		6.20	0.24					99.5
BC14003_Plag1	8.96		6.26	0.18					99.3
BC14003_Plag1	9.56		6.02	0.09					99.6
BC14003_Plag1	9.94		5.64	0.16					99.4
BC14003_Plag1	9.85		5.83	0.18					99.4
BC14003_Plag1	9.51		5.78	0.12					98.8
BC14003_Plag1	9.83		5.93	0.22					99.1
BC14003_Plag1	9.70		5.91	0.18					99.1
BC14003_Plag1	9.96		5.68	0.20					98.7
BC14003_Plag1	10.19		5.59	0.13					99.2
BC14003_Plag1	9.34		6.10	0.25					99.1
BC14003_Plag1	9.08		5.99	0.17					98.9
BC14003_Plag1	8.49		6.63	0.22					99.5
BC14003_Plag1	8.43		6.61	0.19					99.5
BC14003_Plag1	7.33		7.16	0.19					99.6
BC14003_Plag1	8.99		6.12	0.24					98.6
BC14003_Plag2	9.07		6.22	0.25					99.6
BC14003_Plag2	8.57		6.37	0.16					98.9
BC14003_Plag2	8.48		6.47	0.18					99.5
BC14003_Plag2	9.28		6.18	0.18					100.3

Table 13: Electron microprobe plagioclase analyses from NW Flores. All values reported as wt.%.

SAMPLE	SiO_2	TiO_2	ZnO	Al_2O_3	Cr_2O_3	FeO	MnO	MgO
BC14003_Plag2	56.81	0.04	27.16		0.33		0.03	
BC14003_Plag2	56.77	0.03	27.26		0.33		0.04	
BC14003_Plag2	56.95	0.18	26.48		0.31		0.01	
BC14003_Plag2	55.60	0.01	27.76		0.31		0.00	
BC14003_Plag2	56.59	0.02	26.85		0.31		0.03	
BC14003_Plag2	56.02	0.01	27.35		0.43		0.01	
BC14003_Plag3	56.41	0.01	27.17		0.34		0.00	
BC14003_Plag3	56.46	0.01	26.96		0.34		0.00	
BC14003_Plag3	57.57	0.02	26.28		0.40		0.00	
BC14003_Plag3	57.96	0.02	26.24		0.38		0.02	
BC14003_Plag3	56.99	0.01	26.78		0.34		0.04	
BC14003_Plag3	56.61	0.00	27.15		0.34		0.00	
BC14003_Plag3	56.84	0.02	26.97		0.32		0.02	
BC14003_Plag3	61.62	0.03	25.38		0.23		0.02	
BC14003_Plag3	56.73	0.01	27.02		0.32		0.03	
BC14003_Plag4	56.23	0.01	27.34		0.30		0.02	
BC14003_Plag4	53.28	0.01	29.57		0.20		0.00	
BC14003_Plag4	56.55	0.01	27.03		0.36		0.01	
BC14003_Plag4	57.23	0.01	26.64		0.36		0.01	
BC14003_Plag4	57.21	0.03	26.94		0.38		0.02	
BC14003_Plag4	57.19	0.03	25.74		0.43		0.00	
BC14003_Plag4	57.98	0.02	25.75		0.44		0.04	
BC14003_Plag4	58.19	0.03	26.52		0.40		0.02	
BC14003_Plag4	58.52	0.03	25.71		0.46		0.00	
BC14003_Plag4	59.16	0.02	25.43		0.46		0.00	
BC14003_Plag4	58.76	0.01	25.54		0.49		0.01	
BC14003_Plag4	58.44	0.00	25.53		0.44		0.00	
BC14003_Plag4	58.35	0.03	25.46		0.47		0.00	
BC14003_Plag4	56.74	0.01	26.59		0.37		0.02	
BC14003_Plag4	56.61	0.01	26.71		0.36		0.02	
BC14003_Plag4	56.80	0.01	26.58		0.35		0.00	
BC14003_Plag4	56.46	0.00	27.11		0.32		0.03	
BC14003_Plag4	56.28	0.02	27.46		0.30		0.05	
BC14003_Plag6	56.34	0.01	26.97		0.34		0.04	
BC14003_Plag6	57.20	0.01	26.35		0.38		0.02	
BC14003_Plag6	57.24	0.02	25.94		0.40		0.02	
BC14003_Plag6	57.41	0.01	26.13		0.37		0.03	
BC14003_Plag6	57.70	0.01	26.19		0.39		0.02	
BC14003_Plag6	56.34	0.02	27.16		0.36		0.01	
BC14003_Plag6	57.25	0.01	26.21		0.40		0.04	
BC14003_Plag6	56.60	0.02	26.70		0.34		0.00	
BC14003_Plag6	56.36	0.02	27.15		0.33		0.00	
BC14003_Plag6	56.06	0.00	27.33		0.29		0.01	
BC14003_plag7	54.16	0.01	28.46		0.25		0.03	
BC14003_plag7	56.30	0.00	26.72		0.36		0.01	
BC14003_plag7	55.34	0.02	27.81		0.29		0.02	
BC14003_plag7	56.14	0.02	27.30		0.32		0.02	
BC14003_plag7	56.48	0.01	27.45		0.33		0.01	
BC14003_plag7	56.04	0.01	27.60		0.30		0.03	

Table 13: Electron microprobe plagioclase analyses from NW Flores. All values reported as wt.%.

SAMPLE	CaO	BaO	Na_2O	K_2O	P_2O_5	SO_3	Cl	F	TOTAL
BC14003_Plag2	8.72		6.43	0.15					99.7
BC14003_Plag2	8.79		6.49	0.22					99.9
BC14003_Plag2	7.87		6.95	0.25					99.0
BC14003_Plag2	8.98		6.14	0.16					99.0
BC14003_Plag2	8.59		6.54	0.14					99.1
BC14003_Plag2	9.22		6.16	0.17					99.4
BC14003_Plag3	8.78		6.27	0.21					99.2
BC14003_Plag3	8.77		6.37	0.14					99.1
BC14003_Plag3	7.97		6.69	0.16					99.1
BC14003_Plag3	7.90		6.90	0.15					99.6
BC14003_Plag3	8.56		6.30	0.12					99.1
BC14003_Plag3	8.77		6.38	0.30					99.5
BC14003_Plag3	8.73		6.41	0.19					99.5
BC14003_Plag3	5.72		8.85	0.15					102.0
BC14003_Plag3	8.84		6.20	0.26					99.4
BC14003_Plag4	9.10		6.22	0.26					99.5
BC14003_Plag4	11.30		5.00	0.28					99.6
BC14003_Plag4	8.62		6.50	0.14					99.2
BC14003_Plag4	8.52		6.59	0.22					99.6
BC14003_Plag4	8.45		6.48	0.17					99.7
BC14003_Plag4	7.81		6.64	0.29					98.1
BC14003_Plag4	7.65		6.96	0.17					99.0
BC14003_Plag4	7.87		7.14	0.11					100.3
BC14003_Plag4	7.38		7.20	0.23					99.5
BC14003_Plag4	7.17		7.38	0.17					99.8
BC14003_Plag4	6.98		7.34	0.18					99.3
BC14003_Plag4	7.32		6.99	0.10					98.8
BC14003_Plag4	7.15		7.15	0.19					98.8
BC14003_Plag4	8.49		6.48	0.15					98.9
BC14003_Plag4	8.43		6.64	0.19					99.0
BC14003_Plag4	8.50		6.48	0.22					99.0
BC14003_Plag4	8.80		6.31	0.17					99.2
BC14003_Plag4	9.33		6.06	0.16					99.7
BC14003_Plag6	8.78		6.30	0.18					98.9
BC14003_Plag6	8.08		6.81	0.18					99.0
BC14003_Plag6	7.52		6.99	0.20					98.3
BC14003_Plag6	8.02		6.76	0.15					98.9
BC14003_Plag6	7.96		6.63	0.16					99.1
BC14003_Plag6	8.79		6.52	0.31					99.5
BC14003_Plag6	8.13		6.57	0.16					98.8
BC14003_Plag6	8.60		6.55	0.16					99.0
BC14003_Plag6	9.05		6.23	0.22					99.4
BC14003_Plag6	9.09		6.22	0.23					99.2
BC14003_plag7	10.42		5.51	0.37					99.2
BC14003_plag7	8.58		6.50	0.24					98.7
BC14003_plag7	9.57		6.08	0.25					99.4
BC14003_plag7	9.00		6.19	0.26					99.2
BC14003_plag7	9.08		6.20	0.15					99.7
BC14003_plag7	9.24		6.18	0.22					99.6

Table 13: Electron microprobe plagioclase analyses from NW Flores. All values reported as wt.%.

SAMPLE	SiO_2	TiO_2	ZnO	Al_2O_3	Cr_2O_3	FeO	MnO	MgO
BC14003_plag7	56.16	0.01	27.09		0.33		0.06	
BC14003_plag7	56.15	0.01	27.12		0.30		0.00	
BC14003_plag7	55.29	0.02	27.54		0.33		0.01	
BC14003_plag7	55.77	0.01	27.95		0.29		0.00	
BC14003_plag7	56.37	0.02	27.27		0.33		0.00	
BC14003_plag7	56.34	0.01	26.93		0.33		0.06	
BC14003_plag7	55.13	0.04	27.59		0.30		0.01	
BC14003_plag8	56.24	0.02	26.94		0.33		0.03	
BC14003_plag8	56.86	0.01	27.07		0.38		0.03	
BC14003_plag8	56.52	0.00	26.79		0.36		0.00	
BC14003_plag8	56.26	0.17	28.43		0.40		0.00	
BC14003_plag8	56.65	0.01	26.55		0.40		0.00	
BC14003_plag8	56.65	0.21	26.36		0.50		0.02	
BC14003_plag8	57.78	0.02	25.82		0.44		0.00	
BC14003_plag8	56.26	0.01	27.05		0.34		0.03	
BC14003_plag8	55.08	0.02	27.81		0.35		0.01	
BC14003_plag8	56.69	0.01	26.87		0.36		0.04	
BC14003_plag8	56.77	0.02	26.59		0.39		0.04	
BC14003_plag8	59.10	0.01	25.54		0.50		0.03	
BC14003_plag8	58.15	0.02	26.08		0.45		0.03	
BC14003_plag8	58.00	0.01	26.67		0.40		0.00	
BC14003_plag8	56.19	0.01	27.03		0.33		0.00	

Table 13: Electron microprobe plagioclase analyses from NW Flores. All values reported as wt.%.

SAMPLE	CaO	BaO	Na_2O	K_2O	P_2O_5	SO_3	Cl	F	TOTAL
BC14003_plag7	9.10		6.10	0.07					98.9
BC14003_plag7	9.03		6.17	0.19					99.0
BC14003_plag7	9.25		5.98	0.71					99.1
BC14003_plag7	9.74		5.78	0.11					99.7
BC14003_plag7	9.04		6.11	0.15					99.3
BC14003_plag7	8.80		6.40	0.27					99.1
BC14003_plag7	9.61		5.95	0.41					99.0
BC14003_plag8	8.91		6.23	0.21					98.9
BC14003_plag8	8.68		6.44	0.26					99.7
BC14003_plag8	8.70		6.44	0.13					98.9
BC14003_plag8	8.18		6.36	0.38					100.2
BC14003_plag8	8.61		6.42	0.22					98.9
BC14003_plag8	7.79		6.47	0.28					98.3
BC14003_plag8	7.86		6.79	0.18					98.9
BC14003_plag8	8.87		6.34	0.27					99.1
BC14003_plag8	9.60		5.95	0.21					99.0
BC14003_plag8	8.66		6.62	0.14					99.4
BC14003_plag8	8.64		6.38	0.23					99.1
BC14003_plag8	7.21		7.34	0.09					99.8
BC14003_plag8	7.77		7.01	0.17					99.7
BC14003_plag8	8.10		6.90	0.10					100.2
BC14003_plag8	8.78		6.18	0.24					98.8

Table 13: Electron microprobe plagioclase analyses from NW Flores. All values reported as wt.%.

SAMPLE	BC14003_mgt1	BC14003_mgt1	BC14003_mgt1	BC14003_mgt1	BC14003_mgt1	BC14003_mgt1	BC14003_mgt2	BC14003_mgt2	BC14003_mgt2	BC14003_mgt2	BC14003_mgt2	BC14003_mgt2	BC14003_mgt2
TiO_2	8.05	7.53	7.31	7.25	7.37	7.81	7.28	6.78	8.02	7.66	7.52	7.56	7.02
ZnO	0.11	0.06	0.06	0.00	0.05	0.08	0.05	0.08	0.10	0.08	0.04	0.12	0.04
Al_2O_3	1.66	1.82	1.86	1.80	1.90	1.44	1.88	3.45	1.67	1.84	1.75	1.78	1.80
Cr_2O_3	0.00	0.01	0.01	0.03	0.01	0.03	0.00	0.00	0.00	0.00	0.02	0.00	0.00
FeO	76.70	77.84	79.75	78.59	79.11	77.45	77.91	76.57	77.72	78.00	77.58	78.09	78.23
MnO	2.07	1.77	1.72	1.65	1.75	1.87	1.94	1.54	2.59	1.90	1.91	1.97	1.78
MgO	0.03	0.03	0.02	0.05	0.04	0.03	0.04	0.06	0.00	0.01	0.01	0.04	0.05
BaO	0.10	0.09	0.12	0.11	0.08	0.11	0.10	0.10	0.07	0.11	0.14	0.11	0.10
P_2O_5	0.01	0.00	0.01	0.00	0.00	0.00	0.01	0.01	0.01	0.00	0.00	0.00	0.01
SO_3	0.03	0.01	0.01	0.00	0.00	0.00	0.02	0.01	0.04	0.00	0.01	0.00	0.01
Cl	0.00	0.00	0.00	0.00	0.00	0.00	0.00	0.01	0.01	0.00	0.00	0.00	0.01
F	0.23	0.24	0.20	0.30	0.29	0.22	0.22	0.26	0.22	0.27	0.22	0.19	0.26
V_2O_3	0.44	0.47	0.35	0.33	0.40	0.44	0.42	0.39	0.43	0.39	0.36	0.33	0.45
ZrO_2	0.05	0.00	0.00	0.01	0.01	0.00	0.00	0.00	0.03	0.00	0.00	0.00	0.04
TOTAL	89.4	89.8	91.3	90.0	90.9	89.4	89.8	89.2	90.8	90.2	89.5	90.1	89.7

Table 13: Electron microprobe magnetite analyses from NW Flores. All values reported as wt.%

Appendix 4

Appendix 4 as an accompaniment to chapter 6

Contains details of partial melting models

Finero (9406)				Conc.	Degree of melting (F)							
Mineral	**Wt%**	**% Melt**		**(ppm)**	**0.001**	**0.0025**	**0.01**	**0.025**	**0.05**	**0.1**	**0.2**	**0.25**
Ol	0.55	0.1	Sm	1.56	99.17108	92.05723	67.75562	44.34363	28.13873	16.25691	8.813639	7.17182
Cpx	0.05	0.7	Yb	0.81	18.04359	17.63622	15.8473	13.17459	10.28389	7.147395	4.439426	3.732375
Opx	0.25	0.14	La	6.63	1458.186	1106.962	502.1791	239.9683	128.3086	66.45977	33.83789	27.16974
Phlogopite	0.01	0	Sm/Yb	1.925926	5.496194	5.219781	4.27553	3.365846	2.736196	2.274522	1.98531	1.921517
Amph	0.11	0.04	La/Sm	4.25	14.70374	12.02472	7.411623	5.411562	4.559857	4.088094	3.839264	3.788402
Spinel	0.03	0.02										

Table 1: Partial melting model constraints for Finero phlogopite-peridotite (sample 9406, Zanetti et al. 1999).

PNG (61-1h)				Conc.	Degree of melting (F)							
Mineral	**Wt%**	**% Melt**		**(ppm)**	**0.001**	**0.0025**	**0.01**	**0.025**	**0.05**	**0.1**	**0.2**	**0.25**
Ol	0.105	0.104167	Sm	0.005	0.265965	0.24996	0.192146	0.131374	0.086027	0.050893	0.028012	0.022871
Cpx	0.055	0.729167	Yb	0.0195	0.335061	0.329303	0.303246	0.261814	0.213253	0.15555	0.10093	0.085856
Opx	0.825	0.145833	La	0.032	4.916533	4.025724	2.112208	1.082826	0.597504	0.315073	0.161961	0.1303
Spinel	0.025	0.020833	Sm/Yb	0.25641	0.793781	0.759057	0.633629	0.501784	0.403402	0.327178	0.277538	0.266385
			La/Sm	6.4	18.48566	16.1055	10.99274	8.242318	6.945579	6.190946	5.781842	5.697249

Table 2: Partial melting model constraints for Papua New Guinea orthopyroxenite (sample 61-1h, McInnes et al. 2001).

Japan (RT1)				Conc.	Degree of melting (F)							
Mineral	**Wt%**	**% Melt**		**(ppm)**	**0.001**	**0.0025**	**0.01**	**0.025**	**0.05**	**0.1**	**0.2**	**0.25**
Ol	0.623053	0.15	Sm	0.03	18.41585	9.591654	2.824551	1.171507	0.593048	0.298382	0.14966	0.119803
Opx	0.018692	0.2	Yb	0.106	6.365467	5.844873	4.148476	2.624831	1.628175	0.925412	0.496665	0.403251
Chlorite	0.124611	0.1	La	0.19	160.7575	70.87094	18.67128	7.549778	3.78863	1.897769	0.94975	0.759939
Amph	0.17134	0.5	Sm/Yb	0.283019	2.893087	1.641037	0.680865	0.446317	0.364241	0.322431	0.301329	0.297093
Spinel	0.062305	0.05	La/Sm	6.333333	8.729301	7.388813	6.610354	6.444498	6.388408	6.360209	6.346071	6.34324

Table 3: Partial melting model constraints for Japan amphibole-peridotite (sample RT1, Khedr & Arai 2009).

Kamchatka (629)				Conc.	Degree of melting (F)							
Mineral	**Wt%**	**% Melt**		**(ppm)**	**0.001**	**0.0025**	**0.01**	**0.025**	**0.05**	**0.1**	**0.2**	**0.25**
Ol	0.766	0.766	Sm	0.073	27.13444	17.43171	6.252634	2.739243	1.414526	0.71905	0.362546	0.290525
Cpx	0.001	0.001	Yb	0.077	2.819308	2.676199	2.134465	1.519351	1.026378	0.622453	0.348305	0.285446
Opx	0.198	0.198	La	0.107	58.78543	32.23914	9.895688	4.14721	2.107131	1.062152	0.533249	0.426948
Amph	0.024	0.024	Sm/Yb	0.948052	9.624502	6.513609	2.929369	1.802904	1.378173	1.155189	1.040886	1.017795
Spinel	0.01	0.01	La/Sm	1.465753	2.166451	1.849453	1.582643	1.513999	1.489638	1.477159	1.470843	1.469574

Table 4: Partial melting model constraints for Kamchatka orthopyroxene-amphibole-peridotite (sample 629, Ishimaru et al. 2006).

Sunda main				Conc.	Degree of melting (F)								
Mineral	**Wt%**	**% Melt**		**(ppm)**	**0.0001**	**0.001**	**0.0025**	**0.01**	**0.025**	**0.05**	**0.1**	**0.2**	**0.25**
Ol	0.56	0.12	Sm	0.393	17.30545	16.76332	15.9315	12.76453	9.133354	6.195787	3.770421	2.114759	1.734035
Cpx	0.07	0.7	Yb	0.426	11.60775	11.38545	11.03329	9.55549	7.536588	5.573837	3.664926	2.17509	1.80767
Opx	0.32	0.15	La	0.893	170.4148	146.2603	118.3114	60.50332	30.60022	16.7789	8.815469	4.522563	3.637
Spinel	0.05	0.03	Sm/Yb	0.922535	1.490853	1.472346	1.443948	1.335832	1.211869	1.111584	1.028785	0.972263	0.959265
			La/Sm	2.272265	9.847462	8.725021	7.426254	4.739957	3.350381	2.708115	2.33806	2.138572	2.09742

Table 5: Partial melting model constraints for main Sunda Arc front volcano trend.

Sunda Ultra-K				Conc.	Degree of melting (F)								
Mineral	**Wt%**	**% Melt**		**(ppm)**	**0.0001**	**0.001**	**0.0025**	**0.01**	**0.025**	**0.05**	**0.1**	**0.2**	**0.25**
Ol	0.5	0.1	Sm	0.44348	7.407494	7.31936	7.17704	6.541103	5.556426	4.44196	3.170237	2.015926	1.705443
Cpx	0.03	0.65	Yb	0.44872	0.789706	0.789315	0.788663	0.785422	0.779018	0.768573	0.748503	0.711351	0.694124
Opx	0.26	0.15	La	1.22768	115.3866	106.7029	94.81082	60.88345	35.48636	20.93297	11.50021	6.048814	4.889855
Garnet	0.075	0.06	Sm/Yb	0.988322	9.380063	9.273056	9.10026	8.328143	7.132606	5.779488	4.235437	2.833942	2.456971
Phlogopite	0.03	0.01	La/Sm	2.768287	15.57701	14.57817	13.2103	9.307825	6.386545	4.712552	3.627557	3.000513	2.867205
Amph	0.105	0.03											

Table 5: Partial melting model constraints for Sunda Arc rear-arc ultrapotassic volcano trend.